

Springer Series in  
**GEOMECHANICS & GEOENGINEERING**

Qiang Yang  
Jian-Min Zhang  
Hong Zheng  
Yangping Yao (Eds.)

# Constitutive Modeling of Geomaterials

Advances and New Applications

 Springer

# Springer Series in Geomechanics and Geoengineering

---

## Editors

Prof. Wei Wu  
Institut für Geotechnik  
Universität für Bodenkultur  
Feistmantelstraße 4  
1180 Vienna  
Austria  
E-mail: wei.wu@boku.ac.at

Prof. Ronaldo I. Borja  
Department of Civil and Environmental  
Engineering  
Stanford University  
Stanford, CA 94305-4020  
USA  
E-mail: borja@stanford.edu

For further volumes:  
<http://www.springer.com/series/8069>

Qiang Yang, Jian-Min Zhang, Hong Zheng,  
and Yangping Yao (Eds.)

---

# Constitutive Modeling of Geomaterials

Advances and New Applications

 Springer

*Editors*

Qiang Yang  
State Key Laboratory of Hydroscience  
and Engineering  
Tsinghua University  
Beijing  
China

Hong Zheng  
Chinese Academy of Sciences  
Institute of Rock and Soil Mechanics  
Wuhan  
China

Jian-Min Zhang  
State Key Laboratory of Hydroscience  
and Engineering  
Tsinghua University  
Beijing  
China

Yangping Yao  
Department of Civil Engineering  
School of Transportation Science  
and Technology  
Beihang University  
Beijing  
China

ISSN 1866-8755

e-ISSN 1866-8763

ISBN 978-3-642-32813-8

e-ISBN 978-3-642-32814-5

DOI 10.1007/978-3-642-32814-5

Springer Heidelberg New York Dordrecht London

Library of Congress Control Number: 2012945326

© Springer-Verlag Berlin Heidelberg 2013

This work is subject to copyright. All rights are reserved by the Publisher, whether the whole or part of the material is concerned, specifically the rights of translation, reprinting, reuse of illustrations, recitation, broadcasting, reproduction on microfilms or in any other physical way, and transmission or information storage and retrieval, electronic adaptation, computer software, or by similar or dissimilar methodology now known or hereafter developed. Exempted from this legal reservation are brief excerpts in connection with reviews or scholarly analysis or material supplied specifically for the purpose of being entered and executed on a computer system, for exclusive use by the purchaser of the work. Duplication of this publication or parts thereof is permitted only under the provisions of the Copyright Law of the Publisher's location, in its current version, and permission for use must always be obtained from Springer. Permissions for use may be obtained through RightsLink at the Copyright Clearance Center. Violations are liable to prosecution under the respective Copyright Law.

The use of general descriptive names, registered names, trademarks, service marks, etc. in this publication does not imply, even in the absence of a specific statement, that such names are exempt from the relevant protective laws and regulations and therefore free for general use.

While the advice and information in this book are believed to be true and accurate at the date of publication, neither the authors nor the editors nor the publisher can accept any legal responsibility for any errors or omissions that may be made. The publisher makes no warranty, express or implied, with respect to the material contained herein.

Printed on acid-free paper

Springer is part of Springer Science+Business Media ([www.springer.com](http://www.springer.com))

# Contents

## Plenary Speakers

<b>Shear Strength Criteria for Rock, Rock Joints, Rockfill, Interfaces and Rock Masses</b> .....	1
Nick Barton	
<b>Revisiting the Paradigm of Critical State Soil Mechanics: Fabric Effects</b> .....	13
Yannis F. Dafalias, Xiang-song Li	
<b>Disturbed State Concept (DSC) for Constitutive Modeling of Geologic Materials and <i>Beyond</i></b> .....	27
Chandrakant S. Desai	
<b>Three-Dimensional Failure in Geomaterials: Experimentation and Modeling</b> .....	47
Poul V. Lade	
<b>FEM Implementation of Micropolar Hypoplastic Model</b> .....	59
J. Lin, W. Wu	
<b>Failure Mechanism and Control of Geotechnical Structures</b> .....	63
Q. Yang, K.D. Leng, Q. Chang, Y.R. Liu	
<b>Time-Dependent Stress-Strain Behavior of Geomaterials</b>	
<b>Back Analysis of Treporti Test Embankment with a Time Dependent Small Strain Stiffness Constitutive Model</b> .....	89
Thomas Benz, Valentina Berengo, Paolo Simonini, Martino Leoni	
<b>Rate Dependent Elastoviscoplastic Model</b> .....	97
Chandrakant S. Desai, Shantanu M. Sane	

<b>Some Strengths and Weaknesses of Overstress Based Elastic Viscoplastic Models</b> . . . . .	107
T.M. Bodas Freitas, D.M. Potts, L. Zdravkovic	
<b>Comparison of Anisotropic Rate-Dependent Models at Element Level</b> . . . . .	115
Minna Karstunen, Mohammad Rezania, Nallathamby Sivasithamparam	
<b>A Comparison of Four Elastic Visco-Plastic Models for Soft Clay</b> . . . . .	121
David Nash, Matthew Brown	
<b>A Rate-Dependent Viscous Model for Sand</b> . . . . .	125
Fang-Le Peng, P. Chattonjai, Zhen Hua, Ke Tan	
<b>A Review on Creep of Frozen Soils</b> . . . . .	129
Jilin Qi, Songhe Wang, Fan Yu	
<b>Influence of Recycled Asphalt Pavement on Creep Compliance of Hot Mix Asphalt</b> . . . . .	135
Pranshoo Solanki, David Adje, Musharraf Zaman, Zahid Hossain	
<b>Simplified Modelling of Isotache Concept for Consolidation</b> . . . . .	139
Yoichi Watabe, Serge Leroueil	
<b>Nonlinear Creep Behavior of Normally Consolidated Soft Clay</b> . . . . .	145
Ze-Xiang Wu, Yin-Fu Jin, Zhen-Yu Yin	
<b>Review of Elastic Visco-Plastic Modeling of the Time-Dependent Stress-Strain Behavior of Soils and Its Extensions and Applications</b> . . . .	149
Jian-Hua Yin	
<b>Examination on Time-Dependent Soil Models in One-Dimensional Consolidation</b> . . . . .	159
Yixing Yuan, Andrew J. Whittle	
<b>Constitutive Modeling within Critical State Soil Mechanics</b>	
<b>Criterion for Flow Liquefaction Instability</b> . . . . .	167
José E. Andrade, Alfonso M. Ramos, Arcesio Lizcano	
<b>Influence of Grain Breakage on Critical State</b> . . . . .	173
Wei Hu, Zhen-Yu Yin, Christophe Dano, Pierre-Yves Hicher	
<b>Compressible Fluid – An Alternative Concept within CSSM</b> . . . . .	179
Tomislav Ivšić, Astrid Gojmerac Ivšić	
<b>Investigation of Critical States and Failure in True Triaxial Tests of Clays</b> . . . . .	185
Victor N. Kaliakin, Andres Nieto Leal	

Contents	VII
<b>Micromechanics of the Critical State of Granular Materials</b> . . . . .	193
N.P. Kruyt	
<b>A Critical State Sand Model with Elastic-Plastic Coupling</b> . . . . .	199
Ali Lashkari, Ali Golchin	
<b>Influence of Grain Size Distribution on Critical State of Granular Materials</b> . . . . .	207
Gang Li, Carlos Ovalle, Christophe Dano, Pierre-Yves Hicher	
<b>On Simulation of Strain Localization Using Microplasticity Constitutive Models</b> . . . . .	211
Majid T. Manzari, Karma Yonten	
<b>Simulation of Isotropic Cyclic Compression by an Elasto-viscoplastic Constitutive Model Based on the Nonlinear Kinematic Hardening Rules</b> . . . . .	215
Fusao Oka, Sayuri Kimoto	
<b>Rotational Hardening and Uniqueness of Critical State Line in Clay Plasticity</b> . . . . .	223
Mahdi Taiebat, Yannis F. Dafalias	
<b>A Modified Bounding Surface Hypoplasticity Model for Sands</b> . . . . .	231
Gang Wang, Yongning Xie	
<b>Soils in Space</b> . . . . .	239
David Muir Wood	
<b>Unique Quantification of Critical State in Granular Media Considering Fabric Anisotropy</b> . . . . .	247
Jidong Zhao, Ning Guo, Xiang-song Li	
<b>Peculiarities of Limiting States in Simulated Drained and Undrained Assemblies of Elliptical Particles</b> . . . . .	253
Leo Rothenburg, Roberto Olivera-Bonilla	
<b>Multiscale and Multiphysics in Geomaterials</b>	
<b>Microstructural Modeling of Granular Materials with Inner Forces</b> . . . .	259
Pierre-Yves Hicher	
<b>Time Effects Relate to Particle Crushing in Granular Materials</b> . . . . .	265
Poul V. Lade	
<b>A Power Law for Elastic Moduli of Unsaturated Soil</b> . . . . .	271
Ning Lu	

<b>Application and Meaning of the <math>t_{ij}</math> Concept</b> . . . . .	277
Teruo Nakai	
<b>A Simplified Model for Clayey Rocks Having a Plastic Porous Matrix</b> . . .	283
Wanqing Shen, Jianfu Shao, Djimédo Kondo	
<b>Anisotropic Porochemoelectroelastic Solution for Inclined Wellbores with Applications to Operations in Unconventional Shale Plays</b> . . . . .	289
Minh H. Tran, Younane N. Abousleiman	
<b>Modeling Ground-Shell Contact Forces in NATM Tunneling, Based on 3D Displacement Measurements</b> . . . . .	293
Shafi Ullah, Bernhard Pichler, Christian Hellmich	
<b>Discrete Modeling of Fluid-Particle Interaction in Soils</b> . . . . .	297
Jidong Zhao, Tong Shan	
<b>Damage to Failure in Rock Structures</b>	
<b>Realistic Simulation of Progressive Brittle Rock Failure near Excavation Boundary</b> . . . . .	303
M. Cai	
<b>Excavation Damaged Zone Modelling in Claystone with Coupled Second Gradient Model</b> . . . . .	313
Frédéric Collin, Benoît Pardoën	
<b>On the Modeling of Transition from a Diffuse to a Localized Damage</b> . . .	319
Dashnor Hoxha, Amine Sbitti, Senjen Wu, Naima Belayachi, Duc-Phi Do	
<b>A Micromechanical Model for Time Dependent Behavior Related to Subcritical Damage in Quasi Brittle Rocks</b> . . . . .	323
Yaoying Huang, J.F. Shao	
<b>Study on Equivalent Rheological Damage Model for Jointed Mass</b> . . . . .	327
Yaoying Huang, Hong Zheng	
<b>On the Solubilities of Anhydrite and Gypsum</b> . . . . .	333
Serafeimidis Konstantinos, Anagnostou Georg	
<b>Binary Medium Model for Rock Sample</b> . . . . .	341
Enlong Liu, Jianhai Zhang	
<b>Study of Rock Bending Failure Mechanism Based on a Proposed Damage Model</b> . . . . .	349
Hamed Molladavoodi, Ali Mortazavi	
<b>To Which Extend the Failure Mode Originates from Microstructure?</b> . . .	359
François Nicot, Nejib Hadda, Franck Bourrier, Luc Sibille, Félix Darve	

<b>Excavation Damage Zone at High Depths: Field Cases and Coupled Analysis</b> .....	363
Jean Vaunat, Antonio Gens, Benoit Garitte	
<b>A Mohr-Coulomb Failure Criterion for Rocks Subjected to Dynamic Loading</b> .....	367
Kaiwen Xia	
<b>An Elasto-plastic Model and Its Return Mapping Scheme for Anisotropic Rocks</b> .....	371
Wei-ya Xu, Jiu-chang Zhang, Ru-bin Wang, Jin-jian Gu	
<b>Micro-Gas Hypothesis for Behaviors of Rocks under Loading</b> .....	381
Zhong Qi Yue (Quentin)	
<b>Micromechanical Poroplasticity Damage Formulations for Saturated Microcracked Rocks</b> .....	387
Qi-zhi Zhu, Ni Xie, Jian-fu Shao	
<b>Behaviour of Geomaterials</b>	
<b>Achieving High Range Elastic Properties of Soil Mass for More Stable and Durable Geostructure</b> .....	391
Gokul K. Bayan	
<b>Effect of Air Entrapment on Unsaturated Flow in Porous Media</b> .....	399
Pan Chen, Changfu Wei, Jili Wang, Houzhen Wei, Tiantian Ma	
<b>On the Mechanical Behaviour of the Gibraltar Strait Breccias</b> .....	409
Weixin Dong, E. Pimentel, G. Anagnostou	
<b>Estimation of Tri-axial Behaviour of Pilani Soil Using the Results of Direct Shear Test as a Function of Pore Water Content</b> .....	417
K. Kumar	
<b>Discrete Element Investigation of the Asymptotic Behaviour of Granular Materials</b> .....	423
D. Mašín	
<b>Mechanical Behavior of Granular Particles with Different Angularities</b> .....	431
M.M. Mollanouri.Sh, Ali Aaghar Mirghasemi	
<b>Numerical Simulation of Direct Shear Test Using Elliptical Particles</b> . . . .	441
Morteza Naeij, Ali Aaghar Mirghasemi	
<b>Study of Anisotropies Evolution in Direct Shear Test Using Discrete Element Method</b> .....	451
Morteza Naeij, Ali Aaghar Mirghasemi	

<b>A Micromechanics-Based Modeling the Simple Shear Behaviors of Granular Materials</b> .....	461
J.G. Qian, Z.P. You, Maosong Huang	
<b>Evolution of Fabric in the Shearing Process Based on Micromechanics</b> .....	469
Homayoun Shaverdi, Mohd. Raihan Taha, Farzin Kalantary	
<b>Determination of Crystallinity of Alkali Activated Flyash by XRD and FTIR Studies</b> .....	477
D.N. Singh, Bhagwanjee Jha, Kadali Srinivas	
<b>Stress-Dependency of Intergranular Strain</b> .....	483
A.B. Tsegaye, B.W. Ygzaw, Thomas Benz	
<b>On Shear-Volume Coupling in Deformation of Soils</b> .....	491
A.B. Tsegaye, S. Nordal, Thomas Benz	
<b>Influence of Various Experimental Conditions on Shear Behavior of Compacted Sandy Soil under Unsaturated Condition</b> .....	501
Yuan Zhang, Tatsuya Ishikawa, Tetsuya Tokoro, Satoru Shibuya	
<b>Investigation on Strain Localization of Coal Using Micro-finite Difference Modelling</b> .....	507
Yixin Zhao, Jingli Han, Yaodong Jiang, Zhongsheng Tian, You Yu	
<b>Constitutive Model</b>	
<b>An Elasto-Plastic Model for Liquefiable Sands Subjected to Torsional Shear Loadings</b> .....	519
Gabriele Chiaro, Junichi Koseki, L.I. Nalin De Silva	
<b>A Micromechanics Based Model for Cemented Granular Materials</b> ....	527
Arghya Das, Alessandro Tengattini, Giang Nguyen, Itai Einav	
<b>Modelling the Thermo-Plasticity of Unsaturated Soils</b> .....	535
Bertrand François, Lyesse Laloui	
<b>Modeling the Dilatancy of Overconsolidated Clay</b> .....	541
Zhiwei Gao, Jidong Zhao	
<b>Current Situation of Constitutive Model for Soils Based on Thermodynamics Approach</b> .....	547
Xiao-xia Guo, Xiang Sun, Long-tan Shao, Bo-ya Zhao	
<b>Constitutive Modeling of Cemented Sands Using Critical State Soil Mechanics and Generalized Plasticity Concepts</b> .....	553
Amir Hamidi, Ehsan Ravanbakhsh	

<b>Comparison between Feature of Modified Cam-Clay Model and UH Model</b> .....	559
Wei Hou, Yangping Yao	
<b>Experimental Investigation and Three Dimensional Constitutive Modeling of Principal Stress Rotation in Shanghai Soft Clay</b> .....	567
Maosong Huang, Yanhua Liu	
<b>From Internal Structure to Constitutive Modeling of Granular Assemblies</b> .....	577
Xia Li	
<b>Extension of Mohr-Coulomb Model into State Dependent Softening of Sand and Its Application in Large Deformation Analysis</b> .....	583
Xu Li, Yuxia Hu, David White	
<b>A Constitutive Model of Sand Considering the State-Dependent and the Effect of Direction of Principal Stress</b> .....	593
Peng Liu, Maotian Luan, Zhongtao Wang	
<b>An Elastoplastic Constitutive Model of Unsaturated Soils with Coupling of Capillary Hysteresis and Skeletal Deformation</b> .....	599
Tian-tian Ma, Chang-fu Wei, Pan Chen, Hou-zhen Wei	
<b>Explicit Incorporation of Asymptotic States into Hypoplasticity</b> .....	609
D. Mašín	
<b>Simple and Unified Modelong of Time-Dependent Behavior for Various Geomaterials</b> .....	617
Teruo Nakai, Hossain Md. Shahin	
<b>Uniqueness of Numerical Experimental Results and Contribution to Constitutive Model by DEM</b> .....	627
Kiichi Suzuki	
<b>Study on Accelerated Creep Properties and Creep Damage Constitutive Relation for Volcanic Breccias</b> .....	633
Rubin Wang, Weiya Xu, Jiuchang Zhang, Wei Wang	
<b>A Research on the Full State Function Constitutive Relation Model</b> ....	641
Zhenhai Wei, Mengshu Wang, Dingli Zhang	
<b>A Generalized Critical State Model for Gas Hydrate-Bearing Sediments</b> .....	649
Rong-tao Yan, Chang-fu Wei, Hou-zhen Wei, Hui-hui Tian, Er-ling Wu	
<b>A Review of Constitutive Modeling of Bonded Soil</b> .....	657
W.M. Yan	

**A Unified Description of Toyoura Sand** ..... 663  
 Feng Zhang, Bin Ye, Guanlin Ye

**A Structured UH Model** ..... 675  
 Enyang Zhu, Yangping Yao

**Application**

**Incorporation of Soil Suction in Stress-Based Slope Stability Analysis** . . . 691  
 Yong Chen, D. Chan, Yunzhi Tan

**Static and Dynamic Analyses of High Core Rockfill Dams**..... 701  
 Weixin Dong, Yuzhen Yu

**Implementation of Numerical Optimization Techniques in Constitutive Model Calibration** ..... 709  
 Louis Ge, Honghua Zhao, Bata Bate

**Modeling Damage by Crack Nucleation and Growth in Porous Media** ..... 715  
 Dashnor Hoxha, Javad Eslami, Dragan Grgic, Duc-Phi Do

**Large Deformation Analysis of Spudcan Penetration into Sand Overlying Normally Consolidated Clay** ..... 723  
 Pan Hu, Dong Wang, Mark Cassidy, Qing Yang

**Application of Data Mining Techniques for the Development of New Rock Mechanics Constitutive Models** ..... 735  
 T. Miranda, L.R. Sousa, W. Ruggenthen, R.L. Sousa

**Ground Response Curve (GRC) and Excavation Damage Zone Based on an Isotropic Damage Model** ..... 741  
 Hamed Molladavoodi

**Effect of Seismic Wave Form on the Behavior of River Embankment on the Soft Soil Deposit** ..... 751  
 Fusao Oka, P.S. Tsai, Sayuri Kimoto

**Integration Algorithms Based on Drucker-Prager Criterion and Application in Slope Stability Analysis** ..... 757  
 Yuanwei Pan, Yaoru Liu, Jingjuan Qian, Qiang Yang

**Investigation of Behavioral Aspects of Flexible Pavement under Various Conditions by Finite Element Method** ..... 765  
 M.S. Ranadive, A.B. Tapase

**Three Dimensional Implementation of HISS Model in ABAQUS** ..... 771  
 Mingqiang Wang, Jun Yang

**Stability Analysis of Shuiwenzhan Landslide under Water Level Fluctuation and Rainfall in Three Gorges Reservoir** ..... 783  
 Gang Zeng, Shimei Wang, Yong Chen

**Case Study: A Stress Update Algorithm for D-P Constitutive Model** .... 789  
 Xiaohan Zhang

**Plastic Damage of the Surrounding Rock under the Influence of Confined Water Pressure and Mining Disturbance**..... 795  
 Chunhu Zhao

**3D Large Deformation FE Analysis of Spudcan Foundations on Layered Clays Using CEL Approach** ..... 803  
 Jingbin Zheng, Muhammad S. Hossain, Dong Wang

**Erratum**

**Large Deformation Analysis of Spudcan Penetration into Sand Overlying Normally Consolidated Clay** ..... E1  
 Pan Hu, Dong Wang, Mark Cassidy, Qing Yang

**Author Index** ..... 811

# Shear Strength Criteria for Rock, Rock Joints, Rockfill, Interfaces and Rock Masses

Nick Barton

Nick Barton & Associates,  
Oslo, Norway  
nickrbarton@hotmail.com

**Summary.** Although many intact rock types can be very strong, a critical confining pressure can eventually be reached in triaxial testing, such that the Mohr shear strength envelope becomes horizontal. This critical state has recently been better defined, and correct curvature, or correct deviation from linear Mohr-Coulomb has finally been found.

Standard shear testing procedures for rock joints, using multiple testing of the same sample, in case of insufficient samples, can be shown to exaggerate apparent cohesion. Even rough joints do not have any cohesion, but instead have very high friction angles at low stress, due to strong dilation.

Great similarity between the shear strength of rock joints and rockfill is demonstrated, and the interface strength between rockfill and a rock foundation is also addressed.

Rock masses, implying problems of large-scale interaction with engineering structures, may have both cohesive and frictional strength components. However, it is not correct to add these, following linear Mohr Coulomb (M-C) or non-linear Hoek-Brown (H-B) standard routines. Cohesion is broken at small strain, while friction is mobilized at larger strain and remains to the end of the shear deformation. The criterion '*c then tan  $\phi$* ' should replace '*c plus tan  $\phi$* ' for improved fit to reality. In all the above, scale effects need to be accounted for.

**Keywords.** Rock, rock joints, rock masses, shear strength, friction, critical state, cohesion, dilation, non-linear, scale effects.

## 1 Introduction

Figure 1 illustrates a series of simple empirical strength criteria that pre-date Hoek-Brown, and that are distinctly different from linear Mohr-Coulomb, due to their consistent non-linearity. Several of these categories will be addressed in this lecture and extended abstract.

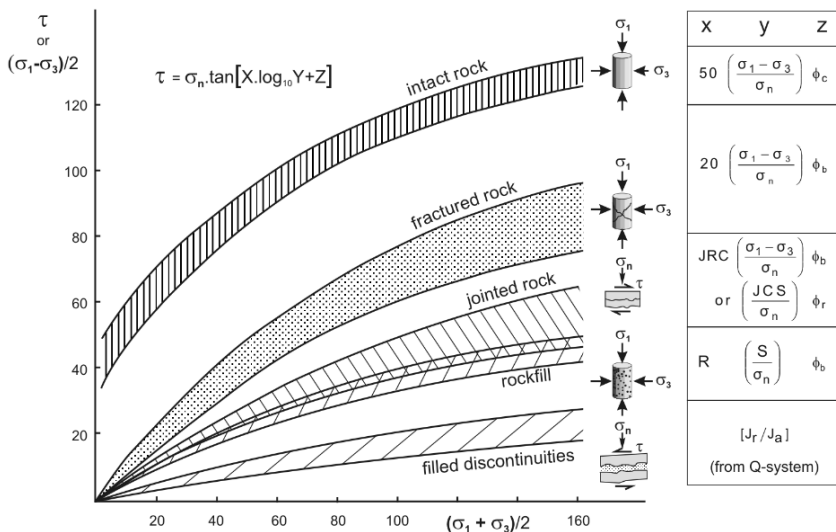


Fig. 1. Simple empiricism, sometimes based on hundreds of test samples, suggested the following ways to express peak shear strength in rock mechanics and rock engineering. Note the general lack of cohesion. Derived from Barton, 1976, and Barton, 2006.

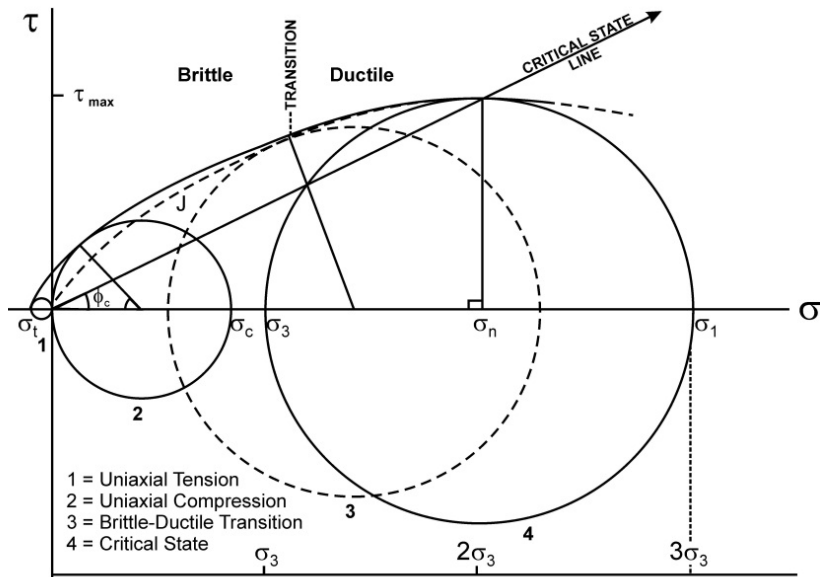
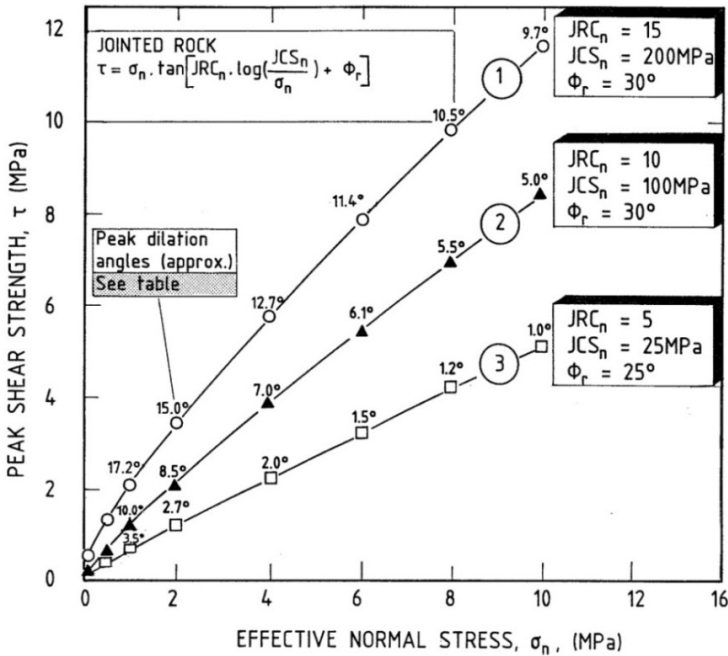


Fig. 2. Critical state line defined by  $\sigma_1 = 3 \sigma_3$  was suggested by numerous high-pressure triaxial strength tests. Note the chance closeness of the unconfined strength ( $\sigma_c$ ) circle to the confining pressure  $\sigma_3$  (critical). Barton, 1976. Note that 'J' represents jointed rock. The magnitude of  $\phi_c$  is  $26.6^\circ$  when  $\sigma_1 = 3 \sigma_3$ .

## 2 Shear Strength of Intact Rock

The shear strength envelopes for intact rock, when tested over a wide range of confining stress, have marked curvature, and eventually reach a horizontal stage with no further increase in strength. This was termed the ‘critical state’ and the simple relation  $\sigma_1 = 3 \sigma_3$  suggested itself, as illustrated in Figure 2. Singh et al., 2011 have now modified the Mohr-Coulomb criterion by absorbing the critical state defined in Barton, 1976, and then quantified the necessary deviation from the linear form, using a large body of experimental test data.

The Singh et al., 2011 development revealed the astonishing simplicity of the following equality:  $\sigma_c \approx \sigma_3$  (critical) *for the majority of rock types*: in other words the two Mohr circles referred to in Figure 2 are usually touching at their circumference. The curvature of peak shear strength envelopes is therefore now more correctly described, so that few triaxial tests are required, and need only be performed at low confining stress, in order to delineate the whole strength envelope.



**Fig. 3.** The scale-effect corrected form of the non-linear Barton 1973 strength criterion, following modification with  $\phi_r$  by Barton and Choubey, 1977, and allowance for scale effects caused by block size. Note the strong dependence of dilation on joint properties.

### 3 Shear Strength of Rock Joints

Figure 3 illustrates the non-linear form of the strength criterion for rock joints. It will be noted that no cohesion intercept is intended. A linear cut-off to the origin is used at very low stress, to represent the extremely high friction angles measured at low stress. It will be noted that subscripts have been added to indicate scale-effect (reduced) values of joint roughness  $JRC_n$  and joint wall strength  $JCS_n$ . This form is known as the Barton-Bandis criterion. Its effect on strength-displacement modelling is shown in Figure 4.

### 4 Shear Strength of Rockfill and Interfaces

Figure 1 showed that there were similarities between the shear strength of rockfill and that of rock joints. This is because they both have 'points in contact', i.e. highly stressed contacting asperities or contacting opposing stones. In fact these contacting points may be close to their crushing strength, such that similar shear strength equations can apply, as suggested in Figure 5

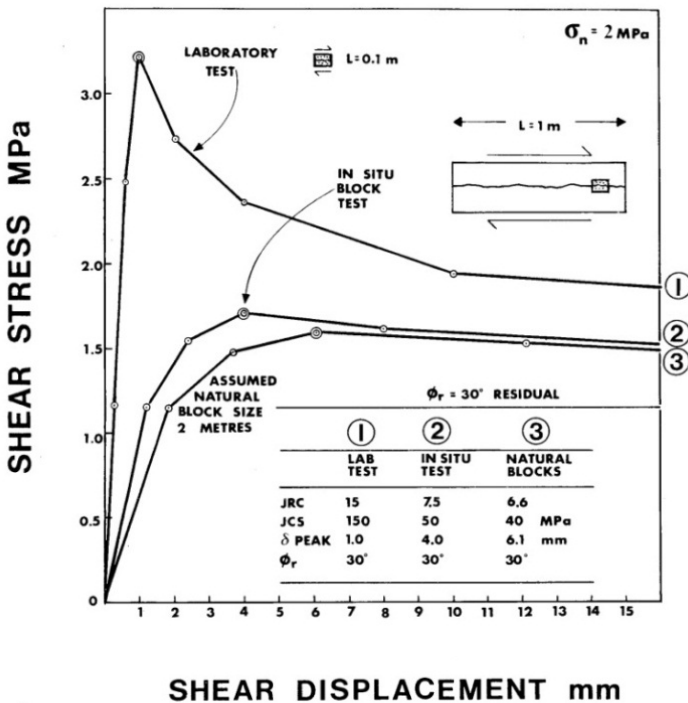


Fig. 4. Laboratory testing, especially of rough joints, may need a strong adjustment (down-scaling) for application in design, due to the block-size related scale effects on JRC and JCS. Barton, 1982

$$\tau/\sigma_n = \tan [JRC \log(JCS/\sigma_n) + \phi_r] \text{ applies to rock joints}$$

$$\tau/\sigma_n = \tan [R \log(S/\sigma_n) + \phi_b] \text{ applies to rockfill}$$

$$\tau/\sigma_n = \tan [JRC \log(S/\sigma_n) + \phi_r] \text{ might apply to interfaces}$$

Because some dam sites in glaciated mountainous countries like Norway, Switzerland, and Austria have insufficient foundation roughness to prevent preferential shearing along the rockfill/rock foundation interface, artificial ‘trenching’ is needed. The preference for interface sliding (JRC-controlled) or failure within the rockfill (R-controlled) is illustrated in Figure 6.

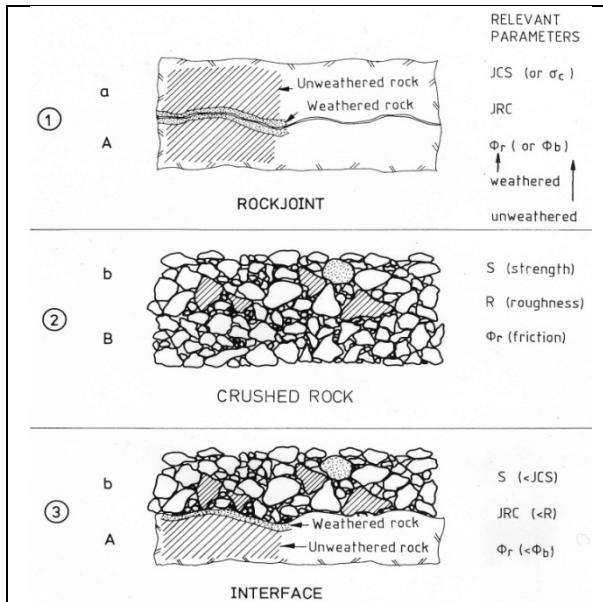


**Fig. 5.** Peak shear strength estimates for three categories of asperity contact: rock joints, rockfill, and interfaces between the two

## 5 Shear Strength and Models of Rock Masses

It has been claimed – correctly – that rock masses are the single most complex of engineering materials utilized by man. The complexity may be due to variable jointing, clay-filled discontinuities, fault zones, anisotropic properties, and dramatic water inrush and rock-bursting stress problems. Nevertheless we have to make some attempt to represent this complexity in models. Two contrasting approaches (to simple cases) are shown in Figures 7 and 8.

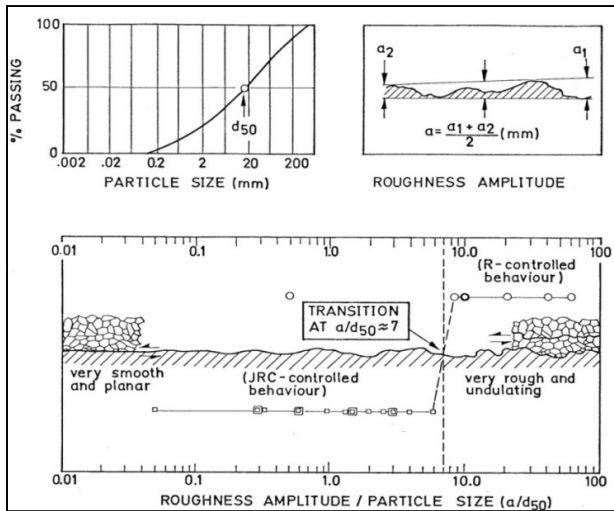


**Fig. 6.** The results of interface/rockfill testing, showing R-controlled and JRC-controlled categories

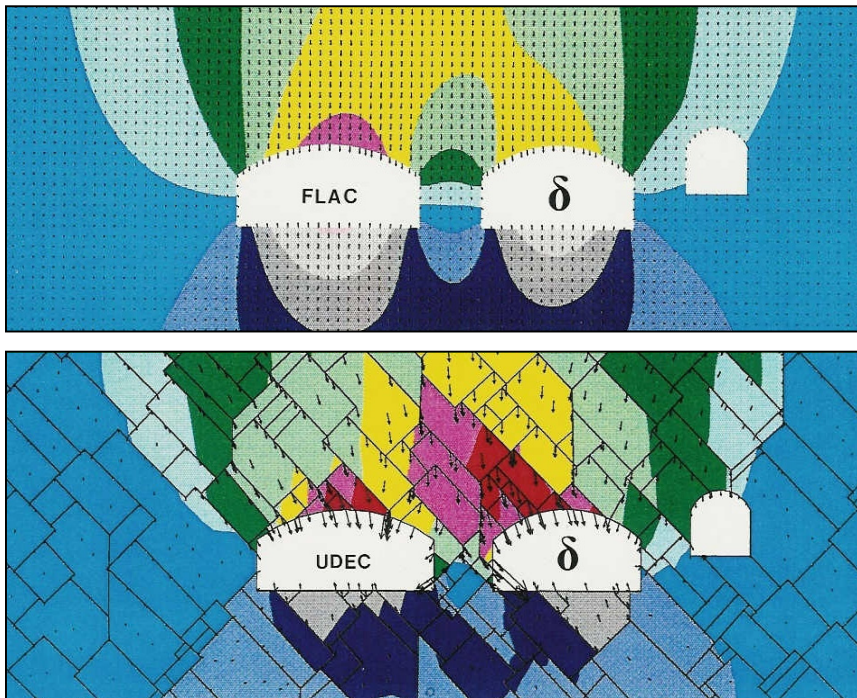


**Fig. 7.** Continuum and discontinuum modelling approaches to the representation of tunneling through an anisotropic rock mass. The increased richness and reality of representing the potential behaviour of jointing, even if exaggerated in 2D, is clear to see.

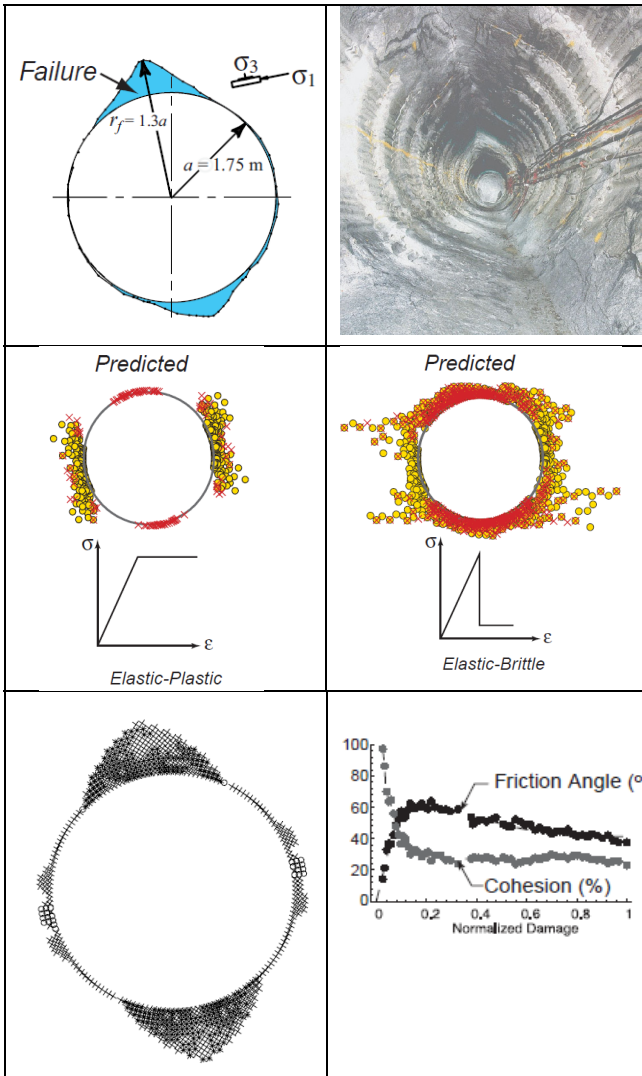


**Fig. 8.** Top: The Canadian URL mine-by break-out that developed when excavating by line-drilling, in response to the obliquely acting anisotropic stresses. This is followed by an important demonstration of unsuccessful modelling by ‘classical methods’ given by Hajiabdolmajid et al., 2000. They followed this with a more realistic degradation of cohesion and mobilization of friction in FLAC.

**5.1 The Limitations of M-C, H-B and  $c$  plus  $\sigma_n \tan \phi$**

Attempts to model ‘break-out’ phenomena such as those illustrated in Figure 8, are not especially successful with standard Mohr-Coulomb or Hoek-Brown

failure criteria, because the *actual phenomena* are not following our long-standing belief in ‘*c plus  $\sigma_n \tan \phi$* ’. The reality is degradation of cohesion at small strain and mobilization of friction (first towards peak, then towards residual) which occur at larger strain. The very important findings of Hajiabdolmajid et al., 2000 are summarised briefly by means of the six figures assembled in Figure 8. The demonstrated shortcomings of continuum modelling with ‘*c plus  $\sigma_n \tan \phi$* ’ shear strength assumptions, should have alerted our profession for change already twelve years ago, but deep-seated beliefs or habits are traditionally hard to change.

Rock masses actually follow an even more complex progression to failure, as suggested in Barton and Pandey, 2011, who recently demonstrated the application of a similar ‘*c then  $\tan \phi$* ’ modelling approach, but applied it in FLAC 3D, for investigating the behaviour of multiple mine-stopes in India. A further break with convention was the application of peak ‘*c*’ and peak ‘ *$\phi$* ’ estimates that were derived directly from mine-logged Q-parameters, using the CC and FC parameters suggested in Barton, 2002. For this method, an estimate of UCS is required, as CC (cohesive component) and FC (frictional component) are derived from separate ‘halves’ of the formula for  $Q_c = Q \times \sigma_c / 100$ . See Table 1.

These much simpler Q-based estimates have the advantage of not requiring software for their calculation – they already exist in the Q-parameter logging data, and the effect of changed conditions such as clay-fillings, can be visualized immediately.

**Table 1.** The remarkable complexity of the algebra for estimating *c*’ and  *$\phi$* ’ with Hoek-Brown GSI-based formulations are contrasted with the simplicity of equations derived by ‘splitting’ the existing  $Q_c$  formula into two parts, as described in Barton, 2002.

( $Q_c = Q \cdot \sigma_c / 100$ , with  $\sigma_{ci}$  expressed in MPa).

FC	$"\phi" \approx \tan^{-1} \left( \frac{J_r}{J_a} \times \frac{J_w}{1} \right)$	(from Q)
	$\phi' = a \sin \left[ \frac{6am_b (s + m_b \sigma'_{3n})^{a-1}}{2(1+a)(2+a) + 6am_b (s + m_b \sigma'_{3n})^{a-1}} \right]$	(from GSI)
CC	$"c" \approx \left( \frac{RQD}{J_n} \times \frac{1}{SRF} \times \frac{\sigma_c}{100} \right)$	(from Q)
	$c' = \frac{\sigma_{ci} \left[ (1+2a)s + (1-a)m_b \sigma'_{3n} \right] (s + m_b \sigma'_{3n})^{a-1}}{(1+u)(2+a) \sqrt{1 + \left( 6am_b (s + m_b \sigma'_{3n})^{a-1} \right)}} / ((1+a)(2+a))$	(from GSI)

**Table 2.** Illustration of parameters CC (MPa ) and FC° for a declining sequence of rock mass qualities, with simultaneously reducing  $\sigma_c$  (MPa). Estimates of  $V_p$  (km/s) and  $E_m$  (GPa) are from Barton, 2002.

RQD	Jn	Jr	Ja	Jw	SRF	Q	$\sigma_c$	$Q_c$	FC°	CC	$V_p$	$E_m$
100	2	2	1	1	1	100	100	100	63	50	5.5	46
90	9	1	1	1	1	10	100	10	45	10	4.5	22
60	12	1.5	2	0.66	1	2.5	50	1.25	26	2.5	3.6	11
30	15	1	4	0.66	2.5	0.1	33	0.04	9	0.3	2.1	3.5

An important part of the verification of the mine stope modelling reported by Barton and Pandey, 2011 was the comparison of the modelling results with the deformations actually measured.

**Table 3.** Empirical equations linking tunnel or cavern deformation to Q-value, with span as input (left), and the ratio of vertical stress and UCS as additional input (right). From Barton, 2002. (Note: In left equation  $\Delta$  is in mm, while span remains in meters, as in left axis of Figure 9. In right equation only:  $\Delta$  mm, span mm, stress and strength in consistent units, e.g. MPa).

$\Delta = \frac{\text{SPAN}}{Q}$ <p>(central trend of all data: approx)</p>	$\Delta_v = \frac{\text{SPAN}}{100Q} \sqrt{\frac{\sigma_v}{\sigma_c}}$ <p>(more accurate estimate)</p>
---	--

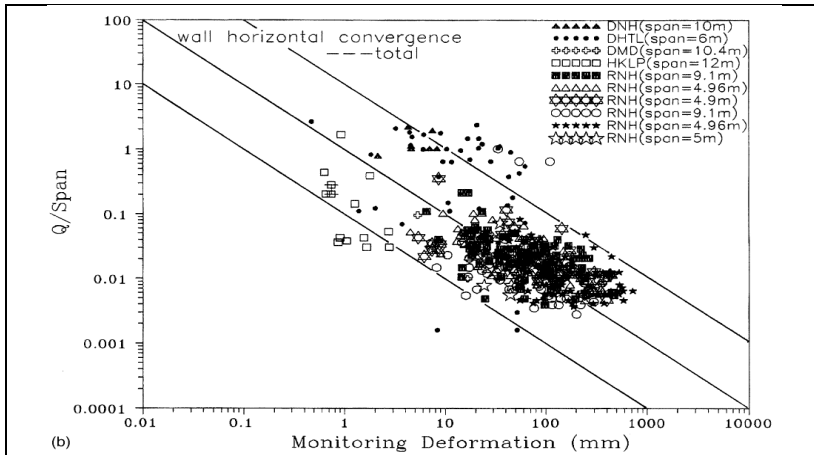


**Fig. 9.** The central (very approximate) data trend of tunnel deformation versus span, modified by rock mass quality Q, can be described by the simplest equation that is possible in rock engineering. See Table 3 (left side).

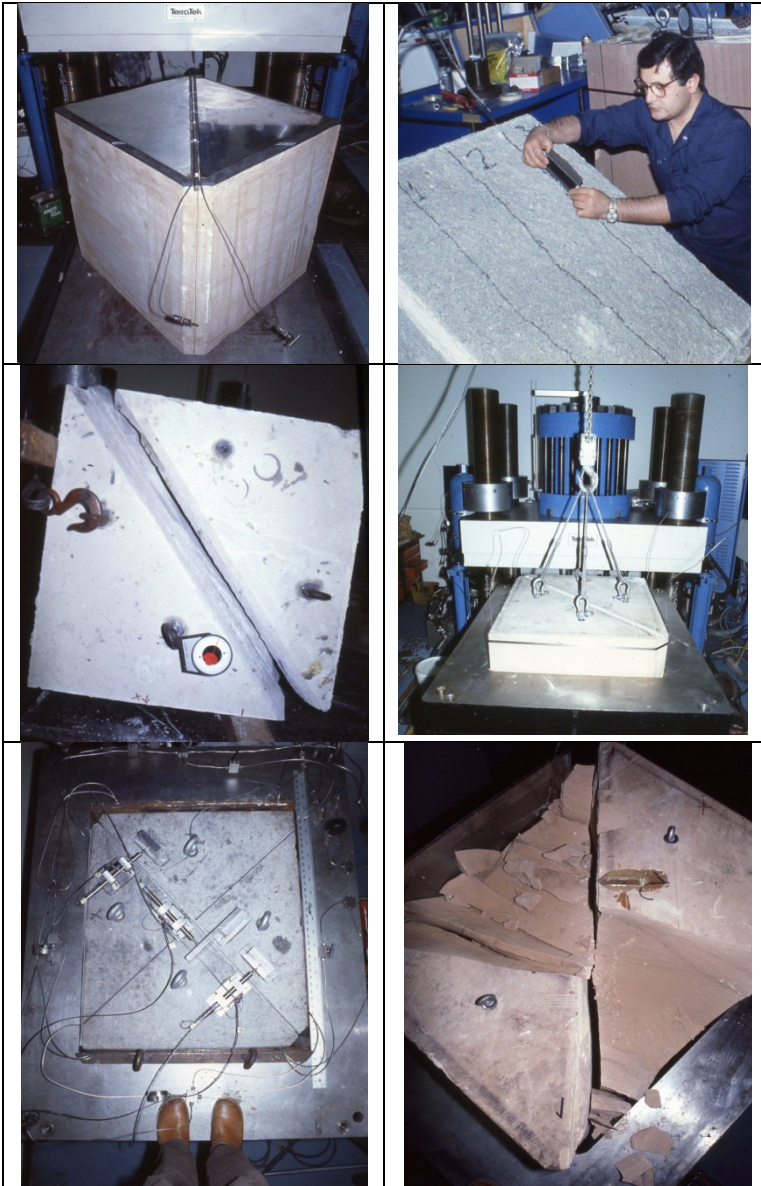


**Fig. 10.** Sample preparation, roughness profiling, tilt testing (at 1 m<sup>3</sup> scale), lowering lightly clamped sample into test frame, LVDT instrumentation, and (a rare) sheared sample. The difficulty of shearing is due to an ignored aspect of stress transformation.

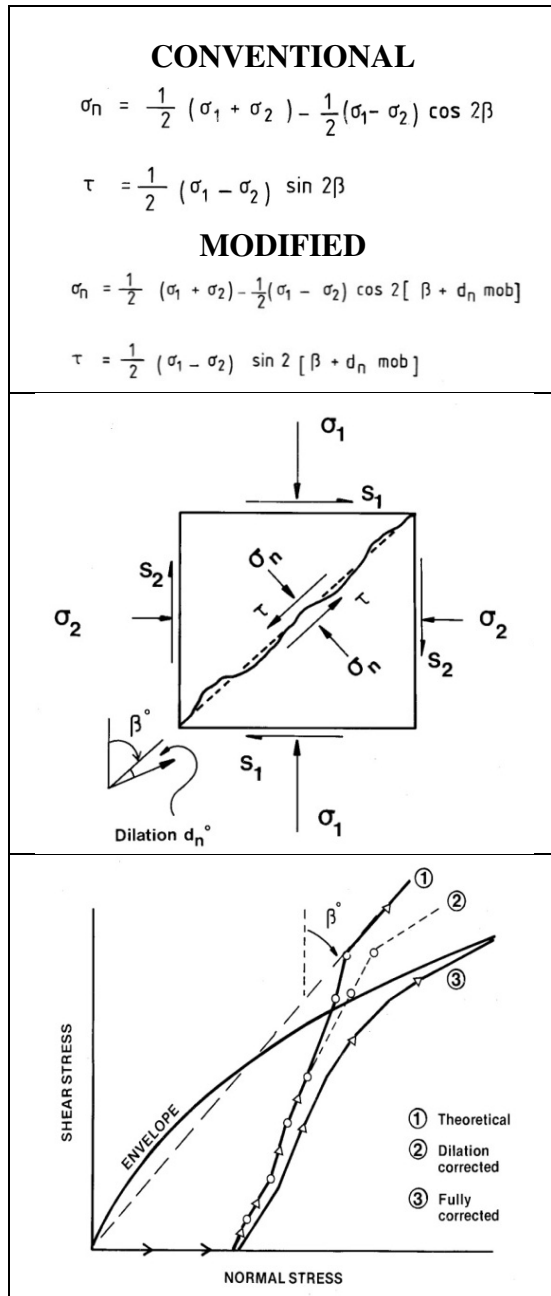


**Fig. 11.** Corrections for out-of-plane dilation and boundary friction, after Bakhtar and Barton, 1984

Recent reviews of pre-excavation modelling for cavern design, and actual cavern performance review for a major metro constructor in Asia, suggest that it is wise to consult these two simple equations, when deliberating over the reality (or not) of numerical models. It is the experience of the writer that distinct element UDEC-MC and UDEC-BB modellers often exaggerate the continuity of modelled jointing (because this is easier than drawing a more representative image of the less-continuous jointing, and digitising the latter). This may result in an order of magnitude error in deformation estimates.

## **6 A Fundamental Geotechnical Over-Sight?**

This paper will be concluded with a subject that concern the transformation of stress from a principal (2D) stress state of  $\sigma_1$  and  $\sigma_2$  to an inclined joint, fault or failure plane, to derive the commonly required *shear and normal stress components*  $\tau$  and  $\sigma_n$ . If the surface onto which stress is to be transformed does not dilate, which might be the case with a (residual-strength) fault or clay-filled discontinuity, then the assumption of co-axial or co-planar stress and strain is no doubt valid. In general this and other assumptions are not valid.

# Revisiting the Paradigm of Critical State Soil Mechanics: Fabric Effects

Yannis F. Dafalias<sup>1</sup> and Xiang-song Li<sup>2</sup>

<sup>1</sup>Dept of Civil and Environmental Engineering, University of California, Davis, CA95616, USA, and Department of Mechanics, School of Applied Mathematical and Physical Sciences, National technical University of Athens, 15773, Athens, Greece.  
jfdafalias@ucdavis.edu

<sup>2</sup>Dept of Civil and Environmental Engineering, Hong Kong University of Science and Technology, Clear Water Bay, Kowloon, Hong Kong, China.  
xсли@ust.hk

## 1 Introduction

In a recent paper Li and Dafalias [1] proposed an Anisotropic Critical State Theory (ACST) as an enhancement of the classical Critical State Theory (CST) for soils, by introducing the requirement that a fabric and loading direction related scalar-valued quantity must reach a critical state value concurrently to the classical requirement of critical state values for the stress ratio  $\eta$  and the void ratio  $e = \hat{e}_c(p)$ . In this process a necessary ingredient is the introduction of a measure of fabric in the form of an evolving fabric tensor, motivated by DEM simulations based on the void vectors concept presented in Li and Li [2]. The so defined fabric tensor was shown theoretically to have a critical state value norm independent of the pressure  $p$  or the specific volume  $v$ , and dependent only on the mode of shearing via a Lode angle expression. A thermodynamic consideration of the critical state in conjunction with Gibbs' condition of equilibrium can provide proof of uniqueness of the critical state line in the  $e$ - $p$  space in regards to various mode of shearing. The enhanced fabric-related critical state condition can be used in a simple, if not unique, way to provide a corresponding constitutive framework for soil plasticity. The objective of this plenary presentation is to briefly outline the premises of the ACST, elaborate more on the motivation and thinking process behind the proposed theory rather than repeat several details that can be found in Li and Dafalias [1], and address several issues associated with current and future research objectives of the ACST.

## 2 Brief Outline of the ACST

At critical state a particulate material keeps deforming in shear at constant volume and stress. In analytical terms this is expressed by

$$\dot{p}=0, \dot{\mathbf{s}}=\mathbf{0}, \dot{\varepsilon}_v=0 \text{ but } \dot{\mathbf{e}}\neq\mathbf{0} \quad (1)$$

where  $p$  is the hydrostatic pressure,  $\mathbf{s}$  the deviatoric part of the stress tensor,  $\varepsilon_v$  the volumetric strain,  $\mathbf{e}$  the deviatoric part of the strain tensor, and a superposed dot implies the rate. The Critical State Theory (CST) by Roscoe *et al.* [3] and Schofield & Wroth [4] proposes that the following conditions must hold at critical state:

$$\eta=\eta_c=(q/p)_c=M \quad \text{and} \quad e=e_c=\hat{e}_c(p) \quad (2)$$

in terms of the triaxial stress variables  $p$  and  $q$ , the stress ratio  $\eta = q / p$ , the void ratio  $e$ , and where  $M$  characterizes the intrinsic frictional coefficient between grain mineral surfaces while  $e_c=\hat{e}_c(p)$  is the critical void ratio which defines the Critical State Line (CSL) in the  $e$ - $p$  plane. For generalization to multi-axial loading one substitutes  $\sqrt{(3/2)\mathbf{s}:\mathbf{s}}$  for  $q$  in the expression  $\eta=q/p$ , and renders  $M$  function of the Lode angle determined by the shearing mode. In some studies under extremely small values of pressure  $p$  in microgravity [5], a dependence of  $M$  on  $p$  was observed, which might be encountered in practice for cases of liquefaction, but such variation will not be considered in this approach although it deserves a more careful examination. The classical CST makes no reference to other fabric related entities than the scalar-valued void ratio. Yet, microstructural studies without exception reveal that an intense orientational fabric formation is present at critical state [6-8], which questions the completeness of the CST.

For a particulate aggregate the fabric can be represented by appropriately defined tensors in both continuum and discrete modes. Adaptation of a discrete definition of fabric tensor  $\mathbf{G}^*$  based on the concept of void vectors by Li and Li [2] to continuum applications yields a tensor  $\mathbf{G}$  with the property that its trace measures the irrecoverable specific volume change  $v^p = 1 + e^p$ , with  $e^p$  the corresponding irrecoverable void ratio change, and its deviator  $\mathbf{F}$  is exclusively a function of the orientational aspects of the aggregates arrangement with no dependence on density. Hence, one can write

$$\mathbf{F} = \mathbf{G} - \frac{v^p}{3} \mathbf{1} \quad (3)$$

Henceforth,  $\mathbf{F}$  will be the fabric tensor while the change of the scalar-valued isotropic part of the fabric associated with volume change  $v^p = 1 + e^p$  will be treated as a separate internal variable. Both evolve in the course of plastic (incrementally irrecoverable) deformation. In order to distinguish between the norm  $F$  and direction  $\mathbf{n}_F$  of  $\mathbf{F}$ , one can write

$$\mathbf{F}=F\mathbf{n}_F, \quad F=\sqrt{\mathbf{F}:\mathbf{F}}, \quad \mathbf{n}_F:\mathbf{n}_F=1, \quad \text{tr}\mathbf{n}_F=0 \quad (4)$$

In general the norm  $F$  will depend the Lode angle  $\theta_F$  associated with  $\mathbf{n}_F$  according to  $\cos\theta_F = \sqrt{6} \text{tr} \mathbf{n}_F^3$ , but based on its foregoing definition will not depend on  $v^p = 1 + e^p$  or the pressure  $p$ .

Motivated by 2D DEM simulations such as in Li and Li [2] and Fu and Dafalias [9], it was postulated by Li and Dafalias [1] that the continuum fabric tensor tends towards a critical state value, which is characterized by a value  $F = F_c$  for the norm and a value  $\mathbf{n}_F = \mathbf{n}$  for the direction,  $\mathbf{n}$  being the so-called loading direction defined by a unit-norm deviatoric tensor along, for example, the direction of the deviatoric plastic strain rate. Based on the properties of the fabric tensor defined above, it follows that  $F_c$  will depend only on  $\theta_F$ . Hence, one can normalize the fabric tensor by  $F_c$  and have that at critical state  $\mathbf{F}_c = \mathbf{n}$  and  $F_c = 1$  for any value of  $\theta_F$ .

Motivated by an approach to account for the relative orientation of loading and fabric tensor directions presented in Li and Dafalias [10] and Dafalias *et al.* [11] for a fixed initial fabric tensor, Li and Dafalias [1] introduced a Fabric Anisotropy Variable (FAV)  $A = \mathbf{F} : \mathbf{n}$ . At critical state it follows that  $A = A_c = 1$  since  $\mathbf{F}_c = \mathbf{n}$ . Thus, the critical state conditions of the CST are augmented by one more related to critical state fabric in reference to current loading direction, providing the following enhanced critical state conditions of the ACST

$$\eta = \eta_c = M, \quad e = e_c = \hat{e}_c(p) \quad \text{and} \quad A = A_c = 1 \quad (5)$$

### 3 Thermodynamic Definition of Critical State and Uniqueness of CSL

The second of Eqs. (5) is the core assumption of critical state theory with or without fabric considerations, and implies the uniqueness of the Critical State Line (CSL) in  $e$ - $p$  space. It is based on experimental evidence, which is nevertheless disputed because of the inherent difficulty to reach a critical state experimentally without localization. In Li and Dafalias [1] a thermodynamic definition of the critical state was used to prove uniqueness of CSL in conjunction with Gibbs' condition of thermodynamic equilibrium, and the procedure is outline below.

The critical state condition (1) states that at critical state, the shear and volumetric responses are completely decoupled, defined by a steady shear flow and a stable equilibrium volumetric state. This condition can be re-expressed within the classical thermodynamics framework by

$$\varpi = \mathbf{s} : \dot{\mathbf{e}} \quad \text{and} \quad pv = C - \Psi \quad (6)$$

where  $\varpi$  is the rate of the per-unit-volume dissipation;  $v$  is the specific volume;  $\Psi$  is the specific (per-unit-mass) Helmholtz free energy; and  $C$  is an energy datum independent of  $v$  (a Gibbs function). Eq. (6)<sub>1</sub> asserts that at critical states the shear work is

solely and completely dissipated, representing a rigid perfectly plastic condition materialized only when Eq. (2)<sub>1</sub> is satisfied; and Eq. (6)<sub>2</sub> describes an exact equilibrium condition, in which all thermodynamic properties are stationary. Eqs. (6) provide a thermodynamic definition of the critical state.

Gibbs asserts that the entropy of a system in equilibrium is the maximum among all the neighboring states with the same internal energy; or alternatively, the internal energy of an equilibrium system is the minimum among all the neighboring states having the same entropy [12]. Application of Gibbs' equilibrium condition to Eq. (6)<sub>2</sub> isothermally suggests that the specific Helmholtz free energy  $\Psi = u - T\vartheta$  is a minimum at critical state, where  $u$ ,  $T$  and  $\vartheta$  are the specific internal energy, the absolute temperature and specific entropy, correspondingly. The specific Helmholtz free energy is in general a function of the specific volume  $v$  as well as other deformation and internal variables, i.e.,  $\Psi = \hat{\Psi}(v, \mathbb{Z})$ , where  $\mathbb{Z}$  represents all relevant variables other than  $v$  and  $p$ . The fabric tensor  $\mathbf{F}$  is included in  $\mathbb{Z}$  since it is not dependent on  $v$  or  $p$ .

It follows from Eq. (6)<sub>2</sub> and Gibbs' equilibrium condition that for a given  $p$ , corresponding to a minimum  $\Psi_c$  (hereafter the subscript 'c' stands for 'at critical state'),  $v_c$  is a maximum with respect to any neighboring states *defined by variation of  $\mathbb{Z}_c$*  but still complying with the critical state condition Eqs. (6). Thus, solving for  $p_c$  at critical state one can re-write Eq.(6)<sub>2</sub> as  $p_c = \hat{p}_c(v_c, \mathbb{Z}_c)$  where for simplicity the datum  $C = 0$ . Because those neighboring states are also critical states as defined by Eqs. (6), they also demand a maximum  $v_c$ . Hence, the only possibility for all those neighboring critical states to satisfy the Gibbs condition is that they have the same value of  $v_c$ , which is the limiting case of the Gibbs condition. Since such "neighboring" critical states have their own neighboring states complying also with Eqs. (6), these "new" neighboring states are also critical states, thus, according to the limiting Gibbs condition are characterized by the same unique value of  $v_c$ . Clearly, such "expansion" of neighboring states can be repeated, resulting in a unique pair of  $p_c$  and  $v_c$  over the entire continuous domain of  $\mathbb{Z}_c$ . Since the fabric tensor  $\mathbf{F}_c$  is one of the variables in  $\mathbb{Z}_c$ , it follows that the presence of fabric anisotropy at critical state has no impact on the critical state line, and accordingly the forgoing equation among  $p_c$ ,  $v_c$  and  $\mathbb{Z}_c$  can be reduced to  $p_c = \hat{p}_c(v_c)$ . Expressing  $v_c$  in terms of the void ratio  $e_c$  and solving for the latter one obtains Eq.(5)<sub>2</sub> with  $p_c = p$  as the equation of the unique CSL. Thus, at critical state the free energy expression becomes the equation of the CSL under Gibbs' equilibrium condition.

It is important to emphasize the significance of having the fabric tensor and its norm independent of specific volume or equivalently of  $p$ , , as defined in Li and Dafalias [1], and dependent only on the Lode angle  $\theta_f$  with its subsequent normalization, in order to prove by use of Gibbs' equilibrium condition the

uniqueness of the CSL. Any coupling of the dependence of the critical state value of the norm of the fabric tensor on specific volume and Lode angle would preclude the exact application of the proof of uniqueness of CSL. How to address such eventuality of coupled dependence will be presented in upcoming publication.

## 4 Evolution of Fabric Tensor

The evolution equation of  $\mathbf{F}$  will be developed within the theory of rate independent plasticity where  $\mathbf{F}$  plays the role of an evolving internal variable. Such evolution will be expressed by a corotational rate in reference to a specific constitutive spin  $\boldsymbol{\omega}$  in order to satisfy objectivity under large deformations and rotations, thus, one can write

$$\overset{\circ}{\mathbf{F}} = \dot{\mathbf{F}} - \boldsymbol{\omega}\mathbf{F} + \mathbf{F}\boldsymbol{\omega} = \langle \lambda \rangle \bar{\mathbf{F}} \quad (7)$$

where a superposed ‘ $\circ$ ’ signifies the corotational rate in association with  $\boldsymbol{\omega}$ , the scalar-valued  $\lambda$  within the Macauley brackets is the plastic multiplier which is a function of stress or strain rate, and  $\bar{\mathbf{F}}$  is a tensor-valued isotropic function of the stress and internal variables due to objectivity.

General guidelines for the specification of the constitutive spin  $\boldsymbol{\omega}$  are based on the theory of Plastic Spin [13]. For small elastic deformations the theory maintains the plausible proposition that  $\boldsymbol{\omega}$  does not have to be equal to the continuum material spin  $\mathbf{W}$ , the anti-symmetric part of the velocity gradient, hence, a plastic spin  $\mathbf{W}^p$  can be defined by  $\mathbf{W} = \boldsymbol{\omega} + \mathbf{W}^p$ . The plastic spin  $\mathbf{W}^p$  is non-zero only when plastic loading occurs, i.e., when  $\lambda > 0$ , hence, one can write  $\mathbf{W}^p = \langle \lambda \rangle \boldsymbol{\Omega}^p$  along the format of Eq. (7). Objectivity requirements render  $\boldsymbol{\Omega}^p$  an isotropic function of the stress and internal variables. Thus, instead of specifying the constitutive spin  $\boldsymbol{\omega}$  that is not objective, one can equivalently specify the  $\boldsymbol{\Omega}^p$  and then obtain  $\boldsymbol{\omega} = \mathbf{W} - \mathbf{W}^p = \mathbf{W} - \langle \lambda \rangle \boldsymbol{\Omega}^p$ . Substitution of the last expression of  $\boldsymbol{\omega}$  in terms of  $\mathbf{W}$  and  $\boldsymbol{\Omega}^p$  in Eq. (7) yields after some simple algebra

$$\overset{\nabla}{\mathbf{F}} = \dot{\mathbf{F}} - \mathbf{W}\mathbf{F} + \mathbf{F}\mathbf{W} = \langle \lambda \rangle (\bar{\mathbf{F}} + \mathbf{F}\boldsymbol{\Omega}^p - \boldsymbol{\Omega}^p\mathbf{F}) \quad (8)$$

where a superposed ‘ $\nabla$ ’ denotes the corotational rate with respect to  $\mathbf{W}$ , otherwise known as the Jaumann rate. Therefore, one needs to specify the form of functions  $\bar{\mathbf{F}}$  and  $\boldsymbol{\Omega}^p$ .

Recall that  $\mathbf{F} = F \mathbf{n}_f$  evolves towards  $\mathbf{n}$ , or equivalently  $F$  evolves towards 1 and  $\mathbf{n}_f$  towards  $\mathbf{n}$ . The foregoing can be incorporated into Eqs. (7) and (8) by setting  $\bar{\mathbf{F}} = c(\mathbf{n} - r\mathbf{F})$ , which, with  $r=1$  at critical state, ensures the evolution of  $\mathbf{F}$  towards  $\mathbf{n}$ , where  $c$  and  $r$  are scalar-valued constitutive parameters (isotropic

functions of the stress and internal variables in general) controlling the pace of evolution and the peak of  $F$ , respectively. With  $r < 1$  at a pre-critical state,  $F$  may reach a peak greater than 1 before it falls to its critical state value of 1 where  $r = 1$ , as observed in DEM simulations for dense specimens.

For the determination of  $\mathbf{\Omega}^p$ , observe first that the principal directions of  $\mathbf{F}$  will tend to rotate towards alignment with those of  $\mathbf{n}$ , if such alignment does not exist to begin with. In addition recall that the  $\mathbf{\Omega}^p$  must be an isotropic function of the stress and internal variables, which in the present general development appear in the form of the loading direction  $\mathbf{n}$  and the fabric tensor  $\mathbf{F}$ . Based on the representation theorems [14], the simplest form of such isotropic anti-symmetric tensor-valued function of two symmetric tensors is given by  $\mathbf{\Omega}^p = \chi(\mathbf{nF} - \mathbf{Fn})$  with  $\chi$  the scalar-valued plastic spin constitutive parameter (again an isotropic function of the stress and internal variables in general). Observe that when  $\mathbf{n}$  and  $\mathbf{F}$  are coaxial, i.e., they have same eigenvectors, they commute, i.e.,  $\mathbf{nF} = \mathbf{Fn}$  and, therefore,  $\mathbf{\Omega}^p = \mathbf{0}$ . It is the non-coaxiality of  $\mathbf{n}$  and  $\mathbf{F}$  that can cause a non-zero plastic spin and by consequence a non-zero constitutive spin given by  $\mathbf{\omega} = -\mathbf{W}^p = -\langle \lambda \rangle \mathbf{\Omega}^p$  when  $\mathbf{W} = \mathbf{0}$ , hence, achieving the tendency for alignment between  $\mathbf{F}$  and  $\mathbf{n}$ . Substitution of  $\bar{\mathbf{F}} = c(\mathbf{n} - r\mathbf{F})$  and  $\mathbf{\Omega}^p = \chi(\mathbf{nF} - \mathbf{Fn})$  in Eq. (8) yields

$$\begin{aligned} \bar{\mathbf{F}} &= \dot{\bar{\mathbf{F}}}\mathbf{n}_F + F\dot{\mathbf{n}}_F = \dot{\mathbf{F}} - \mathbf{WF} + \mathbf{FW} \\ &= \langle \lambda \rangle \left[ c(\mathbf{n} - r\mathbf{F}) - \chi(\mathbf{nF}^2 + \mathbf{F}^2\mathbf{n} - 2\mathbf{FnF}) \right] \end{aligned} \quad (9)$$

One needs the values of  $c$ ,  $r$  and  $\chi$  for the implementation of Eq. (9).

## 5 Effect on Constitutive Modeling

The introduction of the fabric tensor  $\mathbf{F}$  and FAV  $A$ , while enhancing the classical CST by one additional condition as shown in Eqs. (5), it does not answer the question as to how exactly this will benefit a corresponding constitutive framework within the ACST. Of course one can treat the  $\mathbf{F}$  as an internal variable and  $A$  as a joint invariant in the expressions for the free energy, the yield surface, plastic potential and dilatancy, where in combination with other internal variables and invariants can be used to describe the effects of evolving fabric anisotropy. Reaching critical state will not just be considered in the  $e$ - $p$ - $q$  space of CST, but in the enhanced  $e$ - $p$ - $q$ - $A$  space of the ACST. These, however, remain general statements without practical and generic value. The issue is to address the effect of fabric in such a way as to influence directly the constitutive features associated with critical state in a generic way, i.e., in a way that can be applied to various families of constitutive models within the ACST.

A previous approach to address the fabric effect was based on the findings of several prior works by the authors, namely in Li and Dafalias [10], Dafalias *et al.*

[11], Papadimitriou *et al.* [15], which in turn were motivated by several hollow cylinder experimental data that are mentioned in the foregoing references. In these past works the fabric was defined by a fixed initial fabric tensor  $\mathbf{F}$ , thus, addressing only initial inherent anisotropy. Subsequently the concept of an anisotropic state variable  $A_\theta = g(\theta_n)\mathbf{F}:\mathbf{n}$  with  $g(\theta_n)$  an interpolating function of Lode angle  $\theta_n$  of the loading direction  $\mathbf{n}$  was introduced and symbolized also by  $A$ , resembling but not being the same as the FAV  $A$  of the present development. The main role played by  $A_\theta$  was to determine a parallel translation of the CSL in  $e$ - $p$  space, thus, “interpreting” the effect of inherent fabric anisotropy into greater or smaller dilatancy resulting from such relocation of the CSL. Because the  $\mathbf{F}$  was fixed and not allowed to evolve, the translation of the CSL does not change as long as the loading direction  $\mathbf{n}$  remains constant, which means that at critical state one may have various CSL depending on the various  $\mathbf{n}$ . For that reason this approach has been questioned despite the fact it provided a plethora of very good simulations for anisotropic sand response up to a certain strain level.

It was clear that the foregoing multiplicity of the CSL was due to the assumed fixed value of the initial fabric tensor  $\mathbf{F}$ , which was representing initial inherent fabric anisotropy. A proposition by Dafalias and Manzari [16] to introduce an evolving fabric dilatancy tensor was not aiming at the effect of evolving fabric in a general way for all aspects of the material response, but it was only focused on the enhancement of consolidation at reverse loading after dilation in a successful effort to simulate liquefaction. The basic new premises of ACST, however, are based on the evolution of a fabric tensor  $\mathbf{F}$  from some initial value to a critical state value; hence, one may think of the possibility to have an evolving rather than fixed translation of a line in the  $e$ - $p$  space, which played before the role of a distinct and fixed CSL. Now it can be treated as an evolving reference line, called the Dilatancy State Line (DSL), such that the difference of the current void ratio from the void ratio on DSL at same  $p$  can characterize the degree of dilatancy or contractancy of the current state. The evolution of DSL can be coupled to the evolution of the fabric tensor and FAV  $A$  in such a way that when the third critical state condition  $A = 1$  of Eqs. (5) is satisfied, the translating DSL in  $e$ - $p$  space reaches its final critical state position which represents a unique CSL, as it was possible to prove earlier based on Gibbs equilibrium condition. In other words any DSL eventually converges with a unique CSL as critical state is reached according to Eqs. (5). The analytical description of this simple scheme will be described in the sequel.

A different line of thinking, which nevertheless leads to the same result, is as follows. In the theory of critical state soil mechanics a measure of how far is a sample from critical state is defined by the difference  $M - \eta$  stress-ratio wise, while such measure is defined density-wise by the difference  $\psi = e - e_c$ , introduced as the state parameter by Been and Jefferies [17], where  $e$  and  $e_c$  are the current and critical void ratios at same  $p$ . The foregoing differences appear prominently, directly or indirectly, in several constitutive models that are built within the classical critical state framework. The introduction of the FAV  $A$  whose

critical state value is 1, invites the proposition that the difference  $1 - A$  must also play a significant role in the constitutive response as an additional measure of a fabric-wise distance from critical state. The important question then is how to treat this  $1 - A$  difference measure. Must be treated independently from the other two measures  $M - \eta$  and  $\psi = e - e_c$ , or must it be combined with any one or both of them? In other words the fundamental question is whether fabric anisotropy at critical state is handled as a coupled or uncoupled property in regards to  $e$  and  $\eta$ .

A simple but not necessarily unique answer to this fundamental question was provided in Li and Dafalias [1]. It begins by observing that the value of  $\psi$  is instrumental in determining whether a soil sample will dilate or contract upon shearing, and its role is incorporated in various constitutive models such as Jefferies [18], Manzari and Dafalias [19], Gajo and Wood [20], Li and Dafalias [21], to mention a few. For example rendering the peak stress ratio and the dilatancy stress ratio (phase transformation line) direct functions of  $\psi$ , as it was first suggested in Wood *et al.* [22] for the former and Manzari and Dafalias [19] for both within a complete bounding surface plasticity formulation, resulted in successful simulations of a plethora of data at various pressures and densities using the same set of model constants, thus, indicating the importance of the correct use of  $\psi$  in constitutive modeling. Yet, all these models were unable to simulate the drastic difference of response of anisotropic sand samples loaded at various directions by means of hollow cylinder experiments [23]. It was therefore clear that the effect of fabric was not appropriately accounted for in such constitutive models. There were two ways to address this problem. The first was to attempt to introduce the fabric effect into the existing constitutive model structure. Such an approach was incomplete because while improving at the beginning the simulation of anisotropic samples by rendering the dilatancy expression function of  $A$  [15], it could not address differences of the order of more than 500% in stress for the same strain for loading at different directions. It became clear that the issue was more fundamental than initially thought, and one proposition was to actually reconsider the way the role of the state parameter  $\psi$  was introduced in constitutive models. Since the time of its initial inception by Been and Jefferies [17] the question of why fabric does not play a role in the definition of the state parameter  $\psi$  was raised but not answered. Hence, in combination with the idea of a fabric tensor evolving towards its critical state value, the ensuing definition of the FAV  $A$  and its critical state value of 1, together with the search for a role of the aforementioned difference  $1 - A$ , came the parallel idea of introducing a common measure of distance from critical state by means of a combination of density distance  $\psi$  and a fabric anisotropy distance  $\psi_A$  defined by  $\psi_A = \hat{\psi}_A(e, p, A) = \hat{e}_A(e, p)(A - 1)$ , in the form of a new parameter  $\zeta$ , called the Dilatancy State Parameter (DSP) and defined by

$$\zeta = \psi - \psi_A = e - \hat{e}_c(p) - \hat{e}_A(e, p)(A - 1) \quad (10)$$

with  $\hat{e}_A(e, p)$  a scalar-valued parameter function of  $e$  and  $p$  in general, such that at critical state where  $A = 1$  and  $e = \hat{e}_c(p)$ , it follows from Eq. (10) that  $\psi_A = 0$  and  $\zeta = \psi = 0$ . Before critical state the DSP  $\zeta$  substitutes the state parameter  $\psi$  in its role in constitutive modeling. Two important points should be mentioned. First, the specific expression for  $\psi_A$  adopted here is not unique and other forms can be suggested as long as  $\psi_A = 0$  when  $A = 1$  at critical state. Second, observe that while at critical state one has  $\zeta = \psi = 0$ , inversely when  $\zeta = 0$  one may instead have  $\psi = \psi_A$  with  $\psi \neq 0$ . This interesting eventuality was identified as the condition of static liquefaction or steady state condition for very loose samples in Li and Dafalias [1], where one can find a more thorough discussion. Thus, steady state is distinctly differentiated from critical state and defined within this new framework of ACST by a mere consequence of setting  $\zeta = 0$  with  $\psi \neq 0$ .

It can be said that the simple form of Eq. (10) embodies all the essential features of an applicable form of the ACST. Furthermore, it expresses analytically the same exactly concept of a translating DSL introduced earlier by a different line of thinking. The link between these two ways can be seen if the DSP can be expressed by  $\zeta = e - e_d$  with  $e_d$  is the so-called dilatancy void ratio on the DSL. The foregoing and Eq. (10) can be graphically illustrated by Fig. 1 and Fig. 2 taken from Li and Dafalias [1]

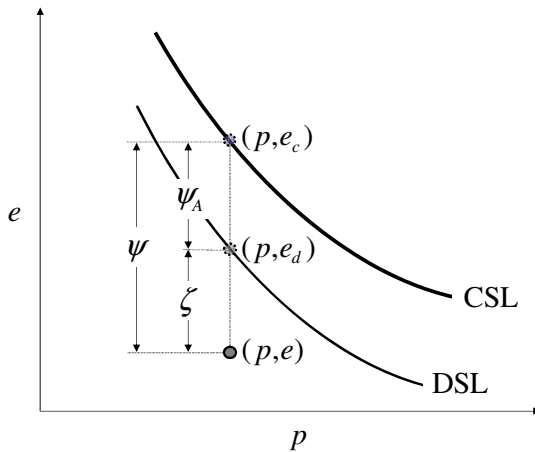


**Fig. 1.** Illustration of the parameters in ACST

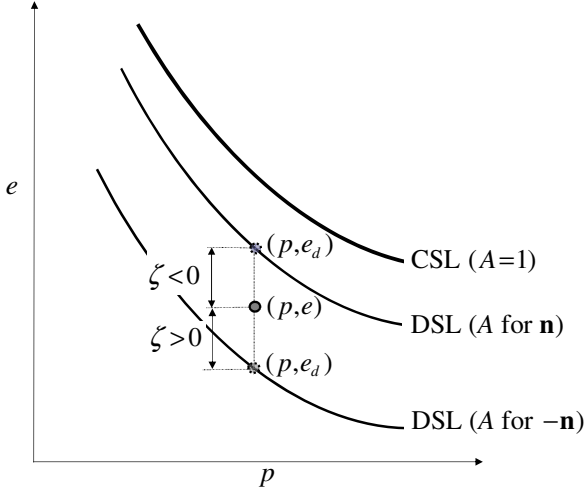


**Fig. 2.** Effects on DSL of a change in loading direction  $\mathbf{n}$  to  $-\mathbf{n}$

Fig. 1 is no more than a direct graphical representation of Eq. (10). Fig. 2 on the other hand, shows another interesting aspect of the theory, namely the effect of changing loading direction. Consider a case where the current values of  $\mathbf{F}$  and  $\mathbf{n}$  specify an  $A > 0$  according to  $A = \mathbf{F} : \mathbf{n}$  that locates a DSL as shown in Fig. 2 by an amount  $\psi_A = \hat{e}_A(e, p)(A - 1)$  as shown in Fig.1 for a given  $p$ - $e$  state. Assume that at this state the loading direction  $\mathbf{n}$  is reversed to  $-\mathbf{n}$ ; the FAV  $A$  will change sign such that the new  $A^* = -A$  will satisfy  $A^* < 0$ , while the  $\psi_A$  will change to  $\psi_A^* = \hat{e}_A(e, p)(A^* - 1) = -\hat{e}_A(e, p)(A + 1)$ , thus, locating the corresponding DSL lower that the previous one, as shown in Fig. 2. It is then possible for the current  $e$  to be located between the two DSL as shown in Fig. 2. It follows that the corresponding DSP  $\zeta$  would be negative or positive according to the loading direction  $\mathbf{n}$  or  $-\mathbf{n}$ , respectively, indicating dilative or contractive trends for the same stress and density state, due only to the change of sign of the loading direction. This is exactly what is often observed in triaxial compression and extension loadings, with the compression being dilative and the extension contractive. This is also what happens in cyclic loading tests upon reversal of shearing direction where dilative response switches to contractive response instantly. In all the cases, however, the corresponding DSL will eventually merge with the CSL when the FAV  $A$  tends towards its critical state value  $A_c = 1$ .

## 6 Future Research Objectives

A very important next step for the validation of the theory is the formulation of complete constitutive models within the framework of ACST. The substitution of

the role of the state parameter  $\psi$  in existing constitutive models by the dilatancy state parameter  $\zeta$  serves as a guiding rule but is not the only way. What is important is to maintain the basic premises of the ACST as expressed by Eqs. (5) in constitutive models of various kinds. Nevertheless, a very simple constitutive model was presented within ACST by Li and Dafalias [1] in the triaxial space, as a first example of the capabilities offered by this new framework. Others will follow.

Other important issues are mainly related to further confirming the attributes of the fabric tensor introduced in ACST either by numerical techniques such as DEM, or experimental techniques such as x-Ray tomographic studies of various aspects of a granular aggregate, such as contact normal orientation distribution, void vectors and particles orientations etc. Such confirmation will include mainly two aspects: the final critical state orientation of the fabric tensor in regards to the loading direction, and the final critical state value of its norm. For both attributes it may be necessary to conduct measurements within shear bands where eventually critical state is reached after large strain. This has been addressed in some 2D DEM simulation by Fu and Dafalias [9].

Conclusions from such studies must be correctly interpreted in terms of what should be the nature of the fabric tensor in its continuum description as an internal variable. It is not just a matter of straightforward transferring DEM or experimental observations to a continuum level because of several issues that preclude such a direct transfer if the theory is to be correct. It should be reminded that some important properties of the fabric tensor in the present theory, such as the decoupling of its critical state norm from the pressure or specific volume, is instrumental in deriving for example the uniqueness of the CSL by use of Gibbs' condition, as recently shown by Li and Dafalias [24]. It is interesting that in the aforementioned reference it was possible to show analytically that the plotting of the critical state norm of the fabric tensor in the  $\pi$ -plane could be reciprocal to the shape of the critical state failure or yield surface. A straightforward transferring of DEM calculations for some definition of fabric tensor, such as the popular contact normal based tensor [25], may lead to some erroneous continuum formulations. A common feature for example of such calculations is the dependence of the critical fabric tensor norm on  $p$ . Without referring to any process off the critical state, this can easily be incorporated in the existing theory by observing that the FAV  $A$  becomes a state function of  $p$  at critical state, thus, the enhanced critical state conditions given by Eqs. (5) can be rephrased with a change of the last condition from  $A=A_c=1$  to  $A=A_c=\hat{A}_c(p)$ , in a similar way to  $e=e_c=\hat{e}_c(p)$ . At first it seems that this is a simple variation of the proposed theory, but in essence it implies more serious aspects which invalidate the proof of uniqueness of CSL by Gibbs' equilibrium condition as already mentioned among other things; it also implies a decoupling of the critical state fabric norm dependence on pressure (or equivalently specific volume) and Lode angle, that has not been shown to be a valid observation. These issues can constitute important future research directions.

## 7 Conclusion

The Anisotropic Critical State Theory (ACST) by Li and Dafalias [1] was outlined, with an emphasis on the way of thinking that lead to this theory, while several details are left out and can be found in the aforementioned publication. The main new idea of ACST is the introduction of a normalized fabric tensor  $\mathbf{F}$  which evolves towards a critical state value norm-wise and direction-wise, thus, introducing one concurrent requirement to those of critical state values for the stress and void ratio of the classical theory. The critical state norm of  $\mathbf{F}$  approaches a normalized value  $F_c=1$ , while the critical state direction of  $\mathbf{F}$  is identical to the loading direction  $\mathbf{n}$ . The introduction of  $\mathbf{F}$  and its evolution was based on various experimental and micromechanical observations on the existence of a strong anisotropic fabric at critical state, notably a recent study of granular fabric by Li and Li [2] based on the concept of void cells. Incorporating the concept and equations of the plastic spin [13], the evolution of  $\mathbf{F}$  was expressed in terms of objective co-rotational rates appropriate for large deformations and rotations normally encountered within shear bands.

The all-important Fabric Anisotropy Variable (FAV) was defined by  $A = \mathbf{F} : \mathbf{n}$  which acquires the value  $A = A_c = 1$  at critical state. The concept of Dilatancy State Line (DSL) was introduced in  $e-p$  space whose difference from the Critical State Line (CSL) depends on  $A$  in such a way that when  $A=1$  at critical state, the DSL becomes identical to the CSL. The contracting or dilating trend of a state depends on the Dilatancy State Parameter (DSP)  $\zeta$ , which is the difference of the current void ratio from the void ratio on the DSL for the same  $p$ , in a role where  $\zeta$  substitutes for the traditional state parameter  $\psi$ . At critical state one has  $\zeta = \psi = 0$  because the DSL converges with the CSL. A corollary of this generic formulation is that the static liquefaction state is shown to occur when  $\zeta = 0$  with  $\psi \neq 0$  thus, it is distinct from the critical state because the fabric anisotropy and void ratio of the former have not yet reached their critical state values. Multiple CSL of past works associated with a fixed initial fabric tensor correspond to interim states of the DSL of the present theory determined by current values of the FAV  $A$ . A thermodynamic proof of the uniqueness of the CSL is presented based on the well-known Gibbs condition of stability. Finally recommendations for future research directions and precautions for correct interpretations of DEM-based observations for continuum description of fabric tensors were presented.

The presentation of the theory was not associated with any specific constitutive model. The key ingredient, the fabric tensor  $\mathbf{F}$ , was used to introduce anisotropy at the critical state in a generic way, and while its role in this respect was instrumental, it should be expected that in various specific constitutive models which can be formulated within ACST, the  $\mathbf{F}$  and the derivative quantity of the FAV  $A$  can play additional constitutive roles fitted to the constitutive model of choice, such as the dependence of the yield function on  $\mathbf{F}$  or  $A$ .

**Acknowledgement.** The research leading to these results has received funding from the European Research Council under the European Union's Seventh Framework Program (FP7/2007-2013) / ERC IDEAS Grant Agreement n° 290963 (SOMEF); and the Research Grant Council of Hong Kong SAR, China, under the grant no. GRF 622910.

## References

- [1] Li, X.S., Dafalias, Y.F.: Anisotropic critical state theory: role of fabric. *J. of Engineering Mechanics*, ASCE 138(3), 263–275 (2012)
- [2] Li, X., Li, X.S.: Micro-macro quantification of the internal structure of granular materials. *J. of Engineering Mechanics*, ASCE 135(7), 641–656 (2009)
- [3] Roscoe, K.H., Schofield, A.N., Wroth, C.P.: On the yielding of soils. *Géotechnique* 8(1), 22–53 (1958)
- [4] Schofield, A.N., Wroth, C.P.: *Critical state soil mechanics*. McGraw-Hill, London (1968)
- [5] Sture, S., Costes, N.C., Batiste, S.N., Lankton, M.R., AlShibli, K.A., Jeremic, B., Swanson, R.A., Frank, M.: Mechanics of Granular Materials at Low Effective Stresses. *J. of Aerospace Engineering*, ASCE 11(3), 67–72 (1998)
- [6] Oda, M.: Initial fabrics and their relations to mechanical properties of granular materials. *Soils and Foundations* 12(1), 17–36 (1972)
- [7] Oda, M.: The mechanism of fabric changes during compressional deformation of sand. *Soils and Foundations* 12(2), 1–18 (1972)
- [8] Masson, S., Martinez, J.: Micromechanical analysis of the shear behavior of a granular material. *J. of Engineering Mechanics*, ASCE 127(10), 1007–1016 (2001)
- [9] Fu, P., Dafalias, Y.F.: Fabric Evolution within Shear Bands of Granular Materials and its Relation to Critical State Theory. *International Journal for Num. and Analytical Methods in Geomechanics* 35, 1918–1948 (2011)
- [10] Li, X.S., Dafalias, Y.F.: Constitutive modelling of inherently anisotropic sand behaviour. *J. of Geotech & Geoenvironmental Engineering*, ASCE 128(10), 868–880 (2002)
- [11] Dafalias, Y.F., Paradimitriou, A.G., Li, X.S.: Sand plasticity model accounting for inherent fabric anisotropy. *J. of Engineering Mechanics*, ASCE 130(11), 1319–1333 (2004)
- [12] Fung, Y.C.: *Foundations of Solid Mechanics*. Prentice-Hall, Englewood Cliffs (1965)
- [13] Dafalias, Y.F.: The plastic spin. *Journal of Applied Mechanics* 53, 865–871 (1985)
- [14] Wang, C.C.: A new representation theorem for isotropic functions. *Archive for Rational Mechanics and Analysis* 36, 166–223 (1970)
- [15] Papadimitriou, A.P., Dafalias, Y.F., Yoshimine, M.: Plasticity modeling of the effect of sample preparation method on sand response. *Soils and Foundations* 40(2), 109–124 (2005)
- [16] Dafalias, Y.F., Manzari, M.T.: A simple plasticity sand model accounting for fabric change effects. *J. of Engineering Mechanics*, ASCE 130(6), 622–634 (2004)
- [17] Been, K., Jefferies, M.G.: A state parameter for sands. *Géotechnique* 35(2), 99–112 (1985)
- [18] Jefferies, M.G.: NorSand: a simple critical state model for sand. *Géotechnique* 43(1), 91–103 (1993)

- [19] Manzari, M.T., Dafalias, Y.F.: A critical state two-surface plasticity model for sands. *Géotechnique* 47(2), 255–272 (1997)
- [20] Gajo, A., Muir Wood, D.: Severn-Trent sand: a kinematic-hardening model for sands: the q-p formulation. *Géotechnique* 49(5), 595–614 (1999)
- [21] Li, X.S., Dafalias, Y.F.: Dilatancy for cohesionless soils. *Géotechnique* 50(4), 449–460 (2000)
- [22] Wood, M.D., Belkheir, K., Liu, D.F.: Strain softening and state parameter for sand modelling. *Géotechnique* 44(2), 335–339 (1994)
- [23] Yoshimine, M., Ishihara, K., Vargas, W.: Effects of principal stress direction and intermediate principal stress on undrained shear behavior of sand. *Soils and Foundations* 38(3), 179–188 (1998)
- [24] Li, X.S., Dafalias, Y.F.: A thermodynamic perspective of critical state in soil mechanics and the uniqueness of critical state line. In: *Third International Workshop on Modern Trends in Geomechanics*, Nottingham, UK, September 4-5 (2012)
- [25] Oda, M.: Fabric tensor for discontinuous geological materials. *Soils and Foundations* 22(4), 96–108 (1982)

# Disturbed State Concept (DSC) for Constitutive Modeling of Geologic Materials and *Beyond*

Chandrakant S. Desai

Regents' Professor (Emeritus), The University of Arizona, Tucson, AZ 85721, USA

**Summary.** The disturbed state concept (DSC) has been used for constitutive modeling of soils (sands and clays). It has been also used for other materials such as rocks, rockfill, asphalt, concrete, silicon, polymers, and interfaces and joints. Because of its generality and unified nature, it has found applications for topics such as active and passive earth pressures, and representation of transfer function for piles. It also can include critical state and self organized criticality (SOC) as special cases. This paper presents a brief description of the DSC and then lists publications by *the Author and Coworkers*, and “*by Other Researchers*” on the DSC and its applications. A review is also presented about other available models for Geomaterials and the rationale for the need and development of the DSC.

**Keywords:** disturbed state concept, generalized plasticity, damage mechanics, constitutive models, engineering materials, geomaterials.

## 1 Introduction

The *disturbed state concept* (DSC) has been published in many technical papers and the book by the author [1]. Hence, the purpose of this paper is mainly to present a brief description of the approach, and concentrate on a compilation of publications and use (by the author and coworkers and other researchers) of the DSC for constitutive modeling of geologic materials (soils and rocks), and *beyond*. Because of its unified and fundamental bases with roots in mechanics and philosophy, it has been used *beyond* geomaterials also, e.g., for modeling interfaces and joints, and other materials such as concrete, asphalt polymers, ceramics, metals and alloys and silicon. It has been also used as a basis for other topics such as derivation of active and passive earth pressures and transfer function for piles. A review of other available constitutive models for geomaterials is followed by a discussion for the rationale for developing the DSC. It is believed that the DSC can be used to model a wide range of materials and can provide a framework in which the critical state (CS) and self organized criticality (SOC) can be considered as special cases.

## 2 Scope

Brief background of the DSC is given first. Then the content of the paper is divided into various categories of publications as (1) Basic and related publications; (2) Soils (sands and clays); (3) Partially saturated soils; (4) Liquefaction-microstructural instability; (5) Rocks and rockfill; (6) Concrete and masonry; (7) Pavement materials; (8) Structured soils; (9) Interfaces and joints; (10) Metals and alloys; (11) Polymers; (12) Ceramics; (13) Silicon with impurities; (14) Load transfer function for piles; (15) Earth pressures; and (16) DSC, critical state (CS) and self organized criticality (SOC).

A review of available constitutive models is presented and their limitations are identified. Then the rationale for developing the unified and hierarchical DSC is discussed.

## 3 Basic Equations of DSC: Unified and Hierarchical

The DSC is a general, unified and hierarchical approach; a schematic of the basis, specifications and use of the DSC is presented in Fig. 1. A brief description follows.

The basic incremental equations in the DSC for constitutive modeling are

$$d \underline{\underline{\sigma}}^a = (1 - D) d \underline{\underline{\sigma}}^i + D d \underline{\underline{\sigma}}^c + dD (\underline{\underline{\sigma}}^c - \underline{\underline{\sigma}}^i) \quad (1a)$$

$$d \underline{\underline{\sigma}}^a = (1 - D) \underline{\underline{C}}^i d \underline{\underline{\varepsilon}}^i + D \underline{\underline{C}}^c d \underline{\underline{\varepsilon}}^c + dD (\underline{\underline{\sigma}}^c - \underline{\underline{\sigma}}^i) \quad (1b)$$

$$d \underline{\underline{\sigma}}^a = \underline{\underline{C}}^{DSC} d \underline{\underline{\varepsilon}}^i \quad (1c)$$

where  $\underline{\underline{\sigma}}$  and  $\underline{\underline{\varepsilon}}$  = stress and strain vectors, respectively, a, i and c denote observed, relative intact (RI) or continuum and adjusted (FA) states in a deforming material element, respectively;  $\underline{\underline{C}}^i$   $\underline{\underline{C}}^c$  denote the constitutive matrices for the RI and FA parts, respectively; and  $\underline{\underline{C}}^{DSC}$  is the coupled constitutive matrix. The coupling between RI and FA parts is represented by the disturbance, D, and dD denotes increment of D.

The disturbance can represent softening or degradation. It can also represent healing or stiffening in the material. It can be expressed in terms of stress, volumetric strain, pore water pressure, nondestructive property (e.g., P and S waves) and entropy [1].

If D = 0, Eq. (1) reduces to

$$d \underline{\underline{\sigma}}^i = \underline{\underline{C}}^i d \underline{\underline{\varepsilon}}^i \quad (2)$$

where  $\tilde{C}^i$  can be represented by elastic, plastic or creep models from continuum mechanics. They are often used as models for the RI behavior. The FA behavior can be represented as having (1) zero strength as in the classical damage model, which is not preferable because it ignores the coupling and may cause computational difficulties, (2) bulk strength as constrained liquid, and (3) as strength under critical state where irrespective of the initial density, the material reaches a critical condition when further shear stress does not cause volume change.

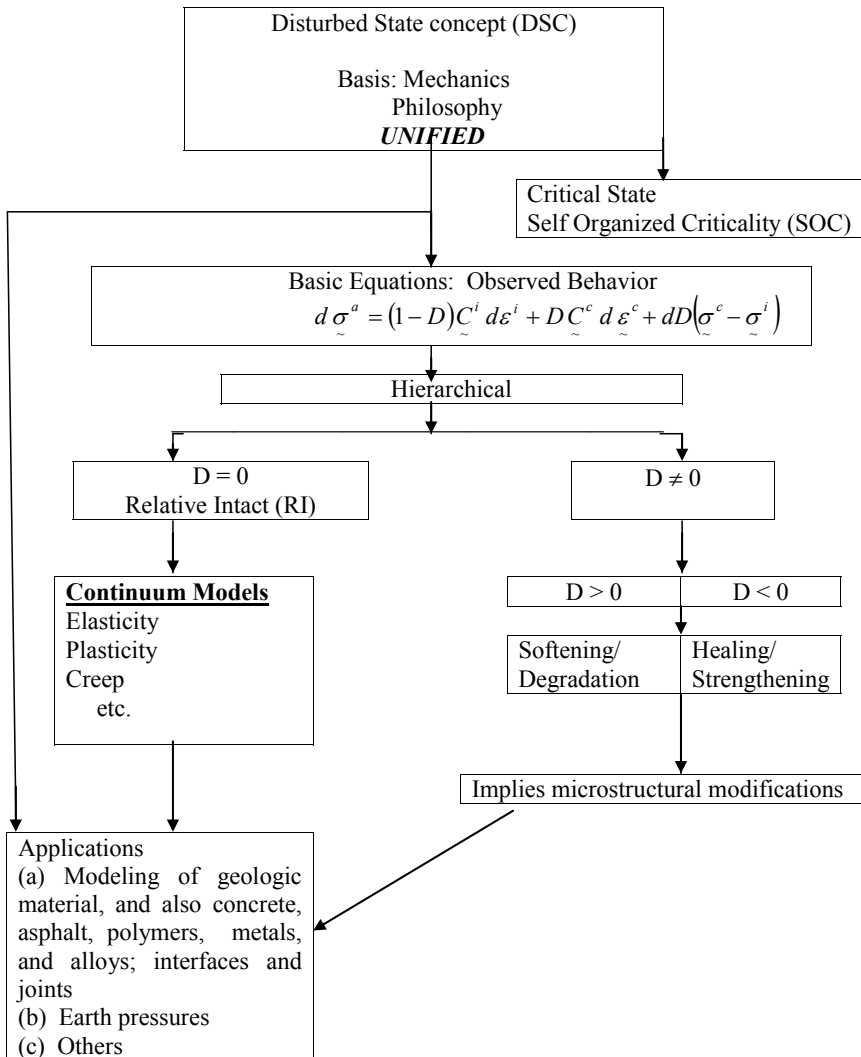


Fig. 1. Schematic of DSC: Basis and Applications

The DSC has been applied by the author and coworkers for a wide range of materials, interfaces and joints. It is implemented in nonlinear finite element procedures. It is validated at the specimen and boundary value (practical) problem levels.

It has also been used by Other Researchers for a wide range of materials and topics.

The first reference list, (I) For DSC, provides *typical* publications by Author and Coworkers, and by Other Researchers. It may be mentioned that some of the publications in the reference list are adopted from the web site; many more may exist beyond the web. The reference list for the subsequent Review is labeled as (II) For Review and Rationale.

## 4 Review and Rationale for Unified and Hierarchical Model

The literature in constitutive modeling for geologic materials (including interfaces and joints), is very wide. It is gratifying to note that since the behavior of geologic media is complex and challenging compared to some of the other engineering materials, considerable research has been accomplished over the last few decades in developing advanced models. Hence, in this review, attempts are made to include some of those significant developments.

Starting with the use of linear elastic models for geomaterials, subsequent developments have taken place for nonlinear (piecewise) elastic, conventional plasticity, continuous yield plasticity, elastoviscoplasticity, hierarchical single surface (HISS) plasticity and anisotropic yielding. To deal with important characteristic of continuities in geomaterials, models based on damage and fracture mechanics, micromechanics or modification of these models to account for coupling or interaction between continuous and discontinuous parts have been proposed. The disturbed state concept (DSC) has been developed as a unified approach to deal *simultaneously* with both continuous and discontinuous parts of the material [1]. A brief review of various models used for geomaterials is given below. It is designed with the aim to lead that at this time, the DSC is considered to be a foremost approach for modeling geomaterials and interfaces/joints.

### (1) Elastic and Earlier Models [97-99]

Around 1960's, when the computer (finite element) methods were first used for solution of geotechnical problems, very often, linear elastic models were used by assuming that the material was isotropic [1]. Here, the stress-strain equation is expressed as

$$\underline{\underline{\sigma}} = \underline{\underline{C}}^e \underline{\underline{\varepsilon}} \quad (3)$$

where  $\underline{\underline{C}}^e$  is the elastic stress-strain or constitutive matrix

## (2) Nonlinear (Piecewise) Elastic Models [100-104]

Realizing that the behavior of geologic material is nonlinear, but assuming that the response was still elastic, various models were proposed by using data points and mathematical functions to simulate the observed stress-strain response. Chief among these models are

(i) Input stress-strain data points on given curves and find (elastic) modulus as slope between data points related to the computed stress or strain [101],

(ii) Simulation of curves using functions like parabola, hyperbola and splines [100,102,103]. Here the elastic moduli are computed as derivatives (or slope) of the function at computed stress or strain, and

(iii) By expressing the elastic moduli as functions of the stress and strain invariants [104].

The nonlinear incremental form is expressed as

$$d \underset{\sim}{\sigma} = \underset{\sim}{C}_t^e d \underset{\sim}{\varepsilon} \quad (4)$$

where  $d$  denotes an increment and  $\underset{\sim}{C}_t^e$  is the tangent constitutive matrix. Models based on hyper- and hypo-elasticity were tried. However, they do not seem to characterize geologic materials successfully.

Although nonlinear (piecewise linear) elastic models allow for nonlinearity, they can not account for factors such as plastic and creep strain, stress path, volume change, different strengths in different directions, and microcracking leading to softening or degradation.

## (3) Conventional Elastoplastic Models [1, 105, 106]

Models like Tresca, von Mises, Mohr-Coulomb and Drucker-Prager are in the category of conventional plasticity. Behavior under these models is assumed to be linear elastic up to a specific yield condition. The material experiences plastic strains thereafter and behaves like a “fluid” under the yield stress. The yield function,  $F$ , in these models is expressed as

$$F = F(J_i, \alpha_i) \quad (5)$$

where  $J_i$  ( $i = 1, 2, 3$ ) denotes invariant of (deviatoric) stress tensor,  $(S_{ij}) \sigma_{ij}$  and  $\alpha_i$  denote an internal variable like plastic strains (accumulated) and plastic work. While these models allow for plastic behavior beyond the yield point, they do not allow for factors such as creep strains, yielding before the yield point, volume change behavior, different strengths in different direction (except for Mohr-Coulomb model), and softening. The incremental constitutive equations are given by

$$d \underset{\sim}{\sigma} = \underset{\sim}{C}_t^{ep} d \underset{\sim}{\varepsilon} \quad (6)$$

where  $\underset{\sim}{C}_t^{ep}$  denotes elastoplastic constitutive matrix.

#### **(4) Continuous Yielding (Hardening) Model [107, 108]**

An important contribution to modeling the behavior of geologic materials was presented in the critical state (CS) behavior, advanced by Roscoe and coworkers [107]. It was found that the soil (clay) which was tested exhibited a behavior involving yielding almost from the start of loading. In other words, each point on the stress-strain behavior was an yield point, thereby removing the specific yield condition in conventional plasticity models. Irrespective of initial density or void ratio, under a given initial confining pressure, the material shows continuous yield response which approaches the critical state (CS) at which there is no further volume (void ratio or density) change under increasing shear. The constitutive matrix for this category is similar to Eq. (6) except that the yield function is different.

The Cap [108] model developed for cohesionless materials allows for continuous yield and irreversible (plastic) deformations from the beginning. However, the CS and Cap models do not allow for different strength under different stress paths or directions, volume change before peak stress, softening or degradation and healing.

#### **(5) Generalized Plasticity-Multi Yield and Boundary Surface Models [109-115]**

The contributions by Mroz, Zienkiewicz and Pastor [109-111] led toward development of generalized plasticity models. Similar advanced models were proposed as boundary and multisurface models in the contributions by Prevost [112], Dafalias and Hermann [113] and Whittle, Pestana and Kavvadas [114, 115]. Most of these models are based on continuum mechanics, with sometimes *ad hoc* schemes, to allow for discontinuities, still with the continuum assumption. The constitutive matrix for this category is similar to Eq. (6) except that the yield function is different.

These models may not be suited for materials involving microcracking, fracture and degradation or softening. Also, most of these models involve multiple surfaces, sometimes with discontinuities in the yield functions, which may cause computational difficulties.

#### **(6) Single Yield Surface and Continuous Yield**

Desai and Coworkers [1,116, 117] have proposed a general function for yield and plastic potential surfaces which culminated into the hierarchical single surface (HISS) plasticity model. The HISS model is considered to contain most of the previous plasticity models as special cases [1]. Matsuoka and Nakai [118] proposed open yield/failure surface dependent on three principal stresses; Lade and Duncan [119] proposed a similar yield/failure surface. Subsequently, Lade and Kim [120] proposed a single yield surface as in the HISS model. The

constitutive matrix for this category is similar to Eq. (6) except that the yield function is different.

These models allow for continuous hardening, but are still based on the assumptions of continuous media. Hence, they may not be suitable for materials involving microcracking, fracture and degradation or softening.

### (7) Creep Behavior

Various models for viscoelastic (ve) (for primary creep), elastoviscoplastic (evp) (for secondary creep), and combined ve and evp, i.e., viscoelasticviscoplastic (vevp), have been proposed. Such models could be used with the conventional and continuous yield characterizations. One of the commonly used models is that due to Perzyna [121], which the same as the evp model is in the multicomponent MDSC [1]. The incremental form of the creep model can be expressed as

$$d \underline{\underline{\sigma}} = \underline{\underline{C}}^{evp} d \underline{\underline{\epsilon}} \quad (7)$$

where  $\underline{\underline{C}}^{evp}$  is combined elastic and viscoplastic matrix. The available creep models are also based on the assumption of continuous media. Hence, they may not be suitable for discontinuities like microcracking and softening.

### (8) Discontinuous Materials

The foregoing models based on theories of elasticity, plasticity and elastoviscoplasticity assume that the material is a continuum. However, a material can contain discontinuities or dislocations or microcracks before and during deformation in which they can coalesce, grow and lead to fracture and failure. In this case, theories of continuum mechanics may not be valid.

A comprehensive review of various models that account for discontinuities in the material can be found in [122]. This book covers details of models based on micromechanics, damage mechanics, Cosserat theory, gradient theory, disturbed state concept, micropolar continua, and non-local damage mechanics. A brief description of some of the models is given below.

**Damage Mechanics.** Kachanov [123] introduced the (classical) damage mechanics; here it is assumed that the damaged part in the material has no strength, which implies that there is no interaction between undamaged and damaged parts. Many investigators [e.g., 124, 125] have used the damage model often by introducing (micro) crack interaction over the behavior of the continuum or undamaged part. The interaction or coupling between continuum (undamaged) and noncontinuum (damaged) parts is essential for reliable (nonlocal) models.

**Fracture Mechanics.** Fracture mechanics is often used to simulate initiation and growth of cracking in a (continuous) material [126, 127]. However, it is usually necessary to introduce *a priori*, a small crack at a selected location(s) from where cracking may initiate and grow. Since locations of cracking depend on the

material behavior, loading conditions, boundary conditions and initial discontinuities, this approach of introducing such initial crack(s) at specific locations may not be realistic.

**Micromechanics.** The concept of defining material behavior (for particles) at the micro level and then define by integration, the macro level behavior is considered to be sound. However, very often, the constitutive law at the microlevel is defined using test data on macro (finite sized) specimens, while the approach requires characterization at the micro level. This may not be realistic.

**Disturbed State Concept.** A description of the DSC is provided earlier. Here a discussion is presented with respect to other available models, reviewed in the foregoing..

**Factors Affecting Material behavior.** As the above review suggests, significant developments have occurred for development and applications of constitutive models for geomaterials. However, the foregoing models (particularly based on the assumption of continuous media) do not account for one or more of the following factors important for behavior of geologic materials, interfaces and joints.

- (1) Elastic, plastic, creep deformations,
- (2) Stress or load path,
- (3) Volume change from contraction to dilation, and before the peak stress,
- (4) Static, repetitive, dynamic (cyclic) loading, environmental loading,
- (5) Microcracking leading to degradation (softening), fracture and failure,
- (6) Healing or strengthening,
- (7) Microstructural instabilities, like liquefaction, and
- (8) Modeling of interfaces and joints using the same framework as for the 'solid' (soil or rock.)

## 5 Rationale for Unified DSC Model

The author and coworkers have used various available models such as nonlinear elastic, elasto-plastic, viscoplastic, critical state, Cap, and anisotropic hardening, and damage mechanics [1,106]. However, it was realized that such models were not capable of accounting for many significant responses exhibited by soils, rocks, interfaces and joints. This led to the development of, first, the unified and hierarchical single surface (HISS) plasticity models that contained most of the available elasticity and plasticity models as special cases. Then the disturbed concept (DSC), was developed, which allows for discontinuities like microcracking, fracture and failure, and healing or strengthening. The DSC is a unified and hierarchical approach that allows for the characterization of both solids (soils and rocks) and interfaces and joints, and also most of the significant factors as listed above.

The basic idea of the DSC and the HISS plasticity models (used for the RI behavior in the DSC) were initiated in [2, 4, 5, 116, 117]. A general basis for yield

and potential functions in plasticity was proposed in [116]. Then the hierarchical single surface (HISS) plasticity model was derived [117]; this approach involves a single yield surface (without discontinuities), that removes the deficiencies posed by other multisurface yield models. The HISS approach removes also many of the limitations of other models such as critical state and Cap; for instance, HISS (associative) model provides volume change transition before the peak stress, different strengths along different stress-paths and modification to include nonassociative behavior and anisotropy [1].

The idea of disturbance was implied in defining the overconsolidated behavior [2], and adopting co-efficient of permeability with pressure (negative and positive) for procedures to solve for free surface seepage problems [4, 5].

The DSC is also based on the idea from physics that the behavior of a material composed of more than one component can be expressed in terms of that of the components. This approach is different from the classical damage mechanics which is based on the idea of physical cracking (or damaged) part which has no strength and does not interact with undamaged part. As discussed in [1], the concept can be considered to have deep roots on philosophy of *Vedas* (India) and *Daoism* (China), for understanding the behavior of matter. In *Vedas*, material is divided into two interacting components, *sat* and *asat*, which means existence and nonexistence; and in *Daoism* the matter is divided into two components, Yin and Yang.

One of the important attributes of the DSC is that its mathematical basis can be used to specialize for interfaces and joints. This is significant because in the past, often different models were adopted for “solids” (soil or rock), e.g., plasticity, and for interfaces, e.g., bilinear elastic, which is inconsistent.

With the above review, it can be concluded that the DSC provides a unified and powerful approach to characterize behavior of soils, rocks, interfaces and joints, by allowing for almost all important factors cited above. It has been applied to model behavior of clays, sands, concrete asphalt, metals, alloys, silicon, polymers and interfaces/joints [1]. Its mathematical and numerical characteristics are also investigated to find that it provides a nonlocal model which is considered to be free from spurious mesh dependence, and also provides for proper convergence [6, 7].

## 6 Presentation at Symposium

Because of various reasons, e.g., the time limitations, this paper contains only a brief review of available models, rationale for the DSC approach, brief description of the DSC with citations of publications by the Author and Coworkers and by Other Researchers. However, the presentation of the paper at the Symposium in Beijing (2012) will cover details such as

- (1) Review of constitutive models for geomaterials and interfaces/joints,
- (2) Basic aspects and equations of the DSC,
- (3) Use for a wide range of materials and for other topics,
- (4) Testing and parameter determination,
- (5) Validations at the specimen level,

- (6) Validations and applications at the boundary value problem level, for a wide range of topics in engineering,
- (7) Topics beyond material modeling, and
- (8) Applications by the author and coworkers and by other researchers.

## 7 Conclusions

A review of various constitutive models for geomaterials, interfaces and joints is included. Description of the DSC approach is presented, and its rationale and advantages are also described. Typical publications by the author and coworkers and by other researchers on the use of the DSC for wide range of materials and topics are included to illustrate general and unified nature of the concept and its usefulness.

### PUBLICATIONS

#### (I) FOR DSC

##### (1) BASIC AND RELATED PUBLICATIONS

- [1] Desai, C.S.: *Mechanics of Materials and Interfaces: The Disturbed State Concept*. CRC Press, Boca Raton (2001)
- [2] Desai, C.S.: A consistent numerical technique for work softening behavior of geologic media. In: *Proc., Int. Conf. on Computational Methods in Nonlinear Mechanics*. Univ. of Texas Press, Austin (1974)
- [3] Desai, C.S., Sherman, W.C.: Unconfined transient seepage in sloping banks. *J. of Soil Mech. and Found. Eng. Division, ASCE* 97(2) (1971)
- [4] Desai, C.S.: Finite element residual schemes for unconfined flow. Short Paper. *Int. J. for Num. Meth. in Eng.* 10 (1976)
- [5] Desai, C.S., Li, G.C.: A residual flow procedure and application for free surface flow in porous media. *Int. J. Advances in Water Resources* 6(1), 27–35 (1983)
- [6] Desai, C.S., Basaran, C., Zhang, W.: Numerical algorithms and mesh dependence in the disturbed state concept. *Int. J. Num. Methods in Eng.* 40 (1997)
- [7] Desai, C.S., Zhang, W.: Computational aspects of disturbed state constitutive models. *Int. J. Computer Methods in Applied Mech. and Eng.* 151, 361–376 (1998)

##### (2) SOILS (SANDS AND CLAYS)

###### By Author and Coworkers

- [8] Wathugala, G.W., Desai, C.S.: Damage based constitutive models for soils. In: *Proc., 12th Canadian Congress on Applied Mechanics*. Carleton Univ., Canada (1989)
- [9] Armaleh, S., Desai, C.S.: Modeling and testing of a cohesionless material using the disturbed state concept. *Int. J. Mech. Behavior of Materials, U.K.* 5(3) (1994)
- [10] Shao, C., Desai, C.S.: Implementation of DSC model and application of analysis of field pile load tests under cyclic loading. *Int. J. Num. Analy. Meth. Geomech.* 44(6), 601–624 (2000)

- [11] Desai, C.S., Wang, Z.: Disturbed state model for porous saturated materials. *Int.J. of Geomech.*, ASCE 3(314) (2003)
- [12] Desai, C.S., El-Hoseiny, K.E.: Prediction of field behavior of geosynthetic-reinforced soil wall. *J. of Geotech. and Geoenv. Eng.*, ASCE 131(6), 209–239 (2005) (Contains DSC modeling for backfill soil and interface between tensar reinforcement and backfill)
- [13] Sane, S., Desai, C.S., Jenson, J.W., Contractor, D.N., Carlson, A.E., Clark, P.V.: Disturbed state constitutive modeling of two pleistocene tills. *Quarterly Science Reviews* 27(3-4), 267–283 (2008)
- [14] Minh, N.H., Suzuki, K., Oda, M., Tobita, T., Desai, C.S.: Numerical simulation using disturbed state concept (DSC) model for softening behavior of sand. *J. of Southeast Asian Geotech. Society* 34(1), 25–35 (2008)
- [15] Akhaveisy, A.A., Desai, C.S., Sadrnejad, S.A., Shakib, H.: Implementation and comparison of generalized plasticity and disturbed state concept for load deformation behavior of foundations. *Scientia Iranica, Transaction A: Civil Engineering* 16(3), 189–198 (2009)
- [16] Desai, C.S., Sane, S., Jenson, J.: Constitutive modeling including creep and rate dependent behavior and testing of glacial tills for prediction of motion of glaciers. *Int. J. of Geomech.*, ASCE 11(6), 465–476 (2011)

### By Other Researchers

- [17] Samieh, A.M., Wong, R.C.K.: Modeling the responses of Athabasca oil sand in triaxial compression tests at low pressure. *Canadian Geotech. J.* 35(2), 395–406 (1998)
- [18] Kim, S.I., Cho, J.S., Park, K.R., Seo, K.B., Lee, J.H.: Simulation of dynamic response of saturated sands using modified DSC model. In: *Proc. 3rd World Congress on Earthquake Eng., Vancouver, Canada* (2004)
- [19] Zhang, Y.T., Wang, C.M., Wang, F., Zheng, H.B.: Stress-strain relationship and analysis of compressive deformation of cohesive soil based on DSC. *Global Geology* 24(2), 200–202 (2005) (in Chinese)
- [20] Zheng, J., Xiurun, G.E., Hong, S.: Application of disturbed state concept to issues in geotechnical engineering. *Chinese J. of Rock Mechanics and Engineering* CNK1:Sun:YSLX:0.2006 – 52-016 (2006)
- [21] Xiang, B.: Coarse grained soil constitutive model based on disturbed state concept and parameters determination. Master's Thesis, Disaster Prevention and Reduction Eng. and Protective Eng., Korea (2006)
- [22] Prochazka, P.P., Valek, M.: Micro-macro behavior of material in soil mechanics. In: *Proc., 5th Int. Conf. on Eng. Computational Technology*, vol. 160. Civil-Comp. Press, Strolingshire (2006)
- [23] Chi, S.H., Xiang, B.: A soil constitutive model based on Disturbed State Concept. *Proc. World Earthquake Eng., Paper CNKI:SUN:SJDC.0.2007-02-021*
- [24] Zheng, J.Y., Ge, S.R., Sun, H.: Meso analysis of rationality of Disturbed State Concept theory considering special area of specimens. *Chinese J. of Geotechnical Eng.*, Paper: CNKI:SUN:YTGC.0.2008-02-018
- [25] Zheng, J.Y., Wu, A.L.: Meroscopic analysis of the utilization of hardening model for a description of softening behavior based on disturbed state concept theory. *J. of Zhejiang Univ. Science A.* 9(9), 1167–1175 (2008)
- [26] Jheng, J., Wu, A.: Finite element analysis of Biot consolidation based on Disturbed State Concept. *Chinese J. of Rock Mech. and Eng.* 8 (2008)

- [27] Tsai, P.M., Lin, P.C.: The optimal material parameters estimation for disturbed state concept model by genetic algorithms. Dept. of Construction Eng., Chaoyang Univ. of Technology, China (2009)
- [28] Yu, X.J., Shi, J.Y., Xu, Y.B.: Modeling disturbed state and anisotropy of natural soft clays. *Rock and Soil Mechanics (China)* 30(11), 3307–3312 (2009)
- [29] Zheng, J.Y.: Macroscopic and mesoscopic parameter introduction into stress-strain relationship description of clayey soils. *J. of Shanghai Jiaotong Univ., Science* (2010)
- [30] Li, J.S., Wang, C.M., Zhang, X.W.: Experimental research in compressive deformation of soft soil based on disturbed state theory. *J. of Jilin Univ. (Earth Science Edition)* CNK1:SUN:CCDZ.0.2010-02-017 (2010)
- [31] Pan, J.: A disturbed state concept of granular material considering physical state. In: *Proc., Int. Conf on Mechanic Automation and Control Engineering*, Wuhan, China, pp. 1268–1271 (2010)
- [32] Wang, G., Pan, J., Tang, B.: An improved method to determine parameters of disturbed state concept constitutive model. *Hydro China Chengdu Eng. Corp., Chengdu* (2010)
- [33] Pan, Y.W., Wang, H.J., Ng, C.W.W.: Effective-stress based dynamic analysis and centrifuge testing of earth dam. *National Chiao-Tung Univ., Hong Kong* (2011) (Powerpoint slides on web)

### **(3) PARTIALLY SATURATED SOILS**

#### **By Author and Coworkers**

- [34] Geiser, F., Laloui, L., Vulliet, L., Desai, C.S.: Disturbed state concept for constitutive modeling of partially saturated porous materials. In: *Proc., 6th Int. Symp. on Numerical Models in Geomech., Montreal, Canada* (1997)

#### **By Other Researchers**

- [35] Zhou, C., Shen, J., Chen, S.S., Chen, T.L.: A hypoplasticity disturbed state model for structural soils. *Chinese J. of Geotech. Eng.* CNKI:SUN:YTGC.0.2004-04-000 (2004)
- [36] Wang, G.X., Xiao, S.F., Huang, H.W., Wu, C.Y.: Study of constitutive model of structural clay based on the disturbed state concept. *Acta Mechanica Solida Sinica* 25(2), 191–197 (2004) (in Chinese)

### **(4) LIQUEFACTION-MICROSTRUCTURAL INSTABILITY**

#### **By Author and Coworkers**

- [37] Desai, C.S., Park, I.J., Shao, C.: Fundamental yet simplified model for liquefaction instability. *Int. J. Num. and Analyt. Meth. in Geomech.* 22, 721–748 (1998)
- [38] Desai, C.S.: Evaluation of liquefaction using disturbed state and energy approaches. *J. of Geotech. and Geoenv. Eng., ASCE* 126(7), 618–631 (2000)
- [39] Park, I.J., Desai, C.S.: Cyclic behavior and liquefaction of sand using disturbed state concept. *J. Geotech. and Geoenv. Eng., ASCE* 126(9), 834–846 (2000)

- [40] Pradhan, S.K., Desai, C.S.: DSC model for soil and interface including liquefaction and prediction of centrifuge test. *J. of Geotech and Geoenv. Eng.*, ASCE 132(2), 214–222 (2006)

### **By Other Researchers**

- [41] Park, I.J., Kim, S.I., Choi, J.S.: Disturbed state concept of saturated sand under dynamic loads. In: *Proc., Earthquake Eng.* (2000)
- [42] Kim, S.I., Choi, J.S., Park, K.B., Seo, K.B., Lee, J.H.: Simulation of dynamic response of saturated sands using modified model. In: *Proc., 13 World Conf. on Earthquake Eng.*, Vancouver, BC, Canada (2004)
- [43] Park, K.B., Park, I.J., Kim, S.I.: Development of modified disturbed state concept model for liquefaction analysis. In: *Geotechnical Eng. for Disaster Mitigation and Rehabilitation*, Korea (2005)
- [44] Park, K., Choi, J., Park, I.J.: Assessment of liquefaction potential based on modified disturbed state concept. *KJCE J. of Civil Engineering* 16(1), 55–67 (2012)

## **(5) ROCKS AND ROCKFILL MATERIALS**

### **By Author and Coworkers**

- [45] Varadarajan, A., Sharma, K.G., Desai, C.S., Hashemi, M.: Analysis of a powerhouse cavern in the Himalayas. *Int. J. of Geomech.*, ASCE 1(1), 109–127 (2001)

### **By Other Researchers**

- [46] Wu, G.: Disturbed state constitutive models of engineering material (I): disturbed state concept and its theory principium and (II) DSC-based numerical simulation of finite element method. *Chinese J. of Rock Mechanics and Eng.* (2002), doi:CNKI:SUN:YSLX.0.2002-06-000
- [47] Varadarajan, A., Sharma, K.G., Venkatachalamy, K., Gupta, A.K.: Testing and modeling of two rockfill materials. *J. of Geotech. and Geoenv. Eng.* 129(3), 206–218 (2003)
- [48] Wu, G., Zhang, L.: Analysis of post-failure behaviors of rock in uniaxial compression using disturbed state concept theory. *J. of Rock Mechanics and Engineering* (2004), doi:CNKI:SUN:YSLX.0.2004.10-007
- [49] Zheng, J.Y., Ge, X.R., Jiang, Y.L., Lu, Y.D.: Parameter calibration and preliminary utilization of disturbed state concept (DSC) method. *J. of Shanghai Univ.*, Index TU452
- [50] Wu, G., Zhang, L.: Studying unloading failure characteristics of a rock mass using the disturbed state concept. *Int. J. Rock Mech. Min. Sci.* 41(3), 437–443 (2004)
- [51] Wu, G., Zhang, L.: Disturbed state model for analysis of the constitutive relationship of sandstone under different strain rates. In: Shen, W.P., Xu, J.Q. (eds.) *Advances in Engineering Plasticity and Its Applications*, pp. 265–270 (2004)
- [52] Wanag, D.L., Ge, X.R.: Application of disturbed state model in stability analysis of 3# section of Three Gorge Dam. *J. of Jiangnan Petroleum Institute (Social Science Edition)* (2005) doi:CNKI: ISSN: 1009-0010.0. 2005-10-032

- [53] Wang, D.L., Ge, X.R.: Constitutive model of rock disturbance status. *J. of Jiangnan Petroleum Institute (Social Science Edition)* (2005), doi:CNKI:ISSN:1009-0010.0.2005-01.030
- [54] Wang, D.L., Shen, J.H., Ge, X.R.: Research on fatigue disturbance model of rock. *J. of Water Resources and Architectural Eng.* (2006), doi:CNKI:SUN:FSJS.0.2006.02-008
- [55] Wu, G., He, G.L.: An elasto-plastic constitutive model of rock based on the disturbed state concept theory. *J. of Hohai Univ. (Natural Sciences)* 40272115 (2008)
- [56] Zhang, J.Y., Wu, A.L.: Descriptions of disturbed state concept of rock stress-strain relationship under compression. *J. of Guangdong Univ. of Technology* (2008)
- [57] Prochazka, P., Trckova, J.: Stress and deformation states in underground structures using coupled modeling. *Acta Geodyn., Geomater.* 5(4), 361–375 (2008)
- [58] Zheng, J.Y., Xiu, R., Sun, H.: Triaxial compressive response description of marble based on disturbed state concept theory (2009), doi:CNKI:SUN:SHJT.0.2008.06-021
- [59] Song, Y., Li, S.C.: Mechanics constitutive model of coal-rock based on disturbed state concept (DSC) theory. *J. of Mining Research and Development* (2009), doi:CNKI:SUN:KYYK.0.2009-05-02S
- [60] Xu, Y.J., Pan, J.J., Chu, X.H., Kong, K.: Study of constitutive model for rockfill material based on the disturbed state concept (2010), doi:CNKI:SUN:GCLX.0.2010-06-027
- [61] Pan, J., Wang, G., Bao, R., Xu, H.: Studies on the disturbed state concept constitutive model of the rockfill materials. In: Boltom, M. (ed.) *Geomechanics and Geotechnics from Micro to Macro*, ch. 14. CRC Press, Boca Raton (2010)
- [62] Wu, A., Hao, Y.: Study of rock stress-strain relationship under uni-axial compression. *Academic Publications* (2011) doi:10.1109/ICETCE.2011.5774319
- [63] Khobklang, P., Virmonsatit, V., Jitsangian, P., Nikaz, H.: Constitutive modeling of hydrated cement treated crush rock base with cyclic-loading behavior. In: *Proc., Int. Conf. on Advances in Geotechnical Eng. (ICAGE 2011)*, pp. 351–356. Curtis Univ., Dept. of Civil Eng., Perth, W. Australia (2011)
- [64] Syed, M.A.: *Constitutive modeling of rockfill materials*. Lap Lambert Academic Publishing (2011) (see web site)

## **(6) CONCRETE AND MASONRY**

### **By Author and Coworkers**

- [65] Akhaveissy, A.H., Desai, C.S.: Nonlinear FE analysis of reinforced concrete structures. *Computers and Concrete* (2011) (submitted)
- [66] Akhaveissy, A.H., Desai, C.S.: Unreinforced masonry walls: nonlinear finite element analysis with unified constitutive model. *Archives of Computational Methods in Eng.* 18(4), 485–502 (2011)
- [67] Akhaveissy, A.H., Desai, C.S.: Application of DSC model for nonlinear analysis of reinforced concrete frames. *J. of Finite Elements in Analysis and Design* 50 (2012)

### **By Other Researchers**

- [68] Huang, H.Y.: Evaluating the bearing behavior of damage structural element with disturbed state concept. Master's Thesis, Department and Institute of Construction Engineering, China (2008)

**(7) PAVEMENT MATERIALS****By Author and Coworkers**

- [69] Desai, C.S.: Unified DSC constitutive model for pavement materials with numerical implementation. *Int. J. Geomech.*, ASCE, E. Masad, A. Scarpas (Guest Editors) 7(2), 83–101 (2007)

**By Other Researchers**

- [70] Guide for mechanistic-empirical design of new and rehabilitated pavement structures, National Cooperative Highway Research Program, TRB/NRC, Washington, DC (2004)
- [71] Shi, J.Y.: Research on the disturbed state concept for soft clay roadbed. In: *Proc., Geohunan Int. Conf.: Challenges and Recent Advances in Pavement Technologies and Transportation*, Changsha Hunan, China (2009)

**(8) STRUCTURED SOILS****By Author and Coworkers**

- [72] Liu, M.D., Carter, J.P., Desai, C.S., Xu, K.J.: Analysis of the compression of structured soils using the disturbed state concept. *Int. J. Num. Anal. Meth. Geomech.* 24(8), 723–735 (2000)

**By Other Researchers**

- [73] Wang, G., Xiao, S., Huang, H., Wu, C.: Study of constitutive model of structural clay based on the disturbed state concept. *Acta Mechanica Solida Sinica* (2004), doi:CNKI:SUN:GTLX.0.2004-02-012
- [74] Wang, C.M., Kuang, S.H., Wang, G.C., Xing, Y.O.: A method for describing consolidated-undrained-shear behavior of structured soil. *Rock and Soil Mechanics (China)* 31(7), 2035–2039 (2010)
- [75] Zhou, C., Shen, Z.J., Chan, S.S., Chen, T.L.: A hypoplasticity disturbed state model for structured soils. *Chinese J. of Geotech. Eng* (2004), doi:CNKI:SUN:YTGC.0.2004-04-000

**(9) INTERFACES AND JOINTS****By Author and Coworkers**

- [76] Desai, C.S., Ma, Y.: Modeling of joints and interfaces using disturbed state concept. *Int. J. Num. Analyt. Methods in Geomechanics* 16(9), 623–653 (1992)
- [77] Desai, C.S., Pradhan, S.K., Cohen, D.: Cyclic testing and constitutive modeling of saturated sand-concrete interfaces using the disturbed state concept. *Int. J. of Geomech.*, ASCE 8(4), 286–294 (2005)

**By Other Researchers**

- [78] El-Sakhawy, N.R., Edd, T.B.: Behavior of shaft-sand interface from local measurements. *Transportation Research Record* 1548, 74–80 (1996)

- [79] Pal, S., Wathugala, G.W.: Disturbed state model for sand-geosynthetic interfaces and application to pull-out tests. *Int. J. Num. Analyt. Meth. Geomech.* 22(15), 1873–1892 (1999)
- [80] Fakharian, K., Eugin, E.: Elasto-plastic modeling of stress-path dependent behavior of interfaces. *Int. J. Num. Analyt. Meth. Geomech.* 24(2), 183–199 (2000)
- [81] Seo, M.W., Park, I.J., Park, J.B.: Development of displacement-softening model for interface shear behavior between geosynthetics. *J. of Japanese Geotech. Society of Soils and Foundations* 44(6), 27–38 (2004)
- [82] Hamid, T.B., Miller, G.A.: Elastoplastic constitutive model for unsaturated soil-steel interface. In: Abousleiman, Chen, Ulm (eds.) *Poromechanics-Giot Centennial (1905-2005)* (2005)

## **(10) METALS AND ALLOYS**

### **By Author and Coworkers**

- [83] Desai, C.S., Chia, J., Kundu, T., Prince, J.: Thermomechanical response of materials and interfaces in electronic packaging, part I: unified constitutive model and calibration, and part II: unified constitutive model, validation and design. *J. of Electronic Packaging, ASME* 119(4), 294–300, 301–309 (1997)
- [84] Basaran, C., Desai, C.S., Kundu, T.: Thermomechanical finite element analysis of problems in electronic packaging using the disturbed state concept, part I: theory and formulation, part II: verification and application. *J. of Electronic Packaging, ASME* 120(1), 41–47, 48–53 (1998)
- [85] Zwick, J.W., Desai, C.S., Ferdie, R.D.: Structural reliability prediction of PBGA solder joints with disturbed state concept. In: *Proc., NAFEMS World Congress 1999*, Newport, RI, USA (1999)
- [86] Desai, C.S., Whitenack, R.: Review of models and the disturbed state concept for thermomechanical analysis in electronic packaging. *J. of Elect. Packaging, ASME* 123(1), 19–33 (2001)
- [87] Desai, C.S., Wang, Z., Whitenack, R., Kundu, T.: Testing and modeling of solders using new device: part I – models and testing, part II – calibration and validation. *J. of Electronic Packaging, ASME* 126(2), 225–231, 232–236 (2004)

### **By Other Researchers**

- [88] Basaran, C.: Unified disturbed state concept for metals and alloys. *J. of the Mechanical Behavior of Materials* 10(5-6), 279–310 (1989)
- [89] Basaran, C., Chandaroy, R.: Finite element simulation of the temperature cycling tests. *IEEE Transactions on Components, Packaging and Manufacturing Technology, Part A* 20(4), 530–536 (1997)
- [90] Lu, H., Ridout, S., Bailey, C., Loh, W.S., Pearl, A., Johnson, M.: Computer simulation of crack propagation in power electronic module solder joints in electronic packaging technology and high density packaging. In: *Proc., Int. Conf., ICEPT-HDP 28–31*, pp. 1–6 (2008)

**(11) POLYMERS****By Other Researchers**

- [91] Vallego, M.J., Tarefdar, R.A.: Predicting failure behavior of polymeric composites using a unified constitutive model. *J. of Mechanics* 27, 379–388 (2011)

**(12) CERAMICS****By Author and Coworkers**

- [92] Desai, C.S., Toth, J.: Disturbed state constitutive modeling based on stress-strain and nondestructive behavior. *Int. J. of Solids Structures* 33(11) (1996)

**(13) SILICON WITH IMPURITIES****By Author and Coworkers**

- [93] Desai, C.,S., Dishongh, T., Deneke, P.: Disturbed state constitutive mdoel for thermomechanical behavior of dislocated silicon with impurities. *J. of Applied Physics* 84(4), 5977–5984 (1998)

**(14) LOAD TRANSFER FUNCTION OF PILES****By Other Researchers**

- [94] Liu, Q., Yang, L., Wu, J.: New model of load transfer function for pile analysis based on disturbed state concept. *Frontiers of Architecture and Civil Eng. in China* 1(4), 443–447 (2007)

**(15) EARTH PRESSURES****By Other Researchers**

- [95] Zhu, J.P., Xu, R.Q., Zhu, K., Li, X.R.: Application of disturbed state concept in calculation of earth pressure. *Eklectronic J. Geotech. Eng (EJEE)* 14, Bund, L (2009)

**(16) DSC, CRITICAL STATE (CS), AND SELF ORGANIZED CRITICALITY (SOC)****By Author and Coworkers**

- [96] Desai, C.S.: Disturbed state, critical state and self organized criticality concept. In: Appendix I in *Mechanics of Materials and Interfaces: The Disturbed State Concept*. CRC Press, Boca Raton (2001)

**(II) FOR REVIEW AND RATIONALE**

- [97] Wilson, E.L.: Finite element analysis of two-dimensional structures. Structural Engineering Laboratory Report No. 63-2. The Univ. of California, Berkeley, CA, USA (1962)

- [98] Sherovd, J.L., Woodward, R.J., Gizieski, S.F., Clevenger, W.A.: In: *Earth and Earth-Rock Dams*, pp. 377–383. John Wiley, New York (1963)
- [99] Clough, R.W., Woodward, R.J.: Analysis of embankment stresses and deformations. *J. Soil Mech. Found. Div.*, ASCE 93(4), 529–549 (1967)
- [100] Kundner, R.L.: Hyperbolic stress-strain response: cohesive soils. *J. Soil Mech. Found. Div.* 89(1), 115–143 (1963)
- [101] Desai, C.S., Reese, L.C.: Analysis of circular footing on layered soils. *J. Soil Mech. Found Div.*, ASCE 96(4) (1970)
- [102] Duncan, J.M., Chang, C.Y.: Nonlinear analysis of stress and strain in soils. *J. Soil Mech. Found. Div.*, ASCE 96(5), 1629–1651 (1970)
- [103] Desai, C.S.: Nonlinear analysis using spline functions. *J. Soil Mech. Found. Div.* 97(2) (1971)
- [104] Nelson, I., Baron, M.L.: Application of variable moduli models to soil behavior. *Int. J. Solids Struc.* 7, 399–417 (1971)
- [105] Drucker, D.C., Prager, W.: Soil mechanics and plastic analysis of limit design. *Q. Appl. Math.* 19(2), 157–175 (1952)
- [106] Desai, C.S., Siriwardane, H.J.: *Constitutive laws for engineering materials*. Prentice Hall, Englewood Cliffs (1984)
- [107] Roscoe, K.H., Schofield, A., Wroth, P.C.: On yielding of granular soils. *Geotechnique* 8, 22–53 (1958)
- [108] DiMaggio, F.L., Sandler, I.S.: Material model for granular soils. *J. Eng. Mech.*, ASCE 97(3), 935–950 (1971)
- [109] Mroz, Z., Zienkiewicz, O.C.: Uniform formulation of constitutive equations for clay and sand. In: Desai, C.S., Gallagher, R.H. (eds.) *Mechanics of Engineering Materials*, pp. 415–450. John Wiley and Sons (1984)
- [110] Pastor, M., Zienkiewicz, O.C., Chang, A.H.C.: Generalized plasticity and the modeling of soil behavior. *Int. J. Num. Analyt. Meth. Geomechanics* 14(3), 151–190 (1990)
- [111] Manzanal, D., Pastor, M., Merodo, J.: Generalized plasticity constitutive model based on state parameter. *CMES Computer Modeling in Engineering Sciences* 55(3), 17–20 (2010)
- [112] Prevost, J.H.: Plasticity theory for soils stress-strain behavior. *J. Eng. Mech.*, ASCE 104(5), 1177–1194 (1978)
- [113] Dafalias, Y.F., Hermann, L.R.: Bounding surface formulation of soil plasticity. In: *Proc., Soil Mechanics – Transient and Cyclical Loads*, G.N. Pande, O.C. Zienkiewicz
- [114] Pestana, J.M., Whittle, A.J.: Formulation for unified constitutive model for clays and sands. *Int. J. Numer. Analyt. Meth. Geomech.* 23, 1215–1243 (1999)
- [115] Whittle, A.J., Kavvas, M.J.: Formulation of MIT-E3 constitutive model for overconsolidated clay. *J. Geotech. Eng.*, ASCE 120(1), 173–198 (1993)
- [116] Desai, C.S.: A general basis for yield failure and potential functions in plasticity. *Int. J. Numer. Analyt. Meth. Geomech.* 4, 361–375 (1980)
- [117] Desai, C.S., Somasundaram, S., Frantziskonis, G.: A hierarchical approach for constitutive modeling of geologic materials. *Int. J. Num. Analyt. Meth. Geomech.* 10(3), 225–257 (1986)
- [118] Matsuoka, H., Nakai, T.: Stress-deformation characteristics of soil under three different principal stresses. *Proc., Jap. Soc. Civil Engrs.* (232), 59–70 (1974)
- [119] Lade, P.V., Duncan, J.M.: Elastoplastic stress-strain theory for cohesionless soil. *J. Geotech. Eng.*, ASCE 101(10), 1037–1053 (1975)

- [120] Lade, P.V., Kim, M.K.: Single hardening constitutive model for frictional materials. III. Comparisons with experimental data. *Computer and Geotechnics* 6, 31–47 (1988)
- [121] Perzyna, P.: Fundamental problems in viscoplasticity. *Adv. in Appl. Mech.* 9, 243–277 (1966)
- [122] Mühlhaus, H.B. (ed.): *Continuum model for materials with microstructure*. John Wiley, Chichester (1995)
- [123] Kachanov, L.M.: *Introduction to continuum damage mechanics*. Martinus Nijhoff Publishers, Dordrecht (1986)
- [124] Bazant, Z.P.: Nonlocal damage theory based on micromechanics of crack interactions. *J. of Eng. Mechanics, ASCE* 120, 593–617 (1996)
- [125] Yang, Q., Chen, X., Zhou, W.Y.: On the structure of anisotropic damage-yield criteria. *Mechanics of Materials* 7, 1049–1058 (2005)
- [126] Gdoutos, E.E.: *Fracture mechanics (solid mechanics and its applications)*. Springer, Germany (2005)
- [127] Scavia, C., Castelli, M.: The use of fracture mechanics for the study of the progressive failure in geomaterials. In: *Proc., 12th Int. Conf. on Comp. Meth. and Advances in Geomech (IACMAG)*, Goa, India (2008)

# Three-Dimensional Failure in Geomaterials: Experimentation and Modeling

Poul V. Lade

Department of Civil Engineering  
The Catholic University of America  
Washington, D.C. 20064, USA  
Lade@cua.edu

**Summary.** Experimental evidence and analyses of result of three-dimensional tests show that the shape of the failure surface for geomaterials such as soils is influenced by the intermediate principal stress, shear banding and cross-anisotropy. True triaxial tests on tall specimens indicated that shear banding played an important role in the shape of the 3D failure surface, and analysis of shear banding under 3D conditions showed that the isotropic failure criterion for homogeneous deformations played an important role in the prediction of shear banding. Shear banding occurs in the hardening regime of the stress-strain behavior in the midrange of  $b$ -values from about 0.18 to approximately 0.85. Thus, the 3D failure surface is not continuous and cannot be described by a single expression, but may be obtained by combining the continuous failure surface with results of predictions of shear banding. Experiments performed in all three sectors of the octahedral plane indicate that pluviated sand exhibits cross-anisotropy with lower strength in the horizontal directions than in the vertical direction. Experiments performed in torsion shear with various inclinations of the major principal stress relative to the bedding planes showed a smooth transition in strength from vertical to horizontal, but with a trough near the orientation where shear bands are parallel to the bedding planes.

**Keywords:** geomaterials, modeling, shear band, shear strength.

## 1 Introduction

Experimental evidence and analyses of result of three-dimensional tests show that the shape of the failure surface for soils is influenced by the intermediate principal stress, shear banding and cross-anisotropy.

A considerable amount of test data is available in the literature concerning the three-dimensional shear strength of sand and clay. Much of this data was produced 20–35 years ago. A review of the strength results shows and it has been known for many years that the failure condition is influenced by the intermediate principal stress. However, other factors clearly play a role in the shape of the three-dimensional failure surface.

From analyses of experimental results from true triaxial tests and from torsion shear tests, it appears that several factors have major effects on the size and shape of the three-dimensional failure criterion. These factors include occurrence of shear banding, boundary conditions and/or slenderness ratio of specimens, cross-anisotropy, and stability of the experimental technique [1]. The factors that relate to the behavior of soils, namely shear banding and cross-anisotropy are reviewed, and a common three-dimensional failure criterion for soils is presented.

## 2 Effects of Intermediate Principal Stress

The  $\varphi - b$  diagram is widely used to represent the variation of peak strength under three-dimensional stress conditions, where the friction angle is  $\varphi = \arcsin[(\sigma_1 - \sigma_3)/(\sigma_1 + \sigma_3)]$ , and  $b = (\sigma_2 - \sigma_3)/(\sigma_1 - \sigma_3)$  indicates the relative magnitude of  $\sigma_2$ . The value of  $b$  varies between 0.0 in triaxial compression and 1.0 in triaxial extension.

Representative  $\varphi - b$  relationships obtained for sands in various studies are indicated on the diagrams in Fig. 1. Basically the friction angle increases with  $b$  from 0 to approximately 0.2, and it continues to increase with decreasing rate until  $b$  is near 0.5 or a little higher, after which it decreases slowly until  $b$  is unity.

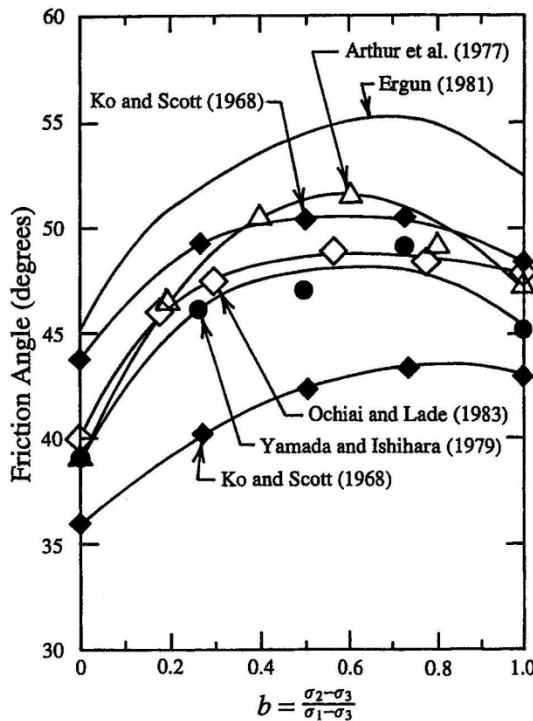


**Fig. 1.** Relationships between friction angle and  $b [= (\sigma_2 - \sigma_3)/(\sigma_1 - \sigma_3)]$  from true triaxial tests on sands with isotropic behavior

### 3 Effects of Shear Banding

For the experimental data shown in Fig. 2, the friction angle increases until  $b$  is near 0.2 after which  $\phi$  becomes constant or it decreases slightly with increasing  $b$ . As  $b$  increases further,  $\phi$  begins to increase again, and it reaches its highest value near  $b = 0.8$  from which it decreases again as  $b$  increases to unity. The friction angles in extension ( $b = 1$ ) shown in Figs. 1 and 2 are considerably higher than those in compression ( $b = 0$ ), and the increases in  $\phi$  are of similar magnitude for the two groups of experimental data. Thus, the difference between the data in Figs. 1 and 2 occurs in the middle section of  $b$ -values.

The reason for this difference has been investigated experimentally. The stress-strain relations obtained from true triaxial tests commonly show continuously decreasing strain-to-failure, more pointed peak, and more rapid strength reduction after the peak for increasing  $b$ -values near and greater than the value at plane strain. This may suggest that pre-failure shear band occurrence is prevalent over a wide range of  $b$ -values. Therefore, failure may be a consequence of the development of shear bands under stress conditions in this midrange of  $b$ -values, and the peak strength may be dependent on the critical condition at which shear banding occurs.

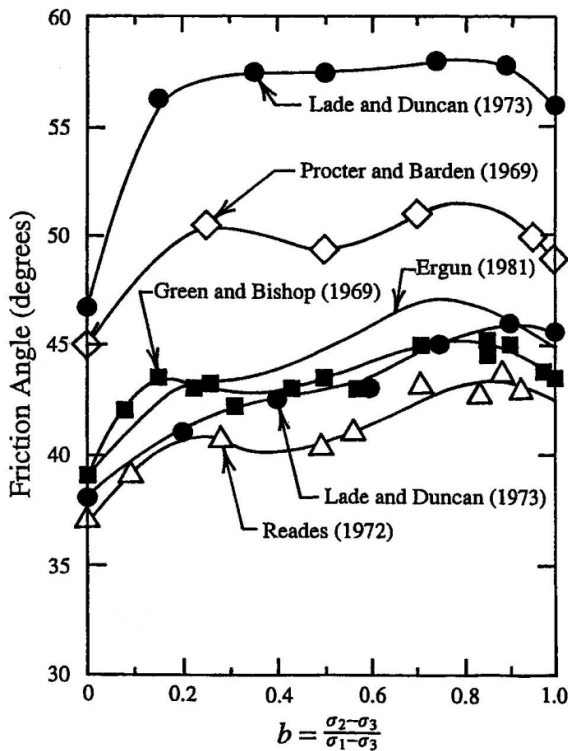
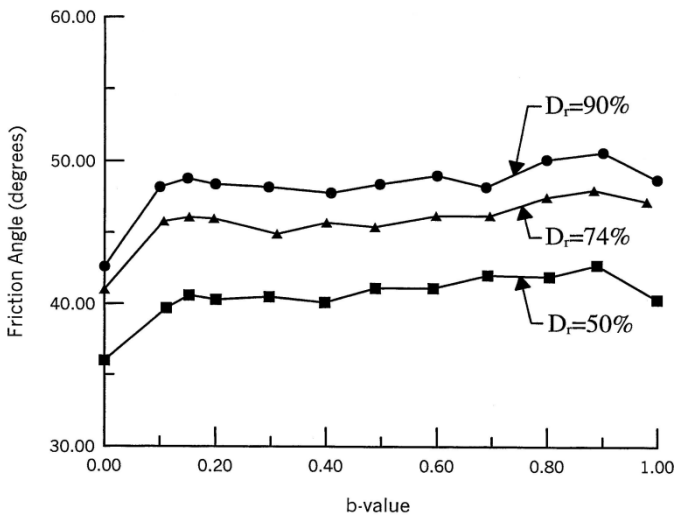


Fig. 2. Relationships between friction angle and  $b [= (\sigma_2 - \sigma_3) / (\sigma_1 - \sigma_3)]$  from true triaxial tests on sands indicating reduction in friction angles in mid-range of  $b$ -values

Experiments have been performed in a true triaxial apparatus on dense, medium dense and loose Santa Monica Beach sand. The cubical triaxial apparatus previously described in [2] was modified to accommodate specimens with a height-to-diameter ratio  $H/D = 2.47$  as explained in [3]. These tall specimens were employed, because shear bands develop more freely and softening behavior is more pronounced in tall and slender specimens. Twelve drained three-dimensional experiments were performed with a constant effective confining pressure of  $\sigma_3' = 49$  kPa and with constant  $b$ -values from 0 to 1.0 for each relative density.

The failure surfaces are shown in Fig. 3 for all three relative densities. They strongly indicate an influence of shear banding in the hardening regime on the peak strength of the material under three-dimensional stress conditions in the midrange of  $b$ -values, including the plane strain condition. It is found in this experimental study that the strength increases as  $b$  increases from 0 to about 0.18, then remains almost constant or even decreases slightly for  $b$  in the range of 0.18 - 0.40. For  $b$  greater than 0.40, the strength increases slowly until  $b$  reaches 0.85, and then decreases slightly at  $b = 1.0$ .

Shear banding initiates in the hardening regime when  $b$  is in the approximate range of 0.18 - 0.85. Failure in these tests is considered to be a consequence of shear banding rather than a continuum response. Thus, peak failure is caused by shear banding in this midrange of  $b$ -values, and a smooth, three-dimensional failure surface is therefore not obtained in general for soils.



**Fig. 3.** Variation of friction angle with  $b$ -value for true triaxial tests on tall prismatic specimens on dense, medium dense, and loose Santa Monica Beach sand with  $\sigma_3' = 49$  kPa

To verify this, the condition for shear band formation proposed in [4] was examined for each test through the computation of the hardening modulus prior to onset of shear banding, as explained in [5]. The predicted shear banding events

were compared with those observed in the experiments, as shown in Fig. 4. In the ranges of low and high  $b$ -values where the shear banding occurs in the softening regime, the smooth peak stress is employed for calculation of the friction angle, while the points of shear banding in the midrange of  $b$ -values correspond to the highest stress point on the stress-strain curves and therefore form the basis for calculation of the friction angles. Thus, shear banding in the hardening regime over the midrange of  $b$ -values clearly produces friction angles that are lower than those anticipated by a smooth failure surface, such as that expected from the failure criterion indicated in [6].

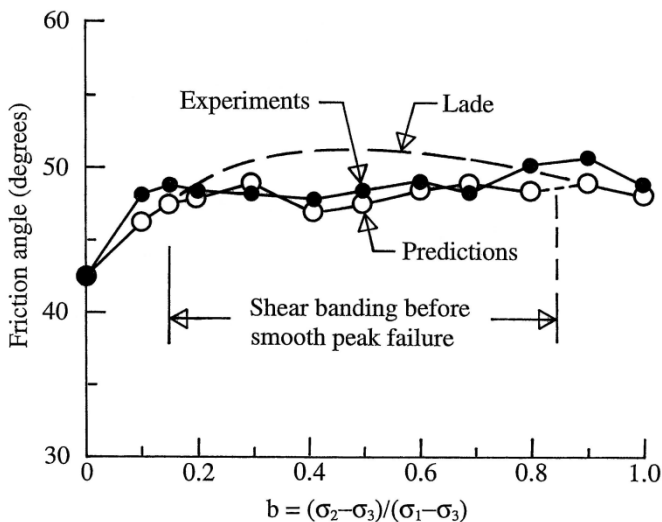


**Fig. 4.** Comparison of measured and predicted friction angles for true triaxial tests on dense Santa Monica Beach sand. Shear banding controls strength in mid-range of  $b$ -values.

This criterion is expressed in terms of the first and the third stress invariants of the stress tensor as follows:

$$\left( \frac{I_1^3}{I_3} - 27 \right) \left( \frac{I_1}{p_a} \right)^m = \eta_1 \quad (1)$$

in which the stress invariants in terms of principal stresses are given as:

$$I_1 = \sigma_1 + \sigma_2 + \sigma_3 \quad (2)$$

$$I_3 = \sigma_1 \sigma_2 \sigma_3 \quad (3)$$

The parameters  $\eta_1$  and  $m$  are constant dimensionless numbers.

In principal stress space, the failure surface is shaped like an asymmetric bullet with the pointed apex at the origin of the stress axes. Fig. 5 shows a comparison of this criterion with the results of true triaxial tests on Cambria sand performed in all three sectors of the octahedral plane. Although this sand was clearly cross-anisotropic in the stress-strain behavior, the failure surface did not exhibit the cross-anisotropic characteristics and no shear banding occurred in the experiments, as explained in [1]. The apex angle for this failure criterion increases with the value of  $\eta_1$ . The failure surface is always concave towards the hydrostatic axis, and its curvature increases with the value of  $m$ . For constant value of  $m$  and increasing  $\eta_1$ -values, the cross-sectional shape in the octahedral plane changes from circular to triangular with smoothly rounded edges in a fashion that conforms to experimental evidence.

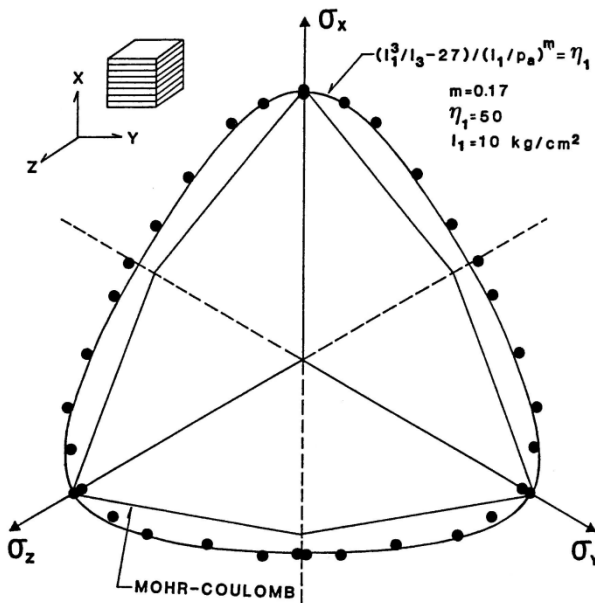


**Fig. 5.** Three-dimensional isotropic failure surface compared with tests on Cambria sand tested in three sectors of the octahedral plane

This failure criterion was a part of the model used to predict the points of shear banding, and these predictions could not have been made with the relative accuracy obtained here unless this criterion had been employed. Thus, the failure criterion, which anticipates the peak failure to be smooth, serves to pull the stress-strain relation up, such that the failure created by shear banding can occur in the hardening regime, i.e. on the way up to smooth peak failure. The failure criterion

in Equation 1 is therefore only correct for low and high  $b$ -values, but for the midrange of  $b$ -values it serves an important role as target (which is never reached due to shear banding) for the condition of smooth peak failure. Exactly where shear banding occurs simultaneously with smooth peak failure between  $b = 0.75$  and  $b = 0.90$  was not determined, but it occurs in this interval of  $b$ -values. The experiments are in agreement with this qualitative and quantitative interpretation of failure in sand under three-dimensional conditions.

Thus, the failure surface for granular material is not a smooth surface that can be described by a single expression, and smooth peak failure is obtained only for the extreme values of  $b$ , while shear banding causes failure in the midrange of  $b$ -values, including plane strain.

### 4 Effects of Cross-Anisotropy

A few sets of data presented in the literature indicate effects of cross-anisotropy. To study effects of cross-anisotropy, true triaxial tests were performed on Santa Monica Beach sand. Dense specimens were prepared by dry pluviation into a special mold, water saturated by the CO<sub>2</sub>-method, and frozen from the bottom up. The specimens were then installed in the cubical triaxial apparatus such that tests could be performed in all three sectors of the octahedral plane [7, 8, 9].

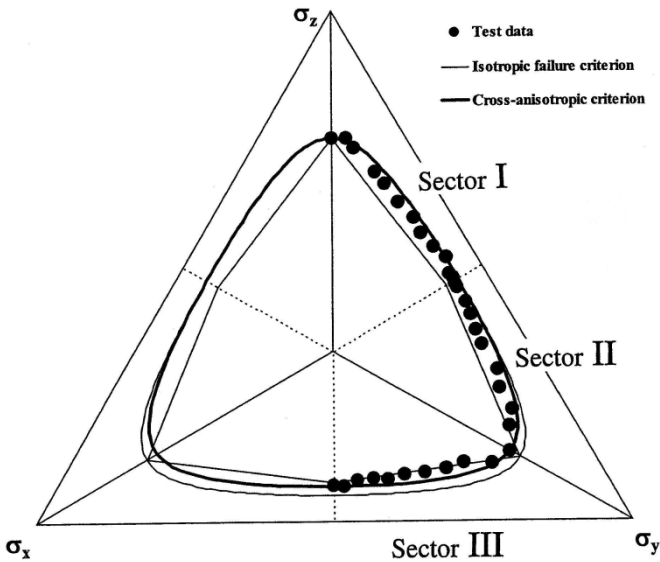


**Fig. 6.** Experimental strength results of true triaxial tests on dense Santa Monica beach sand with cross-anisotropic fabric in octahedral plane

Figure 6 shows the octahedral plane with the strength results plotted on one side of the vertical axis. The Mohr-Coulomb failure criterion and Lade's failure criterion for isotropic soils [6] are also indicated on Fig. 6. Both isotropic criteria have been fitted to the strengths in conventional triaxial compression located at the top of sector I. It is clear that the strength of the sand is affected by cross-anisotropy. Thus, the friction angles in sector III are of magnitudes that fit the friction angle in conventional triaxial compression. In particular, the friction angle in conventional triaxial extension, located at the bottom of sector III, is of similar magnitude as the friction angle in conventional triaxial compression, a result that has been found and confirmed in a multitude of studies performed over the past 40 years using conventional triaxial equipment. Clearly, Figure 6 shows that this result is caused by cross-anisotropic behavior of specimens prepared with cross-anisotropic fabric. Thus, failure in sector III corresponds to lower friction angles than those obtained in sectors I and II.

## 5 Failure Criterion for Cross-Anisotropic Soils

The effects of cross-anisotropic soil structure on the failure of soils loaded under fixed principal stress directions aligned with the principal directions of the cross-anisotropy as well as the effect of principal stress rotation relative to the principal directions of the cross-anisotropic soil, are captured in a failure criterion proposed by Lade [10, 11]. Following the developments of Pietruszczak and Mroz[12, 13], the so-called loading direction relative to the material microstructure directions are specified and defined by a unit vector  $(\ell_1, \ell_2, \ell_3)$ . For cross-anisotropic materials, Pietruszczak and Mroz[12, 13] showed that the expression for the failure criterion becomes:

$$f = \eta_f = \eta_0 \cdot [1 + \Omega_1(1 - 3\ell_2^2)] \quad (4)$$

where  $\eta_0$  and  $\Omega_1$  are constant material parameters. The average value of  $\eta$  is equal to  $\eta_0$  = the radius of a sphere, as shown projected on the octahedral plane in Fig. 7, and the factor  $[1 + \Omega_1(1 - 3\ell_2^2)]$ , which is controlled by the scalar material parameter  $\Omega_1$  and the loading direction  $\ell_2$ , describes the deviation in two dimensions from the sphere (circle in octahedral plane). Thus, the right hand of Eq. 4 describes a shape that is symmetric with regard to the vertical 2-direction, as indicated in Fig. 7.

Combining the expression in Eq. 4 with the expression for the isotropic three-dimensional failure criterion for soils given in Eq. 1 produces the following failure criterion for cross-anisotropic soils:

$$f = \left( \frac{I_1^3}{I_3} - 27 \right) \left( \frac{I_1}{p_a} \right)^m = \eta_0 [1 + \Omega_1(1 - 3\ell_2^2)] \quad (5)$$

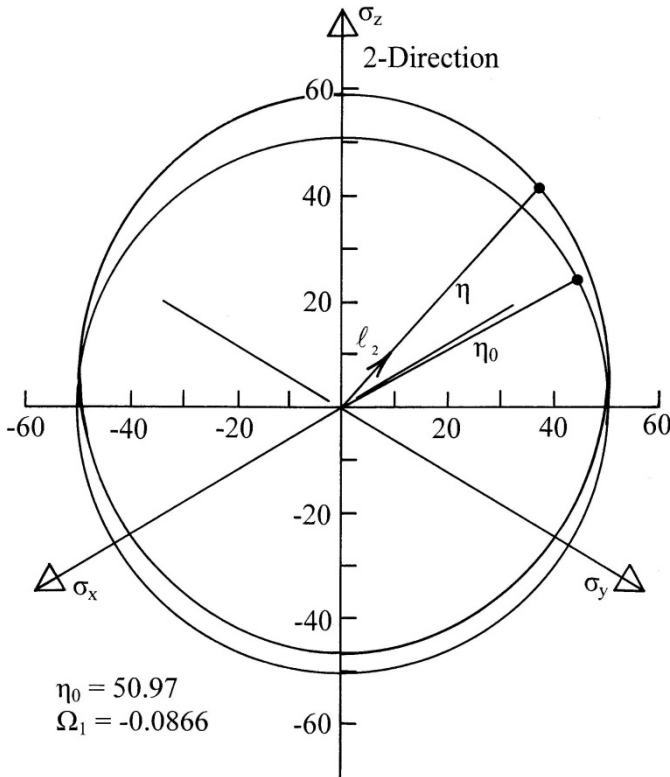


**Fig. 7.** Variation of factor  $\eta = \eta_0 [1 + \Omega_1 (1 - 3\ell_2^2)]$  indicated by the symmetric shape (around the 2-direction) on the octahedral plane for dense Santa Monica Beach sand tested in true triaxial tests

For cross-anisotropic materials tested in common laboratory experiments in which up to 3 different, orthogonal normal stresses and one shear stress can be applied, the expression for  $\ell_2$  becomes:

$$\ell_2 = \sqrt{\frac{\sigma_y^2 \sin^2 \beta + \sigma_z^2 \cos^2 \beta}{\sigma_x^2 + \sigma_y^2 + \sigma_z^2}} \tag{6}$$

in which  $(\sigma_x, \sigma_y, \sigma_z)$  are principal stresses as indicated in Fig. 8.

Comparisons of test data with the failure criterion for the dense Santa Monica Beach sand are indicated in Fig. 6. The material parameters were determined from triaxial compression tests on vertical specimens and one triaxial compression test

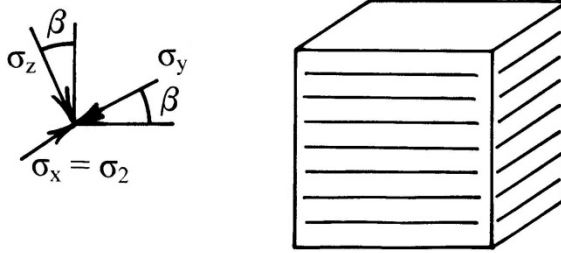


**Fig. 8.** Principal stress conditions possible in true triaxial and torsion shear tests

on a horizontal specimen, as explained in [10]. Fig. 7 shows the variation of the term on the right hand of Eq. 5 for the parameters  $\eta_0 = 50.97$  and  $\Omega_1 = -0.0866$  determined for the dense Santa Monica Beach sand tested in true triaxial tests.

The comparison in Fig. 6 is shown in an octahedral plane. The experimental results and the predictions from the failure criterion are shown for all three sectors. The diagram indicates a good fit for the homogeneous results near  $b = 0$  and  $b = 1$ , while the data in the mid-ranges of  $b$ -values in all three sectors clearly shows the effects of shear banding in the hardening regime, thus resulting in lower friction angles than obtained from the tests with homogeneous deformations. The criterion indicates a friction angle in conventional triaxial extension ( $b = 1$ , sector III) that is  $1.5^\circ$  higher than measured, a result that is acceptable in view of the fact that only the triaxial compression tests were used for parameter determination.

The most noticeable difference between the experimental failure points and the failure criterion, exhibited in Fig. 6, occurs in the mid-ranges of  $b$  where shear banding plays an important role for the shear strength. To analyze the occurrence of shear banding for the dense Santa Monica Beach sand, the homogeneous failure criterion for cross-anisotropic soils presented here is required in the constitutive model to be used for such analyses.

## 6 Effects of Stress Inclination

To study of the behavior of cross-anisotropic sand during shearing with inclined major principal stress direction, a systematic series of torsion shear tests were performed to determine the drained behavior of sand deposited with cross-anisotropic fabric over a range of  $\sigma_1$ -directions relative to vertical from  $\alpha = 0^\circ$  to  $\alpha = 90^\circ$ , and over a full range of intermediate principal stress values as indicated by  $b$  from 0.0 to 1.0. Fig. 9 shows the results of these torsion shear tests. The experiments show a smooth transition in strength as the major principal stress inclination is changed from vertical to horizontal, but with a trough near the orientation where shear bands are parallel to the bedding planes.

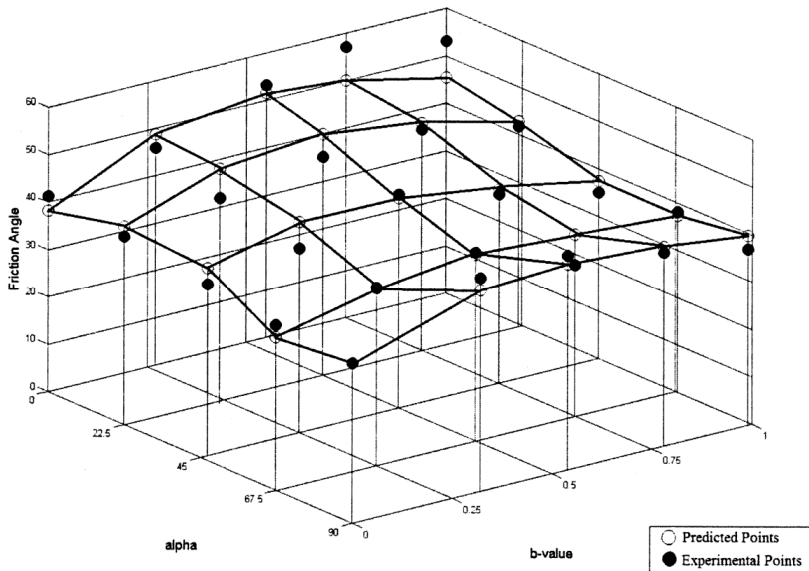


**Fig. 9.** Experimental failure surface from torsion shear tests performed on cross-anisotropic deposits of Fine Nevada sand at a mean normal stress of 100 kPa. A third order expression (Eq. 7) fitted with data points from 25 tests models the failure surface as indicated by the straight lines between points.

The failure criterion in Eq. 5 was augmented to capture this strength variation by a third order expression [14] by expanding the right hand side of the expression:

$$\eta_f = \eta_0 \left[ 1 + \Omega_1 (1 - 3\ell_2^2) + a_1 (\Omega_1 (1 - 3\ell_2^2))^2 + a_3 (\Omega_1 (1 - 3\ell_2^2))^3 \right] \quad (7)$$

in which the parameters  $\eta_0$ ,  $\Omega_1$ ,  $a_1$ , and  $a_3$  are determined by the method of least squares fit based on polynomial regression. The curvature parameter  $m$  in Eqs. 1 and 5 is determined from triaxial experiments with different confining pressures.

## 7 Conclusions

From analyses of experimental results from true triaxial tests on sand, it appears that several factors have major effects on the size and shape of the three-dimensional failure surface and the consequent selection of a representative failure criterion. These factors include the intermediate principal stress, occurrence of shear banding and cross-anisotropy.

The variation of the isotropic three-dimensional strength of sand exhibiting homogeneous behavior (without effects of shear banding) is represented by a smooth triangular failure criterion expressible in terms of the first and the third

stress invariants like that indicated in [6]. Effects of shear banding will cause the failure surface to be “indented” in the midrange of  $b$ -values, possibly extending to  $b = 1.00$ , in all sectors of the octahedral plane. Effects of cross-anisotropic response will result in lower strengths in sector III than in sector I, and the failure surface will appear to have been rotated around the stress origin in the principal stress space. These factors have been reviewed in greater detail in [1], and these effects, as well as the effect of principal stress rotation in physical space, are all captured in a failure criterion for cross-anisotropic soils proposed in [10, 11]. The failure criterion has been further augmented to capture the results of torsion shear tests on cross-anisotropic soil in which the major principal stress is inclined at any angle between vertical and horizontal.

## References

- [1] Lade, P.V.: Assessment of Test Data for Selection of 3-D Failure Criterion for Sand. *Int. J. Num. and Analyt. Meth. Geomech.* 30(4), 307–333 (2006)
- [2] Lade, P.V., Duncan, J.M.: Cubical Triaxial Tests on Cohesionless Soil. *J. Soil Mech. Found. Div., ASCE* 99(SM10), 793–812 (1973)
- [3] Wang, Q., Lade, P.V.: Shear Banding in True Triaxial Tests and Its Effect on Failure in Sand. *J. Engrg. Mech., ASCE* 127(8), 754–761 (2001)
- [4] Rudnicki, J.W., Rice, J.R.: Conditions for the Localization of Deformation in Pressure-Sensitive Dilatant Materials. *J. Mech. Phys. Solids* 23, 371–394 (1975)
- [5] Lade, P.V.: Analysis and Prediction of Shear Banding Under 3D Conditions in Granular Materials. *Soils and Foundations* 43(4), 161–172 (2003)
- [6] Lade, P.V.: Elasto-Plastic Stress-Strain Theory for Cohesionless Soil with Curved Yield Surfaces. *Int. J. Solids Structures* 13, 1019–1035 (1977)
- [7] Abelev, A.V., Lade, P.V.: Effects of Cross-Anisotropy on Three-Dimensional Behavior of Sand. Part I: Stress-Strain Behavior and Shear Banding. *J. Engrg. Mech., ASCE* 129(2), 160–166 (2003a)
- [8] Abelev, A.V., Lade, P.V.: Characterization of Failure in Cross-Anisotropic Soils. *J. Engrg. Mech., ASCE* 130(5), 599–606 (2003b)
- [9] Lade, P.V., Abelev, A.V.: Effects of Cross-Anisotropy on Three-Dimensional Behavior of Sand. Part II: Volume Change Behavior and Failure. *J. Engrg. Mech., ASCE* 129(2), 167–174 (2003)
- [10] Lade, P.V.: Modeling Failure in Cross-Anisotropic Frictional Materials. *Int. J. Solids Structures* 44 (2007a)
- [11] Lade, P.V.: Failure Criterion for Cross-Anisotropic Soils. *J. Geotech. and Geoenv. Engrg., ASCE* 133 (2007b)
- [12] Pietruszczak, S., Mroz, Z.: Formulation of Anisotropic Failure Criteria Incorporating a Microstructure Tensor. *Computers and Geotechnics* 26, 105–112 (2000)
- [13] Pietruszczak, S., Mroz, Z.: On Failure Criteria for Anisotropic Cohesive-Frictional Materials. *Int. J. Num. Analyt. Meth. Geomech.* 25, 509–524 (2001)
- [14] Pietruszczak, S., Peijun, G.: Description of deformation process in inherently anisotropic granular materials. *Int. J. Num. Analyt. Meth. Geomech.* 35 (published on-line November 15, 2011)

# FEM Implementation of Micropolar Hypoplastic Model

J. Lin\* and W. Wu

Institute of Geotechnical Engineering, University of Natural Resources and Life Sciences  
Feistmantelstr. 4, 1180 Vienna, Austria  
jia.lin@boku.ac.at

**Summary.** A constitutive model based on hypoplasticity and micropolar continuum is developed by complex tensor formulations. The new model is simpler than any existing micropolar models. A characteristic length is the only additional material parameter. This model is implemented into ABAQUS and solved by finite element method (FEM). The simulation result of a simple shear test is compared with results of discrete element method (DEM). The comparison shows that the rotations of particles can be fairly well predicted with the micropolar hypoplastic model.

**Keywords:** hypoplasticity, micropolar, constitutive model, granular materials.

## 1 Introduction

In spite of their discrete nature, granular materials can be reasonably well described by continuum models. Recently, hypoplastic model based on nonlinear tensorial functions has attracted much attention [2]. The classical hypoplastic model does not have any internal length scale and therefore cannot account for problems with scale dependence. In granular materials, however, if the domain size is of the order of the mean grain size, the underlying boundary value problem shows scale dependence to some extent. A good example is the formation of shear band in granular materials [1]. There are several approaches to endow the constitutive equation with a characteristic length, e.g. micropolar theory [3], strain gradient theory [8] and nonlocal continuum [9]. The micropolar theory considers the relationship between couple stress and curvature in addition to the stress strain relationship. However, due to the lack of experimental data of micro scale, the couple-curvature relationship cannot be obtained directly. In this paper, the classical hypoplastic model is enhanced with the micropolar variables with the help of a complex formulation [4].

## 2 Formulations

Hypoplastic model is a constitutive model in rate type, which can be expressed as nonlinear tensorial functions:

---

\* Corresponding author.

$$\overset{\circ}{\mathbf{T}} = L(\mathbf{T}) : \mathbf{D} + N(\mathbf{T}) \| \mathbf{D} \| \quad (1)$$

where  $\mathbf{T}$  is the stress tensor,  $\overset{\circ}{\mathbf{T}}$  is objective rate and  $\mathbf{D}$  is the stretching tensor.  $L$  and  $N$  are tensorial functions of  $\mathbf{T}$  and can be obtained with the help of the representation theorems for isotropic tensorial functions. The development and calibration of the model are mainly based on the results of element tests with homogeneous stress and strain. Analog to complex numbers, tensors can also be put into a complex form  $\mathbf{A} + i\mathbf{B}$ , where  $\mathbf{A}$  and  $\mathbf{B}$  are tensors and  $i$  is called the imaginary unit, where  $i^2 = -1$ . In this expression,  $\mathbf{A}$  is called the real part and  $\mathbf{B}$  is called the imaginary part of the complex tensor. If both  $\mathbf{A}$  and  $\mathbf{B}$  are  $n$ th order tensors,  $\mathbf{A} + i\mathbf{B}$  is a  $n$ th order complex tensor. In this way the complex tensors contain the ordinary real tensors while extending them in order to solve problems that cannot be solved with only real tensors. Hence, complex tensors are widely used in theoretical physics and continuum mechanics.

In a micropolar continuum, the statical and kinematical variables  $\mathbf{T}$ ,  $\overset{\circ}{\mathbf{T}}$  and  $\mathbf{D}$  are augmented by the moment stress  $\mathbf{M}$ , its objective rate  $\overset{\circ}{\mathbf{M}}$  and the curvature rate  $\mathbf{K}$ . General stress and strain tensors in complex form substitute into the hypoplastic model, the following complex tensors for the static and kinematic variables can be written out according to the above definition of complex tensors:

$$\mathbf{T}' = \mathbf{T} + i\mathbf{M}/l, \quad \overset{\circ}{\mathbf{T}}' = \overset{\circ}{\mathbf{T}} + i\overset{\circ}{\mathbf{M}}/l, \quad \mathbf{D}' = \mathbf{D} + i\mathbf{K}l \quad (2)$$

Dimension analysis requires that a characteristic length  $l$  need be introduced. The operations for real tensors, such as inner product are defined by Xiao ([5]). Inserting the complex tensors in (2) into the constitutive equation (1) gives rise to

$$\overset{\circ}{\mathbf{T}}' = L(\mathbf{T}') : \mathbf{D}' + N(\mathbf{T}') \| \mathbf{D}' \| \quad (3)$$

All tensors in the above equation have two parts, a real and an imaginary part. By separating the real and imaginary part, two constitutive equations are obtained, one for the stress-strain variables and the other for the moment-curvature variables.

$$\overset{\circ}{\mathbf{T}} = L_1(\mathbf{T}, \mathbf{M}, l) : \mathbf{D} + L_2(\mathbf{T}, \mathbf{M}, l) : \mathbf{K} + N_1(\mathbf{T}, \mathbf{M}, l) \sqrt{\| \mathbf{D} \|^2 + l^2 \| \mathbf{K} \|^2} \quad (4)$$

$$\overset{\circ}{\mathbf{M}} = L_3(\mathbf{T}, \mathbf{M}, l) : \mathbf{K} + L_4(\mathbf{T}, \mathbf{M}, l) : \mathbf{D} + N_2(\mathbf{T}, \mathbf{M}, l) \sqrt{\| \mathbf{D} \|^2 + l^2 \| \mathbf{K} \|^2} \quad (5)$$

The ensuing equations (4) (5) are largely simplified by assuming that the tensors of stress, strain and their rates are symmetric, the tensors of moment stress, curvature and their rates are antisymmetric. These two simplified equations define the micropolar hypoplastic model. This model is simpler than the existing micropolar

models ([3],[6] and [7]). The only additional parameter in this new model is the characteristic length  $l$ . It can be easily determined from the width of shear band. In general, the ensuing equations show coupling between the stress-strain variables and the moment-curvature variables to some extent and are rather complex.

### 3 FEM Implementation and Comparison

This new model is implemented to a 2D FEM element in ABAQUS, each node has three degree of freedom (two translation and one rotation). A simple shear test is simulated with this model. The result is compared with a similar simulation with discrete element method.

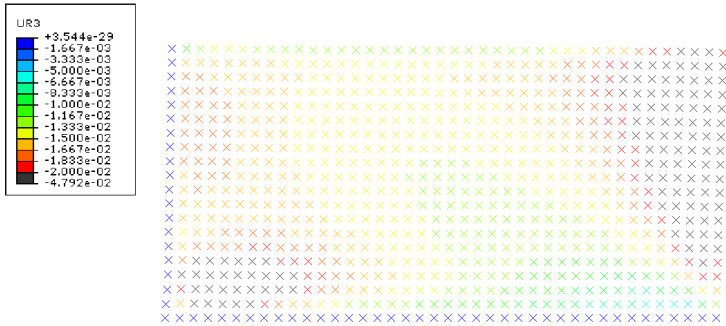


Fig. 1. FEM simulation of simple shear test

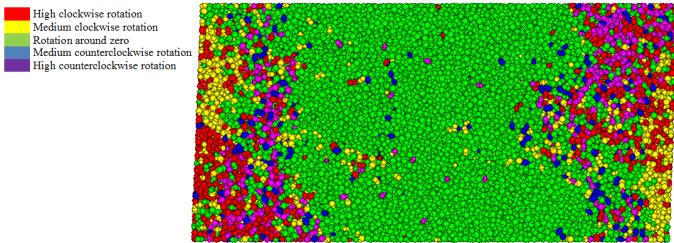


Fig. 2. DEM simulation of simple shear test

Figure 1 is the result of finite element simulation, where crosses are elements, and the colors show the average rotation of the particle. Figure 2 is the result of discrete element simulation, and the colors show the rotation of particles. It can be seen that both FEM and DEM show high rotation on lower left and higher right corner on the sample, while the middle part of the sample is not very significant.

## 4 Conclusions

A new constitutive model for granular materials is developed with complex formulation. This model enhanced the hypoplastic model with micropolar theory. It is simpler than existing micropolar models. Only one additional parameter is needed. The comparison with DEM simulation shows that the new model is able to predict the rotation field in a simple shear test.

## References

- [1] Mühlhaus, H.B., Vardoulakis, I.: The thickness of shear bands in granular materials. *Geotechnique* 37, 271–283 (1987)
- [2] Wu, W., Kolymbas, D.: Numerical testing of the stability criterion for hypoplastic constitutive equations. *Mechanics of Materials* 9, 245–253 (1990)
- [3] Tejchman, J., Bauer, E.: Numerical Simulation of Shear Band Formation with a Polar Hypoplastic Constitutive Model. *Computers and Geotechnics* 19, 221–244 (1996)
- [4] Goddard, J.D.: Granular hypoplasticity with Cosserat effects. In: *AIP Conference Proceedings*, vol. 1227, pp. 323–332 (2010)
- [5] Xiao, H.: On symmetries and anisotropies of classical and micropolar linear elasticities: A new method based upon a complex vector basis and some systematic results. *Journal of Elasticity* 49, 129–162 (1998)
- [6] Tejchman, J., Wu, W.: Numerical study on patterning of shear bands in a Cosserat continuum. *Acta Mechanica* 99, 61–74 (1993)
- [7] Huang, W., Nübel, K., Bauer, E.: Polar extension of a hypoplastic model for granular materials with shear localization. *Mechanics of Materials* 34, 563–576 (2002)
- [8] Osinov, V.A., Wu, W.: Strain-gradient extension of hypoplasticity. *Acta Mechanica* 203(1-2), 37–47 (2009)
- [9] Tejchman, J.: Comparative FE-studies of shear localizations in granular bodies within a polar and non-local hypoplasticity. *Mechanics Research Communications* 31(3), 341–354 (2004)

# Failure Mechanism and Control of Geotechnical Structures

Q. Yang\*, K.D. Leng, Q. Chang, and Y.R. Liu

State Key Laboratory of Hydrosience and Engineering, Tsinghua University, Beijing, China

yangq@tsinghua.edu.cn

**Abstract.** Geotechnical structures are characterized by magnificent scale and complicated configurations and working conditions. Reinforcement design is imperative for such complicated geotechnical structures. To make the reinforcement design effective and targeted, structural failure mechanism under certain actions must be analyzed because reinforcement is essentially aimed at failure control. The deformation reinforcement theory (DRT) provides a feasible solution to determine the structural failure mechanism and corresponding reinforcement force for failure control through elastoplastic finite element analysis. The central concept of DRT is the unbalanced force, which is a set of equivalent nodal forces representing the resistance deficiency of the structure to withstand given actions. The principle of minimum plastic complementary energy (PCE) is proposed: elastoplastic structures under given actions deform tending to the limit steady state at which the unbalanced force is minimized in the sense of PCE. At the limit steady state, the minimized distribution of the unbalanced force reflects the structural failure mechanism, including the failure position and pattern, and determines the optimal reinforcement force to prevent such failure. For geotechnical engineering, DRT can realize a quantitative and pinpoint reinforcement design method and suggest the principles for reinforcement effect evaluation and structural safety monitoring and forecasting. The physical meanings of the principle of minimum PCE and the limit steady state are preliminarily discussed in viscoplasticity and thermodynamics. Four numerical examples and one engineering application verified by geomechanical model test are presented to illustrate the major conclusions.

## 1 Introduction

Geotechnical structures are characterized by magnificent scale and complicated configurations. Take Baihetan arch dam for example, a concrete arch dam of height 289.0m, located at a site where faults and veins are highly developed, more than twenty of which potentially threaten the security of the dam abutments, as shown in Fig.1. Reinforcement design is imperative for such large-scale

---

\* Corresponding author.

geotechnical structures. For this purpose, structural failure mechanism induced by any possible actions must be reflected in three-dimensional (3D) numerical methods, because reinforcement measures are essentially aimed at failure control.

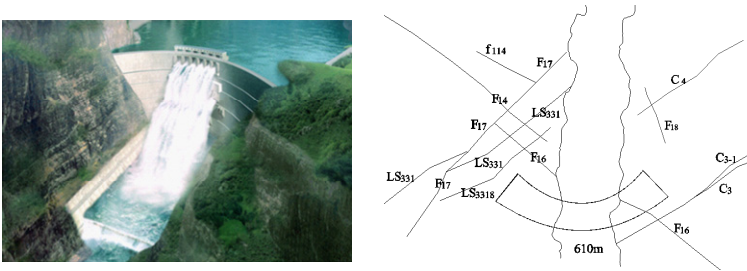


**Fig. 1.** Baihetan high arch dam and the major faults in the abutments

Limit analysis [1-3] may not be so suitable for such complicated structures, but it enlightens some basic points pertaining to structural instability and reinforcement. First, structural stability should be investigated from the generality of instability, which claims a specific stability criterion, as embodied in limit analysis by the upper and lower bound theorems. Second, limit analysis mainly considers rigid-perfect plasticity, which means instability is a structural behavior that is influenced but not dominated by constitutive relations. Finally, as implied by the upper bound theorem, full description of structural instability depends on a collapse or failure mechanism that reflects the position and pattern of the subsequent failure behavior, which is vital to an effective and targeted reinforcement design.

Deformation analyses based on continuum inelasticity can be well applied to large-scale 3D geotechnical structures, among which the finite element method (FEM) is the most comprehensive and adaptable one [4-7]. Nevertheless, a few weaknesses of FEM have long been perceived in practice. On one hand, FEM is efficient in obtaining the structural responses, such as displacement and stress fields and plastic regions, but it is usually difficult to evaluate the global stability of the structure and to determine the structural failure mechanism through these responses. On the other hand, to evaluate the stabilizing effects of the reinforcement measures, the general approach is to model the measures directly, typically, the bolted joints [8] and shotcrete [9]. However, the stabilizing effects obtained by FE analysis are usually much weaker than those observed in engineering practice.

In fact, these problems just dwell in that conventional FEM for elastoplasticity can only turn out the solutions of stable structures. The classical theory of elastoplasticity aims at solving the displacement and stress fields that satisfy all the basic equations in the boundary value problem, including kinematic admissibility, equilibrium condition and constitutive equations. However, the existence of such correct solution implicitly requires that the structure should evolve to a stable state under given actions, namely, a state where no failure occurs. As compensation, we may as well identify instability with non-solution, for example, the non-convergence of the solution algorithm or the singularity of the structural stiffness

matrix [10]. But this definition is obviously not specific enough and still cannot help to determine effective reinforcement measures.

The deformation reinforcement theory (DRT) provides a feasible solution to this problem [11-17]. Basic points of DRT can be loosely summarized as:

- ◆ Structural instability occurs when action is greater than resistance, and the difference between action and resistance defines the unbalanced force;
- ◆ Under given actions, structures deform tending to the limit steady state at which the unbalanced force is minimized;
- ◆ At the limit steady state, the unbalanced force distribution reflects the structural failure mechanism, including the failure position and pattern;
- ◆ The opposite of the unbalanced force determines the optimal reinforcement force to prevent failure.

To embody the very first point, two stress fields must be defined respectively to characterize the external action and the structural resistance, while the standard boundary value problem only involves one stress field. Thus, DRT essentially alters the structure of the standard boundary value problem.

A reinforcement theory should involve two aspects: to locate the most critical area and to determine the required reinforcement force. Owing to the third and fourth points, DRT embodies both the two aspects and thus makes a reinforcement theory for continuum structures. In comparison, the Key Block Theory [18] can be viewed as a reinforcement theory for blocky systems, which proposes that a large blocky system can be stabilized once the key blocks are properly reinforced. To implement such idea, the key blocks are first identified by topology analysis and the reinforcement forces are then determined by limit equilibrium analysis.

In this paper, DRT is introduced in an intelligible logic. In Section 2, a conceptual model of structural instability based on action and resistance is proposed, introduced from the limit equilibrium model of a rigid block and implemented for elastoplastic materials. In Section 3, DRT is established by substantiating this conceptual model in elastoplastic FE analysis, which embodies a quantitative and pinpoint reinforcement design method and suggests the principle for reinforcement effect evaluation. In Section 4, the theoretical basis of the principle of minimum PCE is established in viscoplasticity and some fundamental discussions are made in thermodynamics. In section 5, one engineering application verified by geomechanical model test is presented. The consistency of DRT with observations and existing theories as well as some helpful suggestions for geotechnical engineering are proposed throughout the content.

## **2 Conceptual Model of Structural Instability**

In this section, we propose a conceptual model of structural instability based on action and resistance, which is simple but helpful for understanding the basic points of DRT.

## 2.1 Limit Equilibrium Model of a Rigid Block

Fig.2 shows the limit equilibrium model of a rigid block. Let  $F$  and  $N$  denote the horizontal and vertical actions on the block and  $R$  the horizontal reaction on the contact. The equilibrium condition restricts  $F = R$  while the resistance of the contact requires  $R \leq R_{\max} = \mu N + cA$ , where  $\mu$ ,  $c$  and  $A$  respectively denote the internal friction coefficient, cohesive strength and contact area. Obviously, possible states of the contact include

$$\begin{aligned}
 \text{Stable: } & F < R_{\max} \Rightarrow R = F < R_{\max}; \\
 \text{Limit: } & F = R_{\max} \Rightarrow R = F = R_{\max}; \\
 \text{Unstable: } & F > R_{\max} \Rightarrow R = \text{indeterminate}.
 \end{aligned} \tag{2.1}$$

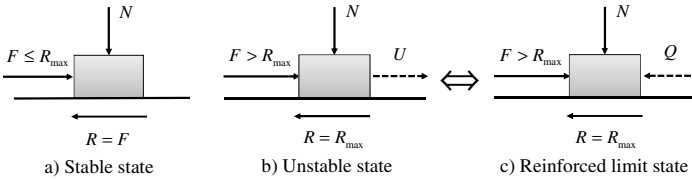


Fig. 2. Stable and unstable states of the rigid contact

As indicated by Equation (2.1c), instability occurs if the action is greater than the resistance, i.e.,  $F > R_{\max}$ , such idea actually borrowed from the reliability theory [19]. Assume that the block is at the critical state just about ready to slip, as we tentatively call it the limit steady state. Base on observations, the reaction at this moment can be assumed to attain the resistance, namely,  $R = R_{\max}$ .

The limit steady state can be interpreted from either the failure or reinforcement points of view. The *unbalanced force* is defined as the deficiency of the resistance to balance the action, denoted  $U$ , which is the driving force of the subsequent failure behavior, as shown Fig.2b,

$$U = F - R = F - R_{\max}. \tag{2.2}$$

On the other hand, if the opposite of the unbalanced force is acted on the block, as shown in Fig.2c, equilibrium regains and a new reinforced limit state is founded. Thus, the unbalanced force can also be understood as the *reinforcement force*,

$$R = R_{\max} = F + Q. \tag{2.3}$$

Their relationship is quite similar to that of the non-equilibrium state and constrained equilibrium state in irreversible thermodynamics [20-22].

In summary, instability occurs if action is greater than resistance. The instability behavior of the contact can be fully described by the postulate of minimum unbalanced force: the contact reacts tending to the limit steady state at which the

unbalanced or reinforcement force is minimized. Note that this postulate naturally encompasses stable states as special cases if the unbalanced force vanishes.

## 2.2 Elastoplastic Material Response

Before extending the conceptual model to structures, we first implement it for elastoplastic materials. For simplicity, we base the formulations on elasto-perfect plasticity with associative flow rule. The constitutive equations may be summarized as

$$\begin{aligned} \dot{\boldsymbol{\varepsilon}} &= \dot{\boldsymbol{\varepsilon}}^e + \dot{\boldsymbol{\varepsilon}}^p, \quad \dot{\boldsymbol{\varepsilon}}^e = \mathbf{C} : \dot{\boldsymbol{\sigma}}; \\ \mathcal{D}^p(\boldsymbol{\sigma}, \dot{\boldsymbol{\varepsilon}}^p) &\geq \mathcal{D}^p(\boldsymbol{\sigma}^{yc}, \dot{\boldsymbol{\varepsilon}}^p), \quad \forall f(\boldsymbol{\sigma}^{yc}) \leq 0, \end{aligned} \quad (2.4)$$

where  $\mathcal{D}^p$  defines the plastic dissipation,  $\mathcal{D}^p(\boldsymbol{\sigma}^{yc}, \dot{\boldsymbol{\varepsilon}}^p) := \boldsymbol{\sigma}^{yc} : \dot{\boldsymbol{\varepsilon}}^p$ . Inequality (2.4c) is known as the principle of maximum plastic dissipation [23], which is a concentrated expression of the flow rule and the Kuhn-Tucker condition.

Let's investigate the discrete form of Equation (2.4). Let  $t$  measure a pseudo-time. Assume that at time  $t_0$  the material state is given by  $\{\boldsymbol{\sigma}_0, \boldsymbol{\varepsilon}_0^p\}$ , which is subjected to a strain increment  $\Delta\boldsymbol{\varepsilon}$  and evolves to a new state  $\{\boldsymbol{\sigma}, \boldsymbol{\varepsilon}^p\}$  during time interval  $\Delta t$ . The linearized plastic strain rate through  $\Delta t$  is

$$\dot{\boldsymbol{\varepsilon}}^p = \frac{\Delta\boldsymbol{\varepsilon}^p}{\Delta t} = \frac{\Delta\boldsymbol{\varepsilon} - \mathbf{C} : (\boldsymbol{\sigma} - \boldsymbol{\sigma}_0)}{\Delta t} = \frac{\mathbf{C} : (\boldsymbol{\sigma}^{eq} - \boldsymbol{\sigma})}{\Delta t}, \quad (2.5)$$

where  $\boldsymbol{\sigma}^{eq}$  is termed the trial elastic stress obtained assuming  $\dot{\boldsymbol{\varepsilon}}^p = 0$ , which can be understood as the *stress action* prescribed on the material point,

$$\boldsymbol{\sigma}^{eq} = \boldsymbol{\sigma}_0 + \mathbf{C}^{-1} : \Delta\boldsymbol{\varepsilon}. \quad (2.6)$$

Applied with Equation (2.5) and after simple manipulations, Inequality (2.4c) can be recast into the following minimization problem whose solution identifies the real stress response  $\boldsymbol{\sigma}$ :

$$\begin{aligned} \min \mathcal{E}_{mat}(\boldsymbol{\sigma}^{yc}), \quad \forall f(\boldsymbol{\sigma}^{yc}) \leq 0, \\ \mathcal{E}_{mat}(\boldsymbol{\sigma}^{yc}) = \frac{1}{2}(\boldsymbol{\sigma}^{eq} - \boldsymbol{\sigma}^{yc}) : \mathbf{C} : (\boldsymbol{\sigma}^{eq} - \boldsymbol{\sigma}^{yc}). \end{aligned} \quad (2.7)$$

Equation (2.7) is known as the closest-point projection method (CPPM) [24-27], which is compatible of elastic responses and holds for hardening plasticity with associative flow rule, as shown in Fig.3.

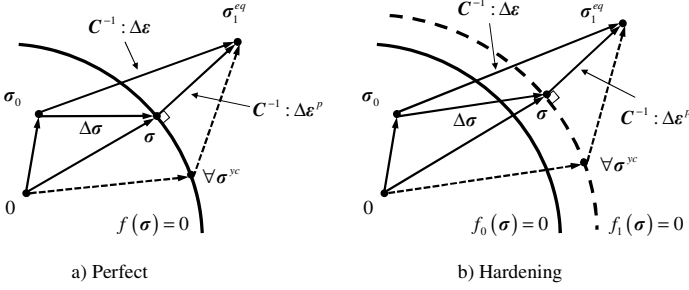


**Fig. 3.** The closest-point projection method for perfect and hardening plasticity

Clearly, the minimization variable  $\sigma^{yc}$  restricted by the yield criterion can be viewed as the *material resistance* while the minimization objective  $\mathcal{E}_{mat}$ , termed the volume density of the plastic complementary energy (PCE), represents the difference between the plastic dissipations of the stress action and the material resistance,

$$\mathcal{E}_{mat} = \mathcal{D}^p(\sigma^{eq}, \Delta\epsilon^p) - \mathcal{D}^p(\sigma^{yc}, \Delta\epsilon^p). \quad (2.8)$$

Thus, instability of a material point can be interpreted as the condition that the stress action is greater than the material resistance in the sense of plastic dissipation:  $\mathcal{E}_{mat} > 0$ ,  $\forall f(\sigma^{yc}) \leq 0$ . This interpretation is similar to the upper bound theorem in limit analysis.

As indicated by the minimization problem, once the material is subjected to a stress action greater than the material resistance, the principle of maximum plastic dissipation requires that the real stress response minimizes the resistance deficiency in the sense of PCE. Therefore, the minimization problem is just an embodiment of the postulate of minimum unbalanced force for elastoplastic materials.

Particularly, the minimization problem can be made explicit for the Drucker-Prager yield criterion. The Drucker-Prager yield function is given by

$$f(\sigma) = \alpha I_1 + \sqrt{J_2} - h, \quad (2.9)$$

where  $I_1 = \text{tr} \sigma$  and  $J_2 = \sigma : \sigma / 2 - I_1^2 / 6$ . If the real stress response  $\sigma$  is determined by Equation (2.7), the following special characteristic can be proved [28],

$$\left. \frac{\partial f}{\partial \sigma} \right|_{\sigma=\sigma} = \left. \frac{\partial f}{\partial \sigma} \right|_{\sigma=\sigma^{eq}}, \quad (2.10)$$

which eventually yields the analytical solution of  $\sigma$ ,

$$\begin{aligned} \sigma &= (1-n)\sigma^{eq} + pI, \quad \text{where,} \\ n &= wG / \sqrt{J_2}, \quad p = -mw + 3nI_1, \\ m &= \alpha(3\lambda + 2G), \quad w = f / (3\alpha m + G), \end{aligned} \tag{2.11}$$

where  $I_1$  and  $J_2$  are invariants of  $\sigma^{eq}$  and  $\lambda$  and  $G$  denote the Lamé constants.

*Example 1. Reinforcement efficiency of a stress state*

Consider a homogenous cylinder subjected to a uniaxial compressive stress of 12.0MPa, as shown in Fig.4. The Drucker-Prager yield criterion is applied with the following material parameters:  $E = 21\text{GPa}$ ,  $\nu = 0.25$ ,  $\alpha = 0.35$ ,  $k = 2\text{MPa}$ , which determines that the uniaxial compressive strength is 8.8MPa.

If the cylinder is reinforced by uniaxial tension, the required tensile stress is 3.2MPa. Alternatively, if the reinforcement stress is determined by Equation (2.7) or equivalently by Equation (2.11), a confining pressure of 0.6MPa is needed, which is only 1/5 of the tensile stress.

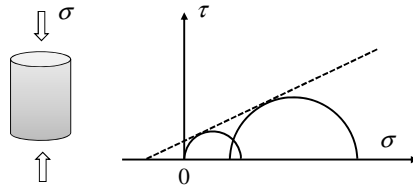


Fig. 4. Reinforcement of a cylinder under uniaxial compression

### 3 Deformation Reinforcement Theory

In this section, we substantiate the conceptual model of structural instability in elastoplastic FE analysis. For simplicity, the problem is restricted in displacement method, which means the kinematic admissibility is naturally satisfied.

#### 3.1 Theory and Examples

Consider a deformable structure of domain  $\mathcal{B}$  subjected to external actions represented by the equivalent nodal force  $\mathbf{F}$ . To embody the conceptual model of structural instability based on action and resistance, two stress field sets are defined, denoted  $S^{eq}$  and  $S^{yc}$ , respectively governed by the equilibrium condition and the yield criterion (considering elasto-perfect plasticity),

$$\begin{aligned} S^{eq} &= \left\{ \boldsymbol{\sigma}^{eq} \mid \mathbf{F} = \int_{\mathcal{B}} \mathbf{B}^T \boldsymbol{\sigma}^{eq} dV \right\}, \\ S^{yc} &= \left\{ \boldsymbol{\sigma}^{yc} \mid f(\boldsymbol{\sigma}^{yc}) \leq 0, \text{ in } \mathcal{B} \right\}, \end{aligned} \quad (3.1)$$

where  $\mathbf{B}$  denotes the displacement gradient matrix. Obviously,  $S^{eq}$  is a stress characterization of external action while  $S^{yc}$  represents structural resistance, both being infinite and convex. The stress state of any non-stationary deformation state should be described by the stress field pair  $(\boldsymbol{\sigma}^{eq}, \boldsymbol{\sigma}^{yc})$ , unless stationarity is reached where they coincide.

In elastoplasticity, the actual stress field is assumed only to satisfy the yield criterion, i.e.,  $\boldsymbol{\sigma} = \boldsymbol{\sigma}^{yc}$ . Hence, the driving force of the deformation process can be termed the *unbalanced force*, also referred to as the residual force in FEM, which is a set of equivalent nodal forces of the difference between the two stress fields,

$$\Delta \mathbf{U} = \int_{\mathcal{B}} \mathbf{B}^T (\boldsymbol{\sigma}^{eq} - \boldsymbol{\sigma}^{yc}) dV = \mathbf{F} - \int_{\mathcal{B}} \mathbf{B}^T \boldsymbol{\sigma} dV. \quad (3.2)$$

As clearly shown in Equation (3.2b), the unbalanced force represents the difference between the external action and the structural resistance. On the other hand, the opposite of the unbalanced force at any deformation state, i.e.,  $\Delta \mathbf{Q} = -\Delta \mathbf{U}$ , is an effective reinforcement force to prevent further deformation.

The principle of minimum PCE is proposed: *under given actions, elastoplastic structures deform tending to the limit steady state at which the unbalanced force is minimized in the sense of PCE*, which is an energy norm of the unbalanced force,

$$\begin{aligned} \min \mathcal{E}(\boldsymbol{\sigma}^{eq}, \boldsymbol{\sigma}^{yc}), \quad \forall \boldsymbol{\sigma}^{eq} \in S^{eq} \text{ and } \forall \boldsymbol{\sigma}^{yc} \in S^{yc}, \\ \mathcal{E}(\boldsymbol{\sigma}^{eq}, \boldsymbol{\sigma}^{yc}) = \int_{\mathcal{B}} \frac{1}{2} (\boldsymbol{\sigma}^{eq} - \boldsymbol{\sigma}^{yc}) : \mathbf{C} : (\boldsymbol{\sigma}^{eq} - \boldsymbol{\sigma}^{yc}) dV. \end{aligned} \quad (3.3)$$

In the above statement, the limit steady state is defined as the deformation state where PCE just reaches its minimum value, as denoted,  $\mathcal{E}_{\min} = \mathcal{E}(\hat{\boldsymbol{\sigma}}^{eq}, \hat{\boldsymbol{\sigma}}^{yc})$ . After the limit steady state, the unbalanced force keeps constant and the structure exhibits steady plastic flow until failure occurs. Note that the limit steady state naturally encompasses stable states as special cases if  $\mathcal{E}_{\min}$  vanishes. Clearly, the principle of minimum PCE is a natural extension of Equation (2.7) to the structural level. One essential difference is that the stress action  $\boldsymbol{\sigma}^{eq}$  should also be treated as a minimization variable.

At the limit steady state,  $\mathcal{E}_{\min}$  makes a quantitative global stability criterion:

$$\mathcal{E}_{\min} = \mathcal{E}(\hat{\boldsymbol{\sigma}}^{eq}, \hat{\boldsymbol{\sigma}}^{yc}) \begin{cases} = 0: & \text{Stable;} \\ > 0: & \text{Instable.} \end{cases} \quad (3.4)$$

Besides, among all stable states where  $\mathcal{E}_{\min}$  vanishes, limit states can be distinguished by the second variation of  $\mathcal{E}_{\min}$  [12, 15]. Therefore,  $\mathcal{E}_{\min}$  makes a scalar function controlling over the global stability of elastoplastic structures.

Meanwhile, the minimized distribution of the unbalanced force at the limit steady state is the driving force of the subsequent failure behavior, which thus concentratedly reflects the structural failure mechanism, including the failure position and pattern. On the other hand, the opposite of the minimized unbalanced force determines the optimal reinforcement force to prevent such failure.

Thus, a visual explanation of the principle of minimum PCE can be proposed: *under given actions, elastoplastic structures deform tending to unleash their maximum resistance while minimizing the unbalanced force or the required reinforcement force.* Clearly, this principle is consistent with the common perceptions and observations on structural failure and reinforcement, for example, the Pan's principles for soil and rock stability [29] and the New Austrian Tunneling Method (NATM) [30, 31], as detailed in the next section.

The relationship between DRT and limit analysis is evident. Equation (3.4) just embodies both the lower and upper bound theorems. At the limit steady state, if  $\mathcal{E}_{\min}$  vanishes, a statically admissible stress field is found, i.e.,  $\sigma = \hat{\sigma}^{eq} = \hat{\sigma}^{yc}$ , indicating that the current load is a lower bound of the limit load. Otherwise, if  $\mathcal{E}_{\min}$  is positive, a failure mechanism is obtained on which the total plastic dissipation of the external action is greater than that of the structural resistance,

$$\mathcal{E}_{\min} = \int_{\mathcal{B}} \mathcal{D}^p(\hat{\sigma}^{eq}, \Delta \epsilon^p) dV - \int_{\mathcal{B}} \mathcal{D}^p(\hat{\sigma}^{yc}, \Delta \epsilon^p) dV > 0, \quad (3.5)$$

which means the current load is an upper bound of the limit load. This also explains the reason why two stress fields must be involved: instability means action is greater than resistance in the sense of total plastic dissipation. On the other hand, DRT also enhances the upper bound theorem, because the failure mechanism obtained by FE analysis is the real failure mechanism with respect to the given action, where the unbalanced force distribution visually reflects the failure position and pattern and determines the optimal reinforcement force.

As proved in Section 4, the principle of minimum PCE holds for associative perfect and hardening plasticity. But non-associative flow rule is universally observed in geomaterials. We may resort to the Radenkovic's theorem [32] to provide a preliminary solution. Radenkovic's first theorem states that, the limit load for a structure made of non-associative material is bounded from above by that for the associative material obeying the same yield criterion. Thus, with the same action and strength, the unbalance force for a non-associative structure should be larger than that for its associative counterpart. Namely, the required reinforcement force should be enlarged in design if non-associative flow rule is considered.

### *Example 2. Homogenous and faulted soil slopes*

In this example, we show the unbalanced force distribution can reflect the failure mechanism. Two soil slopes under dead load are analyzed, one homogenous and the other cut by a fault, as shown in Fig.5. Elasto-perfect plasticity with Drucker-Prager yield criterion is applied with the material parameters given by Table 1.

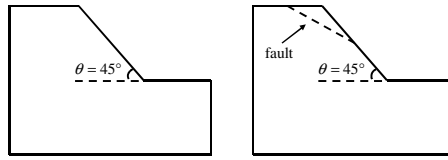


**Fig. 5.** Models of the soil slopes: a) homogenous; b) faulted

**Table 1.** Material parameters of the matrix and the fault

	$E / \text{GPa}$	$\nu$	$\mu$	$c / \text{kPa}$	$\rho / \text{kg/m}^3$
Matrix	10	0.35	0.2	50	2500
Fault	1	0.35	0.1	10	2500

The unbalanced force distribution of the homogenous slope is shown in Fig.6a, which clearly exhibits the shear band of the slope. The unbalanced force distribution of the faulted slope is shown in Fig.6b, which manifests the optimal anchorage direction to stabilize the fault.

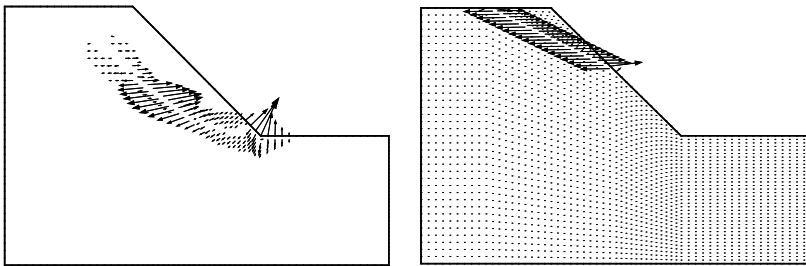


**Fig. 6.** Unbalanced force distribution of the soil slopes: a) homogenous; b) faulted

*Example 3. Semi-infinite foundation*

In this example, we show that the unbalanced force can determine the optimal reinforcement force to prevent failure. Fig.7 shows the slip line solution of a semi-infinite foundation subjected to uniform load  $p$ . Once the load exceeds the limit load  $p_u$ , the uniform pressure  $q$  provided by the embedment can be viewed as a reinforcement force. When  $\varphi = 40^\circ$ , the limit load is increased by  $\Delta p_u = 64.2\Delta q$ . We shall explain such great impact of the reinforcement force.

Fig.8 shows the development of the unbalanced forces in the iterative process when  $p = 1.5p_u$ . At the beginning, the unbalanced forces are concentrated underneath the bearing band and gradually spread sideward and downward with

diminishing magnitudes as the foundation deforms. The final unbalanced forces intensively distribute at the skirted ground surface, pointing upwards, which explains the reinforcement efficiency of the embedment.

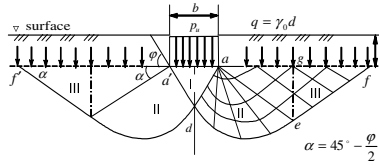


Fig. 7. Slip line solution of semi-infinite foundation subjected to uniform load

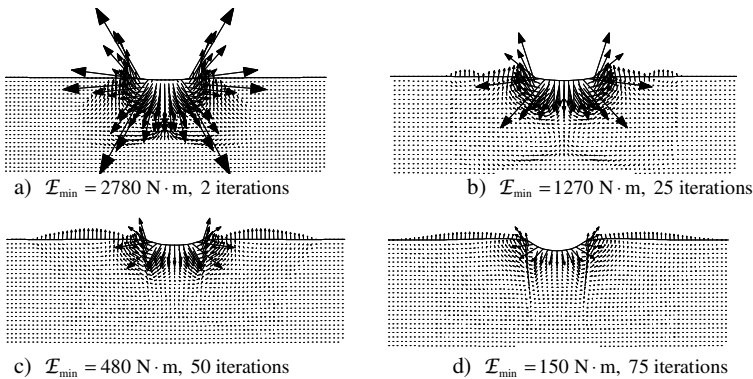


Fig. 8. Development of unbalanced forces of semi-infinite foundation when  $p = 1.5 p_u$

This example also indicates that, reinforcement measures need not to be placed throughout the large plastic region, but only to the real critical areas where unbalanced forces occur. Another illustration is the double underground caverns under dead load, as shown in Fig.9. The unbalanced forces only occur at the pillar and point towards the caverns, clearly reflecting the failure mechanism, while the plastic region has extended to a very wide range. The model tests on anchored tunnels carried out in Ref. [33] also verify the results, as shown in Fig.10. With the same total length of bolts, the short-dense plan is much effective than the long-sparse one to stabilize the surroundings.

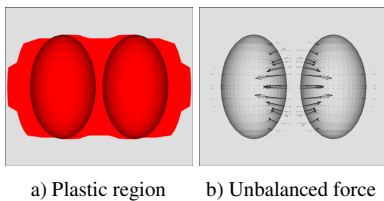


Fig. 9. Plastic region and unbalanced forces of double underground caverns

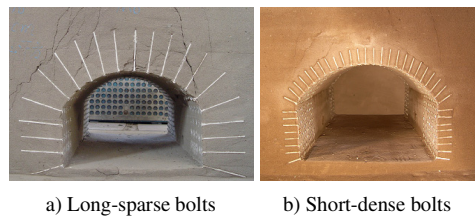


Fig. 10. Fracture pattern of tunnel model reinforced by common bolts [33]

### 3.2 Reinforcement Design and Effect Evaluation

The entire failure procedure of geotechnical structures can be realized by the process of overloading [34] (changing action  $S^{eq}$ ) or strength reduction [5, 6] (changing resistance  $S^{yc}$ ). In the stable states, the times of overloading or strength reduction, denoted  $K$ , can sever as an overall safety factor of a structure. Otherwise, instability can be described by the limit steady state, evaluated with the combination  $(K, \mathcal{E}_{min})$ , which means the structure reaches the safety factor  $K$  with the help of the reinforcement force  $\Delta Q_{min}$ . The  $K \sim \mathcal{E}_{min}$  relation quantitatively characterizes the safety of a structure during the entire failure procedure, as shown in Fig.11, each point on the curve representing a limit steady state. The  $K \sim \mathcal{E}_{min}$  relations of the abutments of the 300m-level high arch dams in China are shown in Fig.12, through which the global stability of the abutments can be comparatively evaluated.

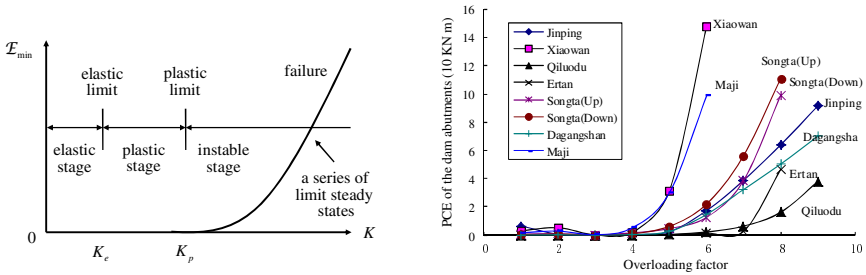


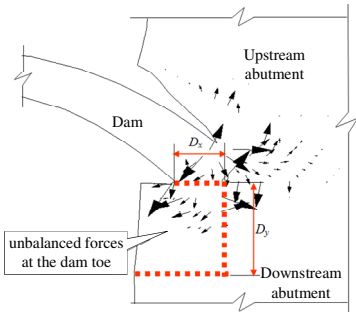
Fig. 11. The  $K \sim \mathcal{E}_{min}$  relation characterizing the failure procedure of a structure

Fig. 12. The  $K \sim \mathcal{E}_{min}$  relations of the high arch dams of 300m-level height in China

There are two limit values of  $K$ , the elastic limit  $K_e$  and the plastic limit  $K_p$ . When  $K \leq K_e$ , the structural response is elastic and the corresponding design method is known as the *strength design* or allowable stress design. Plastic response occurs when  $K$  reaches beyond  $K_e$ , but the structure remains stable if  $K \leq K_p$ , where the design method is known as the *limit design*. If  $K$  increases beyond  $K_p$ , instability occurs and the *reinforcement design* must be carried out. The three design methods deal with different stages of the failure procedure, independent to one another and all indispensable in structural design. Evidently, for geotechnical structures such as slope and tunnel, the reinforcement design is more significant than the first two, because the limit state could be easily exceeded due to various natural or human actions. For example, in engineering classification of rock masses [35, 36], the stability of rock masses are mainly judged by the required reinforcement measures to stabilize them.

DRT actually implements the concept of reinforcement design with the help of unbalanced force. Take the dam toe anchorage design for high arch dams for example. Because of small embedded depth and high stress concentration, the

stability of the dam toes can be very vulnerable and anchorage design is imperative. The unbalanced forces at the dam toe can be statistically summed up at each level to determine the least required anchoring force, as shown in Fig.13. The calculation results for Xiluodu high arch dam (285.5m) is verified by the geomechanical model test and accepted as an important support for the final decision, as shown in Fig.14 and 15.



**Fig. 13.** Unbalance force summation at dam toe for anchorage design **Fig. 14.** An overall view of the foundation excavation of Xiluodu arch dam

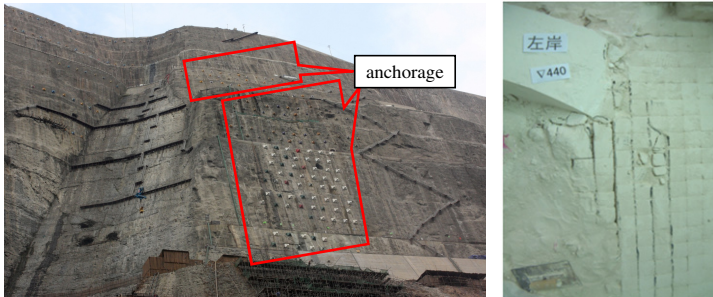


**Fig. 15.** Test results and final anchorage on the left abutment of Xiluodu arch dam

Another notable issue is the effect evaluation of reinforcement measures. Many models have been developed in FEM to simulate the stabilizing effects of the measures, for example, the bolted joints [8] and shotcrete [9]. But the effects obtained by calculations are usually much weaker than those observed in engineering practice. Despite the unrevealed working mechanisms of the reinforcement measures, the inconsistency largely depends on their working conditions.

We propose that *the effects of reinforcement measures must be evaluated in the stage of instability*. In geotechnical engineering, the reinforcement forces provided by the measures are usually self-balancing forces distributed in small regions, for example, the friction piles and bolts. Known from the Saint-Venant's principle, their effects in changing the structural responses such as displacement and stress should be very limited, *if* the reinforced area is initially in a stable state. But this does not mean these reinforcement measures are dispensable. Because once the

structure enters the stage of instability, they will to a large extent stabilize the structure.

## 4 Discussions in Viscoplasticity and Thermodynamics

There are quite a few variational principles proposed for elastoplastic structures [23, 37]. But they essentially differ from the principle of minimum PCE in that they are applicable only for stable states, because all the basic equations in the standard boundary value problem must be referred to in their derivations. In elastoplasticity, the principle of minimum PCE is certainly not a weak form of the standard boundary value problem but more like a postulate, or more exactly, an explanation to the Newton-Raphson method and its derivations [10] through which the unbalanced force is minimized [12, 15].

In fact, the principle of minimum PCE deals with the quasi-static asymptotic stability of deformable structures. Thus, to reveal the physical meaning of this principle, time-dependent deformation process must be investigated, either in viscoplasticity of which elastoplasticity is only a limiting case [38-41], or more generally, in thermodynamics. In this paper, however, we are not able to establish the integrated theoretical basis, but only to make some fundamental discussions.

### 4.1 The Duvaut-Lions Overstress Model

There are mainly two obstacles to manifest the physical meaning of the principle of minimum PCE based on elastoplasticity. First, because no statically admissible stress field exists in the occurrence of instability and stresses violating yield criterion are not admissible in elastoplasticity, two stress fields must be introduced to represent any deformation stress state. This might be an effective description of structural instability but cannot be physically objective. Second, in elastoplastic FE analysis, the deformation process actually takes place in the Newton-Raphson method with time effects neglected. Thus, one may consider that elastoplasticity only focuses on the final deformation state if the algorithmic process is ignored.

Overstress models in viscoplasticity overcome such obstacles. In overstress models of the Perzyna [38] and Duvaut-Lions [39] types, the stress  $\sigma$  is assumed only to satisfy the equilibrium condition and allowed to relax back to the yield surface over time. Here, we apply the Duvaut-Lions model that supports the two stress field method in the most straightforward way. Considering associative flow rule, the Duvaut-Lions model takes the following form,

$$\dot{\epsilon}^{vp} = C : (\sigma - \bar{\sigma}) / \tau, \quad (4.1)$$

where  $\tau$  is a positive parameter and  $\bar{\sigma}$  is the closest point projection of the overstress  $\sigma$  on the yield surface, determined by the minimization problem in Equation (2.7). Obviously, the Duvaut-Lions model is a natural extension of the principle of maximum plastic dissipation [24, 26, 39]: the direction of  $\dot{\epsilon}^{vp}$  coincides with that of  $\dot{\epsilon}^p$  in elastoplasticity and  $\dot{\epsilon}^{vp}$  equals to  $\dot{\epsilon}^p$  when  $\tau = 1$ .

Considering smooth yield surface, one can further obtain the associative orthogonal flow rule,

$$\dot{\boldsymbol{\varepsilon}}^{vp} \propto \left. \frac{\partial f}{\partial \boldsymbol{\sigma}} \right|_{\boldsymbol{\sigma}=\bar{\boldsymbol{\sigma}}}. \quad (4.2)$$

The advantages of the Duvaut-Lions model are obvious. It clearly manifests that the driving force of the viscoplastic deformation is just the difference between the two stress fields of action and resistance. And we show it latter that the Duvaut-Lions form of PCE is fully consistent with that in elastoplasticity. The Perzyna model can be viewed as the penalty formulation of the principle of maximum plastic dissipation [26] and thus the two overstress models are related. In fact, if the Drucker-Prager yield function is used, they are equivalent to each other owing to the property of Equation (2.10). The viscoplastic models of Perzyna and Duvaut-Lions types are often used as an alternative solution to elastoplastic problems. For example, the Perzyna model in Drucker-Prager form was applied by Zienkiewicz and Cormeau [42] to approach to elastoplastic solutions, showing that if the structure can reach a stationary state under given actions, the accuracy is highly acceptable. Silva [43] discussed the viscous regularization of softening elastoplasticity based on the two overstress models. In the next subsection, we show that the equivalence of elastoplasticity and viscoplasticity lays in the principle of minimum PCE, both for stationary and non-stationary cases.

## 4.2 Principle of Minimum PCE in Viscoplasticity

Applying Duvaut-Lions model, the plastic complementary energy is defined as

$$\mathcal{E} = \int_{\mathcal{B}} \frac{1}{2} (\boldsymbol{\sigma} - \bar{\boldsymbol{\sigma}}) : \mathbf{C} : (\boldsymbol{\sigma} - \bar{\boldsymbol{\sigma}}) dV. \quad (4.3)$$

The principle of minimum PCE is proposed: *under time invariant loading and boundary conditions, viscoplastic structures deform tending to the limit steady state at which PCE is minimized. If the minimum PCE turns out to be zero, a new stationary state is reached; otherwise, the structure suffers steady viscoplastic flow by the minimum rate in the sense of PCE until failure occurs.* Note that  $\mathcal{E}$  is non-negative for any deformation states and vanishes only when a stationary state is reached, we only need to prove  $\mathcal{E}$  is monotonically decreasing with time, i.e.,

$$\dot{\mathcal{E}} = \int_{\mathcal{B}} (\dot{\boldsymbol{\sigma}} - \dot{\bar{\boldsymbol{\sigma}}}) : \dot{\boldsymbol{\varepsilon}}^{vp} dV < 0. \quad (4.4)$$

Proof of Equation (4.4):

Time invariant loading and boundary conditions are summarized as

$$\dot{\boldsymbol{f}} = 0, \text{ in } \mathcal{B}; \quad \dot{\boldsymbol{t}} = 0, \text{ on } \partial_{\boldsymbol{\sigma}} \mathcal{B}; \quad \dot{\boldsymbol{u}} = 0, \text{ on } \partial_{\boldsymbol{u}} \mathcal{B}, \quad (4.5)$$

where  $\boldsymbol{f}$  denotes the body force and  $\boldsymbol{t}$  the surface traction. It is easily shown that the following state function must vanish at each moment,

$$\int_{\partial_u \mathcal{B}} \dot{\mathbf{t}} \cdot \dot{\mathbf{u}} dV + \int_{\partial_\sigma \mathcal{B}} \dot{\mathbf{t}} \cdot \dot{\mathbf{u}} dV = \int_{\partial \mathcal{B}} \dot{\mathbf{t}} \cdot \dot{\mathbf{u}} dV = 0. \quad (4.6)$$

Applied with the divergence theorem, and then with the quasi-static momentum equation and the kinematic equation, Equation (4.6) yields

$$\int_{\mathcal{B}} \dot{\boldsymbol{\sigma}} : \dot{\boldsymbol{\varepsilon}} dV = \int_{\mathcal{B}} \dot{\boldsymbol{\sigma}} : (\mathbf{C} : \dot{\boldsymbol{\sigma}} + \dot{\boldsymbol{\varepsilon}}^{vp}) dV = 0. \quad (4.7)$$

Because the first term is always positive except for homogenous creep process, the following inequality is all too obvious,

$$\int_{\mathcal{B}} \dot{\boldsymbol{\sigma}} : \dot{\boldsymbol{\varepsilon}}^{vp} dV < 0. \quad (4.8)$$

Equation (4.7) concentratedly reflects the time invariant loading and boundary conditions and all the basic equations in the boundary value problem except the kinetic equation that specifies the evolution law of the inelastic strain rate. Thus, Inequality (4.8) holds for a wide range of overstress constitutive relations, not limited to Duvaut-Lions and Perzyna model in viscoplasticity.

On the other hand, the loading/unloading condition ensures that

$$\begin{aligned} \text{unloading: } \quad & \dot{\boldsymbol{\varepsilon}}^{vp} = 0 \Rightarrow \dot{\boldsymbol{\sigma}} : \dot{\boldsymbol{\varepsilon}}^{vp} = 0; \\ \text{loading: } \quad & \dot{\boldsymbol{\sigma}} : \dot{\boldsymbol{\varepsilon}}^{vp} \propto \dot{\boldsymbol{\sigma}} : \left. \frac{\partial f}{\partial \boldsymbol{\sigma}} \right|_{\boldsymbol{\sigma}=\bar{\boldsymbol{\sigma}}} \begin{cases} > 0, & \text{hardening;} \\ = 0, & \text{perfect;} \\ < 0, & \text{softening.} \end{cases} \end{aligned} \quad (4.9)$$

Combining Inequality (4.8) and (4.9), we can conclude that Inequality (4.4) holds for perfect and hardening plasticity. End of proof.

Similarly, in viscoplastic FE analysis, the overstress force can be defined corresponding to the unbalanced force in elastoplasticity,

$$\Delta Y = \int_{\mathcal{B}} \mathbf{B}^T (\boldsymbol{\sigma} - \bar{\boldsymbol{\sigma}}) dV = \mathbf{F} - \int_{\mathcal{B}} \mathbf{B}^T \bar{\boldsymbol{\sigma}} dV. \quad (4.10)$$

Obviously, PCE is an energy norm of both the viscoplastic strain rate field and the overstress force. Thus, the principle of minimum PCE can be stated as: *under time invariant loading and boundary conditions, viscoplastic structures deform tending to the limit steady state at which the viscoplastic deformation rate or the overstress force is minimized in the sense of PCE.* If such state is not reinforced, the structure suffers steady viscoplastic flow by the minimum rate until failure occurs. It is just the theoretical basis of the two stress field method and the principle of minimum PCE in elastoplasticity. It is noted that the above derivations and results still hold for the Perzyna model [38]. But the Perzyna form of PCE is not as clear as the Duvaut-Lions form to show the connection between viscoplasticity and elastoplasticity.

In summary, if perfect and hardening plasticity is considered, the equivalence between the viscos and the inviscid solutions dwells in the minimization of PCE. Namely, they both require the structure to unleash its maximum resistance through

deformation trying to reach a stationary state. If no stationary state ever exists, the limit steady state is reached, which is a non-stationary state closest to the stationary condition. However, the minimization processes in the two approaches take different paths, so the solutions cannot be identical, especially for complicated structures. On the other hand, if softening is involved in constitutive relations, the principle of minimum PCE does not hold, and thus, such equivalence needs further investigations. But one thing is clear: PCE increases only when softening develops to a certain level.

The principle of minimum PCE as well as the objectivity of the limit steady state can be evidenced by the typical creep curves for metals [41], as shown in Fig. 16. When the stress is low enough, the creep rate tends to vanish and a stationary state is finally reached. When the stress is mildly higher, after the primary creep, the steady creep takes place over a significant time interval until microstructural damages lead to the tertiary creep. The steady creep can be described by the Norton's law while the tertiary creep can be modeled by introducing the effective stress to characterize damage effects [44]. The limit steady state combines the primary and steady creep stages and the principle of minimum PCE actually governs the primary creep behavior tending to the limit steady state. The asymptotic stability and steady creep of solids are discussed in non-equilibrium thermodynamics in Ref. [22, 45].

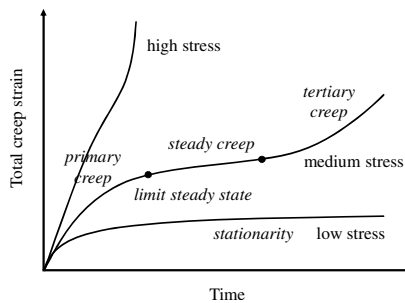


**Fig. 16.** Typical creep curves for metals

### 4.3 Thermodynamical Interpretations

As proposed by Edelen [46], one of the fundamental properties of real material systems, also referred to as the zeroth law of thermodynamics, can be stated loosely as follows: any real material system of finite spatial extent, satisfying reasonable boundary conditions that do not depend explicitly on time, will ultimately evolve to an equilibrium state, *if* such equilibrium state exists uniquely. The principle of minimum PCE makes an effort to extend this proposition to the situations where such equilibrium state does not exist.

In fact, correlations can be found between the principle of minimum PCE and the minimum entropy production theorem by Onsager [47], where the steady states are characterized by minimum rate of entropy production. As verified by

Rajagopal and Srinivasa [48] and Martyushev and Seleznevb [49], the minimum entropy production theorem holds not only for systems of linear reciprocal relation but also for those of Ziegler's principle of maximum dissipation [50]. Thus, the relationship between the principle of minimum PCE and the principle of maximum plastic dissipation is in parallel with that between the minimum entropy production theorem and Ziegler's principle of maximum dissipation.

The inherent connections have been clarified by Yang et al. [51, 52] between the three theories of irreversible thermodynamics including the normality structure by Rice [20], the principle of maximum dissipation by Ziegler [50] and the nonlinear reciprocal relation by Edelen [46]. The common ground of these theories is the presumption of a dissipation potential, which, however, may not hold for geomaterials [53]. The complicated mechanical behaviors of geomaterials should better be studied in a more general thermodynamical framework where rotational entropy flow can be considered. At the structural level, Hamiltonian for green inelastic structures has been proposed [54, 55], which can be viewed as the thermodynamical basis of the principle of minimum PCE.

#### ***4.4 Measurement of Unbalanced Force and Structural Safety Monitoring and Forecasting***

The objectivity of the unbalanced force cannot be validated unless it can be measured. Physical measurement of the unbalanced force can be implemented by measuring the time-dependent deformation rate, which can determine the overstress force through calculations. The overstress force can be viewed as the unbalanced force because both of them represent the current difference between external action and structural resistance. Such measurement of unbalanced force is quite similar to stress measurement, which is achieved by strain measurement and calculations based on the Hooke's law. The similarity between the Duvaut-Lions model and the Hooke's law is obvious, both of which establish a linear relation that enables us to measure stress via strain.

Monitoring and forecasting is vital to the security of geotechnical structures. In conventional monitoring measures and forecasting models, surface displacement is focused, which, however, cannot be effective because it deviates from the structural failure mechanism. It behooves the unbalanced force or the time-dependent deformation rate to be the primary target in structural safety monitoring and forecasting, because they are respectively the driving force and the intrinsic representation of structural failure. Such idea has long been aware in geotechnical engineering. For example, the NATM attaches much importance to the monitoring and control of time-dependent deformation rate.

##### *Example 4. The NATM*

The NATM [30, 31] is a good engineering illustration of the principle of minimum PCE. The central ideas of NATM can be addressed by the typical relation between the required support force and the convergence of the tunnel wall after excavation, as shown in Fig.17. NATM emphasizes that rigid supports should not be installed

too early such that the tunnel could deform to unleash its own resistance. However, the convergence rate should be carefully watched and the rigid supports be carried out in time to prevent unrecoverable damage and collapse. During the convergence process, there is an optimal timing for supporting, which corresponds to the limit steady state if damage effects are not considered. Evidently, the principles of NATM are in full accordance with those of DRT.

In this numerical example, we reproduce the NATM curve by viscoplastic FE analysis. A circular shallow-buried tunnel of radius 5m is modeled, buried at the depth 5m. Excavation is carried out after the loading of gravity. In case A, perfect viscoplasticity given by Equation (4.1) is applied, with  $\gamma = 1.0$  (time scale is not concerned) and  $\Phi = f$ . The Drucker-Prager yield criterion is applied and the material parameters are given in the first line of Table 1. In case B, damage effects are taken into account to reflect the increasing period of the curve. To elaborately consider the damage effects of geomaterials, such as jointed rock masses [56-60] and granular materials [61, 62], fabric tensors can be incorporated as damage variables that provide a simple but powerful description of the microstructures. However, we apply a simple damage model in this example, assuming that the stiffness and strength reductions are both implemented by a single damage variable  $D$ ,

$$E = (1 - D)E_0, \quad \mu = (1 - D)\mu_0, \quad c = (1 - D)c_0, \tag{4.11}$$

and the evolution law of  $D$  is given by

$$D = 1 - \exp\left[-k\left(w^{vp} - w_{th}^{vp}\right)\right], \quad w^{vp} = \left(2/3\boldsymbol{\varepsilon}^{vp} : \boldsymbol{\varepsilon}^{vp}\right)^{1/2}, \tag{4.12}$$

where  $k$  is an positive material parameter and  $w_{th}^{vp}$  defines the damage threshold. In the computation,  $k = 1.2 \times 10^5$  and  $w_{th}^{vp} = 0$ . Fig.18 shows the development of the vertical overstress force of the node located at the tunnel top with respect to its vertical displacement.

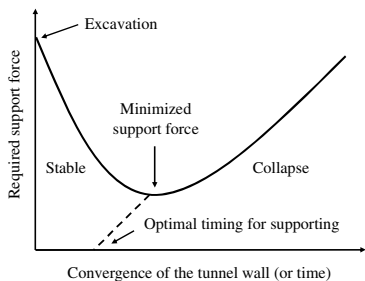


**Fig. 17.** Relation between support force and tunnel convergence in NATM

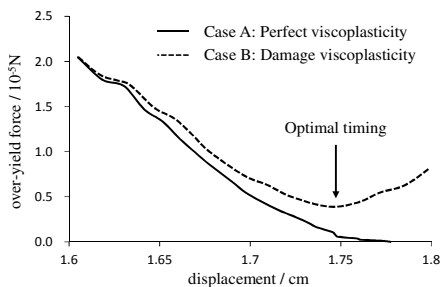


**Fig. 18.** Development of overstress force with respect to displacement at the tunnel top

### 5 Model Test Verification

In this subsection, we introduce an engineering application of DRT to Baihetan arch dam and show the correlations of the results given by FE analysis and geomechanical model test [16].

Baihetan hydropower station is located on the lower reaches of the Jinsha River, China. The height of the concrete double curvature arch dam is 289.0m. Faults and veins are highly developed at the dam site, as shown in Fig.1. The FE model is shown in Fig.19, with the critical faults simulated in detail. The hydrostatic pressure  $P_0$  is overloaded, from  $P_0$  to  $4.0 P_0$  by the increment of  $0.5 P_0$ .

The  $K \sim \mathcal{E}_{\min}$  relation of the model is shown in Fig.20, indicating that the left abutment is much more threatened than the right abutment and the dam body. This result can be verified by the distribution of the cracks and crushed zones at the dam toes obtained by the geomechanical model test, as shown in Fig.21. Fig.22 shows the unbalanced forces at the dam heel and Fig.23 shows the unbalanced force contour and the crack photograph of the bed base surface, proving that the unbalanced forces well predict the position and inception point of the dam heel cracking. Fig.24 shows the magnitude of the unbalanced forces of the faults, indicating that fault F18 on the right and LS3318 on the left are the most critical faults, as validated by the cracks shown in Fig.25.

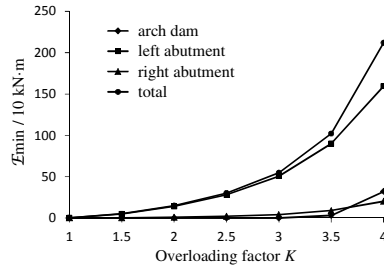
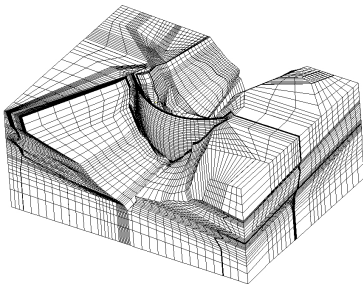


Fig. 19. FE model of Baihetan arch dam, with 94765 nodes and 86522 elements

Fig. 20. The  $K \sim \mathcal{E}_{\min}$  relations of Baihetan arch dam

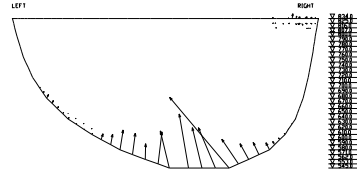
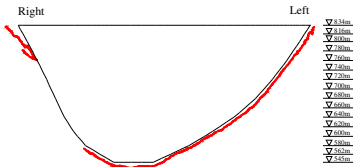


Fig. 21. Cracks and crushed zones at the dam toes obtained by geomechanical model test

Fig. 22. Unbalanced forces at the dam heel at  $3.5P_0$

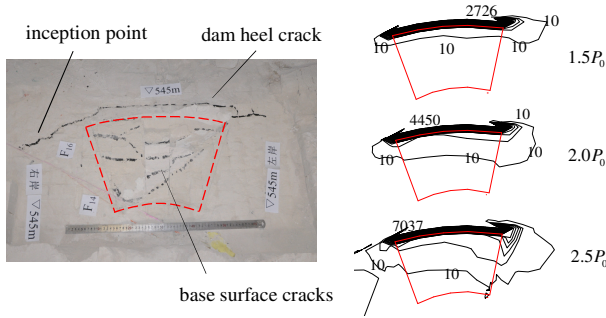


Fig. 23. Unbalanced force contour and crack photograph on the bed base surface

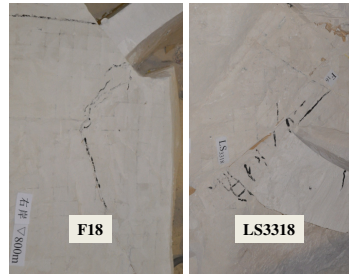
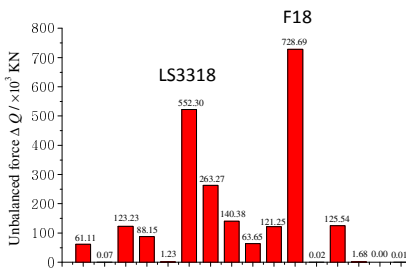


Fig. 24. Magnitude of the unbalanced forces of the faults

Fig. 25. Crack photographs on the right and left abutments

As verified by geomechanical model test, the unbalanced force serves well as a preliminary prediction of structural failure, such as crack inception and propagation and shear crush, while the advanced methods like X-FEM and DEM are currently not available for large-scale 3D geotechnical structures. In 2011, DRT has been incorporated into the latest Chinese Hydraulic Design Manual [63].

## 6 Conclusions

The deformation reinforcement theory (DRT) embodies the concepts of structural instability and reinforcement in 3D elastoplastic FE analysis, which is helpful to the study of failure mechanism and control for large-scale complicated geotechnical structures. The major conclusions of DRT include:

- 1) Two stress fields must be involved respectively to represent external action and structural resistance, because instability occurs when action is greater than resistance in the sense of total plastic dissipation.
- 2) The unbalanced force characterizes the current difference between action and resistance, which is the driving force of the deformation process.

- 3) The principle of minimum plastic complementary energy (PCE): under given actions, structures deform tending to the limit steady state at which the unbalanced force is minimized in the sense of PCE.
- 4) At the limit steady state, the unbalanced force reflects the structural failure mechanism of the structure, including the failure position and pattern. This conclusion is well verified by the geomechanical model test of Baihetan high arch dam.
- 5) The opposite of the unbalanced force determines the optimal reinforcement force to prevent failure, which realizes a quantitative and pinpoint reinforcement design method for geotechnical structures.
- 6) The effects of reinforcement measures must be evaluated in the stage of instability.

The theoretical basis of the principle of minimum PCE is established in viscoplasticity and primarily discussed in thermodynamics. Some fundamental remarks are presented as follows:

- 1) The principle of minimum PCE in viscoplasticity: under time invariant loading and boundary conditions, viscoplastic structures deform tending to minimize PCE at each moment. This principle holds for associative perfect and hardening plasticity.
- 2) The principle of minimum PCE and the objectivity of the limit steady state can be evidenced by the typical creep curve and the principle of NATM.
- 3) The relationship between the principle of minimum PCE and the principle of maximum plastic dissipation is in parallel with that between the minimum entropy production theorem and Ziegler's principle of maximum dissipation.
- 4) Physical measurement of the unbalanced force can be implemented by measuring the time-dependent deformation rate, which is suggested to be the primary target in structural safety monitoring and forecasting.

**Acknowledgments.** This work is supported by the National Natural Science Foundation of China under Projects 50925931, 11172150 and subsidized by the special funds for major state basic research projects with grant No. 2009CB724604.

## References

- [1] Drucker, D.C., Greenberg, H.J., Prager, W.: Extended limit design theorems for continuous media. *Quart. App. Math.* 9, 381–389 (1952)
- [2] Chen, H.F.: *Limit Analysis and Soil Plasticity*. Elsevier, Amsterdam (1975)
- [3] Kamenjarzh, J.A.: *Limit Analysis of Solids and Structures*. CRC Press, Florida (1996)
- [4] Duncan, J.M.: State of the art: limit equilibrium and finite-element analysis of slopes. *J. Geotech. Engrg.* ASCE 122, 577–596 (1996)
- [5] Griffiths, D.V., Lane, P.A.: Slope stability analysis by finite elements. *Geotechnique* 49, 387–403 (1999)

- [6] Dawson, E.M., Roth, W.H., Drescher, A.: Slope stability analysis by strength reduction. *Geotechnique* 49, 835–840 (1999)
- [7] Potts, D.M., Zdravkovic, L.: *Finite Element Analysis in Geotechnical Engineering, Application*. Thomas Telford, London (2001)
- [8] Bickford, J.H.: *An Introduction to the Design and Behavior of Bolted Joints*, 2nd edn. Marcel Dekker, New York (1990)
- [9] Ansell, A.: Chapter 2: A finite element model for dynamic analysis of shotcrete on rock subjected to blast induced vibrations. In: Bernard, E.S. (ed.) *Proc. 2nd Int. Conf. Engrg. Dev., Shotcrete*, Cairns, Queensland, Australia, pp. 15–25. Taylor & Francis (2004)
- [10] Zienkiewicz, O.C., Taylor, R.L., Zhu, J.Z.: *The finite element method: its basis and fundamentals*, 6th edn. Elsevier, Burlington (2005)
- [11] Yang, Q., Liu, Y.R., Chen, Y.R., Zhou, W.Y.: Deformation reinforcement theory and its application to high arch dams. *Sci. China Ser. E—Tech. Sci.* 51, 32–47 (2008)
- [12] Yang, Q., Leng, K.D., Liu, Y.R.: Mechanical basis and engineering significance of deformation reinforcement theory. *Rock and Soil Mech* 32, 1–8 (2011)
- [13] Yang, Q., Leng, K.D., Liu, Y.R.: A finite element approach for seismic design of arch dam-abutment structures. *Sci. China Ser. E—Tech. Sci.* 54, 516–521 (2011)
- [14] Liu, Y.R., Chang, Q., Yang, Q.: Fracture analysis of rock mass based on 3-D nonlinear Finite Element Method. *Sci. China Ser. E—Tech. Sci.* 54, 556–564 (2011)
- [15] Yang, Q., Leng, K.D., Liu, Y.R.: Structural stability in deformation reinforcement theory—fundamentals and applications. In: Khalili, N., Oeser, M. (eds.) *Proc. 13th Int. Conf. on Computer Methods and Advances in Geomechanics*, Melbourne, Australia, pp. 28–35. Centre for Infrastruc. Eng. and Safety, Sydney (2011)
- [16] Guan, F.H., Liu, Y.R., Yang, Q., Yang, R.Q.: Analysis of stability and reinforcement of faults of Baihetan arch dam. *Adv. Mater. Res.* 243-249, 4506–4510 (2011)
- [17] Liu, Y.R., Wang, C.Q., Yang, Q.: Stability analysis of soil slope based on deformation reinforcement theory. *Finite Ele. Ana. Design* 58, 10–19 (2012)
- [18] Goodman, R.E., Shi, G.H.: *Block theory and its application to rock engineering*. Prentice Hall, London (1985)
- [19] O'Connor, D.T.P.: *Practical Reliability Engineering*, 4th edn. John Wiley & Sons, New York (2002)
- [20] Rice, J.R.: Inelastic constitutive relations for solids: An internal variable theory and its application to metal plasticity. *J. Mech. Phys. Solids* 19, 433–455 (1971)
- [21] Yang, Q., Xue, L.J., Liu, Y.R.: Thermodynamics of infinitesimally constrained equilibrium states. *ASME J. App. Mech.* 76, 014502 (2009)
- [22] Yang, Q., Bao, J.Q., Liu, Y.R.: Asymptotic stability in constrained configuration space for solids. *J. Non-Equilib. Thermodyn.* 34, 155–170 (2009)
- [23] Hill, R.: *The mathematical theory of plasticity*. Oxford University, London (1950)
- [24] Simo, J.C., Kennedy, J.G., Govindjee, S.: Non-smooth multisurface plasticity and viscoplasticity, Loading/unloading conditions and numerical algorithms. *Int. J. Numer. Methods Engrg.* 26, 2161–2185 (1988)
- [25] Macari, E.J., Weihe, S., Arduino, P.: Implicit integration of elastoplastic constitutive models for frictional materials with highly non-linear hardening functions. *Mech. Cohesive-frictional Mater.* 2, 1–29 (1997)
- [26] Simo, J.C., Hughes, T.J.R.: *Computational inelasticity*. Springer, New York (1998)
- [27] Armero, F., Perez-Foguet, A.: On the formulation of closest-Point projection algorithms in elastoplasticity. Part I: The variational structure. *Int. J. Numer. Methods Engrg.* 53, 297–329 (2002)

- [28] Yang, Q., Yang, X.J., Chen, X.: On integration algorithm of perfect plasticity based on Drucker-Prager yield criterion. *Engrg. Mech.* 22, 15–19 (2005)
- [29] Chen, Z.Y.: On Pan's principles of soil and rock stability analysis. *J. of Tsinghua Univ. Sci. Tech.* 38, 1–4 (1998)
- [30] Brown, E.T.: Putting the NATM into perspective. *Tunnels & Tunnelling* 22, 9–13 (1990)
- [31] Barton, N., Grimstad, E.: Rock mass conditions dictate the choice between NMT and NATM. *Tunnels & Tunnelling* 26, 39–42 (1994)
- [32] Radenkovic, D.: Limit theorems for a Coulomb material with a non-standard dilatation. *Comptes Rendus de l'Académie des Sciences de Paris* 252, 4103–4104 (1961)
- [33] Gu, J.C., Chen, A.M., Xu, J.M., et al.: Model test study of failure patterns of anchored tunnel subjected to explosion load. *Chinese J. Rock. Mech. Engrg.* 27, 1315–1320 (2008)
- [34] Zhou, W.Y., Yang, R.Q., Yan, G.R.: Stability evaluation methods and criteria in designing large arch dams. *Design Hydroelec. Power Station* 13, 1–7 (1997)
- [35] Barton, N., Lien, R., Lunde, J.: Engineering classification of rock masses for the design of tunnel support. *Rock Mech. Rock Engrg.* 6, 189–236 (1974)
- [36] Bieniawski, Z.T.: *Engineering rock mass classifications: A complete manual for engineers and geologists in mining, civil, and petroleum engineering.* Wiley, Hoboken (1989)
- [37] Washizu, K.: *Variational methods in elasticity and plasticity.* Pergamon, Oxford (1975)
- [38] Perzyna, P.: Fundamental problems in viscoplasticity. *Adv. App. Mech.* 9, 243–377 (1966)
- [39] Duvaut, G., Lions, J.L.: *Inequalities in Mechanics and Physics.* Springer, Berlin (1976)
- [40] Chaboche, J.L.: A review of some plasticity and viscoplasticity constitutive theories. *Int. J. Plast.* 24, 1642–1693 (2008)
- [41] Lubliner, J.: *Plasticity Theory.* Macmillan, New York (1990)
- [42] Zienkiewicz, O.C., Corneau, T.C.: Viscoplasticity—plastic and creep in elastic solids—a unified numerical solution approach. *Int. J. Numer. Methods Engrg.* 8, 821–845 (1974)
- [43] Silva, V.D.: A simple model for viscous regularization of elasto-plastic constitutive laws with softening. *Commun. Numer. Methods Engrg.* 20, 547–568 (2004)
- [44] Kachanov, L.M.: On Creep Rupture Time. *Proc. Acad. Sci., USSR, Div. Eng. Sci.* 8, 26–31 (1958)
- [45] Yang, Q., Chen, X., Zhou, W.Y.: Thermodynamic relationship between creep crack growth and creep deformation. *J. Non-Equilib. Thermodyn.* 30, 81–94 (2005)
- [46] Edelen, D.G.B.: *The College Station Lectures on Thermodynamics.* Texas A&M University, College Station (1993)
- [47] Onsager, L.: Reciprocal relations in irreversible thermodynamics. I. *Phys. Rev.* 37, 405–426 (1931)
- [48] Rajagopal, K.R., Srinivasa, A.R.: On thermomechanical restrictions of continua. *Proc. Math. Phys. Engrg. Sci.* 460, 631–651 (2004)
- [49] Martyusheva, L.M., Seleznevb, V.D.: Maximum entropy production principle in physics, chemistry and biology. *Phy. Rep.* 426, 1–45 (2006)
- [50] Ziegler, H.: Some extremum principles in irreversible thermodynamics. In: Sneddon, N., Hill, R. (eds.) *Prog. Solid Mech.*, vol. 4. North Holland, New York (1963)

- [51] Yang, Q., Tham, L.G., Swoboda, G.: Normality structures with homogeneous kinetic rate laws. *ASME J. App. Mech.* 72, 322–329 (2005)
- [52] Yang, Q., Chen, X., Zhou, W.Y.: Microscopic thermodynamic basis of normality structure of inelastic constitutive relations. *Mech. Res. Commun.* 32, 590–596 (2005)
- [53] Yang, Q., Xue, L.J., Liu, Y.R.: Multiscale Thermodynamic Basis of Plastic Potential Theory. *ASME J. Engrg. Mater. Tech.* 130, 044501 (2008)
- [54] Yang, Q., Guan, F.H., Liu, Y.R.: Hamilton's principle for Green-inelastic bodies. *Mech. Res. Commun.* 37, 696–699 (2010)
- [55] Leng, K.D., Yang, Q.: Generalized Hamilton's principle for inelastic bodies within non-equilibrium thermodynamics. *Entropy* 13, 1904–1915 (2011)
- [56] Yang, Q., Swoboda, G.: An energy-based damage model of geomaterials – I. Formulation and Numerical Results. *Int. J. Solids Struct.* 36, 1719–1734 (1999)
- [57] Yang, Q., Chen, X., Tham, L.G.: Relationship of crack fabric tensors of different orders. *Mech. Res. Commun.* 31, 661–666 (2004)
- [58] Yang, Q., Swoboda, G., Zhao, D., Laabmayr, F.: Damage mechanics of jointed rock in in tunneling. In: Beer, G. (ed.) *Numerical Simulation in Tunnelling*, pp. 117–160. Springer, New York (2003)
- [59] Oda, M.: Fabric tensors for discontinuous geological materials. *Soils Foundat.* 22, 96–108 (1982)
- [60] Lydzba, D., Pietruszczak, S., Shao, J.F.: On anisotropy of stratified rocks: homogenization and fabric tensor approach. *Comput. Geotech.* 30, 289–302 (2003)
- [61] Millet, O., Gu, S., Kondo, D.: A 4th order fabric tensor approach applied to granular media. *Comput. and Geotech.* 36, 736–742 (2009)
- [62] Li, X., Yu, H.S.: Tensorial characterization of directional data in micromechanics. *Int. J. Solids and Struct.* 48, 2167–2176 (2011)
- [63] Yang, Q., Xue, L.J.: Hydraulic Design Manual. In: Zhou, J.P., Dang, L.C. (eds.) *Concrete Dam*, 2nd edn., ch. 5, pp. 176–190. China Water & Power Press, Beijing (2011)

# Back Analysis of Treporti Test Embankment with a Time Dependent Small Strain Stiffness Constitutive Model

Thomas Benz<sup>1,\*</sup>, Valentina Berengo<sup>2</sup>, Paolo Simonini<sup>3</sup>, and Martino Leoni<sup>4</sup>

<sup>1</sup> Norwegian University of Science and Technology (NTNU), 7491 Trondheim, Norway

<sup>2</sup> NET Engineering SpA, Via Squero n.12, 35043 Monselice, Padova Italy

<sup>3</sup> University of Padova, 35122 Padova, Italy

<sup>4</sup> Wesi Geotecnica Srl, Piazza De Gasperi 15/11, 54100 Massa (MS), Italy

thomas.benz@ntnu.no

**Summary.** This paper is concerned with back analysis of a trial embankment on soft soil. The analysis is conducted with and without consideration of small strain stiffness in the time dependent soft soil constitutive model. Whilst in loading during embankment construction small strain stiffness is found to be of minor importance, it is predominant in unloading. In unloading, the small strain enhanced model predicts deformations with considerably higher accuracy than its counterpart without small strain stiffness formulation. The time dependent small strain stiffness model is based on a recently proposed anisotropic creep framework and a strain space based small strain stiffness formulation.

**Keywords:** creep, small strain stiffness, constitutive model, embankment.

## 1 Introduction

Soil stiffness at small strains has been extensively discussed over the past decades. It is well recognized that linear elasticity may only be a valid assumption at very small strains. In practical geomechanics, however, soil stiffness at small strains is not considered thoroughly enough due to a lack of models. This holds particularly true if small strain stiffness is to be considered together with creep. Figure 1 depicts the definition of small and large strains as used in the paper at hand.

Creep, that is deformation at constant effective stress, is another well recognized feature of soil behavior. Creep is clearly evident in soft soils such as clays but it is recognized in hard soils, too. Depending on their loading history, especially soft soils may accumulate very large creep strains. It may therefore seem that creep and small strain stiffness are not closely interconnected. However, if a soil that was subject to creep is subsequently loaded in a reversed direction, e.g. unloading of a foundation or embankment, small strain stiffness becomes an important aspect in creep analysis, too.

---

\* Corresponding author.

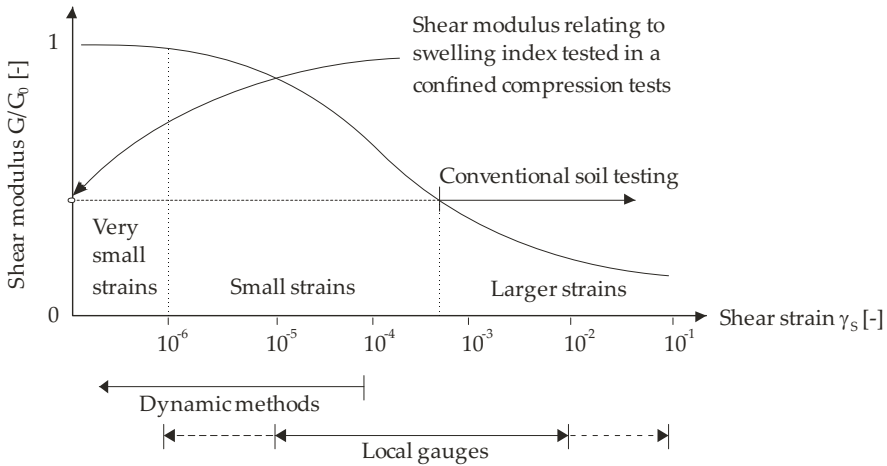


**Fig. 1.** Small strain definition as used in the paper at hand

In literature, several case studies that apparently involve creep and small strain stiffness can be found. One of them is the Treporti test embankment. The Treporti embankment was constructed at the inner border of the Venetian lagoon, imposing a load of more than 100 kPa on the soft ground below. The load was kept constant for more than four years before the embankment was removed. Ground displacements and pore pressure evolution were monitored over time. Creep settlements up to 0.5 m were measured at the site. Back-analyses of the Treporti embankment were published, amongst others, by Cortellazzo et al. [1] and Berengo et al. [2]. Those back-analyses did not include the unloading part of the case study. In fact, the little heave of the embankment upon unloading cannot be explained without considering small strain stiffness.

This paper presents the application of a small strain stiffness enhanced elastoviscoplastic model based on the anisotropic creep framework put forward by Leoni et al. [3] and the small strain stiffness framework proposed by Benz et al. [4] Coupling of these two models is briefly discussed in the next section before the coupled model is applied in back calculating laboratory creep tests as well as the load settlement history of the Treporti test embankment.

## 2 A Small Strain Stiffness Creep Model

The creep framework presented in [3] incorporates elastic stiffness that is defined for large strains. It is implied that elastic bulk stiffness  $K$  depends linearly on effective mean stress. The model's (large strain) swelling index  $\bar{c}_s$

$$\bar{c}_s = \frac{\ln 10 (1+e_0)}{K} p' = \frac{3(1-2\nu) \ln 10 (1+e_0)}{2(1+\nu) G} p' \tag{1}$$

is a function of effective mean stress  $p'$  and initial void ratio  $e_0$  but is constant with respect to strain. Furthermore, it is assumed that recompression index and

swelling index are identical. Note that the elastic quantity  $K$  can alternatively be expressed in shear modulus  $G$  and Poisson's ratio  $\nu$  so that by help of [4] the swelling index of the small strain stiffness enhanced creep model may be defined as:

$$\bar{\bar{C}}_s = \ln 10 (1 + e_0)^{\frac{3(1-2\nu)}{2(1+\nu)}} \left( 1 + \frac{3}{7L} \left| \frac{\gamma}{\gamma_{0.7}} \right| \right)^2 \frac{p'}{G_0} \quad (2)$$

where  $G_0$  is the initial truly elastic (small strain) stiffness,  $\gamma$  is the actual shear strain amplitude since the last load reversal,  $\gamma_{0.7}$  is a reference shear strain at which the secant shear modulus  $G$  has been reduced to  $0.7 G_0$ , and  $L$  is a shape factor:  $L=1$  for primary loading and  $L=2$  for unloading/ reloading [5].

As the swelling index is now a non-linear function of the accumulated shear strain after the last load reversal [4], swelling and recompression lines in  $e - \log \sigma_v'$  show a distinct loop similar to the one observed in experimental data as for example shown in Figure 3. Overbars and double overbar denotes large strain and small strain quantities, respectively. Equation 2 is applied for small strains only:

$$C_s = \begin{cases} \bar{C}_s & \text{for } \bar{\bar{C}}_s > \bar{C}_s \\ \bar{\bar{C}}_s & \text{for } \bar{\bar{C}}_s \leq \bar{C}_s \end{cases} \quad (3)$$

Various choices exist in defining the model's remaining stiffness parameters, e.g. primary and secondary compression indices. In the following, it is assumed that all stiffness parameters - elasto-plastic, elastic, and creep - undergo identical degradation processes in the small strain range.

### 3 Validation: Treporti Test Embankment

The Venetian Lagoon is the enclosed bay of the Adriatic Sea in which the city of Venice is situated. It is around 8% land, including Venice itself and many smaller islands, About 11% is permanently covered by open water, while around 80% consists of mud flats, tidal shallows and salt marshes.

From ground investigations carried out so far, it is believed that the main characteristic of the lagoon soils is determined by a predominant silt fraction, combined with clay and/or sand. These form a chaotic interbedding of different sediments, which basic mineralogical characteristics vary marginally, as a result of similar geological origins and common depositional environment.

Small strain stiffness data of Venetian silts is published in Cola & Simonini [6]. The 1D small strain framework's ability to reproduce stiffness decay curves of Venetian silts is highlighted in Figure 2. Based on the experimental data presented in this figure, the small strain model parameters are quantified as follows:  $G_0 = 60$  MPa,  $\gamma_{0.7} = 0.0001$ .

All remaining model parameters listed in Table 1 are determined as follows: Compression and swelling indices were evaluated on the basis of oedometer tests results, choosing an average characteristic value for the silty layers. The creep

index was obtained from normally consolidated oedometer testing with 24h loading steps. The previous overburden pressure (POP) of 30 relates to in-situ measurements at the embankment test site (Figure 3). POP relates to the overconsolidation ratio (OCR) as follows:

$$OCR = \frac{POP + \sigma_{z,0}'}{\sigma_{z,0}'} \quad (4)$$

where  $\sigma_{z,0}'$  is the actual vertical effective stress. Figure 4 shows back calculations of constant rate of strain (CRS) tests on Venetian soils. Test strain rate is  $10^{-6}$  [s<sup>-1</sup>]. Tests are back calculated with and without the small strain stiffness addition to the creep framework. All calculations make use of the parameters presented in Table 1. However, POP = 30 is replaced with OCR = 1.3 for the laboratory test samples since all samples were loaded and then unloaded in order to get to that specific OCR value before starting CRS testing. The effect of small strain stiffness is most evident in unloading/ reloading loops. Hysteretic behavior is clearly visible.

The Treporti test embankment site is located at the inner border of the Venetian lagoon, very close to the inlet of Lido. The vertically-walled circular test embankment has a diameter of 40 m and a height of approximately 6.5 m, resulting in a surcharge load of slightly more than 100 kPa. Relevant ground displacements together with pore pressure evolution are measured during construction and after. The embankment load was kept constant for more than four years before the embankment was dismantled always monitoring ground displacements.

The ground beneath the embankment was well instrumented. Soil sampling, laboratory testing, and in-situ testing was performed to estimate soil properties [7]. Figure 5 shows a representative soil profile beneath the embankment and the axis-symmetric finite element model. For back calculation, the soil profile is subdivided in coarse grained and fine grained layers. The proposed small strain creep model is applied in fine grained soil layers. The commercially available double hardening Hardening Soil model with small strain stiffness extension, HS-small [8], is applied in coarse grained layers. The small strain stiffness extension of the HS-small model is identical to the one applied to the creep framework. Table 2 summarizes material properties for the HS-small model. As no laboratory test data for the coarse grained soil layers were available, empirical knowledge compiled by Brinkgreve *et al.* [9] is used in determination of those model parameters.

Note that the uppermost sandy lamination that is present on the border of the embankment has been smeared to the centreline, resulting in a reduced thickness. In [2] a slightly different soil profile was chosen on the basis of measured horizontal displacement profiles: A thicker sandy lamination corresponding to the small horizontal displacements measured at the toe of the embankment was assumed. In the current study, however, the soil profile is exclusively based on laboratory and in situ classification tests.

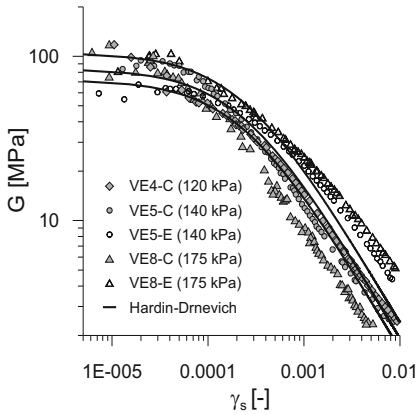


**Fig. 2.** Back analyzed stiffness decay curves (Venetian silts)

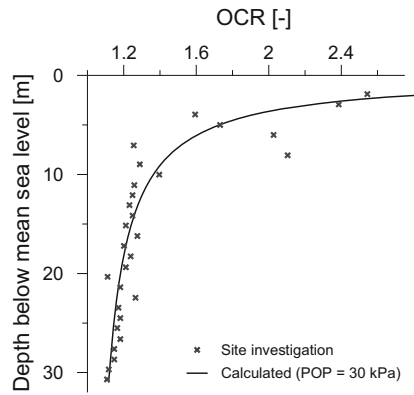


**Fig. 3.** OCR profile at Treporti test site before embankment construction

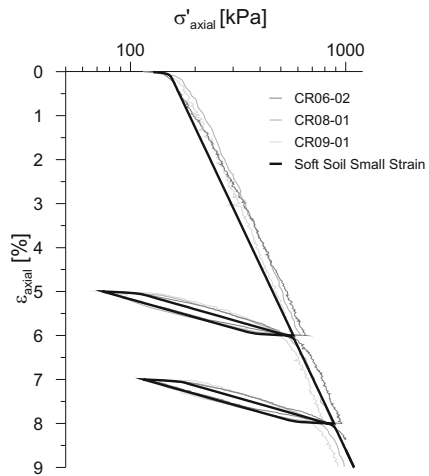
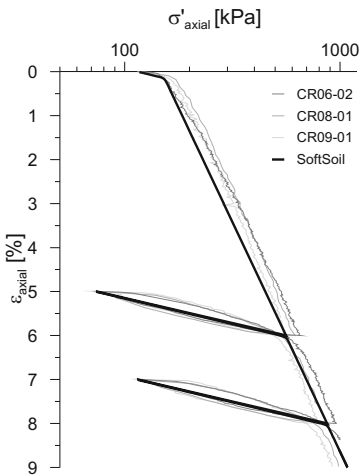


**Fig. 4.** Back calculation of CRS tests

The left mesh boundary depicted in Figure 5 is the calculation model’s symmetry axis. The phreatic level is assumed to be 0.5 m below ground surface. Water flow is only prevented across the symmetry axis. Permeability is assumed to be relatively high as electric piezometer readings during embankment construction did not detect any appreciable increase of pore pressure.

All embankment construction stages are simulated by placing soil layers according to the real construction sequence. Each construction stage follows a consolidation phase. Table 3 gives an overview of the construction sequence.

**Table 1.** Model parameters fine grained soil

$\gamma_{sat}$ [kN/m <sup>3</sup> ]	$C_c$	$C_s$	$C_\alpha$	$\nu$ [-]	POP [-]	$\phi$ [°]	$c$ [kPa]	$\psi$ [°]
18	0.2	0.014	0.006	0.2	30	33	0	0

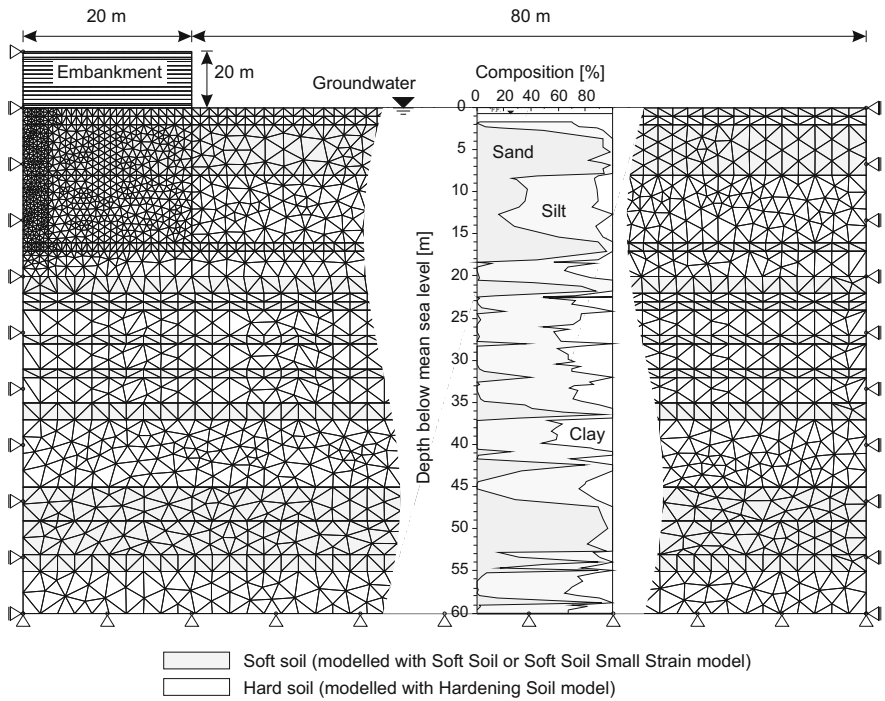


**Fig. 5.** Treporti test embankment. Axisymmetric FE model detailing soil layers

**Table 2.** Model parameters coarse grain soil layers

$\gamma_{sat}$ [kN/m <sup>3</sup> ]	$E_{s0}$ [MPa]	$E_{oed}$ [MPa]	$E_{ur}$ [MPa]	$G_0$ [MPa]	$\gamma_{0.7}$ [-]	$m$ [-]	$\nu$ [-]	POP [-]	$\phi$ [°]	$c$ [kPa]	$\psi$ [°]
18.5	30	30	90	112.5	$1.5 \times 10^{-4}$	0.5	0.2	30	35	1	0

**Table 3.** Construction and removal sequence

Phase	Date	Fill height (m)	Action
0	12 September 2002	0.00	reference measurement
1	12-17 September 2002	0.5	+0.5 m sand
2	23-26 September 2002	1.00	+0.5 m sand
3	1-3 October 2002	1.50	+0.5 m sand
4	9-14 October 2002	2.00	+0.5 sand
5	7-8 November 2002	2.50	+0.5 sand
6	13-18 November 2002	3.00	+0.5 sand
7	27-29 November 2002	3.50	+0.5 sand
8	16-19 December 2002	4.00	+0.5 sand
9	30 December 2002-03 January 2003	4.50	+0.5 sand
10	14-16 January 2003	5.00	+0.5 sand
11	22-25 January 2003	5.50	+0.5 sand
12	4-7 February 2003	6.00	+0.5 sand
13	24-27 February 2003	6.50	+0.5 sand
14	06-10 March 2003	6.70	+0.2 gravel
15	15-29 June 2007	5.40 ca.*	-0.2 gravel,-0.5 sand
16	8-14 July 2007	4.60 ca.*	-0.8 sand
17	22 October-06 November 2007	3.60 ca.*	-1.0 sand
18	9-20 November 2007	2.65 ca.*	-0.95 sand
19	22 February-4 March 2008	1.70 ca.*	-0.95 sand
20	17-21 March 2008	0.75 ca.*	-0.95 sand
21	26-31 March 2008	0.00 *	-0.75 sand

\*measured not in the centreline, but at a distance of 15 m.

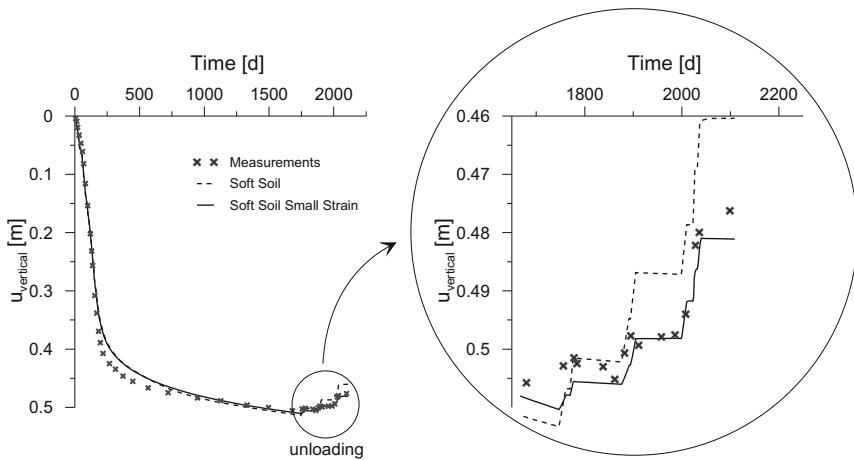


**Fig. 6.** Measured and calculated vertical settlements below the embankment

Figure 6 compares measured and back calculated vertical displacements measured in the middle of the first layer near the embankment centreline. Results are provided for the original creep framework and for the small strain stiffness enhanced creep framework. The final settlement is well-captured by both creep models; little difference is observed in primary loading. However, in unloading the creep model without small strain stiffness formulation overestimates swelling whereas the proposed small strain creep model is in good agreement with measured ground heave.

## 4 Conclusions

In this paper the application of a creep model that accounts for small strain stiffness is described. The small strain stiffness enhanced creep model was implemented in a finite element code and successfully validated in simulating laboratory CRS tests and construction and removal of a 40 m wide test embankment in the Venice lagoon. The overall good agreement obtained between experimental and calculated results indicates that the mechanical behaviour of Venetian subsoil can be well captured when a dedicated stress-strain-time model is adopted for the fine grained subsoil. The model proposed in this paper was capable to enhance calculation results especially in unloading, where it was able to predict reliable results in contrast to its non small strain enhanced counterpart.

## References

- [1] Cortellazzo, G., Ricceri, G., Simonini, P.: Analisi retrospettiva del comportamento del terreno di fondazione di un rilevato sperimentale ubicato nella Laguna di Venezia. In: Proc. XXIII Convegno Nazionale di Geotecnica: Previsione e Controllo del Comportamento Delle Opere, Padova-Abano Terme, pp. 515–522. Patron Editore, Bologna (2007)
- [2] Berengo, V., Leoni, M., Simonini, P., Vermeer, P.A.: Numerical creep analysis of the Treporti test embankment. In: The 2nd International Workshop on Geotechnics of Soft Soils, Glasgow, pp. 371–377. Balkema, Rotterdam (2008)
- [3] Leoni, M., Karstunen, M., Vermeer, P.A.: Anisotropic creep model for soft soils. *Géotechnique* 58(3), 215–226 (2008)
- [4] Benz, T., Vermeer, P.A., Schwab, R.: A small-strain overlay model. *Int. J. Numer. Anal. Meth. Geomech.* 33, 25–44 (2009)
- [5] Hashiguchi, K.: Fundamental requirements and formulations of elastoplastic constitutive equations with tangential plasticity. *Int. J. Plasticity* 9(5), 525–549 (1993)
- [6] Cola, S., Simonini, P.: Some remarks on the behavior of Venetian silts. In: 2nd International Symposium on Pre-failure Behaviour of Geomaterials, IS Torino 1999, pp. 167–174. A. A. Balkema, Rotterdam (1999)
- [7] Simonini, P., Ricceri, G., Cola, S.: Geotechnical characterization and properties of Venice lagoon heterogeneous silts. In: Proc. 2nd Int. Workshop on Characterization and Properties of Natural Soils, Singapore, pp. 2289–2327. Balkema, Rotterdam (2006)
- [8] Benz, T.: Small-Strain Stiffness of Soils and its Numerical Consequences. PhD thesis, Universität Stuttgart (2007)
- [9] Brinkgreve, R.B.J., Engin, E., Engin, H.K.: Validation of empirical formulas to derive model parameters for sands. In: Benz, T., Nordal, S. (eds.) *Numerical Methods in Geotechnical Engineering Numge 2010*, pp. 137–142. CRC Press, Leiden (2010)

# Rate Dependent Elastoviscoplastic Model

Chandrakant S. Desai<sup>1</sup> and Shantanu M. Sane<sup>2</sup>

<sup>1</sup> Regents' Professor (Emeritus), Dept. of Civil Eng. and Eng. Mechanics.,  
The Univ. of Arizona, Tucson, AZ, USA  
csdesai@email.arizona.edu

<sup>2</sup> Energy and Propulsion Technologies, GE Global Research Center, Niskayuna, NY, USA

**Summary.** A rate dependent model for creep behavior using an elastoviscoplastic model is presented. It requires yield surface that is dependent on the rate of strain. It is called dynamic yield surface and is obtained by modifying or correcting the static yield surface. A new method based on creep tests is proposed to define the static yield surface. The model is validated with respect to test data for two materials: a soil (glacial till) and an alloy (solder). The correlations between model predictions and test data are very good. Thus, the proposed model can be used to characterize the behavior of materials that depend on strain rate and creep.

**Keywords:** constitutive models, multicomponent DSC, rate dependence, elastoviscoplastic, static yield surface, dynamic yield surface, validations.

## 1 Introduction

Behavior of many materials depends on rate of loading or strain rate, Fig. 1. The objective of this paper is to develop a constitutive model for rate dependent behavior based on the elastoviscoplastic (evp) characterization for material exhibiting creep.

A unified constitutive model called multicomponent DSC (MDSC) for the creep behavior has been proposed [1]. It contains viscoelastic (ve), elastoviscoplastic (evp) and viscoelasticviscoplastic (vevp) models as special cases. Here, the evp, which is essentially the same as the Perzyna's model [2], is considered for the rate dependent behavior. Such a rate dependent continuum material model can be used to characterize the relative intact (RI) behavior in the MDSC. A brief description of the MDSC is given first. Then the rate dependent evp model and validations are presented.

## 2 Multicomponent (MDSC)

The multicomponent disturbed state concept (MDSC) provides a general model for both primary and secondary creep.

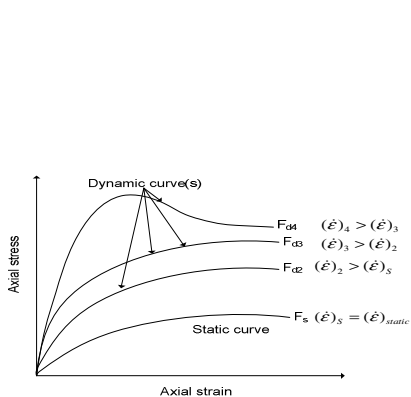


Fig. 1. Rate dependent (dynamic)

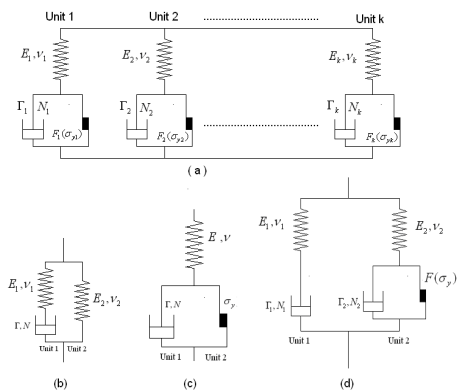


Fig. 2. MDSC: (a) Rheological representation, (b) ve (c) vep, (d) vevp models stress-strain behavior

Figures 2 shows the rheological representation of the MDSC [1]; they show the elastic (E, ν) and creep (Γ N) parameters for the specific model.

The material element is divided into n components or units, and the equilibrium equation for the material element is given by

$$\sigma^a = \sigma_1 \frac{A_1}{A} + \sigma_2 \cdot \frac{A_2}{A} + \dots + \sigma_n \frac{A_n}{A} \tag{1}$$

where  $A_1, A_2 \dots A_n$  are the areas of the units or components ( $A = \sum A_i$ );  $\sigma_i$  ( $i = 1, 2, \dots n$ ) corresponding stresses, and  $\sigma^a$  is the stress corresponding to the applied force  $F^a$ , and  $A$  is the total area. If it is assumed that the width of the units,  $b$ , is the same, Eq. (1) can be written as

$$\sigma^a = \sigma_1 \frac{t_1 b}{\sum t_i b} + \sigma_1 \frac{t_2 b}{\sum t_i b} + \dots \sigma_n \frac{t_n b}{\sum t_i b} \tag{2}$$

where  $t_1, t_2 \dots t_n$  are the thicknesses of each component and  $\sum t_i b$  is the total area of the material element. Equation (2) can be expressed as

$$\sigma^a = \sigma_1 \bar{t}_1 + \sigma_2 \bar{t}_2 + \dots + \sigma_n \bar{t}_n \tag{3}$$

where  $\bar{t}_i$  ( $i = 1, 2, \dots n$ ) is the nondimensionalized thickness of each component.

For the multidimensional case, Eq. (3), can be written in incremental form as

$$d \sigma^a + \bar{t}_1 \tilde{C}^1 d \varepsilon_1 + \bar{t}_2 \tilde{C}^2 d \varepsilon_2 + \dots + \bar{t}_n \tilde{C}^n d \varepsilon_n \tag{4}$$

where  $\tilde{C}^j$  ( $j = 1, 2, \dots, n$ ) is the (tangent) constitutive matrix of each component. If the strain in each component is assumed to be the same, i.e.,  $d\epsilon_i = d\epsilon$ , the relationship can be expressed as

$$d\sigma^a = \tilde{C}_{eq} \cdot d\epsilon \tag{5}$$

where  $\tilde{C}_{eq}$  is the equivalent constitutive matrix  $= \bar{t}_1 \tilde{C}_1 + \bar{t}_2 \tilde{C}_2 + \dots + \bar{t}_n \tilde{C}_n$ .

This case with equal strains in all components is similar to the overlay or mechanical sublayer model proposed in (e.g.,[3])

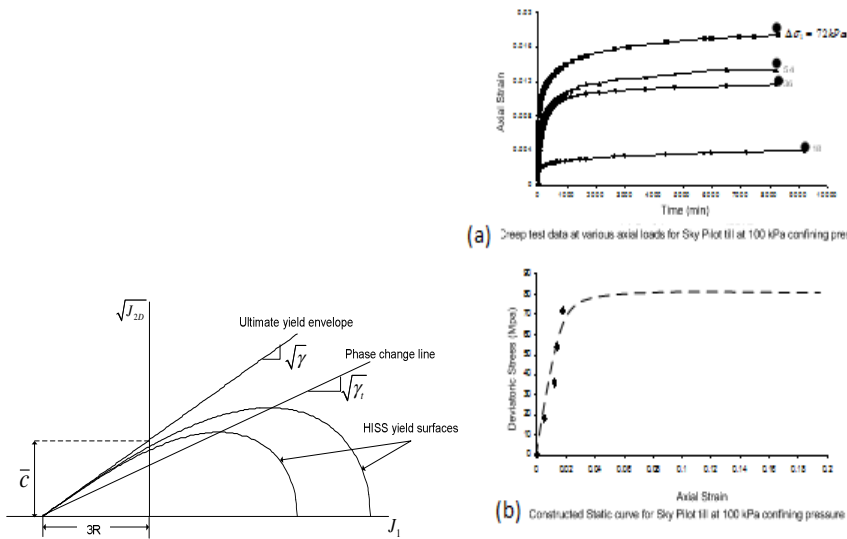


**Fig. 3.** Schematic of HISS yield surfaces

**Fig. 4.** Constructed static stress-strain Behavior

In the DSC model, the incremental equations are given by (e.g.,[1,4]):

$$d\tilde{\sigma}^a = (1 - D)\tilde{C}^i d\tilde{\epsilon}_i + D\tilde{C}^c d\tilde{\epsilon}^c + dD(\tilde{\sigma}^c - \tilde{\sigma}^i) \tag{6}$$

where  $\tilde{\sigma}$  denotes the stress vector,  $\tilde{C}$  constitutive matrix,  $D$  disturbance,  $dD$  rate of disturbance, and  $a, i, c$  the observed, relative intact (RI) and fully adjusted (FA) behavior, respectively; RI and FA are the two components of a material element, and  $\tilde{C}^i$  and  $\tilde{C}^c$  denote constitutive matrices for the RI and FA behavior, respectively.

In the MDSC, the RI behavior  $(C^i)$  in Eq. (6) can be simulated by using one of the above specializations. If disturbance is not involved, Eq. (6) would specialize to one of the creep models for the RI (continuum) behavior. In this paper, a procedure is proposed for the rate dependent creep analysis using the evp specialization. It is used to predict rate dependent creep behavior of a soil (glacial till); the model is also used successfully for an alloy (solder: Sn/3.9Ag/0.6 Cu) [4]; latter is not included here.

### 3 Rate Dependent Creep Model

For the creep (evp) model, the yield surface (at the static state) is given by

$$F = \overline{J_{2D}} - (-\alpha \overline{J_1}^n + \gamma \overline{J_1}^2)(1 - \beta S_r)^{-0.5} = 0 \quad (7)$$

where  $\overline{J_{2D}} = J_{2D} / p_a^2$ ,  $J_{2D}$  is the second invariant of the deviatoric stress tensor and  $p_a$  is the atmospheric pressure;  $\overline{J_1} = (J_1 + 3R) / p_a$  where  $J_1$  is the first invariant of the total stress tensor,  $R$  is the intercept along  $J_1$  axis to define the cohesive strength  $\bar{c}$  (Figure 3);  $n$  is the phase change parameter representing the volume change from compaction to either dilation or no volume change;  $\gamma$  is the parameter related to ultimate yield surface;  $\beta$  is related to shape of  $F$  in the  $\sigma_1 - \sigma_2 - \sigma_3$  space,  $S_r =$  stress ratio =  $\sqrt{27/2} \cdot (J_{3D} / J_{2D}^{3/2})$ ,  $J_{3D}$  is third invariant of the deviatoric stress tensor, and  $\alpha$  is the growth or hardening function; a simple form of  $\alpha$  is given as

$$\alpha = \frac{a_1}{\xi^{\eta_1}} \quad (8a)$$

where  $a_1$  and  $\eta_1$  are hardening parameters and

$$\xi = \sqrt{d\epsilon_{ij}^p d\epsilon_{ij}^p} \quad (8b)$$

where  $\xi$  is the trajectory of or accumulated plastic strains,  $\epsilon_{ij}^p$ , and  $d$  denotes the increment. Figure 3 shows the continuously expanding yield surface with the yield surfaces, phase change line and ultimate envelope.

In evp (e.g., [2,1]) model, the viscoplastic strain rate is given by

$$\begin{aligned} \dot{\epsilon}_{ij}^{vp} &= \Gamma \left( \frac{F_s}{F_0} \right)^N \frac{\partial F_s}{\partial \sigma_{ij}} & \text{if } F > 0 \\ &= 0 & \text{if } F \leq 0 \end{aligned} \quad (9)$$

where  $\dot{\boldsymbol{\varepsilon}}_{ij}^{vp}$  is the viscoplastic strain rate tensor,  $\Gamma$  and  $N$  are material parameters,  $\sigma_{ij}$  is the stress tensor,  $F_s$  is the (static) plastic yield function and  $F_0$  is the term for nondimensionalization.

Yield function  $F$  depends upon the applied stress and plastic strains. It has, initially, a non zero positive magnitude which gradually approaches zero with time and increasing plastic strains. At  $\dot{F} = 0$ , the strain reaches a steady state ( $\dot{\boldsymbol{\varepsilon}}_{vp} = 0$ ). This indicates that the yield function  $F$  should be defined in such a way that it represents combinations of stress and corresponding *steady state strains*.

The static test (at zero strain rate) is usually not available, therefore, it needs to be constructed. Details of the rate dependent model and the procedure to construct the static curve from available creep tests are described below. In the following rate dependent model, it is required to define the static yield surface, as well as the dynamic (rate) yield surfaces,  $F_d$ . A novel procedure is developed to derive the static yield surface from creep test, which is described later.

## 4 Rate Dependent (evp) Model

The behavior of a material is dependent on the rate of loading, Fig. 1. Hence, to model such (creep) behavior, it is necessary to develop the yield surface for the specific (dynamic) strain rate, denoted by  $F_d$ . It is derived by modifying or correcting the static surface,  $F_s$ . Thus  $F_d$  is expressed as (e.g.,[5,4]):

$$F_d(\sigma_{ij}, \alpha, \dot{\boldsymbol{\varepsilon}}_{ij}) = \frac{F_s(\sigma_{ij}, \alpha) - F_R(\dot{\boldsymbol{\varepsilon}}_{ij})}{F_0} = 0 \quad (10)$$

Here  $F_d$  represents the plastic yield function defined at nonstatic or ‘dynamic’ rate,  $F_0$  is the factor used to render the terms nondimensional and  $F_R$  is the modification or correction function. Details of the derivation of  $F_R$  are given below.

## 5 Derivation of $F_R$

Squaring both sides and taking square root of Equation (9) yields,

$$\Gamma \left( \frac{F_s}{F_0} \right)^N = \sqrt{\frac{\left( \frac{d\boldsymbol{\varepsilon}_{ij}^{vp}}{dt} \right)^T \cdot \left( \frac{d\boldsymbol{\varepsilon}_{ij}^{vp}}{dt} \right)}{\left( \frac{\partial F_s}{\partial \sigma_{ij}} \right)^T \cdot \left( \frac{\partial F_s}{\partial \sigma_{ij}} \right)}} \quad (11a)$$

$$\frac{F_s}{F_0} = \left\{ \left( \frac{1}{\Gamma} \right) \cdot \sqrt[1]{ \frac{ \left( \frac{d\epsilon_{ij}^{vp}}{dt} \right)^T \cdot \left( \frac{d\epsilon_{ij}^{vp}}{dt} \right) }{ \left( \frac{\partial F_s}{\partial \sigma_{ij}} \right)^T \cdot \left( \frac{\partial F_s}{\partial \sigma_{ij}} \right) } } \right\}^{\frac{1}{N}} \quad (11b)$$

Thus

$$\frac{F_s}{F_0} - \left\{ \left( \frac{1}{\Gamma} \right) \cdot \sqrt[1]{ \frac{ \left( \frac{d\epsilon_{ij}^{vp}}{dt} \right)^T \cdot \left( \frac{d\epsilon_{ij}^{vp}}{dt} \right) }{ \left( \frac{\partial F_s}{\partial \sigma_{ij}} \right)^T \cdot \left( \frac{\partial F_s}{\partial \sigma_{ij}} \right) } } \right\}^{\frac{1}{N}} = 0 \quad (11c)$$

Comparing Eq. 11(c) with (10):

$$\frac{F_R}{F_0} = \left\{ \left( \frac{1}{\Gamma} \right) \cdot \sqrt[1]{ \frac{ \left( \frac{d\epsilon_{ij}^{vp}}{dt} \right)^T \cdot \left( \frac{d\epsilon_{ij}^{vp}}{dt} \right) }{ \left( \frac{\partial f_s}{\partial \sigma_{ij}} \right)^T \cdot \left( \frac{\partial f_s}{\partial \sigma_{ij}} \right) } } \right\}^{\frac{1}{N}} \quad (12)$$

Equation 12 gives the rate dependent factor  $F_R$  as a function of strain rate. The function,  $F_R$ , decreases as the strain rate decreases and approaches zero as strain rate tends to zero. Concept of zero strain rate is theoretical and it can be considered as a very slow or static rate in practice. Thus we can say that  $F_d$  reduces to  $F_s$  at static rate; hence  $F_s$  may be considered as a special case of  $F_d$  at the static rate. Therefore,  $F_d$  in Eq. (10) can be determined with the knowledge of  $F_R$  and  $F_s$ ; derivation of the latter is given below.

## 6 Yield Surface at Steady State

A novel method developed to define  $F_s$  is described here. Consider a series of creep tests for different applied (constant) stress and given confining pressure or temperature. Figure 4(a) shows such creep tests for the Sky Pilot till at different applied stresses, and confining stress = 100 kPa [4]. It is assumed that the steady or ultimate stress is reached at high time levels; hence, the strains at the steady state are marked as asymptotic to the curves in Fig. 4(a). Hence, the pair, steady strain and the corresponding applied (constant) stress forms a point on the stress-strain curve if the tests were performed at steady (or zero) strain rate. Thus various static strains and applied stress constitutes points on the stress-strain curve at steady strain rate; this curve is called the *constructed* static stress-strain curve,

Figs. 4(b). The constructed curves (at different confining stresses or temperatures) are then used to determine the parameters for the static yield surface, Eq. (7). The static yield surface is used to develop the dynamic yield surface  $F_d$ , Eq. (10), by treating  $F_R$  as the modifying function, as described above. For rate dependent analysis, the dynamic yield surface  $F_d$  is used to derive the elastoplastic matrix in the incremental constitutive equations; Eq. (6) for  $D = 0$ :

$$d \underset{\sim}{\sigma}^i = \underset{\sim}{C}^{i(ep)} d \underset{\sim}{\varepsilon}^i \quad (13)$$

where  $\underset{\sim}{C}^{i(ep)}$  is the elastoviscoplastic (evp) constitutive matrix derived on the basis of the dynamic yield surface,  $F_d$ .

## 7 Laboratory Tests and Parameters

A series of triaxial shear and creep tests were performed on the soil (glacial till) [4,6]. The former were conducted at various confining pressures,  $\sigma'_3 = 100, 200, 300$  and  $400$  kPa; tests for independent (not used to find parameters) were also performed at  $\sigma'_3 = 150$  and  $500$  kPa. The creep tests were performed at  $\sigma'_3 = 100, 200$  and  $400$  kPa and at constant stress at fractions of the peak stresses in respective shear tests; independent validation test was performed at  $\sigma'_3 = 300$  kPa. The parameters for evp model, derived by using the shear and creep test data are given below [4]:

Elastic:  $E = 50,470$  kPa,  $\nu = 0.45$ ;

HISS (RI) for  $F_s$ :  $\gamma = 0.0092$ ,  $\beta = 0.52$ ,  $n = 6.85$ ,  $\bar{c} = 16.67$  kPa

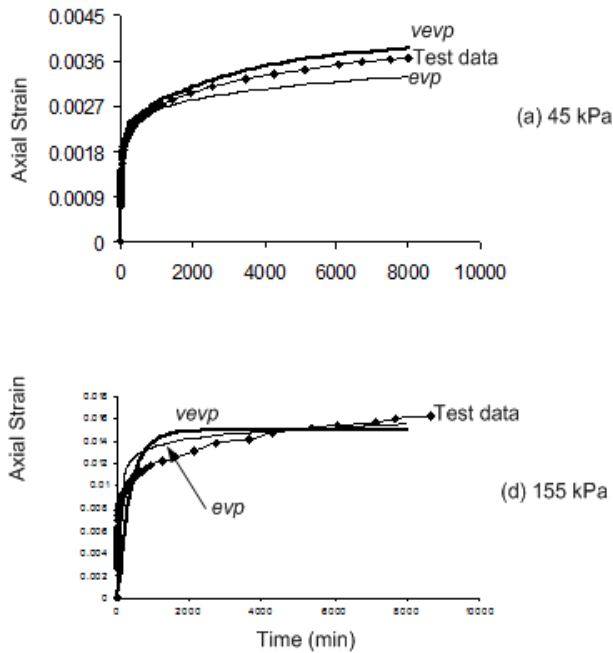
Hardening (RI):  $a_1 = 1.35 \times 10^{-7}$ ,  $\eta_1 = 0.14$

Creep (evp):  $\Gamma = 5.5 \times 10^{-6}$ ,  $N = 1.625$ .

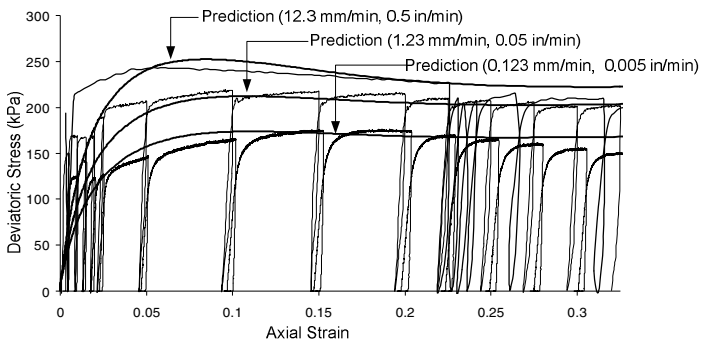
## 8 Validations

The foregoing parameters were used to validate the proposed model by comparing predictions with laboratory test data by integrating Eq. (6). The predictions are compared with test data from which the parameters were determined (Level 1) and with data not used to find the parameters (Level 2); the latter are called independent validations.

Figure 5(a) shows typical comparisons between predictions for tests data at confining pressure = 300 kPa and at two typical applied constant stresses = 45 and 155 kPa. These figures also include predictions by using the vevp model [4]. In Fig. 5(b) are shown comparisons between predictions and test data for stress-strain responses at different strain rates: 0.123, 1.23, 12.3 mm/min. Based on the results, it can be concluded that the proposed rate dependent evp model provides very good correlations with the observed laboratory behavior.



(a) Creep behavior at typical constant stresses



(b) Comparison of back predicted and observed behavior for three strain rates

**Fig. 5.** Comparisons between back predictions and measurements for Sky Pilot till (a) at two constant stresses and  $\sigma_3 = 300$  kPa, and (b) for rate dependent behavior at three strain rate

## 9 Conclusions

Behavior of many materials is dependent on the rate of loading. Various constitutive models can be used to simulate the rate dependence. Here, the elastoviscoplastic (evp) from the general MDSC is used to characterize the behavior that exhibits creep. The evp model for static behavior is based on the yield surface ( $F_s$ ) at static (strain rate = zero) condition.

For rate dependent behavior, the yield surface ( $F_d$ ) is a function of the rate of loading. The rate dependent or dynamic yield surface,  $F_d$ , is obtained by correcting the static surface,  $F_s$ , by introducing a modification or correction function,  $F_R$ . Since the test data at static strain rate is not readily available, a novel method is developed to define the static yield surface,  $F_s$ , by using the steady state conditions in creep tests at different confining pressures and constant axial stresses.

The proposed model is validated with respect to laboratory tests used for finding the parameters and independent tests not used to find the parameters. The model is also used to predict the rate dependent behavior of an alloy (solder) [4], which is not included here. Comparison between the model predictions and the laboratory test data show very good correlation. Hence, it is believed that the proposed model can be used to characterize rate dependent behavior many engineering materials.

**Acknowledgements.** The research in this paper was funded partially by the National Science Foundation, Washington, DC, Award No. EAR-0229889. Participation and assistance of D.N. Contractor, J. Jenson, A. Carlton, P.U. Clark and A. Pandey are gratefully acknowledged.

## References

- [1] Desai, C.S.: Mechanics of materials and interfaces: the disturbed state concept. CRC Press, Boca Raton (2001)
- [2] Perzyna, P.: Fundamental problems in viscoplasticity. *Advances in Applied Mech.* 9, 243–277 (1966)
- [3] Pande, G.N., Owen, D.R.J., Zienkiewicz, O.C.: Overlay models in time-dependent nonlinear material analysis. *Computer and Structures* 7, 435–443 (1977)
- [4] Sane, S., Desai, C.S.: Disturbed state concept for reliability analysis of lead-free solders and prediction of glacial motions. NSF Report, Dept. of Civil Eng. and Eng. Mechs., The Univ. of Arizona, Tucson, AZ, USA (2007)
- [5] Baladi, G.Y., Rohani, B.: Development of an elastic viscoplastic constitutive relationship for earth materials. In: Desai, C.S., Gallagher, R.H. (eds.) *Mechanics of Engineering Materials*, ch. 2, pp. 23–43. John Wiley and Sons Ltd (1984)
- [6] Pandey, A.: Disturbed state modeling for creep response of sub glacial till. M.S. Thesis, Dept. of Civil Eng. and Eng. Mechanics, Univ. of Arizona, Tucson, AZ, USA (2005)

# Some Strengths and Weaknesses of Overstress Based Elastic Viscoplastic Models

T.M. Bodas Freitas<sup>1</sup>, D.M. Potts<sup>2</sup>, and L. Zdravkovic<sup>2</sup>

<sup>1</sup> Instituto Superior Técnico, Portugal  
tmbodas@civil.ist.utl.pt

<sup>2</sup> Imperial College London, UK.

**Abstract.** Various elastic viscoplastic models based on the overstress theory by Perzyna [9] have been proposed and are described in the literature. This paper presents the theoretical formulation of this type of models and highlights the abilities and shortcomings of such models to reproduce the time dependent behaviour of clays observed in the laboratory and the implications that these have when used in the analysis of boundary value problems.

## 1 Introduction

Driven by the increasing use of numerical methods in geotechnical design, various constitutive models have been proposed to simulate the time dependent behaviour of soils, in particular clays, under general stress conditions [8]. Due to its simplicity and flexibility, most of these are elastic viscoplastic (EVP) models based on Perzyna's overstress theory [9]. These models reproduce a unique stress – strain – strain rate relationship that is found to be adequate in reproducing most aspects of the time dependent behaviour (namely creep, stress relaxation and strain rate effects) of natural and reconstituted clays [2].

## 2 Model General Formulation

The basic assumption of EVP models is that the total strain rate  $\dot{\boldsymbol{\epsilon}}_{ij}^T$  is decomposed into an elastic and a viscoplastic component:

$$\dot{\boldsymbol{\epsilon}}_{ij}^T = \dot{\boldsymbol{\epsilon}}_{ij}^{el} + \dot{\boldsymbol{\epsilon}}_{ij}^{vp} \quad (1)$$

where the elastic strain increment,  $\dot{\boldsymbol{\epsilon}}_{ij}^{el}$ , is instantaneous and thus time independent and the viscoplastic strain increment,  $\dot{\boldsymbol{\epsilon}}_{ij}^{vp}$ , is time dependent and irreversible.

According to the viscoplastic theory proposed by Perzyna [9], the viscoplastic strain increment can be evaluated as:

$$\dot{\epsilon}_{ij}^{vp} = \gamma \cdot \langle \Phi(F) \rangle \cdot \frac{\partial f_d}{\partial \sigma'_{ij}} \quad (2)$$

$$\text{Where} \quad \langle \Phi(F) \rangle = \Phi(F) \quad \text{if } F > 0$$

$$\langle \Phi(F) \rangle = 0 \quad \text{if } F \leq 0$$

$\dot{\epsilon}_{ij}^{vp}$  is the viscoplastic strain rate tensor;  $\gamma$  is a fluidity parameter and  $\Phi$  is a function of the overstress,  $F$ , given by the following equation:

$$F = \frac{f_d}{f_s} - 1 \quad (3)$$

where  $f_d$  is the dynamic loading surface (i.e. the loading surface that passes through the current stress state) and  $f_s$  is the static loading surface that defines the region of time independent and pure elastic behaviour (i.e. a yield surface), as shown schematically in Figure 1a. According to Eq. 2 and 3 the viscoplastic strain rate is a function of the distance between the dynamic and the static loading surfaces, and the value of  $\Phi(F)$  is implicitly constant for all stress states located on a given loading surface. The individual strain components are obtained from a potential that is coincident with dynamic loading surface. The size of the static loading surface is the model hardening parameter that varies with the amount of viscoplastic strain.

The overstress theory differs from the plasticity theory as the former does not invoke the consistency rule to derive the equations that govern the deformation behaviour of a soil element. Thus, the current stress state can lie on, above or below the static loading surface. When loading a soil element at a very high strain rate, overstress theory based models will predict that the material response is identical or very close to pure elastic behaviour, as there is no time for time delayed viscoplastic strains to occur. If the fluidity parameter  $\gamma$  or equivalent is set equal to zero then the behaviour is elastic.

The overstress theory is able to mimic strain rate effects in the material's stress-strain response and predicts the phenomena of creep and stress relaxation, provided the processes start from a stress state outside the static loading surface. The main difficulty in applying the overstress theory, in the form described above, is to identify the static yield function, as by definition, it corresponds to loading at a strain rate equal to zero. To overcome this problem, the form of the overstress function may be changed, such that  $F$  is a measure of the distance between the current (dynamic) loading surface,  $f_d$ , and a reference loading surface,  $f_{ref}$ , associated with a finite viscoplastic strain rate value (often coincident with the normally consolidated, NC, state).  $\Phi(F)$  is then evaluated for stress states on, above and below  $f_{ref}$  (i.e. for values of  $F$  larger, smaller or equal to zero). Using this approach, permanent time and rate effects can be reproduced at NC and overconsolidated (OC) stress states.

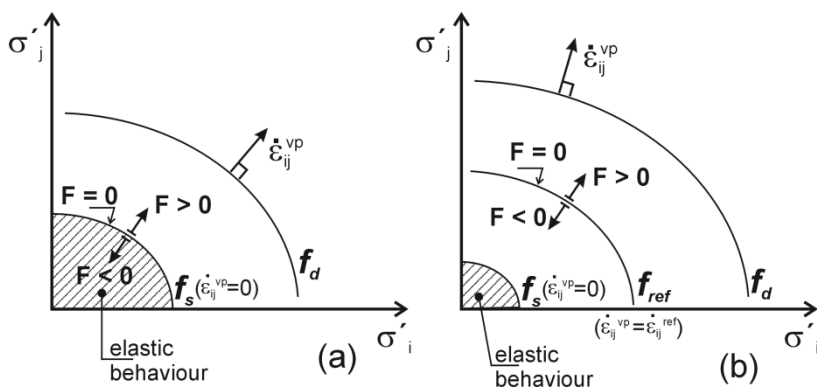


**Fig. 1.** Schematic framework of EVP models. a) original Perzyna model; b) adapted overstress model

If no static loading surface (yield surface) is specified,  $\Phi(F)$  is evaluated for all values of  $F$  (i.e. for all soil states); therefore a soil element left to creep under constant effective stresses is predicted to reach infinite viscoplastic strains at infinite time. [4,12] introduce a static loading surface (yield surface) within the reference loading surface (Figure 1b). The introduction of a yield surface, and thus a region of pure elastic behaviour, implies that there is a limit to the amount of creep strains, which is consistent with the adopted hyperbolic creep law in these works.

$\Phi(F)$  may take a variety of mathematical forms. In some earlier works,  $\Phi(F)$  was taken as an exponential function of overstress and the function constants were obtained by curve fitting laboratory test data. Alternatively  $\Phi(F)$  has been related to the observed creep behaviour under one-dimensional or isotropic stress conditions, a procedure that simplifies significantly the derivation of the model parameters.

In most cases the shape of the loading surface and plastic potential is fixed and mathematically described by the Cam Clay yield surface or the elliptical shape of the Modified Cam Clay surface, and thus once the angle of shearing resistance is set, the undrained shear strength under a given shearing mode is predefined. For many soils this results in a significant divergence between predicted and available undrained shear strength. [4,12] employ flexible functions to describe the loading surface, that can be adjusted through the model parameters, to ensure that both the soil's drained and undrained shear strength are simultaneously well reproduced. In [6] the loading surface has the shape of a rotated ellipse to account for soil anisotropy, the inclination of which varies during loading, with the amount of irrecoverable strain, to reproduce the soil's evolving anisotropy.

### 3 Aspects of Soil Behaviour Simulated by EVP Models

The numerical predictions shown in this paper were obtained using an overstress based model that incorporates some important features, namely: i) a non-linear

creep law based on the concept of equivalent time [11,12] that includes a limit to the amount of drained creep deformation and ii) a flexible loading surface that can reproducing a wide range of shapes in  $p' - J$  stress space (where  $p'$  is the mean effective stress and  $J$  is the deviatoric stress) and incorporates the Matsuoka-Nakai failure criterion in deviatoric stress space. The model was implemented in the Imperial College Finite Element Code, ICFEP [10], and thoroughly validated [4].

Overstress based models reproduce a unique stress-strain-strain rate law and thus mimic permanent rate effects in the soil's stress-strain response (i.e. isotach viscosity); they are suitable to model most features of the time dependent behaviour of natural and reconstituted clays, in the NC and OC state, namely the phenomena of creep, stress relaxation and the effect of strain rate on the stress-strain response, in particular on the soil's pre-consolidation pressure and undrained shear strength.

An interesting feature shown by [4] is that overstress based models predict that the critical state line (CSL) is unique in stress space  $p' - J$  but it is rate dependent in  $p' - e$  space (where  $e$  is the void ratio). Figure 2 shows the model predictions for a series of constant rate of strain (CRS) drained triaxial compression tests on NC and OC samples, isotropically consolidated to 100 kPa, obtained by means of single element finite element analyses, using model parameters typical of a soft clay. Figure 3 shows the state path predicted during the same analyses in  $p' - \varepsilon_{vol}$  space, where  $\varepsilon_{vol}$  is the total volumetric strain. The critical state points lie on the same vertical (i.e. same effective stress) but they move upwards with increasing strain rate, showing that in this space the CSL is rate dependent. However, the distance between CSLs per logarithmic cycle of strain rate is about 0.01 volumetric strain (i.e. 0.025 in void ratio, given that the samples had an initial void ratio equal to 1.5). This value is very small, comparable to the error encountered in void ratio laboratory measurements, suggesting that its experimental verification may not be feasible at present.

Most EVP models include a linear logarithmic creep law; in this case a soil element left to creep under constant effective stresses is predicted to reach infinite viscoplastic strain at infinite time, an assumption that is conservative but obviously unrealistic. Figure 4 shows the results of two drained creep tests under isotropic stress conditions and the numerical predictions obtained when using a linear logarithmic and a hyperbolic creep law (with a limit for the amount of creep volumetric deformation). The adoption of a hyperbolic creep law leads to predictions of long term creep deformations in closer agreement with laboratory and field measurements, particularly for large creep periods [7,11].

[8] note that overstress based models cannot reproduce tertiary compression; however that may be achieved if an adequate creep law is adopted. One obvious limitation of EVP overstress based models is the fact that they cannot mimic accelerating creep and therefore cannot reproduce appropriately undrained creep rupture [1], as discussed in the following section.

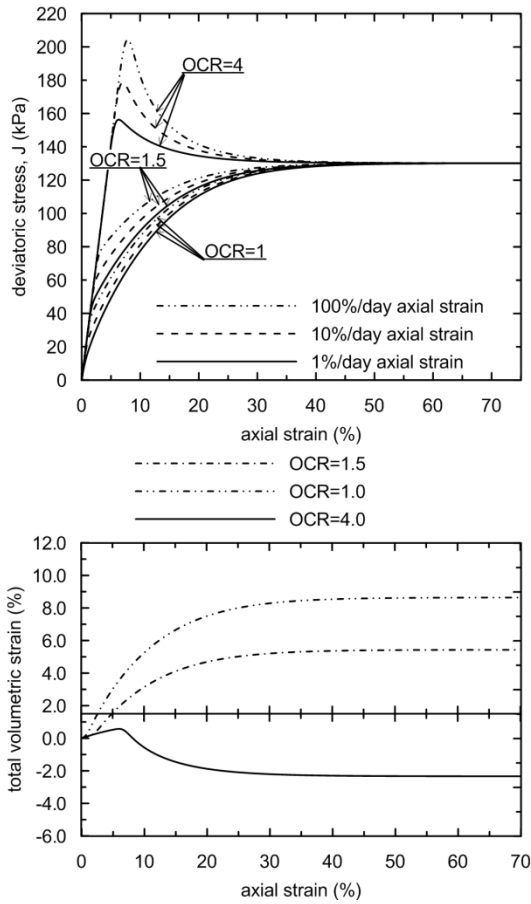


**Fig. 2.** Numerical predictions of CRS drained triaxial compression tests on NC and OC samples; a) stress – strain curves and b) volumetric strain during shearing for samples sheared at 10%/day axial strain

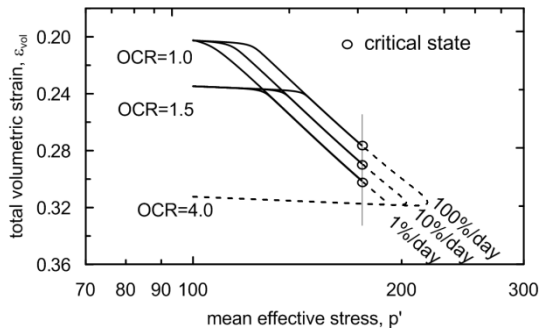


**Fig. 3.** Predicted state paths during drained triaxial compression tests

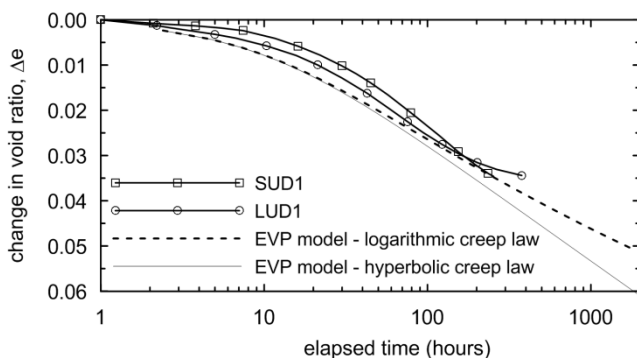


Fig. 4. Drained creep tests on Carse Clay: laboratory test data and numerical predictions

## 4 Application of EVP Models in Boundary Value Problems

There are a limited number of reported cases of the application of EVP models to the analysis of boundary value problems, in particular in conditions close to failure. [3] analysed the short and long-term behaviour of two surface footings on Carse clay [5]. Figure 5 shows the load-displacement curves, measured in the field and predicted by numerical analysis, of one footing that was taken to failure over 3 days. In addition, Figure 5 shows the model predictions obtained when the footing is continuously loaded, after the load test. These results demonstrate some of the shortcomings of EVP models when these are applied in the analysis of boundary value problems:

i) EVP models are unable to predict ultimate failure conditions; in particular, in this case, no ultimate bearing capacity was reached. This derives from the fact that these models are based on a unique stress-strain-strain rate law and thus an increase in strain rate (associated with the proximity to failure) leads to an increase in the available soil undrained strength, which inhibits the occurrence of failure. Therefore, when using EVP models, failure has to be defined using serviceability failure criteria, such as a limit deformation or deformation rate.

ii) The numerical analyses reproduce poorly the soil's stiffer response during the early loading stages. This derives from the fact that the models employed (to the knowledge of the authors similarly to all overstress based EVP models published in the literature) adopt a stress dependent elastic bulk and shear moduli and do not account for their degradation with strain level.

iii) According to the model formulation viscoplastic strains are predicted for all stress states located above the yield surface. Therefore when using the framework described in Fig 1b irrecoverable deformations are likely to be predicted for all (or most) points in the analysis domain as soon as the analysis is initiated (time is applied), even if no external load is prescribed (i.e. exclusively under the initial in-situ stresses). For NC and lightly OC states these deformations will be significant. This is against the experimental evidence that usually an external perturbation is required to initiate significant creep deformations.

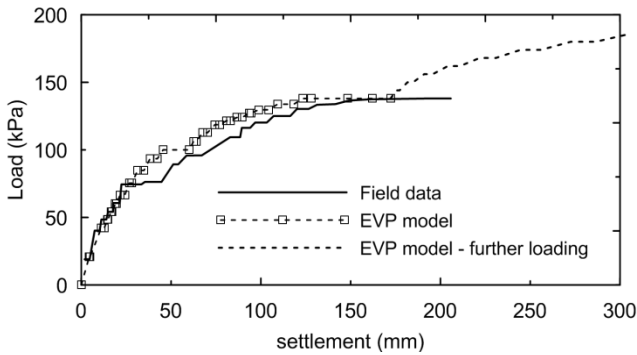


**Fig. 5.** Load displacement curve of a surface footing on Carse Clay: field measurements and numerical predictions

The characterisation and numerical modelling of the time and rate dependent behaviour of clays is complicated by the fact that the behaviour of natural clays is simultaneously influenced by other phenomena such as anisotropy and structure. [13] describe an overstress based model that accounts for soil viscosity, anisotropy and destructuration, aiming to evaluate the relative importance of each feature on the observed behaviour of an embankment on POKO clay. The results suggest that anisotropy and destructuration have a relatively smaller influence on the observed soil response. To date, no studies have been carried out on the numerical modelling of the gain of soil structure during a creep period or during loading at very slow strain rates [7].

## 5 Conclusions

Various overstress based EVP models are described in the literature. These models have been extensively validated and are shown to reproduce adequately most features of the time and rate dependent stress-strain response of natural and reconstituted clay soils, as observed in laboratory tests. However, further work is needed regarding the application of these models in the analysis of boundary value problems.

## References

- [1] Adachi, T., Oka, F., Mimura, M.: Mathematical structure of an overstress elasto-viscoplastic model for clay. *Soils and Foundations* 27(3), 31–42 (1987)
- [2] Augustesen, A., Liingaard, M., Lade, P.V.: Evaluation of the time-dependent behaviour of soils. *Int. Journal of Geomechanics* 4(3), 137–156 (2004)
- [3] Bodas Freitas, T.M.: Numerical modelling of the time dependent behaviour of clays. PhD Thesis. Imperial College, University of London (2008)
- [4] Bodas Freitas, T.M., Potts, D.M., Zdravkovic, L.: A time dependent constitutive model for soils with isotach viscosity. *Computers and Geotechnics* 38(6), 809–820 (2011)

- [5] Jardine, R.J., Lehane, B.M., Smith, P.R., Gildea, P.A.: Vertical loading experiments on rigid pad foundations at Bothkennar. *Geotechnique* 45(4), 573–597 (1995)
- [6] Leoni, M., Karstunen, M., Vermeer, P.A.: Anisotropic creep model for soft soils. *Geotechnique* 58(3), 215–226 (2008)
- [7] Leroueil, S., Kabbaj, M., Tavenas, F., Bouchard, R.: Stress-strain-time rate relation for the compressibility of sensitive natural clays. *Geotechnique* 35(2), 159–180 (1985)
- [8] Liigaard, M., Augustesen, A., Lade, P.V.: Characterization of models for the time dependent behaviour of soils. *Int. Journal of Geomechanics* 4(3), 157–177 (2004)
- [9] Perzyna, P.: Constitutive equations for rate sensitive plastic materials. *Quarterly of Applied Mathematics* 20(4), 321–332 (1963)
- [10] Potts, D.M., Zdravkovic, L.: *Finite element analysis in geotechnical engineering: Theory*. Thomas Telford, London (1999)
- [11] Yin, J.-H.: Non-linear creep of soils in oedometer tests. *Geotechnique* 49(5), 699–707 (1999)
- [12] Yin, J.-H., Zhu, J.: - G and Graham J: A new elastic visco-plastic model for time-dependent behaviour of normally and overconsolidated clays: theory and verification. *Canadian Geotechnical Journal* 39, 157–173 (2002)
- [13] Yin, Z.-Y., Karstunen, M.: Influence of anisotropy, destructuration and viscosity on the behaviour of an embankment on soft clay. In: *Proceedings of the Int Association for Computer Methods and Advances in Geomechanics*, pp. 4728–4735 (2008)

# Comparison of Anisotropic Rate-Dependent Models at Element Level

Minna Karstunen<sup>1,2,3,\*</sup>, Mohammad Rezania<sup>3,4</sup>,  
and Nallathamby Sivasithamparam<sup>3,5</sup>

<sup>1</sup> Department of Civil and Environmental Engineering  
Chalmers University of Technology, SE-412 96 Göteborg, Sweden

<sup>2</sup> Department of Civil and Environmental Engineering  
Aalto University, FI-00076 Aalto, Finland

<sup>3</sup> Department of Civil and Environmental Engineering  
University of Strathclyde, 107 Rottenrow, Glasgow G4 0NG, UK

<sup>4</sup> School of Civil Engineering and Surveying  
University of Portsmouth, Portland Street, Portsmouth PO1 3AH, UK

<sup>5</sup> Plaxis B.V., Delft, 2628 XJ, The Netherlands  
minna.karstunen@strath.ac.uk

**Summary.** Two recently proposed anisotropic rate-dependent models, EVP-SCLAY1 and ACM are used to simulate the stress-strain behaviour of Vanttila clay. The models are identical in the way the evolution of anisotropy is simulated, but differ in the way the rate-effects are taken into account. Based on numerical simulations against element level tests, using objective parameters, suggest that EVP-SCLAY1 is able to give a better representation of the clay response at element tests than ACM in 1D loading, but the latter gives a better prediction for undrained strength.

**Keywords:** constitutive model, creep, consolidation.

## 1 Introduction

Although the geotechnical engineers have been aware of the issues related to creep and rate effects for ages, only relatively recently that comprehensive rate-dependent constitutive models capable of modelling anisotropic natural soils have been proposed (see e.g., [1-5]). The aim of this paper is to compare objectively the predictions by two anisotropic rate-dependent models: EVP-SCLAY1 [4] and ACM [2] at element level. For the sake of simplicity, the effects of apparent bonding and destructuration of the rate-dependent behaviour are ignored, although as demonstrated e.g. by Hinchberger & Qu [3] and Yin et al. [5] this may be necessary for modelling certain phenomena.

---

\* Corresponding author.

## 2 ACM and EVP-Sclay1 Models

In ACM and EVP-SCLAY1 anisotropic surfaces, analogous to the anisotropic yield surface in the rate-independent S-CLAY1 model [6], represent the boundary between large irrecoverable strains and relatively small strains. Subsequent loading that produces irrecoverable strains, may change the anisotropy. In EVP-SCLAY1 [4] within so-called static yield surface (see Fig. 1a) the behaviour is purely elastic. In contrast, in ACM, the bounding surface is called normal consolidation surface NCS (see Fig. 1b) and creep strains occur even in the overconsolidated range.

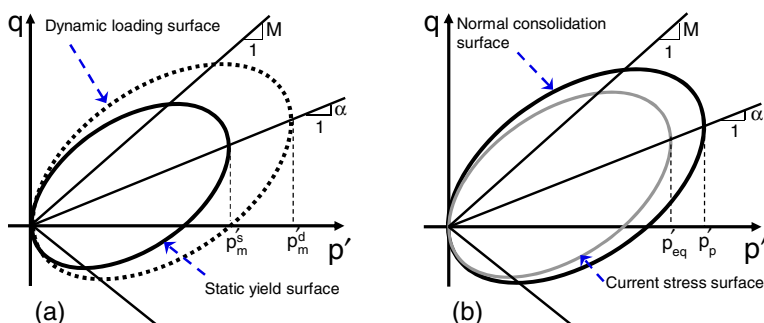


**Fig. 1.** a) Yield surfaces of the EVP-SCLAY1 model; b) Normal consolidation surface and current stress surface of ACM model

The advantage of ACM over EVP-SCLAY1 is that it is possible to derive the soil constants directly from the experimental tests, whilst the viscosity coefficients of EVP-SCLAY1 require some calibration. Both models have been implemented in the Plaxis 2D and 3D finite element code as user-defined soil models.

## 3 Simulations of Vanttila Clay

The model simulations include element level tests on Vanttila Clay [5] which is a highly sensitive ( $S_t > 50$ ) soft clay. Conventional oedometer test results, combined with the results from undrained triaxial tests have been used in determination of average parameter values for the EVP-SCLAY1 and ACM. At a depth of 2.9 m the common parameter values are:  $e_0=3.3$ ,  $\lambda=0.5$ ,  $\kappa=0.057$ ,  $\lambda^*=0.1163$ ,  $\kappa^*=0.0133$ ,  $M=1.35$ ,  $\nu'=0.2$ ;  $\alpha_{K0}=0.52$ ,  $\omega_d=0.91$  and  $\omega=12$ . For ACM  $\mu^*=3.76E-3$  and  $\tau=1$  day, and for EVP-SCLAY1  $N=23$  and  $\mu=4E-3$  ( $\text{day}^{-1}$ ).

Firstly, conventional 1 day oedometer tests on Vanttila clay are simulated with Plaxis 2D 2010 with the user-defined model implementation of EVP-SCLAY1 and ACM. Fig. 2 shows the model prediction against experimental data (vertical strains vs. log-time) for Vanttila clay at a depth of around 2.8-2.9 m. No attempt

has been made to create a best possible match, and the soil constants have been determined independently of the test that is being modelled. For all loading stages simulated, EVP-SCLAY1 appears to give better predictions than ACM. Of course, it would be possible to match ACM with the test data better than done in Fig. 2 by e.g. artificially increasing POP or OCR,  $\tau$  or indeed parameter  $\beta = (\lambda^* - \kappa^*)/\mu^*$ . That however, would be curve-fitting rather than objective model prediction. Fig. 3 in turn shows the model predictions for an undrained shear test of Vanttila clay at constant strain rates. In this case ACM gives a better prediction of the undrained strength than EVP-SCLAY1.

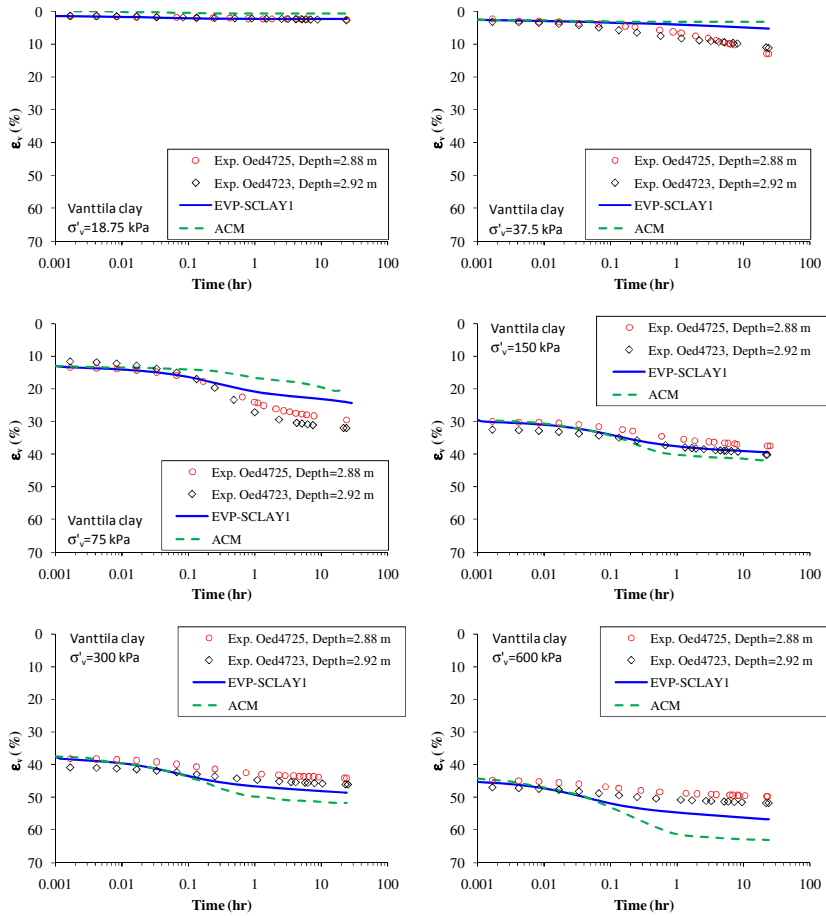
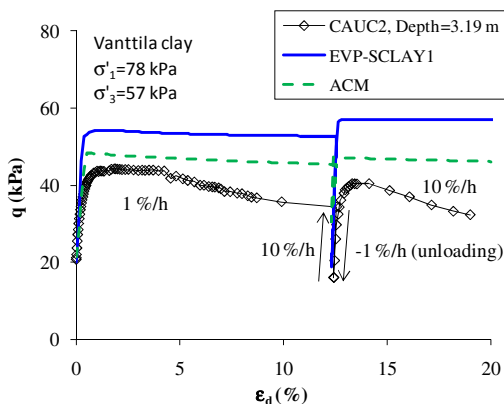


Fig. 2. Conventional oedometer test predictions of Vanttila clay



**Fig. 3.** Comparison of simulations of stress-strain behaviour of Vanttila clay for an undrained triaxial test with constant strain rates

## 4 Conclusions

Two anisotropic rate-dependent models, ACM [2] and EVP-SCLAY1 [4] have been used to simulate element level behaviour of Vanttila clay. EVP-SCLAY1 appears to give marginally better predictions than ACM for 1D loading, whilst ACM gives better prediction of undrained strength. The simulations ignored the effects of apparent bonding and destructuration for the sake of simplicity, which is not always appropriate. Challenge is how to make good predictions with objective parameters values. The compressibility, apparent preconsolidation stress and the tendency of a natural clay to creep is highly dependent on sample quality and further investigations on the effect of sample disturbance to the rate effects and deformations are needed.

**Acknowledgements.** The work presented was carried out as part of a Marie Curie Industry-Academia Partnerships and Pathways projects GEO-INSTALL (PIAP-GA-2009-230638) and CREEP (PIAP-GA-2011-286397). The experimental work was done at Aalto University sponsored by Academy of Finland (Grant 128459).

## References

- [1] Zhou, C., Yin, J.-H., Zhu, J.-G., Cheng, C.-M.: Elastic anisotropic viscoplastic modeling of the strain-rate dependent stress-strain behaviour of K<sub>0</sub>-consolidated natural marine clays in triaxial shear test. *Int. J. Geomech.* 5(3), 218–232 (2006)
- [2] Leoni, M., Karstunen, M., Vermeer, P.A.: Anisotropic creep model for soft soils. *Géotechnique* 58(3), 215–226 (2008)
- [3] Hinchberger, S.D., Qu, G.: Viscoplastic constitutive approach for rate-sensitive structured clays. *Can. Geotech. J.* 46(6), 609–626 (2009)

- [4] Karstunen, M., Yin, Z.-Y.: Modelling time-dependent behaviour of Murro test embankment. *Géotechnique* 60(10), 735–749 (2010)
- [5] Yin, Z.-Y., Karstunen, M., Chang, C.S., Koskinen, M., Lojander, M.: Modeling time-dependent behavior of soft sensitive clay. *J. Geotech. Geoenviron. Eng.* 137(11), 1103–1113 (2011)
- [6] Wheeler, S.J., Nääätänen, A., Karstunen, M., Lojander, M.: An anisotropic elastoplastic model for soft clays. *Can. Geotech. J.* 40(2), 403–418 (2003)

# A Comparison of Four Elastic Visco-Plastic Models for Soft Clay

David Nash<sup>1</sup> and Matthew Brown<sup>2</sup>

<sup>1</sup>Department of Civil Engineering, University of Bristol, Bristol BS8 1TR, U.K.

<sup>2</sup>Arup Geotechnics, 63 St. Thomas Street, Bristol BS1 6HJ, U.K.

**Abstract.** The time-dependent settlement of soft clays following application of surface loading may be modelled using elastic visco-plastic constitutive models to describe the soil behaviour. For applied loadings that increase the stresses to around the in-situ yield stress, the predicted behaviour is strongly influenced by the associated breakdown of clay structure and the way in which this is modelled. Four elastic visco-plastic models have been compared and all calculate the creep rate in fundamentally the same manner by comparison to the state at the same effective stress on a reference isotache.

## 1 Introduction

The prediction of long-term settlements of embankments foundations and fills on soft clays requires a good understanding of the time dependant behaviour of the clay. While a complex finite element analysis may sometimes be necessary, it will often be more appropriate to undertake a one-dimensional analysis of the centre-line conditions. The study reported here explores the implications of the different assumptions made within four constitutive models as the clay is stressed towards and beyond the yield stress, and its structure is gradually damaged.

## 2 A Simple Isotache Model

In the 1-D elastic visco-plastic (EVP) models used in the present study the incremental total strain  $\partial\epsilon$  resulting from a change of vertical effective stress  $\partial\sigma'$  is the sum of the incremental elastic strain  $\partial\epsilon^e$  and the incremental creep strain  $\partial\epsilon^{tp}$ .

In stress-strain-strain rate models the creep strain rate is defined by the relationship of the current soil state to that on a reference isotache at the same effective stress. Under constant effective stress the creep or secondary compression strain  $\epsilon^{tp}$  at time  $t$  is assumed to increase linearly with logarithmic time as given by equation (1):

$$\epsilon^{tp} = \epsilon_{ref} + C \cdot \ln \left( \frac{t}{t_{ref}} \right) \quad (1)$$

where  $C$  is a coefficient of secondary compression, and  $\epsilon_{ref}$  and  $t_{ref}$  define a reference state. In incremental form equation (1) may be expressed as:

$$\dot{\epsilon}^{ip} = \frac{C}{t} \quad \text{and thus} \quad \dot{\epsilon}_{ref}^{ip} = \frac{C}{t_{ref}} \tag{2}$$

The creep strain to the current state from the reference state (equation 1) may then be expressed as:

$$\epsilon^{ip} = \epsilon_{ref} + C \cdot \ln \left( \frac{\dot{\epsilon}_{ref}^{ip}}{\dot{\epsilon}^{ip}} \right) \tag{3}$$

Many of the EVP models described in the literature use a relationship in the form of equation (1) to evaluate the creep rate by reference to a linear isotache but this presents the analyst with the inherent difficulty of deciding the reference time. Use of the logarithmic creep relationship in the form of equation (3) avoids this difficulty. Four EVP models were used in the present study:

1. A 1-D ‘equivalent time’ creep model for unstructured clay (Yin & Graham 1996, Nash & Ryde 2001) denoted Model 3;
2. The Plaxis Soft Soil Creep model for unstructured clay (Vermeer & Neher 1999) denoted SSC;
3. Model 3-d accounting for an initial structure (Nash 2010);
4. The University of Chalmers time resistance creep model accounting for an initial structure (Claesson 2003) denoted Chalmers model.

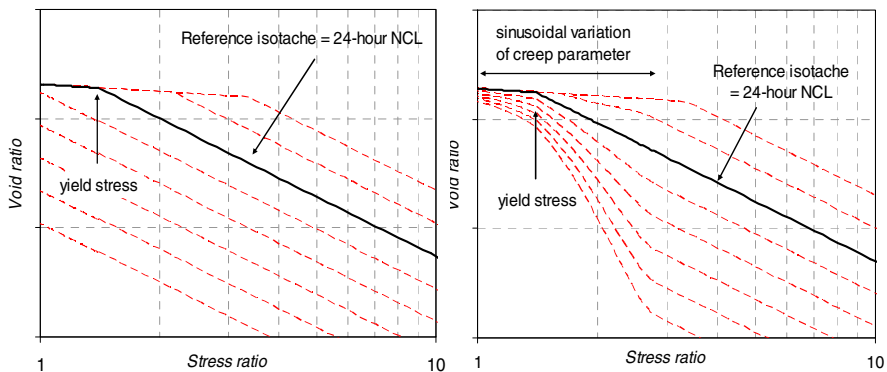


**Fig. 1.** General isotache shapes for EVP models a) without structure and b) with initial soil structure

The Soft Soil Creep model is run within Plaxis; the others have been implemented into the finite difference framework Briscon (Nash & Ryde 2001). All are similar to the simple isotache model described above. The first pair of models do not model destructuration of the clay and use a set of parallel isotaches that are

linear on a plot of void ratio or engineering strain vs  $\log \sigma'_v$ . However this is not a requirement for an EVP analysis and the other pair of models that incorporate de-structuration of the clay use curved isotaches as illustrated in Figure 1.

### 3 Full-Scale Test Predictions

A benchmarking study proposed by the Norwegian Geotechnical Institute, was reported at an international workshop on creep of soft soils held in 2009. Six research groups undertook various creep predictions (Jostad and Degago 2010) for a simplified geometry comprising 10m of sand overlying 30m of soft compressible clay. Variables specified included the applied stress at ground level, initial OCR and drainage conditions. A single oedometer test was provided from which soil parameters were to be determined. The Bristol prediction was described by Nash (2010), but the exercise was recently extended to explore the performance of several EVP models, and to highlight the implications of modelling initial soil structure. Two situations were considered:

1. An initial OCR of 1.4 in the clay, with 0kPa applied stress (creep only).
2. An initial OCR of 1.4 in the clay, with 90kPa applied stress.

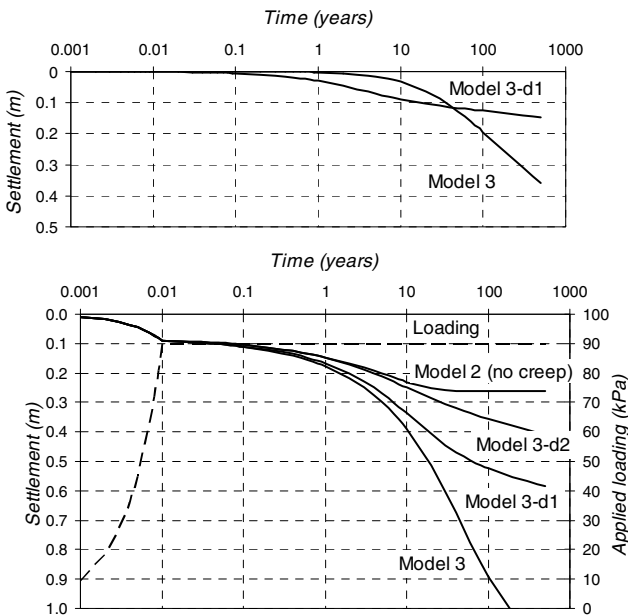


**Fig. 2.** Predicted settlement vs time for a) no load and b) 90 kPa for OCR=1.4 1-D analyses were undertaken that involved creep for 500 years. Each pair of models for *un-structured* and *structured* clay predicted very similar results, confirming that each accounts for creep in a similar manner. Some time-settlement plots are shown in Figure 2 for zero and 90 kPa applied load.

With no applied load (case 1) settlements up to 0.4m were predicted, with the final creep rate for the *unstructured* clay greater than that of *structured* clay. These large settlements seem implausible and result from high creep rates in the initial state. When equivalent age of the clay was increased from 1 day (in model 3 and 3-d1) to 10000 years (model 3-d2) the settlement was negligible. Under 90 kPa applied loading (case 2), models accounting for initial structure predicted circa 50% of the settlement predicted by the structured models, highlighting the importance of representing the initial material structure. Further details are given by (Nash and Brown 2012).

## 4 Conclusions

Four 1-D elastic visco-plastic models have been studied; despite differences in terminology, they are all similar to the simple isotache model described above. Modelling the gradually changing creep behaviour as clay structure is broken down in the over-consolidated state and around the yield stress has a significant effect on strain predictions for over-consolidated material. While a two or three dimensional analysis with a more complex constitutive model may sometimes be necessary, this will often present difficulties in defining representative soil parameters. It may often be appropriate to undertake a one-dimensional analysis of the centre-line conditions like those illustrated here, taking care to use a model such as the two reported above that incorporate the gradual destructure of the clay.

## References

- Claesson, P.: Long term settlements in soft clays. PhD Thesis, Chalmers University of Technology, Gothenburg (2003)
- Jostad, H.P., Degago, S.A.: Comparison of methods for calculation of settlements of soft clay. In: Numerical Methods in Geotechnical Engineering, pp. 57–62. Taylor and Francis, London (2010)
- Nash, D.F.T.: Influence of destructure of soft clay on time-dependant settlements. In: Numerical Methods in Geotechnical Engineering, pp. 75–80. Taylor and Francis, London (2010)
- Nash, D.F.T., Brown, M.A.: The influence of destructure of soft clay on time-dependent settlements – a comparison of some elastic visco-plastic models. Submitted to International Journal of Geomechanics (2012)
- Nash, D.F.T., Ryde, S.J.: Modelling consolidation accelerated by vertical drains in soil subject to creep. Géotechnique 51(3), 257–273 (2001)
- Vermeer, P.A., Neher, H.P.: A soft soil model that accounts for creep. Beyond 2000 in Computational Geotechnics (1999)
- Yin, J.H., Graham, J.: Elastic visco-plastic modelling of one-dimensional consolidation. Geotechnique 46(3), 515–527 (1996)

# A Rate-Dependent Viscous Model for Sand

Fang-Le Peng, P. Chattonjai, Zhen Hua, and Ke Tan

Department of Geotechnical Engineering, Tongji University,  
1239 Siping Road, Shanghai 200092, P.R. China  
pengfangle@tongji.edu.cn

**Summary.** Experimental results show the dense sand exhibits very distinct viscous characteristics. The main viscous aspect of sand includes the effect of the strain rate change, creep and stress relaxation. In order to properly simulate the viscous characteristics, especially the temporary effect of strain rate change, a new visco-elastoplastic constitutive model is presented.

**Keywords:** Dense sand, viscous behavior, constitutive model, loading rate.

## 1 Introduction

Previous research mainly focuses on the creep deformation of dense sand in the long term, which takes time as the primary inherent variable controlling the quantity of deformation. The stress-strain-time behavior of dense sand under various loading histories includes sustained loading for creep, fixed displacement for stress relaxation and monotonic loading with varying strain or displacement rate. For the last case, most of the conventional viscous models of sand fall short, due to the fact that the time,  $t$ , is taken as the inherent variable in those models, it is hard and sometimes even impossible to predict the effect of strain rate on the stress-strain relationship. To realistically portray the time-dependent behavior of sandy ground under monotonic loading, it is necessary to take into account the varying loading strain rate.

## 2 Visco-Elastoplastic Modelling for Sand

According to this non-linear three-component model (see [1]), the stress,  $\sigma$ , consists of inviscid and viscous components,  $\sigma^f$  and  $\sigma^v$ , while the strain rate,  $\dot{\epsilon}$ , consists of elastic and irreversible components,  $\dot{\epsilon}^e$  and  $\dot{\epsilon}^{ir}$ , which can be expressed as:

$$\dot{\epsilon} = \dot{\epsilon}^e + \dot{\epsilon}^{ir} \tag{1}$$

$$\sigma = \sigma^f + \sigma^v \tag{2}$$

The non-linear three-component model consists of the cross-anisotropic hypo-elastic component ( $\mathbf{E}$ ), the energy-based hardening and softening plastic component ( $\mathbf{P}$ ) and the rate-dependent non-linear viscous component ( $\mathbf{V}$ ). For the component  $\mathbf{E}$ , an inherent and stress system-induced cross-anisotropic compliance matrix for elastic strain increments was employed in the present study. The elastic Young's modulus defined for the major principal strain increment taking place in a certain direction is a unique function of the normal stress acting in that direction, while the Poisson's ratios for elastic strain increments change with the changes in the stress ratio. More details about this model can be found in Hoque and Tatsuoka [2]. For component  $\mathbf{P}$ , the inviscid component  $\mathbf{P}$  is formulated based on an isotropic, work-hardening and softening, and non-associated plastic model. The yield function and the irreversible potential function are assumed to be Mohr-Coulomb type and Drucker-Prager type, respectively. The following modified irreversible strain energy is adopted as the work-hardening parameter under plane strain condition, which is stress path-independent:

$$W^{ir*} = \int \frac{\sigma_{ij}^f d\epsilon_{ij}^{ir}}{(p^f / p_a)^n} \approx \int \frac{t^f \cdot d\gamma^{ir} + s^f \cdot d\epsilon_{vol}^{ir}}{(s^f / p_a)^n} \quad (3)$$

Where,  $\sigma_{ij}^f d\epsilon_{ij}^{ir}$  is the irreversible strain energy increment;  $t^f = (\sigma_v^f - \sigma_h^f)/2$  and  $s^f = (\sigma_v^f + \sigma_h^f)/2$ ;  $p_a = 98.1$  kPa;  $d\gamma^{ir}$  and  $d\epsilon_{vol}^{ir}$  are the irreversible shear and volumetric strains;  $n = 0.9$  for Toyoura sand in PSC tests.  $\sigma_v^f$  and  $\sigma_h^f$  are the inviscid vertical and horizontal stresses activated in component  $\mathbf{P}$ , while,  $\sigma_v^v$  and  $\sigma_h^v$  are the viscous vertical and horizontal stresses activated in component  $\mathbf{V}$ . More details about the energy-based model can be found in Peng et al. [3]. For the component  $\mathbf{V}$ , a new viscous model, called the TESRA (Temporary Effect of Strain Rate and Acceleration) model, had been proposed. This means even under the loading conditions, the effects of  $\dot{\epsilon}^{ir}$  and its rate (i.e., irreversible strain acceleration) on the  $\sigma^v$  value become temporary, therefore, the current  $\sigma^v$  value becomes a function of not only instantaneous values of  $\epsilon^{ir}$  and  $\dot{\epsilon}^{ir}$  but also recent strain history. Then, the TESRA viscous stress,  $\sigma_{TESRA}^v$ , can be obtained as:

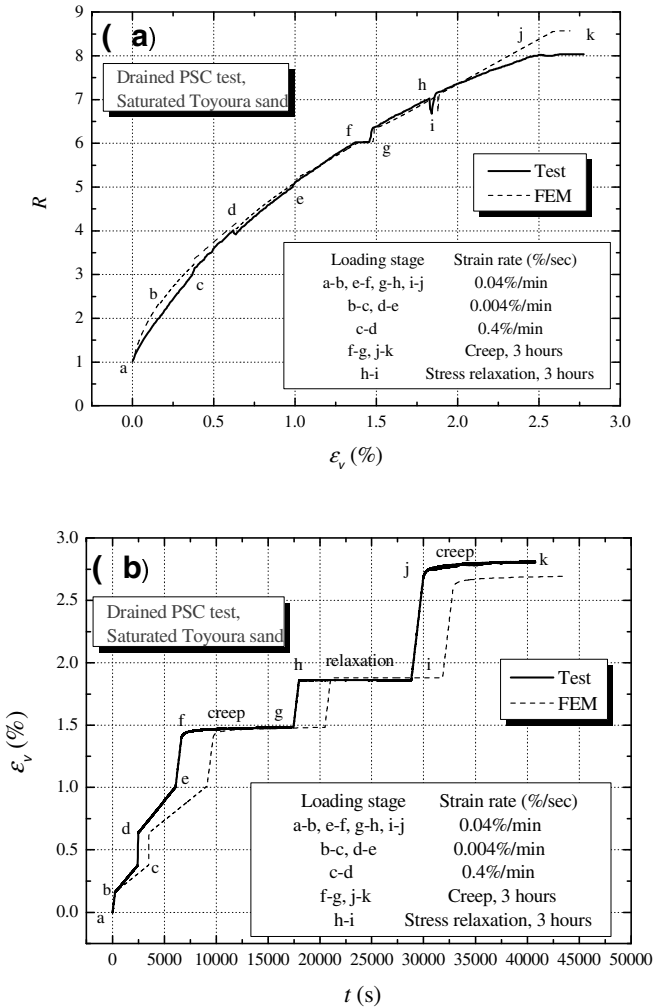
$$\sigma^v = \sigma_{TESRA}^v(\epsilon^{ir}, \dot{\epsilon}^{ir}, h_s) = \int_{\tau=\epsilon_1^{ir}}^{\epsilon^{ir}} [d\sigma_{iso}^v]_{(\tau)} \cdot r_d^{(\epsilon^{ir}-\tau)} \quad (4)$$

Where,  $\epsilon_1^{ir}$  is the initial irreversible strain at  $\sigma^v = 0$ ;  $[d\sigma_{iso}^v]_{(\tau)}$  is the developed viscous stress increment at  $\epsilon^{ir} = \tau$ ;  $r_d$  is the decay parameter that is positive less than unity. In this way, the current value of  $\sigma_{TESRA}^v$  (when  $\epsilon^{ir} = \epsilon^{ir}$ ) depends on the history of  $\epsilon^{ir}$ . More details can be found in Tatsuoka et al [4].

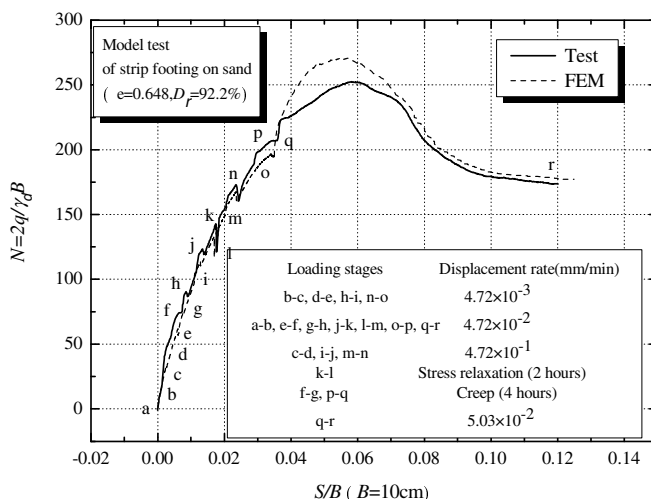
### 3 Fem Simulation and Discussion

Fig.1 compares the time-dependent stress-strain relations for the sand specimen obtained from the corresponding FEM simulations and the plane strain

compression(PSC) test performed by Kongkitkul [5]. It can be seen that the results from the FEM simulations are reasonably agreement with the physical test results. Fig. 2 compares the normalized load-settlement curves obtained from FEM and the physical model test of strip footing on sand performed by Hirakawa [6]. It can be seen that the general trend of the load-settlement curve observed in the test is well reflected by the FEM analysis, especially the response of the sandy foundation at the pre-peak strength region under the effect of variable displacement rate, creep and stress relaxation.



**Fig. 1.** FEM and test results from drained PSC test: (a) R- $\epsilon_v$  relation; (b) time history of  $\epsilon_v$



**Fig. 2.** Normalized load-settlement relations obtained from FEM and the physical model test of strip footing on sand

## 5 Conclusions

In the physical test on sand, the stress-strain curve overshoots when the strain rate suddenly increases and undershoots when decreases. The shooting of the curve behaves quasi-elastic with high instantaneous stiffness. As loading progresses, the shooting gradually decays and rejoins the curve obtained from constant strain rate monotonic loading. A rate-dependent viscous model for sand is proposed, which can simulate rather satisfactorily the viscous behavior of sand exhibited the viscous response of sandy ground, including the effect of the strain (displacement) rate, creep and stress relaxation.

## References

- [1] Di Benedetto, H., Tatsuoka, F., Ishihara, M.: Time-dependent shear deformation characteristics of sand and their constitutive modeling. *Soils and Foundations* 42(2), 1–22 (2002)
- [2] Hoque, E., Tatsuoka, F.: Anisotropy in the elastic deformation of materials. *Soils and Foundations* 38(1), 163–179 (1998)
- [3] Peng, F.L., Siddiquee, M.S.A., Tatsuoka, F., Yasin, S.J.M., Tanaka, T.: Strain energy-based elasto-viscolastic constitutive modeling of sand for numerical simulation. *Soils and Foundations* 49(4), 611–629 (2009)
- [4] Tatsuoka, F., Ishihara, M., Di Benedetto, H., Kuwano, R.: Time-dependent shear deformation characteristics of geomaterials and their simulation. *Soils and Foundations* 42(2), 103–129 (2002)
- [5] Kongkitkul, W.: Effects of material viscous properties on the residual deformation of geosynthetic-reinforced sand [PhD Thesis]. The University of Tokyo, Tokyo (2004)
- [6] Hirakawa, D.: Study on residual deformation characteristics of geosynthetic reinforced soil structures [PhD thesis]. The University of Tokyo, Tokyo (2003) (in Japanese)

# A Review on Creep of Frozen Soils

Jilin Qi\*, Songhe Wang, and Fan Yu

Cold and Arid Regions Environmental and Engineering Research Institute  
Chinese Academy of Sciences  
320 Donggang West Road, Lanzhou, China 730000  
qijilin@lzb.ac.cn

**Summary.** Creep of frozen soils is one of the most important topics in engineering activities when frozen soils are involved. This paper firstly gives a review on the previous studies on creep of frozen soils. It is found that extensive experimental work has been carried out, which has facilitated recognition of creep behaviors of frozen soils. As for modeling, due to so many factors such as soil classification, density, water (ice) content as well as especially temperature, focus has been put on empirical models which often precisely describe creep behaviors of frozen soils under certain conditions but with serious limitations for extension. Closed-form models have been a pursuit while they are more theoretical explorations rather than applications so far. Considering this state of the art, a simple method was proposed in modeling the constitutive relations of frozen soil.

**Keywords:** creep, frozen soil, creep model, hypoplastic model.

## 1 Introduction

Since the past century, many projects were built through the permafrost regions in Qinghai-Tibetan plateau, e.g., highway, oil pipeline, railway and optical cable. With increasing engineering activities in cold regions, there are some new problems when frozen soils are involved. Long-term observation of ground temperature and deformation in Qinghai-Tibetan highway and railway indicated that even when the permafrost table descends insignificantly, i.e., little thaw settlement occurs, considerable deformation was still observed in the embankment. It is found that the settlement is closely related to the warm permafrost layer beneath the embankment. In recent years, people come to realize that thaw settlement due to permafrost degradation is not the only source for the deformation of embankment. Creep of frozen soil under foundation load is also a significant source [1]. As to the high-grade highway in permafrost regions, the deformation of embankment was strictly required. Therefore, creep of warm frozen soil must be taken into

---

\* Corresponding author.

consideration in the settlement analysis. The study on the mechanical properties of frozen soil, especially the creep is in an urgent need for a reasonable description.

## 2 State-of-the-Arts: Creep Model of Frozen Soil

Frozen soil is a special geomaterial with ice inclusions and viscous unfrozen water. It is rather a difficult work to model the complicated stress-strain relationship of frozen soil under loading. So far, creep of geotechnical materials are generally described from microscopic and phenomenological views. As to the microscopic models, thermodynamics and damage mechanics are introduced to reflect the microscopic changes during creep of geo-material, e.g., the theory of rate process [2]. Andersland [3] introduced the thermodynamics into frozen soil mechanics and verified the feasibility of the theory of rate process. Fish [4–5] viewed deformation as entropy change and proposed an exponential creep equation based on the conservation of entropy. He et al. [6] derived a constitutive theory on viscoelastoplastic and damage of frozen soil. Miao et al. [7] studied the damage during creep of frozen soil by electron microscope and deduced a damage evolution equation, taking the variation of ice content into consideration. However, the microscopic variables in the creep models above are difficult to be obtained in laboratory which restrains its application in engineering.

In engineering activities, the phenomenological models are generally used, which is obtained by fitting the experimental data directly or the theory of elastic-visco-plasticity, e.g., Yin-Graham model [8]. Assur [9] put forward a tertiary creep model for frozen soil. Ting [10] then proposed a simpler model which can better describe the creep failure under relatively high stress. According to the turning point in the curve of creep rate versus time, Zhu and Carbee [11] classified the creep of frozen silt as short-term and long-term creep and found that Assure model well described the short-term creep but deviated in the long-term creep. Hereby, the corresponding relationships were established. However, due to so many influencing factors such as soil classification, density, water (ice) content as well as especially temperature, the aforementioned stress-strain relationships are limited for extension. Besides, some scholars described the creep of geo-materials by combing various mechanical elements based on the theory of elastic-visco-plasticity. Vyalov [12] derived a mechanical model to describe the creep of frozen soil. Li et al. [13] deduced a creep model of frozen deep clay on the basis of Nishihara model. This kind of model has clear physical meaning and convenient in programming. Thus, it is recommended in engineering application.

## 3 A Simple Creep Model for Frozen Soil

Under constant load, the frozen soil will respond with an instantaneous deformation initially, followed by a time-dependent deformation, with three periods of time during which the creep rate is (i) decreasing, (ii) remaining essentially constant, and (iii) increasing [14]. The creep of conventional soils display all the

creep stages aforementioned but a relatively long period of viscoplastic flow occurs for frozen soil. The mechanical elements are identified by the creep characteristics of frozen soil above-mentioned. A simple creep model under triaxial conditions can be deduced as follows,

$$e_{ij} = \frac{S_{ij}}{2G_M} + \frac{S_{ij}}{2H_M}t + \frac{S_{ij}}{2G_K} \left[ 1 - \exp\left(-\frac{G_K}{H_K}t\right) \right] \quad (\phi(F) \leq 0)$$

$$e_{ij} = \frac{S_{ij}}{2G_M} + \frac{S_{ij}}{2H_M}t + \frac{S_{ij}}{2G_K} \left[ 1 - \exp\left(-\frac{G_K}{H_K}t\right) \right] + \frac{1}{2H_N} \langle \phi(F) \rangle \frac{\partial Q}{\partial \{\sigma\}} t \quad (\phi(F) > 0)$$

in which,  $G_M$  and  $G_K$  are temperature-dependent shear modulus for Maxwell and Kelvin body, respectively;  $H_M$ ,  $H_K$  and  $H_N$  are temperature-related viscosity coefficients for Maxwell, Kelvin and Bingham body, respectively; and  $Q$  is a plastic potential function.  $\phi(F)$  is the yield function. Previous studies show that a parabolic yield criterion is more applicable for frozen soil [15–16], which is written as:

$$F = \sqrt{3J_2} - c - \sigma_m \tan \varphi + \frac{\tan \varphi}{2p_m} \sigma_m^2$$

in which,  $c$  is the cohesion (MPa);  $\varphi$  is the internal friction angle ( $^\circ$ ) when  $p=0$ ;  $p_m$  is the mean normal stress (MPa) corresponding to the maximum shear strength  $q_m$ ; and  $\sigma_m$  and  $J_2$  are the first principal stress invariant and the second deviatoric stress invariant, respectively. The associated flow rule is also adopted.

Fig. 1 presents the comparison between the experimental data and the fitted curve. It was shown that the fitted curve agrees in general with the experimental data under relatively low stresses but deviates when the tertiary part is considered.

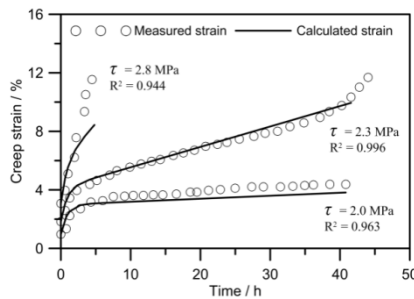


Fig. 1. Experimental verification for frozen sand

### 3 A New Method of Modeling Creep of Frozen Soil

Since the 1980s, the theory of hypoplasticity has been derived from the theory of thermodynamics to model the stress-strain relationships of geomaterials [17– 20]. In this theory, the objective stress rate of geomaterials is assumed to be dependent on the current stress state and strain rate [17]. It directly gives the simple mathematical relationship between stress rate and strain rate, without the hypothesis of

plastic potential, plastic flow rule, hardening rule and yield surface. In recent years, the hypoplasticity theory has been employed in the modeling of conventional soils, e.g., the constitutive relation for sand by Wu and Bauer [21], the model for coarse soil under static and circular loading [22]. The studies indicate that in conventional soil mechanics, the hypoplastic model well describes the stress-strain relations when large plastic deformation of soil occurs under multiple stress paths. Due to the simplicity and openness of this theory, it may help build a constitutive model for the creep of frozen soil influenced by various factors.

## 4 Conclusions

From the review of creep of frozen soils, it can be noticed that creep is a significant source for settlement of cold regions engineering, which is rather a difficult work to be modeled by the method in conventional soil mechanics. After identification of mechanical elements by the typical creep characteristics, a simple creep model under triaxial conditions was proposed in this paper. The verification results show that it well describes the creep behavior of frozen soil. After the introduction of the theory of hypoplasticity, the creep of frozen soil may be modeled, considering multiple influencing factors, e.g., soil classification, density, water (ice) content as well as especially temperature.

## References

- [1] Qi, J.L., Sheng, Y., Zhang, J.M., Wen, Z.: Settlement of embankments in permafrost regions in the Qinghai-Tibetan plateau. *Norw. J. Geogr.* 61, 49–55 (2007)
- [2] Christensen, R.W., Wu, T.H.: Analysis of clay deformation and rate of process. *J. Soil Mech. Found. Div., ASCE*, 90(SM6), 125–157 (1964)
- [3] Andersland, O.B., Akili, W.: Stress effect on creep rates of a frozen clay soil. *Geotechnique* 17(1), 27–39 (1967)
- [4] Fish, A.M.: Kinetic nature of the long-term strength of frozen soils. In: *Proc., 2nd Int. Symp. on Ground Freezing*, Trondheim, Norwegian Institute of Technology, pp. 95–108 (1980)
- [5] Fish, A.M.: Comparison of USSR codes and US Army manual for design of foundation on permafrost. *Cold Reg. Sci. Technol.* 8, 3–24 (1983)
- [6] He, P., Cheng, G.D., Zhu, Y.L.: Constitutive theories on viscoelastoplasticity and damage of frozen soil. *Sci. China (Ser. D)* 42, 38–43 (1999)
- [7] Miao, T.D., Wei, X.X., Zhang, C.Q.: Creep of frozen soil by damage mechanics. *Sci. China (Ser. B)* 25(3), 309–317 (1995)
- [8] Yin, J.H., Graham, J.: Viscous elastic plastic modeling of one-dimensional time dependent behavior of clays. *Can. Geotech. J.* 26, 199–209 (1989)
- [9] Assur, A.: *Some promising trends in ice mechanics. Physics and Mechanics of Ice.* Springer, Berlin (1980)
- [10] Ting, J.M.: Tertiary creep model for frozen sands. *J. Geotech. Geoenviron. Eng.* 109(7), 932–945 (1983)

- [11] Zhu, Y.L., Carbee, D.L.: Creep behavior of frozen silt under constant uniaxial stress. In: Proc., 4th Int. Conf. on Permafrost, Fairbanks, Alaska, pp. 1507–1512 (1984)
- [12] Vyalov, S.S.: Rheological fundamentals of soil mechanics, pp. 234–240. Science Press, Beijing (1986) (in Chinese)
- [13] Li, D.W., Wang, R.H., Zhao, Y.H., Hu, P.: Research on parabolic yield-surface creep constitutive model of artificial frozen soil. *Rock Soil Mech.* 28(9), 1943–1948 (2007)
- [14] Andersland, O.B., Ladanyi, B.: An introduction to frozen ground engineering. Chapman and Hall, New York (1994)
- [15] Fish, A.M.: Strength of frozen soil under a combined stress state. In: Proc., 6th Int. Symp. on Ground Freezing, Beijing, China, vol. 1, pp. 135–145 (1991)
- [16] Ma, W., Wu, Z.W., Sheng, Y.: Strength and creep of frozen soil. *J. Glaciology Geo-cryo.* 16(2), 113–118 (1994) (in Chinese)
- [17] Wu, W., Kolymbas, D.: Numerical testing of the stability criterion for hypoplastic constitutive equations. *Mech. Mater.* 9(4), 245–253 (1990)
- [18] Dafalias, Y.F.: Bounding surface plasticity, I: Mathematical foundation and hypoplasticity. *Eng. Mech. ASCE* 112(9), 966–987 (1986)
- [19] Wu, W., Niemunis, A.: Failure criterion, flow rule and dissipation function derived from hypoplasticity. *Mech. Cohesive-Frict. Mater.* 1(2), 145–163 (1996)
- [20] Masin, D.: A hypoplastic constitutive model for clays. *Int. J. Num. Anal. Meth. Geomech.* 29(4), 311–336 (2005)
- [21] Wu, W., Bauer, E.: A simple hypoplastic constitutive model for sand. *Int. J. Num. Anal. Meth. Geomech.* 18(12), 833–862 (1994)
- [22] Zhang, G., Zhang, J.M., Wu, W.: A hypoplastic model of gravelly soil considering physical state. *Rock Soil Mech.* 29(6), 1530–1534 (2008)

# Influence of Recycled Asphalt Pavement on Creep Compliance of Hot Mix Asphalt

Pranshoo Solanki<sup>1</sup>, David Adje<sup>2</sup>, Musharraf Zaman<sup>2</sup>, and Zahid Hossain<sup>2</sup>

<sup>1</sup> Department of Technology, Illinois State University, Campus Box 5100,  
Normal, Illinois 61790, USA  
psolanki@ilstu.edu

<sup>2</sup> School of Civil Engineering and Environmental Science, The University of Oklahoma,  
202 W. Boyd Street, Room 334, Norman, Oklahoma 73019, USA

**Abstract.** This study explored the influence of recycled asphalt pavement (RAP) on hot mix asphalt (HMA) mixes. One RAP source was used to design Superpave mixes (Oklahoma S3) with a nominal maximum size (NMS) of 19 mm. A total of two mixes, one containing 25% RAP and the other containing 40% RAP, were designed and tested for creep compliance. It was found that at lower temperature, the mix containing 25% RAP content is stiffer, as indicated by higher creep compliance values. At higher temperature, however, the mix containing 40% RAP is stiffer as compared to that containing 25% RAP.

## 1 Introduction

Hot mix asphalt (HMA) is the most widely used paving material in the United States. Each year as much as 100 million tons of HMA are reclaimed during road resurfacing and widening projects. About 80 million tons (80%) are reused as recycled asphalt pavement (RAP). Although RAP has been used in the U.S. for over 25 years, with increased environmental awareness and focus on recycling, its enhanced use in pavement construction has become a topic of national importance. In Oklahoma, the current state of practice is to allow up to 25% RAP for base courses, but none for surface courses. One of the reasons for using a low percentage of RAP in Oklahoma is lack of performance data on mixes with high RAPs (>25%). One of the concerns among agencies is the detrimental effect of RAP on low-temperature performance. Therefore, it is important to evaluate low-temperature performance of mixes containing RAP. In order to utilize RAP containing HMA as a structural pavement component, it is necessary to predict the pertinent properties affecting low-temperature performance of pavement, with reliability. The Mechanistic-Empirical Pavement Design Guide (MEPDG) recommends the evaluation of new material properties for critical low-temperature performance prediction of HMA layers (AASHTO 2004). These properties include creep compliance and indirect tensile strength.

Consequently, the current study explores the effect of different RAP contents on the creep compliance performance of HMA. One RAP source and two Superpave<sup>®</sup> mixes (Oklahoma S3) with a nominal maximum size (NMS) of 19 mm were used. Mixes containing 25% and 40% RAP from a local source were designed and tested.

## 2 Materials and Test Procedure

### 2.1 Materials

The location of the RAP source was I-35 in McClain County (near Purcell), Oklahoma. In addition to the collection of RAP millings, four different types of virgin aggregates, namely, #67 Rocks, 5/8-in. chips, screenings, manufactured sand, and natural sand, and a virgin binder (PG 64-22 OK from Valero, Oklahoma) were collected for mix design and laboratory testing. As noted earlier, a total of two mixes, namely, S3 mix containing 25% RAP (S3-25) and S3 mix containing 40% RAP (S3-40), were prepared. Several trials were attempted where the percentages of blended materials for fulfilling the consensus properties and volumetric mix design requirements were changed in accordance with the AASHTO M 323 requirements. One field site on York Road (near US 77 and Franklin Road) in Norman, Oklahoma was selected for this study. A full depth construction at the site used mixes containing different percentages of RAP. After construction, core specimens were retrieved from the test sections. In this study, the field cores tested for creep compliance had an air void content of  $6\pm 0.5\%$  in accordance with the Oklahoma Department of Transportation OHD L-45 test method.

### 2.2 Creep Compliance

Creep compliance is defined in AASHTO T 322 as “the time-dependent strain divided by the applied stress.” In this study, creep compliance tests were conducted at  $-18^{\circ}\text{C}$ ,  $-10^{\circ}\text{C}$ ,  $0^{\circ}\text{C}$ , and  $10^{\circ}\text{C}$  on cylindrical cores (diameter = 150 mm, height = 45 mm) in accordance with the AASHTO T 322 test method. The test method consists of the application of a static load of fixed magnitude along the diametral axis of a specimen for 100 seconds. A 100 kN (22,000 lb) load cell was used for loading the specimen. The vertical and horizontal deformations were measured by two LVDTs having a stroke length of 5 mm (0.2 in.), attached in the diametrically perpendicular direction. A gauge length of approximately 38 mm (1.5 in.) was used for mounting LVDTs on one face of the specimen. The horizontal and vertical deformations measured near the center of the specimen were used for calculating the tensile creep compliance as a function of time. Figure 1 shows a photographic view of the setup used for conducting the creep test. The master creep compliance curve was created using the time-temperature superposition principle; the time and temperature-dependent material properties can be represented by using reduced time ( $t_r$ ) (Richardson and Lusher 2008).



Fig. 1. Creep Compliance Setup

### 3 Presentation and Discussion of Results

Plots generated for the creep compliance test results are presented in Figures 2 and 3 for S3-25 and S3-40 mixes, respectively. It is evident from Figures 2 and 3 that creep compliance increases with an increase in temperature, as expected (Richardson and Lusher 2008; Vargas 2007, Bonaquist 2011). It is also evident from Figures 2 and 3 that the S3-25 mix is more sensitive to change in temperature than the corresponding higher RAP containing mix (S3-40). For example, an increase in temperature by 28°C (from -18°C to +10°C) increased the creep compliance by approximately 709% and 465% for the S3-25 mix and the S3-40 mix (at 100 seconds), respectively. Also, an increase in temperature by 10°C (from 0°C to +10°C) increased the creep compliance by approximately 550% and 350% for the S3-25 mix and the S3-40 mix (at 100 seconds), respectively.

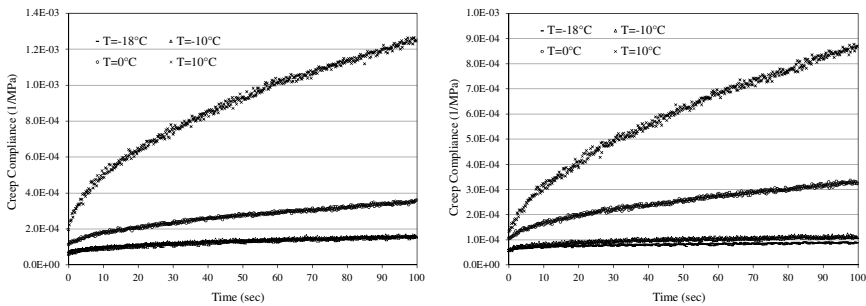
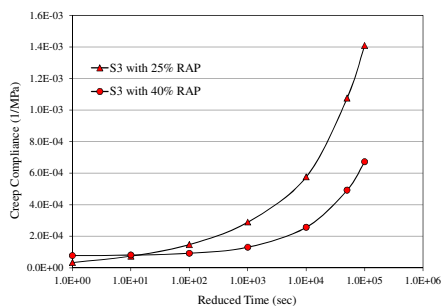


Fig. 2. Variation of Creep Compliance Values of (a) S3-25 Mix and (b) S3-40 with Temperature

Master curves for creep compliance were generated for both S3-25 and S3-40 mixes, as shown in Figure 3. It is clear from Figure 3 that S3-25 mixes showed lower creep compliance values as compared to S3-40 mixes up to a reduced time of 10 seconds (low temperature). Beyond 10 seconds, S3-25 mixes start showing higher creep as compared to the S3-40 mix.



**Fig. 3.** Master Curves

behavior of the S3 mixes with the increase of RAP content in the mixes, is consistent with the observations reported by other researchers (e.g., Richardson and Lusher 2008; Bonaquist 2011).

The differences in creep values between the S3-25 and S3-40 mixes are more pronounced at higher reduced time or temperature. For example, at a reduced time of 100 seconds, the S3-25 mixes had approximately 60% higher creep compliance values as compared to the S3-40 mix. However, the percentage difference between the S3-25 and S3-40 mixes increased to 124% at a reduced time of 10,000 seconds. This

## 4 Conclusions

At relatively low reduced time (temperature  $\leq -10^{\circ}\text{C}$ ), the S3-25 mix showed lower creep compliance values indicating higher stiffness as compared to the S3-40 mix at similar reduced time level (or temperature). At higher reduced time (temperature  $> -10^{\circ}\text{C}$ ), S3-25 mix exhibited higher creep compliance values as compared to S3-40 mix at corresponding reduced time. This indicates relatively higher stiffness of S3-40 mix as compared to corresponding values of S3-25 mix at high temperature ( $> -10^{\circ}\text{C}$ ).

## References

- AASHTO, "Guide for Mechanistic-Empirical Design of New and Rehabilitated Pavement Structures," Final Report prepared for National Cooperative Highway Research Program (NCHRP) 1-37A, Transportation Research Board, National Research Council, Washington DC (2004)
- Bonaquist, R.: Characterization of Wisconsin Mixture Low Temperature Properties for the AASHTO Mechanistic-Empirical Pavement Design Guide. Final Report No. WHRP 11-12, Wisconsin Department of Transportation, Madison, WI (2011)
- Richardson, D.N., Lusher, S.M.: Determination of creep compliance and tensile strength of Hot-Mix Asphalt for Wearing Courses in Missouri. MoDOT Report OR08-18, Missouri Department of Transportation (April 2008), <http://library.modot.mo.gov/RDT/reports/Ri05052/or08018.pdf>
- Vargas, A.: Evaluation of the use of reclaimed asphalt pavement in stone matrix asphalt mixtures, M.S. Thesis. Auburn University, Auburn, AL (2007)

# Simplified Modelling of Isotache Concept for Consolidation

Yoichi Watabe<sup>1</sup> and Serge Leroueil<sup>2</sup>

<sup>1</sup> Port and Airport Research Institute  
3-1-1, Nagase, Yokosuka 239-0826, Japan  
watabe@ipc.pari.go.jp

<sup>2</sup> Laval University  
Québec (Québec), G1V 0A6, Canada  
Serge.Leroueil@gci.ulaval.ca

**Summary.** The authors have proposed a simplified method based on the isotache concept by using a compression curve and a relationship between the preconsolidation pressure and the strain rate. The former and the latter can be obtained from one constant rate of strain consolidation test (CRS test) and one long-term consolidation test (LT test), respectively. The latter is expressed by an equation with three isotache parameters initially determined for Osaka Bay clays but generalized to worldwide inorganic clays with various characteristics.

**Keywords:** long-term consolidation, viscosity, isotache, strain rate.

## 1 Introduction

There are two main approaches for evaluation of the consolidation settlement, and these can be described as follows:

- The constant  $C_{ae}/C_c$  concept [1] with the same strain at the EOP [2]. Here,  $C_{ae}$  denotes the coefficient of secondary consolidation in void ratio. The coupling method of Terzaghi's one-dimensional consolidation theory and constant  $C_{ae}$  concept is classified into this.
- The isotache concept [3], in which a unique relationship between the strain and the preconsolidation pressure is introduced corresponding to strain rate in association with the viscosity. The ratio  $C_{ae}/C_c$  is not necessarily a constant.

In this paper, a simplified model of the isotache concept is introduced and applied to worldwide clays with various characteristics.

## 2 Modelling of Isotache Concept

The very simple equations [4] are used here, but applied to the visco-plastic deformation only. For clarity, the authors employ the  $\varepsilon_{vp} - \log \sigma'_p$  relationship, where

$\varepsilon_{vp}$  is the visco-plastic strain, which is defined as the difference between the total strain  $\varepsilon$  obtained from consolidation test and the elastic strain  $\varepsilon_e$ . We then use Eq.(1).

$$\varepsilon_{vp} = \varepsilon - \varepsilon_e \quad (1a); \quad \frac{\sigma'_v}{\sigma'_p} = f(\varepsilon_{vp}) \quad (1b); \quad \sigma'_p = g(\dot{\varepsilon}_{vp}) \quad (1c)$$

Here,  $\sigma'_v$  is the vertical effective consolidation pressure,  $\sigma'_p$  is the preconsolidation pressure, and  $\dot{\varepsilon}_{vp}$  is the plastic strain rate. In order to obtain the relationships expressed by Eqs.(1b) and (1c), one constant rate of strain consolidation test (CRS test) and one long-term consolidation test (LT test) are required to be performed.

The parameter  $\varepsilon_e$  is defined as the strain expressed by the straight line passing through the points  $(\sigma'_v, \varepsilon) = (1 \text{ kPa}, 0)$  and  $(\sigma'_{v0}, \varepsilon_0)$  on the  $\varepsilon - \log \sigma'_v$  curve. Here,  $\sigma'_{v0}$  denotes the overburden effective stress and  $\varepsilon_0$  denotes the strain at  $\sigma'_v = \sigma'_{v0}$ . The curve expressed by Eq.(1b) is named as ‘‘reference compression curve.’’

A simple model of Eq.(1c) was proposed as a form of Eq.(2) in [5]:

$$\ln \frac{\sigma'_p - \sigma'_{pL}}{\sigma'_{pL}} = c_1 + c_2 \ln \dot{\varepsilon}_{vp} \quad (2)$$

Here,  $c_1$  and  $c_2$  are constants and  $\sigma'_{pL}$  is the lower limit of  $\sigma'_p$ . When  $\dot{\varepsilon}_{vp}$  decreases towards zero in Eq.(2),  $\sigma'_p$  converges towards  $\sigma'_{pL}$ . This equation is consistent with [6] in which it was emphasized that the slope  $\alpha$ , which is defined as  $\Delta \log \sigma'_p / \Delta \log \dot{\varepsilon}_{vp}$  decreases when  $\dot{\varepsilon}_{vp}$  decreases to very small values. In Eq.(2), if it is assumed that the curve passes on certain point, the parameter  $c_2$  is automatically calculated as a dependent variable of  $\sigma'_{pL}$  and  $c_1$ .

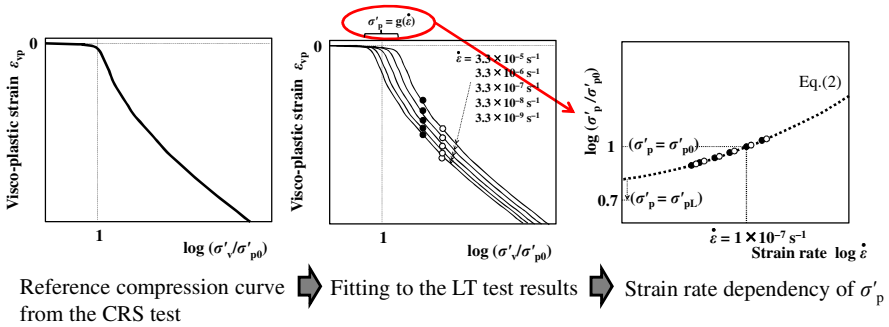


**Fig. 1.** Illustration of the method to evaluate the strain rate dependency of  $\sigma'_p$  from the CRS and LT test results

The consolidation yield stress  $\sigma'_p$  is obtained as a function of  $\dot{\varepsilon}_{vp}$  from the reference compression curve by using the data set of  $\sigma'_v$  and  $\varepsilon_{vp}$ . The procedure to obtain the  $\log \sigma'_p - \log \dot{\varepsilon}_{vp}$  curve from CRS and LT test results is illustrated in Fig.1.

### 3 Applicability to Worldwide Clays

In [5], the proposed method was applied to Osaka Bay clays collected up to 300 m below the seabed. And then, it was found out that the isotache parameters  $c_1$ ,  $c_2$  and  $\sigma'_{pL}$  can be determined for Osaka Bay clays at various depth; i.e.  $\sigma'_{pL}/\sigma'_{p0} = 0.70$  and  $c_1 = 0.935$  (automatically  $c_2 = 0.107$ ). Here,  $\sigma'_{p0}$  is defined as the  $\sigma'_p$  corresponding to an  $\dot{\epsilon}_{vp}$  value of  $1.0 \times 10^{-7} \text{ s}^{-1}$ , which is close to the average strain rate corresponding to 24 h incremental loading consolidation test. The best fitting curve with these common isotache parameters is named as the integrated fitting curve. In [7], the proposed method was applied to worldwide clays with various characteristics. It was found out that the best fitting curve determined for the Osaka Bay clays is available for all the worldwide clays.

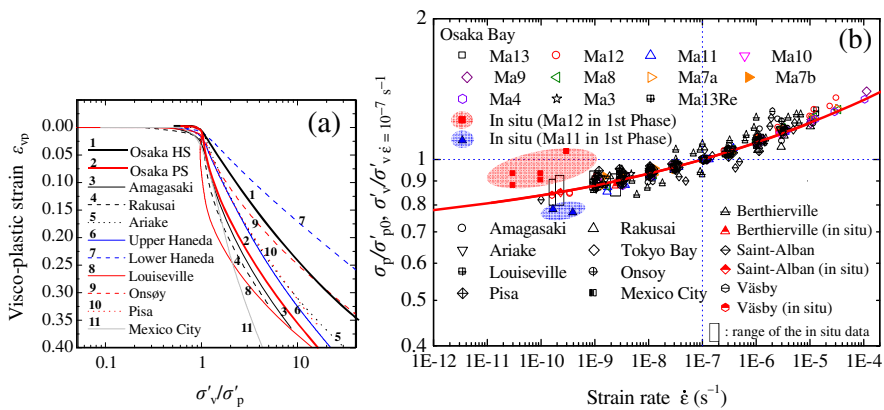


**Fig. 2.** (a) Superimposed reference compression curves for the worldwide clays examined in [5][7], (b) the  $\log \sigma'_p/\sigma'_{p0} - \log \dot{\epsilon}_{vp}$  relationship for all the worldwide clays studied in [5][7], as well as [8] with an interpretation after [6], comparing to the integrated fitting curve with the common isotache parameters determined for the Osaka Bay clays

Fig.2 shows (a) superimposed reference compression curves and (b) the  $\log \sigma'_p/\sigma'_{p0} - \log \dot{\epsilon}_{vp}$  relationship for all the worldwide clays examined in [5][7], as well as field results obtained on Canadian, Swedish and Osaka clays (from [8] with an interpretation after [6]). In this figure, the integrated fitting curve is superimposed. The test results and the integrated fitting curve are compared thoroughly. Note here that because the results are for natural clays, some variability is inevitable. The difference between the test results and the proposed curve is not so significant, indicating that the model is very general for inorganic clays.

### 4 Application to Practical Engineering

In engineering practice, consolidation settlement is generally estimated based on  $e - \log \sigma'_v$  curve obtained from 24 h incremental loading oedometer test which

corresponds to a strain rate of about  $1.0 \times 10^{-7} \text{ s}^{-1}$ . As shown in [7], additional settlement (strain) can be estimated by Eq.(3) and the results are charted in Fig.4 as a function of  $C_c/(1 + e_0)$  and in situ strain rate  $\dot{\epsilon}_{\text{Field}}$ . This chart is very simple and useful in application of isotache concept to engineering practice.

$$\Delta \epsilon = \frac{C_c}{1 + e_0} \log \left[ \frac{\sigma'_{p0}}{\sigma'_{pl}} \left\{ \frac{1}{1 + \exp(c_1 + c_2 \ln \dot{\epsilon}_{\text{Field}})} \right\} \right] \quad (3)$$

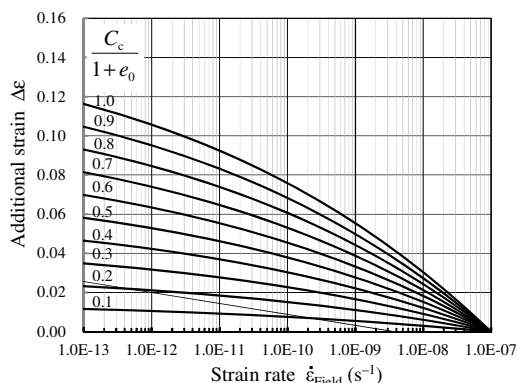


Fig. 3.  $\Delta \epsilon$  as a function of strain rate for different values of  $C_c/(1 + e_0)$ , as given by Eq.(3)

## 5 Conclusions

The authors proposed a simplified method based on the isotache concept by using a compression curve and relationship between the preconsolidation pressure and the strain rate. The latter is expressed by Eq.(2) with three parameters, which have been determined for worldwide inorganic clays with various characteristics. Using this model, additional strains to be applied in the field can be calculated as a function of  $C_c/(1 + e_0)$  and in situ strain rate.

## References

- [1] Mesri, G., Castro, A.: The  $C_a/C_c$  concept and  $K_0$  during secondary compression. *J. of Geotech. Engrg.*, ASCE 113(3), 230–247 (1987)
- [2] Mesri, G., Choi, Y.K.: The uniqueness of the end-of-primary (EOP) void ratio-effective stress relationship. In: *Proc. 11th ICSMFE, San Francisco*, vol. 2, pp. 587–590 (1985)
- [3] Šuklje, L.: The analysis of the consolidation process by the isotache method. In: *Proc. 4th Int. Conf. on Soil Mech. Found. Engrg.*, London, vol. 1, pp. 200–206 (1957)
- [4] Leroueil, S., Kabbaj, M., Tavenas, F., Bouchard, R.: Stress-strain-strain rate relation for the compressibility of sensitive natural clays. *Géotechnique* 35(2), 159–180 (1985)

- [5] Watabe, Y., Udaka, K., Morikawa, Y.: Strain rate effect on long-term consolidation of Osaka bay clay. *Soils Founds* 48(4), 495–509 (2008)
- [6] Leroueil, S.: The isotache approach. Where are we 50 years after its development by Professor Šuklje? In: *Proc. 13th Danube-European Conf. Geotech. Engrg.*, pp. 55–88 (2006)
- [7] Watabe, Y., Udaka, K., Nakatani, Y., Leroueil, S.: Long-term consolidation behavior interpreted with isotache concept for worldwide clays. *Soils Founds* 52(3) (in print, 2012)
- [8] Leroueil, S., Kabbaj, M., Tavenas, F.: Study of the validity of a  $\sigma'_v - \sigma_v - \dot{\epsilon}_v$  model in in situ conditions. *Soils Founds* 28(3), 3–25 (1988)

# Nonlinear Creep Behavior of Normally Consolidated Soft Clay

Ze-Xiang Wu<sup>1,2</sup>, Yin-Fu Jin<sup>1</sup>, and Zhen-Yu Yin<sup>1,\*</sup>

<sup>1</sup> Department of Civil Engineering, Shanghai Jiao Tong University, Shanghai 200240, China

<sup>2</sup> Department of Civil Engineering, North China University of Technology, 100144  
zhenyu.yin@gmail.com

**Summary.** The nonlinear creep behavior of normally consolidated soft clays is investigated. The study is based on conventional oedometer tests on reconstituted clays, which eliminates the influence of soil structure on creep behavior. Furthermore, a simple nonlinear creep formulation is proposed accounting for the volumetric packing of soil assemblies.

**Keywords:** soft clays, creep, consolidation, oedometer test.

## 1 Introduction

Natural soft clays exhibit significant time-dependent deformations under both laboratory and in-situ conditions after the primary consolidation due to the viscosity [1-8]. The secondary compression coefficient  $C_{ac}$  is commonly used in the development of one-dimensional creep models and for the practice.

A constant  $C_{ac}$  was generally considered for reconstituted clays in their studies. It needs to be pointed out that the nonlinear creep formulations by Yin et al.[4] and Kelln et al. [5] imply a decreasing  $C_{ac}$  by time for one applied stress level, while the predicted conventional oedometer test should give an almost same value of  $C_{ac}$  for different applied stress levels bigger than the preconsolidation pressure. However, the  $C_{ac}$  should be decreasing continuously with an increasing soil density to avoid the negative void ratio.

In this study, conventional oedometer tests on several natural soft clays are selected. All tested samples are reconstituted in order to eliminate the influence of soil structure on the evolution of  $C_{ac}$ . We focus on the nonlinear  $C_{ac}$  for different stress levels. Based on all test results, a simple nonlinear creep formulation is proposed accounting for the volumetric packing of soil assemblies.

## 2 Nonlinear Creep Behavior

Conventional oedometer tests on four reconstituted natural soft clays were selected for this study: Haarajoki clay[8], Murro clay[7], Vanttila clay[7] and Hong Kong Marine clay[4].

---

\* Corresponding author.

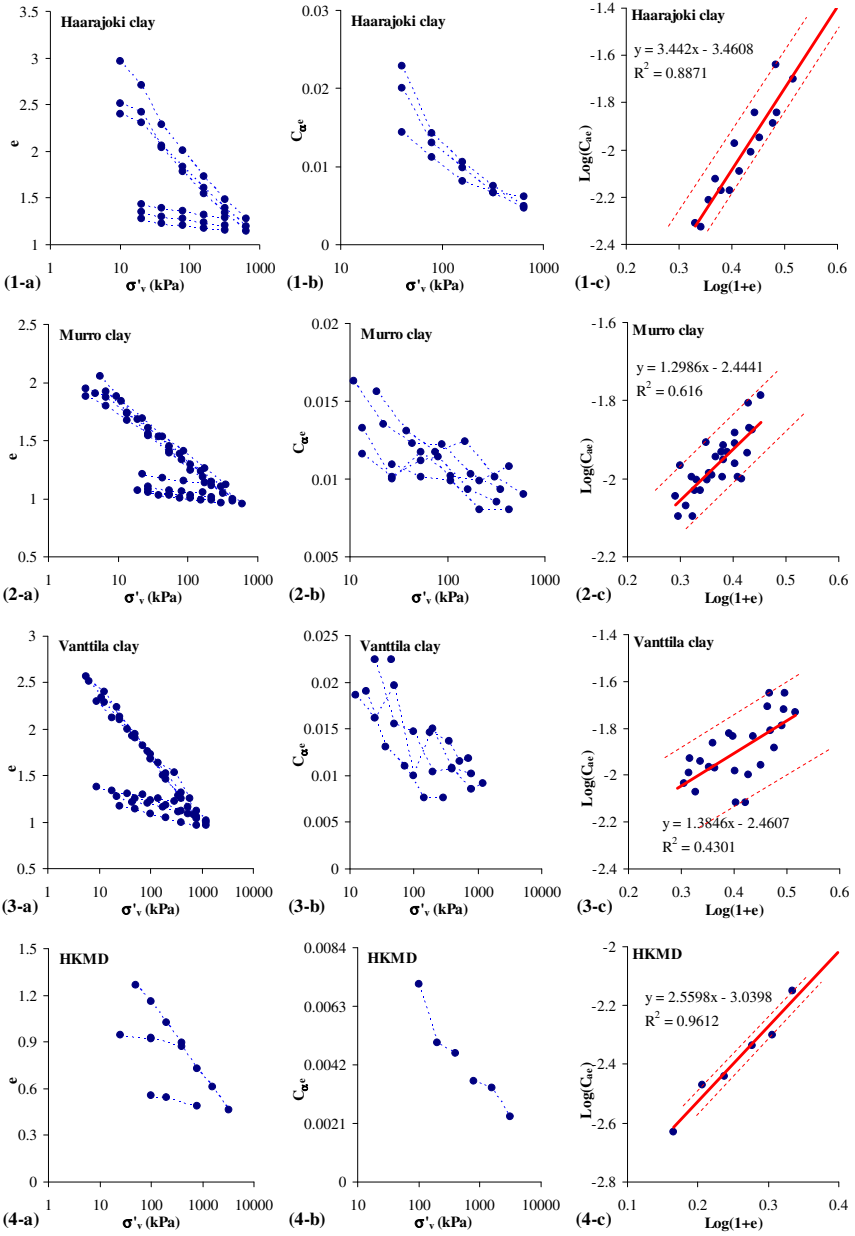


Fig. 1. Results of oedometer tests on different remoulded clays

Figure 1 shows the results of 1 day conventional oedometer tests for all tested clays. The results include  $e$ - $\log\sigma'_v$  curves,  $C_{\alpha e}$ - $\log\sigma'_v$  curves and  $\log(C_{\alpha e})$ - $\log(1+e)$  curves:

- a) From  $e$ - $\log\sigma'_v$  curves, although there is variation of initial void ratio for all clays, for each clay the compressibility of different samples are very similar.
- b) The  $C_{\alpha e}$ - $\log\sigma'_v$  curves were plotted for normally consolidated states ( $\sigma'_v > \sigma'_p$ ). The  $C_{\alpha e}$  decreases with applied stress level for all tested clays with decreasing void ratio.
- c)  $C_{\alpha e}$ - $(1+e)$  was plotted in double log space, where linear relationship can be assumed for all tested clays. Based on that, a new nonlinear creep formulation can be proposed as follows:

$$\frac{C_{\alpha e}}{C_{\alpha e0}} = \left( \frac{1+e}{1+e_0} \right)^m \tag{1}$$

where  $C_{\alpha e0}$  and  $e_0$  are reference values of secondary compression coefficient and void ratio respectively;  $m$  is the material constant representing the slope of  $\log(C_{\alpha e})$ - $\log(e)$  curve, which can be correlated with plastic limit shown in Fig. 2.

If we plot the evolution of  $(\lambda-\kappa)/C_{\alpha e}$  by void ratio (see Figure 3), obviously the  $(\lambda-\kappa)/C_{\alpha e}$  is not a constant. Using the average value of  $\lambda$  and  $\kappa$  for each clay, and applying the proposed nonlinear creep formulation Eq. (2), the theoretical curves were plotted (continuous lines in Figure 3) which fit well with experimental curves. Therefore, the new nonlinear creep formulation improved the assumption of Mesri and Godlewski (1977).

Since the new nonlinear creep formulation accounts for the volumetric packing of soil assemblies by void ratio, the  $C_{\alpha e}$  can decrease with time since the creep deformation results in the reduction of void ratio for an applied stress. Furthermore, the proposed formulation can describe the continuous decrease of  $C_{\alpha e}$  with applied stress level due to the decrease of the void ratio accordingly. Therefore, the proposed formulation can be applied to viscoplastic models to improve the predictive ability of modelling the time-dependent behaviour of soft soils.

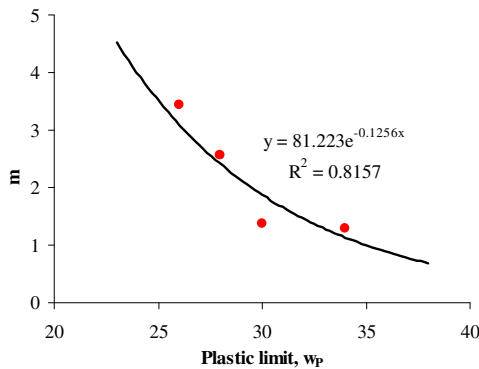


Fig. 2. Correlation between the material constant  $m$  and the plastic limit

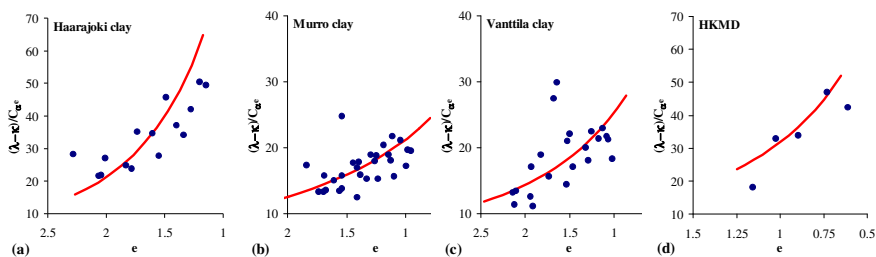


Fig. 3. Evolution of the ratio  $(\lambda-\kappa)/C_{\alpha e}$  with void ratio  $e$  for different remoulded clays

### 3 Conclusions

The nonlinear creep behavior has been investigated by oedometer tests on several soft clays. All clay samples are reconstituted in order to eliminate the influence of soil structure on the evolution of  $C_{\alpha e}$  with applied stress. Based on that, a new nonlinear creep formulation was proposed accounting for the volumetric packing of soil assemblies. The formulation can be further incorporated into creep models to improve the predictive ability.

### References

- [1] Bjerrum, L.: Engineering geology of Norwegian normally-consolidated marine clays as related to settlements of building. *Géotechnique* 17(2), 81–118 (1967)
- [2] Leroueil, S., Kabbaj, M., Tavenas, F., Bouchard, R.: Stress-strain-strain rate relation for the compressibility of sensitive natural clays. *Géotechnique* 35(2), 159–180 (1985)
- [3] Mesri, G., Castro, A.: The  $C_{\alpha}/C_c$  concept and  $K_0$  during secondary compression. *J. of Geotech. Engrg., ASCE* 113(3), 230–247 (1987)
- [4] Yin, J.-H., Zhu, J.-G., Graham, J.: A new elastic visco-plastic model for time-dependent behaviour of normally and overconsolidated clays: theory and verification. *Canadian Geotechnical Journal* 39, 157–173 (2002)
- [5] Kelln, C., Sharma, J.S., Hughes, D., Graham, J.: An improved elastic-viscoplastic soil model. *Can. Geot. J.* 45(21), 1356–1376 (2008)
- [6] Yin, Z.-Y., Hicher, P.Y.: Identifying parameters controlling soil delayed behaviour from laboratory and in situ pressuremeter testing. *International Journal for Numerical and Analytical Methods in Geomechanics* 32(12), 1515–1535 (2008)
- [7] Karstunen, M., Yin, Z.-Y.: Modelling time-dependent behaviour of Murro test embankment. *Géotechnique* 60(10), 735–749 (2010)
- [8] Yin, Z.-Y., Karstunen, M., Chang, C.S., Koskinen, M., Lojander, M.: Modeling time-dependent behavior of soft sensitive clay. *ASCE Journal of Geotechnical and Environmental Engineering* 137(11), 1103–1113 (2011)

# Review of Elastic Visco-Plastic Modeling of the Time-Dependent Stress-Strain Behavior of Soils and Its Extensions and Applications

Jian-Hua Yin

Department of Civil and Structural Engineering, The Hong Kong Polytechnic University  
Hung Hom, Kowloon, Hong Kong, China  
cejhyin@polyu.edu.hk

**Abstract.** This paper presents a brief review of the works of elastic visco-plastic (EVP) modelling of the time-dependent stress-strain behaviour of soils in one-dimensional straining (1D) and in 3D stress state. A few important concepts and their physical meanings are explained. The 1D EVP model is briefly reviewed with a comparison with the classic Maxwell's rheological model. It is found that Yin and Graham's 1D EVP model is an extension of Maxwell's rheological model for considering the nonlinear behaviour of soils. A nonlinear creep function proposed by the author is presented. This function has been used in refined 1D and 3D EVP models. The recent extension of the EVP modelling framework to consider the swelling of a saturated soil is introduced. New developments and applications done by other researchers are also briefly summarized. It is found that, in general speaking, the EVP modelling framework is suitable as a theoretical basis for modelling the time-dependent stress-strain behaviour of many clayey soils. However, this framework shall be modified or extended to consider special characteristics of the viscous behaviour of soils such as swelling of saturated and unsaturated soils and other geomaterials.

**Keywords:** creep, time effects, strain-rate effects, visco-plastic, viscous.

## 1 Introduction

The behaviour of many geomaterials is viscous, resulting in time effects and strain rate effects. An important time-dependent phenomenon is creep - continued deformation under constant loading. In early days, this was often called 'secondary consolidation'. The term 'creep' is preferable because it is referred to the compression of soil skeleton under a constant loading, having nothing to do with consolidation. Creep of soils is due to mainly (a) viscous expulsion of adsorbed water from 'double layers' around clay particles and (b) viscous, non-recoverable re-arrangement and deformation of clay particles and their skeleton. Adsorbed water is highly viscous and does not flow freely under the normal



The “equivalent time” is an important concept here. The “equivalent time” is the time duration” for a soil to creep from the normal consolidation line to a stress-strain state point (say from Point A to Point B), the creep rate at this point is “equal” to the creep rate reached from any other loading history (say from Point A, to Point C and to Point B). In other words, the creep rate of a soil at a stress-strain state point is uniquely related to this state point, independent on the loading history (not related to how to reach to this stress-strain state point). If we can determine the creep rate at a state point from one loading history, the creep rate is the same for any other loading history. This finding, that is, the “equivalent time” concept, has been used to derive 1D elastic visco-plastic models (Yin and Graham 1989, 1994)[2,3].

For counting any time duration, we need a time reference. In the papers by Yin and Graham (1989, 1994)[2,3], they defined a “reference time” line in Figure 2 for counting the “equivalent time”. They have found that the slope of the “reference time” line in the ln(stress) and strain coordinates is about the same as the slope of the normal consolidation line in the same coordinates.

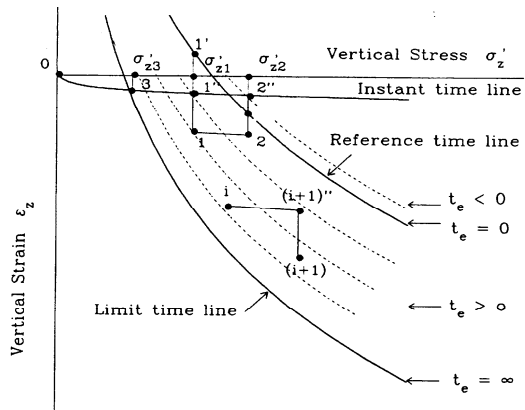


Fig. 2. 1D compression and concepts used in 1D EVP model (after Yin and Graham 1994)

Yin and Graham (1989, 1994)[2,3] pointed out that the ‘instant compression’ in Fig.1 is not the true instant (or elastic) compression line but contains creep compression. The compression from point  $(e_o, p_o)$  to point  $p_c$  is mainly elastic compression and this line is a true “instant compression” line, called “instant time” line in Figure 2.

### 3 Modelling the Time-Dependent Stress-Strain Behavior of Soils in 1D Straining

In elasto-plastic models, the stress-strain is time-independent and total strain increment  $\dot{\epsilon}_z$  are separated into elastic strain increment  $\dot{\epsilon}_z^e$  plus plastic strain increment  $\dot{\epsilon}_z^p$  (time  $dt$  can be removed in the following equation):

$$\dot{\epsilon}_z = \dot{\epsilon}_z^e + \dot{\epsilon}_z^p \tag{1}$$

To model the time-dependent stress-strain behaviour of a viscous soil, some researchers simply add the visco-plastic strain rate  $\dot{\epsilon}_z^{vp}$ :

$$\dot{\epsilon}_z = \dot{\epsilon}_z^e + \dot{\epsilon}_z^p + \dot{\epsilon}_z^{vp} \tag{2}$$

Yin and Graham (1989, 1994)[2,3] have pointed out that the separation of in-elastic strain rate into plastic strain rate  $\dot{\epsilon}_z^p$  and the visco-plastic strain rate  $\dot{\epsilon}_z^{vp}$  has no sound physical basis. In the view by Perzyna (1966)[4], the  $\dot{\epsilon}_z^{vp}$  has included the irreversible strain. The total strain rate shall be divided into two parts:

$$\dot{\epsilon}_z = \dot{\epsilon}_z^e + \dot{\epsilon}_z^{vp} \tag{3}$$

In (3), the time-independent strain rate is the elastic strain rate  $\dot{\epsilon}_z^e$  and the time-dependent strain rate is the visco-plastic strain rate  $\dot{\epsilon}_z^{vp}$ .

One common view is that the creep strain (or “secondary consolidation” settlement) is small in comparison with instant compression (including elastic and plastic compression) (or “primary consolidation” settlement). The author considers the above view is wrong. According to (1), as we know, the plastic strain is much bigger than the instant elastic strain. According to (3), all plastic strain is viscous (creep strain under constant loading), and also much bigger than the instant elastic strain. In this approach, instant compression shall be elastic, shall not include plastic compression. The elastic compression (“instant time” line) is represented by  $\kappa$ -line in plot  $\epsilon_z - \ln(\sigma'_z)$  as shown in

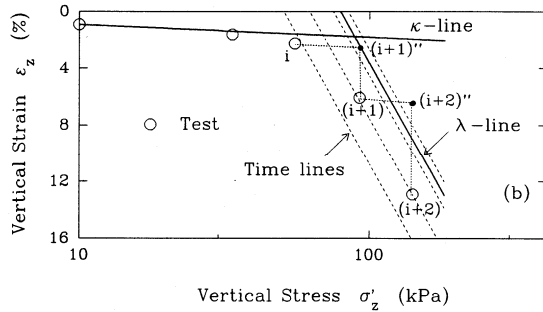


Fig. 3. Relation of strain and log(stress)

Fig.3. The “reference time” line is represented by  $\lambda$ -line in plot  $\epsilon_z - \ln(\sigma'_z)$ . It is seen from Fig.3 that the visco-plastic strain is much bigger than the instant strain rate. The value of  $\kappa$  is 1/5 to 1/10 of the value of  $\lambda$ . Therefore, the creep strain is normally more than five times of the elastic strain. From this point of view, the proper calculation of the creep strain (or creep settlement) is very important.

Based on the above concepts and understandings, Yin and Graham (1989, 1994)[2,3] derived rigorously the constitutive equation of a 1D Elastic Visco-Plastic (1D EVP) model:

$$\dot{\epsilon}_z = \frac{\kappa}{V} \frac{\sigma'_z}{\sigma'_z} + \frac{\psi}{V t_o} \exp(-\epsilon_z \frac{V}{\psi}) (\frac{\sigma'_z}{\sigma'_0})^{\lambda/\psi} \tag{4}$$

where  $\dot{\epsilon}_z$  and  $\epsilon_z$  are vertical strain rate and strain;  $\dot{\sigma}'_z$  and  $\sigma'_z$  are vertical effective stress rate and stress;  $\kappa V$  is a constant related to elastic compression (see Fig.3);  $\lambda V$  is a constant related to a reference time line (approximately the NCL, see Fig.3);  $\sigma'_o$  is a constant at  $\epsilon_z = 0$ , locating the position of the reference time line; and  $\psi V$  and  $t_0$  (in units of time) are two constants related to creep of the soil. More details can be found in Yin and Graham (1989, 1994)[2,3].

In (4), the visco-plastic strain rate is:

$$\dot{\epsilon}_z^{vp} = \frac{\psi}{Vt_0} \exp(-\epsilon_z \frac{V}{\psi}) (\frac{\sigma'_z}{\sigma'_o})^{\lambda/\psi} \tag{5}$$

It is seen from (5) that the visco-plastic strain rate is a function of the stress-strain state  $(\sigma'_z, \epsilon_z)$ , nothing to do with how to reach this state.

It is well known that the classic Maxwell's rheological model can be expressed as:

$$\dot{\epsilon}_z = \frac{\dot{\sigma}'_z}{E} + \frac{\sigma'_z}{\eta} \tag{6}$$

where  $E$  is the elastic modulus and  $\eta$  is a viscous constant. Maxwell's rheological model is derived from a series connection of a spring and a dashpot. In this approach, the total strain rate is divided into elastic strain rate and a visco-plastic strain rate. It is noted that Maxwell's rheological model is not a visco-elastic model since the strain due to the dashpot is not recoverable. Maxwell's rheological model is, in fact, a linear elastic and linear visco-plastic model. Comparing (4) with (6), it is found that Yin and Graham's 1D EVP[2,3] is a nonlinear elastic and nonlinear visco-plastic model, that is, a nonlinear rheological model. Yin and Graham's 1D EVP can be considered to be an extension of the classic Maxwell's rheological model.

The 1D EVP model has been used to simulate time-dependent stress-strain behaviour of a variety of clay soils under different loading condition. For example, the model was used to simulate 1D constant-rate-of-strain (CRSN) tests on Bäckebol Clay (Sällfors (1975)[5] in Fig.4. The modelling results agrees well with measured data. The 1D EVP model in Eqn.(4) can predict soil behaviour under any loading condition, including unloading/reloading, varying rates of strain, consolidation, creep and relaxation.

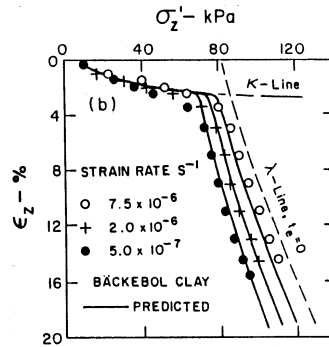


Fig. 4. Strain rate effects from constant-rate-of-strain tests – test data and 1D EVP model results (after Yin and Graham 1989)

One limitation of Eqn.(4) is that creep strains may theoretically become infinite because the model uses logarithmic functions for creep and compression. A nonlinear creep function in (7) can overcome this limitation.

Fig.4 shows data from constant-rate-of-strain (CRSN) tests on Bäckebol Clay (Sällfors 1975) in 1D straining. It is seen that the stress-strain relationships depend on strain-rate. It is seen from the figure that stresses can increase indefinitely with increasing strain rate, and that stress points might actually lie above the “instant compression” line as shown in Fig.1. The data support the idea that the “instant compression” in Fig.1 is not the true “elastic line”.

#### 4 A Nonlinear Creep Function Soils in 1D Straining

A semi-logarithmic function has been commonly used to fit creep strain *vs.* time data. However, when time is infinite, the semi-logarithmic function implies that strains (and therefore settlements) are also infinite. This is certainly incorrect. Long-term creep tests show that the relationship of creep strain (or void ratio) *vs.*  $\log(\text{time})$  is not straight. The slope  $C_{\alpha\epsilon}$  (the coefficient of ‘secondary’ compression) of creep strain *vs.*  $\log(\text{time})$ , decreases with time. Thus, a semi-logarithmic creep function may overestimate creep settlements. Yin (1999) suggested a new function for fitting non-linear creep behaviour of soils[6]:

$$\Delta\epsilon = \psi'_o \ln \frac{t+t_o}{t_o} / (1 + \frac{\psi'_o}{\Delta\epsilon_l} \ln \frac{t+t_o}{t_o}) \quad (7)$$

where  $\Delta\epsilon$  is creep strain and  $t$  is the duration of loading that produces  $\Delta\epsilon$ . In Eqn.(7)  $\psi'_o$ ,  $t_o$  and  $\Delta\epsilon_l$  are three constant parameters. Note that Eqn.(7) is defined at time  $t = 0$ . The subscript ‘ $o$ ’ stands for parameters that have specific meaning at time  $t = 0$ . If  $\ln[(t+t_o)/t_o]$  is taken together as a variable, Eqn.(7) has the form of a hyperbolic function.

#### 5 Modelling Time-Dependent Stress-Strain Behaviour in Triaxial and More General Stress Conditions

Using the separation of elastic and creep strains in Eqn.(3), the concept of ‘equivalent time’ inherent in Fig.1, and the Modified-Cam Clay model, Yin and Graham (1999) derived a three-dimensional Elastic Visco-Plastic (3-D EVP) model[7]:

$$\dot{\epsilon}_{ij} = \dot{\epsilon}_{ij}^e + \dot{\epsilon}_{ij}^{vp} = \left( \frac{1}{2G} \dot{s}_{ij} + \frac{\kappa}{3V} \frac{\dot{p}'}{p'} \delta_{ij} \right) + \frac{\psi}{V t_0} \exp \left[ \left( \epsilon_{vm0}^r + \frac{\lambda}{V} \ln \frac{p'_m}{p_{m0}} - \epsilon_{vm} \right) \frac{V}{\psi} \right] \frac{1}{|2p' - p'_m|} \frac{\partial \mathcal{F}}{\partial \sigma'_{ij}} \quad (8)$$

where  $\dot{\epsilon}_{ij}$  is the total strain rate ( $i = 1,2,3; j = 1,2,3$ );  $\dot{\epsilon}_{ij}^e$  and  $\dot{\epsilon}_{ij}^{vp}$  are the elastic and visco-plastic strain rate;  $\sigma'_{ij}$  is effective stress; the mean effective stress  $p'$  is defined as  $p' = \sigma'_{kk}/3$ ;  $\dot{s}_{ij}$  is the deviator stress rate; the deviator stress  $s_{ij}$  is defined as  $s_{ij} = \sigma'_{ij} - \delta_{ij}\sigma'_{kk}/3$ , where  $\delta_{ij} = 0$  if  $i \neq j$ ,  $\delta_{ij} = 1$  if  $i = j$ ;  $G$  is the elastic shear modulus;  $\kappa/V$  ( $V$  is specific volume),  $\psi/V$ ,  $t_0$ ,  $\lambda/V$ ,  $p'_{m0}$  and  $\epsilon_{vm0}^r$  are model parameters.

The  $F$  in Eqn.(12) is a function describing the visco-plastic flow surface (Yin and Graham 1999):

$$F = p'^2 + \frac{q^2}{M^2} - p'p'_m = 0 \quad (9)$$

where  $M$  is the slope of the Critical State strength envelope in the  $q-p'$  plane; and  $q$  is the generalised deviator stress  $\sqrt{\frac{3}{2}s_{ij}s_{ij}}$ . In Eqn.(12) and Eqn.(13),  $p'_m$  is the mean effective stress at which the flow surface in Eqn.(13) intercepts the  $p'$ -axis in the  $q-p'$  plane. The sub-index 'm' represents the mean stress or volume strain under isotropic stressing conditions, that is,  $p' = p'_m$  with  $q = 0$ . For example,  $\epsilon_{vm}$  in Eqn.(8) is the total volumetric strain under isotropic stressing. Yin and Graham (1999) show that the rate of  $\epsilon_{vm}$  can be expressed

$$\dot{\epsilon}_{vm} = \frac{\kappa}{Vp'_m} \dot{p}'_m + \frac{\psi}{Vt_0} \exp\left[\left(\epsilon_{vm0}^r + \frac{\lambda}{V} \ln \frac{p'_m}{p'_{m0}} - \epsilon_{vm}\right) \frac{V}{\psi}\right] \quad (10)$$

Eqns.(8), (9) and (10) are differential equations of a 3D EVP model for describing time-dependent stress-strain behaviour of clays. The proposed model has been verified using data from a number of soils.

## 6 Extentions and Applications of the above EVP Modelling Works

Yin et al. (2002) extended the 3D EVP model[7] to describe the time-dependent behaviour of normally and overconsolidated clays[8]. Yin and Tong (2011) has extended the 1D EVP model in (4) for constitutive modelling of the time-dependent stress-strain behaviour of saturated soils exhibiting both creep and swelling[9]. The extended model can simulated the loops due to unloading-reloading and the time-dependent swelling under a constant stress due a large unloading step very well. It is noted that there is room for improvement or modification of the EVP models in order to consider the time-dependent characteristic of soils in special conditions such as in unsaturated state, and other geomaterials such as salt rock.

Bodas Freitas et al. (2011) has developed a new elastic visco-plastic model based on the EVP works by Perzyna (1966)[4] and Yin and his co-workers (1989, 1999, 2002)[2,7,8]. Kelln et al. (2008) presented an improved elastic-viscoplastic soil model[11]. They have used this model in finite element analysis of geotechnical structures [12,13].

Nash and Ryde (2001)[14] and Nash and Brown (2012)[15] evaluated different elastic visco-plastic models and used them for modelling consolidation accelerated by vertical drains in soil subject to creep. Hu (2010) applied the 1D EVP model for long-term settlement of soft subsoil clay under rectangular or semi-sinusoidal repeated loading of low amplitude [16]. Matsuda and his co-workers have used the 1D EVP model for consolidation analysis of soft soils with creep and comparison with test data [17,18]. They showed the EVP model can consider the creep of soils well in during and after the primary consolidation.

## 7 Conclusions

The main conclusions in the paper are in the followings: (a) Appreciation of the concepts and their physical meanings in the EVP models are needed for better use or improvement of the models. (b) The 1D EVP model is an extension of Maxwell's rheological model for considering the nonlinear behaviour of soils. (c) The nonlinear function proposed by the author is good for fitting the creep compression of most soft soils in 1D straining. (d) The EVP modelling framework is suitable as a theoretical basis for modelling the time-dependent stress-strain behaviour of many clayey soils. (e) This framework shall be modified or extended to consider special characteristics of the viscous behaviour of soils such as swelling of saturated and unsaturated soils and other geomaterials.

**Acknowledgements.** Financial supports are gratefully acknowledged from The Hong Kong Polytechnic University (A/C: 5-ZG64, G-U663, G-YG60).

## References

- [1] Bjerrum, L.: Engineering geology of Norwegian normally consolidated marine clays as related to the settlements of buildings. *Géotechnique* 17, 83–118 (1967)
- [2] Yin, J.H., Graham, J.: Viscous elastic plastic modelling of one dimensional time dependent behavior of clays. *Canadian Geotechnical Journal* 26, 199–209 (1989)
- [3] Yin, J.H., Graham, J.: Equivalent times and one dimensional elastic visco-plastic modelling of time dependent stress strain behaviour of clays. *Canadian Geotech. Journal* 31, 42–52 (1994)
- [4] Perzyna, P.: Fundamental problems in viscoplasticity, *Advances in Applied Mechanics*, vol. (9), pp. 244–368. Academic Press, New York (1966)
- [5] Sällfors, G.: Preconsolidation pressure of soft, high-plastic clays, Ph.D. thesis. Chalmers University of Technology, Gothenburg, Sweden (1975)
- [6] Yin, J.-H.: Non-linear creep of soils in oedometer tests. *Geotechnique* 49(5), 699–707 (1999)

- [7] Yin, J.-H., Graham, J.: Elastic visco-plastic modelling of the time-dependent stress-strain behaviour of soils. *Canadian Geotech. Journal* 36, 736–745 (1999)
- [8] Yin, J.-H., Zhu, J.G., Graham, J.: A new elastic visco-plastic model for time-dependent behaviour of normally and overconsolidated clays: theory and verification. *Canadian Geotechnical Journal* 39, 157–173 (2002)
- [9] Yin, J.-H., Tong, F.: Constitutive Modelling of the Time-dependent Stress-strain Behaviour of Saturated Soils Exhibiting both Creep and Swelling. *Canadian Geotechnical Journal* 48(12), 1870–1885 (2011) (SCI 105)
- [10] Bodas Freitas, T.M., Potts, D.M., Zdravkovic, L.: A time dependent constitutive model for soils with isotach viscosity. *Computers and Geotechnics* 38(6), 809–820 (2011)
- [11] Kelln, C., Sharma, J.S., Hughes, D., Graham, J.: An improved elastic-viscoplastic soil model. *Can. Geot. J.* 45(21), 1356–1376 (2008b)
- [12] Kelln, C., Sharma, J.S., Hughes, D.: A finite element solution scheme for an elastic-viscoplastic soil model. *Compu. and Geot.* 35, 524–536 (2008a)
- [13] Kelln, C., Sharma, J.S., Hughes, D., Graham, J.: Finite element analysis of an embankment on a soft estuarine deposit using an elastic-viscoplastic soil model. *Can. Geot. J.* 46(12), 357–368 (2009)
- [14] Nash, D.F.T., Ryde, S.J.: Modelling consolidation accelerated by vertical drains in soil subject to creep. *Géotechnique* 51(3), 257–273 (2001)
- [15] Nash, D.F.T., Brown, M.A.: The influence of destructuration of soft clay on time-dependent settlements – a comparison of some elastic visco-plastic models. Submitted to *International Journal of Geomechanics* (2012)
- [16] Hu, Y.Y.: Long-term settlement of soft subsoil clay under rectangular or semi-sinusoidal repeated loading of low amplitude. *Can. Geot. J.* 47(11), 1259–1270 (2010)
- [17] Matsuda, Hiroshi, Baek, W., Baek, J., Sato, Y.: Effect of creep on the settlement-time relation of clay during primary consolidation process. In: *Proceedings of the 42th Japan National Conference on Geotechnical Engineering*, vol. 135, pp. 269–270 (2007) (in Japanese)
- [18] Matsuda, Hiroshi, Baek, W., Baek, J.: Effect of creep on the settlement-time relation during primary consolidation of clay. In: *Proceedings of International Workshop on Constitutive Modelling - Development, Implementation, Evaluation and Application*, Hong Kong, January 12-13, pp. 208–217 (2007)

# Examination on Time-Dependent Soil Models in One-Dimensional Consolidation

Yixing Yuan\* and Andrew J. Whittle

Department of Civil and Environmental Engineering  
Massachusetts Institute of Technology, Cambridge, MA 02139  
Yixing@mit.edu

**Abstract.** This paper reviews the performance of two time-dependent constitutive models in predictions of one-dimensional consolidation. The Soft-Soil Creep model [1] is an example of an elastic-viscoplastic formulation that incorporates a time-dependent state variable to estimate viscoplastic deformation. We show that the SSC model is equivalent to the isotache formulation proposed by Imai [2], as both are based on a unique relationship between stress, void ratio and the viscoplastic component of void ratio rate. Simulations of 1-D consolidation confirm that both models represent Hypothesis B behavior, where the axial strain at the End of Primary (EOP) consolidation is dependent on the depth of the clay layer. The effects of specimen thickness and the phenomenon of pore pressure increase at the start of consolidation are discussed in detail. Our interpretation highlights the importance of assumptions regarding the initial strain rate on the behavior observed at different scales under a given applied increment of loading.

**Keywords:** elastic-viscoplastic, isotache, thickness effect, initial strain rate.

## 1 Introduction

There are many formulations that have been developed to explain the interactions between creep and consolidation behavior of clays that affect the time dependent response at different length scales. In this paper we show that the elastic-viscoplastic formulation used for the Soft-Soil Creep model (SSC; [1]) is equivalent to the Isotache framework proposed by Imai [2]. Isotache concepts can then be used to interpret to predictions using the SSC model.

## 2 Equivalence of SSC and Isotache Formulations

Fig.1 shows a schematic representation of the SSC model for 1-D loading. This model describes the deformation of soil skeleton as a combination of elastic  $\Delta\epsilon^e$

---

\* Corresponding author.



Imai [2] assumed that if the total void ratio rate can be separated into recoverable ( $-\dot{e}^r$ ) and irrecoverable components ( $-\dot{e}^{ir}$ ), a unique linear relationship also holds between ( $-\dot{e}^{ir}$ ) and  $\Gamma$ . This results is expressed by  $\Gamma = a \log(-\dot{e}^{ir}) + b$  with slope  $C_\alpha$ . This relationship can be verified particularly with the data after the End-Of-Primary consolidation (EOP), as the void ratio rate ( $-\dot{e}$ ) reduces to the irrecoverable rate ( $-\dot{e}^{ir}$ ) in secondary compression. Imai’s assumption also holds well within the range of primary consolidation as long as the irrecoverable component is dominant in overall deformation (e.g., after “apparent yield”).

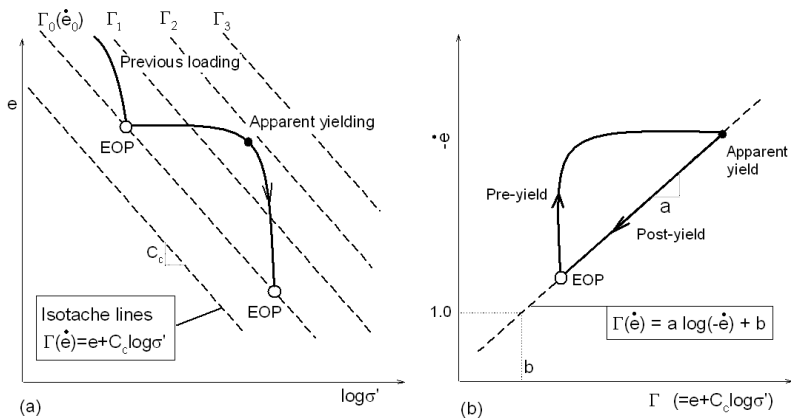


Fig. 2. Schematic representation of Imai’s model [2]: (a) isotaches; (b) isotache-void ratio rate

Table 1 lists the equations of Imai’s Isotaches formulation. Equation b1 shows the separation rule that is essentially equivalent to the SSC model, if ( $-\dot{e}^r$ ) = ( $-\dot{e}^c$ ) and ( $-\dot{e}^{ir}$ ) = ( $-\dot{e}^{vp}$ ). Although the recoverable void ratio is of the same form as SSC (Eqn. b2 vs a2), the irrecoverable component ( $-\dot{e}^{ir}$ ) is obtained through a unique geometric relationship presented in Eqn.b3. In summary, this Isotache model requires four input parameters  $C_c$ ,  $C_s$ ,  $C_\alpha$ , and  $b$  (Fig. 2b).

In order to find the relation between Imai’s model and SSC, the parameter  $b$  in the Isotaches formulation is expressed with initial condition as

$$b = e_0 + C_c \log \sigma'_0 - C_\alpha \log(-\dot{e}_0^{ir}) \tag{2.1}$$

where  $e_0$ ,  $\sigma'_0$  and ( $-\dot{e}_0^{ir}$ ) are initial void ratio, effective stress and irrecoverable void ratio rate, respectively. Substituting Eqn. 2.1 into Eqn. b3, and subtracting the recoverable component ( $-\Delta e^r = C_s \log[\sigma'/\sigma'_0]$ ) from the total void ratio change of ( $-\Delta e = e_0 - e$ ), we obtain the irrecoverable component of void ratio change as:

$$-\Delta e^{ir} = (C_c - C_s) \log \frac{\sigma'}{\sigma'_0} - C_\alpha \log \frac{-\dot{e}^{ir}}{-\dot{e}_0^{ir}} \tag{2.2}$$

Combining Eqns. 2.2 and a4, and assuming ( $-\Delta e^{vp}$ ) = ( $-\Delta e^{ir}$ ), we have an expression of ( $-\dot{e}^{ir}$ ):

$$-\dot{e}^{ir} = \left[ \begin{array}{c} (-\dot{e}_0^{ir}) \left( \frac{\sigma_{p0}}{\sigma'_0} \right)^{\frac{C_c - C_s}{C_\alpha}} \\ \left( \frac{\sigma'_0}{\sigma_p} \right)^{\frac{C_c - C_s}{C_\alpha}} \end{array} \right] \quad (2.3)$$

Through the geometric relation of Isotaches, one can show the first term on the right hand side of Eqn. 2.3 maps the initial irrecoverable void ratio rate ( $-\dot{e}_0^{ir}$ ) to a reference void ratio rate ( $-\dot{e}_{ref}$ ) = 0.434 ( $C_\alpha / \tau_{ref}$ ). Eqn. 2.3 for the Isotache model is then same as SSC model Eqn. a3 and hence, the two formulations are equivalent. We can easily convert the SSC parameters  $\tau_{ref}$  and  $\sigma_{p0}$  with the Isotache parameter b by using Eqn. 2.1 together with

$$-\dot{e}_0^{ir} = \frac{0.434 C_\alpha}{\tau_{ref}} \left( \frac{\sigma'_0}{\sigma_{p0}} \right)^{\frac{C_c - C_s}{C_\alpha}} \quad (2.4)$$

The equivalency between SSC and Imai's model implies these two models are based on the same unique relationship between stress, void ratio, and irrecoverable void ratio rate, as indicated in Eqn. b3.

### 3 Simulation of One-Dimensional Consolidation

Numerical analyses of one-dimensional consolidation are conducted to simulate incremental oedometer tests using the SSC and Isotache models. The differential equations of coupled consolidation are solved using a finite difference method (similar to [4]). The analyses also account for nonlinear variations of hydraulic conductivity with void ratio. The total strain rate is controlled by the distribution of excess pore pressure, whereas the constitutive model determines the viscoplastic (irrecoverable) deformation and the changes in effective stress.

Example calculations have been performed using input parameters corresponding to Yokohama clay (following the calibration of the Isotache model by Hawlader et al. [5]), Table 2. The initial example considers a normally consolidated specimen, with  $\sigma'_0 = 160\text{kPa}$  and  $e_0 = 2.38$ , with zero initial excess pore pressure that is subject to an incremental load,  $\Delta\sigma = 160\text{kPa}$  and consolidates with top drainage only. Since we assume that the specimen is normally consolidated, the SSC state variable  $\sigma_{p0} = \sigma'_0$  and the reference time  $\tau_{ref}$  is determined as 24hr using Eqns. 2.1 and 2.4. It should be noted that the parameter b is not dimensionless, but should be consistent with the stress and time units ([kPa] and [hr] in this case).

**Table 2.** Model input parameters for Yokohama clay (after [5])

$k_0$ [cm/hr]	$C_k$	$C_c$	$C_s$	$C_\alpha$	b*	$\tau_{ref}$ ** [hr]	$\sigma_{p0}$ ** [kPa]
$2.66 \times 10^{-4}$	1.8	1.05	0.11	0.05	4.85	24	160

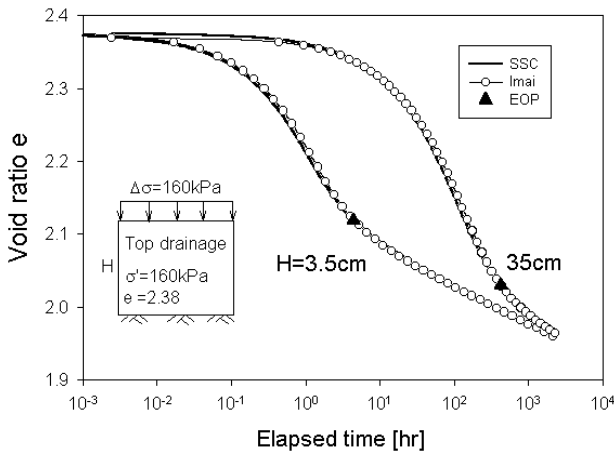
\* Isotache model; \*\*SSC model

Note:  $(e - e_0) = C_k \log(k_v / k_{v0})$

Fig. 3 shows that consolidation curves from SSC and the Isotache model match perfectly for specimens with thickness,  $H = 3.5\text{cm}$  and  $35\text{cm}$ . Both models describe creep with constant  $C_\alpha$  occurring concurrently with primary consolidation and hence, predict larger changes in void ratio at the EOP condition for the thicker specimen, consistent with Hypothesis B [6].

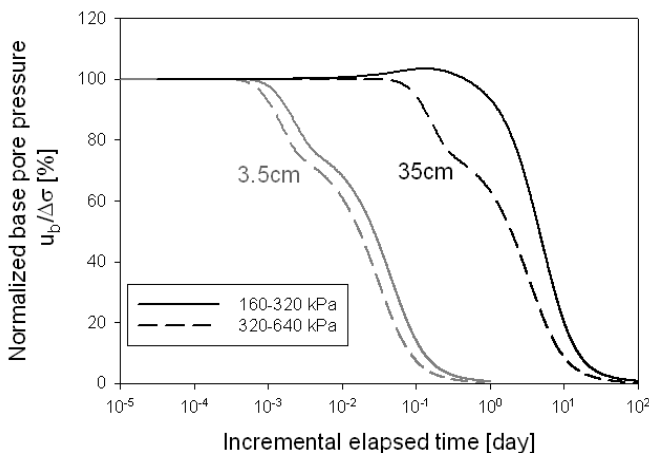
### 4 Thickness Effects

Fig. 4 shows the variation of the normalized base pore pressure ( $u_b/\Delta\sigma$ ) predicted by the SSC model for cases with  $H = 3.5\text{cm}$  and  $35\text{cm}$  for the initial conditions, material parameters and incremental load conditions ( $160 - 320\text{kPa}$ ) described above. Results for the thin specimen ( $3.5\text{cm}$ ) show a monotonically decrease in base pore pressure. In contrast, for  $t \leq 0.5\text{days}$  there is a small increase in  $u_b$  at the base of the thicker specimen ( $35\text{cm}$ ) prior to dissipation.



**Fig. 3.** Variation of void ratio from simulations with SSC and Imai’s model for two different drainage heights: 3.5cm and 35cm

Stolle et al. [7] have found similar behavior using the SSC model. Yin and Graham [8] attribute this behavior to undrained creep that occurs far from the drainage boundary. During undrained creep, the accumulation of viscoplastic strain must be compensated by a reduction in effective stress and hence, to an increase in pore pressure. However, we view this phenomenon differently. It is interesting to note that all prior simulations assume that the initial pore pressures are equal to zero. This assumption is apparently inherited from the Terzaghi consolidation theory, in which the pore pressures become negligible after EOP. This assumption implies no gradient across the specimen and hence, zero strain rate everywhere. However, in reality fully consolidated soil still undergoes secondary



**Fig. 4.** Variation of normalized base pore pressure for specimens with different drainage heights under two increments of load

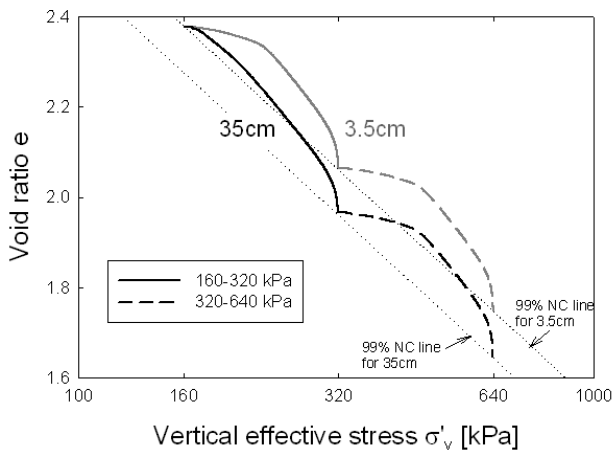


**Fig. 5.** Void ratio-stress paths of consolidating specimens with different heights under two increments of load

compression where the total strain rate is non-zero and is equal to the irrecoverable strain rate due to creep. This important implication from the Isotache formulation is often overlooked in predictions with elastic-viscoplastic models. Therefore, the increase in pore pressure is due to an inconsistency between the initial total strain and viscoplastic strain rates, but is not an intrinsic characteristic of normally consolidated soil.

In order to demonstrate this fact, specimens are firstly consolidated up to 99% pore pressure dissipation under the first increment of load from 160 to 320kPa. A subsequent load increment is applied from 320kPa to 640kPa. Fig. 4 also compares

the normalized variations in base pore pressure for this second load increment. In this case, qualitatively similar behavior occurs for both  $H = 3.5\text{cm}$  and  $35\text{cm}$  specimens. This result occurs because at the end of the first increment, the pore pressure gradient produces sufficient total strain rate to balance the viscoplastic strain rate. There is no undrained creep after the second load increment is applied.

More results can be extracted from the two successive increments of loading: Fig. 5 plots the void ratio-effective stress relations. In the first load increment, the thin and thick specimens start with the same initial effective stress and void ratio, and are initially on the same Isotache. The thicker specimen tends to consolidate for a longer period of time and produces more deformation than the thin specimen at EOP. In the second load increment, the two specimens start at different EOP conditions, (i.e., they are initially on Isotaches with different initial strain rates), as shown in Fig. 5. However, if one plots the incremental change in void ratio for the two specimens during this second load increment, as shown in Fig.6, the two compression curves are almost parallel to each other. Although this result initially appears to conform to Hypothesis A behavior (as suggested in [9]), this is misleading as the initial void ratios of thin and thick specimens are different at the start of the load increment.

These results highlight that predictions using the SSC model vary significantly with the initial strain rate (this finding has also been noted by Degago et al. [10]). In this case we face a dilemma in using SSC to predict field consolidation. For instance, one often calibrates the model based on the experiment results and uses the obtained parameters to predict the field behavior. This procedure relies on the resemblance between the laboratory and the field. However, the initial strain rate in the field will generally differ from the one calibrated in laboratory tests. This difference will eventually cause discrepancies in predictions of consolidation behavior at field scale.

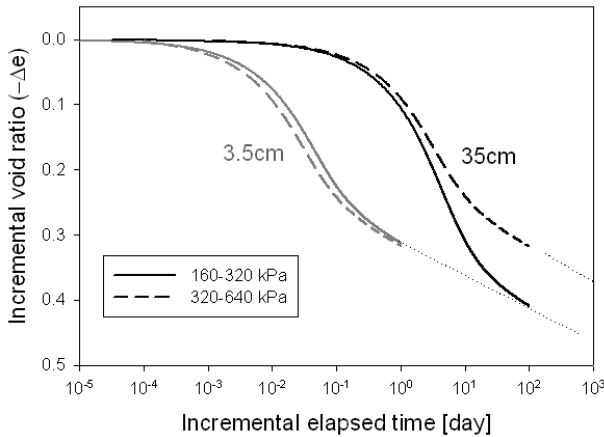


**Fig. 6.** Different relations of incremental void-ratio over time along two continuous increments

## 5 Concluding Remarks

In this paper, we show the formulations of two time-dependent soil models: SSC and Imai's Isotaches model are equivalent. The relationships are developed so that the parameters of two models can be converted from each other. Numerical simulations of one-dimensional consolidation are conducted on normally consolidated Yokohama clay. Two models predict very consistent results, and both are classified as Hypothesis B type models.

Analyses of consolidation under incremental loads using the SSC model generate increases in pore pressures at constant total stress for thick specimens. Using the Isotache concepts we show that this is due to an inconsistency between total and viscoplastic strain rates and can be eliminated in a subsequent load increment when the two strain rates are in equilibrium at the end of the first increment. In this case, the initial conditions for thin and thick specimens are the same in the first increment, but are different in the second increment. The resulting discrepancy between the compression behavior in the two load increments highlights the importance of the assumption of initial strain rate and has important impacts on the application of elastic-viscoplastic models (such as SSC) for predicting consolidation at field scale.

## References

- [1] Vermeer, P.A., Neher, H.P.: A soft soil model that accounts for creep. Beyond 2000 in computational geotechnics: 10 years of PLAXIS International. In: Proceedings of the International Symposium Beyond 2000 in Computational Geotechnics, Amsterdam, The Netherlands, March 18-20, vol. 249 (1999)
- [2] Imai, G.: Analytical examinations of the foundations to formulate consolidation phenomena with inherent time-dependence. *Compression and Consolidation of Clayey Soils*, 891–935 (1995)
- [3] Bjerrum, L.: Engineering geology of Norwegian normally consolidated marine clays as related to settlements of buildings. *Géotechnique* 17(2), 83–118 (1967)
- [4] Yin, J.H., Graham, J.: Elastic-viscoplastic modeling of one-dimensional consolidation. *Géotechnique* 46(3), 515–527 (1996)
- [5] Hawlader, B.C., Muhunthan, B., Imai, G.: Viscosity Effects on One-Dimensional Consolidation of Clay. *International Journal of Geomechanics* 3(1), 99 (2003)
- [6] Ladd, C.C., Foott, R., Ishihara, K., Schlosser, F., Poulos, H.: Stress-Deformation and Strength Characteristics. In: Proc. 9th Int. Conf. Soil Mechn. Fdn. Engng., Tokyo, pp. 421–494 (1977)
- [7] Stolle, D.F.E., Vermeer, P.A., Bonnier, P.G.: A consolidation model for a creeping clay. *Canadian Geotechnical Journal* 36(4), 754–759 (1999)
- [8] Yin, J.H., Graham, J., Clark, J.I., Gao, L.: Modelling unanticipated pore-water pressures in soft clays. *Canadian Geotechnical Journal* 31(5), 773–778 (1994)
- [9] Imai, G., Tang, Y.: A constitutive equation of one-dimensional consolidation derived from inter-connected tests. *Soils and Foundations* 32(2), 83–96 (1992)
- [10] Degago, S., Grimstad, G., Jostad, H.: Use and misuse of the isotache concept with respect to creep hypotheses A and B. *Géotechnique* (10), 897–908 (2011)

# Criterion for Flow Liquefaction Instability

José E. Andrade<sup>1</sup>, Alfonso M. Ramos<sup>2</sup>, and Arcesio Lizcano<sup>3</sup>

<sup>1</sup> Civil and Mechanical Engineering, California Institute of Technology,  
1200 E. California Blvd. Pasadena, CA 91106  
jandrade@caltech.edu

<sup>2</sup> Geophysical Institute, Pontificia Universidad Javeriana, Cra 7 No 42-27 Bogotá, Colombia

<sup>3</sup> Professor, Civil and Environmental Engineering, Universidad de Los Andes,  
Cra 1 No 18 A-12, Bogotá, Colombia

**Abstract.** This paper describes a general liquefaction flow instability criterion for elastoplastic soils based on the concept of loss of uniqueness. We apply the criterion to the general case of axisymmetric loading and invoke the concepts of effective stresses and loss of controllability to arrive at a general criterion for the onset of liquefaction flow. The criterion is used in conjunction with an elastoplastic model for sands to generate numerical simulations. The numerical results are compared with experimental evidence to give the following insights into predicting liquefaction. 1) The criterion proposed clearly and naturally differentiates between liquefaction flow (instability) and cyclic mobility. 2) Flow liquefaction not only depends on the potential of the material to generate positive excess pore pressures, but more importantly, it also depends on the current state of the material, which is rarely predicted by phenomenology.

**Keywords:** Undrained instabilities, elastoplasticity, flow liquefaction, sands.

## 1 Introduction

Liquefaction is one of the most elusive concepts in geotechnics due to its physical complexity and its relatively lax definition. Liquefaction can be associated with phenomena giving rise to loss of shearing resistance or the development of excessive strains, accompanied by increases in excess pore water pressures [1]. Flow liquefaction is associated with a state of instability and sudden increases in strain and pore pressures. In this work, we apply the notion of loss of uniqueness to a general class of isotropic elastoplastic models to derive a specific criterion for the onset of flow liquefaction. By choice, we make no distinction between so-called static liquefaction [2] and cyclic or dynamic liquefaction. The criterion is specialized to the context of classical ‘triaxial’ conditions applicable in the laboratory. The derived criterion is then adapted to a particular elastoplastic model [3] capable of simulating cyclic and monotonic loading in sands.

## 2 Flow Liquefaction Criterion

For the sake of simplicity, we limit the following derivation to infinitesimal and axisymmetric undrained conditions. Loss of uniqueness requires  $[[\dot{\sigma}]] : [[\dot{\epsilon}]] = 0$  [2,4]. Also,  $[[\dot{\epsilon}]] = \dot{\epsilon}^* - \dot{\epsilon}$  is the jump in the strain rate due to potentially duplicate solutions  $(\mathbf{v}^*, \mathbf{v})$  for the velocity field. Further,  $[[\dot{\sigma}]]$  is the jump in the effective stress rate tensor. Now, under triaxial (axisymmetric) conditions, loss of uniqueness reduces to  $[[\dot{p}]] [[\dot{\epsilon}_v]] + [[\dot{q}]] [[\dot{\epsilon}_s]] = 0$ , where  $\dot{\epsilon}_v = \dot{\epsilon}_a + 2\dot{\epsilon}_r$  is the rate of volumetric strain and  $\dot{\epsilon}_s = 2/3(\dot{\epsilon}_a + \dot{\epsilon}_r)$  is the deviatoric component of the strain rate. Also,  $\dot{p} = 1/3(\dot{\sigma}_a + 2\dot{\sigma}_r)$  is the effective pressure rate and  $\dot{q} = \dot{\sigma}_a - \dot{\sigma}_r$  is the deviatoric stress rate.  $\dot{\sigma}_a$  is the axial total stress rate and  $\dot{\sigma}_r$  is its radial counterpart. Assuming a rate form for the constitutive relation, we write the relation between the effective stress rate and the total strain rate such that

$$\begin{Bmatrix} \dot{p} \\ \dot{q} \end{Bmatrix} = \begin{bmatrix} C_{pp} & C_{pq} \\ C_{qp} & C_{qq} \end{bmatrix} \begin{Bmatrix} \dot{\epsilon}_v \\ \dot{\epsilon}_s \end{Bmatrix} \quad (1)$$

where the constitutive matrix is furnished by the specific constitutive model of choice. Further, under undrained conditions, and assuming incompressible fluid and solid constituents, we require that  $\dot{\epsilon}_v = 0$ . Then, by using this fact together loss of uniqueness and equations (1) we get that  $C_{qq} [[\dot{\epsilon}_s]]^2 = 0$  which implies in general that the shear component of the constitutive equation must vanish, i.e.,  $C_{qq} = 0$ . This condition will furnish a general criterion for detecting flow liquefaction instability.

## 3 Constitutive Model

We use the Dafalias-Manzari model [3]. Based on the rates of total volumetric and deviatoric strains, Eq (1) especially adapted to the Dafalias-Manzari constitutive model reads

$$\begin{Bmatrix} \dot{p} \\ \dot{q} \end{Bmatrix} = \frac{1}{\chi} \begin{bmatrix} 3KG + KHp & -3KG\beta \text{sgn}(\dot{\epsilon}_s^p) \\ 3KG\eta & 3GHp - 3KG\beta\eta \text{sgn}(\dot{\epsilon}_s^p) \end{bmatrix} \begin{Bmatrix} \dot{\epsilon}_v \\ \dot{\epsilon}_s \end{Bmatrix} \quad (2)$$

where,  $\chi = 3G + Hp - K\beta\eta \text{sgn}(\dot{\epsilon}_s^p)$ . Loss of uniqueness and the onset of flow liquefaction, when especially adapted to the Dafalias-Manzari model is

$$C_{qq} = \frac{3G(Hp - K\beta\eta \text{sgn}(\dot{\epsilon}_s^p))}{\chi} = 0 \quad (3)$$

which, to be true in general, requires the quantity inside the parenthesis to vanish. From Equation (3) a closed form of the hardening modulus that is able to detect the onset of flow liquefaction can be proposed

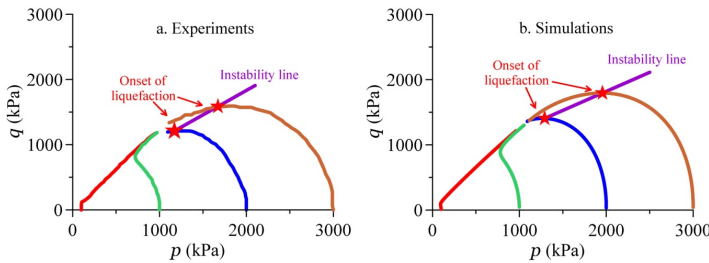
$$H_L = \frac{K\beta\eta}{p} \text{sgn}(\dot{\epsilon}_s^p) \quad (4)$$

## 4 Numerical Simulations

We present numerical simulations using the generalized flow liquefaction adapted to the Dafalias-Manzari model utilizing the limiting hardening modulus (Eq 4). We compare these simulations with different sets of experimental results where monotonic and cyclic stress paths were imposed for Toyoura sand and Dog’s Bay sand, respectively.

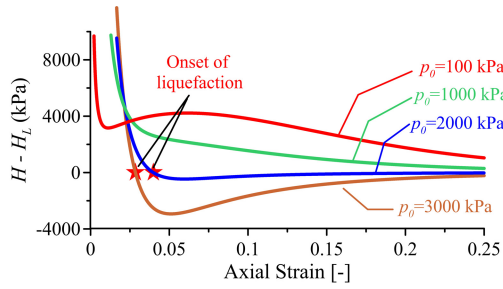
### 4.1 Verdugo and Ishihara (1996) Experiments on Toyoura Sand

Fig 1a shows the experiments with initial void ratio  $e_0 = 0.833$  with mean pressure ranging from  $p_0 = 100$  kPa to  $p_0 = 3000$  kPa [5]. The onset of flow liquefaction, marked by a star symbol in Figure 1a, was obtained at the peak of deviatoric stress, and the instability line was built by joining the points marking the onset of flow liquefaction from each experiment. The instability line is defined as the locus of points at which flow liquefaction is initiated for the same void ratio under undrained triaxial test [6].



**Fig. 1. a:** Experiments in undrained triaxial test for void ratio  $e_0=0.833$  after [5] **b:** Simulations of Verdugo and Ishihara tests

We perform simulations on the Toyoura sand samples (Fig 1b). The onset of flow liquefaction, as well as the instability line in the simulations, was detected by tracking the evolution of the critical hardening modulus and comparing it with the hardening modulus  $H - H_L$ . Fig 2 shows the evolution of the criterion of flow liquefaction for the simulations shown in Fig 1b. It can be observed that only samples at 2000 and 3000 kPa confining pressures are able to liquefy. As observed in the experiments, the samples at lower confinement never reach the onset of liquefaction flow. These results clearly show that the criterion (and model) are able to distinguish between mechanical behaviour corresponding to denser than critical to that of sands that are looser than critical, or contractive. Liquefaction is a function of the state.



**Fig. 2.** Evolution of the flow liquefaction criterion compared to axial strains for simulations of undrained triaxial tests on Toyoura sands. Onset of flow liquefaction is marked at points where  $H$  equals  $H_L$

### 4.2 Qadimi and Coop (2007) Experiments on Dog’s Bay Sand

Fig 3a depicts an undrained cyclic triaxial test performed by [7] using Dog’s Bay sand. It is anisotropically consolidated under a  $K_0$  stress path. The initial state of stresses before the undrained cyclic test was  $q = 1828$  kPa and  $p = 2500$  kPa. The void ratio before the cyclic test was  $e_0 = 0.982$ . The increment of deviatoric stress for the undrained cyclic triaxial test was  $\Delta q = 1000$  kPa. After a couple tens of cycles, the specimen displayed liquefaction flow with a sudden increase in pore water pressure as evidenced by the remarkable drop in effective (Fig 3a). This set of experiments is particularly interesting because it helps illustrate the difference between flow liquefaction and cyclic mobility.

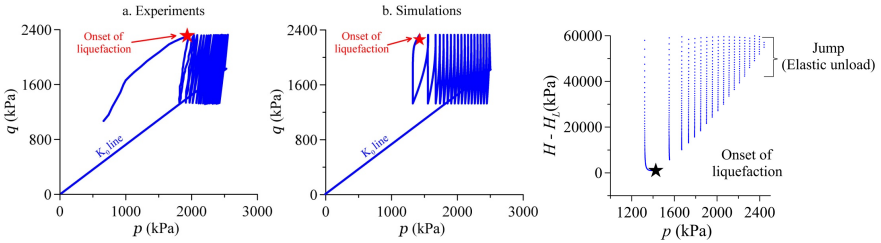


**Fig. 3. a:** Experimental undrained cyclic triaxial test anisotropically consolidated with a  $K_0$  condition of  $e_0 = 0.982$ ,  $\Delta q = 1000$  kPa [7] **b:** Simulation **c:** Evolution of  $H - H_L$  for the simulation of the anisotropically consolidated undrained cyclic triaxial test

Parallel to the anisotropically consolidated test, we performed a simulation (Fig 3b). Similar to the actual experiment, flow liquefaction is detected after 19 cycles. As before, detection of flow liquefaction is signalled by  $H - H_L = 0$ , as shown in Fig 3c. The simulation reproduces faithfully the stress path and the onset of

liquefaction. Additionally, [7] performed an undrained cyclic test after isotropic consolidation. The void ratio for this test was very similar to the above with  $e_0 = 1.22$ . Hence, these two tests provide a backdrop to evaluate the differences between liquefaction flow and cyclic mobility. Fig. 4 shows a simulation of an undrained cyclic triaxial test isotropically compressed at  $p_0 = 1400$  kPa performed by [7]. The increment of cyclic deviatoric stress is  $\Delta q = 280$  kPa. 150 cycles of deviatoric stress were applied. Fig 4b shows the evolution of the criterion for flow liquefaction ( $H - H_L$ ). Although there is a decrease in effective mean pressure as a result of cyclic loading, the criterion for liquefaction flow is never satisfied after 150 cycles.

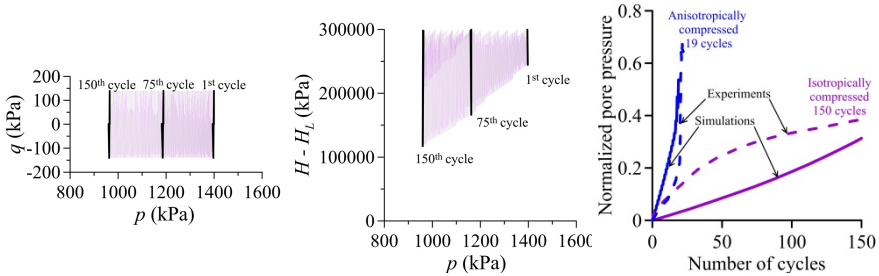


**Fig. 4. a:** Simulation of an undrained cyclic triaxial test isotropically compressed at  $p_0 = 1400$  kPa in Dog’s Bay sand. Initial void ratio  $e_0 = 1.22$ . Increment of deviatoric cyclic stress  $\Delta q = 280$  kPa at 150 loading cycles **b:** Evolution of the criterion for flow liquefaction **c.** Build up of excess pore pressure for the cyclic experiments depicted in Figures 3a and 4. Experiments were performed by [7]

The build up of pore pressure generated in the two previous undrained cyclic triaxial tests was reported by [7] and is redrawn in Fig 4c. The build up of pore pressure obtained in the simulations is superimposed on the figure. It can be seen that the build up of pore water pressures is significantly different for the anisotropically consolidated sample relative to the isotropically consolidated counterpart. There is a sharp increase in pore pressures after a few tens of cycles in the anisotropic sample. This is characteristic of liquefaction flow. On the other hand, as it is characteristic of cyclic mobility, the isotropically consolidated sample displays a smooth increase in pore pressures, without noticeable sudden changes. In fact, as seen in Figure 4c, after 150 cycles, the sample has reached about 50% of the normalized pore pressure increase experienced by the anisotropic sample. This is emblematic of the mechanical difference between liquefaction flow and cyclic mobility. As anticipated by [8], flow liquefaction is an instability obtained as part of structural collapse in a sample of sand. It typically displays sudden increases in strains and excess pore pressure. On the other hand, cyclic mobility is a constitutive response, with accumulation of strains and excess pore pressures without exhibiting measurable instabilities.

## 5 Conclusions

The liquefaction criterion presented herein can detect the onset of liquefaction flow under both monotonic and cyclic conditions without resorting to assumptions *a priori*.

As observed in experiments, both cyclic mobility and flow liquefaction display increases in pore pressures, with cyclic mobility producing gradual pore pressure build-up and flow liquefaction producing sudden pore pressure build-up as a result of material instability. The criterion presented herein captures this difference as a natural result of the state of the material.

The  $H - H_L$  could help predict the liquefaction potential for a given soil based on its state and imposed loading path.

## References

- [1] National Research Council (NRC): Liquefaction of soils during earthquakes. National Academy Press, Washington D.C (1985)
- [2] Andrade, J.E.: A predictive framework for liquefaction instability. *Géotechnique* 59(8), 673–682 (2009)
- [3] Dafalias, Y.F., Manzari, M.T.: Simple plasticity sand model accounting for fabric change effects. *Journal of Engineering Mechanics* 130(6), 622–633 (2004)
- [4] Hill, R.: A general theory of uniqueness and stability in elastic-plastic solids. *Journal of the Mechanics and Physics of Solids* 6(3), 236–249 (1958)
- [5] Verdugo, R., Ishihara, K.: The steady state of sandy soils. *Soils and Foundations* 33, 81–92 (1996)
- [6] Lade, P.V.: Instability and liquefaction of granular materials. *Computers and Geotechnics* 16(2), 123–151 (1994)
- [7] Qadimi, A., Coop, M.: The undrained cyclic behaviour of a carbonate sand. *Géotechnique* 57(9), 739–750 (2007)
- [8] Alarcón-Guzmán, A., Leonards, A., Chameau, L.: Undrained monotonic and cyclic strength of sands. *Journal of Geotechnical Engineering* 114(10), 1089–1108 (1988)

# Influence of Grain Breakage on Critical State

Wei Hu<sup>2\*</sup>, Zhen-Yu Yin<sup>3</sup>, Christophe Dano<sup>1</sup>, and Pierre-Yves Hicher<sup>1</sup>

<sup>1</sup> Research Institute in Civil and Mechanical Engineering, Ecole Centrale de Nantes

<sup>2</sup> State Key Laboratory of Geohazard Prevention and Geoenvironment Protection,  
Chengdu University of Technology, Chengdu, 610059, PR China  
huwei1999@gmail.com

<sup>3</sup> Department of Civil Engineering, Shanghai Jiao Tong University, Shanghai PR China

**Summary.** This paper aims to investigate the influence of grain breakage on the position of the critical state line (CSL). Existing measures of the amount of grain breakage are discussed and a new measure named “relative uniformity” based on the evolution of the uniformity coefficient is proposed. Triaxial tests with different stress paths on granular materials made of limestone grains are carried out. Based on the obtained results, a method for determining the modified relative breakage index and the relative uniformity is proposed using plastic work. A relation between grain breakage measures and the position of the critical state line is then proposed for describing the influence of grain breakage on mechanical properties.

**Keywords:** Critical state, grain breakage, limestone grains.

## 1 Introduction

Grain breakage influences significantly the mechanical behaviour of crushable granular materials. The CSL changing with the grain size distribution (GSD) has been justified by experiments on sand (e.g. Bandini and Coop[1]; Biarez and Hicher[2]) and by numerical simulations using the discrete element method (e.g., Bolton et al. [3]; Kikumoto et al. [7]). The goal of this work is to propose a relation between the evolution of the CSL location and the measure of the amount of grain breakage during loading.

## 2 Definition of Breakage Indexes

Various grain breakage indexes have been proposed in the literature. Here, we retain the modified relative breakage index  $B_r^* = B_r/B_p$  proposed by Einav[6] obtained by replacing, in the definition by Hardin of the indexes  $B_p$  and  $B_r$ , the cut-off line of silt particle size by an ultimate GSD. Since the GSD tends to be fractal according to McDowell and Bolton [8] and Coop et al. [4], the breakage measure  $B_r^*$

---

\* Corresponding author.

varies from zero to one with changes in GSD. This particular aspect might be convenient in practice. We also propose another coefficient called the relative uniformity  $B_u$  based on the uniformity coefficient  $C_u = D_{60}/D_{10}$  which varies with grain breakage, as follows

$$B_u = \frac{C_u - C_{ui}}{C_{uf} - C_{ui}} \quad (1)$$

another coefficient called the relative uniformity  $B_u$  based on the uniformity coefficient where  $C_{ui}$  represents the initial uniformity coefficient;  $C_{uf}$  represents the ultimate uniformity coefficient corresponding to the fractal GSD. Thus,  $B_u$  varies also from zero to one.

### 3 Relation between the Plastic Work and Breakage Index

A possible variable related to the breakage amount can be the plastic work as proposed by Daouadji et al. [4]. We define the plastic work as follows:

$$w_p = \int \left\langle \frac{1}{3} I_1 dI_1'^p + 2\sqrt{J_2} dJ_2'^p \right\rangle \quad (2)$$

where  $I_1$  and  $dI_1'^p$  are the first invariants of the stress tensor and of the incremental plastic strain tensor, respectively;  $J_2$  and  $dJ_2'^p$  are the second invariants of the deviatoric stress tensor and of the incremental plastic deviatoric strain tensor, respectively; the function of MacCauley implies  $\langle F \rangle = (|F| + F)/2$ . If Eq.(2) is adopted, the plastic work can be accumulated during cyclic loading. Monotonic and cyclic triaxial tests were performed on assemblies of limestone grains from a quarry located in Prefontaines, in the centre of France. This material is very crushable. The unit weight of the material is  $17.1 \text{ kN/m}^3$  and the specific weight is  $27.0 \text{ kN/m}^3$ . The prepared samples have an initial uniformity coefficient  $C_u = 1.8$ . The mean grain size is  $D_{50} = 6 \text{ mm}$ . The maximum and minimum void ratios are 1.43 and 0.83, respectively. The initial void ratio  $e_0$  for all tested samples varies from 1.05 to 1.1. Based on the stress-strain curves of all the above mentioned tests, the plastic work is obtained by using Eqs.(2). Then,  $B_u$  and  $B_r^*$  are plotted versus the plastic work, as shown in Fig. 1. For both monotonic and cyclic loading tests, the evolution of GSD can be expressed by a unique function of the plastic work, independent of the loading condition

$$B_u = \frac{w_p}{a + w_p}; \quad B_r^* = \frac{w_p}{b + w_p} \quad (3)$$

with  $a = 6500$  and  $b = 1000$  for Préfontaines gravel.

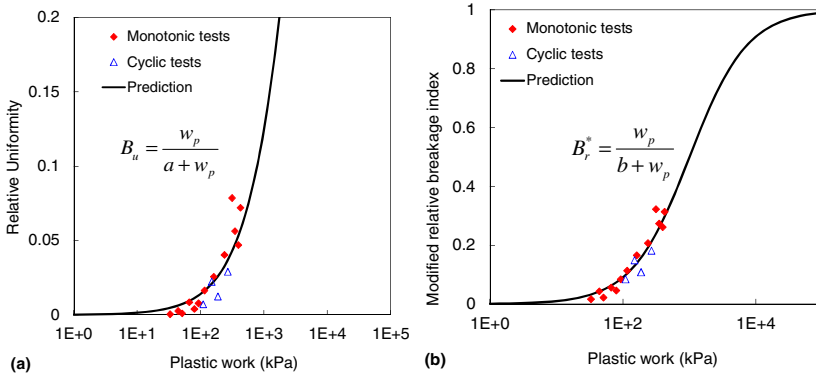


**Fig. 1.** (a) Relation between the plastic work and relative uniformity. (b) Relation between the plastic work and modified relative breakage index.

### 4 Relation between the Plastic Work and Critical State Position

For the tested material, in order to investigate the evolution of the CSL when grain breakage occurs, drained triaxial tests at a confining stress of 100 kPa but with different stress histories were carried out. Based on the  $e-\log p'$  curves of the different tests in Fig.2 with different amount of grain breakage, the hypothesis of a shift of the CSL can be justified. The equation of the CSL can be written as:

$$e_c = e_{ref} - \lambda_c \ln \left( \frac{p'}{p_{at}} \right) \tag{4}$$

where  $e_c$  is the critical void ratio corresponding to the current  $p'$ ;  $e_{ref}$  is the reference critical void ratio for a reference stress (taken equal to  $p_{at}$  for convenience);  $c$  is the slope of the critical state line in the  $e-\ln p'$  plan. For the limestone material, the initial position of the CSL is given by  $e_{ref0} = 1.43$  and  $c = 0.153$ , adopting the correlation of Biarez and Hicher . If the reference critical void ratio for each test is plotted as a function of the breakage measures  $B_u$  and  $B_r^*$  (see Fig. 3), the evolution of the CSL location can be linked to the evolution of GSD, as follows:

$$e_{ref} = e_{ref0} - \Delta e_{ref} \frac{B_u}{c + B_u} ; \quad e_{ref} = e_{ref0} - \Delta e_{ref} \frac{B_r^*}{d + B_r^*} \tag{5}$$

with  $e_{ref0} = 1.43$ ,  $e_{ref} = 0.5$ ,  $c = 0.006$  and  $d = 0.035$  obtained by curve fitting. Substituting Eq.(3) into Eq.(5), the reference critical void ratio can also be directly related to the plastic work, as follows:

$$e_{ref} = e_{ref0} - \Delta e_{ref} \frac{w_p}{ac + (1+c)w_p} \tag{6}$$

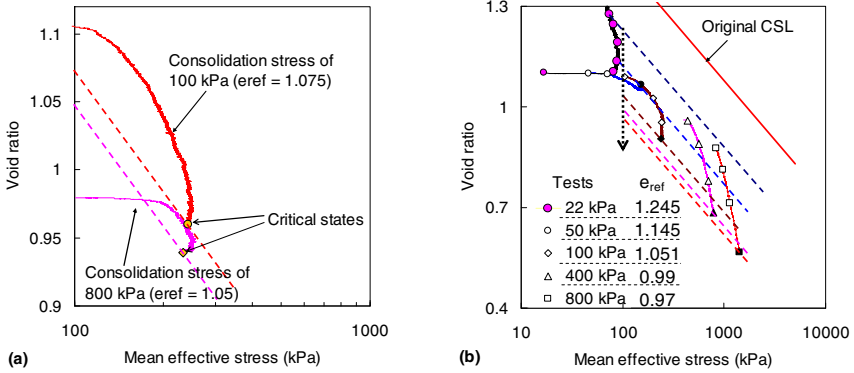


**Fig. 2.** Movement of CSL in  $e$ - $\log p'$  plane for: (a) tests with different consolidation stress histories, (b) tests with different confining stresses

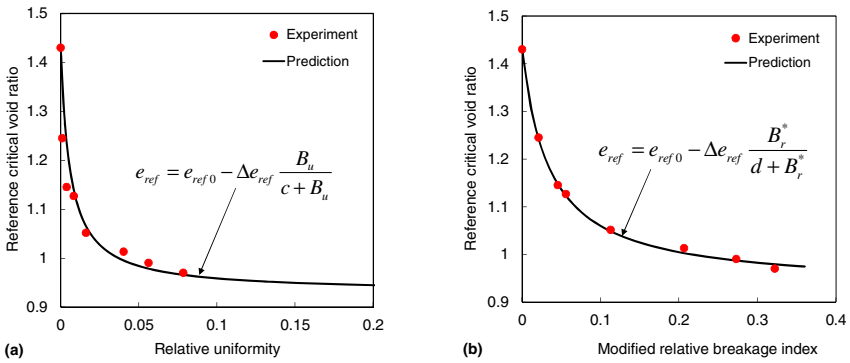


**Fig. 3.** (a) Reference critical void ratio versus relative uniformity, (b) Reference critical void ratio versus modified relative breakage index

## 5 Conclusions

Triaxial tests with different stress paths under both monotonic and cyclic loadings on limestone grain assemblies were carried out. Based on experimental observations, the evolution of the breakage measures  $B_u$  and  $B_r^*$  representing the evolution of GSD due to grain breakage under both monotonic and cyclic loading conditions are shown to be both an hyperbolic function of the plastic work, independently of the nature of the loading. Furthermore, the shift of the critical state line due to grain breakage was also investigated. Based on the results obtained on the limestone grain material, a relation between the breakage measures and the CSL location is proposed. Therefore, the shift of the CSL can be determined at any stage of a given test by calculating the plastic work accumulated from the beginning of the mechanical loading.

## References

- [1] Bandini, V., Coop, W.R.: The influence of particle breakage on the location of the critical state line of sands. *Soils and Foundations* 51(4), 591–600 (2011)
- [2] Biarez, J., Hicher, P.Y.: *Elementary Mechanics of soil behaviors*. Balkma, Rotterdam (1997)
- [3] Bolton, M.D., Nakata, Y., Cheng, Y.P.: Micro- and macro-mechanical behaviour of DEM crushable materials. *Géotechnique* 58(6), 471–480 (2008)
- [4] Coop, M.R., Sorensen, K.K., Bodas Freitas, T., Georgoutsos, G.: Particle breakage during shearing of a carbonate sand. *Géotechnique* 54(3), 157–163 (2004)
- [5] Daouadji, A., Hicher, P.Y., Rahma, A.: An elastoplastic model for granular materials taking into account grain breakage. *European Journal of Mechanics - A/Solids* 20(1), 113–137 (2001)
- [6] Einav, I.: Breakage mechanics- Part I: Theory. *Journal of the Mechanics and Physics of Solids* 55(6), 1274–1297 (2007)
- [7] Kikumoto, M., Muir Wood, D., Russell, A.R.: Particle crushing and deformation behaviour. *Soils and Foundations* 50(4), 547–563 (2010)
- [8] McDowell, G.R., Bolton, M.D.: On the micromechanics of crushable aggregates. *Géotechnique* 48(5), 667–679 (1998)

# Compressible Fluid – An Alternative Concept within CSSM

Tomislav Ivšić<sup>1,\*</sup> and Astrid Gojmerac Ivšić<sup>2</sup>

<sup>1</sup> University of Zagreb, Faculty of Civil Engineering, Kačićeva 26, 10000 Zagreb, Croatia  
tom@grad.hr

<sup>2</sup> University of Zagreb, Faculty of Science, Department of Chemistry,  
Horvatovac 102a, 10000 Zagreb, Croatia  
agi@chem.pmf.hr

**Summary.** In the paper an attempt to introduce an alternative concept for pressure-volume behavior of sands is presented. It is motivated by analogy between sand body and compressible fluid. Included is a brief description of methodology used for developing the concept, which is also applied to current and possible future research topics. The short overview of main findings is outlined with discussion and comments on possible implications for actual understanding of pressure-volume relations. The basic expected relation for studying the stress-strain relations is discussed, and, also, the possible relation between Critical State line and isotropic compression line coming from the proposed model is presented. The need for comprehensive and reliable experimental data is strongly emphasized.

**Keywords:** mineral sand, Critical State, van der Waals fluid.

## 1 Introduction

The mechanical behavior of sands is the subject of intensive research in the field of soil mechanics in order to obtain reliable tools for prediction, basically used in engineering applications. The rich phenomenology of sand behavior is studied through continuum or discrete approach, both of them having advantages and disadvantages, and variable success in description of macroscopic tests on sand samples.

In this paper an alternative concept is presented, aiming to describe the controversial pressure-volume in more consistent way. The classical, phenomenological approach is applied, using experiments on mineral sands. These macroscopic systems involve bulk properties, where continuum idealization can be applied.

The basis for most of the constitutive equations for soils is the concept of solid. The pressure - volume relations are well established and best understood for compressible fluids, making also the basis of classical thermodynamics. The concept proposed in this paper is mostly investigated in terms of compressible fluid. It is also based on “critical state” of soils assuming that the Critical State line (CSL) represents the fundamental state of mineral sands.

---

\* Corresponding author.

## 2 Methodology

The simple constitutive model is presented in Fig.1 [1]. The proposed system consists of a cylinder with compressible fluid (e.g. gas) and a piston with impediment or constraint (e.g. "friction pads"). The mechanical equilibrium of the system can be achieved for any volume of fluid ( $v_f$ ) in the cylinder when combination of forces from constraint ( $F$ ) and from pressure applied on external side of cylinder ( $p_a$ ) balances the pressure (force) inside the cylinder ( $p_f$ ). For the sake of simplicity, isothermal conditions are assumed. Using described mechanism, the same quantity of fluid can be kept in "loose" state (Fig 1a.) when applied pressure is greater then fluid pressure, or "dense" state (Fig 1b.) when applied pressure is less then fluid pressure. The fluid pressure is defined by its state equation for assumed constant temperature.

When the constraint is released without change of applied pressure, the contraction occurs in the first "initial state", and expansion in the second. The process of volume changes stops when the equilibrium of applied and fluid pressure is achieved. Ideally, with no constraint forces, they would balance at the mentioned isotherm. By combination of constraint force and applied pressure, various "paths" in  $p - V$  diagram, also shown in Fig 1c., can be obtained.

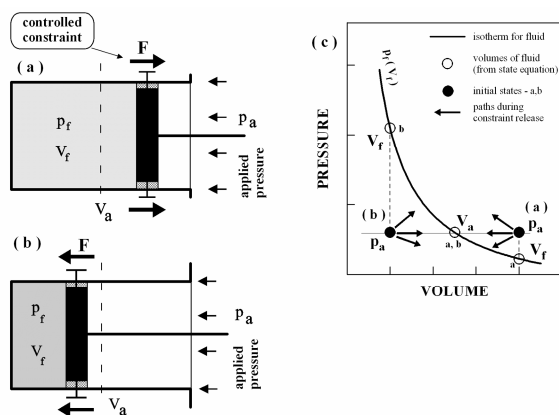


**Fig. 1.** The suggested model of compressible fluid for description of sand volume changes during shear; a) "loose" state, b) "dense" state, c) possible "paths" in  $p - V$  diagram

The most common elastic-plastic model used in soil mechanics is represented by a system of "spring" and "slider". The research methodology is to examine the properties of equivalent spring (leading to soil elasticity), of equivalent slider (soil plasticity), and the coupled effects in various stress paths. This basic model is until today significantly upgraded with various refinements and sophisticated features.

The research for the model of compressible fluid is expected to include similar three directions: a) the properties of the equivalent fluid are examined; b) the properties of the equivalent “impediment”, in direction of loading (overcome of the resistance) and unloading (jamming), and the also the influence of previous loading history; c) finally, the interaction or coupling of these elements in various stress paths can be examined.

The working assumptions and hypotheses should be tested with caution and in small steps, since the dissipation is present in the system, and the “land of irreversibility” is full of uncertainties.

### 3 Recent Findings

The basic hypothesis was the idea of existence of the thermodynamic (internal) pressure in sands as in compressible fluids, defined by state equation of sand (state function) which uniquely relates pressure and volume, depending only on substance (mineral grains) properties. This state equation would correspond to CSL.

The properties of analogous compressible fluid were analyzed by van der Waals equation of state for real gases written in adapted form

$$( p + A / v^2 ) ( v - 1 ) = C \quad (1)$$

where  $p$  is mean (effective) pressure,  $v$  - specific volume,  $A$  and  $C$  are constants in the units of pressure obtained empirically, for any set of corresponding measured data.

The main findings are presented in [1,2] and summarized here:

- the adapted van der Waals equation describes well the pressure-volume relation at critical state of mineral sands for a large range of applied pressures, as well as the common tests in which the deviator stress is proportional to the mean pressure. More over, it is demonstrated that the ratio of appropriate empirical constants  $A/C$  is close to 4 for all tests (as also expected from theory),
- the “stable” state defined by Eq. (1) is in the range of void ratios from 0 to 1
- more regular behavior according to proposed equation is obtained for the tests at elevated and higher pressures despite the grain crushing
- unexpectedly, the quantitative values of constants are of the same order of magnitude as the corresponding constants of gases or other volatile fluids. The constants  $C$  and  $A$  from Eq. (1) obtained experimentally from triaxial tests on mineral sands correlate well with ideal gas properties and molar properties of sands
- it is not expected that the agreements and non-contradictions that are found between compressible fluid and sands can have the physical explanation in the way used for common fluids. This especially applies to thermal behavior where the limits of analogy are most obvious.

## 4 Other Hypotheses

- The adapted van der Waals equation fitting the test results is presented in common  $e$ - $\log p'$  diagram (Fig.2a). The proposed cubic equation predicts the maximal allowable (stable) void ratio of  $e = 1$  for  $A/C = 4$  and  $p' = 0$ , which is not in contradiction with real sands. Also, for very large pressures this equation predicts  $e = 0$  which complies with tests on very high pressures. Using this equation it is also shown that sand follows the basic rule of real compressible fluids i.e. (*corrected*) *pressure*  $\times$  (*corrected*) *volume* = *const.* These features give advantage to this equation instead of common linear  $e$ - $\log p'$  relations. - eventually looser state at near zero pressure could be attributed to additional, structural forces like capillarity, cementation or other surface forces. The differences between “fundamental” and observed states could give some bulk information on the magnitude of these forces.
- Following further the hypothetical analogy with compressible fluids, the stress tensor  $\mathbf{T}$  for sands can be written analogously to compressible viscous (“frictional”) fluid as:

$$\mathbf{T} = -p(v)\mathbf{I} + \mathbf{T}_E \quad (2)$$

where  $\mathbf{T}_E$  is the extra stress tensor, which by means of constitutive equations can be related to strains. Written further in simplified form (with pressures positive), this tensor can be rearranged to

$$\mathbf{T} = p(v)\mathbf{I} + [p_m - p(v)]\mathbf{I} + \mathbf{T}_D \quad (3)$$

where  $p_m$  in the midterm is the mean mechanical pressure, and  $p(v)$  plays the role of thermodynamic pressure obtained by state equation.

This presented separation in spherical and deviatoric part enables the introduction of stress-strain relations for “bulk and shear friction”, analogous to bulk and shear viscosity in viscous fluid (probably with replacement of strain rates with strains).

Consequently, the “pure shear” stress-strain relation could be also obtained experimentally using  $p' = \text{const.}$  triaxial tests, starting from the projection of CSL to  $p'$ - $v$  plane and giving  $dv \approx 0$  during test.

- The deviator stress or stress difference, ( $q$ ), at CSL is directly proportional to the mean pressure ( $p$ ) at CSL as  $q = Mp$ . In triaxial tests it represents the difference of pressures at two perpendicular planes needed to initiate the yielding, i.e. slow flow of sand sample. In the context of hypothetical compressible fluid model from Fig.1 it can be recognized as a measure of constraint (resistance) relieved to obtain the “fundamental” state, defined by state equation  $p(v)$ . This stress difference is obtained for large deformations of sample, where all influences from previous history of sample are lost.

It can also be assumed that “pressure difference” or “resistance” of the same order of magnitude can become visible in similar compression tests where outer deviator is suppressed – the isotropic compression test, where  $q = 0$ . The most similar state of sand, without any previous loading history, is the “loosest” state (Fig. 2a). The isotropic pressure,  $p_{iso}$ , for this state can be written (for the same volume, Fig. 2b) as:

$$\begin{aligned}
 p_{iso} &= p(v) + [p_{iso} - p(v)] = p(v) + \Delta p \\
 p_{iso} &= p(v) [1 + \Delta p / p(v)] = p(v) [1 + M_i]
 \end{aligned}
 \tag{4}$$

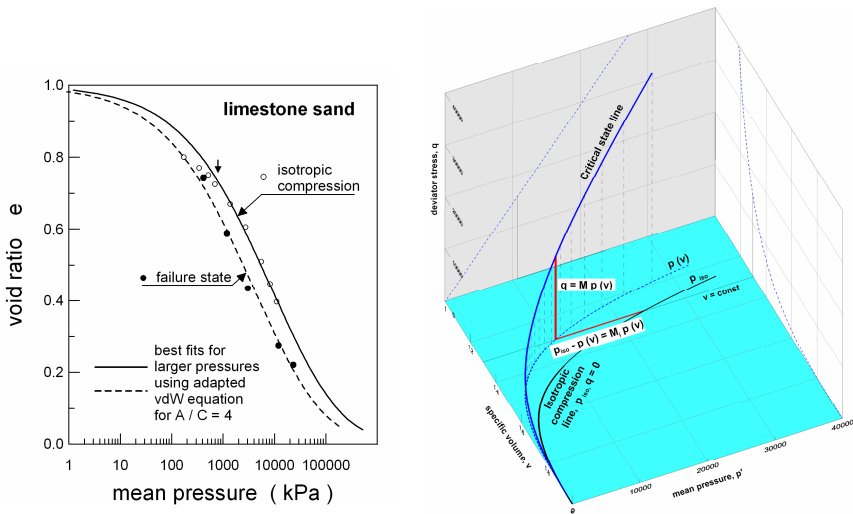


**Fig. 2.** a) The presentation of adapted van der Waals equation in common diagram; b) the relation of isotropic compression and critical state line

In the test series at the elevated pressures [1,2] it was shown that isotropic pressures are practically proportional to mean pressures at critical state. For the same  $A/C$  ratio the proportionality of the constants is the ratio of empirical constants  $C$ .

For the tests on elevated and high pressures the following was obtained:

- limestone sand [3];  $M = 1.51$   $C_{iso} = 24600$   $C_{CSL} = 11100$   $M_i = 1.25$
- Cambria sand [4];  $M = 1.45$   $C_{iso} = 47000$   $C_{CSL} = 15800-27650$   $M_i = 0.7-1.97$
- Ch.River sand [5];  $M = 1.31$   $C_{iso} = 66000$   $C_{CSL} = 21200-35660$   $M_i = 0.85-2.11$

The results show that the same order of magnitude for the pressure difference and stress difference is achieved, proportional to CSL mean pressure.

Other working assumptions for these observations can be formulated about the similarity of the resistance inside the sample (grain friction, granular columns, force chains..), or about the energy and dissipation in the presented stress paths.

## 5 Final Remarks

The concept of compressible fluid and the results presented are based on set of hypotheses and additional assumptions that differ significantly from the common concept of solid used to describe the mechanical soil behavior.

The assumed relations are tested on results of triaxial sand tests collected from published literature. The obtained analogies, similarities and non-contradictions are encouraging to explore other possible consequences of classical phenomenological theories. However, at this stage of research they cannot be understood as a "proof of behavior", but rather as good indicators.

The empirical proofs (or deviations) from proposed relations could come only with increased number of experimental data. It is also to be stressed that experimentally determined macroscopic behavior of soil bodies gives the framework and limits that should be confirmed for models and theories at lower scales.

In this context one should remind the remarks of prof. Scott [6] during Grenoble Workshop in 1982., where he stated the need for comprehensive test series on variety of soils, stored in databanks and available to all researchers.

## References

- [1] Ivšić, T., Galović, A., Kirin, D.: Sand as a compressible fluid. *Physica A* 277, 47–61 (2000)
- [2] Ivšić, T., Gojmerac Ivšić, A.: State equation of mineral sands. *Granular Matter* 14, 37–50 (2012)
- [3] Lo, K.Y., Roy, M.: Response of particulate materials at high pressures. *Soils and Foundations* 13(1), 1–14 (1973)
- [4] Yamamuro, J.A., Lade, P.V.: Drained sand behaviour in axisymmetric tests at high pressures. *J. Geotech. Eng. ASCE* 122(2), 109–119 (1996)
- [5] Vesić, A.S., Clough, G.W.: Behaviour of granular materials under high stresses. *J. Soil Mech. Found. Eng. Div. ASCE* 94(SM3), 661–688 (1968)
- [6] Scott, R.F.: General remarks. In: Gudehus, G., Darve, F., Vardoulakis, I. (eds.) *Results of the Int. Workshop on Constitutive relations for Soils, Grenoble, Balkema, September 1982*, pp. 453–455 (1984)

# Investigation of Critical States and Failure in True Triaxial Tests of Clays

Victor N. Kaliakin\* and Andres Nieto Leal

Department of Civil and Environmental Engineering,  
University of Delaware, Newark, DE 19716 U.S.A.  
kaliakin@udel.edu

**Summary.** A detailed investigation of the true triaxial drained and undrained response of clays has been performed. This paper summarizes the main findings of this investigation, with emphasis placed on ascertaining the existence of critical states and on the variation of the failure state of the clay with principal stress difference.

**Keywords:** true triaxial, clays, shear band.

## 1 Introduction

The applicability of critical state based models in simulating the true triaxial response of clays was questioned in a recent paper [1]. This somewhat controversial conclusion prompted a more detailed investigation of previous studies [2-4] involving the simulation of drained and undrained response of clays under true triaxial stress states using the bounding surface model for cohesive soils.

In particular, the results of several true triaxial testing programs have appeared in the literature. These programs typically investigated the effect of the intermediate principal stress ( $\sigma_2$ ) on the behavior of clays. The relative magnitude of the intermediate principal stress in true triaxial tests may conveniently be expressed by means of the following ratio between deviator stresses:

$$b = \frac{\sigma_2 - \sigma_3}{\sigma_1 - \sigma_3} \quad (1)$$

where it is assumed that  $\sigma_1 \geq \sigma_2 \geq \sigma_3$ . The ratio  $b$  is zero for axisymmetric triaxial compression where  $\sigma_2 = \sigma_3$ , and is equal to unity for axisymmetric triaxial extension in which  $\sigma_1 = \sigma_2$ .

---

\* Corresponding author.

Not all of the true triaxial results appearing in the literature span the entire range from axisymmetric compression ( $b = 0.0$ ) to axisymmetric extension ( $b = 1.0$ ). In addition, not all descriptions of experimental programs provide sufficient details that allow for the numerical simulation of true triaxial test results. Consequently, only the following results of *complete* true triaxial testing programs were used in the aforementioned investigation: 1) Isotropically consolidated, remolded Grundite Clay tested under undrained conditions [5], 2) Isotropically consolidated, remolded Fujinomori Clay tested under drained conditions [6, 7], 3) Isotropically consolidated, remolded Edgar Plastic Kaolinite (EPK) tested under undrained conditions [8], 4) Anisotropically consolidated San Francisco Bay Mud tested under undrained conditions [9, 10], 5) Isotropically overconsolidated, remolded kaolin tested under undrained conditions [11], and 6) Anisotropically normally consolidated kaolin under drained conditions [12].

This paper summarizes the main findings of the aforementioned investigation of true triaxial response of clays. Emphasis is placed on ascertaining the existence of critical states and on the variation of the failure state of the clay with  $b$  value.

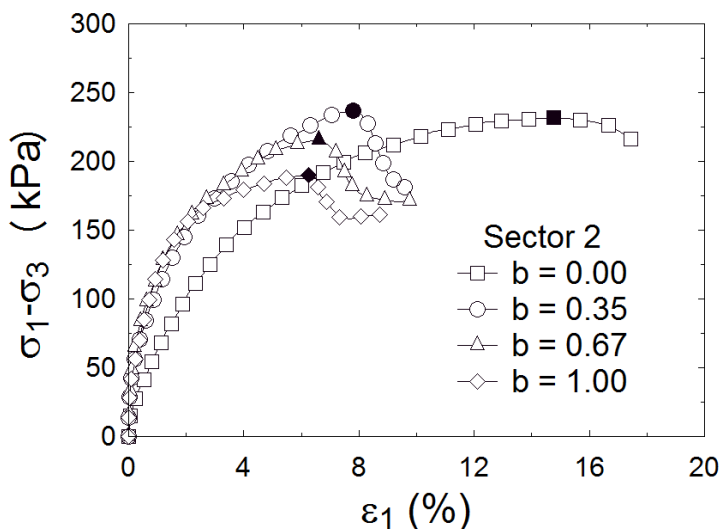


**Fig. 1.** Stress-strain response for true triaxial shearing of anisotropically normally consolidated kaolin [12]

## 2 Presence of Shear Bands

Similar to the axisymmetric triaxial response of clays, the formation of shear bands precludes the attainment of critical states under true triaxial stress states. In particular, shear bands will most commonly occur in “tall” (cuboidal) specimens. Fig. 1 shows typical results obtained by Anantanasakul [12] on anisotropically consolidated kaolin specimens measuring 73 mm by 73 mm by 170 mm, tested

under drained conditions. The formation of shear bands is evident in all but the  $b = 0.0$  test. In Fig. 1 the solid symbols represent the points of effective stress failure; i.e., those states for which the ratio  $\sigma'_1/\sigma'_3$  is maximum. The  $b = 0.0$  test appears to achieve a critical state, characterized by negligible change in principal stress difference with principal strain. This is supported by Fig. 2, which shows that the associated change in volumetric strain is negligible for large values of  $\epsilon_1$ .

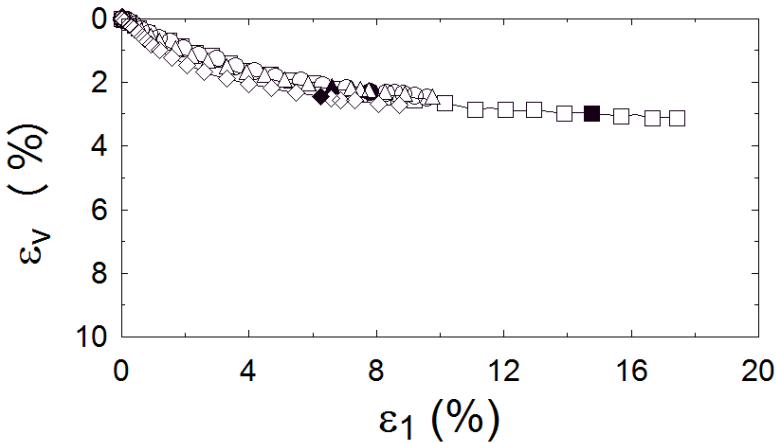


**Fig. 2.** Volumetric strain response for true triaxial shearing of anisotropically normally consolidated kaolin [12]

### 3 Response in Absence of Shear Bands

Since shear bands are typically absent in the true triaxial testing of cubical specimens, the response for such cases is next investigated. Consider the case true triaxial shearing of isotropically consolidated, remolded Grundite clay [5]. Fig. 3 shows typical normalized principal stress difference-strain response, where the principal stress difference is normalized by the initial confining stress of 147.0 kPa. Since no mention of shear band formation was made in discussing the response of Grundite clay [5], it follows that the soil exhibits varying degrees of strain softening. In particular, the  $b = 0.0$  test exhibits very little softening; indeed the specimen appears to have reached critical state. The tests associated with the remaining  $b$  values (0.21, 0.40, 0.70 and 0.95) show more pronounced softening response. Based solely on the normalized principal stress difference-strain response, the existence of a critical state is somewhat debatable. To gain further insight into this issue in Fig. 4 the normalized excess pore pressure is plotted versus the major principle strain. These results indicate that, with the possible exception of the  $b = 0.00$  results, the changes in excess pore pressure with increasing major principal strain become negligible, which is consistent with the existence of a critical state.

Although the results shown in Figs. 3 and 4 are for remolded Grundite clay, the observed trends apply to the other soils listed in Section 1 when subjected to true triaxial stress states. Consequently it is concluded that, in the absence of shear bands, critical states are not always reached with respect to changes in principal stress difference and volumetric strain (under drained conditions) or excess pore pressure (under undrained conditions) with major principal strain.

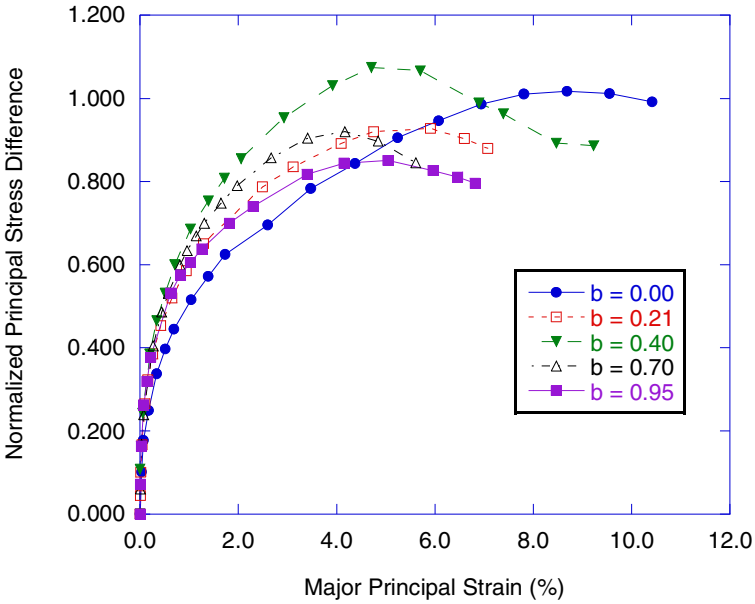


Fig. 3. Normalized stress-strain response for true triaxial shearing of isotropically normally consolidated Grundite clay [5]

### 4 Prediction of Failure States

Assuming that a critical state has indeed been realized, it is necessary to investigate the variation of the failure criterion with the third stress invariant, here taken to be the Lode angle ( $\theta$ ). For a specific value  $\theta$ , the failure surface is commonly assumed to be straight and to coincide with the critical state line. In two-invariant ( $p'$  -  $q$  space), the slope of the critical state line is denoted by  $M$ . The variation of  $M$  with  $\theta$  has traditionally been described by a relation having the following form:

$$M(\theta, k) = g(\theta, k)M_c \tag{2}$$

where  $k = M_c / M_c$ , with  $M_c = M(-\pi/6)$  and  $M_c = M(\pi/6)$  being the values of  $M$  associated with axisymmetric triaxial extension and compression, respectively. The dimensionless function  $g(\theta, k)$  must take on the values  $g(-\pi/6, k) = k$  and

$g(\theta, k) = 1$ . A simple form of this function that has been used in conjunction with several constitutive models for cohesive soils is [13]

$$g(\theta, k) = \frac{2k}{1 + k - (1 - k)\sin 3\theta} \tag{3}$$

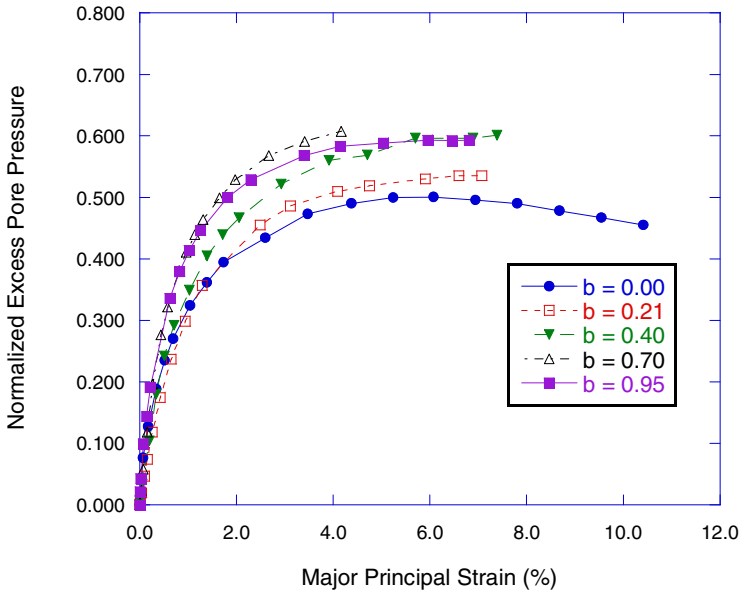


**Fig. 4.** Normalized excess pore pressure-strain response for true triaxial shearing of isotropically normally consolidated Grundite clay [5]

Assuming a purely frictional material,  $M_e$  and  $M_c$  are related to the effective angle of internal friction in axisymmetric triaxial extension ( $\phi'_e$ ) and compression ( $\phi'_c$ ) and according to

$$M_e = \frac{6 \sin \phi'_e}{3 + \sin \phi'_e}, \quad M_c = \frac{6 \sin \phi'_c}{3 - \sin \phi'_c} \tag{4}$$

One fundamental issue in the assessment of critical state based models for simulating the true triaxial response of clays is the suitability of the variation of  $g(\theta, k)$  used in characterizing the variation of the critical state line with  $\theta$ . To this end, the deviator stress ( $q$ ) and mean normal effective stress ( $p'$ ) must be generalized as follows

$$q = \sqrt{\frac{1}{2} [(\sigma_1 - \sigma_2)^2 + (\sigma_2 - \sigma_3)^2 + (\sigma_3 - \sigma_1)^2]} \quad p' = \frac{\sigma_1 + \sigma_2 + \sigma_3}{3} \tag{5}$$

Using eq. (1) in conjunction with (5) gives the following relation at failure [11]:

$$M^*(\phi, b) = \frac{q_f}{p'_f} = \frac{6 \sin \phi \sqrt{1 - b + b^2}}{3 + (2b - 1) \sin \phi} \tag{6}$$

Thus, for given values of  $\phi'_e$  (associated with  $b = 1.00$ ) and  $\phi'_c$  (associated with  $b = 0.00$ ),  $M_e$  and  $M_c$  are computed from (4). Knowing  $\sigma'_1$  and  $\sigma'_3$  at failure for a given value of  $b$ , it follows that  $\phi = \sin^{-1} \left[ \frac{(\sigma'_1 - \sigma'_3)}{(\sigma'_1 + \sigma'_3)} \right]$ . Finally, the value of  $M^*$  for with this failure state and  $b$  value is computed from (6).

The associated value of  $\theta$  is computed from  $\sigma'_1$ ,  $\sigma'_3$  and  $b$  (recall eq. 1). Substituting this  $\theta$  value into (3) and the resulting expression into (2) gives the value of  $M(\theta, k)$ . This value is then compared to the corresponding value of  $M^*$ .

Fig. 5 compares  $M^*$  and  $M$  values for remolded Grundite clay [5] subjected to an initial confining stress of 147.0 kPa. It is evident that (3) does not necessarily yield good agreement between  $M^*$  and  $M$  for all  $b$  values. Similar conclusions have been reached for other clays tested under true triaxial conditions.

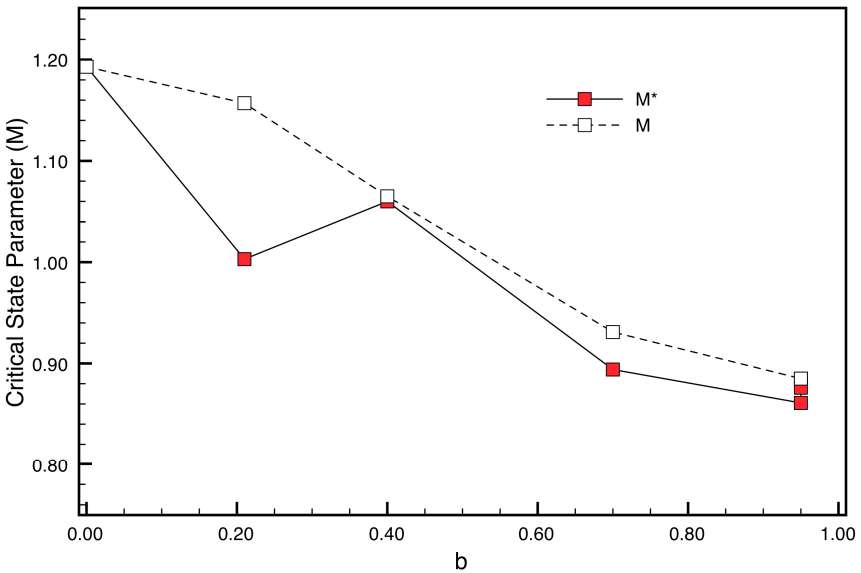


**Fig. 5.** Investigation of failure states for true triaxial shearing of isotropically normally consolidated Grundite clay [5] (initial confining stress = 147.0 kPa)

## 5 Conclusion

This paper has investigated the existence of critical states in conjunction with true triaxial stress states and the variation of the failure state of the clay with  $b$  value. Similar to axisymmetric triaxial response, the formation of shear bands precludes

the attainment of a critical state. In the case of true triaxial stress states, shear bands will commonly occur in cuboidal (“tall”) specimens and in cubical ones.

In the absence of shear bands, critical states are not always reached with respect to changes in principal stress difference and volumetric strain (under drained conditions) or excess pore pressure (under undrained conditions) with major principal strain.

Finally, the function commonly used to account for the variation of the critical state with Lode angle does not always give good agreement with experimentally determined failure states. Consequently, a more accurate representation of the failure surface appears to be warranted.

## References

- [1] Anantanasakul, P., Kaliakin, V.N.: Simulations of 3-D Drained Behavior of Normally Consolidated Clay Using Elastoplastic Models. In: *GeoCongress 2012*, GSP 225, ASCE, pp. 1076–1085 (2012)
- [2] Kaliakin, V.N., Pan, Z.: Assessment of 3-D Predictive Capabilities of Bounding Surface Model for Cohesive Soils. In: *Batra, R. (ed.) Proceedings of the 14th U. S. National Congress on Theoretical and Applied Mechanics*, Blacksburg, VA (2002) (CD-ROM)
- [3] Kaliakin, V.N.: Assessment of Predictive Capabilities of Bounding Surface Model for Cohesive Soils under Complex Stress Paths. In: *Voyiadjis, G.Z., Dorgan, R.J. (eds.) Proceedings of McMat Mechanics and Materials Conference*, Baton Rouge, LA (2005) (CD-ROM)
- [4] Kaliakin, V.N.: Assessment of Model Predictive Capabilities for True Triaxial Shearing of Clay. In: *Ulitsky, V.M. (ed.) Development of Urban Areas and Geotechnical Engineering*, Proceedings of the International Geotechnical Conference, pp. 397–402. St. Petersburg, Russia (2008)
- [5] Lade, P.V., Musante, H.M.: Three-Dimensional Behavior of Remolded Clay. *J. Geotech. Eng. Div., ASCE* 104(GT2), 193–209 (1978)
- [6] Nakai, T., Matsuoka, H.: A Generalized Elastoplastic Constitutive Model for Clay in Three-Dimensional Stresses. *Soils and Foundations* 26(3), 81–98 (1986)
- [7] Nakai, T., Matsuoka, H., Okuno, N., Tsuzuki, K.: True Triaxial Tests on Normally Consolidated Clay and Analysis of The Observed Shear Behavior Using Elastoplastic Constitutive Models. *Soils and Foundations* 26(4), 67–78 (1986)
- [8] Lade, P.V.: Single-Hardening Model with Application to NC Clay. *J. Geotech. Eng. Div., ASCE* 116(3), 394–414 (1990)
- [9] Kirkgard, M.M., Lade, P.V.: Anisotropy of Normally Consolidated San Francisco Bay Mud. *ASTM Geotech. Test. J.* 14(3), 231–246 (1991)
- [10] Kirkgard, M.M., Lade, P.V.: Anisotropic Three-Dimensional Behavior of a Normally Consolidated Clay. *Can. Geotech. J.* 30(5), 848–858 (1993)
- [11] Prashant, A., Penumadu, D.: Effect of Intermediate Principal Stress on Overconsolidated Kaolin Clay. *J. Geotech. and Geoenv. Eng., ASCE* 130(3), 284–292 (2004)
- [12] Anantanasakul, P.: Three-Dimensional Experiments and Modeling of Anisotropic Clay. Ph.D. dissertation, School Civil and Construc. Eng., Oregon State Univ. (2010)
- [13] Gudehus, G.: Elastoplastische Stoffgleichungen für trockenen Sand. *Ingenieur-Archiv* 42(3), 151–169 (1973)

# Micromechanics of the Critical State of Granular Materials

N.P. Kruyt

Department of Mechanical Engineering, University of Twente, P.O. Box 217, 7500 AE Enschede, The Netherlands

[n.p.kruyt@utwente.nl](mailto:n.p.kruyt@utwente.nl)

**Abstract.** The geometrical characteristics of the critical state are studied, using two-dimensional Discrete Element Method simulations. Various simulations have been performed in order to study the effect on the critical-state fabric tensor of interparticle friction and of the type of loading. The results for the fabric tensor, from simulations with different material properties and different loading conditions, collapse to a single curve, where high coordination number corresponds to low fabric anisotropy. This suggests that a limiting fabric state exists that has a geometrical origin. Since high confining pressure leads to high coordination number, this then means that the fabric anisotropy is low. As it is well-known that fabric anisotropy is a main factor contributing to shear strength of granular materials, this geometrical effect explains the (weak) decrease of shear strength with increasing pressure. The contact network determines loops of contacts. Based on simplified loop shapes, two theoretical relations are developed for their geometrical description. These two theories are based on orientational exclusion of contacts and constant-volume deformation of the loops, respectively. These theoretical results bracket loop fabric anisotropies that are obtained from the results of the Discrete Element Method simulations.

## 1 Introduction

In micromechanics of quasi-static deformation of granular materials, relationships are investigated between characteristics at the continuum, macro-scale and the micro-scale of particles and interparticle contacts.

The characteristics at the continuum, macro-scale are the stress and strain tensors. For granular materials consisting of stiff particles, the characteristics at the micro-scale are the (average) forces and relative displacements at contacts, as well as (averages of) the contact geometry. It is well known from experiments and computer simulations that the contact network generally is anisotropic, in particular after deformation.

The micromechanical analysis by Rothenburg & Bathurst [6] showed that the shear strength of granular materials originates from the anisotropy of the contact network as well as from the anisotropy of the distribution of the contact forces.

The evolution of the contact network has been studied previously, for example in [5]. The focus of the current study is on geometrical characteristics of the contact network at the critical state. To this end, two-dimensional Discrete Element Method simulations (DEM for short), as proposed by Cundall & Strack [11], are used to obtain the required detailed information.

## 2 Fabric Tensor

A geometrical characteristic of a contact  $c$  is the branch vector,  $\mathbf{l}^c$ , that connects the centres of two particles in contact. The corresponding unit vector is the contact normal  $\mathbf{n}^c$ . Primary averages of the contact network are (1) the coordination number  $Z$ , i.e. the average number of contacts per particle, and (2) the contact distribution function [2] that describes the orientational distribution of contacts. Alternatively, the fabric tensor that combines these characteristics may be employed [7]. The (symmetric) second-order fabric tensor  $\mathbf{F}$  is defined here by

$$F_{ij} = \frac{2}{N_p} \sum_{c \in C} n_i^c n_j^c, \quad (1)$$

where the sum is over contacts  $c$  in the set of contacts  $C$  in the region of interest and  $N_p$  is the number of particles. Using this definition, it follows that the coordination number  $Z$  is given by  $Z = 2N_c/N_p = F_{11} + F_{22}$ , where  $N_c$  is the number of contacts. Hence, coordination number  $Z$  is the first invariant of the fabric tensor. The second invariant of the fabric tensor,  $A$ , describes the anisotropy of the fabric tensor. In terms of major and minor principal values  $F_1$  and  $F_2$ , respectively, of the fabric tensor we have

$$Z = F_1 + F_2 \quad A = F_1 - F_2. \quad (2)$$

## 3 DEM Simulations

Two-dimensional Discrete Element Method are employed here to obtain the required detailed information on the contact network, and hence on the fabric tensor. Polydisperse assemblies of 50,000 disks are considered. In these DEM simulations periodic boundary conditions are employed in order to suppress the formation of large-scale shear bands, and thus be able to study the behaviour at very large strains.

Various simulations are considered in order to study the effect on the critical-state fabric of: (1) interparticle friction and (2) type of loading. For the first effect isobaric tests are considered with different values for the interparticle friction coefficient  $\mu$

(ranging from 0.1 – 0.5), while for the second effect isobaric, biaxial and isochoric (constant-volume) tests are considered (with the same value for the interparticle friction coefficient,  $\mu = 0.5$ ).

The results from the DEM simulations are analysed with respect to shear strength  $q/p$  (where  $q$  is the deviator of the stress tensor and  $p$  is the mean pressure; in terms of the major and minor principle stresses  $\sigma_1$  and  $\sigma_2$ , respectively, of the stress tensor, we have  $p = (\sigma_1 + \sigma_2)/2$  and  $q = (\sigma_1 - \sigma_2)/2$ ), coordination number  $Z$  and fabric anisotropy  $A$  at the critical state.

The results for the fabric tensor are shown in Figure 1. These results, from simulations with different material properties (interparticle friction) and different loading conditions, (closely) collapse to a single curve. This suggests that a limiting fabric state exists that has a *geometrical origin*.

As expected, the shear strength increases with increasing interparticle friction  $\mu$ , see also 4. The shear strength is approximately the same for the three types of tests, with a slight decrease in shear strength with increasing pressure (increasing from isobaric, biaxial to isochoric test). This trend can be explained as follows: higher pressure  $p$  is associated with higher coordination number  $Z$ . According to the results shown in Figure 1, a higher coordination number corresponds to a lower fabric anisotropy  $A$ . According to the micromechanical analysis in 6 the lower fabric anisotropy and higher coordination number result in lower shear strength  $q/p$ . Recapitulating, these geometrical considerations explain why shear strength  $q/p$  decreases (weakly) with increasing pressure  $p$ .

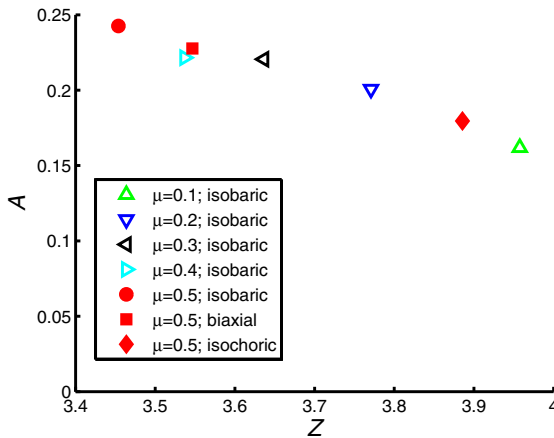


**Fig. 1.** Relation between coordination number  $Z$  and fabric anisotropy  $A$  at the critical state from various DEM simulations. The filled symbols correspond to results from DEM simulations with different loading conditions and identical interparticle friction coefficient  $\mu$ . The other symbols correspond to results from DEM simulations with isobaric loading and different values for the interparticle friction coefficient  $\mu$ .

### 4 Loops

The network of contacts tessellates the area occupied by the two-dimensional assembly into loops (or polygons) of contacts [3]. The average number of sides of the loops,  $L$ , is related to the coordination number  $Z$  (through Euler’s relation for planar graphs):  $L = 2Z/(Z - 2)$ . Thus, high coordination number  $Z$  corresponds to loops with few sides (i.e. low  $L$ ). Some regular loops consisting of equal-sized disks are shown in Figure 2: triangle with three sides (where the angle  $\beta$  must equal  $60^\circ$ ), diamond with four sides and hexagon with six sides.

A loop (fabric) tensor  $\mathbf{H}^l$  for loop  $l$  is defined by

$$H_{ij}^l = \sum_{s \in S^l} n_i^s n_j^s, \tag{3}$$

where the sum is over the sides  $s$  in the set of sides  $S^l$  of loop  $l$ . Note that the trace of the loop tensor,  $H_{11}^l + H_{22}^l$ , equals its number of sides.

Since each contact is part of two loops (when boundary effects are neglected or not present as is the case when periodic boundaries are employed), we have the relation  $2 \sum_{c \in C} n_i^c n_j^c = \sum_l \sum_{s \in S^l} n_i^s n_j^s$ . Thus the fabric tensor in Eq. (II) is related to the loop tensors in Eq. (3) by

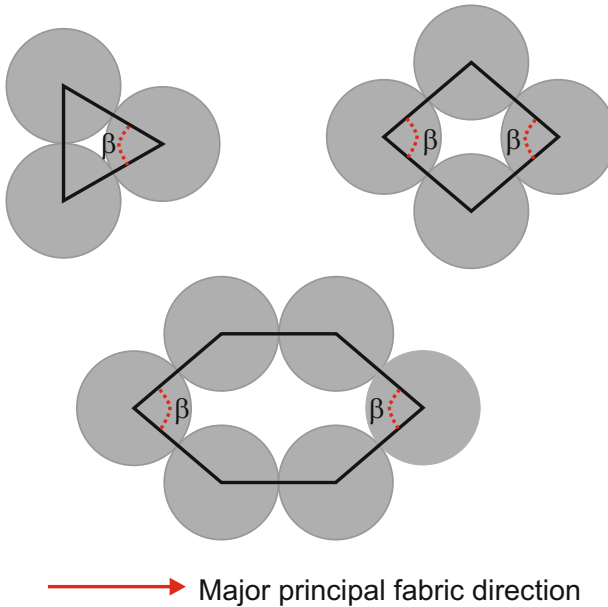


**Fig. 2.** Regular loops consisting of equal-sized disks. Top left: triangle, where the angle  $\beta = 60^\circ$ ; top right: diamond; bottom: hexagon.

$$\frac{L}{Z} F_{ij} = \frac{1}{N_l} \sum_l H_{ij}^l, \tag{4}$$

where  $N_l$  is the number of loops and the relation  $N_p/N_l = L/Z$  has been used. Hence the average loop tensor (given by the right-hand side of Eq. (4)) is directly proportional to the fabric tensor  $\mathbf{F}$ .

For the regular loops shown in Figure 2 the principal values  $H_1$  and  $H_2$  of the loop tensor can be determined: triangles with  $\beta = 60^\circ$ ,  $H_1 + H_2 = 3$  and  $H_1 - H_2 = 0$ ; diamonds,  $H_1 + H_2 = 4$  and  $H_1 - H_2 = 4 \cos \beta$ ; hexagons,  $H_1 + H_2 = 6$  and  $H_1 - H_2 = 4 \cos \beta + 2$ .

Troadec et al [8] emphasized the importance of orientational (or steric) exclusion of contacts to the behaviour of granular materials. This argument leads (strictly) to a value for  $\beta = 60^\circ$ .

Alternatively, the angle  $\beta$  can be determined from the criterion that, at the critical state, the volume is constant. Assuming that the topology of the loops remains unchanged and that the lengths of the sides are constant, we find (after some algebra) that the loops deform at constant volume when  $\beta = 90^\circ$  for diamonds and  $\beta = 120^\circ$  for hexagons. Deformation of the triangle is not possible without disruption or creation of contacts.

These two theories yield expressions for the loop tensor of triangles, diamonds and hexagons. These predictions are compared with the results of the DEM simulation by grouping the loops by their number of sides and computing the corresponding average loop tensors for these groups.

The results from the DEM simulation in Figure 3 show that the anisotropy  $H_1 - H_2$  of the loop increases with their number of sides  $H_1 + H_2$ . The loop tensor of the triangles is isotropic, according to DEM simulation and theories.

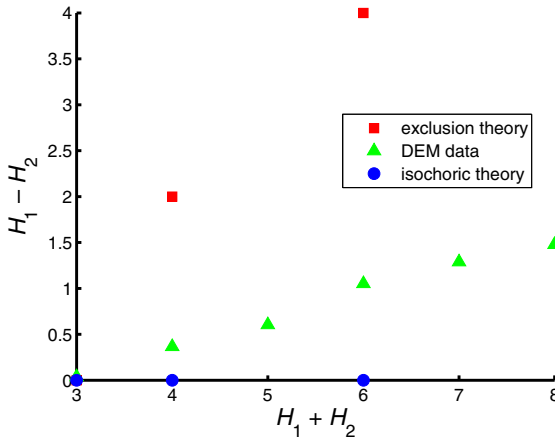


**Fig. 3.** Results for the loop tensor  $\mathbf{H}$  in terms of its principal values  $H_1$  and  $H_2$ : averages from DEM simulation (isobaric;  $\mu = 0.5$ ) at the critical state, theory based on orientational exclusion and theory based on deformation at constant volume (isochoric).

The anisotropy of the loop tensors from the DEM simulations is bracketed by the theories, where the theory based on orientational exclusion forms an upper bound and the theory based on isochoric deformation gives a lower bound. Quantitatively, the results from the DEM simulations are closer to the predictions from the isochoric (constant-volume) deformation theory. Although the prediction of this latter theory forms a trivial bound, the closer agreement (in comparison to the orientational exclusion theory) indicates that it captures essential geometrical characteristics of the contact network at the critical state.

## References

1. Cundall, P.A., Strack, O.D.L.: A discrete numerical model for granular assemblies. *Géotechnique* 9, 47–65 (1979)
2. Horne, M.R.: The behaviour of an assembly of rotund, rigid, cohesionless particles, I and II. *Proceedings of the Royal Society of London A* 286, 62–97 (1965)
3. Kruyt, N.P., Rothenburg, L.: Micromechanical definition of the strain tensor for granular materials. *Journal of Applied Mechanics (Transactions of the ASME)* 63, 706–711 (1996)
4. Kruyt, N.P., Rothenburg, L.: Shear strength, dilatancy, energy and dissipation in quasi-static deformation of granular materials. *Journal of Statistical Mechanics: Theory and Experiment*, P07021 (2006)
5. Kruyt, N.P.: Micromechanical study of fabric evolution in quasi-static deformation of granular materials. *Mechanics of Materials* 44, 120–129 (2012)
6. Rothenburg, L., Bathurst, R.J.: Analytical study of induced anisotropy in idealized granular materials. *Géotechnique* 39, 601–614 (1989)
7. Satake, M.: Constitution of mechanics of granular materials through graph theory. In: Cowin, S.C., Satake, M. (eds.) *US-Japan Seminar on Continuum-Mechanical and Statistical Approaches to Granular Materials*, pp. 47–62. Elsevier, Amsterdam (1978)
8. Troadec, H., Radjaï, F., Roux, S., Charnet, J.C.: Model for granular texture with steric exclusion. *Physical Review E* 66, 041305 (2002)

# A Critical State Sand Model with Elastic-Plastic Coupling

Ali Lashkari\* and Ali Golchin

Department of Civil & Environmental Engineering  
Shiraz University of Technology, Shiraz, Iran  
lashkari@sutech.ac.ir, lashkari\_ali@hamyar.net

**Summary.** Experimental studies have revealed that plastic strains change the elastic properties of granular soils. This observation is an elastic-plastic coupling phenomenon which is considered here through the dependence of a free energy function to a proper hardening parameter. It is shown that implementation of the resulted hyperelastic model in a critical state bounding surface plasticity platform leads to more reasonable simulations.

**Keywords:** sand, bounding surface, elastic-plastic coupling, hyperelasticity.

## 1 Introduction

In liquefaction phenomena, the restrain on volume change necessitates a balance between the elastic and plastic strains. Hence, the elastic portion of behavior has a profound influence in liquefaction analysis. The elastic behavior of granular soils depends on soil density as well as mean principal effective stress. Moreover, the evolution of fabric associated with shear stress affects the elastic response of granular soils (e.g., [1,2]). Several novel constitutive models in the bounding surface plasticity framework have been suggested accounting for the effects of induced anisotropy through modification of elements dealing with the plastic part of behavior such as plastic hardening modulus and dilatancy [3,4]. In these models, however, the elastic portion always remains isotropic even when the mentioned plastic ingredients reach the so-called fully saturated state of anisotropy. It is clear that the assumption of the isotropy of elasticity has been made mainly due to the simplicity. Recently, Lashkari [5] suggested a simple elastic-plastic coupled hypoelastic model and showed that induced anisotropy of elasticity participates actively in sudden loss of strength in liquefaction of dense sands subjected to cyclic loading.

The so-called small strain shear modulus of granular soils (measured at shear strains less than  $10^{-5}$ ) is usually expressed by the following relationship:

$$G = G_0 p_{ref} F(e) \left( \frac{p}{p_{ref}} \right)^{\chi} \tag{1}$$

---

\* Corresponding author.

where  $G_0$  is a dimensionless constant and  $p_{\text{ref}}$  is a reference pressure ( $\approx 101$  kPa).  $F(e)$  imposes the influence of void ratio,  $e$ , on  $G$ . The best known suggestions are  $F(e)=(2.97-e)^2/(1+e)$ , and  $F(e)=(2.17-e)^2/(1+e)$ , respectively, for soils with angular and round grains [6]. Mean principal effective stress,  $p$ , has a great influence on the elastic shear moduli of soils through the term  $(p/p_{\text{ref}})^\chi$ . Hardin & Black [6] recommended  $\chi_0 \approx 0.5$  for sands under extremely low strain levels ( $\leq 10^{-5}$ ) when soil behavior is purely elastic.

Surprisingly, when granular soils are subjected to moderate-large shear strains beyond the pretty small elastic domain, it has been revealed that  $\chi$  is no more constant and increases with the irrecoverable shear strains (e.g., [1,7-9]). Using the available experimental data in the literature, the measured  $\chi$ -shear strain relationship is illustrated in Fig. 1. Evolution of  $\chi$  with irrecoverable shear strains is an evidence of elastic-plastic coupling which is not addressed in the currently available soil elastic models (e.g., [5,10,11]).

## 2 Hyperelasticity with Elastic-Plastic Coupling

In most soil constitutive models, the elastic part of behavior is simulated using Hypoelastic models which do not conserve energy (e.g., [3-5,12]). The remedy for this deficiency is in Hypeleasticity theory in which elastic constitutive equations are derived from free energy functions (e.g., [10,11]). Here, it is assumed that the hyperelastic response of granular media is uniquely defined by a Gibbs free energy function expressed by  $\Gamma = \Gamma(p, q, \chi)$ . Variables  $p (= (\sigma_1 + 2\sigma_3)/3)$  and  $q (= \sigma_1 - \sigma_3)$  are, respectively, mean principal effective stress and deviator stress defined in triaxial space. Now, elastic strain rates are calculated by:

$$\dot{\varepsilon}_v^e = \underbrace{\Gamma_{,pp} \dot{p} + \Gamma_{,pq} \dot{q}}_{\text{recoverable}} + \underbrace{\Gamma_{,p\chi} \dot{\chi}}_{\text{irrecoverable}} \quad ; \quad \dot{\varepsilon}_q^e = \underbrace{\Gamma_{,qp} \dot{p} + \Gamma_{,qq} \dot{q}}_{\text{recoverable}} + \underbrace{\Gamma_{,q\chi} \dot{\chi}}_{\text{irrecoverable}} \quad (2)$$

where  $\varepsilon_v^e (= \varepsilon_1 + 2\varepsilon_3)$  and  $\varepsilon_q^e = 2/3(\varepsilon_1 - \varepsilon_3)$  are, respectively, the elastic volumetric and shear strains.  $X_{,Y}$  is the compact form for operation  $\partial X/\partial Y$ . In Eq. (2),  $\chi$  varies with a proper hardening parameter. Hence, for pure elastic response, one has  $\dot{\chi} = 0$ . The first two terms in each elastic strain rates are recoverable, but the last term (in each) is irrecoverable upon unloading due to fabric evolution associated with loading. Rearrangement of terms yields the following relationship to relate the rates of the stress variables to the rates of the recoverable elastic strains:

$$\begin{Bmatrix} \dot{p} \\ \dot{q} \end{Bmatrix} = \frac{1}{\Gamma_{,pp} \Gamma_{,qq} - \Gamma_{,pq}^2} \begin{pmatrix} \Gamma_{,qq} & -\Gamma_{,pq} \\ -\Gamma_{,pq} & \Gamma_{,pp} \end{pmatrix} \begin{Bmatrix} \dot{\varepsilon}_v^e - \Gamma_{,p\chi} \dot{\chi} \\ \dot{\varepsilon}_q^e - \Gamma_{,q\chi} \dot{\chi} \end{Bmatrix} = \begin{pmatrix} K & J \\ J & 3G \end{pmatrix} \begin{Bmatrix} \dot{\varepsilon}_v^{er} \\ \dot{\varepsilon}_q^{er} \end{Bmatrix} \quad (3)$$

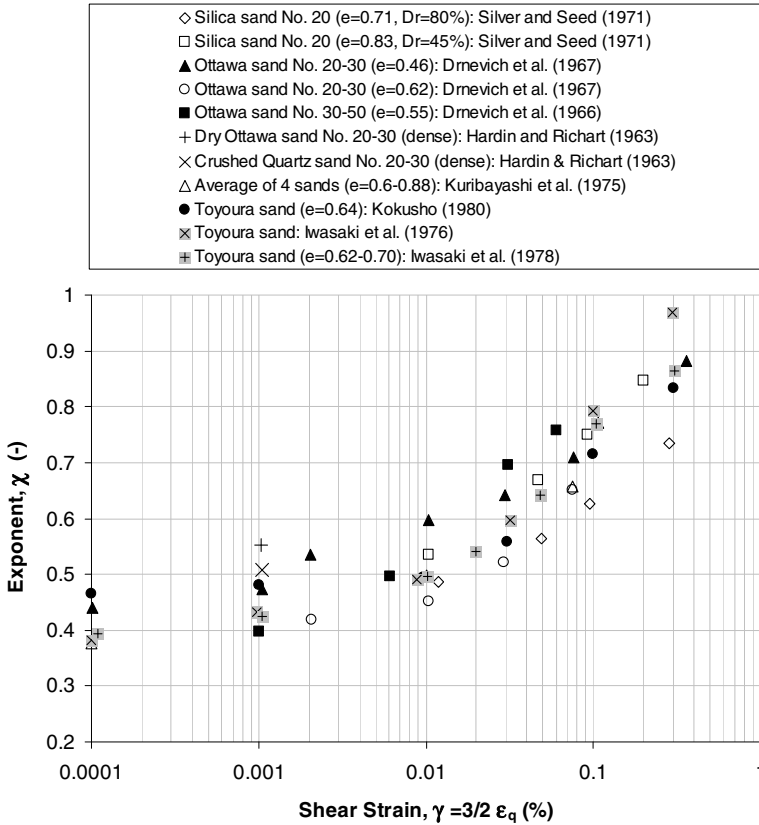


Fig. 1. Effect of shear strain on evolution of  $\chi$  (experimental data after [11])

where  $\dot{\epsilon}_v^{er}$  and  $\dot{\epsilon}_q^{er}$  are recoverable volumetric and deviator elastic strain rates (see Eq. 2).  $K$ ,  $J$ , and  $G$  are, respectively, the elastic bulk, coupling, and shear moduli which are calculated by partial differentiation of the Gibbs free energy function.

The yield function, domain of pure elasticity, in  $q$ - $p$  plane is expressed by:

$$f = |\eta - \alpha| - m = 0 \tag{4}$$

where  $\eta=q/p$  is stress ratio,  $\alpha$  is a hardening parameter, and  $m$  represents the yield function size [3-5]. In the bounding surface platform suggested by Dafalias & Manzari [4], the following constitutive equations control the hardening:

$$\dot{\alpha} = \dot{\eta} = K_p \dot{\epsilon}_q^p = K_p s \langle L \rangle. \tag{5}$$

In Eq. (5),  $\dot{\epsilon}_q^p$  is deviator plastic strain rate, and  $L$  is the plastic multiplier. One has  $s = +1$  if  $\eta - \alpha = m$ , and  $s = -1$  if  $\alpha - \eta = m$ . Finally,  $\langle \rangle$  are Macauley brackets. In this study, plastic modulus,  $K_p$ , is defined by:

$$K_p = h(e) \frac{\alpha^b - s \alpha}{|\alpha - \alpha_m|} \left( \frac{p_{ref}}{p} \right)^{1-\chi} \quad (6)$$

where  $h(e)$  is a function of void ratio,  $\alpha_m$  is the initial value of  $\alpha$  in the most recent loading, and  $\alpha^b$  is the bounding surface back stress ratio. Detailed definition of these terms can be found in [4,5].

It is suggested that  $\chi$  can evolve with  $\alpha$  through the following relationship:

$$\chi = \chi(\alpha) = \chi_0 + (\chi_{max} - \chi_0) \left( \frac{|\alpha|}{|\alpha| + B(\alpha^b - |\alpha|)} \right) \quad (7)$$

where  $B$  is a parameter controlling the pace of  $\chi$  with change in  $\alpha$ . In above equation,  $\chi_0$  and  $\chi_{max}$  are the boundaries of  $\chi$  associated with very small and large shear strains, respectively.

Each strain rate can be parted into the elastic and plastic parts. Now by referring to decomposition presented in Eq. (2), and recalling that plastic strains are irrecoverable upon stress unloading, one has:

$$\begin{aligned} \dot{\epsilon}_v &= \dot{\epsilon}_v^e + \dot{\epsilon}_v^p = \dot{\epsilon}_v^{er} + \overbrace{\dot{\epsilon}_v^{ei} + \dot{\epsilon}_v^p}^{irrecoverable} = \dot{\epsilon}_v^{er} + \dot{\epsilon}_v^i \\ \dot{\epsilon}_q &= \dot{\epsilon}_q^e + \dot{\epsilon}_q^p = \dot{\epsilon}_q^{er} + \underbrace{\dot{\epsilon}_q^{ei} + \dot{\epsilon}_q^p}_{irrecoverable} = \dot{\epsilon}_q^{er} + \dot{\epsilon}_q^i \end{aligned} \quad (8)$$

where  $\dot{\epsilon}_v^i$  and  $\dot{\epsilon}_q^i$  are the volumetric and deviatoric irrecoverable strain rates. Considering Eqs. (5), the irrecoverable strain rates can be written by:

$$\dot{\epsilon}_v^i = \Gamma_{,p\chi} \chi_{,\alpha} K_p \dot{\epsilon}_q^p + \dot{\epsilon}_v^p \quad ; \quad \dot{\epsilon}_q^i = (1 + \Gamma_{,q\chi} \chi_{,\alpha} K_p) \dot{\epsilon}_q^p. \quad (9)$$

None of the existing conventionally available experimental devices and their corresponding testing techniques is capable of direct separating the irrecoverable elastic strain rate from the plastic strain rate in volumetric and shear irrecoverable strain rates. Based on this conclusion, the following definition is made for dilatancy in elastic-plastic coupled geomaterials:

$$d = \frac{\dot{\epsilon}_v^i}{s \dot{\epsilon}_q^i} = \frac{\Gamma_{,p\chi} \chi_{,\alpha} K_p \dot{\epsilon}_q^p + \dot{\epsilon}_v^p}{s(\Gamma_{,q\chi} \chi_{,\alpha} K_p \dot{\epsilon}_q^p + \dot{\epsilon}_q^p)} \quad (10)$$

where  $d$  is dilatancy function [3-5].

### 3 Evaluation

Simulation of three loading/unloading triaxial tests on dense samples of Toyoura sand is studied here. Isotropically consolidated samples ( $p_m=1000$  kPa) were

firstly subjected to shear stress up to  $\approx 25\%$  axial strain. Then, they were unloaded to isotropic stress condition.

To investigate the influence of different elasticity theories on the predictive capacity of constitutive models, several elasticity theories are implemented within the model of Dafalais & Manzari [4]. In Fig. 2(a), predicted stress paths using the model of Manzari & Dafalias [12] are shown. In the first shear loading, fabric is nearly isotropic. Therefore, the model predictions are acceptable. However, prior to unloading, soil fabric reaches a saturate or nearly saturate state of anisotropy. As a result, this model which ignores the influence of anisotropy on both elastic and plastic ingredients is incapable of providing reasonable predictions in the unloading phase. In Fig. 2(b), it can be observed that the modification of plastic modulus by fabric-dilatancy effects in the Dafalias & Manzari [4] model leads to improvement of predictions. However, one may find sharp return of stress paths following the unloading point in measured data which can not be simulated by this model due to the assumption of isotropy in elasticity. As a consequence, the simulated half butterfly loops are not similar to those of data. Predictions by the model of Lashkari [5] with anisotropic hypoelasticity are shown in Fig. 2(c). A reasonable agreement between experiments and simulations indicates the importance of considering the influence of induced anisotropic elasticity on the predictive capacity; however this approach does not conserve energy. Predictions by the implementation of the hyperelastic models of Einav & Puzrin [10] and Houlsby et al. [11] are shown in Fig. 2(d). The sharp return of stress paths following the unloading points indicates that the hyperelastic approaches are capable of considering the effect of induced anisotropy; however it is simply becomes clear that the magnitude of generated anisotropy in these models is inadequate. Finally, predictions by the application of the hyperelastic formulation of this study with the possibility of elastic-plastic coupling are illustrated versus experiments in Fig. 3(a). In the later approach, a modified Einav & Puzrin [10] Gibbs free energy function in the following form is adopted:

$$\Gamma(p, q, \chi) = \frac{p^{2-\chi} - (2 - \chi)p p_0^{1-\chi}}{\bar{K} (2 - \chi)(1 - \chi) p_{ref}^{1-\chi}} + \frac{q^2}{6\bar{G} p_{ref}^{1-\chi} p^\chi} - \frac{q_0(2q p_0 - \chi q_0 p)}{6\bar{G} p_{ref}^{1-\chi} p_0^{1+\chi}}. \quad (11)$$

where  $p_0$  and  $q_0$  are, respectively, values of mean principal effective and deviator stresses at zero elastic strains. It must be noted that despite the original definition of [10],  $\chi$  in this study evolves in 0.45-0.95 range though Eq. (7). The evolution of  $\chi$  with shear strain is shown together with experimental data in Fig. 3(b). Considering that the samples initial state parameter values are relatively the same, nearly identical evolution curves for  $\chi$  are obtained. However, lower curves for samples in loose state are expected which are not presented here. Comparing Fig. 3(a) to Fig. 2(d) indicates that considering the elastic-plastic coupling leads to further generation of anisotropy in elasticity and improvement of simulations.

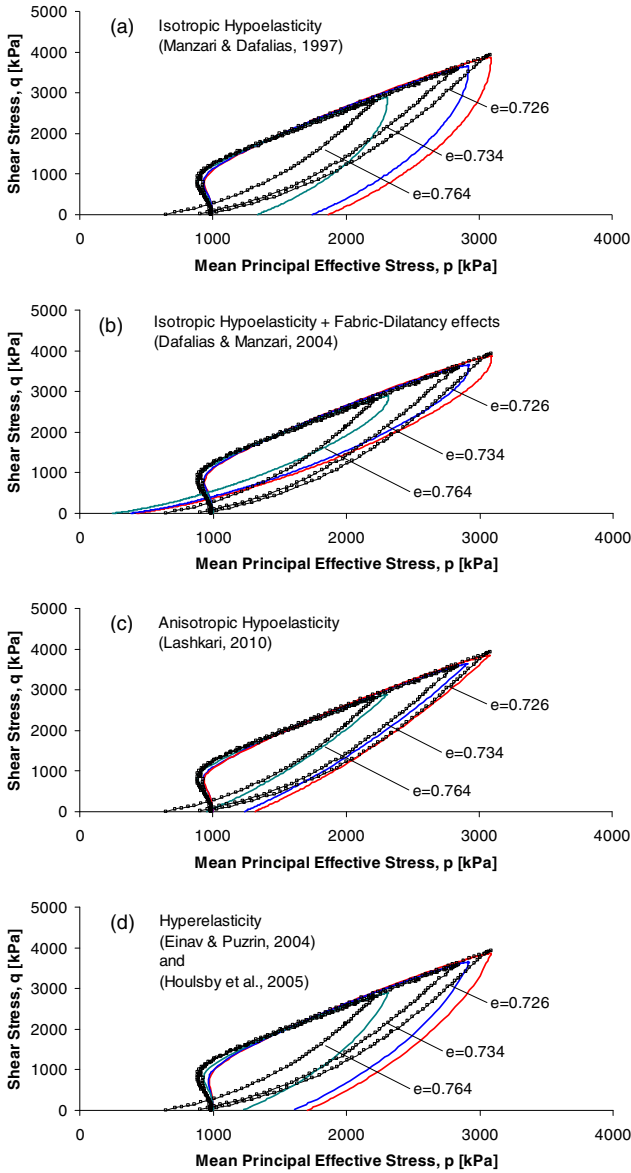


**Fig. 2.** Evaluation of elasto-plastic models with different elasticity theories: (a) isotropic hypoelasticity [12]; (b) isotropic hypoelasticity with fabric-dilatancy effects [4]; (c) anisotropic hypoelasticity of Lashkari [5]; (d) hyperelastic theories of Einav & Puzrin[10] and Housby et al. [11] (data taken from [13])

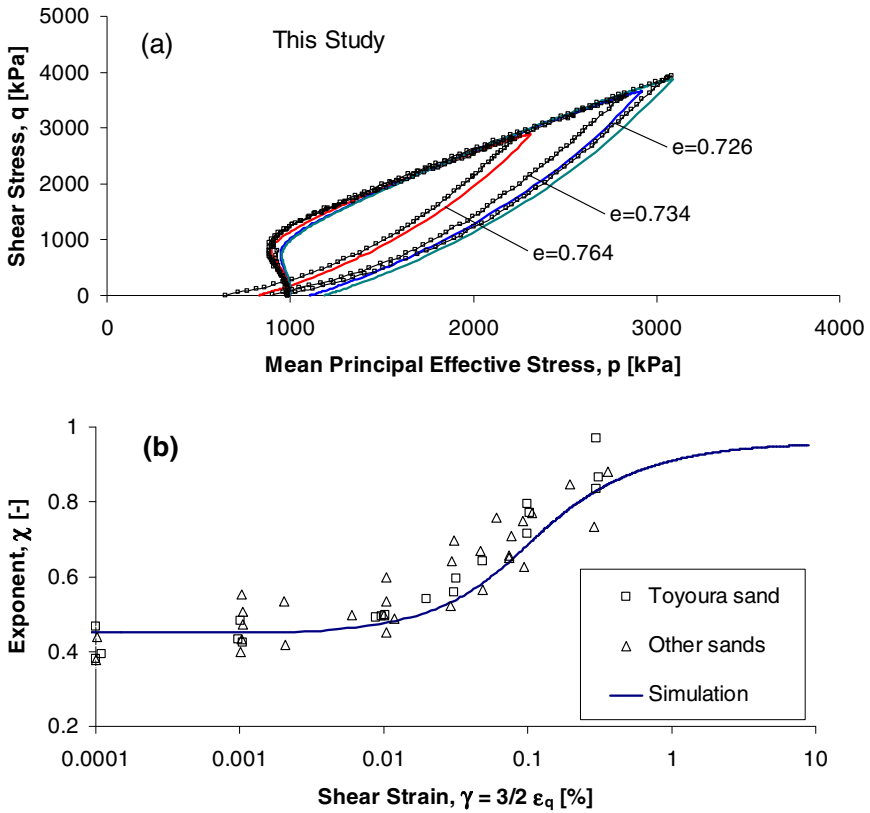


**Fig. 3.** Simulations using the proposed approach of this study: (a) stress paths (data taken from [13]); (b) evolution of  $\chi$  with shear strain (data after [9])

## References

- [1] Koseki, J., Kawakami, S., Nagayama, H., Sato, T.: Change of small strain quasi-elastic deformation properties during undrained cyclic torsional shear and triaxial tests of Toyoura sand. *Soils and Foundations* 40(3), 101–110 (2000)
- [2] Kuwano, R., Jardine, R.J.: On the applicability of cross-anisotropic elasticity to granular materials at very small strains. *Géotechnique* 52(10), 727–749 (2002)
- [3] Papadimitriou, A.G., Bouckovalas, G.D., Dafalias, Y.F.: Plasticity model for sand under small and large cyclic strains. *ASCE Journal of Geotechnical and Geoenvironmental Engineering* 127(11), 973–983 (2001)
- [4] Dafalias, Y.F., Manzari, M.T.: Simple plasticity sand model accounting for fabric change effects. *ASCE Journal of Engineering Mechanics* 130(6), 622–634 (2004)
- [5] Lashkari, A.: A SANISAND model with anisotropic elasticity. *Soil Dynamics and Earthquake Engineering* 30, 1462–1477 (2010)

- [6] Hardin, B.O., Black, W.L.: Sand stiffness under various triaxial stresses. *ASCE Journal of the Soil Mechanics and Foundation Division* 92(SM2), 27–42 (1966)
- [7] Kokusho, T.: Cyclic triaxial test of dynamic soil properties for wide strain range. *Soils and Foundations* 20(2), 45–60 (1980)
- [8] Silver, M.L., Seed, H.B.: Deformation characteristics of sands under cyclic loading. *ASCE Journal of the Soil Mechanics and Foundation Division* 97(SM8), 1081–1098 (1971)
- [9] Ishihara, K.: *Soil behavior in earthquake Geotechnics*. Oxford Science Publications (1996)
- [10] Einav, I., Puzrin, A.M.: Pressure-dependent elasticity and energy conservation in elastoplastic models for soils. *ASCE Journal of Geotechnical and Geoenvironmental Engineering* 130(1), 81–92 (2004)
- [11] Houlsby, G.T., Amorosi, A., Rojas, E.: Elastic moduli of soils dependent on pressure: a hyperelastic formulation. *Géotechnique* 55(5), 383–392 (2005)
- [12] Manzari, M.T., Dafalias, Y.F.: A critical state two-surface plasticity model for sands. *Géotechnique* 47(2), 255–272 (1997)
- [13] Verdugo, R., Ishihara, K.: Steady state of sandy soils. *Soils and Foundations* 36(2), 81–91 (1996)

# Influence of Grain Size Distribution on Critical State of Granular Materials

Gang Li, Carlos Ovalle, Christophe Dano<sup>\*</sup>, and Pierre-Yves Hicher

Research Institute in Civil and Mechanical Engineering  
Ecole Centrale de Nantes  
UMR CNRS 6183, Nantes, France  
christophe.dano@ec-nantes.fr

**Summary.** This paper aims to investigate the influence of grain size distribution (GSD) on the critical state of Hostun sand. Drained triaxial tests were conducted on saturated specimens with different GSD ( $C_u=1.4, 5, 10, 20$ ) under different confining pressures (100, 200, 400 kPa). The experimental results highlight that the critical state of the tested sand predominantly depends on its GSD.

**Keywords:** grain size distribution, critical state, triaxial tests.

## 1 Introduction

Since the pioneering work of Roscoe and Schofield (1958), the critical state concept has been developed and largely regarded as a fundamental framework for the development of constitutive models for soils. Based on this concept, lots of studies have been conducted on crushable soils (see for example Daouadji and Hicher, 1997), which have shown that the GSD of the soil changes during its lifetime by crushing of particles, leading to an increase of the coefficient of uniformity  $C_u$ . These changes influence the basic constitutive properties of the material, in particular the properties such as the critical state which is dependent on the particle size distribution at a given point of the loading history. As the fine content increases and the soil becomes better graded, it has been experimentally shown that the critical state line moves downwards (Biarez and Hicher 1994). Based on these new findings, some new models for crushable soils have been developed (Daouadji et al. 2001). Also, by means of discrete element method (DEM), Wood and Maeda (2007) showed the dependence of the critical state of granular materials on their initial GSD. However, so far, no detailed experimental data confirm these findings obtained by DEM.

This study aims to investigate the influence of initial particle GSD of a granular material on its mechanical behavior in terms of critical state and stress-strain relationship. A series of drained triaxial tests were performed on specimens of Hostun sand. Due to the high strength of Hostun sand particles, grain breakage may be considered as being negligible during shearing under testing loading conditions, permitting to maintain the same GSD all along the mechanical loading.

---

<sup>\*</sup> Corresponding author.

## 2 Testing Program

Samples with different GSD, corresponding to different coefficients of uniformity  $C_u$  ( $d_{60}/d_{10}$ ) varying from 1.4 to 20, with identical mean grain size  $d_{50}$ , were tested (Fig.1a). Three effective confining pressures (CP = 100kPa, 200kPa, 400kPa) were applied. All specimens were prepared by the moist tamping method (Ishihara 1993) in order to obtain very loose specimens.

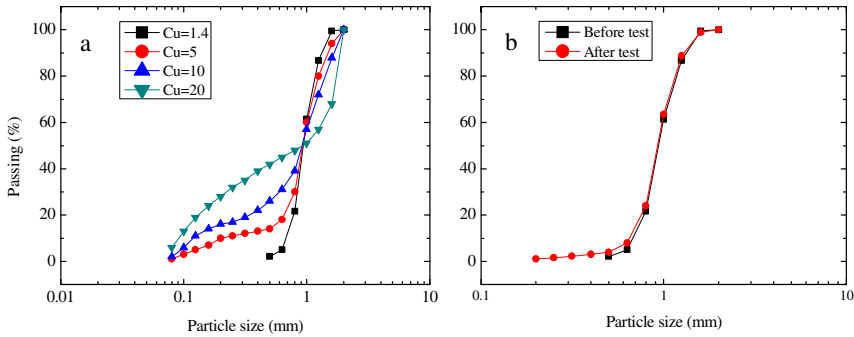


**Fig. 1.** (a) Particle size distribution; (b) GSD ( $C_u=1.4$  CP=400 kPa) before and after test

In order to confirm the assumption of no particle breakage occurring during testing, grain size distributions were systematically measured at the end of each test. As an example, the grain size distribution of one specimen ( $C_u = 1.4$  and confining pressure = 400 kPa), most prone to grain breakage among all the tested specimens, before and after the test is presented (Fig.1b). It shows that no global grain occurred; only a small amount of fines was produced by attrition.

## 3 Results and Discussions

Responses of specimens with different initial void ratios under triaxial compression at the same confining pressure are shown in Fig.2. It can be observed that the two specimens have the same tendency of contracting until the critical state is reached. However, the denser specimen appears less contractive. Although the initial void ratios are different, both specimens reach the same ultimate strength, corresponding to a same final void ratio at critical state.

The comparison of the critical state lines (CSL) obtained for different  $C_u$  (1.4, 5, 10 and 20) in the  $p'-q$  plane is presented in Fig.3a. It can be concluded that the tested specimens exhibit a unique critical stress ratio ( $M = q/p'$ ) upon compression regardless of GSD, except for the case of  $C_u = 20$  which shows a slight deviation with higher maximum stress ratio. The uniqueness of the critical stress ratio confirms that the shear resistance is not influenced by the change in GSD (Bandini and Coop, 2011). The differences obtained for  $C_u$  equals 20, may be due to the heterogeneity of the specimens during preparation, resulting in higher void ratio in the upper part of the sample due to some segregation of the finer part.

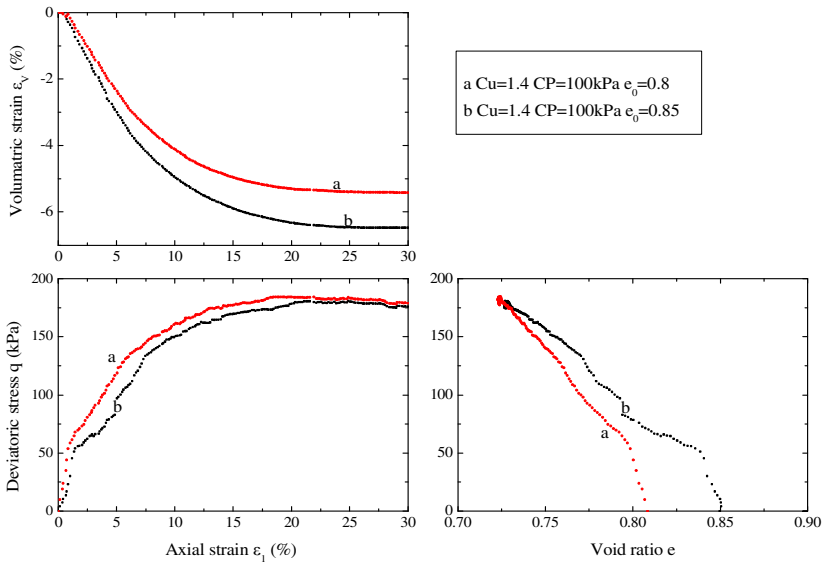


Fig. 2. Mechanical response of specimen with different  $e_0$

The CSL in the  $e-\log p'$  plane for specimens with different  $C_u$  is presented in Fig.3b. It can be found that the location of the CSL varies with the change of  $C_u$ . The higher the  $C_u$  value, the lower the location of the CSL. In other words, a well graded material has a smaller void ratio at critical state than a badly graded one.

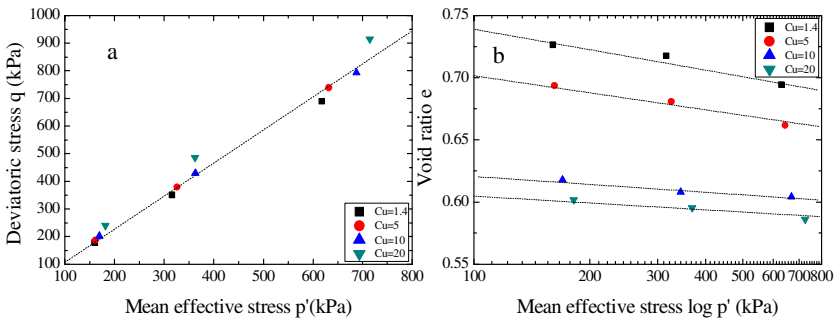


Fig. 3. (a)Critical state lines in  $p'$ -  $q$  space; (b) Critical state lines in  $e-\log p'$  space

### 4 Conclusions

Although the factors influencing the critical state of soils have been widely investigated by means of numerical and experimental approaches, there is still a lack of detailed experimental data addressing the influence of the grain size distribution (GSD) on the critical state of sandy soils. Therefore, the objective of this

experimental study was to investigate the influence of initial GSD on the mechanical properties of non-crushable soils. A series of conventional consolidated-drained triaxial compression tests were carried out on loose saturated Hostun sand specimens with different coefficients of uniformities  $C_u$  (1.4–20). This sand could be regarded as non-crushable under loading conditions used in this study. The experimental results highlight that the critical state of the tested specimens are significantly affected by the changes in GSD. A higher value of  $C_u$  leads to a lower location of the critical state line (CSL) in the  $e$ - $\log p'$  plane while the CSL in the  $p'$ - $q$  plane appears unique regardless of the value of  $C_u$ . In other words, the GSD affects the void ratio at critical state but not the ultimate shear strength or friction angle at critical state.

## References

- [1] Roscoe, K.H., Schofield, A.N., Wroth, C.P.: On the Yielding of Soils. *Géotechnique* 8, 22–53 (1958)
- [2] Daouadji, A., Hicher, P.-Y.: Modelling of grain breakage influence on mechanical behaviour of sand. In: Pietruszczak, Pande (eds.) *Numerical Models in Geomechanics*, Balkema, Rotterdam (1997) ISBN 905410886X
- [3] Biarez, J., Hicher, P.-Y.: *Elementary mechanics of soil behaviour*. A.A. Balkema, Rotterdam (1994)
- [4] Daouadji, A., Hicher, P.-Y., Rahma, A.: Modelling grain breakage influence on mechanical behaviour of granular media. *European Journal of Mechanics, A/Solids* 20, 113–137 (2001)
- [5] Muir Wood, D., Maeda, K.: Changing GSD of soil: effect on critical states. *Acta Geotechnica* 3, 3–14 (2007)
- [6] Ishihara, K.: Liquefaction and flow failure during earthquakes. *Géotechnique* 43(3), 351–415 (1993)
- [7] Bandini, V., Coop, M.R.: The influence of particle breakage on the location of the critical state line of sands. *Soils and Foundations* 51(4), 591–600 (2011)

# On Simulation of Strain Localization Using Microplasticity Constitutive Models

Majid T. Manzari<sup>1</sup> and Karma Yonten<sup>2</sup>

<sup>1</sup> Department of Civil and Environmental Engineering  
The George Washington University  
801 22<sup>nd</sup> Street, NW Washington, DC 20052  
manzari@gwu.edu

<sup>2</sup> Glenn Department of Civil Engineering, Clemson University  
200 Lowry Hall, Clemson SC 29634

**Summary.** The common perception that a regularization method such as strain gradient or micropolar enhancement must be able to produce mesh objective solutions is evaluated within the framework of micropolar plasticity for granular soils. It is shown while this perception holds for micropolar enhancement of classical elastoplasticity constitutive models in which the stress state remains within an elastic domain for a large part of reverse loading. However, micropolar plasticity models that are able to accurately model the reverse loading accounting for large volume change of the soil during reverse loading do not appear to follow the same rule.

**Keywords:** Elastoplasticity, Finite Elements, Localization, Micropolar, Sand, Two-surface plasticity.

## 1 Introduction

A key feature of the stress-strain response of granular materials is their tendency to undergo large volumetric strains in a reverse loading that follows a forward shearing. The ability to model this important feature is missing in majority of classical constitutive models for soils. In recent years, a few constitutive models [1, 2] have attempted to incorporate the volume change of soils in reverse loading. The implication of such modeling capability on emergence and evolution of shear bands within slightly heterogeneous specimens of granular soils is presented in this paper.

Two constitutive models built within the frameworks of micropolar plasticity and critical state soil mechanics are considered. The first model has the ability to properly model the reverse loading while the second one is unable to model the volume change of the soil in reverse loading. The capabilities of these models in simulating the post-localization response of granular soils are evaluated. It is shown that proper modeling of reverse loading will have significant impact on the

post-localization response of the specimen. The commonly accepted notion that an objective regularization method must produce post-bifurcation responses that are independent of discretization (say, in a finite element analysis) will be discussed in the lights of the aforementioned findings.

## 2 Finite Element Analysis of Strain Localization Using Two Different Micropolar Elastoplasticity Models

Consider a biaxial specimen of granular material with slight heterogeneity. Depending on sophistication of the constitutive model, the initial heterogeneity can be defined in terms of a state parameter such as density (void ratio) or simplified strength parameters such as friction angle or cohesion. Here we first consider a simple elastoplastic model that is similar to a non-associated Drucker-Prager model with friction angle and dilatancy that are evolving with a properly defined internal variable such as accumulated plastic shear strain. The model is fully described in Manzari and Regueiro [3] and is referred to as the SMR model. A micropolar version of the model is developed and implemented to evaluate the effectiveness of micropolar plasticity in analysis of strain localization. Figure 1 shows the results of a micropolar finite element analysis with the SMR model. Contours of vertical strain are shown to localize along a shear band whose thickness and orientation remains independent of the finite element mesh density. Figure 2 shows the force-displacement curves obtained from two different mesh densities. It is clear that post-localization response of the soil is independent of the mesh density and a mesh-objective solution is achieved by using micropolar framework.

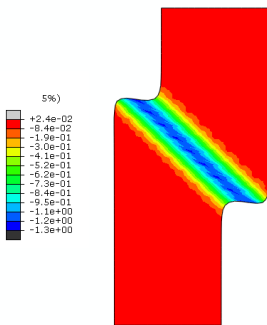


**Fig. 1.** Contours of vertical strain in a plane strain specimen of sand simulated with the micropolar SMR model

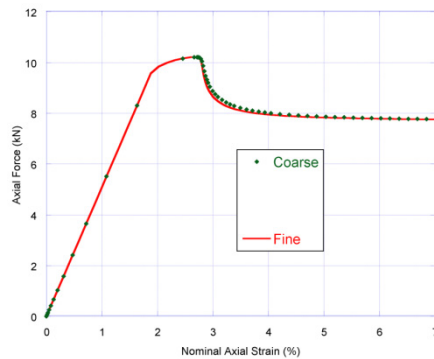


**Fig. 2.** Force-displacement curves obtained by using two different mesh densities and the micropolar SMR model

Similar finite analyses were conducted by using the micropolar version of the critical state two-surface plasticity model [2,4, 5]. The model has recently been implemented in a micropolar hydro-mechanical framework [6, 7] and is shown to produce realistic simulations of post-localization response of sands. Results of the

finite element analyses conducted by using this model are shown in Figure 3. The force-displacement curves no longer follow the same paths once strain localization is triggered. It is interesting to note that the shear band thickness and orientation are still independent of the mesh density (Figure 4) but the force-displacement curves are not.

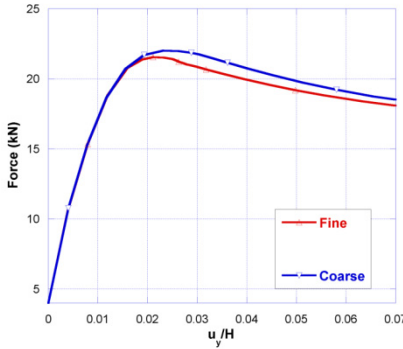


**Fig. 3.** Force-displacement curves obtained by using three different mesh densities and the micro-polar version of the critical state two-surface plasticity model

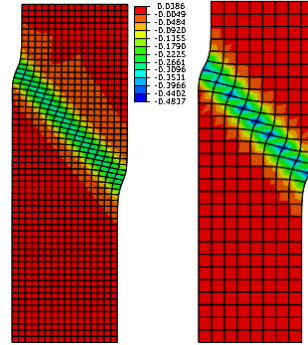


**Fig. 4.** Contours of micro-rotation in biaxial specimens subjected to vertical compression

### 3 Discussion of the Results

Figure 4 presents the contours of micro-rotations within the plane-strain specimen in a post-localization stage. Significant micro-rotations are localized inside the shear band while no micro-rotation is developing outside the band. This localization of micro-rotation, however, does not mean that the soil outside the shear band is in the state of elastic unloading. Due to small size of the yield surface, bulk of the soil outside shear band has passed the elastic unloading and has reached a reverse loading condition in which volumetric plastic strain continue to develop.

This means that unlike classical plasticity models, the area outside shear band is not elastically unloading and the overall force-displacement response is affected by both the softening of the soil inside the shear band and the continuous plastic deformation of the soil outside the band. The plastic deformations and the corresponding hardening of the soil that occur outside the shear band would contribute to the overall force-displacement response depending. This is why mesh density and the accuracy of finite element calculations inside as well as outside the band impact the overall force-displacement curve. It is noted, however, that the noticeable difference between the force-displacement curves for two different mesh densities is mainly for relatively coarse meshes and convergence is expected once the finite element mesh reaches a modest level of fineness.

**Acknowledgement.** The research presented in this paper was supported by the US National Science Foundation Geomechanics and Geomaterials Program directed by Dr. Richard J. Fragaszy. The first author also acknowledges the support from the European Research Council under the European Union's Seventh Framework Programme (FP7/2007- 2013) / ERC Grant Agreement #290963, IDEAS specific program SOMEF.

## References

- [1] Pastor, M., Zienkiewicz, O.C., Leung, K.H.: Simple Model for Transient Soil Loading In Earthquake Analysis. II. Non-Associative Models for Sands. *Int. J. Num. Anal. Meth. Geomech.* 9(5), 477–498 (1985)
- [2] Dafalias, Y.F., Manzari, M.T.: Simple Plasticity Sand Model Accounting for Fabric Change Effects. *ASCE Journal of Engineering Mechanics* 130(6), 622–634 (2004)
- [3] Manzari, M.T., Regueiro, R.A.: Gradient Plasticity Modeling of Geomaterials in a Meshfree Environment. *Mechanics Research Communication* 32, 536–546 (2005)
- [4] Manzari, M.T., Dafalias, Y.F.: A Critical State Two-Surface Plasticity Model for Sands. *Geotechnique* 49(2), 252–272 (1997)
- [5] Manzari, M.T., Dafalias, Y.F.: A Critical State Two-Surface Micropolar Plasticity Model for Sands. In: *Proceedings of 11th International Conference on Fracture*, Torino, Italy (2005)
- [6] Manzari, M.T., Yonten, K.: Analysis of Post-Failure Response of Sands using a Critical State Micropolar Plasticity Model. *Interaction and Multiscale Mechanics* 4(3), 187–206 (2011)
- [7] Manzari, M.T., Yonten, K.: Comparison of Two Integration Schemes for a Micropolar Plasticity Model. *Comp. Meth. Civil Eng.* 2, 21–42 (2011)

# Simulation of Isotropic Cyclic Compression by an Elasto-viscoplastic Constitutive Model Based on the Nonlinear Kinematic Hardening Rules

Fusao Oka\* and Sayuri Kimoto

Civil and Earth Resources Engineering  
Kyoto University  
Kyotodaigaku-katsura 4, Nishikyo-ku, Kyoto, 615-8540  
oka.fusao.2s@kyoto-u.ac.jp

**Abstract.** A cyclic elasto-viscoplastic constitutive model is proposed for saturated soils based on the nonlinear kinematic hardening rules by considering the structural degradation of soil particles. The model is based on the overstress type elasto-viscoplasticity theory and includes deviatoric and volumetric components of kinematical hardening parameters. The performance of the model is verified through the isotropic cyclic compression test of soft clay samples. The simulated results with both the linear and non-linear kinematical hardening can well simulate the cyclic compression behavior of clay, which indicates the capability of the proposed model to reproduce the cyclic behavior of soft clayey soils.

**Keywords:** Cyclic constitutive model, Clayey soils, Viscoplasticity, Kinematical hardening rule, isotropic compression.

## 1 Introduction

The prediction of soft clay behavior is complex due to the rate-dependent and cyclic plastic behaviors. This becomes even more complicated when destructure and microstructural changes of soils are taken into consideration. Several constitutive models have been proposed to describe the rheological behavior of clay under static loading conditions. However, few viscoplastic constitutive models are available for the analysis under dynamic and cyclic loading conditions (e.g., Oka 1992, Modaressi nad Laloui 1997, Oka et al. 2004, Maleki and Cambou 2009). Oka (1992) developed a cyclic elasto-viscoplastic constitutive model for clay based on nonlinear kinematic hardening rules (Armstrong and Frederick 1966, Chaboche and Rousselier 1983). Then, Oka et al. (2004) proposed a cyclic viscoelastic-viscoplastic model by incorporating the viscoelastic feature into the constitutive equations, in which the behavior of clay can be described not only in the range of middle to high level of strain, but also in the range of low level of strain. Despite the ability of these models to explain the

---

\* Corresponding author.

deformation characteristics under cyclic loading conditions, the effect of structural degradation of clay particles was disregarded. Taking into account the structural degradation and microstructural changes, a cyclic elasto-viscoplastic model is developed based on the nonlinear kinematic hardening rules for the changes in both the stress ratio and the mean effective stress. In addition, the kinematic hardening rule for changes in viscoplastic volumetric strain is considered to improve the prediction of the behavior during cyclic loading process.

In the present paper, the overall feature of the cyclic elasto-viscoplastic constitutive model is described. In order to evaluate the capability of the model, modeling of soft clay samples has been evaluated under isotropic cyclic compression.

## 2 Cyclic Elasto-viscoplastic Constitutive Model

The cyclic elasto-viscoplastic constitutive model is based on the concept of structural degradation in the elasto-viscoplastic model (Kimoto and Oka 2005) incorporated with the nonlinear kinematic hardening rules (Armstrong and Frederick 1966, Chaboche and Rousselier 1983). The model considers the structural degradation of the soil skeleton by shrinkage of both the static yield surface and the overconsolidation boundary surface with respect to the accumulation of viscoplastic strain. The model is derived based on an overstress type of viscoplasticity theory (Perzyna 1963) and the associated flow rule. The nonlinear kinematic hardening rules for both the deviatoric and volumetric strain are employed in addition to the viscoplastic strain dependency of elastic shear modulus.

In the constitutive model, Terzaghi's effective stress is used as

$$\sigma_{ij} = \sigma'_{ij} + p\delta_{ij} \quad (1)$$

where  $\sigma_{ij}$  is the total stress tensor,  $\sigma'_{ij}$  is the effective stress tensor,  $p$  is the pore water pressure, and  $\delta_{ij}$  is Kronecker's delta. In addition, total strain rate tensor  $\dot{\epsilon}_{ij}$  is assumed to be divided into two parts, namely,

$$\dot{\epsilon}_{ij} = \dot{\epsilon}_{ij}^e + \dot{\epsilon}_{ij}^{vp} \quad (2)$$

where  $\dot{\epsilon}_{ij}^e$  denotes the elastic strain rate tensor and  $\dot{\epsilon}_{ij}^{vp}$  is the viscoplastic strain rate tensor.

An overconsolidation boundary surface  $f_b$  is used which is defined as the boundary in the stress space between the normally consolidated (NC) region and the overconsolidated (OC) region by

$$f_b = \bar{\eta}_{(0)}^* + M_m^* \ln(\sigma'_m / \sigma'_{mb}) = 0 \quad (3)$$

where  $f_b < 0$  indicates the overconsolidated region and  $f_b \geq 0$  shows the normally consolidated region.  $\bar{\eta}_{(0)}^*$  is the relative stress ratio and is defined as  $\bar{\eta}_{(0)}^* = \{(\eta_{ij}^* - \eta_{ij(0)}^*)(\eta_{ij}^* - \eta_{ij(0)}^*)\}^{1/2}$ ;  $\eta_{ij}^* = s_{ij} / \sigma_m'$  and  $\eta_{ij(0)}^*$  is the value of  $\eta_{ij}^*$  at the end of consolidation.  $M_m^*$  is the value of  $\eta^* = \sqrt{\eta_{ij}^* \eta_{ij}^*}$  at critical state and at which the volumetric strain increment changes from compression to dilation.

To describe the structural degradation of clay, strain softening with the accumulated viscoplastic strain is introduced in addition to strain hardening with the viscoplastic volumetric strain as

$$\sigma_{mb}' = \sigma_{ma}' \exp\left(\frac{1+e_0}{\lambda - \kappa} \varepsilon_v^{vp}\right) \quad (4)$$

$$\sigma_{ma}' = \sigma_{maf}' + (\sigma_{mai}' - \sigma_{maf}') \exp(-\beta z) \quad (5)$$

where  $\sigma_{ma}'$  is assumed to decrease with an increase in the viscoplastic strain. In Equation (5),  $\sigma_{mai}'$  and  $\sigma_{maf}'$  are the initial and the final values for  $\sigma_{ma}'$ , respectively.  $\beta$  is a parameter that stands for the changing rate of  $\sigma_{ma}'$ , while the proportion of  $n = \sigma_{maf}' / \sigma_{mai}'$  provides the degree of possible collapse of the soil structure at the initial state.  $z$  is the accumulation of the second invariant of the viscoplastic strain increment.

Considering the model for monotonic loading conditions (Kimoto and Oka, 2005), the static yield function is obtained by considering the nonlinear kinematic hardening rule for the changes in the stress ratio, in the mean effective stress, and in the viscoplastic volumetric strain as

$$f_y = \bar{\eta}_\chi^* + \tilde{M}^* \left( \ln \frac{\sigma_{mk}'}{\sigma_{my}^{(s)'}} + \left| \ln \frac{\sigma_m'}{\sigma_{mk}'} - y_m^* \right| \right) = 0 \quad \bar{\eta}_\chi^* = \left\{ (\eta_{ij}^* - \chi_{ij}^*)(\eta_{ij}^* - \chi_{ij}^*) \right\}^{1/2} \quad (6)$$

in which  $\sigma_{mk}'$  is the unit value of the mean effective stress,  $y_m^*$  is the scalar kinematic hardening parameter, and  $\sigma_{my}^{(s)'}$  denotes the static hardening parameter.  $\chi_{ij}^*$  is so-called back stress parameter, which has the same dimensions as stress ratio  $\eta_{ij}^*$ . Incorporating the strain softening for the structural degradation, the hardening rule of  $\sigma_{my}^{(s)'}$  can be expressed as

$$\sigma_{my}^{(s)'} = \frac{\sigma_{maf}' + (\sigma_{mai}' - \sigma_{maf}') \exp(-\beta z)}{\sigma_{mai}'} \sigma_{myi}^{(s)'} \quad (7)$$

In the same manner as for the static yield function, the viscoplastic potential function  $f_p$  is given by the similar function as

$$f_p = \bar{\eta}_\chi^* + \tilde{M}^* \left( \ln \frac{\sigma'_{mk}}{\sigma'_{mp}} + \left| \ln \frac{\sigma'_m}{\sigma'_{mk}} - y_m^* \right| \right) = 0 \quad (8)$$

The evolution equation for the nonlinear kinematic hardening parameter  $\chi_{ij}^*$  is given by

$$d\chi_{ij}^* = B^* \left( A^* de_{ij}^{vp} - \chi_{ij}^* d\gamma^{vp} \right) \quad (9)$$

where  $A^*$  and  $B^*$  are material parameters,  $de_{ij}^{vp}$  is the viscoplastic deviatoric strain increment tensor, and  $d\gamma^{vp} = \sqrt{de_{ij}^{vp} de_{ij}^{vp}}$  is the viscoplastic shear strain increment tensor.  $A^*$  is related to the stress ratio at failure, namely,  $A^* = M_f^*$ , and  $B^*$  is proposed to be dependent on the viscoplastic shear strain as

$$B^* = \left( B_{\max}^* - B_1^* \right) \exp\left(-C_f \gamma_{(n)}^{vp*}\right) + B_1^* \quad (10)$$

in which  $B_1^*$  is the lower boundary of  $B^*$ ,  $C_f$  is the parameter controlling the amount of reduction,  $\gamma_{(n)}^{vp*}$  is the accumulated value of the viscoplastic shear strain between two sequential stress reversal points in the previous cycle.  $B_{\max}^*$  is the maximum value of parameter  $B^*$ .

In order to improve the predicted results under cyclic loading conditions, the scalar nonlinear kinematic hardening parameter  $y_m^*$  is adopted (Oka et al., 1999) and is decomposed into two parts such as linear and nonlinear kinematical hardening parameters as

$$y_m^* = y_{m1}^* + y_{m2}^* \quad (11)$$

where  $y_{m1}^*$  is the non-linear and  $y_{m2}^*$  is the linear kinematical hardening parameters. The non-linear and linear kinematical hardening are introduced as

$$dy_{m1}^* = B_2^* \left( A_2^* d\varepsilon_v^{vp} - y_{m1}^* |d\varepsilon_v^{vp}| \right) \quad (12)$$

$$dy_{m2}^* = B_3^* d\varepsilon_v^{vp} \quad (13)$$

where  $A_2^*$  and  $B_2^*$  are material parameters,  $d\varepsilon_v^{vp}$  is the increment of the viscoplastic volumetric strain tensor. The values of  $A_2^*$  and  $B_2^*$  are determined by data-adjusting method from the laboratory test data. In addition, we can use a

linear kinematical hardening rule given in Eq.(13) in which  $B_3^*$  is a hardening parameter.

### 3 Performance of the Proposed Model

Simulation has been performed under cyclic loading histories with several sets of material parameters shown in Table 1. Figs. 1-3 indicate the cyclic behavior of soil under isotropic loading, reloading and unloading conditions with constant loading rate  $\dot{\sigma}'_m = 0.04$  kPa/s; the loading history is  $\sigma'_m = 20 \rightarrow 300 \rightarrow 20 \rightarrow 400$  kPa. In the Fig. 1, only the linear kinematical hardening is considered. It is seen

**Table 1.** Material parameters of Nakanoshima clay

		Case 1	Case 2	Case 3
Initial void ratio	$e_0$		1.373	
Compression index	$\lambda$		0.2173	
Swelling index	$\kappa$		0.0344	
Viscoplastic parameter (1/s)	$C_2$		$1.0 \times 10^{-9}$	
Stress ratio at compression	$M_{mc}^*$		1.143	
Compression yield stress (kPa)	$\sigma'_{mai}$		20	
Viscoplastic parameter	$m'$		22.7	
Scalar hardening parameter	$A_2^*$	0.0	8.0	9.0
Scalar hardening parameter	$B_2^*$	0.0	3.5	1.7
Scalar hardening parameter	$B_3^*$	13.0	0.0	4.0

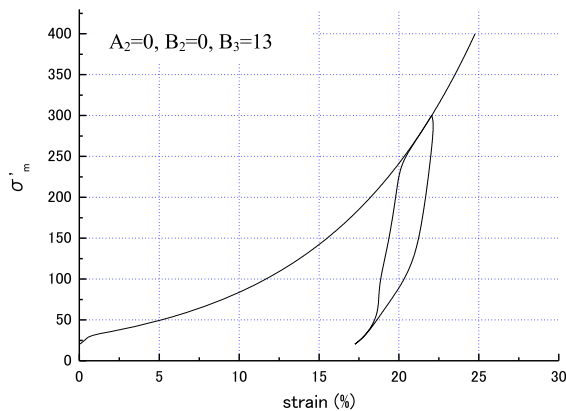


**Fig. 1.** Simulation of isotropic cyclic compression (Case 1)

that the cyclic behavior is well reproduced. In Fig. 2, only the non-linear kinematical hardening parameter is adopted, and in this case we can see the apparent yield value becomes smaller on the reloading curve. Finally, both the non-linear and linear parameters are used in Fig. 3. The simulated result is quite similar to the cyclic compression behavior of soft clay.

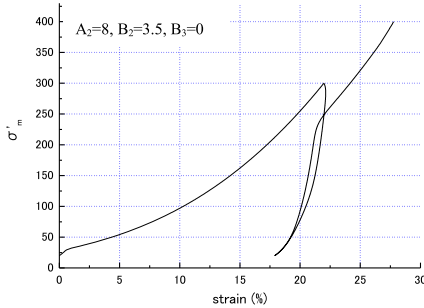


**Fig. 2.** Simulation of isotropic cyclic compression (Case 2)

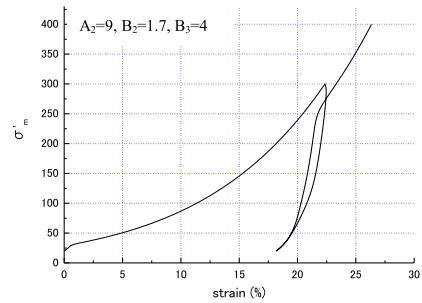


**Fig. 3.** Simulation of isotropic cyclic compression (Case 3)

## 4 Conclusions

A cyclic elasto-viscoplastic model was proposed based on the nonlinear kinematic hardening rules and by considering the structural degradation. The simulated results can well reproduce the isotropic cyclic behavior. It is worth noting that the both the linear and non-linear kinematical hardening parameters are necessary to describe the cyclic behavior of clay. This indicates the ability of the proposed model to predict the behavior of clay under cyclic undrained and drained loading conditions.

## References

- [1] Armstrong, P.J., Frederick, C.O.: A mathematical representation of the multiaxial Bauschinger effect. CEGB Report RD/B/N 731 (1966)
- [2] Chaboche, J.L., Rousselier, G.: On the plastic and viscoplastic constitutive equations; part I and Part II. *J. Pressure Vessel Technol., Trans. ASME* 105, 153–164 (1983)
- [3] Kimoto, S., Oka, F.: An elasto-viscoplastic model for clay considering destructuralization and consolidation analysis of unstable behavior. *Soils and Foundations* 45(2), 29–42 (2005)
- [4] Maleki, M., Cambou, B.: A cyclic elastoplastic-viscoplastic constitutive model for soils. *Geomechanics and Geoengineering: an International Journal* 4(3), 209–220 (2009)
- [5] Mirjalili, M.: Numerical analysis of a large-scale levee on soft soil deposits using two-phase finite deformation theory. PhD thesis. Kyoto University, Japan (2010)

- [6] Modaressi, H., Laloui, L.: A thermo-viscoplastic constitutive model for clay. *Int. J. Numer. Anal. Meth. Geomech.* 21, 313–335 (1997)
- [7] Oka, F.: A cyclic elasto-viscoplastic constitutive model for clay based on the nonlinear kinematic hardening rule. In: Pande, G.N., Pietruszczak, S. (eds.) *Proc. 4th Int. Symposium on Numerical Model in Geomechanics*, Swansea, Balkema, vol. 1, pp. 105–114 (1992)
- [8] Oka, F., Yashima, A., Tateishi, A., Taguchi, Y., Yamashita, S.: A cyclic elasto-plastic constitutive model for sand considering a plastic-strain dependence of the shear modulus. *Geotechnique* 49(5), 661–680 (1999)
- [9] Oka, F., Kodaka, T., Kim, Y.S.: A cyclic viscoelastic–viscoplastic constitutive model for clay and liquefaction analysis of multi-layered ground. *Int. J. Numer. Anal. Meth. Geomech.* 28, 131–179 (2004)
- [10] Perzyna, P.: The constitutive equations for work-hardening and rate sensitive plastic materials. In: *Proc. of Vibration Problems, Warsaw*, vol. 3(4), pp. 281–290 (1963)

# Rotational Hardening and Uniqueness of Critical State Line in Clay Plasticity

Mahdi Taiebat<sup>1</sup> and Yannis F. Dafalias<sup>2</sup>

<sup>1</sup> The University of British Columbia, Vancouver, BC, Canada  
[mtaiebat@civil.ubc.ca](mailto:mtaiebat@civil.ubc.ca)

<sup>2</sup> University of California, Davis, CA, USA and National Technical University of Athens, Zographou, Greece  
[jfdafalias@ucdavis.edu](mailto:jfdafalias@ucdavis.edu)

**Abstract.** Rotational Hardening (RH) is the constitutive ingredient of clay plasticity models which allows the description of more realistic response than typical isotropic models under various loading conditions, and in particular under  $K_0$  consolidation, where isotropic models fail to capture the correct  $K_0$  value. Additional restrictions must be imposed to prevent excessive rotation when loaded at very high stress ratios. One important aspect of a RH law is its ability to obtain a unique critical state line (CSL) in the  $e-p$  space, while maintaining a realistic response before critical state failure. Some RH laws are critically examined and a novel proposition is outlined.

## 1 Introduction

Rotational Hardening (RH) is the term used to indicate the rotation of the yield surface and/or plastic potential surface in stress space as a result of non hydrostatic loading and was first introduced by Sekiguchi and Ohta [1] for clay plasticity. Such loading induces anisotropy due to fabric orientation of the particulate medium, the macroscopic manifestation of which is described by such rotation. RH applies to both sand and clay plasticity models, but in this paper only the case of clays will be considered. RH is expressed in terms of a scalar-valued stress-ratio type constitutive internal variable in triaxial space which is the counterpart of a corresponding tensor-valued variable in multiaxial space, and can be associated with various shapes of yield surfaces. The RH variable obeys rate evolution equations which must satisfy certain restrictions in order to avoid excessive rotation, as well as appropriate saturation values under specific loading conditions such as  $K_0$  loading or loading up to Critical State. In the last case it is important to investigate the effect of RH on the uniqueness of the resulting Critical State Line (CSL) in the void ratio  $e$  versus hydrostatic pressure  $p$  space in regards to loading at different Lode angles, as for example in triaxial compression and extension. This investigation will be the main focus of this presentation.

## 2 Yield Surfaces and Critical State Line

For anisotropic clays there is a plethora of yield surface expressions, whose RH can be studied independently of the particular shape. It will be expedient though to focus on a specific yield surface expression in order to avoid unnecessary generalities which will obscure the main objective of this work. As such the yield surface of a rotated and “sheared” ellipse introduced by Dafalias [2] will be considered, due to its analytical simplicity and success in capturing the yield loci of experimental data for various clays, as well as its dissipation-based derivation. The corresponding analytical expression, after some algebraic manipulations from its original form, reads:

$$f = (q - p\alpha)^2 - (M^2 - \alpha^2)p(p_0 - p) = 0 \tag{1}$$

and is plotted in Fig. 1 for illustration. The  $\alpha$  is the dimensionless stress-ratio type RH variable defining the rotation of the yield surface, and  $p_0$  is the  $p$  coordinate of the intersection of the line with slope  $\alpha$  and the yield surface. The  $\alpha$  and  $p_0$  constitute the two hardening internal variables, the former addressing RH and the latter isotropic hardening due to density changes. For  $\alpha = 0$  Eq.(1) becomes the well known isotropic modified Cam-Clay yield surface expression [3]. Notice that Eq.(1) requires that  $|\alpha| < M$  in order to have real roots for  $q$ . The value of  $M$  is that of triaxial compression  $M_c$  or extension  $M_e$ , for  $\eta = q/p \geq \alpha$  or  $\leq \alpha$ , respectively.

In  $e-\ln p$  space the  $p_0$  variation with  $e$  represents the Normal Consolidation Line (NCL). At this point it is expedient to present the generally accepted rate evolution equation of  $p_0$

$$\dot{p}_0 = \langle L \rangle \frac{1 + e_{in}}{\lambda - \kappa} \frac{\partial f}{\partial p} p_0 \tag{2}$$

where a superposed dot implies the rate,  $L$  in the Macaulay brackets represents the plastic multiplier or loading index, function of the rates of stress or strain,  $e_{in}$  is the initial void ratio and  $\lambda$  and  $\kappa$  are the slopes of the consolidation and rebound lines, respectively, in  $e-\ln p$  space.

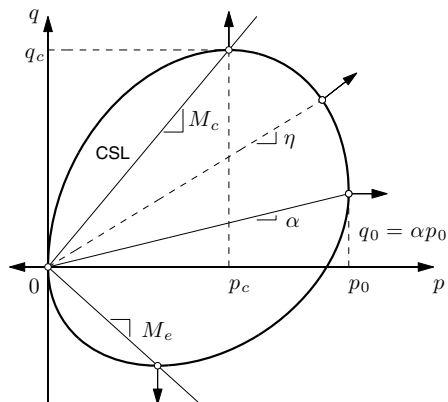


**Fig. 1.** Schematic diagram of the anisotropic yield surface in the  $p$ - $q$  space

As shown in Dafalias(1986), the yield surface of Eq.(2) intersects the critical stress ratio line  $\eta = q/p = M$  at

$$p_c = \frac{1}{2}p_0(1 + \frac{\alpha}{M}); \quad q_c = Mp_c \tag{3}$$

where  $-M$  must substitute for  $M$  in Eq.(3) for the corresponding intersection point in extension. It follows from Eq.(3) that in reference to a fixed NCL represented by the evolution of  $p_0$  in the  $e-\ln p$  space as described by Eq.(1), the location of the corresponding CSL in  $e-p$  space, expressed by  $p_c$  in regards to  $p_0$ , depends on the rotation  $\alpha$  and in particular on the ratio  $\alpha/M$ , assuming of course that the  $\alpha$  has reached a critical state value and does not evolve any further, while simultaneously the  $p_0$  has stopped to evolve based on Eq.(2) since  $\partial f/\partial p = 0$  at point  $(p_c, q_c)$ . Notice from Eq.(3) that for  $\alpha = 0$  it follows that  $p_c = (1/2)p_0$  as in the isotropic Cam-Clay model. This dependence on  $\alpha/M$  must also account for the fact  $M$  is different in compression and extension, and more generally that  $M$  depends on the Lode angle in multiaxial stress space. Other properties of the yield surface of Eq.(1) such as the fact it always intersects the  $\eta = M$  line at the peak  $q$  point where also the  $\partial f/\partial p = 0$ , have been extensively discussed in past publications and are not presented again.

### 3 Rotational Hardening and Uniqueness of Critical State Line

With an eye towards the simulation of undrained stress paths and the attainment of the correct  $\eta_k$  stress ratio under  $K_0$  consolidation, Dafalias [2] proposed the following evolution law for  $\alpha$ :

$$\dot{\alpha} = \langle L \rangle \frac{1 + e_{in}}{\lambda - \kappa} \left| \frac{\partial f}{\partial p} \right| c \frac{p}{p_0} (\eta - x\alpha) \tag{4}$$

where  $c$  is a model parameter controlling the pace of evolution and  $x$  is another model parameter controlling the saturation value of  $\alpha$  under fixed stress ratio  $\eta$  loading, namely  $\alpha = \eta/x$  when  $\dot{\alpha} = 0$ . The absolute value  $|\partial f/\partial p|$  multiplied by  $\langle L \rangle$  implies that the  $\alpha$  evolves only when the plastic volumetric strain rate is not zero, based on the associative flow rule assumption. The term involving  $e_{in}$ ,  $\lambda$ , and  $\kappa$  is placed only for association with the corresponding term in Eq.(2), and could be absorbed in the value of  $c$  if desired.

Under  $K_0$  consolidation, the ratio of volumetric to deviatoric total strain rates must be equal to 3/2. As a result the yield surface on one hand expands as  $p_0$  increases and on the other rotates as  $\alpha$  evolves until the final fixed stress ratio  $\eta_k$  under  $K_0$  is reached; then the rotation stops while the yield surface continues to expand isotropically. Imposing this condition on total strain rate ratios in conjunction with Eq.(4), the elastic relations and associative flow rule for the plastic strain rates, Dafalias [2] derived the equation

$$\alpha_k = \frac{\eta_k}{x} = \frac{\eta_k^2 + 3[1 - (\kappa/\lambda)]\eta_k - M^2}{3[1 - (\kappa/\lambda)]} \tag{5}$$

Knowing the value of  $K_0$  one has  $\eta_k = 3(1 - K_0)/(1 + 2K_0)$  and with  $M$ ,  $\kappa$ , and  $\lambda$  known, Eq.(5) yields the value of  $x$  and the value  $\alpha_k$  of  $\alpha$  after  $K_0$  consolidation. If  $x$  is considered constant, this is the way of its determination; if it is considered variable with  $\eta$ , Eq.(5) yields its value for  $\eta = \eta_k$ .

Another observation related to Eq.(4) addresses the boundness of the rotation of  $\alpha$ . In very large OCR one has  $\eta \rightarrow \infty$  which may suggest that the rate of  $\alpha$  can possibly become infinite, thus, inducing an excessive rotation which might allow for  $\alpha > M$ , unacceptable for the validity of Eq.(1). However, if the  $p$  in Eq.(4) is brought inside the parenthesis one has  $p(\eta - x\alpha) = q - xp\alpha$ , the original expression in [2], which is bounded. Yet, for a value of  $x$  very close to 1 which might allow  $\alpha$  to approach  $M$ , even a bounded term can create problems, hence, the introduction of some additional bounds was postulated in Dafalias *et al.* [4]. If on the other hand  $x$  is sufficiently greater than 1 (say  $x \geq 2$ ), no such possibility exists and the bounds in [4] might be unnecessary.

Under undrained loading after  $K_0$  consolidation, Fig. 2 illustrates the undrained stress paths obtained in this case. Notice that as soon as the stress path reaches the point of intersection of the yield surface with the  $\eta = M$  line, the  $\partial f/\partial p=0$  and according to Eqs. (2) and (4),  $\dot{p} = 0$  and  $\dot{\alpha} = 0$ , thus, Critical State failure occurs because the corresponding plastic modulus obtained from the consistency condition is then zero [2].

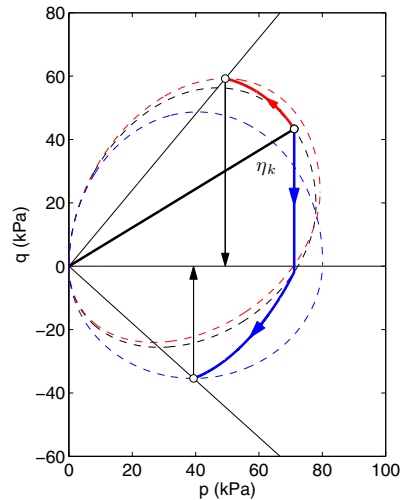


**Fig. 2.** Undrained stress path after  $K_0$  consolidation using anisotropic hardening rule of Eq.(4)

Looking at the undrained stress paths of Fig. 2 one observes that the  $p_c$  value at critical state (refer to Fig. 1 for the definition of  $p_c$ ) is different in compression and extension for the same void ratio  $e$  (due to undrained loading), which implies that

there are two different CSL. In fact it suffices to consider the points of intersection of the rotated yield surface in Fig. 1 with the  $\eta = M$  lines in compression and extension which are points of critical state failure as explained before because of  $\partial f/\partial p = 0$ , and the different values of  $p_c$  imply the existence of different CSL. This can be repeated for several values of  $\alpha$ , creating an infinite number of CSL for each  $\alpha/M$  according to Eq.(3). It is clear that the culprit for this feature is the existence of the term  $|\partial f/\partial p|$  in Eq.(4) which freezes the evolution of  $\alpha$  once at an intersection point with the  $\eta = M$  lines. There was, however, a special reason why the term  $|\partial f/\partial p|$  was introduced in Eq.(4). To illustrate this reason let us remove first this term from Eq.(4) and consequently have as rate equation of evolution for  $\alpha$  the remaining terms, i.e.

$$\dot{\alpha} = \langle L \rangle \frac{1 + e_{in}}{\lambda - \kappa} p_{at} c \frac{p}{p_0} (\eta - x\alpha) \quad (6)$$

where  $p_{at}$  is the atmospheric pressure and was placed in Eq.(6) for dimensional consistency after the removal of  $|\partial f/\partial p|$  from Eq.(4). The discussion on  $K_0$  consolidation and resulting important Eq.(5) are not affected at all by this change. But critical state failure now is obtained not only when  $\dot{p}_0 = 0$  at an intersection point  $\eta = M$ , where  $\partial f/\partial p = 0$ , but also requires  $\dot{\alpha} = 0$  which from Eq.(6) implies that  $\alpha = \eta/x = M/x$  at critical state failure. Setting this value of  $\alpha$  in Eq.(3) one has that at critical state the stress is given by

$$p_c = \frac{1}{2} p_0 \left(1 + \frac{1}{x}\right); \quad q_c = M p_c \quad (7)$$

Eq.(7) shows that the ratio  $p_c/p_0$  is a function of  $x$ , hence, there is a unique CSL which is parallel to the NCL expressed by  $p_0$  in  $e-\ln p$  space, the distance between CSL and NCL defined in terms of the value of  $x$ . Observe that such uniqueness is guaranteed for any Lode angle since the  $x$  is not dependent on it. If  $x$  is a constant, its value can be determined by Eq.(5), as already mentioned. But it is possible to have  $x$  a function of  $\eta$  which provides greater flexibility in specifying different values of  $x$  for the two crucial tests of  $K_0$  consolidation where  $\eta = \eta_k$ , and critical state failure where  $\eta = \eta_c = M$ .

To illustrate the effect of removing  $|\partial f/\partial p|$  from Eq.(4) in order to obtain Eq.(6), it is instructive to run again the simulation of undrained loading after  $K_0$  consolidation using Eq.(6) for the evolution of  $\alpha$ . The results for the undrained stress paths are shown in Fig. 3(a) and it is clear that the same  $p_c$  is obtained at compression and extension, thus, implying the same CSL as discussed above in conjunction with Eq.(7). Notice though the ‘‘hook’’ type of undrained stress path response observed mainly in triaxial extension; similar strong hook-type of simulated response will be observed in both triaxial compression and extension if the undrained loading starts from an isotropically consolidated state. This type of response is not usually observed in reported experiments and its avoidance was the main reason for introducing the  $|\partial f/\partial p|$  term in Eq.(4). The price one had to pay for this, was the multiplicity of CSL, as explained before. The explanation for the hook-type response of

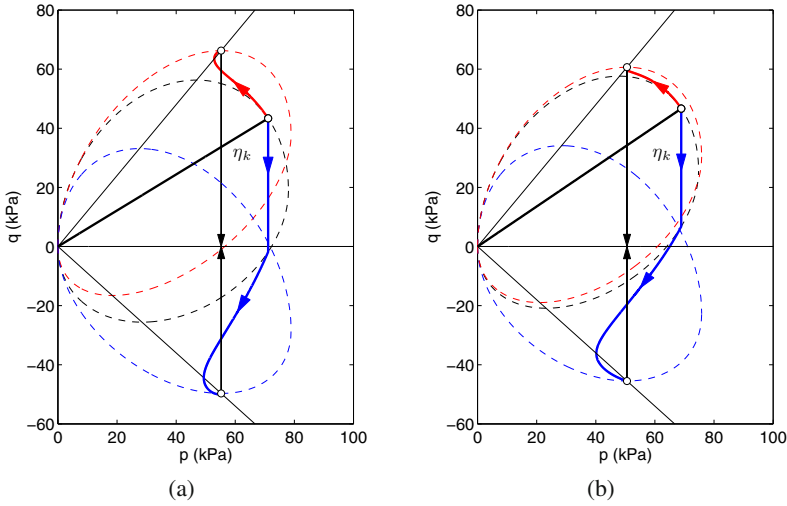


**Fig. 3.** Undrained stress path after  $K_0$  consolidation using anisotropic hardening rules in (a) Eq.(6) and (b) Eq. (8)

the undrained stress paths is easy. When the stress reaches the  $\eta = M$  line, and this happens quite rapidly, the  $\alpha$  has not yet reached its saturation critical state value  $M/x$ , hence, it continues to evolve and consequently the yield surface continues to rotate without change of size because the  $p_0$  remains fixed at  $\eta = M$  where the volumetric plastic strain rate is zero due to  $\partial f / \partial p = 0$ . This continuing rotation causes the stress point to climb up the  $\eta = M$  line until  $\alpha = \eta / x = M / x$ , and the hook shape appears as a result of this climbing. The fact that after  $K_0$  consolidation the yield surface is already rotated in compression, explains why the hook response is less pronounced in compression than in extension because the  $\alpha$  is closer to its saturation critical state value in the former than the latter case. This is also the reason why after isotropic consolidation where no rotation has taken place, the hook-type of response is similarly pronounced in compression and extension.

One, therefore, is faced with the choices to either include the  $|\partial f / \partial p|$  in the rate equation of evolution of  $\alpha$ , as in Eq.(4), in order to avoid the hook-type of undrained stress path response but the price to pay is a multiplicity of CSL, or delete the  $|\partial f / \partial p|$  and use instead Eq.(6) in which case such hook-type of response is observed but the CSL is unique for any Lode angle, which includes the cases of triaxial compression and extension, because the distance of the CSL from the NCL is fixed and defined by Eq.(7) where the  $x$  is independent of such Lode angle.

### 4 Other Propositions

Uniqueness of CSL was achieved by a different RH proposed in Wheeler *et al.* [5], where the same form of yield surface as in Eq.(1) was used, and the rate equation of evolution of  $\alpha$  was given by

$$\dot{\alpha} = \mu \left[ \left( \frac{3\eta}{4} - \alpha \right) \langle \dot{\epsilon}_v^p \rangle + \beta \left( \frac{\eta}{3} - \alpha \right) |\dot{\epsilon}_d^p| \right] \tag{8}$$

where  $\mu$  and  $\beta$  are model constants and the two plastic strain rate terms represent the volumetric and deviatoric parts. Loading at  $\eta \geq M$  induces a non positive volumetric strain rate according to the associative flow rule, [2], and the Macaulay brackets eliminate the first term. Eq. (8) leads to a unique CSL, as pointed out in [5], but also predicts the hook-type of undrained stress path response for the same reasons that Eq.(6) does. This is illustrated in Fig. 3(b) placed next to the corresponding Fig. 3(a) for Eq.(6).

Eq.(6) shows that in order to obtain a unique CSL is not necessary to have the rate of  $\alpha$  depending on both volumetric and deviatoric plastic strain rates, as stated in Wheeler *et al.* [5]. It suffices to formulate the rate equation of  $\alpha$  in such a way as to have its saturation value a function of  $\eta$  that is independent of the Lode angle and becomes a fraction of  $M$  at critical state. Eq.(8) contains four constants, the 3/4 and 1/3 factors in the parentheses, the  $\mu$  and the  $\beta$ , the latter to be determined by the  $K_0$  condition. Eq.(6) on the other hand is simpler and contains only two constants, the  $c$  which is the counterpart of  $\mu$ , and the  $x$ ; this has the following relative disadvantage: when a specific fixed value of  $x$  is obtained by matching the  $K_0$  stress ratio  $\eta_k$  according to Eq.(5), it cannot necessarily accommodate a CSL at a prescribed distance from the NCL, but such CSL is directly specified by Eq.(7) and the value of  $x$ .

To address this disadvantage a new proposition can be made that captures the correct  $K_0$  value and yields a unique CSL, while maintaining the saturation value of  $\alpha$  less than  $M$  for loading at  $\eta \geq M$ . It suffices to render  $x$  a function of  $\eta$  according to the relation:

$$x = \frac{|\eta|}{(M/z)[1 - \exp(-s|\eta|/M)]} \tag{9}$$

with  $z$  and  $s$  being two model constants, which with  $c$  constitute the three constants of Eq.(6). When  $|\eta| \geq M$ , the exponential term is almost zero for an appropriate value of  $s$ , in which case the saturation value  $\eta/x$  for  $\alpha$  becomes  $M/z$  according to Eq. (9), hence, it is maintained always less than  $M$  if  $z > 1$ ; the choice  $z = 3$  yields in such case the same results as Eq. (8). For  $K_0$  consolidation, application of Eq.(5) for  $x$  given by Eq.(9) yields the means to determine  $s$ . Eq.(9) is well defined at  $\eta = 0$  (use L'Hopital rule for the limit as  $\eta \rightarrow 0$ ).

## 5 Conclusion

Elimination of the term  $|\partial f / \partial p|$  from the original rate evolution Eq.(4) of the rotational hardening parameter  $\alpha$  in [2], yields a unique CSL in the  $e-\ln p$  space but it induces a hook-type of undrained stress path response which is not normally observed in clay experiments. The general conclusion is that CSL uniqueness can be guaranteed when the rotational hardening variable  $\alpha$  reaches a saturation value at critical state which is a fraction of  $M$  and independent of the Lode angle. This can be

achieved by various approaches, at the expense of having a hook-type of undrained stress path, one of which is the proposition of Wheeler *et al.* [5] as per Eq.(8), and another aforementioned proposition of Dafalias [2] without the  $|\partial f/\partial p|$  term as per Eq. (6), and an  $x$  which can be either constant or variable with  $\eta$  as per Eq.(9).

**Acknowledgements.** This research received funding from the European Research Council under the European Union's Seventh Framework Program (FP7/2007-2013) / ERC IDEAS Grant Agreement 290963 (SOMEF). The first author acknowledges also support from the Natural Sciences and Engineering Research Council of Canada (NSERC).

## References

- [1] Sekiguchi, H., Ohta, K.: Induced anisotropy and time dependence in clays. In: Constitutive Equations for Soils, Proceedings of 9th ICSMFE (Specialty Session 9), Tokyo, pp. 229–238. JSSMFE (1977)
- [2] Dafalias, Y.F.: An anisotropic critical state soil plasticity model. Mechanics Research Communications 13(6), 341–347 (1986)
- [3] Burland, J.B.: The yielding and dilation of clay. Géotechnique 15(2), 211–214 (1965)
- [4] Dafalias, Y.F., Manzari, M.T., Papadimitriou, A.G.: SANICLAY: simple anisotropic clay plasticity model. International Journal for Numerical and Analytical Methods in Geomechanics 30(12), 1231–1257 (2006)
- [5] Wheeler, S.J., Näätänen, A., Karstunen, M., Lojander, M.: An anisotropic elastoplastic model for soft clays. Canadian Geotechnical Journal 40, 403–418 (2003)

# A Modified Bounding Surface Hypoplasticity Model for Sands

Gang Wang\* and Yongning Xie

Department of Civil and Environmental Engineering  
Hong Kong University of Science and Technology  
Clearwater Bay, Kowloon, Hong Kong SAR, China  
[gwang@ust.hk](mailto:gwang@ust.hk)

**Abstract.** A modified bounding surface hypoplasticity model is developed to capture distinct dilatancy behaviors of sandy soils during various phases of cyclic loading. The model features a new modulus formulation, a phase transformation surface that is dependent on a state variable and soil density. The effects of accumulated plastic strains on the plastic moduli are also considered. The modified model improves simulation of cyclic mobility and post-liquefaction behavior of both loose and dense sands. The model capacity is demonstrated by comparing the model simulations with a series of undrained cyclic simple shear tests on Fraser River sand.

**Keywords:** constitutive model, bounding surface hypoplasticity, cyclic response.

## 1 Introduction

Much progress has been made during the past thirty years to develop advanced constitutive models to simulate the fundamental stress-strain-strength relationships of granular soils. Among them, the bounding surface model developed by Wang *et al.* [1] has been successfully used to simulate fully nonlinear site response [2] and earthquake-induced liquefaction and deformation of earth structures [3]. However, the original model suffers several drawbacks. The model does not prescribe a zero dilatancy at the limit of critical state. Therefore, it is not consistent with the critical state theory and can not properly characterize the dilatancy behavior in liquefied state. Although the original model can simulate cyclic response of loose sands reasonably well, it can not properly model the dilatancy behavior and the cyclic mobility of dense sands. To overcome these difficulties, a modified bounding surface hypoplasticity model based on the original framework of Wang *et al.* [1] is developed in this study.

## 2 Model Formulation

Following [1], the effective stress is represented by the deviatoric stress ratio  $\mathbf{r} = \mathbf{s}/p$ , where  $\mathbf{s} = \boldsymbol{\sigma} - p\mathbf{I}$  is the deviatoric stress tensor,  $p = 1/3tr(\boldsymbol{\sigma})$  is the mean

---

\* Corresponding author.

effective stress. The stress ratio invariant,  $R = \sqrt{1/2\mathbf{r} : \mathbf{r}}$ , is used to define the following bounding surfaces: The failure surface  $R_f$ , which defines the ultimate limit of an admissible  $R$ ; The maximum prestress surface  $R_m$ , which defines the maximum stress ratio experienced by the material. The phase transformation surface  $R_p$ , which defines the location where transformation from contractive to dilative behavior occurs. These bounding surfaces are illustrated in the  $p - J$  space (where  $J = \sqrt{1/2\mathbf{s} : \mathbf{s}} = pR$ ) and stress ratio space in Fig. 1. In Fig. 1(b), the current stress state is represented by vector  $\mathbf{r}$ . A projection center  $\alpha$  is defined as the last stress reversal point, or is set to the origin if the current stress state exceeds the maximum pre-stress surface  $R_m$ , i.e., virgin loading. An image stress point  $\bar{\mathbf{r}}$  is defined as the point projected on the  $R_m$  surface from the projection center  $\alpha$  through the current stress state point  $\mathbf{r}$ . Scaler quantities  $\rho$  and  $\bar{\rho}$  measure the distances between  $\alpha$ ,  $\mathbf{r}$  and  $\bar{\mathbf{r}}$ , and their ratio  $\bar{\rho}/\rho$  will be used in the plastic shear modulus formulation.

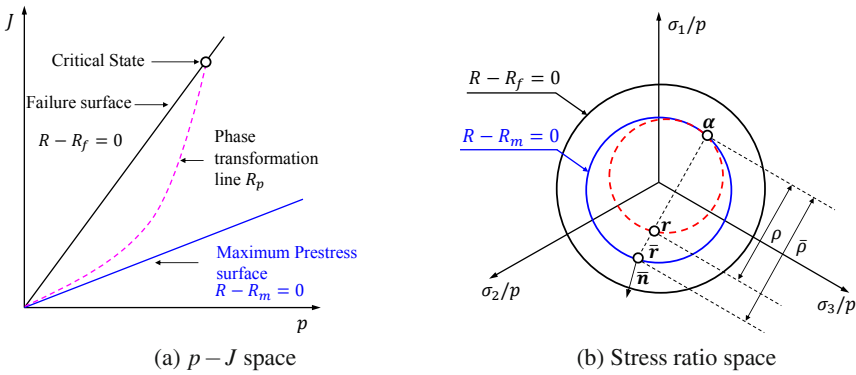


Fig. 1. Bounding surfaces in  $p - J$  space and stress ratio space

The concept of state-dependent dilatancy assumes that  $R_p$  follows the following relationship [4]:

$$R_p = R_f e^{m\psi} \tag{1}$$

where  $\psi$  is a state parameter defined as the difference between the current void ratio  $e_0$  and the critical void ratio  $e_c$  in Fig. 2.  $e_c$  is related to the current mean effective stress  $p$  through the following equation [5]:

$$e_c = e_\Gamma - \lambda \left( \frac{p}{p_a} \right)^\xi \tag{2}$$

where  $e_\Gamma$ ,  $\lambda$  and  $\xi$  are critical state parameters. By examining the laboratory test data, a single value can not be assigned to  $m$  to realistically represent the phase transformation lines of both loose and dense samples. In this study,  $m$  is proposed

to be dependent on the relative density of the sample. Fig. 3 illustrates the phase transformation lines for dense ( $m = 4$ ,  $D_r = 80\%$ ) and relatively loose ( $m = 1.2$ ,  $D_r = 40\%$ ) samples of Fraser River sands. By comparison, the transformation line of the loose sample is much closer to the failure line, indicating it is more contractive than the dense sample.

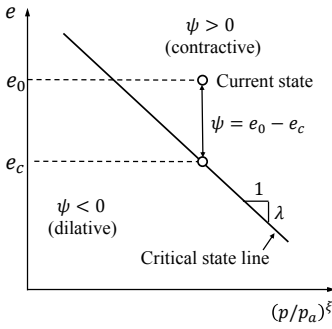


Fig. 2. Critical state line

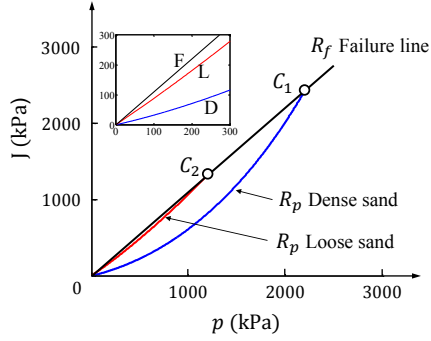


Fig. 3. Phase transformation line

The elastic stress-strain relationship can be written as:

$$\dot{\epsilon}^e = \dot{\epsilon}^e + \frac{1}{3}(tr\dot{\epsilon}^e)\mathbf{I} = \frac{1}{2G}\dot{\mathbf{s}} + \frac{1}{3}\dot{p}\mathbf{I} = \frac{1}{2G}p\dot{\mathbf{r}} + \left(\frac{1}{2G}\mathbf{r} + \frac{1}{3K}\mathbf{I}\right)\dot{p} \quad (3)$$

where  $G$  and  $K$  are elastic shear and bulk moduli, respectively. In this paper, only the plastic strain rate induced by  $p\dot{\mathbf{r}}$  will be considered for simplicity:

$$\dot{\epsilon}^p = \left(\frac{1}{H_r}\bar{\mathbf{n}} + \frac{1}{3K_r}\mathbf{I}\right)(p\dot{\mathbf{r}} : \bar{\mathbf{n}}) \quad (4)$$

where  $H_r$  and  $K_r$  are plastic shear and bulk moduli associated with the deviatoric and volumetric plastic strains. The  $\bar{\mathbf{n}}$  is a deviatoric unit tensor specifying the direction of deviatoric plastic strain rate, defined here as normal to the maximum prestress surface at the image point  $\bar{\mathbf{r}}$  in Fig. 1(b). The  $p\dot{\mathbf{r}} : \bar{\mathbf{n}}$  is loading index. The plastic shear modulus  $H_r$  is defined as:

$$H_r = Gh_r C_H(\xi_q) \left[ \frac{R_f}{R_m} \left(\frac{\bar{\rho}}{\rho}\right) - 1 \right] \left(\frac{p}{p_m}\right)^{1/2} \quad (5)$$

where

$$C_H(\xi_q) = \frac{1}{1 + \alpha\xi_q} \quad \text{and} \quad \xi_q = \int_0^{e^p} \sqrt{\frac{2}{3}} de^p : de^p \quad (6)$$

$h_r$  is a dimensionless material constant,  $C_H(\xi_q)$  accounts for the influence of accumulated deviatoric plastic strain,  $\xi_q$ , on the plastic modulus ( $de^p$  is the deviatoric

plastic strain increment). Parameter  $\alpha$  is used to control the extent of the strain dependence. The strain-dependent term is essential to effectively represent the cyclic mobility. Without the strain-dependent term, a stabilized cyclic stress-strain behavior will eventually be reached under a repeated cyclic loading. Parameter  $\alpha$  is used to control the extent of the strain dependence. A pressure-dependent term  $(p/p_m)^{1/2}$  is included to strengthen the influence of the mean effective stress on the plastic shear modulus, and it can effectively improve the stress-strain hysteresis behaviors.

The plastic bulk modulus  $K_r$  is formulated by modifying the elastic bulk modulus  $K$  as follows:

$$K_r = p_a \frac{1 + e_{in}}{wK} \left( \frac{p}{p_a} \right)^{1/2} = \frac{K}{w} \quad (7)$$

where

$$w = \begin{cases} w_1 = \frac{1}{k_r} \left( \frac{R_m}{R_f} \right)^b \left( \frac{R_p - R}{R_f - R_m} \right), & \text{if } R = R_m \text{ or } R > R_p, \text{ and } \dot{R} > 0 \quad (8a) \\ w_2 = C_K(\xi_v) \left( \frac{R_m + \text{sign}(\dot{R})R}{R_f} \right) \left( \frac{R_p - \text{sign}(\dot{R})R}{R_p + R_m} \right), & \text{otherwise.} \quad (8b) \end{cases}$$

The above formulation controls the volumetric dilatancy of sands. It is noted that  $w_2$  always assume a non-negative value and is used only for a contactive phase.  $w_1$  is used for all dilative phases, but it can also be used prescribe a contractive response if  $R = R_m$  (virgin loading) and  $R < R_p$ . The parameter  $C_K(\xi_v) = d_1(1 + d_2 \tanh(100 \xi_v))$ , where  $\xi_v$  is the plastic volumetric strains accumulated only during dialtive phases,  $d_1$  and  $d_2$  are model parameters whose values may vary with different relative densities. The function  $\tanh$  is used to prescribe a maximum value of the strain-dependent effect.

### 3 Model Simulations

The performance of the proposed model is demonstrated through comparison with a series of cyclic simple shear tests on Fraser River sand conducted at UBC [6]. The test samples were densified to a relative density ( $D_r$ ) of 40% and 81% under applied pressues of 100 kPa and 200 kPa, respectively. Samples were then subjected to cyclic shear for a range of cyclic stress ratios ( $CSR$ ) under constant volume conditions that simulate the undrained response. The calibrated model parameters are summarized in Table 1. The test data and model simulations are presented in Figs. 4 to 5. During the first a few loading cycles, the dense sample ( $D_r = 81\%$ ) exhibits an increasingly stronger contractive phase following each dilative phase. As the effective stress approaches zero, the stress path is repeated following a ‘butterfly’ loop. The shear strain progressively accumulates during each loading cycles, referred to as cyclic mobility. The shape of the stress-strain curve also progressively changes to form a ‘banana’ pattern. On the other hand, the loose sample ( $D_r = 40\%$ ) exhibits

a purely contractive response and continuous reduction of effective stress during the first six cycles. Once the effective stress approaches zero, large cyclic strains suddenly developed. The proposed model demonstrated excellent capability in simulating the effective stress paths and stress-strain behaviors of both dense and loose soil samples.

**Table 1.** Summary of model parameters

Critical state parameters	Phase transformation parameters	Elastic moduli parameters	Plastic shear modulus parameters	Plastic bulk modulus parameters
$e_{\Gamma} = 1.029$	$m = 4$	$G_0 = 208$	$h_r = 0.1$	$k_r = 0.3, \quad b = 0.6$
$\lambda = 0.0404$	$(D_r = 81\%)$	$\nu = 0.05$	$\alpha = 1.5$	$d_1 = 4 \quad (D_r = 81\%)$
$\xi = 0.7$	$m = 1.2$			$d_1 = 1.2$
$R_f = 0.768$	$(D_r = 40\%)$			$(D_r = 40\%)$
				$d_2 = 2$

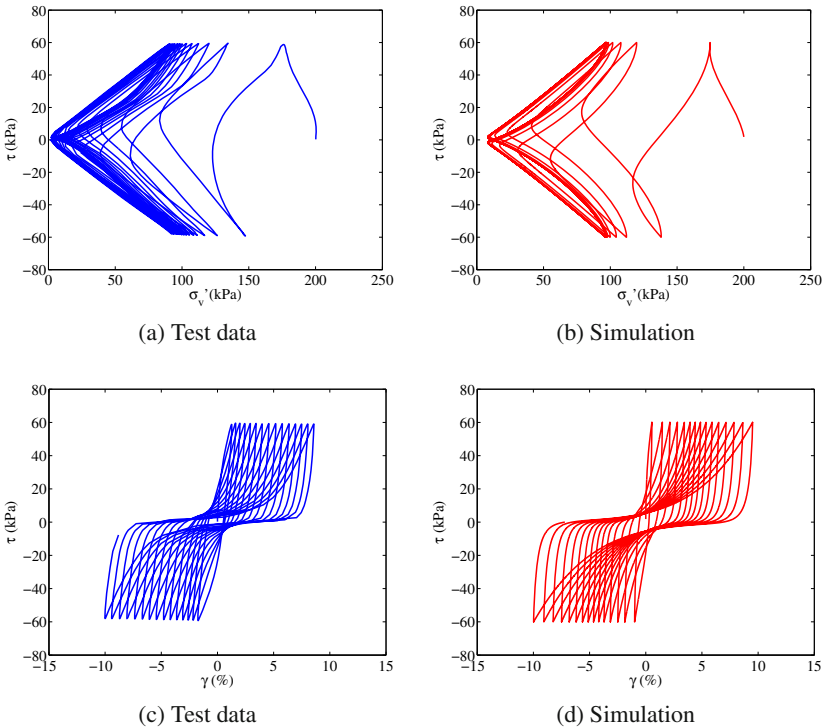


**Fig. 4.** Comparison of test data and model simulation for  $D_r = 81\%$ ,  $p'_0 = 200kPa$ ,  $CSR = 0.3$ . (a)(b) effective stress path, (c)(d) stress-strain curve

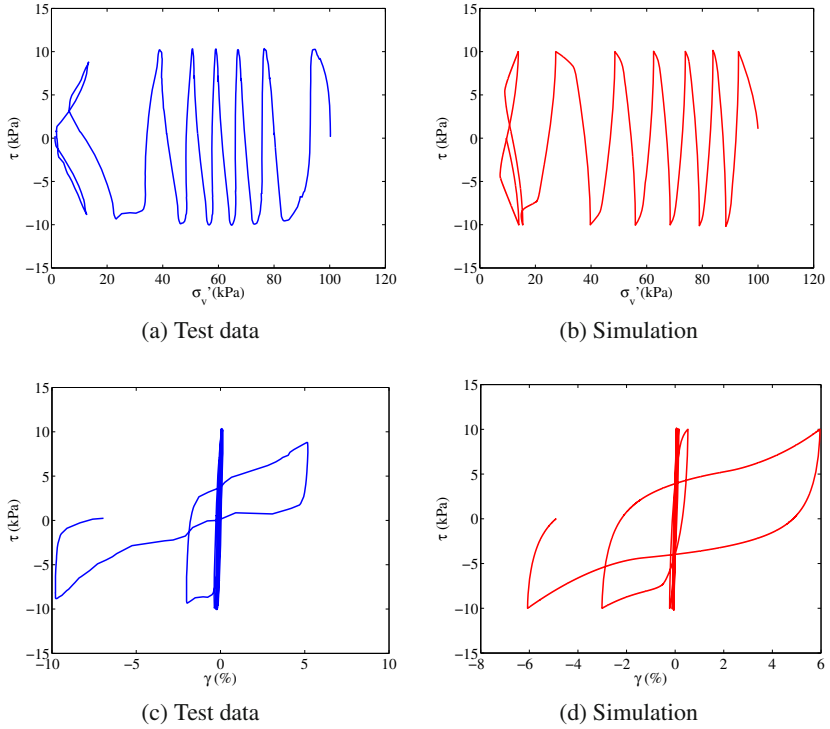


**Fig. 5.** Comparison of test data model simulation for  $D_r = 40\%$ ,  $p'_0 = 100kPa$ ,  $CSR = 0.1$ . (a)(b) effective stress path, (c)(d) stress-strain curve

## 4 Conclusions

The modified bounding surface hypoplasticity model employs a new modulus formulation that improves the simulation of distinct dilatancy behaviors of sandy soils during various phases of cyclic loading. The model demonstrated excellent performance in simulating cyclic mobility and post-liquefaction behavior of both loose and dense sands.

## References

1. Wang, Z.L., Dafalias, Y.F., Shen, C.K.: Bounding surface hypoplasticity model for sand. *Journal of Engineering Mechanics* 116(5), 983–1001 (1990)
2. Li, X.S., Wang, Z.L., Shen, C.K.: A nonlinear procedure for response analysis of horizontally-layered sites subjected to multi-directional earthquake loading. Department of Civil Engineering, University of California, Davis (1992)
3. Wang, Z.L., Makdisi, F.I., Egan, J.: Practical applications of a nonlinear approach to analysis of earthquake-induced liquefaction and deformation of earth structures. *Soil Dynamics and Earthquake Engineering* 26, 231–252 (2006)

4. Li, X.S., Dafalias, Y.F., Wang, Z.L.: State-dependent dilatancy in critical-state constitutive modelling of sand. *Canadian Geotechnical Journal* 36, 599–611 (1999)
5. Li, X.S., Wang, Y.: Linear representation of steady-state line for sand. *Journal of Geotechnical and Geoenvironmental Engineering* 124(12), 1215–1217 (1998)
6. Sriskandakumar, S.: Cyclic loading response of Fraser River sand for validation of numerical models simulating centrifuge tests, Master's thesis. The University of British Columbia (2004)

# Soils in Space

David Muir Wood

University of Dundee, Dundee DD1 4HN, UK

[d.muirwood@dundee.ac.uk](mailto:d.muirwood@dundee.ac.uk)

**Abstract.** Most of the interesting properties of soils and other granular materials arise from the space that exists between and around the individual particles. Tests on mixtures of clay and fine gravel can be interpreted to suggest the loosest degree of packing for which some interaction between particles can occur. Tests on mixtures of sand with flexible fibres show enhanced dilatancy which can be modelled by allowing the fibres to steal some of the void from the sand.

## 1 Introduction

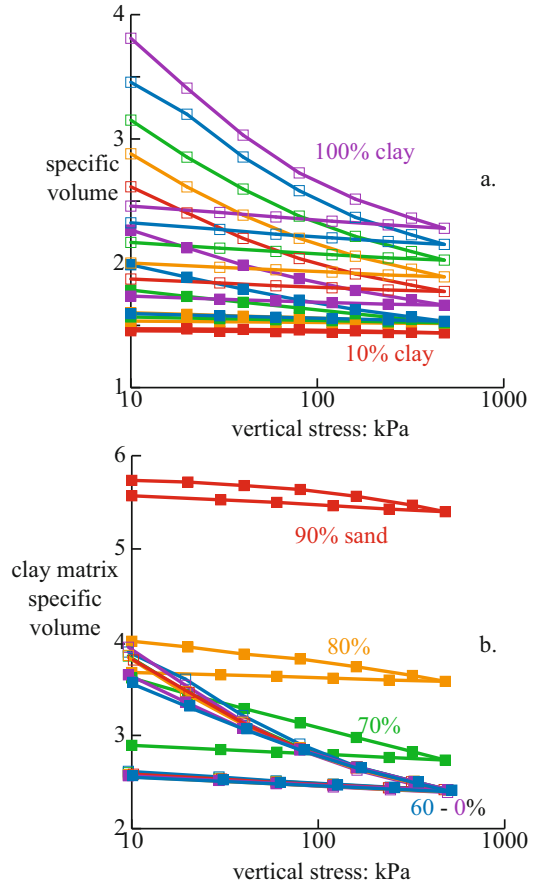
Soils and other granular materials consist of more or less rigid particles surrounded by space (voids). The presence of these voids is the source of many of the surprising aspects of the behaviour of these materials. Soils are formed from particles in space but, for the purposes of analysis of prototype response, have to be treated as continua, using concepts of stress and strain which lose their meaning as the area of inspection shrinks to the order of a few particles. It is this particle-continuum duality that underpins the fascination and challenges for the development of constitutive modelling.

## 2 Mixed-Up Soils

Soil mechanics research has concentrated on ‘simple’ soils - ‘clays’ and ‘sands’ - and has tended to neglect more naturally realistic soils which contain a mixture of soil types. However, it is tempting even with such soils to start with study of some simple mixtures - for example, a mixture of kaolin clay with Leighton Buzzard fine gravel 2mm fraction [8; 9; 10].

Looking at the results of oedometer tests in Figs 1a it is clear that there is a monotonic change in the response as the proportions of clay and gravel are varied. As the sand content increases the one-dimensional stiffness increases. This is expected.

**Fig. 1.** One-dimensional compression of mixtures of kaolin with fine gravel [9]



The usual definitions of specific volume  $v$  and void ratio  $e = v - 1$  are (Fig 2a):

$$v = 1 + e = \frac{V_v + V_g + V_c}{V_g + V_c} = Cv_c + (1 - C) \tag{1}$$

where  $V_c, V_g, V_v$  are the volumes of clay, gravel and voids respectively and  $C = V_c / (V_c + V_g)$  is the proportional clay content (Fig 2). We can improve our understanding of these results if we look at the mixture from the point of view of either the clay or the gravel separately. If we just think of the clay particles and the water-filled voids, and ignore the presence of the gravel particles, we can define a clay matrix void ratio  $e_c$  or clay matrix specific volume  $v_c$  (Fig 2b):

$$v_c = 1 + e_c = \frac{V_v + V_c}{V_c} \tag{2}$$

It is very striking that the one-dimensional compression of the mixture is essentially identical to that of the clay matrix, expressed in terms of clay specific volume  $v_c$ ,

for clay contents of 40-100% (gravel contents of 0-60%) (Fig 1b). Gathering various observations, it seems that the proportional content of the granular gravel component has to be at least 60-70% before the granular particles start to interact and to have an influence on the mechanical response distinct from the occupation of void space.

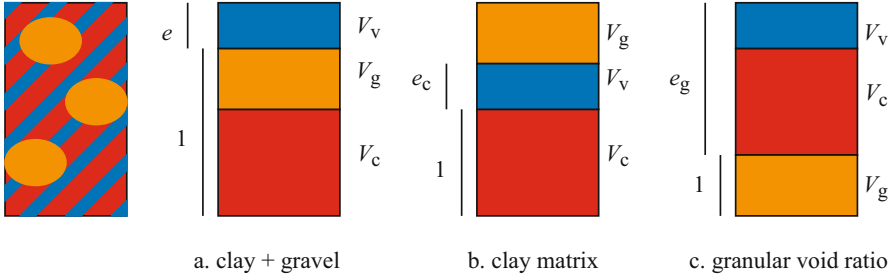


Fig. 2. Clay matrix void ratio  $e_c$  and granular void ratio  $e_g$

We can define a granular specific volume  $v_g = 1 + e_g$  (where  $e_g$  is granular void ratio) (Fig 2c):

$$v_g = 1 + e_g = \frac{V_v + V_c + V_g}{V_g} = \frac{v}{1 - C} = \frac{1}{f_g} \tag{3}$$

where  $f_g$  is the granular volume fraction - the ratio of volume of granular material to the total volume of the mixture (including the voids). This is the specific volume of the gravel treating the volume of the clay as simply a component of the voids. We can deduce:

$$v_c = \left[ \frac{1 - C}{C} \right] \left[ \frac{1 - f_g}{f_g} \right] \tag{4}$$

From Fig 1a it seems that intergranular influence is occurring for  $v \sim 1.6 - 2$  for  $C = 40\%$ , or for  $v \sim 1.6 - 1.7$  for  $C = 30\%$ . From (3) this implies granular specific volume  $v_g \sim 3$  or granular volume fraction  $f_g \sim 0.33$  for initiation of particle interaction.

The densest arrays of spherical particles are face-centred cubic structures for which the volume fraction for spherical particles of single diameter  $d$  with spacing  $s$  is:

$$f_g = \frac{\pi}{3\sqrt{2}} \left( \frac{d}{s} \right)^3 \tag{5}$$

This has a maximum value of 0.74 when  $s = d$ .

If a threshold value of  $f_g \sim 0.33$  is inserted in (5) the critical spacing that emerges is  $s \sim 1.23d$ . The subangular to subrounded particles of gravel in the present study are of course not spherical but it is surprising that the particles have on average to be as close as this before any detectable mechanical interaction occurs.

We can interpret this result as an indication that even at a specific volume of  $v_g \sim 3$  the granular material is able to play some part in the transfer of stress. It is suggested [6], following [11], that the average number of contacts per particle

Fig. 3. Void ratio and coordination number [11]

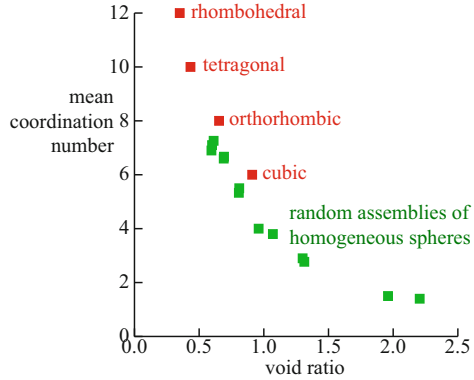
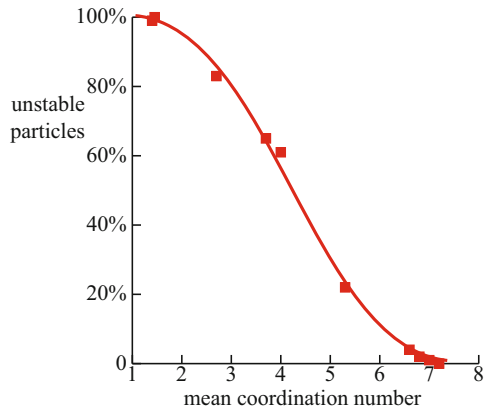


Fig. 4. Coordination number and proportion of unstable particles [11]



(coordination number  $\bar{N}$ ) is inversely proportional to  $v(v - 1)$  (Fig 3). Coordination number below three cannot lead to equilibrium. Oda [11] records the increasing number of particles with fewer than 4 contacts as a function of void ratio or average coordination number (Fig 4). These ‘unstable’ particles are likely to be mobile in the presence of fluid flow, for example, producing scour around the foundation of a structure on the seabed. Oda’s complete instability, corresponding to an average coordination number of about 1.5 (Fig 4), indicates a (granular) void ratio around  $e_g \sim 2$  (Fig 3) or granular specific volume  $v_g \sim 3$  which corresponds with the onset of particle interaction observed for the clay-gravel mixtures (Fig 1a).

Where should the boundary be placed between soil and fluid where scour is occurring? There is a continuous change in density from the seabed soil to the fluid with dispersed suspended particles (Fig 5). In between there is some particle interaction and energy transfer. We might choose to reclaim for geomechanics more of the transition region, using a model extrapolated to this low coordination number regime. The truly fluid behaviour would then be restricted to material in suspension so dilute that no significant particle interactions were occurring, material which has reached the top of Oda’s instability curve (Fig 4).

Fig. 5. Soil-fluid interface

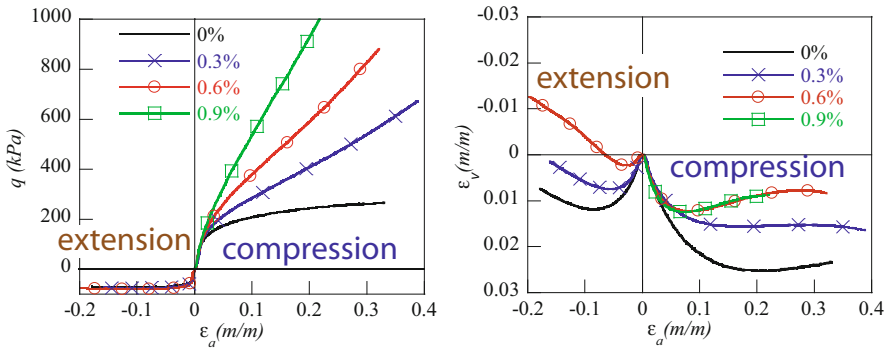
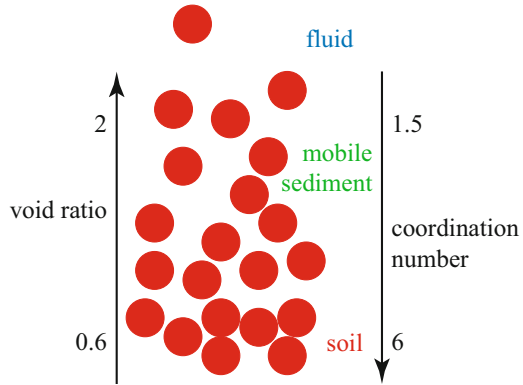


Fig. 6. Drained triaxial tests on sand-fibre mixtures [11; 7]

### 3 Fibres and Roots

It is well known that plant roots are beneficial in their contribution to the stability of slopes. The roots provide some reinforcement to the soil to a certain depth and, provided they remain intact, they provide enhanced strength to the near surface soils. An analogue of the interaction of flexible plant roots with soil is provided by tests on mixtures of sand with flexible polypropylene fibres. Experimentally it is found that the fibre-sand mixture has a higher strength in drained triaxial compression but very little change in strength in triaxial extension (Fig 6). It turns out to be difficult to prepare mixtures with fibres uniformly distributed across all possible orientations: the moist tamping procedure used tends to produce fibres with orientations within about 30° of the horizontal [3]. It is evidently important to know what is the actual distribution of fibre or root orientations. Horizontally oriented fibres provide little reinforcement benefit in triaxial extension tests in which the horizontal strains are expected to be compressive.

However, it is found in triaxial tests and direct shear tests that in the presence of fibres the sand becomes significantly more dilatant (Fig 6). In undrained testing

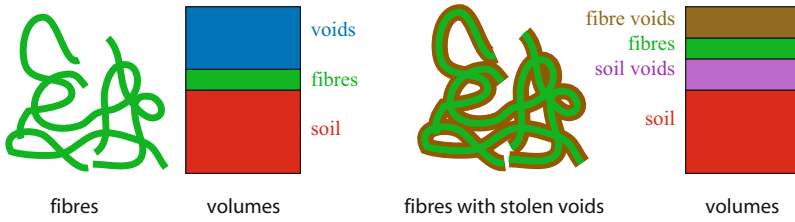


Fig. 7. Assignment of stolen voids to fibres

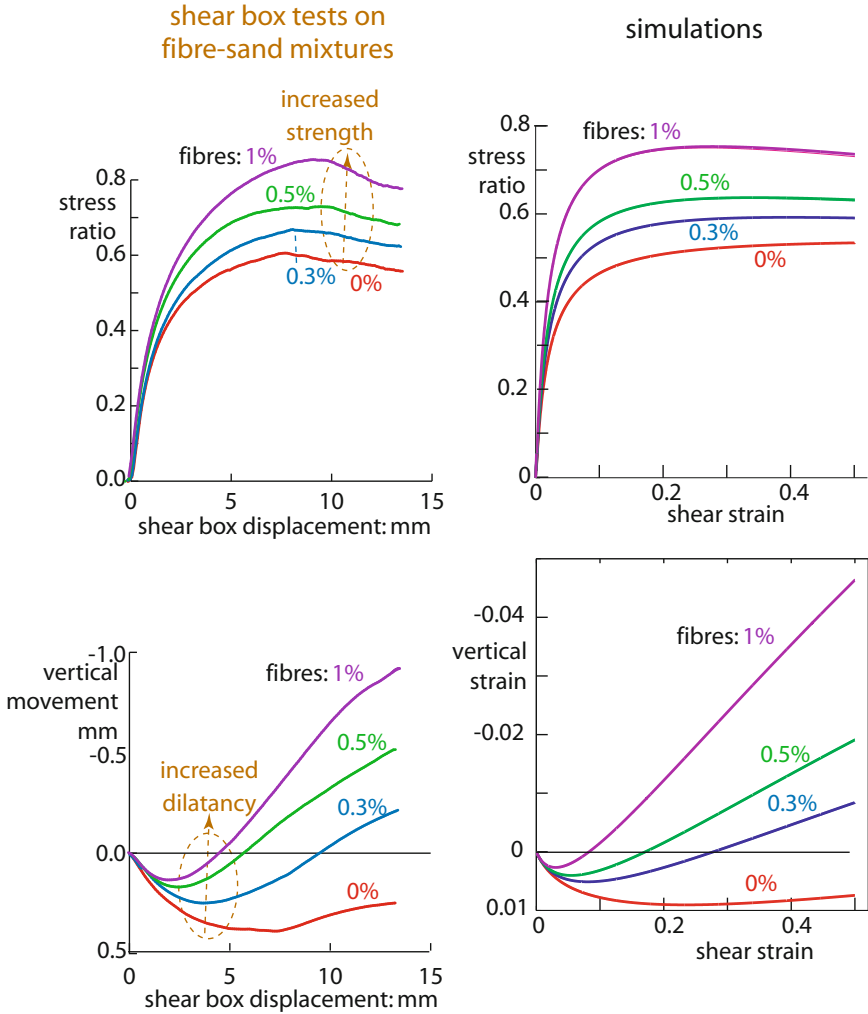


Fig. 8. Simulation of direct shear tests on sand-fibre mixtures

the response is also more dilatant and resistance to liquefaction is correspondingly increased [2]. A consistent means by which these effects can be taken into account in adapting the Severn-Trent sand model (for example) [4; 5] (the constituent sand itself should not see any change in its mechanical response in the presence of the fibres) is to assign part of the void space inalienably to the fibres (Fig 7). Thus the mere presence of the fibres steals some of the void previously available to the sand which consequently feels denser. With such an assumed 'fibrespace' it is possible to make rather satisfactory simulations of the laboratory tests (Fig 8).

## 4 Conclusion

We have encountered two examples of the interaction of soils or other granular materials with the space around the particles. The response of mixtures of clay with fine gravel shows a response governed by the clay matrix up to a surprisingly high proportion of gravel. This result can be interpreted to indicate the density of packing at which particles of a somewhat narrowly graded granular material will begin to interact. This might be used as evidence in support of the extrapolation of soil models to the description of flow of dilute sediments. Plant roots and flexible fibres steal some of the void space from the soil with which they are mixed. It is necessary to take account of these stolen voids in order to produce reasonable simulations of the mechanical response of the mixtures.

Space - or void - is the key common factor in these various applications.

**Acknowledgements.** This paper is a shortened version of an invited lecture presented at the 13th Portuguese National Geotechnical Congress in Lisbon in April 2012.

## References

- [1] Diambra, A., Ibraim, E., Muir Wood, D., Russell, A.R.: Fibre reinforced sands: experiments and modelling. *Geotextiles and Geomembranes* 28(3), 238–250 (2010)
- [2] Diambra, A., Ibraim, E., Russell, A.R., Muir Wood, D.: Modelling the undrained response of fibre reinforced sands. *Soils and Foundations* 51(4), 625–636 (2011)
- [3] Diambra, A., Russell, A.R., Ibraim, E., Muir Wood, D.: Determination of fibre orientation in reinforced sands. *Géotechnique* 57(7), 623–628 (2007)
- [4] Gajo, A., Muir Wood, D.: A kinematic hardening constitutive model for sands: the multi-axial formulation. *International Journal for Numerical and Analytical Methods in Geomechanics* 23(5), 925–965 (1999)
- [5] Gajo, A., Muir Wood, D.: Severn-Trent sand: a kinematic hardening constitutive model for sands: the  $q - p$  formulation. *Géotechnique* 49(5), 595–614 (1999)
- [6] Hicher, P.-Y., Chang, C.: Instability and failure in soils subjected to internal erosion. In: Oka, F., Kimoto, S., Murakami, A. (eds.) *Prediction and Simulation Methods for Geohazard Mitigation*, pp. 325–330. CRC Press, Balkema (2009)
- [7] Ibraim, E., Diambra, A., Muir Wood, D., Russell, A.R.: Static liquefaction of fibre-reinforced sand under monotonic loading. *Geotextiles and Geomembranes* 28(4), 374–385 (2010)

- [8] Kumar, G., Muir Wood, D.: Mechanical behaviour of mixtures of kaolin and coarse sand. In: Fleck, N., Cocks, A. (eds.) IUTAM Symposium on Mechanics of Granular and Porous Materials, pp. 57–68. Kluwer Academic Publishers (1996)
- [9] Kumar, G., Muir Wood, D.: Fall-cone and compression tests on clay-gravel mixtures. *Géotechnique* 49(6), 727–739 (1999)
- [10] Muir Wood, D., Kumar, G.: Experimental observations of behaviour of heterogeneous soils. *Mechanics of Cohesive-Frictional Materials* 5(5), 373–398 (2000)
- [11] Oda, M.: Co-ordination number and its relation to shear strength of granular material. *Soils and Foundations* 17(2), 29–42 (1977)

# Unique Quantification of Critical State in Granular Media Considering Fabric Anisotropy

Jidong Zhao\*, Ning Guo, and Xiang-song Li

Department of Civil and Environmental Engineering, Hong Kong University of Science and Technology, Clearwater Bay, Kowloon, Hong Kong  
jzhao@ust.hk

**Summary.** Classic definition on the critical state of granular soils lacks proper reference to the fabric structure developed at critical state. This paper presents a study on the characteristics of critical state in consideration of fabric anisotropy in granular media, based on Discrete Element Method (DEM) simulations and a *contact-based* fabric tensor. In addition to the unique relation between the critical void ratio and the mean effective stress, we identify a unique relation between the mean effective stress and a fabric anisotropy parameter,  $K$ , defined by the first joint invariant of deviatoric stress tensor and the deviatoric fabric tensor. The relation does not depend on the specific loading paths. The two unique relations combine to present a unique spatial critical state line (CSL) in the 3DI space  $K$ - $e$ - $p$  for a granular material whose projection in the  $e$ - $p$  plane is the unique CSL in classic critical state theory.

**Keywords:** critical state, fabric tensor, anisotropy, spatial critical state line, DEM.

## 1 Introduction

The classic critical state refers to an ultimate state of continuous shear deformation with constant volume under constant stress. This definition of critical state emphasizes only the scalar-valued void ratio (or fabric isotropy) and lacks a proper reference to the behavior of anisotropic fabric. Numerous studies have indicated that the behavior of granular soil is predominantly anisotropic under shear (see [1-3]). The fabric anisotropy has to be considered in the definition of critical state. Motivated by the Anisotropic Critical State Theory (ACST) recently proposed by Li & Dafalias (see [4]), the present study seeks to use DEM to explore the unique characteristics of critical state in consideration of fabric anisotropy.

## 2 Contact-Normal Based Fabric Tensor and Joint Invariants

In a cubic container with rigid walls we generate around 32,000 polydisperse spherical particles with radii ranging from 0.2 mm to 0.6 mm. A linear contact law

---

\* Corresponding author.

with Coulomb's friction governing the sliding is employed. The interparticle friction coefficient adopts a value at 0.5. Isotropic samples with different initial void ratios are prepared using a technique proposed in Guo & Zhao (2012). The obtained samples are monotonically sheared under either drained or undrained (constant volume) conditions. Special numerical schemes are designed to shear the samples at a constant intermediate principal stress ratio  $b = (\sigma_2 - \sigma_3) / (\sigma_1 - \sigma_3)$  loading path. Five cases of  $b$  have been investigated,  $b = 0, 0.25, 0.5, 0.75, 1$ . Constant  $p'$  tests are also carried out to obtain more data points. We employ the contact-based definition of fabric tensor proposed by Satake (see [5]) to characterize the fabric structure:

$$F_{ij} = 15(\phi_{ij} - \delta_{ij}/3)/2, \quad \phi_{ij} = \int_{\Theta} E(\Theta) n_i n_j d\Theta \quad (1)$$

where  $\mathbf{n}$  is the unit normal vector between two contacted particles.  $\Theta$  denotes the orientation of  $\mathbf{n}$  relative to the global coordination system.  $E(\Theta)$  is the distribution probability density function (PDF). The second-order Fourier expansion of  $E(\Theta)$  is adopted to characterize the contact normals such that  $E(\Theta) = (1 + F_{ij} n_i n_j) / (4\pi)$ . The second-order fabric tensor  $F_{ij}$  is deviatoric and symmetric, and will be used to characterize the fabric anisotropy in an assembly. Its invariants and joint invariants with the deviatoric stress tensor are defined below

$$J_1^F = F_{ii} = 0, \quad J_2^F = \frac{1}{2} F_{ij} F_{ji}, \quad J_3^F = \frac{1}{3} F_{ij} F_{jk} F_{ki} \quad (2)$$

$$K_1 = K = \sigma'_{ij} F_{ji}, \quad K_2 = \sigma'_{ij} F_{jk} F_{ki}, \quad K_3 = \sigma'_{ik} \sigma'_{kj} F_{ji}, \quad K_4 = \sigma'_{ik} \sigma'_{kj} F_{jl} F_{li} \quad (3)$$

where  $\sigma'_{ij} = \sigma_{ij} - p' \delta_{ij}$  is the deviatoric stress tensor.

### 3 Results and Discussion

A total of over 80 numerical samples with different initial states (e.g., in terms of density and initial confining pressure) have been sheared to critical state under various monotonic loading paths. All samples reach a relatively steady state with constant stress and constant volume after an axial strain level at around 40% which satisfies the description of classic critical state. The soil state beyond this point has been taken as critical state. While certain degree of fluctuations in the soil response stays at this strain level, averages have been taken for the concerned quantities over a sustained stage of deformation, e.g., for an axial strain ranged between 40%~50%.

Data points for the critical void ratio are correlated to the mean effective stress  $p'$  in Fig. 1a. All data points collapse to a unique linear relation of the following general expression

$$e_c = e_\Gamma - \lambda_e (p'/p_a)^\xi \tag{4}$$

where  $p_a = 101 \text{ kPa}$  is the atmospheric pressure. Similar linear relations have previously been found valid for Erksak sand and Toyoura sand. The second invariant of critical fabric anisotropy,  $F_c = \sqrt{3F_{ij}^c F_{ij}^c / 2}$ , is used to represent the degree of fabric anisotropy. Plotted in Fig. 1b is the correlation between  $F_c$  and  $p'$  at critical state. For each individual case of  $b$ , we observe a dependence of  $F_c$  on the critical mean effective stress according to the following power law:

$$F_c = m_F p'^\zeta \tag{5}$$

where  $m_F$  denotes a parameter dependent on the Lode angle or  $b$ , e.g.,  $m_F = \hat{m}_F(b)$ .  $\zeta = -0.14 \sim -0.09$ . It is readily seen that a unique critical fabric structure independent of loading path is not attainable, according to the current definition of fabric tensor.

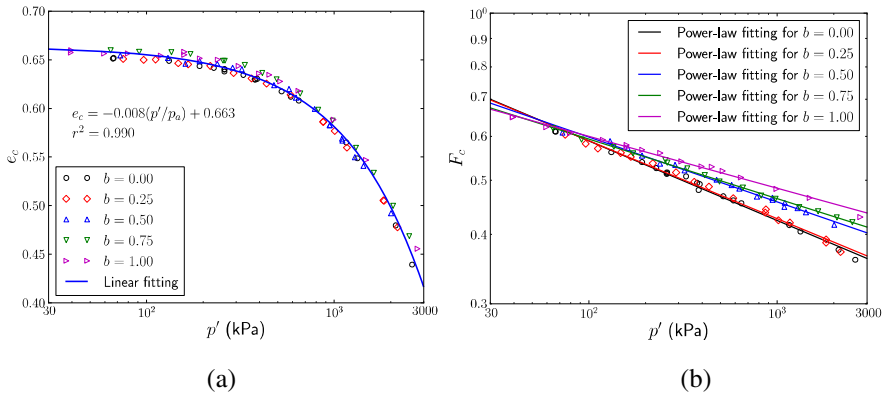


**Fig. 1.** Correlation between the critical void ratio (a) and the critical fabric anisotropy (b) with the mean effective stress

Based on contact-based fabric tensor, no unique property appears to be identifiable for the critical fabric anisotropy alone. However, the first joint invariant,  $K$ , has been found to correlate with  $p'$  at critical state in a unique way, as shown in Fig. 2. A striking power law correlation between the two is found to fit all data well:

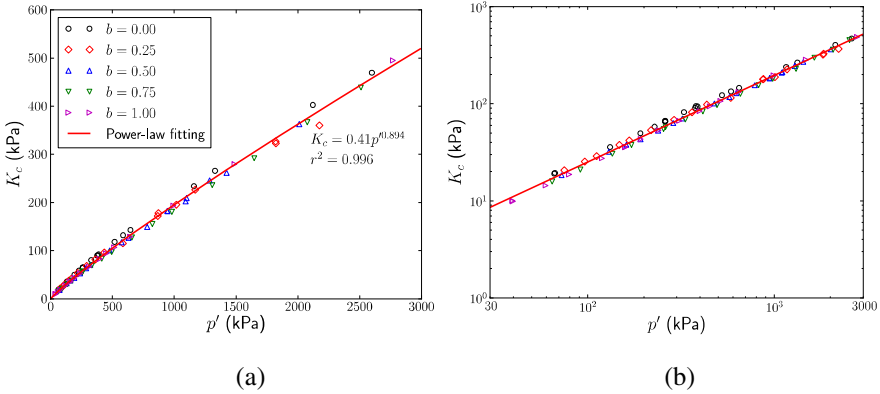


**Fig. 2.** Correlation between the first joint invariant  $K$  and  $p'$  at critical state by a power law fitting: (a) in a natural scale; (b) in a log-log plot

$$K_c = \alpha p'^{\zeta} \tag{6}$$

where  $\alpha = 0.41$  and  $\zeta = 0.894$  for the obtained data. A similar correlation exists for the fourth joint invariant, but no unique correlations can be found for the other two joint invariant. Based on Figs. 1 and 2 as well Eqs. (4) and (6), we see the three quantities  $e_c$ ,  $K_c$  and  $p'$  are actually inter-correlated with one another. A spatial critical curve can then be plotted in the space of  $e_c - p' - K_c$ , as shown in Fig. 3. The projects of this spatial curve onto the plane of  $e_c - p'$  and  $K_c - p'$  gives the unique relation in Figs. 1 and 2 and Eqs. (4) and (6), respectively. This new critical state curve nicely unifies the classic critical state concept with the case in consideration of fabric anisotropy. While a contact-based fabric tensor has been used for the study, how to reconcile the finding with the Anisotropic Critical State Theory in [4] which was derived from a *void-based* fabric tensor is still under investigation.

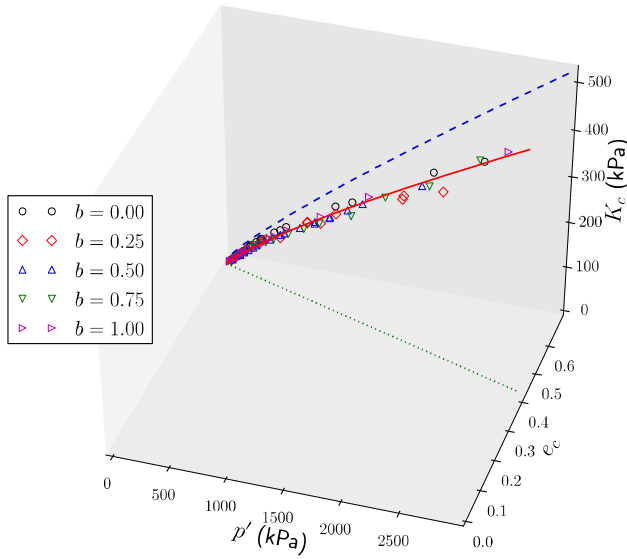


**Fig. 3.** A unique critical state line (CSL) in the space of  $e_c - p' - K_c$

### 4 Conclusion

A unique relation between the first joint invariant of a *contact-based* fabric tensor and the deviatoric stress tensor has been identified at critical state of granular sand. Based on the relation, a unique critical state line (CSL) has been found in the space of  $e_c - p' - K_c$  whose projection in the  $e_c - p'$  plane is the CSL in classic critical state theory. The new CSL provides a practical unique definition of critical state in granular media in consideration of fabric anisotropy.

**Acknowledgement.** This work was supported by Research Grants Council of Hong Kong (GRF 622910).

### References

- [1] Yoshimine, M., Ishihara, K., Vargas, W.: Effects of principal stress direction and intermediate principal stress on undrained shear behavior of sand. *Soils Found.* 38(3), 179–188 (1998)
- [2] Li, X., Li, X.S.: Micro-macro quantification of the internal structure of granular materials. *J. Eng. Mech. ASCE* 135(7), 641–656 (2009)

- [3] Guo, N., Zhao, J.: Signature of anisotropy in granular materials under shear. *Computers & Geotechnics* (under review, 2012)
- [4] Li, X.S., Dafalias, Y.F.: Anisotropic critical state theory: the role of fabric. *J. Eng. Mech. ASCE* 138(3), 263–275 (2012)
- [5] Satake, M.: Fabric tensor in granular materials. In: Vermeer, P.A., Luger, H.J. (eds.) *Deformation and Failure of Granular Materials*, pp. 63–68. Balkema, Rotterdam (1982)

# Peculiarities of Limiting States in Simulated Drained and Undrained Assemblies of Elliptical Particles

Leo Rothenburg<sup>1,\*</sup> and Roberto Olivera-Bonilla<sup>2</sup>

<sup>1</sup> University of Waterloo, 200 University Avenue, Waterloo, Ontario, Canada N2L 2T3

<sup>2</sup> Golder Associates, Burnaby, British Columbia, Canada V5C 6C6

leo.rothenburg@uwaterloo.ca

**Summary.** The study is aimed at characterizing micromechanical characteristics of large shear strain behavior during transition to critical/steady state in simulated granular assemblies. It is demonstrated that there are substantial differences in which various attributes of micromechanical response evolve in drained and undrained situations, pointing to the possibility that volumetric constraints due to presence of fluid in voids may alter mechanisms of large strain behavior in comparison with drained response.

**Keywords:** Critical state, steady state, fabric, elliptical particles, numerical simulations.

## 1 Introduction

There is a substantial body of evidence suggesting that shear deformations transform the internal structure of sands in a way that deformations can eventually continue with no volume change under Mohr-Coulomb-type of stress state. This includes liquefaction of sands, which also involves volume-preserving deformations. Both drained and undrained cases can be typically rationalized within concepts of critical state soil mechanics. However, it is still a hotly debated topic whether the *critical state* identified by Casagrande [1] from drained tests and the *steady state* described by Castro [2] based on undrained testing truly refer to the same state of matter. This cannot be resolved without studying possible differences in grain-level mechanisms involved during drained and undrained deformations. This is addressed in the present article based on numerical simulations of drained and undrained tests on granular assemblies.

## 2 Micromechanics View on the Critical State

Observations on the evolution of intergranular contacts in numerically simulated assemblies clearly suggest that under monotonic shear deformations these systems

---

\* Corresponding author.

evolve towards the state where the number of contacts stabilizes at some level which is independent on the number of contacts initially present, Rothenburg and Kruyt [3]. This behavior mimics transition to steady state in physical systems where the macroscopic measure of packing, the void ratio, was observed to evolve towards the critical value introduced by Casagrande [1]. Although there is only an approximate link between the void ratio and the number of intergranular contacts (taken per particle and expressed as the average coordination number), the observed evolution of the coordination number towards a unique value points to the physical origin of processes during transition to the critical state in sands. When the initial number of contacts is greater than the critical value, contacts are disintegrated under shear deformations, the assembly dilates until the number of contacts stabilizes and deformations proceed at a constant volume. When the number of contacts initially is less than critical, contacts are created and the assembly contracts until the number of contacts stabilizes at critical state.

Observations also suggest that processes of contact creation and disintegration do not cease at critical state. All that happens eventually is that rates of contact creation and disintegration equalize leaving the number of contacts constant. A simple first order kinetic theory based on this view of the transition to steady state remarkably accurately represents the evolution of the coordination number in simulated system [3].

A deeper understanding of transition to critical state comes from the observation that even at relatively low strains the system reaches the state of static determinacy, i.e. the number of contact force components is equal to the number of equations of equilibrium [4]. This immediately links the critical coordination number  $\Gamma_\infty$  to the fraction of contacts where friction is mobilized at critical state. Indeed, in an assembly of  $N$  particles there are  $\frac{1}{2}N\Gamma_\infty$  physical contacts with two force components per contact for plane systems, i.e.  $N\Gamma_\infty$  force components that must satisfy  $3N$  equations of static equilibrium. Presence of mobilized friction in a certain fraction of contacts  $f$  reduces the number of unknown force components by  $\frac{1}{2}fN\Gamma_\infty$ . Equating the number of unknown forces to the number of equations gives the critical coordination number as  $\Gamma_\infty = 6/(2 - f)$ . If friction cannot be mobilized at all, e.g. an infinite friction coefficient, the critical coordination number is expected to be  $\Gamma_\infty = 3$ , in accordance with simulations [3].

When the system is strictly at the boundary of static determinacy (i.e. no redundancy), destruction of a single contact makes it impossible to maintain static equilibrium until a new contact is formed. This contact creation-destruction supports deformations in steady state. It appears that unstable conditions occur all through the assembly and it is manifested in presence of a certain fraction of particles with less than 3 contacts (“rattlers”) whose presence is essential to maintain the system in a mobile state. Different particles likely becomes “rattlers” on and off and this is how statistically homogeneous deformations are maintained.

The described processes of contact creation and disintegration occur in a directional manner, when disintegration of contacts is precipitated by extension strain that tends to disrupt contacts more aligned along the direction of extension. Creation of contacts is more likely in the direction of compression. As a result, contact orientations reach the state of limiting anisotropy, which is unique in the sense that the same anisotropy develops irrespective if the critical state is approached from the “loose” or “dense” side relative to the “critical” coordination number.

### 3 Undrained Simulations

Saturation effects within the DEM scheme were accommodated by assuming that voids are filled with compressible fluid. The fluid transfer between voids occurs as if neighboring voids are connected by channels with the flow rate in proportion to the pressure difference between voids. When the particle skeleton behaves elastically in this model (fixed contacts and no slip) this solid-fluid system behaves according to rules of Bio’s poro-elasticity, which was verified by solving the Trzagli one-dimensional consolidation problem and comparing with the analytical solution. For simulations involving disintegration of contacts and coalescence of voids, the fluid mass balance rules were used. Elliptical particles were used in simulations and interparticle interactions were treated in a non-linear fashion according to Hertz’s law. More details can be found in [5]. The emphasis of this study is on differences in the performance of drained and undrained systems, particularly in relation to conditions in steady state.

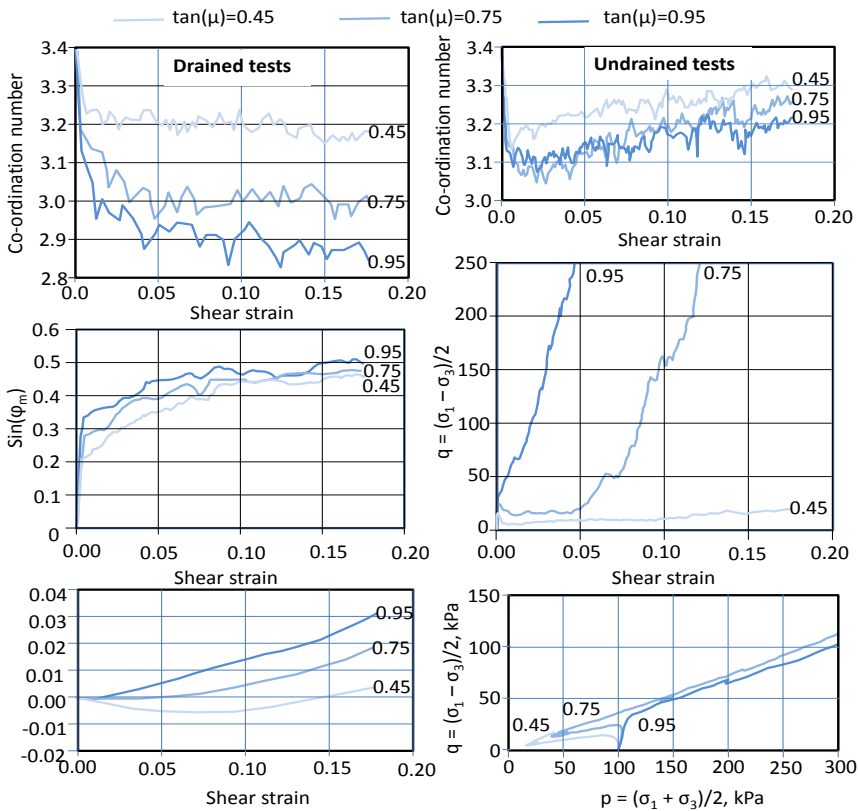


Fig. 1. Drained and undrained simulations with different interparticle friction

Drained and undrained tests in illustrated in Figure 1 give expected patterns for reasonably loose systems, with the friction coefficient not affecting drained behavior qualitatively while completely altering the undrained performance towards liquefaction at the lowest friction angle studied. Perhaps the most remarkable observation from Figure 1 is that *the co-ordination number does not stabilize in undrained tests.*

#### 4 Differences between Drained and Undrained Mechanisms

While basic features of micromechanical response in simulated assemblies are similar in drained and undrained situations, i.e. inter-granular contacts preferentially disintegrate and are spontaneously created to restore local equilibrium, details likely differ. It appears that deformations under strict volumetric control both locally and globally have insufficient freedom to equalize rates of contact creation and disintegration, shifting the process towards disintegration of contacts, until the limit of mechanical stability is reached. This can be observed in simulations detailed in Figure 2 which summarizes tests carried out on assemblies with different initial coordination number, all other attributes the same.

Shear stress versus strain curves at the top of Figure 2 feature normal patterns, with the peak shear strength showing a definitive correlation with the initial coordination number. However, the evolution of coordination number in each of the three tests shows no tendency to reach some common “critical” state. Nevertheless, deformations do occur without volume change and, in the case of the test with the middle peak strength, in steady state. In all these three tests the system attains mobility after peak strength is reached and the coordination number drops by about the same amount in all three tests, as can be seen in the lower right part of Figure 2.

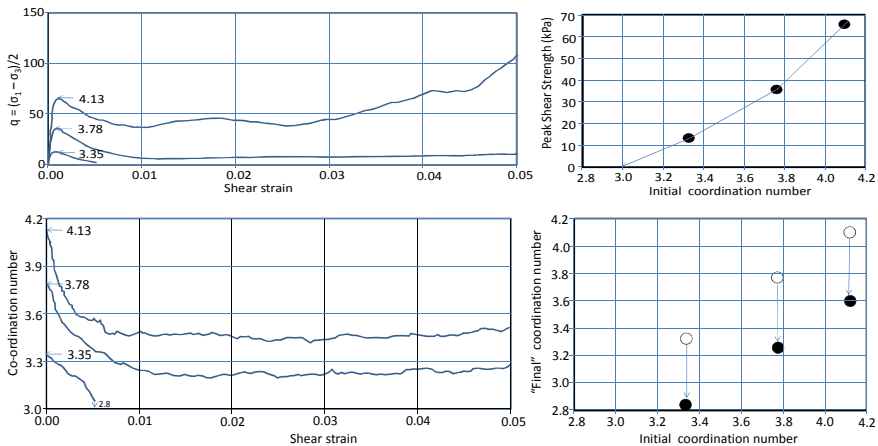


**Fig. 2.** Undrained simulations with different initial coordination number

Perhaps the observed behavior reflects the contact disintegration in a way that leaves some particles not to remain in contact with the skeleton, eventually assuring mobility when their numbers accumulate. In the drained assembly, where local dilation and spontaneous volume reductions are taking place, particles become re-engaged again as part of the load-carrying skeleton. This may not occur in the case of volume-restricted deformations.

## 5 Conclusions

Numerical simulations of undrained granular assemblies show features of micro-mechanical response in steady state that are incompatible with the attributes of critical state as known from drained simulations.

## References

- [1] Casagrande, A.: Characteristics of cohesionless soils affecting the stability of earth fills. In: *Contributions to Soil Mechanics 1925-1940*, pp. 257–276. Boston Society of Civil Engineers (1936)
- [2] Castro, G.: *Liquefaction of Sands*. PhD thesis. Harvard University, Cambridge, Massachusetts (January 1969)
- [3] Rothenburg, L., Kruyt, N.P.: Critical state and evolution of coordination number in simulated granular materials. *Int. J. Solids Structures* 41, 5763–5774 (2004)
- [4] Kruyt, N.P., Rothenburg, L.: Plasticity of granular materials: a structural-mechanics view *Powders & Grains 2009*. In: Nakagawa, M., Luding, S. (eds.) *AIP Conference Proceedings*, vol. 1145, pp. 1073–1076 (2009)
- [5] Olivera-Bonilla, R., Rothenburg, L.: Effects of interparticle friction on the undrained response of granular media. In: Garcia-Rojo, R., McNamara, S., Herrmann, H. (eds.) *Powders and Grains 2005, Conference Proceedings*, pp. 1097–2001 (2005)

# Microstructural Modeling of Granular Materials with Inner Forces

Pierre-Yves Hicher

Research Institute in Civil and Mechanical Engineering UMR CNRS 6183  
Ecole Centrale Nantes-University of Nantes, France  
pierre-yves.hicher@ec-nantes

**Summary.** In this paper, we present a method to take into account the existence of inner forces between grains and their influence upon the mechanical behavior of granular assemblies. Two examples were retained. The first one concerns unsaturated granular materials for which we have considered capillary forces depending on the degree of saturation. The second one concerns extraterrestrial soils for which surface energy forces, such as Van der Waals forces, cannot be neglected due to tiny atmospheric pressure.

**Keywords:** granular materials, capillary forces, surface energy forces, homogenization.

## 1 Introduction

Macroscopic properties of granular materials are governed by the properties of inter-particle contacts. A homogenization technique has been developed to obtain an elastoplastic stress-strain relationship for these types of materials using a static approach. This approach is based on a technique consisting of a localization operator relating the macro stresses to the local contact forces and a homogenization operator relating the grain displacements to the macro strains. Local forces and displacements are related through a constitutive law at the contact level.

## 2 Dry Unbounded Granular Materials

For dry unbounded granular materials under common environmental conditions, the inter-particle forces are solely related to the applied external stresses. Detailed expressions of the homogenization and localization operators, and of the local constitutive law, are given in Chang and Hicher [1]. Comparisons of experimental results and numerical simulations have demonstrated the ability of this model to reproduce accurately the overall mechanical behavior of granular media and to account for the influence of key parameters such as void ratio and mean stress.

### 3 Unsaturated Granular Materials

When a certain amount of water is added to the grain assembly, significant changes, such as an increase in stiffness and strength, can be observed. These changes can be explained by the formation of water menisci between neighboring particles, which creates capillary forces. The amplitude of these capillary forces depends upon the degree of saturation and the morphology at particle level (grain and pore sizes). For modeling the behavior of unsaturated granular materials, capillary forces at the grain contacts are, therefore, added to the contact forces created by an external load. They are calculated as a function of the degree of saturation, depending on the grain size distribution and on the void ratio of the granular assembly. Numerical simulations show that the model is capable of reproducing the major trends of a partially saturated granular assembly under various stress and water content conditions.

In this study, we retained the following expression

$$f_n^{cap} = f_{\max} e^{-c\left(\frac{d}{R}\right)} \quad (1)$$

where  $f_{cap}$  is the capillary force between two neighboring grains, not necessarily in contact,  $f_{\max}$  is the value of  $f_{cap}$  for two grains in contact, and  $R$  is the mean grain radius,  $d$  represents the distance between two grains and is equal to  $l - 2R$ ,  $l$  being the branch length given as a distribution function of the grain size and the void ratio,  $c$  is a material parameter, dependent on the grain morphology and on the water content,  $f_{\max}$  depends on the capillary pressure defined as the pressure jump across the liquid-air interface, on the liquid-air interface surface tension, as well as on the geometry of the menisci governed by the solid-liquid contact angle and the filling angle. In this study, a simplified approach was developed that considers an empirical relation between  $f_{\max}$  and the degree of saturation  $S_r$ , without taking into account the hysteresis along drying and wetting paths

$$\begin{aligned} f_{\max} &= f_0 \frac{S_r}{S_0} && \text{for } 0 < S_r < S_0 \\ f_{\max} &= f_0 \frac{S_0(1-S_r)}{S_r(1-S_0)} && \text{for } S_0 < S_r < 1 \end{aligned} \quad (2)$$

where  $f_0$  and  $S_0$  are material parameters.  $f_0$  depends on the grain size distribution,  $S_0$  represents the degree of saturation at which any further drying of the specimen will cause substantial breaking of the menisci in the pendular domain.  $S_0$  depends on the nature of the granular material. The following empirical expression was proposed by Wu *et al.* [4] for compacted granular materials:

$$(S_r)_{opt} = (-0.65 \log(d_{10}) + 1.5) / 100 \quad (3)$$

in which  $(S_r)_{opt}$  is equivalent to  $S_0$  in Eq. 5,  $d_{10}$  is the effective grain size in mm.

Figure 1 presents numerical simulations of water constant triaxial tests on a silty sand at various degrees of saturation. An overall good agreement with experimental results could be reached, particularly the evolution of the maximum strength as a function of the degree of saturation was well obtained by the model.

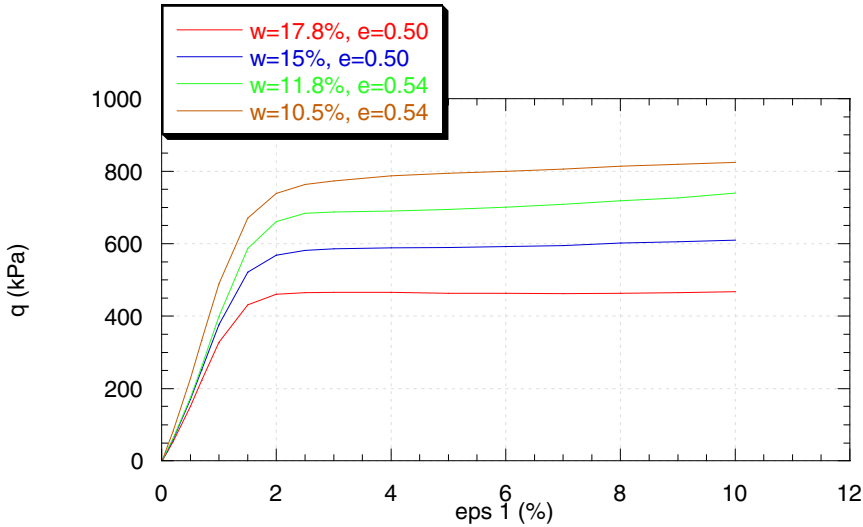


Fig. 1. Influence of the degree of saturation on constant water content triaxial tests on silty sand

### 4 Granular Materials with Surface Energy Forces

Environmental conditions can also modify the behavior of granular media. All materials, with or without a net surface charge, exhibit surface energy forces which act at a very short range. But whereas these forces are negligible for common sand or silty sand on Earth, they play a significant role under tiny atmospheric pressure. The mechanical behavior of the subsurface soil on Moon and Mars is, therefore, expected to be significantly different from that on Earth. The model is then extended to include Van der Waals forces in order to describe the possible behavior of these extraterrestrial soils. Van der Waals forces acting between two particles can be considered as the sum of two terms, one due to the interaction between two flat surfaces of area  $S = \pi a^2$  and one along the remaining surface of the two spheres. Using the Derjaguin approximation for the second term, we obtain the expression of the Van der Waals force between two particles:

$$f = \frac{A}{6D^3} a^2 + \frac{AR}{12D^2} \tag{4}$$

where  $A$  = Hamaker coefficient;  $D$  thickness of molecules layer between two particles;  $R$  = the radius of particles. Hamaker constant  $A$  was estimated to be 4.3

$\times 10^{-20}$  J. for lunar soil and  $1.5 \times 10^{-20}$  J. for terrestrial quartz sand (Perko et al. [3]). The thickness of molecules layer between two particles  $D$  is highly dependent on the atmospheric pressure and composition. On the Moon, the atmospheric pressure is nearly zero, which can lead to a very thin layer of molecules between two particles compared to that under terrestrial environment. Therefore, according to Eq. (4), it is reasonable to expect that the surface energy forces between particles are much higher than those between particles under terrestrial environment. Under these conditions and in accordance with the observations made on the Moon's surface, the model shows that lunar soil has an additional component of shear strength described by a cohesion,  $c$ , higher than the one which could be found on Earth. Besides, because the radius  $a$  of the contact area in Eq. (4) increases with confining stress of a specimen, the surface energy force also increases with confining stress, which indicates that the surface energy force will contribute to the shear strength not only on the cohesive component but also on the frictional component. Figure 2 shows the influence of the distance  $D$  between the particles on the shear strength for soil specimens under 20 kPa confining stress, where  $q_0$  represents the shear strength for soil without surface energy forces and  $q$  represents the shear strength with the effect of surface energy forces.

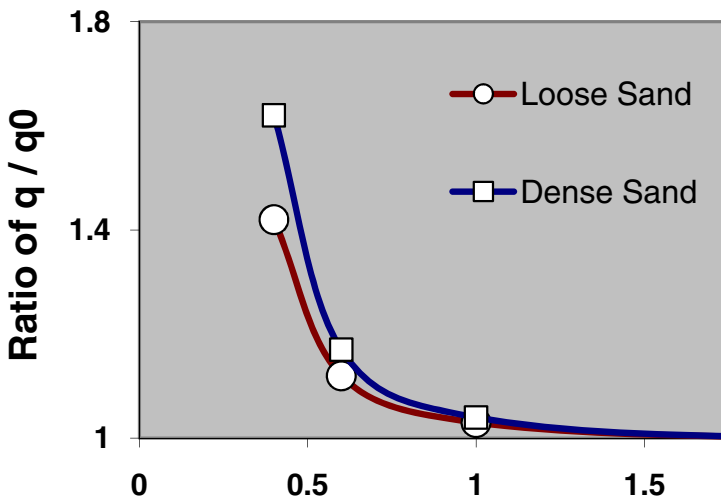


Fig. 2. Effect of distance between particles on shear strength

Predictions of the model indicate that the soil under extremely low atmospheric pressure has an increase of shear strength by several kPa higher than the one which would be present under the atmospheric pressure of the Earth's. This result is in accordance with the general trend observed in situ. The magnitude is in the same order as the measured increase of shear strength for lunar soil simulants tested under the usual atmospheric pressure and under a chamber with ultrahigh vacuum.

## References

- [1] Chang, C., Hicher, P.-Y.: An elastoplastic Model for Granular Materials with Microstructural Consideration. *Int. J. of Solids and Structures* 42(14), 4258–4277 (2005)
- [2] Liao, C.L., Chang, T.P., Young, D., Chang, C.S.: Stress-strain relationship for granular materials bases on hypothesis of best fit. *International Journal of Solids and Structures* 34(31-32), 4087–4100 (1997)
- [3] Perko, H., Nelson, J., Sadeh, W.: Surface cleanliness effect on lunar soil shear strength. *Journal Geotechnical Engineering, ASCE* 127(4), 371–383 (2001)
- [4] Wu, S., Gray, D.H., Richart Jr., F.E.: Capillary effects on dynamic modulus of sands and silts. *Journal of Geotechnical Engrg., ASCE* 110(9), 1188–1203 (1984)

# Time Effects Relate to Particle Crushing in Granular Materials

Poul V. Lade

Department of Civil Engineering  
The Catholic University of America  
Washington, D.C. 20064, U.S.A.  
Lade@cua.edu

**Summary.** Sands exhibit patterns of time effects different from those observed in clays. It appears that time effects in sand are associated with crushing of particles, and a mechanistic picture of time effects in granular materials is constructed in which time effects depend on particle crushing by static fatigue, interparticle friction, and grain rearrangement. The phenomenon of static fatigue or delayed fracture of individual particles seems to be at the root of time effects in sand. While creep and relaxation are caused by the same underlying phenomenon, it appears that results of creep tests cannot be obtained from results of relaxations tests, and vice versa.

**Keywords:** creep, sand, static fatigue, time effects.

## 1 Introduction

Recent research [1-6] shows that time effects in granular materials is different from the viscous behavior observed in clays. The effects of strain-rate, creep and stress relaxation of clays follow a classic pattern of viscous behavior observed for most materials. For granular materials the effects of strain rate or loading rate are observed to be small to negligible, and while creep and stress relaxation are caused by the same phenomenon, namely grain crushing followed by grain rearrangement, the prediction of one phenomenon can apparently not be accomplished on the basis of the other. Presented here is a mechanistic picture in which static fatigue of individual grains together with interparticle friction, and grain rearrangement account for the time effects observed in experimental studies.

## 2 Experiments on Virginia Beach Sand

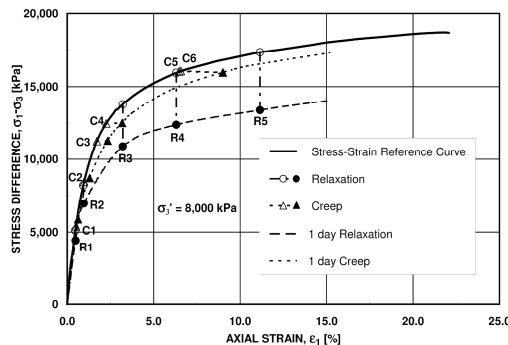
Particle crushing appears to be at the root of time effects in granular materials through the phenomenon of static fatigue. Therefore, a study of Virginia Beach sand, which consists of strong, subangular to subrounded quartz particles, was conducted and sieve analyses were performed to prove that particle crushing relate

directly to the observed time effects. The details of the equipment, specimen preparation and testing procedures are given in [1]. The experiments were performed in a high pressure triaxial cell with an effective confining pressure of 8,000 kPa at which pressure significant crushing occurs in Virginia Beach sand.

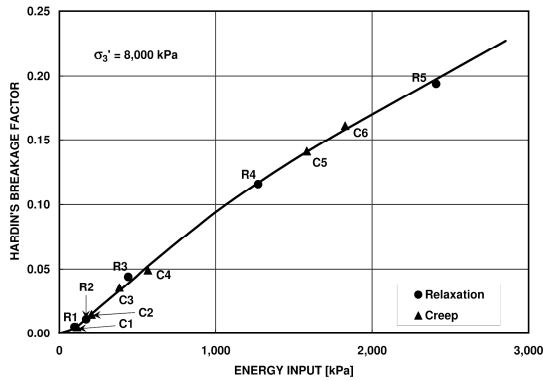
Similar to observations for crushed coral sand [5, 6] and Antelope Valley sand [2], experiments on Virginia Beach sand also indicated that strain rate effects on stress-strain and strength behavior are small [1, 3]. Fig. 1 shows a comparison of creep and stress relaxation effects in Virginia Beach sand. Each of these experiments were performed by shearing a freshly deposited specimen at a constant strain rate of 0.0416%/min up to the point at which the specimen was allowed to creep or to stress relax for one day. The results are plotted from a common stress-strain curve and the initial or final points of each creep and stress relaxation test are indicated by an identification number.

The grain size distribution curves were determined for each of the experiments. Negligible amounts of particle breakage occur during stress relaxation for which negligible strains occur [1], and the observed particle breakage therefore corresponds to the breakage that occurred during shearing up to the point at which the stress relaxation is initiated. The amounts of particle breakage are related to the locations along the stress-strain curve at which the creep and stress relaxation are terminated. To quantify this relationship, the particle breakage is represented by Hardin's particle breakage factor (Hardin 1985) and the locations at which creep and stress relaxation are terminated is represented by the energy input per unit volume of the specimen.

Fig. 2 shows the relation between Hardin's particle breakage and the energy input per unit volume for the experiments shown in Fig. 1. A unique and almost linear relation is observed between the amount of particle breakage and the energy input per unit volume to the specimens, which were all sheared at an effective confining pressure of 8,000 kPa. While stress relaxation occurs with no strains and therefore relates to zero energy input, a portion of the energy input relates to the time-dependent phenomenon of creep. It is therefore evident that time effects are related to the crushing of particles.



**Fig. 1.** Comparison of creep and stress relaxation experiments performed in triaxial compression tests on Virginia Beach sand



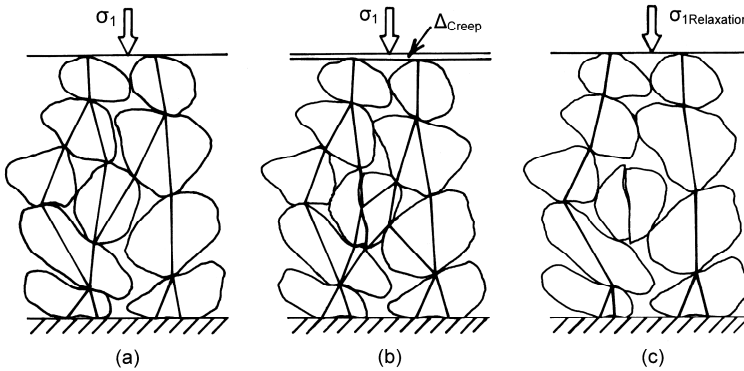
**Fig. 2.** Relation between Hardin’s particle breakage factor and input energy per unit volume of triaxial compression specimens of Virginia Beach sand performed with a confining pressure of 8,000 kPa

Fig. 1 indicates that the observed stress relaxation behavior does not correspond with the measured creep behavior. It is concluded that none of the three sands that have been tested (Antelope Valley sand, crushed coral sand and Virginia Beach sand) exhibits classic viscous effects. Note also that the amounts of disagreement between the stress-strain relations after one day of creep or stress relaxation are quite different for the three sands.

### 3 Mechanistic Picture of Time Effects in Sands

A mechanistic picture of time effects may be constructed on the basis of the phenomenon of particle breakage. Particle breakage may not occur and time effects are negligible in granular materials at very low stresses. Time effects become significant with increasing confining pressure and increasing stress difference.

Fig. 3(a) shows an assembly of grains that have been loaded up to a given stress difference and either creep or stress relaxation occurs from this point. The diagram shows the force chains down through the assembly. The grain in the middle fractures in the beginning of either of these two types of time effects. The responses of the grain assembly are quite different for the two phenomena. Fig. 3(b) shows what happens during creep in which the vertical stress is held constant. The assembly adjusts its structure to carry the vertical stress. This requires adjustment of the grains and it results in some vertical deformation and new force chains are created to match the externally applied stress. The redundancy in the grain structure allows new force chains to be created and engage other grains that may break. But slowly the amount of breakage will reduce and the creep will slow down with time, just as observed in the experiments.



**Fig. 3.** (a) Initial force chains in particle structure and effects of grain crushing in (b) creep test and in (c) stress relaxation test

Fig. 3(c) shows what happens in the stress relaxation experiment. After the grain has broken, the grain structure is not able to carry the vertical stress, but since the assembly is prevented from vertical deformation, the stress relaxes. New force chains are created around the broken grain which does not carry any load. It is the small amount of grain movement in the creep tests that allows new contacts to be created and forces to be carried through the grain skeleton. Without this adjustment and consequent deformation to achieve the adjustment, the grain structure is able to transmit only a reduced load and stress relaxation is the consequence. It can also be seen that if a lower limit to the relaxed stress exists, then it depends on the grain strength rather than its frictional properties.

It may be seen that a relation between creep and stress relaxation does not exist, because the two explanations do not allow a transition from one to the other phenomenon. Thus, Fig. 1 shows that the amounts of creep and the amounts of stress relaxation after one day do not converge towards the same curves. The two sets of curves are quite different and one cannot be obtained from the other.

With only friction (and slippage when the frictional resistance is overcome) and particle breakage (when the strengths of the particles are overcome) as basic behavior constituents, how can the observed time effects be explained for granular materials? Experiments on rock specimens have clearly shown that their strengths are strongly dependent on time. Crushing of single sand particles indicates that they behave similar to rock specimens in the sense that their crushing strengths are time-dependent. This phenomenon is referred to as static fatigue or delayed fracture.

## References

- [1] Karimpour, H., Lade, P.V.: Time effects relate to crushing in sand. *J. Geotec. Geoenvironm. Engrg.*, ASCE 136(9), 1209–1219 (2010)
- [2] Lade, P.V.: Experimental study and analysis of creep and stress relaxation in granular materials. In: *GeoDenver*, ASCE. Denver, Colorado (2007) CD-rom

- [3] Lade, P.V., Karimpour, H.: Static Fatigue Controls Particle Crushing and Time Effects in Granular Materials. *Soils and Found.* 50(5), 573–583 (2010)
- [4] Lade, P.V., Liu, C.-T.: Experimental study of drained creep behavior of sand. *J. Engrg. Mech.*, ASCE 124(8), 912–920 (1998)
- [5] Lade, P.V., Liggio Jr., C.D., Nam, J.: Strain rate, creep, and stress drop-creep experiments on crushed coral sand. *J. Geotech. Geoenvironm. Engrg.*, ASCE 135(7), 941–953 (2009)
- [6] Lade, P.V., Nam, J., Liggio Jr., C.D.: Effects of particle crushing in stress drop-relaxation experiments on crushed coral sand. *J. Geotech. Geoenvironm Engrg.*, ASCE 136(3), 500–509 (2010)

# A Power Law for Elastic Moduli of Unsaturated Soil

Ning Lu

Department of Civil and Environmental Engineering  
Colorado School of Mines  
1700 Illinois Street, Golden, Co, 80401, USA  
ninglu@mines.edu  
<http://inside.mines.edu/~ninglu/>

**Summary.** This paper presents a new power law for describing the dependency of elastic modulus on soil water content. Experimental data of either Young's modulus from 11 different soils are used to examine the validity of the proposed power law. It is shown that the proposed power law can well represent the highly non-linear relation between elastic modulus and soil water content in silty and clayey soils.

**Keywords:** Elastic modulus, Shear modulus, Young's modulus, Resilient Modulus, and Unsaturated soil.

## 1 Introduction

Elastic modulus refers to the stiffness of materials in response to recoverable deformation. In geotechnical engineering, it is often referred to either Young's modulus or shear modulus. Elastic modulus has been considered a fundamental parameter governing the recoverable mechanical behavior of earthen structures. It has been widely used as the basis for calculating settlements for a variety of foundation types bearing on compacted or over consolidated soils following constructions (e.g., [1], [2], and [3]).

In the classical theories, elastic modulus is mainly considered as a function of stress conditions, soil type, and environmental factors. Historically, stress and environmental conditions have been considered as the main factors in some early theories (e.g., [4], [5], and [6]). Despite the strong dependence of elastic modulus on environmental factors shown in many silty and clayey soils in recent studies (e.g., [7] and [8]), few theories or models effectively describing such dependence have been proposed and rigorously tested for different types of soils under variably saturated conditions.

This work will first present some new evidence for the dependence of Young's modulus on soil water content for various soils ranging from sand, to silt and clays. Based on examining these data and some previous experimental data and theories, a power law describing the dependence of elastic modulus on soil water content is proposed and its accuracy for various soils under variably saturated conditions is assessed.

## 2 Evidence on Elastic Modulus-Soil Water Content Relation

The drying cake (DC) test, recently invented by Lu and Kaya [9] for measuring soil water retention curve (SWRC) and hydraulic conductivity function (HCF) as well as Young’s modulus of a compacted disk-shape soil specimen (cake) while drying, is used to measure the dependency of Young’s modulus on water content. The geotechnical properties of the 11 soils are summarized in Table 1. The testing results for Young’s modulus as a function of volumetric water content for these soils are shown in Figs. 1a-1c. Two patterns can be seen from these results. First, Young’s modulus generally monotonically increases with decreasing water content. Take Golden silt (Fig. 1b) for example, Young’s modulus is 2.0 MPa at water content of 0.32 and increases to 2.9 MPa at water content of 0.25 (Fig. 1b), and continues to increase as the cake is drying. At the water content of 0.08, Young’s modulus increases to 5.5 MPa, nearly double of that at the water content of 0.32. Second, low or no plasticity soils like sands and some silts exhibit less change (Figs. 1a and 1b) than those soils with high plasticity like some silts and clays (Figs. 1b-1c).

**Table 1.** Geotechnical properties of 11 different soils

Soils	Classification	LL (%)	PL (%)	PI (%)	G <sub>s</sub>	Porosity	Water content at compaction
Esperance sand	SP	-	-	-	2.65	0.390	0.25
Ottawa sand	SP	-	-	-	2.65	0.380	0.25
Elliot Forest silt	OL	29.0	26.0	3.0	2.55	0.390	0.22
Bonny silt	ML	25.0	21.0	4.0	2.65	0.470	0.29
BALT silt	ML	27.4	21.7	5.8	2.72	0.470	0.29
Iowa silt	ML	33.7	22.4	11.3	2.65	0.450	0.27
Golden silt	ML	31.0	17.0	14.0	2.65	0.440	0.22
Hopi silt	SC	36.0	23.0	13.0	2.68	0.480	0.32
Denver claystone	CH	44.0	23.0	21.0	2.70	0.550	0.39
Georgia kaolinite	CH	44.0	26.0	18.0	2.66	0.580	0.45
Denver bentonite	CH	118.0	45.0	73.0	2.70	0.530	0.32

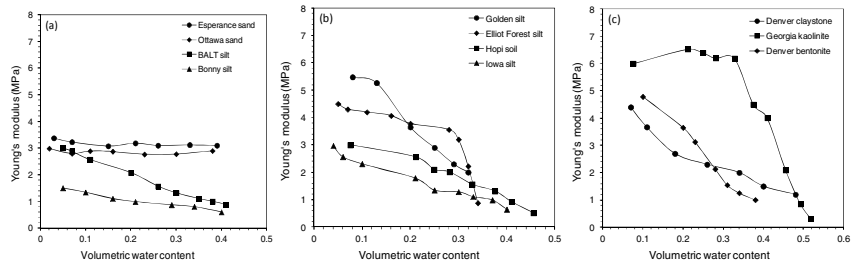


**Fig. 1.** Test results of elastic modulus for various compacted soils as a function of water content from nearly saturated state to dry state for: (a) Young’s modulus for Esperance sand, Ottawa sand, BALT silt, and Bonny silt, (b) Young’s modulus for Golden silt, Elliot Forest silt, Hopi silt, and Iowa silt, and (c) Young’s modulus for Denver claystone, Georgia kaolinite, and Denver bentonite

### 3 The Proposed Power Law for Elastic Moduli

The dependency of elastic modulus on either total or effective stress has been a major focus for saturated soils as stress can modify pore and soil skeleton structures thus the stiffness of soils. However, under unsaturated conditions, effective stress or stress in soil skeleton is affected not only by the total stress, but also by inter-particle stresses called suction stress ([10] and [11]). Suction stress is the effective stress due to variation in soil water content or matric suction ([11], [12], and [13]). Suction stress consists of inter-particle physico-chemical forces, pore water attraction due to matric suction, and surface tension. Therefore, in silty and clayey soils, suction stress is highly governed by soil water content or matric suction. Since the relationship between soil water content and matric suction can be established by SWRC, soil water content may be sufficient as the sole independent variable in describing variation in elastic modulus for unsaturated soil.

From both Young's modulus and resilient modulus results shown in Figs. 1a-1c as well as other recent studies (e.g., [14], [15], and [3]), it is clear that elastic modulus of soils follows a power law decay as the water content increases. It is also observed that elastic modulus is bounded by the two-end members with the maximum occurring at the dry end and the minimum occurring at the wet end. As such, the following power law is proposed:

$$E = E_d + (E_w - E_d) \left( \frac{\theta - \theta_d}{\theta_w - \theta_d} \right)^m \quad (1)$$

where  $E$  stands for Young's modulus, the subscript  $d$  stands for a dry state and  $w$  stands for a wet state, and  $m$  is an empirical fitting parameter. A dry state can be set at practically the driest environment of interest and a wet state can be set near saturated or saturated condition. There are only 3 parameters in equation (1) in order to fully define elastic modulus of any soil. Furthermore 2 of the 3 parameters, namely  $E_d$  and  $E_w$ , have direct physical meaning as they represent the elastic moduli at the wet and dry states. Thus, only one fitting parameter  $m$  in the power law (1) remains to be identified for any soil once the elastic moduli at the dry and wet states are known.

### 4 Experimental Validation of the Proposed Power Law

Fig. 2 shows the least squared-fit of Young's modulus of the 11 soils by equation (1). Fig. 2a shows two sandy soils and two silty soils. The sandy soils have relatively small values of  $m$  (0.01 for Ottawa sand, and 0.2 for Esperance sand), reflecting their insensitivity of Young's modulus with water content. The two silty soils, on the other hand, have moderate values of  $m$  (0.84 for BALT silt and 0.80 for Bonny silt), reflecting their relatively sensitive nature to water content. Take BALT silt for example, Young's modulus is 0.9 MPa at water content of 0.42, but increases to 3.0 MPa at water content of 0.02. As shown, the elastic modulus of all these 4 soils can be well represented by equation (1).

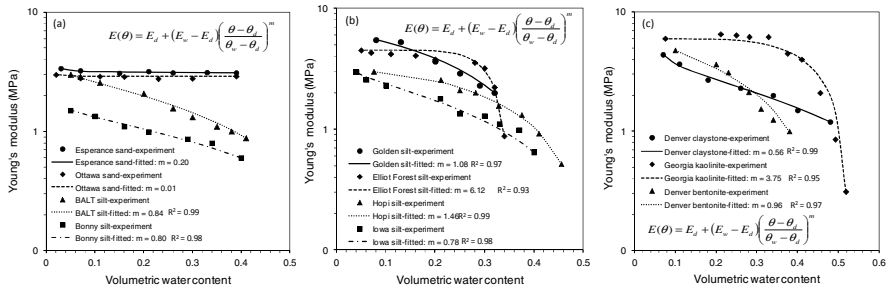


**Fig. 2.** Fitting of Young’s modulus data with the proposed model for various compacted soils: (a) Esperance sand, Ottawa sand, BALT silt, and Bonny silt, (b) Golden silt, Hopi silt, Elliot Forest silt, and Iowa silt, and (c) Denver claystone, Georgia kaolinite, and Denver bentonite

For the 4 silty soil shown in Fig. 2b, the variation of Young’s modulus with the water content shows similar pattern with those 2 silty soils shown in Figure 4a, but the magnitude is slightly higher for 2 of the 4 silty soils (Golden silt and Hopi silt), reflecting high values of  $m$  (1.08 for Golden silt and 1.46 for Hopi silt). Iowa silt has similar range of change in Young’s modulus to the 2 silty soils shown in Fig. 2a and its  $m$  value (0.78) is similar to those two silty soils too. Overall, Young’s modulus of all 4 soils can be well represented by equation (1) as the coefficients of determination  $R^2$  are all  $\geq 0.97$ .

For the 3 clayey soils shown in Fig. 2c, Young’s modulus varies highly non-linearly with the water content, particularly when the water content is high. Denver claystone, a predominately non-expansive illite, has a moderate  $m$  value (0.56) and its variation in Young’s modulus is moderate too, varying from 1.05 MPa at water content of 0.5 to 4.5 MPa at water content of 0.06. Again the least squared-fit between equation (1) and the data are excellent; the coefficients of determination  $R^2$  are  $> 0.93$  for all 3 soils.

## 5 Conclusions

A new power law for describing the dependency of elastic modulus on soil water content is presented. Using the elastic modulus data from 11 different soils, it is shown that the proposed power law can accurately represent the dependency of elastic modulus on soil water content.

## References

- [1] Yoder, E.J., Witczak, M.W.: Principles of Pavement Design, 2nd edn. Wiley, New York (1975)
- [2] Nazarian, S., Yuan, D., William, R.R.: A simple method for determining modulus of base and subgrade materials. In: Resilient Modulus Testing for Pavement Components, ASTM STP 1437, ASTM, West Conshohoken, Pa (2003)

- [3] Schuettpezel, C.C., Fratta, D., Edil, T.B.: Mechanistic corrections for determining the resilient modulus of base course materials based on elastic wave measurements. *Journal of Geotechnical and Geoenvironmental Engineering* 136(8), 1086–1094 (2010)
- [4] Edil, T.B.: Influence of Fabric and Soil-water Potential on Stress-strain Response of Clay, Ph.D. Dissertation, Northwestern University, Evanston, Ill (1973)
- [5] Fredlund, G.D., Bergan, A.T., Sauer, E.K.: The deformation characteristics of subgrade soils for highways and runways in northern environments. *Canadian Geotechnical Journal* 12(2), 213–223 (1975)
- [6] Moossazadeh, J., Witzak, M.W.: Prediction of subgrade moduli for soil that exhibits nonlinear behavior. *Transportation Research Records* 810, Transportation Research Board, 9–17 (1981)
- [7] Mancuso, C., Vassallo, R., d’Onofrio, A.: Small strain behavior of a silty sand in controlled-suction resonant column-torsional shear tests. *Canadian Geotechnical Journal* 39(1), 22–31 (2002)
- [8] Khoury, N.N., Zaman, M.M.: Correlation between resilient modulus, moisture variation, soil suction for subgrade soils. *Transportation Research Record*, Transportation Research Board, Washington, D.C (2004)
- [9] Lu, N., Kaya, M.: A drying cake method for measuring suction stress characteristic curve, soil water retention curve, and hydraulic conductivity function. *Geotechnical Testing Journal* (accepted for publication, 2012)
- [10] Lu, N., Likos, W.J.: *Unsaturated Soil Mechanics*, 556 p. Wiley (2004)
- [11] Lu, N., Likos, W.J.: Suction stress characteristic curve for unsaturated soils. *Journal of Geotechnical and Geoenvironmental Engineering* 132(2), 131–142 (2006)
- [12] Lu, N.: Is matric suction a stress variable? *Journal of Geotechnical and Geoenvironmental Engineering* 134(7), 899–905 (2008)
- [13] Lu, N., Godt, J., Wu, D.: A closed form equation for effective stress in variably saturated soil. *Water Resources Research* (2010), doi:10.1029/2009WR008646
- [14] Sawangsuriya, A., Edil, T.B., Bosscher, P.J.: Modulus-suction-moisture relationship for compacted soils in postcompaction state. *Journal of Geotechnical and Geoenvironmental Engineering* 135(10), 1390–1403 (2009)
- [15] Ng, C.W.W., Xu, J., Yung, S.Y.: Effects of imbibition-drainage and stress ratio on anisotropic stiffness of an unsaturated soil at very small strains. *Canadian Geotechnical Journal* 46(9), 1062–1076 (2009)

# Application and Meaning of the $t_{ij}$ Concept

Teruo Nakai\*

Department of Civil Engineering  
Nagoya Institute of Technology  
Gokiso-cho, Showa-ku, Nagoya, 466-8555, Japan  
nakai.teruo@nitech.ac.jp

**Summary.** Simple and unified method to describe stress-strain behavior in general three-dimensional stress condition, which has been called the  $t_{ij}$  concept, was presented [1]. Since this concept was found out from idea that the frictional law essentially governs soil behavior, its meaning is very clear. Using this concept, any kinds of one-dimensional models and/or three-dimensional models formulated by using ( $p$  and  $q$ ) can be easily extended to general three-dimensional models. Methods for formulating the constitutive model using  $t_{ij}$  and the meanings of the  $t_{ij}$  concept are presented.

**Keyword:** three-dimensional stress condition, modified stress, frictional law.

## 1 Introduction

Most of ordinary models are formulated using the stress invariants ( $p$  and  $q$ ) and cannot describe uniquely the deformation and strength of soils under three different principal stresses. To describe the soil behavior under three different principal stresses, some material parameters in the models are given by a function of the magnitude of the intermediate principal stress. However, such method is not essential in rational modeling. Then, the concept of  $t_{ij}$  has been proposed to describe uniquely the stress-strain behavior in general three-dimensional stress condition [1]. Since the details of this concept were described in the previous papers [e.g., 1, 2] and the recent book [3], outlines of the method to apply this concept to elastoplastic modeling and the meaning of the concept are presented here.

## 2 Application of $t_{ij}$ to Constitutive Model

The plane ABC in Figure 1 is the spatially mobilized plane (SMP) [4] in the three-dimensional stress space, where axes I, II and III imply the directions of three principal stresses ( $\sigma_1$ ,  $\sigma_2$  and  $\sigma_3$ ). At each of the three sides AB, AC and BC of plane ABC, the shear-normal stress ratio is maximized between two principal stresses as shown in Figure 2. Here, the plane AB where the shear normal stress ratio ( $\tau/\sigma$ ) is maximized has been called “Mobilized plane” or “Plane of maximum

---

\* Corresponding author.

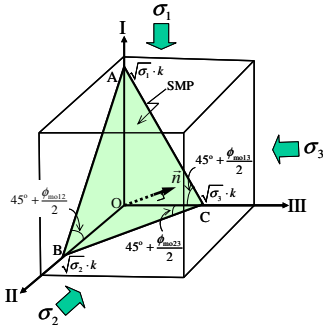


**Fig. 1.** Spatially mobilized plane (SMP) in three-dimensional space

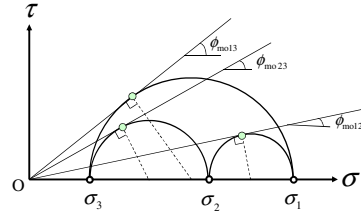


**Fig. 2.** Three Mohr's stress circles under three different principal stresses

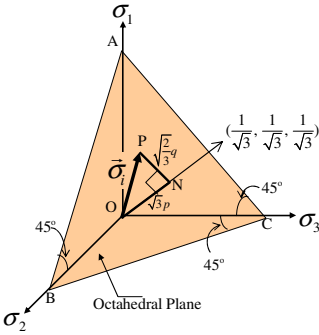


**Fig. 3.** Definitions of  $p$  and  $q$

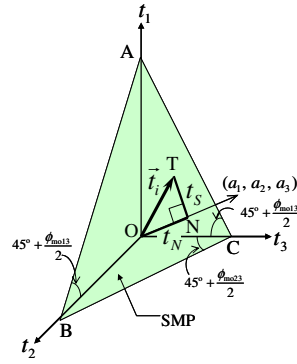


**Fig. 4.** Definitions of  $t_N$  and  $t_S$

mobilization” by Murayama [5], and the three planes AB, AC and BC have been collectively called “Compounded mobilized planes” by Matsuoka [6]. Now, the direction cosines ( $a_1, a_2$  and  $a_3$ ) of the normal to the SMP are given by

$$a_1 = \sqrt{\frac{I_3}{I_2 \sigma_1}}, a_2 = \sqrt{\frac{I_3}{I_2 \sigma_2}}, a_3 = \sqrt{\frac{I_3}{I_2 \sigma_3}} \quad (\text{where } a_1^2 + a_2^2 + a_3^2 = 1) \quad (1)$$

Here,  $I_2$  and  $I_3$  are the second and third invariants of the Cauchy stress  $\sigma_{ij}$ . Also, the unit symmetric tensor,  $a_{ij}$ , whose principal values are given by these direction cosines can be defined.

The modified stress tensor  $t_{ij}$  is then defined by the product of  $a_{ik}$  and  $\sigma_{kj}$  as follows:

$$t_{ij} = a_{ik} \sigma_{kj} \quad (2)$$

Its principal values are given by

$$t_1 = a_1\sigma_1, \quad t_2 = a_2\sigma_2, \quad t_3 = a_3\sigma_3 \quad (3)$$

Now, in most of conventional elastoplastic models, the yield function  $f$  is formulated using the stress invariants ( $p$  and  $q$ ), which are given by the normal and in-plane components of the ordinary stress with respect to the octahedral plane (see Figure 3), and the flow rule is assumed in the  $\sigma_{ij}$  space.

$$f = F(p, \eta = q/p) - H = 0 \quad (4)$$

$$d\varepsilon_{ij}^p = \Lambda \frac{\partial F}{\partial \sigma_{ij}} \quad (5)$$

On the other hand, in the  $t_{ij}$  concept, the stress invariants ( $t_N$  and  $t_S$ ), which are defined as the normal and in-plane components of the modified stress tensor  $t_{ij}$  with respect to the SMP, are employed (see Figure 4). Then, the yield function  $f$  is formulated using the stress invariants ( $t_N$  and  $t_S$ ) instead of ( $p$  and  $q$ ) in such a form as

$$f = F(t_N, X = t_S/t_N) - H = 0, \quad (6)$$

with the flow rule being defined in the  $t_{ij}$  space and not in the  $\sigma_{ij}$  space, i.e.

$$d\varepsilon_{ij}^p = \Lambda \frac{\partial F}{\partial t_{ij}} \quad (7)$$

### 3 Meaning of the $t_{ij}$ Concept

The meaning of the  $t_{ij}$  concept is presented, focusing mostly on the microscopic point of view. Several researchers have shown that induced anisotropy of soils developed during stress changes is characterized by the frequency distribution of the inter-particle contact angles. It has then been shown from microscopic observations (e.g., Oda [7]) that, as the stress ratio increases, the average of the normal directions to the inter-particle contacts gradually concentrate in the direction of the major principal stress ( $\sigma_1$ ).

Figure 5(a) shows schematically the distribution of inter-particle contact normal directions in 2D conditions in a granular material. Considering an equivalent continuum, such a material exhibits anisotropy with rearrangement of contact normal directions since the stiffness in the  $\sigma_1$  direction becomes larger than that in the  $\sigma_2$  direction with an increase of stress ratio as shown in diagram (b). Within the framework of elastoplastic theory, it is reasonable to treat the soil as an isotropic material by introducing the modified stress  $t_{ij}$  in which any induced anisotropy is already taken into consideration. Just like when analyzing seepage in anisotropic soils, the transformation of the stress space into a modified one allows us to revert to isotropic conditions where normality rule applies with the direction of plastic flow being normal to the yield surface (plastic potential). As can be seen from Eq. (1), the principal values of  $a_{ij}$  are inversely proportional to the square root of the respective principal stresses in 2D condition as well. As shown in diagram

(c) referring to an equivalent isotropic material, the stress ratio  $t_1/t_2$  in the modified stress space is smaller than the stress ratio  $\sigma_1/\sigma_2$  in the ordinary stress space, because  $a_1$  is smaller than  $a_2$  as a consequence of Eq. (1). Then, it is reasonable to assume that the flow rule (normality condition) does not hold in the  $\sigma_{ij}$  space but in the  $t_{ij}$  space, because the condition of the anisotropic material under anisotropic stress ratio in diagram (b) can be considered to be the same as that of an equivalent isotropic material under lower modified stress ratio in diagram (c).

Next, we demonstrate the rationale of relating the stress and strain increment invariants to normal and in-plane components of the respective measures in the SMP within the  $t_{ij}$  concept instead of the octahedral plane used in traditional models. The failure behavior of highly cohesive materials such as metals is governed mostly by the deviatoric stress (or shear stress) alone, so that it is generally accepted to analyze failure in the plane where the shear stress is maximized, i.e.  $45^\circ$  plane (in 2D condition), or the average plane where the shear stress arising from two principal stresses is maximized, i.e. octahedral plane (in 3D condition). On the other hand, turning to geomaterials such as soils, failure is governed by Coulomb's friction between particles which relates to the shear to normal stress ratio. Therefore, attention should be paid to the plane where the shear to normal stress ratio is maximized, i.e. the mobilized plane (in 2D condition), or the combination of the three planes where the shear to normal stress ratio between two respective principal stresses is maximized, i.e. the SMP (in 3D condition). From this viewpoint, it is natural to formulate constitutive models using the normal and in-plane components of the stress referred in the SMP. As a consequence, the influence of the intermediate principal stress on induced anisotropy and on the frictional resistance of geomaterials is naturally introduced when the  $t_{ij}$  concept is adopted.

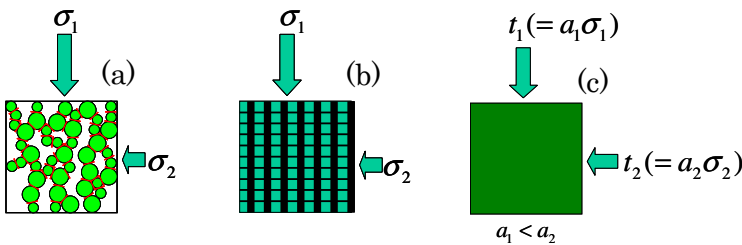


Fig. 5. Anisotropy of soils and its expression

## References

- [1] Nakai, T., Mihara, Y.: A new mechanical quantity for soils and its application to elastoplastic constitutive models. *Soils and Foundations* 24(2), 82–94 (1984)
- [2] Nakai, T.: Modeling of soil behavior based on  $t_{ij}$  concept. In: *Proc. of 13th ARCSMGE, Keynote Paper, Kolkata, vol. 2, pp. 69–89 (2007)*
- [3] Nakai, T.: *Constitutive Modeling of Geomaterials: Principles and Applications*, 376 pages. CRC Press (to be published in July, 2012)

- [4] Matsuoka, H., Nakai, T.: Stress-deformation and strength characteristics of soil under three different principal stresses. In: Proc. of JSCE, vol. 232, pp. 59–70 (1974)
- [5] Murayama, S.: A theoretical consideration on a behavior of sand. In: Proc. of IUTAM Symposium on Rheology and Soil Mechanics, Grenoble, pp. 146–159 (1964)
- [6] Matsuoka, H.: Stress-strain relationship of sand based on the mobilized plane. *Soils and Foundations* 14(2), 47–61 (1974)
- [7] Oda, M.: The mechanism of fabric changes during compressional deformation of sand. *Soils and Foundations* 12(2), 1–18 (1972)

# A Simplified Model for Clayey Rocks Having a Plastic Porous Matrix

Wanqing Shen<sup>1</sup>, Jianfu Shao<sup>1,\*</sup>, and Djimédo Kondo<sup>2</sup>

<sup>1</sup> LML, UMR CNRS 8107, University of Lille, France

<sup>2</sup> IJLRA, UMR CNRS 7190, University of PMC, France

Jian-Fu.Shao@polytech-lille.fr

**Abstract.** This study is devoted to a micro-macro model of plastic deformation in a clayey rock which is composed of a ductile porous clay matrix and linear elastic mineral grains. By making use of nonlinear homogenization methods with a two-step homogenization procedure, we derive a closed form expression of the macroscopic plastic criterion which accounts for the effects of pores and of mineral inclusions simultaneously. Then, a non-associated flow rule is proposed. Comparisons between the predictions of the full micro-macro model and available experimental data show that the proposed model is able to capture the main features of the mechanical behavior of the clayey rock.

## 1 Microstructure of Callovo-Oxfordian (COx) Argillite

Hard clayey rocks, also called argillite, have been largely investigated in the context of feasibility study for geological storage of radioactive wastes. The Callovo-Oxfordian (COx) argillite is a clayey rock involved in the French national research program dealing with the feasibility study of underground waste storage. This rock is characterized by its low hydraulic conductivity and relatively high mechanical strength. Its mineralogical composition varies with the in situ depth and contains three main phases: clay matrix (40 to 50%), calcite (20 to 27%) and quartz grains (23 to 25%). The porosity of COx argillite varies from 11 to 14%. For simplicity, the argillite is schematized at mesoscale as a two phase composite: effective inclusions embedded in the clay matrix. The effective inclusions are assumed elastic rigid, spherical and randomly distributed. The clay matrix is an isotropic elastoplastic porous medium with a typical local porosity value  $f=25\%$ .

## 2 Macroscopic Criterion of Porous Media Reinforced by Rigid Inclusions

In this section, we first aim at determining the macroscopic criterion of a ductile porous medium reinforced by rigid inclusions. According to the above description, the studied material at mesoscale is composed of two phases: the rigid elastic

---

\* Corresponding author.

inclusions and the embedding elastoplastic porous matrix. In the Representative elementary volume  $\Omega$ , the volume fraction of pores, rigid inclusions and of the solid matrix are respectively denoted  $\Omega_p$ ,  $\Omega_i$  and  $\Omega_m$ . The porosity  $f$  of the matrix and the absolute volume fraction  $\rho$  of the rigid inclusions reads:  $f = \Omega_p / (\Omega_p + \Omega_m)$ ,  $\rho = \Omega_i / (\Omega_p + \Omega_m + \Omega_i)$ . The solid phase of the matrix obeys to a Drucker-Prager criterion:

$$F^m(\underline{\underline{\tilde{\sigma}}}) = \tilde{\sigma}_d + T(\tilde{\sigma}_m - h) \leq 0 \quad (1)$$

$\underline{\underline{\tilde{\sigma}}}$  denotes the local stress in the solid phase,  $\tilde{\sigma}_m = \text{tr} \underline{\underline{\tilde{\sigma}}} / 3$  being mean stress,  $\tilde{\sigma}_d = \sqrt{\underline{\underline{\tilde{\sigma}}} : \underline{\underline{\tilde{\sigma}}}}$  generalized deviatoric stress with  $\underline{\underline{\tilde{\sigma}}}_d = \underline{\underline{\tilde{\sigma}}} - \tilde{\sigma}_m \underline{\underline{1}}$ . The symbol " $\sim$ " is used in order to make difference with the microscopic stresses of the solid phase and the mesoscopic stress field attached to the porous medium. The parameter  $h$  represents the hydrostatic tensile strength while  $T$  denotes the frictional coefficient.

By using a nonlinear homogenization technique based on the modified secant method, [1] has shown that, even in the context of non-associated solid phase, the yield criterion of the porous medium having a Drucker-Prager matrix reads as in the associated case:

$$F^{mp} = \frac{1 + 2f/3}{T^2} \sigma_d^2 + \left( \frac{3f}{2T^2} - 1 \right) \sigma_m^2 + 2(1-f)h\sigma_m - (1-f)^2 h^2 = 0 \quad (2)$$

In the present study, this criterion will be used to describe the yield of the elastoplastic behavior of the porous matrix. It remains to build the macroscopic criterion of the whole composite. Since the strength domain  $F^{mp}(\underline{\underline{\sigma}}, f)$  is convex and closed in the stress space, the support function  $\pi^{mp}$  in the porous medium can be expressed as function of the volumetric deformation  $\underline{\underline{d}}_v$  and the norm of the deviatoric deformation  $\underline{\underline{d}}_d$ . In the perspective of application of the modified secant moduli approach, the stress-strain relationship derived from this support function  $\pi^{mp}$  can be put in the following form:

$$\underline{\underline{\sigma}} = \frac{\partial \pi^{mp}}{\partial \underline{\underline{d}}} = 2\mu^{mp} \underline{\underline{d}}_d + k^{mp} \underline{\underline{d}}_v \underline{\underline{1}} + \sigma^p \underline{\underline{1}} \quad (3)$$

$k^{mp}$ ,  $\mu^{mp}$  being the secant bulk and shear moduli, respectively, and  $\sigma^p$  denoting a spherical prestress. The secant moduli are non-uniform, due to their dependence on the heterogeneity of the strain rate field  $\underline{\underline{d}}$ . Following [1], we consider the effective strain rate  $\underline{\underline{d}}^{eff}$  which is an appropriate average of  $\underline{\underline{d}}$  over the porous matrix to capture the effect of the loading on the non-linear stiffness. Therefore, the

effective moduli  $k^{mp} = k_{eq}^{mp}(d_v^{eff}, d_d^{eff})$ ,  $\mu^{mp} = \mu_{eq}^{mp}(d_v^{eff}, d_d^{eff})$  and the spherical prestress  $\sigma^p = \sigma_{eq}^p(d_v^{eff}, d_d^{eff})$ . These quantities depend on the macroscopic strain rate  $\underline{D}$ .

Due to the matrix-inclusions morphology of the material, the macroscopic state equation of the composite can be obtained by using the Hashin-Shtrikman lower bound in the case of rigid inclusions. It follows that:

$$k^{hom} = \frac{3k_{eq}^{mp} + 4\rho\mu_{eq}^{mp}}{3(1 - \rho)}, \quad \mu^{hom} = \mu_{eq}^{mp} \frac{k_{eq}^{mp}(6 + 9\rho) + \mu_{eq}^{mp}(12 + 8\rho)}{6(1 - \rho)(k_{eq}^{mp} + 2\mu_{eq}^{mp})} \quad (4)$$

The effective volumetric and deviatoric strain rates in the porous matrix are defined by the modified secant method as:  $d_v^{eff} = \sqrt{\langle d_v^2 \rangle_{\Omega^{mp}}}$ ,  $d_d^{eff} = \sqrt{\langle d_d^2 \rangle_{\Omega^{mp}}}$ . Following a methodology used by [2], the effective strain rates in the equivalent porous matrix are obtained as:

$$\frac{1}{2}(1 - \rho)d_v^{eff2} = \frac{1}{2} \frac{\partial k^{hom}}{\partial k_{eq}^{mp}} D_v^2 + \frac{\partial \mu^{hom}}{\partial k_{eq}^{mp}} D_d^2, \quad (1 - \rho)d_d^{eff2} = \frac{1}{2} \frac{\partial k^{hom}}{\partial \mu_{eq}^{mp}} D_v^2 + \frac{\partial \mu^{hom}}{\partial \mu_{eq}^{mp}} D_d^2 \quad (5)$$

The resulting macroscopic criterion (of the material made up of the porous matrix and rigid inclusions) takes the form:

$$\Phi = \Theta \Sigma_d^2 + \left( \frac{3f}{2T^2} - 1 \right) \Sigma_m^2 + 2(1 - f)h\Sigma_m - \frac{3 + 2f + 3\rho f}{3 + 2f} (1 - f)^2 h^2 = 0 \quad (6)$$

where  $\Theta = \left[ \frac{1 + 2f/3}{T^2} + \frac{2}{3}\rho \left( \frac{3f}{2T^2} - 1 \right) \right] / \left[ \frac{4T^2 - 12f - 9}{6T^2 - 13f - 6} \rho + 1 \right]$ .

### 3 A Micro-Macro Model with Non-Associated Flow Rule for COx

The macroscopic plastic criterion (6) obtained above is now applied to describe elastoplastic behavior of argillite. In order to complete the formulation of the micro-macro model, we aim at proposing a non-associated flow rule for the COx clayey rock. Inspired by (6), the following plastic potential is suggested:

$$G = \frac{\frac{1 + 2f/3}{Tt} + \frac{2}{3}\rho \left( \frac{3f}{2Tt} - 1 \right)}{\frac{4Tt - 12f - 9}{6Tt - 13f - 6} \rho + 1} \Sigma_d^2 + \left( \frac{3f}{2Tt} - 1 \right) \Sigma_m^2 + 2(1 - f)h\Sigma_m \quad (7)$$

where  $t$  represents the dilatancy coefficient.

Concerning the plastic hardening of the solid phase, modeled via the evolution of the frictional coefficient  $T$  and that of the dilatancy coefficient  $t$  with the equivalent plastic strain  $\varepsilon^p$ , the following forms are proposed:

$$\bar{T} = T_m - (T_m - T_0)e^{-b_1\varepsilon^p}, \quad \bar{t} = t_m - (t_m - t_0)e^{-b_2\varepsilon^p} \quad (8)$$

### 4 Validation of the Micro-Macro Model for the Argillite Cox

A series of uniaxial and triaxial compression tests are now simulated using the proposed model with the non-associated flow rule. Different confining pressures and mineralogical compositions are considered. The model predictions are compared with available experimental data as shown in Figure 1. A good agreement is observed. Various other tests are simulated and shown in [3].

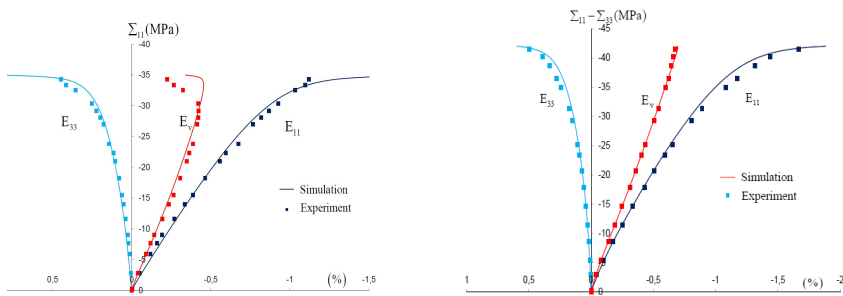


**Fig. 1.** Left-uniaxial compression test with  $\rho=49\%$  at the depth 466.8m; Right-triaxial compression test  $\rho=40\%$  with a confining pressure 10 MPa at the depth 482.2m

### 5 Conclusions

A homogenization-based model is proposed for the elastoplastic behavior of the COx argillite. At the mesoscopic scale, this material is considered as a two phase composite: mineral grains embedded in a porous clay matrix. Two homogenization steps are carried out and allow to formulate at macroscopic scale a closed form expression of the plastic criterion which accounts for the effects of mineral inclusions and the influence of porosity simultaneously. With a non-associated plastic flow rule, the predictions of the model agree with the available experimental data.

### References

[1] Maghous, S., Dormieux, L., Barthélémy, J.F.: Micromechanical approach to the strength properties of frictional geomaterials. Euro. J. of Mech. A/Solid 28, 179–188 (2009)

- [2] Barthlmy, J.F., Dormieux, L.: A micromechanical approach to the strength criterion of Drucker-Prager materials reinforced by rigid inclusions. *Int. J. Numer. Anal. Meth. Geomech.* 28, 565–582 (2004)
- [3] Shen, W.Q.: Modelisations micro-macro du comportement mecanique des materiaux poreux ductiles: application l'argilite du Callovo-Oxfordien. PhD Thesis. University of Lille (2011)

# Anisotropic Porochemoelectroelastic Solution for Inclined Wellbores with Applications to Operations in Unconventional Shale Plays

Minh H. Tran and Younane N. Abousleiman\*

Mewbourne School of Petroleum and Geological Engineering  
PoroMechanics Institute  
University of Oklahoma  
100 East Boyd St., Suite P119, Norman, OK 73019  
yabous1e@ou.edu

**Summary.** In this work, the porochemoelectroelastic theory is applied to analyze instability problems of an inclined wellbore drilled in the laminated and charged saturated chemically active shale formations. Numerical example is given for wellbore drilling in the Woodford gas shale formation. The analysis shows that ignoring either the porochemoelectroelastic effects or the formation anisotropy can lead to inaccurate predictions of potential wellbore integrity problems.

**Keywords:** chemical effects, inclined wellbore, shale, anisotropy.

## 1 Introduction

Wellbore instability problems associated with unconventional shale reservoirs are not the classical type. It is well-known that shale swells and shrinks when exposed to aqueous solutions due to the imbalance of electrochemical potentials between the mildly charged matrix, its pore fluid and the invading fluid. Simultaneously, the effective stresses in the formation are modified which could lead to detrimental effects on the formation integrity. The transversely isotropic nature of shale has also been known to greatly affect the failure zoning around the wellbore. With increasing shale drilling activities for oil and gas production, the chemically active behavior and anisotropic nature of shales have become subjects of extensive research. In this work, the porochemoelectroelastic theory is applied to analyze instability problems of an inclined wellbore drilled in the laminated and charged saturated chemically active shale formations as depicted in Fig. 1.

## 2 Porochemoelectroelasticity

It is well-known that the constituent clay surfaces in the shale matrix contain the negative fixed charge of which the amount can be estimated from the Cation Exchange Capacity (CEC) of the formation [1]. Prior to drilling, the shale formation

---

\* Corresponding author.

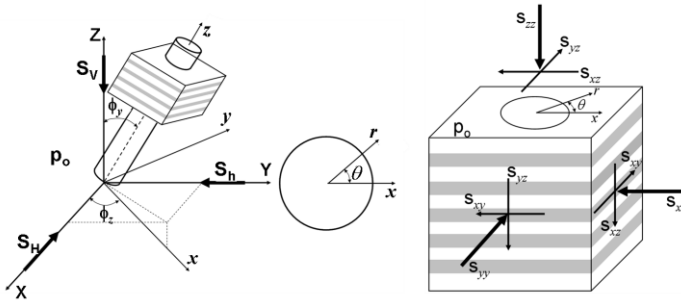


Fig. 1. Problem schematic

contains  $m_{fc}^o$  moles of negative fixed charge, and is saturated with pore fluid with  $m_a^o$  moles of anion and  $m_c^o$  moles of cation at an initial pore pressure  $p_o$  as illustrated in Fig. 2a. The electrical neutrality condition requires the amount of cation in the pore fluid to be greater than the amount of anion.

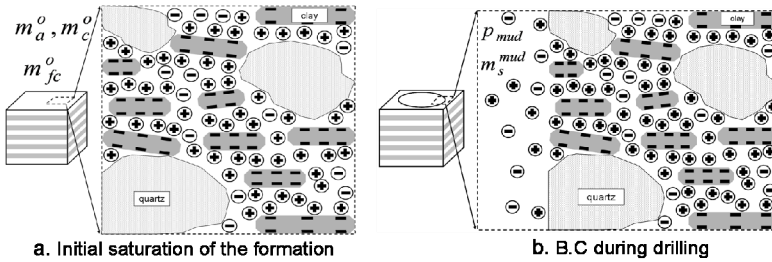


Fig. 2. The initial conditions and boundary conditions at the wellbore wall during drilling

During the drilling process, the wellbore is filled with drilling mud having mud pressure,  $p_{mud}$ , with solute concentration,  $m_s^{mud}$ , as shown in Fig. 2b. The presence of the negative fixed charge creates a discontinuity of ion concentration at the mud-shale interface leading to the development of an osmotic pressure at the wellbore wall. These phenomena are the well-known Donnan equilibrium effect [2]. Based on thermodynamic principle, it can be shown that the porochemoelectroelastic constitutive stress-strain relations share the same form with the original Biot’s poroelastic formulations. The electrochemical effects only enter through the transient nature of the fluid and ion flows due to differences in the electrochemical potentials across the porous medium [1]. The approach has been applied to generalize the 3-D anisotropic poroelastic solutions for inclined wellbores [3] to capture the chemically active behavior of charged saturated shale formations [4].

### 3 Application to Woodford Shale Drilling

The solution is utilized to assess possible wellbore integrity problems for a vertical wellbore in the Woodford shale formation. The gas shale formation is assumed to be at a depth of 2000 m and subject to  $S_V = 50$  MPa,  $S_H = 44$  MPa,  $S_h = 40$  MPa,  $p_o = 19.6$  MPa. The drilling fluid is assumed to be NaCl solution with activity of 0.9 and density of 1.07 g/cc. Laboratory testing shows that the formation CEC is 10 meq./100 grams and the pore fluid activity is 0.87. Other formation properties necessary for modeling are adopted from [5].

Shown in Fig. 3 is the pore pressure distribution along the maximum horizontal stress ( $S_H$ ) direction after 15 minutes into drilling. The pore pressure jump at the wellbore wall is the result of the Donnan equilibrium effect as previous discussed. On the other hand, the pore pressure peak inside the formation is the consequence of water influx from the wellbore into the formation to equalize the salinity difference between the borehole fluid and pore fluid.

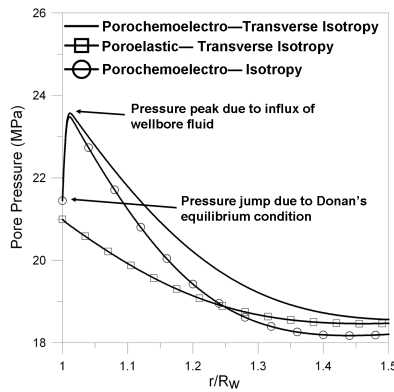


Fig. 3. Pore pressure distribution in the direction of  $S_H$  after 15 minutes into drilling

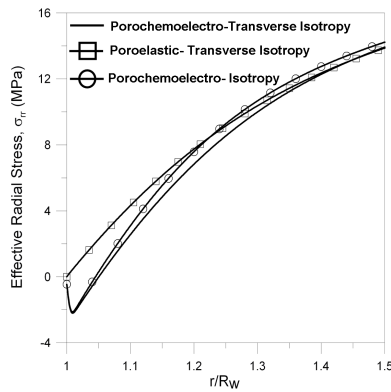


Fig. 4. The effective radial stress in the direction of  $S_H$  15 minutes into drilling

These phenomena result in a region of tensile effective stress near the borehole as shown in Fig. 4 which may lead to wellbore instability such as spalling. The severity of the failure zone is dominantly controlled by the formation CEC and the difference between drilling mud and pore fluid activity. For example, comparison of the porochemoelectroelastic solution with the poroelastic solution ( $CEC = 0$  and zero membrane efficiency) shows that higher formation CEC results in larger failure zone which not only enhances the borehole fluid leak-off into the formation but also results in a near wellbore plastic zone absorbing the hydraulic pressure from the drilling/fracturing mud. This may explain why clay-rich intervals are often reported as more ductile than quartz-rich intervals from LOT or mini-frac test interpretation.

## 4 Conclusions

The analysis shows that ignoring either the porochemoelectroelastic effects or the formation anisotropy can lead to inaccurate predictions of potential wellbore integrity problems. The analysis also explains the observation that clay-rich intervals are often perceived as more ductile than quartz-rich intervals.

**Acknowledgements.** The financial support of the PoroMechanics Industrial Consortium at the University of Oklahoma is gratefully acknowledged.

## References

- [1] Nguyen, V.X., Abousleiman, Y.N.: Incorporating electrokinetic effects in the porochemoelectroelastic inclined wellbore formulation and solution. *Annals of the Brazilian Academy of Sciences* 82, 1–28 (2010)
- [2] Overbeek, J.T.: The Donnan equilibrium. *Progress in Biophysics* 6, 57–84 (1956)
- [3] Abousleiman, Y.N., Cui, L.: Poroelastic solution in transversely isotropic media for wellbore and cylinder. *Int. J. Solids Structures* 35, 4905–4929 (1998)
- [4] Tran, M.H., Abousleiman, Y.N.: Anisotropic porochemoelectroelastic solution for an inclined wellbore drilled in shale - Special issue Olivier Coussy. *J. Appl. Mech* (in press, September 2012)
- [5] Abousleiman, Y.N., et al.: Geomechanics field and lab characterization of Woodford shale: The next gas play. SPE-110120 Presented at the 2007 SPE ATCE, California, November 11-14 (2007)

# Modeling Ground-Shell Contact Forces in NATM Tunneling, Based on 3D Displacement Measurements

Shafi Ullah<sup>1,2</sup>, Bernhard Pichler<sup>1</sup>, and Christian Hellmich<sup>1,\*</sup>

<sup>1</sup> Institute for Mechanics of Materials and Structures

Vienna University of Technology (TU Wien)

Karlsplatz 13/202, A-1040 Vienna, Austria

Christian.Hellmich@tuwien.ac.at

<sup>2</sup> Directorate of Civil Engineering (DCED)

Pakistanian Research and Development Organization

Post Box 1138, Pak Secretariat, Islamabad, Pakistan

**Summary.** Based on an advanced micromechanics-based nonlinear creep model for shotcrete and thin shell kinematics, measured displacement data are first converted into in-plane stress fields throughout a shotcrete tunnel shell driven according to the New Austrian Tunneling Method (NATM). Subsequently, the partial differential equations for local force equilibrium in the cylindrical coordinate directions are solved for the out-of-plane shell stresses, inclusive of the tractions at the ground-shell interface. Results obtained for a NATM-tunnel driven through clayey ground at moderate depth, show that the maximum shear tractions at the ground-shell interface may even exceed the maximum normal tractions ("ground pressure"). At the same time, even a young top heading tunnel shell may act as an arching thrust. We regard our method as a further step in the continuous refinement of interpretation displacement measurements stemming from tunnel monitoring systems for the NATM, on a well-defined mechanical basis. This results in two structural models for top heading excavation stages, which might have the potential to support NATM predesign activities in the future.

**Keyword:** monitoring, micromechanics, ground-shell interaction.

## 1 Introduction

Tunnel shell displacements result from the interaction between the ground and the support system, i.e. they contain information on the frequently complex, usually anisotropic and inhomogeneous ground, as well as on all installed support measures. Herein, we use measured displacements as input for a structural analysis focusing exclusively on the shotcrete tunnel shell [1-3]. In this analysis, 3D tunnel shell displacements referring to discrete measurements points of so-called measurement cross-sections, which are on-site measured in a fixed Cartesian

---

\* Corresponding author.

coordinate system, are first transformed into corresponding shell-specific (radial, circumferential, and axial) displacement components [1]. Then, the latter components are interpolated in time and space, in order to reconstruct the displacement field history of the inner surface of the shell. This is the basis to derive, within the framework of thin shell theory, the strain field history across the bulk of the shotcrete tunnel shell. On the basis of micromechanical material models for shotcrete elasticity, creep, and strength [4-7], which account for initial mixture characteristics (water-to-cement ratio, aggregate-to-cement ratio) and hydration-driven changes in material composition, the aforementioned strain fields are transformed into (in-plane) stress fields. The latter, together with equilibrium conditions applied throughout the bulk of the tunnel shell, provide access to both the normal and in particular the shear traction forces, which are transferred from the rock mass, across the rough, frictional ground-shell interface, onto the shotcrete shell [3]. This is quantified for a cross-section of Sieberg Tunnel described next.

## 2 Sieberg Tunnel

Sieberg tunnel was constructed in the 1990s in Miocene clay at moderate depths, as part of the high-capacity Vienna-Salzburg railway line in Austria. Around the here-considered measurement cross-section MC1452, the overburden depth was about 20 m, and influx of water was rather moderate.

The support system consisted of a shotcrete tunnel shell, exhibiting a thickness of  $h = 30$  cm, with embedded steel fabric reinforcements, and rock bolts. Our investigation focuses on the measurement cross-section MC1452 which is made up of cylindrical shell segments with piece-wise constant curvatures, see Fig. 1 for related geometrical dimensions. In the course of a sequential excavation strategy, the top heading at MC1452 was placed on Dec 14, 1997, followed by the installation of left bench and right bench on Jan 19, 1998 and Jan 21, 1998, respectively. Placement of the invert and, hence, finalization of MC 1452 was carried out a few months later.

For monitoring of 3D displacements, five measurement points (MPs) were installed per MC: Three (MP1, MP2, MP3) were evenly distributed along the top heading, and two (MP4 and MP5) were installed in lower parts of the benches (Fig. 1). This holds also for the preceding measurement cross-section MC1444, with its top heading, left bench and right bench installed on Dec 12, 1997, Jan 18, 1998 and Jan 20, 1998, respectively, in an axial distance of 8 m from MC1452. For the subsequent analyses, we will consider displacement measurements collected at these two MCs between Dec 12, 1997 and Feb 01, 1998, see [3] for details.

## 3 Ground-Shell Interaction at MC1452

The analysis described in the introductory section delivers ground-shell interaction forces providing insight into the structural behavior of MC1452 of Sieberg tunnel [3]. In this context, it is interesting to study the circumferential distributions of

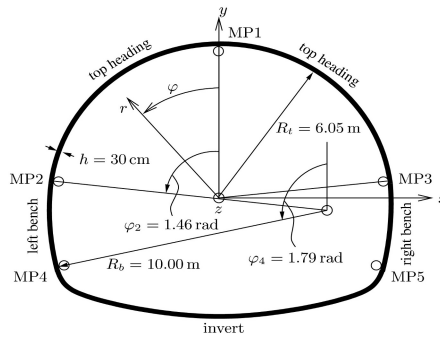


**Fig. 1.** Measurement cross-section of Sieberg tunnel shell: structural dimensions, geometric properties, and locations of measurement points (MPs)

contact stresses on Dec 15, 1997, i.e. one day after the installation of the top heading (at this date, the maximum degree of utilization was reached [3]).

The maximum ground pressure occurs in the crown (-0.83 MPa), and it decreases almost symmetrically towards the feet [Fig. 2(a)]. The circumferential shear contact stresses exhibit local maxima at the left foot (-1.22 MPa) as well as at the right foot (+1.03 MPa) of the top heading. They are acting upward, and their magnitude gradually decreases to almost zero at the crown [Fig. 2(b)]. In other words, the analysis shows that the young tunnel shell takes vertical loads mainly through its crown region, and that these loads are then transferred to the lateral parts of the top heading, where they are effectively back-transferred to the ground via shear stresses.

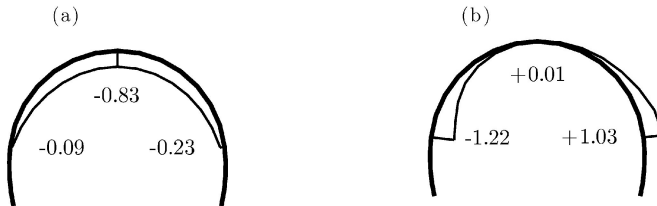


**Fig. 2.** Computed circumferential distributions of ground-shell contact tractions (in MPa) at MC1452 of Sieberg tunnel on Dec 15, 1997: (a) ground pressure; (b) circumferential shear contact stresses

### 3 Structural Model for Top Heading Shells

The described contact stress distributions (Fig. 2) imply (i) that the top-heading shell acts as an arching thrust, a structural element carrying loads exclusively

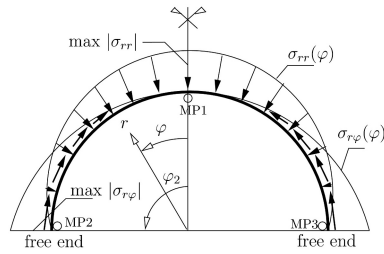


**Fig. 3.** Arching thrust model for top heading under symmetric loading conditions

through normal forces [3] and (ii) that maximum ground shear and maximum ground pressure are related through  $\max|\sigma_{r\phi}| = 2 \max|\sigma_{rr}| / \varphi_2$ , where  $\varphi_2$  denotes the circumferential angle of the top heading feet, see Fig. 3. The shown analysis might well support future (pre)design of top heading tunnel excavations.

## References

- [1] Ullah, S., Pichler, B., Scheiner, S., Hellmich, C.: Shell-specific interpolation of measured 3D displacements, for micromechanics-based rapid safety assessment of shotcrete tunnels. *Computer Modeling in Engineering and Sciences (CMES)* 57(3), 279–316 (2010)
- [2] Ullah, S., Pichler, B., Scheiner, S., Hellmich, C.: Influence of shotcrete composition on load level estimation in NATM tunnel shells: micromechanics-based sensitivity analyses. *International Journal for Numerical and Analytical Methods in Geomechanics* (2012), Article first published online, doi:10.1002/nag.1043
- [3] Ullah, S., Pichler, B., Scheiner, S., Hellmich, C.: Modeling Ground-Shell Contact Forces in NATM Tunneling, Based on 3D Displacement Measurements. *Journal of Geotechnical & Geoenvironmental Engineering* (accepted for publication, 2012)
- [4] Hellmich, C., Mang, H.: Shotcrete elasticity revisited in the framework of continuum micromechanics: from submicron to meter level. *Journal of Materials in Civil Engineering* 17(3), 246–256 (2005)
- [5] Pichler, B., Scheiner, S., Hellmich, C.: From micron-sized needle-shaped hydrates to meter-sized shotcrete tunnel shells: micromechanical upscaling of stiffness and strength of hydrating shotcrete. *Acta Geotechnica* 3(4), 273–294 (2008)
- [6] Scheiner, S., Hellmich, C.: Continuum microviscoelasticity model for aging basic creep of early-age concrete. *Journal of Engineering Mechanics* 135(4), 307–323 (2009)
- [7] Pichler, B., Hellmich, C.: Upscaling quasi-brittle strength of cement-based materials: a multiscale engineering mechanics approach. *Cement and Concrete Research* 41(5), 467–476 (2011)

# Discrete Modeling of Fluid-Particle Interaction in Soils

Jidong Zhao\* and Tong Shan

Department of Civil and Environmental Engineering, Hong Kong University of Science and Technology, Clearwater Bay, Kowloon, Hong Kong  
jzhao@ust.hk

**Summary.** Fluid-particle interaction contributes to important behaviors of soils. This paper presents a numerical method to model the interaction by coupling the Computational Fluid Dynamics (CFD) with the Discrete Element Method (DEM). The particle motion of the granular system is simulated by the DEM, and the CFD solves the locally averaged Navier-Stokes equation for the flow of pore fluid. The interaction between pore fluid and particles is considered by exchange of interaction forces between DEM and CFD. The numerical method is further benchmarked and validated by several geomechanics problems.

**Keywords:** fluid-particle interaction, CFD, DEM, sandpile.

## 1 Introduction

Fluid-particle interaction underpins the key behavior of granular soils in many applications. Conventional approaches have been based on continuum, phenomenological theories of porous media and cannot offer important information at the microscale governing the interacted system of particles and fluid. While the microscopic behavior of the fluid-particle interaction may provide insights to the overall understanding of granular materials, a coupled CFD-DEM numerical tool will be developed in this study to simulate the fluid-particle interactions in granular soils.

## 2 Formulation and Approach

In a particle system simulated by the DEM, the following equations are assumed to govern the translational and rotational motions of a particle:

$$\begin{cases} m_i \frac{d\mathbf{U}_i^p}{dt} = \sum_{j=1}^{n_i^c} \mathbf{F}_{ij}^c + \mathbf{F}_i^f + \mathbf{F}_i^g \\ I_i \frac{d\boldsymbol{\omega}_i}{dt} = \sum_{j=1}^{n_i^c} \mathbf{M}_{ij} \end{cases} \quad (1)$$

---

\* Corresponding author.

where  $\mathbf{U}_i^p$  and  $\boldsymbol{\omega}_i$  denote the translational and angular velocities of particle  $i$ , respectively.  $\mathbf{F}_{ij}^c$  and  $\mathbf{M}_{ij}$  are the contact force and torque acting on particle  $i$  by particle  $j$  or walls, and  $n_i^c$  is the number of total contacts for particle  $i$ .  $\mathbf{F}_i^f$  is the particle–fluid interaction force acting on particle  $i$ , which include both buoyancy force and drag force in the current case.  $\mathbf{F}_i^g$  is the gravitational force.  $m_i$  and  $I_i$  are the mass and moment of inertia of the particle. The Hooke contact law in conjunction with Coulomb’s friction law is employed to describe the interparticle contact behaviour. For the fluid system, the following continuity equation and locally averaged Navier-Stokes equation will be solved by the CFD:

$$\begin{cases} \frac{\partial(n\rho)}{\partial t} + \nabla \cdot (n\rho\mathbf{U}^f) = 0 \\ \frac{\partial(n\rho\mathbf{U}^f)}{\partial t} + \nabla \cdot (n\rho\mathbf{U}^f\mathbf{U}^f) - n\nabla \cdot (\mu\nabla\mathbf{U}^f) = -n\nabla p - \mathbf{f}^p + n\rho\mathbf{g} \end{cases} \quad (2)$$

where  $\mathbf{U}^f$  is the average velocity of a fluid cell,  $\rho$  is averaged fluid density.  $n$  defines the porosity (void fraction).  $p$  is the fluid pressure in the cell;  $\mu$  is the averaged viscosity;  $\mathbf{f}^p$  is the interaction force averaged by the cell volume the particles inside the cell exert on the fluid.  $\mathbf{g}$  is the body force vector.

The drag force and buoyancy force are considered to be the dominant interaction forces between fluid and particles for low Reynolds number pore flows. The following expression is employed for the drag force (see [1-2]):

$$\mathbf{F}^d = \frac{1}{8} C_d \rho \pi d_p^2 (\mathbf{U}^f - \mathbf{U}^p) |\mathbf{U}^f - \mathbf{U}^p| n^{1-\chi} \quad (3)$$

where  $d_p$  is the diameter of the considered particle.  $C_d$  and  $\chi$  depend on the Reynolds number of the considered particle  $\text{Re}_p$

$$C_d = \left( 0.63 + \frac{4.8}{\sqrt{\text{Re}_p}} \right)^2, \quad \chi = 3.7 - 0.65 \exp \left[ -\frac{(1.5 - \log_{10} \text{Re}_p)^2}{2} \right] \quad (5)$$

and  $\text{Re}_p = n\rho d_p |\mathbf{U}^f - \mathbf{U}^p| / \mu$ .

The buoyancy force adopts the following expression:

$$\mathbf{F}^b = \frac{1}{6} \pi \rho d_p^3 \mathbf{g} \quad (6)$$

The general computational scheme is outlined as follows (see also [3]). The fluid phase is discretized with a typical cell size five to ten times of the average particle diameter. At each time step, the DEM package will provide such information as the position and velocity of each individual particle. The position of each particle is then matched with the fluid cell to calculate relevant information of each cell such as the porosity. Eq. (2) is solved by the CFD program for the averaged velocity and pressure for each cell. The obtained averaged velocity and pressure of a cell are then used to determine the drag force and buoyancy force acting on the particles within the cell. Iterative schemes may be required to ensure the convergence of relevant quantities such as fluid velocity and pressure. When a converged result is obtained, the information of the fluid-particle interaction forces will be taken into account for the next step calculation of the DEM part. Ideally, information on interaction forces should be exchanged once after each step of calculation for DEM or CFD. This, however, may be computationally extremely expensive in practice. For most problems, numerical experience indicates that for each CFD computing step, exchange of information after every 100 steps of DEM calculation will ensure sufficient accuracy as well as efficiency. If the time steps for DEM and CFS are sufficiently small, more steps for DEM are also acceptable.

### 3 Benchmarking and Application

Two classic geomechanics problems are first employed to benchmark the proposed CFD-DEM method. One is the one-particle settling in water problem, and the other is the one-dimensional consolidation problem. Analytical solutions to both problems are available in soil mechanics text books. Predictions by the numerical tool for the two problems are compared against the analytical solutions in Figure 1.

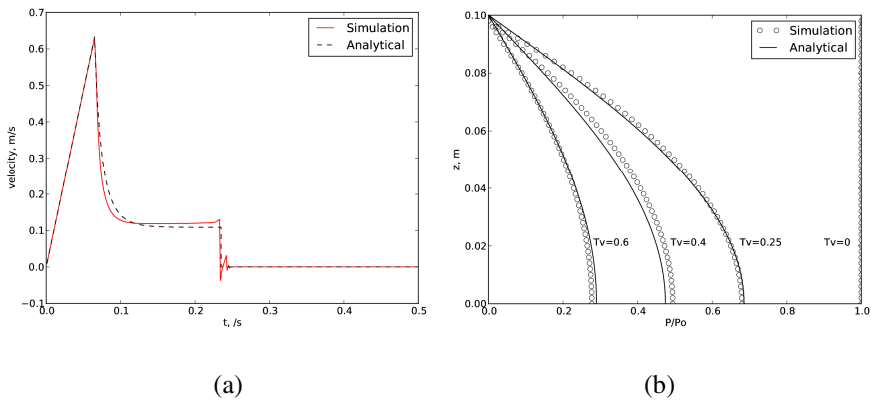


**Fig. 1.** Benchmarking of the CFD-DEM method with analytical solutions for (a) the single-particle settling in water problem; (b) one-dimensional consolidation problem

For the single particle settling problem, it is evident from Figure 1a that the settling velocity of a sphere particle in water predicted by the CFD-DEM agrees well with the analytical solution. Sharp reduction of settling velocity of the particle when it hit the water is accurately captured, along with the settling process in the water. The bounce back from the bottom of the contained is also reproduced well. For the 1D consolidation problem, Figure 1b shows that the simulated dissipation of excess pore water with time also compare reasonably well with the analytical solution. However, it is also noticed (not shown here) that at very early stage of consolidation, i.e., when  $T_v < 0.1$ , the numerical prediction deviates slightly from the analytical solution. This is because the Terzaghi's analytical solution assumes an instantaneous build-up of excess pore pressure throughout the column once the surcharge is applied, whereas the CFD-DEM calculation needs some time to build up the excess pore water.

The CFD-DEM method has also been applied to investigating the formation of sandpile in water. Shown in Figure 2a demonstrates the formation process of a sandpile in water through hopper flow. The case without water has also been simulated for comparison. Meanwhile, the rolling resistance has been regarded important in simulating the sandpiling problem (see [4]), and will be considered here. Presented in Fig. 2b is the pressure dips observed in sandpiles obtained in the various cases. The overall profile of the vertical pressure in the wet case is higher than the dry case. The pressure dip is found to be moderately reduced by the presence of water as compared to the dry case. Consideration of rolling resistance may lead to enhanced pressure dip, and the difference is more appreciable in the wet case than in the dry case. From a further inspection of the force chain network it is found that the presence of water may lead to more homogeneous contact force distribution in the sandpile, which may help to explain the reduced pressure dip in the wet.

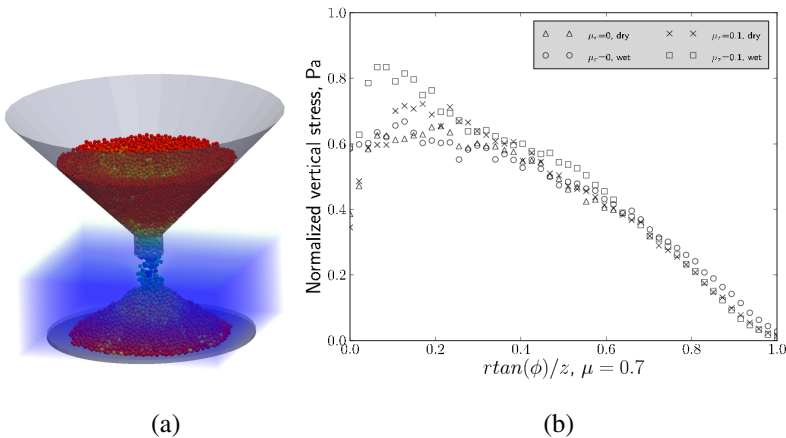


**Fig. 2.** CFD/DEM simulation of sandpiling in water. (a) Schematic of forming a sandpile in water through hopper flow; (b) Comparison of pressure dip in sandpiles formed in dry/wet conditions and with/without consideration of rolling resistance.

## 5 Conclusion

A CFD-DEM numerical tool has been developed to simulate the fluid-particle interaction in granular soils. It was benchmarked by two classic geomechanics problems and was further applied to the sand pile formation in water. It is shown that important behavior of fluid-particle interaction in soils can be well captured.

**Acknowledgement.** The work was supported by Research Grants Council of Hong Kong (GRF 622910).

## References

- [1] De Felice, R.: The voidage function for fluid-particle interaction systems. *Int. J. Multiphase Flow* 20(1), 153–159 (1994)
- [2] Zhu, H., Zhou, Z., Yang, R., Yu, A.: Discrete particle simulation of particulate systems: Theoretical developments. *Chemical Engineering Science* 62(13), 3378–3396 (2007)
- [3] O’Sullivan, C.: *Particulate Discrete Element Modelling: A Geomechanics Perspective*. Spon Press (an imprint of Taylor & Francis), London (2011)
- [4] Zhou, Y.C., Wright, B.D., Yang, R.Y., Xu, B.H., Yu, A.B.: Rolling friction in the dynamic simulation of sandpile formation. *Physica A* 269, 536–553 (1993)

# Realistic Simulation of Progressive Brittle Rock Failure Near Excavation Boundary

M. Cai

Laurentian University, Sudbury, Ontario, Canada  
mcai@laurentian.ca

**Abstract.** Over the last two decades, the importance of rock material heterogeneity on rock strength has been well recognized. Because of the material heterogeneity, local stress concentration is generated from which failure is initiated. In addition to material heterogeneity, geometrical heterogeneity in the form of boundary irregularity must be properly considered when assessing rock strength. This is particularly important for modeling brittle rock failure near excavation boundary. As the tunnel face advance, the maximum tangential stress at the wall increases gradually. Any surface geometrical heterogeneity will increase the stress, which in turn will affect the spalling failure process. It is demonstrated in the present study that when the excavation boundary geometrical heterogeneity is properly considered, in-situ rock strength can be properly interpreted and progressive rock failure process can be realistically simulated using a simple Mohr-Coulomb model for brittle rocks.

## 1 Introduction

As mining and civil tunneling migrate to deep grounds, high-stress-induced rock fracturing is inevitable. A better understanding of rock failure around underground excavations is important for safe and cost-effective construction.

Numerous numerical methods, such as BEM, FEM, DEM, FEM/DEM combined methods have been used to study the brittle rock failure process from crack initiation, propagation, to coalescence leading to failure. Using a discontinuous modeling approach based on micromechanics, it is possible to capture the rock failure process adequately. However, the disadvantages of this approach are that the input material parameters cannot be determined from physical tests and requires a comprehensive calibration effort. The calibrated material parameters are model depended and cannot be generalized and used by other models. In addition, the requirement for computational resources is high.

Hence, continuum modeling approach is still widely used to model rock failure due to its simplicity of model construction, material property determination, and less demand on computing resources. In the continuum modeling approach, a constitutive model is used to describe the mechanical properties of the rock and failure is indicated by the calculated yielding zones. Although many failure criteria

have been proposed, the most widely used ones in rock mechanics are Mohr-Coulomb failure criterion and Hoek-Brown failure criterion [1].

For realistic simulation of progressive brittle rock failure near excavation boundary, what is required is not a complex strength model with dozens of model parameters which are often difficult to be determined uniquely. The material model has to be simple and we must focus on considering other important factors that influence rock strength. Some major factors that influence rock strength include heterogeneity, scale-effect, boundary condition, intermediate principal stress, stress path, loading rate, excavation method, etc. Some factors will be briefly reviewed in the next section.

Fig. 1 presents the design and the actual “as-built” tunnel profiles at one tunnel location in a deep mine in Canada. The tunnel was excavated using drill-and-blast technique. The fact is that, despite all the good intention to design smooth tunnel walls, the actually constructed tunnel boundary profile is very irregular. It is observed that when people construct numerical models to simulate excavation response, they always make a simplification of the excavation profiles. This is necessary in certain situations to simplify the problem and to make the problem solvable. However, over-simplification could result in misinterpreted material properties. One direct consequence is that the field rock strength can be significantly underestimated if the “as-built” boundary is not considered.

This paper attempts to study the problem of in-situ rock strength of massive rocks in a new perspective. A new interpretation of the true in-situ rock strength is presented and this approach is verified using the Mine-by tunnel case history. It is demonstrated in the present study that when the excavation boundary geometrical heterogeneity is properly considered, the in-situ rock strength can be properly interpreted and the progressive rock failure process can be realistically simulated using a simple Mohr-Coulomb model for brittle rocks.

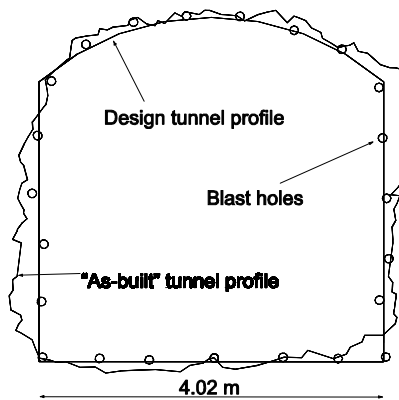


**Fig. 1.** Designed and “as-built” tunnel profiles in a deep mine

## 2 Factors That Influence Rock Strength

### 2.1 Heterogeneity

Over the last two decades, the importance of rock material heterogeneity on rock strength has been well recognized [2-6]. Because of the material heterogeneity, local tensile stress concentration is generated from which failure is initiated. When microscopic strength and deformation variabilities and a gradual loading process are considered, progressive rock failure can be simulated.

Material heterogeneity can be in various forms, ranging from the existence of microcracks, mineral grains of different shapes and sizes with different modulus and strength, contacts of mineral grains, cavities, etc. at a microscopic scale to the existence of veins, contacts of different rock types, large cavities, irregular excavation boundaries, etc. at a macroscopic scale. The impact of heterogeneity to rock strength is that the heterogeneity creates localized stress concentration which facilitates the gradual failure process from damage initiation, propagation, to coalescence. In general, material heterogeneity can be attributed to elastic heterogeneity due to stiffness contrast of different materials, geometrical heterogeneity due to different shape and size of material zones, and contact heterogeneity due to the anisotropy of contact distributions. It is observed that geometrical heterogeneity in the form of boundary irregularity and stress raisers must be properly considered when assessing rock strength. This is particularly important for modeling brittle rock failure near excavation boundary and is the focus of this study.

### 2.2 Scale-Effect

It has been confirmed from laboratory and in-situ tests that there is a scale-effect in rock strength [7-9]. Hoek and Brown [8] proposed to consider the scale-effect of intact rock using the following equation,

$$\sigma_{cD} = \sigma_{c50} \left( \frac{50}{D} \right)^{0.18} \quad (1)$$

where  $\sigma_{c50}$  is the uniaxial compressive strength of a 50 mm diameter sample of the same rock material and  $\sigma_{cD}$  is the uniaxial compressive strength of a sample with a diameter of  $D$  (mm). Test data at a maximum sample diameter of 200 mm show that the rock strength  $\sigma_{c200}$  is about 0.8 times of  $\sigma_{c50}$ . In addition, test data show that the rock strength ratios of  $\sigma_{cD}/\sigma_{c50}$  are almost constant at around 0.8 for  $D$  between 150 and 200 mm. It should be mentioned that Eq. (1) should not be used for  $D > 200$  mm because there are no test data in the dataset used for its development.

### 2.3 Intermediate Principal Stress

Most laboratory test results suggest a significant increase of rock strength due to the intermediate principal stress [10, 11]; a rock strength increase of about 40% to 50% for  $\sigma_3 = 0$  can be seen from their test results. Cai [12] argued, using the

Mine-by tunnel in Canada as an example and applying the strength increase factor from the test by Haimson and Chang [11], that the field rock strength can be enhanced from a laboratory value of 220 MPa to roughly 320 MPa due to effect of the 45 MPa intermediate principal stress acting parallel to the tunnel axis. Field observation does not support such a notion of strength increase. Based on the field observation of rock failure and combined with a 3D numerical simulation using ELFEN [13], Cai [12] concluded that the intermediate principal stress has limited influence on the peak strength of the rock near the tunnel boundary where the minimum principal stress is near zero; large strength increase observed in the laboratory tests was attributed to the end effect of the loading platens.

## **2.4 Stress Path**

For a given rock mass and in-situ stress condition, excavation-induced failure or damage to the rock mass depends on the stress path, which in turn depends on the excavation method employed and sequence adopted. The essence of this dependency is that the mechanical response of elasto-plastic materials is stress-path dependent [14]. Some researchers [15, 16] argue that the complex loading path occurring in the anterior region of a tunnel can lead to a reduction of the in-situ rock strength relative to that obtained from laboratory tests. In the laboratory, the strength is estimated via a simple monotonically increasing loading path where as the in-situ strength is mobilized essentially by unloading the rock mass through a complex loading path involving stress rotation.

## **2.5 Loading Rate**

Rock strength is loading rate dependent [17-19]. Testing results show that the crack propagation stress corresponds to the long-term rock strength [20]. Laigle [21] claimed that because the in-situ loading rate due to tunnel excavation is much lower than the loading rate used in laboratory test, hence, the in-situ strength should be about 50% of the laboratory strength. However, test data show that for loading rate less than  $10^{-1}/s$ , the difference in rock strength is small [22].

# **3 Realistic Simulation of Progressive Brittle Rock Failure at the Mine-by Tunnel**

## **3.1 The Mine-by Tunnel Mystery**

The 3.5 m diameter Mine-by tunnel at the Underground Research Laboratory (URL) in Canada is one of the extensively studied case histories and its contribution to the development of science in rock mechanics is noteworthy. The tunnel was excavated in massive granite without joints and an extensive stress measurement program revealed that the in-situ maximum, intermediate, and minimum principal stresses at the 420 level of the Mine-by tunnel are  $\sigma_1 = 60$ ,  $\sigma_2 = 45$ , and  $\sigma_3 = 11$  MPa, respectively [15]. The tunnel axis is parallel to the intermediate principal stress direction.

According to the Kirsh's solution, the maximum wall tangential stress is  $\sigma_{\max} = 3\sigma_1 - \sigma_3 = 169 \text{ MPa}$ . Because the average uniaxial compressive strength ( $\sigma_c$ ) of the rock is about 220 MPa ( $> \sigma_{\max}$ ) and careful manual excavation was conducted to avoid blasting damage to the rocks, no failure should be expected at the tunnel site. However, well-developed notches occurred in the roof and floor of the tunnel as shown in Fig. 2. This led some researchers [15, 16, 23, 24] believed that the wall rock strength was much lower than 169 MPa. The peak field rock strengths used by these researchers for capturing the notch failure range from 100 to 120 MPa, which was significantly lower than the laboratory strength of 220 MPa. A strength of 100 to 120 MPa is equal to 0.45 to 0.55 of  $\sigma_c$ , a stress level that corresponds to the crack initiation stress. Consequently, some researchers [15] concluded that crack initiation stress can be used to estimate the field spalling strength [24].

As shown in Fig. 2, the wall boundary of the Mine-by tunnel is not smooth, i.e., it is not a "simple" circular tunnel but rather a "complex" circular tunnel. A realistic simulation of the gradual rock failure process must consider modeling details like the non-smooth boundary profile. It is observed that the field rock strength, as approximated by the crack initiation stress, was reached based on interpretation of field data without honoring the true excavation boundary condition in the field. In other words, the influence of geometrical heterogeneity in the form of boundary irregularity was not properly considered in previous studies.

### 3.2 Numerical Model and Material Properties

Hence, an "as-built" FEM model with half-barrels of the perimeter boreholes is constructed in this study (Fig. 3a). In addition, very fine mesh and eight node elements are used to increase the stress analysis accuracy. The in-situ stresses are  $\sigma_1 = 60 \text{ MPa}$ ,  $\sigma_3 = 11 \text{ MPa}$ ,  $\sigma_2 = 45 \text{ MPa}$  (out of plane stress).  $\sigma_1$  is inclined with an inclination angle of  $15^\circ$ . The tunnel excavation in the modeling is completed in 16 stages using the load-split technique in Phase2 [25]. The fixed external boundary is five times away from the tunnel.



Fig. 2. Notch breakouts occurred at the Mine-by tunnel [15]

Instead of using complicated material models with many model parameters, the simple Mohr-Coulomb model with brittle parameters is used to simulate the progressive rock failure observed at the Mine-by tunnel. The elastic modulus is 60 GPa, and the peak and residual cohesions and frictional angles are 59 MPa, 22°, 0.1 MPa, 45°, respectively. The corresponding peak and residual uniaxial compressive strengths (UCS) of the rock are 175 MPa and 0.5 MPa, respectively (see Fig. 3b). For comparison, the peak strength envelope (dashed line with a UCS of 103 MPa) used by Diederichs [24] is also shown Fig. 3b. The maximum tangential wall stress ( $\sigma_{\max} = 169$  MPa) according to Kirsh’s solution and the laboratory rock strength ( $\sigma_c = 220$  MPa) are also indicated in the same figure.

### 3.3 Result and Discussion

The final notch breakout shape, as represented by the yielded elements, is presented in Fig. 4. Both the notch extent and depth on the roof are very close to that recorded from field observation. The degree of failure on the tunnel floor in the field is less than what is simulated in the model because of the influence of excavation debris and gravity on progressive rock failure.

The progressive development of the breakout in the roof is presented in Fig. 5a. For comparison, the recorded notch development from field observation is presented in Fig. 5b. It is seen that the simulated progressive notches development in the roof resemble the actual ones observed in the field. The good correspondence between the model simulation and field observation of the notch shape and its progressive development in the roof demonstrates that the model and the material properties used to reproduce the observed breakout are adequate. In addition, the consideration of the “as-built” tunnel wall boundary is critical for the success of the model simulation.

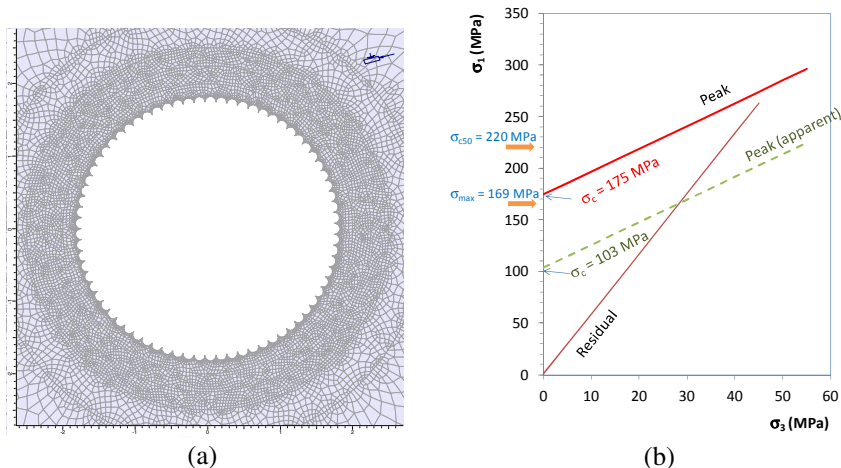


**Fig. 3.** (a) FEM mesh for the Mine-by tunnel simulation with “as-built” wall boundary; (b) peak and residual strength envelopes defined by the brittle Mohr-Coulomb model

When simplified smooth tunnel boundary is used in the numerical simulation, the maximum tangential wall stress is 169 MPa. Because the peak rock strength is 175 MPa, failure will not occur in this case. That is why significantly lower peak rock strength, in the order of 100 to 120 MPa, had to be used by other researchers [15, 16, 23, 24] to simulate the notch breakouts. Obviously, such an interpreted in-situ rock strength is not the “true” rock strength. We call it “apparent” rock strength because an approximation of the true “as-built” tunnel wall boundary is made in the numerical stress analysis. In other words, a numerical “error” was introduced in the interpretation models by ignoring the boundary irregularity. When the model geometry does not honor the reality truthfully, a set of adjusted material parameters has to be used to ensure that the simulation results somewhat resemble the field observation. In the model with “as-built” tunnel wall boundary, the excavation boreholes act as stress concentrators. The maximum principal stress ( $\sigma_1$ ) is greater than 175 MPa at Stage-11 and failure initiates from the borehole that has the largest wall stress. Once the failure is initiated, coupled with further tunnel face advance, spalling failure gradually propagates and eventually forms the notch.

It is seen from this simulation that the assigned “true” peak rock strength to the elements is in the order of 175 MPa, or about  $0.80\sigma_c$ , for  $\sigma_c = 220$  MPa. This makes sense when the scale-effect on rock strength is considered. The laboratory rock strength is often obtained using 50 mm diameter samples. Compared with the actual massive rocks in the field, the strength index represented by  $\sigma_{c50}$  is higher than that from larger samples. On the other hand, if laboratory samples with a diameter of in the range of 150 mm to 200 mm can be tested for  $\sigma_c$ , then this value can be used to represent the “true” in-situ peak rock strength. When test data on large samples are not available,  $(\sigma_c)_{in-situ} = \sigma_{c200} \approx (0.8 \pm 0.05)\sigma_{c50}$  can be used.

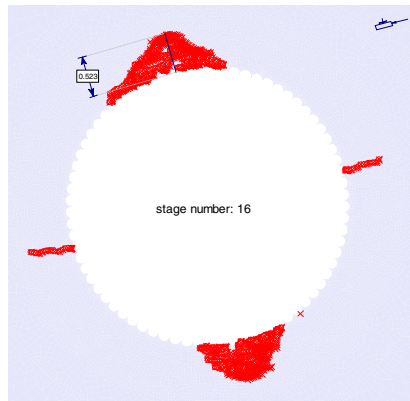
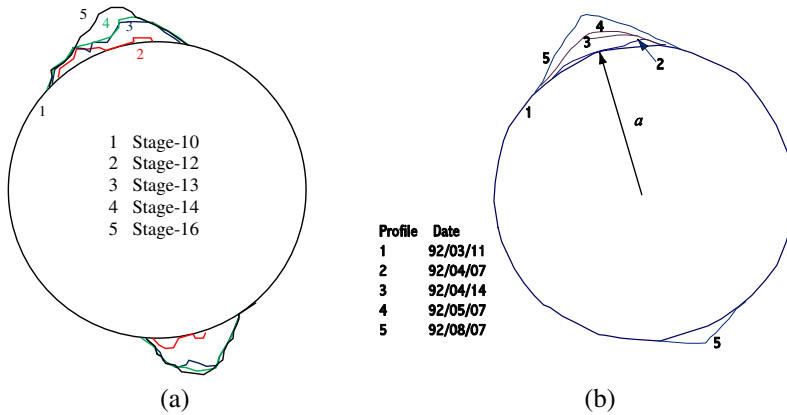


Fig. 4. Final simulated notch shape at the end of excavation (Stage-16)



**Fig. 5.** (a) Simulated progressive development of the notch geometry in the roof and floor; (b) field observation of progressive development of the notch geometry in the roof and floor of the Mine-by tunnel [15]

## 4 Conclusions

Brittle rock failure is a progressive process; it starts from crack initiation and propagation to coalescence of the fractures and eventually reaches the peak strength. Furthermore, for excavation problems, the tangential stress near the excavation boundary is the maximum principal stress. This is the driving force to cause crack initiation, propagation, and coalescence. Any irregularity near the excavation boundary will act as a stress raiser, so that rocks could actually fail at a lower far-field stress level, which means that the actual rock strength should be higher than what is inferred from stress analysis without considering the effect of stress raisers (boundary irregularities).

Using the Mine-by tunnel case history, it is demonstrated in this study that when scale-effect is considered, the in-situ strength for massive crystalline rocks can be approximated by  $(0.8 \pm 0.05)\sigma_c$ . This field spalling strength is significantly higher than the strength value of about  $0.5\sigma_c$  suggested by other researchers. The observed notch in the roof can be captured when the non-smooth tunnel boundary created by perimeter excavation boreholes is considered in the model. The true rock strength is associated with the true excavation boundary condition and excavation process. To simulate the progressive rock failure realistically, it is important to consider all these factors. This study demonstrates the importance of considering the geometrical heterogeneity in the form of excavation boundary irregularity in numerical modeling. Only in this fashion can realistic material properties be used to simulate realistic brittle rock failure process.

**Acknowledgements.** Financial support from Natural Sciences and Engineering Research Council (NSERC) of Canada is greatly appreciated.

## References

- [1] Hoek, E., Brown, E.T.: Practical estimates of rock mass strength. *Int. J. Rock Mech. Min. Sci.* 34(8), 1165–1186 (1997)
- [2] Cundall, P.A.: Modeling of notch formation in the URL Mine-by tunnel, Report to URL/AECL. Itasca Consulting Group Inc., p.15 (1994)
- [3] Tang, C.A.: Numerical simulation of progressive rock failure and associated seismicity. *Int. J. Rock Mech. Min. Sci.* 34, 249–262 (1997)
- [4] Hazzard, J.F., Young, R.P.: Simulating acoustic emissions in bonded-particle models of rock. *Int. J. Rock Mech. Min. Sci.* 37(5), 867–872 (2000)
- [5] Cai, M., Kaiser, P.K., Morioka, H., Minami, M., Maejima, T., Tasaka, Y., Kurose, H.: FLAC/PFC coupled numerical simulation of AE in large-scale underground excavations. *Int. J. Rock Mech. Min. Sci.* 44(4), 550–564 (2007)
- [6] Lan, H.X., Martin, C.D., Hu, B.: Effect of heterogeneity of brittle rock on micromechanical extensile behavior during compression loading. *Geophysical Research* 115(B01202), 1–14 (2010)
- [7] Mogi, K.: The influence of the dimensions of specimens on the fracture strength of rocks. *Bull. Earthquake Res. Inst. (The University of Tokyo)* 40, 175–185 (1962)
- [8] Hoek, E., Brown, E.T.: *Underground excavations in rock*. Institution of Mining and Metallurgy, London (1980)
- [9] Jackson, R., Lau, J.S.O.: The effect of specimen size on the laboratory mechanical properties of Lac du Bonnet grey granite. In: Cunha, A.P. (ed.) *Scale Effects in Rock Masses*. Balkema, Rotterdam (1990)
- [10] Mogi, K.: Effect of intermediate principal stress on rock failure. *J. Geophys. Research*. 72, 5117–5131 (1967)
- [11] Haimson, B.C., Chang, C.: A new true triaxial cell for testing mechanical properties of rock, and its use to determine rock strength and deformability of Westerly granite. *Int. J. Rock Mech. Min. Sci.* 37(1-2), 285–296 (2000)
- [12] Cai, M.: Influence of intermediate principal stress on rock fracturing and strength near excavation boundaries - insight from numerical modeling. *Int. J. Rock Mech. Min. Sci.* 45(5), 763–772 (2008)
- [13] Rockfield Software Ltd.: *ELFEN*. Version 3.7 (2003)
- [14] Cai, M.: Influence of stress path on tunnel excavation response - numerical tool selection and modeling strategy. *Tunnelling and Underground Space Technology* 23, 618–628 (2008)
- [15] Martin, C.D.: Seventeenth Canadian Geotechnical Colloquium: The effect of cohesion loss and stress path on brittle rock strength. *Canadian Geotechnical Journal* 34(5), 698–725 (1997)
- [16] Read, R.S., Chandler, N.A., Dzik, E.J.: In situ strength criteria for tunnel design in highly-stressed rock masses. *Int. J. Rock Mech. Min. Sci.* 35(3), 261–278 (1998)
- [17] Lankford, J.: The role of tensile microfracture in the strain rate dependence of the compressive strength of fine-grained limestone-analogy with strong ceramics. *Int. J. Rock Mech. Min. Sci. & Geomech. Abstr.* 18(1), 173–175 (1981)
- [18] Lajtai, E.Z., Scott Duncan, E.J., Carter, B.J.: The effect of strain rate on rock strength. *Rock Mech. Rock Engng.* 24, 99–109 (1991)
- [19] Cai, M., Kaiser, P.K., Suorineni, F., Su, K.: A Study on the Dynamic Behaviour of the Meuse/Haute-Marne Argillite. *Physics and Chemistry of the Earth* 32(8-14), 907–916 (2007)

- [20] Lajtai, E.Z., Schmidtke, H.: Delayed Failure in Rock Loaded in Uniaxial Compression. *Rock Mech.* 19, 11–25 (1986)
- [21] Laigle, F.: Short-term and delayed behaviors of underground openings - field observations and numerical simulations. In: Hart, P., Varona, P. (eds.) *Proc. 4th International FLAC Symposium*. Paper No. 02-08 (2006)
- [22] Lockner, D.A.: Rock failure. *Rock Physics and Phase Relations, Rock Physics and Phase Relations*. American Geophysical Union, 127–147 (1995)
- [23] Hajiabdolmajid, V., Kaiser, P.K., Martin, C.D.: Modelling brittle failure of rock. In: Girard, J., Liebman, M., Breeds, C. (eds.) *Proc. 4th North American Rock Mech. Symposium*, pp. 991–998 (2000)
- [24] Diederichs, M.S.: The 2003 Canadian Geotechnical Colloquium: Mechanistic interpretation and practical application of damage and spalling prediction criteria for deep tunnelling. *Can. Geotech. J.* 44(9), 1082–1116 (2007)
- [25] Rocscience Inc.: *Phase<sup>2</sup>*. Rocscience Inc., Version 8 (2011)

# Excavation Damaged Zone Modelling in Claystone with Coupled Second Gradient Model

Frédéric Collin\* and Benoît Pardoën\*\*

Argenco Department  
University of Liège  
1, Chemin des Chevreuils B-4000 Liège, Belgium  
f.collin@ulg.ac.be

**Abstract.** Galleries excavation leads to damage and significant properties changes of the host rock. The fracture structure of the excavation damaged zone created around the galleries remains nowadays a major issue especially in the context of underground storage. In order to correctly model the strain localisation, the second gradient local model (regularization method) is used within a hydro-mechanical modelling of a gallery excavation. The numerical results provide information about the strain localisation bands pattern.

**Keywords:** fracturing, numerical modelling, excavation damaged zone, strain localisation.

## 1 Introduction

Gallery excavation in clayey rocks induces stress perturbations that trigger damage propagation. The damage can either be diffuse or localised and can lead to significant changes in the material properties. The excavation process creates the so-called excavation damaged zone (EDZ) in which the mechanical and hydraulic properties are modified. The prediction of the extension and especially of the fracturing structure in this zone remains a major issue.

Since strain localisation in shear band mode is frequently observed in experimental works, the excavation damaged zone can be modelled by considering the development of strain localisation bands.

## 2 Strain Localisation Modelling

Within the framework of classical finite elements, the strain localisation depends on the mesh size and orientation (Collin et al. [1]). An enhanced model, introducing an internal length scale, is thus needed to correctly model the post peak and

---

\* Corresponding author.

\*\* FRIA, FRS-FNRS research fellow.

localisation behaviour. Among the different regularization methods, the second gradient local model (Chambon et al. [2-3]) is used. In the latter, the continuum is enriched with microstructure effects: the kinematics includes the classical one (macro) and the microkinematics ([4-6]). For coupled second gradient model, the two balance equations to be solved (Collin et al. [7]), for every kinematically admissible virtual displacement field  $u_i^*$  and virtual pore water pressure field  $p_w^*$ , read in a weak form:

$$\int_{\Omega} \left( \sigma_{ij} \frac{\partial u_i^*}{\partial x_j} + \Sigma_{ijk} \frac{\partial^2 u_i^*}{\partial x_j \partial x_k} \right) d\Omega = \int_{\Omega} G_i u_i^* d\Omega + \int_{\Gamma_e} (\bar{t}_i u_i^* + \bar{T}_i D u_i^*) d\Gamma \quad (1)$$

$$\int_{\Omega} \left( \dot{M} p_w^* - m_i \frac{\partial p_w^*}{\partial x_i} \right) d\Omega = \int_{\Omega} Q p_w^* d\Omega + \int_{\Gamma_q} \bar{q} p_w^* d\Gamma \quad (2)$$

where  $\sigma_{ij}$  is the total stress field,  $\Sigma_{ijk}$  is the double stress dual of the (micro) second gradient, which needs an additional constitutive law, and  $\Omega$  denotes the current solid configuration (volume).  $G_i$  is the body force per unit volume,  $t_i$  is the external traction (classical) forces per unit area,  $T_i$  is an additional external (double) force per unit area, both applied on a part  $\Gamma_e$  of the boundary of  $\Omega$  and  $D u_i$  is  $u_i$  normal derivative. Further,  $\dot{M}$  is the time derivative of the water mass inside  $\Omega$ ,  $m_i$  is the mass flow,  $Q$  is a sink term and  $\Gamma_q$  is the part of the boundary where the input water mass per unit area  $\bar{q}$  is prescribed.

The total stress field is defined according to Terzaghi's postulate:

$$\sigma_{ij} = \sigma'_{ij} - S_{r,w} p_w \delta_{ij} \quad (3)$$

where  $\sigma'_{ij}$  is the effective stress,  $S_{r,w}$  is the water saturation degree and  $\delta_{ij}$  is the Kronecker symbol. The double stress  $\Sigma_{ijk}$  has no link with the pore water pressure.

The second gradient law gives  $\Sigma_{ijk}$  as a function of the (micro) second gradient. It is a linear elastic law with isotropic linear relationship deduced from (Mindlin [5]) and it depends only on one elastic parameter  $D$ . The shear band width is proportional to this elastic parameter ([2; 8]).

### 3 Numerical Modelling and Results

A hydro-mechanical modelling of a gallery excavation is performed in two-dimensional plane strain state with impervious gallery wall (undrained). It takes into account the hydraulic permeability anisotropy and the initial anisotropic stress state corresponding to a gallery of the Andra underground research laboratory (Meuse/Haute-Marne, France) drilled in Callovo-Oxfordian claystone. The end of excavation corresponds to 5 days of numerical modelling (fig. 1).

A flow model is used to reproduce transfers in porous media. The constitutive mechanical law (first gradient law) used for the clayey rock is an elastoplastic

model with a Drucker-Prager yield surface. It includes friction angle hardening and cohesion softening as a function of the Von Mises equivalent plastic strain.

Several calculations were performed to focus on the influence of second gradient elastic modulus  $D$ , dilatancy  $\psi$  and cohesion softening on the strain localisation. Numerical results emphasize that a cohesion softening is needed to initiate the strain localisation process around the gallery. The second gradient elastic modulus has a significant influence on the width of the shear strain localisation bands appearing around the gallery. Its value has to be chosen carefully regarding the mesh element size. No dilatancy permits the appearance of strain localisation during the excavation whereas, when using dilatancy the strain localisation only appears after the excavation. It emphasizes transient localisation behaviour after the excavation, under constant radial stress at gallery wall (1 atm). It has been observed that excavation process creates rock fractures during the excavation (Blümling et al. [9]) then a value close to  $\psi=0$  seems preferable.

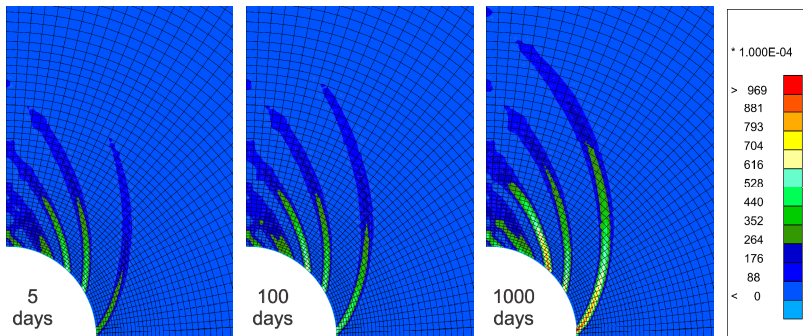


**Fig. 1.** Evolution of strain localisation bands pattern (total deviatoric strain) after the excavation for an elastoplastic model with cohesion softening

The strain localisation structure (fig. 1) exhibits a chevron fracture pattern around the gallery corresponding to *in situ* observations (Cruchaudet et al. [10]). The extension of this excavation damaged zone fairly corresponds to the *in situ* experimental measurements of shear fractures. The final dimensions of the zone are about 0.8 m horizontally and 5.5 m vertically. The extension of the damaged zone based on *in situ* shear fracture measurements is 0.8 m horizontally, 3.9 m and 5.1 m respectively vertically upward and downward (Cruchaudet et al. [10]). Because of the material anisotropic stress state, the chevron fractures are concentrated above the gallery and the convergence is anisotropic. The latter is important during the excavation and keeps increasing afterwards. The comparison between numerical results and experimental measurements realized in the considered gallery (fig. 2) indicates a good matching especially for the vertical convergence.

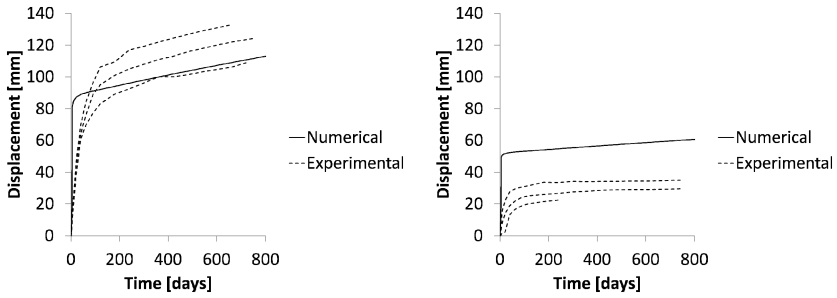


Fig. 2. Matching between numerical results and experimental measurements of the gallery convergence in (left) vertical and (right) horizontal directions

## 4 Conclusion

The excavation damaged zone in claystone had been fairly well modelled with strain localisation. Within this zone, the modelling provides information about the fracture structure and its evolution corresponding to in situ observations. Nevertheless, the rock state and its properties changes still have to be considered. It would be necessary to validate the results with a more accurate modelling of the rock anisotropy and of the hydro-mechanical coupling occurring in this zone (Levasseur et al. [11]). Permeability is probably not homogeneous in the damaged zone and probably depends on a mechanical parameter such as the plastic deformation (Levasseur et al. [12]).

## References

- [1] Collin, F., Levasseur, S., Chambon, R.: Numerical post failure methods in multiphysical problems. *Eur. J. Environ. Civ. Eng.* 13(7-8), 983–1004 (2009)
- [2] Chambon, R., Caillerie, D., El Hassan, N.: One-dimensional localisation studied with a second grade model. *Eur. J. Mech. - A/Solids* 17(4), 637–656 (1998)
- [3] Chambon, R., Caillerie, D., Matsushima, T.: Plastic continuum with microstructure, local second gradient theories for geomaterials: localization studies. *Int. J. Solids Struct.* 38, 8503–8527 (2001)
- [4] Toupin, R.: Elastic materials with couple-stresses. *Arch. Ration. Mech. Anal.* 11, 385–414 (1962)
- [5] Mindlin, R.D.: Micro-structure in linear elasticity. *Arch. Ration. Mech. Anal.* 16, 51–78 (1964)
- [6] Germain, P.: The method of virtual power in continuum mechanics. Part 2 Micro-structure. *SIAM J. Appl. Math.* 25, 556–575 (1973)
- [7] Collin, F., Chambon, R., Charlier, R.: A finite element method for poro mechanical modelling of geotechnical problems using local second gradient models. *Int. J. Numer. Meth. Eng.* 65(11), 1749–1772 (2006)

- [8] Kotronis, P., Collin, F., Bésuelle, P., Chambon, R., Mazars, J.: Local Second Gradient Models and Damage Mechanics: 1D Post-Localization Studies in Concrete Specimens. In: 7th International Workshop on Bifurcation, Instabilities and Degradation in Geomechanics, pp. 127–142 (2007)
- [9] Blümling, P., Bernier, F., Lebon, P., Derek Martin, C.: The excavation damaged zone in clay formations time-dependent behaviour and influence on performance assessment. *Phys. Chem. Earth* 32, 588–599 (2007)
- [10] Cruchaudet, M., Noiret, A., Talandier, J., Gatmiri, B., Armand, G.: OHZ en GED: EDZ initiale et évolution. ANDRA, D.RP.AMFS.11.0016 (2010)
- [11] Levasseur, S., Bésuelle, P., Collin, F., Chambon, R., Charlier, R., Viggiani, C.: EDZ in clayey rocks: which effect on permeability? In: Proceedings of European Commission - Timodaz-Teresa THMC Conference, Luxembourg, September 29-October 01 (2009)
- [12] Levasseur, S., Charlier, R., Frieg, B., Collin, F.: Hydro-mechanical modelling of the excavation damaged zone around an underground excavation at Mont Terri Rock Laboratory. *Int. J. Rock Mech. Min.* 47, 414–425 (2010)

# On the Modeling of Transition from a Diffuse to a Localized Damage

Dashnor Hoxha<sup>\*</sup>, Amine Sbitti, Senjen Wu, Naima Belayachi,  
and Duc-Phi Do

Laboratoire PRISME, Université d'Orléans  
Polytech'Orléans, 8 rue Léonard de Vinci, 45072 Orléans, France  
dashnor.hoxha@univ-orleans.fr

**Abstract.** An approach to model long term hydromechanical behavior of rock masses around underground excavations is proposed. Implemented in a classical finite element numerical code this approach combine in one hand a continuum model to describe the progressive damage and strain localization and a fracture mechanics XFEM based numerical procedure to model the behavior of fractured mass once the macrofracturing takes places.

## 1 Introduction

Numerical modeling is a favorite tool to predict to some extent long term evolution of structures in general and underground excavation in particular. This evolution is particularly important for underground storages of any type (CO<sub>2</sub>, nuclear or urban wastes, etc). While in engineering practice of design of such underground openings continuum mechanics based models are generally sufficient in many cases one reaches at limits of continuum approach once the strain localization took place ([1],[3]). Not only the strain localization leads to numerical difficulties such as solution fluctuation and mesh-dependent results ([1],[2],[4],[7]) but moreover the shear bands associated to this localization continues to follow continuum mechanics laws even if they are considered to be macroscopic fractures ([3], [5]). The strong discontinuity through the fractures is it in that case ill presented by a continuum approach and a direct fracture mechanics approach would be welcomed but often this means shifting towards a discontinuous approach using some suitable numerical tools ([6]). Fracture mechanics based approaches are well suited to describe the evolution of cracks but their use needs to precisely know the initial geometry of cracks. So modeling of transition from a diffuse to a localize damage needs a coupling between continuous and discontinuous approaches. The approach proposed here is suitable for modeling of fracturing initiated by localization which is often the case in underground openings. Similar approaches are thought to work for other conditions.

---

<sup>\*</sup> Corresponding author.

## 2 From Diffuse to Localized Damage

The coupling of diffuse and localized damage is presented schematically in the Fig. 1. It supposes the use of two ingredients: firstly a nonlocal damages model (or any other softening model) in order to describe the diffuse damage and eventually strain localization, secondly a XFEM approach for modeling behavior of fractures and their growth. Of course one could use the XFEM only approach to make full analyses but the numerical cost would be much higher

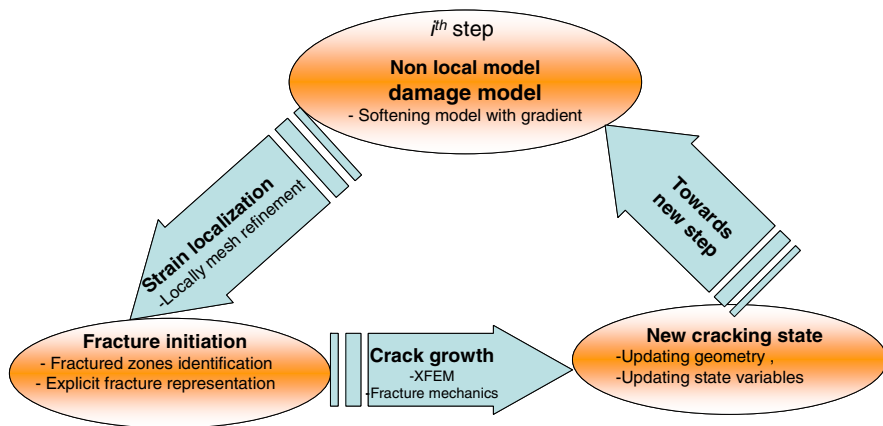


**Fig. 1.** Schematic presentation of continuous –discontinuous approaches coupling

In this work a non local formulation of a Drucker-Prager softening model with a gradient in internal variable is used to describe the nonlinear behavior up to strain localization. In comparison with a classical formulation of constitutive model in a non local model the energy includes in addition to a local term  $W_{loc}$  another term  $W_{gra}(\nabla\chi)$  depending on the gradient of a chosen variable  $\chi$  (in this study it depends on the gradient of equivalent plastic strain) ([5]).

$$W(\underline{\underline{\varepsilon}}, \chi, \lambda, \alpha) = \int_{\Omega} (W_{loc}(\underline{\underline{\varepsilon}}(x), \chi(x)) + W_{gra}(\nabla\chi) + \lambda(\chi - \alpha)) dx \quad (1)$$

In this expression the total energy of the structure is written in a dual form making use of Lagrange multiplier  $\lambda$  and the field  $\alpha$  of gradient dependent variable defined on mesh nodes. The evolution of the hidden variable is defined by solving the problem of energy constrained minimization. Using this formulation for a standard plastic model it is found that normality of plastic flow of local model is maintained for the non local one but the thermodynamic force associated with hidden variable is modified to:

$$F_\chi = -\frac{\partial W(\underline{\varepsilon}, \chi, \lambda, \alpha)}{\partial \chi} = -\frac{\partial W_{loc}(\underline{\varepsilon}, \chi)}{\partial \chi} + (\lambda + r(\alpha - \chi)) \tag{2}$$

with  $r$  being a penalty factor of constrained minimization problem. In practice in order to make use of such formulation it is useful to use a refining mesh strategy in order to assure that the shear band thickness is at least one element. In the Code\_Aster (EDF, France) a special tool is used for this purpose.

Following the approach described in the Fig.1 once the strain localization took place one introduces explicitly fractures and then shift to XFEM by using a level set representation of shear bands. Then fracture mechanics paradigm is used to describe crack growth. Numerically the most suitable criterion for crack growth that under simple assumptions could be used in many situations is the energy restitution rate. For the 2D case treated here, in local base attached to the crack tip assuming a subcritical crack growth one could calculate the rate crack propagation:

$$\begin{cases} V = CG^m (\sin \beta . e_1 + \cos \beta . e_2) \\ \beta = 2 \text{Arc tan} \left[ \frac{1}{4} \left( \frac{K_I}{K_{II}} - \text{sign}(K_{II}) \cdot \sqrt{\left( \frac{K_I}{K_{II}} \right)^2 + 8} \right) \right] \end{cases} \tag{3}$$

with  $G$  being the energy rate  $C$  an  $m$  two model parameters and  $\beta$  is the angle between local crack coordinate system and the global one

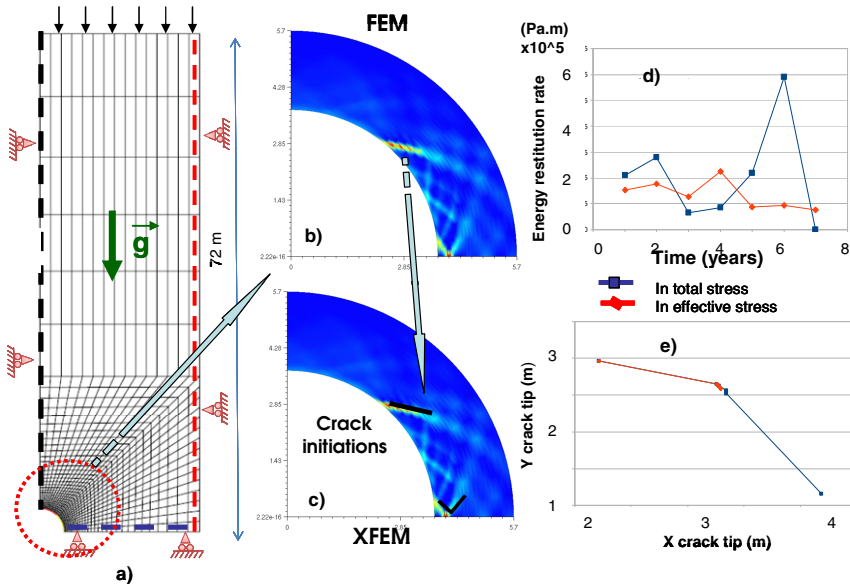


Fig. 2. Fracturing evolution around an excavation in an initially saturated rock massif

### 3 Numerical Application

An illustration of the proposed algorithm is proposed in the Fig. 2.a. A cylindrical tunnel is constructed in a homogenous massif with initial stress state given as it follows  $\sigma_{xx} = \sigma_{yy} = 12MPa$  and  $\sigma_{zz} = 1.3\sigma_{xx}$ . The massif is initially saturated and the water pressure in the gallery level is equal to 5MPa. The rock masses are supposed to follow a Drucker-Prager plastic softening behavior. The excavation of the tunnel is performed in three days and then a ventilation of the gallery is supposed during 7 years which leads in 1m massif désaturation around the excavation and modification of stress and pressure fields in the rock. Consequently, formation of shear bands is observed in the walls of excavation whose persistence and position is controlled by a nonlocal formulation of the model and a selective mesh refining. Figures 2.b and 2.c show the transition from FEM to XFEM paradigm while Fig. 2.d and 2.e show evolution of energy rate restitution and crack tip position evolution as a function of time. For assumption of this analyze estimation of effective stress approach are more optimist than total stress one.

### References

- [1] de Borst, R.: Computation of post-bifurcation and post-failure behavior of strain-softening solids. *Computers and Structures* 25, 211–224 (1987)
- [2] Fernandes, R., Chavant, C., Chambon, R.: A simplified second gradient model for dilatant materials: theory and numerical implementation. *International Journal of Solids and Structures* 45, 5289–5307 (2008)
- [3] Hoxha, D., Giraud, A., Blaisonneau, A., Homand, F., Courtois, A., Chavant, C.: Poroplastic modelling of the excavation and ventilation of a deep cavity. *International Journal for Numerical and Analytical Methods in Geomechanics* 28(4), 339–364 (2004)
- [4] Jirasek, M.: Comparative study on finite elements with embedded discontinuities. *Comput. Methods Appl. Mech. Eng.* 188, 307–330 (2000)
- [5] Kazmyrenko, K.: Modélisation non locale à gradients de variables internes (2010), <http://www.code-aster.org>
- [6] Souley, D., Hoxha, F.: Homand- Distinct element modelling of an underground excavation using a continuum damage model. *Int. J. of Rock Mech. & Min. Sci.* 35, 4–5, Paper No. 26 (1999)
- [7] Pijaudier-Cabot, G., Bazant, Z.P.: Nonlocal damage theory. *Journal of Engineering Mechanics, ASCE* 113, 1512–1533 (1987)

# A Micromechanical Model for Time Dependent Behavior Related to Subcritical Damage in Quasi Brittle Rocks

Yaoying Huang and J.F. Shao

LML, UMR 8107 CNRS, University of Lille, 59655, Villeneuve d'Ascq, France  
College of Civil and Transportation Engineering, HOHAI University, Nanjing China  
jianfu.shao@univ-lille1.fr

**Abstract.** In France, an underground research laboratory is constructed in a clay formation, called Callovo-Oxfordian argillites. In order to evaluate quantitatively the structure durability, it is necessary to achieve a good understanding of the long-term behavior of the material. Subcritical crack growth is one of main causes of time-dependent behavior in rock. In order to rigorous modeling of the time-dependent behavior of studied material, a micromechanical model incorporated subcritical damage propagation is proposed for Callovo-Oxfordian argillites in this paper. In the proposed constitutive model, the argillite is considered as a two phase composite: the clay matrix and the mineral inclusion. Based on experimental observations [1], the clay matrix is described by a time-dependent damage model and the mineral inclusions are described by a linear elastic model. The passage from the micro-scale to the macro-scale is done through different homogenization schemes for studying their influences on the subcritical propagation of cracks.

**Keywords:** argillite, subcritical crack growth, micromechanical model.

## 1 Introduction

In the field of fracture mechanics, crack growth appears when the stress intensity factor reaches the fracture strength of the material. However, slow crack growth also arises when the stress intensity factor is less than the fracture strength. This phenomenon is called subcritical crack growth. Subcritical crack growth is one of main causes of time-dependent behavior in rock [2]. For this reason, taking into consideration the subcritical crack growth in the constitutive model of the rock is important for predict the long-term mechanical behavior of rock structures. The aim of this paper is to propose a micromechanical model of time-dependent damage behavior of the Callovo-Oxfordian argillite. The argillite is then seen as a three phase composite, namely composed of an elastic damaged clay matrix, two different elastic mineral inclusions---calcite and quartz. This micromechanical model takes account of the heterogeneous mineralogical compositions.

## 2 Local Elastic Isotropic Time-Dependent Damage Model for Clay Matrix

In the framework of the thermodynamics, the evolution of damage is determined by a dissipation potential. In the case of time-dependent dissipation, the criterion is used to determine whether the propagation of the microcracks takes place in the clay matrix and further the rate of damage. A linear scalar-valued function of the thermodynamic forces associated with the damage is often adopted as the criterion, and note that the kinetics of evolution of damage is different in tension and compression. Therefore, two damage criteria with exponential form are proposed. In the context of subcritical crack growth, the microcracks propagate with time. Thus, we assume the propagation rate of the microcracks in the clay matrix as a function of the criterion value. Once the value of the damage variable is determined, a secant operator for the damaged clay matrix can be derived from the simple linear relations:  $k(d) = k_0(1-d)$ ,  $\mu(d) = \mu_0(1-d)$ , reads as:  $C_0(d) = 3k(d)J + 2\mu(d)K$ . It's worth noting that the secant operator  $C_0(d)$  is an isotropic tensor, it means that, for the isotropic damaged clay matrix and the spherical inclusion, the Eshelby tensor is also isotropic and it can be evaluated by the following analytical expression:

$$S^0 := 3k_s J + 2\mu_s K \quad (1)$$

$$\text{with } k_s = \frac{k(d)}{3k(d) + 4\mu(d)} \text{ and } \mu_s = \frac{3(k(d) + 2\mu(d))}{5(3k(d) + 4\mu(d))}.$$

## 3 Application to the Different Homogenization Schemes

In this section, we propose to apply three different linear homogenization schemes (Voigt bound [3], dilute scheme [4] and Mori-Tanaka estimation [5]) to the Callovo-Oxfordian argillite. In Fig.1, the axial deformation of the clay matrix without inclusions (legend: Matrix) is larger than that of the composite containing the calcite and quartz inclusions under a constant uniaxial compression. The reinforcing effect of the mineral inclusions in argillite is perfectly obvious. On the contrary, the axial deformation derived from the Voigt upper bound is magnified one thousand times in Fig.1 (legend: Voigt\*1000), but even then it is smaller than that from the others homogenization schemes. That is because the macroscopic elastic properties estimated by Voigt upper bound are greater than that by other schemes. Comparing between the dilute scheme (legend: Dilute) and Mori-Tanaka estimation (legend: M-T), we observe that in the condition of dilute distribution of inclusions, it is fast into the third stage of the creep, the creep rate begins to accelerate very soon under a constant loading. However, with Mori-Tanaka estimation, the curve is more close to the experimental results. The reason causing this difference is that the interactions

between the inclusions are neglected in the dilute scheme, in which the macroscopic axial deformation is larger facing the same damage ratio of the clay matrix.

### 4 Numeric Simulation of Laboratory Tests

The objective of this section is to evaluate the correspondence between the simulation from this micromechanical model and the experimental data. Through the comparisons of different homogenization schemes in previous section, the Mori-Tanaka estimation is considered to be applicable for describing the time-dependent behavior of the argillite induced by propagation of microcracks. One of numeric simulation results is shown by Fig. 2.

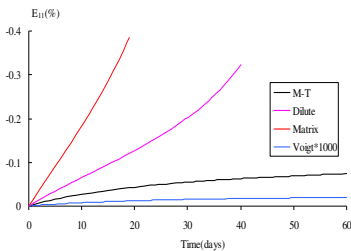


**Fig. 1.** Curves of macroscopic axial strain – time (uniaxial creep test under a constant compression)

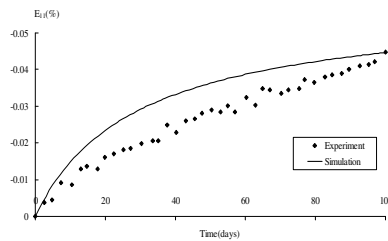


**Fig. 2.** Specimen number: EST 205 GII-05481-01,  $f_{Matrix}=30.4\%$ ,  $f_{Calcite}=36.2\%$ ,  $f_{Quartz}=33.4\%$  (uniaxial creep test under a constant compression  $\Sigma_{11} = -9.9MPa$ )

### 5 Conclusion

The proposed micromechanical model has been tested by three homogenization schemes, and after comparison the results from different schemes, the Mori-Tanaka estimation is adopted for reproduce the experimental data. The simulations of laboratory tests, performed on argillite, have shown a good agreement with experimental data, whereby this time-dependent damage model theoretically proves that the subcritical crack growth is one of main causes of time-dependent behavior in argillite.

### References

1. Abou-Chakra Guery, A., Cormery, F., Shao, J.F., Kondo, D.: A multiscale modeling of damage and time-dependent behavior of cohesive rocks. *Int. J. for Numerical and Analytical Methods in Geomechanics* 33(5), 567–589 (2009)
2. Atkinson, B.K.: Subcritical crack propagation in rocks: theory, experimental results and applications. *J. Struct. Geol.* 4, 41–56 (1982)

3. Voigt, W.: *Über die beziehung zwischen den beiden elasticitat constantan isotroper korper*. Ann. Phys. (Leipzig) 38, 573–587 (1889)
4. Eshelby, J.: *The determination of the elastic field of an ellipsoidal inclusion, and related problems*. Proc. R. Soc. Ser. A 241, 376–396 (1957)
5. Mori, T., Tanaka, K.: *Average stress in matrix and average elastic energy of materials with misfitting inclusions*. Acta Metallurgica 21, 571–574 (1973)

# Study on Equivalent Rheological Damage Model for Jointed Mass

Yaoying Huang<sup>1</sup> and Hong Zheng<sup>2</sup>

<sup>1</sup> School of Hydraulic and Environmental Engineering, Chinese Three Gorges University, Yichang 443002, China  
huangyaoying@sohu.com

<sup>2</sup> Key Laboratory of Geomechanics and Geotechnical and Engineering, Institute of Rock and Soil Mechanics, Chinese Academy of Sciences, Wuhan 43001, China  
hzheng@whrsm.ac.cn

**Summary.** On the basis of the macroscopic continuum theory and the second theorem of damage thermodynamics, the evolution damage functions are proposed for rock and rock joints respectively, postulating that damage is accumulated with increase in visco-plastic strains in rock and rock joints. Here, rock damage is assumed isotropic, but for a joint damage in the normal direction is different from that in the tangential direction. Then, an equivalent rheological damage model is built in terms of effective stresses. The numerical tests show that the equivalent rheological damage model in terms of effective stresses is feasible and is able to simulate the damage evolution of jointed rock mass.

**Keywords:** Jointed rock mass, rheology, equivalent damage, effective stress.

## 1 Introduction

In the past decades, researches on the constitution laws of rocks for coupling damage and rheology have been made thoroughly, but less for jointed rock mass. Observing acoustic emission occurring in creep of salt rock, Szczepanik [1] investigated creep damage of salt rock. Taking into account the mechanism of ductility, damage and rehabilitation of salt rock, Lux and Hou [2] derived the model of damage creep of salt rock from continuum damage mechanics. Using the generalized Bingham creep mode, Xu, et al. [3], suggested a constitution relationship for greenschist through introducing a nonlinear function into the stable creep stage and damage into the speeding creep stage.

On the basis of the macroscopic continuum theory and the second theorem of damage thermodynamics, this study develops an equivalent rheological damage model for jointed rock mass. The derivation is from the hypothesis that visco-plastic deformation is a process of damage accumulation.

## 2 Equivalent Rheological Damage Model for Rock Mass

Rocks and rock joints are totally different in deformation under the action of loads. As a result, the models of damage creep for rocks and rock joints are to be built respectively.

### 2.1 Evolution Damage Functions of Rock Mass

Supposing the process of increase in visco-plastic deformation corresponds to the process of damage accumulation, we will build the evolution functions of rheological damage for rocks and rock joints respectively in the following.

#### 2.1.1 Evolution Function of Rheological Damage of Rock

If rock damage is assumed anisotropic, as is known, the effective stress tensor is asymmetric with nine independent stress components. If, however, rock damage is considered isotropic, the effective stress tensor remains symmetric. For the sake of simplicity in determining parameters, we suppose rock damage is isotropic and define the evolution function of rheological damage of rock as

$$D_r = 1 - \exp[-a_1(\varepsilon^{vp})^{b_1}] \quad (1)$$

where  $a_1$  and  $b_1$  represent damage constants of the rock;  $\varepsilon^{vp}$  denotes the equivalent visco-plastic strain with  $\varepsilon^{vp} = \int \left( \frac{2}{3} d\varepsilon_{ij}^{vp} d\varepsilon_{ij}^{vp} \right)^{\frac{1}{2}}$ .

#### 2.1.2 Evolution Damage Function of Rock Joints

Considering the deformation property in normal direction differs significantly from that in tangential direction, we introduce two evolution damage functions for the normal and the tangential directions respectively. In normal direction, the evolution function of rheological damage is defined as

$$D_{jn} = 1 - \exp[-a_2(\varepsilon_n^{vp})^{b_2}] \quad (2)$$

with  $\varepsilon_n^{vp} \equiv \int |d\varepsilon_n^{vp}|$ ;  $a_2$  and  $b_2$  two damage constants in normal direction.

In tangential direction, the evolution function of rheological damage is defined as

$$D_{j\tau} = 1 - \exp[-a_3(\varepsilon_\tau^{vp})^{b_3}] \quad (3)$$

Here,  $a_3$  and  $b_3$  are two damage constants in tangential direction; and  $\epsilon_{\tau}^{vp} \equiv \int [(d\epsilon_{\tau_1}^{vp})^2 + (d\epsilon_{\tau_2}^{vp})^2]^{\frac{1}{2}}$ ,  $\tau_1$  and  $\tau_2$  represent two tangential unit vectors on the joint perpendicular to each other.

### 2.2 Rheological Damage Model for Rock Mass

According to the hypothesis of strain equivalence, if the material has no damage, stresses are calculated in terms of effective stress  $\tilde{\sigma}$ ; if the material has damage, stresses are calculated in terms of real stress  $\sigma$ . The former assumption will be taken in this study. In this case, the effective stress undertaken by rock reads as

$$\tilde{\sigma}_r = \frac{\sigma_r}{1 - D_r} \tag{4}$$

The effective stresses undertaken by a rock joint are

$$\tilde{\sigma}_n = \frac{\sigma_n}{1 - D_{jn}}, \text{ and } \tilde{\sigma}_{\tau_1} = \frac{\sigma_{\tau_1}}{1 - D_{j\tau}}, \tilde{\sigma}_{\tau_2} = \frac{\sigma_{\tau_2}}{1 - D_{j\tau}} \tag{5}$$

in normal direction and tangential directions, respectively.

Now we suppose the computational model for elastic and visco-plastic deformation is shown in Fig. 1.

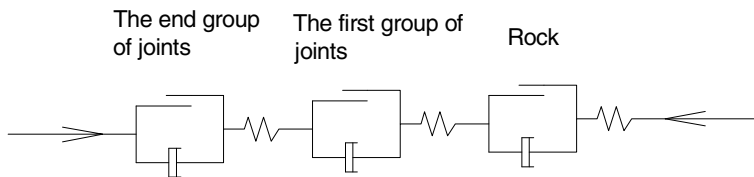


Fig. 1. Equivalent rheological model of jointed rock

The elastic and visco-plastic constitution relation for rock is

$$\Delta\sigma_r = D_r^d (\Delta\epsilon_r - \Delta\epsilon_r^{vp}) \tag{6}$$

where  $D_r^d \equiv (1 - D_r)D_r^0$ ,  $D_r^0$  is the elastic matrix for intact rock,  $\Delta\sigma_r$  is incremental stress vector of rock,  $\Delta\epsilon_r$  and  $\Delta\epsilon_r^{vp}$  are incremental strain vector of rock and incremental visco-plastic strain vector.

Similarly, the elastic and visco-plastic constitution relation for a rock joint is

$$\Delta\sigma_j = D_j^d (\Delta\varepsilon_j - \Delta\varepsilon_j^{vp}) \quad (7)$$

Here,  $D_j^d$  is the elastic damage matrix of the joint, dependent on the normal stiffness  $k_n$  and the tangential stiffness  $k_\tau$  in the intact state, the joint span  $b$ , and  $D_{jn}$  and  $D_{j\tau}$ , see equations (2) and (3).

According to the strain additivity associated with Fig. 1, the total strain of jointed rock mass is the sum of rock strain and joint strain, that is,

$$\Delta\varepsilon = \Delta\varepsilon_r + \sum (T_j)^{-1} \Delta\varepsilon_j \quad (8)$$

where  $T_j$  is a 6×6 matrix determined by the three vectors  $n$ ,  $\tau_1$  and  $\tau_2$  of the joint.

Considering equations (6), (7) and (8), we have

$$\Delta\sigma = D^d (\Delta\varepsilon - \Delta\varepsilon^{vp}) \quad (9)$$

with the composite elastic damage matrix

$$(D^d)^{-1} = (D_r^d)^{-1} + \sum (T_j)^{-1} (D_j^d)^{-1} (T_j^T)^{-1} \quad (10)$$

and the equivalent visco-plastic strain vector

$$\Delta\varepsilon^{vp} = \Delta\varepsilon_r^{vp} + \sum (T_j)^{-1} \Delta\varepsilon_j^{vp} \quad (11)$$

If the jointed rock mass is in the visco-plastic state, we have

$$\dot{\varepsilon}_r^{vp} = \gamma_r \langle F_r \rangle \frac{\partial F_r}{\partial \bar{\sigma}_r} \quad (12)$$

for rock. Here,  $F_r$  represents the yield function of the rock material. In this study, the associated flow rule is adopted. For the rock joint, we have

$$\dot{\varepsilon}_j^{vp} = \gamma_j \langle F_j \rangle \frac{\partial F_j}{\partial \bar{\sigma}_j} \quad (13)$$

Here,  $F_j$  denotes the yield function of the joint material.

### 3 Conclusions

The rheological damage analysis of rock mass can be conducted in terms of effective stress. Nevertheless, the effective stress tensor is asymmetric, leading to the inconvenience of analysis. It is more appropriate that the analysis of rheological deformation is conducted in terms of the real stress but damage must be taken into account.

**Acknowledgements.** This study is supported by the National Basic Research Program of China (973 Program), under the Grant No. 2011CB013505.

### References

- [1] Szczepanik, S.D.: Time-dependent acoustic emission studies on potash. In: Roegies, D. (ed.) *Rock Mechanics as a Multidisciplinary Science*, pp. 471–479. Balkema, Rotterdam (1991)
- [2] Lux, K.H., Hou, Z.: New development in mechanical safety analysis of repositories in rock salt. In: Bennett, R.F. (ed.) *Radioactive Waste Disposal Technologies & Concepts*, pp. 281–286. Springer, Berlin (2000)
- [3] Xu, W., Zhou, J., et al.: Study on creep damage constitutive relation of geenschist specimen. *Chinese Journal of rock Mechanics and Engineering* 25, 3093–3097 (2006)

# On the Solubilities of Anhydrite and Gypsum

Serafeimidis Konstantinos and Anagnostou Georg

ETH Zurich, Switzerland

konstantinos.serafeimidis@igt.baug.ethz.ch

**Abstract.** Claystones containing finely distributed anhydrite swell due to water uptake. Experience shows that the swelling may cause considerable damage and lead to high repair costs. During tunnel excavation, a change in the field conditions occurs, causing the dissolution of anhydrite into its ions and the subsequent precipitation of gypsum crystals. The formation of the latter is (together with water uptake by the clay minerals) the cause of the swelling process. Identifying the conditions under which anhydrite or gypsum is the stable phase is crucial for understanding the process. The current paper presents a thermodynamic model for the individual assessment of anhydrite and gypsum solubilities by additionally considering the partial contact stress between the minerals. The model is verified with experimental and theoretical results from the literature.

## 1 Introduction

The distinguishing characteristic of swelling rocks is their volume increase when coming into contact with water. Anhydritic claystones of the Gypsum Keuper formation are particularly problematic. Their swelling has resulted in damage leading to high repair costs in numerous tunnels (see [1]). It occurs because of the transformation of anhydrite into gypsum crystals via the solution phase, when the anhydrite solubility (i.e. its equilibrium concentration) in the field is higher than that of the gypsum. In general, the solubility of a mineral depends on the temperature, the pressure and the presence of foreign ions in the solution. The chemical reactions of gypsum and anhydrite are



respectively. The system  $CaSO_4 - H_2O$ , with and without salts, has been examined by several authors both theoretically and experimentally (see [2]). Nonetheless, most of the studies are outdated and many of them do not even provide all of the necessary information. Moreover, their results often appear controversial. In the present study, we therefore develop a rigorous thermodynamic model for predicting the solubilities of anhydrite and gypsum by additionally considering the partial contact stress between the minerals, a feature which has so far not been factored in by existing studies. The model predictions are compared with experimental and theoretical results from the literature. The present paper supplements recent

research by the Authors into the kinetics of the reactions (1) and the simultaneous dissolution of anhydrite and precipitation of gypsum in a closed system ([3] [4]).

## 2 Thermodynamic Derivations

### 2.1 Gypsum

The direction of a chemical reaction depends on the difference in the Gibbs free energy  $G$  between the products and the reactants. Any transformation in a system takes place in order to minimize  $G$ , i.e. a chemical reaction will occur spontaneously from a high  $G$  state to a low  $G$  state. The Gibbs Free Energy  $G$  change in a phase is expressed as follows:

$$dG = \mu_i dn_i + V_i dp_i - S dT, \quad (2)$$

where  $S$  is the entropy and  $T$  the temperature of the system. The subscript  $i$  corresponds to the different constituents of the system, while repeated use of  $i$  indicates summation over all constituents. For the gypsum reaction,  $i = Ca^{++}, SO_4^{--}, H_2O$  or  $CaSO_4 \cdot 2H_2O$ . The term  $n_i$  is the number of moles of constituent  $i$  (considered here to be unity) and  $\mu_i$  is the chemical potential. The latter determines how  $G$  changes due to chemical transformations at constant temperature and pressure and is given by  $\mu_i = \mu_i^0 + RT \ln a_i$ , where  $\mu_i^0$ ,  $a_i$  and  $R$  denote the chemical potential at standard state (atmospheric pressure  $p_0 = 0$  and  $T_0 = 298.15$  K), the activity of component  $i$  and the universal gas constant, respectively. The activity of solids and thus of gypsum is unity. The activity of the ions is equal to  $\gamma_i c_i / c_i^0$ , where  $c_i$  is the concentration of the ions,  $c_i^0$  is the concentration at standard state ( $c_i^0 = 1$  mol/l) and  $\gamma_i \leq 1$  is the activity coefficient. The latter is a function of the concentrations of all ions present in the solution (including foreign ions) and accounts for interactions among them. For an extremely dilute solution,  $\gamma_i$  equals unity, which leads to  $a_i = c_i$ . Several theoretical approaches have been proposed in the literature for determining  $\gamma_i$ . For dilute solutions the most common equations are the extended Debye – Hückel and the Davies equations, while for highly saline waters, which is not the case in the present study, the more complicated Pitzer equation is used. For details of the different methods, the reader is referred to Merkel and Planer-Friedrich [5]. Finally, the activity  $a_w$  of water depends on the existence of foreign ions and clay minerals in the system, both of which tend to reduce it. For dilute solutions and in the absence of clay minerals,  $a_w = 1$ .

The term  $V_i dp_i$  in Equation (2), with  $V_i$  denoting the molar volumes of the constituents  $i$ , accounts for the different pressures  $p_i$  that might be exerted on the constituents. In a porous medium, the pore pressure  $p$  is exerted on all constituents  $i$ , while the solid phase (gypsum) is additionally subjected to the contact pressure  $\sigma''$  among the solid grains. The contact pressure  $\sigma''$  is related to the effective stress  $\sigma'$  and can be taken equal to  $\sigma'' / (1 - \phi) = (\sigma - p) / (1 - \phi)$ , where  $\sigma$  and  $\phi$  denote the total stress and the porosity, respectively. The following equation then applies:

$$V_i dp_i = V_{Ca^{++}} dp + V_{SO_4^{--}} dp + 2V_{H_2O} dp + V_{CaSO_4 \cdot 2H_2O} d(p + \sigma^r). \quad (3)$$

Since the molar volumes and entropies remain practically constant, the difference in the Gibbs free energy  $G$  between the products and reactants for the arbitrary temperature  $T$  and pressures  $p_i$  can be calculated by integrating Equation (2):

$$\Delta_{r,G} G|_{T,p,\sigma^r} = \Delta_{r,G} G|_{T_0,p_0,\sigma^r=0}^0 + RT \ln Q_G + \int_{p_0}^p \frac{\partial \Delta_{r,G} G}{\partial p} dp + \int_0^{\sigma^r} \frac{\partial \Delta_{r,G} G}{\partial \sigma^r} d\sigma^r + \int_{T_0}^T \frac{\partial \Delta_{r,G} G}{\partial T} dT, \quad (4)$$

where  $\Delta_{r,G} G|_{T_0,p_0,\sigma^r=0}^0 = \Delta_f G_{SO_4^{--}}^0 + \Delta_f G_{Ca^{++}}^0 + 2\Delta_f G_{H_2O}^0 - \Delta_f G_{CaSO_4 \cdot 2H_2O}^0$  is the difference in the formation Gibbs free energies  $\Delta_f G_i^0$  between products and reactants at standard state (values for  $\Delta_f G_i^0$  can readily be found in the literature, see Table 1) and  $Q_G$  is the activity product ratio ( $Q_G = \gamma_{Ca^{++}} c_{Ca^{++}} \gamma_{SO_4^{--}} c_{SO_4^{--}} a_w^2$ ). The three integrals on the right hand side of Equation (4) read as follows (cf. [6]):

$$\int_{p_0}^p \frac{\partial \Delta_{r,G} G}{\partial p} dp = p \Delta_{r,G} V^0, \quad \int_0^{\sigma^r} \frac{\partial \Delta_{r,G} G}{\partial \sigma^r} d\sigma^r = -\sigma^r V_{CaSO_4 \cdot 2H_2O}, \quad \int_{T_0}^T \frac{\partial \Delta_{r,G} G}{\partial T} dT = -\Delta_{r,G} S^0 (T - T_0), \quad (5)$$

where  $\Delta_{r,G} V^0 = V_{Ca^{++}}^0 + V_{SO_4^{--}}^0 + 2V_{H_2O}^0 - V_{CaSO_4 \cdot 2H_2O}^0$  and  $\Delta_{r,G} S^0 = S_{Ca^{++}}^0 + S_{SO_4^{--}}^0 + 2S_{H_2O}^0 - S_{CaSO_4 \cdot 2H_2O}^0$  are the differences in the molar volumes and entropies, respectively, between products and reactants.

At equilibrium,  $\Delta_{r,G} G|_{T,p,\sigma^r} = 0$  and  $Q_G$  then becomes equal to the equilibrium or solubility constant  $K_G|_{T,p,\sigma^r}$ . From Equations (4) and (5) we obtain:

$$K_G|_{T,p,\sigma^r} = \exp \left[ \frac{1}{RT} \left( -\Delta_{r,G} G|_{T_0,p_0,\sigma^r=0}^0 - p \Delta_{r,G} V^0 + \sigma^r V_{CaSO_4 \cdot 2H_2O}^0 + \Delta_{r,G} S^0 (T - T_0) \right) \right]. \quad (6)$$

**Table 1.** Formation Gibbs free energies, molar volumes and entropies after Anderson [6], with exception the value of  $V_{SO_4^{--}}^0$  which is after Millero [7]

Parameter	Value [kJ/mol]	Parameter	Value [cm <sup>3</sup> /mol]	Parameter	Value [J/mol/K]
$\Delta_f G_{CaSO_4}^0$	-1321.79	$V_{CaSO_4}^0$	45.94	$S_{CaSO_4}^0$	106.7
$\Delta_f G_{CaSO_4 \cdot 2H_2O}^0$	-1797.28	$V_{CaSO_4 \cdot 2H_2O}^0$	74.3	$S_{CaSO_4 \cdot 2H_2O}^0$	194.1
$\Delta_f G_{H_2O}^0$	-237.12	$V_{H_2O}^0$	18	$S_{H_2O}^0$	69.91
$\Delta_f G_{Ca^{++}}^0$	-553.58	$V_{Ca^{++}}^0$	-18.4	$S_{Ca^{++}}^0$	-53.1
$\Delta_f G_{SO_4^{--}}^0$	-744.53	$V_{SO_4^{--}}^0$	13.98	$S_{SO_4^{--}}^0$	20.1

Under the simplifying assumption that the calcium and sulphate ion concentrations are permanently equal during the chemical reaction,  $K_G|_{T,p,\sigma^r} = \gamma_{\pm}^2 c_{eq,G}^2 a_w^2$ , where

$c_{Ca^{++}} = c_{SO_4^{--}} = c_{eq,G}$  is the solubility of gypsum and  $\gamma_{\pm} = \sqrt{\gamma_{Ca^{++}}\gamma_{SO_4^{--}}}$  the mean activity coefficient, which in the present study is calculated according to the Davies equations. In conclusion, the solubility of gypsum at arbitrary temperatures and pressures is calculated by the following equation:

$$c_{eq,G} = (\gamma_{\pm} a_w)^{-1} \sqrt{K_G|_{T,p,\sigma^r}}. \quad (7)$$

## 2.2 Anhydrite

The solubility of anhydrite can be calculated with some minor modifications analogously to Section 2.1. Equation (4) becomes for the anhydrite reaction

$$\Delta_{r,A} G|_{T,p,\sigma^r} = \Delta_{r,A} G|_{T_0,p_0,\sigma^r=0}^0 + RT \ln Q_A + \int_{p_0}^p \frac{\partial \Delta_{r,A} G}{\partial p} dp + \int_0^{\sigma^r} \frac{\partial \Delta_{r,A} G}{\partial \sigma^r} d\sigma^r + \int_{T_0}^T \frac{\partial \Delta_{r,A} G}{\partial T} dT, \quad (8)$$

where  $\Delta_{r,A} G|_{T_0,p_0,\sigma^r=0}^0 = \Delta_f G_{SO_4^{--}}^0 + \Delta_f G_{Ca^{++}}^0 - \Delta_f G_{CaSO_4}^0$ . The three integrals on the right hand side of Equation (8) read as follows:

$$\int_{p_0}^p \frac{\partial \Delta_{r,A} G}{\partial p} dp = p \Delta_{r,A} V^0, \quad \int_0^{\sigma^r} \frac{\partial \Delta_{r,A} G}{\partial \sigma^r} d\sigma^r = -\sigma^r V_{CaSO_4}, \quad \int_{T_0}^T \frac{\partial \Delta_{r,A} G}{\partial T} dT = -\Delta_{r,A} S^0 (T - T_0), \quad (9)$$

where  $\Delta_{r,A} V^0 = V_{Ca^{++}}^0 + V_{SO_4^{--}}^0 - V_{CaSO_4}^0$  and  $\Delta_{r,A} S^0 = S_{Ca^{++}}^0 + S_{SO_4^{--}}^0 - S_{CaSO_4}^0$ . Analogously to Equation (6), the solubility constant

$$K_A|_{T,p,\sigma^r} = \exp \left[ \frac{1}{RT} \left( -\Delta_{r,A} G|_{T_0,p_0,\sigma^r=0}^0 - p \Delta_{r,A} V^0 + \sigma^r V_{CaSO_4}^0 + \Delta_{r,A} S^0 (T - T_0) \right) \right], \quad (10)$$

and, assuming as before that the ion concentrations are equal,  $K_A|_{T,p,\sigma^r} = \gamma_{\pm}^2 c_{eq,A}^2$ .

The solubility of anhydrite at any temperature and pressure conditions then reads as follows:

$$c_{eq,A} = \gamma_{\pm}^{-1} \sqrt{K_A|_{T,p,\sigma^r}}. \quad (11)$$

## 3 Model Verification

The model of Section 2 was tested by comparing the model predictions with experimental data and theoretical predictions obtained by different authors. Figure 1a depicts the equilibrium concentration of anhydrite at different temperatures under atmospheric pressure ( $p = 0$ ) and zero partial stress ( $\sigma^r = 0$ ). In general, the results of the proposed model agree well with the literature data. A greater deviation is observed at low temperatures, where the only available data, however, is that of Kontrec et al. [8]. Similarly, Figure 1b shows the equilibrium concentration of gypsum at atmospheric pressure,  $\sigma^r = 0$  and  $a_w = 1$ . The model predictions are good in this case as well.

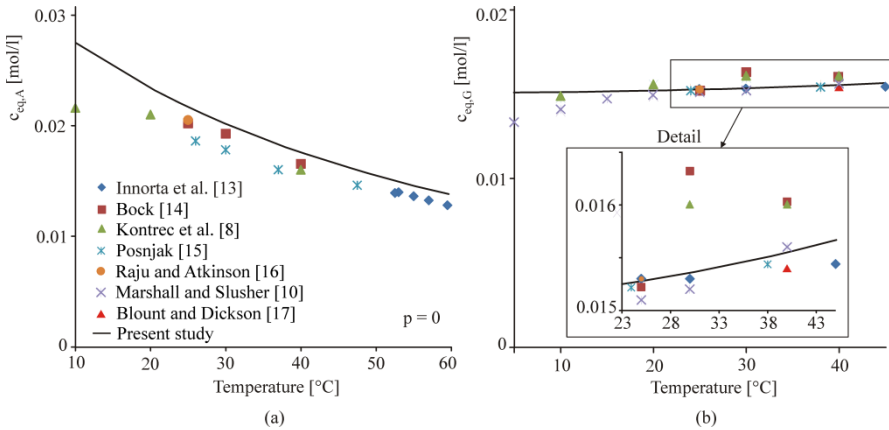


**Fig. 1.** Model verification with literature data at atmospheric pressure: (a) anhydrite and (b) gypsum solubilities as a function of temperature

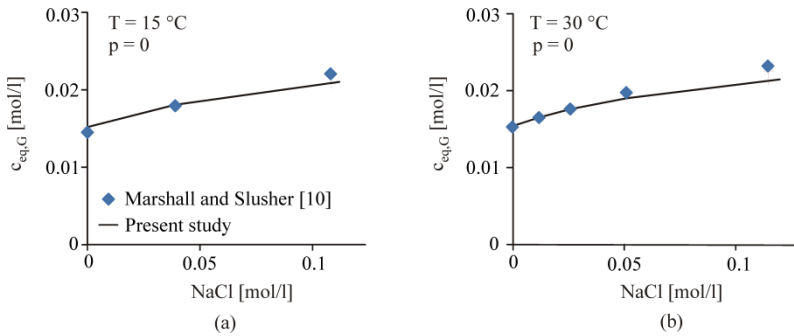


**Fig. 2.** Gypsum solubility at atmospheric pressure as a function of NaCl-molality at (a)  $T = 15\text{ °C}$  and (b)  $T = 30\text{ °C}$

A further verification of the model is shown in Figure 2, which depicts the solubility of gypsum as a function of NaCl-molality at different temperatures. In most existing investigations the molality of NaCl varies between 0 and 6 mol/kg  $\text{H}_2\text{O}$ , which is a common range for saline deposits. However, according to water analysis data from Belchentunnel (see [9]), which has experienced repeated floor heaves and swelling induced damage, the NaCl-molality appears to be relatively low in the Gypsum Keuper ( $< 0.025$  mol/kg  $\text{H}_2\text{O}$ ). Therefore, the verification is restricted to low molalities of NaCl (there is experimental data at such low molalities only for gypsum in Marshall and Slusher [10], where the Davies equation is still applicable (cf. Section 2.1)). The results of the present model once again fit well with the existing experimental data.

### 4 Stable Phase

We study the pressure and temperature conditions under which gypsum and anhydrite co-exist, i.e. have the same equilibrium concentration, in respect of pure water without foreign ions or interactions with clay minerals ( $a_w = 1$ ). The pressure-temperature condition can be derived easily by setting the solubility constant of gypsum (Eq. 6) to that of anhydrite (Eq. 10). Figure 3 shows this condition under the present model as well as under MacDonald [11] and Marsal [12]. The dashed lines assume that there is no contact stress between the mineral grains ( $\sigma'' = 0$ ), i.e. pore pressure alone acts upon the solids (Marsal [12] studied this case alone). The solid lines assume that the solid phase is subject to an additional stress (cf. Section 2). In a similar way to MacDonald [11], we consider lithostatic and hydrostatic total stress and pore pressure conditions under a total unit weight of  $24 \text{ kN/m}^3$  and a water unit weight of  $10 \text{ kN/m}^3$ , respectively. Assuming that the porosity is very low (i.e.,  $\phi \approx 0$ ),  $\sigma'' = 1.4p$ .

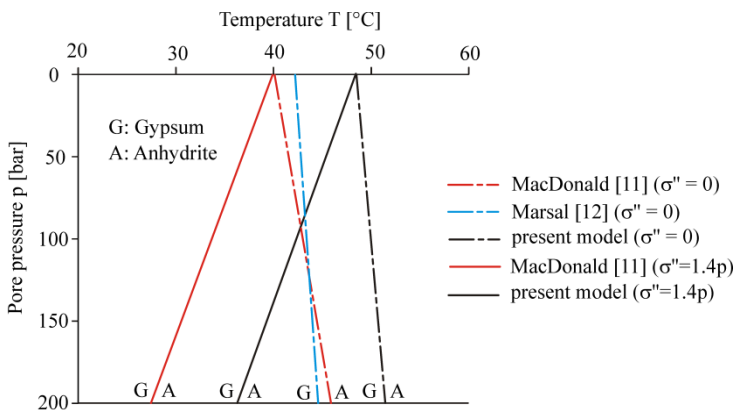


**Fig. 3.** Pressure – Temperature condition at phase equilibrium between anhydrite and gypsum

In both cases (dashed and solid lines of Figure 3) the slopes are almost the same. The minor differences can only be attributed to different thermodynamic values that have been used. According to MacDonald [11] and Marsal [12] anhydrite and gypsum co-exist at atmospheric pressure at a temperature of  $T = 40$  and  $42 \text{ }^\circ\text{C}$ , respectively, while the present model suggests a transition temperature of  $T = 48.85 \text{ }^\circ\text{C}$ . This value is in the middle of the range of the transition temperatures in the literature ( $42 - 60 \text{ }^\circ\text{C}$ , cf. [2]). The difference in the temperature estimates is also a result of the different thermodynamic values assumed.

### 5 Conclusions

A thermodynamic model for estimating anhydrite and gypsum solubility was developed which considers the effect of temperature, pore pressure, and effective

stress. In addition, the model takes account (via the water activity and the ion activity coefficient) of the presence of foreign ions as well as possible interactions with clay minerals. It may serve as a component of more complex models of the swelling process in anhydritic claystones.

## References

- [1] Amstad, C., Kovári, K.: Untertagbau in quellfähigem Fels. Schlussbericht Forschungsauftrag 52/94 des Bundesamts für Strassen ASTRA (2001)
- [2] Freyer, D., Voigt, W.: Crystallization and phase stability of  $\text{CaSO}_4$  and  $\text{CaSO}_4$ -based salts. *Monatshefte für Chemie* 134, 693–719 (2003)
- [3] Serafeimidis, K., Anagnostou, G.: On the kinetics of the chemical reactions underlying the swelling of anhydritic rocks. In: Eurock 2012, Stockholm (2012)
- [4] Serafeimidis, K., Anagnostou, G.: Simultaneous anhydrite dissolution and gypsum precipitation in a closed swelling rock system. In: ARMA 2012, Chicago (in press, 2012)
- [5] Merkel, J.B., Planer-Friedrich, B.: *Groundwater Geochemistry*, 2nd edn. Springer (2008)
- [6] Anderson, G.M.: *Thermodynamics of Natural systems*. University of Toronto, John Wiley and Sons, Inc. (1996)
- [7] Millero, F.J.: *The partial molar volume of electrolytes in aqueous solutions. Water and Aqueous Solution*. Wiley (1972)
- [8] Kontrec, J., Kralj, D., Brečević, L.: Transformation of anhydrous calcium sulphate into calcium sulphate dihydrate in aqueous solutions. *J. of Crystal Growth* 240, 203–211 (2002)
- [9] Wegmüller, M.C.: *Einflüsse des Bergwassers auf Tiefbau/Tunnelbau* (2001)
- [10] Marshall, W.L., Slusher, R.: Thermodynamics of calcium sulphate dihydrate in aqueous sodium chloride solutions, 0–110°C. *J. Phys. Chem.* 70, 4015–4027 (1966)
- [11] MacDonald, G.J.F.: Anhydrite-gypsum equilibrium relations. *Am. J. of Science* 251, 884–898 (1953)
- [12] Marsal, D.: Der Einfluss des Druckes auf das System  $\text{CaSO}_4\text{-H}_2\text{O}$ . *Heidelberger Beiträge zur Mineralogie und Petrographie* 3, 289–296 (1952)
- [13] Innorta, G., Rabbi, E., Tomadin, L.: The gypsum-anhydrite equilibrium by solubility measurements. *Geochim. Cosmochim. Acta* 44, 1931–1936 (1980)
- [14] Bock, E.: On the solubility of anhydrous calcium sulfate and of gypsum in concentrated solutions of sodium chloride at 25°C, 30°C, 40°C and 50°C. *Can. J. Chem.* 39, 1746–1751 (1961)
- [15] Posnjak, E.: The system  $\text{CaSO}_4$ . *Am. J. of Sc.* 5th edition 35, 247–272 (1938)
- [16] Raju, K., Atkinson, G.: Thermodynamics of ‘scale’ mineral solubilities. 3. Calcium sulfate in aqueous NaCl. *J. of Chem. and Engin. Data* 35, 361–367 (1990)
- [17] Blount, C.W., Dickson, F.W.: Gypsum-Anhydrite equilibria in systems  $\text{CaSO}_4\text{-H}_2\text{O}$  and  $\text{CaCO}_3\text{-NaCl-H}_2\text{O}$ . *Am. Mineralogist* 58, 323–331 (1973)

# Binary Medium Model for Rock Sample

Enlong Liu\* and Jianhai Zhang

College of Water Resource and Hydropower  
Sichuan University  
Chengdu, 610065, P.R. China  
liuenlong@scu.edu.cn

**Summary.** Rock materials exhibit strain softening at low confining pressure. How to accurately describe the strain softening of rock materials is very important for rock engineering. A new model, referred to as Binary Medium Model for rock materials, is formulated under the theoretical framework of breakage mechanics for geomaterials. In the model, rock materials is conceptualized as binary medium consisting of bonded blocks and weakened bands which are idealized as bonded elements and frictional elements respectively. During the loading process the bonded elements gradually fracture and transform to be the frictional elements. The deformation properties of the bonded elements are described by ideal elastic-brittle materials and those of the frictional elements are described by hardening elasto-plastic materials. Two sets of breakage parameters, i.e., breakage ratios and strain concentration coefficients, describing the influence of rock structure on the process of failure, are introduced. The proposed model has been used to predict the behavior of sandstone sample in triaxial compression test. By making comparisons of predictions with experimental data it is demonstrated that the new model provides satisfactory modeling of many important features of the behavior of rock materials.

**Keywords:** binary medium model, rock materials, strain softening, breakage parameters.

## 1 Introduction

The failure processes and constitutive properties of rock materials are one of the important problems investigated by the researchers studying on solid mechanics, materials science, geophysics and geological engineering, and the research performed has very profound help in constructing the projects related to rock engineering [1]. There are many constitutive models for rock materials proposed to describe their stress-strain relationship. Based on the results of Drucker and Cam-clay model, Sandler et al. proposed the Cap model for rock materials and the associated algorithm including a FORTRAN subroutine [2, 3]. With the development of damage mechanics and fracture mechanics, many researchers established many constitutive models for rock materials [4-6] including the fracture-damage model,

---

\* Corresponding author.

the coupled elasto-plasticity and damage model, the elasto-brittle-fractal damage model and the statistical damage model. How to describe reasonably the strain softening under low confining pressure and strain hardening under high confining pressure of rock materials, however, is a hot topic and challenging theoretical problem.

A new constitutive model, referred to as Binary Medium Model for rock materials, is formulated here. Rock materials are conceptualized as binary medium consisting of bonded blocks (bonded elements) and weakened bands (frictional elements) here. The deformation properties of the bonded elements are described by ideal elastic-brittle materials and those of the frictional elements are described by hardening elasto-plastic materials. Finally the proposed one has been used to predict the behavior of sandstone sample in triaxial compression test.

## 2 Binary Medium Model for Rock Materials

The rock materials, idealized as binary medium materials, are heterogeneous materials whose constitutive equations can be formulated by using the mesomechanics theory. For a representative element volume (REV), which can be considered as continuum medium macroscopically and includes infinite meso-characteristics microscopically, we can obtain the following relations by the homogenization theory of heterogeneous materials [7]

$$\{\sigma\} = (1 - \lambda)\{\sigma\}_b + \lambda\{\sigma\}_f \quad (1)$$

$$\{\varepsilon\} = (1 - \lambda)\{\varepsilon\}_b + \lambda\{\varepsilon\}_f \quad (2)$$

in which  $\{\sigma\}, \{\varepsilon\}$  are respectively the average stress and strain of the element,  $\{\sigma\}_b, \{\varepsilon\}_b$  are respectively the local stress and strain of the bonded element,  $\{\sigma\}_f, \{\varepsilon\}_f$  are respectively the local stress and strain of the frictional element, and  $\lambda$  is the volumetric ratio of frictional elements.

We define

$$\sigma_m = \sigma_{kk} / 3, \quad \sigma_s = \sqrt{3s_{ij}s_{ij}} / 2 \quad (3)$$

$$\text{and} \quad \varepsilon_v = \varepsilon_{kk}, \quad \varepsilon_s = \sqrt{2e_{ij}e_{ij}} / 3 \quad (4)$$

where  $s_{ij} = \sigma_{ij} - \sigma_{kk}\delta_{ij}/3$ ,  $e_{ij} = \varepsilon_{ij} - \varepsilon_{kk}\delta_{ij}/3$ , and  $\delta_{ij}$  is kronecker symbol.

In the following the stress can be divided into the mean stress and deviatoric stress and the corresponding strain can be divided into the volumetric strain and generalized shear strain respectively. By introducing breakage ratio  $\lambda_v$  and  $\lambda_s$  which reflect respectively the influence of mean stress and deviatoric stress, we can rewrite equation (1) and (2) as the following

$$\sigma_m = (1 - \lambda_v)\sigma_{mb} + \lambda_v\sigma_{mf} \quad (5)$$

$$\varepsilon_v = (1 - \lambda_v)\varepsilon_{vb} + \lambda_v\varepsilon_{vf} \quad (6)$$

$$\sigma_s = (1 - \lambda_s)\sigma_{sb} + \lambda_s\sigma_{sf} \quad (7)$$

$$\varepsilon_s = (1 - \lambda_s)\varepsilon_{sb} + \lambda_s\varepsilon_{sf} \quad (8)$$

where the subscript  $b$  denotes the bonded element and the subscript  $f$  denotes the frictional element.

For the bonded element, the stress-strain relation can be assumed as follows

$$d\sigma_{mb} = K_{m vb}d\varepsilon_{vb} + K_{m sb}d\varepsilon_{sb} \quad (9)$$

$$d\sigma_{sb} = K_{s vb}d\varepsilon_{vb} + K_{s sb}d\varepsilon_{sb} \quad (10)$$

and for the frictional element, the stress-strain relation can be assumed as follows

$$d\sigma_{mf} = K_{m vf}d\varepsilon_{vf} + K_{m sf}d\varepsilon_{sf} \quad (11)$$

$$d\sigma_{sf} = K_{s vf}d\varepsilon_{vf} + K_{s sf}d\varepsilon_{sf} \quad (12)$$

in which  $K_{m vb}$ ,  $K_{m sb}$ ,  $K_{s vb}$ ,  $K_{s sb}$ ,  $K_{m vf}$ ,  $K_{m sf}$ ,  $K_{s vf}$  and  $K_{s sf}$  can be determined by the deformation properties of the bonded element and the frictional element.

Introducing strain concentration coefficients  $c_v$  and  $c_s$ , which satisfy the following expressions

$$\varepsilon_{vb} = c_v\varepsilon_v \quad (13)$$

$$\varepsilon_{sb} = c_s\varepsilon_s \quad (14)$$

From equation (13) and (14) we can obtain

$$d\varepsilon_{vb} = B_v d\varepsilon_v \quad (15)$$

$$d\varepsilon_{sb} = B_s d\varepsilon_s \quad (16)$$

in which  $B_v = c_v^0 + \frac{\partial c_v}{\partial \varepsilon_v} \varepsilon_v^0$  and  $B_s = c_s^0 + \frac{\partial c_s}{\partial \varepsilon_s} \varepsilon_s^0$ .

Through equations (5) to (16), we can obtain the following equations

$$\begin{aligned}
 d\sigma_m = & [(1 - \lambda_v^0)K_{m vb}B_v + K_{mvf} - K_{mvf}(1 - \lambda_v^0)B_v]d\epsilon_v \\
 & + [(1 - \lambda_v^0)K_{msb}B_s + \frac{\lambda_v^0}{\lambda_s^0}K_{msf} - \frac{\lambda_v^0}{\lambda_s^0}K_{msf}(1 - \lambda_s^0)B_s]d\epsilon_s \quad (17) \\
 & - K_{mvf}d\lambda_v \frac{1}{\lambda_v^0}(1 - c_v^0)\epsilon_v^0 - \frac{\lambda_v^0}{\lambda_s^0}d\lambda_s K_{msf} \frac{1}{\lambda_s^0}(1 - c_s^0)\epsilon_s^0 + \frac{d\lambda_v}{\lambda_v^0}(\sigma_m^0 - \sigma_{mb}^0)
 \end{aligned}$$

$$\begin{aligned}
 d\sigma_s = & [(1 - \lambda_s^0)K_{svb}B_v + \frac{\lambda_s^0}{\lambda_v^0}K_{svf} - \frac{\lambda_s^0}{\lambda_v^0}K_{svf}(1 - \lambda_v^0)B_v]d\epsilon_v \\
 & + [(1 - \lambda_s^0)K_{ssb}B_s + K_{ssf} - K_{ssf}(1 - \lambda_s^0)B_s]d\epsilon_s \quad (18) \\
 & - \frac{\lambda_s^0}{\lambda_v^0}K_{svf}d\lambda_v \frac{1}{\lambda_v^0}(1 - c_v^0)\epsilon_v^0 - d\lambda_s K_{ssf} \frac{1}{\lambda_s^0}(1 - c_s^0)\epsilon_s^0 + \frac{d\lambda_s}{\lambda_s^0}(\sigma_s^0 - \sigma_{sb}^0)
 \end{aligned}$$

where the superscript 0 indicates the initial value in a incremental step.

### 3 Determination of Model Paramters

The stress-strain properties of the bonded element can be assumed as be elastic-brittle, which has the following expression

$$d\sigma_{mb} = K_b d\epsilon_{vb} \quad (19)$$

$$d\sigma_{sb} = 3G_b d\epsilon_{sb} \quad (20)$$

where  $K_b$  and  $G_b$  are the bulk modulus and shear modulus of the bonded element respectively, which can be determined by the initial value of the sample tested.

The frictional element is transferred from the bonded element and there are no bonding between them, whose stress-strain properties can be described by the constitutive characteristics of sample broken totally subjected to loading. Here we use the elastic-plastic relationship of the sample to describe it.

The yield surface can be assumed as

$$f_f = \frac{\sigma_{mf}}{\sigma_{sf}} - M_f = 0 \quad (21)$$

in which  $M_f$  are critical stress ratio. The ratio of the plastic volumetric strain to the plastic shear strain of the frictional element can be expressed as

$$d_f = \frac{\Delta \varepsilon_{vf}^p}{\Delta \varepsilon_{sf}^p} = M_f - \eta_f \quad (22)$$

where  $\eta_f = \sigma_{mf} / \sigma_{sf}$  is the effective stress ratio. By equation (21) and (22), we can obtain

$$\Delta \sigma_{mf} = (K_f + A_f K_f^2 \eta_f d_f) \Delta \varepsilon_{vf} - 3A_f K_f G_f d_f \Delta \varepsilon_{sf} \quad (23)$$

$$\Delta \sigma_{sf} = (3A_f K_f G_f \eta_f) \Delta \varepsilon_{vf} + (3G_f + 9A_f G_f^2) \Delta \varepsilon_{sf} \quad (24)$$

where  $K_{mvf} = K_f + A_f K_f^2 \eta_f d_f$  ,  $K_{msf} = -3A_f K_f G_f d_f$  ,  
 $K_{svf} = 3A_f K_f G_f \eta_f$  ,  $K_{ssf} = 3G_f + 9A_f G_f^2$  ,  
 $A_f = 1 / (K_f \eta_f d_f - 3G_f - H_{pf})$  ,  $K_f = G_f \frac{2(1 + \nu_f)}{3(1 - 2\nu_f)}$  is the elastic bulk modulus,  $G_f = P_a G_{0f} (\sigma_c / \sigma_r)^{N_R} (\sigma_{mf} / P_a)^{0.5}$  is the elastic shear modulus,  $H_{pf} = h_f G_f (\frac{M_f}{\eta_f} - 1.0)^{n_f}$  is the hardening modulus,  $P_a$  is the atmosphere pressure,  $\sigma_r$  is the residual strength,  $\nu_f$  is Poisson's ratio,  $G_{0f}$  ,  $N_R$  ,  $h_f$  and  $n_f$  are parameters.

The breakage ratios and strain concentration parameters are assumed as follows

$$\lambda_v = 1 - e^{-a_v \varepsilon_v^{n_v}} \quad (25)$$

$$\lambda_s = 1 - e^{-a_s \varepsilon_s^{n_s}} \quad (26)$$

$$c_v = e^{-t_v \varepsilon_v^{r_v}} \quad (27)$$

$$c_s = e^{-t_s \varepsilon_s^{r_s}} \quad (28)$$

in which  $a_v, a_s, n_v, n_s, t_v, r_v, t_s$  and  $r_s$  are model parameters.

## 4 Testing Verification

For the sandstone samples tested under the confining pressures 2MPa, 10MPa and 50MPa using the apparatus of MTS815 concrete and rock test system, the triaxial results, tested and predicted, are presented in Fig. 1 and Fig. 2. The parameters used in the model are as follows,

$$K_b = K_{b0} (\sigma_{3b} / P_a)^{N_K} , G_b = G_{b0} (\sigma_{3b} / P_a)^{N_G} , K_{b0} = 760.3 \text{MPa} ,$$

$G_{b0} = 3893.0MPa$ ,  $N_K = 0.533$ ,  $N_G = 0.285$ ,  $G_{0f} = 4705$ ,  $N_R = 1.341$ ,  
 $\nu_f = 0.03$ ,  $h_f = 0.56$ ,  $n_f = 4.2$ ,  $M_f = 2.5$ ,  $a_v = 8.0$ ,  $n_v = 0.97$ ,  
 $a_s = 180.0$ ,  $n_s = 1.02$ ,  $t_v = 1.0$ ,  $t_s = 0.95$ ,  $r_v = 2.7$  and  $r_s = 3.25$ .

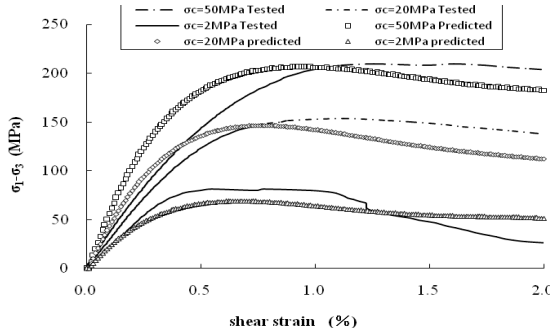


Fig. 1. The deviatoric stress-shear strain relationship

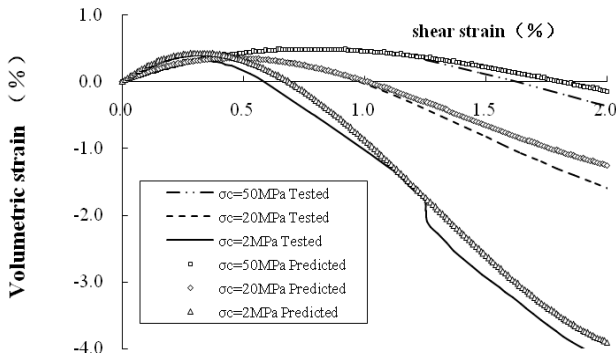


Fig. 2. The volumetric strain-shear strain relationship

## 5 Conclusions

Under the theoretical framework of breakage mechanics for geomaterials, the rock materials is conceptualized as the binary medium consisting of the bonded elements described by ideal elastic-brittle materials and the frictional elements described by hardening elasto-plastic materials respectively. By introducing breakage parameters including breakage ratios and local strain coefficients, a new constitutive model for rock materials is proposed and verified with the triaxial results of sandstone samples, which demonstrated that the proposed model can simulate the constitutive properties of sandstone sample properly.

## References

1. Jaeger, J.C., Cook, N.G.W., Zimmerman, R.W.: *Fundamentals of rock mechanics*. Blackwell Publishing (2007)
2. Sandler, I.S., DiMaggio, F.L., Baladi, G.Y.: Generalized cap model for geological materials. *J. Geotech. Engng. Div. Proc. Am. Soc. Civ. Eng.*, 683–699 (1976)
3. Sandler, I.S., Rubin, D.: An algorithm and a modular subroutine for the CAP model. *Int. J. Numer. Anal. Methods Geomech.* 3, 173–186 (1979)
4. Lu, Y.F., Shao, J.F.: Modelling of anisotropic damage in brittle rocks under compression dominated stresses. *Int. J. Numer. Anal. Methods Geomech.* 26, 645–961 (2002)
5. Wong, T.F., Wong, R.H.C., Chau, K.T., et al.: Microcrack statistics, Weibull distribution and micromechanical modeling of compressive failure in rock. *Mech. Mater* 38, 664–681 (2006)
6. Zhao, Y.: Crack pattern evolution and a fractal damage constitutive model for rock. *Int. J. Rock Mech. Min. Sci* 35, 349–351 (1998)
7. Shen, Z.J., Liu, E.L., Chen, T.L.: Generalized stress-strain relationship of binary medium model for geo-logical materials. *Chinese J. Geotech. Eng.* 27(5), 489–494 (2005)

# Study of Rock Bending Failure Mechanism Based on a Proposed Damage Model

Hamed Molladavoodi\* and Ali Mortazavi

Department of Mining and Metallurgical Engineering  
Amirkabir University of Technology  
424 Hafez Ave, Tehran, Iran  
hamedavodi@aut.ac.ir

**Summary.** The dominant causes of irreversible rock deformations are damage process and plastic flow. Most of the existing elastic-plastic models employed in the analysis and design of rock structures only consider the plastic flow and ignore the full damage process. The common plastic models used to simulate the rock failure, does not model the rock realistically and often the important issues such as stiffness degradation, softening, and significant differences in rock response under tensile and compressive loadings are ignored. In the definition of rock damage yield function, many authors considered only the tensile microcracking. Since quasi brittle materials such as rock degrade under tensile and shear microcracking, separate positive and negative damage yield functions were introduced. The proposed damage yield functions are formulated in the framework of a damage model which was coded in C++ environment and implemented into a commercial code. Accordingly, the proposed model was applied to the simulation of brittle rocks behavior. The three point load bending test of a brittle rock was simulated numerically and numerical findings were presented. The analysis results show a very good match between numerical and experimental observation especially in the post-elastic region.

**Keywords:** Rock damage, Damage yield function, Strain softening.

## 1 Introduction

The macroscopic and phenomenological consequence of damage process is stiffness degradation, softening, and significant difference in tensile and compressive response. In the damage mechanics approach the continuum behavior of a solid is studied within the framework of thermodynamic fundamentals, internal state variables, degradation rule and damage yield function. The main advantage of continuum damage models is that they provide macroscopic constitutive equations, which can be easily implemented and applied to engineering analyses.

In the definition of damage yield function for rocks, many authors (e.g. [1-4]) considered only the tensile microcracking. Since quasi brittle materials such as rock degrade due to shear microcracking, the definition of damage yield function under compressive stress field are vital in the analysis of complex structures.

---

\* Corresponding author.

In this paper, the pseudo logarithmic damage tensor, its associated thermodynamic force, and energy equivalence principle were used in the proposed damage model. Moreover, two separate compressive and tensile damage yield functions were used. The tensile damage yield function proposed by Carol et al. [5,6] was extended to include a compressive damage yield function. The proposed constitutive model was programmed in C++ and implemented into a commercial code. The developed damage model was applied to the analysis of rock damage under three point load bending test condition.

## 2 The Developed Damage Model

In a plane of material, the damage parameter is defined as the ratio of microdefects to entire area. The damage parameter  $D$  ranges between 0 and 1 ( $0 < D < 1$ ). When  $D$  is 0, the rock is undamaged (intact rock), whereas a value close to 1 indicates a rupture of the rock. Experimental observations have highlighted the anisotropic damage in rocks. The anisotropic damage is described by a second order symmetric damage tensor ( $D_{ij}$ ).

The second order symmetric integrity tensor,  $\bar{\phi}_{ij}$ , is defined by the following relation;

$$\bar{\phi}_{ij} = \delta_{ij} - D_{ij} \quad (1)$$

Where  $\delta_{ij}$  are components of Delta Kroneker tensor. The inverse of integrity tensor illustrated by  $\phi_{ij}$  is defined by;

$$\phi_{ip}\bar{\phi}_{pj} = I_{ij} \quad (2)$$

Accordingly, the square root of integrity tensor  $\bar{w}_{ij}$  and the square root of inverse integrity tensor can be written as below:

$$\bar{\phi}_{ij} = \bar{w}_{ik}\bar{w}_{kj}, \quad \phi_{ij} = w_{ik}w_{kj} \quad (3)$$

In the present work, the energy equivalence principle was used to calculate the effective stress ( $\bar{\sigma}_{ij}$ ) and effective strain ( $\bar{\epsilon}_{ij}$ ) in the formulation of the proposed damage model. The nominal stress-strain relationship can be expressed as (see[5-6]);

$$\sigma_{ij} = E_{ijkl} \epsilon_{kl}, \quad E_{ijkl} = \Lambda^0 \bar{\phi}_{ij}\bar{\phi}_{kl} + G^0 (\bar{\phi}_{ik}\bar{\phi}_{jl} + \bar{\phi}_{il}\bar{\phi}_{jk}) \quad (4)$$

where  $\Lambda^0$ ,  $G^0$  are the Lamé constants. The elastic-damage Helmholtz free energy potential is given by the elastic stored energy corresponding to the current secant stiffness and can be written as:

$$\rho\psi = \frac{1}{2} \epsilon_{ij} E_{ijkl} \epsilon_{kl} \quad (5)$$

where  $\rho\psi$  is the elastic-damage free energy potential that. The internal variables are  $\epsilon_{ij}$  and  $\phi_{ij}$  and the thermodynamic associated variables are  $\sigma_{ij}$  and  $Y_{ij}^\phi$ :

$$\sigma_{ij} = \rho \frac{\partial \psi}{\partial \varepsilon_{ij}} = E_{ijkl} \varepsilon_{kl}, \quad Y_{ij}^{\phi} = \rho \frac{\partial \psi}{\partial \phi_{ij}} \quad (6)$$

The rate of degrading dissipation ( $d^{\bullet}$ ) can be expressed as below:

$$\begin{aligned} d^{\bullet} &= \sigma_{ij} \dot{\varepsilon}_{ij} - \rho \dot{\psi} > 0 \\ d^{\bullet} &= -\frac{1}{2} \varepsilon_{ij} E_{ijkl}^{\bullet} \varepsilon_{kl} = \left( -\frac{1}{2} \varepsilon_{ij} \frac{\partial E_{ijkl}}{\partial \phi_{rs}} \varepsilon_{kl} \right) \phi_{rs}^{\bullet} = -Y_{rs}^{\phi} \phi_{rs}^{\bullet} > 0 \end{aligned} \quad (7)$$

The thermodynamic force associated with the inverse of integrity tensor can be written as:

$$-Y_{rs}^{\phi} = \frac{-v^0}{E^0} (\sigma_{kl} \phi_{kl}) \sigma_{rs} + \frac{1+v^0}{E^0} \sigma_{rk} \phi_{kl} \sigma_{ls} \quad (8)$$

For a physically meaningful description of the thermodynamic force conjugate to damage, a pseudo logarithmic damage tensor was introduced. The changes of the pseudo logarithmic damage tensor are defined by Carol et al. [5-6]:

$$L_{rs}^{\bullet} = 2 \bar{w}_{rp} \phi_{pq}^{\bullet} \bar{w}_{qs}, \quad \phi_{pq}^{\bullet} = \frac{1}{2} w_{pr} L_{rs}^{\bullet} w_{sq} \quad (9)$$

The thermodynamic force conjugate to pseudo logarithmic damage tensor ( $y_{rs} = \rho \frac{\partial \psi}{\partial L_{rs}}$ ) was identified.

$$\begin{aligned} d^{\bullet} &= \left( -\frac{1}{2} \sigma_{ij} \frac{\partial E_{ijkl}}{\partial \phi_{pq}} \sigma_{kl} \right) \phi_{pq}^{\bullet} = \left( -\frac{1}{2} \sigma_{ij} \frac{\partial E_{ijkl}}{\partial \phi_{pq}} \sigma_{kl} \right) \left( \frac{1}{2} w_{pr} L_{rs}^{\bullet} w_{sq} \right) = -y_{rs} L_{rs}^{\bullet} > 0 \\ -y_{rs} &= \frac{-v^0}{2E^0} (\bar{\sigma}_{kk}) \bar{\sigma}_{rs} + \frac{1+v^0}{2E^0} \bar{\sigma}_{rk} \bar{\sigma}_{ks} \end{aligned} \quad (10)$$

It is possible to verify the thermodynamic force conjugate to pseudo logarithmic damage as below (see [5-6]):

$$-y_{rs} = \frac{1}{2} \bar{\sigma}_{rk} \bar{\varepsilon}_{ks} \quad (11)$$

## 2.1 Double Damage Functions

A damage function shows the state boundary of the damage development. The damage function consists of two main components of a loading function and a resistant function. It can be described as below:

$$F = f(\text{loading}) - r(\text{resist}) \quad (12)$$

where  $r$  is the current damage threshold (energy barrier), which controls the size of the expanding damage surface (see [7]). The loading function employed by Carol et al. [6] was used to represent the tensile damage as the following:

$$f^+(-\hat{y}_{ij}^+) = \left( \text{tr} \left[ (-\hat{y}_{ij}^+)^{b+1} \right] \right)^{\frac{1}{b+1}} \quad (13)$$

The tensile loading function is based on the positive thermodynamic force conjugate to pseudo logarithmic damage ( $-\hat{y}_{ij}^+$ ). In the above equation,  $b$  is a positive

constant which shows the shape of the damage function. The positive thermodynamic force conjugate to pseudo logarithmic damage are defined as below:

$$-\hat{y}_{ij}^+ = \frac{1}{2} \bar{\sigma}_{ir}^+ \bar{\varepsilon}_{rj}^+ \quad (14)$$

where  $\bar{\sigma}_{ij}^+$ ,  $\bar{\varepsilon}_{ij}^+$  are the positive components of the effective stress and strain tensor respectively. The resistance function of damage function under tensile loading was in an exponential form as below:

$$r^+ = r_{0t} e^{-3k_t L} \quad (15)$$

Where  $r_{0t}$  is the elastic energy associated with peak uniaxial tensile strength ( $\sigma_t$ ) and  $k_t$  is the ratio of elastic energy to the total absorbed energy in the uniaxial tension test.  $L$  is the representative of pseudo logarithmic damage tensor in material. That is defined by:

$$L = \frac{1}{3} tr [\ln(\Phi_{ik} \Phi_{kj})] \quad (16)$$

In the above equation,  $r_{0t}$  is calculated from the following equation:

$$r_{0t} = \frac{\sigma_t^2}{2E_0} \quad (17)$$

In the above equation,  $\sigma_t$  is the peak uniaxial tensile strength and  $k_t$  is determined by:

$$\begin{aligned} b = 0 &\Rightarrow k_t = \frac{r_{0t}}{3g_{ft}} \\ b > 0 &\Rightarrow k_t = \frac{r_{0t}}{g_{ft}} \end{aligned} \quad (18)$$

where  $g_{ft}$  is the area under the tensile uniaxial stress-strain diagram (tensile fracture energy for unit volume).

$$g_{ft} = \int_0^\infty \sigma(\varepsilon) d\varepsilon \quad (19)$$

Hence, the damage function under tensile loading can be written as:

$$F^+ = \left( tr \left[ (-\hat{y}_{ij}^+)^{b+1} \right] \right)^{\frac{1}{b+1}} - r_{0t} e^{-3k_t L} \quad (20)$$

Quasi brittle materials such as rocks damage and fail under compressive and tensile loads. In this work, the tensile loading function was extended to a double tensile and compressive loading function to represent the tensile and compressive damage of rock materials. In the developed damage model, the compressive loading function is defined as below:

$$f^-(-\hat{y}_{ij}^-) = \left( tr \left[ (-\hat{y}_{ij}^-)^{b+1} \right] \right)^{\frac{1}{b+1}} \quad (21)$$

The compressive loading function is based on the negative thermodynamic force conjugate to the pseudo logarithmic damage ( $-\hat{y}_{ij}^-$ ). The negative thermodynamic force associated to pseudo logarithmic damage is defined as below:

$$-\hat{y}_{ij}^- = \frac{1}{2} \bar{\sigma}_{ir}^- \bar{\varepsilon}_{rj}^- \quad (22)$$

The proposed resistance function of damage function under compressive loading is as below:

$$r^- = r_{0c} e^{-3k_c L} \quad (23)$$

where  $r_{0c}$  is the elastic energy associated with peak uniaxial compressive strength ( $\sigma_c$ ) and  $k_c$  is the ratio of elastic energy to total absorbed energy associated with the uniaxial compression test.

In this work, the damage function under compressive loading was proposed in the following form:

$$F^- = \left( \text{tr} \left[ (-\hat{y}_{ij}^-)^{b+1} \right] \right)^{\frac{1}{b+1}} - r_{0c} e^{-3k_c L} \quad (24)$$

The loading function is based on the negative thermodynamic force conjugate to pseudo logarithmic damage (See [8]).

## 2.2 Evolution Rule, Maximum Dissipation Rate

The derivation of the evolution law is based on the physical assumption that a system dissipates the stored energy as quickly as possible. Hence, the energy dissipation rate  $d^*$  shall be maximized under the constraints of damage functions. The maximization can be attained by converting the problem into a minimization problem which can be solved by a Lagrange minimization of  $-d^*$ . By introducing the Lagrange multipliers  $\lambda^\pm > 0$  and redefining the thermodynamic force associated to the pseudo logarithmic damage  $-\hat{y}^\pm$ , the Lagrange function  $\Pi$  becomes:

$$\Pi = -d^* + \lambda^+ F^+ + \lambda^- F^- = (\hat{y}_{ij}^+ + \hat{y}_{ij}^-) L_{ij}^* + \lambda^+ F^+ + \lambda^- F^- \quad (25)$$

and the minimization determines the evolution rule as below:

$$\begin{aligned} \frac{\partial \Pi}{\partial (-\hat{y}_{ij}^+ - \hat{y}_{ij}^-)} &= 0 \rightarrow \\ L_{ij}^* &= \lambda^+ \frac{\partial F^+}{\partial (-\hat{y}_{ij}^+)} + \lambda^- \frac{\partial F^-}{\partial (-\hat{y}_{ij}^-)} = \\ \lambda^+ \frac{(-\hat{y}_{ij}^+)^b}{(\text{tr} [(-\hat{y}_{ij}^+)^{b+1}])^{b/(b+1)}} &+ \lambda^- \frac{(-\hat{y}_{ij}^-)^b}{(\text{tr} [(-\hat{y}_{ij}^-)^{b+1}])^{b/(b+1)}} \end{aligned} \quad (26)$$

where  $\lambda^\pm$  are the damage multipliers that specify the intensity of the increment of the damage variable (See [8]).

### 3 The Model Verification

#### 3.1 Model Geometry and Input Parameters

In order to verify the proposed damage model, a typical standard bending test was simulated. In this test, a rock beam is sited on two standing points at both ends and is subjected to a concentrated load applied at the top and midlength of the sample. A view of the model geometry and employed boundary condition of the test situation is shown in figure 1. A plane stress condition was assumed to analyze the simulated rock beam.

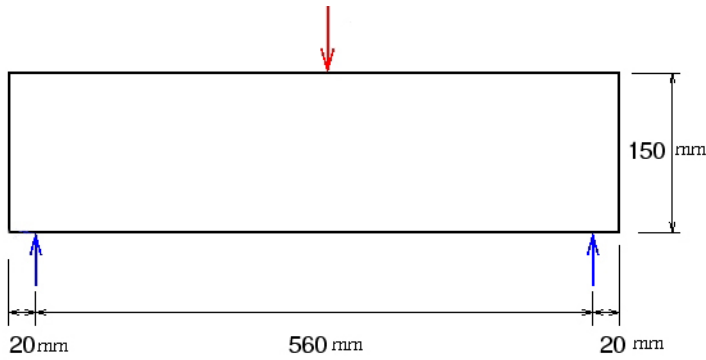


Fig. 1. Model geometry used in the numerical analysis

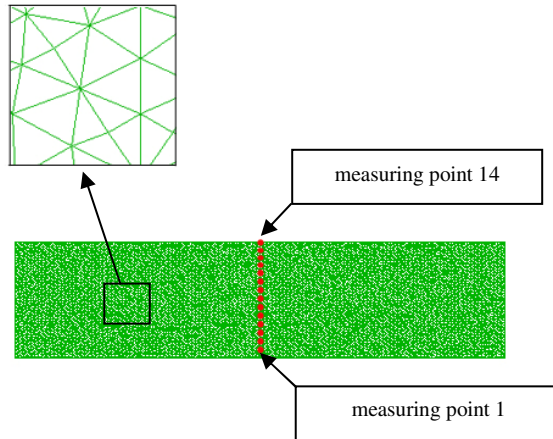


Fig. 2. The discretized rock beam model with their measuring points

In order to assess the local behavior of the sample, series of vertical measuring points were placed at the mid portion of the model as illustrated in Fig. 2. Important variables such as stress and strain components were monitored at these locations. These red measuring points were numbered from down to top of the simulated rock beam as shown in Fig. 2.

In Fig. 2, the rock beam was discretized with triangular elements with an equivalent dimension of 7 mm. A total of 12288 elements were used to discretize the model.

In order to determine the required input parameters, the physical and mechanical properties of a limestone sample reported in Brady & Brown, [9] were selected as a basis. Employing the sophisticated servo-control testing machine, the complete stress-strain behavior of the rock can be determined. A summary of input data consist of physical and mechanical parameters used in the numerical analysis is given in Table 1.

**Table 1.** Rock property data used in the numerical analysis

Bulk modulus (GPa)	Shear modulus (GPa)	Compressive strength (MPa)	Tensile strength (MPa)	Numerical Compressive fracture energy (KPa)	Numerical Tensile fracture energy (KPa)
28.33	13.07	68	6.8	79	5

### 4 Numerical Simulation Results

To illustrate the problem, the principal strain components were evaluated as a function of loading. Fig. 3 shows the change in strain field within the elastic and post-elastic ranges.

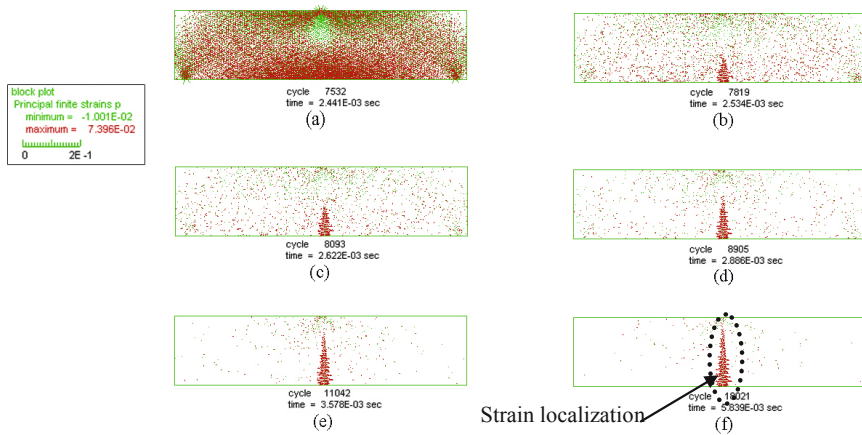


**Fig. 3.** Change in principal strains field as a function of loading

Fig. 3 illustrates both compressive and tensile principal strains distribution within the loaded beam. As shown in Fig. 3, with damage progression the strains are localized in the central area and lower portion of the rock beam. The localized strains are progressively extended to the upper portions of the rock beam. With the extension of damage and strain localization extension toward the top portion of the rock beam, areas of sample outside the damage zone are unloaded. The bifurcation behavior is observed because of the strain localization along the central axis of the rock beam and strain reduction in areas outside of the damage zone. In order to investigate the strain softening behavior, the horizontal stresses and strains were recorded in measuring points. The stress-strain curves are plotted in Fig. 4.

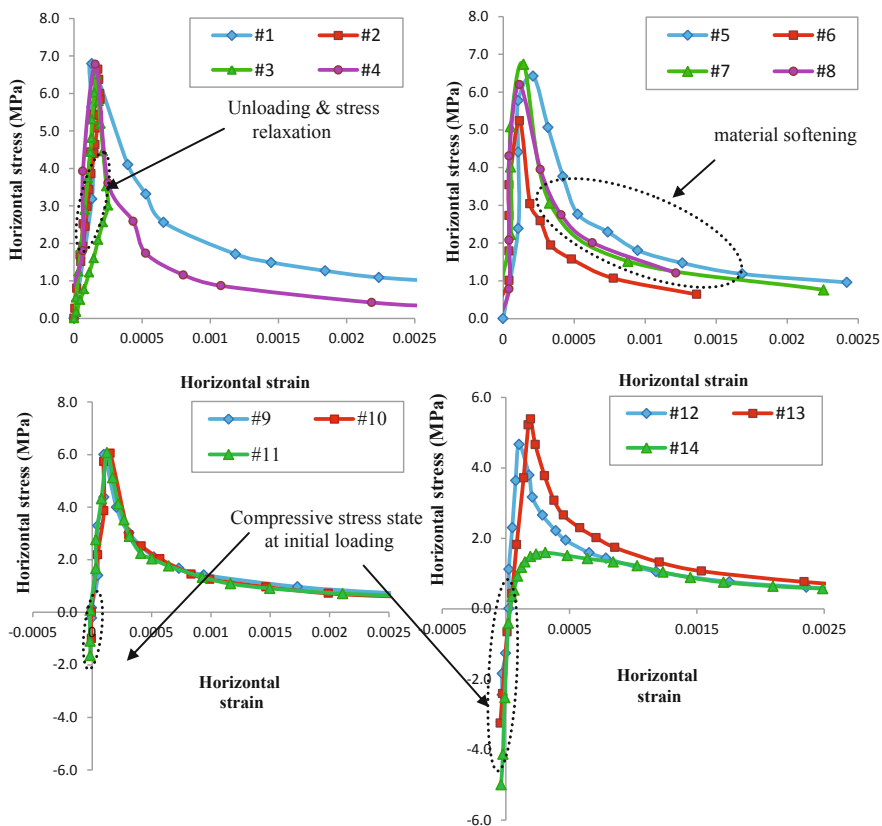


Fig. 4. The horizontal stress - strain diagrams

With regard to the results presented in Fig. 4, at initial stages of loading, all elements of the sample deform homogenously within the elastic region leading to the tensile strength in some elements. Because of the tensile stress concentration in the bottom portion of the rock beam, non-uniform deformations occur within

the sample as a result of strain localization and softening at some zones and unloading at other zones.

Fig.5 shows the state of displacement vectors at various stage of loading in the elastic and post peak (damage) range.

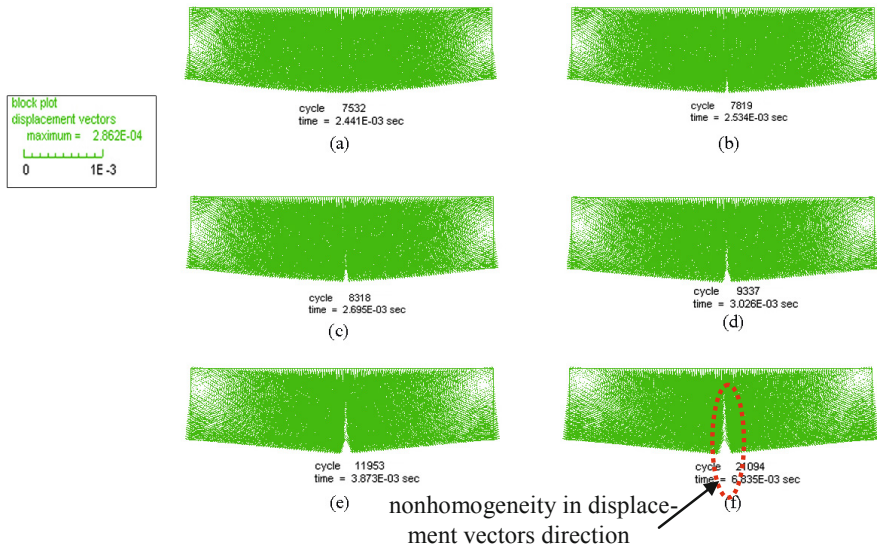


Fig. 5. Variation in displacement vectors demonstrating the fracturing pattern of beam

Fig. 5-a shows the displacement vectors distribution in the elastic range. The effect of the sequential damage process on the displacement vectors field is shown in Fig. 5-b to Fig. 5-f.

## 5 Conclusion

According to the damage theory, the thermodynamic force associated with damage can be described by a thermodynamic force conjugate to pseudo logarithmic damage tensor in a physically meaningful manner. In the presented work, a pseudo logarithmic damage variable was used. The rock material, acting as a quasi brittle material under induced stress condition degrades both in compression and tension. Therefore, for a realistic evaluation of the damage process in rock two distinct damage yield functions under both compressive and tensile loading were proposed. The proposed damage constitutive model was employed to simulate the rock failure mechanism under bending loading conditions. The three point bending test was selected as a basis and simulated numerically. Important governing issues such as occurrence of damage under bending loading condition were described by the proposed model. Strain localization states predicted by the model are in good agreement with practical observations.

## References

- [1] Salari, M.R., Saeb, S., Willam, K.J., Patchet, S.J., Carrasco, R.C.: A coupled elastoplastic damage model for geomaterials. *Comput. Methods Appl. Mech. Engrg.* 193, 2625–2643 (2004)
- [2] Shao, J.F., Chau, K.T., Feng, X.T.: Modeling of anisotropic damage and creep deformation in brittle rocks. *Int. J. Rock Mech. Min. Sci.* 4(3), 582–592 (2006)
- [3] Pellet, F., Hajdu, A., Deleruyelle, F., Besnus, F.: A viscoplastic model including anisotropic damage for the time dependent behaviour of rock. *Int. J. Numer. Anal. Meth. Geomech.* 29, 941–970 (2005)
- [4] Chiarella, A.S., Shao, J.F., Hoteit, N.: Modeling of elastoplastic damage behavior of a claystone. *Int. J. Plast.* 19, 23–45 (2003)
- [5] Carol, I., Rizzi, E., Willam, K.: On the formulation of anisotropic elastic degradation. I. Theory based on a pseudo-logarithmic damage tensor rate. *Int. J. Solids Struct.* 38, 491–518 (2001)
- [6] Carol, I., Rizzi, E., Willam, K.: On the formulation of anisotropic elastic degradation. II. Generalized pseudo-Rankine model for tensile damage. *Int. J. Solids Struct.* 38, 519–546 (2001)
- [7] Wu, J.Y., Li, J., Faria, R.: An energy release rate-based plastic-damage model for concrete. *Int. J. Solids Struct.* 43, 583–612 (2006)
- [8] Mortazavi, A., Molladavoodi, H.: A numerical investigation of brittle rock damage model in deep underground openings. *Engineering Fracture Mechanics* (in press)
- [9] Brady, B.H.G., Brown, E.T.: *Rock Mechanics for underground mining*. Springer (2005)

# To Which Extend the Failure Mode Originates from Microstructure?

François Nicot<sup>1</sup>, Nejib Hadda<sup>1</sup>, Franck Bourrier<sup>1</sup>, Luc Sibille<sup>2</sup>, and Félix Darve<sup>3</sup>

<sup>1</sup> IRSTEA, Grenoble, France

Francois.Nicot@irstea.fr

<sup>2</sup> Institut de Recherche en Génie Civil et Mécanique, Université de Nantes, ECN-CNRS, Nantes, France

<sup>3</sup> UJF-INPG-CNRS, Laboratoire Sols Solides Structures Risques, Grenoble, France

## Abstract

The theoretical study of instabilities in random heterogeneous media has proved to be an interesting pursuit in the development of a proper continuum framework for defining instability in geomaterials. Its influence transcends the scales down to the micro level and extends beyond applications that are being herein contemplated. In this present work, we are specifically interested in establishing a linkage between macroscopic and microscopic instabilities and their respective mathematical expressions through a theoretical analysis which bridges the two scales.

The microstructural investigation of instabilities has already received much attention in the past several years. While one of the ambitions was to elucidate which basic microstructural aspects lead to a macroscopic instability, a prime obstacle is the diversity in the definition of the notion of instability. According to the definition proposed by Bagi (2007), which is in line with Lyapunov's definition, an equilibrium mechanical state of a given material system is considered unstable if its kinetic energy increases in a finite way under an infinitesimal load increase (disturbance). This increase in kinetic energy corresponds to a transition (which is basically a bifurcation<sup>1</sup>) from a quasi-static regime toward a dynamical one (Nicot *et al.*, 2009, Darve *et al.*, 2007; Daouadji *et al.*, 2010). The dynamical regime is associated with a failure process that can be either diffuse or localized.

It is commonly acknowledged, with the exclusion of flutter instabilities, that a general and necessary condition for instability to occur in rate-independent materials is given by the so-called “second-order work criterion”, which corresponds to the loss of positive definiteness of the elasto-plastic tangent constitutive matrix (Hill, 1958). More specifically, excluding flutter instabilities, a necessary and sufficient condition is that (see for instance Nicot *et al.*, 2011a and 2011b):

---

<sup>1</sup> A bifurcation can be defined as a discontinuous change in the response of a given system, under a continuous evolution of both state and loading variables. Other definitions can also be found in the literature.

- The equilibrium state belongs to the bifurcation domain, in which the symmetric part of the tangent constitutive operator admits at least one negative eigenvalue. Indeed, the boundaries of the bifurcation domain are given by the surface where the determinant of that symmetric part of the constitutive operator vanishes first and by the plastic limit condition (vanishing of the constitutive determinant itself). Inside this domain, loading directions exist along which the second-order work takes negative values.
- The loading is controlled by mixed parameters, some being composed of stress components, while the others of strain components.
- The mixed control parameters impose a loading direction associated with a negative value of the second-order work.

The second-order work corresponds to the quadratic form associated with the symmetric part of the tangent elasto-plastic constitutive matrix. Viewed at the macroscopic level where a representative elementary volume (REV) is invoked, the second-order work can be computed as the inner product of the Piola-Kirchhoff incremental stress tensor and the spatial gradient of the incremental displacement.

In non-associated plasticity, it turns out that the elasto-plastic matrix is non-symmetric and as such, the emerging bifurcation domain is bounded by an outer surface given by the plastic limit condition and an inner surface defined by the first vanishing values of the determinant of the symmetric part of the constitutive matrix (Darve *et al.*, 2004; Nicot *et al.*, 2007; Wan *et al.*, 2011). Within such a bifurcation domain, the second order work lends itself to the detection of a variety of unstable states involving either plastic strain localization or diffuse deformation (Nicot and Darve, 2011). In this context, the second order work plays a fundamental role in the analysis of divergence instabilities not only in geomechanics (by virtue of geomaterials being intrinsically non-associated), but also in structural mechanics where the stiffness matrix is non-symmetric due to non-conservative or dissipative forces (Challamel *et al.*, 2010).

Moreover, the microstructural origin of the existence of an unstable state and the dynamical regime that ensues (depending on the loading conditions) is thought to be linked to the stability of elementary grain assemblies at an intermediate, mesoscopic scale (Kuhn and Chang, 2006; Tordesillas and Muthuswamy, 2009; Tordesillas *et al.*, 2010), including both cluster patterns of grains ( $n$ -grains cycles) and linear patterns (force chains). The stability of these patterns directly depends upon the possible relative motion of each grain, and therefore on the constitutive behaviour on the contact scale (Kuhn and Chang, 2006; Valanis and Peters, 1996).

From the above discussion, it becomes clear that a proper local variable that can be related to the macroscopic second-order work is needed as an indicator of local stability. Along these lines, a discrete definition of second-order work was proposed by Nicot and Darve (2007) at the microscopic level (i.e. the grain level), by involving local microstructural variables such as the inter-granular incremental force and the inter-granular incremental displacement at a contact point.

The objective of this communication is to shed light on the microscopic counterparts of the second-order work. Following a micromechanical analysis, it can be

shown that the micromechanical expression of the second-order work is the combination of two terms:

$$W_2 = \sum_{p,q} \mathcal{F}_i^c \delta_i^c + \sum_{p \in V} \mathcal{F}_i^p \delta x_i^p \quad (1)$$

The first term  $\sum_{p,q} \mathcal{F}_i^c \delta_i^c$  involves both contact forces  $\bar{f}^c$  and branch vectors

$\bar{l}^c$  between adjoining grains at every contact ‘c’ between adjoining granules ‘p’ and ‘q’. As branch vectors connect the centers of adjoining grains, this first term depends on the internal particle topology (packing). It can be regarded therefore as a configurational term.

The second term  $\sum_{p \in V} \mathcal{F}_i^p \delta x_i^p$  introduces the incremental unbalanced force  $\bar{\mathcal{F}}^p$  applied to each particle ‘p’. When inertial effects are small (in quasi-static regime for example), the contribution of this term becomes negligible too. However, when rapid particles motions occur, this term is likely to be no longer negligible.

Ignoring thereafter the second term, the term  $\sum_{p,q} \mathcal{F}_i^c \delta_i^c$  constitutes a sound basis to investigate the micromechanical origin of the occurrence of some instability modes in granular assemblies. This investigation is carried out by using a discrete element method that enables to go down to the microscale. Two main aspects are discussed:

- The role of force chains in the destabilization of granular assemblies. In particular, the distribution of the contacts where the local term  $w_2^c = \mathcal{F}_i^c \delta_i^c$  is negative is analysed. It is shown how the distribution scales with the repartition of the so-called weak and strong phases.
- Depending upon the loading conditions, a chaotic or self-organized localized kinematic field can develop once the material has destabilized. First insights are given to understand why the nature of the kinematic field can bifurcate toward a specific pattern.

## References

- Bagi, K.: On the concept of jammed configurations from a structural mechanics perspective. *Granular Matter* 9, 109–134 (2007)
- Challamel, N., Nicot, F., Lerbet, J., Darve, F.: Stability of non-conservative elastic structures under additional kinematics constraints. *Eng. Struct.* 32, 3086–3092 (2010)

- Daouadji, A., AlGali, H., Darve, F., Zeghloul, A.: Instability in granular materials: an experimental evidence of diffuse mode of failure for loose sands. *Journal of Engineering Mechanics (ASCE)* 136(5), 575–588 (2010)
- Darve, F., Servant, G., Laouafa, F., Khoa, H.D.V.: Failure in geomaterials, continuous and discrete analyses. *Comp. Methods Appl. Mech. Engrg.* 193, 3057–3085 (2004)
- Darve, F., Sibille, L., Daouadji, A., Nicot, F.: Bifurcations in granular media, macro-and micro-mechanics. *Compte-Rendus de l'Académie des Sciences – Mécanique* 335, 496–515 (2007)
- Hill, R.: A general theory of uniqueness and stability in elasticplastic solids. *J. Mech. Phys. Solids* 6, 236–249 (1958)
- Kuhn, M.R., Chang, S.C.: Stability, bifurcation, and softening in discrete systems: a conceptual approach for granular materials. *Int. J. of Solids and Structures* 43, 6026–6051 (2006)
- Nicot, F., Darve, F.: Micro-mechanical investigation of material instability in granular assemblies. *Int. J. of Solids and Structures* 43, 3569–3595 (2006)
- Nicot, F., Darve, F.: A micro-mechanical investigation of bifurcation in granular materials. *Int. J. of Solids and Structures* 44, 6630–6652 (2007)
- Nicot, F., Sibille, L., Donzé, F., Darve, F.: From microscopic to macroscopic second-order works in granular assemblies. *Mechanics of Materials* 39(7), 664–684 (2007)
- Nicot, F., Sibille, L., Darve, F.: Bifurcation in granular materials: an attempt at a unified framework. *Int. J. of Solids and Structures* 46, 3938–3947 (2009)
- Nicot, F., Challamel, N., Lerbet, J., Prunier, F., Darve, F.: Bifurcation and generalized mixed loading conditions in geomaterials. *Int. J. of Num. Anal. Methods in Geomechanics* 35(13), 1409–1431 (2011a)
- Nicot, F., Hadda, N., Bourrier, F., Sibille, L., Darve, F.: Failure mechanisms in granular media, a discrete element analysis. *Granular Matter* 13(3), 255–260 (2011b)
- Nicot, F., Darve, F.: Diffuse and localised failure modes, two competing mechanisms, *Int. J. Numer. and Analyt. Meth. In: Int. J. Numer. and Analyt. Meth. in Geomech.* (2011), doi:10.1002/nag.912
- Tordesillas, A., Muthuswamy, M.: On the modeling of confined buckling of force chains. *Journal of the Mechanics and Physics of Solids* 57(4), 706–727 (2009)
- Tordesillas, A., Walker, D.M., Lin, Q.: Force cycles and force chains. *Physical Review E* 81, 011302 (2010)
- Wan, R.G., Pinheiro, M., Guo, P.J.: Elastoplastic modelling of diffuse instability response of geomaterials. *Int. J. of Num Anal Methods in Geomechanics* 35(2), 140–160 (2011)

# Excavation Damage Zone at High Depths: Field Cases and Coupled Analysis

Jean Vaunat<sup>\*</sup>, Antonio Gens, and Benoit Garitte

Department of Geotechnical Engineering and Geosciences,  
Technical University of Catalonia (UPC)  
Building D2, c/ J. Girona, 1-3, 08034 Barcelona  
jean.vaunat@upc.edu

## 1 Introduction

One of the challenges of the modelling of hard soils and soft rocks is the precise reproduction of the Excavation Damage Zone (EDZ) around openings. Characteristics of the EDZ are indeed affected by both fissuration and fracturation, which requires the consideration of a mechanical model based on coupled damage-plasticity. In this abstract, the performance of a composite model developed by Vaunat & Gens [1] for such a purpose is tested by comparison with a large-scale field tests carried out in the Underground Research Laboratory of Meuse/Haute Marne (Callovo-Oxfordian formation, see Armand et al. [2]; Su [3]).

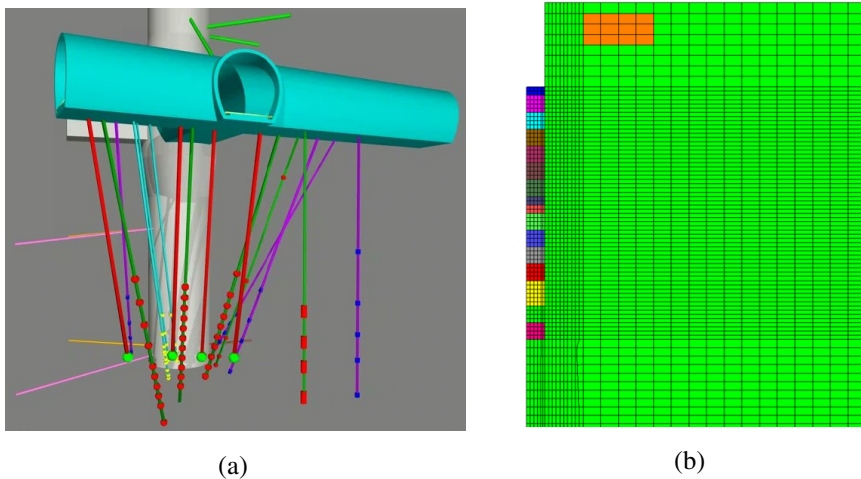


**Fig. 1.** MODEX-REP experiment – a) field test features and b) mesh considered for the modelling

---

<sup>\*</sup> Corresponding author.

The field case forms part of the works carried out during the construction of the access shaft to the underground laboratory of the French National Agency for Nuclear Waste Management. In order to obtain information about the hydro-mechanical response of the clay, the perturbation caused by the shaft advance on the surrounding clay rock was followed by mean of an extensive instrumentation. A layout of the instrumentation is shown in Figure 1.a. Three boreholes equipped with extensometers (red points), one borehole with inclinometer (red squares), four boreholes with pore pressure transducers (blue points) and four boreholes with strain gauge cells (green points) were installed from a lateral niche previous to the excavation of the shaft at the considered depth. Instrumentation campaign is completed by wave velocity survey, hydraulic conductivity measurement by means of pulse tests and installation of radial extensometers after excavation. the simulation of the excavation of the access shaft to Meuse/Haute Marne URL.

**Table 1.** – Values of model parameters used to model an excavation in the Callovo-Oxfordian mudstone

Elastic parameters							
$E^{b0}_{//}$	$E^{b0}_{\perp}$	$E^M_{//}$	$E^M_{\perp}$	$v^b_{//}$ ( $= v^b_{/\perp}$ )	$v^M_{//}$ ( $= v^M_{/\perp}$ )	$\alpha_T$	–
10000 MPa	10000 MPa	2250 MPa	2250 MPa	0.23	0.23	$5.10^{-6}$ $K^{-1}$	–
Viscoplastic and viscodamage parameters							
$R_c^M$	$m^M$	$\eta^M$	$s_T^M$	$\chi$	$r^b_0$	$r^b_1$	$\eta^b$
15 MPa	3	$1.10^6$ MPa.s	–	0.384	0.0005 MPa.m/m	0.04	$1.10^4$ MPa.s

Excavation of the access shaft has been modelled using Code\_bright, a Finite Element code that solves 3D thermo-hydro-mechanical problems in geological media. In the analyses presented, the equations for stress equilibrium, water mass balance and solid mass balance were solved simultaneously, resulting in a hydro-mechanical coupled formulation of a Biot type. The mesh used is depicted in 1.b: it consists of a 2D axisymmetric mesh where the shaft and the lateral niche are represented (the latter in an approximate manner due to the assumption of axisymmetry). Linear elasticity and Hoek & Brown criterion has been considered for the elastoplastic model and isotropic damage model for the damage part. Parameters have been calibrated on the basis of laboratory tests and are summarized in Table 1 (see Vaunat & Gens [1] for parameters significance).

The time evolution of convergence is compared with field measurements in Figure 2. A very good agreement can be observed. In Figure 3, computed and measured angular variation within one point in inclinometer 2208 are (pore

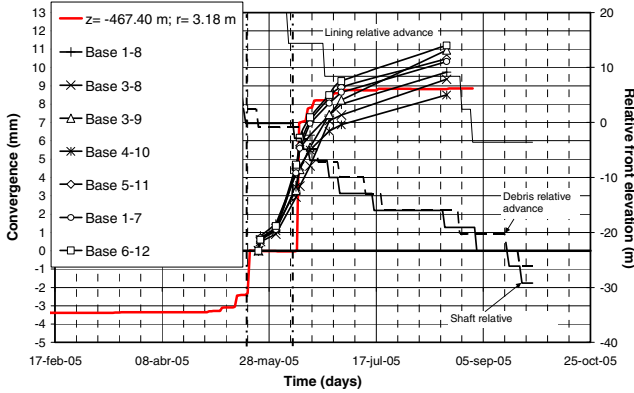


Fig. 2. Shaft convergence: comparison between measurements and numerical results

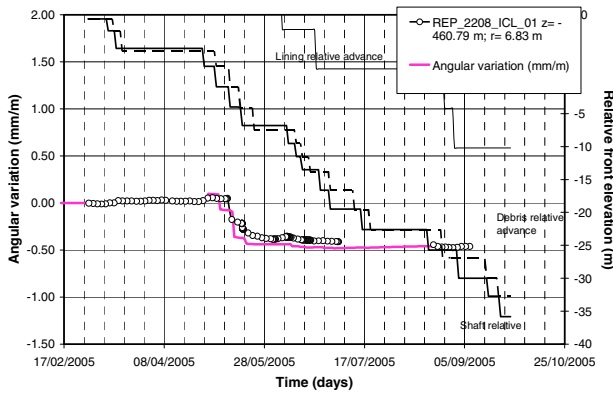


Fig. 3. Deformation close to the shaft: comparison between measurements and numerical results

pressures are discussed in paragraph 2.5.2). In Figure 4, the damage zone predicted by the model is compared with the change in shear wave velocity measured before and after the excavation. Both model and measurements evidence a damage of about 2%. This low value is essentially due to the fact that the Callovo-Oxfordian mudstone has a significant content of carbonates at the level of Modexp experiment.

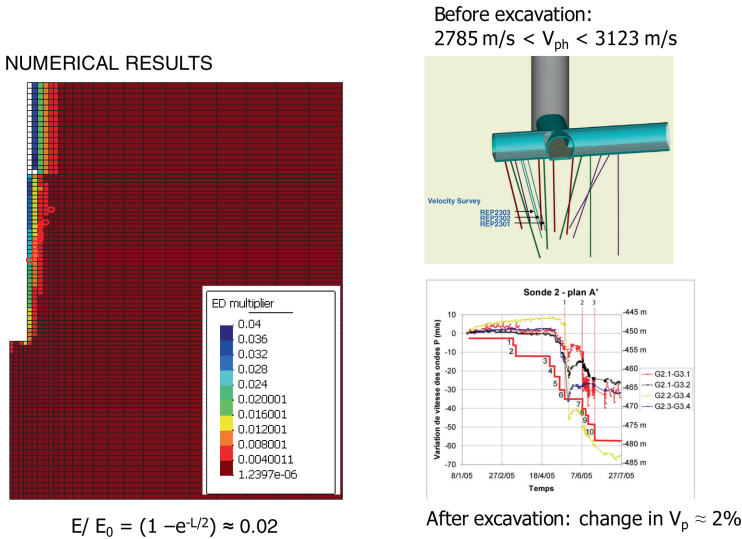


Fig. 4. Damage zone: comparison between measurements and numerical results

## References

- [1] Vaunat, J., Gens, A.: Bond degradation and irreversible strains in soft argillaceous rock. In: Cullighan, P.J., Einstein, H.H., Whittle, A. (eds.) Proceedings of 12th Pan-American Conference on Soil Mechanics and Geotechnical Engineering, Boston, USA, June 23-25, vol. 1, pp. 479–484. Pub. VGE (2003) ISBN 3-7739-5985-0
- [2] Armand, G., Su, K., Wileveau, Y., Delay, J.: Expérimentation REP Résultats des mesures après la phase de fonçage du puits entre les cotes -454 m et -480 m. ANDRA report DRPADPE050855A, Paris, France (2005)
- [3] Su, K.: Development and validation of the constitutive hydromechanical models for Callovo-Oxfordian Argillites: the MODEX-REP Project. ANDRA report, Paris, France (2007)

# A Mohr-Coulomb Failure Criterion for Rocks Subjected to Dynamic Loading

Kaiwen Xia

Department of Civil Engineering  
University of Toronto  
35 St. George St., Toronto, Ontario, Canada M5S 1A4  
kaiwen.xia@utoronto.ca

**Summary.** The classical Mohr-Coulomb failure criterion has been extensively used in various rock engineering applications. To investigate the applicability of the Mohr-Coulomb model to dynamic rock failures, I examined in this work the correlation of the three dynamic rock properties: compressive strength, tensile strength and punch shear strength of Longyou sandstone (LS), obtained using a modified split Hopkinson pressure bar (SHPB) system. Considering the loading rate effect of the rock dynamic properties, the three dynamic properties are compared and correlated. The results show that the famous Mohr-Coulomb criterion can be extended to the dynamic range, given proper conversion of the loading rate.

**Keywords:** dynamic strength, Mohr-Coulomb model; SHPB, punch shear.

## 1 Introduction

Split Hopkinson pressure bar (SHPB) system provides a robust way to measure the dynamic properties of rocks. Invented by Kolsky [1], SHPB is a standard dynamic testing system. Recently, an indirect tensile method, Brazilian disc [2], was employed to acquire the dynamic tensile strength of rock [3-5]. The punch test is a method for measuring shear property of rocks and it has the advantages of the applicability for high strength solids, minimization of the bending stresses on the samples, and facilitation of the sample preparation [6, 7]. We thus adopted the idea of punch tests for metal materials and have successfully designed a dynamic punch shear strength test of rock using SHPB [8].

An important application of the strength measurements is to establish applicable failure criteria. One of most famous criteria, Mohr-Coulomb criterion, has been widely used in numerical simulation and modeling. Because it is well known that the dynamic properties of rocks have a loading rate effects, i.e. the rock strength increases with the loading rate [9], the objective of this paper is to examine the applicability of Mohr-Coulomb criterion to dynamic rock failure cases through the examination of three dynamic strengths of a fine-grained sandstone.

## 2 Split Hopkinson Pressure Bar System

SHPB system is used as the loading device for all dynamic tests in this work. As a standard facility for dynamic testing, SHPB is composed of a striker bar, an incident bar and a transmitted bar (Fig. 1). The striker bar is launched by a low speed gas gun. The impacting of the striker bar on the free end of the incident bar generates a longitudinal compressive wave propagating in the incident bar as the incident wave  $\epsilon_i$ . When the incident wave reaches the bar-specimen interface, part of the wave is reflected back as reflected wave  $\epsilon_r$ , and the remainder passes through the specimen and then enters the transmitted bar as transmitted wave  $\epsilon_t$ . These three waves are measured using strain gauges and used to infer the dynamic response of the material (i.e., stress-strain curve) subsequently.

Using these three waves, the forces  $P_1$  and  $P_2$  on both ends of the specimen can be calculated:

$$P_1(t) = EA[\epsilon_i(t) + \epsilon_r(t)], \quad P_2(t) = EA\epsilon_t(t) \tag{1}$$

where  $E$  and  $A$  are Young's modulus and cross-sectional area of the bars, respectively.

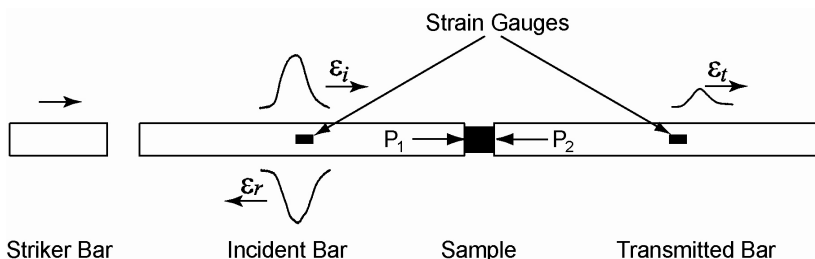


**Fig. 1.** Typical configuration of SHPB. The interaction of the incident wave, transmitted wave and reflective wave leads to the dynamic loadings on the specimen.

## 3 Dynamic Mohr-Coulomb Criterion

Results for dynamic strengths of LS are collected, with dynamic compressive strength measured in this work, dynamic tensile strength reported by Huang et al [5], and dynamic shear strength reported by Huang et al [8]. Based on Mohr-Coulomb theory, the uniaxial compressive strength (UCS)  $\sigma_0$  is given as [10]:

$$\sigma_0 = 2 \tan\left(\frac{\pi}{4} + \frac{\phi}{2}\right)c_0 \tag{2}$$

here  $c_0$  is the cohesion (equal to the shear strength) and  $\phi$  is the internal friction angle. Theoretically, the cohesion  $c_0$  is equal to the pure shear strength. Assuming that the angle of internal friction is a time invariant, the differentiation on both sides of Eq. 2, using the stresses instead of the strengths yields:

$$\frac{d\sigma_c}{dt} = 2 \tan\left(\frac{\pi}{4} + \frac{\phi}{2}\right) \frac{d\tau}{dt} \tag{3}$$

where  $\sigma_c$  is the compressive stress during the dynamic compressive test. One can then convert the dynamic punch shear strength to dynamic UCS (Fig. 2).

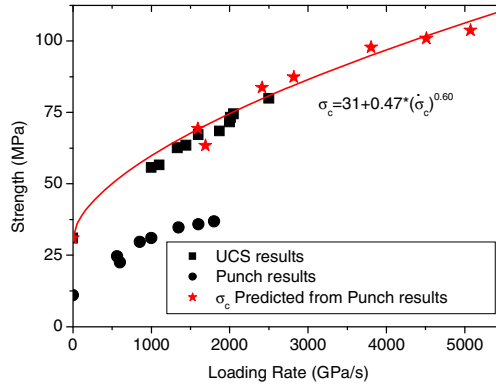


Fig. 2. Dynamic UCS measured and predicted from punch shear strength

Based on the Mohr-Coulomb theory, one can also derive a relation between tensile strength  $\sigma_{t0}$  and shear strength  $c_0$ , and their loading rates:

$$\sigma_{t0} = 2 \cot\left(\frac{\pi}{4} + \frac{\phi}{2}\right) c_0, \quad \frac{d\sigma_t}{dt} = 2 \cot\left(\frac{\pi}{4} + \frac{\phi}{2}\right) \frac{dc}{dt} \tag{4}$$

In a similar way, one can also convert the dynamic punch shear strength to dynamic tensile strength (Fig. 3). It can be seen from the figures that the predicted strength values are consistent with those measured. The observed consistency proves that the Mohr-Coulomb failure criterion can be applied in dynamic conditions, if the loading rates are properly converted.

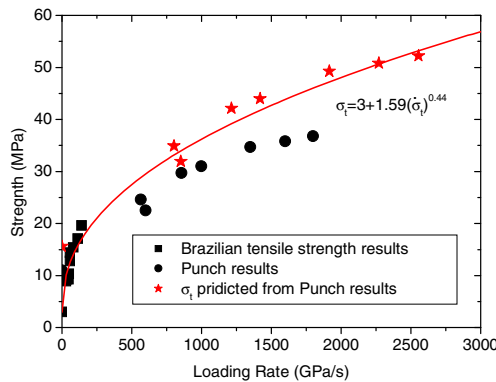


Fig. 3. Tensile strength measured and predicted from punch shear tensile strength

## 4 Conclusion

Dynamic tensile strengths of Longyou Sandstone (LS) are measured and collected. By proper converting the loading rate, these strengths are related and compared. It is showed that the UCS predicted from the punch shear strength of LS matched well with the experimentally measured UCS data, and the tensile strength predicted from the punch shear strength of LS also matched well with the experimental results of dynamic Brazilian tensile strength. We thus conclude that the famous Mohr-Coulomb criterion can be extended to the dynamic range.

Because dynamic material properties are loading rate dependent, it is thus required proper conversion of loading rates in order to apply the Mohr-Coulomb model to dynamic failure. Within the theoretical framework of Mohr-Coulomb model, the relations for converting loading rates are established in this work under the assumption that the internal friction angle is rate independent.

## References

- [1] Kolsky, H.: An investigation of the mechanical properties of materials at very high rates of loading. *Proceedings of the Royal Society A-Mathematical Physical and Engineering Sciences* B62, 676–700 (1949)
- [2] Hobbs, D.W.: The Strength and the Stress-Strain Characteristics of Coal in Triaxial Compression. *J. Geo.* 72(2), 214–231 (1964)
- [3] Cai, M., Kaiser, P.K., Suorineni, F., Su, K.: A study on the dynamic behavior of the Meuse/Haute-Marne argillite. *Phys. Chem. Earth.* 32(8-14), 907–916 (2007)
- [4] Wang, Q.Z., Li, W., Song, X.L.: A method for testing dynamic tensile strength and elastic modulus of rock materials using SHPB. *Pure Appl. Geo.* 163, 1091–1100 (2006)
- [5] Huang, S., Xia, K.W., Yan, F., Feng, X.T.: An Experimental Study of the Rate Dependence of Tensile Strength Softening of Longyou Sandstone. *Rock Mech. Rock Eng.* 43(6), 677–683 (2010)
- [6] Stacey, T.R.: A Simple Device for the Direct Shear-Strength Testing of Intact Rock. *J. S. Afr. I. Min. Metall.* 80(3), 129–130 (1980)
- [7] Sulukcu, S., Ulusay, R.: Evaluation of the block punch index test with particular reference to the size effect, failure mechanism and its effectiveness in predicting rock strength. *I. J. Rock Mech. Min. Sci.* 38(8), 1091–1111 (2001)
- [8] Huang, S., Feng, X.T., Xia, K.W.: A dynamic punch method to quantify the dynamic shear strength of brittle solids. *Rev. Sci. Instrum.* 82, 053901 (2011)
- [9] Dai, F., Huang, S., Xia, K.W., Tan, Z.Y.: Some Fundamental Issues in Dynamic Compression and Tension Tests of Rocks Using Split Hopkinson Pressure Bar. *Rock Mech. Rock Eng.* 43(6), 657–666 (2010)
- [10] Jaeger, J.C., Cook, N.G.W., Zimmerman, R.W.: *Fundamentals of rock mechanics*, 4th edn. Blackwell Publishing Ltd., Malden (2007)

# An Elasto-plastic Model and Its Return Mapping Scheme for Anisotropic Rocks

Wei-ya Xu, Jiu-chang Zhang<sup>\*</sup>, Ru-bin Wang, and Jin-jian Gu

Institute of Geotechnical Engineering, Hohai University, Nanjing 210098, China  
zhangjiuchang@gmail.com

**Summary.** Based on an anisotropic failure criterion that includes a scalar parameter in terms of the mixed invariants of the stress and micro-structure tensors, an elasto-plastic model is suggested for the description of mechanical properties of transversely isotropic rocks. And on the basic principles of return mapping, we deduce the formulations of return mapping suit for transversely isotropic rocks, especially the second derivative of plastic potential function and unsymmetrical consistent constitutive matrix. For application, an experimental program is conducted and several tests of argillite specimens are simulated with various confining pressures and loading orientations. The comparison reveals that the proposed model and its return mapping scheme are suitable for describing the mechanical properties of argillite.

**Keyword:** Anisotropy, Elasto-plasticity, Micro-structure tensor, Return mapping.

## 1 Introduction

In general, rocks with bedding, stratification, layering or foliation are of transversely isotropic materials [1, 2], which have an axis of rotational symmetry with distinctive anisotropy and a plane normal to that axis wherein it is largely isotropic. Over past few decades, many efforts have been undertaken to develop proper failure criterion and establish elasto-plastic constitutive models for them.

Among all the relevant researches [3-10], the criteria and models developed by Pietruszczak et al. [6-8] are more significant, since into their criteria an anisotropic parameter were introduced in terms of the mixed invariants of stress and micro-structure tensors, which can reflect the spatial relations between structure and stress. Because of its manifesting analytical formulations, these criteria have more potential possibilities for developing elasto-plastic models of anisotropic geomaterials. Some original researches have been undertaken by them in this field. Recently, a more sophisticated elasto-plastic model coupled with damage variables was proposed by Chen et al. [10] for the description of strongly anisotropic sedimentary rocks.

Promoted by Krieg and Krieg [12], return mapping schemes have become the most popular ways in isotropic materials due to its effective iteration, high

---

<sup>\*</sup> Corresponding author.

accuracy and numerical stability [12, 13]. It involves first integrating the elastic equations with total strain increments to obtain an elastic predictor. The elastically predicted stresses are then relaxed onto a suitably updated yield surface by correcting, iteratively the plastic strain increments [13]. However, there are few literatures reported about the application of this method in that of anisotropic geomaterials, though it has been achieved well in isotropy.

So in this study an attempt introducing this scheme into anisotropic rocks has been made. Firstly, the scheme is simply encapsulated here. Secondly, on the basis of previous works, a new anisotropic failure criterion including micro-structure tensor is presented and furthermore an associated elasto-plastic model is developed. Finally, the formulation is implemented as a user-material subroutine code which has been applied to simulating the properties of a kind of argillite we tested.

## 2 Fundamentals of Return Mapping Scheme

Here, we take  $F(\sigma_{ij}) = 0$  as failure criterion. For small-strain and perfect plasticity of geomaterials at failure, according to Hooke's law, constitutive relation can be determined by

$$d\sigma_{ij} = D_{ijkl} (d\varepsilon_{kl} - d\varepsilon_{kl}^p) = D_{ijkl} (d\varepsilon_{kl} - d\lambda \frac{\partial G}{\partial \sigma_{kl}}) = D_{ijkl}^{ep} d\varepsilon_{kl} \quad (1)$$

where,  $\sigma_{ij}$ ,  $D_{ijkl}$ ,  $D_{ijkl}^{ep}$  and  $G$  are stress tensor, elastic, elasto-plastic stiffness tensors and plastic potential, respectively.  $\varepsilon_{ij}^e$  and  $\varepsilon_{ij}^p$  are elastic and plastic parts of total strain  $\varepsilon_{ij}$ . In the implementation of return mapping scheme provided in [12, 13], a consistent elasto-plastic constitutive matrix  $D_{ijkl}^{epc}$  is adopted as a substitution of  $D_{ijkl}^{ep}$ . Cited from [12], similarly,  $D_{ijkl}^{epc}$  can be written as

$$D_{ijkl}^{epc} = D_{ijkl}^c - \frac{1}{H} \left( D_{ijkl}^c \frac{\partial F}{\partial \sigma_{pq}} \frac{\partial G}{\partial \sigma_{mn}} D_{mnkl}^c \right); \quad H = \frac{\partial F}{\partial \sigma_{pq}} D_{pqmn}^c \frac{\partial G}{\partial \sigma_{mn}} \quad (2)$$

where  $D_{ijkl}^c$  is so-called consistent stiffness tensor, and it is as follows

$$D_{ijkl}^c = \left( \delta_{ijkl} + \Delta\lambda D_{ijkl} \frac{\partial^2 G}{\partial \sigma_{ij} \partial \sigma_{kl}} \right)^{-1} D_{ijkl} \quad (3)$$

where  $\delta_{ijkl}$  is forth-order Kronecker tensor.  $\partial^2 G / \partial \sigma_{ij} \partial \sigma_{kl}$  is the second derivatives of plastic potential.  $\lambda$  and  $\Delta\lambda$  are the plastic multiplier and its increment. More details about return mapping scheme can be referred to [12, 13].

### 3 Elasto-plasticity for Anisotropic Rocks

#### 3.1 Coordinate Systems and Elastic Theory of Anisotropy

Two coordinate systems are needed to describe properties of transversely isotropic rocks. One is structure system  $Oxyz$  attached to their structures, with its  $z$ -axis as rotational symmetric axis and  $xOy$  plane as transversely isotropic plane (Fig. 1). The other is the global system  $OXYZ$ , obtained by rotating  $Oxyz$  counter-clockwise around the  $x$ -axis with an angle of  $\beta$ . Transversely isotropic rocks have five elastic parameters:  $E_1$ ,  $E_2$ ,  $\nu_1$ ,  $\nu_2$  and  $G_2$  (more details in [1, 2]).

Stress and strain between two different coordinate systems comply with the transformation rule of tensor. In  $Oxyz$ , elastic equation can be described as  $\sigma_{ij}^{xyz} = D_{ijkl} \epsilon_{kl}^{xyz}$ , and in  $OXYZ$ , as  $\sigma_{ij}^{XYZ} = R_{ijkl} \epsilon_{ij}^{XYZ}$ .  $D_{ijkl}$  and  $R_{ijkl}$  are stiffness matrices in  $Oxyz$  and  $OXYZ$ , respectively. The relation between  $R_{ijkl}$  and  $D_{ijkl}$  can be referred in [11]. And finally,  $R_{ijkl}$  will be used to form the global stiffness matrix in the external finite element program.

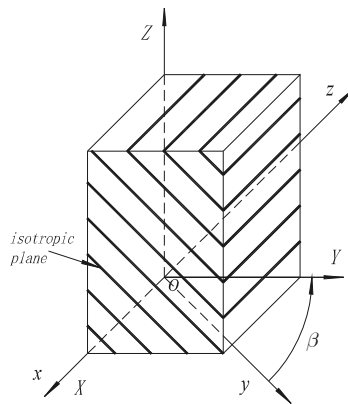


Fig. 1. Structure and global coordinate systems for transversely isotropic rocks

#### 3.2 A New Elasto-plastic Model for Transversely Isotropic Rocks

Pietruszczak and Mroz [6, 7] suggested a generalized formulation of anisotropic failure criterion. Furthermore, Pietruszczak et al. [8] developed a new elasto-plastic model on a non-linear failure criterion for sedimentary rocks with transverse isotropy. In this paper, for simplicity, an associated flow model is suggested with a simpler linear failure function like that in [8], which is

$$F = G = I_1 + c_1 \sqrt{J_2} - c_2 \sigma_c = 0 \quad (4)$$

Here, we assume tensile stress is positive.  $I_1 = \text{tr}(\boldsymbol{\sigma})$ , and  $\sqrt{J_2} = \text{tr}(\mathbf{s}^2)^{1/2}$ .  $c_1$  and  $c_2$  are three material parameters.  $\sigma_c$  is defined as a variable for describing varying strength of uniaxial compression affected by the loading angles, and we take it with the same form in [8]

$$\sigma_c = \hat{\sigma}_c [1 + \zeta + b_1 \zeta^2 + b_2 \zeta^3 + \dots]; \quad \zeta = \frac{A_{ij} \sigma_{ik} \sigma_{jk}}{\sigma_{ij} \sigma_{ij}} \quad (5)$$

where  $A_{ij}$  is the deviatoric part of fabric tensor  $a_{ij}$  of anisotropic geo-materials. More details about  $a_{ij}$  and  $A_{ij}$  can be referred in [6-8].

### 3.3 The First Derivatives of Failure and Plastic Potential Functions

On Eqs. (4), we can derive the first derivatives of failure and plastic potential functions

$$\frac{\partial G}{\partial \sigma_{ij}} = \frac{\partial F}{\partial \sigma_{ij}} = \left( \frac{\partial F}{\partial I_1} \frac{\partial I_1}{\partial \sigma_{ij}} + \frac{\partial F}{\partial \sqrt{J_2}} \frac{\partial \sqrt{J_2}}{\partial \sigma_{ij}} \right) + \left( \frac{\partial F}{\partial \sigma_c} \frac{\partial \sigma_c}{\partial \sigma_{ij}} \right) \quad (6)$$

From Eq. (6), it is evident that the effect of anisotropy is described in the last term. To evaluate this term, we have the following equation according to Eq. (5) and [8]

$$\frac{\partial \sigma_c}{\partial \sigma_{ij}} = \frac{\partial \sigma_c}{\partial \zeta} \frac{\partial \zeta}{\partial \sigma_{ij}} = 2 \hat{\sigma}_c [1 + 2b_1 \zeta + 3b_2 \zeta^2 + \dots] \frac{A_{ki} \sigma_{kj} \sigma_{pq} \sigma_{pq} - A_{pk} \sigma_{pq} \sigma_{kq} \sigma_{ij}}{(\sigma_{pq} \sigma_{pq})^2} \quad (7)$$

### 3.4 The Second Derivative of Plastic Potential Function

In the implementation of return mapping scheme, the second derivative of plastic potential on stress are required and it can be expressed as

$$\frac{\partial^2 G}{\partial \sigma_{ij} \partial \sigma_{kl}} = c_3 \frac{\partial^2 \sqrt{J_2}}{\partial \sigma_{ij} \partial \sigma_{kl}} - c_2 \frac{\partial^2 \sigma_c}{\partial \sigma_{ij} \partial \sigma_{kl}} \quad (8)$$

According to the composite function derivative chain rule, we have

$$\frac{\partial^2 \sigma_c}{\partial \sigma_{ij} \partial \sigma_{kl}} = \frac{\partial^2 \sigma_c}{\partial \zeta^2} \frac{\partial \zeta}{\partial \sigma_{ij}} \frac{\partial \zeta}{\partial \sigma_{kl}} + \frac{\partial \sigma_c}{\partial \zeta} \frac{\partial^2 \zeta}{\partial \sigma_{ij} \partial \sigma_{kl}} \quad (9)$$

Essentially, the second derivative  $\partial^2 G / \partial \sigma_{ij} \partial \sigma_{kl}$ , a forth-order tensor, can be abbreviated as a six-order matrix. Here the matrix, however, is unsymmetrical because in  $\partial^2 \sigma_c / \partial \sigma_{ij} \partial \sigma_{kl}$   $A_{ij}$  is not zero for transversely isotropic rocks. As for isotropy,  $A_{ij}$  will be absent.

**Table 1.** A brief flowchart of the return mapping scheme corresponding to transversely isotropic rocks

1.	In the global system $OXYZ$ , set initial values plastic strain to converged values at end of previous load step, zero the incremental plasticity parameter, create an increment of strain $k = 0, \sigma_{ij(n)}^{XYZ}; \epsilon_{ij(n+1)}^{XYZ p(0)} = \epsilon_{ij(n)}^{XYZ p}, \Delta \lambda^{(0)} = 0, \Delta \epsilon_{ij}^{XYZ}$
2.	Transform $\sigma_{ij(n)}^{XYZ}, \epsilon_{ij(n+1)}^{XYZ p(0)}$ and $\Delta \epsilon_{ij}^{XYZ}$ into the material structure system $Oxyz$ to be $\sigma_{ij(n)}^{xyz}, \epsilon_{ij(n+1)}^{xyz p(0)}$ and $\Delta \epsilon_{ij}^{xyz}$
3.	In the structure system $Oxyz$ , calculate the elastic trial stress $\sigma_{ij(n+1)}^{xyz(0)} = \sigma_{ij(n)}^{xyz} + D_{ijkl} \Delta \epsilon_{kl}^{xyz}$
4.	In $Oxyz$ , at $k$ -th iteration, calculate $F^{(k)}$ . If $ F^{(k)}  > TORL$ , failure GOTO 5; ELSE $\sigma_{ij(n+1)}^{xyz} = \sigma_{ij(n+1)}^{xyz(k)}$ , converged and GOTO 7
5.	In $Oxyz$ , at $k$ -th iteration, calculate plasticity parameter $\Delta \lambda^{(k)}$ and $D_{ijkl}^{c(k)}$ with Eq. (29) in [12]
6.	In $Oxyz$ , at $k$ -th iteration, calculate plastic stress correctors with Eq. (28) in [12], update stress by Eq. (13) in [12], and update plastic strain and plasticity parameter with Eq. (31) in [12]. And then $k = k + 1$ , GOTO 4
7.	In $Oxyz$ , if $\sigma_{ij(n+1)}^{xyz} = \sigma_{ij(n+1)}^{xyz(0)}$ , material is still elastic and $D_{ijkl}^{epc} = D_{ijkl}$ ; ELSE, material is failure, and calculate $D_{ijkl}^{epc}$ with Eq. (3)
8.	Transform $\sigma_{ij(n+1)}^{xyz}, \epsilon_{ij(n+1)}^{xyz p}$ and $D_{ijkl}^{epc}$ into the global system $OXYZ$ , to be $\sigma_{ij(n+1)}^{XYZ}, \epsilon_{ij(n+1)}^{XYZ p}$ and $R_{ijkl}^{epc}$
9.	In $OXYZ$ , OUTPUT $\sigma_{ij(n+1)}^{XYZ}, \epsilon_{ij(n+1)}^{XYZ p}$ and $R_{ijkl}^{epc}$ to external finite element program

**Note:** in superscript ‘ $p$ ’ means plasticity, ‘(0)’ and ‘(k)’ mean the times of iteration. In subscript ‘(n)’ stand for the times of calculating step.

### 3.5 Flowchart of the Return Mapping Scheme to This Model

The formulations provided in the previous sections have been implemented in the form of user-material subroutine code which is called at each integration point of element by an external finite element program. Additionally, a brief flowchart of the return mapping scheme corresponding to transversely isotropic rocks is presented in table 1.

## 4 Tests and Model Parameters

To illustrate the performance of this model, a number of uniaxial and triaxial tests of argillite were conducted. The argillite rock specimens were obtained by drilling at different angles  $\beta$  ( $0^\circ$ ,  $15^\circ$ ,  $30^\circ$ ,  $45^\circ$ ,  $60^\circ$  and  $90^\circ$ ). For triaxial tests, two different initial confining pressures are applied. One is 5MPa, the other 10MPa. Five elastic parameters of argillite were tested by the means of [1, 2], and they are

$$\begin{cases} E_1 = 5.619\text{GPa}, & \nu_1 = 0.213 \\ E_2 = 4.129\text{GPa}, & \nu_2 = 0.187 \\ G_2 = 0.885\text{GPa}, \end{cases} \quad (10)$$

By test, anisotropic argillite strength varies with confining pressures and loading angles which are listed in Table 2. It is easy to determine the parameters of  $\hat{\sigma}_c$  by strength results of uniaxial tests with data-fit approximations (Fig. 2). They are as follows

$$\hat{\sigma}_c = 26.885 \text{ MPa}, \quad A_1 = 0.656, \quad b_1 = 0.214, \quad \text{and} \quad b_2 = -0.563 \quad (11)$$

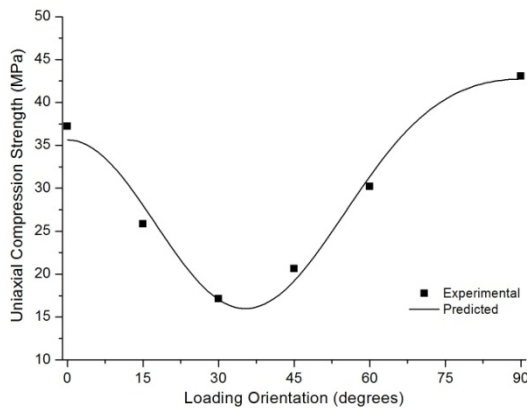


Fig. 2. Variation of uniaxial compression strength with loading orientation

**Table 2.** Major principal stress  $\sigma_1(\beta)$  at failure of argillite (MPa)

$\sigma_3$ (MPa)	$\beta$					
	$0^\circ$	$15^\circ$	$30^\circ$	$45^\circ$	$60^\circ$	$90^\circ$
0	37.22	25.84	17.10	20.61	30.19	43.05
5	48.66	39.49	35.93	38.75	44.13	49.36
10	56.72	54.38	49.03	45.47	53.11	56.84

**Table 3.**  $c_1$  and  $c_2$  of argillite under different loading angles

Parameters	$\beta$					
	$0^\circ$	$15^\circ$	$30^\circ$	$45^\circ$	$60^\circ$	$90^\circ$
$c_1$	4.545	3.913	4.034	4.698	5.494	10.104
$c_2$	1.660	1.207	1.449	1.695	2.225	4.785

The material parameters  $c_1$  and  $c_2$  in failure criterion of Eq. (4) vary with the loading orientations and can be determined by the results of the tests at different confining pressures which is listed in table 2. In this table,  $\sigma_3 = \sigma_x = \sigma_y$  and  $\sigma_1 = \sigma_z$ . We can observe that with the growth of confining pressure, anisotropic degree of argillite in strength becomes lower. By substituting these data into the failure criterion of Eq. (4) with least-squares method, we obtain the values of  $c_1$  and  $c_2$  listed in Table 3.

### 5 Test Results and Simulations

During tests, a large number of intensive data of stress and strain are recorded by computer. For simplicity and clarity, only a few of them are selected as key points which to some extent are capable of showing the deformation behavior of argillite. In order to examine the performance of this model and its formulation of return mapping algorithm, all tests are simulated. A comparison between experiments and numerical simulations are presented in Fig. 3. These graphs are categorized according to loading orientations and in contents describe the relations of deviatoric stress versus strains: they are axial strain  $\epsilon_z$ , radial strains  $\epsilon_x$  and  $\epsilon_y$ . Only for vertical samples ( $\beta = 0^\circ$  shown in Fig. 3a), numerical simulations are strictly isotropic, so there is  $\epsilon_x = \epsilon_y$  and for other samples, including  $\beta = 90^\circ$ ,  $\epsilon_x \neq \epsilon_y$ . This can be observed in other five figures.

We can observe in Fig.3 that the model can well predict the main mechanical properties of transversely isotropic argillite. It is noteworthy that in the phase of

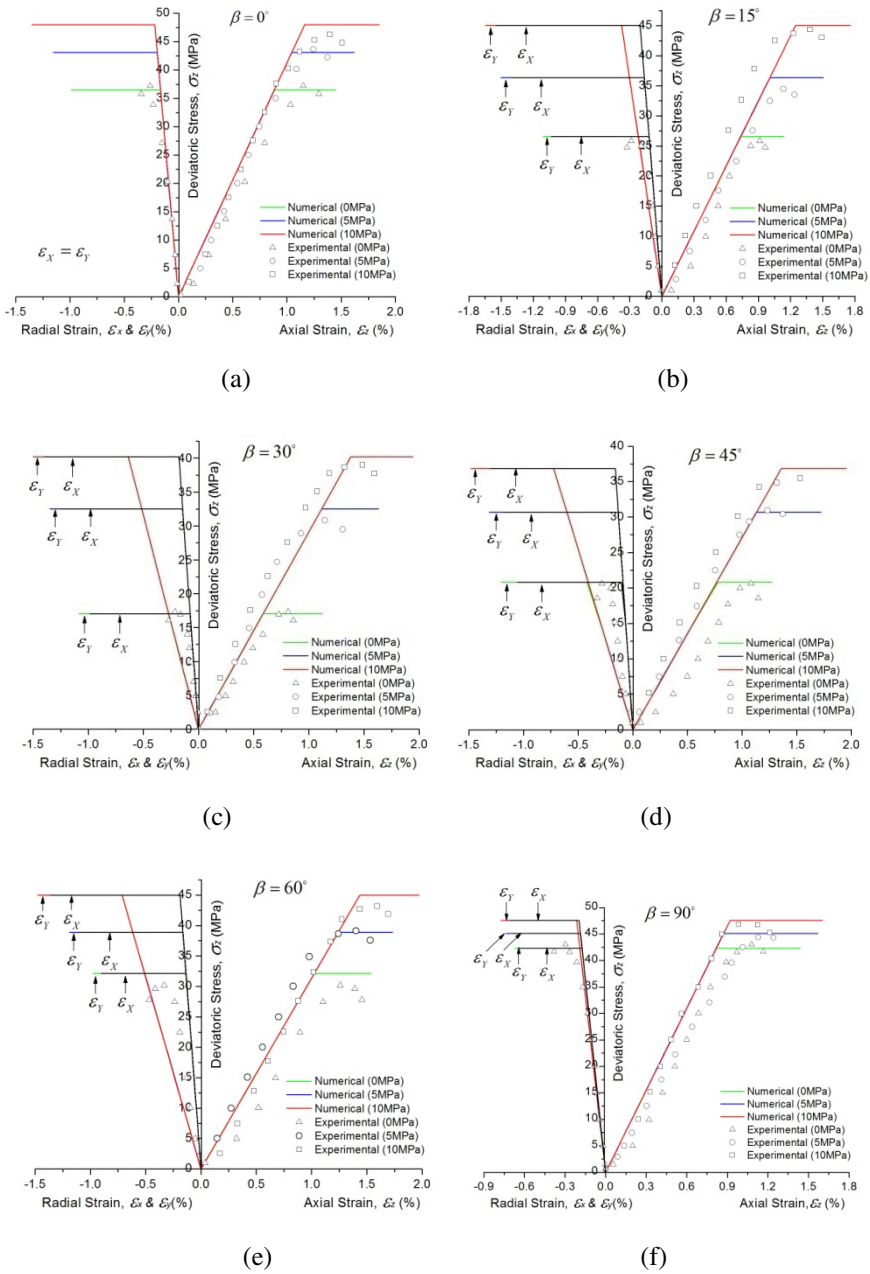


**Fig. 3.** Numerical simulations of tests on argillite rock specimens with different loading orientations

elasticity, the gaps between  $\varepsilon_x$  and  $\varepsilon_y$  are wide when loading orientations are inclined. In the phase of plasticity, however, this disparity will reduce due to the reason of plastic flow. Because this model is of perfect plasticity, when axial stress approaches to failure state, no increase of stress occurs while strains significantly boost. However, once failure strength has been attained, argillite specimens are more likely to crack.

## 6 Conclusions

In this study, we first introduce return mapping scheme into the model of anisotropic rocks and then propose a new perfect associated plasticity model for transversely isotropic rocks. We also deduce the derivatives of anisotropy required in the return mapping scheme. This anisotropic model and its return mapping scheme are performed for the prediction of stress-stress relations of argillite. Good predictions obtained show that the proposed model and its numerical formulations are capable of modeling mechanical properties of argillite. A more sophisticated model needs to be developed in the future, which may well be taking strain hardening or non-associated flow into account, and even the influence of Lode angle. In addition to basically theoretical aspect, much more intensive laboratory investigations are required for further validation of this model and its formulations.

**Acknowledgments.** The study that is presented in this paper was supported by the National Natural Science Foundation of China (Projects: 11172090, 51009052, 51109069), and also supported by a grant from the Major State Basic Research Development Program of China (973 Program: 2011CB013504).

## References

- [1] Amadei, B.: Importance of anisotropy when estimating and measuring in situ stresses in rock. *Int. J. Rock Mech. Min. Sci. & Geomech.* 33(3), 293–325 (1996)
- [2] Hakala, M., Kuula, H., Hudson, J.A.: Estimating the transversely isotropic elastic intact rock properties for in situ stress measurement data reduction: A case study of the Olkiluoto mica gneiss, Finland. *Int. J. Rock Mech. & Min. Sci.* 44(1), 14–46 (2007)
- [3] Duveau, G., Shao, J.F.: A Modified Single Plane of Weakness Theory for the Failure of Highly Stratified Rocks. *Int. J. Rock Mech. & Min. Sci.* 35(6), 807–813 (1998)
- [4] Ramamurthy, T., Rao, G.V., Singh, J.: A strength criteria for anisotropic rocks. In: *Proc. 5th Australia–New Zealand Conf. Geomech., Sydney, vol. 1, pp. 253–257 (1988)*
- [5] Tien, Y.M., Kuo, M.C.: A failure criteria for transversely isotropic rocks. *Int. J. Rock Mech. & Min. Sci.* 38, 399–412 (2001)
- [6] Pietruszczak, S., Mroz, Z.: Formulation of anisotropic failure criteria incorporating a microstructure tensor. *Comput. Geotech.* 26(2), 105–112 (2000)
- [7] Pietruszczak, S., Mroz, Z.: On failure criteria for anisotropic cohesive-frictional materials. *Int. J. Num. Anal. Meth. Geomech.* 25(5), 509–524 (2001)

- [8] Pietruszczak, S., Lydzba, D., Shao, J.F.: Modelling of inherent anisotropy in sedimentary rocks. *Int. J. Solids Struct.* 39(3), 637–648 (2002)
- [9] Gao, Z.W., Zhao, J.D., Yao, Y.P.: A generalized anisotropic failure criterion for geomaterials. *Int. J. Solids Struct.* 47(22-23), 3166–3185 (2010)
- [10] Chen, L., Shao, J.F., Huang, H.W.: Coupled elastoplastic damage modeling of anisotropic rocks. *Comput. Geotech.* 37(1-2), 187–194 (2010)
- [11] Nunes, A.L.L.S.: A new method for determination of transverse isotropic orientation and the associated elastic parameters for intact rock. *Int. J. Rock Mech. & Min. Sci.* 39, 257–273 (2001)
- [12] Krieg, R., Krieg, D.: Accuracies of numerical solution methods for the elastic-perfectly plastic model. *J. Press. Vessel. Technol.* 99, 510–515 (1977)
- [13] Huang, J.S., Griffiths, D.V.: Observations on Return Mapping Schemes for Piecewise Linear Yield Criteria. *Int. J. Geomech.* 8(4), 253–265 (2008)
- [14] Huang, J.S., Griffiths, D.V.: Return Mapping Schemes and Stress Predictors for Failure Analysis in Geomechanics. *J. Eng. Mech.* 135(4), 276–284 (2009)

# Micro-gas Hypothesis for Behaviors of Rocks under Loading

Zhong Qi Yue (Quentin)\*

Department of Civil Engineering  
The University of Hong Kong  
Pokfulam Road, Hong Kong, China  
yueqzq@hku.hk

**Summary.** I propose a micro-gas hypothesis for the mechanism of mechanical and physical behaviors of intact rocks under loading in this paper. The rock behaviors include elastic deformation, brittle cracking, strain hardening, strain softening, ductile deformation, plastic deformation, creep, as well as change from brittle to ductile under confining pressures. The hypothesis is based on the observation that natural gas can be present in micro-voids, micro-pores, lattice boundaries and interfaces of intact rocks and their minerals with various porosities. The coupled interaction between the micro-gas and the rock mineral solids can determine the individual behaviors of intact rocks under loading.

**Keywords:** micro-gas, rock, brittle, crack, ductile, creep.

## 1 Introduction

The physical and mechanical behaviors of intact rocks under loading have been well tested and examined by many researchers over the past 100 years [1-7]. They can be similar, various and/or different. Regularities on the stress-strain relationship of intact rocks have been well summarized in literatures in terms of solid mechanics or continuum mechanics and on the basis of the phenomenological approach. For example, under uniaxial compression, a rock sample would experience an initial setting deformation, a linear elastic deformation, a yielded deformation, then a peak, and a post-failure. After the linear elastic behavior, the rocks may show brittle cracking, strain hardening, strain softening, ductile or plastic deformation. Sometimes, rocks can show creep deformation or stress-relaxation with time. The rock cracking can be either tensile or shear. As the confining pressure increases, rocks (such as marble) can show the brittle to ductile change in the post-peak behavior. They can have residual strengths.

The constitutive relationship for stress-strain in the linear elastic deformation can be well described with the Hooke's law, where some elastic parameters such

---

\* Corresponding author.

as elastic modulus and Poisson's ratio are used. On the other hand, many constitutive or strength models have been proposed and developed to describe and predict the post-peak stress-strain behavior. Examples are the Mohr-Coulomb criterion, the Griffith crack criterion, the Bieniawski criterion, and the Hoek and Brown criterion. A majority of the criteria are empirical in nature. In addition, continuum mechanics theories including elasticity, plasticity, viscoelasticity, rheology and poro-elasticity have been used to describe and predict the ductile or creep deformation or time-dependent deformation in rocks.

In this paper, I propose a micro-gas hypothesis to further describe the mechanism of intact rock behaviors under loading. So, the rock behaviors can be consistently analyzed and more accurately predicted in the future.

## 2 The Micro-gas Hypothesis

Rocks are the lithified solid materials of sedimentary, igneous, or metamorphic origin. They are the constituents of the crust of the Earth. Rocks are formed by combined and cemented minerals or rock particles. A mineral is a naturally-occurring, homogeneous solid that has a definite chemical composition and a distinctive internal crystal structure. Rocks are distinguished by their heterogeneous compositions of different minerals and/or previous rock particles. Hence, rocks and their minerals can have micro-defects of the sizes of millimeters, micro-meters or less, which can be evidenced with the ever non-zero porosity of intact rocks.

The micro-defects include mineral cleavages, particle contact or jointing zones, beddings, foliations, joints, voids, pores, fissures, cracks, inclusions, and impurities. They can be infilled with natural gases (called micro-gases in this paper). They and their micro-gas infillings (inclusions) can be either originated during the rock lithification processes of sedimentary, igneous, or metamorphic origin or developed during secondary tectonic movements. The micro-gases can be  $H_2$ ,  $CH_4$ ,  $N_2$ , He,  $H_2O$ , CO,  $CO_2$ ,  $SO_2$ , and/or air.

The micro-gases have their physical, chemical and mechanical properties including density, pressures, and specific heat ratio. Before excavation, the rocks and their micro-gases have been in a stable, peaceful and equilibrium condition and a seal environment for thousands, hundred thousands, and/or millions years. Due to the high in-situ compressive stresses and long term sealed and stable ground conditions, the pressure of the micro-gases in the micro-defects can equal to the average of the three principal in-situ stresses. The lower limit of the micro-gas pressure can be the atmospheric pressure. Secondly, the micro-gases with higher pressures can have a certain amount of expansion energy and forces. Thirdly, when the micro-gas pressure decreases, their volumes would expand significantly following an inversely proportional law. Such volumetric change of the micro-gases with pressure is totally different with those of rock solids and liquids. The volumes of pressured rock solids and liquids would increase a little once their pressure is reduced to zero (or the atmospheric pressure).

According to elastodynamics and stress wave speeds, the excavation in underground rocks must disturb the rocks and must result sudden changes in the

rock solid elastic stress and strain fields. According to the second law of thermodynamics, such disturbance would definitely and heavily disturb the pressurized micro-gases sealed in the micro-defects and inclusions of intact rocks. Some of the micro-gases can escape and flow out of the intact rocks into the atmosphere. Some can still be sealed and kept in the intact rocks with changed pressures and volumes. These micro-gases that are still trapped in the intact rocks can cause different stress-strain behaviors to the intact rocks when they are subject to reloading. More details on this micro-gas hypothesis in rock mechanics can be found in [8]. As example, the rock behaviors in uniaxial and triaxial compression tests are discussed in detail below.

### 3 Rock Behavior in Uniaxial Compression

As shown in Fig.1, the stress-strain curves between the zero stress and the peak (uniaxial compressive strength for zero (or atmospheric) confining pressure) can be divided into four zones. The curves in the first zone have steadily increasing slopes, which are more noticeable for porous rocks. The curves in the second zone are nearly linear, where the hysteresis is almost zero. In the third zone, the curve slopes slightly decrease and the volumetric strains increase slowly. Some micro-cracks develop stably. In the fourth zone, the curve slopes rapidly decrease and the volumetric strains increase quickly. The micro-cracks develop and propagate quickly, which can be observed with acoustic emissions. The rock strengths reach the peak eventually.

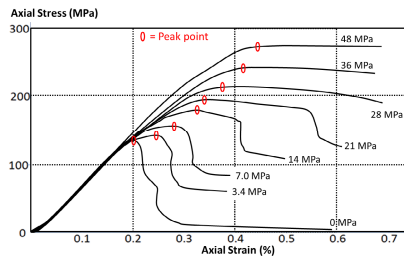


**Fig. 1.** Complete stress-strain curves for unconfined and confined compression tests of Tennessee marble (modified after [1])

However, significant differences in the stress-strain curves are noticeable after the peak, which is the post-peak behavior. For brittle rocks, macro-fractures develop while the peak strengths reduce dramatically. An example of the fractures is given in Fig. 2, where the fractures are tensile roughly along vertical planes. For ductile rocks, large deformation can develop while the peak strengths keep constant. In addition, different specimens of the same intact rocks can have different values for the compressive strength.

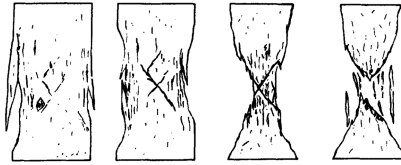


**Fig. 2.** Schematic representation of fracture developments during post-peak in uniaxial compression test of Charcoal Gray granite (after [1])

The above behavior of intact rocks under uniaxial compression can be interpreted and explained with the micro-gas hypothesis. The behavior in the first zone is basically a recovery of the rock expansion deformation caused partially by the unloading and partially by gas escaping during the sampling process. The linear behavior in the second zone can be considered as a stable, equilibrium and harmonic state of the coupled deformation between the rock solids and the micro-gases. The micro-gases are gaining higher and higher pressure while the micro-defects are reducing their volumes under the compression. Once the coupled system reaches its upper limits that it had experienced, new micro-cracks would start. Hence, in the third and fourth zones, the micro-gases would receive higher and higher compression and have gained higher and higher pressures. They would expand laterally and produce micro-tensile/shear cracks along vertical planes. The micro-gases also slip, flow and migrate from originally horizontal micro-defects to newly developed vertical micro-defects within the intact rocks. Because the micro-gas cannot escape the intact rock, the rock strength can keep and increase further in the third and fourth zones. As the axial compressive load increases, more and more micro-gases with higher pressure flow vertically and expand laterally. So, they produce more and more micro-cracks along the rock vertical planes till the peak strength.

At the peak, the axially loaded rock can behave differently from sudden brittle macro-cracking in small strain for brittle rocks to some ductile deformation with large strain for ductile rocks. For brittle rocks, the lateral expansion of the compressed and re-aligned micro-gases can cause the old or new vertical micro-defects to suddenly occur macro-ruptures in tension and eject broken fragments or particles. The tensile crack propagations can be in shear crack modes and form X-shaped ruptures. In the meantime, the trapped micro-gases would escape out of the intact rock. So the rock strength is decreased significantly to the residual strength or to zero.

For ductile rock, the lateral expansion of the compressed and realigned micro-gases can cause the micro-crack walls to deform extensively whilst the micro-gases are still compressed and trapped in the deformed intact rocks. Consequently, the axially loaded rock can keep deformation and maintain the peak strength. Due to the limits in its lateral deformation, the deformed rock would eventually occur macro-ruptures.

## 4 Rock Behavior in Triaxial Compression

The effect of a hydrostatic confining pressure on the stress-strain behavior of rocks can be observed in Fig.1 in triaxial tests. As the confining pressure increases, the peak strength and residual strength increase and their difference reduces. The curve shapes from the first to fourth zones are insensitive to the magnitude of the confining pressure. In the post-peak, the rock brittle behavior at the lower confining pressures gradually changes to the rock ductile behavior as the confining pressure increases to high values.

The conventional mechanisms for such change in the post-peak are local shear failure, inter-granular sliding and true intra-crystalline glide on well-defined, regularly-spaced inclined planes, as well as the grain reorientations [1], where the micro-defects are considered completely empty. These rock behaviors under triaxial compressions can also be described with the micro-gas hypothesis. The confining pressure can balance the lateral expansive force of the micro-gases and make their pressures higher. Hence, the rock strength can be higher and higher and its deformation can be extended elastically.

## 5 Conclusions

In the above, a micro-gas hypothesis is proposed and used to describe the physical and mechanical behaviors of rocks under loading. If they are in confined space, micro-gases can be compressed extensively and gain high pressure. They can become very elastic and preserve a large amount of expansive energy. They can support compressive loads, which can make the rock compressive strength increase or rock deformation become harmonic and ductile. Their expansion power can make rock rupture or crack or split in the interior of rocks. Open micro-defects in rocks can be re-sealed under compressive loading. Their micro-gas (air) can be re-trapped and re-compressed. So, rock compressive strength can be extremely high while rock tensile strength is very low.

## References

- [1] Wawersik, W.R., Fairhurst, C.: A study of brittle rock fracture in laboratory compression experiments. *Int. J. Rock Mechanics and Mining Sciences & Geomechanics Abstracts* 7(5), 561–564 (1970)
- [2] Goodman, R.E.: *Introduction to Rock Mechanics*, 2nd edn. J. Wiley, New York (1989)
- [3] Hudson, J.A. (Editor-in-Chief): *Comprehensive Rock Engineering: Principles, Practice, and Projects*. Pergamon Press, Oxford (1993)
- [4] Wang, S.J., Yang, Z.F., Fu, B.J. (eds.): *China Rock Mechanics and Rock Engineering: Century Achievements*. Hohai University Press, Nanjing (2004)
- [5] Yue, Z.Q., Selvadurai, A.P.S.: On the mechanics of a rigid disc inclusion in a fluid saturated poroelastic medium. *Int. J. Engineering Science* 33(11), 1633–1662 (1995)

- [6] Yue, Z.Q., Chen, S., Tham, L.G.: Finite element modeling of geomaterials using digital image processing. *Computers and Geotechnics* 30, 375–397 (2003)
- [7] Yue, Z.Q., Shang, Y.J., Hu, R.L., Tu, X.B.: Five test methods for porosity of completely decomposed granite in Hong Kong. *Int. J. Rock Mechanics and Mining Science* 41, 393–394 (SINOROCK 2004 Paper 1B 03, CD ROM) (2004)
- [8] Yue, Z.Q.: A possible tensile force and energy source causing rock burst, pressure bump, mine earthquake, rock split, zonal disintegration and large deformation in rock excavations at deep undergrounds with high in-situ stresses. *News Journal of China Society of Rock Mechanics and Engineering* 97(1), 83–89 (2012)

# Micromechanical Poroplasticity Damage Formulations for Saturated Microcracked Rocks

Qi-zhi Zhu<sup>1,3,\*</sup>, Ni Xie<sup>1</sup>, and Jian-fu Shao<sup>2,3</sup>

<sup>1</sup> Université Paris-Est, Laboratoire Modélisation et Simulation Multi Echelle,  
5 Bd Descartes, 77454 Marne-la-Vallée Cedex 2, France

<sup>2</sup> Université Lille 1, Laboratoire de Mécanique de Lille, Boulevard Paul Langevin,  
59655 Villeneuve d'Ascq Cédex, France

<sup>3</sup> Hohai University, College of Civil and Transportation Engineering,  
1-3, Road Xikang, 210098, Nanjing, China  
qizhi.zhu@gmail.com

**Abstract.** We present homogenization-based constitutive thermodynamic formulations for poroplasticity damage modeling of saturated microcracked rocks. Emphases are put upon the case of closed frictional cracks of random distribution. Plastic flow due to frictional sliding, crack propagation characterized by an isotropic damage variable and evolution of pore pressure are coupled naturally and inherently. A simple numerical application is presented to show the predictive ability of the proposed model.

## 1 Introduction

Damage by microcracking and inelastic deformation due to frictional sliding occurring on closed cracks are two essential dissipative mechanisms involved in cohesive-frictional geomaterials such as concrete and rocks. Under compression-dominated loadings, there exists strong coupling between damage and friction-induced plastic deformation. In many engineering applications such as tunnel excavation and geological storages, geomaterials are most often subjected simultaneously to mechanical loadings and variation of pore pressure. For constitutive modeling of material damage and structural failure, it is essential to investigate the coupling between the two mechanically dissipative processes [1-3] and the incorporation of pore pressure variation and its influence on damage evolution and plastic flow [4-5].

In this work, we attempt to derive constitutive thermodynamic formulations for modeling poromechanical behaviors of saturated microcracked rocks. The linear homogenization method is applied to provide the effective properties of the matrix-inclusion system. The continuity conditions in both stress and strain energy are used to determine unknown constants.

---

\* Corresponding author.

## 2 Description of a Matrix-Cracks System

Consider the representative elementary volume (REV) occupying a geometric domain  $\Omega$  and having its boundary  $\partial\Omega$  as a matrix–inclusion system: the matrix phase having the elasticity tensor  $\mathbb{C}^m$  and the inclusion phase being here penny-shaped microcracks. In the linear homogenization context and under isotropic assumption, the inelastic deformation due to opening microcracks  $E^c$  is linked linearly to the uniform macroscopic strain  $E$  such that  $E^c = \mathbb{A}^c : E$  with the global strain concentration tensor  $\mathbb{A}^c$  function of the material constants of the matrix and the isotropic damage variable  $\omega$ . Correspondingly, the effective stiffness tensor of the REV is given by  $\mathbb{C}^{\text{hom}} = \mathbb{C}^m : (\mathbb{I} - \mathbb{A}^c)$  where  $\mathbb{I}$  represents the fourth-order identity tensor.

For dry cohesive-frictional geomaterials, it has been proved that the total strain energy takes the form [2] [3]

$$W = \frac{1}{2}(E - E^c) : \mathbb{C}^m : (E - E^c) + \frac{1}{2}E^c : \mathbb{C}^b : E^c \quad (1)$$

where  $\mathbb{C}^b(\omega)$  is the fourth-order modulus related to the stored energy and given by  $\mathbb{C}^b = [(\mathbb{I} - \mathbb{A}^c)^{-1} : \mathbb{A}^c : \mathbb{S}^m]^{-1}$  with  $\mathbb{S}^m = (\mathbb{C}^m)^{-1}$ . The thermodynamic force associated with the inelastic strain  $E^c$  contains a back-stress term  $\mathbb{C}^b : E^c$  which allows modeling material hardening and softening. In addition, damage evolution and plastic flow will be coupled each other in a strong way.

## 3 Poromechanical Formulations

In the case of open microcracks, the Biot modulus  $1/N$  and the second-order tensor of Biot coefficients  $B$  have been derived by Dormieux and Kondo [5]. For closed frictional microcracks, the system potential energy  $W^*$  takes the form

$$W^* = \frac{1}{2}(E - E^c) : \mathbb{C}^m : (E - E^c) + \frac{1}{2}E^c : \mathbb{C}^b : E^c - \frac{p^2}{2\tilde{N}} - p\tilde{B} : (E - E^c) - p \operatorname{tr} E^c \quad (2)$$

It is proved that the tensor of Biot coefficients  $\tilde{B}$  and the Biot modulus  $1/\tilde{N}$  are respectively related to  $1/N$  and  $B$  in such a way that

$$\tilde{B} = (\mathbb{I} - \mathbb{A}^c)^{-1} : (B - \delta : \mathbb{A}^c) \tag{3}$$

$$\frac{1}{\tilde{N}} = \frac{1}{N} - \delta : \mathbb{S}^s : \mathbb{C}^m : \mathbb{A}^c : \mathbb{S}^s : \delta \tag{4}$$

where  $\delta$  is the second order identity tensor and  $\mathbb{S}^s$  denotes the elastic compliance tensor of the solid phase.

Within the thermodynamic framework of irreversible processes, the following constitutive relations and thermodynamic forces can be obtained by standard differentiations of the potential energy  $W^*$  with respect to the variables:

$$\Sigma = \frac{\partial W^*}{\partial E} = \mathbb{C}^m : (E - E^c) - p\tilde{B} \tag{5}$$

$$F_\omega = -\frac{\partial W^*}{\partial \omega} = -\frac{1}{2} E^c : \frac{\partial \mathbb{C}^b}{\partial \omega} : E^c \tag{6}$$

$$\sigma = -\frac{\partial W^*}{\partial E^c} = \Sigma - \mathbb{C}^b : E^c + p\delta \tag{7}$$

$$\phi - \phi_0 = -\frac{\partial W^*}{\partial p} = \frac{p}{\tilde{N}} + \tilde{B} : (E - E^c) + \text{tr } E^c \tag{8}$$

$\Sigma$  denotes the macroscopic stress tensor and  $\sigma$  the local stress on the closed cracks.  $\phi$  and  $\phi_0$  are the current and initial porosity of the REV, respectively.

### 4 A Numerical Example

A Coulomb-type friction criterion in terms of the driving force (local stress)  $\sigma$  is adopted [3]

$$f(\sigma) = \|s\| + \mu_f \text{tr } \sigma \leq 0 \tag{9}$$

where  $\mu_f$  is the coefficient of friction of the material.

A strain energy release rate-based damage criterion is used

$$f_\omega = \omega_c + (\omega_c - \omega_0) \exp(-\kappa F_\omega) - \omega \leq 0 \tag{10}$$

in which  $\omega_0$  and  $\omega_c$  are the initial and critical values of the damage variable, respectively. For some homogenization scheme, the value of  $\omega_c$  has been discussed in [3]. The model parameter  $\kappa$  is used to control the rate of damage evolution.

Fig. 1 shows numerical predictions of stress-strain curves and evolution of pore pressure for a typical rock in its undrained condition.

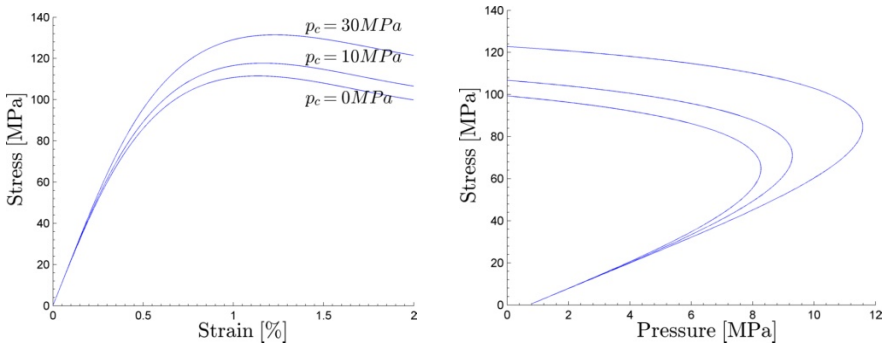


**Fig. 1.** Numerical predictions for an undrained rock: stress-strain curves (left) and evolution of pore pressures (right)

## References

- [1] Pensee, V., Kondo, D., Dormieux, L.: Micromechanical analysis of anisotropic damage in brittle materials. *J. Eng. Mech. ASCE* 128(8), 889–897 (2002)
- [2] Zhu, Q.Z., Kondo, D., Shao, J.F., Pensée, V.: Micromechanical modelling of anisotropic damage in brittle rocks and application. *Int. J. Rock Mech. Min. Sci.* 45, 467–477 (2008)
- [3] Zhu, Q.Z., Shao, J.F., Kondo, D.: A micromechanics-based thermodynamic formulation of isotropic damage with unilateral and friction effects. *Euro. J. Mech. A/Solids* 30(3), 316–325 (2011)
- [4] Dormieux, L., Kondo, D., Ulm, F.J.: *Microporomechanics*. John Wiley & Sons (2006).
- [5] Dormieux, L., Kondo, D.: Micromechanics of damage propagation in fluid-saturated media. *Revue européenne de Génie Civil.* 11, 945–962 (2007)

# Achieving High Range Elastic Properties of Soil Mass for More Stable and Durable Geostructure

Gokul K. Bayan

CSIR- North East Institute of Science & Technology, Jorhat; Assam  
NEIST Branch Laboratory, Itanagar, Arunachal Pradesh, Pin-791 110  
gokul\_kb\_ctk@yahoo.com

**Abstract.** Constitutive behavior soil mass is normally measured in-terms-of its nature of particle size density together with the existence of water quantity. For achieving the best behavior elastic properties are always desirable. Obviously, range of elasticity of soil mass is quite small in comparison to other materials. Hence, it reveals less allowance in every directions of its behavioral expression. Of many, settlement is the principal criterion to put attention for achieving the best safety performance. Three series of R&D works conducted in a model plate load test by using three types of soil mass under various field conditions comprising special form of hard inclusions, to achieve high range elastic properties for road and building foundations is the objective of this paper. Utilization of such achievements generates a system of surface foundation in reality with the projected properties.

## 1 Introduction

Soil mass is a disintegrated geomaterials which express its naturally bonded behavior with its water content. Constitutive particles of soil mass perform individual activities within its stage of micro action phenomenon. Integrated result of such micro action leads to development of macro action. Finally the integrated macro action yields physical behaviour of the soil mass. Such behaviour is found in three different categories. Accordingly, soil mass is known as elastic, plastic or brittle material. In which way micro actions lead to generate macro action and ultimately reveal behaviour, exactly in that way it bears the witness regarding its entity of geological origin in nature. Profoundly, the three forms of behaviors pertaining to elastic or plastic or brittle nature bearing presence of density variation of different particles coexist with water content indicates its utility expressing its aspect of geological origin. Study reveals that such behaviour of geologic origin do not express wide range of variation of properties as and when it is placed for utilization in a remolded state.

To obtain high range elasticity of a soil mass is the objective of this study for yielding the best performed structures like construction of road and building

foundations to be placed at surface level. Accordingly, three series of R&D works conducted in a model Plate Load Test (PLT) by using three types of soil mass under various field conditions comprising special form of hard inclusions. Hard inclusions are more rigid material than soil mass and it is made either of PVC or Steel. Hence, counting of their individual behaviors is beyond scope of this study.

In broad sense, field condition comprises two phases. Treated and untreated phase as the term implies. Physically treated phase includes engineering development of soil mass with hard inclusion to soil mass for generating confined environment of structural soil. It is achieved through development of inner and outer confinements. The complete confined situation created through such stages is known as fully treated structural soil mass (FTSM). This FTSM is the ultimate goal to achieve which yields high range of elastic properties.

In the contexture, Table 1 gives various geotechnical properties of the structural soil used for conducting three series of behavioral tests.

**Table 1.** Properties of structural soil used for conduction of different tests in various condition

Broad division of soil (BDS), their geological origin and physical description of soil samples used	Soil grains as p.c. passing					Basic properties of soil (i.e. Consistency limits) in %			Classification of soil per IS:1498	Result of Standard Proctor Test		Result of Direct shear Test from LB-DST*		SBC of ground from PLT* in (kN/m <sup>2</sup> )
	Grain size in (mm)					W <sub>L</sub>	W <sub>P</sub>	I <sub>P</sub>		OMC	DD in kN/m <sup>3</sup>	C' in N/mm <sup>2</sup>	φ' in degree	
(1) BDS-1. Laterite soil of upper tertiary deposit in local lake; Reddish brown to pale yellowish brown color in wet condition; Inorganic sandy-silt of low compressibility with angular-rounded grains														
(1.1) Reddish brown color soil	93.6	87.3	73.2	35.3	21.8	None-plastic			SM	11.6	18.7	0.6	33.2 <sup>0</sup>	156
(1.2) <i>Pale brown color soil</i>	84.2	90.9	69.3	25.9	16.4	None-plastic			SM	10.5	19.4	1.5	35.0	107
(2) BDS-2. Alluvial soil of recent deposit in local lake; yellowish to blackish grey color in wet condition; Inorganic or organic silty-clay of low compressibility with rounded grains														
(2.1) Yellowish grey color soil	100	100	100	98.7	97.9	32.7	23.4	9.3	CL	18.3	17.8	1.0	29.5 <sup>0</sup>	69.7
(2.2) Blackish grey color soil	100	100	100	97.1	91.5	27.0	21.9	5.1	ML-OL	16.0	18.2	1.1	27.0 <sup>0</sup>	67.7
BDS-3. Colluvial soil of quaternary deposit in local lake; bluish grey to pale grey color in wet condition; Inorganic or organic sandy-silt of low compressibility with angular grains														
(3.1) Pale bluish grey color soil	88.5	81.3	64.5	32.8	24.3	None-plastic			SM	7.25	19.6	0.3	34.99	346

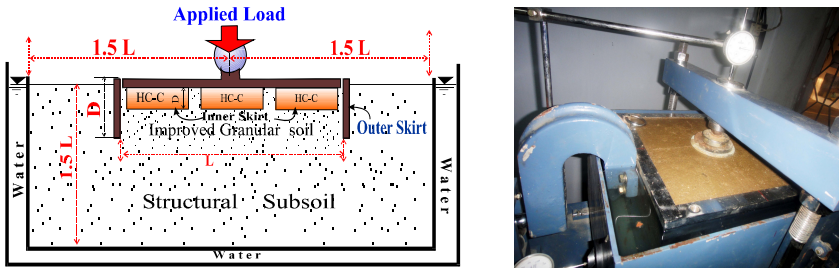
Note: LB-DST\* implies Large Box Direct Shear Test & PLT\* implies model Plate Load Test carried out in the laboratory

## 2 Procedure for Experimental Evaluation of Elastic Behavior of Soil Mass

A good number of model tests in the laboratory were carried out keeping the field condition representative such that observed behaviors can be materialized. In field, for achieving the best performed foundation constructions are normally completed as and when water content in the structural soil mass is closely lower than its optimum content. Moisture closely below optimum is the criterion to fix its stage for development of substructure and subsequently obtaining more elastic behaviors. After development of the structural soil mass with special rigid structure as confining barrier/ skirt to the soil mass, it is found that the water absorption capacity

of soil particles is turning to about stagnant situation. Hence, the chances of attaining its worst situation of cent percent saturation become zero. Because of the applied load on soil mass at this intermediate state of water content with confinement made of impervious rigid material, the soil mass never achieve its plastic limit stage which is the aim to achieve through these efforts.

Under treated phase, a layer of treated soil mass is created and place just below loading plate i.e. foundation level to carryout the series of tests. Fig. 1 illustrating all about whole arrangement of numerical model PLT carried out in the laboratory.



(a) PLT arrangement in Schematic drawing (b) Photograph shows the PLT in LB-DST machine

**Fig. 1** Arrangement for conduction of numerical model plate load tests

This treated layer is named after their process of treatment engaged to generate improved field condition. The process involve consisting of development of inner confining ring as cell type mass particle and outer skirt filling with soil materials. Further, filling materials may also vary in two ways e.g. same type of structural soil to construct the layer and improved quality granular soil (IQGrS) for layer and underneath is site origin structural soil mass.

**Table 2.** Characteristics properties of hard inclusions used in the series of tests

Particulars of items and their materials used to conduct the tests	Dimensions in (mm)			Characteristics Ratio (CR) = Depth to Length	Area within skirts used as individual/group in (mm <sup>2</sup> )	
	Outside Diameter (Length)	Inside Diameter	Depth		For PLT & K-value test	
					As individual/ group inclusion without soil	Used in CBR mould during penetration
1. Outer Skirt of Steel (Sk-1)	115	107	32	0.278	Area of 1 Sk 10386.9	Area (1- Sk) 10386.9
2. Outer Skirt of Steel (Sk-2)	60	54	23	0.383	Area of 1 Sk = 2827.4	Area (1 Sk) 2827.4
3. Inner skirt (HC-C) as cell of PVC						
3(a) PVC-1	40	36	5	0.125	Area of 4 Sk 5026.5	Area (4 Sk), 5026.5
3(b) PVC-2	25	22	5	0.200	Area of 4 Sk 1963.5	Area (4-Sk), 3712.2
3(c) PVC-3	23.5	21	11	0.468	Area of 4 Sk 1828.4	Area (4-Sk), 3712.2
3(d) PVC-4	23.5	21	20	0.851	Area of 4 Sk 1828.4	-
3(e) PVC-3	23.5	21	32	1.36	Area of 4 Sk 1828.4	-
4. Inner skirt HC-C of Steel (STL)	19	17	19	1.000	Area of 7 Sk 1984.7	Area (7-Sk), 3237.1
-Do-	19	17	32	1.68	Area of 7 Sk 1984.7	--

Both inner skirt and outer skirt are defined by their characteristics depth to length ratio (CR). Obviously, the inner confining ring cell is known as cell particle engineered with its depth (D) to diameter (L) ratio, which is termed as ring ratio (RR). This confined soil cell particle is arranged as honey comb cell (HC-C) manner placed in a same plane treated or untreated condition by outer skirting. For different series of tests with various type of soil, this RR is varied at a desired value, e.g. 0.125, 0.20, 0.468, 0.851, 1, 1.36 & 1.68. Table 2 gives an account of the characteristics of hard inclusions used in the present study.

Similarly, in the same treated phase, the outer confinement is defined by skirting barrier filling with structural soil mass inside it with or without HC-C. In special case, when the inside filling is void with HC-C then it is entirely covered by IQGrS or same as its site original subsoil. Hence, besides skirting condition, the engineered filling of such IQGrS placed as a thin layer also follow a ratio of its depth (D) to diameter (L). Thus it is termed as improved granular soil ratio (IGSR). On the other hand, skirting condition of these types is also engineered with its depth (D) to diameter (L) ratio which is termed as skirt ratio (SR). For the whole series of tests conducted under the present study, the SR value considered is mostly one i.e. 0.278 in stead of many. The reason is: it is revealed by evaluated opinion on this aspect that this SR value may be holding good to yield optimum behavior in our present study. Alternately, in general case, the depth of such outer skirt should not exceed the largest diameter of the inner skirted ring use to develop HC-C and placing in single, double or triple layers.

Finally, the permutation and combination of such criteria having RR, SR and IGSR generates many categories of treated soil conditions. Of the many, the treated skirt condition having HC-C process filling with IQGrS is termed as FTSM which is the best. Out of many trials of FTSM with different RR values of HC-C, the combination bearing RR value 1.0 is found to be the best suitable process for obtaining high range elastic properties. Obviously, following engineered conditions were created and are availed to conduct the series of tests:

- Untreated condition – implies PLT without inclusion of RR, SR and IGSR.
- Treated condition – implies PLT with inclusion of RR or SR or IGSR, or combination of two or all with variation of their individual RR values as under:
  - SRB-SF – implies skirt & HC-C ring base surface foundation layer with different values of RR e.g. RR=0.125, RR=0.468; RR=0.851; RR=1; etc.
  - SLRB-SF – implies skirtless but HC-C ring base surface foundation layer with different values of RR e.g. RR-0.468; RR-0.851; RR-1; etc.
  - SGrB-SF – implies skirted granular soil but without HC-C ring base surface foundation layer with different values of IGSR e.g. IGSR-0.299; IGSR-0.187; etc.
  - SRGrB-SF – implies skirt & HC-C ring with improved granular soil filled base surface foundation layer with different values of RR & of IGSR e.g. RR-0.468 & IGSR-0.299; etc.

In reality, the combination of this RR, SR and IGSR as a thin layer to foundation system yields *surface foundation for Road* [5] and *Low rise Buildings upto 12*

storey height [1][2][3]. However, such treatment is extensively differ by principle and application as and when the ground is treated with granular pile/ columns [4].

In the above series of tests so carried out under model PLT set up that placed in a LB-DST machine (Fig. 1), it was tried to maintain the earlier mentioned field situation for each tests conducted (Table 1). The preparation of the tests with selective undisturbed and remolded soil mass is done meticulously to achieve targeted field condition and moisture situation. For the remolded soil, standard compaction procedures were followed and soil layers are placed at moisture content closely lower to OMC. Additional moisture content is allowed to increase by absorption from bottom of the testing soil mass through machine system after setting of all loading and measuring devices (Fig. 1). After a few hours of absorption i.e. approximately crossing about 45% saturation, load versus settlement tests commenced for every trial tests.

### 3 Test Results and Discussion

In total 21 number of model PLT were carried out with three kinds of soil given in Table 1. Because of the page limitation, it is not possible to deal with each test for presentation of their results and discussion. However, for comprehensive understanding how it is achieving the aim and objective of the study, a few number of test results carried out with soil type BDS-1(1.2) i.e. pale brown color soil of laterite origin (Table-1) are presented in Fig. 2. As for illustrative purposes, Fig. 2 shows a series of PLT results which are representative by nature of all series of tests conducted under various field conditions with different soil materials.

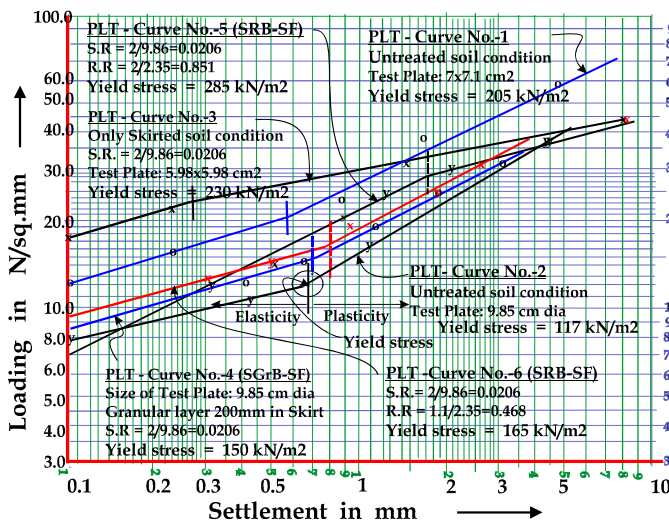


Fig. 2. Load Vs settlement curves representing results of a single type structural soil mass namely Laterite soil of pale brown color

Fig. 2 demonstrating all about seven kinds of test results which represent seven varieties of applied field conditions for a single type of soil. In general, the PLT curve reveals loading intensity (i.e. stress), settlement (i.e. strain) and ultimate elastic stress which is utilized for finding factor of safety (FoS) from geological point of view and final safe bearing capacity (SBC) of the soil used to carry out the PLT. Hence, yield stress is an important expression of soil behaviour which is the maximum elastic stress point of the tested soil mass. Since it is known as critical stress point i.e. end point of elastic behavior of soil mass, therefore, the execution of plastic behavior begins beyond this point. Such critical point is illustrated and marked on curve no. 1 in Fig. 2.

Curve no.1 represents the untreated normal ground and hence, it expresses the geologic original range of elasticity of the soil mass which is prevailing in nature without treatment. The range of elasticity expressed through elastic settlement Vs corresponding stress is the shortest range, which reveals a lower most yielding stress. On the other hand, the higher most range of elasticity expresses by curve no. 3 among the present results. The field condition represented by curve no. 3 is evidently for SRGrB-SF with all form of combination. However, the determining criteria are IGSR, SR & RR. For the present study these values are 0.299, 0.278 & 1.0 respectively. This is the best combined process of soil mass development for construction of surface foundation layer built as Bi-layer footing foundation system [1][2][3] for building and road foundation [5] with high range elasticity.

Study reveals that the achievement of high range elastic behavior of FTSM developed with various types of soil (Table 1) are varied extensively but always reveals many times more that the untreated site ground (Curve No. 1).

## 4 Conclusions

Present study carried out for achieving high range elastic properties of soil mass reveals the following:

- It is possible to enhance the elastic property of naturally occurs soil mass many times (Fig. 2) by treating them with hard inclusion with their characteristics ratio (Table-2) pertaining to RR, SR and IGSR placing them as one thin layer to Bi-layer SF system which reveals stable and durable structures.
- It is concluded that FTSM with the highest combination of various field conditions generates a high elastic property layer to bi-layer foundation system known as surface foundation [1][2][3], which can be used as shallow foundation for multistorey building as well as road foundation as express way.
- Present study as an innovative work attracts more meticulous study in future to achieve more benefit for human developments.

## References

- [1] Bayan Gokul, K.: Design & Detailing of (G+6)-Storeys rcc Building of Er. Ayung Nabam, with Bi-layer Footing Foundation System at Doimukh; M/S Design-Tech Pvt. Ltd, Report No. Report No.DgT/ Nabam/ rcc Building/ 7s-2011 July; Naharlagun; Arunachal Pradesh; India, pp. 1-166 (2011)

- [2] Bayan Gokul, K.: Introduction of bi-layer footing foundation for multistorey RCC building in weak subsoil of lower Himalayan region in India—A case study. In: *Geotechnics for Sustainable Development— Geotech Hanoi 2011*; Phung (Ed.); Construction Publishing House Vietnam; pp. 387–398 (2011) ISBN 978-604-82-000-8
- [3] Bayan Gokul, K.: Failure of a 4-storey RCC Building and its Retrofitting with bi-layer footing foundation under Eq Zone V – A Case study. In: *Proc. of IGS & Cochin University of Science and Technology, IGC 2011, Kochi, Kerala*, pp. 999–1002 (2011)
- [4] Bayan Gokul, K.: Behaviour of Weak soil Foundations Treated with Granular Piles. In: *Proc. 12th Asian Regional Conference, ISSGE (International Society for Soil Mechanics and Geotechnical Engineering)*, Singapore, pp. 443–447 (August 2003)
- [5] Bayan Gokul, K.: Road foundation – a new avenue for its stable and ever-lasting aspect. In: *Indraratna, B., Rujikiatkamjorn, C., Vinod, J.S. (eds.) International Conference on Ground Improvement and Ground Control (ICGI 2012)*, October 30–November 2. U 2012, University of Wollongong, Australia (2012)

# Effect of Air Entrapment on Unsaturated Flow in Porous Media

Pan Chen<sup>1</sup>, Changfu Wei<sup>1,2,\*</sup>, Jili Wang<sup>1</sup>, Houzhen Wei<sup>1</sup>, and Tiantian Ma<sup>1</sup>

<sup>1</sup> State Key Laboratory of Geomechanics and Geotechnical Engineering, Institute of Rock and Soil Mechanics, Chinese Academy of Sciences, Wuhan, Hubei 430071

<sup>2</sup> Guilin University of Technology, Guilin, Guangxi 541004  
{cfwei, pchen}@whrsm.ac.cn

**Summary.** The sizes and connectivity of the pores in porous media such as rock and soil are randomly distributed at microscopic level. Due to this characteristic, the flow of fluids in the porous media is significantly different from the flow characteristics in the ideal single pore model. As important features of seepage, capillary hysteresis and air entrapment generally occur in the porous media experiencing non-monotonic change of water content. Based on the analysis of drying/wetting processes in unsaturated soils, a theoretic model of seepage is developed, in which the effect of air entrapment is taken into account. The theoretical model is implemented into a computer code and a numerical analysis procedure is developed. The model can be used to simulate the unsaturated seepage in soils with the effect of air entrapment under arbitrary change of water content. By comparing the numerical results with measured data, it is shown that the effect of air entrapment is significant on the fluid distribution. The effect of capillary hysteresis and air entrapment should be taken into account in seepage analysis in order to accurately predict the soil-moisture characteristics of soils.

**Keywords:** air entrapment, unsaturated flow, capillary hysteresis, porous media.

## 1 Introduction

The characterization of the content and distribution of fluids in porous media are important for water resources management, plant irrigation and contamination source restoration. The content and distribution of fluids depend upon many factors, among which are capillary hysteresis and air entrapment. Entrapped air is non-continuous air bubbles trapped within the wetting fluid in porous media (e.g., [1]). The effect of trapped air on the fluid flow has been studied by some researchers. Stonestrom and Rubin (1989)[2] showed that the hydraulic conductivity of soils was reduced due to air entrapment. Similar results were observed by others (e.g., [3]). Based on the experimental and numerical simulations, van Geel et al.(1997)[4]

---

\* Corresponding author.

found that the entrapment of LNAPL had an important effect on the distribution of LNAPL spills as the water table fluctuated.

Sharma and Mohamed (2003)[5] found that the content of trapped air depends on the degree of saturation at the previous imbibition point of hydraulic path. The content of the non-wetting phase entrapment can change with drying/wetting cycles (e.g., [6]). In numerical modeling, it is usually found (e.g., [7]) that the calculated saturation and capillary pressure usually does not agree well with experimental data, especially during the wetting process immediately after the drainage of soils. The main reason for this is that the effect of capillary hysteresis and air entrapment commonly occurs in the unsaturated porous media undergoing drying-wetting cycles. Thus far, however, very few models include the effect of air entrapment. Park and Lenhard (1987)[8] developed a scaling model to describe the relations of hysteretic saturation-capillary pressure, which accounts for the effect of entrapment air and oil phase during the wetting progress. The method can significantly improve simulation results. Hence, an accurate model for moisture retention characteristics is crucial in reasonably predicting the distribution of water phase and NAPL in the vadose zone.

Several models have been developed for describing the change of soil-moisture state with the effect of capillary hysteresis in porous media. Among these models, the internal state variable hysteresis model (ISVH-model) was the one derived from thermodynamic theory and internal state variable theory (e.g., [9]). The model can describe well the soil-water characteristic of porous media experiencing drying/wetting cycles. It is noted, however, that in the original ISVH-model the effect of air entrapment was not taken into account. In this paper, a theoretical model of soil-water characteristics, which can simultaneously address capillary hysteresis and air entrapment, is first developed based on ISVH-model. Then the new model is implemented into a finite element code. The numerical procedure is used to analyze the drying/wetting processes in unsaturated soils.

## 2 Theoretical Model

Based on the mercury injection tests on the rocks, Wardlaw and Taylor (1976)[10] found that the content of entrapped mercury is related to the saturation degree of mercury at the transiting point from injection to withdrawal curves. Similar results were observed in unsaturated soils[2]. Based on this observation, we assume herein that (1) the content of air entrapment depends only upon the maximum matric suction the porous medium experienced. (2) The scanning soil-moisture retention curves can be uniquely determined by the closed hysteresis circles corresponding to the previous maximum matric suction. As such, the shape of closed hysteresis loops is not affected by the air entrapment. Based on the above two assumptions, the rate of the change in water content along the drying or wetting scanning curves can be determined by the scanning curves within the closed loop constituted by the main wetting and main drying curve.

The mathematical description is developed based on the above two assumptions. The sketch of the theoretical model is shown in figure 1. The content of air entrapment is related to the maximum matric suction  $s_c^{max}$  that the porous medium previously experienced, as

$$\theta_{entrap}(s_c^{max}) = \theta_{entrap}^{max} - [\theta^{IDC}(s_c^{max}) - \theta^{MDC}(s_c^{max})] \tag{1}$$

where  $\theta_{entrap}(s_c^{max})$  is the volumetric content of air entrapment related to  $s_c^{max}$ ,  $\theta_{entrap}^{max}$  is the maximum volumetric content of air entrapment,  $\theta^{IDC}(s_c^{max})$  is the volumetric water on the primary drying curve corresponding to the transition point  $s_c^{max}$ ,  $\theta^{MDC}(s_c^{max})$  is the volumetric water content on the main drying curve corresponding to the matric suction  $s_c^{max}$ . The translational volumetric water content  $\theta_{tran}(s_c)$  from the point B on the IDC to the point C on the MDC is computed as,

$$\theta_{tran}(s_c) = \theta(s_c) - (\theta_{entrap}^{max} - \theta_{entrap}(s_c^{max})) \tag{2}$$

The change of water content from the point C to I (or the point D to H) in the main hysteretic loop can be calculated undergoing the change of matric suction in the same way as in the literature[9]. The actual water content in the scanning drying (the point E to F) or wetting curves (the point B to G) from the primary drying curve is obtained by the translation method given the change of matric suction, i.e.,

$$\theta(s_c + \dot{s}_c) = \theta_{tran}(s_c + \dot{s}_c) + (\theta_{entrap}^{max} - \theta_{entrap}(s_c^{max})) \tag{3}$$

where  $\dot{s}_c$  is the changing rate of matric suction. The boundary curve equation of the hysteretic loop is given (e.g., [11]).

$$s_c = b \left( \frac{S_r^i - S_r}{S_r - S_r^{irr}} \right)^{1/a} \tag{4}$$

where  $S_r^i = \begin{cases} 1.0 & \text{for IDC} \\ S_r^{MDC} & \text{for MDC} \\ S_r^{MWC} & \text{for MWC} \end{cases}$ ,  $S_r$  is the degree of saturation,  $S_r^{irr}$  is the residual degree of saturation, a, b are the empirical parameters which are obtained from fitting the experimental data.

Thus far, we have developed a theoretical model for capillary hysteresis. For convenience, the model is termed as ISVH-TRAP model hereinafter. The new model accounts for the effect of air entrapment on the liquid flow in porous media.

The ISVH-TRAP model is used to predict the soil-water retention relationship for verifying its effectiveness under arbitrary change of water content. The predictive results are compared with the experimental data from the literature (e.g., [12]) in the figure 2. The model parameters are listed in the table 1. From the figure 2, the predictive curves are coincident with the measured data. It's shown that the ISVH-TRAP model is efficient to simulate the soil-water retention relationship with the effect of capillary hysteresis and air entrapment undergoing the repeated change of hydraulic paths.

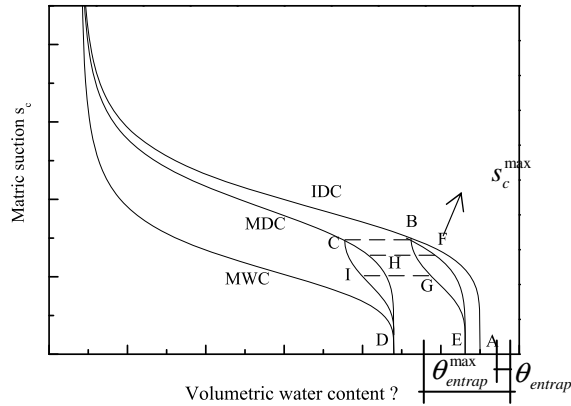
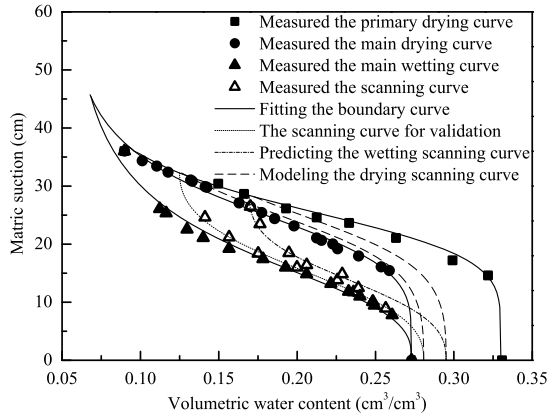


Fig. 1. Schematics of the theoretical model for SWRC

Table 1. Model parameters of sand

Parameters	Symbol	Quantity	Unit
	$n_0$	0.33	
Porosity	$S_r^{irr}$	15.15	-
Residual saturation degree	$S_r^{entrap\ max}$	17.27	%
Maximum air entrapment	$S_r^{MDC}$	82.73	%
content	$S_r^{MWC}$	82.73	%
	$b^{IDC}$	26.92	cm
	$b^{MDC}$	26.86	cm
	$b^{MWC}$	19.44	cm
Model parameters for	$a^{IDC}$	5.56	-
ISVH-TRAP	$a^{MDC}$	4.59	-
	$a^{MWC}$	2.84	cm
	$c$	500	



**Fig. 2.** Hydraulic path in a porous medium subjected to wetting/drying cycles with entrapped air effect

### 3 Numerical Model

The ISVH-TRAP model has been implemented into a finite element code, U-DYSAC2. The code can be used to simulate the transient seepage processes in multiphasic porous media. The finite element formulations and time-stepping procedure are described in details in [11]. The numerical implementation and the validation of the finite element code can also be found in this reference. Here we shall focus on discussing the simulation results.

### 4 Numerical Examples

In order to validate the new numerical model and explore the effect of entrapped air on the unsaturated seepage, the simulated curves using the above-mentioned finite element code are compared with the experimental data. The measured data are obtained from Lenhard et al. (1991)[13] who performed the cyclic drying-wetting tests on a sand column. The height of the sand column is 72 cm. If the horizontal direction is defined as x axis and the vertical direction defined as z axis, the boundary condition can be expressed as

$$\text{Top boundary: } u_x = 0.0 \text{ cm, } q_z^w = 0.0 \text{ cm/h, } p^N = 1 \text{ atm,}$$

$$\text{Two lateral boundaries: } u_x = 0.0 \text{ cm, } q_x^w = 0.0 \text{ cm/h, } p^N = 1 \text{ atm,}$$

$$\text{Bottom boundary: } u_x = u_z = 0.0 \text{ cm, } p_z^w = p(t) \text{ cm, } q^N = 0.0 \text{ cm/h.}$$

where  $u$  is the displacement function,  $q^w$  is the flow of water,  $p^N$  is the pressure of air phase,  $p^w$  is the pressure of water phase.

At the bottom of the column,  $z=0\text{cm}$ . The sand is saturated with the distilled water. After the water table was raised to  $z=72\text{cm}$ , it remained at the same level for 12 hours, and then the experiment started. The repeated change of the bottom pressure  $p_z^W(t)$  with time can be seen in literature (e.g., [13]). The material parameters are given in table 2. The ISVH-TRAP model is used to model the measured soil-water retention curve. The primary drying curve is obtained through fitting the experimental data. The same fitting parameters are used to obtain the main drying curve, but the main wetting curve is different due to the effect of air entrapment. Based on the scattered data available, the main wetting curve is obtained by assuming that  $\alpha^W = 2\alpha^D$  in the VG-mode (e.g., [14]). The model parameters are concluded in table 3.

The change of water content with time at the different heights is shown in the figure 3. The simulation results are given and compared with the experimental data. ISVH-TRAP model represents the hysteresis model considering the effect of air entrapment in the flow analysis. The effect of entrapped air is excluded in the ISVH model. IDC model stands for single drying curve without the effect of hysteretic effect. All the above three models are considered in simulating the seepage processes in the column. Figure 3 shows that the ISVH-TRAP model yields very good results, whereas ISVH and IDC models generally overestimate the degree of saturation. It can be seen from Figure 4 that the hydraulic path is not always along the single primary drying curve due to the effect of capillary hysteresis and air entrapment. Overall, the ISVH-TRAP model yields the best results in all the cases simulated. The ISVH and IDC model fail to predict the tendency of the water distribution. Especially, the simulation results of the IDC model are significantly different from the observed results.

**Table 2.** Material properties of sand

Parameters	Symbol	Quantity	Unit
Density of solid phase	$\rho^S$	2.65E+3	kg/m <sup>3</sup>
Density of water phase	$\rho^W$	1.0E+3	kg/m <sup>3</sup>
Density of air phase	$\rho^N$	1.2	kg/m <sup>3</sup>
Volumetric modulus of skeleton	K	8.33E+3	kPa
Shear modulus of skeleton	G	6.25E+3	kPa
Volumetric modulus of water phase	$K_w$	2.2E+6	kPa
Intrinsic permeability	$k_{sat}$	3.37E-11	m <sup>2</sup>
Dynamic viscosity of water phase	$\nu_w$	1.00E-3	Pa s
Dynamic viscosity of air phase	$\nu_N$	1.80E-5	Pa s
Porosity	$n_0$	0.360	-
Residual saturation degree	$S_r^{irr}$	16.94	%

**Table 3.** Model parameters of sand

Parameters	Symbol	Quantity	Unit
Maximum air entrapment content	$S_r^{max}$	25.0	%
	$S_r^{MDC}$	75.0	%
	$S_r^{MWC}$	75.0	%
	$b^{IDC}$	25.58	cm
Model parameters for ISVH-TRAP	$b^{MDC}$	25.58	cm
	$b^{MWC}$	12.56	cm
	$a^{IDC}$	4.78	-
	$a^{MDC}$	4.78	-
	$a^{MWC}$	4.47	-
	$c$	200	cm

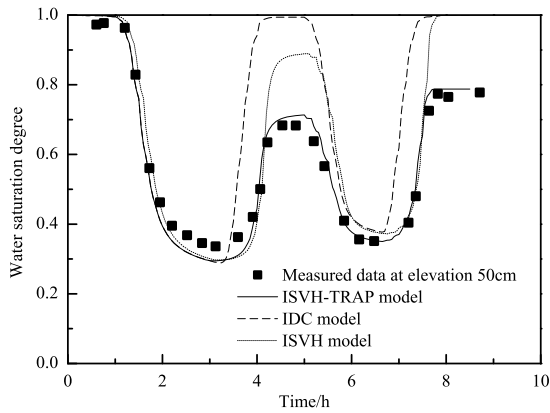


**Fig. 3.** Comparisons of simulations with experimental results

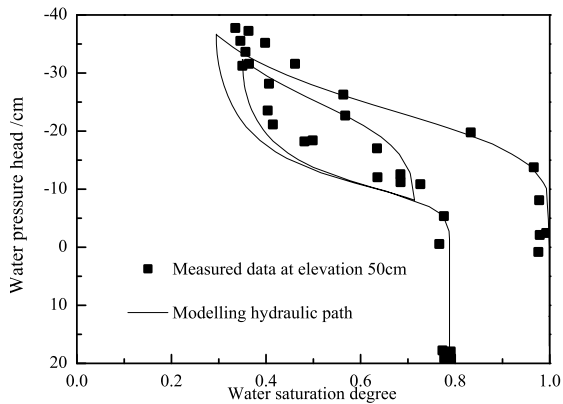


**Fig. 4.** The simulated and measured change of hydraulic paths

The phenomena of capillary hysteresis and air entrapment in soil layers commonly occur under intermittent rainfall infiltration and water table fluctuation conditions. Hence, it is crucial to properly characterize these phenomena in modeling the seepage processes in unsaturated soils.

## 5 Conclusion

A new model for describing the soil-water retention characteristics is developed, and the effect of air entrapment is taken into account. The new model (termed as ISVH-TRAP model) can be used to simulate the change of soil-water state in the unsaturated porous media experiencing cyclic hydraulic paths. The new model is implemented into a finite element code, which can be used to analyze the seepage problem in unsaturated soils with air entrapment. By comparing the numerical simulations with experimental results, it is shown that air entrapment can significantly influence the water content distribution. The effect of capillary hysteresis and air entrapment should be taken into account in modeling the unsaturated flow in unsaturated soils.

**Acknowledgment.** The research is supported by the Natural Science Foundation of China (Grant No. 11072255), and the Natural Science Foundation of GuangXi (No. 11-KF-05).

## References

- [1] Bond, W.J., Collisgeorge, N.: Ponded infiltration into simple soil systems.1. The saturation and transition zones in the moisture-content profiles. *Soil Science* 131(4), 202–209 (1981)
- [2] Stonestrom, D.A., Rubin, J.: Water-content dependence of trapped air in 2 soils. *Water Resources Research* 25(9), 1947–1958 (1989)
- [3] Seymour, R.M.: Air entrapment and consolidation occurring with saturated hydraulic conductivity changes with intermittent wetting. *Irrig. Sci.* 20, 9–14 (2000)
- [4] van Geel, P.J., Sykes, J.F.: The importance of fluid entrapment, saturation hysteresis and residual saturations on the distribution of a lighter-than-water non-aqueous phase liquid in a variably saturated sand medium. *Journal of Contaminant Hydrology* 25(3–4), 249–270 (1997)
- [5] Sharma, R.S., Mohamed, M.H.A.: An experimental investigation of LNAPL migration in an unsaturated/saturated sand. *Engineering Geology* 70(3–4), 305–313 (2003)
- [6] Van Geel, P.J., Roy, S.D.: A proposed model to include a residual NAPL saturation in a hysteretic capillary pressure-saturation relationship. *Journal of Contaminant Hydrology* 58(1–2), 79–110 (2002)
- [7] Kamon, M., Li, Y., Flores, G., Inui, T., Katsumi, T.: Experimental and numerical study on migration of LNAPL under the influence of fluctuating water table in subsurface. In: *Annuals of Disas. Prev. Res. Inst.*, vol. (49)B, pp. 383–392. Kyoto Univ. (2006)
- [8] Parker, J.C., Lenhard, R.J.: A model for hysteretic constitutive relations governing multiphase flow 1: saturation-pressure relations. *Water Resources Research* 23(12), 2187–2196 (1987)

- [9] Wei, C.F., Dewoolkar, M.M.: Formulation of capillary hysteresis with internal state variables. *Water Resource Research* 42, W07405 (2006)
- [10] Wardlaw, N.C., Taylor, R.P.: Mercury capillary pressure curves and the interpretation of pore structure and capillary behaviour in reservoir rocks. *Bulletin of Canadian Petroleum Geology* 24(2), 225–262 (1976)
- [11] Chen, P., Wei, H.Z., Li, H., Xu, Y.B., Wei, C.F.: Effect of capillary hysteresis on two-phase flow in porous media. *Chinese Journal of Rock Mechanics and Engineering* 29(10), 2148–2158 (2010)
- [12] Poulouvalis, A.: Hysteresis of pore water in granular porous bodies. *Soil Science* 109(1), 5–12 (1970)
- [13] Lenhard, R.J., Parker, J.C., Kaluarachchi, J.J.: Comparing simulated and experimental hysteretic two-phase transient fluid flow phenomena. *Water Resources Research* 27(8), 2113–2124 (1991)
- [14] Kool, J.B., Parker, J.C.: Development and evaluation of closed-form expressions for hysteretic soil hydraulic-properties. *Water Resources Research* 23(1), 105–114 (1987)

# On the Mechanical Behaviour of the Gibraltar Strait Breccias

Weixin Dong, E. Pimentel, and G. Anagnostou

Department of Civil, Environmental and Geomatic Engineering  
ETH Zurich  
Wolfgang-Pauli-Strasse 15, 8093 Zurich, Switzerland  
weijie.dong@igt.baug.ethz.ch

**Abstract.** The tunnel planned for the Gibraltar Strait fixed link will cross - among other formations - two paleo-channels filled with breccias. The breccias exhibit poor mechanical properties in the range between stiff clays and weak rocks. The overburden and high pore pressures in-situ may lead, in combination with the low strength of the breccias, to heavy squeezing during construction of the tunnel. The mechanical properties of the breccias were studied using special triaxial tests. The testing technique is very demanding due to the need for pore water control in combination with high applied loads. Neither standard rock nor soil mechanics testing equipment is adequate for this purpose. In addition, the low hydraulic conductivity of the breccias demands extremely low loading rates, which leads to very long test durations. The paper presents and comments on the test results on the strength, volumetric behaviour, consolidation state and hydraulic conductivity of the breccias.

## 1 Introduction

The proposed Gibraltar Strait fixed link consists of a subaqueous tunnel with a length of about 38 km [1]. The actual vertical alignment of the tunnel (B1 in Fig. 1) crosses - among other formations - two paleo-channels at a depth of about 200 m beneath the sea bed. These natural channels are located approximately in the middle of the alignment and are filled with clayey breccias of extremely poor quality. The breccias consist of a chaotic mixture of blocks, stones and stone splinters embedded in a clay matrix, which possesses a low strength and a high deformability [1]. They represent the weakest material in tunnel lithology. Their low strength in combination with the high in-situ pressures (about 200 m below the sea bed and 500 m below sea level, see Fig. 1) makes the breccias highly susceptible to squeezing. This, together with the limited accessibility for pre-exploration or pre-treatment, makes overcoming the breccias one of the key challenges of the project.

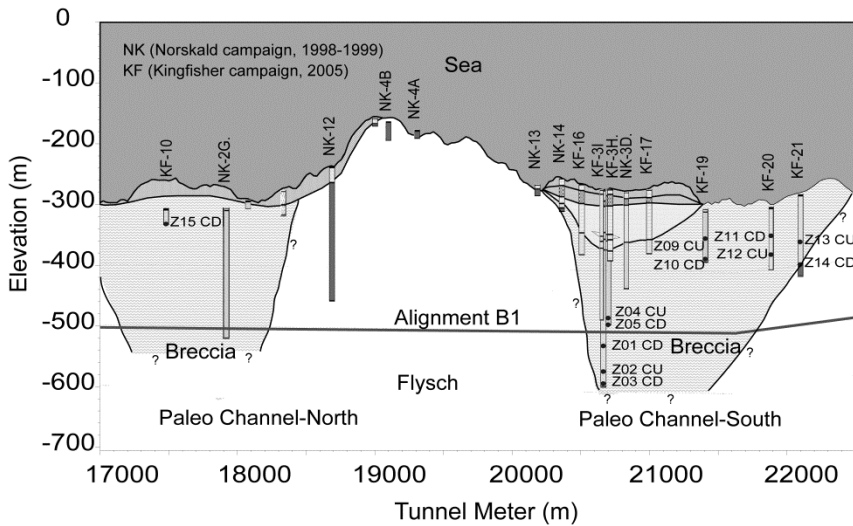


**Fig. 1.** Geological profile of the breccia zones, tunnel alignment and location of samples (after SECEGSA and SNED)

The mechanical properties of the ground were investigated using triaxial compression tests. Due to the dominant role of the clay matrix in the mechanical behaviour of the breccia and the saturated state of the material in situ, the effect of pore pressure (according to the principle of effective stresses) must be considered in testing. The standard triaxial testing apparatuses from soil mechanics or rock mechanics are not adequate for testing this material: Soil mechanics equipment considers only low nominal loads and pressures, while rock mechanics equipment does not allow for control of the pore pressure. In order to overcome these limitations several modifications were carried out on the triaxial testing apparatus [2-7]. The literature contains information about the mechanical behaviour of some weak rocks with highly squeezing potential, such as kakirites [7] and clayshales [2,3,5], but there has been nothing not yet on breccias similar to those from Gibraltar.

The main objective of the paper is to present and analyse the experimental results and the particular characteristics of the weak breccias from the Gibraltar Strait. The paper also introduces some of the features and key procedures involved in the implementation of the triaxial testing technique for weak rocks with low hydraulic conductivity under high stress.

## 2 Laboratory Investigations

The testing material consists of the cores obtained from offshore drilling during the last two exploratory campaigns (the so-called Norskald and Kingfisher campaigns). Figure 1 shows the projected location of the boreholes and the depth of the samples. The cores were stored in the Tarifa Gallery, an exploratory adit with nearly 100% relative humidity. In order to provide additional protection against drying, the cores were wrapped in foil.

The results of grain size analyses indicate that the main constituents of the breccias are silt and clay, accounting for more than 80% of the content, and with a plasticity index  $PI$  of 27% and an activity of 0.77, which corresponds to inactive clays with high plasticity. After testing, the breccias have a porosity  $n$  of 32.5% and a water content  $w$  of 17%. The breccia samples can be indented by thumbnail and peeled by knife. The samples can therefore be classified as stiff clay or weak rock, according to the soil and rock strength classifications from field indices suggested by the ISRM [8].

During the exploration phase of the Gotthard Basetunnel, Vogelhuber [7] modified the equipment of our rock laboratory in order to study the behaviour of kakirites. The research on the breccias from the Gibraltar strait necessitated further improvements. The main improvements were the implementation of a pressure controlled electromechanical pore pressure device and an electronically controlled diamond band saw for the specimen preparation. The latter allows for a vibrationless cutting of the hard inclusions without deforming the clay matrix of the breccias. The pore pressure equipment makes it possible to measure hydraulic conductivity more accurately. This was necessary for testing the breccias, because they exhibit a very low hydraulic conductivity and require extremely low load rates and long test durations (Table 1). After the first two tests, a sample slenderness factor of 1 was chosen for the other tests in order to reduce the testing time. The lower slenderness factor nevertheless introduces friction effects. In order to reduce friction between the end surfaces of the specimen and the loading plates, polished stainless steel plates and a circular latex membrane material with a thickness of 2.6 mm, separated by a film of silicone grease were applied on both ends of the specimen [9].

In order to recreate the in-situ conditions as far as possible and in view of a possible slight drying of the specimens during storage, the specimens were first brought to a saturated state and to a stress level close to the in-situ stress. This was done sequentially by watering, by applying back-pressure and by consolidation. The watering phase allows also for the measurement of the hydraulic conductivity. The pressures for the watering, back-pressure and consolidation phases were determined on the basis of the estimated in-situ mean stress values.

The testing programme consists of multi-stage consolidated-drained (CD) and consolidated-undrained (CU) tests. The chosen axial loading rates were 0.05 - 0.1 mm/h for the CD-tests and 0.1 - 0.2 mm/h for the CU-tests. The adequacy of these loading rates was checked by means of a numerical (hydro-mechanically coupled) experiment (the simulation of the drained shearing of a material exhibiting an extremely low hydraulic conductivity of  $k = 10^{-13}$  m/s). According to the numerical results, the pore pressure distribution in the model is practically homogeneous, which indicates that the chosen loading rate is sufficiently slow to ensure that no relevant excess pore pressure will develop at any time or at any point in the specimen.

Due to the long test duration and the low strength of the breccias some factors, which are usually negligible, must be considered in the evaluation of the results. The duration of each deviatoric loading stage takes 1 - 2 days. For comparison, the kakirites of the Gotthard base tunnel needed only 3 - 4 hours [7]. Since our rock mechanics laboratory is air-conditioned but does not allow for a precise temperature regulation, the temperature may vary by 2 - 3 °C between day and night and

by 3 - 4 °C over the weekend. The temperature changes affect the evaluation of the volumetric strain, which for this equipment is usually calculated on the basis of axial deformation and changes in the oil volume in the cell. With this measuring principle, the error introduced by a temperature difference between day and night will be of the same order of magnitude or even bigger than the measured volumetric strain. Therefore the volumetric strain was calculated via the volume of the water expelled from the sample during shearing and consolidation. Using this method, the error caused by the temperature fluctuation is considerably reduced because, (i), the quantity of water in the testing system is smaller than the quantity of oil and, (ii), water has a lower thermal expansion coefficient than oil. A temperature change of 2 - 3 °C causes an error in the volumetric strain of the specimen of only 0.08 - 0.12%. This method works accurately only if the specimen is saturated and a high back-pressure is applied.

Due to the low strength of the breccias, the axial force measured externally must also be corrected in order to compensate for the effect of the friction between piston and cell wall. The friction force was quantified by a series of calibration tests and depends linearly on the confining pressure. In the following discussion, only the corrected values will be considered.

### 3 Results and Discussion

The hydraulic conductivity and the strength of the specimens are evaluated by means of Darcy's law and the Mohr-Coulomb failure criterion (in terms of effective stresses), respectively. Table 1 summarizes the strength parameters, hydraulic conductivities, loading rates and test durations of the tested samples.

**Table 1.** Strength parameters, hydraulic conductivities, loading rates and test durations

Test Nr.	Test type	Depth of cover [m]	Region	$c'$ [MPa]	$\phi'$ [°]	$k$ [m/s]	Load rate [mm/h]	Test duration [days]
Z01	CD	256	Lower	0.376	14.3	4.88E-12	0.05	35
Z02	CU	298		0.583	7.6	1.05E-11	0.15	76 ( $H/D=2$ )
Z03	CD	318		1.399	9.1	1.42E-12	0.1	97
Z04	CU	212		0.447	12.1	9.36E-13	0.1	93
Z05	CD	223		0.327	9.0	3.76E-13	0.05	54
Z09	CU	49	Upper	0.375	26.0	9.40E-12	0.1	30
Z10	CD	82		0.081	20.2	2.28E-11	0.1	49 ( $H/D=2$ )
Z11	CD	48		0.233	26.4	4.23E-11	0.05	22
Z12	CU	79		0.120	24.5	1.86E-11	0.1	36
Z13	CU	79		0.099	21.8	2.53E-11	0.2	28
Z14	CD	116		0.306	18.9	2.11E-12	0.05	49
Z15	CD	25		0.108	22.2	5.26E-12	0.05	39

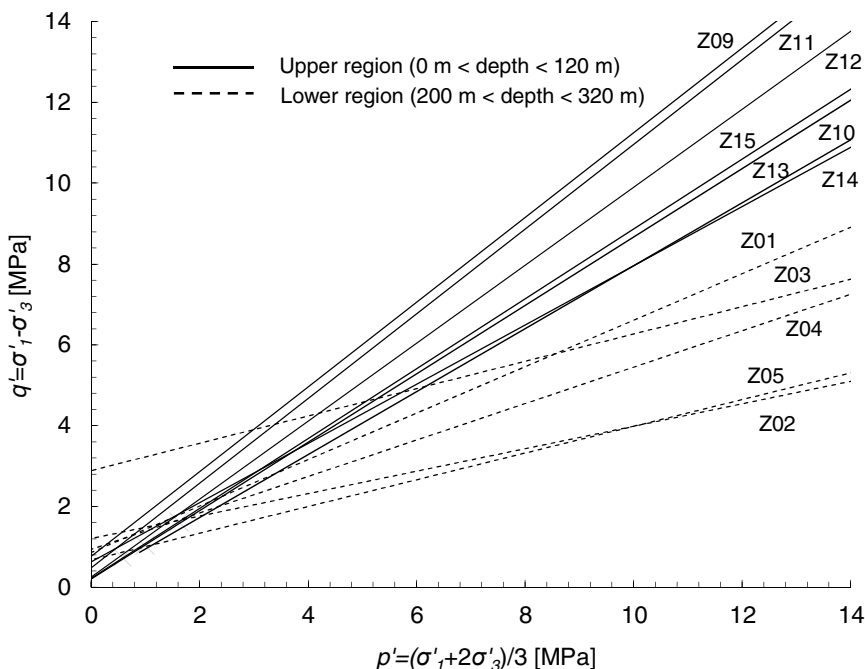
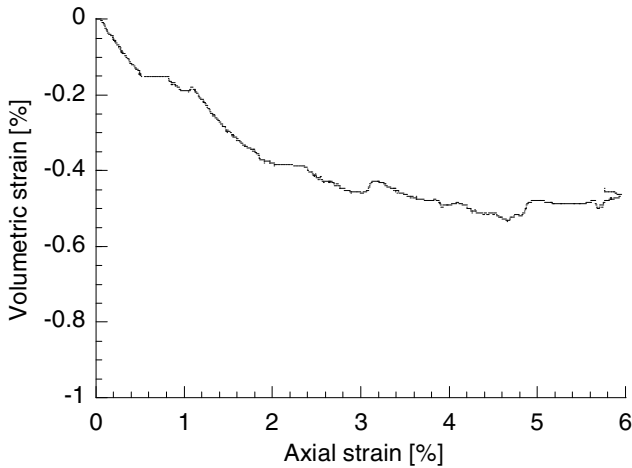


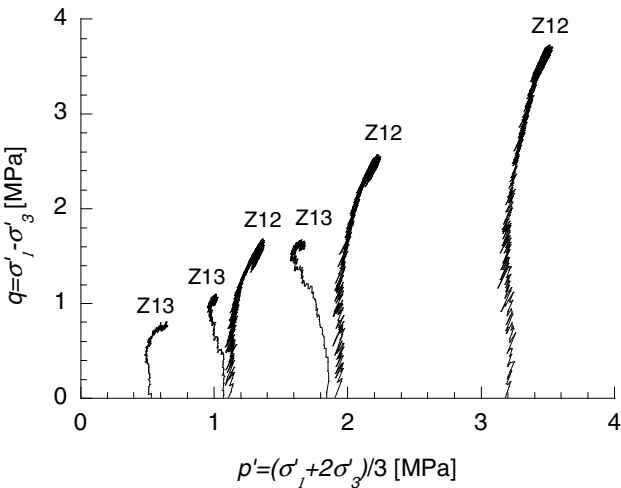
Fig. 2. Strength envelopes of the tested samples

Figure 2 provides an overview of the strength envelopes in the  $p'$ - $q'$  space. The samples can be arranged in two groups: The first group contains the samples from the upper region of the paleo-channel (depth < 120 m, solid lines in Fig. 2); the other samples stem from the lower region (depth between 200 and 320 m, dashed lines in Fig. 2). Samples from the lower region show lower friction angles but higher cohesions. These results indicate that the initial stress strongly influences the properties of the breccias. The planned vertical alignment of the tunnel (B1 in Fig. 1) crosses the breccias at a depth of about 200 m, i.e. at the top of the lower region.

Figure 3 shows the typical volumetric strains for the deviatoric stage of a CD-test (sample Z15). The volumetric strain increases smoothly with the axial strain and shows a slightly contractant behaviour during the whole shearing stage. Figure 4 shows the stress paths of two CU-tests (samples Z12 and Z13) in the  $p'$ - $q'$  space. In the case of the sample Z13, the effective confining pressure  $p'$  decreases before failure, i.e. the pore pressure increases, which means that the behaviour before failure is contractant. The same observation was also made with most of the other CU samples. Sample Z12 is the only exception exhibiting a slightly dilatant behaviour before failure as indicated by the negative excess pore pressure. It is interesting to note, however, that the negative excess pore pressure ceases to increase after failure and that the peak stress and volumetric strain remain approximately constant after reaching failure. Samples Z12 and Z13 therefore exhibit a different volumetric behaviour before failure, but both reach a critical state [10] and have about the same strength parameters.



**Fig. 3.** Typical volumetric strain curve during shearing (Z15, 1st load stage, total radial stress  $\sigma_3 = 2.2$  MPa, back pressure  $u = 2.0$  MPa)



**Fig. 4.** Stress paths for sample Z12 and Z13

The results of the CD and CU triaxial tests show that the breccias behave like normally consolidated or slightly over-consolidated soils. This is plausible because there is no geologic evidence that the breccias from Gibraltar were exposed in the past to considerably higher stresses due to tectonic action or to glacial deposits [11]. The evaluation of Skempton’s pore pressure parameter  $A$ , which denotes the ratio of increment of the pore pressure to the increment of axial stress

during shearing in CU tests [12], provides additional evidence that the breccias are normally or slightly over-consolidated. In the CU-tests,  $A_f$  (i.e.  $A$  at failure) varied between 0.15 - 0.45. The typical  $A_f$  values are 0.5 - 1.0 for normally consolidated soils, 0 - 0.5 for slightly over-consolidated soils and negative for over-consolidated soils [13].

## 4 Conclusions

The breccias from Gibraltar Strait show low strength and are subjected to high initial effective stresses and pore pressures. Furthermore, their hydraulic conductivity is extremely low. They consist of a relatively soft matrix containing hard inclusions. All of this makes specimen preparation and triaxial testing very demanding. According to the test results the breccias behave like normally consolidated or slightly over-consolidated clays. The strength parameters of the breccias seem to depend on the depth. Their volumetric behaviour before failure is mainly contractant and the peak stress and volumetric strain remain approximately constant after reaching failure.

**Acknowledgement.** The authors are very glad to SECEGSA and SNED for permission of to publish the test results and for allowing the presentation of Figures 1 and 2. The authors also wish to express their gratitude to Mr. Roca and Mr. Sandoval from SECEGSA and Mr. Bensaid and Mr. Bahmad from SNED for their support for the research project.

## References

1. Pliego, J.M.: Open Session- The Gibraltar Strait tunnel. *Tunnelling and Underground Space Technology* 20(6), 558–569 (2005)
2. Steiger, R.P., Leung, P.K.: *Critical state shale mechanics* (1991)
3. Aristorenas, G.V.: Time-dependent behavior of tunnels excavated in shale. Ph.D. Thesis, Dept. of Civil and Environmental Engineering, Massachusetts Institute of Technology (1992)
4. Bellwald, P.: A contribution to the design of tunnels in argillaceous rock. Ph.D. Thesis, Dept. of Civil and Environmental Engineering, Massachusetts Institute of Technology (1992)
5. Bonini, M., Debernardi, D., Barla, M., Barla, G.: The Mechanical Behaviour of Clay Shales and Implications on the Design of Tunnels. *Rock Mechanics and Rock Engineering* 42(2), 361–388 (2009)
6. Barla, G., Barla, M., Debernardi, D.: New Triaxial Apparatus for Rocks. *Rock Mechanics and Rock Engineering* 43(2), 225–230 (2010)
7. Vogelhuber, M.: Der Einfluss des Porenwasserdrucks auf das mechanische Verhalten kakiritisierter Gesteine. Zurich, Dissertation ETH Nr. 17079, ETH Zürich (2007)
8. ISRM: Suggested methods for the quantitative description of discontinuities in rock masses. *Int. J. Rock Mech. Min. Sci. & Geomech.* 15, 319-368 (1977)
9. Head, K.: *Manual of soil laboratory testing, volume 2: Permeability, shear strength and compressibility tests*. Pentech Press, New York (1994)

10. Schofield, A., Wroth, P.: *Critical state soil mechanics*. McGraw-Hill, London (1968)
11. Luján, M., Crespo-Blanc, A., Comas, M.: Morphology and structure of the Camarinal Sill from high-resolution bathymetry: evidence of fault zones in the Gibraltar Strait. *Geo-Marine Letters* 31, 163–174 (2011)
12. Skempton, A.: The pore-pressure coefficients A and B. *Géotechnique* 4(4), 143–147 (1954)
13. Vallejo, L.G., Ferrer, M.: *Geological Engineering*. Taylor and Francis, London (2009)

# Estimation of Tri-axial Behaviour of Pilani Soil Using the Results of Direct Shear Test as a Function of Pore Water Content

K. Kumar

Department of Civil Engineering  
Birla Institute of Technology & Science  
Pilani, Rajasthan 333031  
kumarkamalesh10@gmail.com

**Summary.** Shear strength of soils have two distinct components, cohesive component and frictional component. Literature study has been made to study the origin of these components of shear strength based on interparticle interactions. Effect of pore water content onto its shear strength components have been discussed. Standard laboratory experiments are available to determine shear strength components of soil. Direct shear testing and triaxial testing are two such techniques. Triaxial testing better simulates field conditions. However, direct shear testing is more simple to perform. Based on literature study, details of direct shear testing and of triaxial testing has been provided in the study. Using the results of direct shear testing, triaxial behavior of local soil has been estimated as a function of pore water content. Locally available soils of sands and silty clayey type have been collected. Specific size particles from both soil types were taken. For this composition and at 5 different water content, shear strength parameters were determined by conducting direct shear testing. Using the results of direct shear testing, tri-axial testing behavior of soil (as a function of pore water content) for a particular confining stress of 0.03MPa has been determined. Practical significance of the results has also been discussed.

**Keywords:** shear strength, cohesion, friction, triaxial testing, pore water.

## 1 Introduction

Soil has variety of engineering properties which are of use in geotechnical engineering. Shear strength of soil is one such engineering property. It has two components: cohesive and frictional. Cohesion results due to chemical cementation between soil particles and friction arises due to actual mineral contact between soil particles (see [4]). They are determined in the laboratory by conducting standard experiments. Direct shear (simple to perform) and triaxial (better field simulating) are two such standard experimental techniques. From practical point of view use

of simpler experimental technique is always advisable. In direct shear testing, failure shear stresses on failure plane at varied normal stresses are determined and then failure envelope is obtained. In triaxial testing, failure axial stresses at different confining stresses are obtained and then failure envelope is determined. These two failure envelopes are same under similar drainage conditions for same soil. Cohesion and friction are determined from these failure envelopes. Two of the most important factors influencing soil shear strength are its particle size composition and pore water content in it (see [1]). Objective of present study is to understand triaxial behavior of local soil knowing the results of direct shear testing under varied pore water content in it.

## 2 Experimental Investigation

Locally available coarse grained and fine grained soil was used for experimental investigation (see [2]). Coarse grained soil retained on  $150\mu$  sieve (classified as sandy) and fine grained soil retained on  $75\mu$  sieve and on pan (classified as silty clay) was used in the study. The classification is based on the results of dispersion test (see [3]). Water used during experiments was ordinary tap water available in soil mechanics laboratory.

Figure 1 shows soil element under direct shear testing, as well as major & minor principal stresses ( $\sigma_1$  and  $\sigma_3$ ) at failure.  $\theta$  is angle between failure plane and major principal plane.  $\sigma$ - $\tau$  plot for direct shear testing to get cohesion ( $c$ ) and angle of internal friction ( $\phi$ ) has been shown in Fig. 2. It also shows Mohr circle for a particular  $\sigma_3$  and corresponding  $\sigma_1$  at failure which is obtained from triaxial testing.  $\sigma$  and  $\tau$  are failure normal & shear stresses on failure plane.

Five different water contents were used (0%, 6%, 10%, 15% & 20%) while doing direct shear testing. At each water content, sand retained on  $150\mu$  sieve was 50%, silty clay retained on  $75\mu$  sieve was 25% and silty clay retained on pan was 25% by weight. Variation in cohesion and angle of internal friction with pore water content is shown in Table 1.

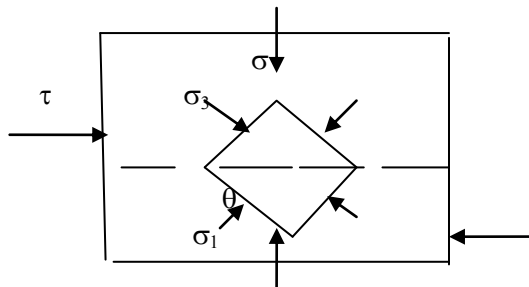


**Fig. 1.** Soil sample under direct shear testing

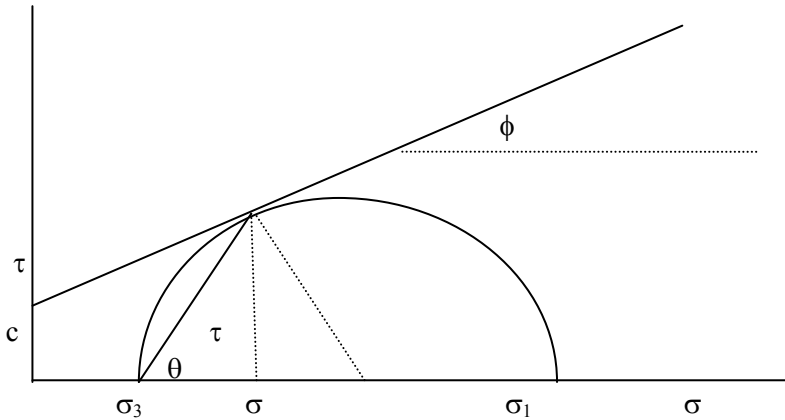


Fig. 2.  $\sigma$ - $\tau$  plot for direct shear testing

### 3 Estimation of Triaxial Behaviour

From Fig. 2, following relations are available (stresses are all total) (see [5]):

$$\theta = 45 + (\phi/2) \tag{1}$$

$$\sigma_1 = \sigma_3(\tan^2\theta) + 2(c)(\tan\theta) \tag{2}$$

$$\sigma = \sigma_1(\cos^2\theta) + \sigma_3(\sin^2\theta) \tag{3}$$

$$\tau = c + \sigma(\tan\phi) \tag{4}$$

During direct shear testing of study, pore water was free to dissipate. Results of study will be applicable for similar drainage condition in triaxial testing. Using Equations (1) to (4), soil behavior during triaxial testing has been calculated as a function of water content for  $\sigma_3 = 0.03$  MPa. Table 1 and Fig. 3 contain the summary of results.

Table 1. Estimation of triaxial behaviour as a function of water content

Pore water content (%)	Cohesion (MPa)	Angle of internal friction (deg)	$\theta$ (deg)	$\sigma_3$ (MPa)	$\sigma_1$ (MPa)	$\sigma$ (MPa)	$\tau$ (MPa)
0	.0062	35.92	62.96	.03	.1394	.0526	.0443
6	.009407	34.47	62.235	.03	.1439	.0547	.0469
10	.0094	36.98	63.49	.03	.1582	.0555	.0512
15	.009045	38.55	64.275	.03	.1667	.0557	.0534
20	.00493	28.92	59.46	.03	.1029	.0488	.0319

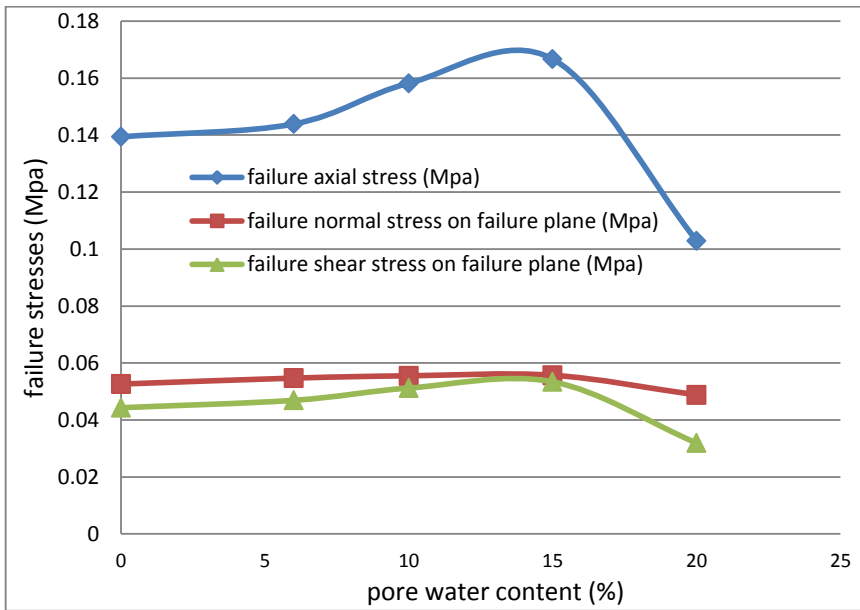


Fig. 3. Variation of failure stresses during triaxial testing

## 4 Conclusions

From Fig. 3, it can be concluded that for Pilani region soil at particle size composition reported in present study, at 15% water content soil will be able to withstand maximum vertical stress before failure if  $\sigma_3 = 0.03$  MPa. This value of  $\sigma_3$  corresponds to average bulk soil density of  $1.45 \text{ T/m}^3$  at a depth of 4.7m with average coefficient of at rest earth pressure value of 0.45. Hence, this amount of water content should be provided for best vertical load carrying capacity of soil. Similar kind of experimental analysis can be carried out for Pilani soil as well as from other region soils at required particle size composition and at required depth to get water content at which soil has maximum vertical load carrying capacity, because in a particular region average bulk density of soil is same.

## References

- [1] Bolton, M.D.: The Strength and Dilatency of Sands. *Geotechnique* 36(1), 65–78 (1986)
- [2] Gayatri, J.: Estimation of Tri-axial Behaviour of Pilani Soil using the Results of Direct Shear Test as a Function of Pore Water Content, Undergraduate Thesis, Birla Institute of Technology & Science, Pi-lani (2006)

- [3] Sehgal, S.B.: A Text Book of Soil Mechanics. CBS Publishers and Distributors, Delhi (1984)
- [4] Venkatapparao, G., Moondra, H.S.: Strength Behavior of Pilani Soil. Indian Geotechnical Journal 6(2), 122–127 (1976)
- [5] Venkatramaiah, C.: Geotechnical Engineering. New Age International Publishers Limited, New Delhi (1995)

# Discrete Element Investigation of the Asymptotic Behaviour of Granular Materials

D. Mašín

Faculty of Science, Charles University in Prague, Czech Republic  
[masin@natur.cuni.cz](mailto:masin@natur.cuni.cz)

**Abstract.** The concept of the asymptotic behaviour of particulate materials is described, including its enhancement considering asymptotic states in extension. A 3D discrete element model with permanent elastic spherical particles is set up. The numerical sample is stretched from different initial states, and the influence of the strain rate direction on the final state is studied. Asymptotic behaviour is clearly observed. The asymptotic stress ratio (including critical state friction angle) is observed not to be constant, but it is a variable depending on the stress level. Existence of extension asymptotic states is observed, and the notion of normal extension line is introduced.

## 1 Introduction

Asymptotic behaviour is one of the most striking features in the behaviour of granular materials. Specific asymptotic states have been known since the early days of soil mechanics. Casagrande [1] observed critical state behaviour of soils – a particular asymptotic state related to constant volume shearing. Schofield and Wroth [2] combined the existence of critical states and compression asymptotic states (revealed in normal compression behaviour) into a unified framework of critical state soil mechanics. More generally, Gudehus et al. [3] understood asymptotic states to be attractors in the behaviour of granular materials, which are independent of the initial state. They proposed that each direction of strain rate with a volume decrease is uniquely linked to a particular asymptotic stress ratio and a particular path in the mean stress vs. void ratio plane (normal compression line). More recently, Gudehus [3] and Gudehus and Mašín [4] have extended the asymptotic state concept into the volume increase (extension) regime.

In this contribution, we present a discrete element study aimed at understanding of the asymptotic behaviour of granular materials. Only the main outcomes of an extensive study are presented due to limited space; more details are given in Mašín [6].

## 2 Asymptotic State Framework

Asymptotic states are defined as that states reached after a sufficiently long proportional stretching, i.e. stretching with a constant direction of the strain rate. Conceptual representation of asymptotic states has been proposed by Gudehus [3] and Gudehus and Mašín [4]. In this work, we focus on axisymmetric stress and deformation states, where the strain rate tensor is fully characterised by axial  $\dot{\epsilon}_a$  and radial  $\dot{\epsilon}_r$  components. Similarly, the stress tensor is given by  $\sigma_a$  (axial stress) and  $\sigma_r$  (radial stress). The strain rate direction may be characterised by an angle  $\psi_{\dot{\epsilon}}$  (see Figure 1a), and the stress obliquity is quantified by the angle  $\psi_{\sigma}$  (Figure 1b).

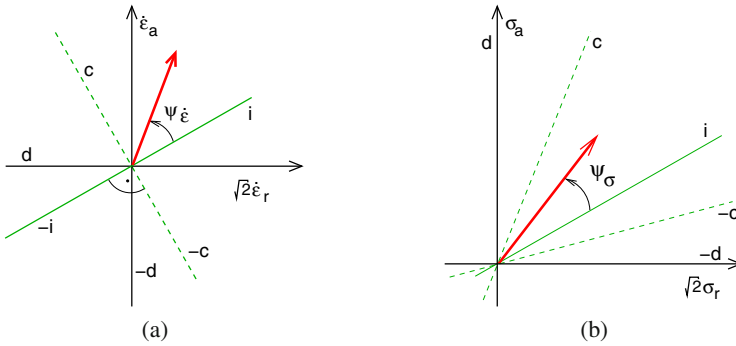


**Fig. 1.** Definition of angles  $\psi_{\dot{\epsilon}}$  and  $\psi_{\sigma}$  [4]. "i" denotes the isotropic direction, "c" denotes the isochoric (constant volume) direction, and "d" denotes the theoretical limit for asymptotic state behaviour

According to the current understanding of the asymptotic behaviour of a granular assembly, proportional deformation (constant  $\psi_{\dot{\epsilon}}$ ) will ultimately lead to an asymptotic state characterised by a constant  $\psi_{\sigma}$ . Each of the asymptotic states also has a unique trace in the mean stress  $p$  vs. void ratio  $e$  plane. Asymptotic states in this plane are traditionally denoted as normal compression lines. All normal compression lines are bound between isotropic normal compression line, attributed to  $\psi_{\dot{\epsilon}(i)}$ , and the critical state line, linked with  $\psi_{\dot{\epsilon}(\pm c)}$  (see Fig. 1 for definition of  $i$  and  $\pm c$  directions).

As suggested by Gudehus [3] (Chapters 2 and 3) and Gudehus and Mašín [4], asymptotic states can also be reached after proportional stretching along extension (volume increase) paths. The stretching directions that lead to extension asymptotic states are depicted in Figure 2. Limiting values of  $\psi_{\dot{\epsilon}}$  and  $\psi_{\sigma}$  are denoted with indices 'd' (asymptotic  $\sigma_r = 0$ ) and '-d' (asymptotic  $\sigma_a = 0$ ) [4]. Each extension asymptotic state is also associated with its trace in the mean stress vs. void ratio plane. In the following, we denote these traces as *normal extension lines* (adopting a parallel with the well-known notion of normal compression lines).

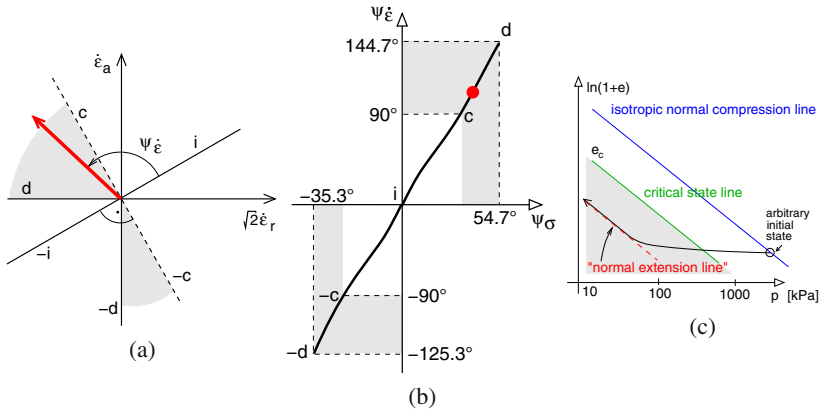


Fig. 2. Graphical representation of extension asymptotic states

### 3 Discrete Element Model of the Asymptotic Behaviour

In order to model the granular assembly, the open-source 3D discrete element software Yade [8] was used. This software utilises the DEM formulation given by Cundall and Strack [2]. We present the results for a specimen consisting of elastic spherical particles. In order to resemble a real granular material, particles of different sizes have been considered following the grain-size-distribution curve of a real sand. The sample consisted of 150000 spherical particles. The periodic cell was cubic, with the initial side length of 31 mm. The specimen in its initial state is depicted in Figure 3.

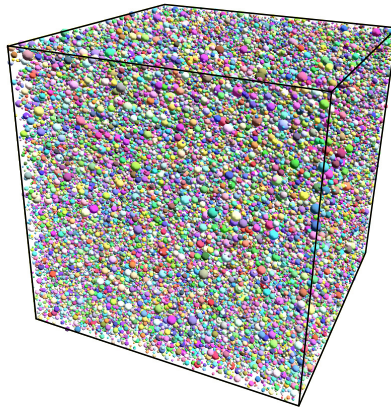
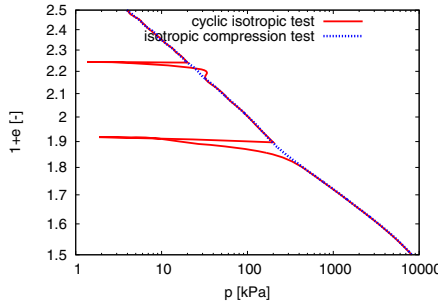


Fig. 3. Periodic cell used in the simulations, consisting of 150000 spherical particles

The contact properties of the spherical particles were governed by a linear elastic perfectly plastic model without cohesion [2], which specifies the contact normal stiffness  $k_n$ , shear stiffness  $k_s$  and friction angle  $\phi$ . These parameters are calculated from the particle properties  $E = 500$  MPa,  $\nu = 0.3$  and  $\phi = 0.5$  Rad. The prescribed particle density was  $\rho_s = 2650$  kg/m<sup>3</sup> and acceleration due to gravity was zero. The cell boundaries were periodic and they were subjected to a constant velocity gradient  $\nabla v$  (constant value of the Euler stretching tensor D). Axisymmetric conditions were applied, such that  $D_{22} = D_{33}$  (subscripts 2 and 3 represent the horizontal directions, 1 the vertical direction). The angle  $\psi_\varepsilon$  can then be calculated by means of Figure 1(a). Local non-viscous damping has been used, with a damping coefficient  $\chi = 0.5$ .

### 4 Modelling Results

Figure 4 shows results on a sample loaded uniformly along the path  $\psi_\varepsilon = 0^\circ$ , together with the results of a test where the loading direction was reversed several times to  $\psi_\varepsilon = 180^\circ$ . The uniformly loaded sample clearly defines an isotropic normal compression line, which is approximately linear in the  $\ln p$  vs.  $\ln(1 + e)$  plane. The sample with the unloading-reloading cycles shows that the isotropic normal is asymptotically approached irrespective of the initial soil density (apart from the minor "overshooting" in the first reloading cycle, which may be attributed to inertia effects). The normal compression behaviour is observed on an assembly of elastic (non-crushable) spheres; it is thus not related to grain crushing. Instead, grain crushing may be regarded as an eventual consequence of stress concentration during loading along the normal compression line.



**Fig. 4.** Monotonous and cyclic (unloading-reloading) isotropic test results ( $\psi_\varepsilon = 0^\circ$  in loading and  $\psi_\varepsilon = 180^\circ$  in unloading)

Secondly, we study the constant volume asymptotic state ( $\psi_\varepsilon = 90^\circ$ ). Figure 5 shows the results of constant volume experiments on normally consolidated (NC) and overconsolidated (OC) samples. These tests are known as undrained triaxial tests in soil mechanics terminology. The samples were first loaded along the  $\psi_\varepsilon = 0^\circ$  path up to the prescribed value of the mean stress. Then, the direction of loading was changed to  $\psi_\varepsilon = 90^\circ$  and the NC samples were sheared until the asymptotic state

was reached. The OC samples underwent  $\psi_\varepsilon = 180^\circ$  unloading before shearing. Figure 5 shows results of the numerical experiments. Although the final states appear to align along a single curve in the  $p$  vs.  $\psi_\sigma$  plane, this curve is interestingly not represented by a constant value of  $\psi_\sigma$ . This implies that the critical state friction angle is not a constant, but a variable dependent on the mean stress. The final states in the  $\ln(1 + e)$  vs.  $\ln p$  plane form a clearly defined critical state line. This line is approximately parallel to the isotropic normal compression line, apart from the larger stresses, where the results are influenced by the final compressibility of the grains and consequent non-negligible overlapping of particles. The asymptotic state is reached irrespective of the initial void ratio (NC and OC samples reach the same state finally).

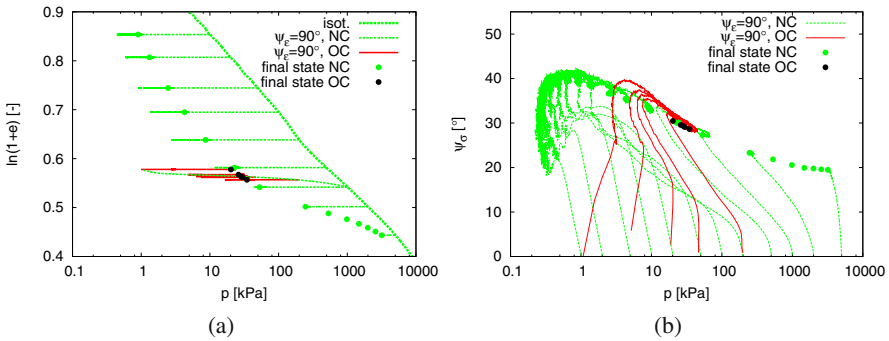


Fig. 5. Results of  $\psi_\varepsilon = 90^\circ$  tests on normally consolidated and overconsolidated samples

In the next set of simulations, we consider a shear test in which the stress path (rather than the strain path) direction is controlled. Namely, experiments with a constant  $\sigma_r$  (drained triaxial tests) have been simulated. The same stretching rate  $D_{11}$  as in the  $\psi_\varepsilon = 90^\circ$  tests was imposed, and  $D_{22} = D_{33}$  were controlled in such a way that  $\sigma_r$  remained constant. After sufficiently long shearing, the specimens reached a state with constant  $\sigma_a$  and constant  $e$ , therefore with constant  $\psi_\sigma$  and with  $\psi_\varepsilon = 90^\circ$  (see Figure 6). Tests on both normally consolidated and overconsolidated samples were considered. The asymptotic states reached by the NC and OC samples coincided for the given  $\sigma_r$  (Figure 6). The asymptotic states reached in constant  $\sigma_r$  tests coincided also with those from  $\psi_\varepsilon = 90^\circ$  tests.

Apart from the asymptotic states in compression, asymptotic behaviour of samples stretched in extension ( $\psi_\varepsilon > 90^\circ$ ) has been investigated. Figure 7 shows the  $\ln(1 + e)$  vs.  $\ln p$  response of these samples. Irrespective of the initial compression stress, all the samples reached well defined asymptotic states. These lines were proposed in Sec. 2 as "normal extension lines". Although they have probably not been observed in experiments yet, they were theoretically predicted and in this study they were confirmed using discrete element simulations.

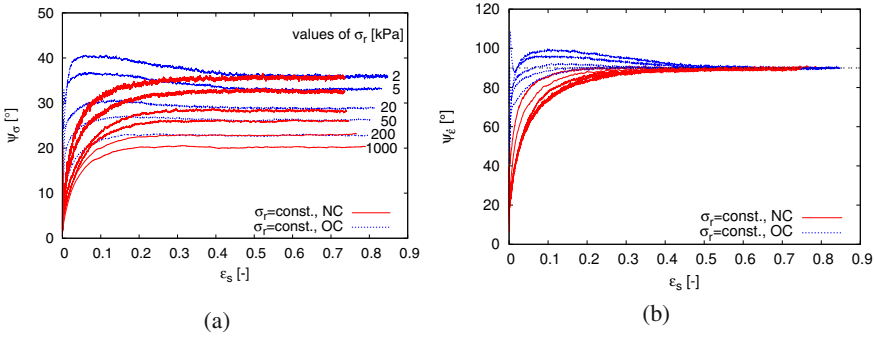


Fig. 6. Results of constant  $\sigma_r$  tests on normally consolidated and overconsolidated samples

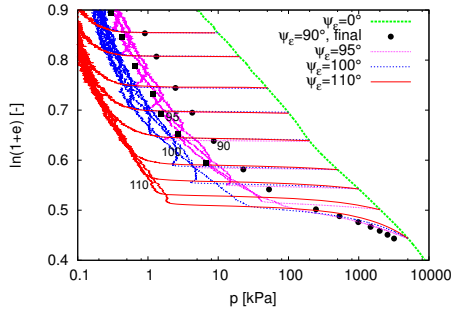
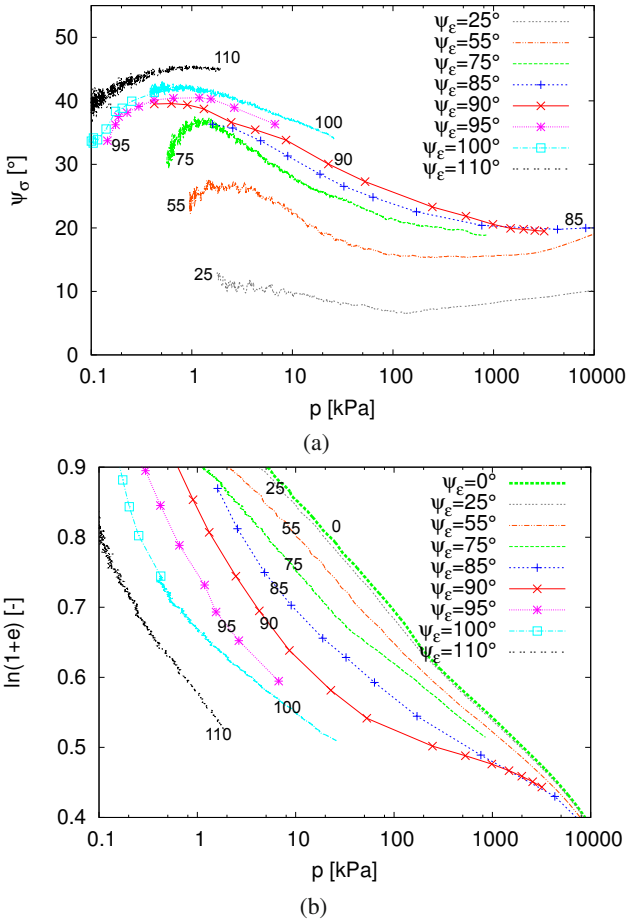


Fig. 7. Extension asymptotic states with  $\psi_\epsilon \geq 90^\circ$  plotted in the  $\ln(1+e)$  vs.  $\log p$  plane, demonstrating existence of the so-called normal extension lines

Figure 8 attempts to summarise the asymptotic states obtained in the described discrete element simulations for various angles of  $\psi_\epsilon$ . Several properties of the observed asymptotic states agree with the concept described in Sec. 2. There are, however, also clear deviations from this concept. As expected, increasing  $\psi_\epsilon$  leads to an increase of the asymptotic stress ratio  $\psi_\sigma$ . Contrary to the theory, however, the asymptotic  $\psi_\sigma$  is for the given  $\psi_\epsilon$  not constant, but it depends on the mean stress level (Fig. 8(a)). Asymptotic states were uniquely defined also in the volumetric plane  $\ln(1+e)$  vs.  $\ln p$ . They are denoted as normal compression lines, critical state line and normal extension lines. The maximum angle of  $\psi_\epsilon$ , for which the asymptotic states could reasonably be studied, was  $\psi_\epsilon = 110^\circ$ . For higher angles, asymptotic state would have been reached at extremely low stresses (below 0.5 kPa), where the results were scattered and unreliable. We thus could not confirm the existence of the limit state denoted as  $\pm d$  in Figure 2(a).



**Fig. 8.** Asymptotic states of an assembly of spherical particles, summary of the DEM simulations

### 5 Conclusions

In the paper, we presented an investigation of the asymptotic properties of granular assemblies. The concept was first introduced, following description of an extensive DEM study. Although the particles were elastic (non-crushable), the asymptotic behaviour was clearly observed. Asymptotic behaviour thus appeared to be an inherent property of the granular assembly, caused primarily by particle rearrangement. The simulations indicated the existence of extension asymptotic states and normal extension lines. Some deviations from the current state-of-the-art were observed: In particular, the asymptotic value of  $\psi_\sigma$  for the given  $\psi_\epsilon$  was not constant, but depended on the mean stress.

**Acknowledgements.** Financial support by the research grants GACR P105/12/1705 and TACR TA01031840 is greatly appreciated.

## References

- [1] Casagrande, A.: Characteristics of cohesionless soils affecting the stability of slopes and earth fills. *Journal of the Boston Society of Civil Engineers*, 257–276 (January 1936)
- [2] Cundall, P.A., Strack, O.D.L.: A discrete numerical model for granular assemblies. *Géotechnique* 29(1), 47–65 (1979)
- [3] Gudehus, G.: *Physical Soil Mechanics*. Springer, Berlin (2011)
- [4] Gudehus, G., Mašín, D.: Graphical representation of constitutive equations. *Géotechnique* 59(2), 147–151 (2009)
- [5] Gudehus, G., Goldscheider, M., Winter, H.: Mechanical properties of sand and clay and numerical intergration methods: some sources of errors and bounds of accuracy. In: Gudehus, G. (ed.) *Finite Elements in Geomechanics*, pp. 121–150. Wiley, Chichester (1977)
- [6] Mašín, D.: Asymptotic behaviour of granular materials. *Granular Matter* (submitted, 2012)
- [7] Schofield, A.N., Wroth, C.P.: *Critical State Soil Mechanics*. McGraw-Hill, London (1968)
- [8] Šmilauer, V., Catalano, E., Chareyre, B., Dorofenko, S., Duriez, J., Gladky, A., Kozicki, J., Modenese, C., Scholtès, L., Sibille, L., Stránský, J., Thoeni, K.: *Yade Documentation*. The Yade Project, 1st edn. (2010), <http://yade-dem.org/doc/>

# Mechanical Behavior of Granular Particles with Different Angularities

M.M. Mollanouri.Sh and Ali Aaghar Mirghasemi\*

School of Civil Engineering, College of Engineering, University of Tehran, Tehran, Iran  
aghasemi@ut.ac.ir

Recent studies show that particle shape and angularity has considerable influence on the mechanical behavior of granular materials. In order to numerical investigation of the particle shape on mechanical behavior of granular particles, a program that is based on Discrete Element Method (DEM) has been developed to model semi-real shape of grains. In this way, the real shape of grain is modeled by combining arbitrary number of overlapping spheres, which are connected to each other in a rigid way. To evaluate the influence of angularity on mechanical behavior of sand two assemblies of sands with different angularities containing rounded grains and high angular grains are considered, and several triaxial tests with different confining pressure and friction coefficient are performed on assemblies. The results demonstrate that the angularity of grains is considerably affecting the behavior of soil.

## 1 Introduction

Recent studies show that particle's shape and angularity have considerable influence on the mechanical behavior of granular materials such as sands [1-4] conducted a comprehensive numerical study on the influence of particle shape and angularity on engineering properties of granular materials. They carried out several biaxial tests on assemblies of different angularity with different confining pressure, friction coefficient, and void ratio. They concluded that under any specified confining pressure, shear strength (or mobilized friction angle), dilation and residual shear strength increase considerably with increasing angularity of grains. Their results showed that shape and angularity of particle have considerable influence on mechanical behavior of granular materials in two dimensions. Holubec and D'Appolonia [5] indicated by testing on sands with varying particle shapes that granular materials with the same relative density could have different mechanical behavior due to angularity. They suggested that the variation of mechanical properties due to shape of particle could be of the same order of magnitude as the variation of properties due to changes in relative density, thus concluded that particle shape could be considered an index property to correlate the properties of granular materials.

Furthermore, Rothenburg and Bathurst [6] reported the results of numerical simulations of planar assemblies of elliptical particles. Packing simulations of the initial assembly showed that the coordination numbers of the generated assemblies increased with increasing eccentricity. Ting et al. [7] reported similar conclusion from isotropic compression and biaxial shear test simulations on assemblies of two-dimensional elliptical particles. Mirghasemi et al. [8] by numerical simulations of polygon-shaped particle assemblies concluded that particle angularity had an important effect on the compressibility and shear strength of the granular media.

In this study irregular shapes of grains are presented to utilize in DEM simulations in order to improve the results of simulation. In most cases of modeling that have been applied so far, grain form is generally considered elliptical, ellipsoidal, polygonal, etc., none of which, however, directly models any irregularly shaped grain, hence will not project the expected mechanical behavior, thus pointing to the need of direct modeling of grains with irregular shapes. Several numerical triaxial tests with different confining pressures and friction coefficients are conducted on the assemblies, and the internal friction angle and maximum volumetric strain are calculated and discussed.

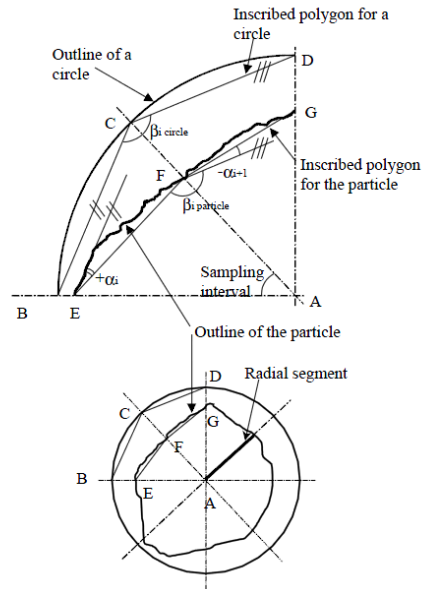
## **2 Particle Shape Consideration**

To investigate the influence of angularity and shape of particles on the mechanical behavior of granular materials, different assemblies with different size and shapes are modeled, and triaxial tests with different parameters are carried out. In the following sections, two categories of assemblies which are used in this research are illustrated. Also, indexes to describe quantitatively the angularity and shape of 3D particles are defined.

### ***2.1 Shape Descriptors in Three Dimensions***

In order to have a quantitative comparison between the shapes of two series of grains, two factors for every category of particles are considered. Three-dimensional descriptors commonly used to characterize shape of particles include the sphericity [9,10] and angularity index [11]. Sphericity, which shows the deviation of the particle from sphere, is the ratio of surface area of a sphere of the same volume as the shape, to actual surface area of the shape [9]. Krumbein [10] defined the sphericity as the ratio of particle volume to that of the smallest circumscribing sphere which is also applied in this paper. Another descriptor for 3D granular particles which shows the number and sharpness of the corners is Angularity Index, which was described by Rao et al. [11]; in this description, three 2D images from three views are captured by image analysis procedure. Then the angularity is calculated as a weighted average of all three views as follows:

**Fig. 1.** Calculation of particle angularity in 2D [12]



$$AI_{particle} = \frac{Ang_{front} \cdot Area_{front} + Ang_{top} \cdot Area_{top} + Ang_{side} \cdot Area_{side}}{Area_{front} + Area_{top} + Area_{side}} \tag{1}$$

Where,  $AI_{particle}$  is the Angularity Index of the particle; the unit for AI is degree. The angularity of a particle which was defined by Sukumaran and Ashmawy [12] is explained in equation 2 and the angle of  $\beta_i$  is demonstrated in Fig. 1.

$$Ang = \sum_{i=1}^N (\beta_{i\ particle} - 180)^2 - \sum_{i=1}^N (\beta_{i\ circle} - 180)^2 \tag{2}$$

The average number of spheres which is used for making a particle, range and average values of sphericity, and angularity index for two series of grains are summarized in Table 1.

**Table 1.** Values of Sphericity and Angularity Index for two series of assemblies

Particles group	Average number of spheres	Shape Description			
		Sphericity Range, %	Sphericity Average, %	Ang. Index Range, %	Ang. Index Average, %
High angular grains	10	88-93	90.2	32-41	37.4
Rounded grains	6	92-97	94.4	19-31	25.5

### 2.2 Granular Particles with Two Categories of Angularity

In this paper, two series of grains with different angularities are considered, including high angular grains and rounded grains. To have a reasonable comparison among assemblies, as shown in Fig. 2, each particle type has equal diameter with different angularities. Therefore, each type of particle in every group has the same diameter but its angularity index and sphericity is different.

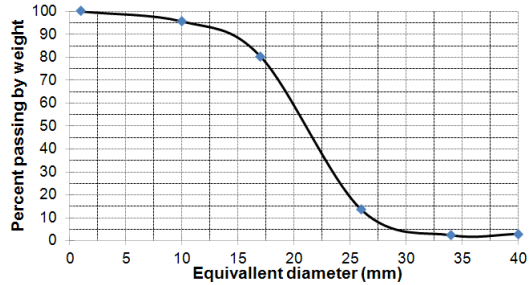
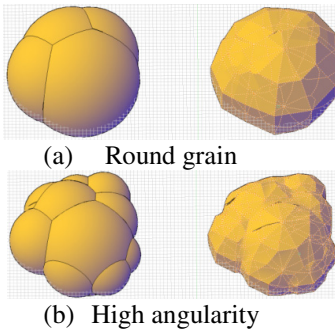


**Fig. 2.** Two different angularity particles, (a) round grain, (b) high angular grain **Fig. 3.** Grain size distribution

To simulate triaxial test numerically, a cubic assembly of particles was generated. In this study 1000 grains, consisting 5 different types with equivalent diameter ranging from 10 to 40 mm, were generated for each series of assembly. The grain size distribution of assemblies is shown in Fig. 3. In this figure, equivalent diameter is the diameter of the sphere which circumscribes each particle.

### 3 Simulated Tests

In order to consider the effects of different factors on mechanical behavior of granular particles, two series of tests were conducted on assemblies with different types of grains: (a) Tests with different confining pressures; (b) Tests with different inter particle friction coefficients. In a triaxial test, the mobilized internal friction angle of a cohesionless material can be determined by Equation (3) as a function of major principal stress:

$$\sin \phi_{mobilized} = \frac{\sigma_1 - \sigma_3}{\sigma_1 + \sigma_3} \tag{3}$$

Major Principal Stresses are determined on the basis of the average stress tensor within an assembly.

The stress tensor of an assembly can be calculated by Equation (4) expressed by Rothenburg [13]:

$$\sigma_{ij} = \frac{1}{V} \sum_c f_i^c l_j^c \quad , i, j = 1, 3 \tag{4}$$

In this equation  $\sigma_{ij}$  is stress tensor,  $V$  is the volume of the assembly,  $f_i^c$  is contact force, and  $l_j^c$  is contact vector between two sphere elements of two grains that are in contact with each other.

On the other hand, volumetric strain,  $\varepsilon_v$ , can be expressed as the ratio between volume of assembly at a specific strain,  $V$ , and the initial volume of assembly,  $V_0$ .  $\varepsilon_v$  can be defined as:

$$\varepsilon_v = \frac{V - V_0}{V_0} \quad (5)$$

### 3.1 Tests with Different Confining Pressures

The simulated tests were conducted in four stages. Initial assemblies are very loose; as it has been mentioned in the previous sections, the program generates particles with no contact. In stage two, in order to compact the initial loose assemblies, the generated assemblies are subjected to a hydrostatic strain rate equal to  $1.0 \times 10^{-7}$ . Compaction is continued until the assembly attains a desired confining pressure i.e. 0.15, 0.5, 1, 2, and 4 MPa. In stage three, zero strain rates in 10,000 cycles are applied in order to bring the particles of each assembly to equilibrium. Afterwards, the assembly of particles is prepared to apply final stage i.e. triaxial test. In the simulated triaxial test, the horizontal stress is maintained constant and the vertical stress is increased by applying deviator strain rate equal to  $0.5 \times 10^{-7}$ .

### 3.2 Tests with Different Friction Coefficients

Parameters used in these simulated tests are reported in Table 2, excluding the friction coefficient which is chosen variant. The first and the second stages of these tests are similar to what is described in section 5.2. In stage 3, assemblies are subjected to isotropic confining pressure equal to 1 MPa with various friction coefficients i.e. 0.1, 0.3, 0.5 and 0.7. Also, in the last stage, triaxial tests are simulated with different friction coefficients with the deviator strain rate of  $0.5 \times 10^{-7}$ .

## 4 Test Results

In order to have a comprehensive comparison, the results of simulated tests are demonstrated in two types of graphs. The first graph shows the sine of the mobilized friction angle ( $\sin\phi_{\text{mobilized}}$ ) versus axial strain ( $\varepsilon_a$ ), and volumetric strain ( $\varepsilon_v$ ) versus axial strain ( $\varepsilon_a$ ) is demonstrated in the second graph.

### 4.1 Results of Tests with Different Confining Pressures

Porosity can be defined as follows:

$$Porosity = \frac{V_{total} - V_s}{V_{total}} \tag{6}$$

Where,  $V_{total}$  is the volume of cubic cell and  $V_s$  is the volume of particles in a cubic cell.

The results of triaxial tests for assemblies with round grains in different confining pressures, as a sample, are shown in Fig. 4. Fig. 5 shows the comparisons among results of triaxial tests for two series of assemblies with the confining pressure of 2 MPa. Variations of mobilized friction angle and volumetric strain rate at the axial strain of 20% with different confining pressures for high angular grains are shown in Fig. 6.

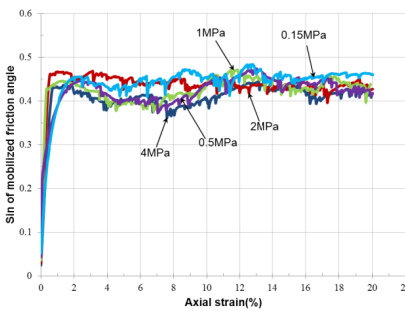


**Fig. 4.**  $\sin\phi_{mobilized}$  versus  $\epsilon_a$  for round grains in different confining pressures and  $\mu = 0.5$

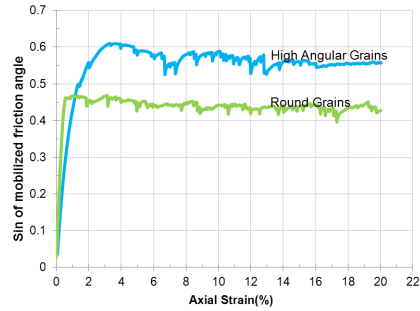


**Fig. 5.**  $\sin\phi_{mobilized}$  versus  $\epsilon_a$  for two series of assemblies in  $\sigma_3 = 2.0 MPa$  and  $\mu = 0.5$

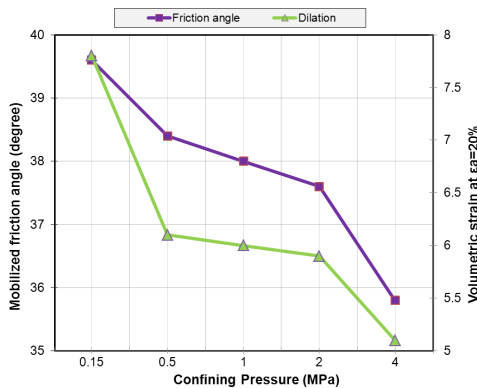


**Fig. 6.** Mobilized fiction angle and dilation in different confining pressure for high angular grains

The following results can be derived from above outputs:

- As shown in Fig. 4 for high angular grains, the mobilized friction angle and dilation decrease while confining pressure increases; similar trends were observed for other assemblies. Fig. 6 shows this trend more obviously for both parameters in different confining pressures. The reason for reduction in both mobilized friction angle and dilation at higher confining pressures is that the higher confining pressures on the assemblies prevent dilation; therefore, it doesn't allow particles to move against each other to produce anisotropy. Less anisotropy in the assembly provides less mobilized friction angle (Rothenburg and Bathurst (1992)).
- As shown in Fig. 5, the mobilized friction angle and maximum volumetric strain increase by increasing angularity. This trend is attributed to the interlocking among particles in higher angularities. In grains with high angularity, a significant interlocking among grains exists which leads to higher shear resistance and dilation of the assembly during triaxial test.

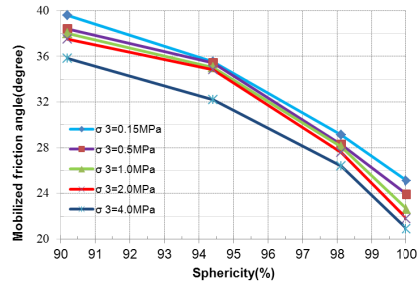
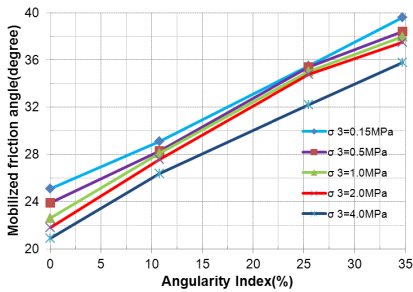


**Fig. 7.** Mobilized friction angle versus angularity index in different confining pressure

**Fig. 8.** Mobilized friction angle versus sphericity in different confining pressure

- Figures. 7 and 8 show that by increasing angularity index and decreasing sphericity, the mobilized friction angle increases. These figures also demonstrate that mobilized friction angle decreases by increasing confining pressure. This reduction is more apparent in higher confining pressures, especially for the confining pressure of 4MPa.

### 4.2 Results of Tests with Different Friction Coefficients

The results of triaxial tests for assemblies with rounded grains with different friction coefficients are shown in Fig. 9 and Fig. 10. The results for all cases are summarized in Tables 2 and 3. Fig. 11 shows the variations of mobilized friction angle and volumetric strain for high angular grains in different friction coefficients.

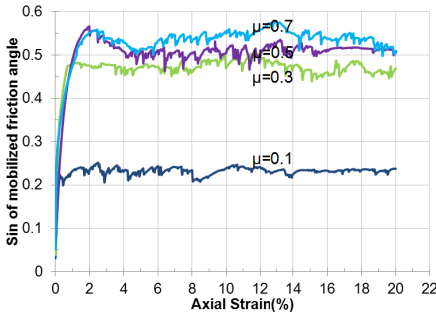


**Fig. 9.**  $\text{Sin}\phi_{\text{mobilized}}$  versus  $\mathcal{E}_a$  for rounded grains in different friction coefficients and  $\sigma_3 = 1.0\text{MPa}$

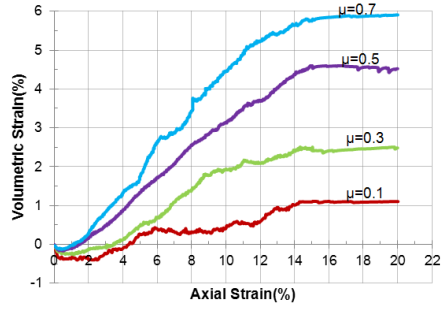


**Fig. 10.**  $\mathcal{E}_v$  versus  $\mathcal{E}_a$  for rounded angular grains in different friction coefficients and  $\sigma_3 = 1.0\text{MPa}$

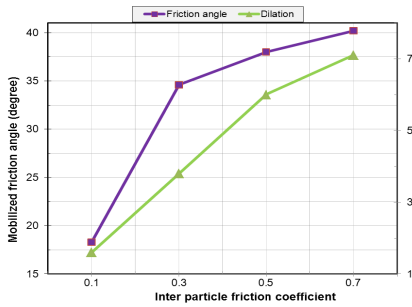


**Fig. 11.** Mobilized friction angle and dilation in different friction coefficient for high angular grains

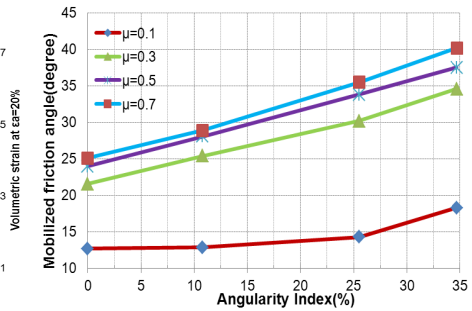


**Fig. 12.** Mobilized friction angle versus angularity index in different friction coefficient

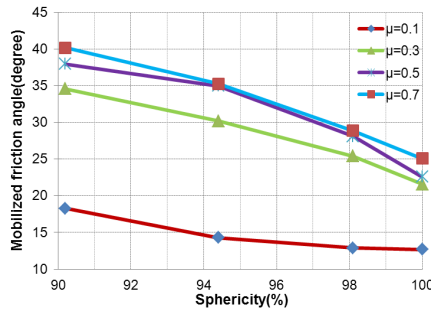


**Fig. 13.** Mobilized friction angle versus sphericity in different friction coefficient

**Table 2.**  $(\phi_{\text{mobilized}})_{\text{max}}$  values for three series of assemblies in different friction coefficients and  $\sigma_3 = 1.0\text{MPa}$

Friction coefficient ( $\mu$ )	Dilation value in $\epsilon_a=20\%$	
	High angular grains	Round grains
0.1	18.3°	12.9°
0.3	34.6°	25.4°
0.5	38.0°	28.1°
0.7	40.2°	28.9°

**Table 3.** Dilation values in  $\epsilon_a=20\%$  for three series of assemblies in different friction coefficients and  $\sigma_3 = 1.0\text{MPa}$

Friction coefficient ( $\mu$ )	Dilation value in $\epsilon_a=20\%$	
	High angular grains	Round grains
0.1	1.6%	0.9%
0.3	3.8%	1.9%
0.5	6.0%	2.9%
0.7	7.1%	4.1%

The following results are derived from the following figures and tables:

- By comparing the values of mobilized friction angle in different friction coefficients, it can be derived that the difference between friction angles decreases by increasing friction coefficients (Fig. 12 and Fig. 13). The main reason is that in granular particles which coefficient friction is less than 0.3, the mobilized friction angle and dilation are less in comparison to particles with higher friction coefficient.
- As shown in Fig. 12 and Fig. 13, by increasing friction angle, the roles of angularity and sphericity for increasing shear strength and dilation are more significant. It demonstrates that in higher friction coefficients, the interlocking between angular grains makes more powerful bonds. It can be concluded that in low friction coefficients, the influence of angularity is not significant, and the influence of angularity is more highlighted by increasing friction coefficient.

## 5 Conclusion

Two categories of grains with different angularities and sphericities consisting of 1000 particles were generated and several triaxial tests with different confining pressures and friction coefficients were performed. The results can be summarized as follows:

- Both mobilized friction angle and dilation have a positive correlation with confining pressure in a constant angularity. This correlation is more highlighted in high angular grains.
- By increasing angularity in a specified confining pressure, mobilized friction angle and dilation increase significantly.
- Increasing angularity in higher friction coefficients is more effective to increase shear strength and dilation of granular particles.

## References

- [1] Roberts, T.A., Beddow, J.K.: Some effects of particle shape and size upon blinding during sieving. *Powder Technology* 2, 121–124 (1968/1969)
- [2] Aoki, R., Suzuki, M.: Effect of particle shape on the flow and packing properties of non-cohesive granular materials. *Powder Technology* 4, 102–104 (1971)
- [3] Liu, L.X., Litster, J.D.: The effect of particle shape on the spouting properties of non-spherical particles. *Powder Technology* 66, 59–67 (1991)
- [4] Abedi, S., Mirghasemi, A.A.: Particle shape consideration in numerical simulation of assemblies of irregularly shaped particles. *Journal of Particology, Particuology* 9(4), 387–397 (2011)
- [5] Holubec, I., D'Appolonia, E.: Effect of particle shape on the engineering properties of granular soils. In: *Proceedings Symposium on Evaluation of Relative Density* 473 Los Angeles, pp. 304–318. American Society for Testing and Materials, ASTM STP 523, Philadelphia (1973)
- [6] Rothenburg, L., Bathurst, R.J.: Micromechanical features of granular assemblies with planner elliptical particles. *Géotechnique* 42(1), 79–95 (1992)
- [7] Ting, J., Khawaja, M., Meachum, L., Rowell, J.: An ellipse-based discrete element model for granular materials. *International Journal for Numerical and Analytical Methods in Geomechanics* 17, 603–623 (1993)
- [8] Mirghasemi, A.A., Rothenburg, L., Matyas, E.L.: Influence of Particle Shape on Engineering Properties of Assemblies of Two-Dimensional Polygon-Shaped Particles. *Géotechnique* 52(3), 209–217 (2002)
- [9] Wadell, H.: Volume, shape, and roundness of rock particles. *J. Geol.* 40, 443–451 (1932)
- [10] Krumbein, W.C.: Measurement and geological significance of shape and roundness of sedimentary particles. *J. Sedimentary Petrol.* 11, 64–72 (1941)
- [11] Rao, C., Tutumluer, E., Kim, I.T.: Quantification of coarse aggregate angularity based on image analysis. *Transportation Research Record*, 1787, Transportation Research Board, National Research Council, Washington DC (2002)
- [12] Sukumaran, B., Ashmawy, A.K.: Quantitative characterization of the geometry of discrete particles. *Geotechnique* 51(7), 619–627 (2001)
- [13] Rothenburg, L.: *Micromechanics of idealized granular system*, PhD dissertation. Carleton University, Ottawa, Ontario, Canada (1980)

# Numerical Simulation of Direct Shear Test Using Elliptical Particles

Morteza Naeij and Ali Aaghar Mirghasemi

School of Civil Engineering, College of Engineering, University of Tehran, Tehran, Iran  
morteza.naeij@gmail.com, aghasemi@ut.ac.ir

**Abstract.** This paper describes the results of numerical simulation of 2D assemblies of elliptical-shaped particles in direct shear test using discrete element method (DEM). The effects of vertical stress, eccentricity and aggregation on the macro behavior of granular materials in direct shear test are investigated. Assemblies of approximately 750 elliptical-shaped particles in random order represent soil specimens. DEM specimens are prepared at four vertical stresses (1, 2, 3 and 5 Kg/cm<sup>2</sup>), six eccentricities (.01, .05, .1, .15, .2 and .25) and three aggregations.

The results indicate that by increasing the vertical stress, volumetric strain and pick friction angle decrease. In addition, simulation results show that by increasing the eccentricity of particles in an assembly, vertical strain, mobilized angle at pick state and packing friction increase due to reaching their maximum value and then decrease. Furthermore, for well-graded assemblies with larger particles, maximum value of friction angle and strength were earned.

**Keywords:** direct shear test, discrete element method, granular soils.

## 1 Introduction

The conventional direct shear box is widely used in geotechnical testing laboratories around the world. This apparatus is used to find the peak and critical state shear strength parameters and dilation characteristics of granular materials. The discrete element method, which simulates the individual dynamics of all particles by numerically integrating their acceleration resulted from all the contact forces, would be an ideal one to obtain stresses and strains or their rates in a granular media while exposing to an external stress.

Discrete element method was introduced by Cundall (1974) and is one of the most popular methods to investigate the behavior of discrete materials and BALL program is the first program that modeled granular material including circular disks, and is written based on DEM (Strak & Cundall, 1978).

For reducing the time of calculation, discrete models use discs or sphere; although, these models do not involve the effect of particle shape on the mechanical behavior. Furthermore, models by disk or sphere particles have excessive freedom to rotate compared with real soils and therefore these assemblies have strength characteristics that are different from real materials.

Adopted ELLIPSE program (Rothenburg & Bathurst 1989) used to investigate the effect of vertical stress, eccentricity and aggregation on the macro behavior of elliptical shaped particles. It was founded that increasing the eccentricity of particles in an assembly lead to an increase in vertical strain, mobilized angle at pick state and packing friction until reaching their peak value and then decrease. However, there are not a linear correlation between these parameters and eccentricity because in greater eccentricity these parameters decreased. In addition, maximum value of friction angle and strength were obtained for well-graded assemblies with larger particles.

## 2 Numerical Simulations

The ELLIPSE program was modified in order to model the direct shear test. For this purpose, the shape of assembly boundary was changed from circular to rectangular, employing six elliptical particles that have great radius and high eccentricity (Fig. 1). The dimensions of simulated shear boxes were determined according to ASTM-D3080 and similar to experimental tests. Each assembly consists of approximately 750 two-dimensional elliptical particles all randomly placed (without any overlap) within the area between six boundary particles. It should be mentioned that in these assemblies the affect of gravity is not considered. The numerical simulations were carried out in four stages. In the first stage, the generated loose assembly was compacted to obtain a dense sample by setting the friction ratio equal to zero. In this stage, a constant compression strain was applied on all boundary particles. These particles move to center of assembly by constant strain rate, and velocity for all particles belonging to the domain is zero.

In the second stage, relaxation was applied to compacted assembly in order to obtain a balanced state in assembly.

Vertical stress was applied on the assembly in the next stage. Top boundary particle moves down when the vertical stress in assembly is lower than defined stress by user.

Finally, the assembly was sheared in the direct shear box model under constant vertical stress. Shear load was applied with a constant rate of strain by moving laterally the upper half of the boundary particles to left side. The normal stress ( $\sigma_n$ ) which was imposed to assembly kept constant during the tests. In two last stages, inter-particle friction coefficient was set to 0.5.

In all stages, the average stress tensor (Rothenburg & Selvadurai 1981) acting on a granular assembly can be computed using equation (3):

$$\sigma_{ij} = \frac{1}{V} \sum_{k=1}^{N_c} f_i^k l_j^k \quad i, j = 1, 2, 3 \quad (3)$$

where  $f_i^k$  is the  $i^{th}$  component of the contact force acting at  $k^{th}$  contact point between two particles;  $l_j^k$  is the  $j^{th}$  component of the branch vector connecting the centroids of two particles forming the  $k^{th}$  contact point (Fig. 2); and  $N_c$  is the total number of contacts, in the volume  $V$  for three dimensional simulation or in the area  $A$  for two dimensional.

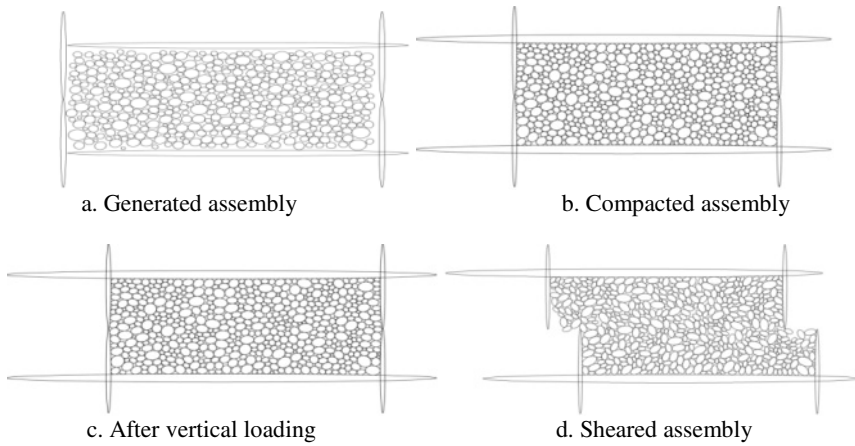


Fig. 1. Different stage of specimen preparing

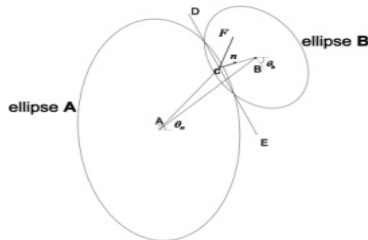


Fig. 2. Schematic view of  $k^{th}$  contact point between two ellipses

Table 1. Input parameters selected for numerical simulation

Properties	values used
Normal Stiffness(MN/mm)	1.75
Shear Stiffness(MN/mm)	1.75
Damping coefficients	4 and 0.01
Density of disks	2000
Friction coefficient	0.5

The parameters used in DEM simulations are listed in Table 1. Both mass and contact damping were used in the simulations to maintain conditions close to static equilibrium.

In order to investigate the effect of vertical stress, samples were sheared in four different vertical stresses 1, 2, 3 and 5 (Kg/cm<sup>2</sup>). Furthermore, the eccentricity for

elliptical-shape particles is set to 0.01, 0.05, 0.1, 0.15, 0.2 and 0.25. ELLIPSE program is not able to analyze samples with disk-shape particles (i.e. eccentricity=0), therefore, eccentricity of 0.01 was supposed to represent disk-shape particles.

To investigate the effect of aggregation on the direct shear test, three different sample grading was considered. Fig (3) illustrates the samples grading.

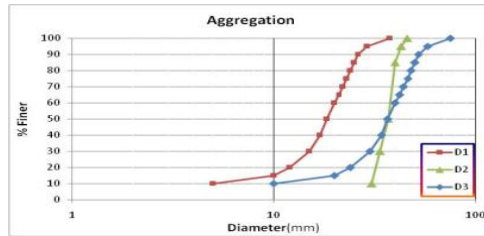


**Fig. 3.** The selected sample grading

In Fig (3), aggregation D1 and D3 are parallel to each other, both composed of 15 types of particles (i.e. 15 different Radius) and differ from each other only in grain size. According to the aggregation curves, these two curves are well graded. Aggregation D2 is uniform and it consisted of six types of particles. Aggregation D3 and aggregation D2 are equal to the amount of  $D_{50}$ .

Before explaining the results, it is needed to describe the naming method of each test (e.g. e10-s1-D1). In all of the names used in this article, e represents the eccentricity of particles and the number after, is eccentricity multiplied by 100. Letter s represents the vertical stress on the assembly and the number after that shows the value of this quantity ( $\text{Kg}/\text{cm}^2$ ). D indicates the experiment aggregation and its number.

### 3 Results and Discussion

#### 3.1 Samples Behavior under Different Vertical Stresses

From Fig (4) it can be deduced that increasing the vertical stress in samples with constant eccentricity and similar aggregation, results in volumetric strain decrease. It can be seen that the maximum vertical strain belongs to sample with  $1 \text{ Kg}/\text{cm}^2$  vertical stress and the minimum to sample with  $5 \text{ Kg}/\text{cm}^2$ . In addition, if horizontal strain exceeds ten percent, volumetric strain rate is approximately zero which indicates no more dilatation in the assembly. As vertical stress increase in a specimen, the slope of vertical-horizontal strain line becomes greater.

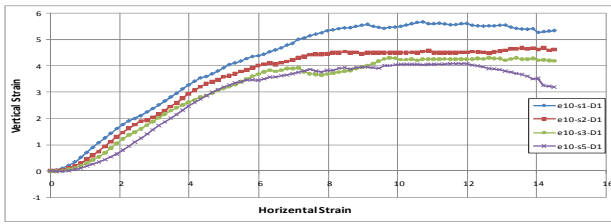


Fig. 4. Vertical Strain changes

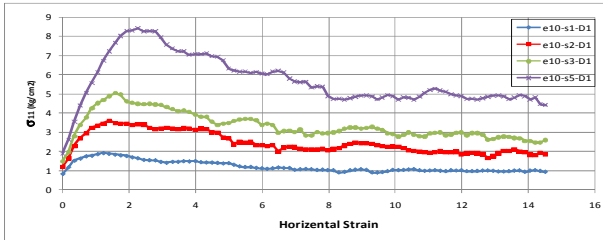


Fig. 5. Horizontal stress changes

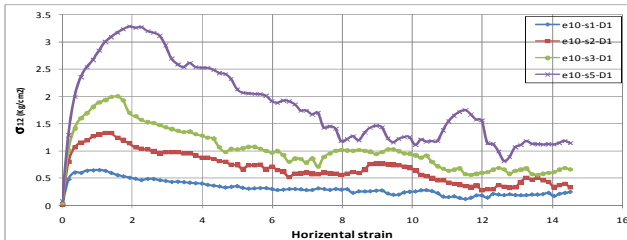


Fig. 6. Shear stress changes

Fig (5) shows that in strains more than ten percent,  $\sigma_{11}$  is approximately equal to  $\sigma_{22}$ . Therefore, it can be deduced that in strain ranges between ten to twelve percent, sample reaches its critical state. Thornton & Zhang (2003, 2007) have shown that horizontal stress at the peak state is greater than vertical stress. Therefore, at peak state, the principal stress angle with vertical axes is more than  $\pi/4$ . Furthermore, as shear strain increases, the horizontal and vertical stresses get close to each other. From Fig (6), it is obvious that as we increase the vertical stress in assemblies, peak mobilized friction angle will decrease. Moreover, maximum of mobilized friction angle with increasing vertical stress is obtained at higher strain.

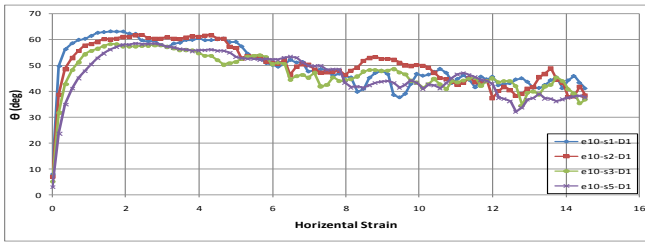


Fig. 7. Principal stress angle with the vertical axis

In Fig (7), principal stress angle changes with the vertical axis (direction of normal stress) are shown. Rotation of principal stress can be easily observed in this Fig. By increasing horizontal strain, principal stress direction starts to increase until reaching to it’s the entire time maximum angle with the vertical axis, and then starts to rotate to reach a critical state in which the angel hovers around  $\pi/4$ . In critical state the stresses  $\sigma_{11}$  and  $\sigma_{22}$  are approximately equal.

### 3.2 Samples Behavior under Different Eccentricity

In this paper due to program limitation, the shape of particle can be controlled just by the eccentricity of the elliptical particles, which can represent the angularity of grains. Figs (9) to (12) show the results of these test simulations.

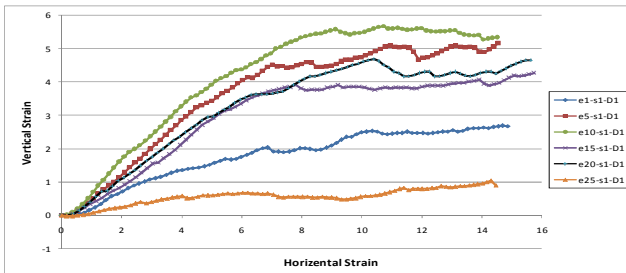


Fig. 9. Vertical Strain changes

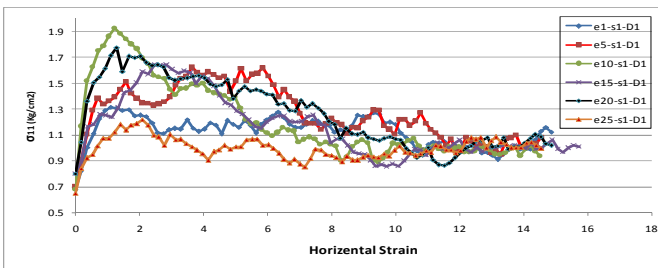


Fig. 10. Horizontal stress changes

It is necessary to explain that the trend of volumetric strain in granular assembly in geotechnical laboratory tests and their simulations are totally dependent on the porosity of the assembly. In this research, preparation of specimens is same for all tests as described before. Therefore, the different packing fractions in assemblies are result of different eccentricity. Packing fraction is the ratio of total particle's area to the total area of direct shear box and values that have been shown in Fig (12) are related to the third stage of simulations.

By considering Fig (9), it can be found that dilatation rate increases in specimens with increasing particles eccentricity. In other words, Fig (9) shows that samples volumetric strains increases with increasing particles eccentricity. However, there is an optimum value for eccentricity that volumetric strains reduce exceeding this optimal amount. Moreover, as it can be observed from Fig (9), if the eccentricity increases to a very large value, the dilatation rate and volumetric strain decrease.

Fig (10) shows that particles with very low eccentricity have less horizontal stresses and by increasing eccentricity of particle,  $\sigma_{11}$  will be increased. This trend continues until eccentricity 0.1 thereafter decreases and in eccentricity of 0.25, horizontal stress reaches to its minimum value.

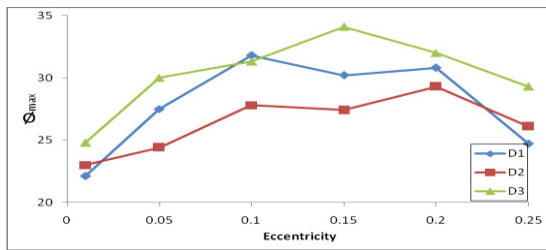


Fig. 11. Maximum mobilized friction angle for s1-D1

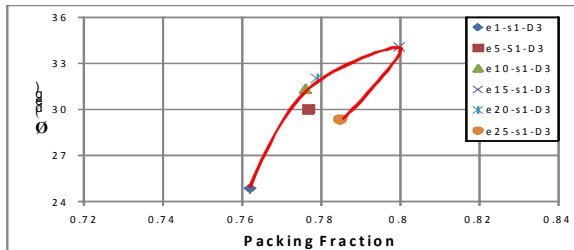


Fig. 12. Packing fraction changes

Peak friction angle in assembly with disk-shape particles is smaller than those of elliptical and polygonal-shape assemblies. It occurs because disk-shape particles have less rolling resistance. Fig (11) shows that assembly with eccentricity 0.1 to 0.2 have maximum peak friction angle and by contrast, assembly with eccentricity 0.01 has minimum peak friction angle in different eccentricity. Considering Fig (11) and

Fig (12), it's obvious that by increasing the eccentricity of specimens for s1-D3 samples, peak friction angle increases but there is an optimum value for this character. Disk-shape particles have minimum angle of internal friction angle and particles with eccentricity of 0.1, 0.15 and 0.2 have maximum internal friction angle in different aggregation. This is obviously the effect of particle shape on soil behavior and its macro parameters.

Fig (12) shows the peak friction angle versus packing fraction in samples s1-D3. In this Fig, the difference between the highest and lowest packing fraction is less than 0.04 and its amounts are almost in same range for most of samples. It can be seen that sample e15-s1-D3 with packing fraction of 0.8, has maximum peak friction angle and the minimum belongs to specimen e1-s1-D3 with packing fraction of 0.76. Furthermore, it's clear that sample e25-s1-D3 has low peak friction angle, whereas, it has higher packing fraction than samples with eccentricity 0.1, 0.15 and 0.2. These results are similar to Rothenburg & Bathurst (1993) for two-dimensional biaxial test and Ng (2005) for triaxial compression test. However, it is different from Yan (2009) where three-dimensional direct shear test formed by cluster shape particles. It is because the elliptical shape particles in Rothenburg & Bathurst (1993) and Ng (2005) always show a convex surface. However, cluster particles in Yan (2009) are formed by joining constitutive spherical balls, which may give more interlocking between particles during loading.

Fig (13) shows the amount of vertical stress versus particle eccentricities at 10% horizontal stress. It can clearly seen that the particle shape is affect the dilation in assembly. By comparing Fig (11) and (13), it can be observed that a very small change in particle eccentricity has large effect on behavior of soil assembly.

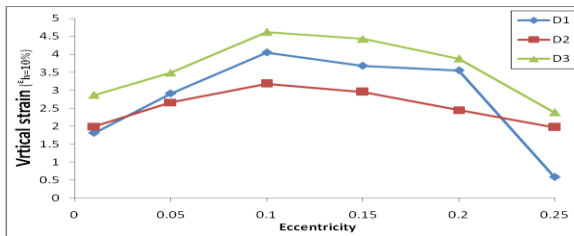


Fig. 13. Vertical strain at  $\epsilon_h=10\%$  for s5

### 3.3 Samples Behavior under Different Aggregation

Figs (14) to (16) show the vertical strain, horizontal stress, shear stress and mobilized friction angel versus horizontal strain for assemblies with different aggregations. The aspect ratio of direct shear box is determined based on ASTM; so it can be expected that the results in this section will be influenced by the aggregation curve and the particles diameter.

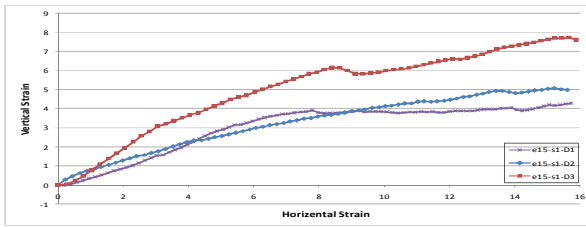


Fig. 14. Vertical Strain changes

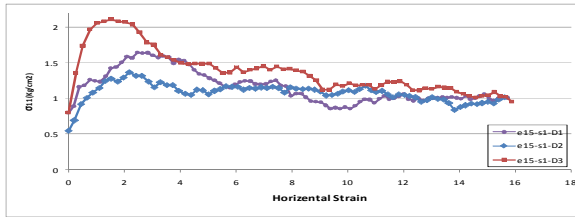


Fig. 15. Horizontal stress changes

Based on the Fig (3), aggregation D1 and D3 are parallel to each other and aggregation D3 has larger particle's diameter. Fig (14) shows that vertical strain increases in specimen with coarser particles. Aggregation D3 and D2 are equal in D50 but the former is well-graded and the other is uniform. Fig (14) shows that D3 have more dilatation behavior. In addition, comparing stresses obtained from three specimens it can be deduced that D3 has maximum horizontal and shear stress whereas D2 has minimum of them. Fig (16) shows that D3 has greater friction angle than two other aggregations during horizontal strain. This result agrees with Bagherzade-Khalkhali & Mirghasemi (2009) where their experimental result of direct shear test on granular assembly shows that with increasing particle diameter in parallel aggregation, friction angle in the particle assembly increases.

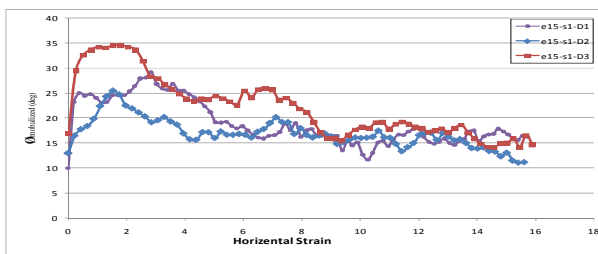


Fig. 16. Mobilized friction angel

## 4 Conclusions

The affect of vertical stress, eccentricity and aggregation on macro behavior of direct shear test is investigated by using numerical simulations based on DEM. Simulation results show that the internal friction angle and dilation in assemblies reduce with increasing the vertical stress.

Generally, the results show that particle eccentricity influences the mechanical behavior of the granular assemblies. The internal friction angle and the sample's dilation increase with growing the particle eccentricity, but there is an optimum value for eccentricity, which thereafter these feature reduced gradually. Similar trend is observed for packing fraction and stress tensor's characters. Optimized eccentricity is between 0.1 and 0.2.

In addition, results demonstrate that aggregation and particle size have important role on macro behavior of soils in direct shear test. Well-graded samples with greater particles show higher strength, peak friction angle and dilation.

## References

- Baghrzadeh-Khalkhali, A., Mirghasemi, A.A.: Numerical and Experimental direct Shear Tests for Coarse-Grained Soils. *Particuology* (7), 83–91 (2009)
- Cundall, P.A.: A Computer Model for Rock Mass Behavior using Interactive Graphics for the Input and output of Geometrical Data, Report Prepared under Contract Number DACW 45-74-c-006, for the Missouri River Division, U.S. Army Corps of Engineers, University of Minnesota (1974)
- Ng, T.T.: Behavior of gravity deposited granular material under different stress paths. *Can. Geotech. J.*, 1644–1655 (2005)
- Rothenburg, L., Bathurst, R.J.: Numerical Simulations of Idealized Granular Assemblies with plane Elliptical Particles. *Computer and Geotechnics* 11, 315–329 (1991)
- Rothenburg, L., Bathurst, R.J.: Influence of Particle Eccentricity on Micromechanical Behavior of Granular Materials. *Mechanics of Materials* (16), 141–152 (1993)
- Rothenburg, L., Selvadurai, A.P.S.: Amicromecanical Definition of the Cauchy Stress Tensor for Particulate Media. In: Selvadurai, A.P.S. (ed.) *Proceedings of the International Symposium on Mechanical Behavior of Structured Media, Part B*, Ottawa, pp. 469–486 (1981)
- Stark, O.D.L., Cundall, P.A.: A Discrete Numerical Mode For Granular Assemblies. *Geotechnique* 29(1), 47–65 (1978)
- Thornton, C., Zhang, L.: Numerical Examinations of Direct Shear Test. *Chem. Eng. Technol.* 26, 2 (2003)
- Yan, W.M.: Fabric Evolution in a Numerical Direct Shear test. *Computers and Geotechnics* (36), 597–603 (2009)
- Zhang, L., Thornton, C.: A Numerical Examination of Direct Shear Test. *Geotechnique* 57(4), 343–354 (2007)

# Study of Anisotropies Evolution in Direct Shear Test Using Discrete Element Method

Morteza Naeij and Ali Aaghar Mirghasemi

School of Civil Engineering, College of Engineering, University of Tehran, Tehran, Iran  
morteza.naeij@gmail.com, aghasemi@ut.ac.ir

**Abstract.** Two-dimensional numerical simulations were conducted by employing the discrete element method (DEM) to study the micromechanical behavior of elliptical-shaped assembly in the direct shear test. The ELLIPSE program (Rothenburg & Bathurst 1989) was adapted and the boundary of assembly was changed to rectangular in order to simulate the direct shear box. In this study, the trend of anisotropy changes and the difference between their principal directions during shear deformation is investigated and the relations between the micromechanics parameters and average stress tensor are argued. The results demonstrate that anisotropy coefficients of soil fabric, contact normal force and contact shear force increase and rotate considerably after shearing starts and reach to their maximum value at peak state. After peak, the shear strength decreases rapidly as the anisotropies of contact normal force and contact shear force. Furthermore, mobilized internal friction angle, which is obtained by assuming non-coaxiality between anisotropy directions, shows better fit with mobilized internal friction angle obtained from average stress tensor.

**Keywords:** direct shear test, discrete element method, anisotropy, fabric, micro-mechanics of soil.

## 1 Introduction

Granular materials are composed of discrete particles which interact only at contact points. Generally, sands and gravels can be behaved as granular media whose present a complex mechanical response when affected by an external force. By increasing the capability of computer techniques, numerical simulation becomes more popular than the above technique to investigate the micromechanical behaviors of granular media. Discrete element method was introduced by Cundall (1974) and is one of the most popular methods to recognize the behavior of discrete materials from a micromechanical point of view. Program BALL has been the first program that modeled granular materials including circular disks, and is written on the basis of DEM (Strak & Cundall, 1978). Various researchers have

been carried out to modify these discrepancies by using non-circular particles, e.g. elliptical-shaped particles (Rothenburg & Bathurst 1993) and polygon-shaped particles (Mirghasemi et al. 2002).

On the other hand for three decades, researchers tried to introduce a link between granular mechanics and continua form of discrete system (Bathurst & Rothenburg 1990, Rothenburg & Bathurst 1993, Ouadfel & Rothenburg 2001, Wang et al. 2007), which analytically connect micro and macro behavior of granular materials. Analytical developments are very useful to consider the effects of external stresses applied to assembly. Bathurst & Rothenburg (1990) introduced anisotropy parameters in discrete media for an assembly containing disk particles and with narrow size distribution by using Fourier series expression presented by Rothenburg (1980) and derived expressions for stress components  $\sigma_{11}$ ,  $\sigma_{22}$  and  $\sigma_{12}$  as functions of anisotropy parameters. Wang et al. (2007) supposed that in the direct shear test the major principal direction of anisotropies are not coincident. Therefore, they showed general expressions for stress components based on anisotropy parameters for disk-shape particles.

## 2 Numerical Simulations

The dimensions of simulated shear boxes determined from ASTM-D3080 and were similar to experimental tests. In addition, the assembly boundary control modes were modified to simulate the conditions of direct shear test. Each assembly consists of approximately 750 two-dimensional elliptical particles with each of them randomly placed within the area surrounded by predefined six boundary particles. The required boundary forces, displacements, or servo-controlled boundary conditions are applied on the boundary particles to simulate the test conditions in different stages.

In the first stage, the generated loose assembly was compacted to obtain a dense sample by setting the inter-particle friction equal to zero. In this stage, a constant compression strain was applied on all boundary particles causing these particles move to the center of assembly. Fig (1.A) shows compacted assembly. Relaxation was applied to compacted assembly to introduce balanced state in assembly in the second stage. (Fig 1.B).

In the third Stage, vertical stress was applied on the compacted assembly (Fig 1.C). Applied vertical stresses on the simulated assemblies were similar to the experimental test in laboratory.

Finally, the assembly was sheared in the direct shear box under constant vertical stress. As shown in Fig 1.D shear load is applied with a constant rate of strain by moving laterally the upper half of the boundary particle to the left side. The normal stress ( $\sigma_v$ ) which was imposed to assembly is kept constant during the test. The imposed shearing force increases from zero to the ultimate value at the failure. In two last stages, a friction coefficient of 0.5 was used.

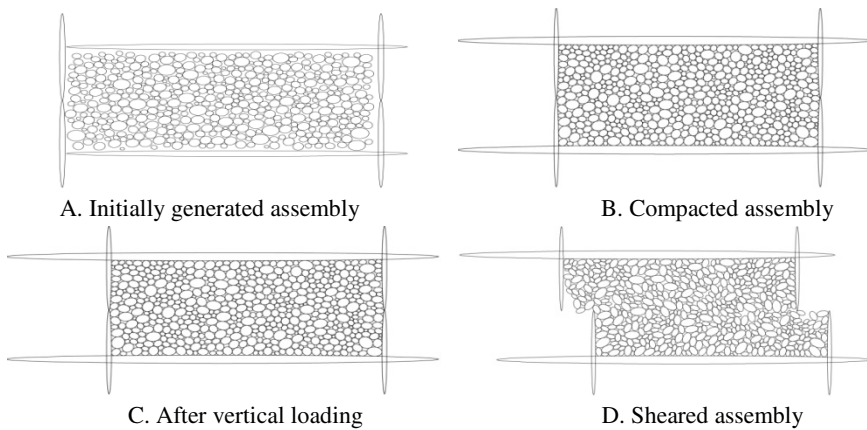


Fig. 1. Different stages of numerical simulation

### 3 Theoretical Backgrounds

The average stress tensor (Rothenburg 1980) which is acting in granular assembly can be computed according to:

$$\sigma_{ij} = \frac{1}{V} \sum_{k=1}^{N_c} f_i^k l_j^k \tag{1}$$

where the term  $V$  represents the volume of the system and it is equal to area of assembly in two dimensional simulation; term of  $f_i^k$  is the  $i^{th}$  component of contact force at the  $k^{th}$  contact point between the two particles;  $l_j^k$  is the  $k^{th}$  component of the branch vector connecting the center of two particles which contact at the  $k^{th}$  contact point (Fig 2) and  $N_c$  is the total number of contacts in the assembly.

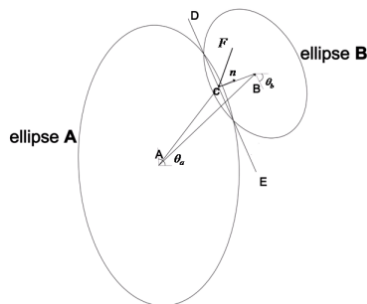


Fig. 2. Schematic view of a contact between two ellipse particles

Rothenburg and Selvadurai(1981) decomposed the average contact force at contact points, in granular system, into an average normal force and average shear force components:

$$f_i(\theta) = f_n(\theta)n_i + f_s(\theta)t_i \quad (2)$$

Satake (1978) introduced a distribution of contacts for a granular system by a three dimensional symmetric second-order fabric tensor. Components of the tensor can be computed on the basis of discrete data of granular system using:

$$F_{ij} = \frac{1}{V} \sum_{c \in V} n_i n_j \quad (3)$$

And Bthurst and Rothenburg (1990) introduced a distribution for an equivalent expression in infinite assemblies approximated equation (3):

$$F_{ij} = m_v \int_V E(\theta) n_i n_j d\theta \quad i, j = 1, 2, 3 \quad (4)$$

In equation (4), term  $E(\theta)$  inrepresents the contact normal distribution in an assembly. Bthurst and Rothenburg (1990) for contact normal force and contact shear force introduced similar distributions to describe the anisotropy of contact force components in a granular assembly. These anisotropy can be obtained either in a discrete way calculating contact normal and contact normal force and contact shear force data for the all particles, or replaced by certain distributions by computing the density distribution functions  $E(\theta)$ ,  $f_n(\theta)$  and  $f_s(\theta)$  for contact normal, contact force components and the equation (1) can be written as:

$$\sigma_{ij} = m_v l_0 \int_0^{2\pi} \{f_n(\theta) n_i n_j + f_s(\theta) n_i t_j\} E(\theta) d\theta \quad (5)$$

$l_0$  is the average contact vector length in assembly for circular or near-circular particles with a narrow size-distribution,  $m_v$  is the contact density,  $n = (\cos \theta, \sin \theta)$  is the unit contact normal vector and  $t$  is the vector perpendicular to  $n$ .

Rothenburg (1980) proposed Fourier expression series expression for density distribution functions as:

$$E(\theta) = \frac{1}{2\pi} \{1 + a \cos 2(\theta - \theta_a)\} \quad (6)$$

$$f_n(\theta) = f_0 \{1 + a_n \cos 2(\theta - \theta_n)\} \quad (7)$$

$$f_s(\theta) = f_0 \{a_w - a_s \sin 2(\theta - \theta_s)\} \quad (8)$$

Where  $f_0$  is the average normal force in assembly. The term  $a_w$  in equation (8) is negligible and Bathurst (1985) showed it for contact shear force in granular assembly as:

$$f_s(\theta) = f_0\{a_s \sin 2(\theta - \theta_s)\} \quad (9)$$

coefficients  $a$ ,  $a_n$  and  $a_s$  are invariant quantity describing second-order anisotropy in the distributions of contact normal, contact normal force and contact shear force. Terms  $\theta_a$ ,  $\theta_n$  and  $\theta_s$  represent principal direction of these anisotropies and also are the Eigen vectors of tensor of anisotropies. The terms  $a$ ,  $a_n$  and  $a_s$  are deviatoric invariant quantity of the contact normal, contact normal force and contact shear force tensors. By substituting Fourier expression of anisotropies into equation (5) and assuming the coaxiality between anisotropies directions and integrating, Bathurst and Rothenburg (1990) obtained the average stress tensor as:

$$\begin{aligned} \sigma_{11} &= P \left\{ 1 + \frac{aa_n}{2} + \frac{1}{2}(a + a_n + a_s) \cos(2\theta_a) \right\} \\ \sigma_{22} &= P \left\{ 1 + \frac{aa_n}{2} - \frac{1}{2}(a + a_n + a_s) \cos(2\theta_a) \right\} \\ \sigma_{12} = \sigma_{21} &= P \left\{ \frac{1}{2}(a + a_n + a_s) \sin(2\theta_a) \right\} \end{aligned} \quad (10)$$

For the direct shear test, Wang et al. (2007) assumed the non-coaxiality between anisotropy directions and derived a general expression. They supposed that  $\theta_a \neq \theta_n \neq \theta_s$  and integrated equation (5). They also generated their expression for narrow size distribution of disk-shape particle in two dimensional

$$\begin{aligned} \sigma_{11} &= p \left\{ 1 + \frac{a.a_n}{2} \cos 2(\theta_a - \theta_n) + \frac{1}{2}[a \cos(2\theta_a) + a_n \cos(2\theta_n) + \right. \\ &\quad \left. a_s \cos(2\theta_s)] - \frac{a.a_w}{2} \sin(2\theta_a) \right\} \\ \sigma_{22} &= p \left\{ 1 + \frac{a.a_n}{2} \cos 2(\theta_a - \theta_n) - \frac{1}{2}[a \cos(2\theta_a) + a_n \cos(2\theta_n) + \right. \\ &\quad \left. a_s \cos(2\theta_s)] + \frac{a.a_w}{2} \sin(2\theta_a) \right\} \\ \sigma_{12} = \sigma_{21} &= p \left\{ \frac{1}{2}[a \sin(2\theta_a) + a_n \sin(2\theta_n) + a_s \sin(2\theta_s)] + \frac{a.a_w}{2} \cos(2\theta_a) \right\} \end{aligned} \quad (11)$$

#### 4 Investigation of Micromechanics Behavior in Direct Shear Tests

Fig (3) shows the polar histogram of sample e10-s1 (In all of the names used in this article, e10 described the eccentricity of particles equal to .1 and after that, letter s represents the vertical stress on the assembly and the number after shows the value of this quantity (Kg/cm<sup>2</sup>)) at the initial stage of shearing, at the maximum friction angle and at the steady state ( $\varepsilon_h = 12\%$ ). It is necessary to mention that the Chinese line around the discrete data represents the Fourier expansion of these data and the angle as shown obtained from Fourier expansion of these data. By comparison between the polar histogram obtained from assembly and Fourier expansion of these distributions, a very good adaptation between these two graphs could be established.

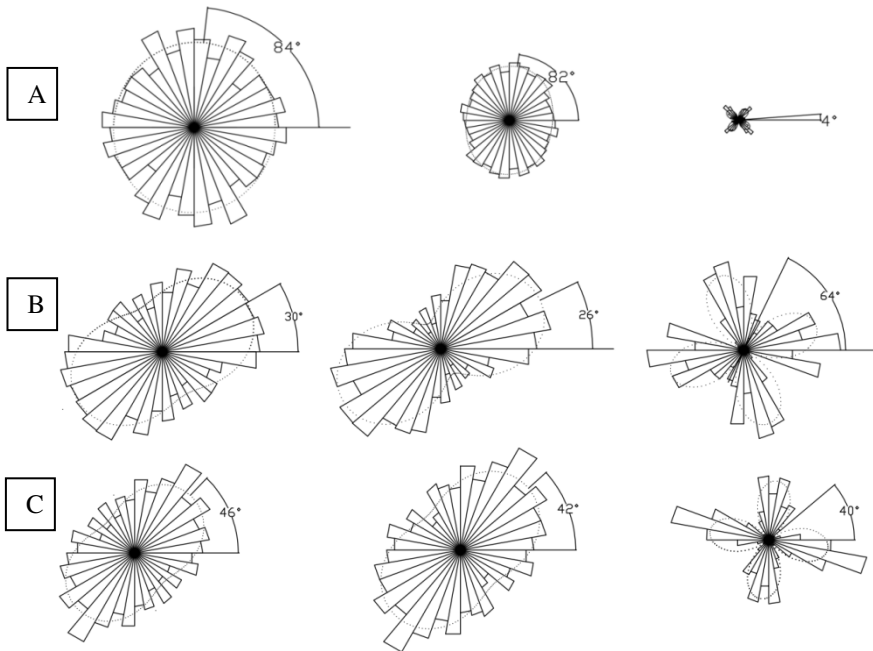


**Fig. 3.** Distribution of contact normal (left), contact normal force (middle) and contact shear force (right) and they Fourier expression in direct shear test: (A) at beginning, (B) at peak state and (C) at  $\varepsilon_h=12\%$ .

By considering Fig (3.A), it is found that at the beginning of shear the anisotropy of contact normal and contact normal forces are coaxial with vertical axes which is the major principal stress in assembly. In this stage the contact shear force anisotropy is very small and its direction with horizontal axes is near to zero. It is because the shear stress is very low.

One of the important results of Fig (3) is that discrete data for anisotropy parameters are similar to Bathurst & Rothenburg (1990) results for the biaxial test by using disk-shape particles and circular boundary. In this Figure the discrete data of different anisotropy are symmetric. Results from Wang et al. (2007) which used disk-shape particles in two-dimensional simulation show that the polar histograms of shear zone for all anisotropy are not totally symmetric. They supposed that in the direct shear test contrary to the Bathurst & Rothenburg (1990) simulated biaxial test, boundary particles movement are not symmetric and it may cause asymmetry in contacts between the particles of assembly and asymmetry in contacts between particles cause asymmetry in the contact forces between the particles. Therefore the histograms of anisotropy may affected by boundary condition. But it cannot be the real reason of this phenomenon because same as a normal contact vector for the first particle, there will be a reverse contact normal vector for the second particle in contact. Thus for each contact there will be two

contact normal vectors in opposite directions. With a short review on the literature it can be observed that in different simulation by using discrete element method for different tests (Ouaifel and Rothenburg 2001, Yang et al. 2008) all anisotropy histograms shown are symmetrical regardless of the type of test and their boundary motions. As mentioned in section (3), Rothenburg and Bathurst (1990) assumed that contact normal and contact normal force is symmetric and therefore the Fourier expansion of these anisotropies is cosine.

### 5 Anisotropy Changes during Sample Shearing

In Fig (4), it is illustrated that at the beginning of shearing stage, shear force is very small compared to axial force. Thus directions of most contact forces are vertical which is the direction of principal stresses. It is also shown that by increasing horizontal strain in assembly, the contact normal orientation with horizontal axes is decreased gradually and at the end of the simulation the change of anisotropy is decreased. In Fig (5), principal stress angle changes with the vertical axis (direction of normal stress) are shown. Rotation of principal stress can be easily observed in this Fig. By increasing horizontal strain, principal stress direction starts to increase until reaching to it's the entire time maximum angle with the vertical axis, and then starts to rotate to reach a critical state in which the angel hovers around  $\pi/4$ . As illustrated in Fig (4.A), at critical state the stresses  $\sigma_{11}$  and  $\sigma_{22}$  are approximately equal.

By considering Fig (6.A) it can be founded that contact normal anisotropy increases and reaches to its maximum value. After peak state, it begins to decrease gradually.

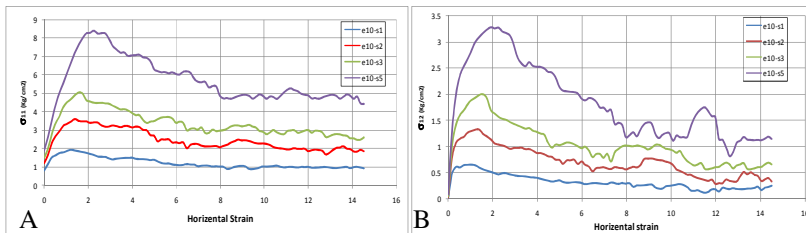


Fig. 4. Cauchy stress tensor changes versus horizontal strain: (A)  $\sigma_{11}$  , (B)  $\sigma_{12}$

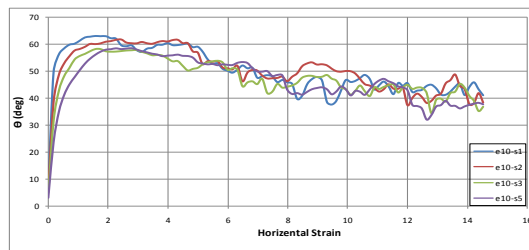
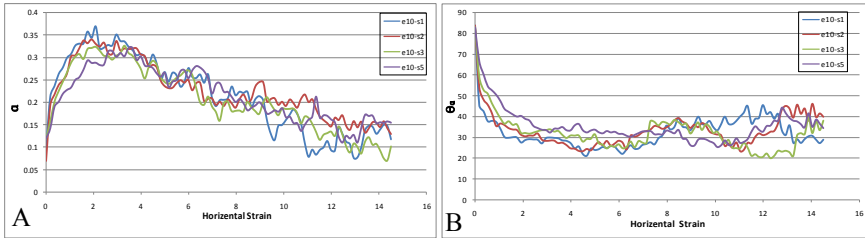
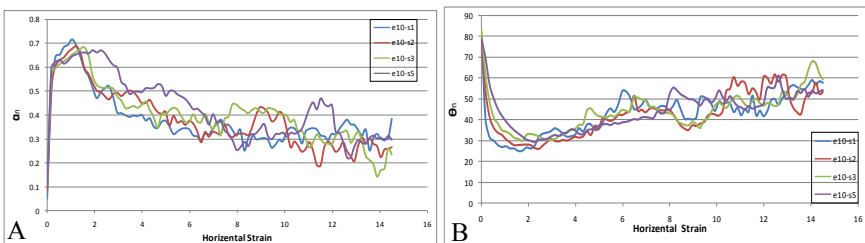


Fig. 5. Principal stress angle with the vertical axis versus horizontal strain

By considering Fig (7.A) it can be found that contact normal force anisotropy increases significantly after horizontal strain begins and reaches to its maximum value at the peak state. After peak state, it begins to decrease rapidly and in horizontal strain greater than 8% the variation is decreased.



**Fig. 6.** Evolution of contact normal anisotropy: (A) magnitude( $a$ ), (B) orientation ( $\theta_a$ )



**Fig. 7.** Evolution of contact normal force anisotropy: (A) magnitude( $a_n$ ), (B) orientation ( $\theta_n$ )

As illustrated in Fig (7.B), contact normal force orientation is near to vertical axes at the beginning of shear stage and by applying shear to assembly, it is decreased rapidly and reached to its minimum value with horizontal axes. By extending the horizontal strain, this orientation rotates rapidly. This Fig also shows that the rotation of contact normal force orientation in higher vertical stress is slower than the lower vertical stress.

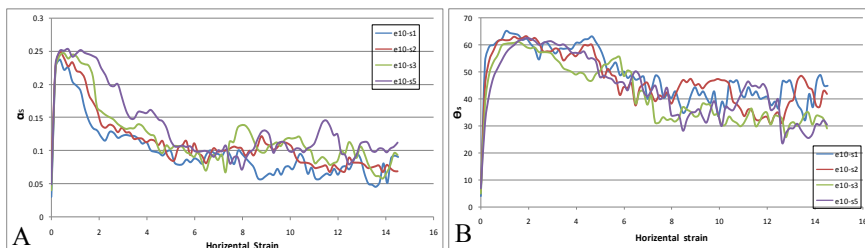


**Fig. 8.** Evolution of contact shear force anisotropy: (A) magnitude( $a_s$ ), (B) orientation ( $\theta_s$ )

Fig (8) shows the magnitude of contact shear force anisotropy and its orientation changes during shearing. At the beginning of this stage, the amount of contact shear force anisotropy is negligible, because no shear strain is applied to the assembly. As mentioned in Section 2 the particle friction ratio is not zero thus by employing vertical stress to the assembly, contact shear force between few particles develops.

### 6 Effect of Anisotropies Non-coaxiality on Mobilized Friction Angle

Fig (9) shows the mobilized friction angle in an assembly in the direct shear test. In this Fig, the mobilized friction angle is computed based on three different methods of average stress tensor (Equation (1), Bathurst and Rothenburg (1990) (Equation 10).which was derived based on only anisotropies magnitude and Wang et al. (2007) which was derived by assuming the non-coaxiality between anisotropies (Equation 11).

Bathurst and Rothenburg (1990) derived their relations for circular or nearly circular particles in narrow size. By considering Fig (9), it can clearly be said that in elliptical-shape assemblies and non-narrow particle size the Fourier expression is sufficiently accurate. The trend of these curves is similar to each other. But the coaxiality assumption between the anisotropies orientation results the higher mobilized friction angle in all simulations especially at peak value and the non-coaxiality shows lower at the peak value.

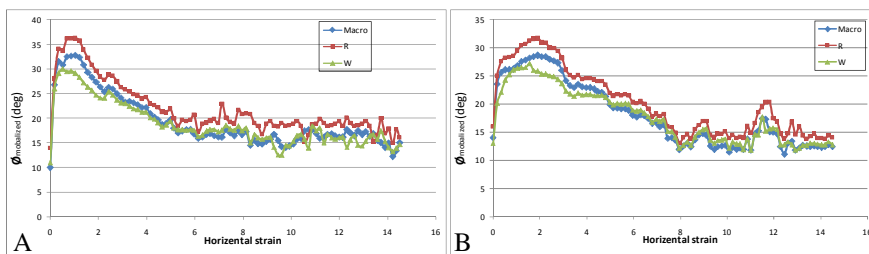


Fig. 9. Mobilized friction angle: (A) different mobilized angle in sample e10-s1, (B) different mobilized angle in sample e10-s5

### 7 Conclusions

In this study, ELLIPSE program (Rothenburg and Bathurst 1989) was modified to simulate the direct shear box. Then, by using this program the variation of anisotropy and their direction was investigated. Results showed that these anisotropy increases immediately when the shear strain is applied. Also, results indicated that the increasing rate of magnitude of anisotropy coefficients was not the same; contact shear force anisotropy was the most sensible and grew fast and contact normal

anisotropy was the less sensitive. The results demonstrated that the magnitudes of anisotropy are affected by the amount of vertical stress. For all anisotropy coefficients by increasing the vertical stress, their magnitudes decreased at the peak shear strength. Also, by increasing the vertical stress in assembly, magnitude of anisotropies reached to its maximum value at larger shear strain.

The principal stress direction as well as the directions of anisotropy rotate during direct shear test simulation. According to simulation results, the trend of variation of orientation of anisotropy is similar to that of principal stress direction.

By assuming the non-coaxiality between anisotropy directions, the mobilized friction angle was more close to mobilized angle which was obtained from average stress tensor. Also, the results demonstrated that proposed relation between mobilized angle which was obtained from average stress tensor and anisotropy parameters are in agreement for assembly of elliptical particles in wide range of particle radii.

## References

- Bathurst, R.J.: A Study of Stress and Anisotropy in Idealized Granular Assemblies, PhD. Dissertation, Queen's University at Kingston, Ontario, Canada (1985)
- Bathurst, R.J., Rothenburg, L.: Observation on Stress-Force-Fabric Relationships in Idealized Granular Materials. *Mechanics of Materials* (9), 65–80 (1990)
- Cundall, P.A.: A Computer Model for Rock Mass Behavior using Interactive Graphics for the Input and output of Geometrical Data, Report Prepared under Contract Number DACW 45-74-c-006, for the Missouri River Division, U.S. Army Corps of Engineers, University of Minnesota (1974)
- Mehrabadi, M.M., Nemat-Nasser, S.: Stress, Dilatancy and Fabric in Granular Materials. *Mechanics of Materials* (2), 155–161 (1982)
- Mirghasemi, A.A., Rothenburg, L., Matyas, E.L.: Influence of Particle Shape on Engineering Properties of Assemblies of Two-Dimensional Polygon-Shaped Particles. *Géotechnique* 52(3), 209–217 (2002)
- Oquadfel, H., Rothenburg, L.: A Stress-Force-Fabric relationship for Assemblies of Ellipsoids. *Mechanics of Materials* 33, 201–221 (2001)
- Rothenburg, L.: Micromechanics of Idealized Granular Systems, Ph.D. Dissertation, Carleton University, Ottawa, Ontario, Canada (1980)
- Rothenburg, L., Bathurst, R.J.: Influence of Particle Eccentricity on Micromechanical Behavior of Granular Materials. *Mechanics of Materials* (16), 141–152 (1993)
- Rothenburg, L., Selvadurai, A.P.S.: Amicromecanical Definition of the Cauchy Stress Tensor for Particulate Media. In: Selvadurai, A.P.S. (ed.) *Proceedings of the International Symposium on Mechanical Behavior of Structured Media, Part B*, Ottawa, pp. 469–486 (1981)
- Satake, M.: Constitution of granular Materials Through the Graph Theory. In: *Theoretical and Applied Mechanics*, vol. 26, p. 257. University of Tokyo Press (1978)
- Stark, O.D.L., Cundall, P.A.: A Discrete Numerical Mode For Granular Assemblies. *Geotechnique* 29(1), 47–65 (1978)
- Wang, J., Dove, J.E., Gutierrez, M.S.: Discrete-Continuum Analysis of Shear Banding in the Direct Shear Test. *Geotechnique* 57(6), 513–526 (2007)
- Yang, Z.A., Li, X.S., Yang, J.: Quantifying and modeling fabric anisotropy of granular soils. *Geotechnique* 58(4), 237–248 (2008)

# A Micromechanics-Based Modeling the Simple Shear Behaviors of Granular Materials

J.G. Qian, Z.P. You, and Maosong Huang

Department of Geotechnical Engineering, Tongji University, Shanghai, 200092, China  
qianjiangu@tongji.edu.cn

**Summary.** For granular materials, their principal directions of stress and inelastic strain rate may become non-coaxial (non-coincident) when subjected to non-proportional loading, e.g., to the simple shear deformation. Non-coaxiality, as an important aspect of anisotropy of granular materials, may also produce significant effects on other plastic behaviors, such as dilatancy of materials. A micromechanics-based framework is developed to model the proportional behaviors. The back stress defined in the classical plasticity is interpreted as contribution of fabric anisotropy and its evolution can be quantified with the deviation of principal direction of stress rate from that of stress. A standard isotropic-hardening model has been modified to be a mixed (isotropic/kinematic) hardening one. As an assessment for validity of the proposed non-coaxial model, this study uses this model to examine the non-coaxial behaviors of the simple shear deformation. It has been found that fabric anisotropy plays significant roles on non-coaxiality as well as dilatancy of granular materials. The degree of non-coaxiality strongly depends on fabric anisotropy under simple shear. Due to fabric anisotropy, both dilatancy also becomes less. All predictions are of agreement with the measured from a series of simple shear tests.

**Keywords:** micromechanics-based model, fabric, simple shear.

## 1 Introduction

The responses of granular materials largely depend on principal direction of stress due to their inherent or induced anisotropy. Experimental observations show that sands exhibit non-coaxiality when rotation of principal stress axis take places(e.g., [1-2]). Coaxiality, which refers to the coincidence of principal directions of stress and inelastic incremental strain, is a fundamental assumption of classical flow theory. However, the conventional flow rule does not agree with experimental evidences.

As early as Hill [3], many studies have devoted to the issue of non-coaxiality. It was found that non-coaxiality facilitates the occurrence of localized failure [4]. Non-coaxiality also has great effects on stress dilatancy and cause less dissipation energy [5]. At the micro level, non-coaxiality was essentially attributed to micro-structure evolutions such as particle rolling within granular soil particles[6].

These past studies, although they have lead to better understanding of non-coaxiality, have left some unexplored facets for non-coaxiality. Little previous work

has been done to account for how to relate non-coaxiality of granular materials to their fabric anisotropy at the micro level. This work, within the context of macro-micro approach, develops micromechanics-based model to estimate anisotropic responses induced by rotation of principal stress direction. Effects of fabric anisotropy on non-coaxiality and dilatancy under simple shear have been estimated.

## 2 Micromechanics-Based Formulation of Stress

At the microscopic level, the stress tensor in a representative volume element (RVE) is associated with the interparticle contact forces as follows[7]:

$$\sigma_{ij} = 2N\bar{l} \int_0^\pi E(\theta) f_i n_j d\theta \quad (1)$$

where  $N$  is the number of contacts in the REV.  $f_i$  is the internal contact force between two particles.  $l_i$  is the contact vector that connects the centroids of two neighbor particles.  $\bar{l}$  and  $n_i$  are the length and unit vector of  $l_i$ , respectively.  $E(\theta)$  defines the orientation distribution of  $n_i$  in the REV.

Without loss of generality, two-dimensional problem is considered. In this case,  $E(\theta)$  and  $f_i$  can be described as follows[8]:

$$E(\theta) = \frac{1}{2\pi} [1 + \omega \cos(2\theta - 2\theta_0)] \quad (2)$$

$$f_i = f^n n_i + f^t t_i \quad (3)$$

where  $\omega$  is the parameter that defines the magnitude of anisotropy and  $\theta_0$  represents the orientation with the maximum distribution density of  $n_i$ .  $f^n$  and  $f^t$  are the normal ( $n_i$ ) and tangent ( $t_i$ ) contact force components, respectively.

The spatial distributions of  $f^n$  and  $f^t$  may be also approximated as follows:

$$f^n = f_0 [1 + a_n \cos 2(\theta - \theta_f)] \quad (4)$$

$$f^t = -f_0 a_t \sin 2(\theta - \theta_f) \quad (5)$$

where  $a_n$  and  $a_t$  are used to describe the degree of anisotropy of distribution of  $f^n$  and  $f^t$  respectively.  $\theta_f$  denotes their principal directions and  $f_0$  is the average value of  $f_n$  in the REV.

Substitution of (2)~(5) into Eq.(1) leads to the stress in the following form:

$$\sigma_{ij} = p\delta_{ij} + s_{ij} = p\delta_{ij} + s_{ij}^f + s_{ij}^a \quad (6)$$

where  $s_{ij}$  is the deviatoric part of  $\sigma_{ij}$  and  $p$  denotes the hydrostatic pressure:

$$p = \sigma_{ii} / 2 = N\bar{l} \int_0^\pi E(\theta) f^n d\theta = N\bar{l}f_0 \quad (7)$$

and

$$s_{ij}^f = pC_{ij}, \quad s_{ij}^a = pF_{ij} \tag{8a, b}$$

with

$$[C_{ij}] = (a_t + a_n) \begin{bmatrix} \cos 2\theta_f & \sin 2\theta_f \\ \sin 2\theta_f & -\cos 2\theta_f \end{bmatrix}, \quad [F_{ij}] = \omega \begin{bmatrix} \cos 2\theta_0 & \sin 2\theta_0 \\ \sin 2\theta_0 & -\cos 2\theta_0 \end{bmatrix} \tag{9a, b}$$

In Eq.(8b),  $F_{ij}$  is introduced to represent the fabric tensor that is symmetric and traceless. Clearly,  $s_{ij}^a$  is referred to the stress related to fabric anisotropy.

Now recall the standard kinematic hardening theory, within which the stress consists of three components, i.e.,

$$\sigma_{ij} = p\delta_{ij} + \tau_{ij} + \alpha_{ij} \tag{10}$$

where  $\tau_{ij}$  and  $\alpha_{ij}$  represent the reduced (deviatoric) stress and the back stress, respectively. With respect to (6), it is reasonable to assume that  $\alpha_{ij}$  is ascribed to  $s_{ij}^a$ .

In order to relate the fabric anisotropy to the back stress, it is necessary to consider two loading cases:

- (1) In the case of proportional loading,  $\theta_0$  coincides with  $\theta_f$  [8] and an isotropic hardening response may be used.
- (2) In the case of non-proportional loading,  $\theta_0$  does not necessarily agree with  $\theta_f$  [9] and a kinematic hardening response tends to be included [10].

With the above considerations, we attempt to relate the back stress to anisotropic fabric by

$$\dot{\alpha}_{ij} = \dot{s}_{ij}^a - \frac{\tau_{ij}\tau_{kl}}{\tau_{ab}\tau_{ab}} \dot{s}_{kl}^a = \dot{F}_{ij} p - \frac{\tau_{ij}\tau_{kl}}{\tau_{ab}\tau_{ab}} \dot{F}_{kl} p \tag{11}$$

where the rate of back stress tensor ( $\dot{\alpha}_{ij}$ ) is normal to the deviatoric reduced stress tensor ( $\tau_{ij}$ ). It implies that  $\dot{\alpha}_{ij}$  vanishes in the case of proportional loading, under which the isotropic-kinematic hardening law holds.

To quantify the back stress, we further define the evolution of the fabric. Oda [11] showed that  $\dot{F}_{ij}$  appears to become proportional to  $\dot{R}_{ij}$  ( $R_{ij}=s_{ij}/p$ ) under proportional loading. For non-proportional loading, it sounds reasonable to assume that the fabric changes with  $\tau_{ij}$  as:

$$\dot{F}_{ij} = a\dot{r}_{ij} \tag{12}$$

where  $r_{ij} = \tau_{ij} / p$ , and  $a$  can be seen as a macroscopic material function that equally governs the degree of fabric anisotropy ( $\omega$ ). For simplicity, here  $a$  is assumed to be constant.

### 3 Micromechanics-Based Mixed-Hardening Model

Based on the above analysis, a simple two-dimensional model with a mixed (isotropic-kinematic) hardening law is proposed here. To this end, we attempt to revise the classical isotropic-hardening law into the mixed-hardening law by replacing the deviatoric stress with the deviatoric reduced stress. As an example, one of isotropic hardening models proposed by Pietruszczak[12] will be reformulated here. The revised yield and plastic potential functions are given as follows:

$$F = \tau - \eta p = 0 \quad (13)$$

$$Q = \tau + \eta_c p \ln(p / p_0) = \text{const} \quad (14)$$

where  $\tau = \sqrt{\tau_{ij}\tau_{ij}} / 2$  with  $\tau_{ij} = s_{ij} - \alpha_{ij}$ ,  $p = \sigma_{ii} / 2$ ,  $i, j = 1, 2$ ,  $p_0$  is initial confining pressure.  $\eta = \eta_f \varepsilon_s^{cp} / (A + \varepsilon_s^{cp})$  with  $\eta_f$ =the failure stress ratio at an ideal state,  $A$ = material constant and  $\varepsilon_s^{cp}$  = plastic shear strain.  $\eta_c$  represents the value of  $\eta$  in the critical state, corresponding to the vanishing rate of plastic volumetric strain.

### 4 Modelling Behaviors of Simple Shear

The above proposed isotropic-kinematic model is intended to model simple shear behaviors of granular materials (made of an assembly of photoelastic cylinders). The simple shear test involves non-proportional loading and has been already reported in details by Oda [2]. As an illustration, the model parameters are given as: Elasticity modulus =25MPa and Poisson's ratio=0.25, and plastic parameters  $\eta_f=0.62$ ,  $\eta_c=0.37$  and  $A=0.0014$ . Fabric anisotropy  $a=0, 0.3, 0.45, 0.48$  are used to reproduce the behaviors of simple shear, respectively.

Fig. 1 shows effects of fabric anisotropy on the difference between principal directions of stress and strain rate under simple shear. Experimental observations have demonstrated that principal directions of stress significantly depart from those of strain rate during the course of shear deformation. The classical plastic model ( $a=0.0$ ) is not capable to reproduce the non-coaxial behaviors. Nevertheless, at very early stage of simple shear, the classical model may also reproduce non-coincidence of principal directions of stress and strain rate. It is essentially due to difference of principal axis of stress and elastic strain rate, which tends to become negligible as the shear strain is increasing. In contrast, the measured non-coaxial behaviors are well simulated by the proposed anisotropic model if an

appropriate degree of fabric anisotropy ( $a$ ) is involved. On the other hand, both experimental observations and theoretical predictions reveals that difference of two principal directions tends to become smaller with increasing shear strain. This particular phenomenon agrees with reported by Roscoe [1].

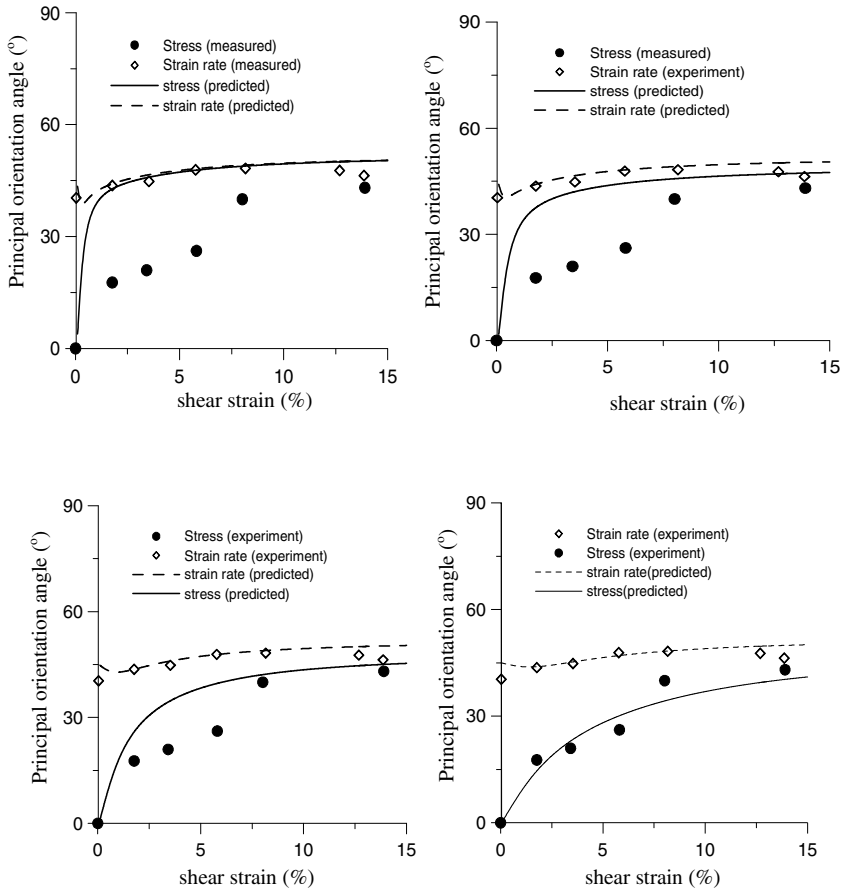


**Fig. 1.** Effect of fabric anisotropy on difference of principal directions of stress and strain rate: (a) Theoretical predictions ( $a=0.0$ ), (b) Theoretical predictions ( $a=0.3$ ), (c) Theoretical predictions ( $a=0.45$ ), (d) Theoretical predictions ( $a=0.48$ ).

Fig.2 demonstrates the effect of fabric anisotropy on dilatancy. Evidently, both compression and dilatancy become less as the degree of fabric anisotropy is increasing. In fact, effects of fabric anisotropy on dilatancy can be associated with the difference of principal directions between stress and strain rate, whose magnitude tends to become larger as the degree of fabric anisotropy is increasing, as

shown in Fig.3. It implies that stronger non-coaxiality may lead to less dilatancy. The dependence of dilatancy on non-coaxiality agrees with macro-micro stress-dilatancy rule earlier proposed by Oda[13]and Gutierrez and Ishihara [5].

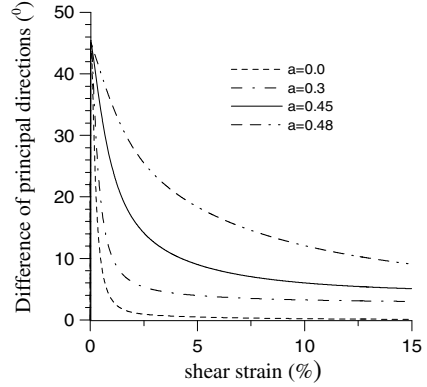
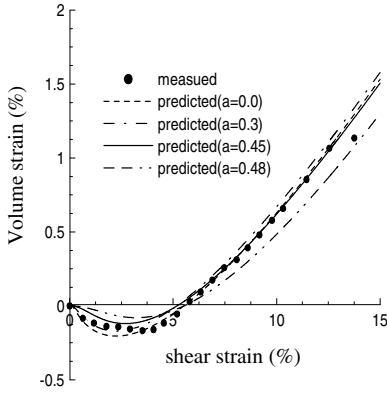


**Fig. 2.** Effect of fabric anisotropy on dilatancy **Fig. 3.** Difference of principal directions between stress and strain rate

Fig.4 further presents theoretical predictions on the microscopic evolution of anisotropic distribution of contact normals. Based on theoretical results in Figs. 2-4,  $a=0.45$  is selected to represent the degree of fabric anisotropy. As shown in Fig.4, the direction of maximum distribution density of contact normals( $\theta_F$ ) continue to change during the process of simple shear. The maximum direction tends to rotate following the change of principal direction of stress ( $\theta_\sigma$ ). Clearly, the theoretical simulations agree well with the experimental measures. At the same time, it should be pointed out that the principal direction of fabric tensor does not agree with that of stress. The difference of their principal directions tends to become larger during the loading of simple shear. Consequently, non-coaxial behaviors are followed.

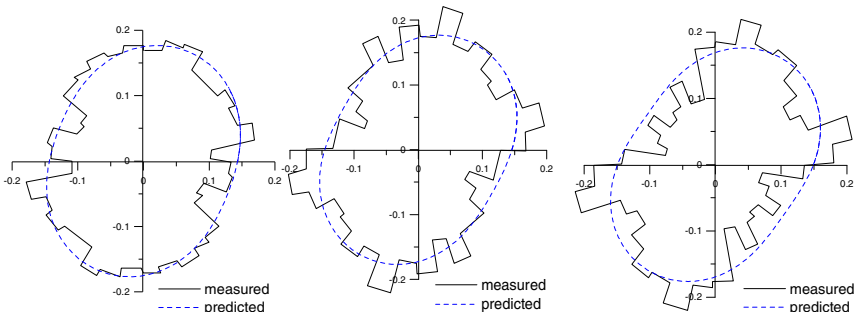


**Fig. 4.** Modeling the evolution of fabric anisotropy ( $a=0.45$ ): (a)  $\gamma=1.82\%$  ( $\theta_\sigma=26.4^\circ$ ,  $\theta_F=21.3^\circ$ ), (b)  $\gamma=3.62\%$  ( $\theta_\sigma=35^\circ$ ,  $\theta_F=29^\circ$ ), (c)  $\gamma=8.0\%$  ( $\theta_\sigma=42.1^\circ$ ,  $\theta_F=35.4^\circ$ )

## 5 Conclusions

Departing from classical continuum theory as well as discrete element method (DEM), this study has proposed a two-dimensional micromechanically-based constitutive framework for the description of induced anisotropy of granular materials. With considerations of micromechanics, fabric anisotropy is essentially linked to kinematic-hardening responses under non-proportional loading. Its component associated with the tangential loading effect appears to coincide with the rate of back stress defined in the classical kinematic-hardening theory. A micromechanics-based mixed hardening model is established and used to capture non-coaxiality and dilatancy under simple shear loading. In general, as shear strain is developing, the degree of non-coaxiality has grown to its peak at the early stage, and subsequently reduces to some critical value. Due to fabric anisotropy, less dilatancy(or compression) is also obtained.

**Acknowledgement.** The work reported in this paper was supported by national natural science foundation of china (grants no. 10972159 and 50825803).

## References

- [1] Roscoe, K.H.: The influence of strain in soil mechanics. *Géotechnique* 20(2), 129–170 (1970)
- [2] Oda, M., Konishi, J.: Rotation of principle stresses in granular material in simple shear. *Soils and Foundations* 14(4), 39–53 (1974)
- [3] Hill, R.: *The Mathematical Theory of Plasticity*. Oxford University Press, Oxford (1950)
- [4] Rudnicki, J.W., Rice, J.R.: Conditions for localization of deformation in pressure-sensitive dilatant materials. *Journal of the Mechanics and Physics of Solids* 23, 371–394 (1975)
- [5] Gutierrez, M., Ishihara, K.: Non-coaxiality and energy dissipation in granular material. *Soils and Foundations* 40, 49–59 (2000)
- [6] Jiang, M.J., Harris, D., Yu, H.S.: Kinematic models for non-coaxial granular materials: Part II: evaluation. *Int. Journal for Numerical and Analytical Methods in Geomechanics* 29(7), 663–689 (2005)
- [7] Christoffersen, J., Mehrabadi, M.M., Nemat-Nasser, S.: A micromechanical description of granular material behavior. *J. Appl. Mech.* 48, 339–344 (1981)
- [8] Rothenburg, L., Bathurst, R.J.: Analytical study of induced anisotropy in idealized granular materials. *Geotechnique* 39(4), 601–614 (1989)
- [9] Nemat-Nasser, S.: A micromechanically-based constitutive model for frictional deformation of granular materials. *J. Mech. Phys. Solids* 48, 1541–1563 (2000)
- [10] Gutierrez, M., Ishihara, K., Towhata, I.: Flow theory for sand during rotation of principal stress direction. *Soils and Foundations* 31, 121–132 (1991)
- [11] Oda, M.: Inherent and induced anisotropy in plasticity theory of granular soils. *Mech. Mat.* 16, 35–45 (1993)
- [12] Pietruszczak, S.: On the undrained response of granular soil involving localized deformation. *Journal of Engineering Mechanics, ASCE* 114, 1292–1298 (1995)
- [13] Oda, M.: On stress-dilatancy relation of sand in simple shear tests. *Soils and Foundations* 15(2), 17–29 (1975)

# Evolution of Fabric in the Shearing Process Based on Micromechanics

Homayoun Shaverdi<sup>1</sup>, Mohd. Raihan Taha<sup>1</sup>, and Farzin Kalantary<sup>2</sup>

<sup>1</sup> Department of Civil and Structure Engineering, University Kebangsaan Malaysia (UKM)  
homayoun\_shaverdi@yahoo.com, profraihan@gmail.com

<sup>2</sup> Department of geotechnical engineering, Khaje Nasir Toosi University of Technology  
fz\_kalantary@yahoo.co.uk

**Abstract.** In this paper a new formulation is presented to encompass the induced anisotropy during shear deformation in granular mass. The fabric anisotropy is affected by a number of parameters such as the mobilized stress ratio, internal friction angle, and the state of fabric. Non-coaxiality between stress and fabric tensor is included in this equation. This proposed formulation is derived by considering the interaction of particles across a potential sliding plane at micro-level. It is further developed to incorporate the initial fabric anisotropy. The changes of fabric in the presence of inherent anisotropy will be predicted by these equations. Verifying of the formulation is presented with numerical simulations and experimental tests.

**Keywords:** induced anisotropy, inherent anisotropy, degree of anisotropy, micromechanic, granular materials.

## 1 Introduction

Micromechanical characteristics (or fabric) of the granular materials have a great effect on the behavior of their shearing mechanism (e.g., [1-4]). The effect of fabric on the shearing mechanism has been attributed to two types of anisotropy i.e., inherent anisotropy and induced anisotropy. These two types of anisotropy first were known by Casagrande & Carillo [5]. The inherent anisotropy was established through the sedimentation of non-spherical particles and were measured based on the apparent long axes. Induced anisotropy is a result of applied shear loads and formation of a new structure in the contact normals to resist against these loads. To quantify the induced anisotropy, many attempts have been done (e.g., [2,6,7-9]). Using an assembly of irregular discs Biarez & Wiendieck [6] performed a biaxial compression test. They have found that the contact normals tend to concentrate parallel to the direction of the maximum compression. Oda [1] also, observed a similar behavior for natural sands in triaxial

compression test. Biarez & Wiendieck [6] approximated the distribution of the contact normals by an ellipse where the principal axes of ellipse agree well with principal stress axes. Matsuoka & Geka [3] used a triangle as an approximation for the distribution of the contact normals. Using distinct element method (DEM) Rothenburg & Bathurst [7] showed that this distribution of the contact normals can be represented by a peanut-shaped function. Arthur et al. [10] and Wan & Guo [9] used the ellipse that was prepared by Biarez & Wiendieck [6] to calculate the fabric tensor and its evolution. However, in this study we used the peanut-shaped function that has already been proposed by Rothenburg & Bathurst [7], but we developed it to direct the calculation of the fabric.

## 2 Quantifying Fabric Anisotropy in the Hardening Process

Hardening in the granular materials is attributed to the changes of contact normals or induced fabric anisotropy ([8,11]). The Creation of new column-like rows in the granular mass is a result of unevenly transmission of the axial load in the vertical direction. To quantify the changes of the contact normals (or column-like rows) Kanatani [12] proposed the following equation:

$$F_{ij} = \int_0^{2\pi} n_i n_j E(\theta) d\theta \quad (1)$$

where  $n_i$  and  $n_j$  are the directions of the contact normals with respect to the Cartesian components  $X$  and  $Y$  respectively;  $E(\theta)$  implies the contact normals distribution. The equation proposed by Rothenburg & Bathurst [7] to show the contact normals distribution is as follows:

$$E(\theta) = (1/2\pi)(1 + \alpha \cos 2(\theta - \theta_f)) \quad (2)$$

where  $\alpha$  is the degree of anisotropy and  $\theta_f$  is the major principal direction of the fabric tensor. The ratio between the major principal value  $F_1$  and the minor principal value,  $F_3$  of the fabric tensor can be presented as follows:

$$\left(\frac{F_1}{F_3}\right)_{ind} = \frac{1 + (1/2)\alpha \cos 2(\theta_\sigma - \theta_f)}{1 - (1/2)\alpha \cos 2(\theta_\sigma - \theta_f)} \quad (3)$$

where  $\theta_\sigma$  is the major principal direction of the compressive stress. The parameters  $\alpha$  and  $\theta_f$  were obtained from the equations proposed by Taha & Shaverdi [13]. These equations are not presented here due to the limitation of the space and presented elsewhere. The magnitude of anisotropy  $\alpha$  obtained is based on the micro-level analysis, and to calculate this parameter, all the main factors such as the ratio of shear to normal stress, the interparticle mobilized friction angle and the non-coaxiality between the stress and the fabric were taken into account.

Oda [8] also, presented a general function to calculate fabric anisotropy but he did not explicitly proposed an applicable equation in which the relations between the main factors are known.

### 3 Inherent Anisotropy

A numerous experimental data show that the shear strength in the granular materials depends on the inherent anisotropy (e.g., [1,2,4,11,14,15]). This is due to the fact that non-spherical particles are sedimented nearly parallel to the horizontal surface under the gravitational force. Inherent anisotropy remains near to unchanged during plastic shear deformation up to failure ([8]). Although Roscoe & Schofield [16] and Oda [17] observed that non-spherical particles tend to be limited rotation perpendiculars to the direction of a maximum principal stress (compression). To quantify the inherent anisotropy by the particle orientation a tensor  $(F_{ij})_{inh}$  is introduced as follows:

$$(F_{ij})_{inh} = \int_{\Omega} m_i m_j E(m) d\Omega \tag{4}$$

where  $m_i$  and  $m_j$  are the inclinations of the apparent long axes of particle  $m$  with respect to the Cartesian components  $X$  and  $Y$  respectively;  $E(m)$  is the distribution function of particles,  $\Omega$  is  $4\pi$  for three dimensions (3D) and  $2\pi$  for 2D problems.

### 4 Shearing in the Presence of Inherent Anisotropy (Combination of Inherent and Induced Anisotropy)

When a sample has a non-coaxiality between the stress and the particle deposition (inherent anisotropy) undergoes shearing, the contact normals rotate to concentrate in the maximum compression direction, hence we have both inherent and induced anisotropy. In this case, the ratio of  $F_1 / F_3$  is obtained from the following equation:

$$(F_1 / F_3) = (F_1 / F_3)_{inh} \cdot (F_1 / F_3)_{ind} \tag{5}$$

The above ratio  $(F_1 / F_3)$  must be used in the constitutive modeling. The parameter  $(F_1 / F_3)_{ind}$  changes with the shearing process because  $\alpha$  and  $\theta_f$  change with the external shear load. The above equation shows the evolution of the fabric in the shearing process in the granular mass. Verification with the numerical simulation and the experimental test show the validity of the above equation.

### 4.1 Verification with Numerical Simulation

Using numerical simulation Guo [18] shows the evolution of principal fabric ratio  $F_1 / F_3$  and the rotation of principal fabric direction of Ottawa sand with  $e_o = 0.65$  and  $(F_1 / F_3)_{inh} = 1.33$ , for two bedding angles,  $\beta = 30^\circ$  and  $60^\circ$  at the same confining stress of  $\sigma_3 = 200kg / cm^2$  in triaxial compression tests. In Fig.1 and Fig.2 these simulations are shown. By applying equation (5), we can predict and simulate this fabric evolution.

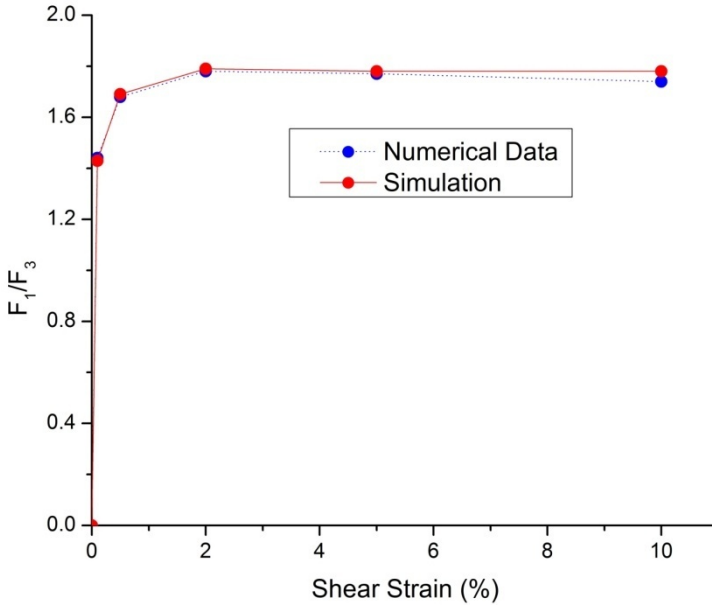
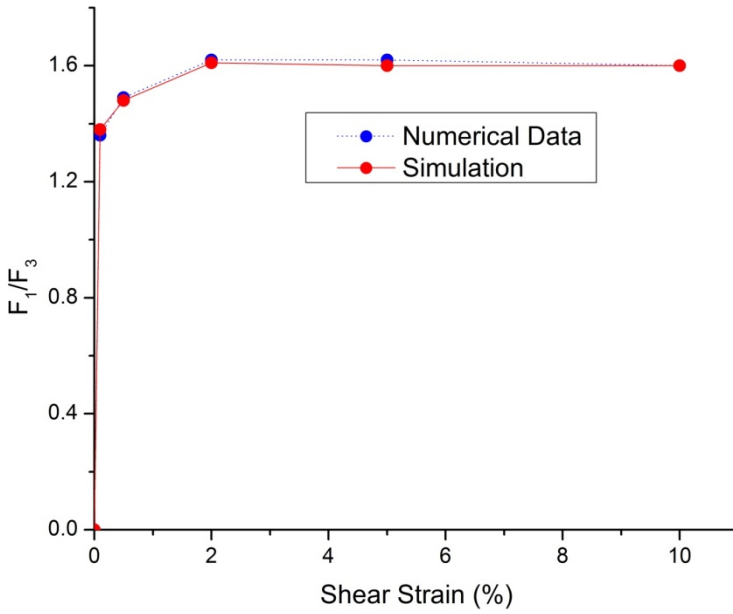


Fig. 1. Compares numerical simulation and the proposed equation for  $\beta = 30^\circ$ , (Data from Guo [18])

### 4.2 Verification with Experimental Test

Oda [17] conducted some experimental tests to study the mechanism of fabric changes in sands by triaxial compression tests. He used uniform sand which was composed of quartz and feldspar grains with rounded to sub-rounded shapes. The size of these grains varies from 0.84mm to 1.19mm. He considered the ratio  $S_z / S_x$  as a fabric characteristic of anisotropic granular sand. This ratio is the same as the ratio  $F_1 / F_3$  that was used in this study. The comparison between the magnitudes obtained from the experimental test and the calculation by using equation (5) reveals the validity of these formulations. The comparison between simulation and experimental tests are shown in Fig. 3 and Fig. 4.



**Fig. 2.** Compares numerical simulation and the proposed equation for  $\beta = 60^\circ$ , (Data from Guo [18])

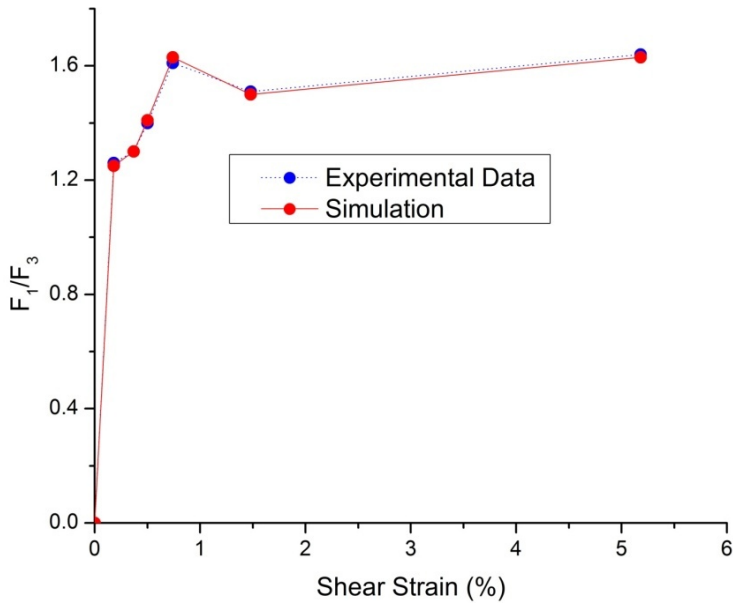


**Fig. 3.** Compares experimental test and the proposed equation for tapping method, (Data from Oda (1972a))

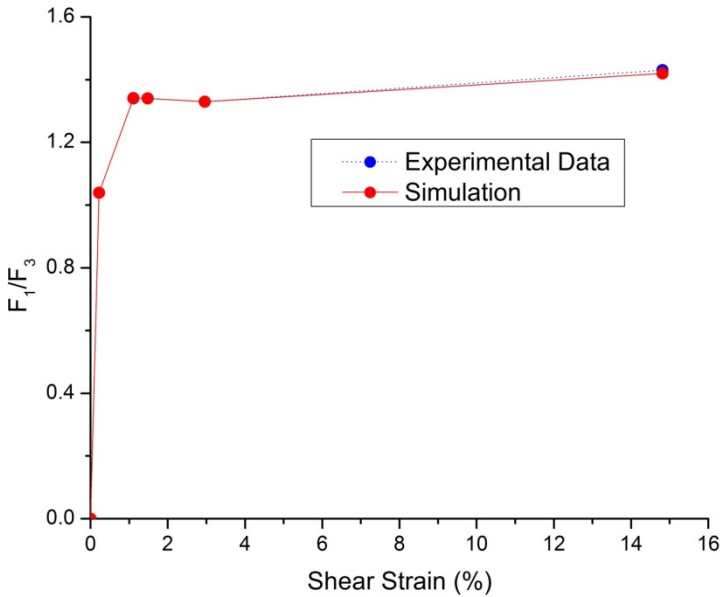


**Fig. 4.** Compares experimental test and the proposed equation for plunging method, (Data from Oda (1972a))

## 5 Conclusion

The equation presented can predict the evolution of the contact normals during shear deformation in the granular mass. The mobilized stress ratio  $\tau / \sigma$  on the spatial mobilized plane (SMP), the internal friction angle  $\phi_{\mu mob}$ , and the non-coaxiality between stress and fabric are the main factors that affect the evolution of fabric ([8]). These parameters were included in the equation to calculate the evolution of fabric. The effect of inherent anisotropy also, was included to account this element on the evolution of the contact normals. This equation was compared with numerical simulations and experimental tests to show its validity.

## References

- [1] Oda, M.: Initial fabrics and their relations to mechanical properties of granular materials. *Soils and Foundations* 12(1), 17–36 (1972a)
- [2] Matsuoka, H.: A microscopic study on shear mechanism of granular materials. *Soils and Foundations* 14(1), 29–43 (1974)
- [3] Matsuoka, H., Geka, H.: A stress-strain model for granular materials considering mechanism of fabric change. *Soils and Foundations* 23(2), 83–97 (1983)

- [4] Yoshimine, M., Ishihara, K., Vargas, W.: Effects of principal stress direction and intermediate principal stress on undrained shear behavior of sand. *Soils and Foundations* 38(3), 179–188 (1998)
- [5] Casagrande, A., Carillo, N.: Shear failure of anisotropic materials, *J. Boston Soc. Civ. Engrs* 31, 122–135 (1944)
- [6] Biarez, J., Wiendieck, K.: La comparaison qualitative entre l'anisotropie mécanique et l'anisotropie de structure milieux pulvérulents. *C. R. Acad. Sci.* 256, 1217–1220 (1963)
- [7] Rothenburg, L., Bathurst, R.: Analytical study of induced anisotropy in idealized granular Materials. *Geotechnique* 39(4), 601–614 (1989)
- [8] Oda, M.: Inherent and induced anisotropy in plasticity theory of granular soils. *Mechanics of Materials* 16(1-2), 35–45 (1993)
- [9] Wan, R., Guo, P.: Effect of microstructure on undrained behaviour of sands. *Canadian Geotechnical Journal* 38(1), 16–28 (2001)
- [10] Arthur, J.R.F., Koenders, M., Wong, R.K.S.: Anisotropy in particle contacts associated with shearing in granular media. *Acta Mechanica* 64(1), 19–29 (1986)
- [11] Oda, M., Nemat-Nasser, S., Konishi, J.: Stress-induced anisotropy in granular mass. *Soils and Foundations* 25(3), 13 (1985)
- [12] Kanatani, K.I.: Distribution of directional data and fabric tensors. *International Journal of Engineering Science* 22(2), 149–164 (1984)
- [13] Taha, M.R., Shaverdi, H.: The evolution of fabric in the presence of the rotation of principal stress in the simple shear tests (submitted to published)
- [14] Arthur, J.R.F., Menzies, B.K.: Inherent anisotropy in sands. *Geotechnique* 22(1), 115–128 (1972)
- [15] Oda, M., Koishikawa, I., Higuchi, T.: Experimental study of anisotropic shear strength of sand by plane strain test. *Soils and Foundations* 18(1), 25–38 (1978)
- [16] Roscoe, K.H., Schofield, A.N.: In stress-strain behavior of soils, Roscoe symposium memorial. *Geotechnique* 14(2), 143–167 (1964)
- [17] Oda, M.: The mechanism of fabric changes during compressional deformation of sand. *Soils and Foundations* 12(1), 1–19 (1972b)
- [18] Guo, P.: Modelling granular materials with respect to stress-dilatancy and fabric: A fundamental approach, civil engineering department. Alberta, University of Calgary. Phd. Thesis (2000)

# Determination of Crystallinity of Alkali Activated Flyash by XRD and FTIR Studies

D.N. Singh<sup>1,\*</sup>, Bhagwanjee Jha<sup>1</sup>, and Kadali Srinivas<sup>2</sup>

<sup>1</sup> Department of Civil Engineering, Indian Institute of Technology, Bombay  
Powai, Mumbai, Maharashtra, India-400 076  
dns@civil.iitb.ac.in

<sup>2</sup> Research Scholar, Civil Engineering Department, Indian Institute of Technology, Bombay,  
Powai, Mumbai-400 076, India

**Abstract.** Alkali activation of a flyash causes dissolution of its mineral constituents and also, significant transition in the characteristics of the residue. As a result, the residue attains the crystallinity, which is different from the ash. In order to quantify the final crystallinity, peak intensity of a mineral present in the X-ray diffractograms (XRD) of these samples has been demonstrated to be a useful parameter. In this context this paper presents a methodology to determine crystallinity of the residue by employing XRD and the Fourier transform infrared (FTIR) analysis of these samples. Also, this study establishes that such activation causes significant changes in the structural framework, which confirms formation of flyash zeolites (viz., Na-P1, hydroxysodalite and cancrinite), as well.

**Keywords:** crystallinity, peak intensity, wave number, flyash, residue.

## 1 Introduction

Flyash has been opined to be an inert material, which interacts severely with an alkali during the hydrothermal treatment at 100 °C (e.g., [1]). Also, physico-chemico-mineralogical and structural transitions occur from flyash to its activated residue [2]. In this context, XRD and FTIR analysis tools are helpful to evaluate these transitions [3-7]. In fact, a variation in the XRD hints for conversion of amorphous to crystalline phases and vice-versa, whereas, that in the FTIR corresponds to some structural bond deformations [3-7]. Hence, present challenge is to evaluate corresponding variation in mineral's crystallinity (VIC), which has been earlier calculated in comparison to a reference material [2]. However, it should be noted that referred material, in general, is different from the treated ash in methodology of synthesis and mineralogy. Hence this manuscript attempts to eliminate the use of any reference material and calculate the VIC of a mineral. Also, this study intends to fix superiority of one of the tools as compared to another.

---

\* Corresponding author.

## 2 Materials and Methods

The flyash used in this study was collected from the hoppers of a thermal power plant in central Maharashtra, India. The alkali (NaOH) used for the study was supplied by Thomas Baker Chemicals Pvt. Ltd., Mumbai. A homogeneous mixture of 25g of the ash and 250ml of 0.5M NaOH was imparted hydrothermal treatment at 100 °C, in an open refluxed system. After the treatment, the slurry was filtered by using Watman filter paper No. 42. The residues were characterized for chemical composition, mineralogy, structural vibration modes and morphology with the help of a X-ray fluorescence (XRF) spectrometer set up (Phillips 1410, Holland), a XRD spectrometer (Phillips 2404, Holland), a FTIR spectrometer (Perkin Elmer make, Paragon 1000 PC) and a field emission gun-scanning electron microscopy (FEG-SEM) set up (JEOL JSM-7600F, Japan), respectively [1]. Accordingly, the results of the XRF study are presented in Table 1. The XRD patterns of these samples are depicted in Fig. 1(a), from which the minerals have been identified by using JCPDS (1994) search files [1]. Also, obtained FTIR spectra in terms of transmittance (%) are presented in Fig. 1(b). Micrographs of the flyash and the residues are presented in Fig. 2(a) and Fig. 2(b,c), respectively.

**Table 1.** Major oxides present in flyash and the residue

Sample	Al <sub>2</sub> O <sub>3</sub>	SiO <sub>2</sub>	Fe <sub>2</sub> O <sub>3</sub>	Na <sub>2</sub> O	K <sub>2</sub> O	BaO	CaO	TiO <sub>2</sub>
Flyash	26.00	63.80	5.1	0.05	0.66	0.14	1.88	1.52
Residues	25.50	58.30	5.0	5.53	0.63	0.09	1.63	1.51

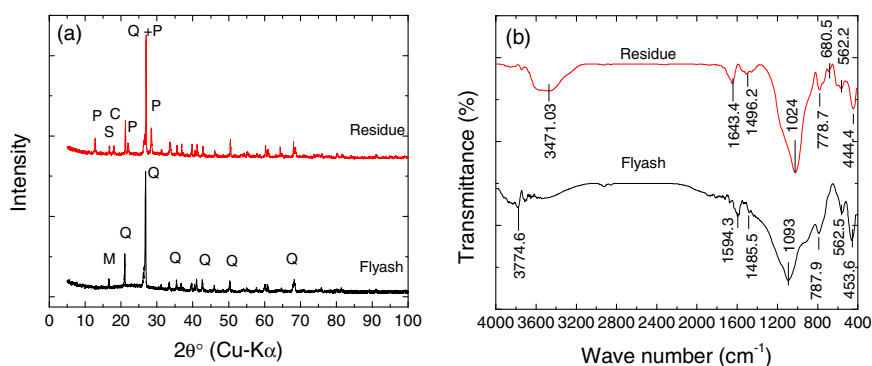


**Fig. 1.** Transition in the flyash and the residue based on (a) XRD patterns and (b) FTIR spectra

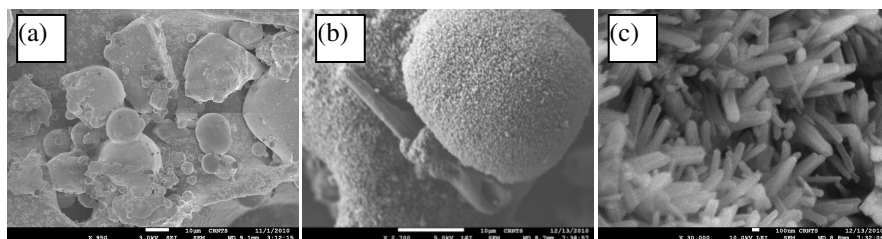


**Fig. 2.** FEG-SEM micrographs of these samples at different magnifications (a) flyash  $\times 950$ , (b) residues  $\times 2700$  and (c) residues  $\times 30000$

### 3 Results and Discussions

From the data presented in Table 1 it can be noticed that dissolution of silica (by 5.2%) and alumina (by 0.5%) from the flyash has occurred, which reveals its chemical transitions. In addition, Fig. 1(a) exhibits few new peaks near many  $2\theta$  values (viz., 12.77, 16.95, 17.98, 22.01, 28.40, 33.78, 50.45 and  $64.34^\circ$ ). As per the JCPDS (1994) match, these peaks correspond to some flyash zeolites designated as **P** (Na-P1) and **C** (Cancrinite), as marked in the XRD patterns. Hence, conversion of few mineral phases from amorphous to crystalline is expected and hence the VIC, as well. In addition, Fig. 2(c) also exhibit clusters of new orthorhombic crystalline morphologies (other than flyash as depicted in Fig. 2a) projecting out of the surface of the residue particles. Further, Fig. 1(b) reveals disappearance of some bands from the flyash and appearance of new bands in the residue. In addition, variations in the full width at half maximum (FWHM) of these bands and their intensity (in terms of decrease in transmittance) are noticeable. Thus, all these changes can be attributed to significant variation in the mineral structures, their external linkages and the VIC also.

#### 3.1 VIC Computation from XRD

In order to evaluate the mineralogical transition, the XRD pattern data have been reanalyzed as per methods described in [2-4]. The average peak areas (calculated by multiplying peak intensity and FWHM) of ten significant peaks are listed in Table 2. From Table 2 the VIC from the ash to the residue is correlated with the percentage changes in the sum of areas e.g.,  $\{(a-b)/a\} \times 100 = 9.87\%$ , peak intensity e.g.,  $\{(c-d)/c\} \times 100 = -34.9\%$  and FWHM e.g.,  $\{(e-f)/e\} \times 100 = 38.2\%$ . Thus, lower change in the area of the peaks reveals majority of amorphous minerals (up to 90.13%) in the residue. Also, an increase in the peak intensity (by 34.9%) corresponds to a reduction in the FWHM (by 38.2%). Hence, average of these results reveals an increase in crystallinity up to 36.5%. Thus, it can be opined that every 1% increase in the area of the XRD pattern may correspond to 3.69% increase in the crystallinity of the sample.

**Table 2.** XRD peak parameters of the flyash and its activated residue

2 $\theta$ ( $^{\circ}$ )	FWHM (2 $\theta^{\circ}$ )	Peak intensity	Peak area	2 $\theta$ ( $^{\circ}$ )	FWHM (2 $\theta^{\circ}$ )	Peak intensity	Peak area
<b>Flyash</b>				<b>Residue</b>			
16.63	0.2007	174	34.92	12.83	0.1673	350	58.55
21.04	0.2007	621	124.63	21.22	0.1338	722	96.60
26.83	0.2007	2733	548.51	26.31	0.1673	326	54.53
33.45	0.2007	171	34.32	26.63	0.1004	496	49.79
35.45	0.2007	244	48.97	26.99	0.1506	2955	445.02
39.66	0.2342	172	40.28	28.43	0.1171	632	74.00
41.05	0.2007	266	53.38	33.56	0.1673	291	48.68
42.67	0.2676	218	58.33	50.47	0.1004	437	43.87
50.30	0.2342	233	54.56	60.26	0.1004	285	28.61
68.36	0.3346	198	66.25	68.06	0.2007	296	59.40
Notations	c <sup>s</sup> =2.2748	c <sup>#</sup> =5030	a <sup>*</sup> =1064	Notations	f <sup>s</sup> =1.4053	d <sup>#</sup> =6790	b <sup>*</sup> =959

\* sum of areas, #sum of peak intensity, \$ sum of FWHM.

### 3.2 VIC Computation from FTIR

A reanalysis of data of Fig. 1(b) is done in Table 3 based on methods from [5-7]. From this table, the VIC from the ash to the residue is correlated with the percentage changes in the sum of band areas e.g.,  $\{(j-k)/j\} \times 100 = 0.94\%$ , band intensity e.g.,  $\{(n-p)/p\} \times 100 = -30.35\%$  and FWHM e.g.,  $\{(r-s)/r\} \times 100 = -21.25\%$ . Hence as demonstrated in [6], a minor change in the area may be due to majority of amorphous solids in the residue. In addition to this, an increase in the band intensity (by 30%) and its FWHM (i.e., broadness by 21%) as well, confirms an average value of the VIC equal to 25.8%. Thus, it can be opined that for every 1% increase in the area of an FTIR spectrum, the VIC increases by 27.44%, which is higher than that from the XRD by 23%. Accordingly, the FTIR spectrum is opined to be more sensitive tool for the evaluation of the VIC. However, quantitatively, value of the VIC from the XRD pattern is observed to be higher than that from the FTIR spectrum.

**Table 3.** FTIR spectrum band parameters for the flyash and the residue

Wave Number (cm <sup>-1</sup> )	Intensity (%)	FWHM (cm <sup>-1</sup> )	Band area	Wave Number (cm <sup>-1</sup> )	Intensity (%)	FWHM (cm <sup>-1</sup> )	Band area
<b>Flyash</b>				<b>Residue</b>			
3774.6	6	127	762	3471.0	12	314	3768
1494.3	6	49	294	1643.4	9	78	702
1485.5	1.5	10	15	1496.2	4	98	392
1093	39	425	16575	1024	48	256	12288
787.9	6	40	240	778.1	8	78	624
562.5	8	38	304	680.5	1	20	20
453.6	13.5	49	661	562.2	5	60	300
Not any				444.4	10	58	580
Notations	s <sup>s</sup> =80	n <sup>#</sup> =738	j <sup>*</sup> =18851	Notations	r <sup>s</sup> =97	p <sup>#</sup> =962	k <sup>*</sup> =18674

\* sum of areas, #sum of peak heights, \$ sum of full wave half maximum (FWHM) of absorption bands, - not any.

## 4 Conclusions

Based on the results and discussions presented above, the following conclusions can be derived.

- The FTIR spectrum and the XRD pattern result in change in crystallinity up to 27.44% and 3.69%, respectively corresponding to every 1% change in their areas.
- The percentage change in area is higher in the XRD pattern than the FTIR spectrum due to a treatment, whereas, an FTIR spectrum is more sensitive to any change in the crystallinity.

## References

- [1] Jha, B., Singh, D.N.: A review on synthesis, characterization and industrial application of flyash zeolites. *J. of Mater. Educ.* 33(1-2), 65–132 (2011)
- [2] Ojha, K., Pradhan, N.C., Samanta, A.N.: Zeolite from flyash: synthesis and characterization. *Bull. Mater. Sci.* 27(6), 555–564 (2004)
- [3] Camacho, W., Karlsson, S.: Simultaneous determination of molecular weight and crystallinity of recycled HDPE by infrared spectroscopy and multivariate calibration. *J. of Appl. Polymer Sc.* 85, 321–327 (2002)
- [4] Larsen, S.C.: Nanocrystalline zeolite and zeolite structures: synthesis, characterization and applications. *J. Phys. Chem.* C111, 18464–18474 (2007)
- [5] Meaurio, E., Lopez-Rodriguez, Sarasua, J.R.: Infrared spectrum of poly (L-lactide): application to crystallinity studies. *Macromolecules* 39, 9291–9301 (2006)
- [6] Starkweather, H.W., Ferguson, R.C., Chase, D.B., Minor, J.M.: Infrared spectra of amorphous and crystalline poly (tetrafluoroethylene). *Macromolecules* 18, 1684–1686 (1985)
- [7] He, Y., Inoue, Y.: Novel FTIR method for determining the crystallinity of poly (E-caprolactone). *Society of Chemical Industry. Polym. Int.* 49, 623–626 (2000)

# Stress-Dependency of Intergranular Strain

A.B. Tsegaye<sup>1</sup>, B.W. Ygzaw, and Thomas Benz<sup>1</sup>

<sup>1</sup> Norwegian University of Science and Technology, Trondheim, Norway

**Abstract.** Various experimental results show that small strain stiffness and its decay with shear strain depend on confining pressure amongst other factors. In this paper, a selection of experimental evidence is briefly discussed. The Intergranular Strain formulation by Niemunis & Herle (1997) for the hypoplastic theory is extended for the same effect and evaluated. Furthermore, application of the concept to elastoplastic models is discussed.

## 1 Introduction

Generally, stiffness of soils depends on stress (*e.g.*, Ohde 1939, Janbu 1963). It has also been noticed that stiffness of soils at small strains is stress dependent (Hardin & Richart 1963).

The trend of the normalized shear modulus is often taken as a characteristic curve of secant (sometimes also tangent) shear modulus reduction with shear strain. Generally, the rate of decay of the normalized shear modulus of soils with shear strain may be affected by several state variables. In literature, the influence of various variables has been investigated (see, *e.g.*, Vucetic & Dorby 1991, Lansivaara 1999, and Benz 2007) which may be summarized as

$$\frac{G}{G_{\max}} = f(\gamma, p, I_p, e_0, OCR, \text{grain characteristics, etc.}). \quad (1)$$

where  $G_{\max}$  is maximum shear modulus,  $\gamma$  is shear strain,  $p$  is confining stress,  $I_p$  is plasticity index,  $e_0$  is initial void ratio,  $OCR$  is overconsolidation ratio to mention some.

The normalized shear modulus decays with shear strain while the rate of decay decreases with confining pressure, plasticity index (for plastic soils), void ratio, and overconsolidation ratio,  $OCR$  (see *e.g.*, Daredeli 2001, Vucetic & Dorby. 1991).

In this paper, the treatment is restricted only to effect of confining pressure  $p$ . Some experimental evidence on the effect of confining pressure is briefly discussed in the next section. Then the Intergranular Strain concept proposed by Niemunis & Herle (1997) for the hypoplastic theory is discussed and a simple way of applying similar technique to elastoplastic theories is treated. Next the evolution of the normalized shear modulus is extended for the effect of confining

pressure, which the original formulation does not consider. For illustration, the data presented in the following section (Figure 1) are numerically back calculated using the extended Intergranular Strain model.

## 2 Experimental Evidence of Influence of Mean Normal Stress on the Rate of Decay of Small Strain Stiffness

Various experimental studies show that the decay of normalized shear modulus in the small strain region is influenced by confining pressure (*e.g.*, Iwasaki *et al.* 1978, Kokusho 1980, Ni 1987, Darendeli *et al.* 2001, Stokeo *et al.* 2004).

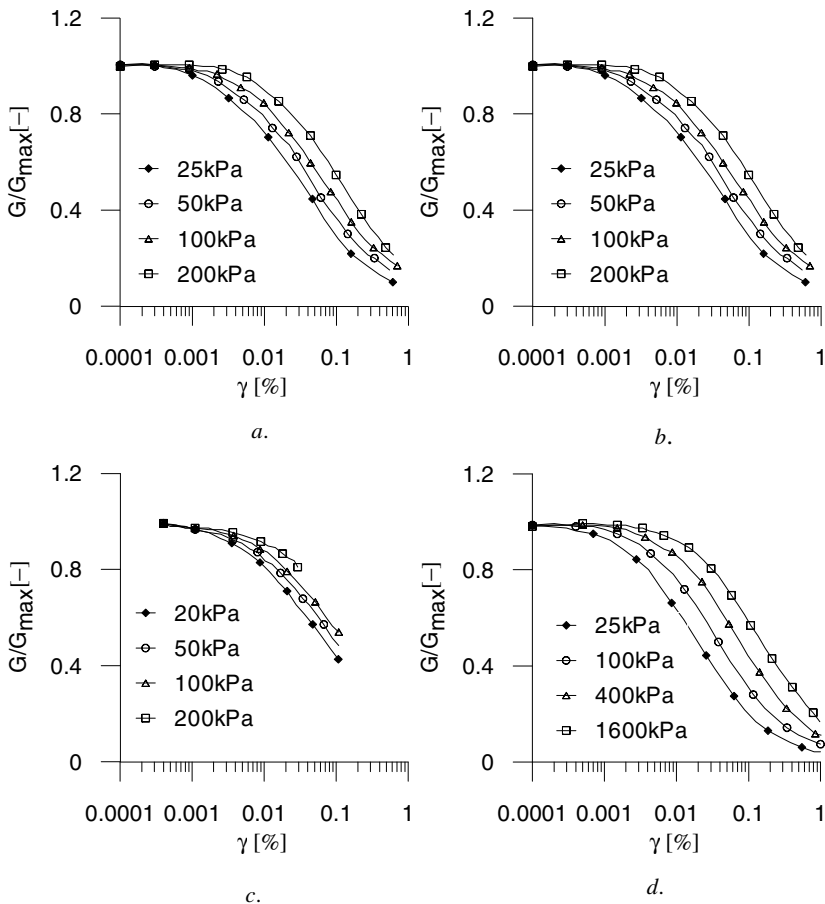


**Fig. 1.** Plots of normalized shear modulus with shear strain a) after Iwasaki *et al.* (1978), b) after Kokusho (1980), c) after Ni (1987), d) after Darendeli (2001)

Iwasaki *et al.* (1978) performed resonant column and torsional shear tests on hollow specimens of saturated clean Toyoura sand under drained conditions with confining pressure ranging from 25 kPa to 200 kPa. The tests indicate that the rate of decay of the normalized shear modulus with shear strain decreases with increasing confining pressure (Figure 1a). Kokusho (1980) investigated the effect of confining pressure on normalized shear modulus reduction on the same sand using a cyclic triaxial test in the confining pressure range 20 kPa to 300 kPa. The test results show a similar effect (Figure 1b). The combined resonant column and torsional shear tests by Ni (1987) on a clean sand show a similar effect of confining pressure on the normalized shear modulus (Figure 1c). The combined resonant column and torsional shear tests by Darendeli *et al.* (2001) on silty sand cover a relatively wider range of confining pressure (from 25 kPa to 1600 kPa). The measured effect of confining pressure is in line with the previous test results (Figure 1d)

In general, the various experiments show that the higher the confining pressure the lower is the rate of decay of the stiffness in the small strain regime. If parameters need be material constants, as advocated in several hypoplastic models and recently in some elastoplastic models, then this influence needs to be considered in the constitutive equations. As will be shown later, the existing Intergranular Strain formulation is insensitive to confining pressure hence the trend is unique for a given set of the Intergranular Strain parameters. The effect of confining pressure can be introduced in a simple way as will be shown later in this paper.

### 3 The Intergranular Strain Formulation for the Hypoplastic and Elastoplastic Models

Niemunis & Herle (1997) introduced a new tensorial state variable to the hypoplastic theory, which they called Intergranular Strain. The proposed model is formulated in strain space and is a one brick type model (Simpson 1992).

The various assumptions are depicted in Figure 2. The recent deformation history is stored in the Intergranular Strain tensor with a generalized evolution rule that Niemunis & Herle (1997) defined as

$$\overset{\circ}{\mathbf{h}} = \begin{cases} (\mathbf{I} - \hat{\mathbf{h}} \otimes \hat{\mathbf{h}} \rho^{\beta_r}) : \dot{\boldsymbol{\varepsilon}}, & \hat{\mathbf{h}} : \dot{\boldsymbol{\varepsilon}} > \mathbf{0} \\ \dot{\boldsymbol{\varepsilon}}, & \hat{\mathbf{h}} : \dot{\boldsymbol{\varepsilon}} < \mathbf{0} \end{cases}, \rho = \frac{\|\mathbf{h}\|}{R} \tag{2}$$

where  $\mathbf{I} = \frac{1}{2}(\delta_{ij}\delta_{kl} + \delta_{ik}\delta_{jl})$ ,  $\hat{\mathbf{h}} = \mathbf{h}/\|\mathbf{h}\|$  is the direction of the Intergranular Strain,  $R$  is a material constant and  $\beta_r$  is a parameter that controls the Intergranular Strain evolution rate. The symbol  $\otimes$  denotes the dyadic product, and the colon: denotes the scalar product between two tensors. When (as in the original formulation) the rate of deformation is used as measure of strain rate the evolution rule in Equation (2) is objective.

Assuming a linear decrease of the normalized shear modulus  $G/G_{\max}$  with  $\rho^\chi$  and linear increase with direction,  $\mathbf{f}(\boldsymbol{\theta}) = \hat{\mathbf{h}} \otimes \hat{\mathbf{h}} : \mathbf{d}$ , where  $\chi$  is model parameter for

non-linearity of the tangent stiffness degradation with  $\rho$ ; and  $\mathbf{d}$  is the direction of the current strain rate (See Figure 2), the interpolated hypoplastic stiffness  $\mathbf{M}$  is given by (Niemunis & Herle 1997)

$$\mathbf{M} = [m_R - \rho^\chi (m_R - m_T)] \mathbf{L} + \rho^\chi \begin{cases} (1 - m_T) \mathbf{L} : \hat{\mathbf{h}} \otimes \hat{\mathbf{h}} + \mathbf{N} \otimes \hat{\mathbf{h}}, & 0^\circ \leq \theta \leq 90^\circ \\ (m_R - m_T) \mathbf{L} : \hat{\mathbf{h}} \otimes \hat{\mathbf{h}}, & 90^\circ \leq \theta \leq 180^\circ \end{cases} \quad (3)$$

The matrices  $\mathbf{L}$  and  $\mathbf{N}$  are the linear and non linear parts of the hypoplastic stiffness tensor. The tensorial quantities  $\mathbf{L}$  and  $\mathbf{N}$  depend generally on tensorial and state dependent scalar functions of a particular hypoplastic model (See *e.g.*, Wolfersdorff 1996, Masin 2005). Detail derivation of Equation (3) is given in Tsegaye *et al.* (2010a). In the formulation of the Intergranular Strain, five parameters are involved, namely  $-m_R$ ,  $m_T$ ,  $\beta_r$ ,  $R$  and  $\chi$ . The procedures to determine these parameters are presented in Niemunis (2003). Some elaborations and alternative ways of obtaining some of the parameters are presented in Tsegaye *et al.* (2010a).

A similar approach can be devised for elastoplastic models. In elastoplastic theory, the tangent stiffness tensor  $\mathbf{C}^{ep}$  can be written as

$$\mathbf{C}^{ep} = \mathbf{C}^e + \mathbf{C}^p \quad (4)$$

where  $\mathbf{C}^e$  is elastic stiffness tensor, and  $\mathbf{C}^p$  is the plastic stiffness tensor.

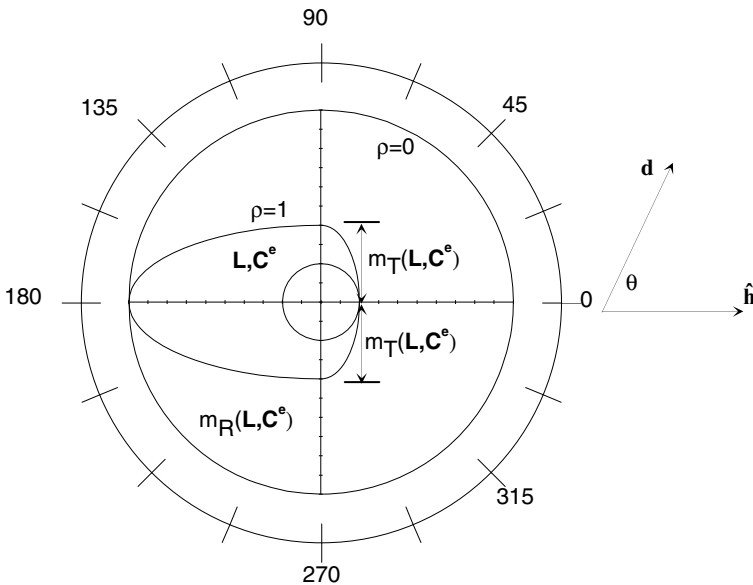


**Fig. 2.** Stiffness interpolation with the direction and magnitude of the Intergranular Strain (for  $N = 0$ )

For rate independent materials  $\mathbf{C}^p$  can be obtained from the so called consistency condition as

$$\mathbf{C}^p = -\frac{1}{\frac{\partial f}{\partial \boldsymbol{\sigma}} : \mathbf{C}^e : \frac{\partial g}{\partial \boldsymbol{\sigma}} - H} \mathbf{C}^e : \frac{\partial g}{\partial \boldsymbol{\sigma}} \otimes \frac{\partial f}{\partial \boldsymbol{\sigma}} : \mathbf{C}^e \quad (5)$$

where  $g$  is plastic potential function,  $f$  is yield function and  $H$  is plastic modulus.

Then the elastic stiffness  $\mathbf{C}^e$  can be substituted in terms of the linear hypoplastic stiffness  $\mathbf{L}$  and  $\mathbf{C}^p$  can be substituted in terms of  $\mathbf{N} \otimes \hat{\mathbf{h}}$  in Equation (3) with a slight adjustment on the plastic modulus,  $H$ , as

$$H_h = \left[ m_R - \rho^\chi (m_R - m_T) \right] H + \rho^\chi H \begin{cases} (1 - m_T) \hat{\mathbf{h}} : \mathbf{d}, & \hat{\mathbf{h}} : \mathbf{d} \geq 0 \\ (m_R - m_T) \hat{\mathbf{h}} : \mathbf{d}, & \hat{\mathbf{h}} : \mathbf{d} \leq 0 \end{cases} \quad (6)$$

### 3.1 Extension of Intergranular Strain for Influence of Confining Pressure

In the original formulation of the Intergranular Strain, the normalized shear modulus is insensitive to the effect of confining pressure for a set of the Intergranular Strain parameters. This can be easily deduced from the following equations (Tsegaye *et al.* 2010a). derived for monotonic shear deformation

$$\gamma_{G/G_R} = R(1 + \rho) + R \sum_{n=1}^{\infty} \frac{1}{n\beta_r + 1} \rho^{n\beta_r + 1} \quad (7)$$

$$\rho = \left\{ \frac{m_R}{m_R - 1} (1 - G/G_{\max}) \right\}^{\frac{1}{\chi}}, \quad (8)$$

where  $\gamma_{G/G_{\max}}$  is the shear strain for a given normalized shear modulus  $G/G_{\max}$ .

Equations (7) and (8) imply that the decay of  $G/G_{\max}$  with  $\gamma_{G/G_{\max}}$  is unique for a given set of the Intergranular Strain parameters regardless of the confining pressure. Therefore, one requires a different set of parameters to capture the effect of confining pressure.

As can be seen from Figure 3, the parameter,  $\beta_r$ , controls the rate of evolution of Intergranular Strain. Here it is proposed to introduce the influence of confining pressure by updating this particular parameter as

$$\beta_r = \beta_r^{ref} \left( \frac{p + c \cot \varphi_c}{p_{ref}} \right)^{-m_3} \quad (9)$$

where  $\beta_r^{ref}$  is a parameter at the reference pressure  $p_{ref}$  and  $m_\beta$  is parameter that takes the sensitivity of  $\beta_r$  for confining pressure. The parameter  $m_\beta$  can be a function of plasticity index. *i.e.*, the higher the plasticity index, the higher should  $m_\beta$  be. Considering the influence of plasticity index can be important especially in hypoplastic models for clays (*e.g.*, Masin 2005) and elastoplastic models for clays (*e.g.*, Grimstad & Degago 2010).

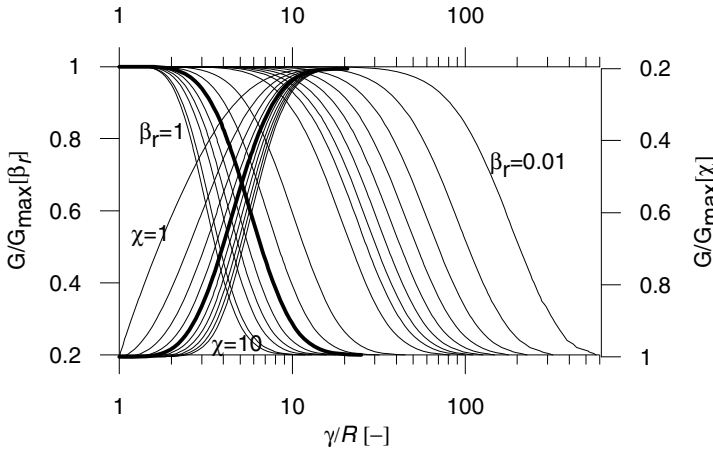


**Fig. 3.** Effect of the parameters  $\chi$  and  $\beta_r$  on the tangent stiffness degradation curve (Tsegaye *et al.* 2010). The reference curves (in bold) are for  $m_R = 5, \chi = 6, \beta_r = 0.5$

The data presented above are simulated by using the extended Intergranular Strain formalism. For all simulations,  $R = 10^{-4}, m_R = 5, m_T = 2.5$  and  $\chi = 1$  are used. The values of  $\chi$  and  $\beta_r^{ref}$  obtained in this study (Table 1) are lower compared to values reported elsewhere. The reason is that for higher values of the parameter  $\chi$  and  $\beta_r^{ref}$  the trend and the rate of decay of the normalized shear modulus are highly unrealistic and do not follow experimental results.

**Table 1.**  $\beta_r^{ref}$  and  $m_\beta$  for the tests presented in Figure 1

Sand Data	$\beta_r^{ref}$	$m_\beta$	Source
Figure 1a, Toyoura sand	0.17	0.5	Iwasaki, <i>et al.</i> (1978)
Figure 1b & 1c	0.12	0.4	Kokusho (1980), Ni (1987), respectively
Figure 1d	0.3	0.5	Darendeli <i>et al.</i> (2001)

As shown in Figure 4, the effect of confining pressure on the rate of decay of the normalized shear modulus is fairly captured by the modified model.

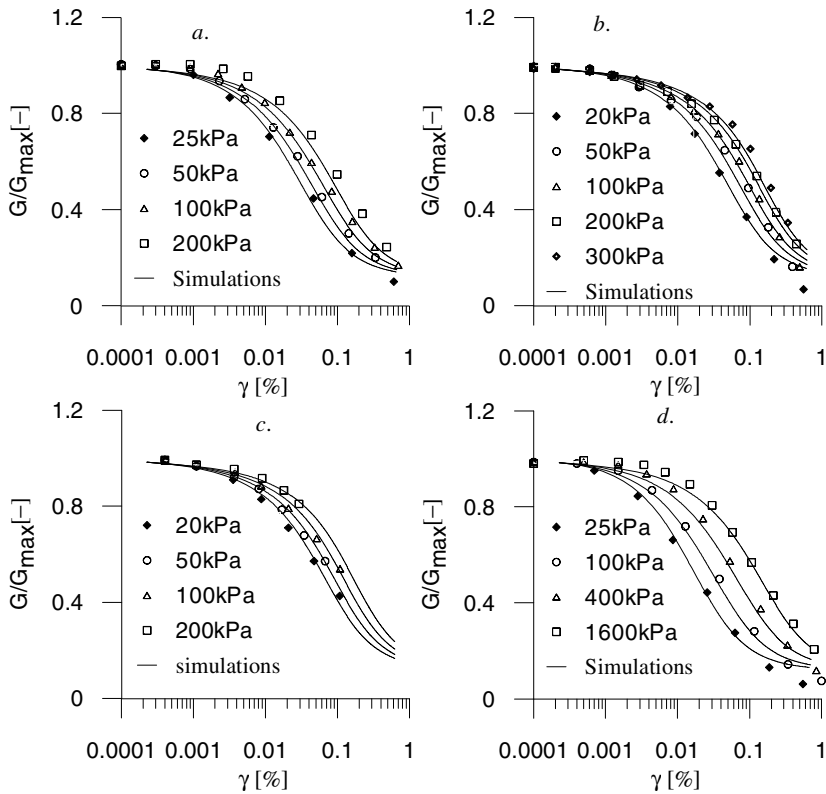


**Fig. 4.** Numerical and experimental plots of normalized secant shear modulus with shear strain using the modified Intergranular Strain formulation (parameters in Table 1)- a) Iwasaki *et al* (1978), b) Kokusho (1980), c) Ni (1987) and d) Darendeli *et al* (2001)

## 4 Summary and Conclusion

The Intergranular Strain formulation considers a relatively higher stiffness at small strain and during change of loading direction. For a given set of parameters, the Intergranular Strain formulation gives a unique evolution of the decay of the normalized shear modulus with shear strain. The rate of decay and the trend of evolution of the normalized shear modulus with shear strain are somewhat different from trends obtained from laboratory investigations. This aspect requires further research. In this paper a simple modification to the Intergranular Strain formalism is presented so that the influence of mean normal stress on the evolution of the normalized shear modulus is incorporated. Furthermore, a possible way of applying the Intergranular Strain to elastoplastic models is briefly discussed. The

implication of the current extension on cyclic responses must be further investigated. For clayey soils, the new parameter  $m_{\beta}(PI, OCR, \dots)$  can be generally a function of plasticity index and overconsolidation ratio.

## References

- [1] Benz, T.: Small-strain stiffness and its numerical consequences. PhD Thesis. Stuttgart University, Germany (2007)
- [2] Darendeli, M.B., Stokoe II, K.H., Rathje, E.M., Roblee, C.J.: Importance of confining pressure on nonlinear soil behavior and its impact on earthquake response predictions of deep sites. In: XVth International Conference on Soil Mechanics and Geotechnical Engineering, August, Istanbul, Turkey (2001)
- [3] Grimstad, G., Degago, S.A.: A non associated creep model for structured anisotropic clays (n-SAC). In: 7th European Conference on Numerical Methods in Geotechnical Engineering, Trondheim, Norway, pp. 3–8 (2010)
- [4] Hardin, B.O., Richart, F.E.: Elastic wave velocities in granular soils. Proc. ASCE: Journal of the Soil Mechanics and Foundations Division 89(SM1), 33–65 (1963)
- [5] Iwasaki, T., Tatsuoka, F., Takagi, Y.: Shear Moduli of Sands under Cyclic Torsional shear Loading. Soils and Foundations 18(1), 39–56 (1978)
- [6] Janbu, N.: Soil Compressibility as determined by oedometer and triaxial tests. In: Proc. 3rd ECSMFE, vol. 1, pp. 19–25 (1963)
- [7] Kokusho, T.: Cyclic Triaxial Test of Dynamic Soil Properties for Wide Strain Range. Soils and Foundations 20(2), 45–60 (1980)
- [8] Lansivaara, T.: A study of the mechanical behavior of soft clay. PhD Thesis, Norwegian University of Science and Technology, Norway (1999)
- [9] Masin, D.: A hypoplastic constitutive model for clays. Int. J. Numer. Anal. Meth. Geomech. 29, 311–336 (2005)
- [10] Ni, S.-H.: Dynamic properties of sand under true triaxial stress states from resonant column/torsional shear Tests, PhD. Dissertation, University of Texas at Austin (1987)
- [11] Niemunis, A.: Extended hypoplastic models for soils. Bochum University Soil Mechanics and Geotechnics (2003)
- [12] Niemunis, A., Herle, I.: Hypoplastic model for cohesionless soils with elastic strain range. Mech. Res. Comm. 2(4), 279–299 (1997)
- [13] Ohde, J.: Zur Theorie der Druckverteilung im Baugrund. GBauingenieur 20, 451 (1939)
- [14] Stokoe, K.H., Darendeli, M.B., Gilbert, R.B., Menq, F.-Y., Choi, W.-K.: Development of a new family of normalized modulus reduction and material damping curves. In: Proc., NSF/PEER Int. Workshop on Uncertainties in Nonlinear Soil Properties and their Impact on Modeling Dynamic Soil Response, Univ. of California at Berkeley (2004)
- [15] Simpson, B.: Retaining structures: displacement and design. The 32<sup>nd</sup> Rankine lecture. Géotechnique 42(4), 541–576 (1992)
- [16] Tsegaye, A.B., Molenkamp, F., Brinkgreve, R.B.J., Bonnier, P.G., de Jager, R., Galavi, V.: Modeling liquefaction behaviour of sands by means of hypoplastic model. In: 7th European Conference on Numerical Methods in Geotechnical Engineering, Trondheim, Norway, pp. 81–87 (2010a)
- [17] Vucetic, M., Dobry, R.: Effect of Soil Plasticity on Cyclic Response. ASCE. Journal of Geotechnical Engineering 117(1), 89–107 (1991)
- [18] Wolffersdorff, P.A.: A hypoplastic relation for Granular Materials with a Predefined Limit State Surface. Mechanics of Cohesive-Frictional Soils 1(3), 251–271 (1996)

# On Shear-Volume Coupling in Deformation of Soils

A.B. Tsegaye, S. Nordal, and Thomas Benz

Norwegian University of Science and Technology, Trondheim, Norway  
anteneh.tsegaye@ntnu.no

**Abstract.** Mathematical formalisms of shear-volume coupling for geomaterials, also known as stress-dilatancy relationships, are central components to a majority of constitutive models for soils. This paper investigates various stress-dilatancy formulations comparatively such that the consequence of adopting them in constitutive modeling can be easily understood.

**Keywords:** Stress-dilatancy, dissipation, constitutive models.

## 1 Introduction

Upon shearing, soils compact, dilate, or may deform without change in volume. The latter state is usually referred to as the critical state. Until the critical state is reached, often significant volume change can be observed that affects soil deformation behavior significantly (*e.g.*, strength, pore pressure generation, *etc.*)

A list of variables that may affect the quantitative aspect of shear-volume coupling of soils, referred also as stress-dilatancy relationships, has been proposed by Li & Dafalias (2000). Adding some variables that were not considered in Li & Dafalias (2000) but suggested in other literature (*e.g.*, Rowe 1962, Shimizu 1982, Gutierrez & Ishihara 2000), the dilatancy behavior of soils, quantified as a ratio of volumetric strain rate  $\dot{\epsilon}_v$  to deviatoric strain rate  $\dot{\epsilon}_q$  may be given by

$$\frac{\dot{\epsilon}_v}{\dot{\epsilon}_q} = f(\eta, e, p, \Delta, Q, c, C_i, OCR, m_s, etc.), \quad (1)$$

where  $\eta$  is stress ratio,  $e$  is void ratio,  $p$  is confining pressure,  $\Delta$  is non-coaxiality between principal stresses and principal strain rates,  $Q$  is evolving tensor of anisotropy,  $c$  is cohesion,  $C_i$  are intrinsic material constants (*e.g.*, values at the critical state, grain characteristics, *etc.* that undergo little change during deformation),  $OCR$  is the overconsolidation ratio and  $m_s$  is shear mode. The influence of confining pressure and void ratio is often considered via a derived state variable,  $\Psi$ , called state parameter (Been & Jefferies 1985).

In this paper only some of the variables, such as  $\eta$ ,  $m_s$ ,  $C$ ,  $e$ ,  $p$ ,  $\Delta$ , in Equation (1) are investigated in terms of some basic classical stress-dilatancy equations (Taylor 1948, Rowe 1962, Roscoe & Schofield 1963, Houslyby 1993) and some extended forms. The various formulations are comparatively studied and some of the underlying assumptions are exposed. Sign convention of soil mechanics, *i.e.*, compression positive and tension negative, is adopted throughout the paper.

## 2 Effect of Stress-Ratio and Shear Mode

In this section, stress-dilatancy relationships that stem from Taylor's (1948) work hypothesis, Rowe's (1962) minimum energy ratio hypothesis and some modified forms, and Houslyby's (1991, 1993) work hypothesis are comparatively presented. In light of these hypotheses the relationship between dilatancy and stress ratio, which is a principal variable in various stress-dilatancy relationships, is investigated. In addition, the influence of shearing modes implied in the hypotheses is discussed.

### 2.1 The Taylor, The Cam-Clay and the Houslyby Work Hypotheses

According to Taylor, the shear strength of sands is due to the internal frictional resistance between grains and interlocking. Sands generally undergo increase in volume when the  $\phi$ -obliquity condition (*phase transformation point*) is reached, and the part of the shearing stress that is acting to overcome interlocking may also be said to be supplying the energy that is being expended in volume increase as Taylor puts it. Taylor demonstrated his hypothesis in a direct shear box test of Toyoura sand subjected to a vertical load  $\sigma_n A$  of shear area  $A$ . A thickness increase  $\Delta h$  of the sample is recorded for shearing displacement  $\Delta l$ . He argues that the strain energy  $\Delta W_e$  used for the volume expansion must be supplied by a portion  $\tau_e$  of the total shear stress  $\tau_t$  such that

$$\Delta W_e = \sigma_n A \Delta h = \tau_e A \Delta l = \tau_{cv} A \Delta l - \tau_t A \Delta l, \quad (2)$$

where  $\tau_{cv}$  is the shear stress observed at constant volume shearing. In relating shear stress  $\tau_t$  and  $\tau_{cv}$  to normal stress  $\sigma_n$  by the mobilized friction angle  $\varphi_m$  and the friction angle at constant volume shearing  $\varphi_{cv}$ , respectively and furthermore selecting appropriate strain rate measures  $\dot{\epsilon}_n$  for normal strain rate and  $\dot{\gamma}$  for shear strain rate and rearranging Equation (2) leads to

$$\frac{\dot{\epsilon}_n}{\dot{\gamma}} = \tan \varphi_{cv} - \tan \varphi_m \quad (3)$$

Taylor's work hypothesis can be extended for different shear modes, for example for triaxial extension, triaxial compression and 2D plane strain modes as

$$\dot{W} = p \dot{\epsilon}_v + q \dot{\epsilon}_q = M_{cv}^{m_s} p \dot{\epsilon}_q, \quad (4)$$

where  $p = (r_1\sigma_1 + r_3\sigma_3)/(r_1 + r_3)$  &  $q = (\sigma_1 - \sigma_3)/(3 - r_1r_3)$  are mean stress and deviatoric stress; and  $\dot{\epsilon}_v = r_1\dot{\epsilon}_1 + r_3\dot{\epsilon}_3$  &  $\dot{\epsilon}_q = 2(\dot{\epsilon}_1 - \dot{\epsilon}_3)/(r_1 + r_3)$  are volumetric strain rate and deviatoric strain rate, respectively; and

$$M_{cv}^{m_s} = \frac{3r_1r_3 \sin \varphi_{cv}}{3 - (r_3 - r_1) \sin \varphi_{cv}} \tag{5}$$

where  $r_i$  are such that  $r_1 = r_3 = 1$  for 2D plane strain,  $r_1 = 2r_3 = 2$  for triaxial extension and  $2r_1 = r_3 = 2$  triaxial compression.

If the constant volume friction angle is replaced by the critical state friction angle, the triaxial compression case is identical to the work hypothesis put forward by Roscoe & Schofield (1963) used in the original Cam-Clay model and hence is also referred to as the Cam-Clay work hypothesis.

Equation (4) can be extended for intermediate shear modes by introducing a Lode angle dependent function -which is trivial but not pursued in this paper. From the work hypothesis in Equation (4), considering the critical state friction angle,  $\varphi_c$  in terms of the constant volume friction angle  $\varphi_{cv}$ , follows

$$\frac{\dot{\epsilon}_v}{\dot{\epsilon}_q} = M_c^{m_s} - \eta, \tag{6}$$

where  $\eta = q/p$  is the stress ratio.

Houlsby (1991, 1993), in an attempt to capture effect of different types of shear modes, proposed a work hypothesis of the form

$$\dot{W} = \frac{2}{3} \tan \varphi_{cv} \sqrt{\sum_{i=1}^3 \sum_{j=1}^3 \sigma_i \sigma_j (\dot{\epsilon}_i - \dot{\epsilon}_j)^2}, \tag{7}$$

where  $\varphi_{cv}$  is the constant volume friction angle in triaxial compression and  $\sigma_i, \sigma_j$  and  $\dot{\epsilon}_i, \dot{\epsilon}_j$  are principal stress components and principal strain rate components ( $i = 1, 3, j = 1, 3$ ). For triaxial compression, 2D plane strain and triaxial extension shear modes, Equation (7) can be rearranged to

$$N_\psi = \frac{3N_\sigma - 2\sqrt{2} \tan \varphi_{cv} \sqrt{m_s N_\sigma}}{3m_s + 2\sqrt{2} \tan \varphi_{cv} \sqrt{m_s N_\sigma}} \tag{8}$$

where  $N_\psi = -\dot{\epsilon}_3/\dot{\epsilon}_1$ ,  $N_\sigma = \sigma_1/\sigma_3 = (1 + \sin \varphi_m)/(1 - \sin \varphi_m)$ , and  $\varphi_m$  and  $m_s$  are mobilized friction angle and shear mode coefficient ( $m_s = 1$  for plane strain,  $m_s = 2$  for triaxial compression and  $m_s = 0.5$  for triaxial extension), respectively.

To compare the two approaches, a function  $f_\psi$  is defined as

$$f_\psi := \frac{m_s N_\psi - 1}{m_s N_\psi + 1}. \tag{9}$$

Equation (9) will be referred to as dilatancy function for easier reference.

In Figure 1, the extended Taylor's work hypothesis shows a distinct difference in the stress-dilatancy behaviour of the different shear modes. This approach also gives a good platform for bounding surface plasticity models. As long as the critical state friction angle is shear mode independent the phase transformation happens at a unique friction angle, whereas Houlsby's work hypothesis gives a slightly different phase transformation angle in the plane strain condition.

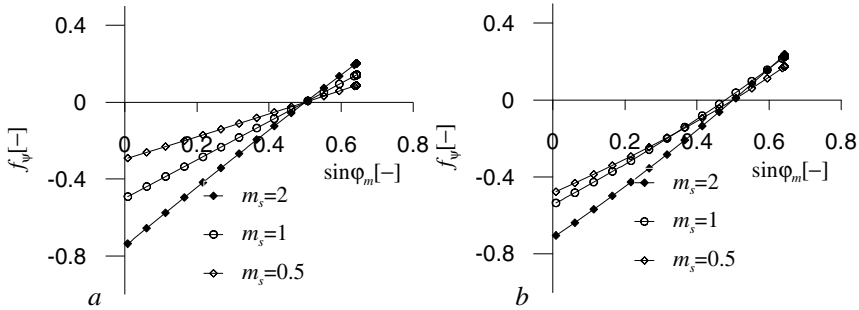


**Fig. 1.** Plots of evolution of dilatancy function for different shear modes a) extended Taylor work hypothesis and b) Houlsby's work hypothesis,  $\varphi_{cv} = 30^0$

## 2.2 Rowe's Stress-Dilatancy Theory and Some Modifications

Considering a pack of orderly arranged steel rods (Figure 2) and spheres, Rowe (1962) obtained "the ratio of the work done per unit volume of the major principal stress to the work done by minor principal stress by the assembly" as:

$$K = -m_s \frac{\sigma_3 \dot{\epsilon}_3}{\sigma_1 \dot{\epsilon}_1} = \frac{\tan(\varphi_\mu + \beta)}{\tan \beta} \quad (10)$$

where  $\varphi_\mu$  is the interparticle friction angle,  $\beta$  is the direction of interparticle sliding plane relative to the major principal stress direction as depicted in Figure 2, and  $m_s$  is shear mode coefficient as defined in Equation (8).

Further, Rowe (1962) established the relationship between  $\varphi_\mu$  and  $\beta$  by considering the variation  $\partial K / \partial \beta = 0$  which in general yields

$$\beta = (2n-1) \frac{\pi}{4} - \frac{\varphi_\mu}{2}, \quad n = 1, 2, 3, \dots \quad (11)$$

Substituting Equation (11) into Equation (10) for  $n = 1$  gives

$$K = \tan^2 \left( \frac{\pi}{4} + \frac{\varphi_\mu}{2} \right). \quad (12)$$

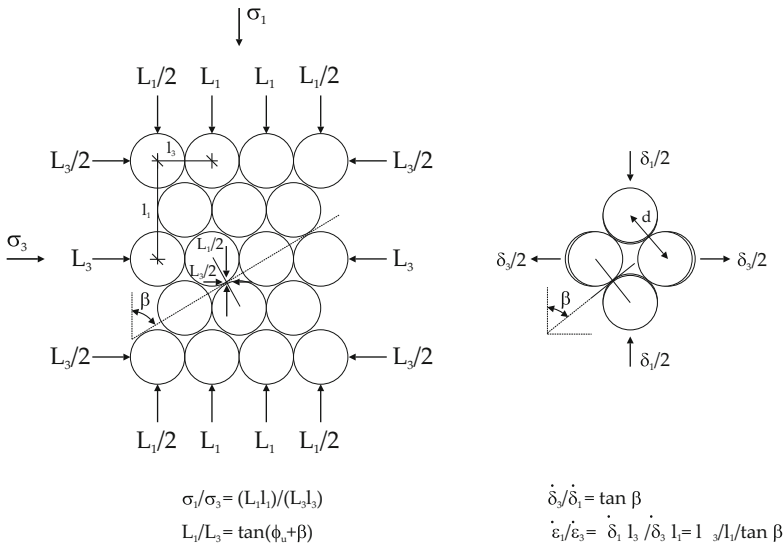


Fig. 2. A pack of orderly arranged cylindrical bars (after Rowe 1962)

The objections towards Rowe’s minimum energy ratio hypothesis are first on the hypothesis itself (e.g., de Jong 1976) and secondly its consequence as it appears to restrict the value of  $\beta$  which is fabric dependent (e.g., Guo & Wan 2007). De Jong (1976) argued that there was no reason to accept the minimum energy ratio hypothesis prior to rigorous proof. The fact that “test results seem to support the relation”, led de Jong to the speculation that “there might exist another reason for the validity of the relation.” He considered a set of constraints, which he called, friction rules, in his approach. In short, de Jong’s approach is to maximize the function

$$\varphi = \arctan(K \tan \beta) - \beta, \tag{13}$$

that is obtained by rearranging Equation (10). Thus de Jong (1976), considering the variation  $\partial\varphi/\partial\beta = 0$  and setting  $\varphi_{\max} = \varphi_\mu$ , arrived at the same expression as Rowe’s, i.e., Equation (12).

Note that de Jong’s derivation requires a constant energy ratio,  $K$ , in addition to the friction rules he stated. Hence the conclusion that the validity of Rowe’s theory is due to friction rules alone is questionable. In addition, the claim that the interparticle friction angle,  $\varphi_\mu$ , is the maximum friction angle is not supported by experiments.

Niiseki (2001) derived the same expressions in a direct variational approach. In Niiseki’s approach, the friction angle to be used in the stress-dilatancy equation appears to be constant volume friction angle, not the interparticle friction angle. Furthermore, the constant volume friction angle can be shear mode dependent.

Rearranging Equation (12) in light of the definition in Equation (9) and substituting  $\varphi_c$  in terms of  $\varphi_\mu$  one obtains

$$f_\psi = \frac{\sin \varphi_m - \sin \varphi_c}{1 - \sin \varphi_m \sin \varphi_c} \tag{14}$$

Notice that the dilatancy function  $f_\psi = -\sin \psi_m$ , where  $\psi_m$  is the dilatancy angle (Figure 3a). Here it is deemed necessary to mention two things. First, in contrast to both the extended Taylor’s and Houlsby’s work hypotheses, Equation (14) implies that  $f_\psi$  is shear mode independent for a unique critical state friction angle,  $\varphi_c$ . Secondly, the presentation of  $f_\psi$  as the sine of an angle does not hold for the extended Taylor work hypothesis and Houlsby’s work hypothesis as both can be greater than one for  $\varphi_c > 37^\circ$  for the triaxial compression deformation mode.

In Figure 3b the Cam-Clay (extended Taylor) work hypothesis, Houlsby’s work hypothesis and Rowe’s stress-dilatancy equation are compared in triaxial compression. Before the phase transformation, Rowe’s stress-dilatancy equation appears less contractive than the other two.

In literature, it is reported that Rowe’s stress-dilatancy is over contractive at lower mobilization levels (e.g., Schanz 1998, Soreide 2003, Wehnert 2006). However, this seems to be the case especially in double hardening elastoplastic models where volumetric strain is contributed not only from the shear-volume coupling but also the volumetric hardening. Volumetric hardening adds up a significant amount of contraction. Since the numerical approach to double hardening models involves mostly Koiter’s (Koiter 1960) rule, i.e., contributions are arithmetically added when both the volumetric hardening and the shear hardening are active, it is difficult on which mechanism to put the blame on. The propositions of Schanz (1998), Soreide (2003) and Wehnert (2006) are to effect down the mobilized dilatancy in the contractive region (See Figure 4). These approaches have also been discussed in Benz (2007). In Schanz (1998) the shear-volume coupling was restricted only to the dilative regime so that contraction is solely contributed from the cap whereas Wehnert (2006) considered a lower bound of  $f_\psi = -0.07$ .

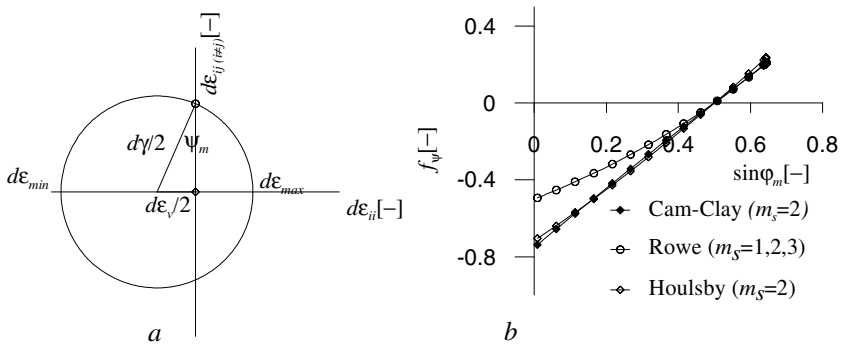


**Fig. 3.** a) Rowe’s dilatancy angle in Mohr’s strain circle b) comparison of various stress-dilatancy relationships for triaxial compression condition ( $\varphi_\mu = \varphi_{cv} = 30^\circ$ ).

In both approaches, liquefaction type behaviours cannot be captured. Soreide's approach is to scale Equation (14) by a factor  $(\sin \varphi_m / \sin \varphi_p)^{\tilde{p}}$ , where  $\tilde{p}$  is a parameter and  $\varphi_p$  is the peak friction angle. The peak friction angle, however, is a state dependent quantity which means that samples of the same soil at different initial states (especially dilative samples) require different values of  $\varphi_p$ . Indications are also that Soreide's parameter may be state dependent.

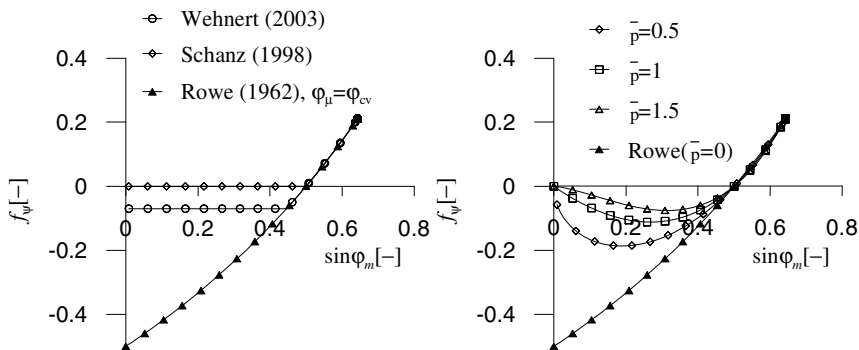


Fig. 4. Modifications on Rowe's stress-dilatancy equation.  $\varphi_\mu = \varphi_{cv} = 30^\circ$  is considered

### 3 Effect of Density and Pressure

Another aspect considered in literature is the effect of density and pressure. The formulations investigated above consider stress ratio as the only independent variable in the stress-dilatancy relationships. Hence all have a unique phase transformation point (with the exception of Houlsby's work hypothesis that gives a slightly different phase transformation point for 2D plane strain case). However, experiments show that the phase transformation point depends on density and pressure (see e.g., Li & Dafalias 2000). Modifications to account for effect of density and pressure have been proposed in literature.

Rowe (1962) introduced a density dependent friction angle,  $\varphi_f$ , in place of the interparticle friction angle,  $\varphi_\mu$ , in the interval  $\varphi_\mu \leq \varphi_f \leq \varphi_{cv}$ , where  $\varphi_{cv}$  is the constant volume friction angle.

Wan & Guo (1998) proposed a modified energy ratio by considering  $\sin \varphi_{cv} = f_{sd} \sin \varphi_c$ , where  $\varphi_c$  is the critical state friction angle,  $f_{sd} = (e/e_c)^{\alpha_{GW}}$  is the Guo-Wan state function,  $e$  is void ratio,  $e_c$  is void ratio at the critical state for the same confining pressure and  $\alpha_{GW}$  is a model parameter.

Li & Dafalias (2000) emphasized the fact that dilatancy is not uniquely related to stress ratio alone. In what they have called ‘state dependent dilatancy’ Li & Dafalias (2000) put forward a generalized expression  $\dot{\epsilon}_v/\dot{\epsilon}_q = f(\eta, e, Q, C)$ . They also proposed a particular stress-dilatancy equation by modifying the Cam-Clay work hypothesis as

$$\frac{\dot{\epsilon}_v}{\dot{\epsilon}_q} = \frac{d_0}{M_c} \left( M_c e^{m_{LD}\Psi} - \eta \right), \quad (15)$$

where  $d_0$  and  $m_{LD}$  are the Li-Dafalias material parameters and  $\Psi$  is the state parameter (Been & Jefferies 1985). Similar state dependent stress-dilatancy formulations have been put forward, *e.g.*, Manzari & Dafalias (1997), Li (1997), Li *et al.* (1998).

#### 4 Effect of Non-coaxiality

In all stress-dilatancy equations discussed in this paper, principal stresses and principal strain rates are assumed coaxial. However, in anisotropic media, non-coaxiality has been observed through experimental studies (*e.g.*, Roscoe *et al.* 1967, Roscoe 1970, Matsuoka *et al.* 1988, and Gutierrez *et al.* 1991) and numerical micromechanics (*e.g.*, Cundal & Strack 1979, Thornton & Barnes 1986, Arthur *et al.*, 1986, Thornton & Zhang 2006, Yu 2008, Wang *et al.* 2007).

De Jong (1976) questioned the validity of assumption of coaxiality in Rowe’s stress-dilatancy theory. Later Gutierrez & Wang (2009) proposed a non-coaxial version of Rowe’s stress-dilatancy equation such that  $\sin \hat{\psi}_m = c \sin \psi_m$  where  $c$  is the Gutierrez-Ishihara non-coaxiality parameter. Gutierrez & Ishihara (2000) introduced non coaxiality into Taylor’s work hypothesis such that the stress ratio in the stress-dilatancy equation is given by  $\hat{\eta} = c\eta$ . Obviously, the two modifications are considerably different. This issue requires further investigation.

#### 5 Summary and Conclusions

In this paper stress-dilatancy equations that stem from Taylor’s work hypothesis, Rowe’s minimum energy ratio hypothesis are investigated. In addition Housby’s work hypothesis which is relatively new compared to the other two is studied. For ease of visualization, the well known shear modes such as triaxial compression, triaxial extension and 2D plane strain cases are considered. Furthermore, extensions of the basic equations for effect of density, pressure and non coaxiality of principal stresses and principal strain increments are briefly discussed. The dilatancy function presented in this paper enables an objective comparison of the various presented stress-dilatancy equations. The comparative presentation and illustrative graphs presented are in a spirit to ease the use of them in constitutive models.

## References

- [1] Arthur, J.R.F., Koenders, M.A., Wong, R.K.S.: Anisotropy in particle contacts associated with shearing in granular media. *Acta Mechanica* 64(1-2), 19–29 (1986)
- [2] Been, K., Jefferies, M.: A state parameter for sands. *Géotechnique* 35(2), 99–112 (1985)
- [3] Benz, T.: Small-strain stiffness and its numerical consequences. PhD Thesis. Stuttgart University, Germany (2007)
- [4] Cundal, P.A., Strack, O.D.L.: A discrete numerical model for granular assemblies. *Géotechnique* 29(1), 47–65 (1979)
- [5] De Josselin de Jong, G.: Rowe's stress-dilatancy equation based on friction. *Géotechnique* 26(3), 527–534 (1976)
- [6] Guo, P., Wan, R.: A rational approach to stress–dilatancy modelling using an explicit micromechanical formulation. In: Exadaktylos, G.E., Vardoulakis, I.G. (eds.) *Bifurcations, Instabilities, Degradations in Geomechanics*. Springer, Berlin (2007)
- [7] Gutierrez, M., Ishihara, K.: Non-coaxiality and energy dissipation in granular materials. *Soils Found.* 40(2), 49–59 (2000)
- [8] Gutierrez, M., Ishihara, K., Towhata, I.: Flow theory of sand during rotation of principal stress direction. *Soils Found.* 31(4), 121–132 (1991)
- [9] Gutierrez, M., Wang, J.: Non-coaxial version of Rowe's stress-dilatancy relation. *Granular Matter* 11(2), 129–137 (2009)
- [10] Gutierrez, M., Wang, J.: Non-coaxial version of Rowe's stress-dilatancy relation. *Granular Matter* 11(2), 129–137 (2009)
- [11] Houlsby, G.T.: How the dilatancy of soils affects their behaviour. In: *Proc. 10th ECSMF, Florence*, vol. 4, pp. 1189–1202 (1991)
- [12] Houlsby, G.T.: Interpretation of dilation as a kinematic constraint. In: Kolymbas (ed.) *Modern Approaches of Plasticity*, pp. 119–138. Elsevier, New York (1993)
- [13] Koiter, W.T.: General theorems of elastic-plastic solids. In: Snedon, I.N., Hill, R. (eds.) *Progress in Solid Mechanics*, vol. 1, pp. 165–221. North Holland, Amsterdam (1960)
- [14] Li, X.S., Dafalias, Y.F., Wang, Z.L.: State dependent dilatancy in critical state constitutive modeling of sand. *Can. Geotech. J.* 36(4), 599–611 (1999)
- [15] Li, X.S., Dafalias, Y.F.: Dilatancy for cohesion less soils. *Géotechnique* 50(4), 449–460 (2000)
- [16] Manzari, M.T., Dafalias, Y.F.: A critical state two surface plasticity model for sands. *Géotechnique* 47(2), 255–272 (1997)
- [17] Niisek, S.: Formulation of Rowe's stress-dilatancy equation based on plane of maximum mobilization. In: *Powders and Grains 2001: Proc. 4th Int. Conf. on Micromechanics of Granular Media*. Sendai., pp. 213–216 (2001)
- [18] Roscoe, K.H., Schofield, A.N.: Mechanical behaviour of an idealized 'wet' clay. In: *Proc. Eur. Conf. Soil Mech. Found. Engng.*, Wiesbaden, vol. 1, pp. 47–54 (1963)
- [19] Roscoe, K.H., Basset, R.H., Cole, E.R.L.: Principal axes observed during simple shear of sand. In: *Proc. 4th ECSMF, Oslo*, pp. 231–237 (1967)
- [20] Roscoe, K.H.: The influence of strains in soil mechanics. *Géotechnique* 20(2), 129–170 (1970)
- [21] Rowe, P.W.: Stress-dilatancy relation for static equilibrium of an assembly of particles in contact. *Proc. R. Soc. A*-269, 500–527 (1962)

- [22] Shimizu, M.: Effect of overconsolidation on dilatancy of a cohesive soil. *Soils Found.* 22(4), 121–135 (1982)
- [23] Soreide, O.K.: Mixed hardening models for frictional soils. PhD thesis, Norwegian University of Science and Technology (NTNU), Trondheim (2003)
- [24] Schanz, T.: Zur Modellierung des mechanischen Verhaltens von Reibungs-materialien. *Mitt. Inst. Für Geotechnik*, vol. 45. Universität Stuttgart (1998)
- [25] Taylor, D.W.: *Fundamentals of soil mechanics*. J. Wiley and Sons, New York (1948)
- [26] Thornton, C., Barnes, D.J.: Computer simulated deformation of compact granular assemblies. *Acta Mechanica* 64(1-2), 45–61 (1986)
- [27] Thornton, C., Zhang, L.: A numerical examination of shear banding and simple shear non-coaxial flow rules. *Phi. Mag.* 86(21-22), 3425–3452 (2006)
- [28] Wehnert, M.: Ein Beitrag zur drainerten und undrainierten analyse in der Geotechnik. PhD thesis. Universität Stuttgart (2006)
- [29] Wan, R., Guo, P.J.: A simple constitutive model for granular soils: Modified stress-dilatancy approach. *Computers & Geotechnics* 22(2), 109–133 (1998)
- [30] Wang, J., Yu, H.S., Langston, P.: Non-coaxial behaviour of granular material in simple shear tests using DEM. In: *Conference on Analysis of Discontinuous Deformation and Application to Mining and Civil Engineering*, Beijing, pp. 157–161 (2007)
- [31] Yu, H.S.: Non-coaxial theories of plasticity for granular materials. In: *Proc. 12th IACMAG*, Goa, pp. 361–378 (2008)

# Influence of Various Experimental Conditions on Shear Behavior of Compacted Sandy Soil under Unsaturated Condition

Yuan Zhang<sup>1,\*</sup>, Tatsuya Ishikawa<sup>1</sup>, Tetsuya Tokoro<sup>2</sup>, and Satoru Shibuya<sup>3</sup>

<sup>1</sup> Faculty of Engineering, Hokkaido University, Sapporo, Japan  
Kita 13, Nishi 8, Kita-ku, Sapporo, Hokkaido, Japan 060-8628  
yuanzhang11115@eng.hokudai.ac.jp

<sup>2</sup> Tomakomai National College of Technology, Tomakomai, Japan

<sup>3</sup> Graduate School of Engineering, Kobe University, Kobe, Japan

**Abstract.** The objective of this paper is to examine the influences of moisture content, loading speed, and degree of compaction on the shear behavior of compacted sandy soil under unsaturated conditions. A series of triaxial compression tests with various experimental conditions were carried out by using triaxial apparatus for unsaturated soil. The test results show that the shear strength of unsaturated soil decreases with the increase in moisture content and increases due to increment of loading speed. The effect of degree of compaction is also discussed. The results reveal that moisture content, loading speed, and degree of compaction have strong influences on the shear behavior of unsaturated sandy soil.

## 1 Introduction

In order to prevent collapse of river dike caused by flood and heavy rainfall, it is indispensable to clarify infiltration characteristic and deformation-strength characteristics of embankment materials under unsaturated condition as well as saturated condition. Kiyohara et al. (2010) [1] discussed the influence of soil structure on the shear strength behavior of volcanic soils under unsaturated condition. Nishimura et al. (2012) [2] performed some kinds of laboratory element tests for unsaturated soils using a cellulose filter, and were able to confirm the validity of using the filter as substitute for a ceramic disk. Kimoto et al. (2011) [3] carried out a series of monotonic and cyclic loading tests on sandy soil to evaluate the effects of the initial suction, the confining pressure, and the degree of compaction under fully undrained conditions. However, there are few researches for the behavior of unsaturated soils under constant water content condition.

This paper examines the changes in the mechanical behavior of unsaturated sandy soil caused by moisture content, loading speed, and degree of compaction

---

\* Corresponding author.

by conducting the constant water content (CW) triaxial compression tests using the pressure membrane method with a triaxial apparatus for unsaturated soils [4], and evaluates the effects of these factors on the shear behavior of embankment materials and the deterioration of river dike.

## 2 Experimental Method

### 2.1 Preparation of Test Specimens

In this research, fine grained gravelly sand (YodogawaBC) used at Yodogawa dike reinforcement work was employed as a test sample. Figure 1 shows the grain size distribution curve of the test sample which maximum grain size is 9.5mm along with the physical properties. Figure 2 shows the compaction curve of YodogawaBC derived from the compaction test with A-b method (JIS A 1210:2009).

A test specimen was prepared as follows. A test specimen, which size was 70mm in diameter and 170mm in height, was produced by the compaction method with 4.5 pounds rammer at three different moisture contents, namely “dry condition” ( $w=11.7\%$ ), “optimum condition” ( $w=13.9\%$ ), and “wet condition” ( $w=16.2\%$ ) as shown in Figure 2. The degree of compaction ( $D_c$ ) adopted in this research is 90.2% and 83.6%, respectively.

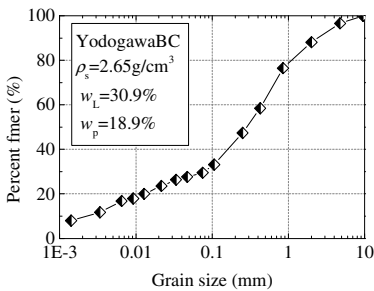


Fig. 1. Grain size distribution of test sample

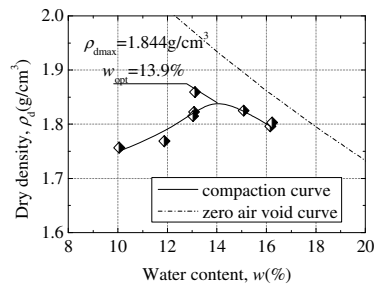


Fig. 2. Compaction curve of test sample

### 2.2 Test Method

First, after setting a test specimen in the triaxial cell, the specimen was isotropically consolidated under a prescribed net normal stress ( $\sigma_{net}$ ) of 49kPa or 98kPa until suction value become constant. Here, the  $\sigma_{net}$  is defined as  $\sigma_{net} = \sigma_c - u_a$ ,  $\sigma_c$ : confining pressure,  $u_a$ : pore air pressure (=atmospheric pressure). Next, the specimen was continuously sheared by applying an axial load at the prescribed axial strain rate ( $\dot{\epsilon}_a$ ), namely 0.033, 0.072, and 0.459%/min, until the axial strain reaches 15%. During the shear, pore air was allowed to drain, while pore water is not allowed to drain.

### 3 Results and Discussions

#### 3.1 Stress-Strain Behavior

Figure 3a and 3b show the influence of moisture contents on relationships between the deviator stress ( $q$ ), the suction ( $s$ ), the volumetric strain ( $\epsilon_v$ ), and the axial strain ( $\epsilon_a$ ) obtained from CW triaxial tests of  $D_c=90.2\%$  under  $\sigma_{net}$  of 49kPa and 98kPa, respectively. With an increasing axial strain, the deviator stress sharply increases to the peak strength. As moisture content ( $w$ ) increases, peak shear strength ( $q_{max}$ ) decreases and positive dilatancy becomes clear, regardless of  $\sigma_{net}$ .

Moreover, suction initially decreases with the increment of axial strain, and it subsequently increases regardless of  $w$  and  $\sigma_{net}$ . Finally, the suction reaches a constant value after deviator stress increases to the peak strength. Comparing the results with different moisture contents at the same  $\epsilon_a$ , the suction decreases with increasing moisture content in the same order of  $q_{max}$ , irrespective of  $\sigma_{net}$ . This indicates that moisture content influences the shear behavior of compacted fine grained gravelly sand.

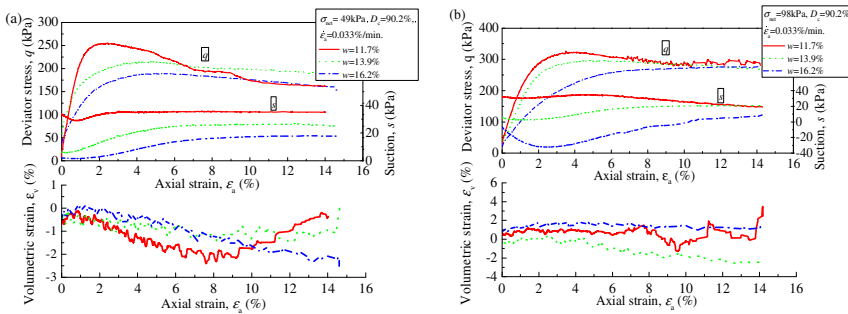


**Fig. 3.** Influence of moisture content on shear strength and suction under (a)  $\sigma_{net}=49kPa$  and (b)  $\sigma_{net}=98kPa$

Figure 4 shows the influence of loading speed on the  $q-\epsilon_a-\epsilon_v-s$  relationships of  $D_c=83.6\%$  obtained from CW triaxial tests in optimum condition at  $\sigma_{net}$  of 49kPa by comparing the results under different loadings speeds. With the decrease in loading speed, the peak strength decreases and the suction during shear tends to increase. Figure 5 shows the influence of degree of compaction on the  $q-\epsilon_a-\epsilon_v-s$  relationships obtained from CW triaxial tests in optimum condition at  $\sigma_{net}$  of 49kPa by comparing the results of  $D_c=83.6\%$  with that of  $D_c=90.2\%$ . In comparison with the result under higher degree of compaction, obvious peak point is not observed in the  $q-\epsilon_a$  relationship under lower degree of compaction. In contrast, with the increasing of degree of compaction, the peak strength increases. At high strain level, the suction tends to increase with the increase in degree of compaction.

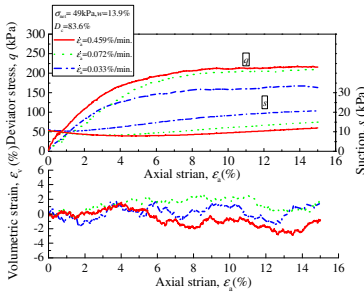


**Fig. 4.** Influence of loading speeds on shear strength and suction under  $\sigma_{net}=49\text{kPa}$

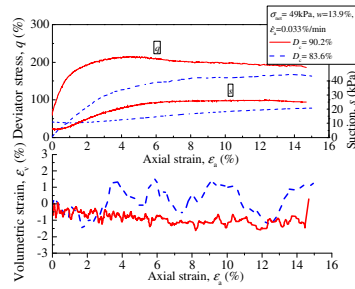


**Fig. 5.** Influence of degree of compaction on shear strength and suction under  $\sigma_{net}=49\text{kPa}$

### 3.2 Influence on Strength Parameters

In this research, Bishop’s effective stress equation as expressed by Equation 1 [5] was applied to calculate the effective stress in unsaturated soils.

$$\sigma' = (\sigma - u_a) + \chi(u_a - u_w) \tag{1}$$

$$\chi = \frac{S_r - S_{r0}}{S_{r,max} - S_{r0}} \tag{2}$$

Where,  $\sigma'$  is the effective stress,  $\sigma$  is normal stress,  $u_a$  is pore air pressure,  $u_w$  is the pore water pressure,  $\chi$  is Bishop’s effective stress parameters as shown in Equation 2.  $S_r$  is degree of saturation,  $S_{r0}$  is the residual degree of saturation,  $S_{r,max}$  is the maximum degree of saturation ( $\approx 100\%$ ). In this study,  $S_{r0}$  is 46.0% which was derived from soil-water characteristic curve of YodogawaBC as shown in Figure 6. Besides, Mohr-Coulomb’s failure criterion in terms of effective stress as expressed by Equation 3 was adopted to calculate the strength parameters, namely internal friction angle ( $\phi'$ ) and cohesion ( $c'$ ).

$$\sigma'_{1f} - \sigma'_{3f} = 2c' \cos \phi' + (\sigma'_{1f} + \sigma'_{3f}) \sin \phi' \tag{3}$$

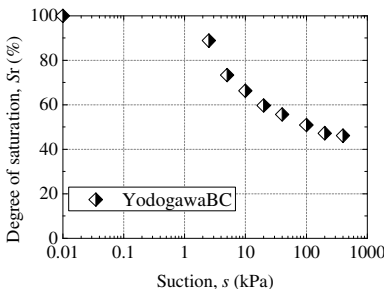


**Fig. 6.** Soil-water characteristic curve of YodogawaBC

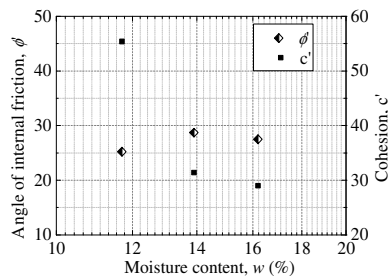


**Fig. 7.** Effects of moisture content on strength parameters

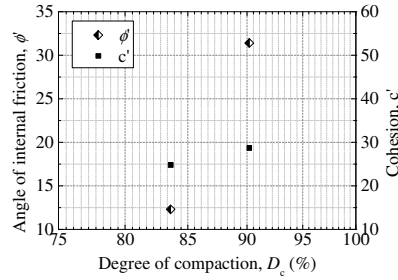
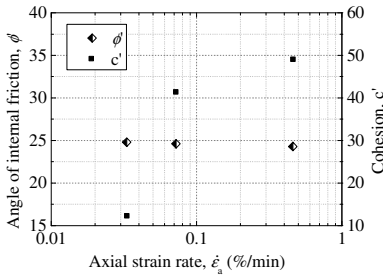


**Fig. 8.** Effects of loading speed on strength parameters

**Fig. 9.** Effects of degree of compaction on strength parameters

Figures 7 to 9 compare the internal friction angles and the cohesion under various experimental conditions. The following trends can be seen as a general shear behavior from Figure 7 to 9; In Figure 7, with the increment of moisture content, the  $c'$  decreases, while the  $\phi'$  is largely unchanged. In Figure 8, with the increase in loading speed, the  $c'$  increases, while the  $\phi'$  is nearly unchanged. In Figure 9, with increasing degree of compaction, both the  $c'$  and the  $\phi'$  increase. Accordingly, moisture content, loading speed, and degree of compaction seriously affect the  $c'$ . These results are attributed to the difference in the suction during shear.

### 4 Conclusions

The following finding can be obtained.

1. The shear strength of compacted sandy soil under unsaturated conditions decreases with the increase in moisture content and it increases due to increment of loading speed, and degree of compaction.
2. During shear, the suction tends to increase with the increase of moisture content and with the increase of degree of compaction, while in different loading speeds, with increase loading speed, the decrease in suction is observed.
3. Moisture content and loading speed seriously affect the  $c'$ , with increase of moisture content and loading speed the  $c'$  decrease. While the  $\phi'$  is unchanged with the moisture content and loading speed regardless of degree of compaction.

### References

[1] Kiyohara, Y., Kazama, M., Uzuoka, R.: Strength of behavior of undisturbed volcanic cohesive soil under unsaturated condition. In: Proc. Unsaturated Soils, pp. 115–120. Taylor & Francis Group, London (2010)

[2] Nishimura, T., Koseki, J., Fredlund, D.G., Rahardjo, H.: Microporous membrane technology for measurement of soil-water characteristic curve. Geotech. Test J. 35(1), 61–77 (2012)

- [3] Kimoto, S., Oka, F., Fukutani, J., Yabuki, T., Nakashima, K.: Monotonic and cyclic behavior of unsaturated sandy soil under drained and fully undrained condition. *Soils Found.* 51(4), 663–681 (2011)
- [4] Ishikawa, T., Tokoro, T., Ito, K., Miura, S.: Testing methods for hydro-mechanical characteristics of unsaturated soils subjected to one dimensional freeze-thaw action. *Soils Found.* 50(3), 421–440 (2010)
- [5] Bishop, A.W.: The principal of Effective Stress. *Norwegian Geotech. Inst.* 32, 1–5 (1960)

# Investigation on Strain Localization of Coal Using Micro-finite Difference Modelling

Yixin Zhao<sup>1,2,3,\*</sup>, Jingli Han<sup>3</sup>, Yaodong Jiang<sup>1,3</sup>, Zhongsheng Tian<sup>3</sup>, and You Yu<sup>3</sup>

<sup>1</sup> State Key Lab of Coal Resources and Safe Mining, China University of Mining and Technology, D11 Xueyuan Road, Beijing 100083, China

<sup>2</sup> State Key Laboratory for Geomechanics and Deep Underground Engineering, China University of Mining and Technology, D11 Xueyuan Road, Beijing 100083, China

<sup>3</sup> School of Mechanics and Civil Engineering, China University of Mining and Technology, D11 Xueyuan Road, Beijing 100083, China  
zhaoyx@cumtb.edu.cn

**Summary.** The behavior of saturated coal under compressive loads is very important for evaluating the coal mass stability and mining hazards control. This paper presents a numerical study of localized deformation process in saturated coal sample. Our approach combines X-ray micro-computed tomography (microCT) imaging with micro-finite difference analysis (microFDA). The three-dimensional images of a coal sample before compression were acquired by microCT scanner. Then the images were used to create finite difference model. The material properties of different groups in saturated coal were assumed based on previous experiments results. Finally, the FLAC<sup>3D</sup> code was employed calculate the strain localization features. The model was used to examine the material's structural response to compressive loading by studying the stress distributions and material deformation. Results indicate that the nature of internal material distribution in coal sample affect failure features greatly. It also shows that a diffuse, wide shear strain localization band progressively thinning during the failure process.

**Keywords:** Saturated coal, Compression test; Strain localization, X-ray micro-computed tomography, Micromechanical modeling, Finite difference modeling

## 1 Introduction

The localization of deformation into thin zones of intense shearing is a very common phenomenon in Geomaterials [1]. It has been studied by many researchers since the strain localization phenomenon is an important issue for

---

\* Corresponding author.

onset of failure problems [1-6]. Nowadays, Water Injection is widely applied in mining hazards control, Coal Bed Methane (CBM) development and Coal Bed Carbon Dioxide Sequestration engineering. In these applications, the mechanical behaviors and failure features of saturated coal are very important factors for evaluating feasibility of these methods [7].

In order to provide better understanding on the strain localization of saturated coal and associated effect on the failure modes, a numerical study of localized deformation process in saturated coal sample was carried out in the current investigation. Our approach combines X-ray micro-computed tomography (microCT) imaging with micro-finite difference analysis (microFDA). It is based on Mimics (Materialise Inc. France) and FLAC<sup>3D</sup> (ITASCA Inc. USA). To obtain an accurate FD model geometry, a multiple-threshold segmentation approach is employed. The 3D model is reconstructed manually with Mimics program. Results indicate that the nature of internal material distribution in coal sample affect failure features greatly. It also shows that a diffuse, wide shear strain localization band progressively thinning during the failure process. The failure modes of saturated coal showed that the specimen underwent ductile deformation dominated by cross shear splitting as primary mode of failure and tensile failure as a secondary mode. The results highlight the need to consider possible strength degradation of the coal in well wall stability control or in coal pillar stability analyses due to water saturation.

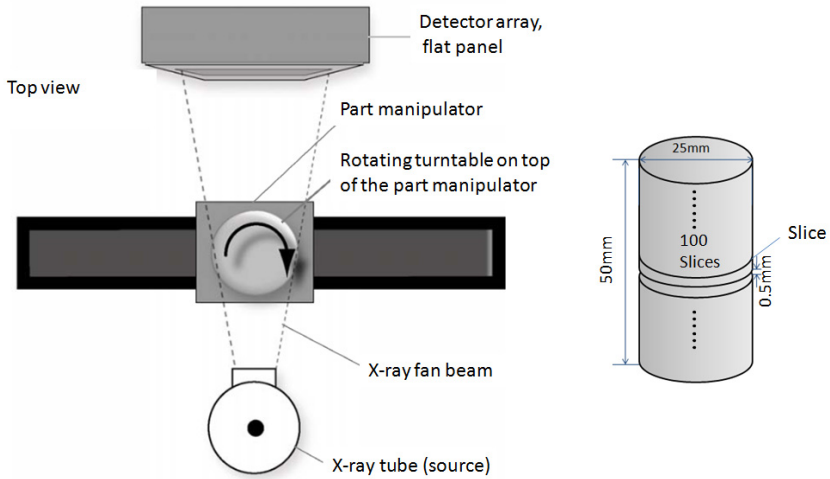
## 2 Methods

### 2.1 *MicroCT scanning*

In this study, cylindrical core samples of bituminous coal, 50mm in height and 25mm in diameter, were scanned using an ACTIS-225FFI microCT scanner manufactured by BIR Corporation of USA. The minimum resolution of the scanner is 10  $\mu\text{m}$  for an object of 4.8mm [8]. However, the resolution at the operation conditions stated here is approximately  $30 \times 30 \mu\text{m}^2$ . The scanner operated at 180KV and 200 $\mu\text{A}$ . The reconstruction matrix consisted of 1024 by 1024 pixels. The scanning time was 9s per slice. Slice thickness and slice spacing are both 0.5mm. The coal is normally composed of three basic components, i.e. the pores, coal matrix, and minerals. Since the grey value of a voxel is a measure of the density of the material, it can be used to threshold the image into two or more sections. Fig.1 shows the schematic diagram of the microfocus X-ray CT and the layout of scanned slices in the specimen.

### 2.2 *Creation of FD Model Geometry from CT Images*

A three-dimensional reconstruction of the sample is generated by collecting a series of radiographs of the coal. A total of 100 slices of scanned coal were



Part rotates in X-ray fan beam cross-section to take image data from all angles

**Fig. 1.** Schematic diagram of MicroCT scanning device and the layout of slices

reconstructed using the Mimics<sup>TM</sup> software in order to generate a 3D volume. The computed tomography data can be visualized as an image stack, which represents parallel cross sections of the scanned sample. In the achieved slice images, light colored areas correspond to materials with higher CT number, and higher density, in comparison to coal itself, as shown in Fig.2a. During the processing, careful and repetitious adjustments were made to make sure that the upper and lower thresholds are universal for all slices of the sample.

In Mimics program, material groups were assigned based on the grey values in the microCT images. Hence, the three-dimensional model consisted of different groups was generated respectively, as shown in Fig.2b. Surface meshes were then created for the solid model and internal pores. Surface meshes were transformed from triangular elements wrapping the solid model and the pore boundaries [8]. On the basis of the optimized surface meshes, mapping algorithm was adopted to generate four nodes tetrahedral element meshes. The number and quality of tetrahedral elements can be controlled by the mesh size during generation of volume meshes. The total number of elements and nodes used were 770,895 and 124,302, respectively. Then, the three-dimensional model was output. The output format can be identified by ANSYS easily. However, considering the requirements by FLAC<sup>3D</sup> code, the interface program was wrote and employed to import constructed model into FLAC<sup>3D</sup> code. The three- dimensional element mesh models are shown in Fig.2c. Moreover, Fig.3 depicts the procedures of our modeling process.

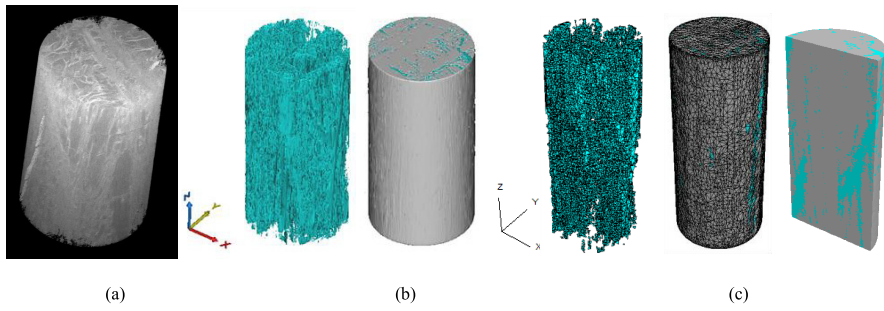


**Fig. 2.** 3D representative microstructures photo achieved by microCT scanner and modeling process. (a) Representative 3D microstructure of the specimen shows the mineral structure in the sample. (b) 3D models of inclusion material and coal wall reconstructed by Mimics software (inclusion material is shown at left). (c) 3D element mesh models constructed by FLAC<sup>3D</sup> code. From left to right, the models are meshed inclusion group, meshed body including coal wall and inclusion groups, and vertical cross-section of FLAC<sup>3D</sup> model before being meshed.

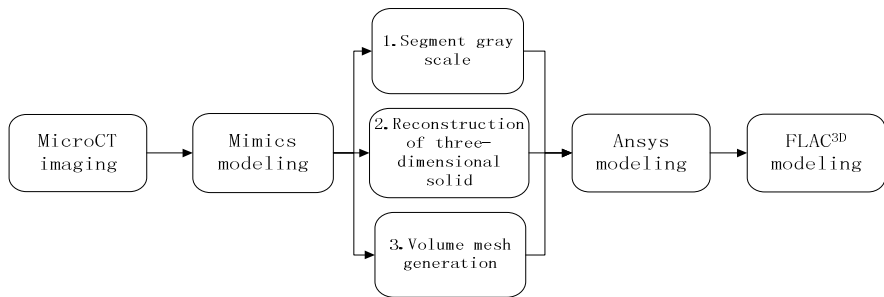


**Fig. 3.** Schematic procedures of modeling process combined MicroCT imaging with finite difference analysis

### 2.3 Material Properties

The coal samples are from No.9 seam in Tangshan coal mine, Hebei Province. Water injection is normally applied in No.9 seam to reduce the potentialities of coal bumps. So the failure features of saturated coal can help to understand the deformation behaviors of coal pillar, which has been injected water. In our simulations, material properties and element types were assigned to volume meshes. Two different materials were modeled: coal wall and mineral inclusions. The coal wall is comprised of reactive maceral components and inert maceral components. The mineral inclusions are much denser than the carbon walls and so the two materials were easily differentiated based on their gray values [9].

In the current simulation, the Young's modulus of the dry coal wall was calculated based on experimentally validated values. Other properties of dry

sample are shown in Table 1. It was assumed that the Cohesion and the Friction angle for wet sample were 10% and 70% lower than the corresponding properties for dry sample, as suggested by some experimental studies that used statics analysis for the determination of wet coal properties [10]. Because data on the elastic properties of mineral inclusions are completely lacking, the assumed properties were also used and listed in Table 1. Isotropic coal wall and mineral inclusions elastic properties were assumed.

The influence of the water to the inclusion properties was neglected. Based on the statics investigation, the classic stress-strain curves of the dry coal and saturated coal under uniaxial compression loading were shown in Fig.4. Moreover, the constitutive model of the inclusions was set as the Mohr-Coulomb model, but for the coal wall the strain-soft model was employed. In the latter model the cohesion, friction, dilation and tensile strength may soften after the onset of plastic yield by a user defined piecewise linear function, as shown in Fig.5 [11].

**Table 1.** Mechanical parameters used for numerical model

	Property	Young's modulus (GPa)	Poisson's Ratio	Tensile strength (MPa)	Cohesion			Friction angle		
					Original value (MPa)	Softening rate (%)	Residual value (MPa)	Original value (deg.)	Softening rate (%)	Residual value (deg.)
Wet	Inclusion	5.32	0.25	3.34	6.45	-	-	34.6	-	-
	Coal wall	3.3	0.38	0.16	1.02	5	0.102	36	0.5	30
Dry	Inclusion	5.32	0.25	3.34	6.45	-	-	34.6	-	-
	Coal wall	3.4	0.38	0.20	1.13	5	0.113	51	0.5	43

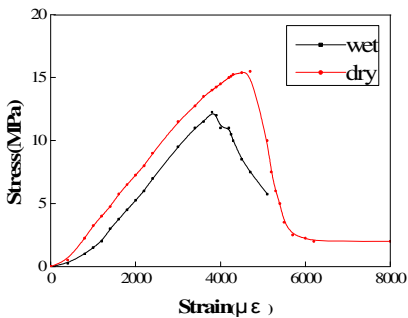


**Fig. 4.** Stress-strain curves of saturated and dry coals under uniaxial compressive loading condition

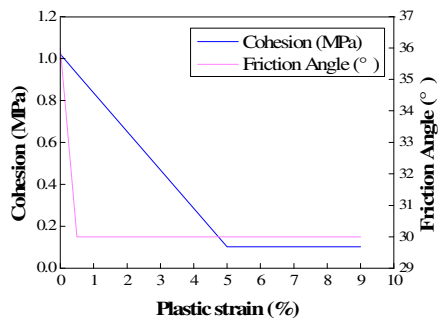


**Fig. 5.** Variation of cohesion and friction angle with plastic strain

## 2.4 Loads and Boundary Conditions

The horizontal displacements of bottom and top nodes are held to be zero. The side nodes are assigned free to simulate the uniaxial compressive condition. In our model the loading was controlled by the vertical displacements of the top and the bottom boundaries. All the top and bottom nodes are assigned a compressive displacement speed of  $5 \times 10^{-5}$  mm/step. Here the step is the time unit in the FLAC<sup>3D</sup> code. The schematic view of loading and boundary condition is shown in Fig.6.

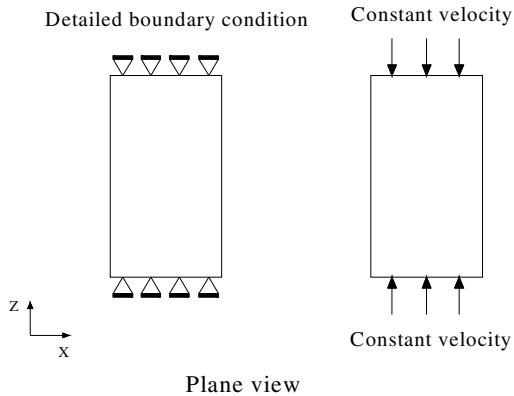


**Fig. 6.** Schematic view of the loading and boundary condition

## 2.5 Simulation

The uniaxial compression test has been extensively used to measure the strength and deformation properties of solid media. In our simulation, the microCT scans of coal sample to create numerical model with geometries that accurately reflect those of the material. The distributions of mineral inclusions, pores or cleats and the coal wall are modeled at the scan resolution. The model was constructed to simulate the characterization of strain localization of saturated coal under compressive loading condition. As the understanding of deformation features of saturated coal can help us evaluate the stability of roadways or coal mass in underground coal mining. The distributions of stress, strain, plastic region and shear strain rate can be obtained by numerical analysis.

## 3 Results

Fig.7 illustrates the variation of vertical displacement in the coal medium. It is found that the variation of displacement occurs obviously after the stress reaches

the second ‘peak’ value. The final vertical displacement shows that the outer of model has smaller deformation than the inside positions near cylinder axis. This is mainly caused by the inclusion materials distribution. In order to show the influence of material distribution on the deformation more clearly, Fig.8 presents the vertical stress distribution in the model. It shows the instantaneous vertical stress (along z axis, i.e., the direction of loading) variation with the loading process. High stress concentration in the areas of mineral inclusions was observed. It is also noted that coal wall tend to have low stress concentrations within them.

Fig.9 shows the accumulated plastic region for each loading state in the model during the compression process. Note that plastic regions in the first four images (top row of Fig.9) do not traverse the sample. It can be found that the unstable failure process possibly initiated at second ‘peak’ value. Fig.10 shows the shear strain rate in the model variation with the compressive loads. The images clearly show the evolution of the localized band cross traverses the sample. It is worth noting that this is an incremental analysis, therefore indicates the deformation active in each shear strain increment. This is different from what can be seen with accumulated plastic failure changes shown in Fig.9.

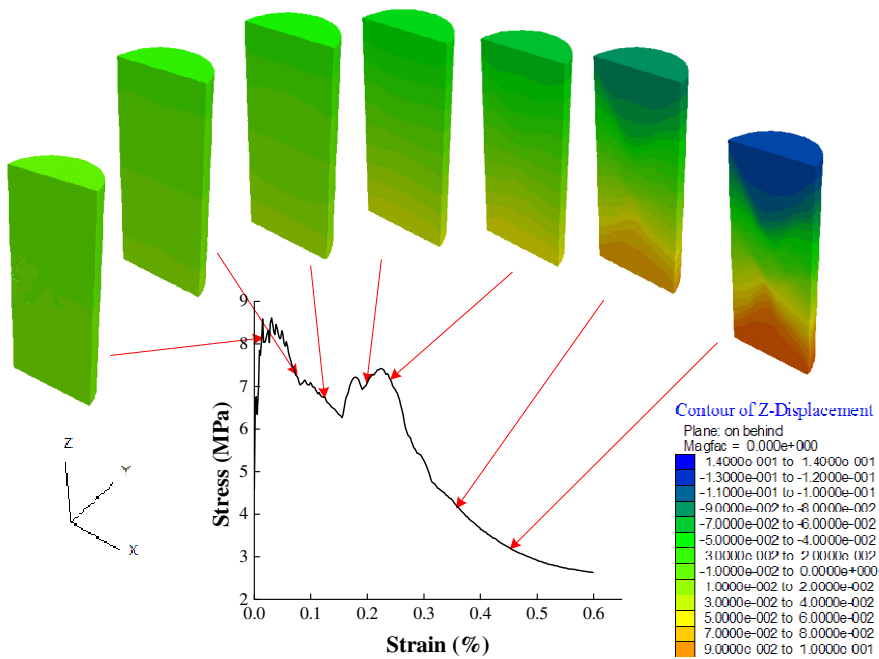


Fig. 7. Vertical displacement distributions in the sample during the loading process

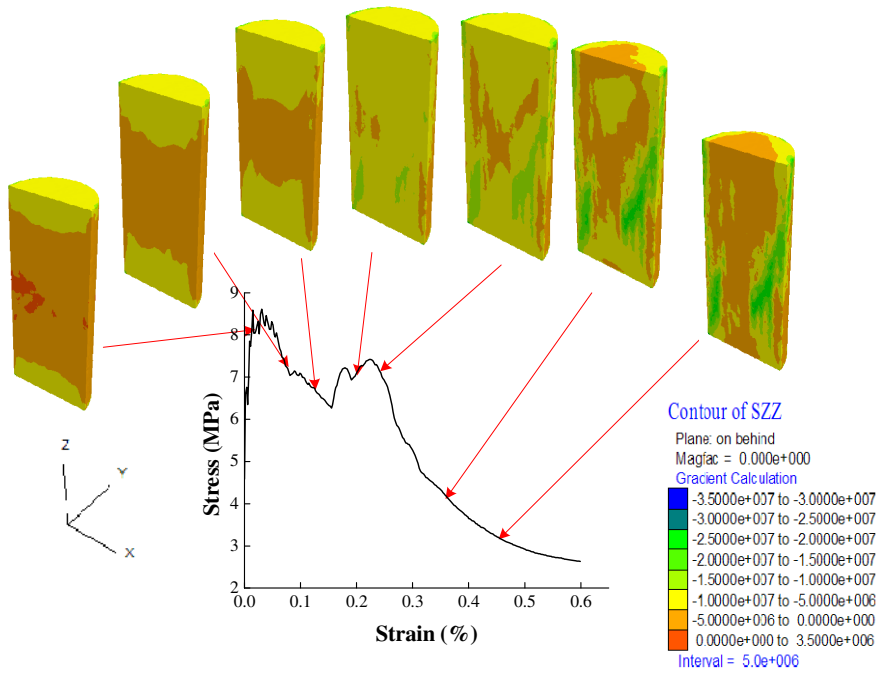


Fig. 8. Vertical stress distributions in saturated coal sample

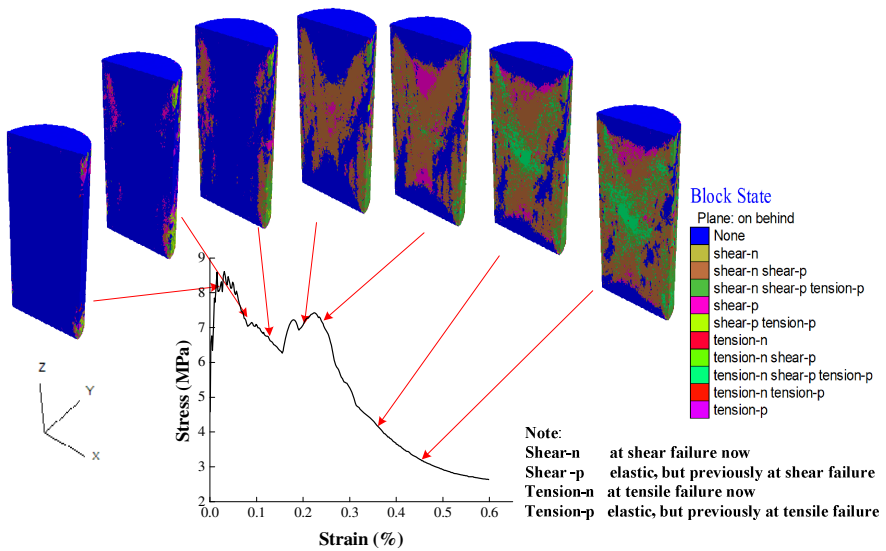


Fig. 9. Plastic regions in saturated coal sample during the loading process

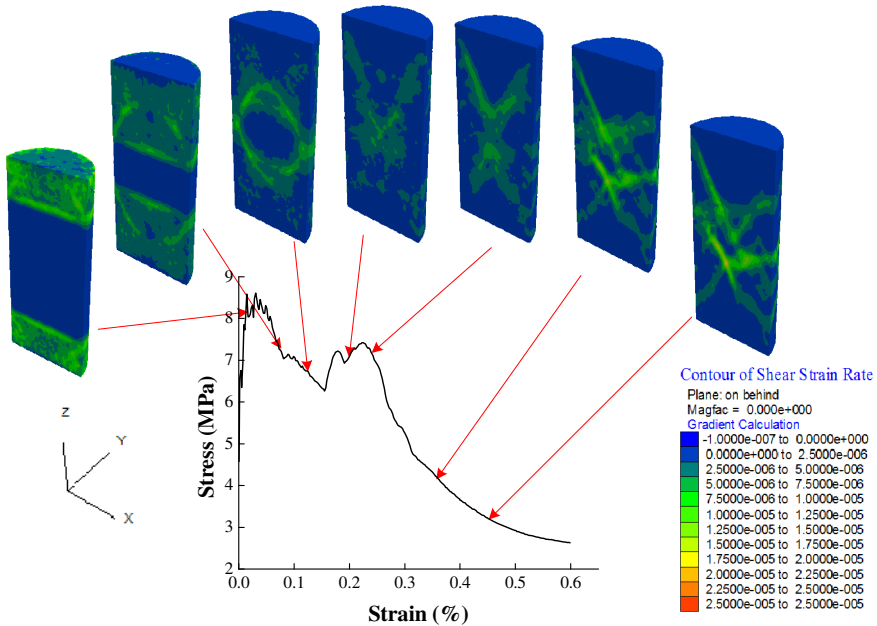


Fig. 10. Shear strain rate distributions in the sample with compressive loads variation

## 4 Discussion

It is worth noting that as a preliminary attempt, in this study a three-dimensional finite difference model was built to investigate the stress, deformation and plastic region evaluation of coal sample during the compression loading process. The results can serve as a reference for future studies on the micro-mechanics behaviors, the deformation and failure mechanism of coal media. The method can also be employed to model the effects of material and geometry at the microstructural level on material strength and behavior under various loads [9, 14].

However, these results must be combined with data gleaned by more conventional methods, both at the macro-scale and the micro-scale [12, 13]. Moreover, some limitations of this method should be mentioned. First, as the structural information from data sets acquired by microCT were used to construct models of coal, the size of coal sample should be suitable for microCT scanner. So this method may not be suit for analysis of mechanical behaviors of coal mass or large samples which are hardly scanned by CT. Secondly, the voxel grouping is performed in our model [9]. Only the largest group is of interest for finite difference analysis so the smaller groups are deleted. This process may also cause error in the material distribution in our model, which will affect the accuracy of results. Third, the mechanics properties of different groups in each type of coal are hardly achieved by conventional test methods. Thus, some properties and related

constitutive model have to be assumed, which may cause the numerical simulation results different with the experiment results. In consequence, further work should be done to validate applicability of this method.

## 5 Conclusion

The objective of this work was to observe and quantify the onset and evolution of localized deformation processes in saturated coal materials. The key element of our approach is combining microCT imaging with finite difference analysis. This allows us not only to create detailed, high resolution models of actual coal sample, but also to assess the evolving 3D deformation and stress distribution throughout loading. Incremental analysis of consecutive steps reveals that the heterogeneity of specimen affects stress and deformation distributions obviously. It indicates that a diffuse, wide band progressively thinning after peak. The degree of such structure seems related to the nature of internal material distribution. The failure mode of saturated coal showed that the specimen underwent ductile deformation dominated by cross shear splitting as primary mode of failure and tensile failure as a secondary mode.

**Acknowledgements.** The research was financially supported by the Major State Basic Research Development Program Fund (No. 2010CB226804, No. 2010CB226801), National Natural Science Foundation of China (No. 51174213), New Century Excellent Talents in Ministry of Education Support Program of China (No. NCET-10-0775), State Key Laboratory for Geomechanics and Deep Underground Engineering Open Research Fund (No. SKLGDUEK1021) and Fundamental Research Funds for the Central Universities.

## References

- [1] Viggiani, G., Besuelle, P., Hall, S.A., et al.: Sand deformation at the grain scale quantified through X-ray imaging. In: Alshibili, K.A., et al. (eds.) *Proceedings of the Third Workshop on X-Ray CT for Geomaterials*, New Orleans, March 1-3, pp. 1–16. John Wiley & Sons, Hoboken (2010)
- [2] Alshibli, K.A., Sture, S., Costes, N.C., et al.: Assessment of localized deformation in sand using X-ray computed tomography. *Geotechnical Testing Journal* 23, 274–299 (2000)
- [3] Fan, H.J., Xiao, S.X., Peng, K.: Study on constitutive model of rock sample in uniaxial compression based on strain localization. *Chinese Journal of Rock Mechanics and Engineering* 25, 2,634–2,641 (2006)
- [4] Wang, X.B.: Numerical simulation of influence of material imperfection on strain localization. *Rock and Soil Mechanics* 27, 1,241–1,247 (2006)
- [5] Kodaka, T., Oka, F., Otani, J., et al.: Experimental study of compaction bands in diatomaceous mudstone. In: Desrues, J., et al. (eds.) *Proceedings of the Second*

- Workshop on X-Ray CT for Geomaterials, Aussois, October 4-7, pp. 255–261. ISTE, London (2006)
- [6] Higo, Y., Oka, F., Kimoto, S., et al.: Visualization of strain localization and microstructures in soils during deformation using microfocus X-ray CT. In: Alshibili, K.A., et al. (eds.) Proceedings of the Third Workshop on X-Ray CT for Geomaterials, New Orleans, March 1-3, pp. 43–51. John Wiley & Sons, Hoboken (2010)
  - [7] Xie, W.B., Zheng, B.S.: Analysis of strain localization to induce rock burst. *Journal of Mining & Safety Engineering* 25, 468–471 (2008)
  - [8] Zhao, Y.X., Jiang, Y.D.: Acoustic emission and thermal infrared precursors associated with bump-prone coal failure. *International Journal of Coal Geology* 83, 11–20 (2010)
  - [9] Tsafnat, N., Tsafnat, G., Jones, A.S.: Micro-finite element modeling of coke blends using X-ray microtomography. *Fuel*. 87, 2,983–2,987 (2008)
  - [10] Wu, Y.K., Wang, S.K., Zhang, W.B.: Discussion on mechanism of rock burst prevention by water infusion. *Journal of China Coal Society* 2, 69–80 (1989)
  - [11] Wang, H.W., Poulsen, B.A., Shen, B.T., et al.: The influence of roadway backfill on the pillar strength by numerical investigation. *International Journal of Rock Mechanics & Mining Sciences* 48, 443–450 (2011)
  - [12] Tsafnat, N., Tsafnat, G., Jones, A.S.: Automated mineralogy using finite element analysis and X-ray microtomography. *Miner Eng.* 22, 149–155 (2009)
  - [13] Tsafnat, N., Amanat, N., Jones, A.S.: Analysis of coke under compressive loading: A combined approach using micro-computed tomography, finite element analysis, and empirical models of porous structures. *Fuel*. 90, 384–388 (2011)
  - [14] Ju, Y., Wang, H.J., Yang, Y.M., et al.: Numerical simulation of mechanisms of deformation, failure and energy dissipation in porous rock media subjected to wave stresses. *Sci. China Tech. Sci.* 53, 1,098–1,113 (2010)

# An Elasto-plastic Model for Liquefiable Sands Subjected to Torsional Shear Loadings

Gabriele Chiaro<sup>1</sup>, Junichi Koseki<sup>2</sup>, and L.I. Nalin De Silva<sup>3</sup>

<sup>1</sup> Research Fellow, Centre for Geomechanics and Railway Eng., University of Wollongong, Northfields Ave., 2522 NSW, Australia

gchiaro@uow.edu.au

<sup>2</sup> Professor, Institute of Industrial Science, University of Tokyo, Japan

koseki@iis.u-tokyo.ac.jp

<sup>3</sup> Senior Lecturer, Dept. of Civil Eng., University of Moratuwa, Sri Lanka

nalinds@uom.lk

**Summary.** This paper presents a modeling procedure for simulating the monotonic undrained torsional shear behavior of sands, including stress-strain relationship, and excess pore water pressure generation, while considering the void ratio and stress level dependence of stress-strain-dilatancy behavior of sand. A unique set of soil parameters is required by the model to satisfactorily predict the undrained behavior of loose and dense Toyoura sand over a wide range of initial void ratios and confining pressures, as proven by simulating experimental data produced by the authors and found in the literature.

## 1 Introduction

It is well known that sand behaves differently under different density states and confining pressures [1–5]. During shearing, loose sand exhibits a contractive behavior with strain-softening. Instead, dense sand dilates while showing strain-hardening.

Although there have been a number of comprehensive model developed in geomechanics, to predict in a very reliable manner the complex response of sands undergoing monotonic loading conditions for a large range of initial void ratios and confining pressures without the need to change the soil parameters remains to be a major challenge.

In models based on generalized plasticity [6, 7], complex mathematical formulations are used. In addition, the same sand is usually considered as different material depending on density and stress level, so that a large number of soil parameters is required. Alternatively, one of advantages of critical-state constitutive models [8, 9] is their ability to predict soil behavior over a range of densities and confining pressures by using a single set of soil parameters. [10] proposed a unified model based on critical state and generalized plasticity. Nevertheless, there may be debates over the uniqueness of critical state line. In addition the majority of such predictive model has been validated only for the case of triaxial loadings.

As an alternative, [11] used a generalized hyperbolic equation (GHE) to simulate the stress-strain behavior of Toyoura sand under drained plane strain compression loadings. Later, the GHE approach was successfully used by [12, 13] for simulating the drained/undrained monotonic/cyclic torsional shear behavior of Toyoura sand for the case of loose and dense Toyoura sands (considered as two different materials).

In this paper, a simple (i.e. use of non-complex mathematical formulations and of small number of soil parameters) elasto-plastic model able to predict all the characteristics of Toyoura sand behavior in monotonic undrained torsional shear tests over a wide range of void ratios and confining pressures using a unique set soil parameters under the GHE approach is proposed.

## 2 Proposed Model

### 2.1 Modeling of Stress-Strain Behavior of Sand

In this current study, the GHE approach was used to simulate the highly non-linear undrained stress-strain response of Toyoura sand subjected to torsional shear loadings. GHE has been proposed by [11] in the form:

$$y = \frac{x}{1/C_{1(x)} + x/C_{2(x)}} \quad (1)$$

where  $x$  and  $y$  represents a normalized plastic shear strain function and a normalized shear stress ratio function, respectively. Note that, in Eq. (1), for normally consolidated uncemented sand, similar to Toyoura sand, the elastic strain component (see Appendix) may be neglected.

$C_{1(x)}$  and  $C_{2(x)}$  are two strain-dependent parameters, which for the case of torsional shear loadings can be formulated as follows:

$$C_{1(x)} = \frac{C_{1(0)} + C_{1(\infty)}}{2} + \frac{C_{1(0)} - C_{1(\infty)}}{2} \cos\left\{\frac{\pi}{(\alpha/x)^a + 1}\right\} \quad (2)$$

$$C_{2(x)} = \frac{C_{2(0)} + C_{2(\infty)}}{2} + \frac{C_{2(0)} - C_{2(\infty)}}{2} \cos\left\{\frac{\pi}{(\beta/x)^b + 1}\right\} \quad (3)$$

All the coefficients in Eqs. (2) and (3) can be determined by fitting the experimental data plotted in terms of  $y/x$  vs.  $x$  relationship as explained in details in [11].

To characterize the GHE while accounting for the void ratio and confining stress level dependence of sand behavior, the same  $x$  and  $y$  functions employed by [14] were adopted:

$$y = \frac{(\tau / p')}{(\tau / p')_{\max}} \tag{4}$$

$$x = \gamma^p / \gamma_R, \quad \gamma_R = \frac{(\tau / p')_{\max}}{(G_0 / p_0')} \tag{5}$$

where  $\gamma^p$  is the plastic shear strain;  $\tau$  is the shear stress;  $p'$  and  $p_0'$  are the current and initial effective mean principal stress, respectively;  $(\tau/p')_{\max}$  is the peak shear stress in the plot  $\tau/p'$  vs.  $\gamma^p$ ; and  $G_0$  is the initial shear modulus.

A number of formulations have been reported in literature to express the shear modulus as a function of void ratio and confining pressure [2, 9, 10, 14]. In here, for the case of undrained torsional shear loadings, the following formulation is proposed for  $G_0$ :

$$G_0 = G_{R0} \frac{f(e_0)}{f(e_{R0})} \left( \frac{p_0'}{p_{R0}'} \right)^n = 7828 \frac{(2.17 - e_0)^2}{1 + e_0} (p_0')^{0.508} \tag{6}$$

where  $e_0$  is the initial void ratio at the corresponding  $p_0'$ ;  $f(e_0) = (2.17 - e_0)^2 / (1 + e_0)$  as defined by [15]; and  $n$  is a material parameter.  $G_{R0}$  is a reference initial shear modulus at the corresponding void ratio ( $e_{R0}$ ) and confining pressure  $p_{R0}'$ . For Toyoura sand subjected to undrained torsional shearing, [13] reported the following values:  $G_{R0} = 80000$  kPa at  $f(e_{R0=0.828}) = 0.985$  and  $p_{R0}' = 100$  kPa; and  $n = 0.508$ .

Referring to results of torsional simple shear tests, [16] evaluated the friction angle at failure ( $\varphi$ ) over a wide range of void ratios and confining pressures. They observed that the pressure-dependence of  $\varphi$  is very small, while the density-dependence is predominant. In a similar manner to [16], in this study it was found that the angle of shear resistance at failure  $\{\varphi' = \tan^{-1}(\tau/p')_{\max}\}$  varies significantly with the void ratio, while the pressure-dependence can be neglected. By fitting the test results, the void ratio dependence of shear strength,  $(\tau/p')_{\max}$ , was formulated as follows:

$$(\tau / p')_{\max} = 0.67 \frac{(2.17 - e_0)^2}{1 + e_0} \tag{7}$$

## 2.2 Stress-Dilatancy Relations of Sand under Torsional Shear

Volume change in drained shear can be considered as the mirror image of pore water pressure build-up during undrained shear. Change of volumetric strain in different stage of loading can be described by the stress-dilatancy relationship, which relates the dilatancy ratio ( $-d\varepsilon_{\text{vol}}^d/d\gamma_{\text{vol}}^p$ ) to the stress ratio ( $\tau/p'$ ) [17, 18].

For the case of torsional shear [19] proposed the following empirical linear stress-dilatancy relationship:

$$\frac{\tau}{p'} = N_d \left( -\frac{d\varepsilon_{vol}^d}{d\gamma^p} \right) + C_d \quad (8)$$

where  $N_d$  and  $C_d$  are the gradient and the intercept in the plot  $(-d\varepsilon_{vol}^d/d\gamma^p)$  vs.  $(\tau/p')$ , respectively. Note that, when  $(\tau/p') < C_d$  soils behaves contractive, while when  $(\tau/p') > C_d$  soils behaves dilative. Alternatively,  $(\tau/p') = C_d$  corresponds to zero dilatancy state (i.e. phase transformation state [20]).

[5] reported that, for a given material, the mobilized angle of shear resistance at zero dilatancy,  $\varphi'_{PTL} = \tan^{-1}(\tau/p')_{PTL}$ , is independent of stress level and density. As a consequence,  $C_d = (\tau/p')_{PTL}$  can be regarded as a constant, and in this current study,  $C_d$  was chosen as 0.6 (i.e. for Toyoura sand,  $\varphi'_{PTL} = 31^\circ$  [21]).

In the proposed model, by fitting test results reported in [12, 13], the void ratio dependence of  $N_d$  was formulated as follows:

$$N_d = 5.793 - 5e_0 \quad (9)$$

### 2.3 Modeling of Pore Water Pressure Generation

In modeling the undrained cyclic shear behavior it was assumed that the total volumetric strain increment ( $d\varepsilon_{vol}$ ) during the undrained loading, which consists of dilatancy ( $d\varepsilon_{vol}^d$ ) and consolidation/swelling ( $d\varepsilon_{vol}^c$ ) components, is equal to zero. Therefore the following equation is valid during undrained loading:

$$d\varepsilon_{vol} = d\varepsilon_{vol}^c + d\varepsilon_{vol}^d = 0 \quad (10)$$

Experimental evidences suggest that the bulk modulus  $K (= dp'/d\varepsilon_{vol}^c)$  can be expressed as a unique function of  $p'$ :

$$K = \frac{dp'}{d\varepsilon_{vol}^c} = K_0 \frac{f(e)}{f(e_0)} \left( \frac{p'}{p_0'} \right)^{m_k} \quad (11)$$

where  $K_0$  is the bulk modulus at  $p_0'$ ;  $f(e)$  and  $f(e_0)$  are the void ratio function at current and reference stress state, respectively; and  $m_k$  is a coefficient to model the stress-state dependency of  $K$ .

Considering that  $f(e) = f(e_0)$  in undrained tests, and that the volumetric strain component due to consolidation/swelling is the mirror image of the one due to dilatancy ( $d\varepsilon_{vol}^c = -d\varepsilon_{vol}^d$ ), the generation of pore water pressure during undrained shearing was evaluated as follows:

$$dp' = K_0 (p' / p_0')^{m_k} (-d\varepsilon_{vol}^d) = K_0 (p' / p_0')^{m_k} \left( \frac{\tau}{p'} - C_d \right) \frac{d\gamma^p}{N_d} \tag{12}$$

An empirical formulation, Eq. (13), was adopted to account for density and pressure dependence of the bulk modulus, similarly to the case of  $G_0$  in Eq. (7). For Toyoura sand subjected to undrained torsional shearing, [14] reported the following values:  $K_{R0} = 47000$  kPa at  $f(e_{R0=0.828}) = 0.985$  and  $p_{R0}' = 100$  kPa; and  $m_k = 0.5$ . Therefore, substituting those values in Eq. (12) yields:

$$K_0 = K_{R0} \frac{f(e_0)}{f(e_{R0})} \left( \frac{p_0'}{p_{R0}'} \right)^{m_k} = 4772 \frac{(2.17 - e_0)^2}{1 + e_0} (p_0')^{0.5} \tag{13}$$

### 3 Model Calibration and Validation

A single set of soil parameters (i.e. GHE parameters), as listed in Table 1, was used to simulate the behavior of loose and dense sand consolidated at different confining pressure level and sheared under undrained torsional shear conditions.

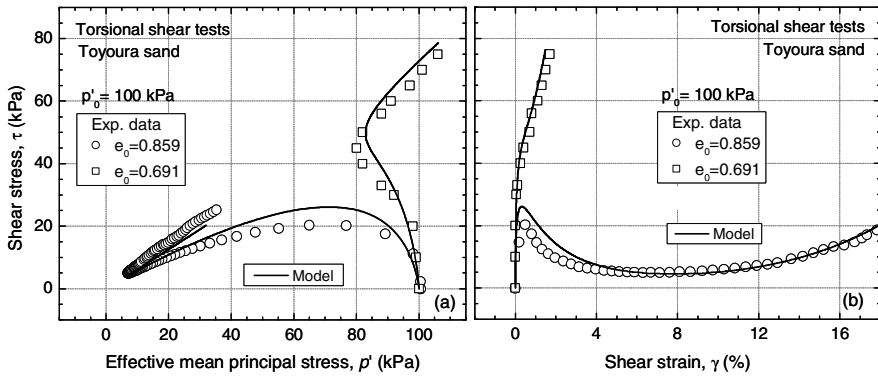
The soil parameters were determined by fitting the results of a monotonic undrained torsional shear tests conducted on a loose Toyoura sand specimen ( $e_0 = 0.828$ ,  $Dr = 45.5\%$ ), which was isotropically consolidated at  $p_0' = 100$  kPa. Note that, tested Toyoura sand specimens refer to batch I, with  $e_{max} = 0.992$ ,  $e_{min} = 0.632$  and  $G_S = 2.65$ .

**Table 1.** GHE parameters for Toyoura sand

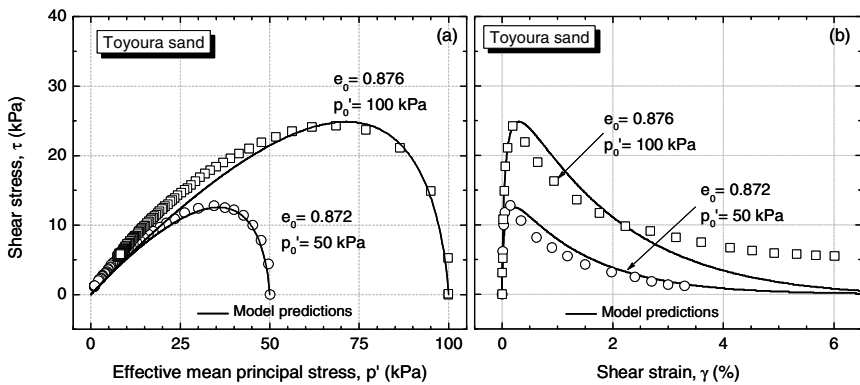
$C_{1(0)}$	$C_{1(\infty)}$	$C_{2(0)}$	$C_{2(\infty)}$	$\alpha$	$\beta$	$a$	$b$
4	0.123	0.102	1.2	0.01073	0.85012	0.2	0.2

Fig. 1 compares predicted and observed (by the authors) behavior of Toyoura sand consolidated to  $p_0' = 100$  kPa at two different void ratios of  $e_0 = 0.691$  (dense,  $Dr = 84\%$ ) and  $0.859$  (loose,  $Dr = 37\%$ ). Fig. 1 shows that, the overall soil behavior of loose (contractive with strain-softening) and dense (dilative with strain-hardening) Toyoura sand specimens consolidated at the same confining pressure was well simulated by the model.

To confirm the model performance, two test results presented by [4] for very loose Toyoura sand specimens ( $e_0 = 0.872-0.876$ ) consolidated to  $p_0' = 50$  kPa and  $100$  kPa were simulated. Note that, the Toyoura sand used by [4] was of different batch from the one used by the authors, thus the index properties were slightly different (i.e.  $e_{max} = 0.977$  and  $e_{min} = 0.597$ ). In Fig. 2, the model predictions are compared with the laboratory test results. It can be seen that, despite the differences in index soil properties of Toyoura sand, the model was able to satisfactorily predict the behavior of very loose sand until the offset of liquefaction.



**Fig. 1.** Undrained monotonic torsional shear behavior of Toyoura sand consolidated to  $p'_0 = 100$  kPa: (a) effective stress path; and (b) stress-strain relationship



**Fig. 2.** Undrained monotonic torsional shear behavior of Toyoura sand consolidated to a void ratio  $e_0 = 0.872-0.876$  (from [4]): (a) effective stress path; and (b) stress-strain relationship

### 4 Conclusions

Under shearing, loose sand exhibits a contractive behavior with strain-softening, while dense sand shows dilative behavior with strain-hardening. To predict in a very consistent manner the complex response of sands subject to shearing while accounting for void ratios and stress level dependency is not an easy task.

In this paper, based on GHE approach, an elasto-plastic model to predict the monotonic undrained torsional shear behavior of sand was proposed. The model employs only a unique set of soil parameters to satisfactorily predict the behavior of Toyoura sand over a wide range of initial void ratios and confining pressures, including contractive behavior with strain-softening (loose sand), dilative behavior with strain-hardening (dense sand) and liquefaction occurrence (very loose sand).

**Acknowledgments.** The authors gratefully acknowledge the financial support provided by the Ministry of Education, Culture, Sport, Science and Technology of Japan. The authors also would like to thank A/Prof. Takashi Kiyota for providing useful data for loose Toyoura sand. Special appreciation goes to Mr. Takeshi Sato for his highly cooperative assistance in the laboratory testing.

## Appendix

For normally consolidated uncemented sand, the elastic shear strain ( $\gamma^e$ ) is very small. In this study,  $\gamma^e (= \Sigma d\gamma^e)$  was found to be in the order of 0.03% for loose Toyoura sand ( $e_0 = 0.828$ ;  $p_0' = 100$  kPa) at the peak stress state, and of 0.11% for dense sand Toyoura sand ( $e_0 = 0.691$ ;  $p_0' = 100$  kPa) subjected to a stress state of  $\tau = 100$  kPa.

The elastic component was calculated by Eqs. (14) and (15), as formulated in the recently developed quasi-elastic constitutive model proposed by [22]:

$$d\gamma^e = d\tau / G \quad (14)$$

$$G = G_0 \frac{f(e)}{f(e_0)} \left( \frac{\sqrt{\sigma_z' \sigma_r'}}{\sigma_0'} \right)^n \approx G_0 \left( \frac{p'}{p_0'} \right)^{0.508} \quad (15)$$

where  $G$  is the actual shear modulus;  $f(e_0)$  and  $f(e)$  are the initial and current void ratio functions, note that  $f(e) = f(e_0)$  in undrained tests;  $G_0$  is the initial shear modulus at  $f(e_0)$  and  $\sigma_0'$ ;  $\sigma_z'$  and  $\sigma_r'$  are the vertical and radial effective stress, respectively; and  $n$  is a material parameter.

## References

- [1] Tatsuoka, F., Muramatsu, M., Sasaki, T.: Cyclic undrained stress-strain behaviour of dense sands by torsional simple shear stress. *Soils Found.* 22(2), 55–70 (1982)
- [2] Ishihara, K.: Liquefaction and flow failure during earthquakes. *Geotechnique* 43(3), 351–415 (1993)
- [3] Verdugo, R., Ishihara, K.: The steady state of sandy soils. *Soils Found.* 36(2), 81–92 (1996)
- [4] Yoshimine, M., Ishihara, K.: Flow potential of sand during liquefaction. *Soils Found.* 38(3), 189–198 (1998)
- [5] Georgiannou, V.N., Tsomokos, A., Stavrou, K.: Monotonic and cyclic behaviour of sand under torsional loading. *Geotechnique* 58(2), 113–124 (2008)
- [6] Pastor, M., Zienkiewicz, O.C., Chan, A.H.C.: Generalized plasticity and modeling of soil behavior. *Int. J. Numer. Analyt. Meth. Geomech.* 14(3), 151–190 (1990)
- [7] Ling, H.I., Liu, H.: Pressure-level dependency and densification behavior of sand through a generalized plasticity model. *J. Eng. Mech., ASCE* 129(8), 851–860 (2003)
- [8] Jefferies, M.G.: Nor-sand: a simple critical model for sand. *Geotechnique* 43(1), 91–103 (1993)

- [9] Imam, S.M.R., Morgenstern, N.R., Robertson, P.K., Chan, D.H.: A critical-state constitutive model for liquefiable sand. *Can. Geotech. J.* 42, 830–855 (2005)
- [10] Ling, H.I., Yang, S.: Unified sand model based on the critical state and generalized plasticity. *J. Eng. Mech., ASCE* 132(12), 1380–1391 (2006)
- [11] Tatsuoka, F., Shibuya, S.: Deformation characteristics of soils and rocks from field and laboratory tests. In: *Proc. 9th Asian Regional Conf. SMFE, Bangkok, Thailand, vol. 2*, pp. 101–170 (1992)
- [12] De Silva, L.I.N.: Deformation characteristics of sand subjected to cyclic drained and undrained torsional loadings and their modeling. PhD. Thesis. University of Tokyo (2008)
- [13] Chiaro, G.: Deformation properties of sand with initial static shear in undrained cyclic torsional shear tests and their modeling. PhD. Thesis. University of Tokyo (2010)
- [14] Chiaro, G., De Silva, L.I.N., Kiyota, T., Koseki, J.: An elasto-plastic model to describe the undrained cyclic behavior of saturated sand with initial static shear. In: *Proc. 5th Int. Sym. Deformation Characteristics Geomaterials, Seoul, Korea, vol. 2*, pp. 1026–1033 (2011)
- [15] Hardin, B.O., Richart, F.E.: Elastic wave velocities in granular soils. *J. Soil Mech. Found. Div., ASCE* 89(SM1), 33–65 (1963)
- [16] Pradhan, T.B.S., Tatsuoka, F., Horii, N.: Strength and deformation characteristics of sand in torsional simple shear. *Soils Found.* 28(3), 131–148 (1988)
- [17] Shahnazari, H., Towhata, I.: Torsion shear tests on cyclic stress-dilatancy relationship of sand. *Soils Found.* 42(1), 105–119 (2002)
- [18] Pradhan, T.B.S., Tatsuoka, F., Sato, Y.: Experimental stress-dilatancy relations of sand subjected to cyclic loading. *Soils Found.* 29(1), 45–64 (1989)
- [19] Nishimura, S., Towhata, I.: A three-dimensional stress-strain model of sand undergoing cyclic rotation of principal stress axes. *Soils Found.* 44(2), 103–116 (2004)
- [20] Ishihara, K., Tatsuoka, F., Yasuda, S.: Undrained deformation and liquefaction of sand under cyclic stresses. *Soils Found.* 15(1), 29–44 (1975)
- [21] Chiaro, G., Koseki, J., Sato, T.: Effects of initial static shear on liquefaction and large deformation properties of loose saturated Toyoura sand in undrained cyclic torsional shear tests. *Soils Found.* 52(3) (2012)
- [22] HongNam, N., Koseki, J.: Quasi-elastic deformation properties of Toyoura sand in cyclic triaxial and torsional loadings and their modeling. *Soils Found.* 45(5), 19–38 (2005)

# A Micromechanics Based Model for Cemented Granular Materials

Arghya Das<sup>\*</sup>, Alessandro Tengattini, Giang Nguyen, and Itai Einav

Particles and Grains Laboratory, The University of Sydney, Sydney, Australia  
arghya.das@sydney.edu.au

**Summary.** Cemented Granular Materials (CGMs) consist of a particle skeleton and a solid matrix partially filling the interstitial space. In this broad class we encounter a number of typical geotechnical materials such as sedimentary rocks (Sandstones, Conglomerates and Breccia) as well as naturally and artificially cemented sands. These materials, while showing a brittle behavior under shearing at low confining pressures, are ductile at high confinements. The micro mechanisms involved, that are cement disaggregation, grain crushing and fragment rearrangement, are known to be different in these two cases.

Several constitutive models based on the elasto-plastic framework have been developed to describe the behavior of CGMs. However lack of correlations between the underlying failure mechanisms and the only internal variable (plastic strain), results in the use of parameters that are hard to physically identify, let alone to calibrate.

In this paper, we tackle the constitutive modeling of CGMs from a more physical angle, which starts from a micro mechanical observation of grain and cement failure, to a statistical homogenization of grain scale quantities for the constitution of their continuum counterparts. In particular, while the established Continuum Breakage Mechanics approach lends itself to the description of grain crushing process, a novel definition of damage for the cement phase is introduced and shown to be measurable. The whole formulation of the new constitutive model is confined in a thermo-mechanical framework, with explicit links between the internal variables (breakage, damage and plastic strain) and the evolving microstructure of the material. As a consequence, the model possesses only a few physically identifiable and experimentally measurable parameters. The behavior of the model is assessed against experimental observations and its novel features are highlighted.

## 1 Introduction

Despite the small volume fraction that the cement phase usually occupies in CGMs, the presence of a solid matrix bridging the particles substantially changes the mechanical response of the granular phase, putting this class of materials in between classical soil and rock mechanics.

---

<sup>\*</sup> Corresponding author.

Given the practical importance of artificially cemented granular materials and the abundance of the naturally occurring ones e.g. in hydrocarbon reservoirs, their behaviors have been investigated by several authors experimentally, numerically and analytically. These materials, while showing a brittle behavior under shearing at low confining pressures, are ductile at high confinements. The main underlying micro mechanisms, according to Menéndez et al. [1], are cement damage, grain crushing and fragment rearrangement, and are known to be different in these two cases.

Shear at low confining pressures facilitates the fracture of cement bridges among the grains, locally releasing degrees of freedom in the system which can be followed by fragment reorganization. Such process, by progressively removing the resistant contribution of the cement bridges, leads to an overall softening of the specimen. On the other hand high confining pressures result in grain crushing, pore collapse and, as known, consequently lead to hardening. Several constitutive models based on the elasto-plastic framework have been developed to capture such a complex behavior. To cite some, in last two decades Nova and his group [2–5] have developed a set of constitutive models for CGMs based on continuum mechanics, successfully predicting the behavior of bonded geomaterial like Calcarene. However lack of correlations between the underlying microscopic failure mechanisms and the only inelastic internal variable (plastic strain), results in the use of a wide set of parameters that are hard to physically identify, let alone to calibrate.

The literature also presents several numerical models used to describe the micromechanics of CGM failure such as those based on the Discrete Element Method (DEM) [6–8], Lattice Element Method (LEM) [9] and FEM. All those approaches, despite the remarkable insight they allow, lack a proper description of one or more of the cited microscale failure mechanisms and are computationally too expensive for real scale engineering problems.

In this paper, we propose a continuum constitutive model for CGMs which starts from the micro mechanical observation of grain and cement failure and introduces separate internal variables for these different mechanisms through statistical homogenization. By introducing such physical understanding of the micro-mechanics underlying the macroscopic response, we minimize the number of required parameters that have now a clear and measurable physical meaning. The formulation is confined within a thermo-mechanical framework, ensuring the respect of two of the few irrefutable laws of physics. The model response is assessed against experimental observations and its novel features are highlighted.

## 2 Internal Variables Representing the Failure

As shown by Einav [10], an effective way to describe grain crushing is through tracking the evolution of the grain size distribution, *gsd*. In Continuum Breakage Mechanics this tracking is proposed through the use of a scalar internal variable, named *Breakage B*, defined as the ratio between the areas under the cumulated probability density functions (*cdf*), as in Fig.1a. From *B* the *gsd* can be deduced at any time given the initial and final *cdf*:

$$F^G(x, B) = F_0^G(x)(1 - B) + F_u^G(x)B \tag{1}$$

where  $x$  is the grain diameter and  $F_0^G(x)$ ,  $F_u^G(x)$  and  $F^G(x)$  are the initial, final and current *cdf* of the granular assembly.

For CGMs the behavior of the granular part is inherently different from that of the cement as grain disaggregation leads to the reorganization of fragments and new column-like stress patterns develop, being the only bearing capacity of the grains in compression. On the other hand cement can also resist in tension but when cracks develop in it, its resistance and stiffness is deteriorated. When fragments detach from the cement bridges the modest volume fraction of the cement render the mechanical contribution of its fragments to the force network negligible. To describe such behavior damage models are generally used. In its simplest classical description damage of a given surface within a unit volume can be seen as the ratio between the void matrix area and the total area of that surface. Such description, sensible for continuum and homogeneous materials, becomes ambiguous in CGMs due to the high porosity of the material. Acknowledging the behavior of the cement we can take into account only the effectively working cement, mechanically equivalent to the total cracked one. At this point it is possible to define at any time an effective cement size distribution. Similarly to Breakage we can introduce a scalar variable Damage  $D$ , defined as the area ratio in Fig 1a. It follows then:

$$F^C(A, D) = F_0^C(A)(1 - D) + F_u^C(A)D \tag{2}$$

Once again we can in first approximation suppose that the evolution of the cement disaggregation process will affect the whole cement area range  $A$  so that we can introduce the fractional independence of  $D$ . The initial cement distribution  $F_0(A)$  can for example be detected in a sample through the use of X-Ray tomographic imaging. The final distribution  $F_u(A)$  can be hypothesized as a Heaviside function centered at zero, meaning that the theoretical final state is a completely uncemented granular material. Such assumption simplifies the solution of the constitutive model and can be considered reasonable in several naturally occurring conditions [11]. Fig. 1b depicts the distribution of cement area and corresponding damage evolution.

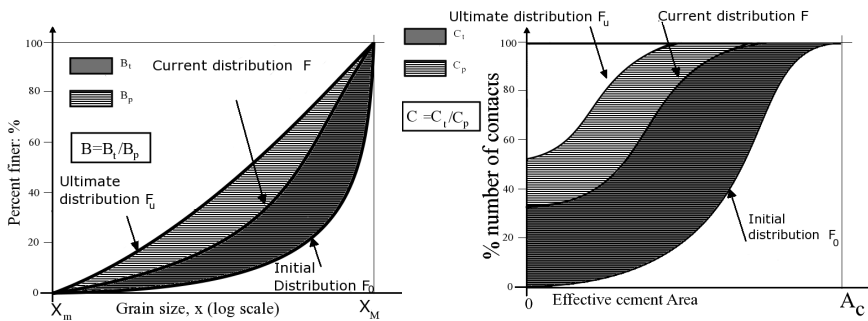


**Fig. 1.** (a) Evolution of grain size distribution and breakage definition. (b) Evolution of cement area distribution and damage definition

### 3 Model Description

We modified the statistical homogenization scheme developed in Einav [10] to integrate the above internal variables in a thermodynamics-based constitutive model. The fundamental assumption that the elastic energies in the grains scale with their sizes remains unchanged as numerically shown in Topin [9]. For this two-phase material it is further assumed that the strain in each phase is the same as the macroscopic one resulting in the macroscopic stress being the volume averaged one to meet the Hill-Mandel condition [13]. Details on the thermo-mechanical formulation and the statistical homogenization will be covered in a forthcoming paper. Only the model description is presented here. Adopting the pressure-dependent elasticity in Einav [12], the constitutive equations of the model can be written as follows:

(a) *The stress-strain relationship is:*

$$q = f_G 3p_r G_G (1 - \vartheta B) \left( \frac{K_G \varepsilon_v^e}{2} + 1 \right) \varepsilon_s^e + f_C 3p_r G_C (1 - D) \left( \frac{K_C \varepsilon_v^e}{2} + 1 \right) \varepsilon_s^e \quad (3)$$

$$p = f_G p_r (1 - \vartheta B) \left[ \left( \frac{K_G \varepsilon_v^e}{2} + 1 \right)^2 + \frac{3}{4} G_G K_G \varepsilon_s^{e2} \right] + f_C p_r (1 - D) \left[ \left( \frac{K_C \varepsilon_v^e}{2} + 1 \right)^2 + \frac{3}{4} G_C K_C \varepsilon_s^{e2} \right] \quad (4)$$

where  $f_C$  and  $f_G$  are the volume fractions of cement and grain respectively;  $K_G, G_G, K_C$  and  $G_C$  are the elastic stiffness parameters for grain and cement and  $p_r$  is the reference pressure at which the granular materials are initially compacted (conveniently taken as 1 kPa).

(b) *Yield surface:*

$$y = \frac{E_B (1 - B)^2}{E_{CB}} + \frac{E_D (1 - D)^2}{E_{CD}} + \frac{q^2}{(Mp)^2} - 1 \leq 0 \quad (5)$$

where  $E_B$  and  $E_D$ , named respectively Breakage Energy and Damage Energy are, a measure of the total strain energy necessary to move the respective distribution from the initial to the final state.

$$E_B = \vartheta_G \left[ \frac{2p_r}{3K_G} \left( \frac{K_G \varepsilon_v^e}{2} + 1 \right)^3 + \frac{3p_r G_G}{2} \left( \frac{K_G \varepsilon_v^e}{2} + 1 \right) \varepsilon_s^{e2} \right] f_G \quad (6)$$

$$E_D = \left[ \frac{2p_r}{3K_C} \left( \frac{K_C \varepsilon_v^e}{2} + 1 \right)^3 + \frac{3p_r G_C}{2} \left( \frac{K_C \varepsilon_v^e}{2} + 1 \right) \varepsilon_s^{e2} \right] f_C \quad (7)$$

where  $E_{CB}$  and  $E_{CD}$ , critical breakage and damage energies are the energy thresholds at which the respective phases initiate the inelastic processes;  $M$  is critical state parameter of the material and  $\vartheta$  is grading index which can be determined directly from the grain size distribution [10].

(c) *Flow rules:*

$$\delta B = 2\delta\lambda(1-B)^2 \cos^2 \omega / E_{CB} \quad (8)$$

$$\delta \varepsilon_s^p = 2\delta\lambda q / (Mp + c(1-D))^2 \quad (9)$$

$$\delta \varepsilon_v^p = \delta\lambda E_B (1-B)^2 \sin^2 \omega / (E_{CB} p) \quad (10)$$

$$\delta D = 2\delta\lambda(1-D)^2 / E_{CD} \quad (11)$$

where  $\omega$  is the coupling angle between Breakage and the volumetric component of the plastic compaction as in Einav [12] and  $\delta\lambda$  is the non negative multiplier.

## 4 Model Calibration and Constitutive Responses

The model is assessed against the experimental data for Calcarenite documented in [3]. The model parameters: grain stiffness coefficients and grain-cement elastic stiffness ratio ( $G_G = 2100$ ,  $K_G = 1697$ ,  $\eta = 4.7$ ), critical energies ( $E_{CB} = 5.51$  kPa and  $E_{CD} = 25.01$  kPa) are obtained from the experimental stress-strain responses. The grading index ( $\vartheta = 0.8$ ) is determined from the known initial *gsd* and the commonly accepted assumption of a fractal distribution for the ultimate state. Grain solid fraction ( $f_G = 0.8$ ) is deduced from literature. The critical state parameter ( $M = 1.35$ ) and the coupling angle ( $\omega = 80^\circ$ ) are deduced from the friction angle [12].

As shown in Figure 2(a-d), the model constitutive responses during K0 consolidation, as well as the initial yield surface, are in good quantitative agreement with the experimental data. The observed mismatch after yield can be attributed to localization as observed in Lagioia and Nova [3] and therefore they are a specimen feature rather than the material constitutive response.

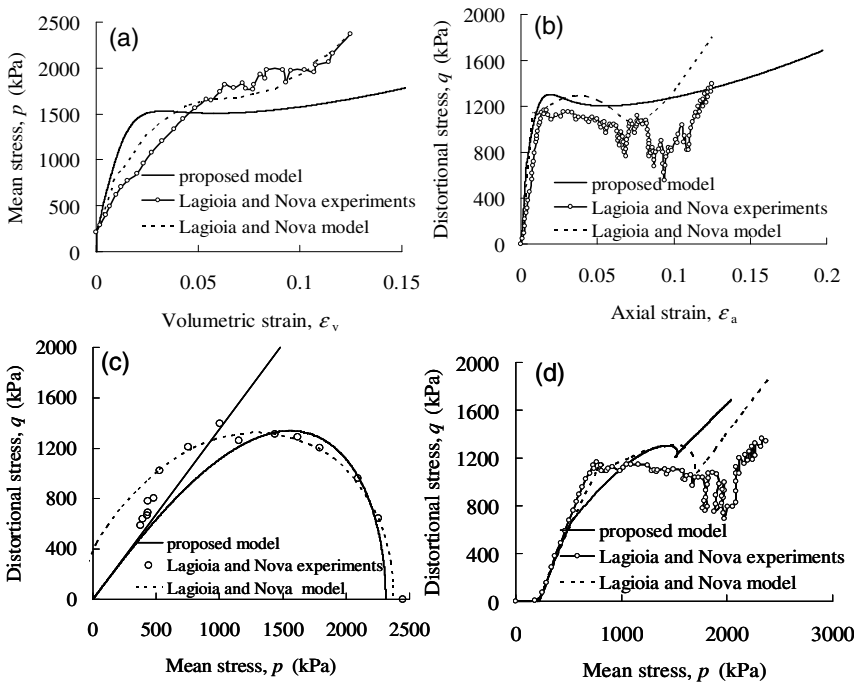


**Fig. 2.** (a) Mean stress vs. volumetric strain response. (b) Distortional stress vs. axial strain response. (c) Initial yield surface. (d) Stress path for  $K_0$  consolidation

### 5 Effects of Stiffnesses, Critical Energies on Constitutive Responses

While the effect of many constitutive parameters have already been delineated in Einav [10,12], it is interesting to note how the critical energy ratio  $k = E_{CD}/E_{CB}$  and the stiffness ratio  $\eta = K_C/K_C (G_G/G_C)$  influence the material behavior in an isotropic compression tests. In Fig.3a it is shown how the energy ratio affects the evolution of the internal variables, so that even if, due to the coupling, the processes start simultaneously, increasing  $E_{CD}$  will slow down the damaging process and thus stiffening the material (Fig. 3b) in inelastic regime. On the other hand an increase of the stiffness of the cement does not influence the relative increment of the internal variables, as can be proved from flow rules (eq. 8 – 11), but affects both the critical pressure and, as expected, the overall stiffness.

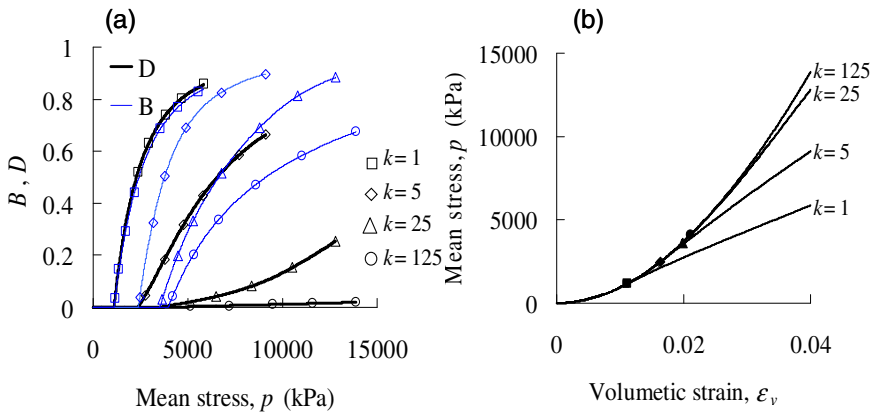


**Fig. 3.** Effects of  $k=E_{CD}/E_{CB}$  on model responses in isotropic compression: a) Evolution of the internal variables, b) Volumetric stress-strain response

## 6 Conclusions

A novel constitutive model for cemented granular material is proposed in this paper. The distinctive choice of the internal variables representing the grain scale failure processes allow a better understanding of the evolution of the material structure under different loading conditions. The physical perspective implies a clear identification for all parameters, reducing their number and facilitating their evaluation. The remarkable capability of the constitutive response of the model to reproduce experimental results is very promising in the perspective of a further numerical simulation of the test conditions, where the inhomogeneous response of the specimen can be captured.

## References

- [1] Menéndez, B., Zhu, W., Wong, T.-F.: Micromechanics of brittle faulting and cataclastic flow in Berea sandstone. *Journal of Structural Geology* 18, 1–16 (1996)
- [2] Vatsala, A., Nova, R., Murthy, B.R.S.: Elastoplastic Model for Cemented Soils. *Journal of Geotechnical and Geoenvironmental Engineering* 127, 679–687 (2001)
- [3] Lagioia, R., Nova, R.: An experimental and theoretical study of the behaviour of a calcarenite in triaxial compression. *Géotechnique* 45, 633–648 (1995)
- [4] Nova, R., Castellanza, R., Tamagnini, C.: A constitutive model for bonded geomaterials subject to mechanical and/or chemical degradation. *International Journal for Numerical and Analytical Methods in Geomechanics* 27, 705–732 (2003)
- [5] Gens, A., Nova, R.: Conceptual bases for a constitutive model for bonded soils and weak rocks.pdf. In: Anagnostopoulos, A., Frank, R., Kalteziotis, N., Schlosser, F. (eds.) *Geotechnical Engineering of Hard Soils -Soft Rocks*, pp. 485–494. Balkema, Rotterdam (1993)

- [6] Jiang, M.J., Yan, H.B., Zhu, H.H., Uti, S.: Modeling shear behavior and strain localization in cemented sands by two-dimensional distinct element method analyses. *Computers and Geotechnics* 38, 14–29 (2011)
- [7] Marketos, G., Bolton, M.D.: Compaction bands simulated in Discrete Element Models. *Journal of Structural Geology* 31, 479–490 (2009)
- [8] Estrada, N., Lizcano, A., Taboada, A.: Simulation of cemented granular materials. I. Macroscopic stress-strain response and strain localization. *Physical Review E* 82, 1–11 (2010)
- [9] Topin, V., Delenne, J.-Y., Radjai, F., Brendel, L., Mabil, F.: Strength and failure of cemented granular matter. *The European Physical Journal E, Soft. Matter.* 23, 413–429 (2007)
- [10] Einav, I.: Breakage mechanics—Part I: Theory. *Journal of the Mechanics and Physics of Solids* 55, 1274–1297 (2007)
- [11] Coop, M.R., Atkinson, J.: The mechanics of cemented carbonate sands. *Geotechnique* 43, 53–67 (1993)
- [12] Einav, I.: Breakage mechanics—Part II: Modelling granular materials. *Journal of the Mechanics and Physics of Solids* 55, 1298–1320 (2007)
- [13] Hill, R.: Acceleration waves in solids. *Journal of the Mechanics and Physics of Solids* 10, 1–16 (1962)

# Modelling the Thermo-plasticity of Unsaturated Soils

Bertrand François<sup>1</sup> and Lyesse Laloui<sup>2</sup>

<sup>1</sup> BATirDepartment, Université Libre de Bruxelles, Belgium

<sup>2</sup> SoilMechanicsLaboratory, Ecole Polytechnique Fédérale de Lausanne, Switzerland  
lyesse.laloui@epfl.ch

**Abstract.** This paper presents a highly-coupled thermo-plasticity model for unsaturated soils. The effect of temperature on the mechanics of unsaturated soils is briefly addressed. Then the equations of the developed model, so-called ACMEG-TS, are detailed. Finally, the model is validated by the means of comparisons with experiments. This constitutive model constitutes an effective tool for modelling the thermo-hydro-mechanical (THM) behaviour of geomaterials involved in the confinement of nuclear waste disposal.

## 1 Introduction

The geomaterials that will be involved in the confinement of radioactive waste in deep geological formations will be submitted to strong thermal, hydraulic, and mechanical modifications. Those modifications may produce a significant change of the characteristics of the confinement barrier, partially due to thermo-plasticity effects in the confining soil [Laloui et al. 2008]. Following the need for understanding and quantifying such effects, a constitutive model that deals with the thermo-mechanical modelling of unsaturated soils is proposed [François and Laloui 2008].

## 2 Thermo-plasticity in Soils

The thermal effects on the mechanical response of soils must be considered not only in terms of reversible phenomena, but also in term of thermo-plasticity. The predominant effect of temperature on the behaviour of fine-grained soils is the causation of successively lower void ratios with temperature increasing for a given stress level. The normally consolidated lines at different temperatures are parallel and shifted to the left with increasing temperature. As a consequence, in a normally consolidated state, the soil undergoes thermal hardening (i.e. densification) upon heating in order to reach the normally consolidated line corresponding to the current temperature. Under undrained conditions, the generation of pore water pressure upon heating is a consequence of a higher thermal expansion coefficient

of water than of the mineral phase. Also, thermo-plastic processes may induce additional pore water pressure. Moreover, the deviatoric behaviour of soils may also be affected by temperature variations [Hueckel et al. 2008].

In addition to the effect of temperature on the saturated soils, the unsaturated conditions bring additional thermo-hydro-mechanical couplings in the materials. In particular, the water retention capacity of soils decreases with increasing temperature.

From an experimental study of the combined effects of suction  $s$  and temperature  $T$  on the preconsolidation pressure, Salager et al. (2008) deduced logarithmic functions to describe the evolution of  $p'_c$  with temperature and suction:

$$p'_c(s, T) = \begin{cases} p'_{c0} \{1 - \gamma_T \log [T / T_0]\} & \text{if } s \leq s_e \\ p'_{c0} \{1 - \gamma_T \log [T / T_0]\} \{1 + \gamma_s \log [s / s_e]\} & \text{if } s \geq s_e \end{cases} \quad (1)$$

where  $p'_{c0}$  is the preconsolidation pressure at ambient temperature  $T_0$  and for suction lower than the air-entry value  $s_e$ .  $\gamma_T$  and  $\gamma_s$  are material parameters.

### 3 The Constitutive Equations

The developed model uses the generalized effective stress approach [Bishop 1959, Nuth and Laloui, 2008]:

$$\sigma'_{ij} = (\sigma_{ij} - p_a \delta_{ij}) + S_r (p_a - p_w) \delta_{ij} \quad (2)$$

where  $\sigma_{ij}$  is the total external stress tensor,  $p_a$  and  $p_w$  the air and water pore pressures, respectively,  $\delta_{ij}$  Kroenecker's symbol and  $S_r$  the degree of saturation.

The model, called ACMEG-TS, is based on an elasto-plastic-framework. The elastic part of the deformation is expressed as follows:

$$d\epsilon_{ij}^e = E_{ijkl}^{-1} d\sigma'_{kl} - \beta_{T,ij} dT \quad (3)$$

The first term of Equation (3) may follow from total stress or fluid pressure variations while the second term is related to the thermo-elastic strain of the material, through the thermal expansion coefficient vector,  $\beta_{T,ij} = (1/3) \beta'_s \delta_{ij}$ .

The plastic mechanism of the material is induced by two coupled hardening processes: an isotropic and a deviatoric one. Using the concept of multi-mechanism plasticity, both mechanisms may induce volumetric plastic strain. Therefore the total volumetric plastic strain rate  $d\epsilon_v^p$  is the coupling variable linking the two hardening processes. The yield functions of the two mechanical, thermo-plastic mechanisms have the following expressions (Figure 1):

$$f_{iso} = p' - p'_c r_{iso} \quad ; \quad f_{dev} = q - Mp' \left( 1 - b \text{Log} \frac{d p'}{p'_c} \right) r_{dev} = 0 \quad (4)$$

where  $p'_c$  is the preconsolidation pressure.  $b$ ,  $d$  and  $M$  are material parameters.  $p'_c$  depends on the volumetric plastic strain,  $\epsilon_v^p$ , in addition to temperature and suction:

$$p'_c = p'_c(s, T) \exp(\beta \epsilon_v^p) \quad (5)$$

where  $\beta$  is the plastic compressibility modulus and  $p'_c(s, T)$  is expressed in Equation (1).  $r_{iso}$  and  $r_{dev}$  are the degree of mobilization of the isotropic and the deviatoric mechanisms and are hyperbolic functions of the plastic volumetric strain induced by the isotropic and the deviatoric mechanisms, respectively [Hujeux 1979; Laloui and François 2008].

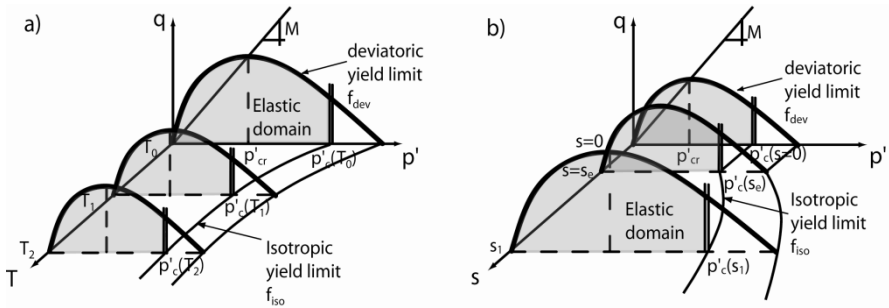


**Fig. 1.** Effect of (a) temperature and (b) suction on the shape of coupled mechanical yield limits

In terms of water retention response, desaturation is also addressed as a yielding phenomenon. As long as the soil is drying, suction increases, and the degree of saturation,  $S_r$ , tends to decrease mainly when the air-entry suction  $s_e$  is reached. Under re-wetting, a hysteretic phenomenon occurs, also represented by a yielding process (Figure 2). A wetting-drying cycle activates two successive yield limits in the  $(S_r - s)$  plane ( $f_{dry}$  and  $f_{wet}$ , along the drying and wetting paths, respectively):

$$f_{dry} = s - s_d = 0 \quad ; \quad f_{wet} = s_d s_{hys} - s = 0 \quad (7)$$

where  $s_d$  is the drying yield limit and  $s_{hys}$  a material parameter considering the size of the water retention hysteresis. Because air-entry suction of the materials

depends on temperature and dry density,  $s_d$  is a function of temperature and volumetric strain [François and Laloui 2008]:

$$s_d(T, \varepsilon_v) = s_{d0} \{1 - \theta_r \log [T/T_0] - \theta_e \log [1 - \varepsilon_v]\} \quad (8)$$

where  $\theta_r$  and  $\theta_e$  are material parameters describing the evolution of air-entry suction with respect to temperature and volumetric strain, respectively. If the initial state is saturated, the initial drying limit  $s_{d0}$  is equal to air-entry suction  $s_e$  and increases when suction overtakes  $s_e$  as follows:

$$s_d = s_d(T, \varepsilon_v) \exp(-\beta_h \Delta S_r) \quad (9)$$

where  $\beta_h$  is the slope of the desaturation curve in the  $(S_r - \ln s)$  plane (Figure 2).  $s_d(T, \varepsilon_v)$  is described by Equation (8).

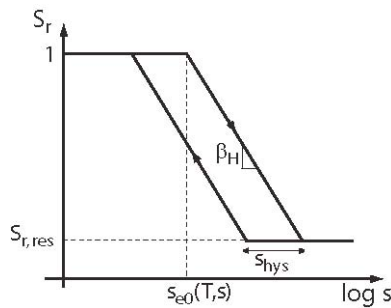


Fig. 2. Schematic representation of water retention curve modelling

### 4 Numerical Simulations

The proposed model has been extensively validated with the results of different non-isothermal experiments under saturated and unsaturated conditions [François and Laloui 2008; François 2008]. In this section, comparison between numerical simulations and experimental results on compacted FEBEX bentonite is briefly proposed. Figure 3a compares the numerical simulations with oedometric compression tests at different suctions ( $T = 22^\circ\text{C}$ ). The compression paths clearly show the enhancement of elastic domain when suction increases. Figure 3b reproduces the numerical simulation of oedometric compression tests at two temperatures under 127 MPa of suction.

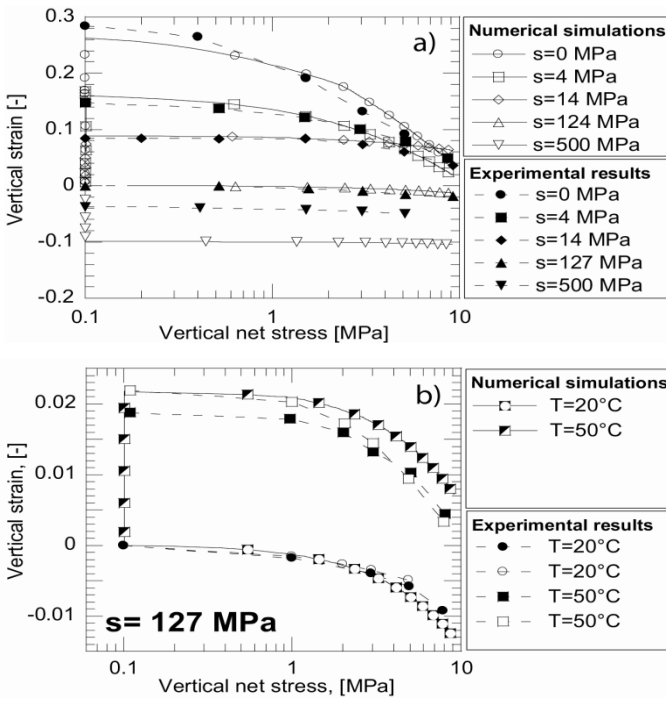


Fig. 3. Numerical simulations of oedometric compression tests of FEBEX bentonite at (a) different suctions and (b) different temperatures. Comparisons with experiments.

## 5 Conclusions

When a soil is simultaneously submitted to stress, suction and temperature variations, several coupling effects are involved in its global response. Those interactions have been introduced in a unified constitutive framework, so-called ACMEG-TS, including two interconnected aspects (a mechanical and a water retention framework) linked through a generalized effective stress expression. This constitutive approach has been confronted with experimental results through numerical predictions which tend to proof the accuracy of the developed model. ACMEG-TS constitutes an effective constitutive tool for modelling the THM behaviour of geomaterials.

## References

[1] Bishop, A.W.: The principle of effective stress. *TecniskUkeblad* 39, 859–863 (1959)  
 [2] François, B.: Thermo-plasticity of fine-grained soils at various saturation states: Application to nuclear waste disposal. PhD Thesis, EPFL, Lausanne, Switzerland (2008)

- [3] François, B., Laloui, L.: ACMEG-TS: A constitutive model for unsaturated soils under non-isothermal conditions. *International Journal for Numerical and Analytical Methods in Geomechanics* 32, 1955–1988 (2008)
- [4] Hueckel, T., François, B., Laloui, L.: Explaining thermal failure in saturated clays. *Géotechnique* 61(10), 831–844 (2008)
- [5] Hujeux, J.C.: Calcul numérique de problèmes de consolidation élastoplastique. PhD Thesis, EcoleCentrale, Paris (1979)
- [6] Laloui, L., François, B.: ACMEG-T: A soil thermo-plasticity model. *Journal of Engineering Mechanics* 135(9), 932–945 (2008)
- [7] Laloui, L., François, B., Nuth, M., Peron, H., Koliji, A.: A thermo-hydro-mechanical stress-strain framework for modelling the performance of clay barriers in deep geological repositories for radioactive waste. In: 1st European Conf. on Unsaturated Soils, Durham, United Kingdom, pp. 63–80 (2008)
- [8] Lloret, A., Romero, E., Villar, M.: FEBEX II Project: Final report on thermo-hydro-mechanical laboratory tests. *Publicación técnica* 10/2004, ENRESA (2004)
- [9] Nuth, M., Laloui, L.: Effective Stress Concept in Unsaturated Soils: Clarification and Validation of a Unified Framework. *International Journal of Numerical and Analytical Methods in Geomechanics* 32(7), 771–801 (2008)
- [10] Salager, S., François, B., El Youssoufi, M.S., Laloui, L., Saix, C.: Experimental investigations on temperature and suction effects on compressibility and pre-consolidation pressure of a sandy silt. *Soils and Foundations* 48(4), 453–466 (2008)

# Modeling the Dilatancy of Overconsolidated Clay

Zhiwei Gao\* and Jidong Zhao

Department of Civil and Environmental Engineering, Hong Kong University of Science and Technology, Clearwater Bay, Kowloon, Hong Kong  
gzwce@ust.hk

**Summary.** The dilatancy of clay has long been considered as a function of the current stress state independent of the loading history. Experimental evidence, however, indicates the dilatancy behavior of over-consolidated (OC) clay bears close correlation with the overconsolidation ratio (OCR) of the soil. This paper presents a simple dilatancy relation for OC clays based on the modified Cam-clay (MCC) model. The dilatancy relation is integrated into a bounding surface model to predict the behavior of OC clays. With only three extra parameters added to the MCC model which can be easily calibrated by triaxial compression tests, the new model is shown to offer good predictions for the experimental data.

**Keywords:** Overconsolidation, clay, dilatancy, bounding surface model.

## 1 Introduction

The term dilatancy was first used by Reynolds [1] to describe the different behavior of volumetric change observed in dense and loose granular assemblies subjected to shear. Dilatancy has been regarded key to the characterization of strength and deformation of soils. Based on drained shear tests on sand, Taylor [2] has shown that there are two sources attributable to the peak strength of sand, one being the inter-particle friction and the other the dilatancy (or interlocking). Later, Rowe [3] developed his seminal stress-dilatancy theory highlighting the important contribution of dilatancy to soil strength and the mobilized friction in the loading process. Not uniquely tagged to sand only, stress dilatancy has been discussed for clay as well (e.g., [4]). In this study, a simple dilatancy relation for OC clay will be proposed based on the MCC model [5]. The new relation can be easily used in conjunction with either the bounding surface or the subloading surface models for OC clay. A demonstrative bounding surface model is developed with the implementation of this dilatancy relation.

---

\* Corresponding author.

## 2 A Simple Dilatancy Relation for OC Clay

In several studies on OC clay using bounding surface, the ratio  $R = r/\bar{r}$  has been used as a key variable to characterize the degree of overconsolidation, where  $r$  and  $\bar{r}$  denote the distances of the current and image stress point from the mapping center, respectively. Smaller  $R$  corresponds to higher degree of overconsolidation. By adopting the origin of the  $p-q$  plane as the mapping center, this  $R$  will be employed as a descriptor for the degree of overconsolidation, where  $p$  and  $q$  denote the mean and deviatoric stress, respectively. Based on this definition of  $R$ , we propose the following dilatancy relation for OC clay

$$D = \frac{d\varepsilon_v^p}{|d\varepsilon_q^p|} = \frac{M_d^2 - \eta^2}{2\eta} \quad (1)$$

where

$$M_d = M_c R^m \quad (2)$$

where  $\eta (= q/p)$  is the stress ratio;  $M_c$  is the critical state stress ratio in triaxial compression and  $m$  is a non-negative material constant. The dilatancy relation expressed above has the following features: (a) For Normally consolidated (NC) clays with the stress state on the bounding surface, Equation (2) is recovered to the dilatancy relation of the MCC model as  $M_d = M_c$ ; (b) As the degree of overconsolidation increases,  $R$  decreases, so do  $M_d$  and  $D$ . This indicates that the response of a clay with higher degree of overconsolidation would be more dilative at the same stress ratio  $\eta$  [6]; (c) At the critical state, the clay becomes NC and the stress state lies on the bounding surface ( $R = 1$ ) with  $\eta = M_c$ , and thus,  $D = 0$ .

## 3 A Bounding Surface Model for Overconsolidated Clay

Based on the dilatancy equation in Equations (1) and (2), a bounding surface model for OC clay is developed here. We will use the  $\alpha - \gamma$  yield surface proposed by Collins [7] as the bounding surface with the assumption of  $\alpha = \gamma$ ,

$$\bar{f} = \frac{(\bar{p} - \alpha \bar{p}_0/2)^2}{[(1-\alpha)\bar{p} + \alpha \bar{p}_0/2]^2} + \frac{\bar{q}^2}{M_c^2 [(1-\alpha)\bar{p} + \alpha \bar{p}_0/2]^2} - 1 = 0 \quad (3)$$

where  $\bar{p}_0$  denotes the size of the bounding surface;  $\bar{p}$  and  $\bar{q}$  are respectively the mean stress and deviatoric stress at the image point. Following Dafalias and Herrmann [8], the same isotropic hardening law as in the MCC model is assumed for  $\bar{p}_0$ ,

$$d\bar{p}_0 = \frac{1+e}{\lambda-\kappa} \bar{p}_0 d\epsilon_v^p \tag{4}$$

where  $\lambda$  and  $\kappa$  are the compression and swelling indices, respectively;  $d\epsilon_v^p$  is the plastic volumetric strain increment. An associated flow rule in the deviatoric plane will be employed,

$$d\epsilon_q^p = \langle dL \rangle \frac{\partial \bar{f}}{\partial \bar{q}} \tag{5}$$

where  $dL$  is the loading index;  $d\epsilon_q^p$  is the plastic deviatoric strain increment;  $\langle \rangle$  are the McCauley brackets. The plastic modulus at the image stress point,  $\bar{K}_p$  is expressed as

$$\bar{K}_p = -\frac{\partial f}{\partial \bar{p}_0} \frac{(1+e)\bar{p}_0}{(\lambda-\kappa)} D_{R=1} = -\frac{(1+e)\bar{p}_0}{(\lambda-\kappa)} \frac{\partial f}{\partial \bar{p}_0} \frac{\partial f}{\partial \bar{q}} \frac{(M_c^2 - \bar{\eta}^2)}{2\bar{\eta}} \tag{6}$$

The expression for the plastic modulus at the current stress state  $K_p$  is simply assumed to be of the identical form of  $\bar{K}_p$  by simply replacing  $M_c$  by a virtue peak stress ratio  $M_v$ ,

$$K_p = -\frac{(1+e)\bar{p}_0}{(\lambda-\kappa)} \frac{\partial f}{\partial \bar{p}_0} \frac{\partial f}{\partial \bar{q}} \frac{(M_v^2 - \eta^2)}{2\eta} \tag{7}$$

where  $M_v$  is related to  $R$  according to

$$M_v = M_c R^{-n} \tag{8}$$

where  $n$  is a non-negative model parameter. For OC clay,  $K_p$  is dependent on the difference between the current stress ratio  $\eta$  ( $=\bar{\eta}$ ) from the virtue peak stress ratio  $M_v$  attainable at the current degree of overconsolidation defined by  $R$ . Since  $R \leq 1$ , the virtue peak stress ratio  $M_v$  in Equation (11) is a decreasing function of  $R$  and thus an increasing function with the degree of overconsolidation [6].

### 4 Model Verification

Shown in Fig. 1 is the comparison between our model predictions with the test data on the Boston blue clay (data from [6]). Good agreement can be observed. In the figures,  $\epsilon_a$  is the axial strain and  $p_c$  is the maximum consolidation pressure. The model parameters are listed in Table 1, where  $\nu$  is the Poisson ratio and  $\Gamma$  is the void ratio at the reference mean stress  $p_r$  on the normal consolidation line.

**Table 1.** Model parameters for Boston blue clay

$M_c$	$\lambda$	$\kappa$	$\nu$	$\Gamma (p_r \text{ (kPa)})$	$\alpha$	$m$	$n$
1.353	0.184	0.036	0.1	1.01 (300)	0.68	0.3	1.5

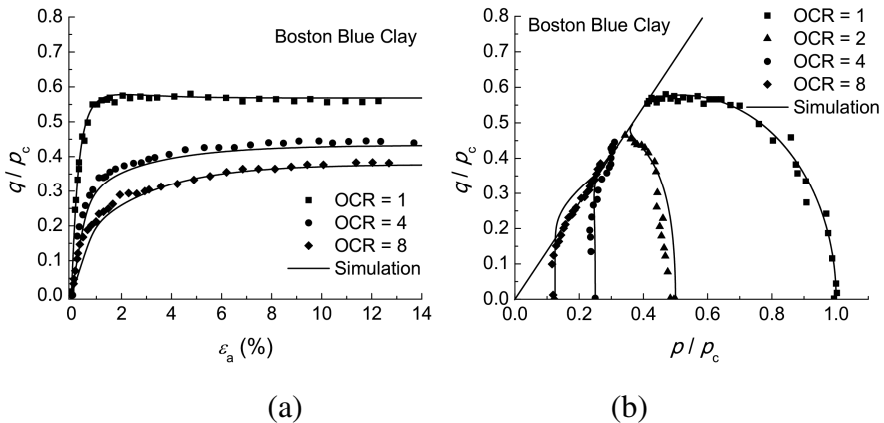


**Fig. 1.** Comparison between the model simulation and test results on Boston blue clay (data from Pestana et al. (2002)): (a) the  $\epsilon_a - q/p_c$  relations and (b) the effective stress paths

### 5 Conclusion

A simple dilatancy relation for OC clay is proposed and used in a predictive bounding surface model. The model has been demonstrated to predict the behavior of OC clays well as compared to test data. Future work will be done on modeling the behavior of structured soils (e.g., [9]).

**Acknowledgements.** This work was supported by Research Grants Council of Hong Kong (under grant no. 623211).

## References

- [1] Reynolds, O.: On the dilatancy of media composed of rigid particles in contact. With experimental illustrations. *Phil. Mag.* 20, 469–482 (1885)
- [2] Taylor, D.W.: *Fundamentals of soil mechanics*. Wiley, New York (1948)
- [3] Rowe, P.W.: The stress-dilatancy relation for static equilibrium of an assembly of particles in contact. *Proc. Roy. Soc. London A269*, 500–527 (1962)
- [4] Schofield, A.N.: The Mohr-Coulomb error. In: *Proc. Symp. on Mechanics and Geotechnics*, LMS Ecole Polytechnique, Paris, vol. 23, pp. 19–27 (1998)
- [5] Roscoe, K.H., Burland, J.B.: On the generalized stress-strain behavior of 'wet' clay. In: *Engineering Plasticity*, pp. 535–609. Cambridge University Press, Cambridge (1968)
- [6] Pestana, J.M., Whittle, A.J., Gens, A.: Evaluation of a constitutive model for clays and sands: Part II – clay behaviour. *Int. J. Numer. Anal. Meth. Geomech.* 26, 1123–1146 (2002)
- [7] Collins, I.F.: Elastic/plastic models for soils and sands. *Int. J. Mech. Sci.* 47, 493–508 (2005)
- [8] Dafalias, Y.F., Herrmann, L.R.: Bounding surface plasticity II: Application to isotropic cohesive soils. *J. Eng. Mech.* 112(12), 1263–1291 (1986)
- [9] Gao, Z.W., Zhao, J.D.: Constitutive modeling of artificially cemented sand by considering fabric anisotropy. *Computer and Geotechnics* 41, 57–69 (2012)

# Current Situation of Constitutive Model for Soils Based on Thermodynamics Approach

Xiao-xia Guo, Xiang Sun, Long-tan Shao, and Bo-ya Zhao

Department of Engineering Mechanics  
Dalian University of Technology  
No.2 Linggong Road, Ganjingzi, Dalian Liaoning, P. R. C.  
whanyuer@163.com

**Abstract.** Traditional constitutive models of soils were based on Drucker's Stability Postulate and the theory of plastic potential. The yield condition, flow rule and hardening law are determined independently and contradict each other sometimes, which results the probability of violating thermodynamics laws. Thermodynamic-based constitutive models for soils are newly developed constitutive models. This approach has the advantage that the models are guaranteed to obey the laws of thermodynamics by use of dissipative incremental function and free energy function, while retrospective criteria need not be applied. The development history of constitutive models based on thermodynamic approach is outlined, the recent study situations are analysed, and the classification of the models is discussed which indicate a broad field of applications to modeling constitutive behavior for soils.

**Keywords:** thermodynamic, soil constitutive model, dissipation function.

## 1 Defect of Traditional Soil Constitutive Model

The soils have extremely complicated physical properties including anisotropism and discontinuity. As a result, the stress-strain relationship of soils is non-linear and non-elastic. The deformation and strength relates not only to the stress-deformation state, but to the stress history, loading rate, drainage condition and consolidation state[1].

Since the middle of the last century, many researchers have developed a large amount of elasto-plastic model of soil, but few of them have been utilized by engineers. There are two types of the traditional soil plastic theory: 1) plastic potential theory and 2) Drucker's postulate. Because plastic potential theory is obtained through a simple imitation of the elastic potential theory, it has no rigorous theoretical foundation. Huang found that Drucker's postulate is independent of the thermodynamic theorem assumption [2]. Not all materials must satisfy these two assumptions. Zheng and Liu proved that neither Drucker's postulate nor traditional plastic mechanics can be applied to geotechnical materials. The single yield surface model based on the traditional plasticity theory is unable to reflect the Geotechnical

deformation properties, whether the associated flow rule is utilized [3]. Appearance of non-associated flow rule and multi-yield surface model modified traditional plastic theories. However, this modification is only based on empirical model of rock and soil mechanics test results. Rigorous theory is not built for the absence of clearer relationship between plastic and non-associated. In these theories, plastic potential surface tend to be arbitrarily assumed [4-7].

## **2 Trends in the Application of a Thermodynamic Approach in Geotechnical Constitutive Model**

The generalized thermodynamics has been applied in more and more research fields. In recent years, this method is used in construction of geotechnical constitutive model. Ziegler and Wehrli [8-9] described the Coulomb material with generalized thermodynamics. Few years later French researchers including Maguin Besseling, van der Giessen, Lemaitre and Chaboche developed this theory to make it more rigorous [10,11,12]. Housby applied thermodynamic approach to soil constitutive theory and showed the free energy function and dissipation function corresponding to the modified Cambridge model [13,14,15]. Then, he applied it in large deformation problems and three-dimensional problems. A rate independent theoretical framework was established by Collins and Housby. It was proved that if dissipation function is independent to the true stress space, associated flow rule in true stress space can be used to conduct constitutive equations of the rate-independent materials without considering elasto-plastic coupling, or else, non-associated flow rule should be used. In addition, they analyzed different Gibbs free energy function expression forms under the condition of considering elastoplastic decoupling and pointed out that the rate-independent dissipation function is a homogeneous function of the plastic strain increment [16].

There are two ways to apply the thermodynamics approach in the soil constitutive model. One way is that the concept of the yield surface plastic potential and hardening function are used as usual as before, but the laws of thermodynamics should be treated as an additional constraint of constitutive model. Collins and Housby found that this method is very cumbersome and lack of versatility [16]. Another way is to assume free energy function and dissipation energy function directly. By this way, the yield surface, the flow rule expressed in dissipative stress space and the true stress space can be derived by these two energy functions and constitutive equations can satisfy the law of thermodynamics automatically.

## **3 Research Status of Thermodynamic Approach**

Elastic constitutive based on the thermodynamics approach: Housby established an energy conservative elastic model based on the elastic energy conservation principle. Variation of the soil shear modulus can be described by this model and non-conservative behavior can't be caused. At the same time, it is considered that the shear modulus is proportional to the pressure in this model [17,18,19,20]. Borja

derived a nonlinear elastic model of the clay based on summarizing Houlsby's hyperelastic approach [21]. Einav proposed a general Gibbs free energy function, and indicated how to join the elastic to plastic model to make the elasto-plastic model automatically satisfy the laws of thermodynamics [22,23].

Rate-independent and rate-dependent elasto-plastic model based on the thermodynamics: Houlsby and Puzrin considered that either Helmholtz free energy function or Gibbs free energy function, combined with dissipation function or yield function defined in dissipative stress space, can be applied to construct a complete constitutive model and deduced the theoretical framework of rate-independent material [24]. Collins and Hilder deduced general form of dissipation function of rate-independent material according to that dissipation function of rate-independent material is a homogeneous function of the plastic strain increment. They also discussed how to build the isotropic constitutive model and the anisotropic constitutive model with thermodynamics approach. Then, a micro scale interpretation of plastic free energy was given by Collins [25]. Wang discussed the reason why the associated flow rule should not be applied to geomaterials by analyzing the relationship between the principle of maximum plastic work and the principle of maximum entropy production rate [26]. Houlsby and Puzrin constructed an elasto-plastic model to describe the effect of time by applying hyperplastic mechanics. In this case, free energy function is the same as that of rate-independent materials, however, dissipation function is divided into force potential function and flow potential function. These two potential functions can be linked by the Legendre-Fenchel transform [24,27,28].

Development of modified Cambridge model based on thermodynamics: Collins [29,30] used dimension analysis approach to discuss dissipation function of the original Cambridge model and the modified Cambridge model respectively. It was emphasized that original Cambridge model dose not satisfy law of thermodynamics because dissipation caused by compression is not considered in the model. Collins proposed  $\alpha$  model in order to consider the modification of yield function and  $\beta$  model to consider the relationship between shear stress and harding. Combining  $\alpha$  and  $\beta$  model, dissipative stress and principle of dissipation during deformation were discussed by Collins [31]. Collins and Muhunthan applied hyperplastic theory to analyse the relationship between soil dilatancy and anisotropy. They pointed out that in the anisotropic analysis, the soil critical state line should be divided into PTL (or CSL) and RTL (DFL). On the PTL (phase translation line), soil dilatancy angle is 0. However, on the RTL (Renold-Taylor line), soil anisotropy angle is equal to the dilatancy angle [32]. Wang [33] extended the traditional clay model to modified model in which influence of  $k_0$  consolidation factor can be considered. Three parameters ( $n_0$ ,  $R$  and  $R^*$ ) which describe the anisotropy of the soft clay and two parameters ( $m$  and  $a$ ) which describe evolution of internal variables were introduced into the Wang's model.

Thermodynamics of multiphase medium model: Li [34,35] considered relationship between storage energy and dissipation based on single-phase medium thermodynamic approach and micro-mechanics. In this model, different potential functions for soil skeleton and pore fluid respectively are defined and coupling of work, energy and dissipation in different phases is considered. Buscarnera [36] built

a strain hardening constitutive model of unsaturated sands model framework by thermodynamic approach to solve the mechanical instability of the unsaturated materials, especially the volume failure caused by hydraulic fracture.

Thermodynamic model based on micromechanics: Collins [29] developed the thermodynamic approach by the introduction of stored plastic work or the freezing of elastic energy concept considering the stress non-homogeneity and strain non-homogeneity in micro scale. It is concluded that plastic work is not totally used for dissipation but some is used for storage. At the micro scale, the stored plastic work is the freezing elastic energy among particles. Only when plastic loading applied on the material, can the freezing energy be reverted. Kong and Collins [37] divided plastic volumetric strain increment of sand into stress-induced volumetric strain and shear strain induced by the plastic volumetric strain increment (Reylonds dilatancy) and added non-work constraints related with Reylonds dilatancy to constitutive model. Thus, the constitutive model can not only describe Reylonds effect but predict the induced anisotropy. Besides, they also proposed the concept of the "Reynolds-Taylor state" which is generalization of critical state for the concept of the classical isotropic theory.

Dynamics model based on thermodynamics: Puzrin and Houlsby [38,39] constructed a multi-yield surface constitutive framework by extension of single yield surface model, and introduced some concepts such as internal function and energy functional in order to make stress-strain curve more smooth. Thus, Masing effect and ratcheting effect can be easily described. Guo [40] modified Hardin-Drnevich mode by thermodynamics approach and defined the concept of threshold strain. Two threshold strains separate dissipation process into three parts to analyze different dissipation in different parts.

## 4 Conclusion

The model which is built based on thermodynamics framework satisfies thermodynamics law automatically and has general application. Once two energy functions, free energy function and dissipation function, are ascertained, all the factor of elasto-plastic constitutive model including elastic stress-strain relationship, yield conditions, flow law and hardening law can be ascertained, so lots of arbitrary assumptions such as Drucker's postulate and plastic potential functions can be discarded. Although the application of thermodynamics approach in geotechnical engineering was spread in just a few years, it has shown powerful vitality and broad prospects of development. Soil constitutive model based on the thermodynamic approach is still in the early stage of development, it is necessary to carry out in-depth study.

## References

- [1] Luan, M.-T.: Thinking on some fundamental mechanics issues on geotechnical engineering. *Journal of Dalian University of Technology* 39(2), 309–317 (1999)
- [2] Huang, S.-J.: Thermodynamics and the postulates of stability in plasticity. *Acta Mechanica Solida Sinica* 9(2), 95–101 (1988)

- [3] Liu, Y.-X.: Study of several basic problems in constitutive theory of geomaterials. *Chinese Journal of Geotechnical Engineering* 23(1), 45–48 (2001)
- [4] Zheng, Y.-R., Liang, K.: Componental plastic mechanics-generalized plastic mechanics. *Chinese Journal of Geotechnical Engineering* 22(3), 269–274 (2001)
- [5] Zheng, Y.-R.: Theory of generalized plastic mechanics. *Rock and Soil Mechanics* 21(2), 188–192 (2000)
- [6] Zheng, Y.-R.: New development of geotechnical plastic mechanics. *Chinese Journal of Geotechnical Engineering* 25(1), 1–10 (2003)
- [7] Zheng, Y.-R.: Several problems about geotechnical plastic. *Geotechnical Engineering Field* 5(4), 14–16 (2002)
- [8] Ziegler, H.: An introduction to thermomechanics. North-Holland, Amsterdam (1983)
- [9] Ziegler, H., Wehrli, C.: The derivation of constitutive relations from the free energy and the dissipation function. *Advances Applied Mechanics* 25, 183–238 (1987)
- [10] Maugin, G.A.: The thermomechanics of plasticity and fracture. Cambridge University Press, Cambridge (1992)
- [11] Besseling, J.F., Giessen, E.V.D.: Mathematical modelling of inelastic deformation. Chapman and Hall, London (1994)
- [12] Lemaitre, J., Chaboche, J.L.: Mechanics of solid materials. Cambridge University Press, Cambridge (1990)
- [13] Houlsby, G.T.: A study of plasticity theories and their applicability to soils. University of Cambridge, Cambridge (1981)
- [14] Houlsby, G.T.: A derivation of the small-strain incremental theory of plasticity form thermodynamics 109–118 (1982)
- [15] Houlsby, G.T.: Interpretation of dilation as a kinematic constraint. In: Kolymbas, D. (ed.) *Modern Approaches to Plasticity*, pp. 119–138 (1993)
- [16] Collins, I.F., Houlsby, G.T.: Application of thermomechanical principles to the modeling of geomaterials. *Proc. Royal Society of London, Series A* 453, 1975–2001 (1997)
- [17] Houlsby, G.T.: The use of a variable shear modulus in elastic-plastic models for clays. *Comput. Geotech.* 1, 3–13 (1985)
- [18] Houlsby, G.T., Amorosi, A., Rojas, E.: Elastic moduli of soils dependent on pressure: a hyperelastic formulation. *Geotechnique* 55(5), 383–392 (2005)
- [19] Houlsby, G.T., Puzrin, A.M.: Principles of hyperplasticity: an approach to plasticity theory based on thermodynamic principles. Springer, London (2006)
- [20] Graham, J., Houlsby, G.T.: Anisotropic elasticity of a natural clay. *Geotechnique* 33, 165–180 (1983)
- [21] Borja, R.I., Tamagnini, C., Amorosi, A.: Coupling plasticity and energy conserving elasticity models for clays. *Journal of Geotechnical and Geoenvironmental Engineering* 123(10), 948–957 (1997)
- [22] Einav, I., Puzrin, A.M.: Pressure-dependent elasticity and energy conservation in elastoplastic models for soils. *Journal of Geotechnical and Geoenvironmental Engineering* 130(1), 81–92 (2004)
- [23] Einav, I.: Application of thermodynamical approaches to mechanics of soils. Technion-Israel Institute of Technology, Israel (2002)
- [24] Houlsby, G.T., Puzrin, A.M.: A thermomechanical framework for constitutive models for rate-independent dissipative materials. *International Journal of Plasticity* 16(9), 1017–1047 (2000)

- [25] Collins, I.F., Hilder, T.: A theoretical framework for constructing elastic/plastic constitutive models of triaxial tests. *International Journal for Numerical and Analytical Methods in Geomechanics* 26(11), 1313–1347 (2002)
- [26] Wang, Q.-S.: Research on soft clays' constitutive relations based on hyperplasticity. Zhejiang University, ZheJiang (2007)
- [27] Houlsby, G.T., Puzrin, A.M.: Rate-dependent plasticity models derived from potential functions. *Journal of Rheology* 46, 113–126 (2002)
- [28] Puzrin, A.M., Houlsby, G.T.: Rate-dependent hyperplasticity with internal functions. *Journal of Engineering Mechanics* 129(3), 252–263 (2003)
- [29] Collins, I.F., Tai, A.: What has thermo-mechanics to offer geomechanics, 281–288 (2005)
- [30] Collins, I.F., Kelly, P.A.: A thermomechanical analysis of a family of soil models. *Geotechnique* 52(7), 507–518 (2002)
- [31] Collins, I.F.: A systematic procedure for constructing critical state models in three dimensions. *International Journal of Solids and Structures* 40(17), 4379–4397 (2003)
- [32] Collins, I.F., Muhunthan, B.: On the relationship between stress–dilatancy, anisotropy, and plastic dissipation for granular materials. *Geotechnique* 53(7), 611–618 (2003)
- [33] Wang, L.-Z., Shen, K.-L.: A constitutive model of K<sub>0</sub> consolidated structured soft clays. *Chinese Journal of Geotechnical Engineering* 29(004), 496–504 (2007)
- [34] Li, X.S.: Thermodynamics-based constitutive framework for unsaturated soils. 1: Theory. *Geotechnique* 57(5), 411–422 (2007)
- [35] Li, X.S.: Thermodynamics-based constitutive framework for unsaturated soils. 2: A basic triaxial model. *Geotechnique* 57(5), 423–435 (2007)
- [36] Buscarnera, G., Nova, R.: An elastoplastic strainhardening model for soil allowing for hydraulic bonding-debonding effects. *International Journal for Numerical and Analytical Methods in Geomechanics* (2008)
- [37] Liang, K., Collins, I.F.: Thermomechanical approach to modeling constitutive behaviors of geomaterials. *Rock and Soil Mechanics* 29(7), 1732–1740 (2008)
- [38] Puzrin, A.M., Houlsby, G.T.: A thermomechanical framework for rate-independent dissipative materials with internal functions. *International Journal of Plasticity* 17(8), 1147–1165 (2001)
- [39] Puzrin, A.M., Houlsby, G.T.: Fundamentals of kinematic hardening hyperplasticity. *International Journal of Solids and Structures* 38(21), 3771–3794 (2001)
- [40] Chi, S.-C., Guo, X.-X., Yang, J., Lin, G.: Study on small strain characteristics and threshold strain of dynamic Hardin-Drnevich model for soils. *Chinese Journal of Geotechnical Engineering* 30(2), 243–249 (2008)

# Constitutive Modeling of Cemented Sands Using Critical State Soil Mechanics and Generalized Plasticity Concepts

Amir Hamidi\* and Ehsan Ravanbakhsh

Department of Engineering  
Kharazmi University  
P.O.Box 15614, Tehran, Iran  
hamidi@tmu.ac.ir

**Summary.** In present research, a constitutive model is developed for prediction of the mechanical behavior of saturated cemented sands according to generalized plasticity and critical state soil mechanics concepts. The model is based on differences between normal consolidation curves of cemented and uncemented soil in  $e$ - $\ln p'$  space. In order to consider the effects of cementation, six new parameters are added to the generalized plasticity model proposed by Manzanal et al. [1]. Deviatoric stress-axial strain besides volumetric strain-axial strain curves are predicted and compared with experimental data for verification. Results show fairly good performance of presented model.

**Keywords:** constitutive model, generalized plasticity, cemented sand, critical state.

## 1 Introduction

In the recent years significant studies have been performed regarding the behavior of cemented soils. Clough et al. [2], Coop and Atkinson [3], Cuccovillo and Coop [4], Huang and Airey [5], Consoli et al. [6], Schnaid et al. [7], Haeri et al. [8], Hamidi and Haeri [9] and Baxter et al. [10] are among related studies. Oka [11] provided a viscoplastic constitutive theory based on the stress history tensor. Gens and Nova [12] considered an isotropic behavior for bonded soils and weak rocks. Vatsala et al. [13] rendered an elastoplastic model for the bonded and cemented soils in which the cemented soil behavior was considered equal to the combination of both the uncemented soil part and the cemented bonds behavior. Haeri and Hamidi [14] provided a constitutive model for gravely sands dividing the behavior of cemented soil to uncemented part and cemented bonds. The objective of current paper is modification of Manzanal et al. [1] generalized plasticity model by addition of some new parameters to model the shear behavior of cemented sands.

---

\* Corresponding author.

## 2 Critical State Framework

Figure 1 represents a schematic curve for changes of void ratio with mean effective stress for cemented and uncemented samples as illustrated by Liu and Carter [15]. In present model, difference of void ratios is added to the uncemented soil one. Generalized plasticity model of Manzanal et al. [1] is used as the base model for uncemented sand. Also changes are made in state parameter, flow rule, hardening function and elastic parameters using six extra parameters.

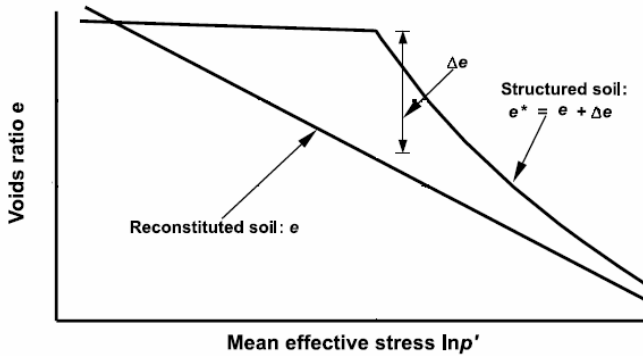


Fig. 1. Idealization of the isotropic compression behavior of reconstituted and structured soils (Liu and Carter [15])

## 3 Modification of the Generalized Plasticity Model

In this part, Manzanal et al. [1] model is modified for predicting the mechanical behavior of cemented soil. Shear modulus is modified based on Saxena *et al.* [7]:

$$G_C = G_S + \Delta G_C \tag{1}$$

$$\Delta G_C = \frac{172CC^{0.88} P_a \left( \frac{P_0}{P_a} \right)^{0.515e - 0.13CC + 0.285}}{(e - 0.5168) \left( \frac{P_0}{P_a} \right)}, CC < 2 \tag{2}$$

$$\Delta G_C = \frac{773CC^{1.2} P_a \left( \frac{P_0}{P_a} \right)^{0.698e - 0.04CC - 0.2}}{e \left( \frac{P_0}{P_a} \right)}, 2 \leq CC \leq 8 \tag{3}$$

where  $G_C$  is the shear modulus of lightly cemented sand,  $G_S$  is shear modulus of sand alone and  $\Delta G_C$  is increase of shear modulus due to cementation effect.  $CC$  is cement content in present and  $e$  is void ratio. Also, the bulk modulus of cemented soil is modified according to Hamidi and Hassanzadeh [16].

$$K_C = K_S + \Delta K_C \tag{4}$$

$$\Delta K_C = (-0.1CC)D_r + 31CC \tag{5}$$

$K_C$  is bulk modulus of lightly cemented sand,  $K_S$  is bulk modulus of sand,  $\Delta K_C$  is bulk modulus increase due to cementation and  $D_r$  is relative density.

Due to the upward movement of *NCL* in *e-Ln p'* space with increase in cementation, the following form can be considered for difference of the cemented and uncemented soil behavior during compression.

$$\psi^* = e^* - e_{cs} \tag{6}$$

$$e^* = e + \Delta e \tag{7}$$

$$\Delta e = A.CC^B \text{Exp}(-C.P_0) \tag{8}$$

where *A*, *B* and *C* are additional model parameters. Flow rule is also changed considering *d<sub>0</sub>* parameter in Manzanal et al. [1] model as follows:

$$d_g = \frac{d_0^*}{M_g} \cdot (\eta_{PTS} - \eta) \tag{9}$$

$$d_f = \frac{d_0^*}{M_f} \cdot (\eta_{PTS} - \eta) \tag{10}$$

$$d_0^* = d_0 - d = d_0 - D.CC^{\zeta_c^*} \tag{11}$$

where *D* is model parameter and  $\zeta_c^*$  is considered 0.25 for cemented soil. *M<sub>f</sub>* can be determined for cemented condition according to the following equations:

$$\frac{M_f}{M_g} = h_1^* - h_2 \left( \frac{e}{e_{cs}} \right)^\beta \tag{12}$$

$$h_1^* = h_1 \text{Exp}(E.CC) \tag{13}$$

where *E* is an additional model parameter. Hardening modulus of the base model is considering as bellows by change in parameter  $\beta_v^*$ :

$$H_v = H_{v0} \cdot \left[ M_g \text{Exp}(-\beta_v^* \psi^*) - \eta \right] \tag{14}$$

$$\beta_v^* = \beta_v + (F.P_0) \tag{15}$$

### 4 Model Validation

Schnaid *et al.* [9] have reported series of consolidated drained triaxial tests on a sandy soil obtained from Porto Alegre in southern Brazil with uniformity coefficient of 32 and specific gravity of 2.7. The soil is classified as non plastic silty sand. Artificially cemented specimens were made by adding Portland cement. All

samples have been isotropically consolidated under a range of confining pressures between 20 to 100 kPa. Table 1 shows additional model parameters for cemented soil and Table 2 shows model parameters for the uncemented soil. Figures 2-a to 2-c represent the comparisons of experimental data and model simulations for drained triaxial compression tests on 0%, 1.0% and 3.0% cemented soil in different effective confining pressure. Confining pressures of 20 and 100 kPa were used for calibration and model was tested using confining pressure of 60 kPa. Fairly good agreement can be observed between the experimental and predicted data.

**Table 1.** Additional model parameters for cemented soil

A	B	C	D	E	F
0.09	0.56	0.03	2.15	0.30	0.20

**Table 2.** Model constants for experimental data of Schnaid et al. [7]

$G_{eso}$	$K_{evv}$	$M_g$	$e_\Gamma$	$\lambda$	$\xi_c$	$d_0$	$m$	$h_1$	$h_2$	$H'_0$	$\beta'_0$	$\beta$	$H_{v0}$	$\beta_v$	$\alpha$	$\beta_0$	$\beta_1$
110	115	1.5	0.6	0.03	0.6	3.5	3.5	1.3	0.5	110	2.2	1.8	120	5.3	0.5	0	0

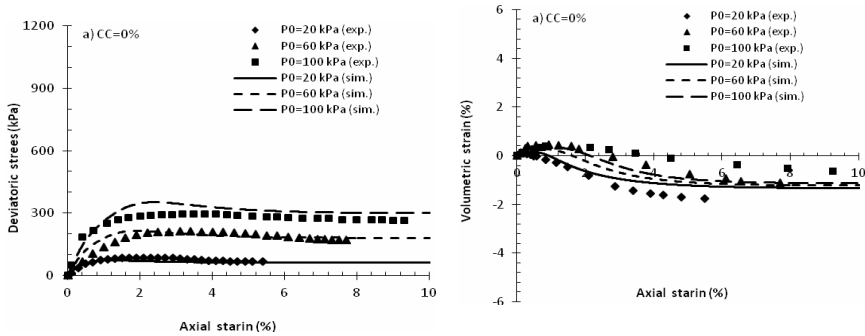


**Fig. 2-a.** Comparison between model predictions and drained triaxial of Schnaid et al. [7] for the uncemented soil

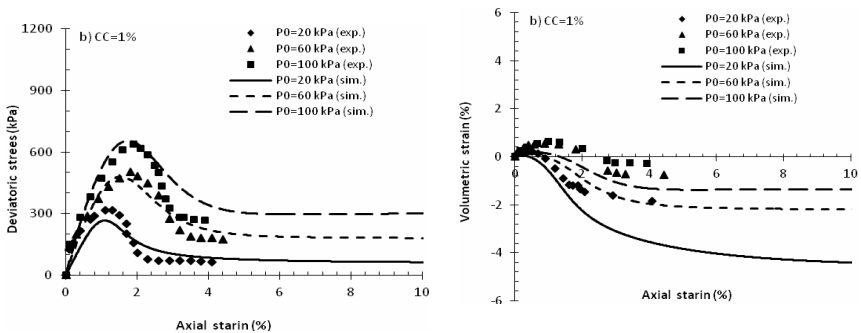


**Fig. 2-b.** Comparison between model predictions and drained triaxial of Schnaid et al. [7] for soil cemented with 1.0% Portland cement

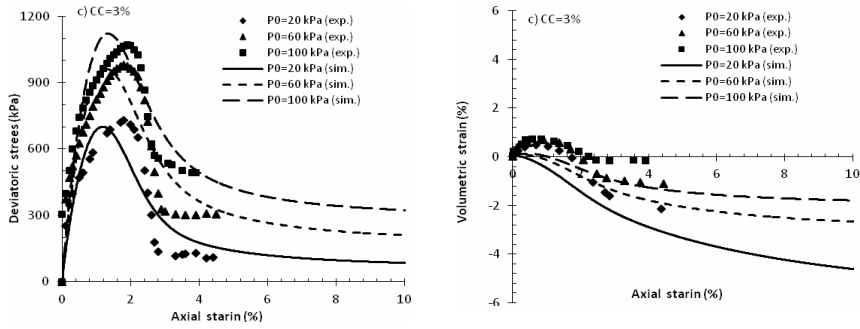


Fig. 2-c. Comparison between model predictions and drained triaxial of Schnaid et al. [7] for soil cemented with 3.0% Portland cement

### 5 Conclusions

In this study, a model has been proposed to determine the mechanical behavior of the cemented, sandy soil. The principles of modeling are based on a generalized plasticity model in keeping with the existing difference in the isotropic compression curve related to the cemented soil and the uncemented soil in  $e-Inp'$  plane. One of the model characteristics is determination of cemented soil parameters based on cement content. The model can be applied in numerical calculations and boundary value problems in geotechnical engineering. Deviatoric stress-axial strain and volumetric strain-axial strain curves have been predicted in a fairly good manner for drained condition.

### References

- [1] Manzanal, D., Fernandez Merodo, J.A., Pastor, M.: Generalized plasticity state parameter-based model for saturated and unsaturated soils. Part 1: Saturated state. *Int. J. Numeric Analytic Meth. Geomech.* 35(12), 1347–1362 (2011)
- [2] Clough, G.W., Kuck, W.M., Kasali, G.: Silicate-stabilized sands. *J. Geotech. Engrg. ASCE* 105(1), 65–82 (1979)
- [3] Coop, M.R., Atkinson, J.H.: The mechanics of cemented carbonate sands. *Geotechnique* 43(1), 53–67 (1993)
- [4] Cuccovillo, T., Coop, M.R.: On the mechanics of structured sands. *Geotechnique* 49(6), 741–760 (1999)
- [5] Huang, J.T., Airey, D.W.: Properties of artificially cemented carbonate sand. *J. Geotech. Geoenv. Engrg. ASCE* 124(6), 482–499 (1998)
- [6] Consoli, N.C., Prietto, D.M., Ulbrich, L.A.: Influence of fiber and cement addition on behavior of sandy soil. *J. Geotech. Geoenv. Engrg. ASCE* 124(12), 1211–1214 (1998)
- [7] Schnaid, F., Prietto, P.D.M., Consoli, M.H.T.: Characterization of cemented sand in triaxial compression. *J. Geotech. Geoenv. Engrg. ASCE* 127(10), 857–867 (2001)

- [8] Haeri, S.M., Hamidi, A., Tabatabaee, N.: The effect of gypsum cementation on the mechanical behavior of gravely sands. *Geotech. Test J. ASTM* 28(4), 180–190 (2005)
- [9] Hamidi, A., Haeri, S.M.: Stiffness and deformation characteristics of a cemented gravely sand. *Int. J. Civil Engrg.* 6(3), 159–173 (2008)
- [10] Baxter, C.D.P., Sharma, R.S., Moran, K., Vaziri, H., Narayanasamy, R.: Use of  $A=0$  as a Failure criterion for weakly cemented soils. *J. of Geotech. Geoenv. Engrg. ASCE* 137(2), 161–170 (2011)
- [11] Oka, F.: An elasto-viscoplastic constitutive model for clay using a transformed stress tensor. *Mech. Materials* 16(1&2), 47–53 (1993)
- [12] Gens, A., Nova, R.: Conceptual bases for a constitutive model for bonded soils and weak rocks. *Geotech. Engrg. of Hard Soils-Soft Rocks* (1993)
- [13] Vatsala, A., Nova, R., Srinivasa Murthy, B.R.: Elastoplastic model for cemented soils. *J. Geotech. Geoenv. Engrg. ASCE* 127(8), 679–687 (2001)
- [14] Haeri, S.M., Hamidi, A.: Constitutive modeling of cemented gravely sands. *Geomech. and Geoengng.: An Int. J.* 4(2), 123–139 (2009)
- [15] Liu, M.D., Carter, J.P.: A structured Cam clay model. Research Report. University of Sydney (2002)
- [16] Hamidi, A., Hasanzadeh, A.: Investigating the compressibility and volume change behavior of cemented sands. *Modarres J. Civil Engrg.* 11(3), 15–26 (2011)
- [17] Saxena, S.K., Avramidis, A., Reddy, K.R.: Dynamic moduli and damping ratios for cemented sands at low strains. *Can. Geotech. J.* 25(2), 353–368 (1988)

# Comparison between Feature of Modified Cam-Clay Model and UH Model

Wei Hou<sup>1</sup> and Yangping Yao<sup>2</sup>

<sup>1</sup> National Academician & Masters Research Office, BGI Engineering Consultants Ltd., Beijing 100038, China

<sup>2</sup> Department of Civil Engineering, Beihang University, Beijing 100191, China  
houwei\_bgi@163.com

**Summary.** Based on researching the features of the modified Cam-clay model and UH model, the mechanism of models modeling the behaviors of the over-consolidated (OC) clays can be revealed. For the OC clays, the curves predicted by the modified Cam-clay model have abrupt changing points, so the model cannot model continue and gradual changing process well. UH model can rationally model many characteristics of the OC clays well, including shear dilatancy, strain-hardening and softening, and stress path dependence behavior.

**Keyword:** over consolidation; elasto-plasticity, modified Cam-clay model, UH model.

## 1 Introduction

The over-consolidated (OC) clays reveal many characteristics, such as strain-hardening /softening, shear dilatancy and so on. Based on the modified Cam-clay model and the concept of the subloading surface, Yao etc. [1-3] have proposed UH model for normally consolidated (NC) clays and OC clays. UH model, which is the same as the modified Cam-clay model for NC clays, can describe behaviors of OC clays well.

The modified Cam-clay model [4] can exhibit the behaviors of OC clays to a certain extent, but the predicted results have abrupt changing points and the peak strength is rather higher than test data. In this paper, the features of the modified Cam-clay model and UH model for the OC clays have been revealed in detail.

## 2 Modified Cam-Clay Model

### 2.1 Yield Surface and Plastic Potential Surface

With an associate flow rule, the yield surface and the plastic potential surface of the modified Cam-clay model are written as:

$$f = g = \ln \frac{p}{p_0} + \ln \left( 1 + \frac{q^2}{M^2 p^2} \right) - \frac{1}{c_p} \varepsilon_v^p = 0 \tag{1}$$

where  $p$  is the mean stress;  $q$  is the deviatoric stress;  $M$  is the stress ratio at the characteristic state point;  $c_p = (\lambda - \kappa)/(1 + e_0)$ ,  $\lambda$  is the slope of the normal compression line (NCL);  $\kappa$  is the slope of the unloading line;  $e_0$  is the initial void ratio;  $p_0$  is the pre-consolidation stress.

### 2.2 Features of the Modified Cam-Clay Model for OC Clay

In order to reveal the Mechanism of the modified Cam-clay model in describing the behaviors of NC clay and OC clay, a example is adopted on assumption that initial deviatoric stress  $q$  is zero and the mean stress  $p$  equals to constant in loading process.

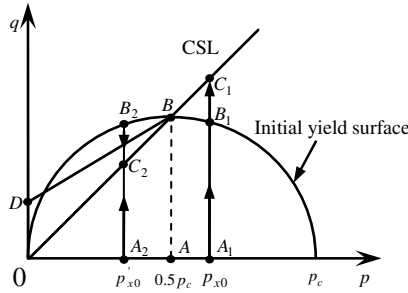


Fig. 1. Stress paths and initial yield surface

As shown in Fig. 1, for NC clay,  $p_{x0} = p_c$ , where  $p_{x0}$  is the length of the major axes of the yield surface in the initial condition;  $p_c$  is the pre-consolidation stress. The stress point is on the yield surface and deformation is elastio-plastic all the time.

The initial yield surface and the critical state line intersect at the point B whose projection at  $p$  axis is the point A ( $p = 0.5 p_c$ ). For OC clay, when the initial stress point is on right side of the point A ( $0.5 p_c \leq p_0 = p_{x0} < p_c$ ) and OCR is small, as shown in Fig.1, the stress path is from the point A to the point B. As the stress point is in the initial yield surface at this time, the relationship of the stress-strain is elastic and the initial yield surface do not move. When the stress point arrives at the point  $B_1$  on the initial yield surface with loading, the relationship of stress-strain changes into elastio-plastic deformation. The yield surface extends with increasing stress until the point  $B_1$  arrives at the point  $C_1$  on the critical state line.

When the initial stress point is on left side of the point A ( $p_0 = p_{x0} < 0.5p_c$ ) and OCR is big, the stress path is from the point A<sub>2</sub> to the point B<sub>2</sub> which is corresponding to the peak strength and the deformation is elastic. Later the deviatoric stress  $q$  decreases and the stress path is from the point B<sub>2</sub> to the point C<sub>2</sub> when the deformation change elastic to elastio-plastic. As the strength of OC clay is determined according to the yield surface but the Hvorslev line. As the projection of point A<sub>2</sub> on the Hvorslev line is lower than that on the yield surface, the predicted peak strength is rather higher.

### 3 UH Model

#### 3.1 Yield Surface and Hardening Parameter

UH model includes two yield surfaces, namely the reference yield surface and the current yield surface. The plastic volumetric strain  $\epsilon_v^p$  is chosen as the hardening parameter for the reference yield surface. A unified hardening parameter  $H$  is adopted in the current yield surface. The reference yield function can be written as:

$$\bar{f} = \ln \frac{\bar{p}}{\bar{p}_{x0}} + \ln \left[ 1 + \frac{\bar{q}^2}{M^2 \bar{p}^2} \right] - \frac{1}{c_p} \epsilon_v^p = 0 \tag{2}$$

where  $\bar{p}_{x0}$  is constant and corresponds to the length of the major axes of the reference yield ellipses in the initial condition when  $\epsilon_v^p = 0$ .  $\bar{p}_{x0}$  is equal to the pre-consolidation stress under the initial isotropic compression condition ( $\eta_0 = 0, \bar{p}_{x0} = \bar{p}_0$ );  $\bar{p}$  is the mean stress and  $\bar{q}$  is the deviatoric stress at the reference yield surface.

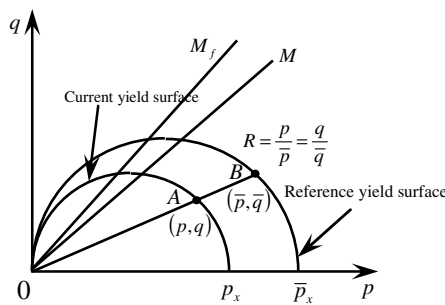


Fig. 2. Current yield surface and reference yield surface

The foundation of the current yield surface is written as:

$$f = \ln \frac{p}{p_{x0}} + \ln \left[ 1 + \frac{q^2}{M^2 p^2} \right] - \frac{1}{c_p} H = 0 \quad (3)$$

Where  $p_{x0}$  is the initial value of  $p_x$  with  $\varepsilon_v^p = 0$  and  $H = 0$ ;  $p_{x0} = p_0$  under the initial isotropic compression condition ( $\eta_0 = 0$ ). The unified hardening parameter is written as:

$$H = \int dH = \int \frac{M_f^4 - \eta^4}{M^4 - \eta^4} d\varepsilon_v^p \quad (4)$$

where

$$\left. \begin{aligned} M_f &= 6 \left[ \sqrt{\frac{k}{R} \left( 1 + \frac{k}{R} \right)} - \frac{k}{R} \right] \\ R &= \frac{p}{\bar{p}_0} \left( 1 + \frac{\eta^2}{M^2} \right) \exp \left( -\frac{\varepsilon_v^p}{c_p} \right) \\ k &= \frac{M^2}{12(3-M)} \end{aligned} \right\} \quad (5)$$

where  $M_f$  is the potential failure stress ratio;  $R$  is over-consolidated parameter.

### 3.2 Features of UH Model for OC Clay

The interrelationship among OC parameter  $R$ , potential failure stress ratio  $M_f$  and unified hardening parameter  $H$  is as shown in Fig.3. Since OC clays with different OC degree may have different potential failure stress ratio, the value of  $M_f$  is related to  $R$ . Besides, the unified hardening parameter  $H$  is related to the potential failure stress ratio  $M_f$ . Thus,  $H$  is affected by  $M_f$ . Meanwhile, the evolution of unified hardening parameter  $H$  (related with  $\varepsilon_v^p$ ) determines the relative locations between the current yield surface and the reference yield surface, which conversely influences the evolution law of OC parameter  $R$ . As a result, a circulatory relationship among OC parameter  $R$ , potential failure stress ratio  $M_f$  and unified hardening parameter  $H$  is established, as shown in Fig.3. This interdependent relationship is still valid when the OC clay becomes the NC clay.

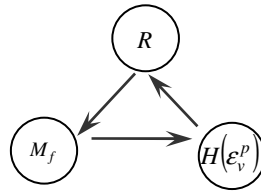


**Fig. 3.** Relationship of over-consolidated parameter, potential strength and hardening parameter

The parameters in UH model are the same as those in the modified Cam-clay model. For NC clay, UH model can regress to the modified Cam-clay model.

### 4 Test Results and Model’s Predictions

The predicted results and test data [5] under drained triaxial condition for the clay with  $OCR = 4,8$  are plotted in Fig. 4. Material parameters can be shown in table 1. It can be seen that the stress-strain relationship predicted by the modified Cam-clay model has an abrupt change and obvious higher peak strength, but UH model can model the foundational behaviors of OC clay as well.

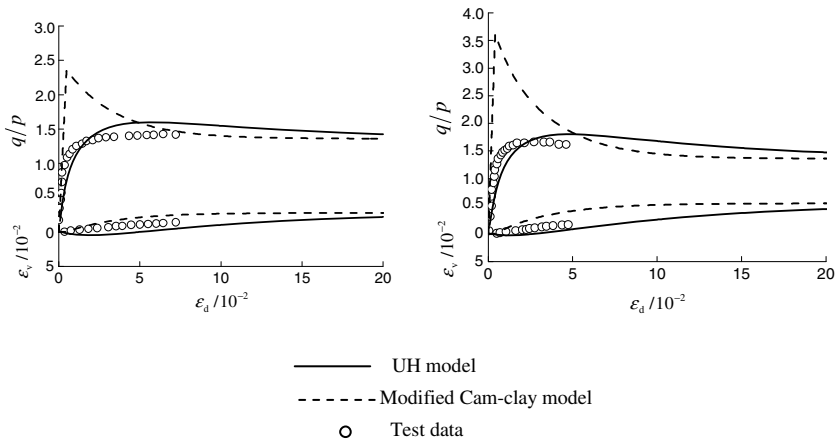


**Fig. 4.** Comparison of predicted results and test data. (a)  $OCR=4$ , (b)  $OCR=8$ .

**Table 1.** Material parameters of Fujinomori clay

$\lambda/(1+e_0)$	$\kappa/(1+e_0)$	$\nu$	$N$	$M$
0.0508	0.0112	0.2	0.83	1.36

The test data [6] under undrained triaxial condition for the clay with OCR=1~8.1 can be illustrated in Fig.5. The results predicted by the modified Cam-clay model and UH model can be shown in Fig.6 and Fig.7 respectively. Material parameters can be shown in table 2.

From Fig.6 it can be shown that the deformation predicted by the modified Cam-clay model at initial stage is elastic and the mean stress  $p$  does not change. For OC clay with small value of OCR, the mean stress  $p$  decreases with the positive pore water pressure after yield ding. For OC clay with big value of OCR, the mean stress  $p$  increases with the negative pore water pressure after stress point arriving yield surface. The predicted results have abrupt changes and cannot display gradually evolution process.

**Table 2.** Material parameters of Kaolin clay

$\lambda$	$\kappa$	$\nu$	$M$	$e_0$	$p_0$ (kPa)
0.240	0.045	0.2	0.896	1.27	689.02

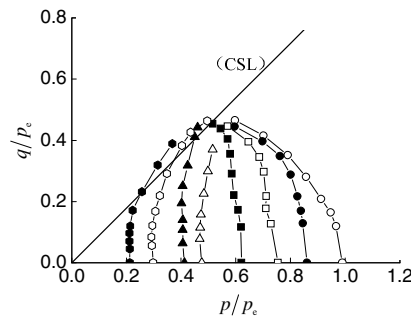


**Fig. 5.** Stress paths under undrained condition

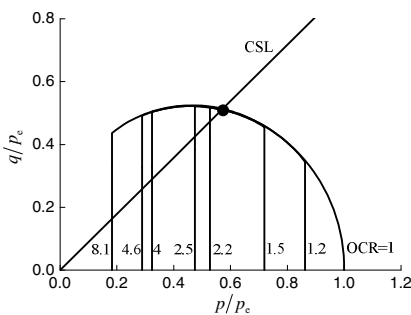


**Fig. 6.** Predicted results by modified Cam-clay model

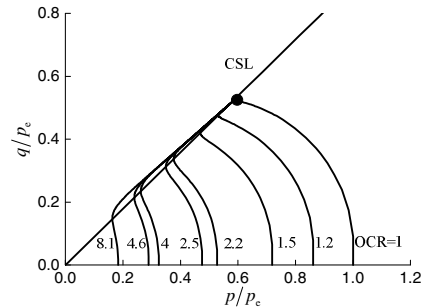


**Fig. 7.** Predicted results by UH model

In Fig.7, the relationship of stress-strain predicted by UH model is elastio-plastic. For the small initial value of OCR, the mean stress  $p$  decreases with positive pore water pressure all the time. For the big initial value of OCR, when the stress ratio is smaller than the characteristic state ratio the mean stress  $p$  decreases with positive pore water pressure. When the stress ratio is bigger than the critical state ratio the mean stress  $p$  increases until the stress point arrives at the critical state line. The predicted result corresponds to the test data as well.

## 4 Conclusions

Comparing with the predicted results of models, it can be seen that those predicted by the modified Cam-clay model have abrupt changes and cannot display gradually evolution process, but UH model can model the many characteristics of the OC clays well, including shear dilatancy, strain-hardening and softening, and stress path dependence behavior.

## References

- [1] Yao, Y.P., Hou, W.: Basic mechanical behavior of soils and their elastoplastic modeling. *Rock and Soil Mechanics* 30(10), 2881–2902 (2009)
- [2] Yao, Y.P., Hou, W., Luo, T.: Unified hardening model for soils. *Chinese Journal of Rock Mechanics and Engineering* 28(10), 2135–2151 (2009)
- [3] Yao, Y.P., Hou, W., Zhou, A.N.: UH model: three-dimensional unified hardening model for overconsolidated clays. *Geotechnique* 59(5), 451–469 (2009)
- [4] Roscoe, K.H., Burland, J.B.: On the generalised stress-strain behaviour of an ideal wet clay. In: Heyman, J., Leckie, F.A. (eds.) *Engineering Plasticity*, pp. 535–609. Cambridge University Press, Cambridge (1968)
- [5] Nakai, T., Hinokio, M.: A simple elastoplastic model for normally and over consolidated soils with unified material parameters. *Soils and Foundations* 44(2), 53–70 (2004)
- [6] Mroz, Z., Norris, V.A., Zienkiewicz, O.C.: Application of an anisotropic hardening model in the analysis of elasto-plastic deformation of soils. *Geotechnique* 29(1), 1–34 (1979)

# Experimental Investigation and Three Dimensional Constitutive Modeling of Principal Stress Rotation in Shanghai Soft Clay

Maosong Huang<sup>1,2,\*</sup> and Yanhua Liu<sup>1,2</sup>

<sup>1</sup> Department of Geotechnical Engineering, Tongji University, Shanghai 200092, China

<sup>2</sup> Key Laboratory of Geotechnical and Underground Engineering of Ministry of Education, Tongji University, Shanghai 200092, China  
mshuang@tongji.edu.cn

**Abstract.** This paper focuses on the study on the deformation behavior and strength character of natural Shanghai soft clay undergoing principal stress axes rotation. Undrained hollow cylinder shear tests were performed on natural Shanghai soft clay under isotropically and anisotropically consolidated conditions to investigate the effects of principal stress rotation. Effects of coefficient of intermediate principal stress and rotational angle of principal stress axes on the stress-strain behavior and strength characteristics of soft clay were studied. Test results show that the stress-strain behavior and undrained strength characteristics of soft clay vary significantly with the coefficient of intermediate principal stress and rotational angle of principal stress axes. The three-dimensional anisotropic bounding surface model for natural soft clay proposed by the authors is adopted to simulate the behaviors of Shanghai soft clay under principal stress rotation. Comparisons between simulations and experiments are given to further demonstrate the validity of the model.

## 1 Introduction

Principal stress rotation often occurs in many geotechnical engineering problems and may affect the behavior of soils significantly. In order to better understand the behavior of Shanghai soft clay under the rotation of principal stress direction, experimental studies of the effect of principal stress rotation on the three dimensional mechanical behavior of Shanghai soft clay should be conducted. Both conventional triaxial tests on solid cylindrical specimens and true triaxial tests on cubical soil specimens have been widely used to investigate soil behaviors without the rotation of principal stress. Hollow cylinder devices can simulate the condition of principal stress rotation and have been used for many researchers [2,3]. Most of them were focused on the laboratory tests on reconstituted soils. Some experiments on natural clays were reported for example London clay by Nishimura et al. [4]. Obviously however, the experimental investigation on the natural clays has been much less intensive due to difficult preparation of high quality undisturbed hollow cylindrical

---

\* Corresponding author.

sample. It should also be pointed out that the tests reported by the above mentioned literature were conducted on the hollow cylindrical samples with the same inner and outer cell pressures. In fact, independent control over the inner and outer cell pressures is important for the study of the three-dimensional soil behaviors.

The Modified Cam-clay (MCC) model has been widely for the constitutive modeling of remolded clay under isotropic consolidation condition. Numerous constitutive models that account for plastic anisotropy of natural clays have been proposed, in which S-CLAY1 model proposed by Wheeler et al. [5] is a relatively simple elastoplastic anisotropic model. The form of yield curve used by Wheeler et al. [5] was identical to that suggested by Dafalias [6]. Several researchers developed constitutive models based on the MCC model for natural soils within the framework of kinematic hardening, which consider simultaneously the anisotropic and structural effect on the mechanical behavior of natural soils. Those models can in general achieve good results but often at a cost of complexity. An alternative approach to avoid this complexity is to remove the kinematic hardening yield surface, only preserving the bounding surface. Huang et al. [1] introduced a simple bounding surface plasticity to reproduce the yielding and stress-strain behavior of the structured Shanghai soft clay. The degradation of the clay structure was modeled with an internal variable that allows the size of bounding surface to decay with accumulated plastic strain. An anisotropic tensor and rotational hardening law were incorporated into the bounding surface formulation with an associated flow rule. Such a simple model was verified by the undrained and drained conventional triaxial tests without considering the rotation of principal stress.

In this paper, undrained hollow cylinder shear tests were performed on natural Shanghai soft clay under isotropically and anisotropically consolidated conditions to investigate the effects of principal stress rotation. The three-dimensional anisotropic bounding surface model proposed by Huang et al. [1] is then adopted to simulate the behaviors of Shanghai soft clay under principal stress rotation. Comparisons between simulations and experiments are finally given to further support the model.

## 2 Hollow Cylinder Tests on Natural Shanghai Soft Clay

### 2.1 Specimens and Test Programme

Soil samples were taken at the site of a foundation pit in Shanghai in a depth of 14 m, and all the samples were undisturbed soil samples from the gray mucky clay layer of Shanghai stratum. The samples were extracted by cutting with PVC pipe. The vertical stress in situ was calculated as 140 kPa according to the density and thickness of above layers. The properties of the undisturbed soil samples can be found in Huang et al. [1].

In this paper, the influences from the coefficient of intermediate principal stress  $b$  and the rotational angle of principal stress axes  $\delta$  on the relationship of stress-strain and the strength characteristics of soft clay are studied by experimental investigation. A series of undrained shear tests with different values of  $b$  and  $\delta$

was undertaken by the stress control loading module of the GDS Hollow Cylinder Apparatus. Both isotropic and anisotropic ( $K_0=0.6$ ) consolidation modes were performed on the hollow thin-wall soil samples. During the shearing process, the mean stress  $P$ , the coefficient of intermediate principal stress  $b$  and the rotational angle of principal stress axes  $\delta$  were kept constant, while the deviatoric stress  $q$  was increasing. Mean effective consolidation stress  $p'_0=150\text{ kPa}$  was adopted in all the tests, and the test programme in more detail is presented in Table 1. There are some restricted loading areas of the test instrument. According to the suggestions of Symes [7], the restricted areas where the difference of internal and external pressure is large are avoided when determining the loading stress paths. The soil specimens have the dimensions: 100 mm in outer diameter, 60 mm in inner diameter and 200 mm in height.

**Table 1.** Undrained hollow cylinder shear test programme

consolidation mode	anisotropic consolidation					isotropic consolidation				
$b$	0.5					0.5				
$\delta$ ( $^\circ$ )	0	30	45	60	90	0	30	45	60	90
consolidation mode	isotropic consolidation									
$b$	0					1.0				
$\delta$ ( $^\circ$ )	0	30	45				45	60	90	
consolidation mode	isotropic consolidation									
$\delta$ ( $^\circ$ )	0			45			90			
$b$	0	0.2	0.5	0	0.5	1.0	0.5	0.7	1.0	

## 2.2 Test Results

The test results are divided into groups by the consolidation mode, the coefficient of intermediate principal stress  $b$  and the rotational angle of principal stress direction  $\delta$ . Test results of three groups including anisotropic consolidation  $b=0.5$ , isotropic consolidation  $b=0.5$  and isotropic consolidation  $b=\sin^2 \delta$  are presented in this paper. In order to consider the combined effect of strain components during torsion, the generalized shear strain is adopted when analyzing the test data. As required by the test instrument for a proper control over  $b$ , the initial generalized shear stress  $q$  in the tests under isotropic consolidation was set as 10 kPa.

**2.2.1 Anisotropic Consolidation  $b = 0.5$**

Fig. 1 shows the tests results for anisotropic consolidation ( $K_0=0.6$ ) and  $b = 0.5$  at different rotational angles of principal stress direction  $\delta$ , in which Fig. 1(a) gives the undrained effective stress path curves, and Fig. 1(b) shows the undrained stress-strain curves. When  $b$  is fixed, the stress path curves and stress-strain curves vary for different  $\delta$ . It can be seen from the effective stress path curves that relative significant difference in the failure stress ratio between  $\delta = 0^\circ, 90^\circ$  and  $\delta = 30^\circ, 45^\circ, 60^\circ$ . This is caused by the restricted torsional displacement range of the test instrument, at the same time, strain localization occurs in the specimens when  $b = 0.5$ . Therefore, it is hard for the peak value of stress ratio at different  $\delta$  to reach the critical state. The critical line shown in Fig 1 is only for the greatest value of the peak stress ratio from the tests, and it is indeed different from the theoretical critical state line.

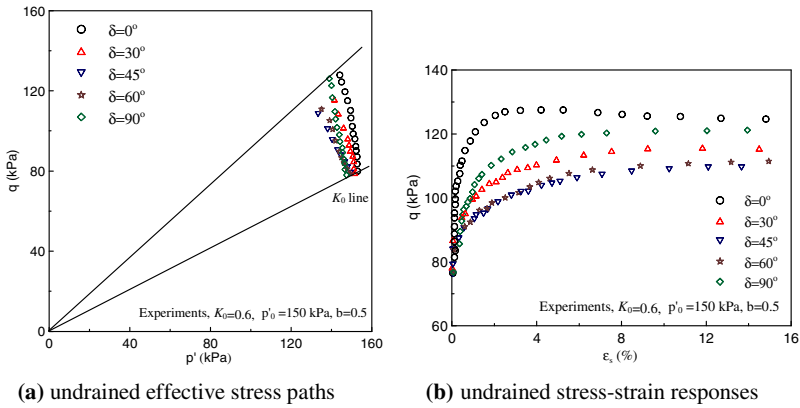


**Fig. 1.** Measured curves for the tests under anisotropic consolidation and  $b = 0.5$  at different rotational angles of principal stress direction

**2.2.2 Isotropic Consolidation  $b = 0.5$**

Fig 2 shows the tests results of isotropic consolidation and  $b = 0.5$  at different rotational angles of principal stress direction  $\delta$ , in which Fig. 2(a) shows the undrained effective stress path curves, and Fig. 2(b) gives the undrained stress-strain curves. The variation trend and existing problems are similar with the tests under anisotropic consolidation and  $b = 0.5$ . However, peak shear strengths under isotropic consolidation mode is lower, and the variation of peak strengths with  $\delta$  is not so significant as in Fig. 1.

**2.2.3 Isotropic consolidation  $b = \sin^2 \delta$**

In the hollow cylinder tests where inside and outside pressures are maintained at the same value, the rotational angle  $\delta$  is related to the parameter  $b$  as  $b = \sin^2 \delta$ ,

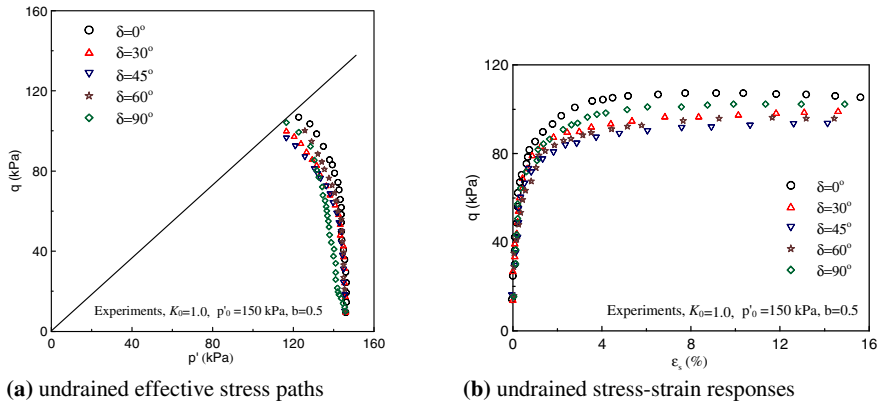


**Fig. 2.** Measured curves for the tests under isotropic consolidation and  $b=0.5$  at different rotational angles of principal stress direction

and hence the independent control over  $b$  and  $\delta$  cannot be realized. Fig. 3 shows the tests results of isotropic consolidation and  $b = \sin^2 \delta$  at different rotational angles of principal stress direction  $\delta$ , in which Fig. 3(a) shows the undrained effective stress path curves, and Fig. 3(b) gives the undrained stress-strain curves.

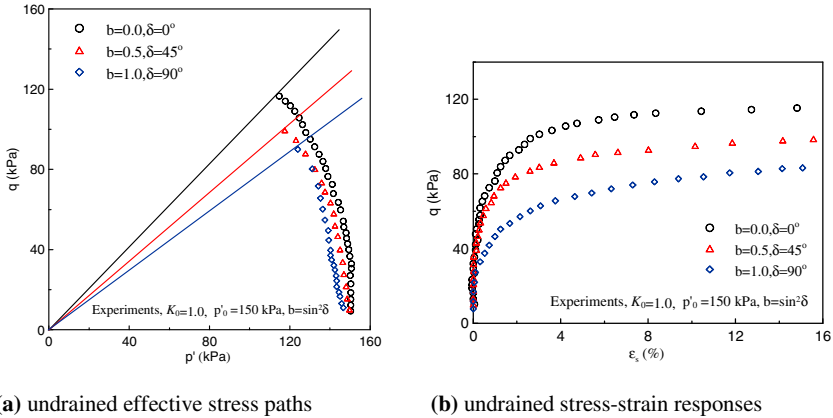


**Fig. 3.** Measured curves for the tests under anisotropic consolidation and  $b = \sin^2 \delta$  at different rotational angles of principal stress direction

When  $\delta$  increases from  $0^\circ$  to  $90^\circ$ ,  $b$  increases from 0 to 1, and the failure stress ratio decreases, while the undrained shear strength also decreases gradually. It reflect combined effects of the coefficient of intermediate principal stress  $b$  and the rotational angle of principal stress direction  $\delta$  on the undrained

stress-strain relation and strength characteristics of soft clay. In fact, for many hollow cylinder apparatus in the early time, the inner pressure and outer pressure cannot be controlled independent, and they must be kept same in the test [3]. Under this condition, the test results cannot purely reflect the effects of  $b$  or  $\delta$ .

### 3 Model Simulations

Based on the three-dimensional anisotropic bounding surface model for natural soft clay proposed by Huang et al. [1], the undrained hollow cylinder shear tests for different coefficients of intermediate principal stress and different rotational angles of principal stress direction are simulated. Comparisons between simulations and experiments are given to further demonstrate the validity of the model. Model parameters used in the simulation are identical to those used by Huang et al. [1].

#### 3.1 Anisotropic Consolidation $b = 0.5$

Fig 4 shows simulation results of the undrained hollow cylinder shear tests of Shanghai soft clay under anisotropic consolidation ( $K_0=0.6$ ) and  $b = 0.5$  at different rotational angles of principal stress direction  $\delta$ , in which Fig. 4(a) gives the undrained effective stress path curves, and Fig. 4(b) shows the undrained stress-strain curves. Although some glitches exist, this model can reflect the trend of undrained stress path and undrained stress-strain relation at different rotational angles of principal stress direction  $\delta$  quite well as a whole. As mentioned above, because of the restricted torsional displacement range of the test instrument and the slight strain localization when  $b = 0.5$ , it is hard for the peak value of stress ratio to reach the critical state. As a result, the calculated  $M(\theta_\alpha)$  line is higher, and the relative peak strength values are larger than the the measured ones.

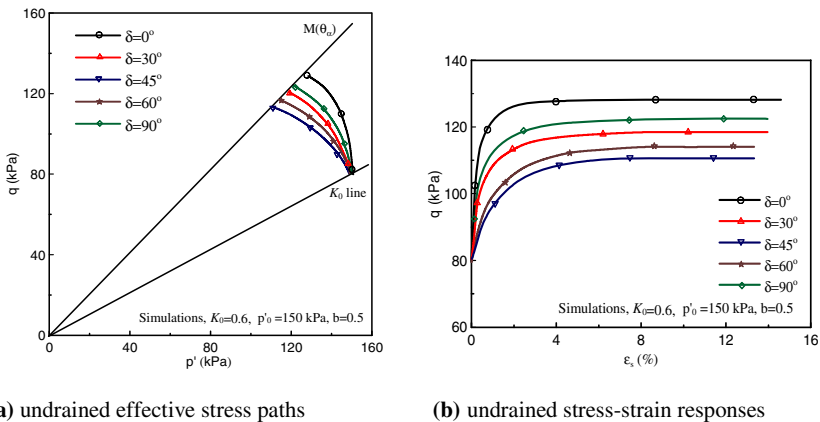


**Fig. 4.** Simulated curves for the tests under anisotropic consolidation and  $b = 0.5$  at different rotational angles of principal stress direction

### 3.2 Isotropic Consolidation $b = 0.5$

Fig. 5 shows the simulation results of the undrained hollow cylinder shear tests of Shanghai soft clay under isotropic consolidation and  $b = 0.5$  at different rotational angles of principal stress direction  $\delta$ , in which Fig. 5(a) gives the undrained effective stress path curves, and Fig. 5(b) shows the undrained stress-strain curves. The response trends calculated by the model accord well with the measurements. Similar problems exist as those occurred in the case of anisotropic consolidation.

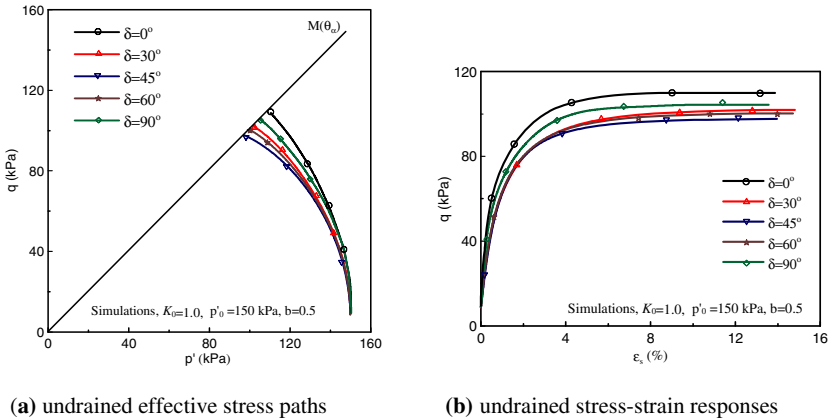


**Fig. 5.** Simulated curves for the tests under isotropic consolidation and  $b = 0.5$  at different rotational angles of principal stress direction

### 3.3 Isotropic Consolidation $b = \sin^2 \delta$

Fig 6 shows the simulation results of the undrained hollow cylinder shear tests of Shanghai soft clay under isotropic consolidation and  $b = \sin^2 \delta$  at different rotational angle of principal stress direction  $\delta$ , in which Fig. 6(a) gives the undrained effective stress path curves, and Fig. 6(b) shows the undrained stress-strain curves. Again, the response trends calculated by the model accord well with the measurements. When the coefficient of intermediate principal stress  $b$  changes as  $0 \rightarrow 0.5 \rightarrow 1.0$ ,  $\delta$  changes as  $0^\circ \rightarrow 45^\circ \rightarrow 90^\circ$ , and the loading state changes from axisymmetric compression state to pure shear state to axisymmetric tension state. Both the critical stress ratio and the peak shear strength decreases gradually with the increase of  $b$ . Significant reduction of the undrained shear strength is found when  $b = 0 (\delta = 0^\circ)$  changes to  $b = 0.5 (\delta = 45^\circ)$ .

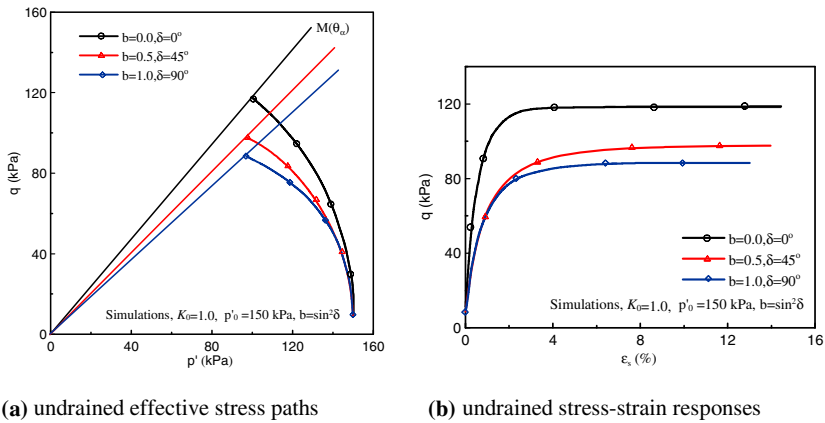


**Fig. 6.** Simulated curves for the tests under isotropic consolidation and  $b = \sin^2 \delta$  at different rotational angles of principal stress direction

## 4 Conclusions

A series of undrained tests were performed on hollow cylinder specimens made of natural Shanghai clay to deeper insight into the effect of principal stress rotation. The test data were presented to demonstrate the effects of coefficient of intermediate principal stress and rotational angle of principal stress axes on stress-strain behavior and strength characteristics of soft clay. Those clearly showed that undrained shear strengths were significantly influenced by the rotation angle of principal stress axes, especially for the cases under anisotropic consolidation conditions. For a constant coefficient of intermediate principal stress, the undrained shear strength initially decreases with increasing the value of rotational angle up to  $45^\circ$  after which the undrained shear strength decreases for the rotational angle larger than  $45^\circ$ . In the case of the same inner and outer cell pressures in a hollow specimen, combination of axial and torsional load can rotate the principal stress and alternate the coefficient of intermediate principal stress simultaneously. It leads to a continuous decrease of undrained shear strength with the increase of rotational angle of principal stress. The comparisons between theoretical predictions of the three-dimensional anisotropic bounding surface model proposed by the first author and experimental results revealed the predictive capability of the constitutive model for the effects of principal stress rotation of natural soft clay.

## References

- [1] Huang, M., Liu, Y., Sheng, D.: Simulation of yielding and stress-strain behavior of Shanghai soft clay. *Computers and Geotechnics* 38(3), 341–353 (2011)
- [2] Zdravkovic, L., Jardine, R.J.: The effect on anisotropy of rotating the principal stress axes during consolidation. *Geotechnique* 51(1), 69–83 (2001)

- [3] Lin, H., Penumadu, D.: Experimental investigation on principal stress rotation in Kaolin clay. *Journal of Geotechnical and Geoenvironmental Engineering*, ASCE 131(5), 633–642 (2005)
- [4] Nishimura, S., Anh-Minh, N., Jardine, R.J.: Shear strength anisotropy of natural London Clay. *Geotechnique* 57(1), 49–62 (2007)
- [5] Wheeler, S.J., Naatanen, A., Karstunen, M., et al.: An anisotropic elastoplastic model for soft clays. *Canadian Geotechnical Journal* 40, 403–418 (2003)
- [6] Dafalias, Y.F.: Anisotropic critical state soil plasticity model. *Mech. Res. Commun.* 13(6), 341–347 (1987)
- [7] Symes, M.J.: Rotation of principal stresses in sand, Ph.D. Dissertation, Imperial College of Science, Technology and Medicine, London, UK (1983)

# From Internal Structure to Constitutive Modeling of Granular Assemblies

Xia Li\*

Materials, Mechanics and Structures Research Division, Process and Environmental Research Division, Faculty of Engineering, The University of Nottingham, University Park, Nottingham NG7 2RD, UK  
xia.li@nottingham.ac.uk

**Abstract.** How to incorporate the impact of the internal structure into the constitutive modeling has attracted much research interest. Towards the grand challenge of developing a constitutive models embedded with particle-scale mechanism, this paper mainly concerns about the internal structure and its role in constitutive modeling. The investigations to be reported address issues including (1) why the internal structure is important; (2) how the internal structure should be quantified; (3) how to reflect the impact of internal structure in constitutive modeling.

**Keywords:** Internal structure, Fabric tensor, Stress-force-fabric Relationship, Granular Materials.

## 1 Introduction

The internal structure has been considered as an important factor contributing to the complicity of the stress-strain response of granular materials in particular to the anisotropic soil behavior observed in situ and in laboratory [1]. The internal structure is a generic terminology until Oda [2] pointed out there are three sources of anisotropy, i.e., the distribution of the contact normals, the shape of the particles and the shape of the voids. The interest in soil internal structure has boosted in the last few decades alongside the development of advanced soil constitutive modeling better predicting the complicated soil behavior. There are many recent progresses in the area. The current paper is limited by presenting some of the recent works in the Nottingham Centre for Geomechanics to attract more interesting discussions in this topic.

## 2 Micro-structural Definition of Stress/Strain Tensors

A granular material can be considered as an assembly of granulate particles interacting at point contact. The stress-strain behavior is the continuum-scale

---

\* Corresponding author.

manifest of particle-scale force-displacement model. The importance of internal structure could hence be interpreted as the bridge-up between the continuum scale stress and strain to the particle-scale contact forces and particle displacement [3].

The stress tensor evaluated as average over the volume  $V$  can be expressed as

$$\bar{\sigma}_{ij} = \frac{1}{V} \left( \sum_{P \in V} \sum_{c \in P} \mathbf{v}_i^{Pc} f_j^{Pc} + \sum_{P \in V} \mathbf{R}_{ij}^P \right). \quad (1)$$

where  $f_i^{Pc}$  is the force acting at the contact point  $c$  of the particle  $P$ ,  $\mathbf{v}_i^{Pc} = \mathbf{X}_i^P - \mathbf{x}_i^c$  is the vector from the contact point  $c$  to the particle centre  $\mathbf{X}_i^P$ . The term  $\sum_{P \in V} \mathbf{R}_{ij}^P$  takes into account the effect to particle rotation in dynamic conditions. The derivation of the stress expression is based on Newton's second law of motion. It is valid for both static and dynamic analyses.

The micro-structural expression of the displacement gradient tensor, valid for any 3D tessellation of the granular assembly into polyhedral elements has been derived as:

$$\bar{e}_{ij} = \frac{1}{V} \sum_{M \in V} \sum_{S^M} \sum_{L^{\Delta S}} \chi_i \Delta u_j \quad (2)$$

where  $\Delta \mathbf{u}$  represents the relative displacements between a pair of particles;  $\boldsymbol{\chi} = -\mathbf{h} \times \mathbf{v} / 2$  is an area vector,  $\mathbf{h} = \mathbf{x}_0^{\Delta S} - \mathbf{x}_0^{\Delta L}$  is the vector from the line reference point  $\mathbf{x}_0^{\Delta L}$  to the surface reference point  $\mathbf{x}_0^{\Delta S}$ .  $\mathbf{v} = \mathbf{X}^M - \mathbf{x}_0^{\Delta L}$  is the vector from the line reference point  $\mathbf{x}_0^{\Delta L}$  to the centre of the micro-elements  $\mathbf{X}^M$ . The micro-structural expression of the strain tensor is obtained by removing the rotation from  $\bar{e}_{ij}$ , i.e.,  $\bar{\epsilon}_{ij} = \frac{1}{2} (\bar{e}_{ij} + \bar{e}_{ji})$ .

Reflecting on Oda's statement, the contact vector existing in the micro-structural definition of the stress tensor is closely linked with the distribution of contact normal, the shape of the void space is closely linked to the area vector  $\boldsymbol{\chi}$  when the void cell system [4] is used as the tessellation system, while the particle shape is believed to indirectly contribute to the afore-mentioned two aspects.

### 3 Quantification in Terms of Fabric Tensor

After identifying the relevant geometrical variables, the next step is its macro-scale quantification. Following the directional statistical theory [5, 6], the directional distribution of contact normal density  $e^c(\mathbf{n})$  can be approximated using the compacted form as:

$$E^c(\mathbf{n}) = \frac{1}{E_0} F_{i_1 i_2 \dots i_n}^c n_{i_1} n_{i_2} \dots n_{i_n} \tag{3}$$

or the form of orthogonal decomposition as:

$$E^c(\mathbf{n}) = \frac{1}{E_0} \left[ 1 + D_{i_1 i_2}^c n_{i_1} n_{i_2} + \dots + D_{i_1 i_2 \dots i_n}^c n_{i_1} n_{i_2} \dots n_{i_n} + \dots \right] \tag{4}$$

$F_{i_1 i_2 \dots i_n}^c$  and  $D_{i_1 i_2 \dots i_n}^c$  are referred to as the direction tensor and the deviatoric direction tensor for contact normal density, respectively.

Discrete element method has been used to simulate the response of granular materials to proportional loading and non-proportional loading paths, the results from directional analyses suggest that an expression of Eq. (4) with the first two terms is sufficient to accurately approximate the directional distributions of contact normals. This leads to the conclusion that a 2<sup>nd</sup> rank symmetric tensor is sufficient to be used as the statistical measure of the contact normal distributions.

In two dimensional spaces, a symmetric and deviatoric tensor  $D_{i_1 \dots i_n}^c$  only has two independent components. The direction tensor could be expressed as

$$D_{i_1 i_2}^c = d_2^c \begin{pmatrix} \cos \phi_2^c & \sin \phi_2^c \\ \sin \phi_2^c & -\cos \phi_2^c \end{pmatrix} \tag{5}$$

And the directional distribution of the contact normal probability density  $E^c(\mathbf{n})$  becomes:

$$E^c(\mathbf{n}) = \frac{1}{2\pi} \left[ 1 + d_2^c \cos(2\theta - \phi_2^c) \right] \tag{6}$$

where  $d_2^c$  characterizes the degree of anisotropy and  $\phi_2^c$  gives information on phase angles.

### 4 Stress-Force-Fabric Relationship

Directional statistical analyses have also been conducted on the directional distribution of contact vectors and contact forces, as well as the statistical dependence between contact vectors and contact forces along each direction. The observation suggests an isotropic statistical dependence between contact forces and contact vectors along each direction, i.e., the effect of the statistical dependence between contact vectors and contact forces could be taken into account by approximating  $P^{ij}(\mathbf{n}) = \zeta$ , a direction independent variable. And only limited terms are necessary to characterize the directional distributed contact vectors and contact forces. [7]

In two dimensional spaces, imposing the symmetric condition of Cauchy stress tensor, i.e.,  $\sigma_{12} = \sigma_{21}$ , the stress tensor could be expressed as:

$$\sigma_{ij} = \frac{\omega N}{2V} \zeta v_0 f_0 \left[ (1 + C) \delta_{ij} + G_{ji}^f + G_{ij}^v + \frac{1}{2} D_{ij}^c \right] \quad (7)$$

where  $\omega$  is the coordination number,  $N$  is the number of particles,  $C$  is a scalar reflecting the joint product of direction tensors,  $G_{ji}^f, G_{ij}^v, D_{ij}^c$  are deviatoric direction tensor in relation to the anisotropy in mean contact force, mean contact vector and contact normal density, respectively. This expression is referred to as the stress-force-fabric relationship following the preceding work done by Rothenburg and Bathurst [8].

The stress-force-fabric relationship expressed explicitly the contribution of fabric tensor into the stress of granular material, and hence strength. It could be used to develop fabric-based failure criterion. Derivation of the stress-force-fabric relationship in three dimensional spaces is part of our future research plan.

## 5 Summary

This paper addresses issues in regarding to internal structure based on the particle-scale mechanics and homogenization theory. Following the micro-structural definitions, the role of internal structure could be understood as the geometrical linkage between the macro-scale stress and strain to the particle-scale contact forces and particle displacements. The quantification of the relevant geometrical information could be achieved by using the directional statistical theory. Direction tensors are proposed to characterize features on the internal structure. The direction tensor based on the contact normal density is of prominent important to the stress and hence strength of granular materials. The general stress-force-fabric relationship has been derived to facilitate the development of fabric-based constitutive relationship. However, there are still much work to be done, in particular on the kinematic aspect, i.e., the deformation and strain of granular materials.

## References

- [1] Casagrande, A., Carrillo, N.: Shear failure of anisotropic materials. In: Proceedings of Boston Society of Civil Engineers, vol. 31, pp. 74–87 (1944)
- [2] Oda, M., Nemat-Nasser, S., Konishi, J.: Stress-induced anisotropy in granular masses. *Soils and Foundations* 25(3), 85–97 (1985)
- [3] Li, X., Yu, H.S., Li, X.S.: Macro-micro relations in granular mechanics. *International Journal of Solids and Structures* 46(25-26), 4331–4341 (2009)
- [4] Li, X., Li, X.-S.: Micro-macro quantification of the internal structure of granular materials. *Journal of Engineering Mechanics* 135(7), 641–656 (2009)

- [5] Kanatani, K.: Distribution of directional data and fabric tensors. *Journal of Engineering Science* 22(2), 149–164 (1984)
- [6] Li, X., Yu, H.-S.: Tensorial Characterisation of Directional Data in Micromechanics. *International Journal of Solids and Structures* 48(14-15), 2167–2176 (2011)
- [7] Li, X., Yu, H.-S.: General stress-force-fabric relationship for two-dimensional granular materials. *International Journal of Solids and Structures* (under review, 2012)
- [8] Rothenburg, L., Bathurst, R.J.: Analytical study of induced anisotropy in idealized granular materials. *Geotechnique* 39(1), 601–614 (1989)

# Extension of Mohr-Coulomb Model into State Dependent Softening of Sand and Its Application in Large Deformation Analysis

Xu Li\*, Yuxia Hu, and David White

University of Western Australian, Perth, Australia  
ceXuLi2012@gmail.com

**Summary.** State transformation is common in soil shearing problem and causes much difficulty in soil description in numerical simulation. For characterizing the state transformation of sand, dilatancy angle and friction angle are linked with soil state parameter, i.e. the difference between current void ratio and void ratio at critical state. Further, state dependent dilatancy angle and friction angle are introduced into classical MC model. The new model shows robust stability in large deformation analysis and offers prediction matching the softening/hardening behavior of sand in laboratory tests, as well as the penetration resistance of spudcan into soil.

**Keywords:** Large deformation analysis, critical state, dilatancy angle, soften, harden.

## 1 Introduction

Referring to soil critical state, soil can be characterized as a dense or loose state. During shearing, dense sand dilates and shows higher strength, i.e. peak resistance. A series of sand models was developed for characterization of soil state dependent shearing behavior, including (Jefferies 1993; Manzari and Dafalias 1997; Samieh and Wong 1997; Li et al. 1999; Ling and Yang 2006). These models have displayed great advantage in capture the soil non-linear hardening and cyclic loading response in single element test. However, in simulating large deformation of soils, the major concern of sand constitutive model is the stability in numerical simulation. If the soil model involves many parameters, where some have physical meanings and some don't, the utilization of these models in practical applications becomes difficult.

Mohr-Coulomb (MC) model has been used successfully in simulating large penetration of foundations on clay and loose sand over clay soils (Yu et al. 2009) and shows robust stability in the large deformation finite element (LDFE) simulation with using remeshing and interpolating technique with small strain (RITSS) method (Hu and Randolph 1998a, 1998b).

---

\* Corresponding author.

In this paper, the critical state concept will be incorporated into the classical MC model. State dependent dilatancy angle and friction angle will be used to capture the phase transformation of sand. The new Critical State Mohr-Coulomb (CSMC) model will be validated against laboratory triaxial and biaxial test data. After the validation, the CSMC model will be applied to spudcan large penetration analysis on sand over clay soils.

## 2 Critical Mohr-Coulomb Model

### 2.1 State Dependent Dilatancy Angle and Friction Angle

Bolton (1986) drew an empirical relation between the soil peak friction angle and soil dilatancy angle,

$$\phi_p \approx \phi_c + a\psi \quad (1)$$

where  $\phi_p$  is peak friction angle;  $\phi_c$  is critical friction angle;  $a$  is 0.8 for plain strain condition, and  $a$  is 0.5 for triaxial test condition. Later a thorough study of the test data of Touyouura sand (Chakraborty and Salgado 2010) gives  $a$  value of 0.62 for both plain strain and triaxial conditions. However the empirical constant  $a$  seems to vary with material. For material with larger critical friction angle,  $a$  seems to be smaller. According to Taylor (1948), friction is considered a source of energy dissipation. Thus,

$$\tan \phi = \tan \phi_c + \tan \psi \quad (2)$$

Because Eq. 2 can fit experimental data very well and do not involve any empirical parameter (Fig. 1), it is selected in this paper. The dilatancy angle of sand can be linked to the soil state parameter,  $\gamma$ , which is defined as (Been and Jefferies 1985):

$$\gamma = e - e_c \quad (3)$$

where  $e$  is the current void ratio;  $e_c$  is the critical state void ratio at current stress. Further, a non-linear fashion between dilatancy angle and state parameter can be drawn from experimental data (Fig. 2):

$$\tan \psi \approx A(1 - \exp^{\text{sign}(\gamma)m|\gamma|^n}) \quad (4)$$

in which  $A$ ,  $m$ ,  $n$  are three constants.

Following eq. 4, the mobilised dilatancy angle is dependent on three parameters:  $A$ ,  $m$  and  $n$ . As demonstrated in Fig. 3, the parameter  $A$  serves as a scale factor to the dilatancy angle, and it has strong influences to dilatancy angle in both negative and positive regions of the state parameter  $\gamma$ , i.e. to both dense and loose sands. In eq. 4,  $n$  is a parameter controlling the curve shape;  $m$  is a parameter majorly influenced the curve shape with positive state parameter, i.e. loose sand.

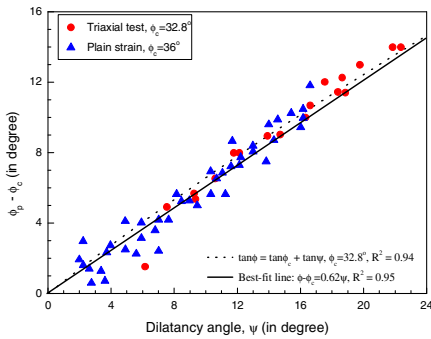


Fig. 1. Dilatancy angle of Touyouura sand

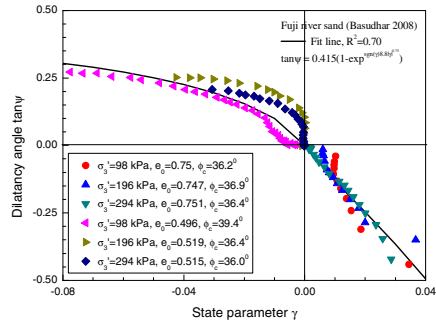


Fig. 2. State dependent dilatancy angle after yield

### 2.2 Critical State Line (CSL) of Sand

Li and Wang (1998) proposed a power equation to describe the CSL of sand, as

$$e_c = e_\Gamma - \lambda \left( \frac{p'}{p_a} \right)^\xi \tag{5}$$

where  $e_c$  is the critical void ratio at mean effective stress  $p'$ ;  $e_\Gamma$  is the critical void ratio at zero mean effective stress;  $p_a$  is a reference pressure, which is normally taken as,  $p_a = 101$  kPa, the atmospheric pressure for convenience;  $p'$  is the mean effective stress;  $\lambda$  is the slope of CSL in  $e$  versus  $(p'/p_a)^\xi$  plane, which is similar to the concept of compression index;  $\xi$  is a dimensionless constant. In this paper,  $\lambda$  is also termed as compression index and  $\xi$  is termed as compression power for convenience. Eq. 5 shows good accuracy when fitting to experimental data (Li et al. 1999; Ling and Yang 2006). Fixing  $\xi$  as 0.75,  $\lambda$  and  $e_\Gamma$  are fitted and listed in Table 1 for the six different sands. By examining the values of  $C_u$  and  $\lambda$ , the following approximation can be found:

$$\lambda = 0.01C_u \tag{6}$$

### 2.3 Critical State Mohr-Coulomb Model

Utilizing eqs. 2~5, state dependent dilatancy angle and friction angle can be determined. They can be further involved in classical MC model or other modified MC model. The hardening parameter can be calculated as,

**Table 1.** Calibration of CSL for six sands

Sand	$C_u$	$D_{50}$	$e_{max}$	$e_{min}$	CSL fitted		
					$e_r$	$\lambda$	$R^2$
1	1.7	0.17	0.98	0.60	0.93	0.016	0.99
2	1.8	0.33	0.84	0.52	0.78	0.014	0.90
3	1.5	0.12	1.02	0.67	0.94	0.014	0.97
4	1.5	0.3	0.86	0.57	0.83	0.014	0.98
5	4.36	0.33	0.99	0.54	0.90	0.048	0.94
6	1.6	0.33	0.86	0.53	0.85	0.015	0.90

1: Toyoura (Verdugo and Ishihara 1996); 2: Erksak (Been et al. 1991); 3: Leighton buzzard(Been et al. 1991); 4: Sydney (Chu 1995); 5: Tung-chung (Li and Wang 1998); 6: Monterey 0# (Riemer and Seed 1997).

$$H = 2 \sin \psi (1 + e) A m n \exp^{sign(\gamma) m |\gamma|^n} |\gamma|^{n-1} \frac{\partial f}{\partial \tan \phi} \quad (7)$$

where  $f$  is the yield function, e.g. in classical MC mode,

$$f = \sigma_1 (1 + \sin \phi) + \sigma_3 (\sin \phi - 1) \quad (8)$$

In this paper, the hyperbolic Mohr-Coulomb (HPMC) was used. The detailed implementation of HPMC can be found in Abbo and Sloan (1993).

### 3 Validation of CSMC

#### 3.1 Single Element Test

In single element test, a unit element is considered to under tri-axial loading process. Fig. 4 shows the model prediction against laboratory test data for Athabasca soil sand. It is apparent that the critical state hyperbolic Mohr-Coulomb model (CSHMC) can predict the peak strength and the residual strength of the soil very well. However, the model prediction shows much sharp peak comparing to the corresponding experimental result. This is because the CSHMC model has not introduced any bonding surface concept. The transition from an elastic state to a plastic state is sharp. Since the model is aiming at simulating the post-peak shearing behaviours of sand for large deformation analysis, it is clearly shown that the post-peak shear behaviour can be modelled satisfactorily.

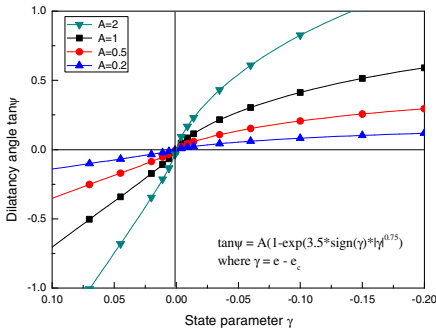


**Fig. 3.** Effect of parameter A on dilatancy angle

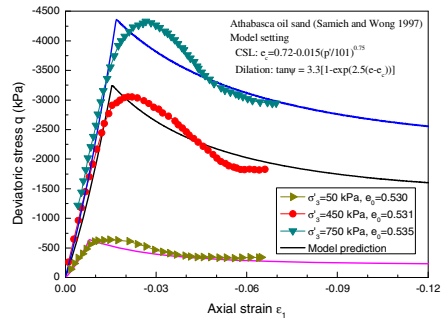


**Fig. 4.** Drained triaxial test results of Athabasca oil sand

### 3.2 Bi-axial Test

Bi-axial test is carried out utilizing FEM method together with the RITSS algorithm for Ottawa sand (Alshibli et al. 2003). In the simulation, sample was of 200 mm in height and 100 mm in width. Sample was loaded from both ends with a displacement step of 0.0001mm. The sample shape was updated and remeshed every 100 steps. Constant confining pressure  $p_0$  was applied to both sides of the sample. To simulate the bi-axial test in reality, fully rough boundary is considered, i.e. four corner points were restrained in horizontal direction.

The model parameters is calibrated by single element test for Ottawa sand (Alshibli et al. 2003) and further used in the bi-axial test. The close match of the model prediction to the experimental data for single element triaxial test provides a set of model parameters as  $A = 0.36$ ,  $m = 8$ ,  $n = 0.75$  (Fig. 5). When this set of parameters was applied to the bi-axial element test conditions, a much lower peak is observed. However, when the parameter A was increased from 0.36 to 0.6, the CSHMC model shows a similar peak as the experimental data (Fig. 6). This can be justified that different parameters might be needed for triaxial and biaxial test conditions, since Bolton (1986) has also suggested that, when estimating the peak friction angle  $\phi_p$  using Eq. 1, the a value is 0.8 for plain strain (biaxial) condition and 0.5 for triaxial condition. Again, the post-peak shear behaviours are captured very well.

Fig. 7 depicts the shear band formed in biaxial tests when CSHMC model was employed. Single shear band is formed first at 2% axial-strain and evolves into double shear band at 8% axial-strain. This phenomenon is consist with the observation in Alshibli et al. (2003), in which single shear band is clearly observed at about 10% axial-strain and cross double shear band is clearly observed at about 20% axial-strain.

The soil in the shear band yields and dilates gradually. The void ratio of soil in shear band increases gradually and approaches to the critical void ratio 0.61.

The dilatancy angle decreases continuously until the soil reaches the critical state, as well as the friction angle.

However, the soil outside the shear band remains the initial void ratio, i.e. 0.54. That’s to say, the local strain in shear band is much different with that of whole sample. The local strain, which can be captured by single element test under bi-axial loading condition, is much higher (as shown in Fig. 6). The single element test result shows a slow decrease in the principal stress ratio after its peak than that in biaxial test. In fact, the measured axial strain in laboratory should be an apparent value.

Strain localization is critical in explaining some laboratory test results where after the peak, the deviatoric stress  $q$  often decreases to a stable value much earlier for axial strain than that does for volume strain (Samieh and Wong 1997; Salgado et al. 2000; Alshibli et al. 2003). In Alshibli et al. (2003), the stress start to flocculates around that value after 10% axial strain, otherwise the volume strain continuously increases even over 25% axial strain. Once a “central” shear band of soil at critical state is formed, the apparent shear strength of whole sample reaches the critical value. However the volume of whole sample still increases with yielding of soil in marginal shear band (Fig. 5).

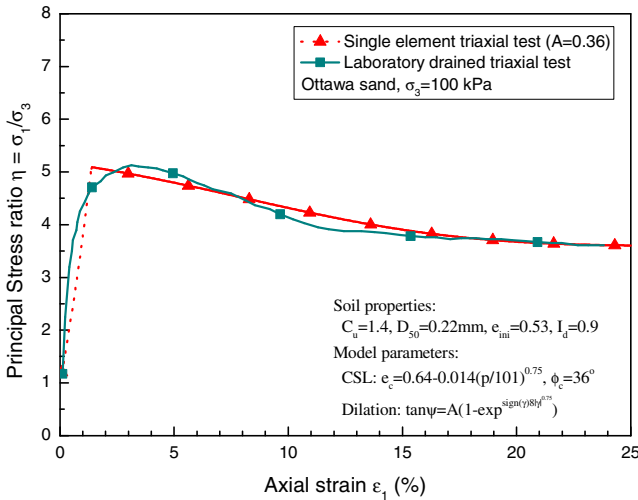


Fig. 5. Model parameter calibration by single element test (tri-axial test)

## 4 Application in Spudcan Penetration into Sand Overlaying Clay Problem

### 4.1 Problem Statement

Spudcan foundations are a common foundation type found in jackup rigs in offshore oil/gas explorations. The spudcan foundations on layered soils, especially on sand over clay soils, normally possess a risk of punch-through failure. K.K.

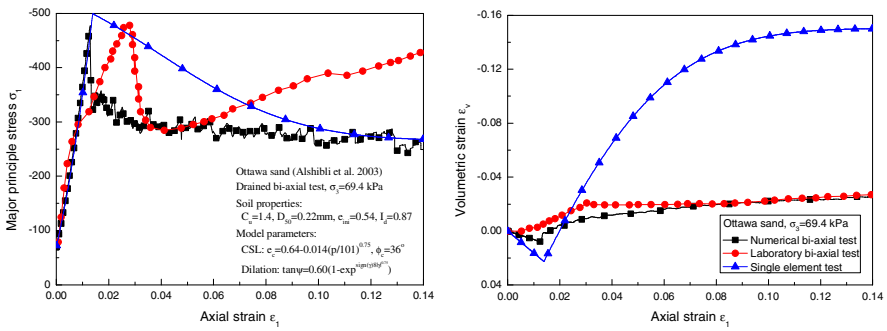


Fig. 6. Plane strain experiments of Ottawa sand: (a)  $\sigma_1$ - $\epsilon_1$  relation; (b)  $\epsilon_v$ - $\epsilon_1$  relation

Lee (2007) conducted series of centrifuge tests of spudcan penetration in sand over clay stratum. Numerical simulation results, which is carried out using AFENA finite element package (Carter & Balaam, 1995) together with RITSS method, are compared with these test results to validate the new CSHMC model. In the simulation, CSHMC was used to describe the sand behaviour, and the clay obeyed Tresca yield criteria.

Lee (2007) used a super fine silica sand with  $d_{50}$  of 0.19 mm,  $C_u$  of 1.7, maximum void ratio of 0.75, and minimum void ratio of 0.45. In case 1, the initial relative density of sand is 0.92; the depth of sand layer is 6.2 m; the shear strength of clay increases with depth and obeys (Lee 2007),

$$S_u = 16 + 2.1z \tag{9}$$

where  $z$  is the depth of clay, which is counted from the surface of clay layer. In numerical simulation, the critical state line (CSL) was taken as:  $e_c = 0.68 - 0.017(p'/101)^{0.75}$ ; the critical friction angle was taken as  $27^\circ$ ; the dilation is taken as  $\tan\psi = 0.8(1 - \exp(\text{sign}(\gamma)5|\gamma|^{0.5}))$ .

The numerical result can match the test data very well, as shown in Fig. 8. That's to say, the CSHMC can capture the peak penetration resistance and post-peak softening of penetration resistance very well.

Fig. 9 shows the dilatancy angle fields in the soil. It's clear that the dilatancy angle in shear band decreases with yielding and at last reaches to 0 at deep penetration. Some strong sand has been trapped under the spudcan and moves together into deeper clay. When the yield zone reaches the clay layer, the spudcan penetration resistance reaches a peak value. After that, the resistance becomes to decrease as the yield zone moves into the clay layer underneath where the strength is lower than that in upper sand layer. After the whole spudcan has been embedded into the clay layer, the spudcan penetration resistance shows a valley value. Further, spudcan penetration resistance grows up because of the increasing strength with depth of clay.

Fig. 10 shows penetration resistance profiles with different dilatancy parameters of sand. If the sand has higher dilatancy angle, the spudcan penetration resistance shows higher peak. Because the sand will reach its critical state and reach a same critical state friction angle, the spudcan penetration resistance profiles coin at deep penetration.

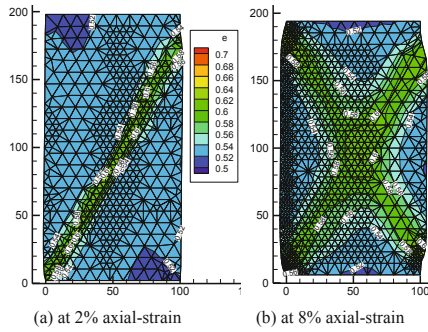


Fig. 7. Shear bound evolution during shearing

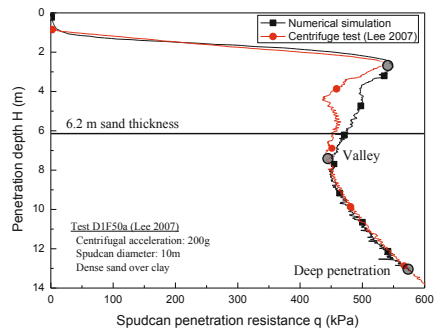


Fig. 8. Penetration resistance profile for spudcan penetration into sand over clay

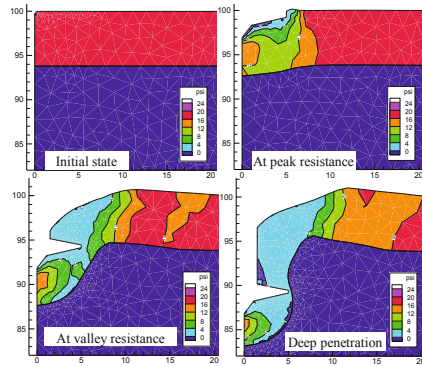


Fig. 9. Dilatancy angle fields in soils

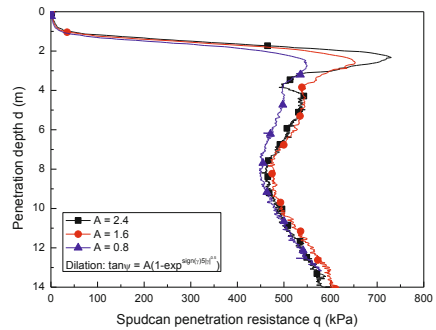


Fig. 10. Peak resistance varied with dilation of sand

## 5 Conclusions

In this paper, the classic Mohr-Coulomb model is extended to simulate soil hardening and softening behaviour with critical state basis. Soil friction angle and dilatancy angle are linked with soil state parameter and further used in MC model. New critical state Mohr-Coulomb model is verified by single element test and large deformation finite element analysis with RITSS method. CSMC model can simulate the state transformation of sand and is able to capture the peak resistance and post-peak softening of sand. The CSMC can be easily applied to large deformation analysis with RITSS method and shows good stability.

**Acknowledgement.** This study is supported by the Australian Research Council (ARC) Discovery Projects Proposals (DP1096764) and Open Funds Projects from Key Laboratory for River Dynamics and Hydraulic Engineering, Tsinghua University (sklhse-2011-D-01).

## References

- Abbo, A.J., Sloan, S.W.: A Smooth Hyperbolic Approximation to the Mohr-Coulomb Yield Criterion. *Computers and Structures* 54(3), 427–441 (1995)
- Alshibli, K.A., Batiste, S.N., Sture, S.: Strain localization in sand: plane strain versus triaxial compression. *Journal of Geotechnical and Geoenvironmental Engineering* 129(6), 483–494 (2003)
- Been, K., Jefferies, M.G.: A state parameter for sands. *Géotechnique* 35(2), 99–112 (1985)
- Been, K., Jefferies, M.G., Hachey, J.: The critical state of sands. *Geotechnique* 41(3), 365–381 (1991)
- Bolton, M.D.: The strength and dilatancy of sands. *Geotechnique* 36(1), 65–78 (1986)
- Carter, J.P., Balaam, N.P.: AFENA users manual: Geotechnical Research Center. University of Sydney (1995)
- Hu, Y.X., Randolph, M.F.: H-adaptive FE analysis of elasto-plastic non-homogeneous soil with large deformation. *Computers and Geotechnics* 23(1-2), 61–83 (1998a)
- Hu, Y.X., Randolph, M.F.: A practical numerical approach for large deformation problems in soil. *International Journal for Numerical and Analytical Methods in Geomechanics* 22(5), 327–350 (1998b)
- Li, X.S., Dafalias, Y.F., Wang, Z.L.: State-dependent dilatancy in critical-state constitutive modelling of sand. *Canadian Geotechnical Journal* 36(4), 599–611 (1999)
- Ling, H.I., Yang, S.: A unified sand model based on critical state and generalized plasticity. *Journal of Engineering Mechanics* 132, 1380–1391 (2006)
- Li, X.S., Wang, Y.: Linear representation of steady-state line for sand. *Journal of Geotechnical and Geoenvironmental Engineering* 124(12), 1215–1217 (1998)
- Manzari, M.T., Dafalias, Y.F.: A critical state two-surface plasticity model for sands. *Géotechnique* 47(2), 255–272 (1997)
- Riemer, M.F., Seed, R.B.: Factors affecting apparent position of steady-state line. *Journal of Geotechnical and Geoenvironmental Engineering* 123(3), 281–287 (1997)
- Samieh, A.M., Wong, R.C.K.: Deformation of Athabasca oil sand in triaxial compression tests at low effective stresses under varying boundary conditions. *Canadian Geotechnical Journal* 34, 985–990 (1997)
- Taylor, D.W.: *Fundamentals of soil mechanics*. Wiley, New York (1948)
- Verdugo, R., Ishihara, K.: The steady state of sandy soils. *Soils Foundation* 36(2), 81–91 (1996)
- Wang, Z.L., Dafalias, Y.F., Shen, C.K.: Bounding surface hypoplasticity model for sand. *Journal of Engineering Mechanics, ASCE* 116(5), 983–1001 (1990)

# A Constitutive Model of Sand Considering the State-Dependent and the Effect of Direction of Principal Stress

Peng Liu<sup>\*</sup>, Maotian Luan, and Zhongtao Wang

Institute of Geotechnical Engineering, School of civil Engineering,  
Dalian University of Technology  
Dalian, China, 116024  
lp-536@163.com

**Abstract.** Based on the theory of critical state, the state parameter considering the direction of principal stress during shear is introduced into dilatancy equation and the plastic hardening modulus expression to develop a new constitutive model for sand which can display the influence of the shearing direction of principal stress. By comparison with the related experimental data and analyzing, the method on simulating the stress-strain relationship under the different shearing direction of principal stress is proved to be correct and accurate.

**Keyword:** direction of principal stress, state parameter, dilatancy.

## 1 Introduction

Yoshimine et al. (1998)[1] and Nakata et al. (1998)[2] performed a series of hollow cylinder undrained torsional tests on Toyoura sand, which showed the shearing direction of principal stress has a significant impact on deformation and strength of sand. Leng et al. (2006)[3], Luan et al. (2007)[4] pointed out the sand displayed different stress-strain relationship and dilatancy character when the direction of the principal stress during shear was different through a series of undrained and drained monotonic shear tests in the different direction of principal stress using the static and dynamic universal triaxial and torsional shear apparatus.

In order to reflect the effect of the direction of principal stress direction on the shear behaviour of sand, based on the critical state theory a new state parameter contained the direction of the principal stress during shear is put forward, and a constitutive model considering the state-dependent and effect of the direction of principal stress is established. A group of monotony shear tests in different fixed direction of principal stress is simulated using the proposed constitutive model. By comparison with experimental data, the method is proved to be correct and accurate.

---

<sup>\*</sup> Corresponding author.

## 2 Effect of Direction of Principal Stress on Dilatancy

The direction of principal stress can be indicated by the direction angle of principal stress, which is the angle of the maximum principal stress from the vertical. Fig. 1 and Fig. 2 show the typical effect of direction of principal stress on the dilatancy of sand and stress-strain relationship. In the undrained monotonic triaxial tests, the samples are at the same initial state with the same initial void ratio and initial mean effective stress, but the direction angle of principal during shear is different. When the direction angle of principal stress become larger, the behavior became clearly softer and more contractive. On the other hand, when the direction angle of principal stress get smaller, the behavior showed strong strain-softening and more dilative.

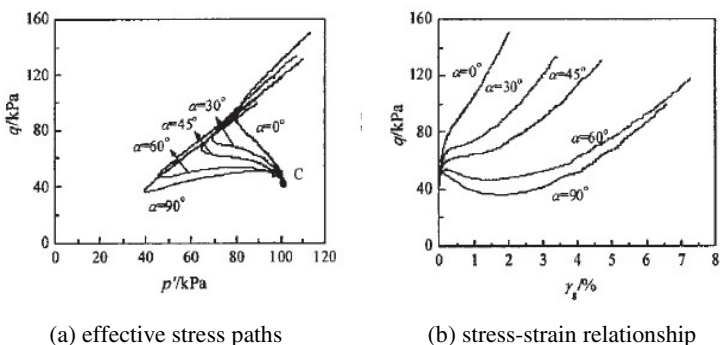


**Fig. 1.** The dependency of effective stress paths on the direction of the principal stress (LUAN, 2007[4])

Lots of experiment results [1-4] display a law that the sand become more contractive with the direction angle of principal stress increased under drained or undrained condition

Based on the analysis of large quantities of test data, the initial state parameter is suggested to be corrected, and the correction factor can be used an experience expression as

$$\psi'_0 = k \frac{\tan \frac{1}{2} \left( \alpha_0 + \frac{\psi_0}{|\psi_0|} \alpha \right)}{\tan \left( \frac{1}{2} \alpha_0 \right)} \psi_0 \tag{1}$$

Where  $k$ ,  $\alpha_0$  are model parameter,  $\psi_0 = e_0 - e_c = e_0 - \left( e_{\Gamma} - \lambda_c \left( \frac{p'}{p_a} \right)^{\xi} \right)$  is initial state parameter,  $\alpha$  is angle of principal stress.

The new state parameter can be expressed as

$$\psi' = \psi'_0 + \frac{\left(\frac{p'}{p_a}\right)^\xi - \left(\frac{p'_0}{p_a}\right)^\xi}{\left(\frac{p'_0}{p_a}\right)^\xi - \left(\frac{p'_c}{p_a}\right)^\xi} \psi'_0 + (e - e_0) \tag{2}$$

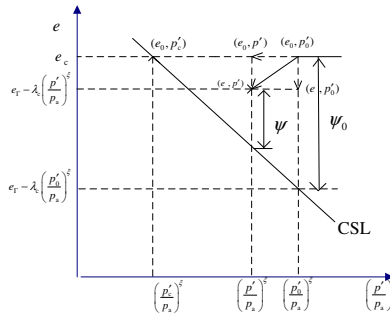


Fig. 2. An arbitrary stress path in  $e - \left(\frac{p'}{p_a}\right)^\xi$  space for loose sand

### 3 Constitutive Model

By the theory of plasticity, the relationship between the stress and strain increments can be expressed as

$$\begin{cases} d\varepsilon_v = d\varepsilon_v^e + d\varepsilon_v^p = \frac{dp'}{K} + \frac{1}{K_p} \left( \frac{\partial f}{\partial p'} dp' + \frac{\partial f}{\partial q} dq \right) \cdot d \\ d\varepsilon_q = d\varepsilon_q^e + d\varepsilon_q^p = \frac{dq}{3G} + \frac{1}{K_p} \left( \frac{\partial f}{\partial p'} dp' + \frac{\partial f}{\partial q} dq \right) \end{cases} \tag{3}$$

With  $K$  and  $G$  the elastic bulk and shear modulus given by

$$\begin{cases} G = G_0 \frac{(2.97 - e)^2}{1 + e} \sqrt{p' p_a} \\ K = G \frac{2(1 + \nu)}{3(1 - 2\nu)} \end{cases} \tag{4}$$

where  $G_0$  is a material constant,  $e$  is current void ratio,  $p_a$  is standard atmospheric pressure.

The yield criterion can be written as

$$f = q - \eta p' \tag{5}$$

in which  $q$  is generalized shear stress,  $p'$  is mean effective stress,  $\eta$  is effective stress ratio.

For the plastic modulus the follow constitutive relation is proposed by Wan [5]

$$K_p = \frac{hGe^{n\psi'}}{\eta} (M_c e^{-n\psi'} - \eta) \tag{6}$$

where  $h = h_1 - h_2 e$ ,  $h_1$  and  $h_2$  are two material constants,  $n$  is a positive model parameters,  $M_c$  is critical stress ratio.

The state-dependent dilatancy function proposed by Li and Dafalias (2000) [6] is used

$$d = \frac{d_0}{M_c} (M_c e^{m\psi'} - \eta) \tag{7}$$

in which  $d_0$  and  $m$  are positive modeling parameters,  $m$  is a positive model parameters

### 4 Simulation by the Model

With undrained test for example, the state parameter can be expressed as

$$\psi' = \psi'_0 + \frac{\left(\frac{p'}{p_a}\right)^\xi - \left(\frac{p'_0}{p_a}\right)^\xi}{\left(\frac{p'_0}{p_a}\right)^\xi - \left(\frac{p'_c}{p_a}\right)^\xi} \psi'_0 \tag{8}$$

in which  $\psi'_0 = k \frac{\tan \frac{1}{2} \left( \alpha_0 + \frac{\psi_0}{|\psi_0|} \alpha \right)}{\tan \left( \frac{1}{2} \alpha_0 \right)} \psi_0$

There are thirteen material constants in the model. In this paper a unified set of model parameters tested by Li (2000) [6] listed in Table 1 will be used to simulated test by Nakata (1998) [2]

**Table 1.** Model parameters of sand

Elastic parameters		Critical state parameters			Hardening parameters			Dilatancy parameters		Direction f principal stress parameters		
$G_0$	$\mathcal{V}$	$M_c$	$\lambda_c$	$e_T$	$\xi$	$h_1$	$h_2$	$n$	$d_0$	$m$	$k$	$\alpha_0$
125	0.25	1.25	0.02	0.86	0.7	3.45	3.34	1.1	0.38	1	1	60

Initial void ratio  $e = 0.7$  , initial mean effective stress  $p' = 200\text{kPa}$  , the direction of principal stress  $\alpha = 0^\circ, 30^\circ, 45^\circ, 60^\circ, 75^\circ, 90^\circ$  , Predicted by the proposed model shear properties of Toyoura sand under undrained condition with different directions of principal stress can be seen in Fig.3.

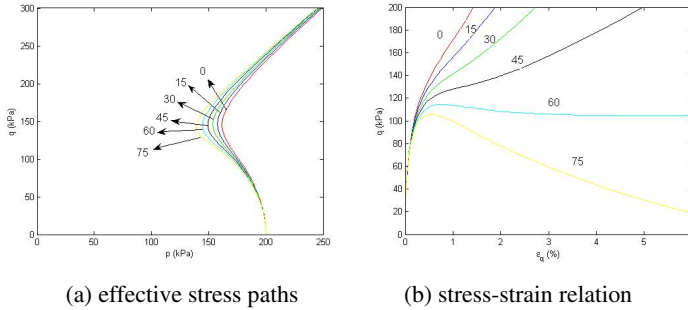


**Fig. 3.** Predicted by the proposed model shear properties of Toyoura sand under undrained condition with different directions of principal stress

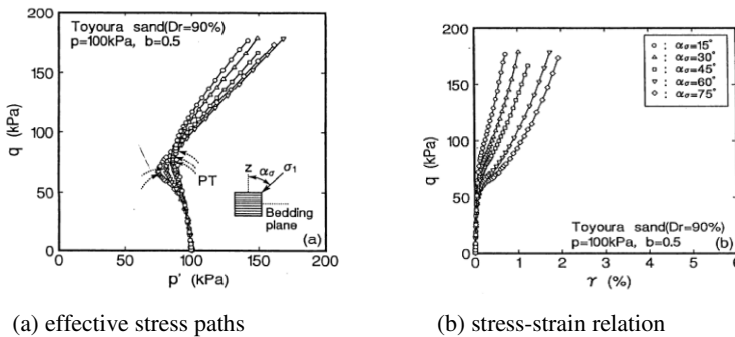


**Fig. 4.** Measured shear properties under undrained conditions (Nakata, 1998)

**References**

- [1] Yoshimine, M., Ishihara, K., Vargas, W.: Effects of principal stress direction and intermediate principal stress on undrained shear behavior of sand. *Soils and Foundations* 38(3), 179–188 (1998)
- [2] Nakata, Y., Hyodo, M., Yasufuku, N.: Flow deformation of sands subjected to principal stress rotation
- [3] Leng, Y., Luan, M.-T., Xu, C.-S., et al.: A comparative study on drained and undrained shear behavior of saturated sands. *Journal of Disaster Prevention and Mitigation Engineering* 28(2), 144–151 (2008) (in Chinese)

- [4] Luan, M.-T., Xu, C.-S., He, Y., et al.: Experimental study on effect of direction of the principal stress on undrained behavior of saturated loose sand under monotonic shearing. *Chinese Journal of Geotechnical Engineering* 28(9), 1085–1089 (2006) (in Chinese)
- [5] Wan, R.G., Guo, R.G.: A simple constitutive model for granular soils: modified stress-dilatancy approach. *Computers and Geotechnics* 22(2), 109–133 (1998)
- [6] Li, X.S., Dafalias, Y.F.: Dilatancy for cohesionless soil. *Geotechnique* 50(4), 449–460 (2000)

# An Elastoplastic Constitutive Model of Unsaturated Soils with Coupling of Capillary Hysteresis and Skeletal Deformation

Tian-tian Ma<sup>1</sup>, Chang-fu Wei<sup>1,2,\*</sup>, Pan Chen<sup>1</sup>, and Hou-zhen Wei<sup>1</sup>

<sup>1</sup> State Key Laboratory of Geomechanics and Geotechnical Engineering, Institute of Rock and Soil Mechanics, Chinese Academy of Sciences, Wuhan 430071, China

<sup>2</sup> Guilin University of Technology, Guilin 541004, China

cfwei@whrsm.ac.cn

**Abstract.** A constitutive model of unsaturated soils coupling skeletal deformation and capillary hysteresis is developed based on the modified Cam-clay model. To describe the effect of capillary hysteresis on skeletal deformation, an evolution equation is first developed for the degree of saturation to characterize the soil-water states under arbitrary drying/wetting conditions, and then a new hardening function is proposed, in which the matric suction and the degree of saturation as well as the plastic volumetric strain are simultaneously introduced to represent the hardening effect. It is shown that the proposed hardening function can properly capture the difference of preconsolidation pressure under different soil-water states and effectively describe the effect of drying/wetting history on the skeletal deformation. Theoretical simulations are compared to the experimental data available in the literature, showing that the new model captures very well the main features of unsaturated soil behavior. Unlike other unsaturated soil models, the new model treats the degree of saturation as an internal variable, whose evolution equation explicitly accounts for the capillary hysteresis. The new model can smoothly transit to the modified cam-clay model of saturated soils when the degree of saturation becomes one. The new constitutive model is implemented into a finite element code, U-DYSAC2, in which the displacement of solid skeleton, pore pressure and air pressure are primary nodal unknowns. An implicit algorithm is developed to integrate the constitutive relation at the Gaussian-point level. The proposed numerical procedure is used to simulate a typical two-dimensional unsaturated soil problem, illustrating the applicability and capabilities of the new numerical procedure.

## 1 Introduction

Sufficient experimental evidence shows that there exists complicated coupling effect between deformation and seepage processes in unsaturated soils [1]. To address such a problem, two coupling constitutive functions must be established, namely the stress-strain relation and the soil-water characteristic curve.

---

\* Corresponding author.

Alonso et al [2] developed the BBM model based on the modified Cam-clay model. This model adopted two independent sets of stress variable, and introduced the so-called Loading-Collapse (LC) yield curve to express the hardening effect of suction. Although the BBM model can capture the main features of unsaturated soil, the stresses and strains adopted therein are not properly conjugated [3]. To resolve this issue, based on the BBM model, Nuth and Laloui [4] and Sheng et al. [5] used a Bishop's type effective stress instead of net stress as an independent stress variable. These models still used LC yield curve to describe wetting-induced collapse phenomenon under different stress states of unsaturated soils, without explicitly considering the effect of capillary hysteresis.

Based on experimental results, Wheeler [1] pointed that the effect of capillary hysteresis on the stress-strain relation is significant. He then suggested that cyclic soil-water characteristic function should be included in the elastoplastic constitutive model of unsaturated soil to describe the effect of the cyclic variation in water content on the skeletal deformation.

The major difference between a saturated soil and an unsaturated soil resides in the fact that the latter depends not only on its stress history but also on the hydraulic path that it has experienced. Recently, Wei and Dewoolkar [6] identified a link between the capillary hysteresis and an intrinsic dissipation process in unsaturated soils, and developed an internal-variable model of capillary hysteresis, allowing the capillary hysteresis and skeletal deformation to be simulated in a unified framework of elastoplastic theory.

In this paper, a theoretical framework is presented that can simulate plastic deformation and capillary hysteresis in a coupling and hierarchical way. The smooth transition from unsaturated to saturated state could be achieved in this model. This new model is implemented in the finite element code, U-DYSAC2, where an implicit algorithm is developed to integrate the constitutive relation at the Gaussian-point level. A numerical model of unsaturated soil is established, in which displacement, pore water pressure and pore air pressure are viewed as basic unknowns.

## 2 A Constitutive Model Coupling Capillary Hysteresis and Plastic Deformation

### 2.1 Stress State Variables

Effective stress  $\sigma'_{ij}$  and matric suction  $s_c$  are adopted as stress state variables, defined respectively as

$$\sigma'_{ij} = (\sigma_{ij} - u_a \delta_{ij}) + S_r (u_a - u_w) \delta_{ij} \quad (1)$$

$$s_c = u_a - u_w \quad (2)$$

where  $\sigma_{ij}$  is the total stress tensor;  $\sigma'_{ij}$  is the effective stress tensor;  $S_r$  is the degree of saturation;  $u_a$  and  $u_w$  are pore gas pressure and pore water pressure, respectively;  $\delta_{ij}$  is the Kronecker delta;  $s_c$  is the matric suction. Houlsby [3] proposed that stress state variables ( $\sigma'_{ij}, S_c$ ) and strain variables ( $\epsilon_{ij}, S_r$ ) are work-conjugated, where  $\epsilon_{ij}$  is the strain tensor.

## 2.2 Effect of Matric Suction and Saturation on Soil Hardening

Microscopically, the stabilizing effect of meniscus water rings is related to the quantity of the rings and the surface tension. Here coefficient  $(1 - S_r)$  is introduced to represent the quantity of meniscus water rings. Moisture distribution in an unsaturated soil depends upon its wetting/drying history [7]. So considering the effect of saturation only is insufficient. To represent the capillary effect at a constitutive level, a formulation is assumed to account for the effect of matric suction and degree of saturation on the preconsolidation pressure (capillarity-induced hardening), i.e.,

$$p_c = p_{c0}(\epsilon_v^p)h(\epsilon_v^p, S_r, s_c) \quad (3)$$

where  $p_c$  and  $p_{c0}$  are the preconsolidation pressures at partial saturation and full saturation respectively; Hardening parameter  $h$  is a function of plastic volume strain, degree of saturation and matric suction, which is assumed as

$$h(\epsilon_v^p, S_r, s_c) = r - (r - 1) \exp \left\{ -m \left\langle 1 - \frac{\epsilon_v^p}{\epsilon_{v\max}^p} \right\rangle \frac{(1 - S_r)s_c}{(1 - S_r^{irr})} \right\} \quad (4)$$

where  $r$  is the ratio of preconsolidation pressures at residual water content and full saturation;  $m$  is the growth rate of preconsolidation pressure with the degree of saturation and suction;  $\epsilon_v^p$  is the plastic volume strain;  $\epsilon_{v\max}^p$  is the maximum plastic volume strain;  $S_r^{irr}$  is the residual degree of saturation;  $\langle \rangle$  is Maccauley bracket, defined as  $\langle x \rangle = xH(x)$ , where  $H(x)$  is Heaviside function.

Equation (4) has the following features: (1) when  $s_c$  is smaller than the air entry value,  $S_r = 100\%$  and  $h = 1.0$ , implying that capillary effect is trivial;  $p_c$  equals to  $p_{c0}$ ; (2) when air enters into soil, the variations of  $s_c$  and  $S_r$  are drastic, which has great influence on the preconsolidation pressure; (3) when the water content approaches to the residual value, the value of  $h$  changes gently with  $s_c$  and  $S_r$  and finally tends to a stable value. These features are

consistent with the experimental observations [4]. The effect of  $s_c$  and  $S_r$  on the preconsolidation pressure diminishes gradually with the increasing of  $\epsilon_v^p$ . When  $\epsilon_v^p$  reaches the maximum  $\epsilon_{v\max}^p$ , the influence of  $s_c$  and  $S_r$  on preconsolidation pressure disappears, implying that the soil is very dense and the capillary effect is negligible.

This framework is based on the modified Cam-clay model, in which the yield function is

$$f = q^2 + M^2 p'(p' - p_c) \tag{5}$$

Experimental data shows that the critical state line of an unsaturated soil is consistent with that of its saturated counterpart.

Elastic volume strain and shear strain are given by

$$d\epsilon_v^e = \frac{\kappa}{v} \frac{dp'}{p'}; \quad d\epsilon_q^e = \frac{1}{3G} dq \tag{6}$$

where  $\lambda$  is the virgin compression index;  $\kappa$  is the swell/recompression index;  $v$  is specific volume;  $G$  is the elastic shear modulus.

An associated flow rule is adopted herein, i.e.,

$$d\epsilon_v^p = \frac{\lambda - \kappa}{v} \frac{dp_{c0}}{p_{c0}}; \quad d\epsilon_q^p = \frac{2q}{M^2(2p' - p_c)} d\epsilon_v^p \tag{7}$$

The hardening rule is assumed as

$$p_c(\epsilon_v^p, S_r, S_c) = p_{c0}(\epsilon_v^p) h(\epsilon_v^p, S_r, S_c) \tag{8}$$

$$p_{c0}(\epsilon_v^p) = p_{c0}^* \exp\left(\frac{v}{\lambda - \kappa} \epsilon_v^p\right) \tag{9}$$

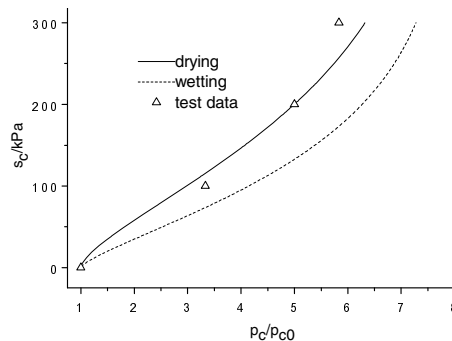


Fig. 1. Comparison of LC curve calculated and test data

The effect of suction and saturation on the preconsolidation pressure is shown in Fig.1. The experimental data in the figure are obtained from Wheeler and Sivakumar [8]. The figure shows that the preconsolidation pressure under drying is smaller than that under wetting, since the degree of saturation is larger due to capillary hysteresis.

### 2.3 The Effect of Deformation on SWCC

Wei and Dewoolkar [6] developed a simple and practical capillary hysteresis internal variable model based on the thermodynamics and porous media theory. The model can account for the effect of volumetric strain on the soil-water characteristics *via* slight modification. To this end, we first note that

$$dS_r = d\left(\frac{V_w}{V_v}\right) = \frac{dV_w}{V_v} - \frac{V_w}{V_v} \frac{dV_v}{V_v} \tag{10}$$

where  $n$  is void ratio. The first term expresses the effect of matric suction variation on the degree of saturation, while the second term describes the effect of deformation on the degree of saturation. Neglecting the effect of elastic deformation, equation (10) becomes

$$dS_r = -\frac{ds_c}{K_p(s_c, S_r, \hat{n}, \epsilon_v^p)} + \frac{S_r}{n} d\epsilon_v^p \tag{11}$$

where  $\hat{n}$  expresses direction of hydraulic path;  $K_p$  is given by

$$K_p(S_c, S_r, \hat{n}) = \bar{K}_p(S_r, \hat{n}) + \frac{c|S_c - \bar{S}_c(S_r, \hat{n})|}{r(S_r) - |S_c - \bar{S}_c(S_r, \hat{n})|} \tag{12}$$

where  $\bar{K}_p(S_r, \hat{n})$  is the slope of boundary curve;  $c$  is a positive material parameter which is used to describe the scanning curves;  $r(S_r)$  is the matric suction difference of the two boundaries corresponding to the current degree of saturation.

### 3 Model Verification

Sun et al. [9] have performed a series of isotropic compression and wetting-collapse tests, the results of which are used to verify the above-developed model. Comparison of model simulations and experimental data is shown in Figure 2(a). There are two stress paths, i.e., A-B-C-E and A-B-D-E. A-B and A-D are isotropic compression at  $s_c = 147kPa$ , while B-C and D-E are wetting ( $s_c = 147kPa \rightarrow 0$ ) at  $p_{net} = 98kPa$  and  $p_{net} = 196kPa$ , respectively. C-E is isotropic compression at full saturation.

Figure 2(b) shows that the sample slightly rebounds in the early beginning, and collapse occurs when the stress state touches the yield surface during wetting. This is because the effective stress decreases slower than the preconsolidation pressure. Figure 2(c) shows that the degree of saturation increases with the increase of net stress due to the plastic strain. The measured SWCC and the model simulation are shown in figure 2(d).

Triaxial compression and wetting test results and model simulation are shown in Figure 3. The model simulation shows that the axial strain is slightly underestimated, whereas the lateral strain is overestimated. When the soil sample is wetted to 0 kPa, the model predicts that the saturation is 1.0. This is inconsistent with the measurement. This discrepancy is probably due to the effect of trapped air, implying that slight improvement of the new model is required.

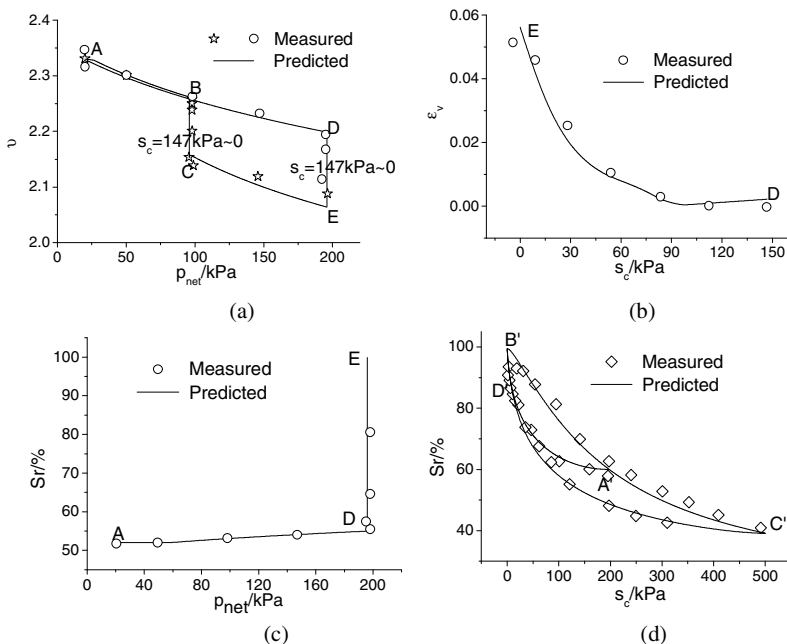


Fig. 2. Isotropic compression and collapse test

### 4 Numerical Analysis

The new constitutive model is implemented into a finite element code, U-DYSAC2 [10], in which the constitutive model was integrated by using an implicit algorithm proposed by Borja and Lee [11], namely the closest point projection algorithm.

A typical two-dimensional problem is analyzed. The boundary condition and the finite element mesh are shown in Fig.4.

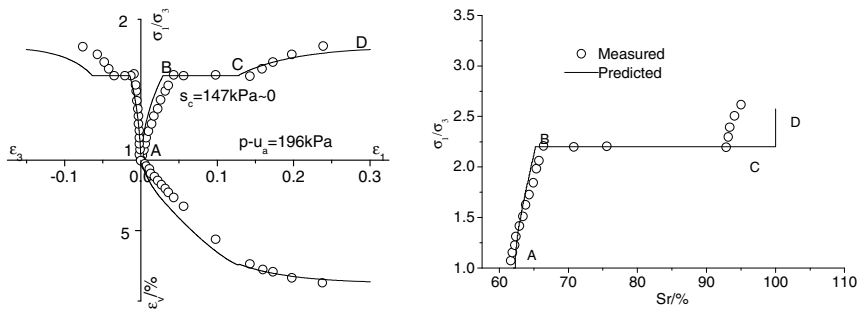


Fig. 3. Triaxial compression and wetting test

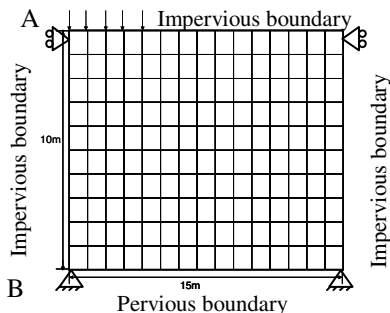


Fig. 4. Finite element mesh and boundary condition for two-dimensional problem

The developments of displacement and pore water at the left boundary are given in Fig.5. Clearly, the displacement near the force boundary is significantly larger than other areas. In the beginning, both displacement and pore water pressure increase quickly, and increase further with time, until finally approach to a steady

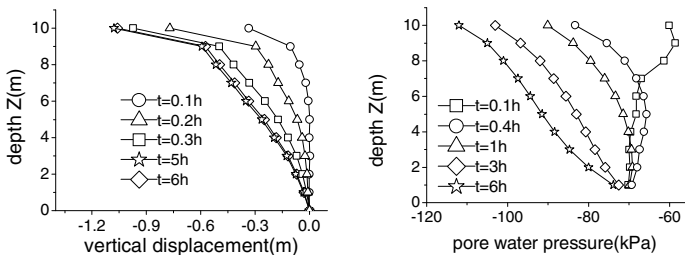


Fig. 5. Surface settlement, Pore pressure at section A-B at different time

state. This phenomenon explains that the load is beared by pore fluid at first and then transferred to the soil skeleton with time. The corresponding degree of saturation and pore air pressure have the similar trend. Remarkably, the model simulations are consistent with previous results (e.g., Zaman et al. [12])

## 5 Conclusion

A constitutive model of unsaturated soils, which addresses the coupling of capillary hysteresis and skeletal deformation, is developed based on the modified Cam-clay model. The new model avoids using a LC curve, usually adopted in traditional models, so that the model becomes more physically meaningful and can be more easily implemented. To consider the hardening effect of capillarity, two new parameters are introduced, which can be easily determined by experiments. Other parameters can be obtained by conventional mechanical and hydraulic tests. By comparing the model simulations with experimental results, it is shown that the model describe well the mechanical and hydraulic behavior of unsaturated soils.

The new model has a hierarchical structure. When ignoring the effect of deformation, the model degenerates into a model describing the soil-water characteristics only; when the soil becomes fully saturated, the model transits smoothly into the modified Cam-clay model of saturated soils.

The constitutive model is implemented into a finite element code by using an implicit algorithm, and it can be used to analyze the seepage and deformation coupling problem of unsaturated soils.

**Acknowledgments.** The research is supported by the Natural Science Foundation of China (Grant No. 11072255) and the Natural Science Foundation of Guangxi (Grant No. 2011GXNSFE018004).

## References

- [1] Wheeler, S.J.: Inclusion of specific water volume within an elastoplastic model for unsaturated soils. *Canadian Geotechnical Journal* 33(1), 42–57 (1996)
- [2] Alonso, E.E., Gens, A., Josa, A.: A constitutive model for partially saturated soils. *Geotechnique* 40(3), 405–430 (1990)
- [3] Houlsby, G.T.: The work input to an unsaturated granular material. *Geotechnique* 47(1), 193–196 (1997)
- [4] Nuth, M., Laloui, L.: Advances in modelling hysteretic water retention curve in deformable soils. *Computers and Geotechnics* 35(6), 835–844 (2008)
- [5] Sheng, D., et al.: Unsaturated soils: From constitutive modelling to numerical algorithms. *Computers and Geotechnics* 35(6), 810–824 (2008)
- [6] Wei, C.F., Dewoolkar, M.M.: Formulation of capillary hysteresis with internal state variables. *Water Resources Research* 42(7), W07405.1–W07405.16 (2006)
- [7] Cadoret, T., et al.: Fluid distribution effect on sonic attenuation in partially saturated limestones. *Geophysics* 63(1), 154–160 (1998)

- [8] Wheeler, S.J., Sivakumar, V.: An elasto-plastic critical state framework for unsaturated soil. *Geotechnique* 45(1), 35–53 (1995)
- [9] Sun, D.A., et al.: Collapse Behavior of Compacted Clays in Suction-Controlled Tri-axial Tests. *Geotechnical Testing Journal* 27(4), 1–9 (2004)
- [10] Wei, C.F.: Static and dynamic behavior of multiphase porous media: governing equations and finite element implementation, Ph.D. Dissertation. University of Oklahoma (2001)
- [11] Borja, R.I., Lee, S.R.: Cam-Clay plasticity, Part 1: Implicit integration of elasto-plastic constitutive relations. *Computer Methods in Applied Mechanics and Engineering* 78(1), 49–72 (1990)
- [12] Zaman, M., et al.: Consolidation settlement of bridge approach foundation. *Journal of Geotechnical Engineering* 117(2), 219–240 (1991)

# Explicit Incorporation of Asymptotic States into Hypoplasticity

D. Mašín

Faculty of Science, Charles University in Prague, Czech Republic

[masin@natur.cuni.cz](mailto:masin@natur.cuni.cz)

**Abstract.** A rearrangement of the hypoplastic constitutive equation is proposed that enables the incorporation of an asymptotic state boundary surface of an arbitrary pre-defined shape into the model, with any corresponding asymptotic strain rate direction. This opens the way for further development of hypoplastic models. Predictions of a new clay hypoplastic model based on the proposed approach are shown for demonstration.

## 1 Introduction

Over the past two decades, hypoplasticity has proven to be a powerful approach to predict the nonlinear behaviour of soils. Early hypoplastic models were developed from sound physical assumptions by means of trial-and-error procedures (see Kolymbas (1991) [7]). These models represented the soil behaviour reasonably well, but their parameters did not have any clear physical meaning. Throughout the development of hypoplasticity, several milestones can be identified, and these are often related to predictions of asymptotic states (see Gudehus and Mašín (2009) [4], Mašín (2012) [10]). Following the earlier work by Gudehus (1996) [2] and Niemunis (2002) [14], Mašín and Herle (2005) [13] analysed asymptotic response of the clay hypoplastic model from Mašín (2005) [9]. They found that the predicted asymptotic states depended on the material parameters, while only isotropic and critical states were pre-defined. The complete shape of the asymptotic state boundary surface (ASBS) thus could not be prescribed *a priori*, as is normal in elasto-plastic models. This property of hypoplasticity has been regarded as its serious limitation.

A procedure for explicit incorporation of any pre-defined asymptotic states into hypoplasticity has recently been developed by Mašín (2012) [12], and adopted in a development of a particular clay hypoplastic model in Mašín (2012) [11]. Primary outcomes of this research are presented in this contribution.

## 2 Explicit Incorporation of Asymptotic States into Hypoplasticity

A procedure for explicit incorporation of the asymptotic states into hypoplasticity has been proposed by Mašín (2012) [12], and we will adopt this approach herein. A general formulation of the hypoplastic model may be written as [2]

$$\dot{\mathbf{T}} = f_s (\mathcal{L} : \mathbf{D} + f_d \mathbf{N} \|\mathbf{D}\|) \quad (1)$$

where  $\dot{\mathbf{T}}$  and  $\mathbf{D}$  represent the objective (Zaremba-Jaumann) stress rate and the Euler stretching tensor respectively,  $\mathcal{L}$  and  $\mathbf{N}$  are fourth- and second-order constitutive tensors,  $f_s$  is the factor controlling the influence of mean stress (barotropy factor) and  $f_d$  is the factor controlling the influence of relative density (pyknotropy factor).

To evaluate the model response at the ASBS, we will interpret it in the stress space normalised by the size of the constant void ratio cross-section through the ASBS. It is given by the Hvorslev equivalent pressure  $p_e$ , defined as a mean stress at the isotropic normal compression line at the current void ratio  $e$ . The normalised stress thus reads  $\mathbf{T}_n = \mathbf{T}/p_e$  and it follows [11] that

$$\dot{\mathbf{T}}_n = \frac{\dot{\mathbf{T}}}{p_e} - \frac{\mathbf{T}}{p_e^2} \dot{p}_e \quad (2)$$

In the following, we assume normal compression lines linear in the  $\ln(1+e)$  vs.  $\ln p/p_r$  plane [1] ( $p_r$  is the reference stress of 1 kPa). The isotropic normal compression line can be written as

$$\ln(1+e) = N - \lambda^* \ln(p_e/p_r) \quad (3)$$

where  $N$  and  $\lambda^*$  are model parameters. It follows that

$$p_e = p_r \exp \left[ \frac{N - \ln(1+e)}{\lambda^*} \right] \quad (4)$$

and thus

$$\dot{p}_e = -\frac{p_e}{\lambda^*} \left( \frac{\dot{e}}{1+e} \right) = -\frac{p_e}{\lambda^*} \text{tr} \mathbf{D} \quad (5)$$

Combination of (5), (2) and (1) implies that

$$\dot{\mathbf{T}}_n = \frac{f_s}{p_e} (\mathcal{L} : \mathbf{D} + f_d \mathbf{N} \|\mathbf{D}\|) + \frac{\mathbf{T}}{p_e \lambda^*} \text{tr} \mathbf{D} \quad (6)$$

During asymptotic stretching the stress state remains fixed in the  $\mathbf{T}_n$  space [13], provided the constant void ratio cross-sections through the ASBS differ only in size and not in shape. This condition implies  $\dot{\mathbf{T}}_n = 0$ . It then follows from (6) that

$$-\frac{\mathbf{T}}{\lambda^*} \text{tr} \mathbf{D}^A = f_s (\mathcal{L} : \mathbf{D}^A + f_d^A \mathbf{N} \|\mathbf{D}^A\|) \quad (7)$$

where  $f_d^A$  is the value of  $f_d$  at the ASBS and  $\mathbf{D}^A$  is the asymptotic strain rate corresponding to the given stress state. Eq. (7) can be manipulated in the following way:

$$-\left(\frac{\mathbf{T}}{\lambda^*} \text{tr} \mathbf{D}^A + f_s \mathcal{L} : \mathbf{D}^A\right) = f_s f_d^A \mathbf{N} \|\mathbf{D}^A\| \tag{8}$$

$$-\mathcal{A} : \mathbf{D}^A = f_s f_d^A \mathbf{N} \|\mathbf{D}^A\| \tag{9}$$

$$-\mathcal{A} : d = f_s f_d^A \mathbf{N} \tag{10}$$

where

$$\mathcal{A} = f_s \mathcal{L} + \frac{\mathbf{T}}{\lambda^*} \otimes 1 \tag{11}$$

$$d = \frac{\mathbf{D}^A}{\|\mathbf{D}^A\|} \tag{12}$$

Eq. (10) implies that

$$\mathbf{N} = -\frac{\mathcal{A} : d}{f_s f_d^A} \tag{13}$$

Combining (13) with (11) yields an alternative expression of the hypoplastic model

$$\dot{\mathbf{T}} = f_s \mathcal{L} : \mathbf{D} - \frac{f_d}{f_d^A} \mathcal{A} : d \|\mathbf{D}\| \tag{14}$$

An arbitrary shape of the ASBS can be incorporated into hypoplasticity with the aid of Eq. (14), by appropriate specification of the dependence of  $f_d^A$  on the void ratio and stress ratio. The corresponding asymptotic direction of the strain rate is then prescribed by  $d$ .

### 3 Proposed Asymptotic States

A particular shape of the ASBS and the corresponding strain rate direction has been proposed by Mašin (11). Due to the limited space, we do not present herein their full mathematical formulations, but instead we describe their main characteristics. The ASBS is characterised by

- Deviatoric (constant mean stress) cross-sections through the ASBS, which correspond to the failure criterion by Matsuoka and Nakai (8).
- Mobilised friction angle  $\varphi_m$  is equal to the critical state friction angle  $\varphi_c$  at  $p_e/p = 2$  (where  $p_e$  is the Hvorslev equivalent pressure). This also implies position of the critical state line in the  $\ln p$  vs.  $\ln(1 + e)$  plane.
- $\varphi_m$  for  $p_e/p \rightarrow \infty$  limit to  $\varphi_m \rightarrow 90^\circ$ . This ensures that the ASBS does not span into the tensile stress region.
- The surface is  $C^1$  continuous everywhere except the  $\mathbf{T} = 0$  state.

The proposed shape of the ASBS, whose mathematical formulation is presented in Ref. [11], is in Fig. 1(a) plotted for the axisymmetric stress state in the normalised stress plane  $p/p_e$  vs.  $q/p_e$  for different critical state friction angles. Its shape is compared with the shape of the ASBS by the Modified Cam-clay model. The ASBS has the desired properties. In particular, unlike the ASBS of the Modified Cam-clay model, it is bound by the  $\varphi_m = 90^\circ$  state, which means it is bound within the compression stress range. Different 3D views of the ASBS in the principal stress space are show in Fig. 2

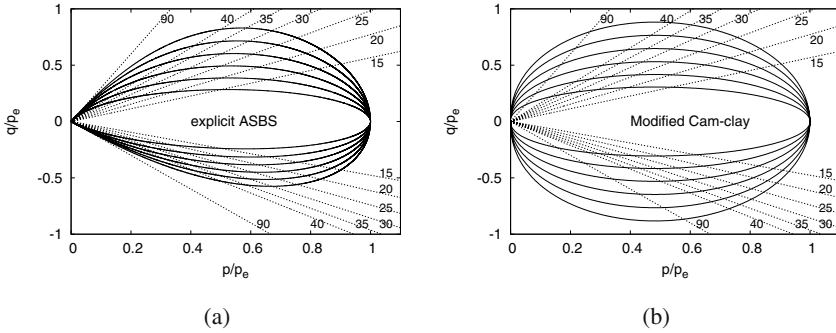


Fig. 1. Asymptotic state boundary surfaces for different critical state friction angles  $\varphi_c$ . Proposed model (a) and a Modified Cam-clay model (b)

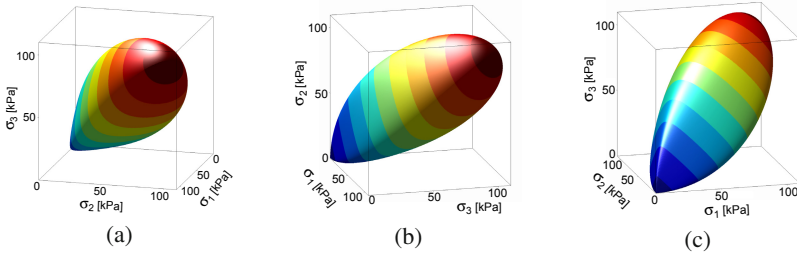


Fig. 2. Principal stress space 3D plots of the ASBS of the proposed model for  $\varphi_c = 25^\circ$

The proposed asymptotic strain rate direction  $d$  has the following properties:

- It predicts zero volumetric strains ( $\text{tr}d = 0$ ) for  $\varphi_m = \varphi_c$ .
- It predicts zero shear strains ( $\text{dev}d = 0$ ) for  $\varphi_m = 0^\circ$ .
- The  $K_0$  state closely agrees with the Jáký [6] formula

$$K_0 = 1 - \sin \varphi_c \tag{15}$$

- The  $\pm d$  states, introduced by Gudehus [3] (Chapters 2 and 3), are properly considered in both the triaxial compression and extension regime. For details, see [3, 4, 10].
- $d^A$  has radial deviatoric direction.

Figure 3 shows  $K_0$  values predicted by the proposed [11], original [9] and Modified Cam-clay models for different values of  $\varphi_c$ . The proposed model predicts  $K_0$  practically coinciding with the Jáký [6] equation (15). Both the original and Cam-clay models overpredict  $K_0$ .

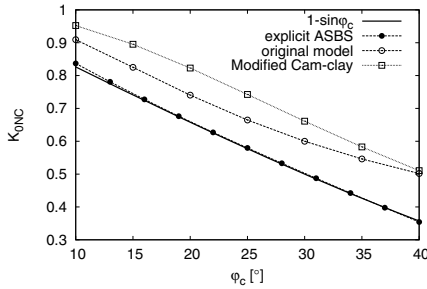


Fig. 3.  $K_0$  values for different  $\varphi_c$  predicted by the proposed, original and Modified Cam-clay models

### 4 Model Formulation

General rate formulation of the model is given by Eq. (14). The tensor  $\mathcal{L}$  is represented by isotropic elasticity: that is

$$\mathcal{L} = \mathcal{I} + \frac{\nu}{1 - 2\nu} \mathbf{1} \otimes \mathbf{1} \tag{16}$$

where the parameter  $\nu$  controls the proportion of bulk and shear stiffness. Effectively, it regulates the shear stiffness, since the bulk stiffness in the model is controlled by the parameters  $\lambda^*$  and  $\kappa^*$  (as shown later). The asymptotic strain rate direction  $d$  has been described in Sec. 3. The following expression for the factor  $f_d$ , which governs the non-linear behaviour inside the state boundary surface, is chosen:

$$f_d = \left( \frac{2p}{p_e} \right)^\alpha \tag{17}$$

where  $\alpha = 2$  is controlling the influence of OCR on non-linear response inside the ASBS. The value of  $f_d^A$  and the asymptotic strain rate direction  $d$  is calculated to follow the proposed asymptotic state formulation, described in Sec. 3.

The last component of the model to be defined is the factor  $f_s$ . It is specified following Ref. [12] to ensure that the slope of the isotropic unloading line in the  $\ln(1 + e) - \ln p$  plane, for unloading starting from the isotropic normally consolidated

state, is given by  $\kappa^*$ . Algebraic manipulations with the above tensorial equations reveal that

$$f_s = \frac{3p}{2} \left( \frac{1}{\lambda^*} + \frac{1}{\kappa^*} \right) \frac{1-2\nu}{1+\nu} \tag{18}$$

The model requires five parameters, with the same physical interpretation as the parameters of the Modified Cam-clay model:  $\varphi_c$ ,  $\lambda^*$ ,  $\kappa^*$ ,  $N$  and  $\nu$ .  $\varphi_c$  is the critical state friction angle;  $\lambda^*$  is the slope of the isotropic normal compression line in the plane  $\ln(1+e)$  vs.  $\ln p$ ;  $\kappa^*$  controls slope of unloading line in the same plane;  $N$  is the value of  $\ln(1+e)$  at the isotropic normal compression line for  $p = p_r = 1$  kPa; and finally the parameter  $\nu$  controls the shear stiffness.

### 5 Model Predictions

Figure 4 shows the shape of the ASBS, together with response envelopes [4] for different states of stress and overconsolidation. It shows the ASBS predicted by the proposed and original clay hypoplastic models. The original model produces response envelopes which rotate with increasing stress deviator, whereas the proposed model adopts isotropic elasticity, which means that the shape of the response envelopes is not affected by the stress state. This is caused by the different formulation of the tensor  $\mathcal{L}$  in the proposed and original models. It influences the model predictions inside the ASBS, and causes the proposed model to better reproduce the experimental data.

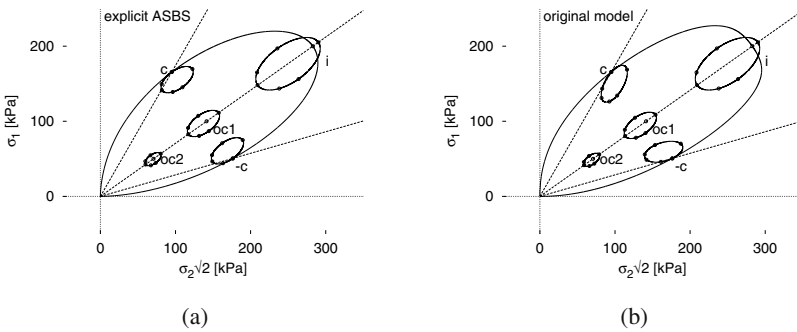


**Fig. 4.** The shape of ASBS of the original and proposed models, plotted together with response envelopes at the isotropic (*i*) and critical ( $\pm c$ ) asymptotic states and in two overconsolidated (*oc*) states

Figure 5 shows predictions of the undrained triaxial tests on the clay from Dortmund, Germany. The experimental data and predictions by the original model have been presented by Herle et al. [5]. The predicted stress paths differ in the way the asymptotic state is approached, but both predictions represent the experimental data reasonably well. More significant difference is clear from the predicted shear strain

vs. deviatoric stress curves. The proposed model predicts accurately the decrease of the tangent shear modulus with shear strain. On the other hand, the original model represents the stress-strain curve relatively poorly, as it underestimates the original stiffness and also the rate of the stiffness degradation.

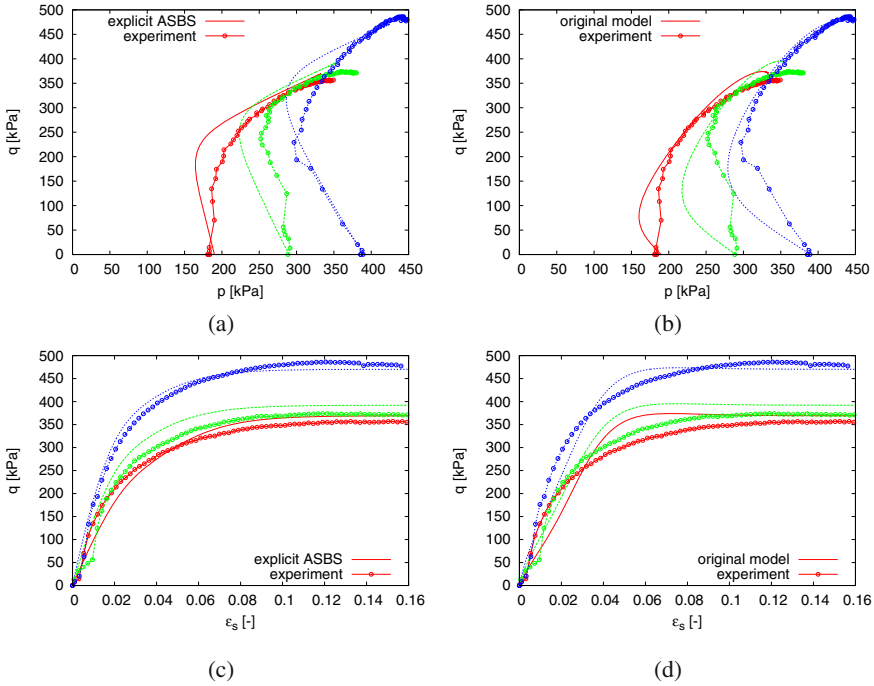


**Fig. 5.** Undrained triaxial tests on overconsolidated Dortmund clay and their representation by the proposed and original models. Experimental data from [5]

## 6 Conclusions

A new hypoplastic model for fine-grained soils has been described. The model is based on an approach which enables us to specify explicitly the asymptotic state boundary surface and corresponding asymptotic strain rate direction. The model eliminates several shortcomings of the original clay hypoplastic model from [9] and improves its predictions, while using equivalent material parameters. The main advantage of the new model is in the independent formulation of the individual model components. The new model is thus more suitable to form a basis for further developments and enhancements.

**Acknowledgements.** Financial support by the research grants GACR P105/12/1705 and TACR TA01031840 is greatly appreciated.

## References

- [1] Butterfield, R.: A natural compression law for soils. *Geotechnique* 29(4), 469–480 (1979)
- [2] Gudehus, G.: A comprehensive constitutive equation for granular materials. *Soils and Foundations* 36(1), 1–12 (1996)
- [3] Gudehus, G.: *Physical Soil Mechanics*. Springer, Berlin (2011)
- [4] Gudehus, G., Mašín, D.: Graphical representation of constitutive equations. *Geotechnique* 59(2), 147–151 (2009)
- [5] Herle, I., Mašín, D., Kostkanová, V., Karcher, C., Dahmen, D.: Experimental investigation and theoretical modelling of soft soils from mining deposits. In: Chung, C.-K., Jung, Y.-H., Kim, H.-K., Lee, J.-S., Kim, D.-S. (eds.) *Proc. 5th International Symposium on Deformation Characteristics of Geomaterials*, Seoul, Korea, vol. 2, pp. 858–864 (2011)
- [6] Jáky, J.: Pressures in silos. In: *Proc. 2nd Int. Conf. Soil Mechanics*, Rotterdam, vol. 1, pp. 103–107 (1948)
- [7] Kolymbas, D.: Computer-aided design of constitutive laws. *International Journal for Numerical and Analytical Methods in Geomechanics* 15, 593–604 (1991)
- [8] Matsuoka, H., Nakai, T.: Stress–deformation and strength characteristics of soil under three different principal stresses. In: *Proc. Japanese Soc. of Civil Engineers*, vol. 232, pp. 59–70 (1974)
- [9] Mašín, D.: A hypoplastic constitutive model for clays. *International Journal for Numerical and Analytical Methods in Geomechanics* 29(4), 311–336 (2005)
- [10] Mašín, D.: Asymptotic behaviour of granular materials. *Granular Matter* (submitted, 2012)
- [11] Mašín, D.: Clay hypoplasticity with explicitly defined asymptotic states. *Acta Geotechnica* (submitted, 2012)
- [12] Mašín, D.: Hypoplastic cam-clay model. *Géotechnique* (in print, 2012)
- [13] Mašín, D., Herle, I.: State boundary surface of a hypoplastic model for clays. *Computers and Geotechnics* 32(6), 400–410 (2005)
- [14] Niemunis, A.: *Extended Hypoplastic Models for Soils*. Habilitation thesis. Ruhr-University, Bochum (2003)

# Simple and Unified Modelong of Time-Dependent Behavior for Various Geomaterials

Teruo Nakai\* and Hossain Md. Shahin

Department of Civil Engineering  
Nagoya Institute of Technology  
Gokiso-cho, Showa-ku, Nagoya, 466-8555, Japan  
nakai.teruo@nitech.ac.jp

**Summary.** A simple model to describe time-dependent behavior for various kinds of soils is presented. The present model can describe various time-dependent behaviors not only of normally consolidated soil but also of over consolidated and naturally deposited soils in the same manner without violating the objectivities. To consider the influence of over consolidation, the subloading surface concept defines a state variable  $\rho$  which represents the influence of density. To describe the behavior of naturally deposited soil, another state variable  $\omega$  which represents the bonding effect, is introduced. The validity of the present models is verified using various kinds of simulations of time-dependent behavior in one-dimensional and three-dimensional conditions.

**Keyword:** time-dependent behavior, density, bonding.

## 1 Introduction

It is known that under one-dimensional consolidation (or isotropic consolidation) remolded normally consolidated clay shows typical strain-hardening elastoplastic behavior, therefore, clay is assumed to be non-linear elastic material in the region where the current stress is smaller than the yield stress (over consolidation region). However, clay shows elastoplastic behavior even in over consolidation region. Furthermore, natural clay behaves intricately compared with remolded clay which is used in laboratory tests, because natural clay develops a complex structure in its deposition process. Such structured clay can exist in a region where its void ratio is greater than that of non-structured normally consolidated clay under the same stress condition. This type of structured clay shows more brittle and more compressive behavior than non-structured clay. Remolded clay and natural clay also show time-dependent behavior such as secondary consolidation and strain rate effect. In the present paper, we will demonstrate simple and unified methods to take

---

\* Corresponding author.

into account various features of geomaterials including the influence of over-consolidation, the bonding effect and the strain rate effects in the constitutive models.

## 2 Modeling of Structured Clay

Figure 1 shows a typical  $e - \ln\sigma$  relation of natural clay schematically. Asaoka et al. [1] developed a model to describe such structured soils, introducing subloading surface concept [2] and superloading surface concept developed by them to the Cam-clay model. In their modeling, a factor related to the over consolidation ratio (corresponding to non-real density but imaginary density) has been introduced to increase the stiffness, and a factor related to the soil skeleton structure has been introduced to decrease the stiffness.

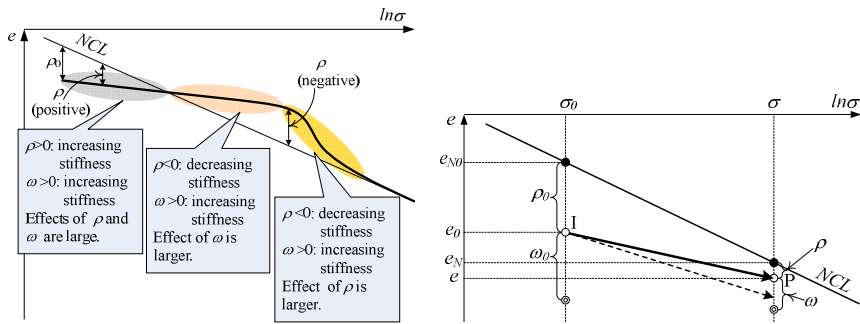


**Fig. 1.** Void ratio ( $e$ ):  $\ln\sigma$  relation in structured clay **Fig. 2.** Change of void ratio in structured clay

Figure 2 shows the change of void ratio when the stress condition moves from the initial state I ( $\sigma = \sigma_0$ ) to the current state P ( $\sigma = \sigma$ ). Here,  $e_0$  and  $e$  are the initial and current void ratios of structured soil, and  $e_{N0}$  and  $e_N$  are the corresponding void ratios on the normally consolidation line. It can be understood that the structured soil is stiffer than non-structured over consolidated soil, when the initial void ratio  $e_0$  are the same. Then, the change in void ratio for structured soil indicated by the arrow with solid line is smaller than that for non-structured over consolidated soil (arrow with broken line). Now, the state variable  $\rho (= e_N - e)$  which represents the effect of the density is defined by the difference between the void ratio on NCL and the current void ratio of the soil at the same stress. The initial value of the state variable is expressed as  $\rho_0 = e_{N0} - e_0$ . To describe such increase in stiffness of structured soil, we introduce an imaginary increase of density  $\omega$  (initial value  $\omega_0$ ) which represents the effect of the bonding, in addition to the real density  $\rho$ .

When stress condition moves from  $\sigma_0$  to  $\sigma$ , the plastic change of void ratio ( $-\Delta e)^p$  for the clay is obtained (referring to Figure 2).

$$\begin{aligned}
 (-\Delta e)^p &= (-\Delta e) - (-\Delta e)^e = \{(e_{N_0} - e_N) - (\rho_0 - \rho)\} - (-\Delta e)^e \\
 &= \lambda \ln \frac{\sigma}{\sigma_0} - (\rho_0 - \rho) - \kappa \ln \frac{\sigma}{\sigma_0}
 \end{aligned} \tag{1}$$

Here,  $(-\Delta e)^e$  is the elastic change of void ratio, and  $\lambda$  and  $\kappa$  denote compression and swelling indices. Therefore, yield function for the soil is expressed as:

$$F + \rho = H + \rho_0 \quad \text{or} \quad f = F - \{H + (\rho_0 - \rho)\} = 0 \tag{2}$$

in which,  $F$  and  $H$  denote the terms of stress and plastic change in void ratio.

$$F = (\lambda - \kappa) \ln \frac{\sigma}{\sigma_0}, \quad H = (-\Delta e)^p \tag{3}$$

From the consistency condition ( $df=0$ ) at the occurrence of plastic deformation with satisfying Eq. (2), the following equation is obtained:

$$df = dF - \{dH - d\rho\} = (\lambda - \kappa) \frac{d\sigma}{\sigma} - \{d(-\Delta e)^p - d\rho\} = 0 \tag{4}$$

Now, it can be considered that the evolution rule of  $\rho$  with the development of plastic deformation for structured soil is determined using both  $\rho$  and  $\omega$ . Then, the evolution rules of  $\rho$  and  $\omega$  can be given in the following form, using increasing functions  $G(\rho)$  and  $Q(\omega)$  which satisfy  $G(0)=0$  and  $Q(0)=0$ , respectively:

$$d\rho = -\{G(\rho) + Q(\omega)\} \cdot d(-e)^p \tag{5}$$

The evolution rule of  $\omega$  is also given as follows using the same function  $Q(\omega)$ :

$$d\omega = -Q(\omega) \cdot d(-e)^p \tag{6}$$

Equations (4) and (5) give the increment of the plastic change in void ratio as

$$d(-e)^p = \frac{\lambda - \kappa}{1 + G(\rho) + Q(\omega)} \cdot \frac{d\sigma}{\sigma} \tag{7}$$

The increment of total change in void ratio is expressed as the summation of the plastic components  $(-\Delta e)^p$  and the elastic component  $(-\Delta e)^e$ .

$$d(-e) = d(-e)^p + d(-e)^e = \left\{ \frac{\lambda - \kappa}{1 + G(\rho) + Q(\omega)} + \kappa \right\} \frac{d\sigma}{\sigma} \tag{8}$$

As shown in Eq. (8), positive  $\rho$  and  $\omega$  have effects to increase stiffness of soil, because  $G(\rho)$  and  $Q(\omega)$  are positive when both  $\rho$  and  $\omega$  are positive. At the first stage ( $\rho > 0$  and  $\omega > 0$ ), the stiffness of the soil is much larger than that of remolded NC soil because of the positive values of  $G(\rho)$  and  $Q(\omega)$ . When the current void ratio becomes the same as that on NCL ( $\rho = 0$ ), the stiffness of the structured soil is still greater than that of remolded NC soil (because of  $\omega > 0$ ). In this stage ( $\rho < 0$  and

$\omega > 0$ ), the effect to increase the stiffness by positive value of  $\omega$  is larger than the effect to decrease the stiffness by negative value of  $\rho$ . After this stage, the effect of  $\omega$  becomes small with the development of plastic deformation. The effect of  $\rho$  to reduce the stiffness becomes prominent (because  $\rho < 0$ ). Finally, the void ratio approaches to that on NCL, because  $\rho$  and  $\omega$  converge to zero. Such feature of structured soil can be described by extending the defined domain of the increasing function  $G(\rho)$  to the negative value of  $\rho$  - e.g.,  $G(\rho)$  and  $Q(\omega)$  are given by increasing functions. That is to say, though  $Q(\omega)$  is monotonically approaching to zero with the development of plastic deformation,  $G(\rho)$  has an effect to the current void ratio to approach to that on NCL, regardless the sign of  $\rho$ .

### 3 Modeling of Time-Dependent Behavior

Time-dependent behavior of soils has been formulated employing elasto/viscoplastic theories such as non-stationary flow surface model (e.g., [3]) and over-stress model (e.g., [4]). We will formulate the time-dependent behavior of soils not using the past elasto/viscoplastic theories but by an extension of the above-mentioned formulation for the structured soils. Figure 3 shows a time-dependent behavior of normally consolidated clay in one-dimensional condition schematically. It is well known that the normally consolidation line (NCL) shifts due to strain rate (rate of plastic change in void ratio  $(-e')^p$ ), and the void ratio ( $e$ ) changes linearly against time on a log scale ( $\ln t$ ) under creep condition. In order to model these features, introducing a state valuable  $\psi$  which is given by a function of strain rate as shown in Fig. 4. Here,  $\psi_0$  is the initial value of  $\psi$ , and point I and point P indicate the initial state ( $\sigma = \sigma_0$ ,  $e = e_0$  and  $\psi = \psi_0$ ) and the current state ( $\sigma = \sigma$ ,  $e = e$  and  $\psi = \psi$ ), respectively. By referring to this figure, the plastic change of void ratio  $(-\Delta e)^p$  in which the above features should be considered is expressed as.

$$\begin{aligned} (-\Delta e)^p &= (-\Delta e) - (-\Delta e)^e = \{(e_{N0} - e_N) - (\rho_0 - \rho)\} - (-\Delta e)^e \\ &= \left\{ \lambda \ln \frac{\sigma}{\sigma_0} + (\psi - \psi_0) - (\rho_0 - \rho) \right\} - \kappa \ln \frac{\sigma}{\sigma_0} \\ &= \lambda \ln \frac{\sigma}{\sigma_0} - (\rho_0 - \rho) - (\psi_0 - \psi) - \kappa \ln \frac{\sigma}{\sigma_0} \end{aligned} \quad (9)$$

Therefore, the following equation holds between  $F$  and  $H$ :

$$F + \rho + \psi = H + \rho_0 + \psi_0 \quad \text{or} \quad f = F - \{H + (\rho_0 - \rho) + (\psi_0 - \psi)\} = 0 \quad (10)$$

Consistency condition ( $df=0$ ) gives

$$df = dF - \{dH - d\rho - d\psi\} = (\lambda - \kappa) \frac{d\sigma}{\sigma} - \{d(-e)^p - d\rho - d\psi\} = 0 \quad (11)$$

Now, referring to Fig. 3, we can give the distance  $(\psi - \psi_0)$  in Fig. 4 as a function of the elapsed time  $t$  or the rate of plastic change in void ratio  $(-e')^p$ :

$$\left\{ \begin{aligned} \psi - \psi_0 &= \lambda_\alpha \ln \frac{t}{t_0} = \lambda_\alpha \ln t - \lambda_\alpha \ln t_0 \quad , \text{or,} \\ \psi - \psi_0 &= \lambda_\alpha \ln \frac{(-\dot{e})_0^p}{(-\dot{e})^p} = \{-\lambda_\alpha \ln(-\dot{e})^p\} - \{-\lambda_\alpha \ln(-\dot{e})_0^p\} \end{aligned} \right. \quad (12)$$

Here,  $\lambda_k$  is the secondary compression index. The increment  $d\psi$  is expressed as

$$d\psi = \frac{\partial \psi}{\partial t} dt = \lambda_\alpha \frac{1}{t} dt = (-\dot{e})^p dt \quad (13)$$

It is assumed that Eq.(12) holds for the normally consolidated soil and the over consolidated soil and naturally deposited soil. Substituting Eqs. (5) and (13) into Eq. (11), we can obtain the increment of the plastic change of void ratio as:

$$d(-e)^p = \frac{(\lambda - \kappa) \frac{1}{\sigma} d\sigma + (-\dot{e})^p \cdot dt}{1 + G(\rho) + Q(\omega)} \cong \frac{(\lambda - \kappa) \frac{1}{\sigma} d\sigma + (-\dot{e})^{p*} \cdot dt}{1 + G(\rho) + Q(\omega)} \quad (14)$$

Here,  $(-\dot{e})^{p*}$  denotes the rate of the plastic change of void ratio in the previous calculation step. Finally, the total increment of void ratio is given as:

$$d(-e) = d(-e)^p + d(-e)^e = \left( \frac{\lambda - \kappa}{1 + G(\rho) + Q(\omega)} + \kappa \right) \frac{d\sigma}{\sigma} + \frac{(-\dot{e})^{p*}}{1 + G(\rho) + Q(\omega)} dt \quad (15)$$

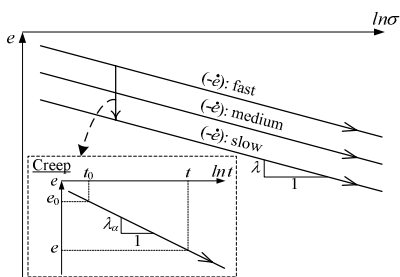


**Fig. 3.** Time dependent behavior of normally consolidated clay

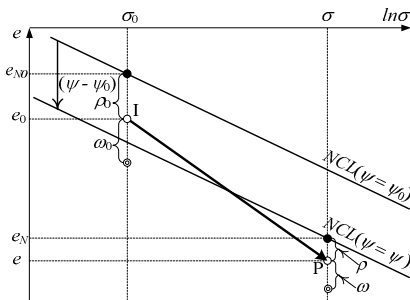


**Fig. 4.** Change of void ratio in structured clay with time dependent behavior

For easy and simple numerical calculations, the known rate  $(-\dot{e})^{p*}$  in the previous step is used in stead of the current rate, as described in Eqs. (14) and (15). The error caused using the previous rate is negligible in the calculations, because an incremental method with small step is used, and some error in the present step is automatically corrected in the next step. The validity of the proposed time-dependent model is checked by some simulations of one-dimensional constant strain rate consolidation tests and conventional oedometer tests. Assuming Fujinomori clay which was used in the previous experimental verification of

constitutive models (e.g., [5], [6]), following material parameters are employed in the numerical simulations – compression index  $\lambda=0.104$ , swelling index  $\kappa=0.010$  and void ratio on NCL at  $\sigma=Pa=98\text{kPa}$  (atmospheric pressure)  $N=0.83$ . The parameter for density  $a=100$  and the degradation parameter of bonding  $b=40$  are used.

Figure 5(a) shows  $e$ - $\log\sigma$  relations for different strain rates in normally consolidated clay under drained condition. Here, the coefficient of secondary compression  $\lambda_\alpha=0.0030$ . It is seen that with the increase of strain rates the resistance to compression increases, and the lines of constant strain rate are parallel to each other which are commonly seen in laboratory tests. It is also seen that when the strain rate changes at a certain point, the curve follows exactly the same path the new rate is supposed to follow. This is valid for both increasing and decreasing the strain rates, and in the case where the strain rate is increased the simulation gradually reaches the target curve following the phenomenon of ‘isotache’. Therefore, it can be said that the proposed model can well produce the strain rate dependency. Figure 5(b) illustrates the results of structured clay ( $\alpha_0=0.20$ ). Here, the initial void ratios are 0.73. It is found that the apparent pre-consolidation stress  $P_c$  increases with the increase of strain rate.

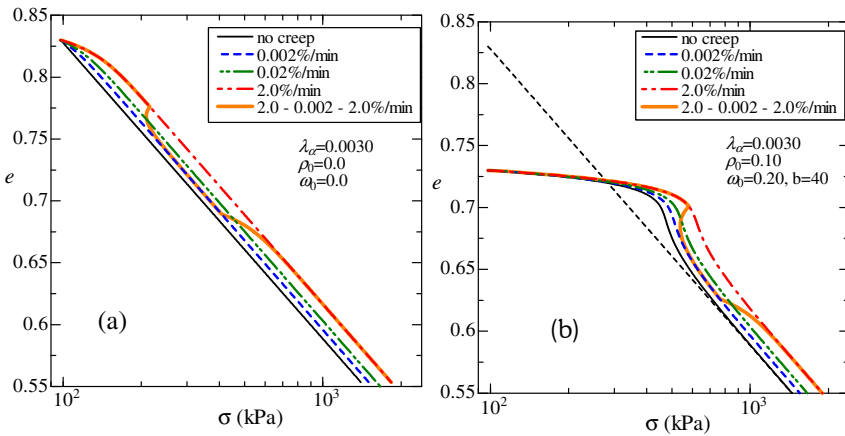


**Fig. 5.** Strain rate effects in normally consolidated clay, over consolidated clay and natural clay

To investigate the consolidation characteristics of clays, one-dimensional soil-water coupled finite element analyses of oedometer tests with instantaneous loading of constant vertical stress is carried out. The height  $H$  of the sample is divided into elements thicknesses of 0.1cm as shown in Fig. 6, and drainage is allowed at the top boundary, and the bottom boundary is considered as undrained condition. In order to make the coefficient of consolidation  $c_v$  constant during normal consolidation, regardless of the stiffness of the soil, following relationship between the coefficient of permeability  $k$  and the current void ratio  $e$  is used in simulations.

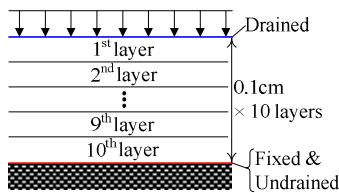


Fig. 6. Finite element mesh

$$k = k_0 \cdot \exp\left(\frac{e - e_{N0}}{\lambda_k}\right) \tag{16}$$

In Eq. (16),  $e_{N0}=0.83$ ,  $k_0=1.0 \times 10^{-5}$ cm/min and  $\lambda_k=0.104$ , which is the same as the compression index  $\lambda$ .

Figure 7 shows  $e$ - $\log t$  response of conventional oedometer tests for normally consolidated clay, where the initial stress is 98kPa and the sudden stress increment is 98kPa. The vertical axis represents the void ratio as a mass. It is seen that the delayed consolidation occurs when the time effect is considered, which shows creep behavior of soil. The larger the value of  $\lambda_\alpha$  the more the delay in consolidation is observed. During secondary consolidation the slopes of the curves are the same as the coefficient of secondary compression which are employed in the simulations. Figure 8 represents the computed  $e$ - $\log t$  relation of normally consolidated clay for different heights of the sample. This figure describes the well-known effects of sample height [7]. Some time after the load is applied, the consolidation curves for different sample heights converge to a single curve. This tendency of  $e$ - $\log t$  curves under different sample heights corresponds to the curve referred to as “Type B” by [7]. Figure 9 shows the results of over consolidated clay (OCR=1.7). After the excess pore water pressure dissipates, the slope of the curve 0020 for the over consolidated clay becomes much flatter than that of the normally consolidated clay, as is cleat in Fig. 9, but becomes steeper again over time. These

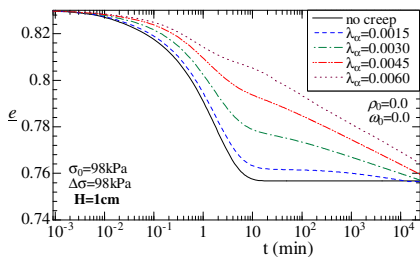


Fig. 7. Simulation of oedometer tests on NC clays different  $\lambda_\alpha$

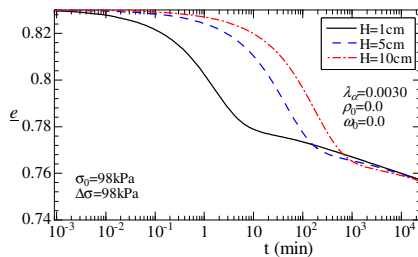


Fig. 8. Simulation of oedometer tests on for NC clays for different height of sample

results of the simulation appear to be in good agreement with the experimental results of Hiroshima clay b in Fig. 10 [8]. Figure 11 shows the computed  $e$ - $\log t$  response of non-structured and structured clays in normally consolidated and over consolidated states. It is seen that although the behavior of the normally consolidated structured clay (OCR=1.0) is different from that of the normally consolidated non-structured clay under small stress increment, not much difference is noted

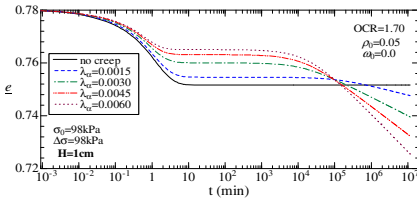


Fig. 9. Simulation of oedometer tests on OC clay

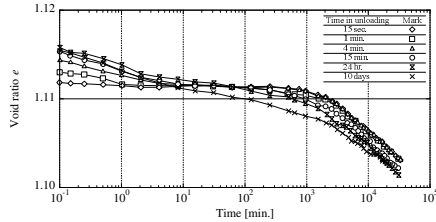


Fig. 10. Experimental results of oedometer tests on OC clay ([8])

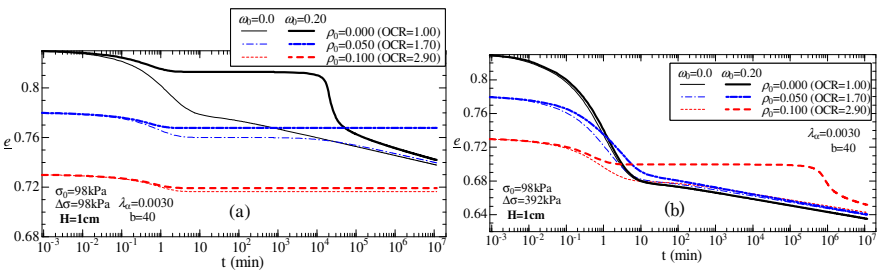


Fig. 11. Simulation of oedometer tests on non-structured and structured clays: (a)  $\Delta\sigma/\sigma_v=1$  (b)  $\Delta\sigma/\sigma_v=4$

between them under large stress increment. On the other hand, the behavior of over consolidated clays (OCR=2.9) is highly influenced by the effect of the structure (bonding) not under small stress increments but under large stress increments.

### 4 Conclusions

As one-dimensional model a simple method to describe the behavior of over consolidated soil and structured soil is presented by using the state variables of density ( $\rho$ ) and bonding ( $\omega$ ), and their monotonous evolution rules. Next, introducing the state variable ( $\psi$ ) which fixes the position of NCL depending on the strain rate, the model is extended to one considering time-dependent behavior for not only normally consolidated soil but also for over consolidated soil and structured soil.

The validities of these models have been checked by the simulations of one-dimensional compression tests on clays with different initial densities, bonding effects and strain rate. These models can easily be extended to three-dimensional ones by introducing the  $t_{ij}$  concept [9]. The detailed explanation of the present 1D and 3D modeling is presented in [10] [11] and [12].

## References

- [1] Asaoka, A., Noda, T., Yamada, E., Kaneda, K., Nakano, M.: An elasto-plastic description of two distinct volume change mechanisms of soils. *Soils and Foundations* 42(5), 47–57 (2002)
- [2] Hashiguchi, K.: Constitutive equation of elastoplastic materials with elasto-plastic transition. *Jour. of Appli. Mech. ASME* 102(2), 266–272 (1980)
- [3] Sekiguchi, H.: Rheological characteristics of clays. In: *Proc. of 9th ICSMFE, Tokyo*, vol. 1, pp. 289–292 (1977)
- [4] Adachi, T., Oka, F.: Constitutive equation for normally consolidated clays based on elasto/viscoplasticity. *Soils and Foundations* 22(4), 57–70 (1982)
- [5] Nakai, T.: Modeling of soil behavior based on  $t_{ij}$  concept. In: *Proc of 13th ARCSMGE, Keynote Paper, Kolkata*, vol. 2, pp. 69–89. *Keynote Paper, Kolkata* (2007)
- [6] Nakai, T., Hinokio, T.: A simple elastoplastic model for normally and over consolidated soils with unified material parameters. *Soils and Foundations* 44(2), 53–70 (2004)
- [7] Ladd, C.C., Foott, R., Ishihara, K., Poulos, H.G.: Stress-deformation and strength characteristics. In: *Proc. of 9th International Conf. on Soil Mech. and Foundation Eng., Tokyo*, vol. 1, pp. 421–494 (1977)
- [8] Yoshikuni, H., Moriwaki, T., Ikegami, S., Tajima, S.: The effect of stress history on the secondary compression characteristics of over consolidated clay. *Proc of Annual Meeting on JGS 1*, 381–382 (1990)
- [9] Nakai, T., Mihara, Y.: A new mechanical quantity for soils and its application to elastoplastic constitutive models. *Soils and Foundations* 24(2), 82–94 (1984)
- [10] Nakai, T., Shahin, H.M., Kikumoto, M., Kyokawa, H., Zhang, F., Farias, M.M.: A simple and unified one-dimensional model to describe various characteristics of soils. *Soils and Foundations* 51(6), 1129–1148 (2011a)
- [11] Nakai, T., Shahin, H.M., Kikumoto, M., Kyokawa, H., Zhang, F., Farias, M.M.: A simple and unified three-dimensional model to describe various characteristics of soils. *Soils and Foundations* 51(6), 1149–1168 (2011b)
- [12] Nakai, T.: *Constitutive Modeling of Geomaterials: Principles and Applications*, 376pages. CRC Press (to be published in July, 2012)

# Uniqueness of Numerical Experimental Results and Contribution to Constitutive Model by DEM

Kiichi Suzuki

Department of Civil and Environmental Engineering, Saitama University,  
255 Shimo-Okubo, Sakura-ku, Saitama City, Saitama, 338-8570 Japan  
ksuzuki@mail.saitama-u.ac.jp

**Summary.** It is necessary to guarantee the uniqueness of the solution by DEM. At first, this paper aims to make sure the uniqueness for biaxial compression test with oval particles using parametric study. It was found that the strain rate has an important role comparing with other affecting factors. Secondly, the simulations were conducted until large strain to study the initiation of shear band formation and the existence of steady state. It was clarified that the initiation of the shear band formation occurs around the peak strength for dense material and the steady state does not necessarily exist.

**Keywords:** DEM, shear band, strain rate, uniqueness.

## 1 Introduction

It has been a long time since Discrete Element Method (DEM) had been expected as a numerical experimental tool instead of laboratory element test, however, it is hard to say that the validity and efficiency is well established. The principal reason comes from the accuracy of the results, because DEM has been so far used to clarify the material behavior qualitatively not quantitatively. Therefore, at first, this paper aims to make sure the uniqueness for biaxial compression test with oval particles using parametric study. The simulated results were investigated both macro-mechanically and micro-mechanically. It should be especially noticed that the damping used in DEM is just spurious numerical damping. Then the unbalanced force was used for tracing the convergence condition. Secondly, the simulations were conducted until large strain to study especially the initiation of shear band formation and the existence of steady state using two initial void ratios (i.e., dense and loose).

## 2 Numerical Experiments

### 2.1 Numerical Method

A free software code Oval is used. Oval has been basically developed by Kuhn [1] based on the principle proposed by Cundall and Strack [2]. 8,192 egg-shaped oval particles with a ratio of the height to the width of 0.6 are used. The specimens were isotropically compressed until a stress of 100 kN/m<sup>2</sup>, and then the vertical strain was gradually given under constant horizontal stress. The calculation conditions are shown in Table 1. The accuracy was traced using the unbalanced resultant force index (Ng [3]) as,

$$I_{uf} = \sqrt{\frac{\frac{1}{N_p} \sum_{p=1}^{N_p} (f_{res}^p)^2}{\frac{1}{N_c} \sum_{c=1}^{N_c} (f^c)^2}} \quad (1)$$

**Table 1.** Calculation conditions

Shape	Oval
Number	8,192
Diameter $d$	2.0~10.0 × 10 <sup>-3</sup> m
Density $\rho_s$	2.65 × 10 <sup>3</sup> kg/m <sup>3</sup>
Initial void ratio $e_0$	0.1121, 0.2462
Spring constant $k_n, k_s$	1.0 × 10 <sup>8</sup> N/m
Coefficient of friction	
Between particles $\mu_p$	0.6
Between particle and wall $\mu_w$	0.0
Damping constant $h$	0.08
Time $\Delta t$	1.0 × 10 <sup>-5</sup> s

where  $N_p, N_c$  = number of particles and number of contacts, respectively.

$f_{res}^p, f^c$  = unbalanced force and contact force, respectively. The virtual damping force used as numerical damping is included in the unbalanced force. Several textbook can be referred for the detail of DEM (e.g., O'Sullivan [4]).

The stress and strain quantities for the biaxial compression test are defined similarly with that for 3-dimensional problems as follows:

$$p = \frac{\sigma_v + \sigma_h}{2}, q = \sigma_v - \sigma_h \quad (2a)$$

$$d\epsilon_{vol} = \frac{-\Delta e}{1+e_0}, d\bar{\epsilon} = \frac{1}{2}(d\epsilon_v - d\epsilon_h) \tag{2b}$$

where,  $p, q$  = mean and equivalent (or deviator) stresses,  $\sigma_v, \sigma_h$  = vertical and horizontal stresses,  $\epsilon_{vol}, \bar{\epsilon}$  = volumetric and equivalent strains,  $\Delta e, e_0$  = incremental and initial void ratios, respectively.

## 2.2 Results and Discussion

Fig. 1 shows the stress ratio and unbalanced resultant force index versus the equivalent strain by different strain rates for dense material. The strain rate of  $0.004 \text{ s}^{-1}$  can obtain the unique solution for this model, then the unbalanced resultant force index was below 0.0005. Fig. 2 shows the stress ratio, volumetric strain, void ratio  $e$ , effective void ratio  $\bar{e}$ , coordination number  $Z$ , and slip coordination number  $S$  versus equivalent strain by two strain rates of  $0.004 \text{ s}^{-1}$  and  $4.0 \text{ s}^{-1}$  until an equivalent strain of 0.8 (80 %) for dense and loose specimens. The slip coordination number defines the number of slip contact per particle. There is “double strain softening” curve as pointed based on the experimental results by Suzuki and Yamada [5]. The steady state does not necessarily exist while it seems exist for the larger strain rate although it does not give the uniqueness of solution.

Fig. 3 shows the stress ratio, volumetric strain and slip coordination number versus equivalent strain until 0.02 (2 %). Fig. 4 shows the transition of contact force distribution at points  $a, b, c$  and  $d$  which was described in the figure of stress ratio-equivalent strain. The slip coordination number starts to reduce with fluctuation around the phase transformation stress ratio at point  $b$  and the initiation of shear band formation occurs around the peak stress ratio at point  $c$ , as described based on an image analysis using laser speckle technique by Yoshida [6]. It will be possible to establish more sophisticated constitutive model based on the analytical evolution of the numerical experimental results by DEM in the near future.

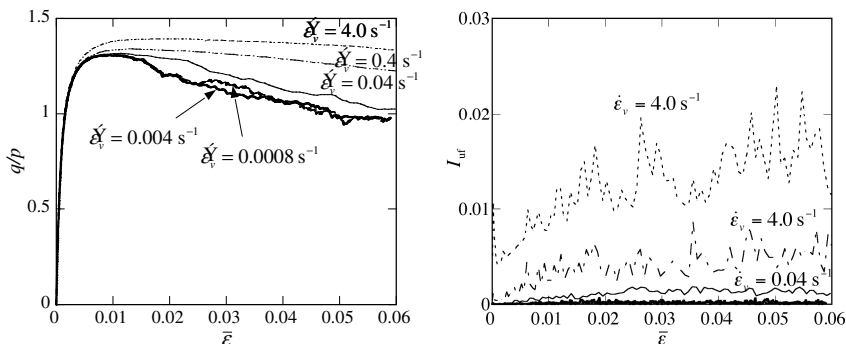


Fig. 1. Influence of strain rate

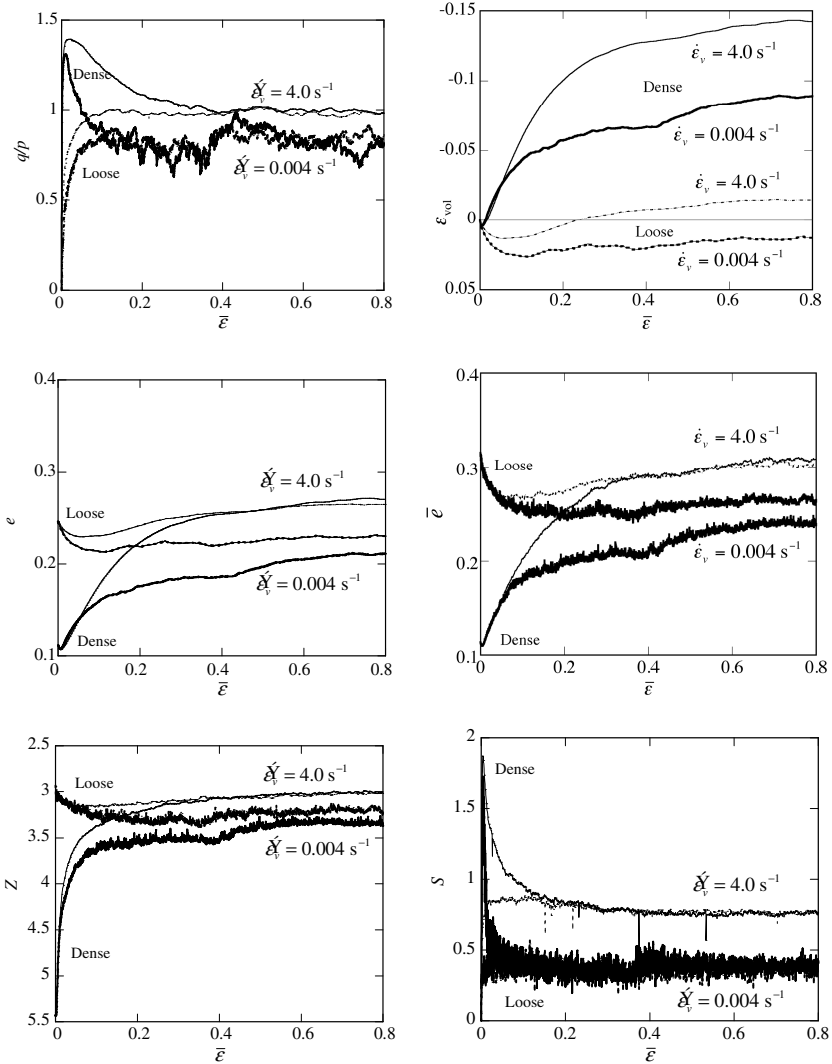


Fig. 2. Various responses until an equivalent strain of 80 %

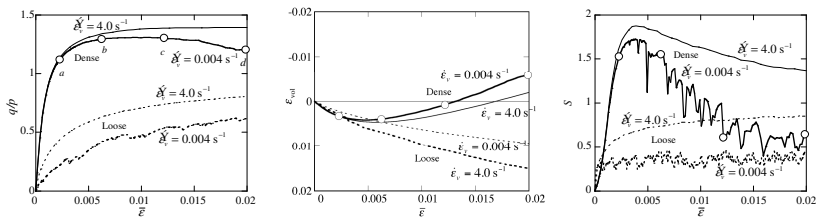


Fig. 3. Enlarged responses until an equivalent strain of 2 %

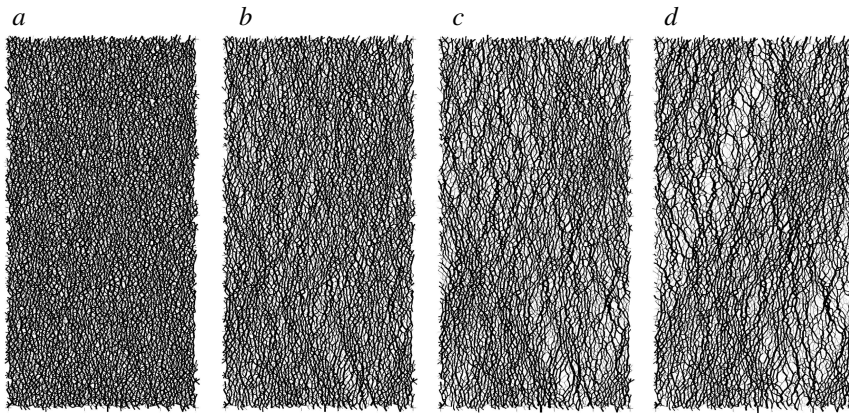


Fig. 4. Transition of contact force distribution until an equivalent strain of 2 %

### 3 Conclusions

The following conclusions were obtained for the above numerical experiments for two initial void ratios using oval particle.

1. The strain rate has a significant effect on the shear behavior especially after peak strength.
2. The steady state does not necessarily exist, strictly speaking.
3. The localization begins around the phase transformation stress ratio and the initiation of the shear band formation occurs around the peak strength.

**Acknowledgement.** The author would like to thank M. R. Kuhn, Professor, University of Portland, U.S.A. for his valuable advices.

### References

- [1] Kuhn, M.R.: Oval and OvalPlot: Programs for analyzing dense particle assemblies with the discrete element method (2002), <http://faculty.up.edu/kuhn/oval/oval.html>
- [2] Cundall, P.A., Strack, O.D.L.: A discrete numerical model for granular assemblies. *Géotechnique* 29(1), 47–65 (1979)
- [3] Ng, T.-T.: Input parameters of discrete element methods. *J. Eng. Mech., ASCE* 132(7), 723–729 (2006)
- [4] O’Sullivan, C.: *Particulate discrete element modelling; A geomechanics perspective*. Spon Press (2011)
- [5] Suzuki, K., Yamada, T.: "Double strain softening" and "Diagonally crossing shear bands" of sand in drained triaxial tests. *Int. J. Geomech., ASCE* 6(6), 440–446 (2006)
- [6] Yoshida, T.: *Strain localization and shear banding during failure of sand*, D. Eng. Thesis, Univ. Tokyo (1995) (in Japanese)

# Study on Accelerated Creep Properties and Creep Damage Constitutive Relation for Volcanic Breccias

Rubin Wang<sup>1,2,\*</sup>, Weiya Xu<sup>1</sup>, Jiuchang Zhang<sup>1</sup>, and Wei Wang<sup>1</sup>

<sup>1</sup> Institute of Geotechnical Engineering, Hohai University, Nanjing 210098, China

<sup>2</sup> College of Water Conservancy and Hydropower Engineering, Hohai University, Nanjing 210098, China

rbwang\_hhu@foxmail.com

**Summary.** In order to know about the accelerated creep properties of volcanic breccias, triaxial compression rheological experiments are carried out on rock servo-controlled triaxial rheology equipment. Based on the experimental results, the accelerated creep phase of creep curve of volcanic breccias is analyzed. It is shown that the strain rate increases sharply, the rock damage rapidly increases; the acoustic emission dramatic increases with the increase of time during the stage of accelerated creep, and the accelerated growth of rock damage leads to the sharp increase of creep rate. Then based on the accelerated creep deformation, the relation of damage variable versus time is obtained, and the creep damage constitutive equation of volcanic breccias is established. It is shown that the established nonlinear creep damage models based on time function is correct and reasonable.

**Keyword:** Volcanic breccias, Accelerated creep properties, Creep damage model.

## 1 Introduction

Rock creep property is a hot topic and key point in rock mechanics and engineering field, especially the accelerated creep deformation and creep-damage property of brittle rock, it can offer the theoretical basis in order to forecast and predict the long-term stability of rock engineering [1-3]. For instance, the granite of Three Gorges Project [4], greenschist and marble of Jinping Hydropower Project [5], and hornblende plagioclase gneiss of Xiaowan Hydropower Project [6], the experimental data of these cases have shown that the hard brittle rocks under high stress condition all possess comparatively obvious creep feature: initial attenuation creep deformation, stabilization creep deformation and accelerated creep deformation. In the classic creep models, the creep deformation is generally

---

\* Corresponding author.

described by the viscoplastic theory [7, 8]. The viscoplastic constitutive relations only are used to describe initial attenuation creep deformation and stabilization creep deformation, but they do not take into account creep damage related to accelerated creep deformation.

As the typical rock for the dam foundation, underground cavern group and high rock slope of Huangdeng Hydropower Project in southwestern China, volcanic breccia is the major complex geological media, and its creep mechanical property is the very important factor to influence the long-term stability and safety of the project. In order to know about the creep properties, especially the accelerated creep properties of volcanic breccias, triaxial compression rheological experiments are carried out on rock servo-controlled triaxial rheology equipment. Then based on the accelerated creep deformation, the creep damage constitutive relation of volcanic breccia is obtained.

## 2 Accelerated Creep Properties of Volcanic Breccias

Based on the triaxial creep experimental results of volcanic breccias specimens, the accelerated creep curve under confining pressure of 4MPa is showed in Fig.1, and exhibits three classical stages of creep at creep failure stress level of 107.5MPa: the initial attenuation creep phase, the stabilization creep phase and the accelerated creep phase. As can be seen from the graph in Fig. 1(a), after staying attenuation creep deformation for a while (In general, this time is very short.), the creep deformation enters the stabilization creep phase for a long time. As the creep time further increases, the creep deformation enters the accelerated creep phase. From Fig.1 (b), it can also be found that the creep rate is experienced a gradual decrease to keep from relative stability, and to gradually increase until the process of destruction.

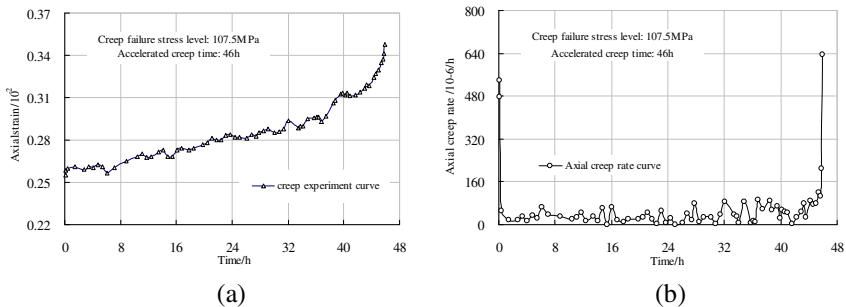


**Fig. 1.** Complete axial accelerative creep curves of volcanic breccia and relation between axial creep rate and time under confining pressure 4MPa

Rock damage is tend to be aggravated continuously, and finally causes rock failure, and rock failure is a damage accumulation process in which rock material property deteriorates continuously. The acoustic emission energy can be comprehensive described the occurrence intensity of micro-cracks of rock. The characteristic-shape

curve of acoustic emission event vs time for salt rock under uniaxial creep test is obtained as shown in Fig.2 [9, 10]. From the Fig.2, we conclude that during the stage of accelerated creep, the acoustic emission dramatic increases. It is shown that the accelerated growth of rock damage leads to the sharp increase of creep rate.

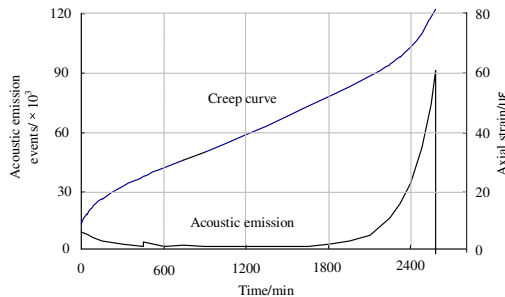


**Fig. 2.** Characteristic-shape curve of acoustic emission event vs time for salt rock under uniaxial creep test [9]

### 3 Creep Damage Variable and Damage Evolution Equation

Under different confining pressure, the total axial stain of rock specimen can be expressed the sum of instantaneous strain and total creep strain, i.e.

$$\epsilon = \epsilon_e + \epsilon_c \tag{1}$$

where  $\epsilon_e$  represents the instantaneous strain;  $\epsilon_c$  is the total creep strain.

Based on the analysis of the results of triaxial rheological tests using specimens of volcanic breccia, the total creep strain can be described as follows:

$$\epsilon_c = \begin{cases} \epsilon_a + \epsilon_s & \sigma < \sigma_s \\ \epsilon_a + \epsilon_s + \epsilon_d & \sigma \geq \sigma_s \end{cases} \tag{2}$$

where  $\epsilon_a$  is initial attenuation creep strain;  $\epsilon_s$  is stabilization creep strain and  $\epsilon_d$  is damage-induced accelerated creep strain;  $\sigma_s$  is the long-term strength of volcanic breccia.

In the classic creep models, it is considered that the properties of attenuation creep and stabilization creep can be better reflected by using the generalized Kelvin rheological model, the creep equation is

$$\epsilon_{c1} = \epsilon_a + \epsilon_s = \frac{\sigma_0}{E_1} + \frac{\sigma_0}{E_2} \left( 1 - \exp\left( -\frac{E_2}{\eta_2} t \right) \right) \tag{3}$$

where  $\epsilon_{c1}$  is the sum of attenuation creep strain and stabilization creep strain;  $E_1, E_2, \eta_2$  are creep parameters;  $\sigma_0$  is a constant stress.

Experiments confirm that the creep damage of rock is possessed correlation with creep time. According to the properties of creep damage of volcanic breccias, the accelerated creep strain in this case can be defined in following equation:

$$\epsilon_d = \frac{\epsilon_{c1}}{1-D} H(t-t^*) \tag{4}$$

where  $D$  represents the creep damage variable;  $t^*$  is the initial time value from stabilization creep strain to accelerated creep strain;  $H(\ )$  is Heaviside function, its expression is

$$H(t-t^*) = \begin{cases} 0 & t \leq t^* \\ 1 & t > t^* \end{cases} \tag{5}$$

Creep damage variable based on time function can be described as follows:

$$D_t = 1 - \exp(-at^b) \tag{6}$$

where  $a, b$  are parameters of rock material. Eq. (6) is described the relation between creep damage variable and accelerated creep time.

According to the above analysis, the creep damage of volcanic breccias is defined as

$$D = \begin{cases} 0 & t \leq t^* \\ 1 - \exp(-a(t-t^*)^b) & t > t^* \end{cases} \tag{7}$$

The relation of damage variable versus creep time is as shown in Fig.3. Based on Eq. (7) and the complete axial accelerative creep curves of volcanic breccia, the relation of damage variable versus time is obtained, as shown in Fig.3. In accordance with the curve in Fig.3, we can conclude that the relationship between creep damage variable of rock and creep time is demonstrated by exponential function, and then the test results agree well with theoretical curve.

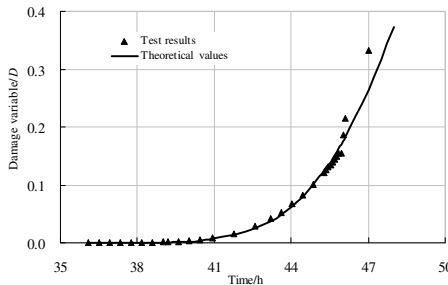
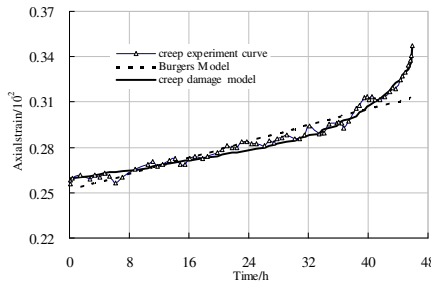


Fig. 3. Relation of damage variable with creep time of volcanic breccias



**Fig. 4.** Comparison between results calculated by creep damage model and experimental results

### 4 Creep Damage Constitutive Relation for Volcanic Breccias

From the Fig.1, we can see that under high stress state, the rock creep is not a linear function, but also in the attenuation creep phase and accelerated creep phase is showed the nonlinear characteristics, so the generalized Kelvin rheological model is not used to describe the whole process of rock creep deformation.

The creep damage constitutive equation of volcanic breccias is established as follows:

- (1) When the creep deformation in the attenuation creep phase and stabilization creep phase,  $D = 0$ , by using Eqs(2)~(5), the creep damage equation can be obtained

$$\varepsilon(t) = \frac{\sigma_0}{E_1} + \frac{\sigma_0}{E_2} \left( 1 - \exp\left(-\frac{E_2 t}{\eta_2}\right) \right), t \leq t^* \tag{8}$$

- (2) When the creep deformation in the accelerated creep phase, the internal damage of rock increases sharply, and should consider the action of damage on rock. In this case,  $D > 0$ , by using Eqs(2)~(7), the creep damage equation can be obtained

$$\left\{ \begin{aligned} \varepsilon(t) &= \left( \frac{\sigma_0}{E_1} + \frac{\sigma_0}{E_2} \left( 1 - \exp\left(-\frac{E_2 t}{\eta_2}\right) \right) \right) \left( 1 + \frac{1}{1-D} \right) & t > t^* \\ D &= 1 - \exp(-a(t-t^*)^b) \end{aligned} \right. \tag{9}$$

### 5 Experimental Verification

Based on the nonlinear creep stain-stress curve as shown in Fig.1(a), the material parameters of the creep damage constitutive equations (8) and (9) are obtained by using the method developed in [11], which is shown in Table 1.

**Table 1.** Parameters of creep damage model of volcanic breccias specimen

Confining pressure (MPa)	Stress level (MPa)	$E_1$ (GPa)	$E_2$ (GPa)	$\eta_2$ (GPa·d)	$a$	$b$
4	107.5	42.3	143.7	7.5E+3	2.6 E-6	4.9

Based on the material parameters as shown in Table 1, the creep data is calculated by the proposed creep damage model and Burgers model, and the comparison curve between the results calculated by creep damage model and experimental results is shown in Fig.4. From the Fig.4, we can conclude that the test results agree well with theoretical curve. Therefore, it is shown that the established creep damage model based on time function is correct and reasonable, and the creep damage equation can be better reflected the complete phases of the attenuation creep, stabilization creep and accelerated creep.

## 6 Conclusions

According to the accelerated creep properties of volcanic breccias and creep damage analysis, the relationship between creep damage variable of rock and creep time is demonstrated by exponential function, and the creep damage constitutive equation of volcanic breccias is established. The experimental verification shows that the established creep damage equation can be better reflected the complete phases of the attenuation creep, stabilization creep and accelerated creep.

**Acknowledgement.** Thanks are given to Projects (11172090, 51009052, 51109069) supported by the National Natural Science Foundation of China; 973 Project (2011CB013504) supported by a grant from the Major State Basic Research Development Program of China.

## References

- [1] Wang, S.J., Yang, Z.F., Fu, B.J.: Century Achievements of Rock Mechanics and Engineering in. Hohai University Press, Nanjing (2004) (in Chinese)
- [2] Sun, J.: Rock rheological mechanics and its advance in engineering applications. Chinese Journal of Rock Mechanics and Engineering 26(6), 1081–1106 (2007) (in Chinese)
- [3] Fabre, G., Pellet, F.: Creep and time-dependent damage in argillaceous rocks. International Journal of Rock Mechanics & Mining Sciences 43, 950–960 (2006)
- [4] Xu, P., Xia, X.L.: Study on creep characteristics of granite in lock zone of three gorges project. Journal of Yangtze River Scientific Research Institute 12(2), 23–29 (1995) (in Chinese)
- [5] Yang, S.Q., Xu, W.Y., Xie, S.Y., et al.: Studies of triaxial rheological deformation and failure mechanism of hard rock in saturated state. Chinese Journal of Geotechnical Engineering 28(8), 962–969 (2006) (in Chinese)

- [6] Jiang, Y.Z., Xu, W.Y., Wang, R.H.: Investigation on rheological mechanical properties of hornblende plagioclase gneiss. *Rock and Soil Mechanics* (S1), 339-345 (2011) (in Chinese)
- [7] Cristescu, N.D., Hunsche, U.: *Time-effects in rock mechanics*. Wiley, England (1998)
- [8] Shao, J.F., Chau, K.T., Feng, X.T.: Modeling of anisotropic damage and creep deformation in brittle rocks. *International Journal of Rock Mechanics & Mining Sciences* 43, 582–592 (2006)
- [9] Szczepanik, S.D.: Time-dependent acoustic emission studies on potash. In: Roegies, D. (ed.) *Rock Mechanics as a Multidisciplinary Science*, pp. 471–479. A. A. Balkema, Rotterdam (1991)
- [10] Yang, C.H., Daemen, J.K., Yin, J.H.: Experimental investigation of creep behavior of salt rock. *International Journal of Rock Mechanics & Mining Sciences* 36(2), 336–341 (2000)
- [11] Xu, W.Y., Zhou, J.W., Yang, S.Q., et al.: Study on creep damage constitutive relation of greenschist specimen. *Chinese Journal of Rock Mechanics and Engineering* 25(S1), 3093–3098 (2006) (in Chinese)

# A Research on the Full State Function Constitutive Relation Model

Zhenhai Wei<sup>1,\*</sup>, Mengshu Wang<sup>2</sup>, and Dingli Zhang<sup>3</sup>

<sup>1</sup> Beijing Jiaotong University, Beijing, 100044, China

<sup>2</sup> Logistics Academy Beijing 100858, China  
wzhai@vip.sina.com

**Summary.** For materials of granular characteristics, structural problem is one key and difficult point of the present study. In the paper, the full state function theory for material structure is proposed based on investigation on the state of material structure as the starting point. The full state function of material structure is a function reflecting the material structure properties, so it also can reflect the variation rules of material mechanics and geometric characteristics when materials are affected by external effect, which is the constitutive relation of materials. The constitutive relation set up based on the full state function is shortened as full constitutive relation, because for constitutive relation the structural characteristics of materials are taken into consideration. Besides the constitutive relation that takes material structure into account that can be deduced on the basis of the full state function theory, the constitutive relation of which the form is identical to that of classical theory can also be deduced when materials deteriorate as classical ideal elastic-plastic materials. The proposed theoretical method enables the change of dynamic process analysis of structural change into state analysis and the establishment of bridge and method to analyze the relationship between particle structure scale and macro scale. In addition, it also lays a foundation for the solution of material structural problems macroscopically.

**Keywords:** constitutive, model, state function.

## 1 Introduction

Classical elastic-plastic theory suggests that material is even, continuous and infinitely dividable, that is to not consider material structure. But any material in reality, whether metal materials with macroscopically uniform and continuous structure or granular materials with very strong structure characteristics, all has certain complex structure form on a certain scale. Thus we can see that the research object of classical elastic-plastic theory is a simple material with no constitutive property, but any material in reality is one kind of complex material with constitutive property.

---

\* Corresponding author.

The research on characteristics of complex materials with constitutive property in the field of mechanics is one key and difficult problem [1~6]. Particularly, many scholars have made a great deal of research on the constitutive relationship problem which is one of the most important bases for material mechanics performance analysis [2~8]. But due to constraint of the past classical theoretical thinking and limitation of thinking ways, people have been trying to set up solutions based on past classical theory. The solution dependent on classical theory witnessed no substantial progress for a long time because of the great difference between the constitutive property of materials and classical theoretical analysis basis[5~8].

Starting from the concept of material structure, this paper takes material structure state as the basis for discussion & analysis of problems and the analysis of material constitutive property as that of complex material mechanics, which offers some preliminary exploration to the constitutive property problem of materials.

## 2 Basic Assumption of the Model and Full State Function

The constitutive relation model based on the full state function of material structure is mainly based on the assumptions as follows:

- (1) All adjacent points reflected in the structure state points of phase space are all structural states that can be evolved into during the process of structure evolution and deformation, which means that adjacent points are the state points that the structure can evolve into;
- (2) The full state function of material structure is macroscopically continuous and smooth or at least one-order smooth;
- (3) The elastic modulus of structure in loading and unloading is identical;
- (4) The change of structural geometrical states can be expressed by way of strain.

Based on the above four assumptions, the full state potential function composed of the elastic modulus of structure, structure critical strength and material structure strain is established:

$$\Phi ( D_{ijkl}^e, \sigma_{ij}^s, \varepsilon_{ij}^p ) = 0 \quad (1)$$

This function reflects the relation between various mechanical and physical parameters in consideration of the constitutive property of material, which is the basis for establishment of the full constitutive relationship.

## 3 Full Constitutive Relation Model

Full state potential function is used to establish a curved face equation in phase space determined by elastic modulus, structure critical strength and strain tensor:

$$\Phi ( D_{ijkl}^e, \sigma_{ij}^s, \varepsilon_{ij}^p ) = 0$$

This is also a characteristic function used to describe the mechanical properties of materials. The full constitutive relation is defined as the tangent plane equation of full state function on curved surface determined by structure elastic modulus, structure critical strength and strain tensor, namely:

$$\frac{\partial\Phi}{\partial D_{ijkl}^e}(D_{ijkl}^e - D_{ijkl}^{e0}) + \frac{\partial\Phi}{\partial \sigma_{ij}^s}(\sigma_{ij}^s - \sigma_{ij}^{s0}) + \frac{\partial\Phi}{\partial \varepsilon_{ij}^p}(\varepsilon_{ij}^p - \varepsilon_{ij}^{p0}) = 0 \tag{2}$$

In which,  $D_{ijkl}^{e0}$ ,  $\sigma_{ij}^{s0}$ ,  $\varepsilon_{ij}^{p0}$  are the coordinate values on curved surface of the selected points, respectively.

Supposing that  $dD_{ijkl}^e = D_{ijkl}^e - D_{ijkl}^{e0}$ ,  $d\sigma_{ij}^s = \sigma_{ij}^s - \sigma_{ij}^{s0}$ ,  $d\varepsilon_{ij}^p = \varepsilon_{ij}^p - \varepsilon_{ij}^{p0}$ , an equation of incremental form can be obtained:

$$\frac{\partial\Phi}{\partial D_{ijkl}^e}dD_{ijkl}^e + \frac{\partial\Phi}{\partial \sigma_{ij}^s}d\sigma_{ij}^s + \frac{\partial\Phi}{\partial \varepsilon_{ij}^p}d\varepsilon_{ij}^p = 0 \tag{3}$$

Then, i, j, k and l are the sub-signs of summation. Obviously, the formula is the

dot product of vectors  $\frac{\partial\Phi}{\partial D_{ijkl}^e}$ ,  $\frac{\partial\Phi}{\partial \sigma_{ij}^s}$ ,  $\frac{\partial\Phi}{\partial \varepsilon_{ij}^p}$  and  $dD_{ijkl}^e$ ,  $d\sigma_{ij}^s$ ,  $d\varepsilon_{ij}^p$ . This is the

material constitutive model in incremental form considering the constitutive property of materials. The equation reflects the relationship among the elastic modulus increment  $dD_{ijkl}^e$  of material structure, critical strength increment  $d\sigma_{ij}^s$  and strain increment  $d\varepsilon_{ij}^p$  of geometric distortion.

Compared with classical plasticity theory, the model considers not only stress increment and strain increment but also the incremental change of material elastic modulus, which is the reason why it is called the full constitutive relation model. Material experiments indicate that, as long as any ordinary material has obvious structural characteristics, its elastic modulus is always a changeable variable. And it is just this changeable variable that makes materials express more complex characteristics. Thus this point is fully considered for the full constitutive relation deduced from full state potential function with consideration to the material constitutive property.

#### 4 A Discussion on Some Special Cases of the Full Constitutive Relation Model

The full constitutive relation model is a kind of constitutive relation model in consideration of the material constitutive property. In classical theory, the material constitutive property is not considered for elastoplastic materials, which is apparently only a special case of materials with constitutive property. The full

constitutive relationship is a material constitutive relation with universal significance, so it probably can reflect the special case. Here a brief discussion is discussed in this aspect.

Through experiment, we can find that the stress-strain curve of ordinary metal material has the following characteristics. When load is affected, the stress-strain relation is a linear relationship, that is, the deformation at the time is a plastic deformation. After entering into a yield state, it begins to produce plastic deformation. The stress-strain will decline along a straight line if it is unloaded to zero, but the strain will retain part residual strain. The analysis of stress-strain relation which is loaded and unloaded each time finds that the loading and unloading lines are in parallel (or basically in parallel). This reflects that the elastic modulus of metal material is identical or the same in the sense of macro statistics.

When  $D_{ijkl}^e$  is a constant and  $dD_{ijkl}^e = 0$ , Formula (3) can be changed into the following formula:

$$\frac{\partial\Phi}{\partial\sigma_{ij}^s}d\sigma_{ij}^s + \frac{\partial\Phi}{\partial\varepsilon_{ij}^p}d\varepsilon_{ij}^p = 0 \tag{4}$$

Considering that the total strain of this material is

$$d\varepsilon_{ij} = d\varepsilon_{ij}^e + d\varepsilon_{ij}^p = \frac{d\sigma_{kl}^s}{D_{ijkl}^e} + d\varepsilon_{ij}^p, \text{ we can obtain } d\varepsilon_{ij}^p = d\varepsilon_{ij} - \frac{d\sigma_{kl}^s}{D_{ijkl}^e}.$$

And this value can be substituted into the above formula(4):

$$\frac{\partial\Phi}{\partial\sigma_{ij}^s}d\sigma_{ij}^s + \frac{\partial\Phi}{\partial\varepsilon_{ij}^p}(d\varepsilon_{ij} - \frac{d\sigma_{kl}^s}{D_{ijkl}^e}) = 0 \tag{5}$$

After sorting, we can obtain:

$$\left(\frac{\partial\Phi}{\partial\sigma_{ij}^s}D_{ijkl}^e - \frac{\partial\Phi}{\partial\varepsilon_{ij}^p}\right)d\sigma_{ij}^s = -\frac{\partial\Phi}{\partial\varepsilon_{ij}^p}D_{ijkl}^e d\varepsilon_{kl} \tag{6}$$

In order to explicitly express the relation of  $d\sigma_{kl}^s$ ,  $d\varepsilon_{ij}$ , two sides of the equation are

multiplied by vector  $\left(\frac{\partial\Phi}{\partial\sigma_{ij}^s}D_{ijkl}^e - \frac{\partial\Phi}{\partial\varepsilon_{ij}^p}\right)$  and the following formula is obtained:

$$\begin{aligned} &\left[\left(\frac{\partial\Phi}{\partial\sigma_{ij}^s}D_{ijkl}^e - \frac{\partial\Phi}{\partial\varepsilon_{ij}^p}\right)\left(\frac{\partial\Phi}{\partial\sigma_{ij}^s}D_{ijkl}^e - \frac{\partial\Phi}{\partial\varepsilon_{ij}^p}\right)\right]d\sigma_{ij}^s = \\ &-\left[\left(\frac{\partial\Phi}{\partial\sigma_{ij}^s}D_{ijkl}^e - \frac{\partial\Phi}{\partial\varepsilon_{ij}^p}\right)\frac{\partial\Phi}{\partial\varepsilon_{ij}^p}D_{ijkl}^e\right]d\varepsilon_{ij} \end{aligned} \tag{7}$$

Obviously, the value in this square bracket is a scalar quantity, therefore:

$$d\sigma_{ij}^s = - \frac{\left( \frac{\partial\Phi}{\partial\sigma_{ij}^s} D_{ijkl}^e - \frac{\partial\Phi}{\partial\varepsilon_{ij}^p} \right) \frac{\partial\Phi}{\partial\varepsilon_{ij}^p} D_{ijkl}^e}{\left( \frac{\partial\Phi}{\partial\sigma_{ij}^s} D_{ijkl}^e - \frac{\partial\Phi}{\partial\varepsilon_{ij}^p} \right) \left( \frac{\partial\Phi}{\partial\sigma_{ij}^s} D_{ijkl}^e - \frac{\partial\Phi}{\partial\varepsilon_{ij}^p} \right)} d\varepsilon_{ij} \tag{8}$$

Then:

$$\begin{aligned} D_{ijkl}^{ep} &= - \frac{\left( \frac{\partial\Phi}{\partial\sigma_{ij}^s} D_{ijkl}^e - \frac{\partial\Phi}{\partial\varepsilon_{ij}^p} \right) \frac{\partial\Phi}{\partial\varepsilon_{ij}^p} D_{ijkl}^e}{\left( \frac{\partial\Phi}{\partial\sigma_{ij}^s} D_{ijkl}^e - \frac{\partial\Phi}{\partial\varepsilon_{ij}^p} \right)^2} \\ &= D_{ijkl}^e - \frac{\left( \frac{\partial\Phi}{\partial\sigma_{ij}^s} D_{ijkl}^e - \frac{\partial\Phi}{\partial\varepsilon_{ij}^p} \right)^2 D_{ijkl}^e + \left( \frac{\partial\Phi}{\partial\sigma_{ij}^s} D_{ijkl}^e - \frac{\partial\Phi}{\partial\varepsilon_{ij}^p} \right) \frac{\partial\Phi}{\partial\varepsilon_{ij}^p} D_{ijkl}^e}{\left( \frac{\partial\Phi}{\partial\sigma_{ij}^s} D_{ijkl}^e - \frac{\partial\Phi}{\partial\varepsilon_{ij}^p} \right)^2} \tag{9} \\ &= D_{ijkl}^e - \frac{D_{ijpq}^e \frac{\partial\Phi}{\partial\sigma_{pq}^s} \frac{\partial\Phi}{\partial\sigma_{rs}^s} D_{rskl}^e D_{ijkl}^e}{\left( \frac{\partial\Phi}{\partial\sigma_{ij}^s} D_{ijkl}^e - \frac{\partial\Phi}{\partial\varepsilon_{ij}^p} \right)^2} \end{aligned}$$

For ideal elastic-plastic materials,  $\Phi$  and  $\varepsilon_{ij}^p$  are irrelevant and  $\frac{\partial\Phi}{\partial\varepsilon_{ij}^p} = 0$ . Then,

the above formula can be translated into a form identical to that in classical elastic-plastic theory, where the full state function is same to the yield function. Thus we can obtain the following formula:

$$D_{ijkl}^{ep} = D_{ijkl}^e - \frac{D_{ijpq}^e \frac{\partial F}{\partial\sigma_{pq}^s} \frac{\partial F}{\partial\sigma_{rs}^s} D_{rskl}^e}{\frac{\partial F}{\partial\sigma_{ij}^s} D_{ijkl}^e \frac{\partial F}{\partial\sigma_{kl}^s}} \tag{10}$$

In which, For represents the yield function.

Through observation, we can find that  $D_{ijkl}^{ep}$  expression here is exactly the same to the elastic-plastic modulus in classical plasticity theory in form [9], but the basis and concept from which the two are deduced are completely different. In terms of the classical plasticity theory, the elasto-plastic modulus tensor expression is deduced from the assumed plastic potential function. But the elastic-plastic modulus tensor expression here is deduced in consideration of the concept of material constitutive property and obtained after simplification with  $D_{ijkl}^e$  as a constant. In other words, the structural elastic modulus of a material remains unchanged macroscopically during the deformation process.

## 5 Conclusions

The full state function theory concerning material structure proposed through the previous analysis and discussion in this paper, especially the full material constitutive relation obtained based on the full state function theory, is an analysis method that contains the classical plasticity theory and considers the impact of material constitutive property. The method proposed offers a new thought to solve the material structural problem. Its significance lies in that:

(1) In this study, a new feasible way of thinking to find methods to solve the material structural problem is put forward, and the dynamic process analysis of material structure is converted into the state analysis of it. Therefore, the difficulty of analysis is greatly reduced. The analysis of dynamic change process of material structure is a very complicated problem involving such aspects as the granular motion in material structure, the change of structural form, and the connection status among granules. So far, there is no good solution for the problem. The proposed full state theory offers a new method to solve the problem from another direction.

(2) The full state theory offers the key concepts and methods concerning the transition from the structural analysis of granular scale to the analysis of macro parameters. The constitutive relation and microscopic structural characteristics which are needed for the macro analysis have been puzzling us for so long a time. Many scholars have been exploring how to establish an effective transition bridge between the two. The full state theory solves the problem fundamentally.

(3) In order to consider the material structural problem, the full state theory suggests a new solution and method macroscopically. Macroscopically, the expression of full state function can be obtained through the determination of material elastic modulus, structural critical strength and geometrical form changes so as to lay the foundation for establishment of the full constitutive relation that takes material structure into consideration. To solve the material structural problem, many scholars also once put forward many macroscopic methods to solve the problem, but all the methods fail to possess general significance. The proposed full state function theory enables the foundation for solving this problem.

The material structural problem especially the dynamic change of material structures is a very complex problem. The discussion in this paper is just a kind of tentative research. Thus, further research is needed for structural dynamic changes and possible states of structures. Many questions concerning the full state function itself remain unsolved, and even many concepts still require further deliberation and discussion.

## References

- [1] Hill, R.: *The Mathematical Theory of Plasticity*. Oxford University Press, London (1950)
- [2] Wei, Z., Wang, M., Zhang, D.: Research on the Constitutive Model of the Granular Material. In: *Proceedings of the Twentieth National Conference on Structural Engineering, China*, pp. II093–II103 (2011)
- [3] Jones, H.: Rapid solidification of metals and alloys, pp. 78–80. Inst of Metallurgists, London (1982)
- [4] Sun, B.-A., Wang, W.-H.: On the plastic deformation mechanism of metallic glasses. *Phys.* 39(9), 628–630 (2010)
- [5] Qian, J.-G., Huang, M.-S.: Micro-macro mechanistic analysis of plastic anisotropy in soil. *Rock and Soil Mechanics* 32(supp.2), 88–94 (2011)
- [6] De Josselin de tong, G.: The double sliding free rotating model for granular assemblies. *Geotechnique* 21(3), 155–162 (1971)
- [7] Wang, Q., Wang, F.-Y., Xiao, S.-F.: A Quantitative Study of the Microstructure characteristics of Soil Andits Application to the Engineering. *Journal of Chengdu University of Technology* 28(2), 148–153 (2001)
- [8] Cen, W.-J., Zhu, Y.-M., Wang, X.-X.: A new type of constitutive theory for granular soil. *Rock and Soil Mechanics* 28(9), 1801–1806 (2007)
- [9] Liu, L., Ma, Z., Kong, Y.: Engineering Forming Theory of Elastic-Plactic Materials. *Journal of Northwestern Polytechnical University* 17(2), 205–209 (1999)

# A Generalized Critical State Model for Gas Hydrate-Bearing Sediments

Rong-tao Yan, Chang-fu Wei<sup>\*</sup>, Hou-zhen Wei, Hui-hui Tian, and Er-ling Wu

State Key Laboratory of Geomechanics and Geotechnical Engineering, Institute of Rock and Soil Mechanics, Chinese Academy of Sciences, Wuhan 430071, China  
cfwei@whrsm.ac.cn

**Summary.** Methane gas hydrate, usually found beneath permafrost and in marine continental margin sediments worldwide, has attracted interest as a possible energy resource and as a potential agent in climate change and seafloor instability. Here, in order to describe the mechanical behavior of gas hydrate-bearing sediments (GHBS), an elastoplastic model is proposed based on the framework of a critical state model. The presence of gas hydrate can increase yield stress, enhancing the cohesion, peak strength and stiffness of the sediments. Therefore, GHBS is considered as the bonded material in the proposed model. A new bonding strength parameter is introduced into the yield function to evaluate the effect of gas hydrate on the yield behavior of the earth materials. Bonding strength of the GHBS subjected to mechanical loading and/or hydrate dissociation may be drastically reduced, causing strain softening after peak strength. Dilatancy is assumed to be a function of the bonding strength and the stress ratio, instead of the single parameter stress ratio, which can reflect the direction of plastic strain increment more realistically. The proposed model can transform into the modified Cam Clay model when hydrate saturation reduces to zero. Finally, the proposed model has been used to predict the stress-strain behaviors of GHBS in triaxial tests, and it is demonstrated that the proposed model has the capability to describe the behavior of GHBS.

**Keywords:** gas hydrate, sediments, critical state model.

## 1 Introduction

Gas hydrate, a crystalline solid composed of natural gas and hydrogen-bonded water molecules, is formed at the relatively high pressure and low temperature conditions present along many continental margins and in the permafrost regions. As a potential source of fuel, hydrate dissociation can destabilize hydrate layer and potentially result in large landslides and soil failures [1]. Due to the practical importance and fundamental interest of analyzing submarine stability, more and more research efforts have been devoted to investigating the response of gas-hydrate-bearing sediments (GHBS) to thermal and mechanical disturbances[1, 2].

---

<sup>\*</sup> Corresponding author.

Gas hydrate may cement sediments when it reaches at sufficient concentrations, and the strength and stiffness tend to increase with hydrate saturation  $S_h$ . Besides, growth habit can have a profound effect on sediment properties. In contrast, when hydrate in the sediment dissociates, the strength and stiffness will decrease, which induces a landslide[3-7].

In order to estimate the slope stability, it is essential to develop a numeric simulator including formation and/or dissociation behavior of hydrate, thermal properties of the reservoirs, permeability and mechanical behaviors of the reservoirs and so on[2]. Therefore, a constitutive model which can describes stress-strain relationship of hydrate-bearing sediments have to be developed.

In this paper, a general elastoplastic constitutive model is developed to describe the mechanical behavior of GHBS subjected to mechanical loading and/or hydrate dissociation in the framework of the modified Cam clay model, and the performance of the constitutive model is demonstrated by comparing the theoretical simulations with experimental data on the mechanical behavior of GHBS.

## 2 Structure of the Constitutive Model

There are three distribution modes of hydrate in sediments: 1) pore-filling, Hydrate grows freely in the pore spaces without bridging neighboring particles; 2) loading-bearing, Hydrate bridges the neighboring grains and contributes mechanical stability to the grains skeleton by becoming part of the load-bearing framework; 3) cementation, Hydrate grows at inter-granular contacts. The pore-filling mode has no effect on the strength of GHBS at low hydrate saturation. It may become a loading-bearing mode when hydrate saturation is above a critical saturation 25-30% [8].

Here GHBS is considered as a bonded soil regardless of the hydrate formation mode. Based on the previous researches for bonded soils[9-11], a constitutive framework for GHBS is presented based on the framework of the modified Cam clay model. It is assumed that the deformation of the GHBS is infinitesimal and the strain increment can be decomposed into an elastic part  $d\epsilon^e$  and a plastic part  $d\epsilon^p$ , i.e.,

$$d\epsilon = d\epsilon^e + d\epsilon^p \quad (1)$$

### 2.1 Elastic Behavior

According to the theory of elastoplasticity, only elastic deformation occurs for stress excursions within yield boundary. The elastic response is expressed as:

$$d\epsilon_v^e = [\kappa_h / (1+e)p] dp \quad (2-a)$$

$$d\epsilon_s^e = dq/3G = [3(1 - 2\nu)(1 + e)p] \cdot dq/[2(1 + \nu)\kappa_h] \tag{2-b}$$

where  $\kappa_h$  is the gradient of unloading or swelling line of GHBS,  $e_v$  is the void ratio and  $\nu$  is the Poisson’s ratio and independent of hydrate saturation[4]. Due to the cementation of hydrates to soils, the stiffness may be enhanced [7]. Therefore  $\kappa_h$  is assumed to be a function of hydrate saturation  $s_h$ , i.e.,

$$\kappa_h = \kappa_0 \cdot e^{\zeta \cdot (s_h - 0.25 \cdot L)} \tag{3}$$

Here,  $\kappa_0$  is the gradient of unloading or swelling line for soils without hydrates,  $\zeta$  is a material parameter and can be acquired by fitting Eq. (3) with experimental data.  $L$  is the index of hydrates formation mode,  $L=0$  for cementation and  $L=1$  for pore filling.

### 2.2 Yield Function for GHBS

In order to account for the influence of hydrate formation on the mechanical behavior for GHBS, we introduce a parameter called bonding strength  $p_b$  to modify the mean effective stress as

$$p^* = p + p_b \tag{4}$$

Thus, the modified stress ratio can be written as

$$\eta^* = q/p^* = q/(p + p_b) \tag{5}$$

Based on the framework of the modified Cam clay model, the yield function for GHBS is given by [10-11]

$$f = p^* (p^* - p_b - p_c - p_m) + q^2 / M^2 \tag{6}$$

$$p_m = k \cdot p_b \tag{7}$$

In Equations (6)-(7),  $p_c$  plays a role similar to the preconsolidation pressure for uncemented soils,  $p_m$  controls the growth rate of the size of the initial elastic domain resulting from the intergranular bonding, and  $k$  is a model parameter and assumed to be 1.0 here for simplicity.  $M$  is the gradient of the failure envelope in the q-p plane, and a lot of experimental results demonstrated that  $M$  is independent of hydrate saturation [3-6]. The yield surface for GHBS is illustrated in the Fig. 1.

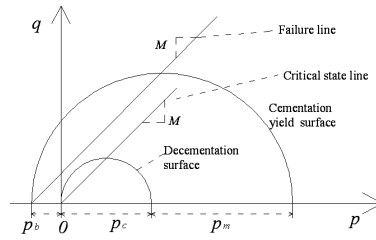


Fig. 1. Effect of hydrate cementation yield and decementation on yielding

### 2.3 Harding Rule and Decementation Law

Based on the results of triaxial compression tests [4-7], GHBS samples clearly show the effects of decementation and dilatance. To capture these features, deviatoric plastic strain,  $\epsilon_s^p$ , is introduced into the hardening rule, which is expressed as

$$dp_c = [(1 + e) p_c / (\lambda_h - \kappa_h)] \cdot [d\epsilon_v^p + M(1 - e^{-\xi \cdot p_b}) d\epsilon_s^p] \tag{8}$$

where  $\lambda_h$  is the plastic compressibility coefficient of GHBS. Sultan & Garziglia [8] suggested that

$$\lambda_h = \lambda_0 [1 - (1 - \lambda_1 / \lambda_0) (1 - \exp(-\beta \cdot (S_h - 0.25 \cdot L)))] \tag{9}$$

Here,  $\lambda_0$  is the plastic compressibility coefficient of the soils without hydrates,  $\lambda_1$  is the plastic compressibility coefficient of hydrate phase and equal to 0.00147 [17],  $\beta$  defines the slope of change of the compressibility with the hydrate saturation.

A decementation process can be divided into two steps: (1) Local decementation takes place before the peak strength, and (2) the collapse of hydrate cementation occurs once the peak strength is arrived.

Here, the content of decementation is assumed to be related to the plastic deviatoric strain  $\epsilon_s^p$ , and the following equation is proposed to describe the phenomenon, i.e.,

$$dp_b = p_b (-\rho_b \cdot d\epsilon_s^p) \tag{10}$$

where  $\rho_b$  is a material parameter. In order to distinguish the two steps of decementation,  $\rho_b$  is assumed a value of  $k_1$  or  $k_2$ , which is shown in Fig.2.

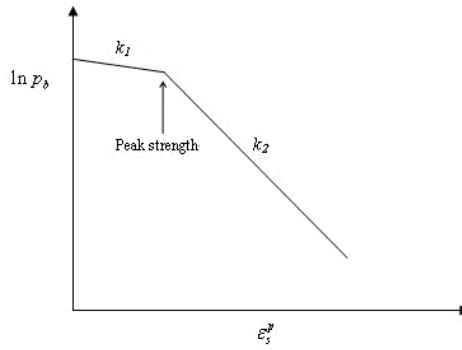


Fig. 2. Schematic diagram for variation of  $p_b$  with plastic strain

### 2.4 Defining $p_b$

Here it is proposed that  $p_b$  varies with hydrate saturation  $S_h$  according to the following relationship:

$$p_b = A \cdot (S_h - 0.25 \cdot L)^B + C \tag{11}$$

where  $A, B, C$  are model parameters, which can be determined by fitting Eq. (11) with experimental data.  $L$  is the index of hydrates formation mode,  $L=0$  for cementation and  $L=1$  for pore filling.

### 2.5 Flow Rule

Li and Dafalias [13] pointed out that dilatancy  $d$  depends not only upon stress ratio  $\eta$ , but also upon the internal state of material. Hereby,  $p_b$  is introduced into the dilatancy  $d$  as an internal state variable, and an equation is given to describe the dilatancy  $d$  for GHBS:

$$d = d(\eta^*, p_b) = M e^{-\xi \cdot p_b} - \eta^* \tag{12}$$

where  $\xi$  is a model parameter.

## 3 Parameter Determination

Summarily, 12 parameters are introduced into the proposed model, and they are  $\lambda_0, \kappa_0, \nu, M, \zeta, \beta, A, B, C, \xi, k_1, k_2$ . The first four model parameters ( $\lambda_0, \kappa_0, \nu, M$ ) are intrinsic soil properties, which are independent of the hydrate saturation. These parameters have the same meaning as those adopted in the Modified Cam Clay

model, and can be easily determined.  $\zeta$  and  $\beta$  are determined by fitting the  $\kappa_h - S_h$  and  $\lambda_h - S_h$  curves with the results of isotropic compression/swelling tests on the GHBS samples at two different hydrate saturation.  $A, B, C$  can be calculated from the curve of  $p_b - S_h$  at three different hydrate saturation, the  $p_b$  of the sample can be deduced from the initial yield point on the stress-strain curve.

Parameter  $\xi$  significantly affects the plastic strain direction, but has no distinctive effect on the stress-strain relationship. Parameter  $k_1$  represents local dementation and has slight effect on the peak strength and the dilatancy. Parameter  $k_2$  influences the strain-softening behavior in such a way that the deviatoric stress decreases more rapidly with a larger  $k_2$ . Parameters  $\xi, k_1$  and  $k_2$  can be estimated from the stress-strain relationship.

### 4 Verification of the GHBS Model

The constitutive model developed was used to simulate the results of triaxial drained tests, which were performed by Masui et al. [14]. The model parameters are listed in Table 1. In Figures 3 and 4, the model simulations are compared with experimental data.

**Table 1.** Model parameters of the GHBS model for GHBS (from Masui et al.,2008)[14]

Parameters	Values		parameters	Values	
	Type A	Type B		Type A	Type B
$e$	0.65	0.65	$B$	0.7	0.7
$\lambda_0$	0.02	0.02	$C$	0.9	0.55
$\kappa_0$	0.012	0.012	$M$	1.2	1.2
$\beta$	2.0	2.0	$\xi$	0.6	0.42
$\zeta$	-1.395	-1.395	$k_1$	0.2	0.2
$\nu$	0.15	0.15	$k_2$	5	5
$A$	3.5	8.255			

In Figure 3, the soil samples with different hydrate saturations (marked as type A) are formed by pore filling; in Figure 4, the soil samples with different hydrate saturations (marked as type B) are formed by cementation. It can be seen that the model predictions agree very well with the experimental data, showing that the proposed model is capable of capturing the main features of the behavior of GHBS, such as the increase of stiffness, peak shear strength, dilatancy and strain softening effect.

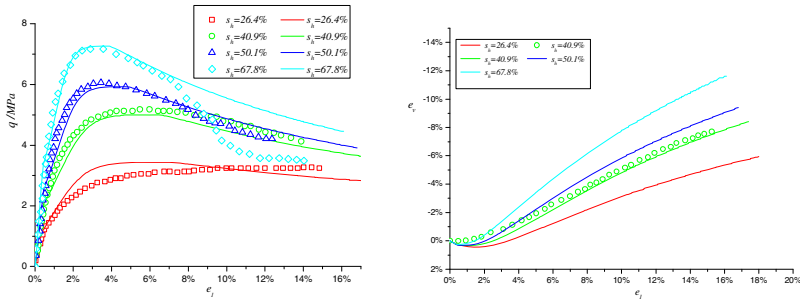


**Fig. 3.** Comparison of experimental and simulated triaxial drained test results (Type A) [14]. Circles represent experimental data, and solid curves represent simulations.

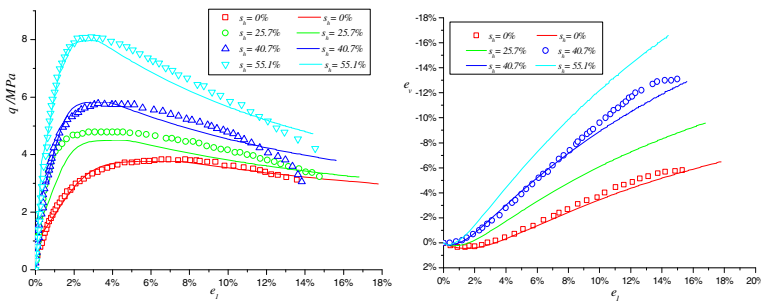


**Fig. 4.** Comparison of experimental and simulated triaxial drained test results (Type B) [14]. Circles represent experimental data, and solid curves represent simulations.

### 5 Conclusions

In this study, an elastoplastic model is proposed based on the framework of the modified Cam clay model, in which GHBS is considered as a bonded material. A new bonding strength parameter is introduced into the yield function to evaluate the effect of gas hydrate on the yield behavior of the GHBS, and dilatancy is assumed to be a function of the bonding strength and the stress ratio. It is demonstrated that the proposed model can captures very well the main features of the behavior of GHBS samples.

**Acknowledgments.** The research is supported by the Natural Science Foundation of China (Grant No. 41102199) and the Breeding Project of “135” Program of IRSM, CAS.

### References

- [1] Sloan, E.D.: Introductory overview: Hydrate knowledge development. *American Mineralogist* 89(8-9), 1155–1161 (2004)
- [2] Sultan, N., et al.: Effect of gas hydrates melting on seafloor slope instability. *Marine Geology* 213(1-4), 379–401 (2004)

- [3] Winters, W.J., et al.: Physical properties of sediment containing methane gas hydrate. In: 229th National Meeting of the American-Chemical-Society, San Diego, CA, Am. Chem. Soc (2005)
- [4] Masui, A., et al.: Mechanical properties of sandy sediment containing marine gas hydrates in deep sea offshore Japan. In: 7th ISOPE Ocean Mining and Gas Hydrates Symposium, Lisbon, Portugal, International Society Offshore & Polar Engineers (2007)
- [5] Winters, W.J., et al.: Physical properties and rock physics models of sediment containing natural and laboratory-formed methane gas hydrate. *American Mineralogist* 89(8-9), 1221–1227 (2004)
- [6] Winters, W.J., et al.: Methane gas hydrate effect on sediment acoustic and strength properties. *Journal of Petroleum Science and Engineering* 56(1-3), 127–135 (2007)
- [7] Yun, T.S., et al.: Mechanical properties of sand, silt, and clay containing tetrahydrofuran hydrate. *Journal of Geophysical Research-Solid Earth* 112(B4) (2007)
- [8] Grozic, J.L.H., Ghiassian, H.: Undrained shear strength of methane hydrate-bearing sand; preliminary laboratory results. In: Proceedings of the 63rd Canadian Geotechnical Conference, GEO 2010, Calgary (2010)
- [9] Gens, A., Nova, R.: Conceptual Bases for a Constitutive Model for Bonded Soils and Weak Rocks. In: Anagnostopoulos, A., Schlosser, F., Kaltefleiter, N., Frank, R. (eds.) *Geotechnical Engineering of Hard Soils - Soft Rocks*, vol 1 - Geological Features, Investigation and Classification; Mechanical Properties and Behaviour, pp. 485–494. A a Balkema, Rotterdam (1993)
- [10] Liu, M.D., Carter, P.: A structured cam clay model. Research Report - University of Sydney, Department of Civil Engineering (814), 1–67 (2002)
- [11] Suebsuk, J., et al.: Modified Structured Cam Clay: A generalised critical state model for destructured, naturally structured and artificially structured clays. *Computers and Geotechnics* 37(7-8), 956–968 (2010)
- [12] Durham, W.B., et al.: The strength and rheology of methane clathrate hydrate. *Journal of Geophysical Research* 108(B4), 2182 (2003)
- [13] Li, X.S., Dafalias, Y.F.: Dilatancy for cohesionless soils. *Geotechnique* 50(4), 449–460 (2000)
- [14] Masui, A., et al.: Effects of methane hydrate formation on shear strength of synthetic methane hydrate sediments. In: Proceeding of the Fifteenth International Offshore and Polar Engineering Conference, Seoul, Korea, pp. 19–24 (2005)

# A Review of Constitutive Modeling of Bonded Soil

W.M. Yan

Department of Civil Engineering, The University of Hong Kong, HKSAR, China  
ryanyan@hku.hk

**Abstract.** Inter-particle bonds exist in both naturally and artificially cemented geomaterials. The bonds affect the mechanical response of the materials and make it differ from the remolded counterparts. In this paper, some recently proposed constitutive models for bonded soils are reviewed from the perspective of yield surface, flow rule and hardening law. The approach of phenomenological and thermomechanical modeling is discussed. The use of discrete element method to shed light on the modeling issue is explored.

## 1 Introduction

Since the development of the critical state framework ([1,2]) and many decades of extensive investigation on the mechanical behavior, many constitutive models which successfully capture the key aspects of the soil response have been proposed for remolded soils from a continuum perspective. Many of them have been implemented into a variety of numerical packages to study the laboratory- or field-scale boundary value problems. It has been well recognized that geomaterials in its natural or intact state behave distinctly different from their remolded counterparts. Increasing research effort has been spent to understand the mechanical behavior of bonded soils ([3–6]) and recently on the development of the constitutive model ([7–9]). In this study, three recently developed constitutive models for bonded soils are reviewed from the perspective of modeling approach: phenomenological v.s. thermomechanical modeling. Lastly, the use of discrete element analysis to shed light on the issue is explored.

## 2 Plasticity Model for Particulate Materials

In continuum solid mechanics, there are three essential ingredients for a plasticity model. They are (1) yield surface, (2) flow rule and (3) hardening law. Yield surface refers to a boundary (usually convex) in the stress space to differentiate elastic and elasto-plastic behavior. For particulate materials which are frictional in nature, the yield surface, defined in the stress space, can be represented by

$f(\boldsymbol{\sigma}, \zeta_n) = 0$  where  $\boldsymbol{\sigma}$  describes the stress state and  $\zeta_n$  is a set of hardening parameters (which can be scalar, tensorial or a combination of both). Consider a stress state on the yield surface. The quantity  $(\partial f / \partial \boldsymbol{\sigma}) : d\boldsymbol{\sigma} > 0, = 0,$  and  $< 0$  denotes plastic loading, neutral loading and elastic unloading, respectively. Flow rule defines the direction of the plastic strain increment  $d\boldsymbol{\varepsilon} = \lambda (dg / d\boldsymbol{\sigma})$  when subject to a plastic loading where  $g$  is the flow potential and  $\lambda$  is a positive scalar factor of proportionality called the loading index. One will have the associative flow rule when  $g = f$ , and non-associative otherwise. Note that choosing the associative flow rule is merely for convenient in most cases and there is no sound theoretical background. Hardening law describes the evolution of yield surface through the evolution of  $\zeta_n$  with the plastic work (work hardening) or the plastic strain  $\boldsymbol{\varepsilon}^P$  (strain hardening, which is more commonly adopted). The condition of consistency  $df = 0$  holds, as shown in Eq. (1), and  $\partial \zeta_n / \partial \boldsymbol{\varepsilon}^P$  is referred to as the hardening law.

$$df = \frac{\partial f}{\partial \boldsymbol{\sigma}} : d\boldsymbol{\sigma} + \frac{\partial f}{\partial \zeta_n} \frac{\partial \zeta_n}{\partial \boldsymbol{\varepsilon}^P} \cdot d\boldsymbol{\varepsilon}^P = 0 \quad (1)$$

### 3 Yield Surface

A general approach which has been adopted in the modeling of bonded soils is the use of an enlarged yield surface when compared to the remolded ones. When a phenomenological approach is used, such enlargement is ad-hoc. Baudet and Stallebrass [7] employed the sensitivity framework concept which uses a scaling factor  $s \geq 1$  (sensitivity) to enlarge the yield surface of the remolded one ([10]). Note that  $s$  characterizes the degree of bonding and it is a hardening parameter which degrades with plastic loading. The soil could approach a metastable structure when subject to shear when  $s \rightarrow s_f \neq 0$ . In their model, tensile strength of the bonded soil is not considered. Yu et al. [8] used two additional parameters ( $p_c$  and  $p_t$ ) to expand the yield surface of the remolded soil to both positive and negative direction of the mean stress axis. The parameters, describing the initial condition, characterize the additional strengths (both compressive and tensile) of the soil provided by the bonds.

On the other hand, the thermomechanical approach ([11,12]) as adopted in Yan and Li [9] provides an energy-consistent framework for the development of models for dissipative materials. The proposal of yield surface in the stress space is no longer ad-hoc. Yet, it is resulted from the balance of dissipative stress work and internal material dissipation in the dissipative stress space based on a dissipation function. The yield surface is then mapped from the dissipative stress space to the

actual stress space though the introduction of back stress, which accounts for the energy stored in the dissipative material. In the case of bonded soils, inter-particle bonds contribute to this back-stress. The yield surface is expanded to both compression and tension sides of the mean stress axis due to the introduction of back stress, which is now theoretically sound. It is worth noting that in the two versions of Cam-clay models for remolded soils, their yield functions are also derived based on energy dissipation (see [13]).

## 4 Flow Rule

Like many other soil models, perhaps for simplicity, associative flow rule is employed in Baudet and Stallebrass [7]. Yu et al. [8], on the other hand, adopted a non-associative flow rule in which a plastic potential function is derived following the stress-dilatancy relationship proposed by Rowe [14]. When a thermomechanical approach is used, following Ziegler [15], associative flow rule is necessarily in the dissipative stress space. Any ad-hoc introduction of associative or non-associative flow rule in the actual stress space becomes redundant and improper. Clearly, through the introduction of back stress for the mapping between the dissipative and the actual stress, non-associative flow rule in the actual stress space holds in general (see also the discussion in [11]).

## 5 Hardening Law

The evolution of bonding is usually defined in an incremental form. Baudet and Stallebrass [7] defined  $\delta s / s \propto \delta \mathcal{E}^p$  while Yu et al. [8] defined  $\delta p_c / p_c \propto \delta \mathcal{E}^p$ . In both models,  $\delta \mathcal{E}^p$  is the plastic strain increment which takes both volumetric and deviatoric components into consideration ( $\delta \mathcal{E}^p = \sqrt{(\delta \mathcal{E}_v^p)^2 + (\delta \mathcal{E}_q^p)^2}$ ). Yu et al. [8] further defined the hardening/softening of remolded soil as  $\delta p_0 / p_0 \propto (\delta \mathcal{E}_v^p + \omega \delta \mathcal{E}_q^p)$  where  $p_0$  denotes the size of the yield surface of the remolded soil and  $\omega$  is a factor to be calibrated which represents the relative contribution of  $\delta \mathcal{E}_q^p$  to the evolution of  $p_0$ . Theoretically it means that a complete destructuration (or metastable structure in [7]) can only occur at infinitely large plastic strain. Furthermore, such hardening law ( $\delta \zeta_b / \zeta_b \propto \delta \mathcal{E}^p$ ) implies a form of exponential decay of the bond characterizing parameter  $\zeta_b$  with the cumulative plastic strain.

Yan and Li [9] adopted a slightly different approach. An internal variable  $\xi_b$ , which is an accumulated plastic deformation, is introduced to reflect the bonding condition.

$$\xi_b = p_{\text{atm}} \int \sqrt{\frac{\delta \boldsymbol{\varepsilon}^P : \delta \boldsymbol{\varepsilon}^P}{(p - p_b - p_0/2)^2}} \quad (2)$$

where  $p_{\text{atm}}$  is a reference pressure taken at the atmospheric condition,  $\delta \boldsymbol{\varepsilon}^P$  is the plastic strain increment,  $p$  is the mean normal stress,  $p_b$  describes the increase in size of the yield surface into the tension region due to bonding, and  $p_0$  characterizes the size of the yield surface. The hardening parameter  $p_0$  and  $p_b$  can be expressed as a function of  $\xi_b$  and their hardening with plastic loading can then be derived. One can see that  $\xi_b = 0$  at the soil's intact state (usually the initial state of a simulation). Besides,  $\xi_b = \infty$  is used to simulate the complete destructuration of the material, which can be happened either (1) at a very large plastic strain level ( $\int \sqrt{\delta \boldsymbol{\varepsilon}^P : \delta \boldsymbol{\varepsilon}^P} \rightarrow \infty$ ) or (2) when  $p = p_b + p_0/2$  as defined in their model formulation. The first condition happens in which a progressive bond breakage takes place, for instance an isotropic or oedometric compression. The second condition, which offers a unique feature of the model, is able to model an abrupt (brittle) failure of the bonded materials in which a complete destroy of bonds occurs abruptly. Such behavior cannot be modeled by [7,8].

## 6 Insights from Discrete Element Analysis

In the past decade, discrete element method (DEM) has become an important tool to understand the soil behavior from a microscopic perspective ([16]). It is believed that with the ability of quantifying microscopic parameters of a granular assemblage, DEM could shed light on the development of constitutive models for bonded soils, which has been found successful in cohesionless granular assemblages ([17]). Yan [18] presented a simple three-dimensional DEM analysis on a bonded assemblage subject to triaxial deviatoric shearing. The data of a drained compression test is re-analyzed and the evolution of bond breakage is shown in Figure 1. It can be seen that the bond counts (bond survival) resembles an exponential decay with strain, which echoes the evolution of hardening parameters ( $s$ ,  $p_c$ ,  $p_b$  etc) in the aforementioned models. It clearly reveals the physical origins of these hardening parameters at the particulate level (bond counts). More importantly, the DEM analysis backs up the use of the current mathematical form of the hardening law. It is expected that further discrete element analyses could help understand the interplays among the bond strength, bond degradation, bond structure, and the model constants in a continuum model.

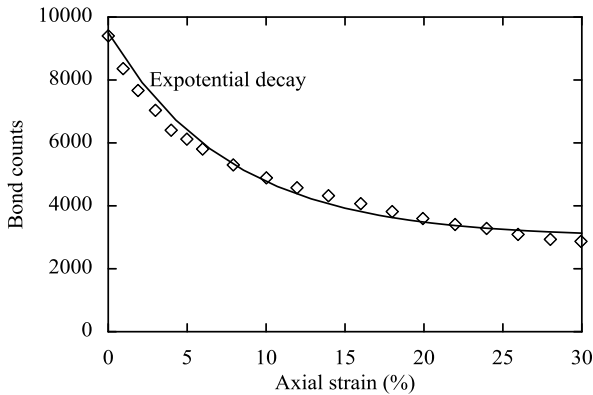


**Fig. 1.** Evolution of the bond breakage during a DEM analysis on bonded assemblage

## 7 Summary

In this paper, the development of constitutive modeling of bonded geomaterials is discussed from the perspective of phenomenological and thermomechanical approach. Different approaches that work out the main ingredients of a continuum plasticity model are evaluated with the help of three recently developed models. The use of discrete element analysis to shed light on the issue is also discussed.

## References

- [1] Roscoe, K.H., Schofield, A.N., Wroth, W.P.: On the yielding of soils. *Géotechnique* 8(1), 22–53 (1958)
- [2] Schofield, A.N., Wroth, C.P.: *Critical state soil mechanics*. McGraw-Hill, London (1968)
- [3] Burland, J.B.: On the compressibility and shear strength of natural clays. *Géotechnique* 40(3), 329–378 (1990)
- [4] Leroueil, S., Vaughan, P.R.: The general and congruent effects of structure in natural soils and weak rocks. *Géotechnique* 40(3), 467–488 (1990)
- [5] Burland, J.B., Rampello, S., Georgiannou, V.N., Calabresi, G.: A laboratory study of the strength of four stiff clays. *Géotechnique* 46(3), 491–514 (1996)
- [6] Callisto, L., Calabresi, G.: Mechanical behaviour of a natural soft clay. *Géotechnique* 48(4), 495–513 (1998)
- [7] Baudet, B.A., Stallebrass, S.: A constitutive model for structured clays. *Géotechnique* 54(4), 269–278 (2004)
- [8] Yu, H.S., Tan, S.M., Schnaid, F.: A critical state framework for modelling bonded geomaterials. *Geomech. Geoeng: An Int. J.* 2(1), 61–74 (2007)
- [9] Yan, W.M., Li, X.S.: A model for natural soil with bonds. *Géotechnique* 61(2), 95–106 (2011)
- [10] Cotecchia, F., Chandler, R.J.: A general framework for the mechanical behaviour of clays. *Géotechnique* 50(4), 431–447 (2000)

- [11] Collins, I.F., Houlsby, G.T.: Application of thermomechanical principles to the modelling of geotechnical materials. *Proc. R. Soc. London Ser. A* 453, 1975–2001 (1997)
- [12] Houlsby, G.T., Puzrin, A.M.: A thermomechanical framework for constitutive models for rate-independent dissipative materials. *Int. J. Plasticity* 16, 1017–1047 (2000)
- [13] Collins, I.F., Kelly, P.A.: A thermomechanical analysis of a family of soil models. *Géotechnique* 52(7), 507–518 (2002)
- [14] Rowe, P.W.: The stress-dilatancy relation for static equilibrium of an assembly of particles in contact. *Proc. R. Soc. London* 269, 500–527 (1962)
- [15] Ziegler, H.: An introduction to thermomechanics. North-Holland, Amsterdam (1985)
- [16] O’Sullivan, C.: Particulate discrete element modelling: a geomechanics perspective. CRC Press (2011)
- [17] Yan, W.M., Dong, J.: Effect of particle grading on the response of an idealized granular assemblage. *Int. J. Geomech.* 11(4), 276–285 (2011)
- [18] Yan, W.M.: Yield surface expansion due to bonding in granular material. In: Inaugural Int. Conf. Eng. Mech. Instit., Minnesota, CD-ROM (2008)

# A Unified Description of Toyoura Sand

Feng Zhang<sup>1</sup>, Bin Ye<sup>2</sup>, and Guanlin Ye<sup>3</sup>

<sup>1</sup> Nagoya Institute of Technology, Nagoya, Japan

<sup>2</sup> Tongji University, Shanghai, China

<sup>3</sup> Shanghai Jiaotong University, Shanghai, China

**Summary.** In this paper, the mechanical behavior of sand, was systematically described and modeled. Without losing the generality of the sand, a specific sand called as Toyoura sand, a typical clean sand found in Japan, has been discussed in detail. In the model, the results of conventional triaxial tests of the sand under different loading and drainage conditions were simulated with a fixed set of material parameters. The model only employs eight parameters among which five parameters are the same as those used in Cam-clay model. Once the parameters are determined with the conventional drained triaxial compression tests and undrained triaxial cyclic loading tests, and then they are fixed to uniquely describe the overall mechanical behaviors of the Toyoura sand, without changing the values of the eight parameters irrespective of what kind of the loadings or the drainage conditions may be. The capability of the model is discussed in a theoretical way.

## 1 Introduction

In recent years, research on constitutive model for soils has been developing very quickly. Some works in particular are worthy of mention in advance. Hashiguchi and Ueno (1977), Hashiguchi (1989) proposed the concept of “subloading”, making it possible to describe the overconsolidation of soils easily and efficiently. Asaoka et al. (1998), Asaoka et al. (2000a), and Asaoka et al. (2000b) proposed the concept of “superloading”, together with the concept of subloading, making it possible not only to describe overconsolidation, but also to explain the effect of the soil structure commonly observed in naturally deposited soils, which is one of the main reasons why soils may differ greatly from place to place. Zhang et al. (2007) proposed a new constitutive model for sand, in which in addition to the concept of superloading related to the soil skeleton structure (Asaoka et al., 1998) and the concept of subloading related to the density (Hashiguchi and Ueno, 1977), a new approach to describe the stress-induced anisotropy was introduced. Based on the model, mechanical behavior of fictional sand subjected to different loadings under different drainage conditions were simulated to verify if the model was suitable to describe the general behavior of the sand with one set of definite parameters (Zhang et al., 2010). Particular attention was paid to the description of the

sand subjected to cyclic loading under undrained conditions, that is, for loose sand, liquefaction happens without transition from contractive state to dilative state; for medium dense sand, cyclic mobility occurs while for dense sand, liquefaction will not occur.

The influence of intermediate stress was carefully investigated which leads to the establishment of  $t_{ij}$  models (Nakai, 1989). Apart from the  $t_{ij}$  concept (Nakai and Mihara, 1984), Yao et al (2008) and Wan et al (2010) discussed the influence of intermediate stress and proposed a concept of transform stress (TS) by which it is also possible to describe this dependency. The advantage of TS concept is that the constitutive model established in  $p$ - $q$  stress space can be easily extended to true triaxial stress space without any change or adding of material parameters. In this paper, the authors try to use the model (Zhang et al., 2007), to describe the overall mechanical behaviors of Toyoura Sand, a typical clean sand, in a unified way. In other words, all the behavior of Toyoura Sand, no matter what loading and drainage conditions may be, its mechanical behavior is described with a fixed set of material parameters. The model proposed by Zhang et al (2007) is firstly given in an infinitesimal strain level. Then the influence of intermediate principal stress is taken into consideration by adopting the TS concept. It is important to be emphasized here that the eight material parameters involved in the model, will be constant no matter what kind of loading or drainage conditions may be.

## 2 Constitutive Model of Sand

Here just a brief description of the yield surfaces is given as shown in Figure 1 and Figure 2.

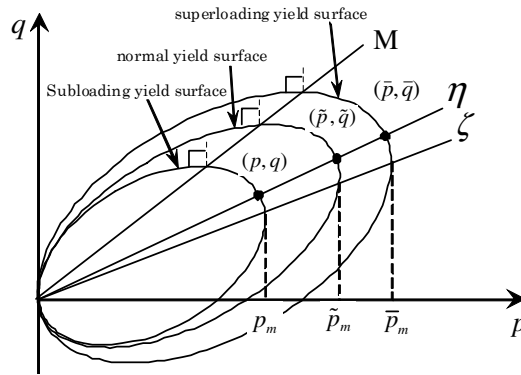


**Fig. 1.** Subloading, normal and superloading yield surfaces in  $p$ - $q$  plane adopted in the present model

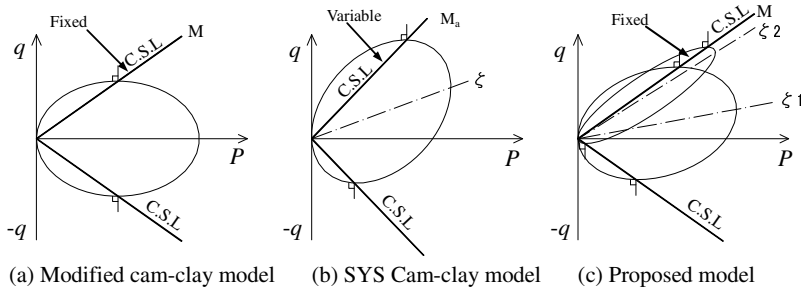


**Fig. 2.** Changes in the subloading yielding surfaces at different anisotropy  $\zeta$

The similarity ratio of the superloading yield surface to normal yield surface  $R^*$  and the similarity ratio of the superloading yield surface to subloading yield surface  $R$  are the same as those in the work by Asaoka et al. (2002), namely,

$$R^* = \frac{\tilde{p}}{p} = \frac{\tilde{q}}{q}, \quad 0 < R^* \leq 1 \tag{1}$$

$$R = \frac{p}{\bar{p}} = \frac{q}{\bar{q}}, \quad 0 < R \leq 1 \tag{2}$$

$$\frac{\bar{q}}{\bar{p}} = \frac{\tilde{q}}{\tilde{p}} = \frac{q}{p} \quad (\text{Similarity of yield surfaces}) \tag{3}$$

where  $(p, q)$ ,  $(\tilde{p}, \tilde{q})$  and  $(\bar{p}, \bar{q})$  represent the present stress state, the corresponding normally consolidated stress state and the structured stress state at  $p$ - $q$  effective stress space respectively, which is only related to a conventional triaxial stress ( $\sigma_{22} = \sigma_{33}, q = \sigma_{11} - \sigma_{33}$ ).

The normally yield surface is given in the following form as:

$$f = \ln \frac{\sigma_m}{\sigma_{m0}^*} + \ln \frac{M^2 - \varsigma^2 + \eta^{*2}}{M^2 - \varsigma^2} + \ln R^* - \ln R - \frac{\varepsilon_v^p}{C_p} = 0 \tag{4}$$

$$\eta^* = \sqrt{\frac{3}{2} \hat{\eta}_{ij} \hat{\eta}_{ij}}, \quad \hat{\eta}_{ij} = \eta_{ij} - \beta_{ij}, \quad \eta_{ij} = \frac{S_{ij}}{\sigma_m}, \quad \sigma_m = p = \sigma_{ii} / 3 \tag{5}$$

$$\eta = \sqrt{\frac{3}{2} \eta_{ij} \eta_{ij}}, \quad \varsigma = \sqrt{\frac{3}{2} \beta_{ij} \beta_{ij}} \quad C_p = \frac{\lambda - \kappa}{1 + e_0} \tag{6}$$

The consistency equation for the subloading yield surface can then be given as:

$$df = 0 \Rightarrow \frac{\partial f}{\partial \sigma_{ij}} d\sigma_{ij} + \frac{\partial f}{\partial \beta_{ij}} d\beta_{ij} + \frac{1}{R^*} dR^* - \frac{1}{R} dR - \frac{1}{C_p} d\varepsilon_v^p = 0 \tag{7}$$

- It is very clear from Figure 2 that the flat ratio of the elliptical yield surface changes with the value of anisotropy.

1) Evolution rule for stress-induced anisotropic stress tensor  $\beta_{ij}$

The following evolution rule for the anisotropic stress tensor is defined as:

$$d\beta_{ij} = \Lambda \frac{\sqrt{6}Mb_r(M - \varsigma)\hat{\eta}_{ij}}{C_p(M^2 - \varsigma^2 + \eta^{*2})\sigma_m} \tag{8}$$

From Equation(9), it is known that anisotropy will stop its development at the time when  $\varsigma$  approaches to  $M$ .

2) Evolution rule for degree of structure  $R^*$

$$dR^* = \Lambda \frac{2aMR^*(1 - R^*)\eta^*}{C_p(M^2 - \varsigma^2 + \eta^{*2})\sigma_m} \tag{10}$$

Here,  $a$  is a parameter that controls the rate of the collapse of the structure during shearing. From the definition, it is clear that the structure of a soil will never be regained once it has been lost.

3) Evolution rule for degree of overconsolidation  $R$

The changing rate of overconsolidation is assumed to be controlled by two factors, the plastic component of stretching and the increment in anisotropy.

$$dR = \Lambda \frac{-mM \ln R \sqrt{6\eta^{*2} + \frac{1}{3}(M^2 - \eta^2)^2}}{C_p(M^2 - \varsigma^2 + \eta^{*2})\sigma_m} \left[ \frac{(\sigma_m / \sigma_{m0})^2}{(\sigma_m / \sigma_{m0})^2 + 1} \right] + R \frac{\eta}{M} \frac{\partial f}{\partial \beta_{ij}} d\beta_{ij} \tag{11}$$

$$\Lambda = \frac{\frac{\partial f}{\partial \sigma_{ij}} E_{ijkl} d\varepsilon_{kl}}{h_p + \frac{\partial f}{\partial \sigma_{ij}} E_{ijkl} \frac{\partial f}{\partial \tilde{\sigma}_{kl}}} \tag{12}$$

$$h_p = \frac{1}{C_p(M^2 - \varsigma^2 + \eta^{*2})\sigma_m} [M_s^2 - \eta^2] \tag{13}$$

where,  $m$  is a parameter that controls the losing rate of overconsolidation  $R$  during shearing.

The loading criteria are given as:

$$\begin{cases} \Lambda > 0 & \text{loading} \\ \Lambda = 0 & \text{neutral} \\ \Lambda < 0 & \text{unloading} \end{cases} \quad (14)$$

The above Equations were discussed in conventional triaxial stress space. Then the TS concept proposed by Yao et al (2008) was adopted to taken into consideration of the intermediate stress dependency. The detailed description about this model in TS space is omitted because of the same form of the equations in the conventional triaxial stress space. Details can be referred to the works by Yao et al (2008) and Wan et al (2010). In the following section, all the calculations are carried out in TS space.

### 3 Determination of Material Parameters

Among the eight parameters involved in the model, five parameters,  $M$ ,  $N$ ,  $\lambda$ ,  $\kappa$  and  $v$  are the same as in the Cam-clay model. The other three parameters and their functions are listed as follows.

- $a$  : Parameter that controls the collapse rate of structure
- $m$  : Parameter that controls the losing rate of overconsolidation
- $b_r$  : Parameter that controls the developing rate of stress-induced anisotropy

**Table 1.** Material parameters of Toyoura Sand

Compression index $\lambda$	0.050
Swelling index $\kappa$	0.0064
Critical state parameter	1.30
Void ratio $N$ ( $p=98$ kPa on <i>N.C.L.</i> )	0.87
Poisson's ratio	0.30
Degradation parameter of overconsolidation state $m$	0.01
Degradation parameter of structure $a$	0.50
Evolution parameter of anisotropy $b_r$	1.50

These three parameters have clear physical meanings and can be determined by undrained triaxial cyclic loading tests and drained triaxial compression tests. Parameter  $m$  can be determined based on the losing rate of overconsolidation of soil sample in conventional triaxial compression tests. Parameter  $a$  can be determined

based on the collapse rate of the structure of the soil sample formed in its natural depositary process, as shown in the work by Asaoka et al (2002). Parameter  $b_r$  can be determined based on the developing rate of the stress-induced anisotropy of the soil sample in undrained triaxial cyclic loading tests. The detailed can be referenced to the work by Zhang et al (2010, 2011). The material parameters of Toyoura Sand used in this paper is shown in table 1.

## 4 Verification of the Model by Tests

### 4.1 Confining-Stress Dependency of Sand in Undrained Monotonic Loading Test

It is reported in the research by Verdugo and Ishihara (1996) that under the same void ratio, the sand behaves like a loose sand if the confining stress is large and the sand behaves like dense sand if the confining stress is small. Such a phenomenon originally defined by Ishihara (1993) is called as “confining-stress dependency of sand”. The mechanical behavior of sands with the same density but different confining stresses can also be reproduced uniquely with one set of the same material parameters in all different conditions by simulation as shown in Figure 5. The simulated results on the whole coincide well with the test results by Verdugo and Ishihara (1996) in Figure 4 quantitatively and qualitatively.

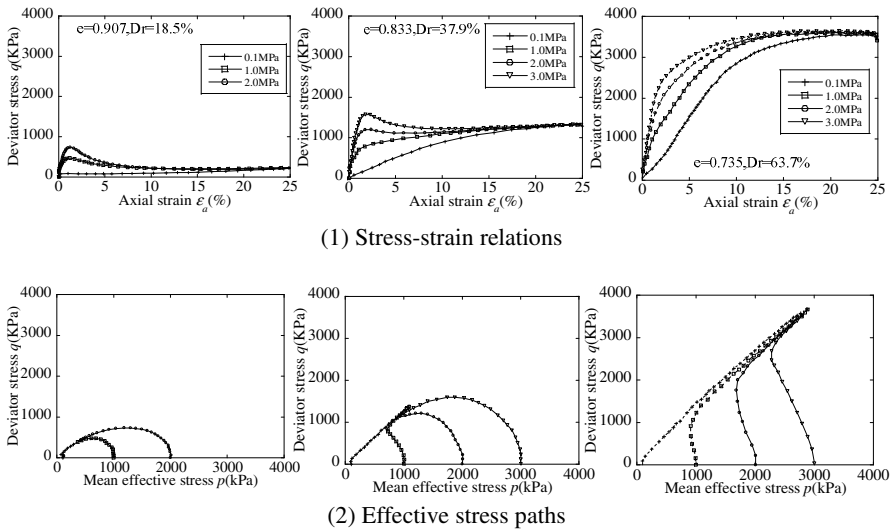


**Fig. 4.** Test results of stress paths and stress-strain relations of Toyoura Sand with the same void ratio but different confining stress in undrained triaxial compression test (Verdugo and Ishihara, 1996)

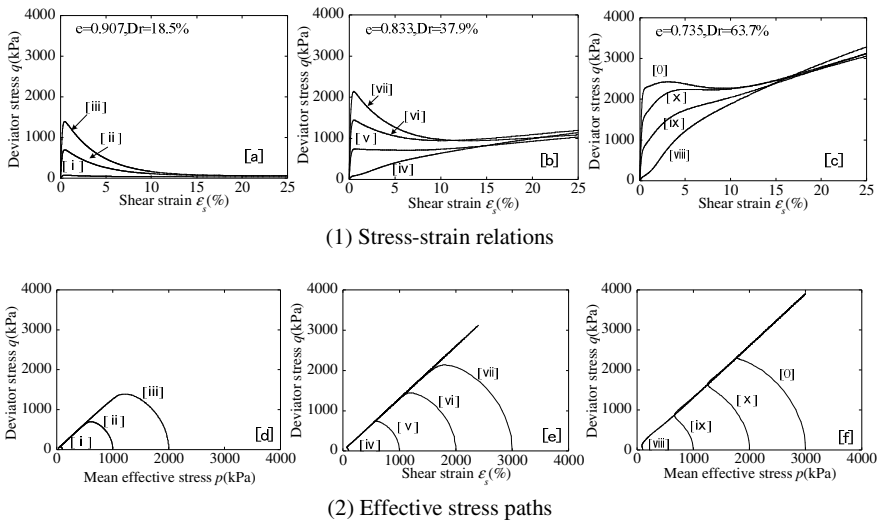


Fig. 5. Simulation of the test results in Figure 4

### 4.2 Sand Subjected to Drained Cyclic Loading

The behaviors of dense sand subjected to drained cyclic loading under constant mean effective stress were simulated. As can be seen in Figure 7, the overall characteristics of the sand predicted by the present model, for instance, the changes in dilatancy and stress-strain relations, agree qualitatively well with the test results in Figure 6 by Hinokio (2000), but showing a slight over-estimation of volume strain.

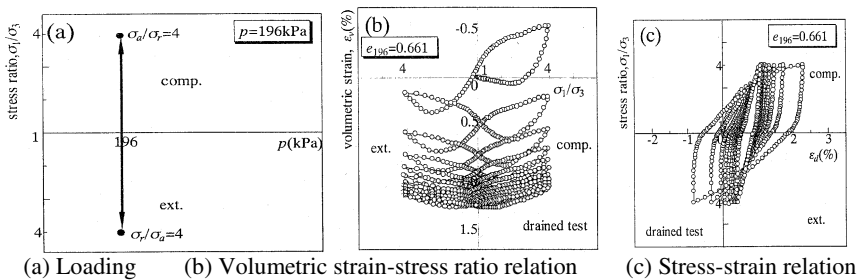


Fig. 6. Test results of dense sand in drained cyclic loading tests (Hinokio, 2000)

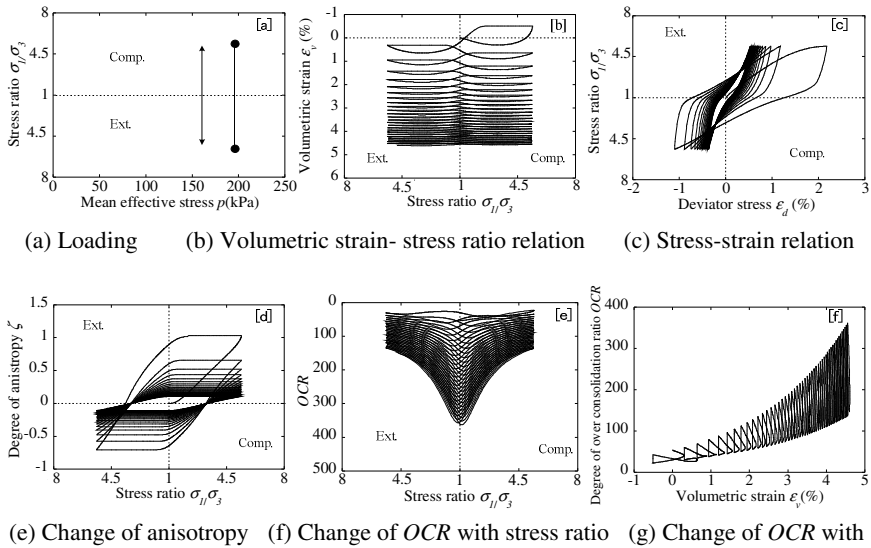


Fig. 7. Simulation of the test results in Figure 6

## 5 Performance of the Model

### 5.1 Influence of Density

Eight groups of sands with different densities are simulated in cyclic loading tests with a confining stress of 196 kPa. The amplitude of the cyclic loading in shear stress ratio ( $q / 2p_0$ ) is 0.12. Figure 8 shows the stress paths and stress-strain relations of the sands with different densities in undrained tests. It is clear from the figures that very loose sands ([1] & [2]) generate a large failure strain along the path directly towards the zero effective stress state without transition from contractive state to dilative state. For relatively loose sands ([3] & [4]), they also generate large failure strain at last but transition from contractive state to dilative state. However, for medium dense sands ([5] & [7]), cyclic mobility occurs and the strain increases gradually to a relatively larger scale. On the other hand, the dense sand ([8]) only generates a small amount of strain and never shows cyclic mobility. Therefore, the mechanical behavior of sand subjected to undrained cyclic loading can be uniquely and properly described by the constitutive model under the condition that all the material parameters are kept constant.

### 5.2 Influence of Stress-Induced Anisotropy

The stress-induced anisotropy has great influence on the mechanical behavior of sand subjected to consequential loadings. This influence can be investigated

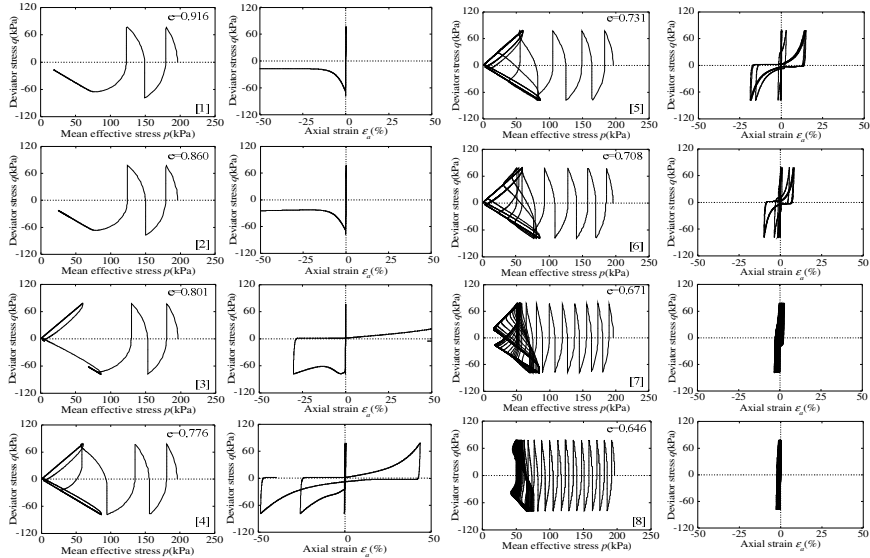
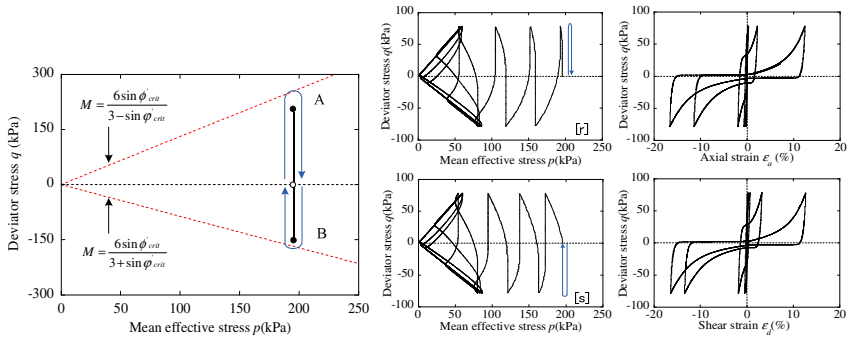


**Fig. 8.** Stress paths, stress-strain relations of the sand specimens with different densities subjected to cyclic triaxial test under undrained condition



(a) Effective stress paths (b) Stress-strain relations

**Fig. 9.** Prescribed loading path under drained condition

**Fig. 10.** Influence of initial anisotropic

through two sand samples [r] and [s], which have almost the same properties in the state variables but different stress-induced anisotropy  $\zeta_0$  at the beginning of undrained triaxial cyclic loading tests. A different stress-induced anisotropy is obtained by different loading direction of the samples [r] and [s] as shown in Figure 9. Then different behaviors of the samples with different stress-induced anisotropy under undrained condition by simulation are shown in Figure 10. Further discussion about the influence of the stress-induced anisotropy can be referred to the work by Ye et al (2011).

### 5.3 Influence of Structure

Four sands [2], [4], [7] and [8] are considered to identify the influence of the structure. Sands [2], [4], [7] and [8] with the structure, are marked by [a], [b], [c] and [d]. While the sands without the structure marked by [e], [f], [g] and [h] are almost the same as the sands marked by [2], [4], [7] and [8], that is  $R^*$  is always equal to 1.0. As to the mechanical behavior of the sands with the structure shown in Figure 11(1), very loose sand will fail along the way directly towards the original, the zero effective stress state in the effective stress space, before the cyclic mobility has a chance to occur; Medium dense sand shows cyclic mobility; Dense sand will never show cyclic mobility. Comparing the behavior of the set of sands without the structure as shown in Figure 11(2) with those in Figure 11(1), it is implicated that the liquefaction behavior of loose sand is impossible to be described properly when the structure is not considered. For dense sand, though the structure does not affect the behavior of the sand in the cyclic mobility region so much as the loose sand, the shape of the effective stress path is affected more or less.

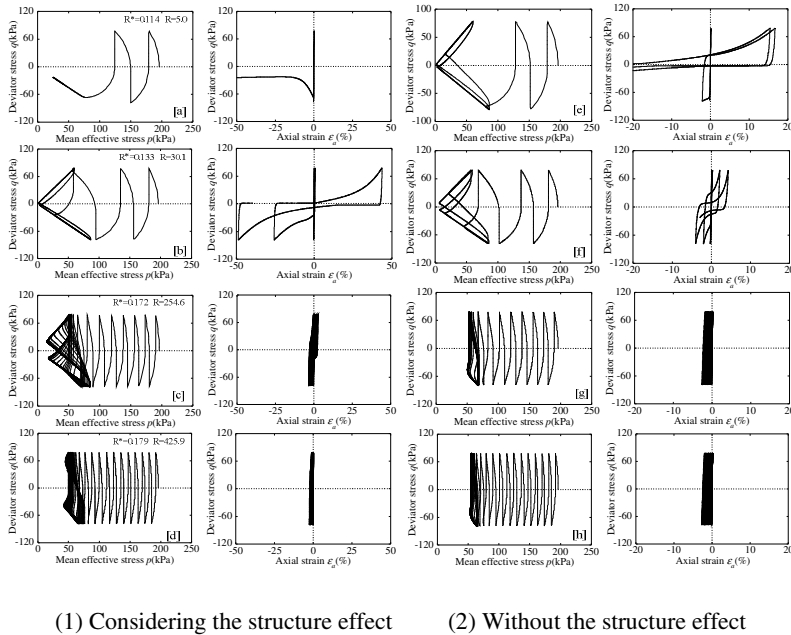


Fig. 11. Influence of the structure

### 5.4 Difference between Clayey Soils and Sandy Soils

According to the works by Asaoka et al. (2000a), the difference between clayey soils and sandy soils depends on the rate of loss in overconsolidation and the rate

of the collapse of the structure during static shearing. For sandy soils, the rate of loss in overconsolidation is very slow, while the rate of the collapse of the structure is very fast. On the contrary, for clayey soils, the rate of loss in overconsolidation is very fast, while the rate of the collapse of the structure is very slow.

A set of soils with the same initial conditions but different values for  $a$  and  $m$ , which control the changing rates of overconsolidation and the collapse of the structure, are investigated for their behavior when subjected to cyclic loading under undrained conditions. Figure 12 shows the different behavior of soils from sandy soil to clayey soil subjected to cyclic loading under undrained condition. From the figure, it is very clear that by changing parameters  $a$  and  $m$ , the difference between sandy soils and clayey soils can be easily and uniquely identified.

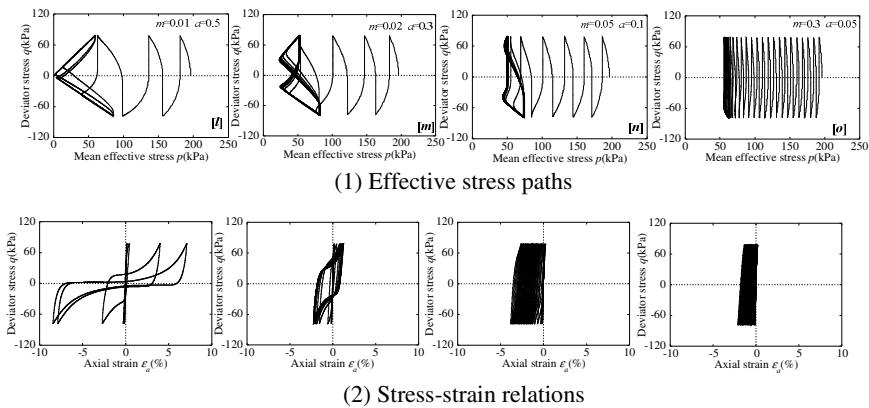


Fig. 12. Difference between clay and sand

## 6 Conclusions

In this paper, the capability of the model to give a unified description of the overall behaviors with fixed values of eight parameters is verified. By introducing the TS concept, the influence of intermediate principal stress on mechanical behavior of sand can be properly taken into consideration, without changing any value of the material parameters if compared with those adopted in conventional triaxial stress condition.

It cannot say that the model can perfectly describe the various behaviors of Toyoura Sand, but that the model can give a unified description of Toyoura Sand with quite satisfactory accuracy only by using eight material parameters with fixed value. On the other hand, in some very specific aspects, such as the non-coaxial property, which have been pursued for years by many researchers, should be done in future to verify the applicability of the model.

## References

- Asaoka, A., Nakano, M., Noda, T.: Super loading yield surface concept for the saturated structured soils. In: Proc. of the Fourth European Conference on Numerical Methods in Geotechnical Engineering-NUMGE 1998, pp. 232–242 (1998)
- Asaoka, A., Nakano, M., Noda, T.: Superloading yield surface concept for highly structured soil behavior. *Soils and Foundations* 40(2), 99–110 (2000a)
- Asaoka, A., Nakano, M., Noda, T., Kaneda, K.: Delayed compression/consolidation of naturally clay due to degradation of soil structure. *Soils and Foundations* 40(3), 75–85 (2000b)
- Asaoka, A., Noda, T., Yamada, E., Kaneda, K., Nakano, M.: An elasto-plastic description of two distinct volume change mechanisms of soils. *Soils and Foundations* 42(5), 47–57 (2002)
- Hashiguchi, K., Ueno, M.: Elastoplastic constitutive laws of granular material, Constitutive Equations of Soils. In: Murayama, S., Schofield, A.N. (eds.) *Pro. 9th Int. Conf. Soil Mech. Found. Engrg., Spec. Ses. 9, Tokyo*, pp. 73–82. JSSMFE (1977)
- Hashiguchi, K.: Subloading surface model in unconventional plasticity. *Int. J. of Solids and Structures* 25, 917–945 (1989)
- Nakai, T., Mihara, Y.: A new mechanical quantity for soils and its application to elastoplastic constitutive models. *Soils and Foundations* 24(2), 82–94 (1984)
- Nakai, T.: An isotropic hardening elastoplastic model for sand considering the stress path dependency in three-dimensional stresses. *Soils and Foundations* 29(1), 119–137 (1989)
- Nakai, T., Hinokio, M.: A simple elastoplastic model for normally and over consolidated soils with unified material parameters 44(2), 53–70 (2004)
- Hinokio, M.: Deformation characteristic of sand subjected to monotonic and cyclic loadings and its application to bearing capacity problem, Doctoral Thesis, Nagoya Institute of Technology, 141–144 (2000) (in Japanese)
- Ishihara, K.: Liquefaction and flow failure during earthquake. In: *The 33rd Rankine Lecture, Geotechnique* (1993)
- Verdugo, R., Ishihara, K.: The steady state of sandy soils. *Soils and Foundations* 36(2), 81–91 (1996)
- Wan, Z., Yao, Y.P., Wang, N.D., Ye, B.: 3-D Zhang's model based on the TS method. *Soils and Foundations* (2010) (in printing)
- Yao, Y.P., Sun, D.A., Matsuoka, H.: A unified constitutive model for both clay and sand with hardening parameter independent on stress path. *Computers and Geotechnics* 35(2), 210–222 (2008)
- Ye, B., Ye, G.L., Zhang, F.: Numerical modeling of changes in anisotropy during liquefaction. *Soils and Foundations* (2011) (in printing)
- Zhang, F., Ye, B., Noda, T., Nakano, M., Nakai, K.: Explanation of cyclic mobility of soils: approach by stress-induced anisotropy. *Soils and Foundations* 47(4), 635–648 (2007)
- Zhang, F., Jin, Y., Ye, B.: A try to give a unified description of Toyoura sand. *Soils and Foundations* 50(3), 679–693 (2010)
- Zhang, F., Ye, B., Ye, G.L.: Unified description of sand behavior. *Frontiers of Architecture and Civil Engineering in China* 5(2), 121–150 (2011)

# A Structured UH Model

Enyang Zhu and Yangping Yao

Department of Civil Engineering  
Beihang University  
No.37 Xueyuan Road, Beijing, China, 100191  
junesun@ce.buaa.edu.cn, ypyao@buaa.edu.cn

**Summary.** Based on the UH model, a structured UH model is formulated to express the constitutive relation of structured clay. The keynote of the work is presenting a moving normal compression line (MNCL) in void ratio-mean effect stress plan. The MNCL is a straight line parallel to and higher than the normal compression line (NCL) of reconstituted clay. The difference between the MNCL and the NCL is defined as structure potential. As structure decay, the MNCL gradually declines and finally achieves to the NCL when the structure decays completely. In considering the temporal stress history, the MNCL, instead of NCL, is referred to determine the quasi-over-consolidation stress. By adopting a simple law of the structure potential evolution, void collapse due to the structure decay can be described. In the structured UH model, only 2 more parameters than that of the Cam-clay model are introduced, which are respectively structure potential and its decay rate factor. Comparisons of the model predictions and tests results indicate that the structured UH model is qualified in capturing the main behaviors of the structured clay.

**Keywords:** structured clay, constitutive relation, structure decay, plasticity, UH model.

## 1 Introduction

Natural clay behaves quite differently from artificial reconstituted clay. It is said that the properties of a natural clay differ from its intrinsic properties due to the influence of soil structure [1]. Thus, either in theoretical study or in practical engineering, structure is necessary to be considered. Nevertheless, many distinguished constitutive models are formulated specific to ideal and homogeneous reconstituted clay. The classical Cam-clay model is one of them [2]. Although the Cam-clay model is formulated specific to the normally consolidated clay, due to its strictness, clearness and simplicity, even now the Cam-clay model is still widely referred in engineering. Thus formulating structured constitutive model on the bases of the Cam-clay model will not only enhance the completeness of the Cam-clay family but also make the formulated model more applicable in practical engineering. And this idea had been accepted by many researchers [3-10].

Based on the Cam-clay model, the UH model was formulated specific to over-consolidated clay, whose parameters are the same as the Cam-clay model [11]. By model verifications, the UH model is qualified in continuously and reasonably describing many behaviors of over-consolidated clay, such as hardening, softening, positive or negative dilation, un-drained stress path and repeated loading etc. Considering that the structured clay in the nature also be influenced by the stress history more or less, thus it might be realizable to develop a structured constitutive model from a constitutive model specific to over-consolidated clay. Therefore, a structured UH model developed from the UH model is formulated tentatively in this paper.

Before further study, only isotropic structure is considered in the structured UH model. All the stresses mentioned in the paper are effective stresses. It is defined that  $\sigma_1, \sigma_2, \sigma_3$  represent principle stresses, and  $\varepsilon_1, \varepsilon_2, \varepsilon_3$  represent principle strains. All of stresses and strains are positive for compression. The mean effective stress  $p$ , deviator stress  $q$ , volume strain  $\varepsilon_v$  and deviator strain  $\varepsilon_d$  are given by

$$p = \frac{1}{3}(\sigma_1 + \sigma_2 + \sigma_3) \quad (1)$$

$$q = \frac{1}{\sqrt{2}} \sqrt{(\sigma_1 - \sigma_2)^2 + (\sigma_1 - \sigma_3)^2 + (\sigma_2 - \sigma_3)^2} \quad (2)$$

$$\varepsilon_v = \varepsilon_1 + \varepsilon_2 + \varepsilon_3 \quad (3)$$

$$\varepsilon_d = \frac{\sqrt{2}}{3} \sqrt{(\varepsilon_1 - \varepsilon_2)^2 + (\varepsilon_1 - \varepsilon_3)^2 + (\varepsilon_2 - \varepsilon_3)^2} \quad (4)$$

In addition, since that the UH model is firstly formulated in  $p - q$  stress space and then be reasonably made three-dimensional by transformed stress [12], the structured UH model also follows suit. So in this paper, the structured UH model is only introduced in  $p - q$  stress space.

## 2 Moving Normal Compression Line

The structure effect in one-dimensional compression is well illustrated by Wesley's tests [13] in Fig.1, where  $e$  represents void ratio and  $\sigma_v$  represents vertical stress. As shown in Fig.1, the structured clay can hold greater void ratio than the reconstituted one at the same stress. This viewpoint has also been agreed by some other researchers [14-16]. In the initial compression phase, decrease of void ratio of

the structured clay is not obvious. As compression going on, change of void ratio transforms from slight reduction to sharp reduction gradually, and finally the compression line of the structured clay tends to combine with that of the reconstituted clay.

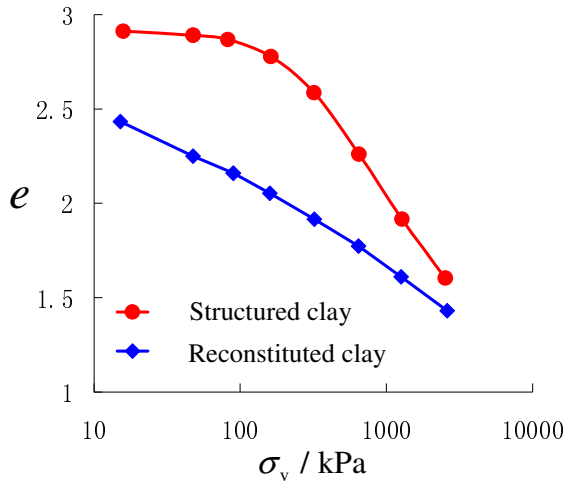


Fig. 1. One-dimensional compression tests (Wesley, 1974)

Stress-strain relationship under isotropic compression is analogous to that under one-dimensional compression. Relationships of  $e$  and  $p$  in isotropic compression on normally consolidated clay, over-consolidated clay and structured clay, are illustrated in Fig.2. The relationship of  $e$  and  $p$  for normally consolidated clay is a straight line expressed by normal compression line (NCL) in  $e - \ln p$ , which is widely referred in the critical state soil mechanics. According to the isotropic compression behaviors of over-consolidated clay and the corresponding description by the UH model, the gradient of compression line of the over-consolidated clay increases gradually and finally tents to the gradient of NCL as the compression going on [11]. In the meanwhile, by referring to the NCL, current stress states pass through points  $r_0, r_1, r_2$  and  $r_3$  one another, with the corresponding pre-consolidation stress states passing through points  $r'_0, r'_1, r'_2$  and  $r'_3$  one another. However, the structured clay behaves differently. For the compression on the structured clay, initially the void ratio does not decrease remarkably as compression on over-consolidated clay. Then the compression line of the structured clay passes through the NCL and holds a greater void ratio than the NCL at the same stress. Afterwards, the gradient of compression line firstly increases to a value greater than the gradient of NCL and then decreases to the gradient of NCL gradually. All of these are observed in Fig.1 and indicated in Fig.2.

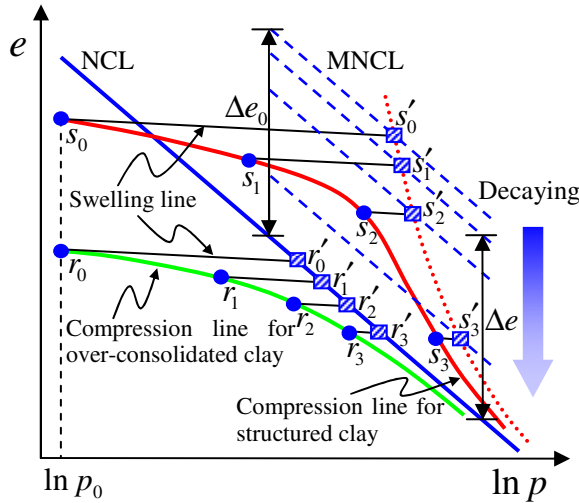


Fig. 2. Illustration of MNCL

The over-consolidation phenomenon presented in the initial phase of the structured clay compression attributed to both structure formulation and stress history is very common in the nature and should be considered in the structured UH model. This is the main reason of formulating a structured UH model from the UH model specific to over-consolidated clay.

In compression on the over-consolidated clay, the NCL is used for reference. Corresponding to the current stress state locating on point  $r_i$  ( $i = 0, 1, 2, 3$ ), the pre-consolidation stress is determined by point  $r'_i$ . Comparing with the reference effect of the NCL in over-consolidated clay compression, a moving NCL (MNCL) in  $e - \ln p$  plan used for reference as well is presented in this paper. MNCL is a straight line parallel to and higher than NCL, which represents current normal consolidation state corresponding to the current structure. The height difference between the MNCL and the NCL indicates the structure degree, which is defined as structure potential and expressed by  $\Delta e$ . As compression going on, the MNCL declines with structure decaying, and finally the MNCL and NCL coincide when the structure decays completely. Similar to the over-consolidated clay compression, the MNCL is applied to determine the so called pre-consolidation stress for the structured clay. Due to the MNCL being moving and related to the structure, here the so called pre-consolidation stress for the structured clay is different from the traditional one, which is named quasi-pre-consolidation stress. As shown in Fig.2, corresponding to the current stress state point  $s_0, s_1, s_2$  and  $s_3$  for the structured clay, the quasi-pre-consolidation stress state locates on point  $s'_0, s'_1, s'_2$  and  $s'_3$  respectively. In loading, that every quasi-pre-consolidation stress state locating on different MNCLs presents the process of the declining of the MNCL due to structure decay.

Just as indicated in Fig.2, there are 2 motions occur in loading on the structured clay. One is the approaching of point  $s_i$  and point  $s'_i$  ( $i = 0, 1, 2, 3$ ) and the other is the declining of the MNCL. The compound of these two motions formulates the particular isotropic compression line of the structured clay. The law of the approaching of point  $s_i$  and point  $s'_i$  can be described similarly as the UH model. And the description of the declining of the MNCL is actually the evolution of  $\Delta e$ . Being of great importance in considering structure decay, the evolution of  $\Delta e$  will be introduced later in the structured UH model formulating.

### 3 The Structured UH Model

The main work of extending the UH model to consider structure is making the reference line (MNCL) to be moving which is the essential of the structured UH model.

Isotropic compression is also applied in the following introduction. As indicated in Fig.3, plastic void ratio increment  $de^p$ , resulted from the isotropic stress increment  $dp = p_2 - p_1$ , is composed of two parts. One part due to loading with the temporal MNCL being static is represented by  $de^{ps}$ , and the other part attributed to the declining of the MNCL due to structure decay (which is assumed to be unrecoverable and plastic) is represented by  $d(\Delta e)$ .

$$de^p = de^{ps} + d(\Delta e) \tag{5}$$

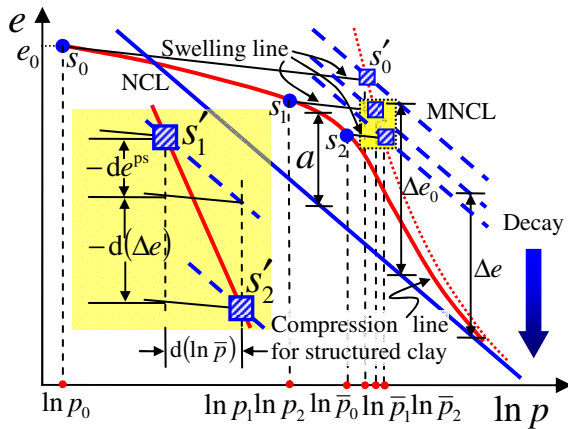


Fig. 3. Two parts of void ratio increments of structured clay in isotropic compression

By extension, equation (5) can also be applied in three-dimensional condition. Thus, the total plastic strain increment  $d\epsilon_i^p$  is composed of  $d\epsilon_i^{ps}$  due to loading with the temporal MNCL being static and  $d\epsilon_i^{pc}$  due to structure decay.

$$d\epsilon_i^p = d\epsilon_i^{ps} + d\epsilon_i^{pc} \quad (i = 1, 2, 3) \tag{6}$$

Since in this paper the constitutive relation is taken into account only in  $p - q$  stress plan, just plastic volume strain  $\epsilon_v^p$  and plastic deviator strain  $\epsilon_d^p$  are involved.

$$d\epsilon_v^p = d\epsilon_v^{ps} + d\epsilon_v^{pc} \tag{7}$$

$$d\epsilon_d^p = d\epsilon_d^{ps} + d\epsilon_d^{pc} \tag{8}$$

In equations (7) and (8),  $d\epsilon_v^{ps}$  and  $d\epsilon_d^{ps}$  are respectively plastic volume strain increment and plastic deviator strain increment due to loading with the temporal MNCL being static; while  $d\epsilon_v^{pc}$  and  $d\epsilon_d^{pc}$  are respectively plastic volume strain increment and plastic deviator strain increment due to structure decay.

The plastic strain increments  $d\epsilon_v^{ps}$  and  $d\epsilon_d^{ps}$  are calculated with the temporal MNCL being static. This is similar to the calculation described by the UH model. Therefore, in the structured UH model, plastic strain increments  $d\epsilon_v^{ps}$  and  $d\epsilon_d^{ps}$  can be calculated similarly.

In the structured UH model, there are two yield surfaces as the UH model. The current yield surface  $f$  passing through the current stress point  $(p, q)$  and the reference yield surface  $\bar{f}$  passing through the reference stress point  $(\bar{p}, \bar{q})$  are indicated in Fig.4. The similarity ratio of the current yield surface and the reference yield surface is  $R$ .

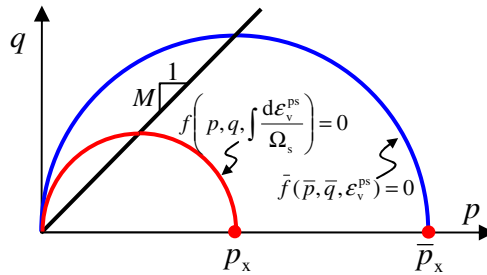


Fig. 4. Yield surfaces of the structured UH model

Functions of this two yield surfaces are written as:

$$f = c_p \left( \ln \frac{p}{p_0} + \ln \frac{M^2 + \eta^2}{M^2} \right) - H = 0 \tag{9}$$

$$\bar{f} = c_p \left( \ln \frac{\bar{p}}{\bar{p}_0} + \ln \frac{M^2 + \bar{\eta}^2}{M^2} \right) - \varepsilon_v^{ps} = 0 \tag{10}$$

In equation (9) and (10),  $c_p = (\lambda - \kappa)/(1 + e_0)$ ;  $\lambda$  and  $\kappa$  are respectively the gradients of compression and swelling line of reconstituted clay in  $e - \ln p$  plan;  $e_0$  is the initial void ratio; stress ratios  $\eta = q/p$  and  $\bar{\eta} = \bar{q}/\bar{p}$ ; parameter  $M$  is critical state stress ratio;  $p_0$  and  $\bar{p}_0$  are respectively the initial intercepts of the current yield surface and the reference yield surface on  $p$  axis; While hardening parameter  $H$  is expressed as:

$$H = \int dH = \int \frac{d\varepsilon_v^{ps}}{\Omega_s} \tag{11}$$

In equation (11), parameter  $\Omega_s = R^{4(M_f - \eta)} \cdot \frac{M^4 - \eta^4}{M_f^4 - \eta^4}$ ;  $M_f$  is inner variable

named potential failure stress ratio, which can be expressed as a function of  $R$  according to the UH model [17, 18].

$$M_f = 6 \left[ \sqrt{\frac{\chi}{R} \left( 1 + \frac{\chi}{R} \right)} - \frac{\chi}{R} \right] \tag{12}$$

where  $\chi = M^2 \sqrt{[12(3 - M)]}$ . Comparing with the parameter  $\Omega (= (M^4 - \eta^4)/(M_f^4 - \eta^4))$  in the UH model [11], the parameter  $\Omega_s$  expressed in equation (11) is a little different. A factor  $R^{4(M_f - \eta)}$  is added into parameter  $\Omega_s$  to increase the modulus. More details about the factor  $R^{4(M_f - \eta)}$  will be discussed later. Referring equation (9) and (10), parameter  $R$  can be calculated by

$$R = \frac{p}{\bar{p}_0} \left( 1 + \frac{\eta^2}{M^2} \right) \exp \left( - \frac{\varepsilon_v^{ps}}{c_p} \right) \tag{13}$$

Differentiating equation (9), the plastic volume strain increment  $d\varepsilon_v^{ps}$  due to loading with the temporal MNCL being static for structured clay can be solved

$$d\varepsilon_v^{ps} = \Omega_s \cdot \left( \frac{\partial f}{\partial p} dp + \frac{\partial f}{\partial q} dq \right) \tag{14}$$

The deviator strain  $\epsilon_d^{ps}$  compounds with  $\epsilon_v^{ps}$  by dilation equation of the Cam-clay model [2].

$$\frac{d\epsilon_v^{ps}}{d\epsilon_d^{ps}} = \frac{M^2 - \eta^2}{2\eta} \tag{15}$$

In the calculation of volume strain  $\epsilon_v^{pc}$ , the evolution law of  $\Delta e$  is necessary as indicated in Fig.3. According to the investigation of structure decay, two features should be followed by the evolution law of  $\Delta e$ : (a) Since the structure decay is unrecoverable, the value of  $\Delta e$  must be monotonously decreasing; (b) Since the MNCL finally combines with NCL when the structure decay completely, the rate of decay of  $\Delta e$  should tends to be zero as  $\Delta e$  tends to be zero.

According to the structured UH model, as loading going on in drained test, firstly the current yield surface expands with  $(\partial f / \partial p)dp + (\partial f / \partial q)dq > 0$  until  $\eta = M_f$ . After that, stress ratio  $\eta$  begins to decrease gradually and the current yield surface shrinks with  $(\partial f / \partial p)dp + (\partial f / \partial q)dq < 0$  and  $\eta > M_f$ . Finally stress ratio  $\eta$  achieves to the critical state stress ratio  $M$ . Bases on the above, an evolution of  $\Delta e$  decaying with the expansion of the current yield surface is abstracted here.

$$d(\Delta e) = -\rho \cdot \Delta e \cdot R^4 \cdot \left\langle \frac{\partial f}{\partial p} dp + \frac{\partial f}{\partial q} dq \right\rangle \tag{16}$$

In equation (16),  $\rho$  is a parameter that describes the rate of structure decaying; a factor  $R^4$  here is applied to consider the quasi-over-consolidation effect to structure decay. In addition, Macaulay brackets are used here to ensure the non-negativity, which is defined as

$$\langle x \rangle = \begin{cases} x & x \geq 0 \\ 0 & x < 0 \end{cases} \tag{17}$$

As indicated in Fig.3, in isotropic compression for instance, current stress states  $s_i$  declines with the quasi-pre-consolidation stress states  $s'_i$  synchronously. Thus the volume strain increment  $d\epsilon_v^{pc}$  attributed to structure decay can be solved directly from  $d(\Delta e)$ .

$$d\epsilon_v^{pc} = \Omega_c \left\langle \frac{\partial f}{\partial p} dp + \frac{\partial f}{\partial q} dq \right\rangle \tag{18}$$

where  $\Omega_c = \rho \cdot \Delta e \cdot R^4 / (1 + e_0)$ .

It is assumed for simplicity that plastic strain attributed to the structure decay is isotropic. Therefore, structure decay leads to no deviator strain.

$$d\epsilon_d^{pc} = 0. \tag{19}$$

Substituting equation (14) and (18) into equation (7), the plastic volume strain increment  $d\epsilon_v^p$  for the structured clay is obtained:

$$d\epsilon_v^p = \Omega_s \left( \frac{\partial f}{\partial p} dp + \frac{\partial f}{\partial q} dq \right) + \Omega_c \left\langle \frac{\partial f}{\partial p} dp + \frac{\partial f}{\partial q} dq \right\rangle \tag{20}$$

Substituting equation (15) and (19) into equation (8), the plastic deviator strain increment  $d\epsilon_d^p$  for the structured clay is obtained:

$$d\epsilon_d^p = \Omega_s \cdot \frac{2\eta}{M^2 - \eta^2} \cdot \left( \frac{\partial f}{\partial p} dp + \frac{\partial f}{\partial q} dq \right) \tag{21}$$

Here is the appropriate opportunity to explain the factor  $R^{4(M_f - \eta)}$  in detail. Considering both equations (9) and (11), total differentiating equation (13), then the increment of parameter  $R$  is obtain

$$dR = \frac{R}{c_p} \cdot \left( \frac{M_f^4 - \eta^4}{M^4 - \eta^4} \cdot \frac{1}{R^{4(M_f - \eta)}} - 1 \right) \cdot d\epsilon_v^{ps} \tag{22}$$

Considering the plastic deviator strain increment  $d\epsilon_d^p = d\epsilon_d^{ps}$  is always positive as loading and according to equation (24), the evolution of parameter  $R$  (always  $< 1$ ) is expressed as follows.

When  $0 < \eta < M$  ,  $d\epsilon_v^{ps} > 0$  by equation (15), and

for  $\left( \frac{M_f^4 - \eta^4}{M^4 - \eta^4} \cdot \frac{1}{R^{4(M_f - \eta)}} - 1 \right) > 0$ , thus  $dR > 0$ ;

When  $M < \eta < M_f$  ,  $d\epsilon_v^{ps} < 0$  by equation (15), and

for  $\left( \frac{M_f^4 - \eta^4}{M^4 - \eta^4} \cdot \frac{1}{R^{4(M_f - \eta)}} - 1 \right) < 0$ , thus  $dR > 0$ ;

When  $\eta > M_f$  in softening,  $d\mathcal{E}_v^{ps} < 0$  by equation (15), and for  $\left(\frac{M_f^4 - \eta^4}{M^4 - \eta^4} \cdot \frac{1}{R^{4(M_f - \eta)}} - 1\right) < 0$ , thus  $dR > 0$  is also satisfied. These reasonably and necessarily indicate the non-negativity of increment  $dR$  in the whole loading process and insure the monotonic of the quasi-over-consolidation decay.

However, if the factor  $R^{4(M_f - \eta)}$  is changed for another factor  $R^\alpha$  (where  $\alpha$  is a constant positive value), the monotonic of the quasi-over-consolidation decay in loading might be disturbed. As  $\eta > M_f$ ,  $0 < \frac{M_f^4 - \eta^4}{M^4 - \eta^4} < 1$ . And in the whole process of loading,  $\frac{1}{R^\alpha} > 1$  is satisfied. So in this condition, inequality  $\left(\frac{M_f^4 - \eta^4}{M^4 - \eta^4} \cdot \frac{1}{R^\alpha} - 1\right) < 0$  might not be always satisfied. This is the essential purpose for adding the factor  $R^{4(M_f - \eta)}$ .

The elastic volume strain increment  $d\mathcal{E}_v^e$  and the elastic deviator strain increment  $d\mathcal{E}_d^e$  follow Hook's law.

$$\begin{cases} d\mathcal{E}_v^e = \frac{1}{K} dp \\ d\mathcal{E}_d^e = \frac{1}{3G} dq \end{cases} \tag{23}$$

In equation (23),  $K = (1 + e_0)p/\kappa$ ,  $G = 3(1 - 2\nu)(1 + e_0)p/[2\kappa(1 + \nu)]$ , and  $\nu$  is Poisson's ratio.

Considering equation (20), (21) and (23), the incremental expression of the structured UH model in  $p - q$  plan is:

$$\begin{cases} d\varepsilon_v = \Omega_s \cdot df_{pq} + \Omega_c \cdot \langle df_{pq} \rangle + \frac{1}{K} dp \\ d\varepsilon_d = \Omega_s \cdot \frac{2\eta}{M^2 - \eta^2} \cdot df_{pq} + \frac{1}{3G} dq \end{cases} \quad (24)$$

where  $df_{pq} = (\partial f / \partial p) \cdot dp + (\partial f / \partial q) \cdot dq$ .

### 4 Parameters

There are 7 parameters in the structured UH model, which are  $\lambda$ ,  $\kappa$ ,  $M$ ,  $\Gamma$ ,  $\nu$ ,  $\Delta e_0$  and  $\rho$ . The first 5 parameters are the same as the Cam-clay model or the UH model, which are well documented, thus they will not be investigated here. For describing the structure and its decay, 2 new parameters  $\Delta e_0$  and  $\rho$  are introduced in the structured UH model. The initial structure potential  $\Delta e_0$  is applied to reflect the initial degree of structure. Parameter  $\rho$  is applied to express the rate of structure decay.

As the structured UH model follows the UH model, elasto-plastic strains are produced both in normally consolidated state and over-consolidated state, which have been illustrated in Fig.2. Thus for structured clay, even loading at quasi-over-consolidated state, structure decays. Therefore, as indicated in Fig.3, the initial structure potential  $\Delta e_0$  is surely larger than the value  $a$  which is the greatest difference of the void ratio between the NCL and the isotropic compression line of the structured clay in  $e - \ln p$  plan. So the initial structure potential  $\Delta e_0$  can not be obtained directly from the isotropic compression test on structured clay. Moreover, even  $\Delta e_0$  is determined, different value of  $\rho$  can also influence the simulated value of  $a$  by the model. So parameters  $\Delta e_0$  and  $\rho$  are some degree interfered each other.

Consequently, before further study, the practical method to determine the 2 new parameters is trial and error. Trying different couples of  $\Delta e_0$  and  $\rho$ , the one makes the best simulation of the isotropic compression test on the structured clay is chosen as the model parameter.

### 5 Verifications

Behavior of void ratio change from structure decay in compression is one of the main differences between structured clay and reconstituted clay. Thus compression test with constant stress ratio  $\eta$  [19] and one-dimensional compression test [20] on Leda clay are recommended to compare with the model predictions in Fig.5. The parameters for Leda clay in constant stress ratio compression are listed in Table 1,

and the constant stress ratios  $\eta$  are 0, 0.63 and 1 respectively. In addition, the Leda clays in the two tests come from different location, so structures of them are surely a little different. Thus the structure parameters for one-dimensional compression on Leda clay is  $\Delta e_0 = 0.748$  and  $\rho = 31$ .

**Table 1.** Parameters for Leda clay (for constant stress ratio compression)

$\lambda$	$\kappa$	$M$	$\Gamma$	$\nu$	$\Delta e_0$	$\rho$
0.223	0.03	1.2	2.338	0.25	0.771	14

Prediction of constitutive relationship in triaxial compression is also necessary for model verification. Tests on Corinth canal marl [21] are cited here and compared with model predictions in Fig.6 and Fig.7. Parameters for Corinth canal marl are listed in Table 2. Fig.6 indicates the isotropic compression and Fig.7 indicates the conventional triaxial compression with the confining pressures  $\sigma_3$  being respectively 98kPa, 294kPa, 903kPa, 1500kPa and 4000kPa.

**Table 2.** Parameters for Corinth canal marl

$\lambda$	$\kappa$	$M$	$\Gamma$	$\nu$	$\Delta e_0$	$\rho$
0.04	0.008	1.3	0.775	0.25	0.123	110

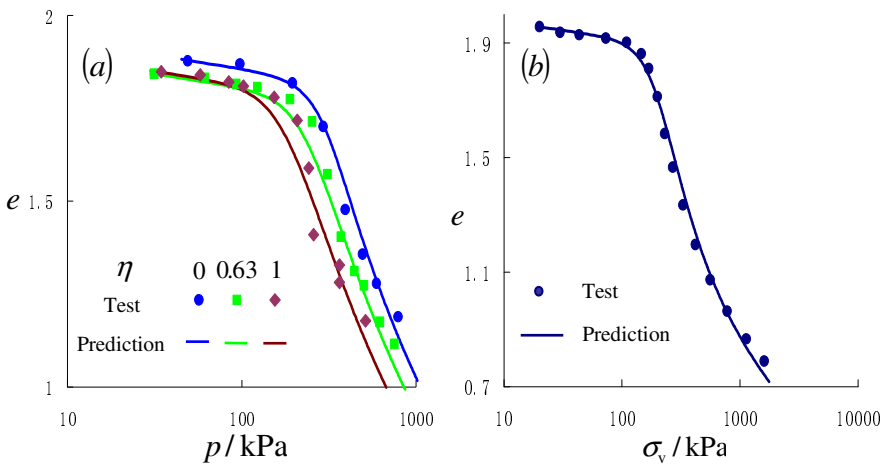


**Fig. 5.** Compression test: (a) Constant stress ratio compression (Walker and Raymond, 1969), (b) One-dimensional compression (Yong and Nagaraji, 1977).

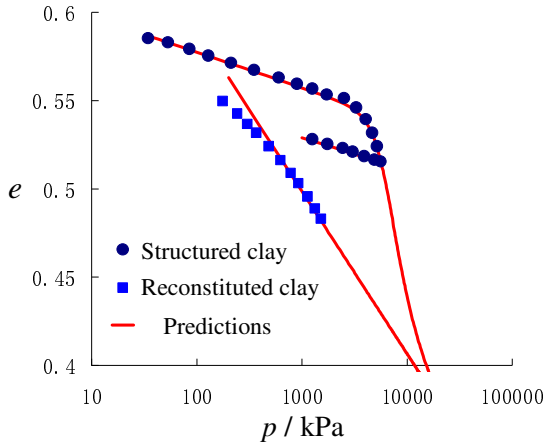


Fig. 6. Isotropic compression (Anagnostopoulos et al. 1991)

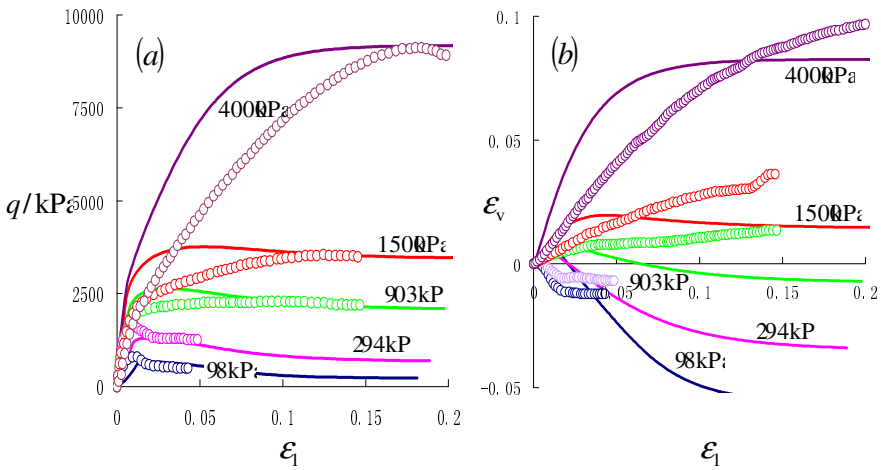


Fig. 7. Conventional triaxial compression (Anagnostopoulos et al. 1991)

It can be seen from Fig.5 to Fig7 that the structured UH model is qualified in capturing the main behaviors of the structured clay.

## 6 Conclusions

By adopting the initial structure potential  $\Delta e_0$  to express the structure degree and the parameter  $\rho$  to describe the structure decay rate, the UH model is extended to the structured UH model, which has the following characteristics.

- (a) Referring to the MNCL instead of referring to the static NCL in  $e - \ln p$  plan, structure effect and its decay are considered into the constitutive model.
- (b) The structured UH model can continuously simulate hardening, softening, positive/negative dilation and void collapse etc. of the structured clay.
- (c) As the structure and the quasi-over-consolidation all decay completely, the structured UH model degrades into the Cam-clay model.

**Acknowledgements.** This study was supported by the national natural science foundation of china (grant no. 11072016; no. 51179003), and the specialized research fund for the doctoral program of higher education of china (grant no. 20091102110030).

## References

- [1] Burland, J.B.: On the compressibility and shear strength of natural clays. *Geotechnique* 40(3), 329–378 (1990)
- [2] Roscoe, K.H., Burland, J.B.: On the generalized stress-strain behaviors of an ideal wet clay. In: Heyman, J., Leckie, F.A. (eds.) *Engineering Plasticity*, pp. 535–609. Cambridge University Press, Cambridge (1968)
- [3] Liu, M.D., Carter, J.P.: A structured Cam Clay model. *Canadian Geotechnical Journal* 39(4), 1313–1332 (2002)
- [4] Carter, J.P., Liu, M.D.: Review of the structured cam clay model. In: *ASCE Conference Proceedings: Proceedings of the Sessions of the Geo-Frontiers, Soil Constitutive Models: Evaluation, Selection, and Calibration*, pp. 99–132 (2005)
- [5] Asaoka, A., Nakano, M., Noda, T.: Superloading yield surface concept for highly structured clay behavior. *Clays and Foundations* 40(2), 99–110 (2000)
- [6] Kavvandas, M., Belokas, G.: An anisotropic elasto-plastic constitutive model for natural clays. In: Desai, C.S. (ed.) *Proceedings of the 10th International Conference on Computer Methods and Advance in Geomechanics*, vol. 1, pp. 335–340. Balkema, Tucson (2001)
- [7] Kavvandas, M., Amorosi, A.: A constitutive model for structured clays. *Geotechnique* 50(3), 263–273 (2000)
- [8] Sivakumar, V., Doran, I.G., Graham, J.: The effect of anisotropic elasticity on the yielding characteristics of overconsolidated natural clay. *Canadian Geotechnical Journal* 38(1), 125–137 (2001)
- [9] Baudet, B., Stallebrass, S.: A constitutive model for structured clays. *Geotechnique* 54(4), 269–278 (2004)
- [10] Suebsuk, J., Horpibulsuk, S., Liu, M.D.: A critical state model for overconsolidated structured clays. *Computers and Geotechnics* 38(5), 648–658 (2011)
- [11] Yao, Y.P., Hou, W., Zhou, A.N.: UH model: Three-dimensional Unified Hardening Model for Overconsolidated Clays. *Geotechnique* 59(5), 451–469 (2009)
- [12] Matsuoka, H., Yao, Y.P., Sun, D.A.: The Cam-clay models revised by the SMP criterion. *Clays and Foundations* 39(1), 81–95 (1999)
- [13] Wesley, L.D.: Discussion of Wallace. *Geotechnique* 24(1), 101–105 (1974)
- [14] Mesri, G., Rokhsar, A., Bohor, B.F.: Composition and compressibility of typical samples of Mexico City clay. *Geotechnique* 25(3), 527–554 (1973)

- [15] Leroueil, S., Vaughan, P.R.: The general and congruent effects of structure in natural clays and weak rocks. *Geotechnique* 40(3), 467–488 (1990)
- [16] Liu, M.D., Carter, J.P.: Virgin compression of structured clays. *Geotechnique* 49(1), 43–57 (1999)
- [17] Yao, Y.P., Li, Z.Q., Hou, W., Wan, Z.: Constitutive model of over-consolidated clay based on improved Hvorslev envelope. *Journal of Hydraulic Engineering* 39(11), 1244–1250 (2008)
- [18] Yao, Y.P., Gao, Z.W., Zhao, J.D., Wan, Z.: Modified UH model: Constitutive modeling of overconsolidated clays based on a parabolic Hvorslev envelope (2012), doi: 10.1061/(ASCE) GT. 1943-5606.0000649
- [19] Walker, L.K., Raymond, G.P.: Anisotropic consolidation of Leda clay. *Canadian Geotechnical Journal* 6(3), 271–286 (1969)
- [20] Yong, R.N., Nagaraj, T.S.: Investigation of fabric and compressibility of a sensitive clay. In: *Proceedings of the International Symposium on Soft Clay*, Asian Institute of Technology, pp. 327–333 (1977)
- [21] Anagnostopoulos, A.G., Kalteziotis, N., Tsiambaos, G.K., Kavvadas, M.: Geotechnical properties of the Corinth Canal marls. *Geotechnical and Geological Engineering* 9(1), 1–26 (1991)

# Incorporation of Soil Suction in Stress-Based Slope Stability Analysis

Yong Chen<sup>1,\*</sup>, D. Chan<sup>1,2</sup>, and Yunzhi Tan<sup>1</sup>

<sup>1</sup> China Three Gorges University, Key Laboratory of Geological Hazards of Three Gorges Reservoir Area, Ministry of Education, Yichang, Hubei 443002, China

<sup>2</sup> Distinguished Professor, Department of Civil and Environmental Engineering, University of Alberta, Edmonton, AB T6G 2W2, Canada  
ychen5@ualberta.ca

**Abstract.** A procedure is developed where stresses from a finite element analysis are incorporated into a limit equilibrium framework to evaluate the stability of unsaturated soil slopes. Based on a known seepage field and pore pressure distribution in the slope, an independent stress-deformation analysis is performed using the Barcelona Basic Model (Alonso et al, 1990 [1]) to calculate the internal stresses in the slope. Subsequently, slip surfaces from the limit equilibrium analysis are introduced using a series of rectangle planes. The maximum and minimum principal stresses at the centre of each plane can be calculated from the internal stresses and they are introduced into the slope stability analysis depending on the stress level relative to the strength of the unsaturated soils. Finally, a parametric study is carried out to show the effect of suction on the calculated factor of safety.

## 1 Introduction

Most of the slope soils are unsaturated near the ground surface, therefore stability of slopes are inevitably affected by the state of saturation of the soil and the contribution of suction to shear strength of the material. The objective of this research is to introduce a procedure that combines an elasto-plastic finite element stress analysis with limit equilibrium method to calculate the factor of safety of an unsaturated soil slope. The method is used to analyze a documented case for verification of the proposed method.

### 1.1 Slope Stability Analysis Methods

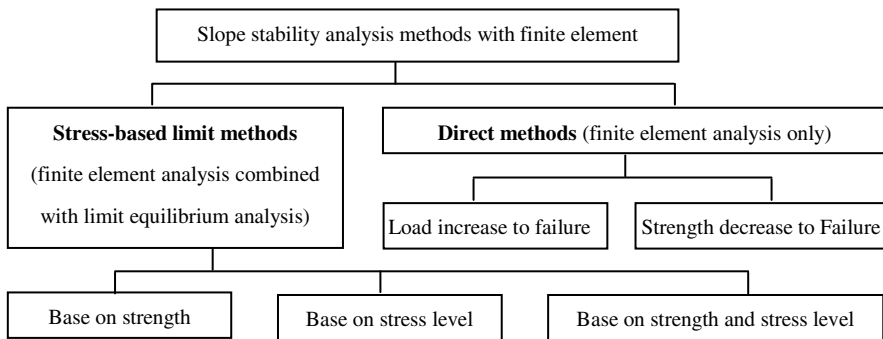
Many methods are available to evaluate the stability of a slope ranging from the method of slices (Fellenius 1936, Bishop 1955) [2, 3] to more rigorous numerical methods such as stress-based finite element methods which alleviate assumptions

---

\* Corresponding author.

on interstices forces. Fredlund et al 1997 [4] identified four important advantages in using the stress-based methods versus the traditional method of slices: (i) The stress versus strain relationship of the soils is included in the analysis, (ii) the entire geometry is used in the calculation of the stress state within the soil mass, (iii) the factor of safety equation is determinate and requires no further assumptions to complete the calculation, and (iv) the factor of safety equation is linear because the normal stresses along the slip surface are known.

The slope stability methods with finite element have been categorized as either direct methods or stress-based methods. Stianson (2008)[5] listed the development of the finite element methods of slope stability using the flowchart shown in Fig. 1.



$$F_s = \frac{\sum (c' + \sigma' \tan \phi') \cdot \Delta L}{\sum \tau \cdot \Delta L} \quad F_s = \frac{\sum (\Delta L)}{\sum \left[ \frac{(\sigma_1' - \sigma_3')}{(\sigma_1' - \sigma_3')_f} \cdot \Delta L \right]} \quad F_s = \frac{\sum [(c' + \sigma' \tan \phi') \cdot \Delta L]}{\sum \left[ \frac{(\sigma_1' - \sigma_3')}{(\sigma_1' - \sigma_3')_f} (c' + \sigma' \tan \phi') \Delta L \right]}$$

Fig. 1. Summary of the finite element procedures for computing the factor of safety in slope stability analysis (Stianson, 2008)

### 1.2 Constitutive Model of Unsaturated Soil

When it had been realized that behavior of unsaturated soils is dominated by effective stress and suction, numerous attentions on unsaturated soils have been paid to the establishment of constitutive model. Based on the concepts of two stress state variables and constitutive surfaces, Fredlund (1979)[6] presented the isotropic linear elastic constitutive model for unsaturated soils. However, unsaturated soils often demonstrate irrecoverable behavior that cannot be explained by unique elastic state surfaces. Alonso et al (1987, 1990) [1,7]proposed the first elasto-plastic framework for unsaturated soils in qualitative form. The framework was subsequently developed into a full mathematical model which later is called the Barcelona Basic Model (BBM). The BBM successfully captured many characteristics of unsaturated soils under drained condition and received extensive acceptance. Since then, many

elasto-plastic models have been developed (Wheeler and Sivakumar 1995; Cui and Delage 1996; Bolzon et al 1996; Vaunat et al 2000a; Wheeler et al 2003; Gallipoli et al 2003; Sheng et al 2008)[8-14]. Meanwhile, various numerical methods have been proposed based on BBM with different mathematical formulations (Li et al 1999; Vaunat et al 2000b; Khalili and Loret 2001; Sheng et al 2003)[15-18].

## 2 The Constitutive Equations for BBM of Unsaturated Soils

The BBM can be used to compute the deformation when the net mean stress  $p$ , deviatoric stress  $q$  and matric suction  $s$  are changed. The model has eleven parameters and the details about the yield loci, hardening laws, flow rules, elastic and plastic strain definitions and the identifications of the parameters can be found in Alonso et al (1990)[7]. Some of the important descriptions are expressed as follows:

(1) The consolidation curve: 
$$dv = \lambda_s \frac{ds}{s + p_{at}}$$
 for concretion of suction

increase, and  $dv = \kappa_s \frac{ds}{s + p_{at}}$  for dry and wetting reversals, where  $\lambda_s$  and  $\kappa_s$  are

respectively the compression and swelling index with suction change, and can be taken as constants,  $p_{at}$  is the atmospheres pressure.

(2) The loading-collapse (LC) yield locus: 
$$\frac{p_0(s)}{p^c} = \left( \frac{p_0(0)}{p^c} \right)^{\frac{[\lambda(0)-\kappa]}{\lambda(s)-\kappa}}$$
, where  $\kappa$  is

the elastic swelling index respect to  $p$ ;  $p_0$  is the mean stress where the yield locus intersect the  $p$  axis,  $p_0(0)$  and  $p_0(s)$  are respectively the pre-consolidation net mean stress under saturated and unsaturated state;  $p^c$  is the reference stress.  $\lambda(s) = \lambda(0)[(1-r)\exp(-\beta s) + r]$ , where,  $\lambda(0)$  is the compression index of saturated soil;  $r$  and  $\beta$  are the parameter that can be confirmed from  $\lambda(s)$  of different suction  $s$ .

(3) The hardening laws: 
$$\frac{d\alpha_0^*}{\alpha_0^*} = \frac{v}{\lambda(0) - \kappa} d\epsilon_V^p \quad \text{and} \quad \frac{ds}{s + p_{at}} = \frac{v}{\lambda_s - \kappa_s} d\epsilon_V^p$$
, where  $d\epsilon_V^p$

is the plastic volumetric strain increment.

(4) The critical state line:  $q = M(p - p_s)$ , where  $M$  is the slope of the critical state line and is the same as that of Modified Cam Clay Model (MCM).  $p_s$  is the intercept of the  $p$  axis and is given as  $p_s = ks$ , with  $k$  being a constant for describing the increase in cohesion with suction.

(5) The yield equation of hypersurface is: 
$$q^2 - M^2(p + p_s)(p_0 - p) = 0$$

where  $q$  is the shear stress,  $p$  is the mean stress,  $M$  is the friction parameter.

The generally expression for the constitutive model of an elasto-plastic material is given by:

$$\{d\sigma\} = \left[ \begin{array}{c} [D_e] \cdot \left\{ \frac{\partial \Phi}{\partial \sigma} \right\}^T \left\{ \frac{\partial Q}{\partial \sigma} \right\} \cdot [D_e] \\ [D_e] - \frac{[D_e] \cdot \left\{ \frac{\partial \Phi}{\partial \sigma} \right\}^T \left\{ \frac{\partial Q}{\partial \sigma} \right\} \cdot [D_e]}{A + \left\{ \frac{\partial \Phi}{\partial \sigma} \right\}^T [D_e] \left\{ \frac{\partial Q}{\partial \sigma} \right\}} \end{array} \right] \cdot \{d\epsilon\} = [D_{ep}] \{d\epsilon\} \quad (1)$$

where  $D_e$  is the usual elastic constitutive matrix,  $\Phi$  is the loading function,  $Q$  is the plastic potential function, and under the condition of associated flow rules, the yield function is  $F = \Phi = Q$ ,  $d\sigma$  is the increment of stress,  $d\epsilon$  is the increment of strains, and  $A$  is the hardening/softening modulus.

For BBM, substituting the loading collapse yield locus of the unsaturated soil into the yield surface equation, it can be shown that:

$$\frac{q^2}{M^2(p + p_s)} + p = p_0 = p^c \left( \frac{p_0^*}{p^c} \right)^{\frac{\lambda - \kappa}{\lambda(s) - \kappa}} \quad (2)$$

The hardening laws can be rewritten as follow:  $p_0^* = p^c \cdot \exp\left(\frac{1 + e_0}{\lambda - \kappa} \epsilon_{vp}^p\right)$  (3)

where  $e_0$  is the initial void ratio of the material.

If Eq. (3) is substitute into Eq. (2), the three- dimensional yield equation can be expressed as:

$$\Phi = \ln[q^2 + M^2(p + p_s)p] - \ln[M^2(p + p_s)p^c] - \frac{1 + e_0}{\lambda(s) - \kappa} \epsilon_{vp}^p = 0 \quad (4)$$

and  $\frac{d\Phi}{d\sigma_x} = \frac{M^2(p + p_s)^2 - q^2}{3(p + p_s)[q^2 + M^2(p + p_s)p]} + \frac{3(\sigma_x - p)}{q^2 + M^2 p(p + p_s)} \Big|_{x,y,z}$ ,  $\frac{d\Phi}{d\tau_{xy}} = \frac{6\tau_{xy}}{q^2 + M^2 p(p + p_s)} \Big|_{x,y,z}$  (5)

If considering plastic volumetric strain  $\epsilon_{vp}^p$  as the hardening variable, the hardening modulus is found to be:

$$A = - \frac{d\Phi}{d\epsilon_{vp}^p} \frac{d\Phi}{d\sigma} = \frac{1 + e_0}{\lambda(s) - \kappa} \frac{d\Phi}{d\sigma} \quad (6)$$

### 3 Stability Analysis of Unsaturated Soils Slope

Regardless of load increase or strength decrease, the direct method of calculating the factor of safety using the finite element technique must decide on whether the failure or critical state of soil is satisfied. In numerical calculation, this criterion will not be satisfied exactly and the results are affected by the rate and accuracy of convergence. Consequently, the factor of safety along a slip surface (Fs) in this

study can be calculated based on the stress field in the slope, as shown in formula (7). The location of the slip surface may not coincide with the finite element mesh. A series of rectangular planes is used to approximate the slip surfaces. An interpolation scheme is used to calculate the stress components at the centroid of the rectangular planes based on the stresses at the Gaussian integration points in the finite element analysis.

$$F_s = \frac{\sum (\Delta A)}{\sum \left[ \frac{(\sigma_1' - \sigma_3')}{(\sigma_1' - \sigma_3')_f} \cdot \Delta A \right]} \tag{7}$$

According to the strength criterion of unsaturated soil proposed by Fredlund, when a node is in a critical state, the major principal stress can be determined from:

$$\sigma_{1f} = \sigma_3 \tan^2 \left( 45^\circ + \frac{\phi}{2} \right) + 2 \cdot (c + s \cdot \tan \phi_b) \tan \left( 45^\circ + \frac{\phi}{2} \right) \tag{8}$$

where  $(\sigma_1 - \sigma_3)_f$  the diameter of Mohr's stress circle at critical state,  $c$  and  $\phi$  are the cohesion and friction of the saturated material,  $\phi_b$  is the friction angle corresponding to the matrix suction  $s$ .

## 4 Example of Stability Analysis of an Unsaturated Slope

### 4.1 The Example and Its Parameters

An example is presented here to illustrate the procedure of the above scheme and to demonstrate its effectiveness in calculating the factor of safety of an unsaturated slope. This example has been analyzed by Chen (2003)[19]. A slope based on the work by Chen with a slope gradient of 1:2 (V:H) is shown in Figure 2, where a potential slip surface is defined by path DCBA. The phreatic line is located at the bottom of the soft layer. An isoline of pore water pressure is assumed in Figure 3. The model parameters are listed in Table 1 (Chen et al. 2009)[20].

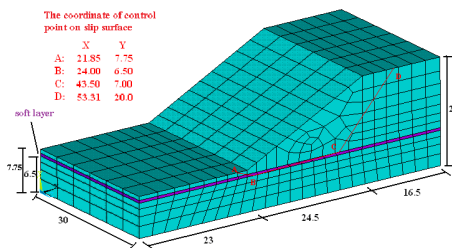


Fig. 2. Finite element grid of example slope

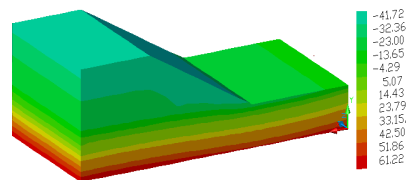


Fig. 3. The isolines of slope pore water pressure (kPa)

**Table 1.** Parameters of BBM and mechanics

parameters	$P_0^*/\text{kPa}$	$\lambda$	$P^*/\text{kPa}$	$K$	$r$	$\beta/\text{kPa}^{-1}$	$\lambda s$	$K_s$	$s_0/\text{kPa}$	$k$	$M$
value	17.0	0.0612	10.0	0.012	0.0125	0.325	0.0506	0.0069	35.0	0.46	0.974
parameters	$E$ (main body / soft layer)		$\mu$	$\gamma$	$N/m^3$	$c$ (main body / soft layer)		$\phi$ (main body / soft layer)		$\phi_b$	
value	60000 / 2000		kPa	0.25	18.84	28.5 / 0		kPa		20 / 10	10

### 4.2 Influence of the Suction to the Stress and Deformation

According to the distribution of pore water pressure, the positive  $u_w$  is considered as the static water pressure, and the negative  $u_w$  as the suction ( $s = -u_w$ ), the stress and deformation of the unsaturated slope under the action of gravity can be calculated using the finite element method. Two constitutive models have been used, the BBM model and the Modified Cam Clay Model (MCC). The MCC model is used to calculate the stresses and deformation in saturated soils without suction. Comparison of the result comparison between BBM and MCC is shown in Table 2. The difference has occurred between effective stresses distributions depending on the saturated or unsaturated constitutive model selected in the finite element analysis, meanwhile, the displacement of X and Y direction base on BBM are less than those based on MCC, which seems that the unsaturated soil are more strong than the saturated. In fact, the phenomena happen just because the suction considering makes the yield stress and hardening modulus increasing.

**Table 2.** Range of stresses and deformations in the slope using two models

Soil Saturation	Max and Min $\sigma'_{xx}$ (kPa)	Max and Min $\sigma'_{yy}$ (kPa)	X Displacement (mm)	Y Displacement (mm)
MCC Saturated Soil with No Suction	-112.1 ~ 2.4	-284.4 ~ -4.0	-30 ~ -1.6	-130 ~ -6.8
BBM Unsaturated Soil With Suction	-113.4 ~ -3.1	-287.0 ~ -14.1	-23.8 ~ -2.1	-113.9 ~ -6

### 4.3 Stability of Unsaturated Soil Slope

The slip surface is dispersed as shown in Fig. 4 where the area and center point location of each rectangle planes can be ascertained to calculate the factor of safety along this slip surface.

In this study, the contributions of soil suction can be divided into two parts. The first part is the change of the effective stresses in the soil, which can be reflected from the different results between the saturated and unsaturated constitutive model, as shown in Table 2. The second part is the contribution to an increase in the strength of the soil which is expressed as  $s \cdot \tan \phi_b$ .

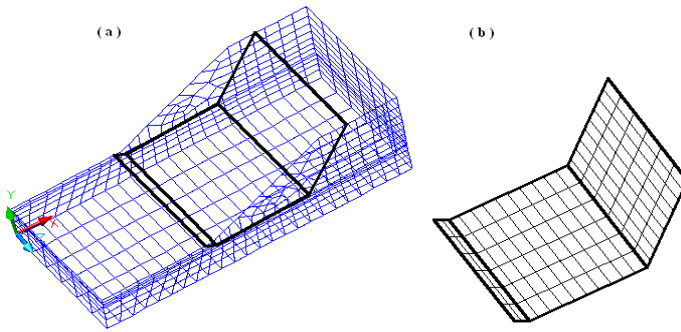


**Fig. 4.** The information of appointed slide surface: (a) position relation between the surface and slope (b) the grid of surface

The calculated factors of safety along the slip surface shown in Figure 4 are given in Table 3 based on different methods. From this table, we can summarize the following: (i) the factors of safety without considering the influence of suction is within the range of values presented by Chen (2003); (ii) the factor of safety increases when the strength criterion of unsaturated soils is included in the constitutive model; (iii) the factors of safety is the highest, 1.54, when both including soil suction in the deformation analysis and using the Fredlund strength criterion.

**Table 3.** The factors of safety along appointed slide surface

Methods <sup>#</sup>	Factors of safety	statistical answer of the example slope *		
		index	ALL (29)	JANBU (10)
MCC + M- C	1.38	Average Value	1.292	1.252
BBM + M- C	1.44	Standard Deviations	0.064	0.060
MCC + Fredlund	1.47	minimum value	1.197	1.197
BBM + Fredlund	1.54	maximum value	1.450	1.333

# M-C: Mohr-Coulomb strength criterion, Fredlund- strength criterion proposed by Fredlund.

\* Chen (2003) [19]: There are 29 calculations from different researchers in which 10 have adopted the JANBU method.

## 5 Conclusion

A procedure has been developed where stresses from a finite element analysis are incorporated into a limit equilibrium method to evaluate the stability of unsaturated soil slopes. In addition, the effect of suction is considered both in the stress-deformation

analysis and limit equilibrium analysis. The factor of safety can be computed based on stress level method from the finite element analysis thus relieving the assumption on the inter-slice forces. The proposed method is used to analyze a slope and compare with published results. It is found that the method based on constitutive model and strength criterion provides a higher estimate on the factor of safety, about 10% higher, than the traditional methods. This procedure can also be applied in evaluating the stability of slopes due to moisture infiltration and evaporation.

**Acknowledgments.** The research is financially supported by the science research project of ministry of education of hubei province, china (d20121303).

## References

- [1] Alonso, E.E., Gens, A., Hight, D.W.: Special problem soils general report. In: 9th European Conf. on Soil Mechanics, Dublin, vol. 3, pp. 1087–1146 (1987)
- [2] Fellenius, W.: Calculations of the stability of earth dams. In: Transactions of the 2nd Congress on Large Dams, Washington, D.C., vol. 4, pp. 445–463 (1936)
- [3] Bishop, A.W.: The use of the slip circle in the stability analysis of slopes. *Geotechnique* 5(1), 7–17 (1955)
- [4] Fredlund, D.G., Scoular, R.E.G., Zakerzadeh, N.: Using finite element stress analysis to compute the factor of safety. In: Proceedings of the 52nd Canadian Geotechnical Conference, Regina, Sask, October 25–27, pp. 73–80. Canadian Geotechnical Society, Richmond (1997)
- [5] Stianson, J.R.: A three-dimensional slope stability method based on finite element stress analysis and dynamic programming. Ph.D. dissertation. University of Alberta, Edmonton, Canada (2008)
- [6] Fredlund, D.G.: Second Canadian Geotechnical Colloquium: Appropriate concepts and technology for unsaturated soils. *Canadian Geotech. J.* 16(1), 121–139 (1979)
- [7] Alonso, E.E., Gens, A., Josa, A.: A constitutive model for partially saturated soils. *Geotechnique* 40(3), 405–430 (1990)
- [8] Wheeler, S.J., Sivakumar, V.: An elasto-plastic critical state framework for unsaturated soil. *Geotechnique* 45(1), 35–53 (1995)
- [9] Cui, Y.J., Delage, P.: Yielding and plastic behaviour of an unsaturated compacted silt. *Geotechnique* 46(2), 291–311 (1996)
- [10] Bolzon, G., Schrefler, B.A., Zienkiewicz, O.C.: Elastoplastic soil constitutive laws generalised to partially saturated states. *Geotechnique* 46(2), 279–289 (1996)
- [11] Vaunat, J., Romero, E., Jommi, C.: An elastoplastic hydro-mechanical model for unsaturated soils. In: *Experimental Evidence and Theoretical Approaches in Unsaturated Soils*, pp. 121–138. Balkema, Rotterdam (2000a)
- [12] Wheeler, S.J., Sharma, R.S., Buisson, M.S.R.: Coupling of hydraulic hysteresis and stress-strain behaviour in unsaturated soils. *Geotechnique* 53(1), 41–54 (2003)
- [13] Gallipoli, D., Gens, A., Sharma, R., Vaunat, J.: An elastoplastic model for unsaturated soil incorporating the effects of suction and degree of saturation on mechanical behaviour. *Geotechnique* 53(1), 123–135 (2003)

- [14] Sheng, D., Fredlund, D.G., Gens, A.: A new modeling approach for unsaturated soils using independent stress variables. *Canadian Geotechnical Journal* 45(4), 511–534 (2008)
- [15] Li, X.K., Thomas, H.R., Fan, Y.: Finite element method and constitutive modeling and computation for unsaturated soils. *Computer Methods in Applied Mechanics and Engineering* 169(1), 135–159 (1999)
- [16] Vaunat, J., Cante, J.C., Ledesma, A., Gens, A.: A stress point algorithm for an elastoplastic model in unsaturated soils. *International Journal of Plasticity* 16(2), 121–141 (2000b)
- [17] Khalili, N., Loret, B.: An elasto-plastic model for non-isothermal analysis of flow and deformation in unsaturated porous media: Formulation. *Int. J. Solids Struct.* 38, 8305–8330 (2001)
- [18] Sheng, D., Smith, D.W., Sloan, S.W., Gens, A.: Finite element formulation and algorithms for unsaturated soils. Part II: Verification and application. *Int. J. Numer. and Anal. Meth. Geomech.* 27(9), 767–790 (2003)
- [19] Chen, Z.Y.: Soil slope stability analysis. China Water Power Press, pp. 365–370 (2003)
- [20] Chen, Y., Liu, D.F., Wang, S.M.: The elastoplastic constitutive model parameter of unsaturated soils and its finite element methods. *Rock and Soil Mechanics* 30(2), 555–560 (2009)

# Static and Dynamic Analyses of High Core Rockfill Dams

Weixin Dong\* and Yuzhen Yu

State Key Laboratory of Hydrosience and Engineering, Tsinghua University,  
Beijing 100084, China  
diy080808@163.com

**Summary.** Static and dynamic numerical calculations were performed to study the dynamic response of a high core rockfill dam. 3-dimensional static analyses of an ideal high core rockfill dam were conducted using Duncan-Chang's E-B model. Then based on the initial static stress field, dynamic analyses of the dam subjected to earthquakes were conducted with the program EB3D in traditional way of visco-elastic model and Equivalent Linear Method. The dynamic response of the high core rockfill dam in the whole process of earthquake was analyzed with program FEMEPDYN, which is based on elasto-plastic model and Nonlinear Method. The dynamic behavior of the high core rockfill dam during the earthquake was analyzed, and the seismic characteristics of response were investigated. Compared with traditional Equivalent Linear Method, it is shown that the Nonlinear Method is more reasonable in describing the dynamic response of high core rockfill dam subjected to the earthquake motion.

**Keywords:** static and dynamic analyses, high core rockfill dam, Duncan-Chang's E-B model, elasto-plastic model.

## 1 Introduction

A number of high concrete faced rockfill dams (CFRDs) and core earth dams with the height of more than 200~300m are being under construction or to be built in Southwest China in the Himalayas seismic belt with potentially heavy seismic activity. For instance, Wenchuan earthquake with a magnitude of 8.0 caused large permanent deformation to Zipingpu Dam, a CFRD.

Traditional soil model for dynamic analysis is equivalent viscous-elastic model in which the non-linear behavior of the soil is modeled using an equivalent linear procedure to describe changes in the shear modulus and damping ratio with strain [e.g., 1-4]. It has a clear concept and has been used in many engineering projects. Nevertheless, it can't be used directly to calculate cumulative pore pressure and residual deformation.

---

\* Corresponding author.

Soil is more a kind of elasto-plastic material. Elasto-plastic model can reflect the anisotropy and the dilatancy of soil effectively. Generalized plasticity model was proposed by Morz and Zienkiewicz, and developed into Pastor-Zienkiewicz III model [5] later. Pastor-Zienkiewicz III model is a simple elasto-plastic model whose parameters are easy to determine.

## 2 Static Analyses

In order to conduct dynamic analysis, an initial stress field is needed. In this study, a nonlinear elastic model was used to provide initial stress field.

### 2.1 Analysis Method and Parameters

First, a simplified high earth rockfill dam Nuozhadu which is under construction in Southwest China was discretized, as shown in Fig.1 and Fig.2.

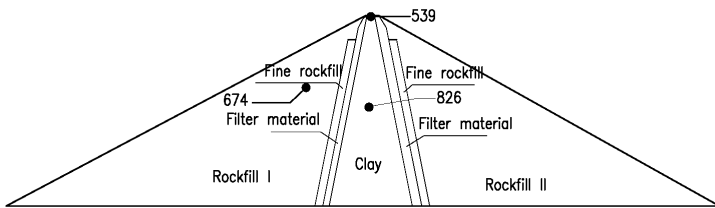


Fig. 1. Material partition

Static analysis was conducted on the simplified dam, with programs based on Duncan-Chang’s E-B model [6], which is widely used in geotechnical engineering. The properties of dam materials are shown in Table 1.

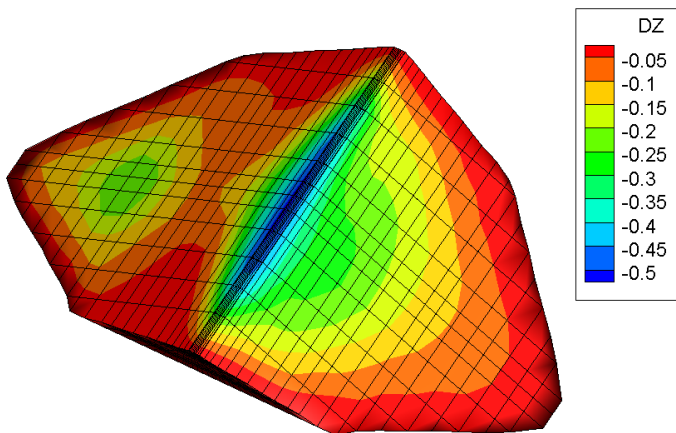


Fig. 2. Model grid of the simplified dam

**Table 1.** Parameters of Duncan-Chang’s E-B model

material	$\phi'(^{\circ})$	$\Delta\phi(^{\circ})$	$R_f$	$K$	$n$	$K_b$	$m$
Rockfill I	54.37	10.47	0.72	1425	0.260	540	0.16
Rockfill II	50.60	10.20	0.76	1530	0.175	376	0.10
Fine Rockfill	53.04	10.10	0.78	1240	0.176	254	0.10
Filter	54.10	11.30	0.78	1450	0.176	350	0.15
Clay	39.47	11.83	0.78	421	0.560	299	0.25

### 2.2 Stress and Deformation Results

Fig. 3 and Fig. 4 show the numerical results of finite element analyses. After the reservoir impounded, due to the water pressure on upstream dam, displacement along river directs to the downstream on the whole, and the largest displacement is about 1.09m. The largest settlement occurs in the middle of core wall with a value of about 2.70m. Because of the big differences of modulus between rockfill and clay, there exists obvious arching effect in the core wall. Effective stress in upstream shell is low and stress level ( $S = (\sigma_1 - \sigma_3) / (\sigma_1 - \sigma_3)_{ultimate}$ ) is high.

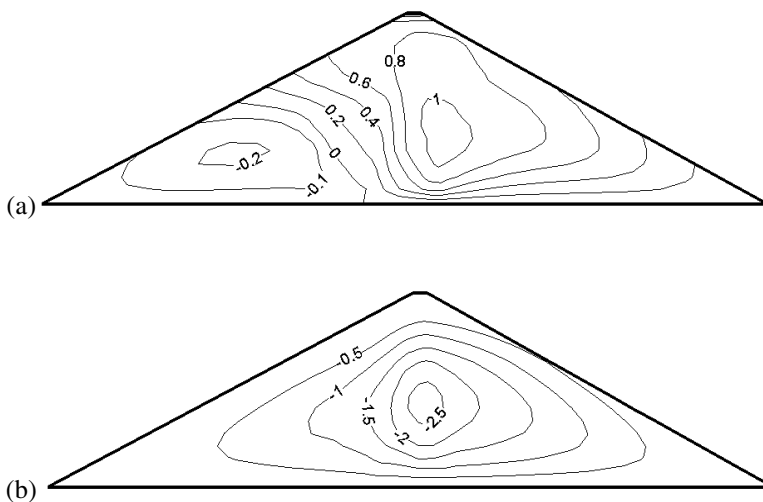


**Fig. 3.** Displacement distribution of maximum section: (a) displacement along river (m) and (b) vertical displacement (m)

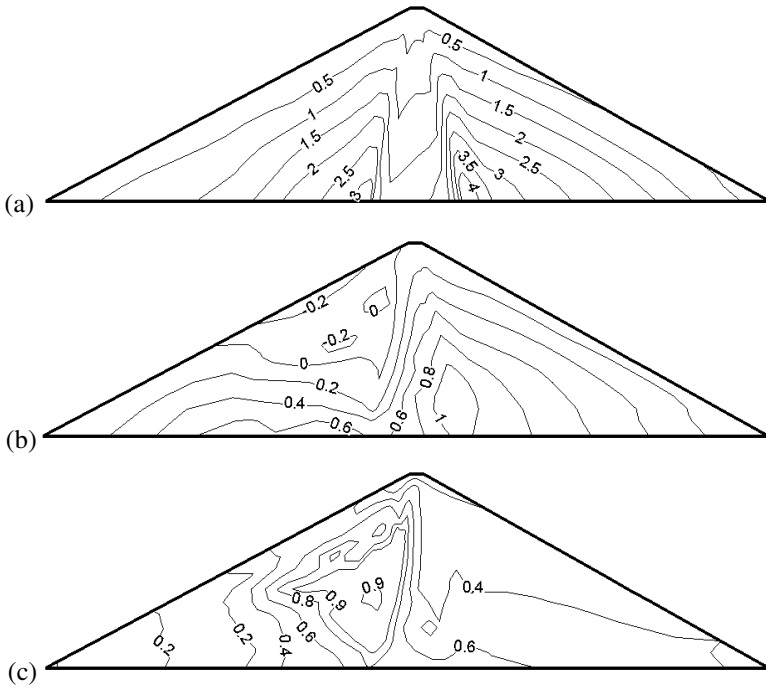


**Fig. 4.** Stress distribution of maximum section: a) Major principle stress (MPa) (b) Minor principle stress (MPa) and (c) Stress level defined previous

### 3 Visco-elastic Dynamic Analyses

#### 3.1 Earthquake Wave and Model Parameters

Earthquake wave was applied at the base of the dam with a peak acceleration of about  $2.86\text{m/s}^2$  and lasting for 20 seconds, as shown in Fig.5.

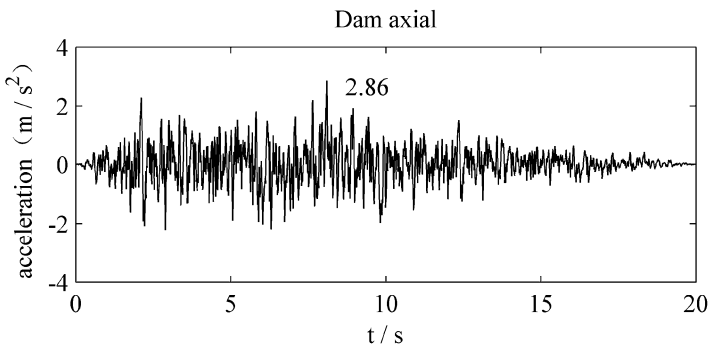


**Fig. 5.** Earthquake wave

Based on the initial stress field obtained from Duncan-Chang’s E-B model static analysis, the behaviors of both the shell and core of the dam were represented in the following.

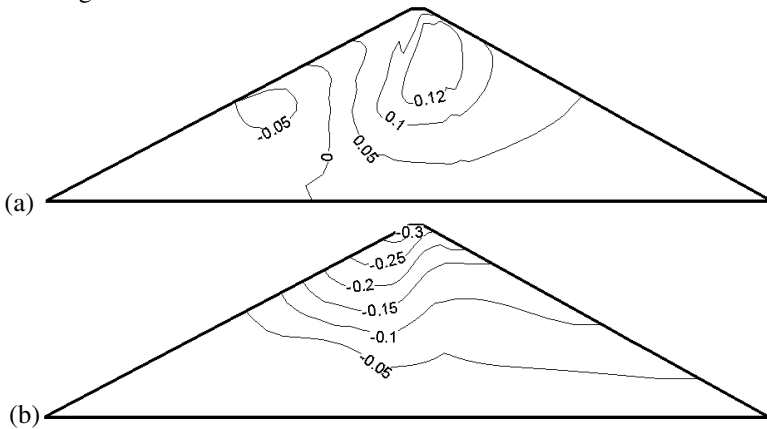


**Fig. 6.** Residual deformation: (a) displacement along river (m) and (b) vertical displacement (m)

## 4 Elasto-plastic Dynamic Analyses

### 4.1 Initial Stress Field

FEMEPDYN is 3D dynamic consolidation finite element program, which is based on Pastor-Zienkiewicz III Generalized plasticity model, Biot dynamic consolidation theory, large strain theory [7]. As program FEMEPDYN can only be used to conduct dynamic analysis, the initial stress field obtained from Duncan-Chang’s E-B model static analysis was provided for dynamic analysis. However, the initial stress field needs modification as tensile stress and excessive stress level exist in upstream shell and upstream core, respectively, as shown in Fig.4. Improved stress field was used to conduct dynamic analyses [8].

### 4.2 Residual Deformation

Displacement distributions are described in Fig.7, which present some differences compared with Fig.6. For instance, the maximum horizontal displacement along river occurs on the surface of downstream shell, which is more reasonable as downstream shell is lack of restraint. Fig.1 shows the distribution of vertical displacement, and the maximum settlement occurs in the middle of the dam crest.

### 4.3 Acceleration and Excess Pore Pressure Response

FEMEPDYN can calculate real-time acceleration and excess pore pressure response, which equivalent linear method is incapable of calculating directly. Empirical equations are used in Equivalent Linear Method for calculating residual

deformation and pore pressure. Acceleration responses of two monitoring points in the core, numbered 826 and 539 as shown in Fig.1, are given as Fig.8. The peak acceleration of 539# is about two times larger than 826#, which accords with the general law that acceleration amplification at dam crest is the largest. The excess pore pressure response of monitoring point 674# is shown in Fig.9, which represents the accumulating process of excess pore pressure.

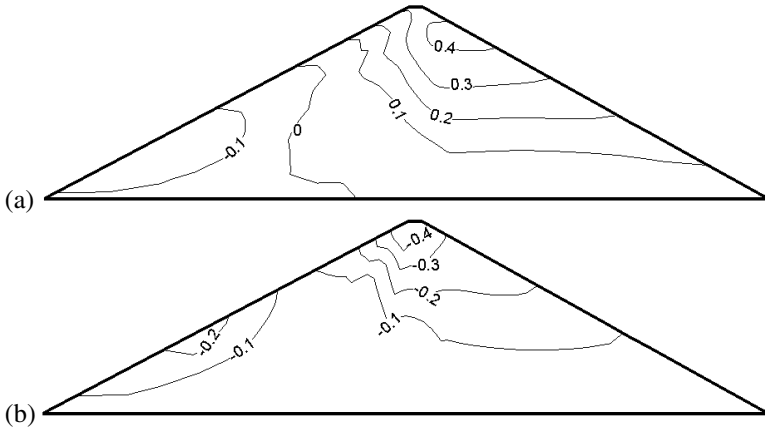


**Fig. 7.** Residual deformation: (a) displacement along river (m) and (b) vertical displacement (m)

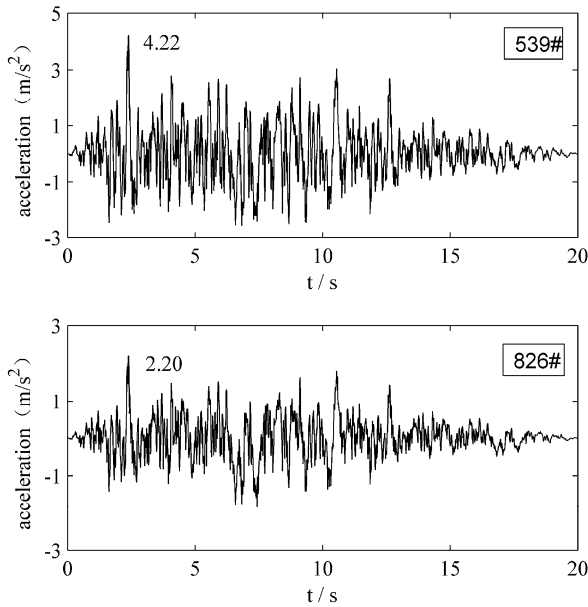


**Fig. 8.** Acceleration response

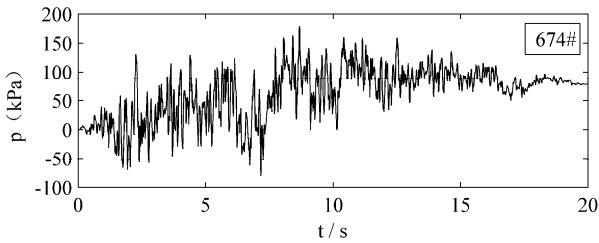


Fig. 9. Excess pore pressure response

## 5 Conclusions

This paper included static and dynamic analyses of a simplified high core rockfill dam. Static analyses were conducted with Duncan-Chang's E-B model. Based on the initial stress field obtained from previous static analyses, dynamic analyses of the dam subjected to earthquake motion were conducted with traditional equivalent visco-elastic model and nonlinear elasto-plastic model.

Static analyses show, there exists obvious arching effect in the core wall, and effective stress in upstream shell is low and stress level is high. The improved initial stress field obtained from Duncan-Chang's E-B model static analysis was provided for dynamic analysis. FEMEPDYN can calculate real-time acceleration and excess pore pressure response, which equivalent linear method is incapable of deriving directly, and the result given by FEMEPDYN is more reasonable.

## References

- [1] Seed, H.B.: Methods of earthquake resistant design of earth dam. J. SMFD, ASCE 92, 45–60 (1966)
- [2] Idriss, I.M., Seed, H.B.: Seismic response of horizontal soil layers. SMFD, ASCE 94, 1003–1031 (1968)
- [3] Finn, W.D.L.: Dynamic response analysis of saturated sands. In: Pande, G.N., Zienkiewicz, O.C. (eds.) Soil Mechanics-Transient and Cyclic Loads, pp. 105–132. John Wiley & Sons Ltd (1982)
- [4] Finn, W.D.L., Kwork, W., Martin, G.R.: An effective stress model for liquefaction. J. GED, ASCE 103, 517–533 (1977)
- [5] Zienkiewicz, O.C., Mroz, Z.: Generalized plasticity formulation and applications to geomechanics. Mechanics of Engineering Materials, 655–679 (1984)
- [6] Duncan, J.M., Chang, C.Y.: Nonlinear analysis of stress and strain in soils. Journal of the Soil Mechanics and Foundations Division 96(5), 1629–1653 (1970)
- [7] Li, R.J.: A study on the aseismic reinforcement mechanism of stabilizing piles in soil slope. Tsinghua University (2008)
- [8] Bian, F.: Elasto-plastic FEM analysis of dynamic response of high earth-rockfill dams during earthquake. Tsinghua University (2010)

# Implementation of Numerical Optimization Techniques in Constitutive Model Calibration

Louis Ge<sup>1</sup>, Honghua Zhao<sup>2</sup>, and Bata Bate<sup>3</sup>

<sup>1</sup> National Taiwan University, Taiwan  
louisge@ntu.edu.tw

<sup>2</sup> Dalian University of Technology, China  
zhaoh@dlut.edu.cn

<sup>3</sup> Missouri University of Science and Technology, USA  
bateba@mst.edu

**Abstract.** When a conventional method such as linear regression is insufficient to identify the constants and parameters of an advanced constitutive model, numerical optimization techniques are often used. In employing numerical optimization to constitutive model calibration, an objective function essentially needs to be formulated in the form of nonlinear least squares where the sum of the differences between the measured and computed data points are quantified. When a minimum value of the objection function is obtained, the corresponding variables are the optimized model constants and parameters. Due to the complexity in the format of objective functions in constitutive model calibration, gradient-based methods are seldom used. In this paper, non-gradient based methods namely Direct algorithm was implemented to calibrate a modified Cam-Clay model against laboratory data.

## 1 Introduction

Optimization problems are generally defined as minimizing the objective function  $f(\mathbf{x})$  subject to decision variable vector  $\mathbf{x}$  (e.g., [1]). Numerical optimization algorithms can be categorized into three groups according to the type of information needed in searching for the minimum of the objective functions. The simplest way to minimize the objective function is to randomly choose a sufficiently large number of candidate vectors  $\mathbf{x}$  and evaluate the objective function for each of them. This approach is often referred to zero-order methods, where random search methods, Rosenbrock methods, Complex methods, and Powell's methods are of this kind.

If the information of the gradient of the objective function is implemented into the optimization algorithm, it is referred to first-order-methods. The gradient of the objective function can be obtained by either finite difference computations or analytical solutions. First-order methods are usually more efficient than zero-order methods; however, they can perform poorly for objective functions that have discontinuous first derivatives. Steepest Descent methods, Conjugate Direction Methods (or Fletcher-Reeves Methods), Variable Metric methods (Davidon-Fletcher-Powell or Broydon-Fletcher-Goldfarb-Shanno Methods) belong to this category.

Second-order Methods, also called Newton's methods, use the information of the second derivatives of the objective function (Hessian matrix  $H$ ) throughout the optimization process. If the Hessian matrix can be calculated relatively easily, Newton's Method is usually the most preferred approach due to its efficiency and stability.

Due to the nature of incremental format of most elasto-plasticity constitutive drivers, the objective functions are not explicitly defined. This causes the difficulty in calculating the first and second derivatives of objective functions when first-order methods and second-order methods are used.

## 2 The Objective Function

It is then straightforward to formulate the objective function as the sum of distances from computed points to their adjacent experimental point in the stress strain space as shown in Figure 1.

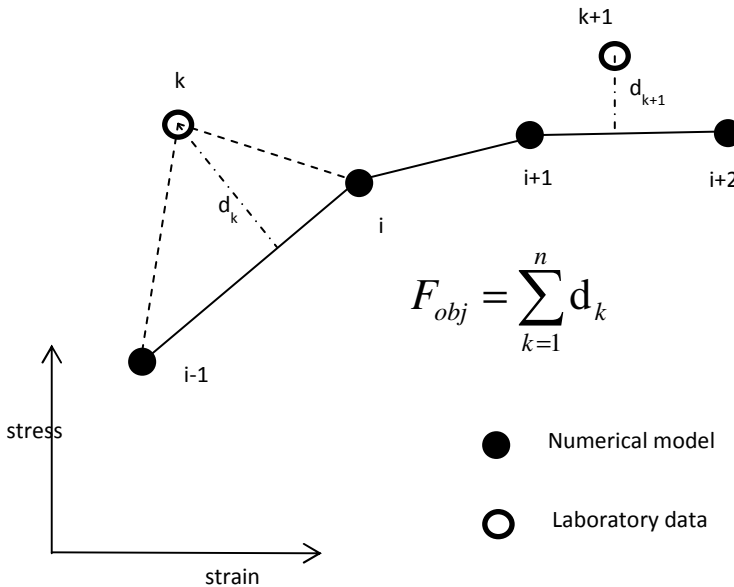


Fig. 1. Illustration of the objective function used in this study

## 3 Direct Optimization Algorithm

The Direct optimization algorithm was motivated by a modification to Lipschitzian optimization [2]. The algorithm does not require any knowledge of the gradient of the objective function. It uses a sampling technique on points in the domain and uses the previously obtained information to determine where to go. A Matlab script of

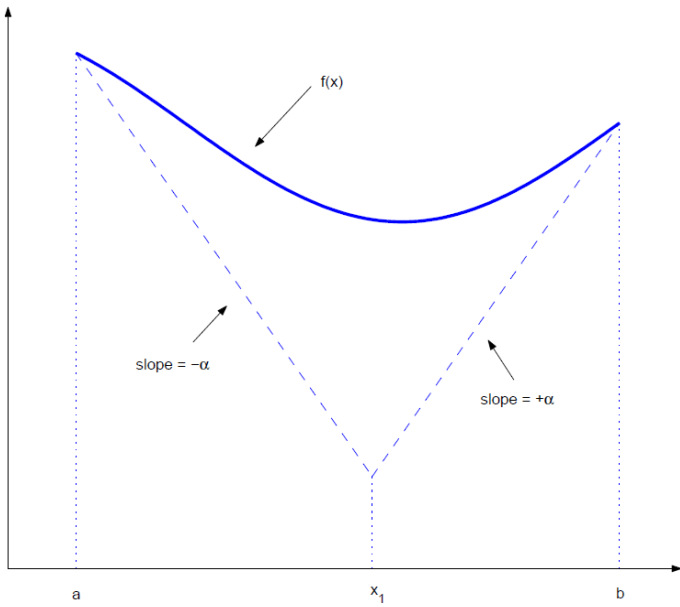


Fig. 2. An initial lower bound using Lipschitz constant (adopted from Finkel, 2003)

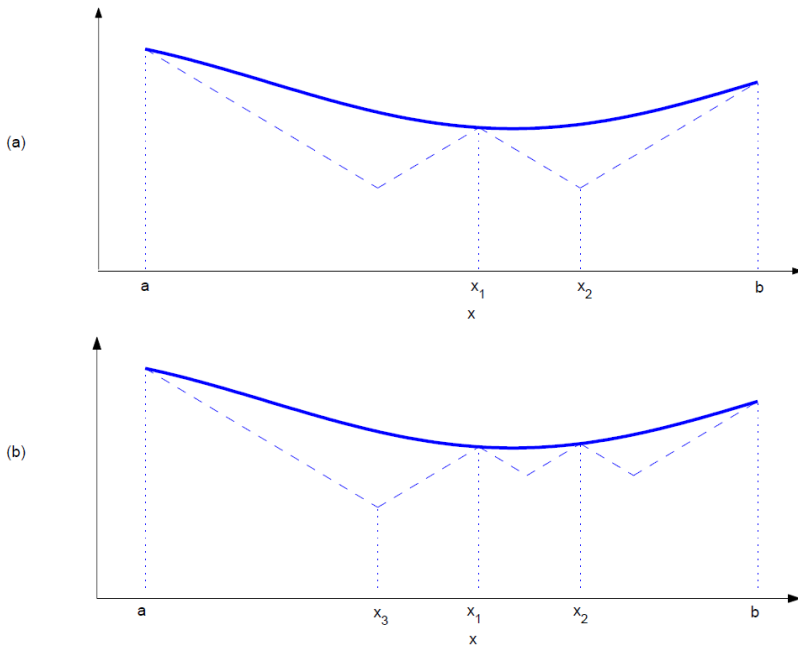
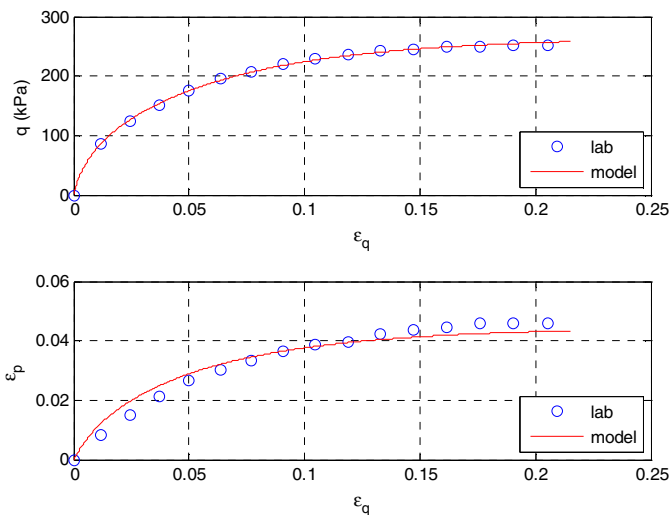


Fig. 3. The Shubert's algorithm (adopted from Finkel, 2003)

Direct algorithm used in this study was directly obtained at [http://www4.ncsu.edu/~ctk/Finkel\\_Direct/](http://www4.ncsu.edu/~ctk/Finkel_Direct/) [3]. The spirit of the Lipschitzian optimization with Shubert algorithm can be demonstrated through Figure 2 below, where the intersection of the two lines with slope  $+\alpha$  and  $-\alpha$  provides an estimate of the minimum of the function  $f$ . Shubert's algorithm repeats in the region between  $a$  and  $x_1$  and the region between  $x_1$  and  $b$ . Figure 3 shows a couple of iterations of this process, as given in the user guide of the Direct algorithm (Finkel, 2003).

## 4 Calibration Example

A set of consolidated drained triaxial test data was used to calibrate a modified Cam Clay model. The confining pressure was set as 207 kPa. All 5 model parameters were calibrated against lab test data at the same time with upper and lower bounds. The bounds and optimized values are listed in the table below. The upper and lower bounds were carefully selected as first screening on model calibration. The range of bounds has a direct influence on the iteration time. Generally, the wider the bound range, the longer time it requires to complete the calibration process. It is also noted that the form of objective function consists two parts. One is computed from the deviatoric stress versus deviatoric strain curve and the other is from the volumetric strain versus deviatoric strain curve. Figure 4 displays the calibrated stress-strain curves compared with the laboratory test data which show a good agreement in general. As shown in Figure 5, after around 15 iterations, the value of the objective function reached a stable value where a global minimum was determined within the given bounds.



**Fig. 4.** Laboratory test results and calibrated model stress-strain curves

**Table 1.** Bound constraints and optimized values for model parameters

	Lower Bound	Upper Bound	Optimized Value
$\lambda$ (isotropic compression index)	0.06	0.08	0.0763
N (specific volume at $p^* = 1$ kPa)	1.8	2.2	2.0073
$\kappa$ (isotropic recompression index)	0.013	0.017	0.0149
G (shear modulus)	4000	6000	5259
M (critical state slope)	0.8	1.0	0.8963

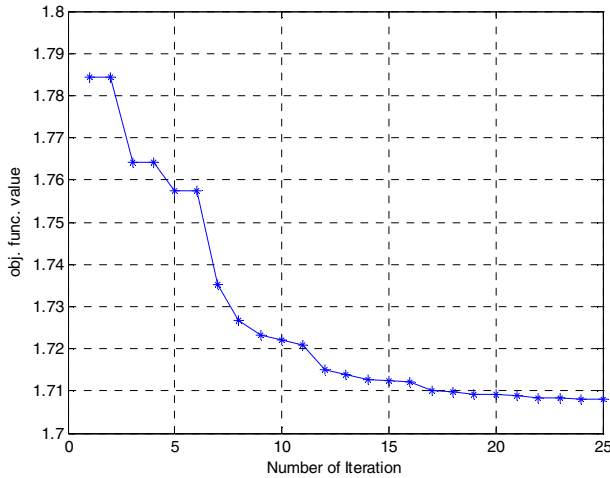


**Fig. 5.** Iteration statistics for incremental Direct objective function

## 5 Conclusions

A non-gradient based numerical optimization algorithm was successfully implemented in calibrating a constitutive model. The implementation was simple and straightforward. The formulation of the objective function follows the conventional least square equation. The performance of the iteration depends on the number of parameters and their corresponding upper and lower bounds. As the optimized model parameters also depend on the selection of initial bounds, the optimized values are not unique for a given calibration. It should be borne in mind that use of this technique is for fine tuning of constitutive model calibration.

## References

- [1] Nocedal, J., Wright, S.: Numerical Optimization. Springer, New York (1999)
- [2] Perttunen, C.D., Jones, D.R., Stuckman, B.E.: Lipschitzian optimization the lipschitz constant. Journal of Optimization Theory and Application 79(1), 157–181 (1993)
- [3] Finkel, D.E.: Direct optimization algorithm user guide (2003), [http://www4.ncsu.edu/~ctk/Finkel\\_Direct/](http://www4.ncsu.edu/~ctk/Finkel_Direct/)

# Modeling Damage by Crack Nucleation and Growth in Porous Media

Dashnor Hoxha<sup>1,\*</sup>, Javad Eslami<sup>2</sup>, Dragan Grgic<sup>3</sup>, and Duc-Phi Do<sup>1</sup>

<sup>1</sup> Laboratoire PRISME, Université d'Orléans, 8 rue Léonard de Vinci, 45072, Orléans France

<sup>2</sup> Laboratoire L2MGC, Université Cergy-Pontoise, 5 Mail Gay-Lussac, 95011 Neuville-sur-Oise France

<sup>3</sup> Laboratoire LaEGO, rue doyen Marcel Roubault, 54501 Vandoeuvre –les-Nancy, France  
dashnor.hoxha@univ-orleans.fr

**Abstract.** While crack propagation is considered as the predominant mechanism of damage in quasi brittle rocks, recent observation on cracking evolution on porous rocks have shown that nucleation of new cracks and back-sliding mechanism of cracks are perhaps as important as the crack propagation. The model proposed here tends to explain the laboratory results that could not be explained within framework of crack-sliding model. A crack nucleation mechanism is then considered to generate an increasing number of cracks based upon a statistical distribution of strain energy cumulated on grain to grain contacts. The increasing role of crack growth and crack coalescence is modeled by an avalanche like mechanism that leads finally to the failure of a porous rock. Predictions of the model are compared with experimentally results in terms of strains and acoustic emission

## 1 Introduction

Even if crack nucleation and crack growth are widely accepted to be two principal mechanisms of cracking evolution the later is more often considered in modeling of brittle and quasi brittle fracture of solids. Among models of crack propagation those based on the well known sliding crack model are perhaps the most used in practice ([12], [14], [9], [3], [15], [13]). It is found that various forms of sliding wing crack model could describe quite well, at least qualitatively, experimental results from direct crack observations on post-mortem mechanically tested samples in terms of crack density and stress-strain curves ([18], [6]). However for a class of geomaterials the nucleation of new cracks is an important mechanism to be considered in order to explain experimental data and observations. For example in a comparative study on sliding crack model, Golshani et al ([5]) have concluded that the crack growth only is not sufficient to explain the dilatancy observed experimentally on brittle solids. Homand et al. ([7]) and Hoxha et al. ([8]) direct post-mortem crack

---

\* Corresponding author.

observations on mechanically tested granite samples have found that crack number increase during loading while mean crack evolves moderately confirming previous observation ([19]). Recently Eslami et al. ([4]) have published some interesting laboratory data on crack monitoring on a porous limestone under increasing mechanical loading using acoustic emission (EA) records and continuous measurements of compressive and shearing ultrasonic wave velocities (UWV). They found that up to failure acoustic emission are localized randomly on the samples. During a loading path anisotropy of UWV is clearly increased as applied stress increases, in full accord with all previous studies. When, from a given stress level, a sample is unloaded, the anisotropy of UWV decreases and fully disappears once the stress is fully removed, even if all UWV records show a global decrease of velocities indicating a damage of rock. These observations could not be explained in the framework of sliding crack model and calls for a suitable modeling framework.

## 2 Principal Hypothesis of Model

Basically three phases of cracking evolution on rock under stress are distinguishable: for low stress level there is no crack growth but existing cracks produce some extra strains as compared to the rock matrix because of crack closure and slide. For moderate stress levels the nucleation of new cracks is produced following the weakest links either inside rock grains or in grain boundaries. Finally, beyond a critical crack density, crack interactions leads to crack coalescence and to a catastrophic crack growth.

In this work in a notable difference with previous works on rock damage, the propagation of cracks during short term is neglected up to crack coalescence and in accord with above mentioned laboratory results on porous rocks, the crack nucleation is considered to be the principal mechanism of cracking evolution.

Porous rocks as natural heterogeneous materials contain in their natural state voids and crack-like flaws of various shapes. In what it follows we consider that all these structure imperfections are either spherical cavities (pores) or oblate ellipsoidal voids (cracks). Moreover cracks are grouped in crack-families each of them representing cracks with the same (approximately) orientation. Each crack is characterized by a characteristic length (its radii  $a$ ) and its shape coefficient  $\varepsilon$  ( $\varepsilon=c/a$ ) with  $c$  being the smaller radii of the ellipsoid representing the crack). In many cases shape coefficient of cracks  $\varepsilon$  is so small that the oblate ellipsoids could be approximated by so called penny-shape cracks. At any moment a crack could be either open (i.e its opposed surfaces are not in contact) or closed (full recovery of normal stiffness only through crack faces is supposed).

## 3 Non Linear Anisotropic Elastic Response of Fractured Rock with Closing Cracks

In order to model an anisotropic response of cracked solid while in loading path and yet an isotropic overall response when full unload an elastic closure of existing

cracks in solid is supposed. Using a homogenization scheme and supposing a solid with pores and cracks it is possible to obtain an expression for the elastic stiffness as a function of the crack density. For example for Mori-Tanaka scheme the expression for such a solid is :

$$C^{\text{hom},M-T} = \left[ (1 - f_p) C_s + \sum_{i,Cl} \frac{4}{3} \pi d_i T_i \right] : \left[ I + f_p \cdot A_p^D + \sum_{i,Cl} \frac{4}{3} \pi d_i T_i + \sum_{i,Op} \frac{4}{3} \pi d_i T_i \right]^{-1} \quad (1)$$

In this expression  $C_s$  is the fourth order stiffness tensor of the matrix,  $f_p$  is the porosity of rock  $d_i$  the crack density of  $i^{th}$  crack family ( $d_i = N_i a_i^3$ ), fourth order tensors  $T_i'$  and  $T_i$  are so called localization tensors associated respectively with penny shape closed and opened cracks while  $A_p^D = [I - S]^{-1}$  is the fourth order tensor of localization for a pore expressed in terms of Eshelby's tensor  $S$ . Detailed expressions for each of fourth order tensors for various shapes of inclusions/voids could be found in specialized literature ([20], [2]).

The principal result from (1) is that the behavior of a cracked solid, even when no crack nucleation or propagation is considered would be highly nonlinear because of the changes of cracks status. Under hypothesis adopted here it is possible to calculate for a crack family with orientation vector  $\underline{n}_i$  and for a macroscopic stress  $\underline{\Sigma}$ , a critical shape coefficient of cracks ( $\epsilon_{cr}$ ) such that all cracks with an inferior shape coefficient be closed ([2]) :

$$\epsilon_{cr}(\underline{n}_i, \underline{\Sigma}) = \frac{1}{(1 - f_p)} \underline{n}_i : (T_i : C_s^{-1} : \underline{\Sigma}) \underline{n}_i \quad (2)$$

For the case of an isotropic compression test ( $\underline{\Sigma} = \Sigma \cdot 1$ ) the equation (2) reads :

$$\epsilon_{cr}(\Sigma) = \frac{4(1 - \nu_s^2)}{3k_s(1 - f_p)\pi(1 - 2\nu_s)} \Sigma \quad (3)$$

with  $k_s$  and  $\nu_s$  being the bulk modulus and Poisson ratio of solid matrix

This equation could be used to deduce the initial distribution of crack shapes using an isotropic compression test resolving the expression of effective bulk modulus against density of open cracked as a function of effective bulk modulus  $k^{\text{hom}}(\underline{\Sigma})$ , bulk modulus of matrix solid  $k_s$  and its shear modulus  $\mu_s$  :

$$d_{ouv}(\underline{\Sigma}) = - \frac{3(3k_s + \mu_s)(3k^{\text{hom}}(\underline{\Sigma})k_s f^p + 4k^{\text{hom}}(\underline{\Sigma})(1 + f^p)\mu_s - 4k_s(1 - f^p)\mu_s)}{16k^{\text{hom}}(\underline{\Sigma})k_s(3k_s + 4\mu_s)} \quad (4)$$

In what it follows an initial description of crack shapes is supposed known and identified following above described procedure. If the total density of cracks is  $d_o^c$  the normalized density of opened cracks when all cracks of a shape coefficient inferior to a critical value  $\epsilon_{cr}$  are closed and its homologue for a crack family are:

$$d^{op,c}(\underline{\epsilon}_{cr}) = 1 - \frac{\sum_i d_{\epsilon_i}^{el,c}}{d_o^c} \quad d_{\epsilon_i}^c(\underline{\epsilon}_{cr,ni}, \underline{n}_i) = 1 - \frac{\sum_i d_{\epsilon_i}^c}{d_o^c(\underline{n}_i)} \quad (5)$$

The equations (1) to (5) describe evolutions of a cracked porous solid supposing that no intersection between cracks or between cracks and pores occur. For a given applied stress the intersection of cracks produces some extra-strains as compared to isolated ones. Considering two crack families with normal  $\underline{n}_j \underline{n}_j$  the extra strains is produced from the sliding  $w_i$  of one family due to the opening  $\omega_j$  of the other one (Fig 1). If the number of crack intersection for families  $i$  and  $j$  is  $N^{i,j}$  the extra strain is:

$$\underline{\epsilon}^{slid.op} = \sum_i \frac{1}{2} N^{i,j} \cdot \underline{\epsilon}^{i,j} = \sum_i \frac{1}{2} N^{i,j} \cdot \left( \frac{1}{2} w_i (\underline{n}_i \otimes \underline{\tau}_i + \underline{\tau}_i \otimes \underline{n}_i) + \omega_j \cdot \underline{n}_j \otimes \underline{n}_j \right) \quad (6)$$

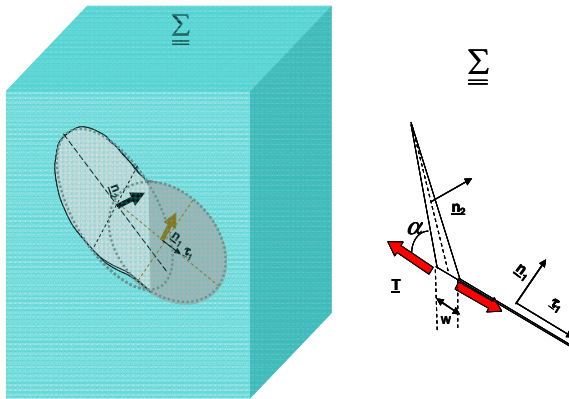


**Fig. 1.** Simplified calculation scheme for extra strains due to crack intersection

The extra strain for all cracks is calculated by summation over all crack families giving a crack family opening  $\Omega_i$ , and sliding  $W_i$ . The relation between extra-opening  $\Omega_i$ , their sliding  $W_i$  and applied macroscopic stress could be found using techniques proposed for wing cracks (see for example [3])

### 4 Crack Nucleation and Coalescence

In a heterogeneous material, cracks nucleate either in the contact of grains that could not accommodate accumulated differential strains, or following structural weakness ([1], [8]). The nucleation of new cracks is related to the distribution of structural weakness on one hand and to the locally stress state on the other hand [11], [18]). From the same works it is observed that the rate of crack nucleation is almost linear in the first stages of applied stress and shifts toward an exponential-like trend from some strain level ([10]). The energy-release based fracture models

show that when considering the failure as a self-organized random structure the rate of energy release close to the critical point (failure) follows a power-law function decorated by log-periodic oscillations ([17]).

Consequently following expression for the evolution of crack density due to crack nucleation is proposed:

$$\begin{cases} d = d_0(1 + k_t(\sigma_{ecv} - \sigma_0)) & \text{if } \sigma_0 < \sigma_{ecv} < \sigma_{lim} \\ d = d_0(1 + k_t(\sigma_{ecv} - \sigma_0)) + \chi \left( \frac{\sigma_{ecv} - \sigma_{lim}}{\sigma_{lim}} \right)^M & \sigma_{ecv} > \sigma_{lim} \end{cases} \quad (7)$$

In this expression  $k_t$  and  $\chi$  are two parameters of the model controlling the rate of crack nucleation along with the exponent  $M$ , while  $\sigma_0, \sigma_{lim}, \sigma_{ecv}$  are three functions of macroscopic stress  $\underline{\Sigma}$ . In the simplest case for materials no sensitive to intermediate stress these functions coincide with Von Mises stress. For rocks however they should be also function of other stress invariants and in this work they are supposed to be Druker-Prager like function..

The strains due to coalescence are calculated by replacing a crack array under compression with a crack oriented in the direction of maximal stress and loaded by a tensile force ([9]):

$$\underline{\underline{\varepsilon}}_{co} = \left( \sum_{i=1}^n \zeta d(\underline{n}_i) \Omega_i \right) \cdot (\underline{e}_1 \otimes \underline{e}_1 + \underline{e}_2 \otimes \underline{e}_2) \quad (8)$$

In this equation it is supposed that a crack family contributes to overall all strains by its fraction  $\zeta$  (a scalar parameter of model) and total opening of this family  $\Omega_i$  calculated as summation over all openings calculated in eq. 6. This mechanism is activated on the same conditions as the crack cataclastic nucleation (eq. 7)

## 5 Numerical Simulations

For comparison purposes published data on a porous limestone are used ([4]). In order to follow the cracking state 15 crack families uniformly distributed on the unit sphere are used as suggested in Zhu et al. ([20]).

Identifying the effective bulk function  $k^{hom} = k^{hom}(\underline{\Sigma})$  from experimental results of hydrostatic compression test (for example by a fitting of stress-volumetric strain), introducing this function in (4) and combining this one with (3) one obtain finally an estimation of initial crack shape distribution. (Fig. 2):

$$d_{eq}^c(\underline{\varepsilon}_{cr}) = Exp(-b \cdot \underline{\varepsilon}_{cr}) \quad (10)$$

Stress strain curve predictions as compared with those obtained experimentally on compression tests (maximal compression in direction 3) are shown in the figure 3 along with predictions of stiffness coefficients (Voigt notations). A quite good accord between numerical predictions and experimental data is found (in numerical predictions only monotonic loading is considered).

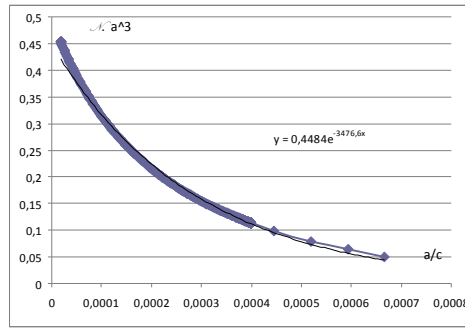


**Fig. 2.** Crack density distribution from laboratory data on isotropic compression test (full line is fitted equation)

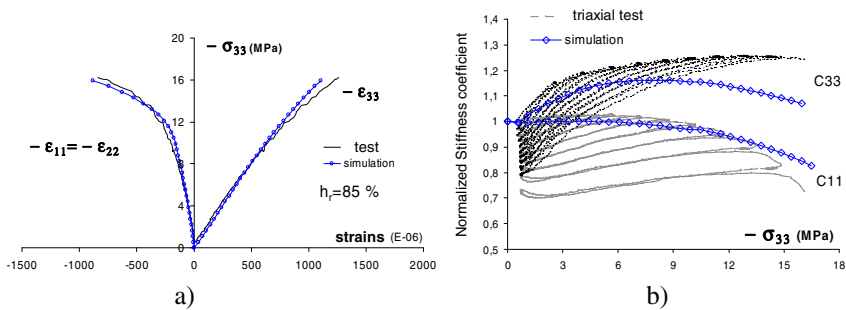


**Fig. 3.** a) Stress strains curves of triaxial compression test b) evolution of stiffness coefficients during compression tests on limestone samples

## References

- [1] Zimmermann, A., Carter, W.C., Fuller, E.R.: Damage evolution during microcracking of brittle solids. *Acta Mater.* 49, 127–137 (2001)
- [2] Deudé, V., Dormieux, L., Kondo, D., Maghous, S.: Micromechanical approach to non-linear poroelasticity: application to cracked rocks. *J. Eng. Mech.* 128(8), 848–855 (2002)
- [3] Dyskin, A.V., Germanovich, L.N., Ustinov, K.B.: A 3-D model of wing crack growth and interaction. *Eng. Fract. Mech.* 63, 81–110 (1999)
- [4] Eslami, J., Grgic, D., Hoxha, D.: Estimation of the damage of a porous limestone from continuous (P- and S-) wave velocity measurements under uniaxial loading and different hydrous conditions. *Geophysical Journal International* 183(3), 1362–1375 (2010)
- [5] Aliakbar, G., Okui, Y., Oda, M., Takemura, T.: A micromechanical model for brittle failure of rock and its relation to crack growth observed in triaxial compression tests of granite. *Mechanics of Materials* 38, 287–303 (2006)

- [6] Hadley, K.: Comparison of calculated and observed crack densities and seismic velocities in westerly granite. *Journal of Geophysical Research* 81(20), 3484–3494 (1976)
- [7] Homand, F., Hoxha, D., Belem, T., Pons, M.N.: Geometric analysis of damaged microcracking granites. *Mech. Mater.* 32, 361–376 (2000)
- [8] Hoxha, D., Lespinasse, M., Sausse, J., Homand, F.: A microstructural study of natural and experimentally induced cracks in a granodiorite. *Tectonophysics* 395, 99–112 (2005)
- [9] Kemeny, J.M., Cook, N.G.W.: Micromechanics of deformation in rocks. In: Shah (ed.) *Toughening Mechanisms in Quasi-Brittle Materials*, pp. 155–188. Kluwer Academic Publishers, Dordrecht (1991)
- [10] Kraft, R.H., Molinari, J.F., Ramesha, K.T., Warner, D.H.: Computational micromechanics of dynamic compressive loading of a brittle polycrystalline material using a distribution of grain boundary properties. *Journal of the Mechanics and Physics of Solids* 56, 2618–2641 (2008)
- [11] Lauterbach, B., Gross, D.: The role of nucleation and growth of microcracks in brittle solids under compression: a numerical study. *Acta Mechanica* 159, 199–211 (2002)
- [12] Nemat-Nasser, S., Obata, M.: Microcrack model of dilatancy in brittle materials. *Journal of Applied Mechanics, Transactions ASME* 55(1), 24–35 (1988)
- [13] Paliwal, B., Ramesh, K.T.: An interacting micro-crack damage model for failure of brittle materials under compression. *J. Mech. Phys. Solids* 56, 896–923 (2008)
- [14] Renaud, V., Kondo, D., Henry, J.P.: Computations of effective moduli for microcracked materials: a boundary element approach. *Computational Materials Science* 5(1-3), 227–237 (1996)
- [15] Sai, S., Sia, N.-N.: Dynamic compressive strength of silicon carbide under uniaxial compression. *Materials Science and Engineering, A* 317, 140–144 (2001)
- [16] Bieler, T.R., Eisenlohr, P., Roters, F., Kumar, D., Mason, D.E., Crimp, M.A., Raabe, D.: The role of heterogeneous deformation on damage nucleation at grain boundaries in single phase metals. *International Journal of Plasticity* 25, 1655–1683 (2009)
- [17] Yukalova, V.I., Mourab, A., Nechad, H.: Self-similar law of energy release before materials fracture. *Journal of the Mechanics and Physics of Solids* 52, 453–465 (2004)
- [18] Wong, T.: Geometric probability approach to the characterization and analysis of microcracking in rocks. *Mechanics of Materials* 4(3-4), 261–276 (1985)
- [19] Zhao, Y.: Crack pattern evolution and a fractal damage constitutive model for rock. *International Journal of Rock Mechanics and Mining Sciences* 35(3), 349–366 (1998)
- [20] Zhu, Q.Z., Kondo, D., Shao, J.F.: Homogenization-based analysis of anisotropic damage in brittle materials with unilateral effect and interactions between microcracks. *Int. J. Numer. Anal. Meth. Geomech.* 33(5), 749–772 (2009)

# Large Deformation Analysis of Spudcan Penetration into Sand Overlying Normally Consolidated Clay

Pan Hui<sup>1,\*</sup>, Dong Wang<sup>1</sup>, Mark Cassidy<sup>1</sup>, and Qing Yang<sup>2</sup>

<sup>1</sup> Centre for Offshore Foundation Systems, The University of Western Australia, Australia

<sup>2</sup> Dalian University of Technology, China

panhu@civil.uwa.edu.au

**Summary.** Inverted conical spudcan footings are the most popular foundation for jack-up platforms in the offshore industry. Before a jack-up can be located at a site, the penetration resistance during spudcan installation must be accurately predicted. This is usually performed using bearing capacity formulae from industry standards, with the use of site-specific numerical modelling not yet common place. In this paper, the Mohr-Coulomb sand model and Tresca clay model are incorporated with a large-deformation approach called the Coupled-Eulerian Lagrangian (CEL) method within the commercial package ABAQUS. It is used to simulate the installation process of spudcans in sand overlying clay. The robustness of this large-deformation analysis method is validated against published results of numerical analyses of spudcan penetration into clay. This comparison is performed to show that the numerical simulations are suited to capture the behaviour of spudcan penetration into seabeds. A series of parametric studies are then conducted to investigate the potential for punch-through during spudcan penetration in sand overlying clay. The influence of soil properties, such as the friction and dilation behaviour of sand, the normalised sand thickness and the undrained shear strength of clay, on the bearing capacity of the spudcan, the soil failure mechanism and the depth of peak penetration resistance are discussed.

**Keywords:** spudcan, sand, clay, bearing capacity.

## 1 Introduction

The installation of the spudcan footings of mobile jack-up platforms is challenging due to complex seabed profiles. One of the main potential problems during preloading in a seabed composed of stratified sediments, in which a strong layer overlays a weak layer, is a large and sudden uncontrolled penetration. This catastrophic incident in jack-up units is referred to as ‘punch-through’. The soil

---

\* Corresponding author.

profile composed of sand overlying clay is particularly conducive to such behaviour and is a common cause of spudcan punch-through (Osborne et al. [1]).

In current practice, the bearing capacity of a spudcan at a particular depth is usually evaluated by assuming that the spudcan is wished-in-place, as specified in the ISO (2012) [2] guideline. However, this assumption is not reasonable for spudcans in multiple-layer soils. In the case of a stronger sand layer overlying soft clay, soil heave is formed gradually on the shoulder of a spudcan. When the spudcan moves into the underlying clay, a sand plug becomes trapped underneath the spudcan effectively increasing the size of the footing and transferring load deeper into the clay. These types of large deformation processes make it important to develop numerical or analytical methods to accurately predict the bearing resistances of spudcans in problematic soil conditions.

Spudcan penetration in sand overlying clay has been studied by testing models using both physical centrifuge and numerical finite element (FE) approaches. Using centrifuge tests, Craig and Chua [3] investigated the failure mechanism in terms of the penetration depth beyond the original soil interface. A slightly tapered sand plug with a depth approximately equal to the initial sand layer thickness was found to have moved into the clay layer underneath the spudcan. By employing the PIV technique in a centrifuge, the failure mechanisms of spudcan foundations were reported in Teh et al. [4]. Teh et al. [5] proposed that the ‘bearing resistance – penetration depth’ profile can be determined by three key resistances and corresponding depths from full spudcan tests. Based on an extensive series of dense sand overlying clay tests, Lee [6] presented a semi-empirical formula to calculate the peak penetration resistance,  $q_{\text{peak}}$  and then employed a simple method to predict the complete penetration resistance profile. To replicate the continuous penetration process of spudcan on sand overlying clay, various large-deformation finite element (LDFE) approaches, which make no a priori assumptions about the failure mechanisms, were used. Yu et al. [7] employed an approach termed Remeshing and Interpolation Technique with Small Strain (RITSS) to study the shape of the sand plug. Qiu et al. [8, 9] incorporated a hypoplastic constitutive model into the Coupled Eulerian-Lagrangian (CEL) method in commercial package ABAQUS/Explicit, to simulate the entire penetration process. Tho et al. [10] compared numerical penetration resistances and soil flow mechanisms with centrifuge results. In this paper, the CEL method is also used to explore the factors that influence the failure mechanisms of spudcans penetrating into sand overlying normally consolidated (NC) clay.

## 2 Numerical Method

In the CEL analysis, the structural spudcan element was taken as a Lagrangian body, and the soil was discretised within an Eulerian mesh. The Eulerian mesh was composed of 8-node linear brick elements with reduced integration and hourglass control. The Eulerian domain prior to calculation was composed of two parts: one part was initially occupied by soil materials and the other part was materially void. An Eulerian element may be partially void or shared by more than one material. Therefore, material assignment fields must be predefined to specify

the volume fractions of different materials in each element. Unlike in Lagrangian elements, materials can flow into or out of Eulerian elements freely during the analysis. Due to geometrical symmetry, only a quarter of the spudcan was considered in the three-dimensional analysis. A thin layer of void elements (i.e., material-free) was set above the original seabed surface to cover the soil berm induced by spudcan penetration. The penetration process was modelled with a displacement-controlled mode.

The contact between the structural element and soils in the following analysis was described using the ‘general contact’ algorithm, and the interface was assumed to be smooth. The Eulerian-Lagrangian contact formulation in ABAQUS is based on an enhanced immersed boundary method (Dassault Systèmes [11]). The contact algorithm automatically tracked and updated the interfaces between the Lagrangian body and the soils.

### 3 Validation with Previous Studies

Comparisons with previous studies were performed to confirm the suitability of the CEL for geotechnical large-deformation problems and provide confidence in the numerical results. In the analyses, the clay layer was normally consolidated with undrained shear strength that increases with the depth as follows:

$$s_u = s_{um} + kz \tag{1}$$

where  $s_{um}$  is the undrained shear strength of the clay at the mud-line,  $k$  is the soil strength gradient and  $z$  represents the soil depth. The clay was treated as an elastic-perfectly plastic material obeying the Tresca yield criterion. The Poisson’s ratio of the clay was taken as 0.49 to approximate a constant volume under the undrained condition, and the Young’s modulus was set as  $E = 500s_u$ .

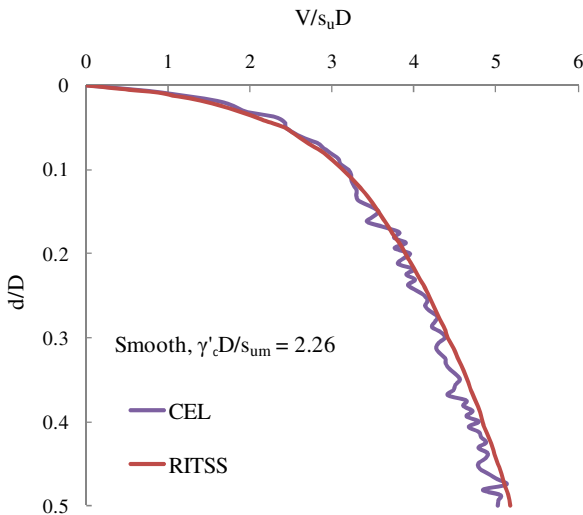
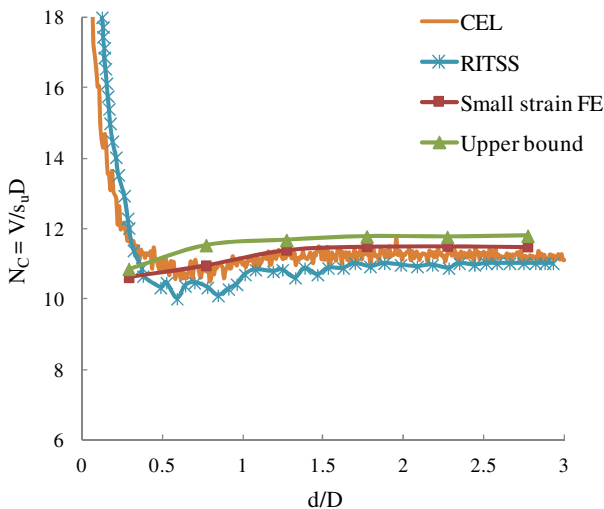


Fig. 1. Comparison of pipeline penetration resistances from RITSS and CEL

The first benchmark case was the penetration of a pipeline in NC clay, which was simulated by Wang et al. [11] using the RITSS approach. The parameters were: pipe diameter  $D = 0.8$  m; submerged unit weight of clay  $\gamma'_c = 6.5$  kN/m<sup>3</sup>;  $s_{um} = 2.3$  kPa and  $k = 3.6$  kPa/m. The pipe was penetrated to an embedment depth of  $d = 0.5D$ . The normalised load-displacement response from the CEL is presented together with that by Wang et al. [12] in Fig. 1, in which  $V$  indicates the penetration resistance. These two LDFE approaches provide roughly equivalent curves, although the CEL curve shows oscillations to some degree. The numerical oscillation was also observed in almost all other applications of the CEL (Qiu et al. [8, 9]; Tho et al. [10]).

The second benchmark case was that of spudcan penetration in NC clay. Mehryar and Hu [13] also employed the RITSS approach to simulate the penetration of a spudcan with diameter  $D = 14$  m. The submerged unit weight of clay was  $\gamma'_c = 7$  kN/m<sup>3</sup>, and the undrained strength parameters were  $s_{um} = 0$  and  $k = 2$  kPa/m. The penetration depth was defined as zero when the lowest level of the spudcan maximum sectional area touches the soil in Mehryar and Hu [13]. The bearing capacity factors from CEL and RITSS are compared in Fig. 2, in which the results of the traditional small-strain FE approach and plasticity limit analysis for the pre-embedment spudcan (Mehryar and Hu [13]) are also plotted. The capacity factor predicted by the CEL is slightly higher than that predicted by the RITSS as  $d/D > 0.4$ , and both load-displacement curves converge to the capacity factor  $N_c = 11$  at  $d/D = 3$ . The  $N_c$  values obtained from both LDFE approaches are a little lower than the factors for the wished- in-place spudcans, i.e., the bearing capacity may be overestimated if the continuous penetration process is neglected. The soil strength profile at a penetration depth of  $3D$  is shown in Fig. 3. It is observed that the soil disturbed by the spudcan penetration is approximately two times the spudcan diameter. The soil flow mechanism is extended to the seabed surface at a shallow penetration depth, but the flow mechanism changes gradually to become localised around the spudcan after deeper penetration.



**Fig. 2.** Bearing capacity factors of a spudcan in NC clay using different methods

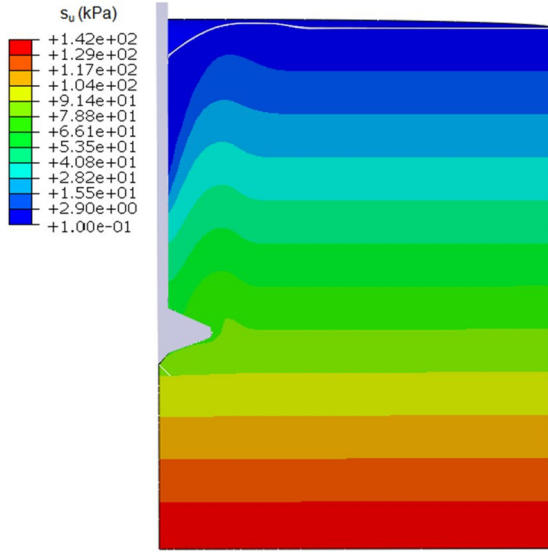


Fig. 3. Undrained strength profile at a spudcan penetration depth of 3D

### 4 Parametric Study

A series of parametric studies were undertaken to explore spudcan penetration into sand overlying NC clay, with the key factors varied in the following manner:

- sand thickness:  $H_s = 3$  and  $4.8$  m;
- sand friction angle:  $\phi' = 30, 34$  and  $38^\circ$  to represent typical loose, medium and dense sand, respectively;
- clay strength at sand-clay interface:  $s_{um} = 10, 20$  and  $40$  kPa. The strength gradient was selected as a typical constant value of  $k = 1.5$  kPa/m.

The sand was considered as an elastic-perfectly plastic material obeying the Mohr-Coulomb yield criterion. The Young’s modulus was set to  $E_{sand} = 50$  MPa and Poisson’s ratio was  $0.3$ . The submerged unit weight of sand and clay were set to  $\gamma'_s = 10$  kN/m<sup>3</sup> and  $\gamma'_c = 7$  kN/m<sup>3</sup>, respectively. The diameter of the spudcan was  $6$  m and the other dimensions are detailed in Fig. 4. The relationship between the internal friction angle and the dilation angle was derived from the following empirical expression:

$$\begin{aligned} \psi &= \phi' - 30^\circ \text{ for } \phi' > 30^\circ \\ \psi &= 0 \text{ for } \phi' \leq 30 \end{aligned} \tag{2}$$

In the following analysis, the penetration of the spudcan,  $d$ , is measured from the tip of the spudcan spigot where it touches the soil surface.

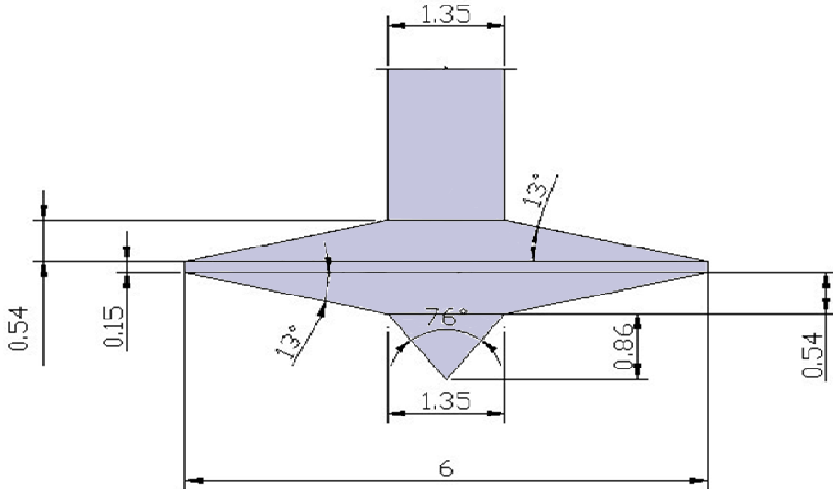
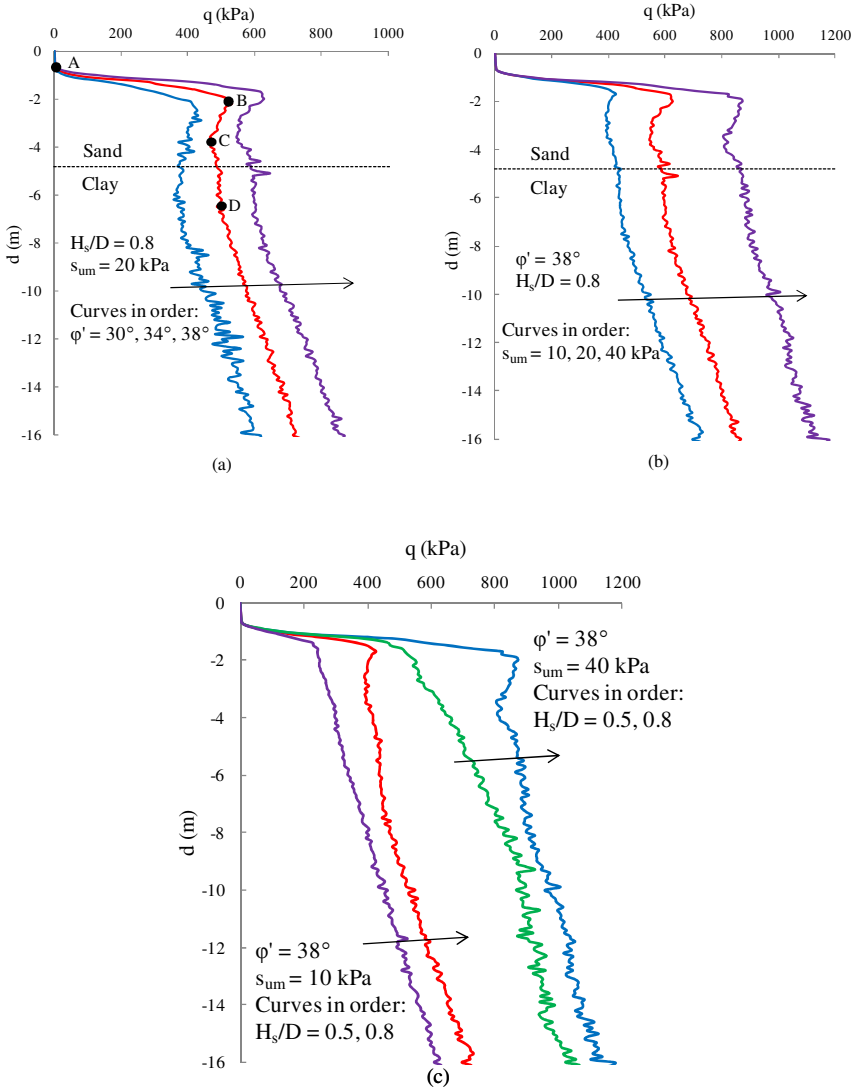


Fig. 4. Dimensions of the spudcan in the parametric study (distances in m)

#### 4.1 Effects of the Three Key Factors on the Penetration Resistance Profile

Fig. 5(a) shows the influence of the internal friction angle of sand on the bearing resistance profile. The penetration resistance, regardless of whether it is occurring in sand or clay, is enhanced by the friction angle of the sand. For  $s_{um} = 20$  kPa, punch-through failures occur against all three friction angles. On the ‘load-displacement’ curves indicating punch-through, the penetration distance from the occurrence of peak resistance to where the resistance comes back to the peak value is defined as the ‘rapid penetration depth’. This rapid penetration depth is approximately 5.6 m for the three internal friction angles in Fig. 5(a). It is commonly believed that a soil profile involving dense sand overlying clay is more prone to causing punch-through failure, but the punch-through phenomenon also occurs in loose sand overlying clay in this study.

The bearing resistance increases with increasing undrained strength of the underlying clay, as shown in Fig. 5(b). When  $\phi' = 38^\circ$  and  $H_s/D = 0.8$ , the peak bearing resistance for  $s_{um} = 40$  kPa is as high as 875 kPa, which is approximately 2 times that for  $s_{um} = 10$  kPa. Punch-through was observed in all three cases, and the depths of peak bearing resistance fall within the narrow range of  $d/D = 0.28 - 0.33$ . After the lowest level of the spudcan maximum sectional area reaches the original sand-clay interface, the gradients of the penetration resistance profiles are nearly independent of  $s_{um}$ .



**Fig. 5.** Penetration resistance profiles showing (a) effect of the friction angle of sand, (b) effect of the undrained strength of clay, (c) effect of the normalised sand thickness

The normalised sand thickness is an important factor affecting the peak penetration resistance and the occurrence of punch-through, as demonstrated in Fig. 5(c). The figure indicates that peak resistance  $q_{peak}$  increases with  $H_s$ . The reason for this trend is that wider extensions of stress in the upper sand layer are

mobilised to contribute to a larger  $q_{\text{peak}}$  for a higher sand thickness  $H_s/D$ . In the cases with  $H_s/D = 0.5$ , the resistance increases during penetration, suggesting no potential punch-through, and safe installation of a jack-up rig is deemed possible. A more obvious reduction in penetration resistance is exhibited during the post-peak stage whilst the peak resistance is enhanced by a higher  $H_s/D$ . Thus, catastrophic punch-through failure is more likely to occur with a higher  $H_s/D$  ratio. Spudcan bearing pressures for modern jack-ups are reported to be in the range of 200 to 600 kPa (Randolph et al. [14]). In Fig. 5(a)-(c), the  $q_{\text{peak}}$  values predicted by the CEL analyses are within this range, except in one case ( $\phi' = 38^\circ$ ,  $H_s/D = 0.8$ ,  $s_{\text{um}} = 40$  kPa).

#### ***4.2 Failure Mechanism of Spudcan Penetration into Sand Overlying NC Clay***

A typical case with  $\phi' = 34^\circ$ ,  $H_s/D = 0.8$  and  $s_{\text{um}} = 20$  kPa in Fig. 5(a) is used here to explain the punch-through failure mechanism of spudcan penetration into sand overlying NC clay. The bearing resistance increases sharply at the early stages until the spudcan spigot is fully penetrated into the sand surface (point A), a penetration depth of  $0.14D$ . The soil movement at this stage is very limited and falls within the sand layer. After that, the resistance continues to increase with increasing depth until  $q_{\text{peak}}$  is achieved at point B, where  $d/D = 0.33$ . The magnitude of  $q_{\text{peak}}$  is determined by the sand frustum pushed into the underlying clay at a dispersion angle; consequently, the peak resistance depends on both the sand and clay strengths in Fig. 5. The subsequent penetration leads to a marked reduction in bearing resistance up to a penetration depth of  $0.6D$  (point C). Next, the resistance gradually increases from point C to point D, accompanied by the intrusion of a sand wedge into the clay. When the lowest level of the spudcan maximum sectional area reaches the underlying clay layer (point D), the sand plug, together with the spudcan forms a composite foundation. The surrounding clay flows upwards, driven by the sand plug moving downwards. This reverse interaction would form an obvious shear plane along the periphery of the sand plug and the side friction developed along the periphery of the plug must be incorporated to assess the bearing capacity (Craig and Chua [3]). A linear increase in bearing resistance commences from point D and ends at a penetration depth of  $2.67D$ . Knowing the sand plug height,  $h$ , becomes essential not only to determine the resistance given by the side friction component, but also to assess the end bearing resistance based on an appropriate value of  $s_u$ . In this example, the height of the sand plug is approximately 4 m (see Fig. 6), which is equivalent to  $0.83H_s$ , and this observation shows reasonably good agreement with the result of  $0.9H_s$  reported by Teh [15].

### 4.3 Depth of Peak Penetration Resistance

In this section, the depths corresponding to peak penetration resistances in the parametric study are compared with the predictive equation by Teh et al. [5]. In practice, the peak resistance and corresponding penetration depth must be quantified in routine design. Teh et al. [5] proposed that the distance from the occurrence of  $q_{peak}$  to the original sand-clay interface was  $0.88H_s$  based on a series of centrifuge tests. Thus, the depth of the peak penetration resistance relative to the lowest level of the spudcan maximum sectional area is:

$$d_{peak} = 0.12H_s \tag{3}$$

It is again noted that the depth of peak resistance here is defined relative to where the tip of the spudcan spigot touches the soil. Due to different definitions of zero depth, the  $d_{peak}$  measured from the numerical resistance profile should be converted to the definition used by Teh et al. [5] to maintain consistency. Fig. 7 is a summary of the penetration depths required to mobilise  $q_{peak}$  from the CEL study, together with Teh’s equation. The CEL results show consistent agreement with Equation 3, except in one loose sand case. The reason for this discrepancy may be that the equation of Teh et al. [5] was based only on the tests for dense sand overlying clay.

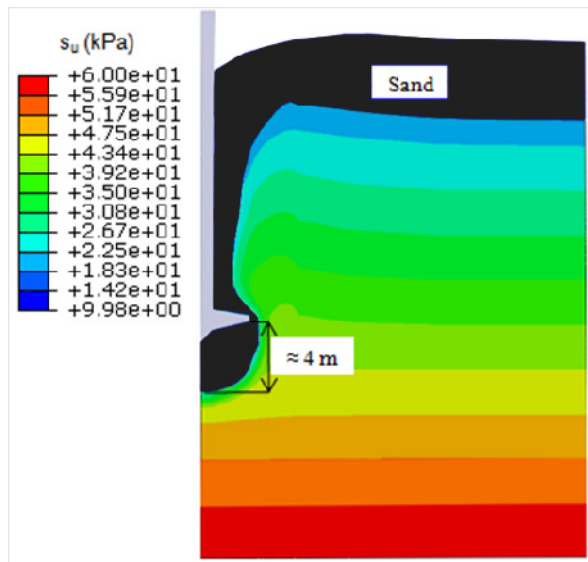


**Fig. 6.** Undrained strength profile of clay layer at a penetration depth of  $2.5D$  ( $\phi' = 34^\circ$ ,  $H_s/D = 0.8$ ,  $s_{um} = 20$  kPa)

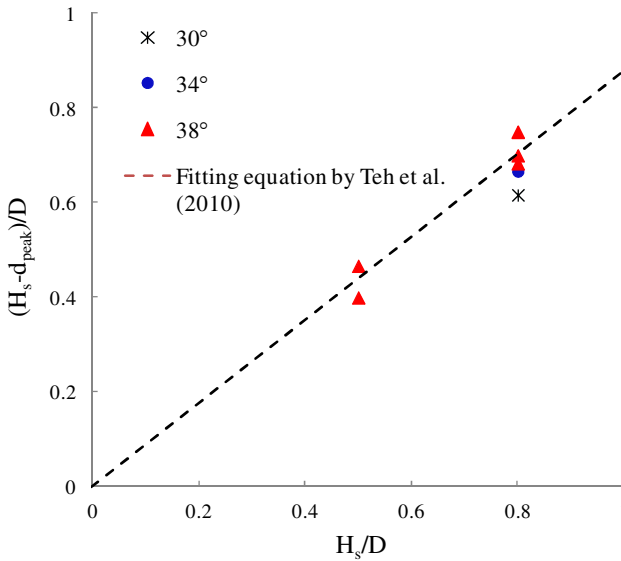


**Fig. 7.** Normalised depth of peak penetration resistance,  $d_{peak}$ , in relation to the normalised sand layer thickness,  $H_s/D$

## 5 Conclusions

This paper reports the results of a CEL analysis investigating the potential for punch-through in spudcan foundations penetrating through sand into NC clay.

The peak bearing resistance increases with the internal friction angle of sand, undrained shear strength of clay and normalised sand thickness. Punch-through failure may occur in loose sand overlying clay, and the rapid penetration depth observed in loose sand is close to that observed in dense sand. The gradients of the penetration resistance profiles are nearly independent of  $s_{um}$  when the lowest level of the spudcan maximum sectional area penetrates into the clay layer. The normalised sand thickness is a key factor controlling the occurrence of punch-through: while no punch-through was found at  $H_s/D = 0.5$ , it is more likely to occur at larger  $H_s/D$  values, and the consequences are more serious because a more rapidly achieved penetration depth would be expected at these values. The penetration depths, when measured against peak resistances from a parametric study, fit well with the existing empirical equation.

**Acknowledgements.** This work forms part of the activities of the Centre for Offshore Foundation Systems (COFS), which is supported by the State Government of Western Australia and The Lloyd's Register Educational Trust as a Centre of Excellence, and now forms one of the primary nodes of the Australian Research Council Centre of Excellence in Geotechnical Science and Engineering. The authors are grateful for this support.

## References

- [1] Osborne, J.J., Houlby, G.T., Teh, K.L., Bienen, B., Cassidy, M.J., Randolph, M.F., Leung, C.F.: Improved guidelines for the prediction of geotechnical performance of spudcan foundations during installation and removal of jack-up units. In: Offshore Technology Conference (OTC), OTC 20291, Houston, Texas (2009)
- [2] ISO/FDIS 19905-1: Petroleum and natural gas industries – Site-specific assessment of mobile offshore unit. Part 1: Jack-ups. International Organization for Standardization (2012)
- [3] Craig, W.H., Chua, K.: Deep penetration of spud-can foundation on sand and clay. *Geotechnique* 40(4), 541–556 (1990)
- [4] Teh, K.L., Cassidy, M.J., Leung, C.F., Chow, Y.K., Randolph, M.F., Quah, C.: Revealing the bearing capacity mechanisms of a penetrating spudcan through sand overlying clay. *Geotechnique* 58(10), 793–804 (2008)
- [5] Teh, K.L., Leung, C.F., Chow, Y.K., Cassidy, M.J.: Centrifuge model study of spudcan penetration in sand overlying clay. *Geotechnique* 60(11), 825–842 (2010)
- [6] Lee, K.K.: Investigation of potential spudcan punch-through failure on sand overlying clay soils. PhD thesis, The University of Western Australia, Perth (2009)
- [7] Yu, L., Hu, Y., Liu, J.: Spudcan penetration in loose sand over uniform clay. In: Proceedings of the 28th International Conference on Ocean, Offshore and Arctic Engineering, Hawaii, USA (2009)
- [8] Qiu, G., Henke, S.: Controlled installation of spudcan foundations on loose sand overlying weak clay. *Marine Structures* 24(4), 528–550 (2011)
- [9] Qiu, G., Henke, S., Grabe, J.: 3D FE analysis of the installation process of spudcan foundations. In: Proceedings of the 2nd International Symposium on Frontiers in Offshore Geotechnics, Perth, WA, pp. 685–690 (2010)
- [10] Tho, K., Leung, C.F., Chow, Y.K., Swaddiwudhipong, S.: Eulerian finite element technique for analysis of jack-up spudcan penetration. *Int. J. Geomech.* (2012), doi:10.1061/(ASCE)GM.1943-5622.0000111
- [11] Dassault Systèmes.: ABAQUS. Version 6.10 Analysis Manual (2010)
- [12] Wang, D., White, D.J., Randolph, M.F.: Large deformation finite element analysis of pipe penetration and large-amplitude lateral displacement. *Can. Geotechnical J.* 47(8), 842–856 (2010)
- [13] Mehryar, Z., Hu, Y.: Penetration analysis of spudcan foundation in NC clay. In: The 20th International Offshore and Polar Engineering Conference, Kitakyushu, Japan, May 26-31 (2002)
- [14] Randolph, M.F., Cassidy, M.J., Gourvenec, S., Eribrich, C.T.: Challenges of offshore geotechnical engineering. In: Proceedings of the 16th International Conference on Soil Mechanics and Geotechnical Engineering (16ICSMGE), Osaka, September 12-16, pp. 123–176. Millpress Science, Rotterdam (2005)
- [15] Teh, K.L.: Punch-through of spudcan foundation in sand overlying clay. PhD thesis, National University of Singapore, Singapore (2007)

# Application of Data Mining Techniques for the Development of New Rock Mechanics Constitutive Models

T. Miranda, L.R. Sousa<sup>\*</sup>, W. Ruggenthen, and R.L. Sousa

State Key Laboratory for Geomechanics and Deep Underground Engineering, Beijing, China, and University of Porto, Portugal  
16 Tsinghua East Road, Haidian District, Beijing, China, 100083  
ribeiro.e.sousa@gmail.com

**Summary.** Data Mining (DM) techniques have been successfully used in many fields and more recently also in geotechnics with good results in different applications. They are adequate as an advanced technique for analysing large and complex databases that can be built with geotechnical information within the framework of an overall process of Knowledge Discovery in Databases (KDD). A KDD process is carried out in the context of rock mechanics using the geotechnical information of two hydroelectric schemes built in Portugal and at DUSEL (Deep Underground Science and Engineering Laboratory). The purpose was to find new models to evaluate strength and deformability parameters and also empirical geomechanical indexes. Databases of geotechnical data were assembled and DM techniques used to analyse and extract new and useful knowledge. The procedure allowed developing new, simple, and reliable models for geomechanical characterization using different sets of input data which can be applied in different situations of information availability.

**Keywords:** Data Mining, rock masses, models.

## 1 Introduction

The determination of geomechanical parameters of rock masses for underground structures is still subject to high uncertainties that are related to geotechnical conditions and construction aspects. An accurate determination of the geomechanical parameters is important for an efficient and economic design of the support of the underground excavation and for the excavation itself. The methodologies used to obtain the parameters are based on laboratory and in situ tests and the application of empirical methodologies. The methods are based on an overall description of the rock mass and on the determination of key parameters that can be related to strength and deformability of the ground medium [1-3].

---

<sup>\*</sup> Corresponding author.

Data Mining (DM) techniques have been successfully used in many fields but rarely in geotechnics. They are advanced techniques which allow analyzing large and complex databases like the ones it is possible to build with geotechnical information. Examples of DM techniques include simple multiple regression, Artificial Neural Networks (ANN) and Bayesian networks (BN).

## 2 Data Mining and Geotechnical Engineering

The formal and complete analysis process, called Knowledge Discovery in Databases (KDD), defines the main procedures for transforming raw data into useful knowledge. DM is just one step in the KDD process concerned with the application of algorithms to the data to obtain models even though normally for simplification sake, the KDD process is referred as DM. The application of DM techniques aim at the extraction of useful knowledge in the form of models or patterns from observed data and it is very important that this knowledge is both novel and understandable.

These tools allow a deep analysis of complex data, which would be otherwise very difficult using classical statistics tools or through one or even a panel of human experts, who could overlook important details. However, the computational process can not completely substitute human experts. Computational tools are only a complement which allows the automatic finding of patterns and models embedded in the data. The knowledge discovered in the process must be explainable in the light of science and experience and must always be validated before being used in other applications.

The KDD process consists of the following steps: i) Data selection: the application domain is studied and relevant data are collected; ii) Pre-processing: noise or irrelevant data are removed (data cleaning) and multiple data sources may be combined (data integration); iii) Transformation: data are transformed in appropriate forms for the DM process; iv) DM: intelligent methods are applied to extract models or patterns; v) Interpretation: results from the previous step are studied and evaluated.

DM is a relatively new area of computer science that is positioned at the intersection of statistics, machine learning, data management and databases, pattern recognition, artificial intelligence, and other areas. There are several DM techniques, each with their own purposes and capabilities. Examples of these techniques include Decision and Regression Trees, Rule Induction, Neural and Bayesian Networks, Support Vector Machines, K-Nearest Neighbors, Learning Classifier Systems, and Instance-Based algorithms [1-3].

## 3 Application to Underground Hydroelectric Schemes

The results of two KDD processes are presented where geotechnical data gathered in two important underground work recently built in the North of Portugal in predominantly granite rock masses. New alternative regression models were developed using multiple regression (MR) and artificial neural networks (ANN) for the analytical calculation of strength and deformability parameters and the RMR index [1]. These

models were built up considering different sets of input data, allowing their application in different scenarios of data availability. Most of the models use less information than the original formulations but maintain a high predictive accuracy, which can be useful in the preliminary design stages in any case where geological/geotechnical information is limited. The application of DM also provided insight to the most influential parameters for the behaviour of the rock mass of interest.

For the first case, Venda Nova II hydroelectric scheme [1] (Fig. 1), the goal was to develop models for the calculation of strength and deformability parameters (friction angle -  $\phi'$ ; cohesion -  $c'$ ; deformability modulus -  $E$ ) while for the second case, Bemposta II hydroelectric scheme [4] (Fig. 2), the parameters of interest were the values of RMR and  $E$ .

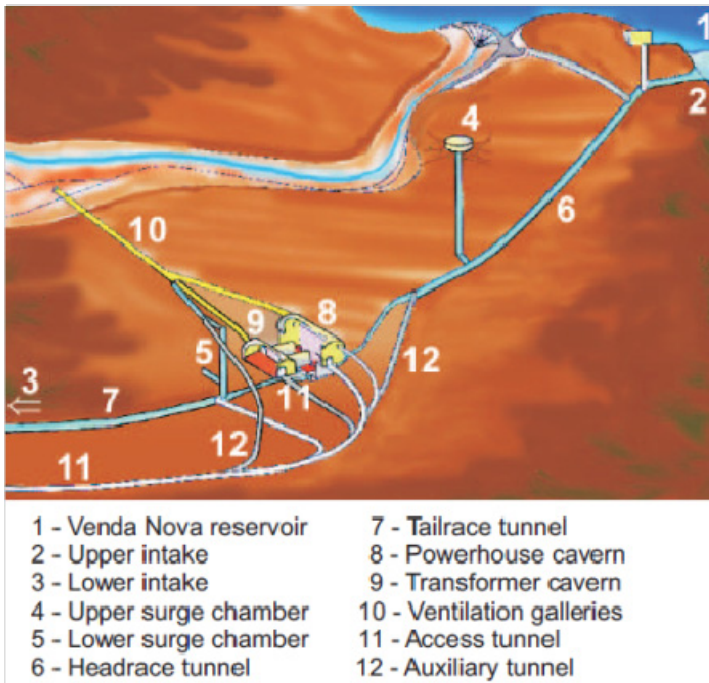


**Fig. 1.** Venda Nova II underground complex [1]

For Venda Nova II scheme the SAS Enterprise Miner software was used [1]. The evaluation of the developed models was performed using the results provided by this software and complementary calculations and spreadsheets. The data were organized and structure in a database composed by 1,230 examples and twenty-two attributes [1]. The models obtained for the granite rock formations are presented in detail in publications [1, 2].

For Bemposta II, also mainly in granite formations, the database is composed by 286 lines with RMR values and their parameters, 270 lines with  $Q$  values and their parameters, and 686 lines with values of SMR and parameters  $P_1$  to  $P_5$  and adjustment factor AF [2]. The models obtained are presented in detail in publication [2].

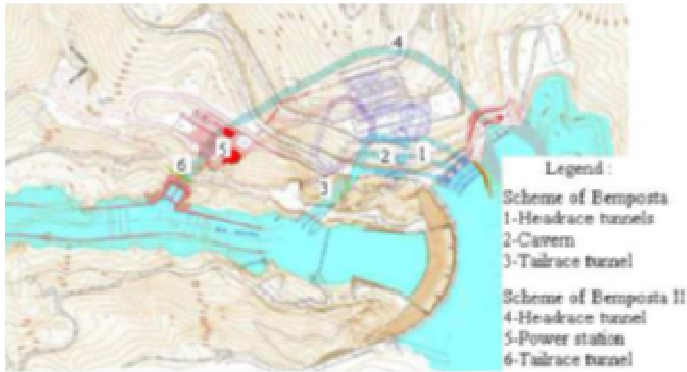


Fig. 2. Bemposta II hydroelectric scheme [4]

#### 4 New Models for Dusel

During the preliminary design for the evaluation of the DUSEL that was considered for siting at the former Homestake gold mine in Lead, SD [5], a large database of geotechnical data was produced. The geotechnical database was analyzed using these innovative data mining tools and new and useful models were developed [3]. The laboratory was seen as a multi-discipline facility with particle physics providing the lead but other disciplines being a significant part of the facility, including geomicrobiology, geosciences, and geoengineering. The possibilities for how the non-physics sciences would participate were described in detail in the EarthLab report to the NSF [5], (Fig. 3).

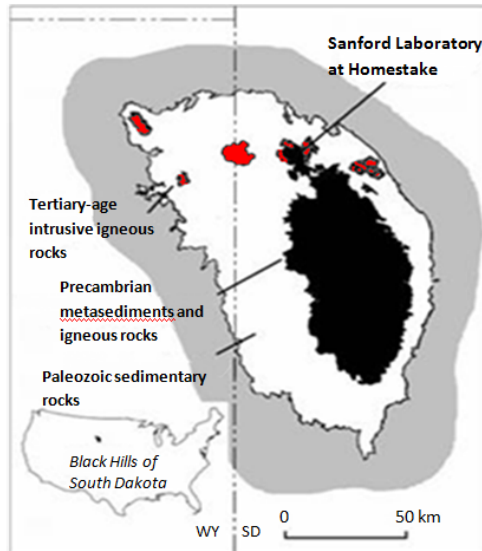
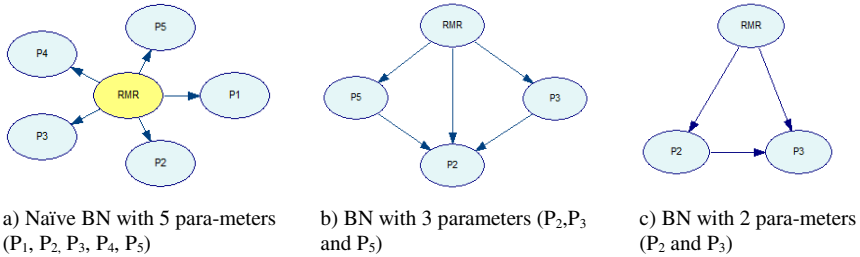


Fig. 3. Location of the Sanford Laboratory in the Black Hills, SD [2]

The developed models are presented in detail in publication [3]. The database included 128 cases gathered from a mapping program conducted at 4850 Level from LFA – Lachel Felice and Associates [3]. The DM algorithms used were ANN, SVM and BN. Several BN were learned and tested for predicting RMR values using software GeNIe. Fig. 4 shows the structure of learned models using different number of parameters.



**Fig. 4.** Learned BN

## 5 Conclusions

In the preliminary stages of design in the context of rock mechanics, the decision regarding the geomechanical parameter values and other important indexes is normally based on limited information. Thus, the use of data from past projects to help in this task appears as a rational solution to mitigate this problem. The application of DM techniques to well organised data gathered from large geotechnical works like underground structures can provide the basis for the development of models that can be very useful in future projects.

The main achievements of this work are pointed out in the next items [1, 2, 3].

- Development of new and reliable regression models based on MR and ANN algorithms for the calculation of the geomechanical parameters  $\phi'$ ,  $c'$  and E and RMR index.
- Enhancement of the understanding of the main parameters related to the behavior of the granite rock masses.
- The relevance of the Q index for determining rock mass strength parameters was already known since the relation  $\tan(J_r/J_a)$  is used to approximate the inter block shear strength
- The results of some expressions concerning the calculation of E were compared. A methodology to define a single final value for this parameter was established and validated with the results of reliable in situ tests.

- Using a database in the scope of the DUSEL project, new geomechanical models for the prediction of rock mass quality indexes, namely RMR, Q and GSI were developed using DM. The MR, ANN and SVM algorithms. With the data available it was possible to learn a BN that has the goal of predicting RMR. The results of the preliminary analysis show the potential of BN as predictors and confirm the results of DM algorithms. One of the great advantages of BN over other methods is the ability to facilitate the combination of domain knowledge and data.

## References

- [1] Miranda, T.: Geomechanical parameters evaluation in underground structures. Artificial intelligence, Bayesian probabilities and inverse methods. PhD thesis. University of Minho, Guimarães, Portugal, 291p. (2007)
- [2] Miranda, T., Sousa, L.R.: Application of Data Mining techniques for the development of new geomechanical characterization models for rock masses. In: Sousa, Vargas, Fernandes, Azevedo (eds.) Innovative Numerical Modelling in Geomechanics, 20p. (2012)
- [3] Sousa, L.R., Miranda, T., Ruggenthen, W., Sousa, R.L.: Models for geomechanical characterization of the rock mass formations at DUSEL using Data Mining techniques. In: ARMA Symposium, Chicago, vol. 14 (2012)
- [4] Lima, C., Resende, E., Esteves, C., Neves, J.: Bemposta II Powerhouse Shaft. Geotechnical Characterization, Design and Construction. In: 12th Int. Congress on Rock Mechanics, Beijing, October 19-22, 6p. (2011)
- [5] McPherson, B., Elsworth, D., Fairhurst, C., Kelsler, S., Onstott, T., Roggenthen, W., Wang, H.: EarthLab: A subterranean laboratory and observatory to study microbial life, fluid flow, and rock deformation, A Report the National Science Foundation, NSF, Washington, DC, 60 (2003)

# Ground Response Curve (GRC) and Excavation Damage Zone Based on an Isotropic Damage Model

Hamed Molladavoodi\*

Department of Mining and Metallurgical Engineering  
Amirkabir University of Technology  
424 Hafez Ave, Tehran, Iran  
hamedavodi@aut.ac.ir

**Summary.** Analysis of stresses and displacements around underground openings is necessary in a wide variety of civil and geotechnical, petroleum and mining engineering problems. In addition, an excavation damaged zone (EDZ) is generally formed around underground openings even in the absence of blasting effects. The dominant cause of irreversible deformations in brittle rocks is damage process.

One of the most widely used methods in tunnel design is the convergence–confinement method (CCM) for its practical application. The elastic–plastic models are usually used in the convergence–confinement method as a constitutive model for rock behavior. The common plastic models used to simulate the rock behavior, does not model the rock realistically and often the important issues such as stiffness degradation and softening are ignored. Therefore, the use of damage constitutive models in the convergence–confinement method is essential in the design process of rock structures. In this paper, the basic concepts of continuum damage mechanics are outlined. Then a solution for a circular tunnel under hydrostatic stress field, with consideration of a damage model for rock mass has been developed. The ground response curve was calculated based on an isotropic damage model. The radius of excavation damage zone was evaluated with the proposed damage model. The convergence–confinement method based on damage model can consider the effects of post-peak rock behavior on the ground response curve and excavation damage zone. The rock brittleness effect on the ground response curve and excavation damage zone can be considered with developed damage model in the convergence–confinement method.

**Keywords:** Damage mechanics, Convergence–confinement method, Strain Softening, Brittleness.

## 1 Introduction

The convergence confinement method (CCM) is an effective analytical tool for the underground openings design. It consists of three basic components: longitudinal

---

\* Corresponding author.

deformation profile (LDP), support characteristic curve (SCC) and ground response curve (GRC). The study of the interaction between support and tunnel can easily be carried out using the convergence–confinement method. The GRC, which describes the relationship between decreasing of inner pressure and the increasing of radial displacement of tunnel wall, is generally evaluated by analytical methods based on axial symmetry plane strain assumption (see [1]).

Many studies have been conducted on the tunnel convergence–confinement method. These available studies, although distinguished from different failure criteria, post-failure behaviors and solution methods, are generally based on the plasticity theory (e.g., [2-7]).

The main cause of irreversible changes in quasi-brittle materials such as rock is the damage process occurring within the material (see [8]). The macroscopic and phenomenological consequence of damage process is stiffness degradation, dilatation, & softening. In this paper, the ground response curve (GRC) was formulated based on the damage mechanics theory.

The construction of a long circular tunnel under a hydrostatic in situ stress condition can be considered as an axial symmetry plane strain problem. According to different fictitious inner pressure provided by the tunnel face and the support, elastic and damage zone will be created around the tunnel. Fig.1 schematically illustrates a general case in the existence of regions.

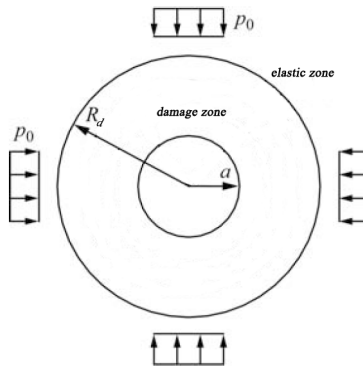


**Fig. 1.** Schematic representation of the rock mass zones after tunnel excavation

In Fig. 1,  $P_0$  is the hydrostatic in situ stress;  $a$  &  $R_d$  are the radii of the tunnel and the elastic-damage interface respectively.

## 2 A Damage Constitutive Model

In this model, the rock in pre failure region behaves linear elastic. With stress increment, the stress state attained to the failure criteria. The failure criterion in this model is assumed Mohr-Coulomb failure criterion as following:

$$F = \sigma_1 - k_\phi \sigma_3 - f_c(D) = 0 \tag{1}$$

where  $\sigma_1, \sigma_3$  are maximum and minimum principal stresses respectively.  $k_\phi$  is a constant frictional coefficient calculated as below:

$$k_\phi = \frac{1 + \sin \phi}{1 - \sin \phi} \tag{2}$$

In Eq. (1),  $f_c(D)$  is the resistant function of failure surface depending on the rock damage variable ( $D$ ). In damage mechanics, rock stiffness is gradually degraded with damage progression. The stiffness modulus of damaged rock is calculated as following:

$$E = (1 - D)E_0 \tag{3}$$

where  $E_0$  and  $E$  are the rock stiffness modulus of intact and damaged rock respectively. The range of damage variable ( $D$ ) is between 0 (intact rock) to 1 for completely damaged rock.

In softening region, the rock strength degrades as power law function with strain increment. The rock stress- strain curve under uniaxial compressive strength is illustrated in Fig. (2).

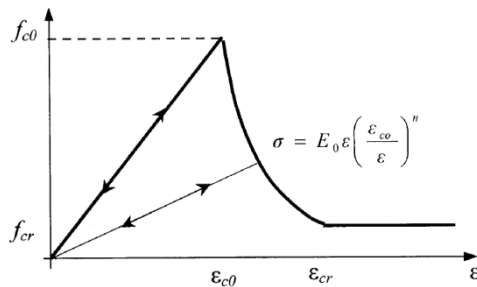


**Fig. 2.** The rock stress-strain curve with Power-law softening and residual strength at post-peak region (see [9])

The residual strength coefficient ( $\lambda$ ) is defined as the fraction of residual ( $f_{cr}$ ) to peak strength ( $f_{c0}$ ) (see [9]).  $\epsilon_{c0}$  is the strain at peak strength ( $f_{c0}$ ). In Fig. 2, the post-peak rock stress-strain curve consists of two regions. In first part, the rock strength decreases as power law softening with strain increment. After the rock strength decreases to residual strength (corresponding to  $\epsilon_{cr}$ ), it is fixed to residual strength in second region. Based on Zhu & Tang, [9], the stress-strain curve in softening region is described with decreasing and power-law relation:

$$\sigma = E_0 \cdot \left(\frac{\epsilon_{c0}}{\epsilon}\right)^b \cdot \epsilon \tag{4}$$

where  $b$  is rock brittleness parameter. Based on Eq. (4), the strain corresponding to residual strength ( $\epsilon_{cr}$ ) can be expressed as

$$\epsilon_{cr} = \frac{\epsilon_{c0}}{(b-1)\sqrt{\lambda}} \tag{5}$$

With comparison of Eqs. (3) & (4), the damage evolution rule is explained as below:

$$D = \begin{cases} 0 & \epsilon < \epsilon_{c0} \\ 1 - \left(\frac{\epsilon_{c0}}{\epsilon}\right)^b & \epsilon_{c0} \leq \epsilon < \epsilon_{cr} \\ 1 - \frac{\lambda\epsilon_{c0}}{\epsilon} & \epsilon_{cr} \leq \epsilon \end{cases} \tag{6}$$

In above equation, the damage evolution law is defined based on total strain. The shear damage evolution is always related to maximum compressive strain (see [9]). Based on tunnel loading status, the tangential strain ( $\epsilon_\theta$ ) is substituted to the uniaxial compressive strain ( $\epsilon$ ) in Eq. (6). The mechanical behavior of rock in bi-axial compression and confinement state of tunnel is associated with increasing of rock strength and strain corresponding to the peak strength. Therefore, the tangential strain at interface of the elastic and damage zone ( $\epsilon_{\theta e}$ ) can be substituted to  $\epsilon_{c0}$  in Eq. (6). As a result, Eq. (6) can be rewritten as below:

$$D = \begin{cases} 0 & \epsilon_\theta < \epsilon_{\theta e} \\ 1 - \left(\frac{\epsilon_{\theta e}}{\epsilon_\theta}\right)^b & \epsilon_{\theta e} \leq \epsilon_\theta < \epsilon_{cr} \\ 1 - \frac{\lambda\epsilon_{\theta e}}{\epsilon_\theta} & \epsilon_{cr} \leq \epsilon_\theta \end{cases} \tag{7}$$

Based on Eq. (4), the rock strength ( $f_c$ ) in softening region can be formulated as

$$f_c = E_0 \left(\frac{\epsilon_{c0}}{\epsilon_\theta}\right)^b \cdot \epsilon_\theta \tag{8}$$

Based on Molladavoodi & Mortazavi, [10], the brittleness parameter is defined as following

$$b = \frac{r_0}{g_f - r_0} \tag{9}$$

In above equation,  $r_0$  is elastic energy associated with peak strength ( $f_{c0}$ ) can be calculated from the following equation:

$$r_0 = \frac{f_{c0}^2}{2E_0} \tag{10}$$

In Eq. (9),  $g_f$  is the area under the compressive uniaxial stress–strain diagram (compressive fracture energy for unit volume). The relation between minimum and maximum principal strains in elastic zone is defined by Poisson’ ratio ( $\nu$ ).

After microcracks creation and progression in damage zone, the ratio between minimum and maximum principal strains increases. In damage zone, these relations can be expressed as

$$d\varepsilon_r = -f d\varepsilon_\theta \tag{11}$$

Based on the isotropic damage mechanics, the parameter ( $f$ ) within damage zone can be written as (see [11])

$$f = \frac{\nu^0}{1-D} \tag{12}$$

Where  $\nu^0$  is Poisson' ratio of intact rock.

### 3 Analyses of Ground Responses

#### 3.1 Elastic Zone

The elastic solution for the excavation of cylindrical cavities in a hydrostatically loaded medium is given by Lamé' solution (see [12]). It applies to the elastic region of this problem (where  $r > R_d$ ). The stress distributions in this region can be expressed as

$$\sigma_r = P_0 - (P_0 - \sigma_{re})\left(\frac{R_d^2}{r^2}\right) \tag{13}$$

$$\sigma_\theta = P_0 + (P_0 - \sigma_{re})\left(\frac{R_d^2}{r^2}\right) \tag{14}$$

where  $\sigma_r$  and  $\sigma_\theta$  are the stresses in radial and tangential directions;  $P_0$  is in situ and initial isotropic stress of region, and  $\sigma_{re}$  denotes the radial stress at the elastic- damage interface ( $R_d$ ). The distributions of radial strains ( $\varepsilon_r$ ), tangential strains ( $\varepsilon_\theta$ ), and radial displacement ( $u$ ) is expressed as below

$$\varepsilon_r = -\frac{(P_0 - \sigma_{re})}{2G_0} \left(\frac{R_d^2}{r^2}\right) \tag{15}$$

$$\varepsilon_\theta = \frac{(P_0 - \sigma_{re})}{2G_0} \left(\frac{R_d^2}{r^2}\right) \tag{16}$$

$$u = \frac{(P_0 - \sigma_{re})}{2G_0} \left(\frac{R_d^2}{r}\right) \tag{17}$$

where  $G_0$  is the shear modulus of intact rock. Since the radial and tangential stresses at the elastic-damage interface ( $r = R_d$ ) should satisfy the Mohr-Coulomb criterion in Eq. (1), it leads to

$$\sigma_{re} = \frac{2P_0 - f_{c0}}{k_\phi + 1} \tag{18}$$

$$\sigma_{\theta e} = 2P_0 - \frac{2P_0 - f_{c0}}{k_\phi + 1} \tag{19}$$

Based on Eqs. (15) & (16), the radial and tangential strains at the elastic and damage zones interface ( $r = R_d$ ) can be calculated as below

$$\varepsilon_{re} = -\frac{(P_0 - \sigma_{re})}{2G_0} \tag{20}$$

$$\varepsilon_{\theta e} = \frac{(P_0 - \sigma_{re})}{2G_0} \tag{21}$$

### 3.2 Damage Zone

It is required to solve for the stresses and displacements in the damage zone to obtain the ground response curve. Assuming a state of plane strain and axial symmetry around the tunnel opening, the strain-displacement compatibility equation in polar coordinate system can be expressed as

$$\varepsilon_\theta = \frac{u}{r}, \quad \varepsilon_r = \frac{du}{dr} \tag{22}$$

Because of the complex stress-strain relation in damage zone, it not possible to find closed-form solutions to the stress and strain distributions. In this condition, a numerical solution proposed by Brown et al. [2] was used. This numerical solution includes a stepwise procedure that calculates the stresses, strains, and displacements on the boundaries of a number of annular rings. The damage zone is divided to a number of annular rings. Based on Fig. 3, ring ( $j-1$ ) lies between normalized radii  $\rho_{(j)} = r_{(j)}/R_d$  and  $\rho_{(j-1)} = r_{(j-1)}/R_d$ . The displacement, strain, and stress at the normalized radius  $\rho_{(j)}$  can be written as  $u_{(j)}$ ,  $\varepsilon_{\theta(j)}$ ,  $\varepsilon_{r(j)}$ ,  $\sigma_{\theta(j)}$ , and  $\sigma_{r(j)}$ .

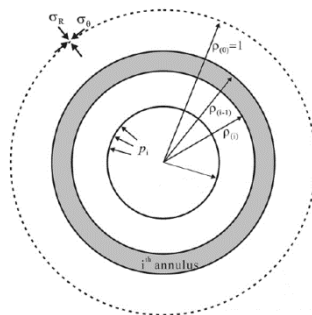


Fig. 3. Normalized damage zone with finite number of annuli

Based on Eq. (22) and damage zone division to annular rings, the strain-displacement relations at normalized radii  $\rho_{(j)}$  and  $\rho_{(j-1)}$  is as following

$$\varepsilon_{\theta(j)} = \frac{u_{(j)}}{\rho_{(j)}}, \varepsilon_{r(j)} = \left(\frac{du}{d\rho}\right)_j \quad (23)$$

If the annular rings are considered quite thin, an approximate relation can be written as below

$$\frac{u_{(j-1)} - u_{(j)}}{\rho_{(j-1)} - \rho_{(j)}} = \frac{1}{2} \left[ \left(\frac{du}{d\rho}\right)_{(j-1)} + \left(\frac{du}{d\rho}\right)_{(j)} \right] \quad (24)$$

If the displacement expression and its derivative calculated by Eq. (23) is substituted in above equation, Eq.(24) can be rewritten as

$$\rho_{(j)} = \frac{2\varepsilon_{\theta(j-1)} - \varepsilon_{r(j-1)} - \varepsilon_{r(j)}}{2\varepsilon_{\theta(j)} - \varepsilon_{r(j-1)} - \varepsilon_{r(j)}} \cdot \rho_{(j-1)} \quad (25)$$

In a step of numerical calculation, the tangential strain ( $\varepsilon_{\theta}$ ) increased as  $d\varepsilon_{\theta}$ . The tangential strain increment ( $d\varepsilon_{\theta}$ ) selected an arbitrary small value. The tangential strain increment is as below

$$d\varepsilon_{\theta} = \varepsilon_{\theta(j)} - \varepsilon_{\theta(j-1)} \quad (26)$$

In the strain-softening region, the radial strain can be calculated as following

$$d\varepsilon_{r(j)} = -f \cdot d\varepsilon_{\theta(j)} \quad (27)$$

The parameter ( $f$ ) is calculated based on Eq. (12). At elastic-damage boundary ( $\rho = \rho_{(1)} = 1$ ), the principals strains ( $\varepsilon_{\theta(1)}, \varepsilon_{r(1)}$ ) are given by Eqs. (20) & (21).  $\varepsilon_{\theta(2)}, \varepsilon_{r(2)}$  and  $\rho_{(2)}$  can be calculated using an arbitrary small value ( $d\varepsilon_{\theta}$ ) and based on Eqs. (25), (26), and (27). With increment of tangential strain, the damage variable increases and the rock strength decreases based on Eqs. (7) & (8) respectively. Then the parameter ( $f$ ) is estimated based on the updated damage variable. The stress states in the softening region should satisfy the Mohr-Coulomb failure criterion. The failure criterion can be expressed with the radial and circumferential stresses,  $\sigma_r$  and  $\sigma_{\theta}$ , such as

$$F = \sigma_{\theta} - k_{\phi}\sigma_r - f_c = 0, \quad \sigma_{\theta} = k_{\phi}\sigma_r + f_c \quad (28)$$

The differential equation of equilibrium must be satisfied by the rock stress state as below

$$\frac{d\sigma_r}{d\rho} + \frac{\sigma_r - \sigma_{\theta}}{\rho} = 0 \quad (29)$$

In above equation, the tangential stress ( $\sigma_{\theta}$ ) is substituted from Eq. (28). It leads to

$$\frac{d\sigma_r}{d\rho} + \frac{(1-k_{\phi})\sigma_r + f_c}{\rho} = 0 \quad (30)$$

By dividing the damage zone with a number of thin annular rings (Fig.3), the above equation can be rewritten between normalized radii  $\rho_{(j-1)}$  and  $\rho_{(j)}$  as following

$$\frac{\sigma_{r(j)} - \sigma_{r(j-1)}}{\rho_{(j)} - \rho_{(j-1)}} + \frac{(1 - k_\phi) \left[ \frac{\sigma_{r(j)} + \sigma_{r(j-1)}}{2} \right] + f_{c(j)}}{\left[ \frac{\rho_{(j-1)} + \rho_{(j)}}{2} \right]} = 0 \quad (31)$$

After some manipulation on above equation, the solution for  $\sigma_{r(j)}$  is as below

$$\sigma_{r(j)} = \sigma_{r(j-1)} - 2 \left( \frac{\rho_{(j-1)} - \rho_{(j)}}{2\rho_{(j)} + k_\phi(\rho_{(j-1)} - \rho_{(j)})} \right) \cdot f_{c(j)} \quad (32)$$

where  $f_{c(j)}$  is the post-peak rock strength can be calculated based on Eq. (8). The radial stress on the outer boundary of the first annulus in which ( $\rho = \rho_{(1)} = 1$ ) is given by Eq. (18). Using this as the starting point, successive values of  $\sigma_{r(j)}$  may be calculated from Eq. (32) for the normalized radii determined from Eq. (25). When  $\varepsilon_\theta$  reaches the residual strain ( $\varepsilon_{cr}$ ) on Eq. (5), the rock strength is considered constant at the residual strength ( $f_{cr}$ ).

The stepwise process was repeated several times to determine completely the stresses, strains, and displacements in damage and residual zones. After  $n$  times calculation, the last  $\sigma_{r(j)}$ , i.e.  $\sigma_{r(n)}$ , reaches the internal support pressure value,  $P_i$  which is acting on the excavation surface of the opening with radius  $a$ . The damage radius  $R_d$  can be obtained from the following relation:

$$R_d = \frac{a}{\rho_{(n)}} \quad (33)$$

The convergence of the tunnel wall can be calculated as below

$$u_{(n)} = \varepsilon_{\theta(n)} \cdot a \quad (34)$$

## 4 Application

In order to show the applicability of the proposed damage model in evaluation of the ground reaction curve and excavation damage zone, a typical circular tunnel of radius  $a = 5 \text{ m}$  was considered. This tunnel is excavated in a fair to good quality rock at depth which the in situ hydrostatic stress is  $P_0 = 55 \text{ MPa}$ . Table.1 shows the rock mass properties used to solution. Similar conditions could exist in the deep tunnel projects.

**Table 1.** The rock mass properties used to solution

$E_0$ (GPa)	$\nu$	$\phi$	$f_{c0}$ (MPa)	$\lambda$	Brittleness ( $b$ )
30	0.22	25	50	0.1	1-3

This problem was solved assuming that the idealized rock mass behavior shown in Fig. 2 applies to the rock mass. A principal strain increment of  $d\varepsilon_{\theta(j)} = 0.01 \varepsilon_{\theta(j-1)}$  was used in Eqs. (28) & (29). The influence of brittleness parameter ( $b$ ) on ground response curve (GRC) and development of the damage zone was investigated. Fig. 4 shows important effect of brittleness parameter ( $b$ ) on ground response curves (GRC).

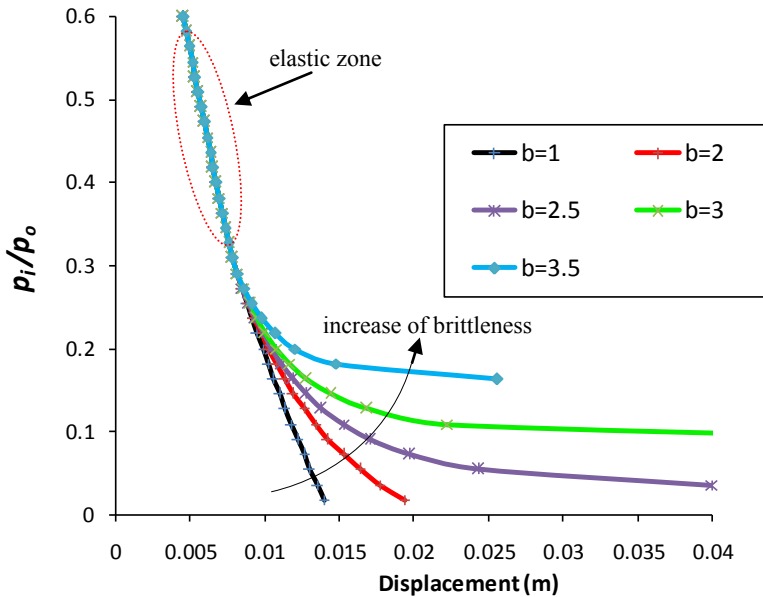


Fig. 4. Ground response curves at different brittleness parameters

The influence of internal support pressure on tunnel wall displacements can be seen in Fig. 4. With decrease of fictitious inner support pressure ( $P_i$ ), the tunnel wall convergence increases. In Fig.4, also the effect of brittleness on ground response curve (GRC) is illustrated. The first parts of all ground reaction curves with any brittleness parameters are same. The first sections of GRCs are relevant to the elastic behavior so they are not dependent on the brittleness parameter ( $b$ ). The second sections of ground response curves are related to the damage zone so there is a bifurcation point on the ground response curves (GRCs) after elastic behavior. Because of different brittleness parameters in ground response curves analysis, the ground response curves are not similar in damage zone. It is evident in Fig.4 that tunnel wall convergence increases with brittleness increment. In a brittle rock exhibiting rapid loss strength with strain increment, the capacity of absorbed fracture energy at post-peak region decreases so the tunnel wall convergence increases.

## 5 Conclusions

The conditions associated with complex rock openings are such that the rock material, acting as a quasi brittle material, damages and its stiffness modulus gradually degrade. According to different inner pressure, elastic and damage zones will be created around the tunnel. The developed damage model was implemented into a convergence-confinement method (CCM). The analytical method was formulated based on the damage mechanics theory. The stress and displacement distributions were calculated in damage zone. The damage zone radius was estimated based on the damage mechanics.

The developed method was implemented to evaluate the ground reaction curve (GRC) under typical conditions. The analysis results are in good agreement with the predicted governing ground reaction. The comparison of results shows that the developed method has good capabilities in predicting damage region around deep tunnel. Additionally, the model input data can be determined more easily.

## References

- [1] Guan, Z., Jiang, Y., Tanabasi, Y.: Ground reaction analyses in conventional tunneling excavation. *Tunnelling and Underground Space Technology* 22, 230–237 (2007)
- [2] Brown, E., Bray, J., Landayi, B., Hoek, E.: Ground response curves for rock tunnels. *ASCEJ. Geotech. Eng. Div.* 109(1), 15–39 (1983)
- [3] Oreste, P., Peila, D.: Radial passive rockbolting in tunnelling design with a new convergence confinement model. *Int. J. Rock Mech. Min. Sci. Geomech. Abstr.* 33(5), 443–454 (1996)
- [4] Jiang, Y., Yoneda, H., Tanabashi, Y.: Theoretical estimation of loosening pressure on tunnels in soft rocks. *Tunnelling and Underground Space Technology* 16(2), 99–105 (2001)
- [5] Detournay, E.: Elastoplastic model of a deep tunnel for a rock with variable dilatancy. *Rock Mech. Rock Engng.* 1986(19), 99–108 (1986)
- [6] Carranza-Torres, C., Fairhurst, C.: The elasto-plastic response of under ground excavations in rock masses that satisfy the Hoek-Brown failure criterion. *Int. J. Rock Mech. Min. Sci.* 36(6), 777–809 (1999)
- [7] Alonso, E., Alejano, L., Varas, F., Fdez-Manin, G., Carranza-Torres, C.: Ground reaction curves for rock masses exhibiting strain softening behavior. *Int. J. Numer. Anal. Meth. Geomech.* 27(13), 1153–1185 (2003)
- [8] Shao, J.F., Chau, K.T., Feng, X.T.: Modeling of anisotropic damage and creep deformation in brittle rocks. *Int. J. Rock Mechanics & Mining Sciences* 43, 582–592 (2006)
- [9] Zhu, W.C., Tang, A.: Micromechanical model for simulating the fracture process of rock. *Rock Mech. Rock Engng* 37(1), 25–56 (2004)
- [10] Molladavoodi, H., Mortazavi, A.: A damage-based numerical analysis of brittle rocks failure mechanism. *Finite Elements in Analysis and Design* 47, 991–1003 (2011)
- [11] Carol, I., Rizzi, E., Willam, K.: On the formulation of anisotropic elastic degradation. I. Theory based on a pseudo-logarithmic damage tensor rate. *Int. J. Solids and Structures* 38, 491–518 (2001)
- [12] Timoshenko, S., Goodier, J.: *Theory of Elasticity*. McGraw-Hill, New York (1970)

# Effect of Seismic Wave Form on the Behavior of River Embankment on the Soft Soil Deposit

Fusao Oka<sup>\*</sup>, P.S.Tsai, and Sayuri Kimoto

Department of Civil and Earth Resources Engineering, Kyoto University  
Kyoto, Japan, 615-8540  
oka.fusao.2s@kyoto-u.ac.jp

**Summary.** we have analyzed model river embankments on the clayey foundation with different ground water tables using a dynamic liquefaction analysis method. We have found that the effects of the water saturated region in the bank and the duration time of earthquake motion on the deformation behavior of river embankments are important. The results are consistent with the investigation results of the feature of the deformation and failure of the embankments due to the 2011 off the Pacific coast Tohoku Earthquake.

**Keywords:** River embankment,, Soft soil deposit, Liquefaction, Clayey soil, Great East Japan earthquake disaster.

## 1 Introduction

The 2011 Tohoku Earthquake damaged many soil made infra-structures such as river dikes, road embankment, railway foundations and coastal dikes. In Miyagi prefecture many river embankments on the soft clayey deposit have been damaged. But its reason is not clear. In this paper, we have analyzed model river embankments on the clayey foundation with different ground water tables using a dynamic liquefaction analysis method. We have found that the effects of the water saturated region in the bank and the duration time of earthquake motion on the deformation behavior of river embankments are important. The results are consistent with the investigation results of the feature of the deformation and failure of the embankments due to the 2011 off the Pacific coast Tohoku Earthquake.

Taking account of the investigation of the soil profile and the water table in the damaged embankments, the reason of the damage is a liquefaction of the water-saturated region bounded by the soft clay layers with smaller permeability. The effect of the water-saturated region is pointed out by Sasaki et al.(1994). This region extends to the lower part of the embankments which have been settled below water table. The water table in the embankments which is higher than ground surface is formed by the rain fall and the capillary etc.

---

<sup>\*</sup> Corresponding author.

## 2 Numerical Analysis

In this section, we have numerically analyzed the deformation behavior of river embankments during earthquakes using a soil-water coupled finite element analysis method. In the numerical simulation of the dynamic behavior of ground, we used a liquefaction analysis program “LIQCA2D011” which has been developed by Oka et al.(Oka et al., 2005,2011) using the u-p formulation.

For the constitutive model for soils, we have used a cyclic elasto-plastic model for sandy soils(Oka et al., 1999) and a cyclic elasto-viscoplastic model for clayey soils (Kimoto, Sahbodagh, Mirjalili, and Oka 2012) based on the previous model(Oka et al., 2004) We have analyzed model river embankments with different soil profiles and water tables. In addition, we have studied the effect of saturated region in the embankment considering the duration of earthquakes.

Figure 1 shows the model of the river embankment and the finite element mesh used in the analysis. In the simulations we used different soil profiles with the clayey subsoil because the ground profiles of the many damaged embankments in Miyagi prefecture includes clayey soil layer about 10m thick.

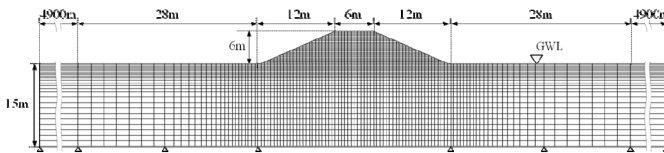


Fig. 1. Finite element and boundary conditions

Figure 2 shows the different soil profiles that taking account of the soft clay deposit and the high water level. The soil ground is composed of liquefiable loose sandy soil and soft clay. In Figure 2, Type 1 illustrates the a levee embankment on the clayey foundation and Type 3 shows the case in which the embankment is settled and ground water level is in the embankment. Type 3 corresponds to the typical case of severely damaged embankment due to the 2011 off the Pacific coast Tohoku Earthquake.

Figure 3 shows the input earthquake motions; Input 1 is an earthquake record obtained during the 1995 Kobe earthquake at a depth of 33m of Higashi Kobe Ohashi. Input 2 is the earthquake record at a depth of 80m obtained at Tajiri ; MYGH06, KiK-net, during the last Tohoku Earthquake 2011 (NIED). The features of these waves are that the duration time of Input 2 is very long more than 2 min, which is longer than Input 1 but the maximum acceleration of Input 1 is larger than that of Input 2.

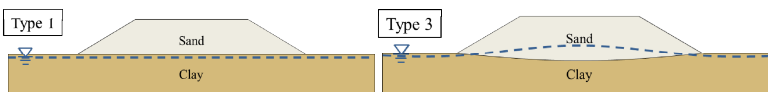


Fig. 2. Soil profile and water table

In the simulation, we adopted four simulation cases with two different soil profiles and earthquake motions. Numerical cases are CASE 1-A: seismic wave=Input 1, soil profile:Type 1, CASE 1-B: seismic wave=Input 1, soil profile:Type 3, CASE 2-A: seismic wave=Input 2, soil profile:Type 1, CASE 2-B: seismic wave=Input 2, soil profile:Type 3. The material parameters used in the analysis is as follows:

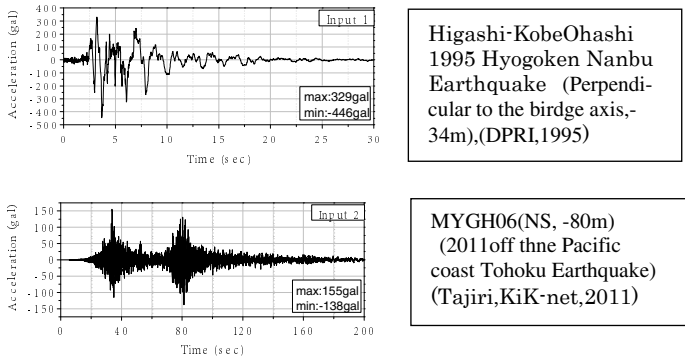


Fig. 3. Input earthquake motions

For sandy soil: Density  $(t/m^3)= 1.8 / 2.0$ , Water permeability  $k (m/s)= 2.20 \times 10^{-5}$ , Initial void ratio  $e_{0}=0.8$ , Compression index  $\lambda=0.0250$ , Swelling index  $\kappa=0.0003$ , Normalized initial shear modulus  $G_0 / \sigma'_{m0} (kPa)= 761$ , Stress ratio at Maximum Compression  $M_m^*=0.909$ , Stress ratio at failure  $M_f^* =1.229$ , Quasi-overconsolidation ratio  $OCR^*=\sigma'_{mai} / \sigma'_{m0}=1.0$ , Hardening parameter  $B_0^*, B_1^*, C_f =2000, 40, 0$ , Structure parameter  $\sigma'_{maf} / \sigma'_{mai}$ ,  $\beta=0.5, 50$ , Control parameter of anisotropy  $C_d=2000$ , Parameter of Dilatancy  $D_0^*$ ,  $n=1.0, 4.0$ , Reference Value of Plastic Strain  $\gamma_r^{Ps}=0.005$ , Reference Value of Elastic Strain  $\gamma_r^{Es}=0.003$

For clayey soil: Density  $(t/m^3)= 1.7$ , Water permeability  $k (m/s)= 5.77 \times 10^{-11}$ , Initial void ratio  $e_{0}=1.25$ , Compression index  $\lambda=0.341$ , Swelling index  $\kappa=0.019$ , Normalized initial shear modulus  $G_0 / \sigma'_{m0} (kPa)= 75.2$ , Stress ratio at critical state  $M_m^*=1.24$ , Quasi-overconsolidation ratio  $OCR^*=\sigma'_{mai} / \sigma'_{m0}=1.0$ , Hardening parameter  $B_0^*, B_1^*, C_f =100, 40, 10$ , Structure parameter  $\sigma'_{maf} / \sigma'_{mai}$ ,  $\beta=0.3, 3.6$ , Viscoplastic parameter  $m' =24.68$ , Viscoplastic parameter (1/s)  $C_1= 1.00 \times 10^{-5}$  Viscoplastic parameter (1/s)  $C_2=3.83 \times 10^{-6}$ , Hardening parameter  $A_2^*, B_2^* =5 .9, 1.8$ , Strain-dependent modulus parameter  $\alpha, r=10, 0.4$ .

For the earthquake record Input 1, larger deformation occurred in the ground type 1. The settlement of the center top of the ground is maximum for Case 2-B. For the earthquake record Input 2, the maximum settlement of the top of the

embankment and the maximum horizontal displacement of the toe of the embankments are obtained for Case2-B. For Case 2-A, the settlement of the top of the embankment is small and less than others. In Figure 4, the vertical displacement-time profiles of the top of the embankment for all cases. The trend of the horizontal displacement is similar to the vertical settlement.

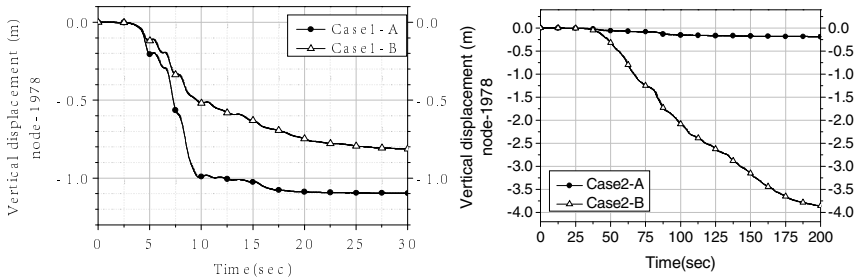


**Fig. 4.** Vertical displacement-time profiles of center top and the toe of the embankment

For case 2-B, liquefaction occurred in the water saturated region in the embankment. From the above discussions, it is worth noting that the water saturated region leads to the larger settlement of river embankment and the larger deformation/failure. This deformation behavior is consistent with the damaged embankments such as the embankments due to the 2011 off the Pacific coast Tohoku Earthquake. From the numerical results of Case 1-A and Case 2-A, we can say that the duration time of the earthquake significantly affects the deformation characteristics of the river embankment-subsoil layer system. Of course the amplitude of the earthquake is an important factor for the damage.

### 3 Conclusion

From the numerical results, it has been found that the water saturated region in the embankments leads to the larger settlement of river embankment and the larger deformation/failure. This deformation behavior is consistent with the pattern of the damaged embankments due the 2011 off the Pacific coast Tohoku Earthquake. In addition, the earthquake wave form such as duration time affects the deformation characteristics of the river embankment-subsoil layer system. Of course the amplitude of the earthquake is an important factor for the damage.

### References

- [1] Kimoto, S., Sahbodagh, K.B., Mirjalili, M., Oka, F.: A cyclic elasto-viscoplastic constitutive model for clay considering the nonlinear kinematic hardening rules and the structural degradation. *Int. J. Geomech.* (submitted, 2012)

- [2] LIQCA Research and Development Group (Representative: F.Oka Kyoto University) (2011), User's manual for LIQCA2D11 (2011) (in Japanese)
- [3] Sasaki, Y., Ohsaki, H., Nishikawa, J.: Embankment failure by the Kushiro-Oki earthquake of January 15,1993. In: Performance of Ground and Soil Structures During Earthquakes, ed. by TC4, pp. 61–68 (1994)
- [4] Tohoku Regional development Bureau of MLIT (2011), Material-3, Interim Report by the 3rd investigative commission for the restoration of the river dikes of Kitakami river etc., July 29, 2011, pp.18–19 (2011) (in Japanese)

# Integration Algorithms Based on Drucker-Prager Criterion and Application in Slope Stability Analysis

Yuanwei Pan<sup>1</sup>, Yaoru Liu<sup>1,\*</sup>, Jingjuan Qian<sup>2</sup> and Qiang Yang<sup>1</sup>

<sup>1</sup> State Key Laboratory of Hydroscience and Engineering  
Tsinghua University, Beijing 100084, China

pyw10@mails.tsinghua.edu.cn, {liuyaoru, yangq}@tsinghua.edu.cn

<sup>2</sup> Ning Xia Guo Dian CSI New Energy Development Co., LTD.  
Yingchuan, 750001, Ningxia, China  
ngxqianjj@163.com

**Summary.** In this paper, an incremental analysis method of perfect elasto-plastic constitutive relation based on Drucker-Prager criteria is adopted in nonlinear finite element computation, which is of first-order accuracy and unconditional stable. This method converges for either small load steps or large load steps. The method was embedded into a 3D nonlinear FEM software named TFINE and applied to stability analysis of Dagangshan high slope. Both theoretical analysis and numerical example show that the method is suitable for limit analysis and can achieve high accuracy to large load increment.

**Keywords:** integration algorithm, analytic solution, slope, stability.

## 1 Introduction

A whole class of structure analysis in geotechnical engineering, such as the bearing capacity of foundation, soil pressure, slope stability and dam foundation stability, is of limit analysis problem. In the field of elastic-plastic analysis, limit analysis corresponds to perfect elasto-plastic analysis employing associated flow rule. Drucker-Prager yield criteria is widely used for rock and soil materials and still attracts many researchers today [1]. One of the key problems of elastic-plastic

---

\* Corresponding author.

numerical analysis is constitutive relation integration, which directly influences the precision and convergence of elastic-plastic computation.

The paper uses a method of perfect elasto-plastic incremental analysis based on Drucker-Prager criteria, which directly deduces analytic solution of transitional stress according with associated flow rule, without forming elastic-plastic increment matrix [2,3]. This method has good convergence no matter for small or large load step size. With the method stated above, stability analysis of Dagangshan high slope based on FEM is provided, while multi-grid method [4] is used to calculate safety factor of slope.

## 2 Constitutive Relation and Analytic Solution

### 2.1 Perfect Elasto-plastic Constitutive Relation Integration

Elastic-plastic finite element computation is embodied by a series of iterative programs approaching genuine solution. Figure 1 shows a typical iterative step. Suppose that initial stress of certain Gaussian point in the initial iterative step is  $\sigma_0$  and  $f(\sigma_0) \leq 0$ . By imposing a strain increment  $\Delta \epsilon$  on initial state, the elastic loading stress state is  $\sigma_1 = \sigma_{ij}^e = \mathbf{D} : (\epsilon_0 + \Delta \epsilon)$ , where  $\mathbf{D}$  is an elastic tensor. If  $f(\sigma_1) > 0$ , the strain increment  $\Delta \epsilon$  results in plastic loading. For this iterative step, the plastic strain increment is  $\Delta \epsilon^p$ , then the adjusted stress can be written as

$$\sigma = \sigma_{ij} = \mathbf{D} : (\epsilon_0 + \Delta \epsilon - \Delta \epsilon^p) = \sigma_1 - \mathbf{D} : \Delta \epsilon^p \tag{1}$$

As the strain increment progress  $0 \rightarrow \Delta \epsilon$  is linear, the corresponding stress increment progress  $\sigma_0 \rightarrow \sigma_1$  is linear too, thus stress state  $\hat{\sigma}$  exists which satisfies the equation  $f(\hat{\sigma}) = 0$ . Associated flow rule  $\Delta \epsilon^p = d\lambda \frac{\partial f}{\partial \sigma}$  can be written in incremental form:

$$\Delta \epsilon^p = \int_{\lambda(\hat{\sigma})}^{\lambda(\sigma_1)} \frac{\partial f}{\partial \sigma} d\lambda = \Delta \lambda \frac{\partial f}{\partial \sigma} \Big|_{\sigma=\hat{\sigma}} \tag{2}$$

According to mean value theorems for integration, equation (2) can hold exactly if  $\partial f / \partial \sigma$  is determined by a proper stress state from  $\hat{\sigma}$  to  $\sigma_1$ .

An approximate method determines representative value of  $\frac{\partial f}{\partial \sigma}$  by  $\sigma_1$ :

$$\Delta \epsilon^p = \Delta \lambda \frac{\partial f}{\partial \sigma} \Big|_{\sigma=\sigma_1} \tag{3}$$

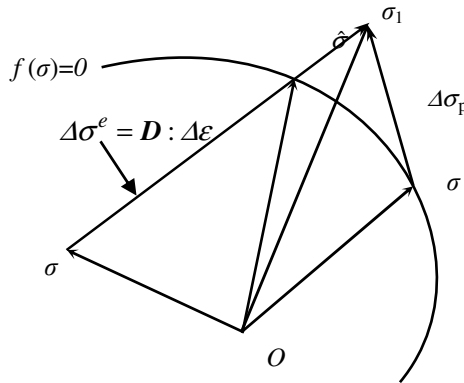


Fig. 1. Diagram of elastic-plastic stress adjustment

### 2.2 Constitutive Relation Integration Based on Drucker-Prager Criteria

Drucker-Prager yield criteria can be expressed as:

$$f = \alpha I_1 + \sqrt{J_2} - k \leq 0 \tag{4}$$

where  $I_1 = \sigma_{ii}$ ,  $J_2 = s_{ij}s_{ij} / 2$ .  $s_{ij}$  is the stress deviator.  $\alpha$  and  $k$  can be determined from internal friction angle  $\varphi$  and cohesive strength  $c$  of materials by using Mohr-Coulomb criteria.

The normal of yield surface can be expressed as

$$m_{ij} = \frac{\partial f}{\partial \sigma_{ij}} = \alpha \delta_{ij} + \frac{s_{ij}}{2\sqrt{J_2}} \tag{5}$$

We can obtain following expression from equation (1) and (3):

$$\Delta \sigma^p = \sigma_1 - \sigma = \mathbf{D} : \Delta \epsilon^p = \Delta \lambda \mathbf{D} : \mathbf{m}_1 \tag{6}$$

Equation (6) is actually the generalized Hooke's law. According to equation (5), for isotropic elastic tensor, equation (6) can be divided as

$$\frac{1}{3}(\sigma_{ii}^1 - \sigma_{ii}) = 3K\alpha\Delta\lambda$$

$$s_{ij}^1 - s_{ij} = 2G \frac{s_{ij}^1}{2\sqrt{J_2^1}} \Delta\lambda \tag{7}$$

where K and G are the bulk modulus and shear modulus, respectively. The adjustment of stress deviator and hydrostatic pressure are associated by  $\Delta\lambda$ . From equation (7) we can obtain another expression:

$$s_{ij} = \left(1 - \frac{G\Delta\lambda}{\sqrt{J_2^1}}\right) s_{ij}^1 \tag{8}$$

**2.3 Analytic Solution of Adjusted Stress**

$I_1$ ,  $J_2$  can be written as follows according to equation (9) and (10):

$$I_1 = \sigma_{ii} = \sigma_{ii}^1 - 9K\alpha\Delta\lambda = I_1^1 - 9K\alpha\Delta\lambda$$

$$\sqrt{J_2} = \sqrt{J_2^1} - G\Delta\lambda \tag{9}$$

Given the following conditions:

$$f(\boldsymbol{\sigma}) = 0, \quad \boldsymbol{\sigma} = \boldsymbol{\sigma}_1 - \Delta\lambda \mathbf{D} : \left. \frac{\partial f}{\partial \boldsymbol{\sigma}} \right|_{\boldsymbol{\sigma}=\boldsymbol{\sigma}_1} \tag{10}$$

the adjusted stress can be determined.

$$\boldsymbol{\sigma} = \sigma_{ij} = (1 - q)\sigma_{ij}^1 + p\delta_{ij} \tag{11}$$

where

$$q = \frac{w\mu}{\sqrt{J_2}}, \quad p = -mw + \frac{1}{3}nI_1, \quad m = \alpha(3\lambda + 2\mu), \quad w = \frac{f}{3\alpha m + \mu} \cdot J_2,$$

$I_1$  and  $f$  are all determined by  $\boldsymbol{\sigma}_1$ , and  $\lambda$  and  $\mu$  are Lamé constants.

Therefore, for each iterative step, stress increment is:

$$\Delta \sigma = \sigma_1 - \sigma = q\sigma_{ij}^1 - p\delta_{ij} \quad (12)$$

## 2.4 Comparison with Other Methods

As for the process of stress adjustment, above analytic solution of transitional stress based on Drucker-Prager criteria is equivalent to linear prediction-radial return method[5]; as for the constitutive relation integration strategy, it is equivalent to the closest point projection method (CPPM) [6], which has first-order precision and is unconditionally stable. As a special instance of generalized midpoint rule (GMR), the CPPM can be adaptive to big strain increment. In the elastic-plastic finite element computation process of geotechnical engineering, load step is very large in general. But the above-stated method is fit for limit analysis, and it can keep a very high level of numerical stability and precision as large load step is adopted. If fine load step division is adopted, the procedure is a strictly perfect elasto-plastic increment computation. When large load increment is adopted, what obtained is a static safe stress field which accord with associated flow rule on average; in the convergence field, the maximum load possibly imposed on is close to limit load and tends to be safer.

## 3 Application in Stability Analysis of Rock Slope

On the base of above-stated slope stability analysis method, a computation program TFINE has been compiled, and successfully applied in high slope stability computation and analysis of Dagangshan Hydropower Station.

Finite element computation model of right bank slope of Dagangshan includes 59661 elements and 63566 nodes as shown in Fig.2. The distribution of key faults is illustrated in Fig.3. There are two key slide blocks formed as follows:

- Slide block 1 The sixth fractures sets  $+\beta_{43} + f_{231}$
- Slide block 2 The sixth fractures sets  $+\beta_4 + f_{231}$ .

The steps of excavation are fully simulated, while stress distribution and forces acting on slip surface can be obtained by multi-grid method. Table.1 shows the forces and safety factors of slide blocks.

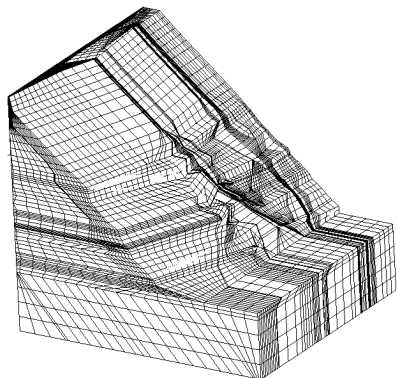


Fig. 2. Calculation mesh

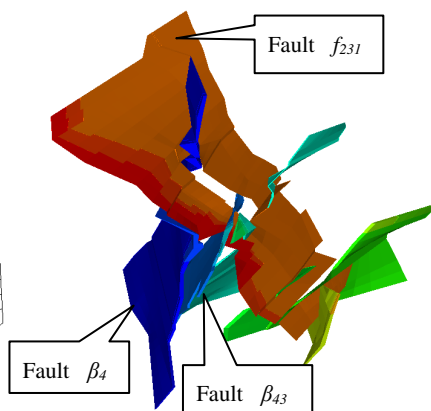


Fig. 3. Distribution of key faults

Table 1. Data and safety factors of blocks

Excavation Process		Unexcavated	Excavated to dam crest elevation	Excavated to spandrel elevation	Fully Excavated
Slide block 1	Composite slip forces ( $\times 10^4 \text{N}$ )	3948917	3422729	2817335	2928772
	Composite slip resistance ( $\times 10^4 \text{N}$ )	5460435	5009779	3971732	3787988
	Block safety factor	1.383	1.463	1.410	1.293
Slide block 2	Composite slip forces ( $\times 10^4 \text{N}$ )	2103067	1339700	1404200	1404559
	Composite slip resistance ( $\times 10^4 \text{N}$ )	2746294	2107285	2085897	2085891
	Block safety factor	1.306	1.572	1.485	1.485

According to the data in Table 1, the slide blocks are significantly influenced by excavation. With the reduction of gravity load, the safety factors of both blocks increase while the slope is excavated to dam crest elevation. After that the safety factors decrease as slope excavation goes on and effect of toe excavation become significant.

As the incremental analysis method is fit for large load step, the computation progress is of high convergence. The result shows that the computation keeps a very high level of numerical stability and precision while the excavation procedure is simulated.

## 4 Conclusions

The method of perfect elasto-plastic incremental analysis based on Drucker-Prager criteria is equivalent to the CPPM, which has first-order precision and is unconditionally stable. Both theoretical analysis and numerical example show that the method is suitable for limit analysis, which can achieve high numerical stability and accuracy to large load increment, such as water load on arch dam or excavation of high slope.

**Acknowledgments.** The work reported here was supported by the National Science Foundation of China with Grant No. 50823005 and China National Funds for Distinguished Young Scientists with grant No. 50925931.

## References

- [1] Hjjaj, M., Fortin, J., de Saxce, G.: A complete stress update algorithm for the non-associated Drucker-Prager model including treatment of the apex. *Int. J. Eng. Sci.* 41, 1109–1143 (2003)
- [2] Chen, X., Yang, Q., Huang, Y.S.: Sub-incremental method for perfect elasto-plastic material based on D-P yield criteria. *Chin. J. Rock Mech. Engr. Supp.* 2, 2465–2469 (2002)
- [3] Yang, Q., Chen, X., Zhou, W.Y.: Elastic-plastic basis of geotechnical engineering reinforcement analysis. *Rock Soil Mech.* 26(4), 553–557 (2005)
- [4] Yang, Q., Zhu, L., Xue, L.J.: Application of limit equilibrium method to stability analysis of Jinping high slope based on 3D multi-grid method. *Chin. J. Rock Mech. Engr.* 24(2), 5313–5318 (2005)
- [5] Schreyer, H.L., Kulak, R.F., Kramer, J.M.: Accurate numerical solutions for elastic-plastic models. *J. Pressure Vessel Technol.* 101(2), 226–234 (1979)
- [6] Ortiz, M., Popov, E.P.: Accuracy and stability of integration algorithms for elastoplastic constitutive relations. *Int. J. Numer. Methods. Eng.* 21(9), 1561–1576 (1985)

# Investigation of Behavioral Aspects of Flexible Pavement under Various Conditions by Finite Element Method

M.S. Ranadive\* and A.B. Tapase

College of Engineering, Pune, K.B.P.College of Engineering & Poly., Satara, India  
msrtunnel@yahoo.co.in, tapaseanand@gmail.com

**Summary.** Basic aim of this paper is to develop a tailor made program for design and analysis of flexible pavements using finite element method which will enhance the scope to use variety of combinations of materials, conditions, and various parameters which correlates with the actual conditions on the field. The conditions which affect the flexible pavement are variation of wheel loading, temperature, seepage, varying thickness, etc. Both positive and negative change in temperature during day time and night time as well as due to seasonal changes will be considered. The water seeps through sub grade which results in decrease in life of pavement by reduction in sub grade modulus. The effect of water table will be studied on swelling and shrinkage property of sub grade. Similarly performance of pavement will be checked by varying thicknesses of asphalt concrete, and base layers. The capillary water held in pores of concrete pavement may cause failure of pavement by freezing and thawing action. The effect of wheel loading cannot be neglected as severe pavement damage is because of higher axle loads. However from the past studies and through the recommendations of the AASHTO code of practice the actual wheel load and their combinations could be shortlisted.

The complex characteristic of the present day systems therefore demands an application of analytical tool which can accommodate the details of the complex system. In this connection it should be noted that the versatile finite element solution technique holds a bright promise. Therefore it is proposed to discuss at length the application of the finite element method towards design of the flexible pavements.

**Keywords:** Flexible pavement, parameters, finite element method.

## 1 Introduction

Pavement design involves many uncertainties, variabilities and approximations regarding material properties, traffic loads, sub grade strength, seepage, drainage conditions, construction procedures, and climatic factors [7]. A good design is one that provides the expected performance with appropriate economic consideration.

---

\* Corresponding author.

Pavement design procedures depend heavily on empirical relationships based on long-term experience and field tests such as AASHO Road Test [1]. The properties of material used in pavement are strongly dependent on temperature. The data obtained from Indian Metrological Department (IMD, Pune) clearly focuses on the seasonal and diurnal fluctuations in weather conditions. Therefore, assuming an average temperature while design or analysis of the pavement is empirical. Instead of that detailed knowledge of temperature distribution in various layers allows for more sophisticated specification of various materials along with bituminous material grade which ultimately prove to be economical solution to rising pavement construction cost. From the literature available it is clear that the temperature variation in the top layer is larger than the variation within the base and sub base layers. Secondly, the influence of the moisture content within the base, sub base and sub grade layer is larger than the temperature variation [7]. The complex characteristics of the present day system demands an application of analytical tool which can accommodate the details of the complex system. In this paper the basic aim is to discuss the optimum design process for flexible pavement. The design is obviously based on the structural response against the variety of structural action.

## 2 Finite Element Methodology

It is apparent from details presented in fig 1.1 that the finite element method of solution constitutes a primary component of the design process.

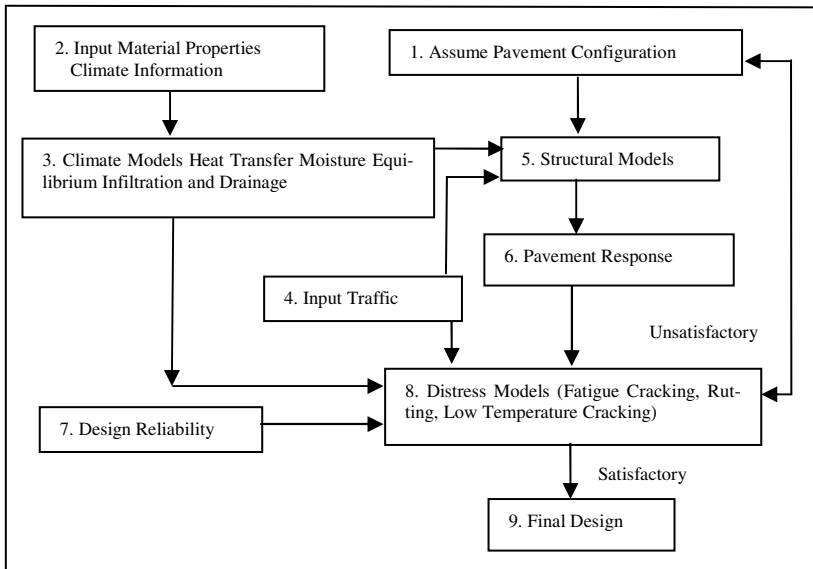


Fig. 1. Methodology of calibrated mechanistic procedure for flexible pavement design [4]

Finite element solution technique is conducted through three stages of the analysis those are as follow.

### 2.1 Idealization of the System Being Investigated

Depending upon the required type of analysis the finite element idealization for the pavement system being analyzed is developed by means of the elements drawn from the element library. A variety of element types are provided in its element library. The two dimensional, three dimensional, axi-symmetrical, and infinite elements compatible with the two or three dimensional elements are to be used as and when required for the analysis.

The scope for variety of material types that may be encountered in the built up of the pavement system are almost indefinite in number. With respect to the actual problem same practically useful data can be extracted from available literature for further investigation including the elastic modulus and Poisson's ratio of various available soil conditions like homogenous elastic soils, idealized cohesion less soil, cohesive soils, etc. [4, 5].

### 2.2 Formulation and Solution of Equation Governing the Phenomenon Being Investigated

The thermal studies in a continuum are basically governed by a heat transfer phenomenon. The governing equation being

$$\frac{\partial T}{\partial t} = \alpha \nabla^2 T \quad (2.1)$$

Wherein, T denotes temperature and t the time.  $\alpha$  is a function of thermal conductivity and  $\nabla^2$  is standard Laplace operator.

In general it would be quite in order to assume that as far as the temperature flow is concerned the continuum elements are homogenous and isotropic. With this the following details could be provided.

- a. A situation similar to plane strain in (x, y) space offers facility for two dimensional analysis with the temperature flow confined to a vertical plane. For this the governing equation would be as shown below

$$\frac{\partial T}{\partial t} = \alpha \left[ \frac{\partial^2 T}{\partial x^2} + \frac{\partial^2 T}{\partial y^2} \right] \quad (2.2)$$

- b. In the cylindrical co-ordinate system (r, z) the governing equation for the heat transfer is as shown below

$$\frac{\partial T}{\partial t} = \alpha \left[ \frac{\partial^2 T}{\partial r^2} + \frac{1}{r} \frac{\partial T}{\partial r} + \frac{\partial^2 T}{\partial z^2} \right] \quad (2.3)$$

c. In case of three dimensional (x, y, z) space the governing equation for the heat transfer is shown below

$$\frac{\partial T}{\partial t} = \alpha \left[ \frac{\partial^2 T}{\partial x^2} + \frac{\partial^2 T}{\partial y^2} + \frac{\partial^2 T}{\partial z^2} \right] \quad (2.4)$$

d. To modify the finite element analysis software which could calculate the temperature at any point in the three layer system of the pavement by employing available data having characteristics like sunshine, air temperature, seasonal variation, daily variation for the past few years available from observatory. The modified program could then be further connect to the deformation segments of the analysis software.

At sites susceptible to the phenomenon of frost and thawing the forces arising out of such development needs to be considered as a part of thermal analysis. Directly some water due to rainfall may enter the subbase and subgrade reason due to cracks in the upper layers. Over a period this would lead to accumulation of water in the subbase subgrade continuum and the same also need to be disposed of safely. Though the drains and other devices are provided the problem would be that of steady state seepage flow creating gradients velocities seepage pressure, etc. This in term could effect by imparting weakness to continuum material as also the deflection that may developed due to the seepage forces. For evaluation of this effects finite element seepage analysis is essential. The governing equations for the seepage flow are as follows.

a. A situation similar to plane strain in (x, y) space offers facility for two dimensional analysis with the steady state seepage over a vertical plane. For this the governing equation would be as shown below

$$\left[ k_x \frac{\partial^2 h}{\partial x^2} + k_y \frac{\partial^2 h}{\partial y^2} \right] = 0 \quad (2.5)$$

b. In the cylindrical co-ordinate system ( r, z) the governing equation for the steady state seepage is as shown below

$$\left[ k_x \frac{\partial^2 h}{\partial r^2} + \frac{k_r}{r} \frac{\partial h}{\partial r} + k_z \frac{\partial^2 h}{\partial z^2} \right] = 0 \quad (2.6)$$

c. In case of three dimensional (x, y, z) space the governing equation for the steady state seepage is shown below

$$\left[ k_x \frac{\partial^2 h}{\partial x^2} + k_y \frac{\partial^2 h}{\partial y^2} + k_z \frac{\partial^2 h}{\partial z^2} \right] = 0 \quad (2.7)$$

**Note:** In the above equations  $h$  denotes the head of water and  $k_x, k_y, k_r$  and  $k_z$  represent coefficients of permeability in  $x, y, r$  and  $z$  directions respectively. The equations relate to steady state seepage flow in case of homogenous but anisotropic elements.

For solution of these equations the finite element analysis software which could calculate the entities such as distribution of seepage pressures, gradients and exit gradients is required. The same however would be easily developed by minor modifications to various deformation analysis programs.

### ***2.3 Evaluation of the Structural Response Required for under Taking the Design Process***

With the solution of governing equation having being derived the element stresses and element strains are evaluated by means of equation 2.8

$$\begin{aligned} [\xi] &= [B][\partial \varepsilon] \\ [\sigma] &= [C][E] \end{aligned} \quad (2.8)$$

Wherein  $[\xi]$  represents element strain vector at the Gauss integration point and  $[\sigma]$  represents element stress vector and the Gauss integration point.

By employing the interpolation characteristics of the elements the modulus of elasticity and the Poisson's ratio at the element nodes are extrapolated by using their respective values and the Gauss integration points. Finally employing direct averaging technique the strains and stresses at the nodes of the idealized system are established. The nodal displacements provide information regarding the deflection suffered which in term helps in analyzing the phenomenon of rutting. On the other hand the nodal stresses help in carrying out analysis for phenomenon of fatigue.

## **3 Conditions for Analysis**

While dealing with the loading conditions various parameters like axle load, wheel load, tire surface contact pressure, tire imprint and contact area, variation in layer thickness and sub grade conditions, should be considered along with temperature variation, moisture content for the analysis. Though the legal axle load limits in India ranges between 6 tones to 18 tons for axles of commercial vehicles, the actual axle loads operating on highways in India are much higher due to lack of enforcement. A simulation model is proposed so that in the countries like India having four seasons and a fluctuating daily temperature can be analyzed at the same time pavement temperature at several depths within the pavement along with its effect on mix design can be studied before actual construction [2]. Characteristics of subgrade for various layers will be different which are proposed to be various cases for analysis [5].

## 4 Conclusions

From the details provided above it is clear that to develop rational and economic design of pavement system various types of finite element analysis would be required to make an integral tailor made analysis software. The analysis software should be capable of performing both the linear and nonlinear analysis.

## References

- [1] American Association of State Highway Officials AASHTO: AASHTO guide for design of pavement structures, AASHTO, Washington, D.C. (1993)
- [2] Chiasson, A.D., Yavuztук, C., Ksaibati, K.: Linearized approach for predicting thermal stresses in asphalt pavements due to environmental conditions. *J. Materials in Civil Eng., ASCE* 20(2), 118–127 (2008)
- [3] Das, A., Pandey, B.B.: M-E design of bituminous road: and Indian perspective. *Journal of Transportation Engineering, ASCE* 125(5) (1999)
- [4] Yang, H.H.: *Pavement Analysis and Design*, 2nd edn. Pearson Education, Inc., and Dorling Kindersley Publishing, Inc. (2008)
- [5] Ranadive, M.S., Parikh, S.K.: Modeling of Geotechnical Materials in Respect of Finite Element Analysis of Tunnel Deformations. *J. of the Institution of Engineers* 82, 139–144 (2001)
- [6] Reddy, K.S., Pandey, B.B.: Lateral placement of commercial vehicle on national highways, HRB Bulletin No.7, Indian Road Congress, New Delhi
- [7] Tarefdar, R.A., Nayan, S., Stormont, J.C.: Evaluation of subgrade strength and pavement designs for reliability. *J. of Transportation Eng., ASCE* 136(4), 379–391 (2010)

# Three Dimensional Implementation of HISS Model in ABAQUS

Mingqiang Wang\* and Jun Yang

Department of Civil Engineering, Tsinghua University, Beijing, 100084, China  
wangmingqiang666@sina.com

**Abstract.** The yield surface of hierarchical single surface (HISS) model is a single smooth function, which overcomes the singularity of so-called cap model. The HISS model and the main parameters influence on the yield surface were introduced. Tests on one Gauss Point are produced by MATLAB, and the stress path and yield surface are measured during loading process. Based on the further development platform provided by ABAQUS, the HISS model was programmed into a three dimensional user-material subroutine (UMAT). Three kinds of triaxial tests (HC, TC and TE) and several proportional loading tests of Munich sand were simulated by ABAQUS with the developed model. The stress-strain relationships obtained by ABAQUS were compared real with experiments results. The numerical predictions show good agreement with the observed behavior in experiments, which verified the UMAT and proved the applicability of HISS model to sands. The three dimensional implementation of HISS model in ABAQUS provides the commercial FEM code a new optional constitutive law for the elastoplastic problems in soil mechanics.

**Keywords:** HISS model, ABAQUS, three dimensional UMAT, triaxial tests, proportional loading

## 1 Introduction

Mohr-Coulomb criterion and Drucker-Prager criterion are two classic plasticity models for soils. Although these two models can characterize the influence of hydrostatic pressure on the shear strength, the assumption of normality with respect to these two criterions implies a substantial volumetric plastic strain rate as long as any plastic strains are occurring and the material with these two models would never yield under hydrostatic pressure loading. Drucker and Prager[1] proposed that the true yield surface of a soil is a 'cap' over the open end of the Mohr-Coulomb wedge. By the concepts of 'cap', several models are proposed for geologic materials, such as Cam-Clay model and Sandler model. One of the major shortcomings of all these 'cap' models is that the yield and ultimate surfaces are expressed by the separate yield functions involving a point of intersection or discontinuity. This may give rise to nonuniqueness of the normal at the point of

---

\* Corresponding author.

intersection. Thus the increment of the plastic strain is not defined at the point of intersection of the two surfaces. Special mathematic methods are needed when these ‘cap’ models are implemented. However this problem can be overcome by defining the entire deformation process through evolution of a single yield function. Desai[2,3] proposed a hierarchical approach for constitutive modeling that allows for progressive development of model of higher grades corresponding to different levels of complexities. This model has one single continuous yield surface. Thus every point on the surface has a unique normal direction, which overcomes the mathematic problems of ‘cap’ models.

ABAQUS is a suite of powerful engineering simulation programs, based on the finite element method, which can solve problems ranging from relatively simple linear analyses to the most challenging nonlinear simulations. A lot of user subroutines are provided in ABAQUS as a further development platform. The user-defined mechanical material behavior (UMAT) is provided by means of an interface whereby any mechanical constitutive model can be added to the library. The UMAT must update the stresses and solution-dependent state variables to their values, and must provide the material Jacobian matrix,  $\partial\sigma / \partial\varepsilon$ , for the mechanical constitutive model at the end of an increment. Pan Jiajun[4] has developed a two dimensional implementation of the HISS model in ABAQUS. In this paper, based on the further development platform, three dimensional implementation of HISS model in ABAQUS was developed for the first time. Also some triaxial tests and proportional loading tests were simulated, and the results of the tests were compared with the ones observed in experiments. The numerical predictions show good agreement with the observed behavior in experiments, which verified the UMAT.

## 2 The Hierarchical Single Surface Model

Desai and his coworkers have developed a hierarchical approach for constitutive modeling that allows for progressive development of model of higher grades, which can characterize isotropic materials, anisotropic materials, associative flow rule, non-associative flow rule, isotropic hardening, kinematic hardening and strain softening, corresponding to different levels of complexities. The basic  $\delta_0$  model exhibit isotropic hardening behavior and associative flow rule for isotropic materials. Considered that the associative rule can produce excessive plastic strain, only the non-associative model  $\delta_1$  was involved in this paper. The yield function  $F$  of the HISS model proposed by Desai[5] is written as

$$F = \frac{J_2}{P_a^2} - \left[ -\alpha \cdot \left( \frac{I_1}{P_a} \right)^n + \gamma \cdot \left( \frac{I_1}{P_a} \right)^2 \right] \cdot (1 - \beta S_r)^{-0.5} \quad (1)$$

where  $J_2 = s_{ij}s_{ji} / 2$  ;  $I_1 = \sigma_{ii}$  ;  $S_r$  is the stress ratio,  $S_r = 3\sqrt{3}J_3J_2^{-1.5} / 2$  ;  $J_3 = s_{ij}s_{jk}s_{ki} / 3$  ;  $P_a=101\text{kPa}$ , is standard atmospheric pressure;  $\gamma$  and  $\beta$  are ultimate constants;  $n$  is phase change constant;  $\alpha$  is hardening parameter; the expression for  $\alpha$ , which allows for improved simulation of response under proportional loading paths, was proposed by Desai and Hashmi[6],

$$\alpha = a_1 \exp\left(-\eta_1 \xi \left(1 - \frac{\xi_D}{a_2 + \eta_2 \xi_D}\right)\right) \tag{2}$$

where  $a_1, a_2, \eta_1, \eta_2$  are hardening constants; effective plastic strain  $\xi = \int (d\epsilon_{ij}^p d\epsilon_{ij}^p)^{1/2}$ , the deviatoric part  $\xi_D = \int (de_{ij}^p de_{ij}^p)^{1/2}$ , volumetric part  $\xi_V = \int (d\epsilon_{kk}^p d\epsilon_{ii}^p / 3)^{1/2}$ .

For the  $\delta_1$  model with non-associative flow rule, the plastic potential function  $Q$  is defined as

$$Q = \frac{J_2}{P_a^2} - \left[ -\alpha_Q \left(\frac{I_1}{P_a}\right)^n + \gamma \left(\frac{I_1}{P_a}\right)^2 \right] (1 - \beta S_r)^{-0.5} \tag{3}$$

where  $\alpha_Q = \alpha + \kappa(\alpha_0 - \alpha)(1 - r_v)$ , in which  $\alpha_0$  is the value of  $\alpha$  at the end of initial loading, and  $\kappa$  is a non-associative constant;  $r_v = \xi_V / \xi$ .

Influences of parameter  $\alpha, \beta, \gamma$  and  $n$  on  $F$  were analyzed by MATLAB. In the analysis, only the value of the parameter which is discussed could change, and the values of the other parameters kept constant. The material constants are presented in Table 1.

**Table 1.** Material constants for Leighton Buzzard sand

$E/\text{kPa}$	$\nu$	$\gamma$	$\beta$	$n$
79238	0.29	0.10212	0.36242	2.5
$a_1$	$a_2$	$\eta_1$	$\eta_2$	$\kappa$
0.0351	0.0047	450	1.02	0.29

The size of yield surface is controlled by the hardening parameter  $\alpha$ . The yield surface reaches the ultimate state, which is a rounded-triangular cone with an open end and two straight lines in  $p$ - $q$  space, as  $\alpha$  equals to zero.

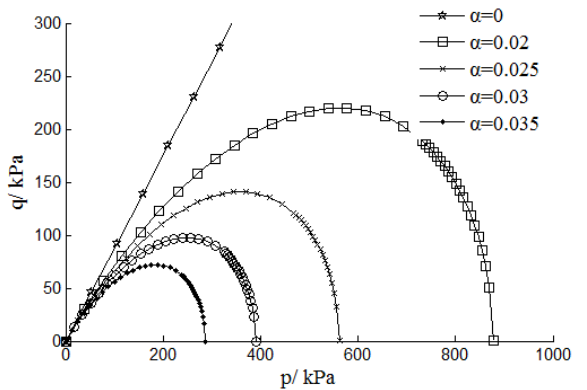


**Fig. 1.** Influences of parameter  $\alpha$  on  $F$  in  $p$ - $q$  space

The shape of yield surface in  $\pi$ - plane is controlled by parameter  $\beta$ . The yield surface is a circle when  $\beta$  equals to zero, otherwise the shape is a rounded-triangle in  $\pi$ - plane. The parameter  $\beta$  can exhibit the behavior that the geo-materials have different strengths under different stress paths.

The ultimate parameter  $\gamma$  is related to the ultimate strength of the material[7]. It denotes the slope of the ultimate yield surface. The phase parameter  $n$  determines the apex of the yield surface in  $p$ - $q$  space. Parameter  $n$  is related to the stress state at which the material response changes from compaction to dilation. Also, both  $\gamma$  and  $n$  influence the size of yield surface in  $p$ - $q$  space.

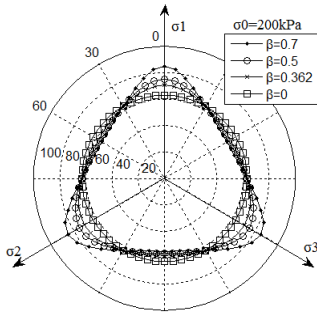


Fig. 2. Influences of parameter  $\beta$  on  $F$  in octahedral space

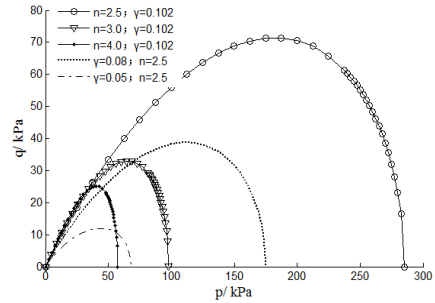


Fig. 3. Influences of parameter  $\gamma$  and  $n$  on  $F$  in  $p$ - $q$  space

### 3 Elastoplastic Relationship

The total strain increment is the sum of elastic strain increment and plastic strain increment,

$$d\epsilon_{ij} = d\epsilon_{ij}^e + d\epsilon_{ij}^p \tag{4}$$

Stress increment is related to the elastic strain increment by the Hooke's law,

$$d\sigma_{ij} = C_{ijkl}^e d\epsilon_{kl}^e \tag{5}$$

In non-associative plasticity, the plastic strain increment can be expressed as,

$$d\epsilon_{ij}^p = \lambda \frac{\partial Q}{\partial \sigma_{ij}} \tag{6}$$

The consistency condition,

$$dF = \frac{\partial F}{\partial \sigma_{ij}} d\sigma_{ij} + \frac{\partial F}{\partial \xi} d\xi + \frac{\partial F}{\partial \xi_D} d\xi_D = 0 \tag{7}$$

Combining Eqs.(4), Eqs.(5), Eqs.(6) and Eqs.(7), we got,

$$\lambda = \frac{\frac{\partial F}{\partial \sigma_{ij}} C_{ijkl}^e d\varepsilon_{ijkl}}{\frac{\partial F}{\partial \sigma_{pq}} C_{pqrs}^e \frac{\partial Q}{\partial \sigma_{rs}} - \frac{\partial F}{\partial \xi} \gamma_Q - \frac{\partial F}{\partial \xi_D} \gamma_{QD}} \tag{8}$$

where  $\gamma_Q = (\frac{\partial Q}{\partial \sigma_{ij}} \frac{\partial Q}{\partial \sigma_{ij}})^{1/2}$ ;  $\gamma_{QD} = ((\frac{\partial Q}{\partial \sigma_{ij}})_D (\frac{\partial Q}{\partial \sigma_{ij}})_D)^{1/2}$

The elastoplastic relationship is expressed as,

$$d\sigma_{ij} = C_{ijkl}^{ep} d\varepsilon_{kl} \tag{9}$$

where

$$C_{ijkl}^{ep} = C_{ijkl}^e - \frac{C_{ijmn}^e \frac{\partial Q}{\partial \sigma_{mn}} C_{uvkl}^e \frac{\partial F}{\partial \sigma_{uv}}}{\frac{\partial F}{\partial \sigma_{pq}} C_{pqrs}^e \frac{\partial Q}{\partial \sigma_{rs}} - \frac{\partial F}{\partial \xi} \gamma_Q - \frac{\partial F}{\partial \xi_D} \gamma_{QD}} \tag{10}$$

### 4 Programming

The diagram of the algorithm is presented in Figure 4.

- ① Compute the elastoplastic matrix  $C^{ep}$ .
- ② Based on the strain increment delivered from ABAQUS and the elastoplastic matrix, compute the stress increment and the new total stress  $\sigma_i = \sigma_{i-1} + d\sigma_i$ .
- ③ Based on the new stress state, check whether  $F \leq 0$  or  $F > 0$ , if  $F \leq 0$ , the point experiences elastic loading or unloading, and go to step④; if  $F > 0$ , the point is loading elastoplastically, and go to step⑤.
- ④ For  $F \leq 0$ , the hardening parameters remain unchanged, the total stress vector is set equal to  $\sigma_i = \sigma_{i-1} + d\sigma_i$ , the elastoplastic matrix  $C^{ep}$  is set equal to  $C^e$ , and go to step⑨.

⑤ For  $F > 0$ , check if the point is elastic or yielded at the start of the current increment. This is done by checking the value of a flag IFLAG, which is equal to zero for the former case and one for the latter. For IFLAG=0, go to step⑥, if IFLAG=1, go to step⑦;

⑥ The material is elastic at the start of current increment and will yield during this increment. The stress increment that just caused the material yielding in this increment and the corresponding elastic strain are figured out. The rest of the strain increment which actually causes the material yielding is also recorded. The initial yield stress is determined using the Newton-Raphson method. It is done iteratively using the expressions for  $n$ th iteration:

$$\sigma_{i-1}^n = \sigma_{i-1}^{n-1} + \delta_n d\sigma_i \quad (11)$$

where

$$\delta_n = - \frac{F(\sigma_{i-1}^{n-1}, \alpha_{i-1}^{n-1})}{\left\{ \frac{\partial F}{\partial \sigma} \right\}^T \{d\sigma_i\}} \quad (12)$$

Set  $\sigma_{i-1}^0 = \sigma_{i-1}$ , the iterations are stopped when convergence is reached, i.e.  $F(\sigma_{i-1}^n, \alpha_{i-1}^{n-1}) \leq 10^{-6}$ . The actual strain increment that will cause yielding is determined as follows:

$$d\varepsilon_i' = d\varepsilon_i - \left( \sum_n \delta_n \right) [C^e]^{-1} d\sigma_i \quad (13)$$

The stress state  $\sigma_{i-1}^n$  after the convergence and strain increment  $d\varepsilon_i'$  are set equal to  $\sigma_{i-1}$  and  $d\varepsilon_i$ , respectively. Now go to step⑦.

⑦ The stress increment is calculated by  $\sigma_i = \sigma_{i-1} + C_{i-1}^{ep} d\varepsilon_i$ , the effective plastic strain increment and its deviatoric and volumetric parts are computed by  $\xi_i = \xi_{i-1} + d\xi$ ,  $\xi_{Di} = \xi_{D(i-1)} + d\xi_D$  and  $\xi_{Vi} = \xi_{V(i-1)} + d\xi_V$ . Update the hardening parameter  $\alpha_i$ . Check if  $F(\sigma_i, \alpha_i) \leq 10^{-6}$ ? If yes, compute  $C_i^{ep}$ , and go to step⑨; If no, go to step⑧.

⑧ Apply the drift correction using the method of Potts and Gens[8]. The stress vector at the end of the drift correction is set equal to  $\sigma_i$ , and go to step⑨.

⑨ Record and save the stress state, strain, effective plastic strain and other state variables. This increment ends.

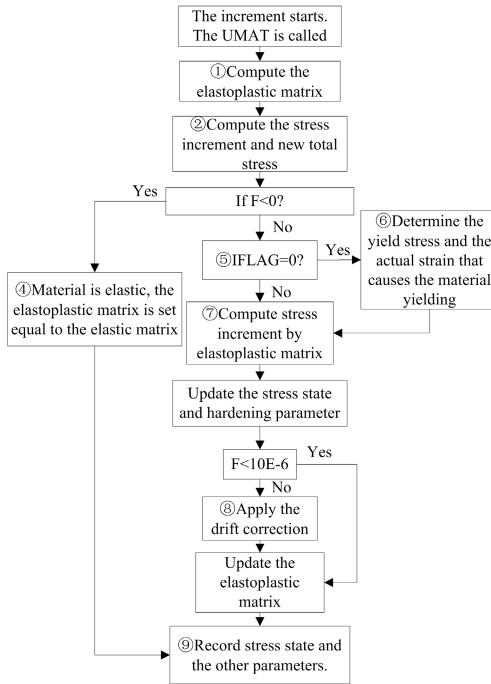


Fig. 4. Flow diagram of the algorithm

## 5 Development of Yield Surface during a Load Circle

A load circle to a Gauss point was simulated by MATLAB to check how the yield surface changed during the loading and unloading process. A strain increment vector was given, and the stress increment was obtained through the elastoplastic relationship. The change of the yield surface was observed during loading, unloading and reloading. The Leighton Buzzard sand was used in this analysis, and the material constants are presented in Table 1.

An initial hydrostatic stress state was set to the Gauss point before loading. In the entire process, three total strain increments were given to simulate loading, unloading and loading reversely, unloading again and reloading, respectively. The development of the yield surface, stress path and stress-strain relationship observed in the process are presented in Fig.5 and Fig.6.

According to the stress path in the elastic region, we know that the loading process is like a triaxial compression, and reversed loading is like a triaxial extension. The yield stresses of point B and C are different, which exhibits that the material has different yield stress under different stress paths. Further, the material has different strength according to the different failure envelope under different stress paths. This behavior is described by the ultimate parameter  $\beta$ . If  $\beta$  equals to zero, the shape of yield surface in octahedral plane is a circle, which means that the material has the same strength under any stress path if the mean pressure keeps

constant. In this analysis,  $\beta$  was not equal to zero, and the shape of yield surface in octahedral is a rounded-triangle, which means that the strength is related to the stress path. From Fig.5, the yield surface expands uniformly without distortion and translation during the loading process, so the model presents isotropic hardening.

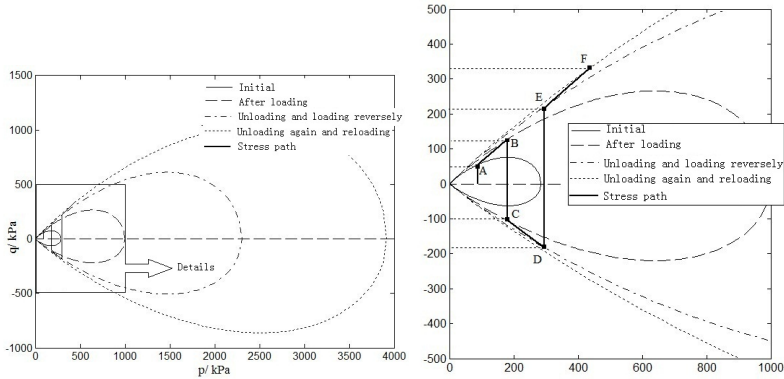


Fig. 5. Changes of the yield surface during a load circle

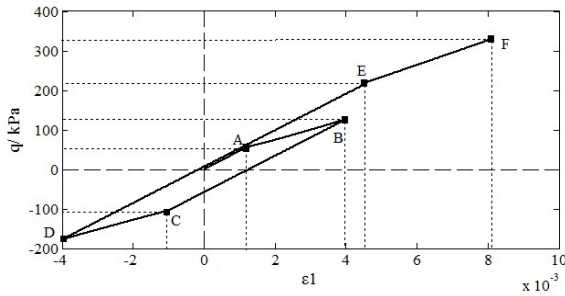


Fig. 6. Stress-strain response during a load circle

## 6 Verification of the Model through Triaxial Tests

Triaxial tests can present the loaded-deformation during the entire loading process until the material fails[9]. So triaxial tests can be used to measure the strength of the material and describe the stress-strain relationship during the loading process. Also, different loading conditions and stress paths can be simulated by the corresponding triaxial tests. Proportional loading is another kind of triaxial test. In proportional loading tests, the ratio of the ambient pressure and the major principal stress must be a constant  $K$  during the entire loading process.

$$\sigma_c / \sigma_a = \Delta\sigma_c / \Delta\sigma_a = K .$$

Three triaxial tests (HC, TC and TE) and some proportional loading tests were simulated by ABAQUS calling UMAT. The element type C3D8 was used. The FEM predicted results were compared with the ones observed from experiments by Hashmi[10]. The material that Hashmi used is Munich Sand, of which the constants are presented in Table 2.

**Table 2.** Material constants for Munich sand

$E/kPa$	$\nu$	$\gamma$	$\beta$	$n$
113685	0.36	0.1051	0.747	3.2
$a_1$	$a_2$	$\eta_1$	$\eta_2$	$\kappa$
0.00499	$2.26 \times 10^{-6}$	1355	1.11	0.35

The stress-strain relationship predicted by ABAQUS and comparisons with the experiment results of three triaxial tests and five proportional loading tests are presented in Fig.7 to Fig.14. According to the comparisons, the stress-strain behaviors show good agreement with the ones observed in laboratory by Hashmi, which verified the UMAT and the applicability of the model to describe the mechanic behavior of sand .

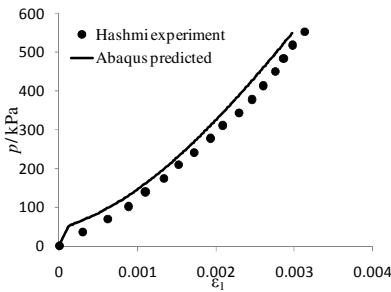


**Fig. 7.** Comparison of stress-strain relationship of HC test

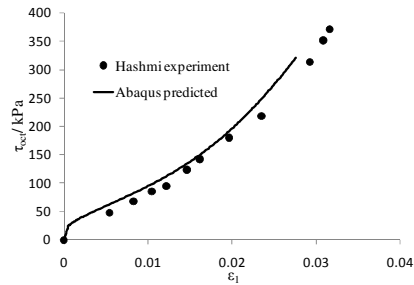


**Fig. 8.** Comparison of stress-strain relationship of PL ( $\sigma_3 / \sigma_1 = 0.424$ )

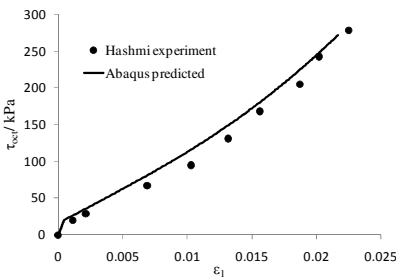


**Fig. 9.** Comparison of stress-strain relationship of PL ( $\sigma_3 / \sigma_1 = 0.274$ )

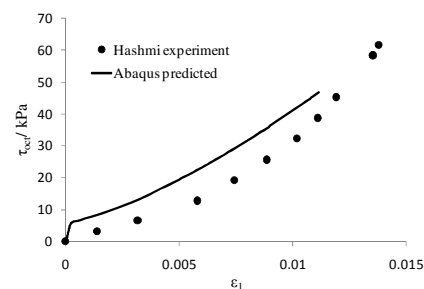


**Fig. 10.** Comparison of stress-strain relationship of PL ( $\sigma_3 / \sigma_1 = 0.792$ )

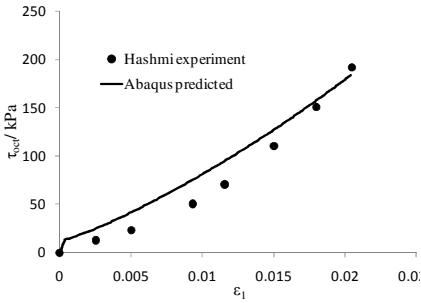


**Fig. 11.** Comparison of stress-strain relationship of PL ( $\sigma_3 / \sigma_1 = 0.6$ )

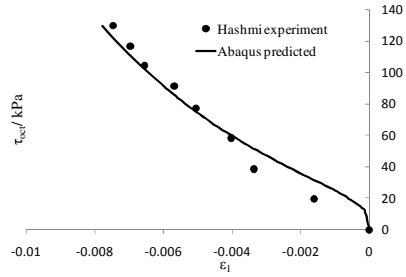


**Fig. 12.** Comparison of stress-strain relationship of PL ( $\sigma_3 / \sigma_1 = 3.0$ )

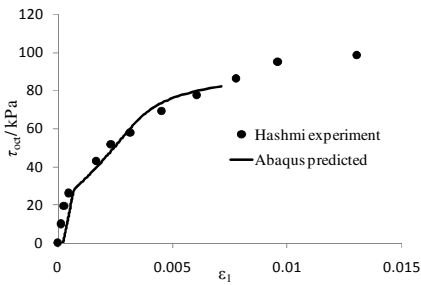


**Fig. 13.** Comparison of stress-strain relationship of TC test

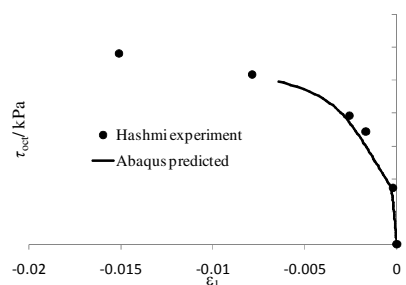


**Fig. 14.** Comparison of stress-strain relationship of TE test

## 7 Conclusions

The HISS model and the influences of main parameters to yield surface are introduced. A three dimensional UMAT was development on the further development platform provided by ABAQUS. Three triaxial tests and five proportional loading tests were simulated by ABAQUS calling UMAT, which was programmed by FORTRAN. According to the good agreement between the numerically predicted results and the experimentally observed ones, we can confirm the validity of the UMAT and the applicability of the model to describe the mechanic behavior of sand. When the three dimensional UMAT developed in this paper are used in triaxial compression test and triaxial extension test, the strength of material can be obtained exactly, but it can't present the stress-strain relationship under large strain condition. The programmed model needs further optimization and the robustness of the model in three dimensional boundary problems should be enhanced.

**Acknowledgments.** This project is supported by the National Natural Science Foundation of China under Grant No. 50908123 and Tsinghua University under Grant No. 2010Z01001.

## References

- [1] Drucker, D.C.: On Uniqueness in the Theory of Plasticity. *Quart. Appl. Math.* 14, 35–42 (1956)
- [2] Desai, C.S., Somasundaram, S., Frantziskonis: A Hierarchical Approach for Constitutive Modeling of Geologic Materials. *Int. J. Num. Analyt. Meth. In. Geomech.* 10, 225–257 (1986)
- [3] Desai, C.S., Wathugala, G.W.: Factors Affecting Reliability of Computer Solutions with Hierarchical Single Surface Constitutive Models. *Computer Methods in Applied Mechanics and Engineering* 82, 115–137 (1990)
- [4] Pan, J.-J., Rao, X.-B.: Implementation and verification of HISS model in ABAQUS. *Rock and Soil Mechanics* 30(12), 532–535 (2009)
- [5] Desai, C.S., Sharma, K.G.: Implementation of Hierarchical Single surface  $\delta_0$  and  $\delta_1$  Models in Finite Element Procedure. *Int. J. Num. Analyt. Meth. in Geomech.* 15, 649–680 (1991)
- [6] Desai, C.S., Hashmi, Q.S.E.: Analysis, Evaluation, and Implementation of a Nonassociative Model for Geologic Materials. *International Journal of Plasticity* 5, 397–420 (1989)
- [7] Liu, X., Cheng, X.H.: Numerical Modeling of Nonlinear Response of Soil. Part 1: Constitutive Model. *International Journal of Solids and Structures* 42, 1849–1881 (2005)
- [8] Potts, D.M., Gens, A.: A Critical Assessment of Methods of Correcting for Drift From the Yield Surface in Elasto-Plastic Finite Element Analysis. *Int. J. Num. Analyt. Meth. in. Geomech.* 9, 149–159 (1985)
- [9] Li, G.: *Advanced Soil Mechanics*. Tsinghua University Press, Beijing (2004)
- [10] Hashmi, Q.S.E.: *Nonassociative Plasticity Model for cohesionless Materials and Its Implementation in Soil-Structure Interaction*. University of Arizona, Tucson (1987)

# Stability Analysis of Shuiwenzhan Landslide under Water Level Fluctuation and Rainfall in Three Gorges Reservoir

Gang Zeng, Shimei Wang, and Yong Chen\*

College of Civil Engineering & Architecture, China Three Gorges University  
8 University Ave, Yichang, Hubei Province, P.R. China  
cy Yonger@126.com

**Abstract.** Water is the most active and positive factors to landslide happened, reservoir water level fluctuation and rainfall are the main predisposing factors for landslide instability. Water level fluctuation can produce uplift effect and dynamic water pressure effect to the soils and rainfall infiltration can reduce the matric suction in unsaturated zone. Based on the situation of Three Gorges reservoir operation, Geo-studio software is used to study the changes of the internal flow seepage field in different lifting speeds and the variation of stability under the effect of reservoir water lift and rainfall of Shuiwenzhan landslide in Three Gorges reservoir.

**Keywords:** rainfall, water level fluctuation, shuiwenzhan landslide, stability analysis.

## 1 Introduction

Landslide is a common geological disaster. Landslides which induced by reservoir are common things in domestic and foreign countries, Qianjiangping landslide and Vaiont large landslide in Italy are typical examples [1-2]. Three Gorges reservoir is an area where landslide and other geological disasters always happen. Three Gorges Dam is almost completed in 2009 and begins to normal operations, reservoir water level before Three Gorges dam changes in 145m-175m-145m and the fluctuations ranged from 30m, what's more, the process of lifting water level is likely to have a stable original landslide instability[3]. Therefore, studying the problem that water level lift and rainfall in reservoir area on the deformation to landslide instability is an urgent need of important engineering application issues. In this paper, saturated - unsaturated seepage and shear strength of unsaturated soil theory and FEM analysis software Geo-slope are used.

## 2 Basic Profile of the Landslide

Shuiwenzhan landslide is located in the Township of Xingshan County, on the right bank tributary of Xiangxi river, the landslide distribution elevation is

---

\* Corresponding author.

150~430m, and the landslide rear elevation is 380~420m as a platform, and landslide terrain in front of the steep angle is 18~28° front straight the river. The landslide front width is 490m, trailing edge width is 150m, average width is 300m, the length is about 700m, thickness is about 10~50m, the area of the landslide is  $20 \times 10^4 \text{ m}^2$ , volume is  $480 \times 10^4 \text{ m}^3$ . Plane shape of the landslide is seemed as an elongated tongue, and the main slip direction is  $73^\circ$ . The landslide profile map is shown in Figure 1.

### 3 Numerical Calculations

In this part, the theory of saturated - unsaturated seepage and unsaturated soil shear strength are used [4].

#### 3.1 Computational Model

According to the Geological Survey report of the landslide, The horizontal length is 700m and edge of the vertical height is 450 m. Therefore, the calculation interval is  $0 < X < 700\text{m}$ ,  $50 < Y < 450$ . Model material is simplified for three partitions: sliding body, sliding belt and sliding bed (bedrock) .It shows in figure 2. Finite element analysis software ANSYS is used for two-dimensional finite element grid partition. And the total division of four-node plane grid cells is 4497, and node 4652. The information from nodes and elements is imported into Geo-Studio software and get the calculation grid map of the landslide. It shows in figure 3 below.

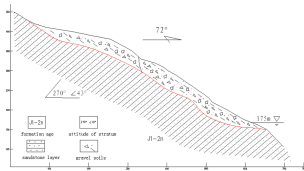


**Fig. 1.** Profile map of the Landslide

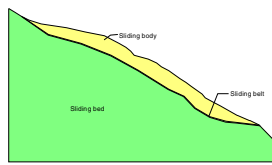


**Fig. 2.** Model material simplified map

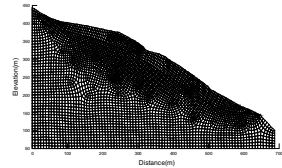


**Fig. 3.** Computing grid map

#### 3.2 Unsaturated Seepage Parameters

Soil water characteristic curve and permeability coefficient of unsaturated soil is important parameters in expressing properties of unsaturated seepage. SWCC is a curve used to describe the relationship between volume of soil saturation and water content or matrix suction. The permeability coefficient of unsaturated soil is

reflected the speed of hydraulic conductivity in unsaturated soil zone. Unsaturated flow parameters of sliding body and sliding belt are shown as Table 1 to Table 4.

**Table 1.** Relationship between  $\theta$  and  $-h$  of sliding body

$\theta$	0.114	0.118	0.131	0.154	0.166	0.18	0.193	0.25
$-h$	750	550	330	150	80	40	20	0

**Table 3.** Relationship between  $\theta$  and  $-h$  of sliding belt

$\theta$	0.11	0.114	0.121	0.151	0.172	0.198	0.22	0.27
$-h$	800	500	300	150	80	40	20	0

**Table 2.** Relationship between  $k_r$  and  $-h$  of sliding body

$k_r$	1.002E-05	1.739E-05	3.231E-05	6.551E-05	1.491E-04	3.980E-04
$-h$	100	90	80	70	60	50
$k_r$	7.051E-04	2.794E-03	1.789E-02	2.599E-01	4.500E+00	
$-h$	40	30	20	10	0	

**Table 4.** Relationship between  $k_r$  and  $-h$  of sliding belt

$k_r$	1.247E-08	2.164E-08	4.021E-08	8.152E-08	1.855E-07	4.952E-07
$-h$	100	90	80	70	60	50
$k_r$	1.669E-06	8.141E-06	2.226E-05	3.234E-04	5.600E-03	
$-h$	40	30	20	10	0	

### 3.3 Seepage Simulation Conditions

This study is mainly considered the influence of seepage field for water level fluctuation. According to the control program of Three Gorges Reservoir, every September to October is reservoir impounding period, water level rises from 145 m to 175 m ; Before flood season in June each year , reservoir water level slows down from 175 m to 145m. That is called storage in winter and relief in summer. Simulate the following conditions:

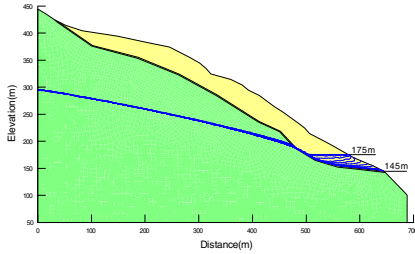
Condition 1 : body load and surface load and water level before dam rises in 1 m/d and 2 m/d from 145 m to 175 m;

Condition 2 : body load and surface load and water level before dam falls in 1 m/d and 2 m/d from 175 m to 145 m;

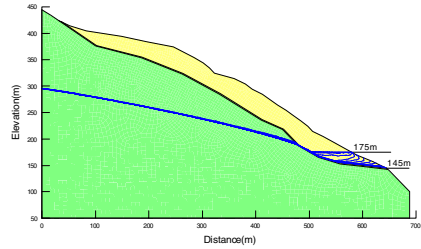
Condition 3 : body load and surface load and water level before dam rises in 1 m/d from 145 m to 175 m and Superimpose Hundred years, fifty years, twenty years, and ten years once of rainfall.

### 3.4 Seepage Calculation

According to water level fluctuation seepage simulation conditions, the following is results of water table below landslide movements with changes in water level.

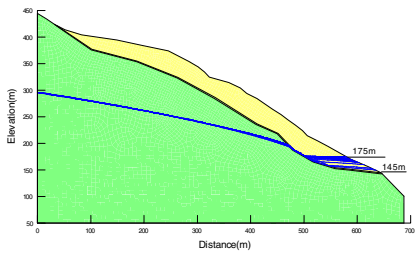


(a) rises in 1 m/d

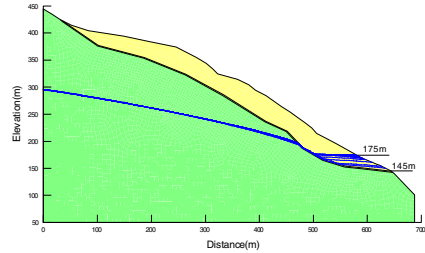


(b) rises in 2 m/d

**Fig. 4.** Underground water level for different times when reservoir water levels rises in different speeds



(a) falls in 1 m/d



(b) falls in 2 m/d

**Fig. 5.** Underground water level for different time when reservoir water levels falls in different speeds

### 3.5 Coupled Seepage and Stress Fields of Landslide Stability Calculation

Boundary conditions of stress calculated are as follows: left and right borders fix horizontal displacement; lower boundary fixed level and vertical displacements; the

**Table 5.** Physical and mechanical parametric

material	$\gamma$ , kN/m <sup>3</sup>	$c$ , kPa	$\phi$ , °	$E$ , MPa	$\mu$	$\phi^b$ , °
sliding body	21.9	13.2	26	21	0.2	16
sliding belt	20.6	21.6	21	18.5	0.32	12
sliding bed	25.8	1480	40.1	5100	0.23	...

**Table 6.** Effects of different rainfall intensity on landslide stability

rainfall intensity /mm/d	rainfall duration /d				
	1	2	3	4	5
q=350	1.027	0.985	...	...	...
q=200	1.023	0.999	...	...	...
q=150	1.025	1.014	0.98	...	...
q=120	1.038	1.031	1.024	0.993	...

upper border is free. The finite element method of slope stability analysis module Slope / w is used to calculate safety factor of the landslide. Landslide calculated parameters are shown in Table 5.

Safety factor of landslide with water level lift curve are shown in Fig 6, Fig 7 and Table 6.

### 3.6 Seepage Calculation Analysis

As Fig 4 shows, underground water level changes in wade range of the landslide body, and rises with reservoir water level rises. Compared fig 4 (a) and (b), the bigger rate reservoir water level rises, the more decrease of depth dipped into underground water level.

As Fig 5 shows, underground water level of landslide body decline with the decline of reservoir water level, and lags behind the rate of decline to reservoir water level drop. Compared fig 5 (a) and (b), it is known that the bigger speed reservoir water level drop, underground water level lags more behind reservoir water.

### 3.7 Stability Calculation Analysis

Fig 6 shows that safety factor of landslide rise as water level decreases. And the reservoir water level increased more slowly, the speed of safety factor reduced more quickly. That is to say, the slower rate of increasing, the more disadvantage for stability of the landslide.

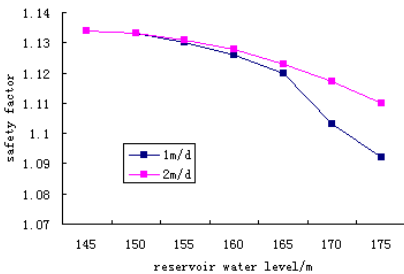


**Fig. 6.** Relationship between stability of landslide and rising velocities of reservoir water level

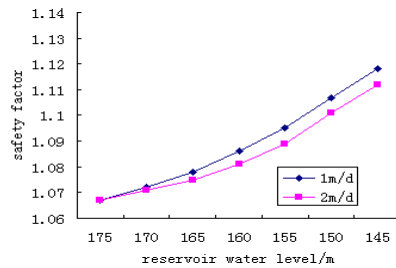


**Fig. 7.** Relationship between stability of landslide and descending velocities of reservoir water level

Fig 7 shows that safety factor of landslide increases with reservoir water level decline, and decline more slowly, stability of the landslide is bigger.

Table 6 shows that, as rainfall holding time increases and rainfall intensity increases, the landslide stability factor continuously decreases.

## 4 Conclusions

(1)The changes of Three Gorges reservoir water level have great impact of the seepage of the landslide body. The water table of the landslide is rising and falling with reservoir water and lags behind reservoir water lift.

(2)Safety factor of the landslide decreases with reservoir water rise. The more reservoir water rate increase, the greater stability of the landslide; safety factor increases with reservoir water drop, and the smaller rate of decline in reservoir water, the better stability of the landslide .This is consistent to rapid rise and slow drop of Three Gorges reservoir water level. And safety factor of the landslide decreases rapidly with rainfall intensity increases and rainfall holding time increases,

**Acknowledgements.** This research is supported by National Natural Science Foundation of China (50839004), Three research projects of geological disasters in Three Gorges Reservoir Area (201001008) and Ministry of Water Resources nonprofit industry research and special funding projects (SXKY3-2-1).

## References

- [1] Liao, Q.-L., Li, X., Lee, S., Dong, Y.-H.: Occurrence, geology and geomorphy characteristics and origin of Qianjiangping landslide in three gorges reservoir area and study on ancient landslide criterion. *Chinese Journal of Rock Mechanics and Engineering* 24(17), 3146–3153 (2005)
- [2] Zhong, L.-X.: Enlightenments from the accident of Vaiont landslide in Italy. *The Chinese Journal of Geological Hazard and Control* 5(2), 77–84 (1994)
- [3] Liu, X.-X., Xia, Y.-Y., Zhang, X.-S., Guo, R.-Q.: Effects of drawdown of reservoir water level on landslide stability. *Chinese Journal of Rock Mechanics and Engineering* 24(8), 1439–1444 (2005)
- [4] Fredlund, D.G., Rahardjo, H.: *Soil Mechanics for Unsaturated Soils*, Chen, Z.-Y., et al (transl.). China Architecture and Building Press

# Case Study: A Stress Update Algorithm for D-P Constitutive Model

Xiaohan Zhang

Civil and Environmental Engineering  
Carnegie Mellon University  
5000 Forbes Ave, Pittsburgh, PA 15213  
zxiaohan@andrew.cmu.edu

**Abstract.** A special stress update algorithm, called closet point project (CPP), for D-P constitutive model is studied with some numerical examples comparing CPP results with corresponding analytical solution. CPP is found to have uniformly consistency and unconditional numerical stability. We found that this algorithm is especially effective when used in geotechnical projects, which usually sees large step loading or unloading and requires strongly both stability and accuracy. A simple numerical example is given in the end for demonstration.

**Keywords:** stress update, nonlinear finite element, closet point project.

## 1 Introduction

Stress update algorithm is a key to nonlinear finite element method. Basically it is a numerical integration of instantaneous stress increment in order to obtain stress for next time step, given  $H = \text{grad } u$  at current time step often combined with Newton-Raphson. Most stress update algorithms require implicit integration to find solution to a dummy variable. Implicit stress update algorithm takes advantage in good numerical stability. However, they are extremely time consuming, considering that such implicit solving happens on each gauss point at each time step. On the other hand, explicit algorithms are fast but don't guarantee on stability. Aside from classifying stress update algorithm by their implicit or explicit, they are usually categorized into generalized midpoint method and generalized trapezoid method. Note that, by selecting different control parameters, those two methods can be either explicit or implicit as well. The algorithm CPP on which we focus here, is a special case of generalized midpoint method. By looking into its property and characteristic of linear plasticity D-P constitutive model, we obtain several interesting and useful observations.

This work is organized in the following way: In first part, an analytical solution is derived, based on linear plasticity D-P constitutive model. In the second section, CPP is formulated. Numerical stability and uniformly consistency proof is given. In the end we show some numerical examples by comparing CPP with corresponding analytical solution.

## 2 Analytical Solution for Stress Update of Linear Plasticity D-P

We begin with the general formula of D-P constitutive equation:

$$F(\sigma, \alpha) = \alpha I_1 + \sqrt{J_2} - c$$

Take derivative in stress space, in physical sense, we obtain normal of yield surface.

$$\frac{\partial F}{\partial \sigma_{ij}} = \alpha \delta_{ij} + \frac{s_{ij}}{2\sqrt{J_2}}$$

Consistency condition requires:

$$\dot{F} = \frac{\partial F}{\partial \sigma} : \dot{\sigma} = 0$$

Note  $\dot{\sigma} = E : (\dot{\varepsilon} - \varepsilon^p) = E : (\dot{\varepsilon} - \frac{\partial F}{\partial \sigma} \dot{\lambda})$ , by manipulating terms and applying consistency condition we have expression for plastic scalar

$$\dot{\lambda} = \frac{\frac{\partial F}{\partial \sigma} : E : \dot{\varepsilon}}{\frac{\partial F}{\partial \sigma} : E : \frac{\partial F}{\partial \sigma}}$$

Substitute it back to get updated stress, we have the following:

$$\begin{aligned} \dot{\sigma}_{ij} &= E_{ijkl} \left[ \dot{\varepsilon}_{kl} - \dot{\lambda} \left( \alpha \delta_{ij} + \frac{s_{kl}}{2\sqrt{J_2}} \right) \right] \\ &= \left[ \left( K - \frac{2}{3}G \right) \delta_{ij} \delta_{kl} + G(\delta_{ik} \delta_{jl} + \delta_{il} \delta_{jk}) \right] : \left[ \dot{\varepsilon}_{kl} - \dot{\lambda} \left( \alpha \delta_{ij} + \frac{s_{kl}}{2\sqrt{J_2}} \right) \right] \\ &= (K \varepsilon_{kk} - 3\alpha K \dot{\lambda}) \delta_{ij} + 2G \dot{\varepsilon}_{ij} - G \frac{s_{ij}}{\sqrt{J_2}} \dot{\lambda} \end{aligned}$$

Here we shall consider special case and make two assumptions: H1) strain rate in each updating step is always a constant. This is true for any time independent FEM calculation. H2) hardening or softening is not considered. Under such assumptions, can derive ODE for deviator part of stress and variable  $\varphi$

$$\frac{\dot{\tau}_c}{\tau_c} = \left| \frac{\sin \frac{1}{2} \varphi}{\sin \frac{1}{2} \varphi_c} \right|^{1-m} \left| \frac{\cos \frac{1}{2} \varphi}{\cos \frac{1}{2} \varphi_c} \right|^{1-n} > 0, \quad m = 2 - \frac{G}{H}(1+\nu), \quad n = 2 - \frac{G}{H}(1-\nu)$$

$$\text{sign}(\sin \varphi) \frac{\frac{1}{2} \dot{\varphi}}{\left| \sin \frac{1}{2} \varphi \right|^m \left| \cos \frac{1}{2} \varphi \right|^n} = - \frac{G\sqrt{2} \|\dot{e}\|}{\tau_c} \frac{1}{\left| \sin \frac{1}{2} \varphi_c \right|^{m-1} \left| \cos \frac{1}{2} \varphi_c \right|^{n-1}}$$

$\varphi$  has a physical meaning in principle stress space. Let  $S_e$  and  $S_c$  be deviator part of increment stress and current stress. Let  $S$  be deviator part of updated stress. Then  $\varphi$  is defined such as:

$$S : S_e = 2\tau\tau_e \cos \varphi \quad \tau = \sqrt{J_2}$$

Physically an angle of  $S$  off  $S_e$ . Up to now, we have got a changing upper limit integral for  $\varphi$  such as:

$$f(\varphi) = \int_{\varphi_c}^{\varphi} \text{sign}(\sin \varphi) \frac{0.5\varphi_t}{\left| \sin 0.5\varphi_c \right|^{m-1} \left| \cos 0.5\varphi_c \right|^{n-1}}$$

Note that normally this function doesn't have analytical solution. However, giving credit to continuity, we can obtain solution up to any order of accuracy. In section 3, we use Matlab to solve  $\varphi$ , substitute it back to get coefficient A and B. Obtaining updated stress by combining consistency condition.

### 3 Stability and Accuracy Analysis

Since CPP is a special case of generalized midpoint method, we start by looking into generalized midpoint method formulation:

$$\begin{aligned} \sigma_{n+1} &= D : (\varepsilon_{n+1} - \varepsilon_{n+1}^p) \\ \varepsilon_{n+1}^p &= \varepsilon_n^p + \lambda \gamma_{n+\alpha} \\ q_{n+1} &= q_n + \lambda h_{n+\alpha} \\ \phi_{n+1} &= 0 \end{aligned}$$

Where,  $n+1$  stands for new step, and  $n$  current.  $\varepsilon_{n+1}$  is known quantity in finite element method and

$$\begin{aligned} r_{n+\alpha} &= r((1-\alpha)\sigma_n + \alpha\sigma_{n+1}, (1-\alpha)q_n + \alpha q_{n+1}) \\ h_{n+\alpha} &= h((1-\alpha)\sigma_n + \alpha\sigma_{n+1}, (1-\alpha)q_n + \alpha q_{n+1}) \end{aligned}$$

It can be seen that generalized midpoint is basically a prediction-correction method. When  $\alpha = 1$  generalized midpoint method becomes CPP. Next we analyze

its numerical stability: Let  $B_{n+\alpha} = \left(\frac{\partial \gamma}{\partial \sigma}\right)_{n+\alpha}$  Dot  $d\sigma_n = -D : d\varepsilon_n^p$  with  $C = D^{-1}$ ,

$$\Rightarrow (C - \lambda(1 - \alpha)B_{n+\alpha}) : d\sigma_n = d\lambda\gamma_{n+\alpha} + (C + \alpha\lambda B_{n+\alpha}) : d\sigma_{n+1}$$

We have incremental plastic scalar:

$$d\lambda = \frac{\eta_{n+1} : (C + \alpha\lambda B_{n+\alpha})^{-1} : (C - \lambda(1 - \alpha)B_{n+\alpha}) : d\sigma_n}{\eta_{n+1} : (C + \alpha\lambda B_{n+\alpha})^{-1} : \gamma_{n+\alpha}}$$

$$\text{Let } P = I - \frac{(C + \alpha\lambda B_{n+\alpha})^{-1} : \gamma_{n+\alpha}}{\eta_{n+1} : (C + \alpha\lambda B_{n+\alpha})^{-1} : \gamma_{n+\alpha}}$$

$$\Rightarrow d\sigma_{n+1} = P : (C + \alpha\lambda B_{n+\alpha})^{-1} : (C - \lambda(1 - \alpha)B_{n+\alpha}) : d\sigma_n$$

One can show that P is a project tensor with  $\|P\| = 1$ . We obtain the following important observation, showing that as long as  $\alpha \geq 0.5$  generalized midpoint method guarantees unconditional stability:

$$\|d\sigma_{n+1}\| \leq \left| \frac{1 - \alpha}{\alpha} \right| \|d\sigma_n\| = C \|d\sigma_n\|$$

Finally, CPP based on D-P can be derived easily by letting  $\alpha = 1$ . Notice that it has automatic stability due to what has been derived for generalized midpoint method.

$$\sigma = \sigma^1 - \Delta\lambda D : \frac{\partial f}{\partial \sigma} \Big|_{\sigma = \sigma}$$

Consequently,

$$\sigma = \sigma^1 - \Delta\lambda D : \left( \alpha \delta_{ij} + \frac{s_{ij}}{2\sqrt{J_2}} \right)$$

Notice that

$$\sigma_{ij}^1 = \frac{1}{3} \sigma_{ii}^1 + s_{ij}^1 \text{ and } \sigma_{ij} = \frac{1}{3} \sigma_{ii} + s_{ij}$$

The equivalent form of CPP is

$$\frac{1}{3} (\sigma_{ii}^1 - \sigma_{ii}) = 3K\alpha\Delta\lambda \text{ and } s_{ij}^1 - s_{ij} = \frac{G\Delta\lambda}{\sqrt{J_2}} s_{ij}$$

An important observation here is that

$$\frac{\partial f}{\partial \sigma} \Big|_{\sigma=\sigma} = \frac{\partial f}{\partial \sigma} \Big|_{\sigma=\sigma^1}$$

which is a special characteristic of D-P constitutive model.

Making use of this property, we can rewrite CPP as following:

$$\sigma = \sigma^1 - \Delta\lambda D : \frac{\partial f}{\partial \sigma} \Big|_{\sigma=\sigma^1}$$

What is shown here is a modified CPP for D-P model. It has advantages in that it is explicit and has unconditional stability.

### 4 Numerical Examples

Iso-error map is generated to examine accuracy of CPP. Figure 1,2 are subjected to strain increment along meridian plane. Figure 3,4 increment along  $\pi$  plane.

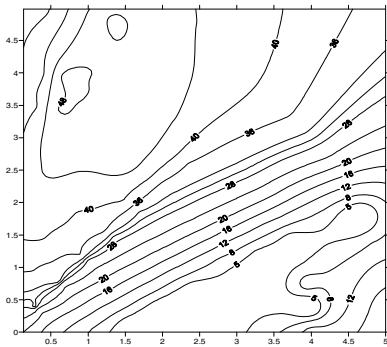


Fig. 1.  $\phi$

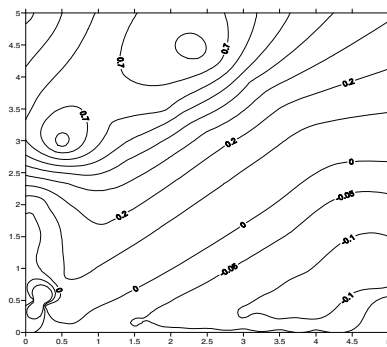


Fig. 2.  $\tau$

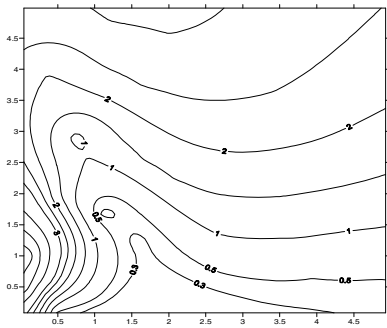


Fig. 3.  $\phi$

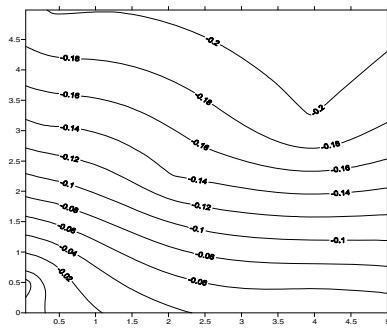


Fig. 4.  $\tau$

## 5 Conclusions

We have proof that CPP has unconditional numerical stability as well as consistency. One interesting observation we made about CPP for D-P model, a model that is popular in geotechnical engineering, is that the derivative of yield function w.r.t updated deviator part of stress is same as trial stress.

Numerical results show that, when strain increment deviate little from initial yield stress, CPP possesses high accuracy. Most important, it is independent of loading step size. This is an ideal property for large nonlinear finite element simulations.

## References

- [1] Ortiz, M., Popov, E.P.: Accuracy and stability of integration algorithms for elastoplastic constitutive relations. *IJNME* (1985)
- [2] Yang, Q., Chen, X., Zhou, W.Y.: A practical 3D elasto-plastic increment method in FEM based on D-P yield criteria. *Chinese Journal of Geotechnical Engineering* (2002)

# Plastic Damage of the Surrounding Rock under the Influence of Confined Water Pressure and Mining Disturbance<sup>\*</sup>

Chunhu Zhao

Xi'an Research Institute of China Coal Technology & Engineering Group corp Xi'an  
Yanta Road(N)52, Xian city, Shanxi Province China 710054  
zhaochunhu51002@163.com

**Summary.** Simulated rock stress and deformation characteristics in influence of mining disturbances, water pressure and crustal stress by use of Comsol4.2a the multi-physics coupling finite element simulation software. The results showed that:(1)the water pressure is fixed conditions, the plastic damage scope in stress concentration zone where was formed by mining disturbance is were greater than the mining floor ,and with an extension of the scope of mining, the scope of plastic failure zone in the rock surrounding which including the vertical and horizontal was increased;(2)Stope width is fixed conditions, with the water pressure increases, resulting in the surrounding rock mechanical strength decrease, As rock water pressure increases, resulting in the surrounding rock mechanical strength decrease, and increase the scope of the plastic collapse and plastic damage within the fault zone intensified.

**Keywords:** fluid- solid coupling,deformation, stress,comsol.

## 1 Introduction

In recent years, safety mining activities affected by the high earth temperature, high underground stress, high hydraulic pressure of the karst and mining disturbances under the conditons of deep mining. And high-pressure groundwater pressure, underground stress, and mining disturbances are the main factors that affect the underground surrounding rock stress and deformation in deep mining. In fact, mutual restraint and mutual influence between this three factors, finally, and result in groundwater-solid coupling effect[1]. Generally, In order to prevent pressurized water broke into the mine tunnel,mine mining activities pre-leaving a certain thickness of the coal seam that based on empirical formula, This empirical formula was summarized drawn from the experience which only takes into account of the

---

<sup>\*</sup> This paper is supported by the Key Program of National Natural Science Foundation of China (51034003).

aquifer water pressure and seam tensile strength[3-7], it does not consider the changed stress caused by actual mining disturbance or the groundwater-solid coupling effect. Thus, it has some defects in the specific mining activities. many study and engineering practice show that fluid-solid coupling analysis is more closer to the actual situation.

In this paper, the flow-solid coupling was introduced into the tunnel excavation analysis for the underground rock stress field and groundwater seepage field, combination of rock elastic-plastic mechanics and fluid dynamics theory, the multi-physics coupling software Comsol4.2a was applied which based on the finite element numerical simulation method, then, paper simulated stope surrounding rock stress and the plastic damage changes under the influence of different water pressures and different mining disturbance range.

## 2 Mathematical Model

Thus, fluid reflected the two aspects impact which lead to the deformation of the solid medium: (1) the underground water pressure (including hydrostatic and hydrodynamic pressure) imposed load on the solid skeleton, and the pressure changes will cause the overall deformation displacement for porosity or fractured media in solid; (2) the existence of the internal water pore pressure, changing the constitutive characteristics of fractured rock mass, thereby affecting solid deformation[8,9]. Therefore, the size and gradient of the pore water pressure has a direct impact on the rock mass stress-strain relationship. mathematical model of mass rock flow-solid coupling should include the percolation model of the fluid and solid stress model. First to introduce the following assumptions: a. groundwater seepage in the infinitesimal segment to follow Darcy's law, and comply with the non-linear Darcy's law in the entire section; b. porous media is mainly composed of solid and fluid part in the underground, and groundwater seepage was considered as single-phase saturated flow; ③ geotechnical pore water pressure and crustal stress to follow the amendment of the Terzaghi effective stress principle; ④ Solid skeleton volume of the saturated porous media deformation equal to the deformation of the pore. Then, the mathematical model can be simplified as follows:

Groundwater seepage field equation: Rock mass displacement equation:

$$\nabla \left[ \frac{\rho K}{\mu} \nabla p \right] = 0 \quad (1)$$

$$G \nabla^2 u + \frac{G}{1-2\nu} \nabla * (\nabla u) - \alpha \nabla p = 0 \quad (2)$$

The formula: “ $K$ ” is the absolute permeability of porous media ( $\mu m^2$ );  $M$  is the fluid viscosity ( $Pa.s$ ); and  $\rho$  is the fluid density ( $g/cm^3$ ), “ $P$ ” is the groundwater pressure ( $Pa$ ); “ $G$ ” is the shear modulus; “ $\nu$ ” is the Poisson ratio of the medium, “ $\alpha$ ” is the Biot coefficient, its value depends on the compression performance of the

material.and, “ $G=2E(I+v)$ ”, “ $E$ ”is the elastic modulus,  $u$  is the displacement in x-axis, the y-axis and z-axis direction. And the“ $\nabla P$ ”reflected the impact of the water seepage field in solid skeleton, its essence is that the pore pressure generated in the fluid flow affected the stress field of the solid skeleton, thereby affecting the deformation of the solid skeleton. These formulas are based on the expression of the Biot classical percolation theory, According to the study of practical problems, and definitions specific to the conditions for determining solution, Then it can computer simulation for the problem.

The rock mass plastic damage criterion adopted amendments to the CM (mohr-coulomb) guidelines [11]:

$$F = \alpha_1 I_1 + \sqrt{J_2} - K_1 = 0 \tag{3}$$

and :

$$I_1 = \sigma_1 + \sigma_2 + \sigma_3 = \sigma_x + \sigma_y + \sigma_z, \quad J_2 = \frac{1}{6} [(\sigma_1 - \sigma_2)^2 + (\sigma_2 - \sigma_3)^2 + (\sigma_3 - \sigma_1)^2]$$

$$\alpha_1 = \tan \varphi / \sqrt{9 + 12 \tan^2 \varphi}, \quad \kappa_1 = 3c / \sqrt{9 + 12 \tan^2 \varphi}$$

In this paper, the simulation criterion of plastic damage in rock, applied the rock mass stress (*solid.sp*) above the coal layer; according to the Terzaghi effective stress principle, applied rock effective stress (*poro.sp*)in the aquifer below the faultusing.

### 3 Case Model

#### 3.1 The Physical Problem

According to Fig.1, Define the hydraulic conductivity thrust fault width is 20m, The seam thickness is 5m, the sandstone thickness is 320m (ie z-axis direction) which above in the coal seam , Impermeable layer thickness is 30m which under the coal seam, model thickness in the Y-axis direction is 500m.and the tunneling coal lane advancing step by step to the right-side where closed to the water-filled fault.

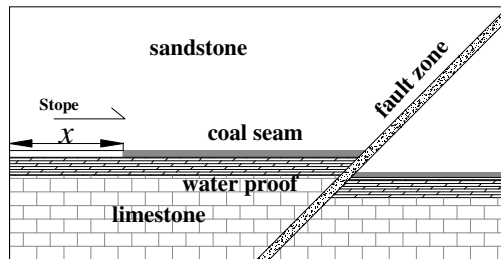


Fig. 1. Physical model diagram

This paper does not study tunneling coal lane wheher occur a suddenly water inrush from coal layer floor or fault damage which caused by confined nature of Ordovician limestone water, The goal of the problem is the research that analysis the rock stress distribution and plastic damage characteristics in the influence of dynamic mining disturbances and fault with water pressure. with expand the scope of plastic failure, rock water blocking water capacity reduced, may be lead to the floor failure or fault activation of hydraulic conductivity, Therefore, there is the high possibility of water inrush occurs.

### 3.2 The Determine Conditions for This Problems

The initial conditions: hydraulic conductivity fault zones and the limestone aquifer defined as the seepage zone, the region  $p_{l(t=0)}=p_0$ ; the whole region are the stress zone,  $u_{l(t=0)}=0$ ,  $p_0$  is a porous medium initial underwater pressure,  $p_0=2\text{MPa}$ ,  $u$  is the displacement.

Boundary conditions:  $p_b=p_1$  (vadose zone);  $u_b=u_l$ ,  $p_1$  is water pressure on the boundary, the water pressure is  $p_1=4\text{MPa}$  in the model of the underside,  $u_l$  is the displacement on the boundary, the underside of the model was set as a fixed boundary which displacement is 0, the model top surface (including the upper part of the fault) was defined as the free boundary which directly connected with the atmosphere, the free boundary pressure is atmospheric pressure (0.1MPa), the model on all sides of the surface is defined as the roller boundary which only in the vertical displacements(z-axis direction),but the horizontal displacement is 0. In this model, the groundwater stress  $p$  was load to solid displacement equations in form of a “volume force”, Unlike the solid medium by the “surface force”, the “volume force” was load to physical distribution in the power of the media within the model, and all computing nodes is governed by the pore water pressure  $p$ , as the solid additional stress  $\sigma'=-p$ , "-" show the pressure of pore water pressure direction contrary to the principal stress direction of the solid.

### 3.3 Establishment of Model

Underground mass rock physical and mechanical properties parameters in the model shown in Table 1, Fig.2 shows the simulation region subdivision map,the model encrypted split coal seam and fault zones where were the key areas.

**Table 1.** Fluid and solid parameters table

Rock mass	density ( $\text{kg/m}^3$ )	E(MPa)	Poisson's ratio	Permeability (mD)	Porosity
Sand stone	2580	12370	0.21	\	\
Coal seam	1350	3200	0.2	\	\
Water proof	2530	3360	0.22	\	\
Fault zone	774	2700	0.4	1500	0.35
Lime stone	2620	2530	0.23	500	0.12

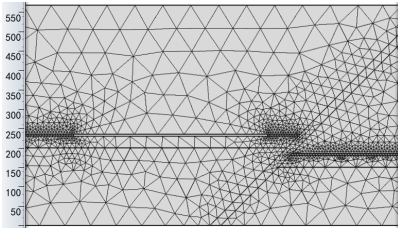


**Fig. 2.** Model district split schematic

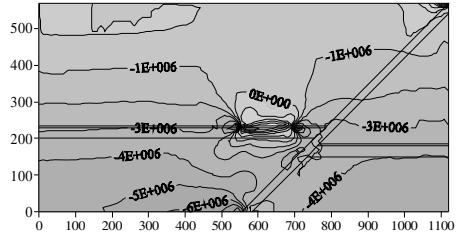


**Fig. 3.**  $p_1=4\text{MPa}$ ,  $x=700$  rock stress contours (unit: Pa)

The simulation defined “x” as a “Global parameters” in the model, it calculated model once time in steady-state when “x” every per a sliding scale of 50m, The range of x values is 600~720 m (from coal seam to the fault distance is 150 ~ 30m, in other side the  $x_1=550\text{m}$  was fixed). and “ $p_1$ ” as “Global parameters” too, it calculated model once time in steady-state when “ $p_1$ ” every per a sliding scale of 2MPa, The range of “ $p_1$ ” values is 0~8Mpa.

## 4 Simulation and Analysis

### 4.1 The Stress of the Rock Mass under the Mining Disturbance

In this model, Stress refers to the first principal stress of the vertical, and displacement was total displacement, define the tensile stress is the "+" and compressive stress is "-", and downward displacement of the "+" or up to "-".

Shown in Fig.3: there were stress concentration phenomenon which due to mining activities in the stope surrounding. The most obvious on both sides of the stope and reached to the maximum, and the stress from the compressive stress into the mining empty district tensile stress .

### 4.2 The Plastic Failure of the Rock Mass under Different Mining Disturbance

In this situation, the model define  $p_1=4\text{Mpa}$  as a fixed water pressure boundary at the bottom. and other hydraulic boundarys remains the same, fixed  $x_1=550\text{m}$  at end left of stope. according to the modified C-M guidelines, Scanning  $x_2$  parameters, mapping the contour map of the  $F'$  value, remove the  $F' < 0$  in the computational domain, retained the  $F' \geq 0$  region which is the plastic damage model area.

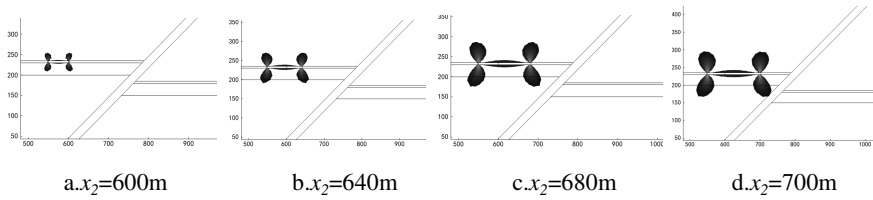


**Fig. 4.** The plastic damage zone in different mining width ( $p_1=4\text{MPa}$ )

**Table 2.** The tables plastic zone in different mining width ( $p_1=4\text{MPa}$ )

Location (m)		Plastic damage of the maximum vertical distance (m)	
$X_2$	width	Middle of the stope	Stress concentration zone
600	50	1.7	11.7
620	70	3.2	23.8
640	90	4.5	35.6
660	110	5.0	46.2
680	130	5.3	52.5
700	150	6.2	57.4

Fig.4 shown the different stope width of the surrounding rock plastic damage distribution, the results show that the surrounding rock plastic damage occurs mainly in the stope at both ends of the stress concentration area, the maximum vertical extension of parts of 20~25m at both ends of the lateral; stope internal top floor plastic range is smaller, but large extended position in the middle of the stope; and with the increase of the width of the stope, the larger the plastic collapse range, as shown in Figure 4d, when  $x = 700\text{m}$ , the right end of the plastic extends to the fault zone within the rock plastic yield, there is the fault water pressure breakthrough in coal pillar into the stope possible. different stope width statistics in Table2, both ends of the stope and central backplane plastic failure of the largest vertical distance: the case of  $x=700\text{m}$  when the largest vertical of the middle of the stope plastic zone deep was 6.2m, both ends reached to 57.4m.

### 4.3 The Plastic Failure of the Rock Mass under Different Water Pressure

Fixed both ends of the stope, location ( $x_1=550\text{m}$   $x_2=700\text{m}$ ), according to the modified C-M guidelines, Scanning  $P_1$  parameters, mapping the contour map of the  $F'$  value, remove the  $F' < 0$  in the computational domain, retained the  $F' \geq 0$  region that is the plastic damage model area.

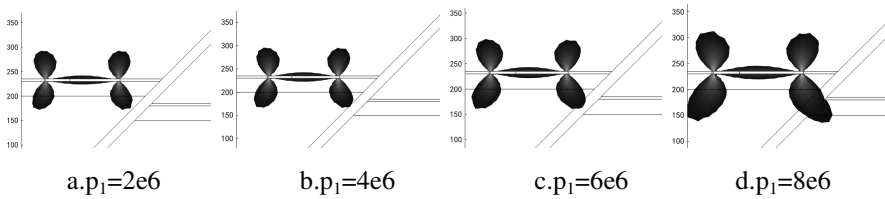


Fig. 5. The plastic damage zone in different water pressure

Table 3. The tables plastic zone in different water pressure ( $p_1=4\text{MPa}$ ,  $x_2=700\text{m}$ )

Water pressure (MPa)	Plastic damage of the maximum vertical distance (m)	
	Middle of the stope	Stress concentration zone
2	4.9	53.0
4	6.2	57.4
6	7.8	70.6
8	11.2	87.4

Fig.5 was the distribution of plastic damage in different hydraulic conditions. the results show that surrounding rock and surrounding rock plastic damage morphology is mainly affected by mining disturbance control, According to the rock mass failure criterion ,the effective stress decreases due to increasing water pressure[10-12], so that the surrounding rock mechanical strength decreases, and the plastic destruction zone was expanded. For example, Fig.5c, when  $p_1=6\text{MPa}$ , the right end of the plastic zone extends to the fault zone, as shown in Fig.5d,  $p_1$  increases to  $8\text{MPa}$ , the plastic zone of rapid expansion in the fault zones, indicating that the fault zone plastic damage intensified by lower mechanical strength of rock mass and the higher water pressure. Maximum vertical distance statistics in Table3 in different water pressure: the greater the water pressure, the greater the distance of vertical damage

## 5 Conclusion

This paper simulated underground mass rock stress and plastic damage characteristics in the influence of disturbances in the mining, water pressure and crustal stress by use of Comsol4.2a the multi-physics coupling finite element simulation software. Initially draw the following conclusions:(1)the water pressure is fixed conditions, the plastic damage scope in stress concentration zone where was formed by mining disturbanceis were greater than the mining floor ,and with an extension of the scope of mining, the scope of plastic failure zone in the rock surrounding which including the vertical and horizontal was increased;(2)Stope width is fixed conditions,with the water pressure increases, resulting in the surrounding rock mechanical strength decrease, As rock water pressure increases, resulting in the surrounding rock mechanical strength decrease, and increase the scope of the plastic collapse and plastic damage within thefault zone intensified.(3)

Ductile failure of rock mass surrounding rock mechanical strength decrease under the influence of high pressure water, may be pressure water to break through the seam floor or impermeable coal pillar into the stope may.

## References

- [1] Hu, W.: Minewater hazard control theory and method, pp. 20–21. China coal industry publishing house, Beijing (2005)
- [2] Xu, Y.: Introduction to rock mass hydraulics. Southwest Jiaotong University Press, Chengdu (1995)
- [3] Li, J.-G., Wang, Y.-Y., Wang, H.: Study of rheological model of porous medium of deep rock. *Rock and Soil Mechanics* 29(9), 2355–2358 (2008)
- [4] Wang, Y.-Y., Qi, J., Yang, C.-H., et al.: A study of nonlinear creep law in deep rocks. *Rock and Soil Mechanics* 26(1), 117–121 (2005)
- [5] Yin, S.-X., Wu, Q., Wang, S.-X.: Hydrogeological and mechanical basics of water inrush from karstic collapse columns in Northern China. *Journal of China Coal Society* 29(2), 182–185 (2004) (in Chinese)
- [6] Gucs, S., Zhou, H.: Study of coupling model of seepage field and stress-field for rolled control concrete dam. *Applied Mathematics and Mechanics (English Edition)* 26(3), 355–363 (2005)
- [7] He, M.-C., Xie, H.-P., Peng, S.-P., et al.: Study on rock mechanics in deep mining engineering. *Chinese Journal of Rock Mechanics and Engineering* 24(16), 2803–2813 (2005)
- [8] Yin, S.-X., Wu, Q., Wang, S.-X.: Hydrogeological and mechanical basics of water inrush from karstic collapse columns in Northern China. *Journal of China Coal Society* 29(2), 182–185 (2004) (in Chinese)
- [9] Zhan, Y., Liu, H., You, C.: FluidSolid coupling analysis of the safety of the waterproof coal pillar. *Chinamining Magazine* 19(04), 89–92 (2010)
- [10] Yang, T.-H., Tang, C.-A., Xu, T., et al.: Seepage characteristic in rock failure. *Science in China Press*, 141–145 (2004) (in Chinese)
- [11] Gu, C.S., Su, H.Z., Zhou, H.: Study of coupling model of seepage field and stress-field for rolled control concrete dam. *Applied Mathematics and Mechanics (English Edition)* 26(3), 355–363 (2005)
- [12] Yuan, L., Li, Z., Wu, H.: Seepage mechanics and Application. China Building Materials Industry Press, Beijing (2001)

# 3D Large Deformation FE Analysis of Spudcan Foundations on Layered Clays Using CEL Approach

Jingbin Zheng, Muhammad S. Hossain<sup>\*</sup>, and Dong Wang

Centre for Offshore Foundation Systems  
The University of Western Australia  
35 Stirling Highway, Crawley, Perth, WA 6009, Australia  
muhammad.hossain@uwa.edu.au

**Abstract.** Spudcan foundations are used widely to provide support at the seabed for independent legged jack-up rigs. In order to explore the continuous load-penetration profile and mobilised soil failure patterns, simulating deep penetration of spudcans during preloading a jack-up rig, large deformation finite element (LDFE) analyses are essential. This paper investigates continuous penetration of circular spudcan foundations in single and two-layer clay deposits. An LDFE approach termed Coupled Eulerian-Lagrangian (CEL) approach in commercial package Abaqus was used. For implementing the CEL approach, a 3D model was created, in which only one fourth of the whole model was considered accounting for the geometric symmetry. Parametric LDFE analyses were performed encompassing the range of practical interest. The results from 3D CEL approach were compared with the previously published results from axisymmetric LDFE analyses using the RITSS (remeshing and interpolation technique with small strain) approach. The good agreement obtained shows that the CEL approach is capable in analysing complicated large deformation problems.

**Keywords:** bearing capacity, clays, failure mechanisms, 3D large deformation finite element analysis, spudcan foundations, CEL.

## 1 Introduction

Deep penetration of spudcan foundations and circular footings on layered clays has attracted attention from a number of researchers. The investigations have been carried out chiefly through model tests. More recently the problem has been addressed through continuous penetration finite element (FE) analysis. These include the studies on deep penetration of strip and circular footings by Wang & Carter [1] and on spudcan foundations by Hossain & Randolph [2]. In both studies, 2D axisymmetric analyses were carried using remeshing and interpolation technique with small strain (RITSS; see [3]) coupled with the finite element package AFENA (see [4]). This method falls within what are known as Arbitrary Lagrangian-Eulerian (ALE) methods. In order to avoid mesh distortions due to large deformation,

---

<sup>\*</sup> Corresponding author.

frequent remeshing and interpolation of historical variables are essential. This also allowed the regenerated mesh to fit into the updated boundary with continuous penetration.

Recently, Coupled Eulerian-Lagrangian (CEL) approach is available in commercial package Abaqus/Explicit to carry out continuous penetration analysis circumventing the difficulties related to LDFE analysis (see [5]). Different from the conventional ALE methods, in the CEL approach, the soil materials are covered by an Eulerian mesh, whereby the mesh nodes are fixed in space and the soil materials flow through the elements. The layer interfaces are tracked as the materials flow within the mesh by computing the volume fraction of each material in each element. As such, mesh distortions that occur in traditional Lagrangian analysis can be avoided.

## 2 Numerical Analysis

Spudcan penetration analyses were performed in Abaqus Version 6.10. All simulations were three dimensional (3D) since the current CEL approach is only for a 3D element type EC3D8R. Analyses were also undertaken for a circular footing mainly for validating against the results from analyses using the RITSS approach. The axisymmetric soil domain was chosen as  $9.2D$  in diameter and  $7.5D$  in depth to ensure that the boundaries were well outside the plastic zone. By considering the symmetry inherent, only a quarter sector was involved in all analyses.

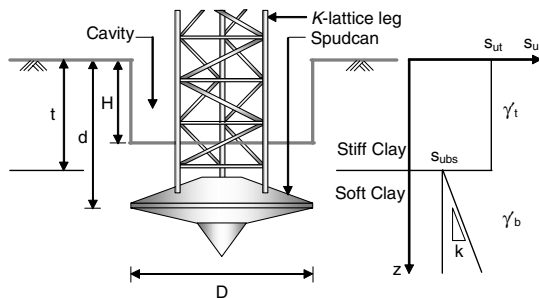


Fig. 1. Schematic of embedded spudcan showing idealised open cavity

### 2.1 Geometry and Parameters

This study has considered a spudcan foundation of diameter  $D$ , penetrating into a two-layer deposit as illustrated schematically in Fig. 1, where the top layer of clay with uniform undrained shear strength  $s_{ut}$ , submerged unit weight  $\gamma'_t$  and thickness  $t$  is underlain by a clay layer of uniform undrained shear strength  $s_{ub}$ , submerged unit weight  $\gamma'_b$  and (nominally) infinite depth. The nomenclature for a deep-penetrating circular footing is consistent, except the footing was modelled as a cylindrical object with smooth rigid shaft and the soil weight was ignored. This did

not allow the soil to flow back above the footing, i.e.  $d = H$  in Fig. 1. The spudcan and circular footing were 12 m and 10 m diameter, respectively. All dimensionless parameters are given in Table 1.

Penetration analyses were also carried out on single layer non-homogeneous clay. The undrained shear strength,  $s_u$ , was taken as varying linearly with depth, i.e.  $s_u = s_{um} + kz$ ; where  $s_{um}$  is the soil strength at the mudline and  $k$  is the rate of increase of  $s_u$  with depth  $z$ .  $s_{u0}$  is the soil strength at the spudcan base level (lowest point of the largest section). All the explored parameters are summarised in Table 2.

**Table 1.** Parameters for LDFE analyses on uniform-over-uniform clay

Analysis	$s_{ub}/\gamma'_b D$	$s_{ub}/s_{ut}$	$t/D$	$\gamma'_b/\gamma'_t$	Base
Spudcan	0.36	0.2, 0.4, 0.6, 0.8	0.25, 0.5, 0.75	0.87	Rough
Circular footing	-	0.2, 0.4, 0.6, 0.8	0.25, 0.5, 0.75, 1	Weightless	Smooth

**Table 2.** Parameters for LDFE analyses on single layer non-homogeneous clay

Analysis	Case 1	Case 2	Case 3	Case 4	Case 5	Case 6	Case 7	Case 8
$s_{um}/\gamma' D$	0.143	0.143	0.095	0.029	0.025	0.020	0.015	0
$kD/s_{um}$	0	1	2	5	10	15	20	$\infty$
Base	Smooth							

## 2.2 Details of FE Modelling

The CEL approach allows both the Eulerian and Lagrangian bodies in a FE model and the Eulerian body undergoes Lagrangian and Eulerian phases in each increment. In CEL analysis, a Lagrangian body, e.g. spudcan, travels through an Eulerian soil material(s) and hence no element distortion occurs during the advancing process.

An elasto-perfectly plastic constitutive model, Tresca model, was used to simulate the undrained penetration of foundations in clay. The yield function can be represented as:

$$F = J \cos \theta - s_u \quad (1)$$

The function plots a regular hexagonal cylinder in the principal stress space, where  $s_u$  is the undrained strength of clay and  $J$  and  $\theta$  are deviatoric stress and Lode's angle respectively:

$$J = \sqrt{\frac{1}{6} [(\sigma_1 - \sigma_2)^2 + (\sigma_2 - \sigma_3)^2 + (\sigma_3 - \sigma_1)^2]} \quad (2)$$

$$\theta = \tan^{-1} \left\{ \frac{1}{\sqrt{3}} [2(\sigma_2 - \sigma_3)/(\sigma_1 - \sigma_3) - 1] \right\} \quad (3)$$

where  $\sigma_1$ ,  $\sigma_2$  and  $\sigma_3$  are principle stresses. All the analyses adopted a Poisson’s ratio  $\nu = 0.49$  to approximate constant soil volume under undrained conditions. A uniform stiffness ratio of  $E/s_u = 500$  was considered throughout the clay profile. The coefficient of earth pressure at rest was taken as 1.

To balance computational accuracy with efficiency, element size of 0.1D was adopted adjacent to the spudcan. When the horizontal distance from the spudcan centre approaches a radius of the foundation, a bias meshing strategy was used.

### 3 Penetration in Uniform-Over-Uniform Clay

#### 3.1 Bearing Response

The load-penetration responses are presented in terms of normalised net bearing pressure,  $q_{net}/s_{ub}$ , as a function of normalised penetration depth,  $d/D$  (see Fig. 1 for definitions), with  $q_{net}$  calculated as:

$$q_{net} = P/A - \gamma'_t V/A \tag{4}$$

where  $P$  is the penetration resistance,  $V$  is the volume of the embedded spudcan including shaft and  $A$  is the largest cross-section area of the spudcan.

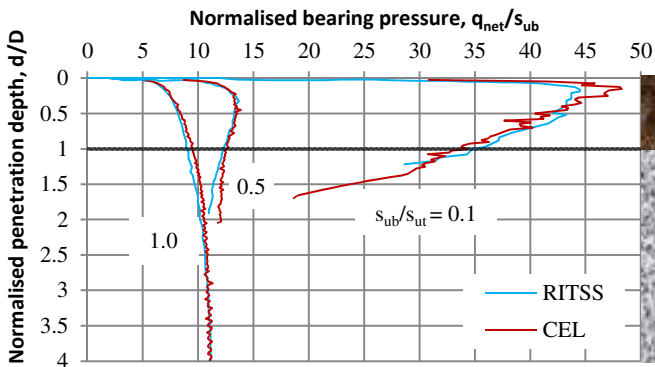


Fig. 2. Comparison between CEL and RITSS approach: circular footing on layered soils

#### 3.2 Circular Footing

Three analyses were performed for weightless soil to compare with the results from the RITSS approach (see [1]). Figure 2 shows the normalised bearing pressure for a smooth circular footing (and smooth shaft) penetrating into layered soils with thickness ratio  $t/D = 1$  and strength ratio  $s_{ub}/s_{ut} = 0.1, 0.5$  and  $1$ . Both sets of results are in excellent agreement, confirming the accuracy of the results using the CEL approach.

Figure 3 shows the effect of the strength ratio on the form of the penetration resistance profile, illustrating the results of various strength ratios  $s_{ub}/s_{ut} = 0.2, 0.4, 0.6, 0.8$ , but for a constant thickness ratio of  $t/D = 0.5$ . For higher strength ratio of  $s_{ub}/s_{ut} = 0.8$ , the normalised bearing resistance increases monotonically with penetration depth, while for  $s_{ub}/s_{ut} \leq 0.6$ , the profiles show a potential for punch-through. The smaller the strength ratio, the severer the punch-through will be.

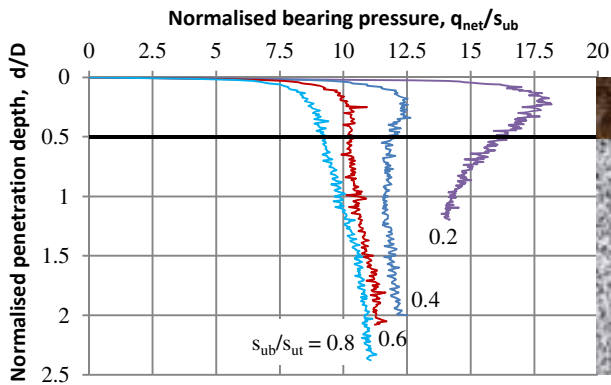


Fig. 3. Effect of strength ratio ( $s_{ub}/s_{ut}$ ) on bearing response: circular footing ( $t/D = 0.5$ )

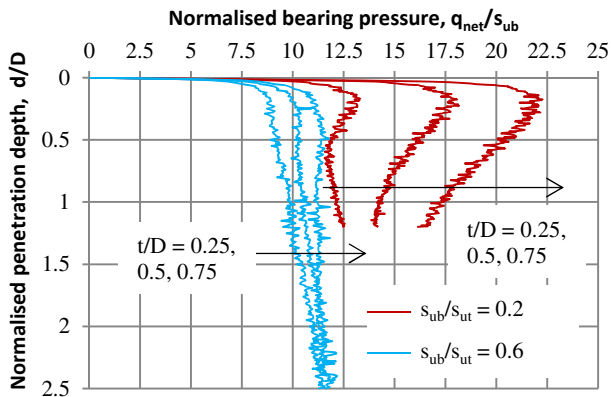


Fig. 4. Effect of thickness ratio ( $t/D$ ) on bearing response: circular footing

To explore the effect of the relative thickness of the upper layer, bearing resistance profiles are plotted in Fig. 4 for a range of thickness ratios of  $t/D$  from 0.25 to 0.75. Two clusters of curves are illustrated for two strength ratios. For lower strength ratio of  $s_{ub}/s_{ut} = 0.2$ , the potential for punch-through exists for all thickness ratios, a marked reduction in bearing resistance occurs after a local maximum. The severity of punch-through, i.e. the gradient of reduction in bearing resistance, increases with  $t/D$ . For higher strength ratio of  $s_{ub}/s_{ut} = 0.6$ , a reduction

in bearing resistance can be seen for  $t/D \geq 0.5$ , while the resistance increases with depth for a very thin crust of  $t/D = 0.25$ .

### 3.3 Spudcan

For spudcan penetration in clay, along with the load-displacement profiles, the limiting cavity depth above the foundation should be considered. Hossain & Randolph [2] reported that the onset of back-flow above the spudcan may be taken as the (average) stable cavity depth after deep penetration of the spudcan, which was also observed in this study. Figures 5 and 6 demonstrate the effects of the strength ratio and thickness ratio on the form of the load-penetration response and the depth of backflow. The results from analyses using the RITSS approach (see [2]) are also included in the figures for comparison. The deformed soils captured in the CEL analyses are also added in the figures for interpretation. Excellent agreement can be seen in terms of depth of backflow and load penetration response for the full penetration depth, with variations in both regards mostly less than 5%. Once again this confirms the accuracy of the results from CEL.

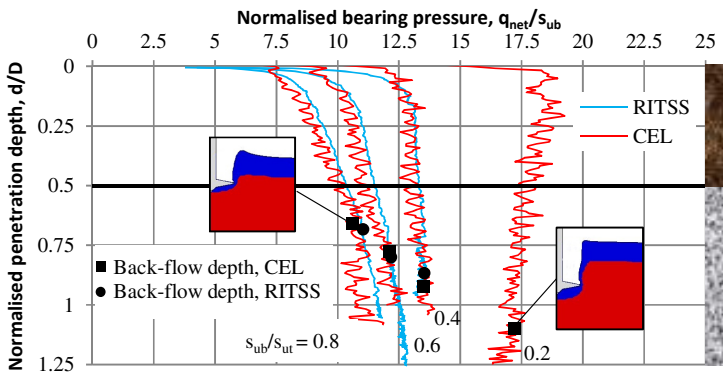


**Fig. 5.** Effect of strength ratio ( $s_{ub}/s_{ut}$ ) on bearing response: spudcan foundation ( $t/D = 0.5$ )

For the same thickness ratio (see Fig. 5), the depth of back-flow and the potential for punch-through increase as the strength ratio decreases. For  $s_{ub}/s_{ut} = 0.2$ , the bearing capacity starts to reduce within the top layer, indicating the potential for punch-through failure for a jack-up installation in the field. Fig. 6 shows the effect of the thickness ratio. For a strength ratio of  $s_{ub}/s_{ut} = 0.4$ , the potential for punch-through failure in the stronger layer increases with increasing thickness ratio. For  $t/D \leq 0.5$ , all three profiles rise monotonically in the upper stiff layer. However, for  $t/D \geq 0.75$ , a peak in penetration resistance followed by some reduction (punch-through) occurs before the spudcan penetrates in the lower layer. The depth of backflow increases as the thickness ratio increases.

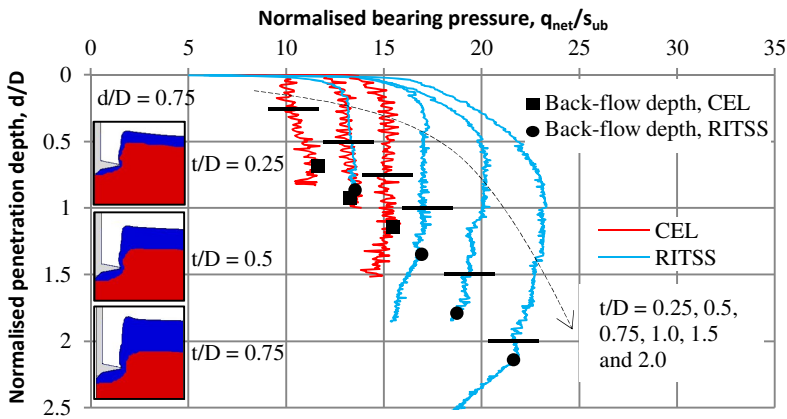


Fig. 6. Effect of thickness ratio ( $t/D$ ) on bearing response: spudcan foundation ( $s_{ub}/s_{ut} = 0.4$ )

### 4 Penetration in Non-homogeneous Clay

The results from spudcan penetration in single layer non-homogeneous clay are shown in Fig. 7. The net bearing pressure,  $q_{net}$ , is normalised by the local soil strength at the spudcan base level,  $s_{u0}$ . At deep embedment, all curves merge together regardless of degree of soil strength non-homogeneity,  $kD/s_{um}$ , and give a unique limiting value of 10.6. This is somewhat 7% lower than the design value, 11.3, proposed by Hossain & Randolph [6] using the RITSS approach.

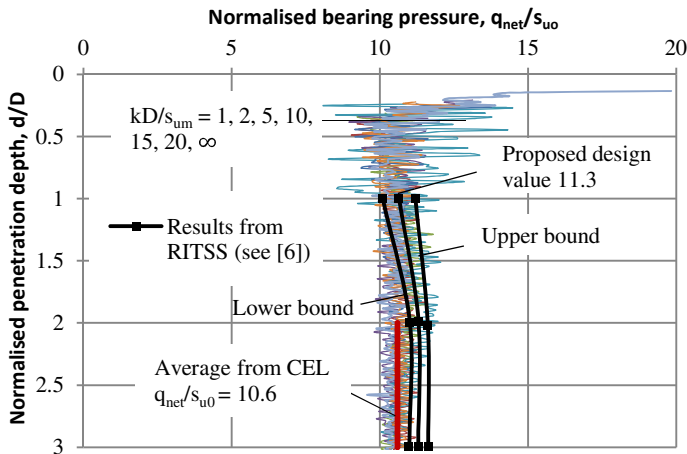


Fig. 7. Load-penetration curves for various soil strength non-homogeneity factors: spudcan foundation on single layer clay

## 5 Conclusions

This paper has reported the results from LDFE analyses using the CEL approach for spudcan foundation and circular footing deep penetration in 2-layer uniform-over-uniform clay and single layer non-homogeneous clay. The aim was to validate the outcomes against the existing results from LDFE analyses using the RITSS approach. Excellent agreement was obtained between the results from these two approaches in terms of the depth of potential punch-through and back-flow and the effects of the thickness ratio and strength ratio. These confirm the capability of the CEL approach for undertaking analysis in single and double layer soils. This research is being extended for spudcan penetration in 3 and 4 layer soils, and incorporating the effects of strain rate and softening.

**Acknowledgements.** The research presented here was undertaken with support from the Australian Research Council (ARC) and the industry partner Keppel Offshore and Marine, Singapore through the ARC Linkage Project LP110100174. The work forms part of the activities of the Centre for Offshore Foundation Systems (COFS), currently supported by the State Government of Western Australia and The Lloyd's Register Educational Trust as a Centre of Excellence, and now forming one of the primary nodes of the ARC Centre of Excellence for Geotechnical Science and Engineering. This support is gratefully acknowledged.

## References

- [1] Wang, C.X., Carter, J.P.: Deep penetration of strip and circular footings into layered clays. *Int. J. Geomech.* 2(2), 205-232 (2002)
- [2] Hossain, M.S., Randolph, M.F.: Deep-penetrating spudcan foundations on layered clays: numerical analysis. *Géotechnique* 60(3), 171-184 (2010)
- [3] Hu, Y., Randolph, M.F.: A practical numerical approach for large deformation problems in soil. *Int. J. Numer. Anal. Methods Geomech.* 22(5), 327-350 (1998)
- [4] Carter, J.P., Balaam, N.P.: AFENA user's manual. Center for Geotechnical Research, The University of Sydney (1990)
- [5] Qiu, G., Henke, S., Grabe, J.: Application of a Coupled Eulerian-Lagrangian approach on geomechanical problems involving large deformations. *Computers and Geotechnics* 38, 30-39 (2011)
- [6] Hossain, M.S., Randolph, M.F.: New mechanism-based design approach for spudcan foundations on single layer clay. *J. Geotech. and Geoenv. Eng.* 135(9), 1264-1274 (2009)

# **Erratum: Large Deformation Analysis of Spudcan Penetration into Sand Overlying Normally Consolidated Clay**

Pan Hui<sup>1</sup>, Dong Wang<sup>1</sup>, Mark Cassidy<sup>1</sup>, and Qing Yang<sup>2</sup>

<sup>1</sup> Centre for Offshore Foundation Systems, The University of Western Australia, Australia

<sup>2</sup> Dalian University of Technology, China

panhu@civil.uwa.edu.au

Q. Yang et al. (Eds.): Constitutive Modeling of Geomaterials, SSGG, pp. 723–733.  
springerlink.com

© Springer-Verlag Berlin Heidelberg 2013

---

**DOI 10.1007/ 978-3-642-32814-5\_106**

In the original version, the first author name was misspelt in this paper. It should read as: Pan Hu.

---

The original online version for this chapter can be found at  
[http://dx.doi.org/10.1007/978-3-642-32814-5\\_95](http://dx.doi.org/10.1007/978-3-642-32814-5_95)

---

# Author Index

- Abousleiman, Younane N. 289  
Adje, David 135  
Anagnostou, G. 409  
Andrade, José E. 167
- Barton, Nick 1  
Bate, Bata 709  
Bayan, Gokul K. 391  
Belayachi, Naima 319  
Benz, Thomas 89, 483, 491  
Berengo, Valentina 89  
Bourrier, Franck 359  
Bo-ya, Zhao 547  
Brown, Matthew 121
- Cai, M. 303  
Cassidy, Mark 723, E1  
Chan, D. 691  
Chang, Q. 63  
Chattonjai, P. 125  
Chen, Pan 399, 599  
Chen, Yong 691, 783  
Chiaro, Gabriele 519  
Collin, Frédéric 313
- Dafalias, Yannis F. 13, 223  
Dano, Christophe 173, 207  
Darve, Félix 359  
Das, Arghya 527  
Desai, Chandrakant S. 27, 97  
De Silva, L.I. Nalin 519  
Do, Duc-Phi 319, 715  
Dong, Weixin 409, 701
- Einav, Itai 527  
Eslami, Javad 715
- François, Bertrand 535  
Freitas, T.M. Bodas 107
- Gao, Zhiwei 541  
Garitte, Benoit 363  
Ge, Louis 709  
Gens, Antonio 363  
Georg, Anagnostou 333  
Golchin, Ali 199  
Grgic, Dragan 715  
Gu, Jin-jian 371  
Guo, Ning 247
- Hadda, Nejib 359  
Hamidi, Amir 553  
Han, Jingli 507  
Hellmich, Christian 293  
Hicher, Pierre-Yves 173, 207, 259  
Hossain, Muhammad S. 803  
Hossain, Zahid 135  
Hou, Wei 559  
Hoxha, Dashnor 319, 715  
Hu, Pan 723, E1  
Hu, Wei 173  
Hu, Yuxia 583  
Hua, Zhen 125  
Huang, Maosong 461, 567  
Huang, Yaoying 323, 327
- Ishikawa, Tatsuya 501  
Ivšić, Astrid Gojmerac 179  
Ivšić, Tomislav 179

- Jha, Bhagwanjee 477  
 Jiang, Yaodong 507  
 Jin, Yin-Fu 145  
  
 Kalantary, Farzin 469  
 Kaliakin, Victor N. 185  
 Karstunen, Minna 115  
 Kimoto, Sayuri 215, 751  
 Kondo, Djimédo 283  
 Konstantinos, Serafeimidis 333  
 Koseki, Junichi 519  
 Kruyt, N.P. 193  
 Kumar, K. 417  
  
 Lade, Poul V. 47, 265  
 Laloui, Lyesse 535  
 Lashkari, Ali 199  
 Leal, Andres Nieto 185  
 Leng, K.D. 63  
 Leoni, Martino 89  
 Leroueil, Serge 139  
 Li, Gang 207  
 Li, Xia 577  
 Li, Xiang-song 13, 247  
 Li, Xu 583  
 Lin, J. 59  
 Liu, Enlong 341  
 Liu, Peng 593  
 Liu, Yanhua 567  
 Liu, Yaoru 757  
 Liu, Y.R. 63  
 Lizcano, Arcesio 167  
 Long-tan, Shao 547  
 Lu, Ning 271  
 Luan, Maotian 593  
  
 Ma, Tian-tian 399, 599  
 Manzari, Majid T. 211  
 Mašin, D. 423, 609  
 Miranda, T. 735  
 Mirghasemi, Ali Aaghar 431, 441, 451  
 Molladavoodi, Hamed 349, 741  
 Mollanouri.Sh, M.M. 431  
 Mortazavi, Ali 349  
  
 Naeij, Morteza 441, 451  
 Nakai, Teruo 277, 617  
 Nash, David 121  
 Nguyen, Giang 527  
 Nicot, François 359  
 Nordal, S. 491  
  
 Oka, Fusao 215, 751  
 Olivera-Bonilla, Roberto 253  
 Ovalle, Carlos 207  
  
 Pan, Yuanwei 757  
 Pardoën, Benoît 313  
 Peng, Fang-Le 125  
 Pichler, Bernhard 293  
 Pimentel, E. 409  
 Potts, D.M. 107  
  
 Qi, Jilin 129  
 Qian, J.G. 461  
 Qian, Jingjuan 757  
  
 Ramos, Alfonso M. 167  
 Ranadive, M.S. 765  
 Ravanbakhsh, Ehsan 553  
 Rezania, Mohammad 115  
 Rothenburg, Leo 253  
 Ruggenthén, W. 735  
  
 Sane, Shantanu M. 97  
 Sbitti, Amine 319  
 Shahin, Hossain Md. 617  
 Shan, Tong 297  
 Shao, Jian-fu 283, 323, 387  
 Shaverdi, Homayoun 469  
 Shen, Wanqing 283  
 Shibuya, Satoru 501  
 Sibille, Luc 359  
 Simonini, Paolo 89  
 Singh, D.N. 477  
 Sivasithamparam, Nallathamby 115  
 Solanki, Pranshoo 135  
 Sousa, L.R. 735  
 Sousa, R.L. 735  
 Srinivas, Kadali 477  
 Suzuki, Kiichi 627  
  
 Taha, Mohd. Raihan 469  
 Taiebat, Mahdi 223  
 Tan, Ke 125  
 Tan, Yunzhi 691  
 Tapase, A.B. 765  
 Tengattini, Alessandro 527  
 Tian, Hui-hui 649  
 Tian, Zhongsheng 507  
 Tokoro, Tetsuya 501

- Tran, Minh H. 289  
Tsai, P.S. 751  
Tsegaye, A.B. 483, 491
- Ullah, Shafi 293
- Vaunat, Jean 363
- Wang, Dong 723, 803, E1  
Wang, Gang 231  
Wang, Jili 399  
Wang, Mengshu 641  
Wang, Mingqiang 771  
Wang, Ru-bin 371, 633  
Wang, Shimei 783  
Wang, Songhe 129  
Wang, Wei 633  
Wang, Zhongtao 593  
Watabe, Yoichi 139  
Wei, Chang-fu 399, 599, 649  
Wei, Hou-zhen 399, 599, 649  
Wei, Zhenhai 641  
White, David 583  
Whittle, Andrew J. 159  
Wood, David Muir 239  
Wu, Er-ling 649  
Wu, Senjen 319  
Wu, W. 59  
Wu, Ze-Xiang 145
- Xia, Kaiwen 367  
Xiang, Sun 547  
Xiao-xia, Guo 547  
Xie, Ni 387  
Xie, Yongning 231  
Xu, Wei-ya 371, 633
- Yan, Rong-tao 649  
Yan, W.M. 657  
Yang, Jun 771  
Yang, Q. 63  
Yang, Qiang 723, 757, E1  
Yao, Yangping 559, 675  
Ye, Bin 663  
Ye, Guanlin 663  
Ygzaw, B.W. 483  
Yin, Jian-Hua 149  
Yin, Zhen-Yu 145, 173  
Yonten, Karma 211  
You, Z.P. 461  
Yu, Fan 129  
Yu, You 507  
Yu, Yuzhen 701  
Yuan, Yixing 159  
Yue (Quentin), Zhong Qi 381
- Zaman, Musharraf 135  
Zdravkovic, L. 107  
Zeng, Gang 783  
Zhang, Dingli 641  
Zhang, Feng 663  
Zhang, Jianhai 341  
Zhang, Jiu-chang 371, 633  
Zhang, Xiaohan 789  
Zhang, Yuan 501  
Zhao, Chunhu 795  
Zhao, Honghua 709  
Zhao, Jidong 247, 297, 541  
Zhao, Yixin 507  
Zheng, Hong 327  
Zheng, Jingbin 803  
Zhu, Enyang 675  
Zhu, Qi-zhi 387